

# WIRELIN FORMATION TESTING & WELL DELIVERABILITY

GEORGE STEWART

PennWell®

**Disclaimer.** The recommendations, advice, descriptions, and the methods in this book are presented solely for educational purposes. The author and publisher assume no liability whatsoever for any loss or damage that results from the use of any of the material in this book. Use of the material in this book is solely at the risk of the user.

Copyright© 2012 by  
PennWell Corporation  
1421 South Sheridan Road  
Tulsa, Oklahoma 74112-6600 USA

800.752.9764  
+1.918.831.9421  
sales@pennwell.com  
www.pennwellbooks.com  
www.pennwell.com

Marketing: Jane Green  
National Account Executive: Barbara McGee

Director: Mary McGee  
Managing Editor: Stephen Hill  
Production Manager: Sheila Brock  
Production Editor: Tony Quinn  
Book Designer: Susan E. Ormston  
Cover Designer: Jesse Bennett

Library of Congress Cataloging-in-Publication Data

Stewart, George, 1940-  
Wireline formation testing and well deliverability / George Stewart.  
p. cm.  
Includes bibliographical references and index.  
ISBN 978-1-59370-230-4  
1. Petroleum--Geology. 2. Oil reservoir engineering. 3. Oil wells--Testing. 4. Petroleum--  
Migration. 5. Managed pressure drilling (Petroleum engineering) I. Title.  
TN870.5.S7445 2011  
622:3382--dc22

2010011728

All rights reserved. No part of this book may be reproduced, stored in a retrieval system,  
or transcribed in any form or by any means, electronic or mechanical, including  
photocopying and recording, without the prior written permission of the publisher.

Printed in the United States of America

1 2 3 4 5 16 15 14 13 12

## Contents

---

<b>Acknowledgments</b> .....	xix
<b>Chapter 1. Radial Flow in Porous Media</b>	
Introduction .....	1
Well performance diagram .....	2
Darcy's law .....	5
Steady-state Linear Flow of an Incompressible Fluid .....	8
Steady-state Radial Flow .....	14
Basic well model .....	14
Boundary conditions .....	15
Steady-state radial flow of an incompressible fluid .....	15
Well productivity .....	19
Well inflow performance .....	20
Volume average pressure in steady-state flow .....	20
Semi-steady-state Radial Flow .....	22
Introduction .....	22
Semi-steady-state solution .....	23
Formation compaction .....	27
Drainage areas and virtual no-flow boundaries .....	30
Well Inflow in terms of average pressure .....	35
Well Productivity in a Bounded Drainage Area .....	36
Generalized form of the semi-steady-state inflow equation .....	37
Analytical formulae for Dietz shape factors .....	40
Wellbore Damage and Improvement Effects .....	46
Introduction .....	46
Near-wellbore altered zone .....	46
Water-sensitive authigenic clays .....	49
Dimensionless skin factor .....	52
Analytical skin formulae .....	53
Well Productivity with Skin Effects .....	58
Steady-state radial flow .....	58
Semi-steady-state radial flow .....	59
Deviation From True Radial Flow .....	61
Effects of partial well completion .....	61
Combination of formation damage and partial completion .....	64
Water and Gas Coning .....	69
Effect of Well Deviation .....	72

Fractured Wells . . . . . 74

Horizontal Wells . . . . . 76

    Horizontal well spanning a rectangular drainage area . . . . . 76

    Horizontal well in general position in a drainage area . . . . . 82

    Pseudo-radial skin factor . . . . . 85

    Wedge-shaped drainage areas . . . . . 87

    Field examples. . . . . 87

    Horizontal well completions . . . . . 90

    Friction in the wellbore . . . . . 90

Compartmentalized Horizontal Well . . . . . 92

Reservoir Heterogeneity . . . . . 101

Well Inflow Performance at High Production Rates . . . . . 106

    Steady-state radial non-Darcy flow. . . . . 107

    Correlations for the inertial resistance coefficient. . . . . 108

    Non-Darcy radial flow in oil field units . . . . . 109

    Influence of damaged zone. . . . . 111

    Partially completed well . . . . . 113

    Steady-state well inflow performance relation . . . . . 114

    Equations in field units . . . . . 115

Notes. . . . . 116

**Chapter 2. Skin Factor in Perforated and Fractured Wells**

The Effect of Perforations on Well Productivity . . . . . 117

    Introduction . . . . . 117

    Perforating systems . . . . . 117

    Perforated completions. . . . . 124

    Fluid mechanics of the API test. . . . . 128

    Effects of underbalance on perforation flow . . . . . 134

    Perforation characteristics . . . . . 136

    Perforation skin factor  $S_{pe}$ . . . . . 136

Approximate Model of the Skin Factor in a Perforated Completion . . . . . 138

    Introduction . . . . . 138

    Spherical steady-state flow . . . . . 143

    Steady-state radial and linear flow . . . . . 146

    Perforated completion. . . . . 147

    Darcy flow shape factors. . . . . 150

    Perforation damage . . . . . 152

    Effect of a radial, uniform altered region . . . . . 155

    Non-Darcy flow . . . . . 159

    Spherical non-Darcy flow shape factors. . . . . 163

    Non-Darcy flow into an open-hole completion . . . . . 166

    Correlations for the inertial resistance coefficient. . . . . 167

    Linear flow in a gravel-packed perforation tunnel. . . . . 169

    Effect of loss control material (LCM) on gravel-pack skin . . . . . 176

    Maximum allowable perforation velocity . . . . . 179



External cylindrical gravel pack. . . . . 184  
 Identical perforation and formation properties . . . . . 185  
 Effective perforation length . . . . . 188  
 Geometric or Completion Skin Factors . . . . . 193  
     Effect of a limited entry. . . . . 193  
     Slant well effect. . . . . 196  
     Combination of limited entry and slant well. . . . . 199  
 Summary of Oil Well Skin Factor Analysis . . . . . 201  
 Horizontal Well Behavior . . . . . 202  
 Hydraulically Fractured Wells . . . . . 204  
     Pseudoradial skin of finite conductivity fractures . . . . . 204  
     Fractured well spanning a rectangular drainage area . . . . . 215  
     Limited-height fractures . . . . . 217  
     In situ proppant permeability . . . . . 219  
     Hemi-pseudoradial flow . . . . . 219  
     Non-Darcy effect in fractured wells . . . . . 220  
     Hydraulic fracturing to overcome formation damage—skin bypass fracture . . . . . 226  
     Performance of fractured wells in tight gas sands . . . . . 228  
     Choked fracture . . . . . 233  
     Flow convergence in the fracture . . . . . 234  
     Fractured wells with gravel packs . . . . . 244  
     Technology of combined fracture and gravel packs. . . . . 250  
     Fractured horizontal wells . . . . . 252  
     Application of Skin Factor Model . . . . . 255  
 Notes. . . . . 258

**Chapter 3. Well Inflow Performance Relations**

Oil Well Inflow Performance Relation . . . . . 261  
     Single layer IPR for semi-steady-state conditions . . . . . 261  
     Transient IPR . . . . . 265  
     Composite IPR of a stratified system . . . . . 272  
     Horizontal wells with vertical fractures . . . . . 274  
 Extension to Gas Well Inflow Performance. . . . . 275  
     Concept of pseudopressure . . . . . 275  
     Treatment of non-Darcy flow . . . . . 285  
     Steady-state gas well inflow performance . . . . . 292  
      $p^2$  form of the normalized pseudopressure function. . . . . 293  
     High-pressure gas well inflow . . . . . 296  
     Summary of gas well non-Darcy skin analysis . . . . . 298  
     Generation of the gas well deliverability curve. . . . . 299  
     Backpressure equation . . . . . 301  
 Two-phase incompressible flow. . . . . 302  
     Two-phase incompressible flow pseudopressure function. . . . . 309  
 Two-Phase Compositional Flow . . . . . 311

Radial steady-state Darcy flow . . . . .	312
Spherical steady-state non-Darcy flow . . . . .	320
Behavior of the pseudopressure function . . . . .	323
Gas-condensate relative permeability . . . . .	329
Gas-condensate well inflow behavior . . . . .	335
Rate-dependent relative permeability curves . . . . .	339
Non-Darcy effect in gas-condensate wells . . . . .	351
Fractured gas-condensate wells . . . . .	353
Solution Gas Drive . . . . .	353
Introduction . . . . .	353
Oil well producing below the bubble point . . . . .	354
Vogel correlation . . . . .	354
Fetkovich method . . . . .	358
Gas Wells Producing Water . . . . .	360
Gas–water two-phase pseudopressure . . . . .	360
Critical gas velocity . . . . .	365
Blowdown limit model . . . . .	367
Standing water column . . . . .	370
Three-phase Flow . . . . .	371
Concept of a Superwell . . . . .	375
Peaceman well model in numerical simulation . . . . .	376
Deliverability of proximate wells . . . . .	380
Well performance index . . . . .	387
Wedge-shaped drainage systems . . . . .	387
Multilayer case . . . . .	390
Notes . . . . .	393
 <b>Chapter 4. Gas Reservoir Material Balance</b>	
Introduction . . . . .	395
Volumetric reserves calculation . . . . .	396
Gas Material Balance . . . . .	397
Case 1—No water influx . . . . .	399
Abnormally pressured gas reservoirs . . . . .	402
Differential form of the material balance . . . . .	406
Nonlinear regression . . . . .	411
Error in rate measurement and allocation . . . . .	413
Case 2—Natural water influx . . . . .	413
Areal pressure variation . . . . .	417
Variable Rate Draw-down Analysis for Aquifer Influx . . . . .	418
Interpretation methodology . . . . .	419
Principle of superposition . . . . .	419
Radial Aquifer Models . . . . .	421
Aquifer influence functions . . . . .	421
Aquifer material balance . . . . .	425

Infinite-acting behavior . . . . .	426
Classical cumulative influx superposition . . . . .	428
Laplace space convolution . . . . .	432
Fetkovich model . . . . .	434
Test problem . . . . .	435
Effect of the invaded zone . . . . .	438
Further Aquifer Types . . . . .	443
Outcropping radial aquifers . . . . .	443
Linear Aquifer . . . . .	444
Fetkovich linear aquifer . . . . .	446
Determination of aquifer parameters . . . . .	447
Deconvolution method . . . . .	448
Extended buildups . . . . .	449
Reservoir limit testing . . . . .	449
Aquifer complicating features . . . . .	450
Case Studies . . . . .	452
Field example 1—Duck Lake field (D-1) . . . . .	452
Field example 2—South Wilburton Field . . . . .	454
Residual Gas Saturation in Water-Drive Gas Reservoirs . . . . .	457
Simultaneous Equation Differential Material Balance . . . . .	459
Theoretical treatment . . . . .	459
Synthetic test problem . . . . .	463
Application to gas storage projects . . . . .	465
Synthetic gas storage problem . . . . .	466
Runga–Kutta ODE integration . . . . .	469
Edge water drive . . . . .	470
Field example . . . . .	471
Second synthetic test problem . . . . .	471
Nonlinear regression . . . . .	474
Well Rate Strategy . . . . .	474
Well rate constrained by IPR–VLP relations . . . . .	474
Material balance shooting . . . . .	479
Production-constrained depletion . . . . .	481
Gas sales contract involving a swing factor . . . . .	482
Determination of the end-of-the-plateau period . . . . .	485
Material balance iteration including swing . . . . .	486
Synthetic test problem . . . . .	487
Addition of new wells . . . . .	490
High-pressure gas reservoirs . . . . .	490
Introduction . . . . .	490
Basic material balance model . . . . .	491
Effect of compressibility variation with stress . . . . .	492
Field examples . . . . .	501
Observation Wells in a Gas Reservoir . . . . .	503
Notes . . . . .	503

**Chapter 5. General Mechanistic Reservoir Material Balance**

Introduction .....	505
Black Oil Model .....	506
Classical Schilthuis Material Balance .....	510
Compositional Material Balance .....	512
Solution gas-drive cell .....	512
Black oil model as an isochoric flash .....	519
Integration of the Material Balance Equation .....	520
Undersaturated liquid behavior .....	523
Well models in the material balance cell .....	524
Synthetic test problem .....	526
Critical gas saturation $S_{gc}$ .....	530
Variable rate production data .....	532
Nonlinear regression .....	533
Integration with a Production Network Model .....	534
Evolution of a Secondary Gas Cap .....	534
Upward percolation of free gas .....	534
Synthetic example .....	539
Inclusion of a primary gas cap .....	539
Addition of a coning model .....	545
Nonlinear regression .....	549
Gas and Gas-condensate Reservoirs .....	549
Depletion above the dew point .....	549
Retrograde condensation without gravity segregation .....	550
Gravity segregation of condensate .....	555
Dry gas injection (recycling) .....	556
Gas Recycling with a Displacement Model .....	563
Aquifer Influx .....	570
Undersaturated reservoir case .....	570
Reservoir pressure below bubble point .....	575
Inclusion of a coning or displacement model .....	577
Dry Gas Reservoir with Active Water Drive .....	580
Associated water model .....	585
Tuning of Material Balance Model .....	585
Notes .....	586

**Chapter 6. Coning and Displacement Models in the Material Balance Context**

Introduction .....	587
Addington Gas Coning Model for Vertical Wells .....	588
Theoretical background .....	588
Yang and Wattenbarger Water Coning Model for Vertical Wells .....	593
Theoretical Background .....	593
Synthetic example .....	597

Empirical Displacement Model . . . . .	599
Unit mobility areal sweep . . . . .	599
Synthetic examples . . . . .	603
Layered systems . . . . .	604
Waterflooding below the bubble point . . . . .	609
Multiple well situations . . . . .	610
Matching field water-cut data . . . . .	614
Notes . . . . .	614

## Chapter 7. Decline Curve Analysis

Introduction . . . . .	615
Constant Wellbore Pressure Testing . . . . .	617
Semi-infinite behavior . . . . .	619
Empirical Rate–Time Equations . . . . .	620
Minimum economic rate $q_{sc}$ . . . . .	625
Exponential decline for a single-compartment system . . . . .	625
Decline rates . . . . .	628
Transformation to cumulative production . . . . .	628
Production database . . . . .	631
Change in production conditions—stimulation . . . . .	633
Field examples . . . . .	635
Fetkovich Type Curve for Depletion . . . . .	638
Nonzero decline curve exponent . . . . .	643
Semi-Steady-State Depletion . . . . .	645
Agarwal–Gardner Decline Type Curves . . . . .	651
Liquid solution decline type curves for radial flow . . . . .	651
Constant terminal pressure data and equivalent time . . . . .	652
Gas reservoir data . . . . .	654
Fractured wells . . . . .	656
Decline type curves based on cumulative production . . . . .	656
Application to gas reservoirs . . . . .	660
Application to field data . . . . .	665
Notes . . . . .	666

## Chapter 8. Distributed Pressure Measurement

Introduction . . . . .	667
Principles of WFT Distributed Pressure Measurement . . . . .	668
Wireline formation tester . . . . .	668
Simplified (Single-phase) Supercharging Analysis . . . . .	671
Rapid Local Permeability Estimation . . . . .	677
Background to Permeability Estimation . . . . .	681

Review of RFT Permeability Interpretation . . . . .	682
Drawdown analysis . . . . .	682
Build-up analysis . . . . .	684
Drawdown versus Buildup . . . . .	685
New developments in RFT interpretation. . . . .	688
Method of Analysis of Field Data . . . . .	690
Discussion of Results . . . . .	693
RFT draw-down versus core permeability. . . . .	693
RFT Build-up versus core permeability . . . . .	695
Conclusions . . . . .	697
Notes. . . . .	698

## **Chapter 9. Exploration Applications of Distributed Pressure Measurement**

Introduction . . . . .	699
Gravity–Capillary Equilibrium . . . . .	700
Effect of a residual oil saturation $S_{or}$ . . . . .	706
Detection of mobile hydrocarbon. . . . .	712
Oil wet behavior . . . . .	713
Tar mat detection. . . . .	715
Additional field examples . . . . .	717
Forced Gradient Technique . . . . .	721
Depth measurement errors . . . . .	727
Multiple well analysis. . . . .	727
Statistical analysis of multiwell WFT data. . . . .	731
Perched Contacts and Trapped Water . . . . .	733
Naturally Fractured Reservoir . . . . .	738
Dynamic Aquifers and Tilted Contacts . . . . .	739
Introduction . . . . .	739
North Field, Qatar . . . . .	740
Other Field Examples of Dynamic Aquifer Effects . . . . .	744
Overpressured Reservoirs. . . . .	748
Notes. . . . .	750

## **Chapter 10. Field Development Applications of Distributed Pressure Measurement**

Introduction . . . . .	751
Introductory Field Examples in Produced Reservoirs . . . . .	752
Single-phase Flow. . . . .	755
Uniform vertical permeability . . . . .	755
Identification of Permeability Barriers . . . . .	760
Semi-steady-state differential depletion . . . . .	762
Reservoir simulation . . . . .	767

Two-phase flow . . . . .	768
Vertical saturation equilibrium . . . . .	768
Countercurrent two-phase flow . . . . .	769
Cocurrent upward two-phase flow . . . . .	774
Accuracy In Gradient Determination . . . . .	777
Use of WFT Interpretation for Reservoir Description . . . . .	779
Introduction . . . . .	779
Early field examples of RFT applications in the North Sea . . . . .	782
Horizontal barrier detection in reservoir testing . . . . .	793
Partially communicating faults . . . . .	795
Lumped Parameter Material Balance Model . . . . .	805
Two-block depletion test . . . . .	810
Two-layer two-block system . . . . .	812
Further North Sea Field Examples . . . . .	815
High Slant Wells . . . . .	819
Notes . . . . .	828

## **Chapter 11. Production Logging and Layered Systems**

Introduction . . . . .	831
Some Reservoir Engineering Applications of Production Logging . . . . .	838
Layer skin distribution . . . . .	842
Zonation . . . . .	845
Direct measurement of layer pressures . . . . .	847
Profile control . . . . .	851
Flow concentration and integration of well testing with production logging . . . . .	851
Well workover . . . . .	851
Flowing gradient surveys . . . . .	852
Selective Inflow Performance . . . . .	853
Single-phase flow . . . . .	853
Gas well quadratic IPRs . . . . .	861
Two-phase flow . . . . .	863
Integration with transient well testing and core analysis . . . . .	871
Borehole video camera . . . . .	874
Notes . . . . .	874

## **Chapter 12. Wireline Formation Testing (WFT) Permeability Interpretation**

Basic Spherical Flow Theory . . . . .	875
Spherical flow analysis . . . . .	886
Vertical Observation Probe and Point Source . . . . .	909
Limited Entry Model . . . . .	926
Straddle Packer Active Zone Response (Limited Entry Model) . . . . .	936

NGWFT Testing in Argentina . . . . .	937
Field Case 1 . . . . .	938
Field Case 2 . . . . .	942
Field Case 3 . . . . .	943
Dual Permeability Model . . . . .	944
Nonlinear Regression. . . . .	949
Finite Element Numerical Models. . . . .	950
Wellbore Storage and Numerical Models . . . . .	954
Behavior of a Sink Probe . . . . .	955
FEM Simulation of the Active Probe Response . . . . .	958
Effect of a Single Horizontal Barrier . . . . .	961
Tuned Analytical Model for an Active (Flowing) Confined Probe . . . . .	964
Spherical Flow Skin Effects. . . . .	965
Absence of Radial Flow Regime . . . . .	976
Stewart and Wittman Depth of Investigation Analysis . . . . .	976
Nonintersecting Fracture Model . . . . .	979
Horizontal Wells. . . . .	987
Probe–Probe Arrangement in a Horizontal Well. . . . .	992
Straddle Packer in a Slant Well . . . . .	996
Slant Well Observation Probe . . . . .	1013
High Slant Well Behavior . . . . .	1015
Notes. . . . .	1016

*The following chapters are on the accompanying CD-ROM.*

**Chapter 13. Reservoir Engineering Aspects of Production**

Basic Reservoir Engineering . . . . .	1017
Introduction . . . . .	1017
In-Fill Drilling. . . . .	1019
Layered Reservoirs . . . . .	1022
Introduction . . . . .	1022
Some Reservoir Engineering Applications of Production Logging. . . . .	1028
Layer Skin Distribution. . . . .	1032
Zonation . . . . .	1035
Direct Measurement of Layer Pressures . . . . .	1036
Profile Control . . . . .	1040
Well Workover . . . . .	1040
Flowing Gradient Surveys. . . . .	1040
Selective Inflow Performance. . . . .	1041
Single-phase Flow . . . . .	1041



Gas Well Quadratic IPRs ..... 1049

Two-Phase Flow ..... 1051

Integration with Transient Well Testing and Core Analysis..... 1058

Borehole Video Camera ..... 1060

Water Shut-off Treatments..... 1060

Sandface Shutoff..... 1060

Crossflow Reservoirs..... 1062

Coning Situations..... 1066

Through Tubing Casing Patch..... 1069

Deep Set Gel Treatment..... 1069

Ghawar Workover Program..... 1071

Pressure Maintenance..... 1074

Reservoir Depressurization ..... 1077

Completion Efficiency and Optimization ..... 1079

    Introduction ..... 1079

    Justification of a Workover..... 1085

Horizontal and Fractured Wells..... 1086

    Semi-Steady-State Deliverability of Horizontal Wells..... 1086

    Transient Deliverability..... 1095

    Effect of Isolated Natural Fractures ..... 1101

    Compartmentalization and Gas Cap Effects..... 1107

    Hydraulically Fractured Wells..... 1109

    Horizontal Wells with Multiple Hydraulic Fractures ..... 1119

    Sand Control Completions..... 1120

Horizontal Gas Well Deliverability ..... 1128

    Infinite Conductivity Wellbore ..... 1128

    Wellbore Friction ..... 1140

    Lumped Parameter Vertical Lift Model..... 1148

Intelligent Wells ..... 1152

Notes..... 1157

**Chapter 14. Compartmentalized Material Balance**

Introduction ..... 1159

Complex Reservoirs ..... 1164

    Oil field units..... 1169

    General form of the commingled well model..... 1169

    State space representation of the complex material balance ..... 1171

    Forcing functions ..... 1174

    Solution of the State Space System..... 1175

    Subsidiary variables ..... 1177

    Natural water influx..... 1178

    Gas cap drive..... 1180

    Gas field units..... 1184

    Solution gas drive..... 1184

    Cumulative production and influx ..... 1184

Cellular Systems .....	1187
Three-cell problem.....	1187
Idealized cellular system.....	1189
Extended buildup in a compartmentalized reservoir .....	1192
Average (steady-state) permeability of a cellular system .....	1196
Effective interblock transmissibility .....	1197
Apparent semi-steady-state of well cell alone.....	1199
Field Example .....	1200
Linear Flow Theory .....	1202
Generalized complex material balance .....	1208
Automatic Matching .....	1215
Production Constrained Convolution .....	1220
Restart facility.....	1225
Cell of specified pressure history.....	1225
Desuperposition .....	1226
Material Balance in Terms of Pseudopressure and Pseudotime .....	1231
Commingled wellbore model for gas wells .....	1234
Transient Production.....	1238
Notes.....	1239

## **Chapter 15. Reservoir Characterization from Underbalanced Drilling Data**

Introduction .....	1241
Transient Well Model .....	1243
Lumped Parameter Wellbore Model.....	1246
Distributed Parameter Wellbore Model.....	1257
Transient Formation Model .....	1259
Application to Underbalanced Drilling .....	1272
Demonstration Simulation.....	1277
Synthetic Three-Zone Problem .....	1281
Distributed Pressure Situation .....	1284
Synthetic Five-Zone Problem.....	1291
Limited Entry Model .....	1294
Horizontal Wells.....	1298
Field Data .....	1304
Canadian Example.....	1304
Middle East Example, Well A.....	1305
Final Buildup .....	1308
Notes.....	1310

## Chapter 16. Effect of Mud Filtrate Invasion on WFT Measured Pressure

Introduction .....	1311
Filtrate Invasion Model.....	1312
Simulation of the Invasion Process .....	1320
Water-Based Mud .....	1320
Oil-Based Mud .....	1328
Field Examples Showing Capillary Pressure Effects.....	1332
Water-Based Mud .....	1332
Oil-Based Mud .....	1343
Supercharging Analysis.....	1346
Basic Theory .....	1346
Halford and Stewart Method .....	1351
Field Example of Advanced Supercharging Analysis.....	1355
Thick Oil–Water Transitions in Carbonate Zones.....	1357
Modeling of Mud Fluid Loss and Invasion .....	1358
Modern Theory of Dynamic and Static Filtration .....	1358
Mathematical Formulation of an Invasion and Supercharging Model.....	1366
Model Predictions .....	1369
Unusual Far East Oil Appraisal Well Example .....	1372
Notes.....	1375

## Chapter 17. Tight Gas and Coal Bed Methane (CBM)

Introduction .....	1377
Stress-Dependent Permeability.....	1378
PanSystem Pseudo Model.....	1390
Inclusion of Wellbore Storage .....	1410
IFO Field Example .....	1417
Forecasting of Production.....	1433
Slug Testing .....	1437
Boundary Effects Combined with SDPP .....	1448
Skin Effect in CBM Wells .....	1452
Interference Testing to Elucidate Areal Anisotropy.....	1466
Extended Production Testing.....	1481
Horizontal Wells in CBM .....	1482
Hydraulically Fractured Horizontal Wells .....	1483
Application of New-Generation Wireline Formation Testers in CBM.....	1492
Notes.....	1496

<b>Index.....</b>	<b>I–1</b>
-------------------	------------

# 1

## Radial Flow in Porous Media

---

### Introduction

The basis of modern reservoir engineering lies in the quantitative description of unsteady-state, multiphase fluid flow in heterogeneous porous media under the influence of pressure as well as gravitational and capillary forces. In the general case, the flow pattern is spatially three dimensional and three separate phases—oil, water and gas—may be flowing simultaneously in the reservoir. Indeed, the complexity of the situation may be succinctly described by the statement:

- three dimensions
- three phases
- three forces

The solution of such formidable flow problems can be obtained only numerically using sophisticated simulation techniques. The only redeeming feature of reservoir flow is that it is essentially laminar in nature resulting in a linear relation between local superficial fluid velocity and potential gradient.

However, in certain circumstances the reservoir flow is much simpler in character and can be modeled on a reduced basis involving only one space dimension, one mobile phase, and one prevailing force. The best example of this approach is the radial flow which takes place in the vicinity of an individual well open to flow in the oil zone. Prior to any water breakthrough and provided the pressure is everywhere above the bubble point, the only flowing phase is oil. The connate water initially present is rendered immobile by capillary forces and the oil flow is determined solely by pressure gradient. The flow is essentially horizontal and, where water or gas coning is not appreciable, the one-dimensional assumption is a good approximation.

Radial flow in the vicinity of the well bore has a great influence on the productivity of a particular well. The well inflow model, which is the relation between the three key variables of flowing bottom-hole pressure, oil production rate, and average reservoir pressure, is the quantitative expression of productivity and it is the purpose of this treatment to develop such

models. In petroleum engineering, the difference between average reservoir pressure and flowing bottom-hole pressure is known as the *drawdown*. The productivity index (PI) is usually defined as the oil production rate per unit pressure drawdown. In some circumstances, this quantity is a constant and the well inflow model assumes a particularly simple form.

The useful application of radial flow models is obviously dependent on making a reasonable estimate of the extent of the region around a given well over which the flow is radially symmetric. The areal movement of fluids within a reservoir is determined by the overall well pattern and spacing, as well as the location of faults, fractures, and reservoir boundaries.

Analytical radial flow models are often used in conjunction with numerical reservoir simulators whose grid size is much too large to follow the local flow in the vicinity of a well whose diameter is perhaps two orders of magnitude smaller than the grid point spacing. Gross areal or vertical flow in the reservoir is defined by the simulator, and the well inflow models appear as pressure-dependent source terms in the appropriate blocks.

## Well performance diagram

In this chapter, attention will be focused on the factors that control the deliverability of a well under approximately steady-state conditions. The importance of well deliverability can be appreciated by considering the problem of defining the number of wells necessary to develop a field. In figure 1–1, a typical development of a large offshore field is illustrated where a number of deviated wells are drilled from separate platform locations in order to cover the whole reservoir. The economics of such highly front-end-loaded projects require that the oil production be brought up as quickly as possible to a plateau level which corresponds approximately to 10% of recoverable reserves per annum. In order to achieve the plateau rate as quickly as possible, wells may be predrilled from a semisubmersible vessel and tied into a subsea manifold located some small distance from the main platform. When the platform is completed, these wells can be brought in immediately to give maximum early production. The requisite number of wells is determined by dividing the overall plateau production by the obtainable rate per well; hence the well deliverability is of great importance in the design of an offshore development. For expensive projects in deep waters, the overriding issue in the study of economic viability is the individual well rate; for example, in the early days of the North Sea exploitation program a figure of 5,000 bbl/day was often quoted as a ball-park estimate of the minimum economic well rate for offshore development. However, in the current circumstances where small fields are being targeted, the minimum economic rate must be determined for each individual case and such factors as water depth, oil price, pipeline tariff, distance to existing facilities, and total recoverable reserves all play an important role in the project economics. The design problem then is to find the number of producing wells  $N_P$  such that

$$\sum_{i=1}^{N_P} q_{s,i} = q_s^{\text{tot}} \quad \text{where } q_s^{\text{tot}} \text{ is the desired plateau oil production rate at surface conditions.}$$

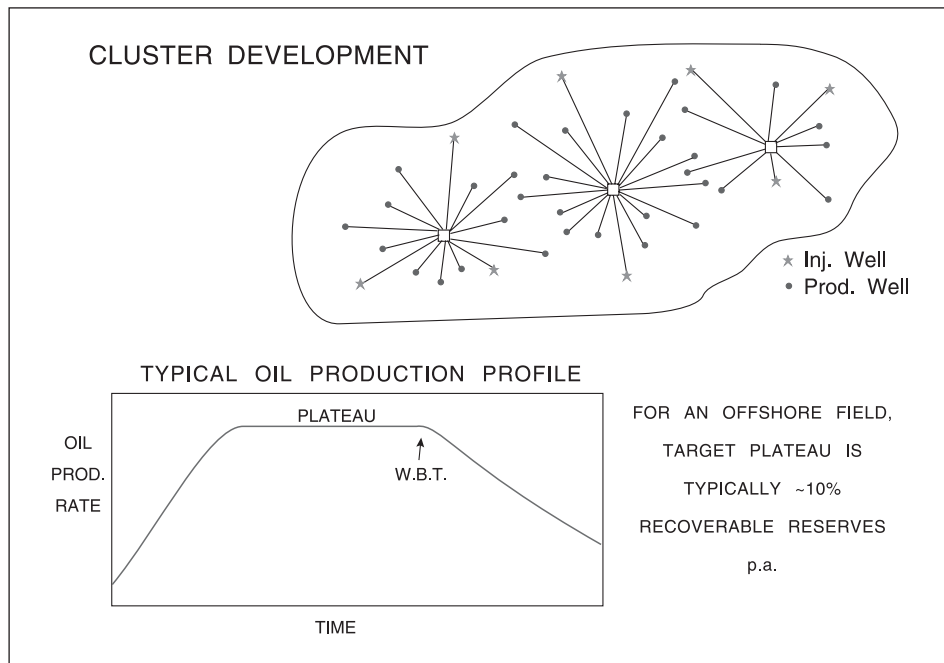


Fig. 1-1. Typical oil production profile from a large offshore reservoir

In order to sustain oil production at a plateau level, the reservoir pressure must usually be maintained by water injection, and hence in figure 1-1 peripheral water injection wells are also indicated, and it is just as important to get water into the reservoir as it is to get oil out. In a balanced water flood, the total rate of water injection on an in situ basis is equal to the total oil production rate; thus,

$$\sum_{j=1}^{NI} q_{w,j} + q^{aq} = B_o q_s^{tot} \quad (1-1)$$

assuming the formation volume factor for water to be essentially unity. Here,  $q^{aq}$  is the natural water influx from the aquifer,  $B_o$  is the oil formation volume factor, and  $NI$  is the number of water injection wells. The required number of water injectors  $NI$  can be fixed only if the strength of the natural water drive  $q^{aq}$  can be estimated; this is one of the most difficult prediction tasks in reservoir engineering. The end of the period of plateau oil production is associated with water breakthrough (WBT) at the producing wells.

In a system without artificial lift, the steady-state rate that can be achieved by a well is basically determined by two resistances in series as illustrated in figure 1-2. Here, fluid flows from the reservoir at pressure  $p_r$  to a wellbore where the bottom-hole pressure is denoted  $p_{wf}$  and then to the surface and into a separator at pressure  $p_s$ . The well rate at stock tank (surface) conditions is denoted  $q_s$ , and the basic production problem is to predict  $q_s$  given the reservoir and surface pressure. The first resistance is due to radial flow in the porous medium, i.e., rock, and the pressure drop  $p_r - p_{wf}$  required for this process is known as the *drawdown*. In oil wells, the flow in the porous medium is laminar (except at very high rate through a limited entry) and there is

a linear relation between flow and pressure drop which leads to the definition of productivity index  $J_{ss}$ ; thus,

$$q_s = J_{ss}(p_r - p_{wf}) \tag{1-2}$$

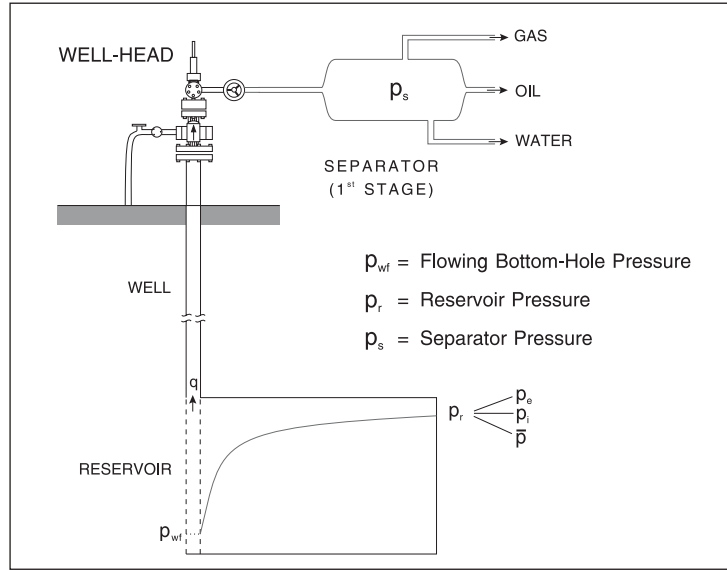


Fig. 1-2. Reservoir to separator flow system

This simple equation linking the flow rate and pressure drop is known as the *inflow performance relation* (IPR). Flow in the tubing is more complicated, and the relation between the oil volumetric flow rate at standard conditions  $q_s$  and the overall pressure difference for vertical lift  $p_{wf} - p_s$  is nonlinear. In general, the vertical lift performance (VLP) may be written symbolically as

$$p_{wf} - p_s = f_{VLP}(q_s) \tag{1-3}$$

and sophisticated computer programs are used to model multiphase flow in the tubing and hence to define this functional relationship. In essence, the problem of determining the production rate of a well is to solve Eqs. (1-2) and (1-3) simultaneously for  $q_s$  and  $p_{wf}$  given  $J_{ss}$  and the function  $f_{VLP}$ . The process is best illustrated on a well performance diagram as shown in figure 1-3; this was first proposed by Gilbert,<sup>1</sup> who is recognized as the father of petroleum production engineering. A well performance diagram is simply a plot of  $p_w$  versus surface flow rate  $q_s$ . Rearranging the definition of the well PI, i.e., Eq. (1-2), shows that the IPR is a straight line of the form

$$p_{wf} = p_r - \frac{1}{J_{ss}} q_s \tag{1-4}$$

while the nonlinear VLP may be written as

$$p_{wf} = p_s + f_{VLP}(q_s) \tag{1-5}$$

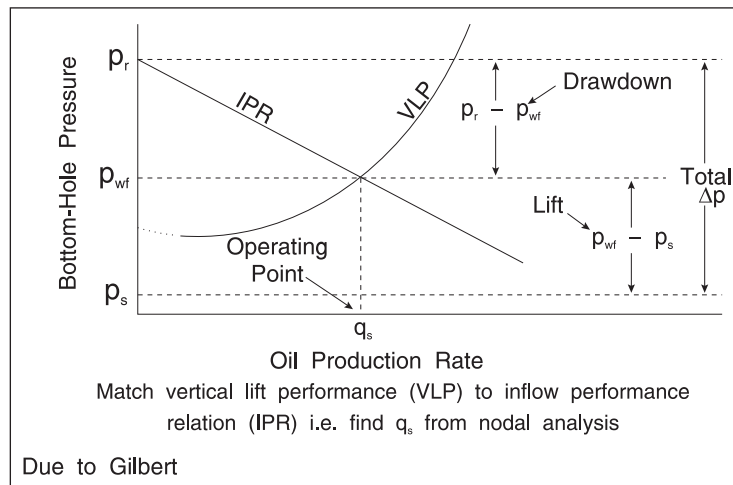


Fig. 1–3. Well performance diagram

The simultaneous solution of these two equations is the intersection of the respective lines on the well performance diagram; this is known as the *well operating point*. The total pressure drop available for flow  $p_r - p_s$  has been divided between radial flow in the porous media and vertical flow in the tubing; the bottom-hole pressure  $p_{wf}$  adjusts so that the flow predicted by the two models (1–2) and (1–3) is the same. This calculation of the operating point by matching the IPR and VLP relations for specified reservoir and separator pressures is known as *nodal analysis* in production engineering.

In this chapter, attention will be concentrated on the phenomena that control the PI ( $J_{ss}$ ) of the well, and therefore the subject of radial flow in porous media will be treated in detail. However, it should always be remembered that the actual well rate is fixed by the simultaneous solution of the IPR and VLP curves.

## Darcy's law

The basic equation describing the laminar, creeping flow of a single-phase fluid in a porous medium is Darcy's law, which takes the form

$$\frac{q}{A} = u = -\frac{k}{\mu} \left( \frac{dp}{dx} - \rho g \frac{dD}{dx} \right) = -\frac{k}{\mu} \frac{d\psi}{dx} \quad (1-6)$$

where the quantity  $\psi = p - \rho gD$  is known as the *potential*; here  $D$  is true vertical depth and  $\rho$  is the fluid density. The potential  $\psi$  is used in the formulation of multiphase reservoir flow equations and it allows for the effect of gravity on the motion. The permeability  $k$  is a property of the porous medium dependent on the nature of the flow channels, while the viscosity  $\mu$  is a property of the fluid. For linear horizontal flow, as illustrated in figure 1–4, there is no effect of gravity and the equation becomes simply

$$\frac{q}{A} = -\frac{k}{\mu} \cdot \frac{dp}{dx} \quad (1-7)$$



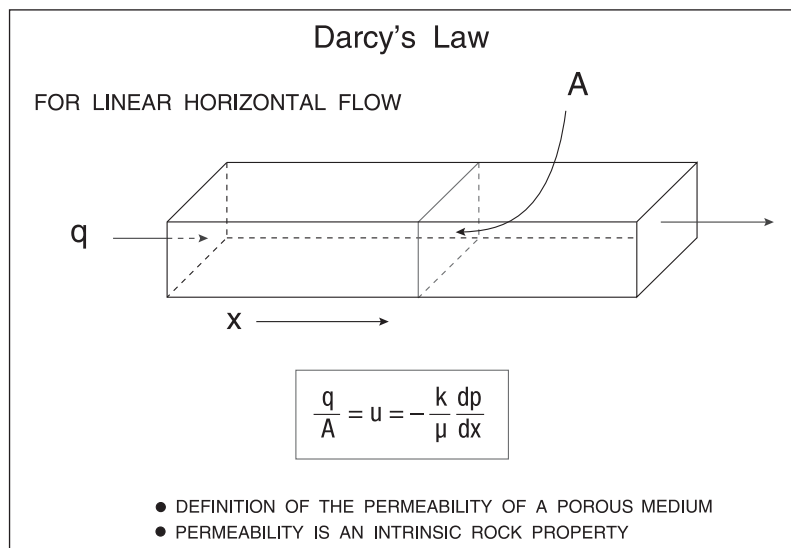


Fig. 1-4. Laminar single-phase flow in a porous medium

The permeability is a measure of the ease with which a fluid will flow through the medium; the higher the permeability, the higher the flow rate for a given pressure gradient. The permeability is a statistical average of the fluid conductivities of all the flow channels in the medium. This average conductivity takes into account the variations in size, shape, direction, and interconnections of all the flow channels. While obviously a number of pores or flow channels must be considered in obtaining a statistically average permeability, it is convenient to consider the permeability as the property of a point in the medium. In a typical laboratory experiment, the permeability of a 25-mm-diameter rock sample or core is measured. In a homogeneous medium, the permeability at all points is the same, while in a heterogeneous medium the local permeability varies from point to point.

In the SI system, the quantities entering Darcy's law have the following units:

q = flow rate (in situ conditions)	:	m <sup>3</sup> /s
A = cross-sectional area	:	m <sup>2</sup>
u = superficial fluid velocity	:	m/s
μ = fluid viscosity	:	Ns/m <sup>2</sup>
p = pressure	:	Pa
x = space co-ordinate in flow direction	:	m
k = permeability	:	m <sup>2</sup>

Historically, the common laboratory units have been as shown below:

q : cm <sup>3</sup> /s	p : atm
A : cm <sup>2</sup>	x : cm
u : cm/s	μ : cp
k : darcy	

This system, known as *darcy units*, and the SI system are consistent and no dimensional factors arise. Since most reservoir rocks have a permeability less than 1 darcy, the millidarcy (md) is often employed as a practical unit. However, another set of units called *reservoir or field units* is also widely used in which the quantities are expressed as follows:

$$\begin{array}{ll} q_s : \text{ bbl/day (stock tank)} & p : \text{ psi} \\ A : \text{ ft}^2 & x : \text{ ft} \\ k : \text{ md} & \mu : \text{ cp} \end{array}$$

This system is not consistent, and Darcy's law takes the form

$$\frac{q_s B}{A} = - \frac{1.127 \times 10^{-3} k}{\mu} \cdot \frac{dp}{dx} \quad (1-8)$$

for horizontal flow; here B is the oil formation volume factor and the quantity  $q_s B$  is simply the in situ volumetric flow rate  $q$ . The unit conversion constant of  $1.127 \times 10^{-3}$  or its reciprocal 887.2 frequently occurs in equations involving Society of Petroleum Engineers (SPE) field units. The ratio  $k/\mu$  entering Eq. (1-8), which is a combination of a rock property and a fluid property, is known as the *mobility*.

Darcy's law, i.e., Eq. (1-7), is the low-Reynolds-number limit of the more general flow in porous media equation due to Forcheimer:

$$\frac{dp}{dx} = - \frac{\mu}{k} u_r - \beta \rho u_r^2 \quad (1-9)$$

where  $\beta$  is a second rock property termed the *inertial resistance coefficient*, which has dimensions of  $L^{-1}$ , e.g.,  $\text{ft}^{-1}$  in field units. The first term on the right-hand side of Eq. (1-9) is the viscous component, while the second term is the non-Darcy component. The non-Darcy term is important only if  $\beta \rho u_r$  is comparable to  $\mu/k$ , i.e., if

$$\text{Re}'' = \frac{k \beta \rho u_r}{\mu} > 0.1 \quad (1-10)$$

Here,  $\text{Re}''$  is a modified Reynolds number for porous media. This condition is only ever satisfied for fluids of low viscosity near the wellbore where the velocity is high. The physical interpretation of non-Darcy flow has been elucidated by Sketne,<sup>2</sup> who has shown that the inertial (acceleration) terms in the Navier–Stokes equation for laminar flow in a porous medium become important at Reynolds numbers, based on the pore throat dimension, greater than unity. The nature of the motion in a porous medium is illustrated in figure 1-5, where the proper fluid dynamic definition of darcy flow is seen to be creeping laminar flow; there is no question of turbulence being involved in porous medium situations. Non-darcy flow near the sandface in gas wells is the origin of the rate-dependent skin factor treated later in this chapter.

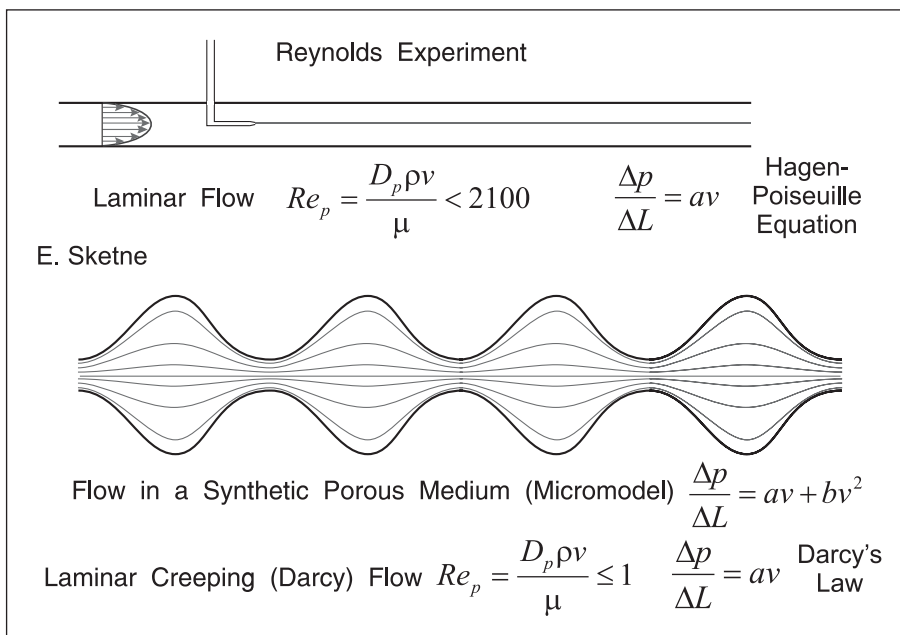


Fig. 1-5. Flow in a synthetic porous medium

## Steady-state Linear Flow of an Incompressible Fluid

Steady-state flow occurs when the flow rate and pressure at each point in the medium are constant with time. In steady-state flow, there is no net accumulation of mass anywhere within the system. The mass rate of flow into any volume element is equal to the mass rate of flow of fluid out. Many laboratory experiments are performed under steady-state conditions in cylindrical cores or sandpicks. The flow through such a system is linear and one dimensional.

In the steady state, isothermal flow of a single, incompressible fluid in a linear system, as shown in figure 1-6, not only is the mass flow rate constant with position, but the volumetric flux  $u = q/A$  is also constant. The differential equation which describes horizontal flow is

$$\frac{q}{A} = - \frac{k}{\mu} \frac{dp}{dl} \tag{1-11}$$

which on assuming the permeability  $k$  to be constant (homogeneous medium) and separating the variables becomes

$$\frac{q}{A} dl = - \frac{k}{\mu} dp \tag{1-12}$$

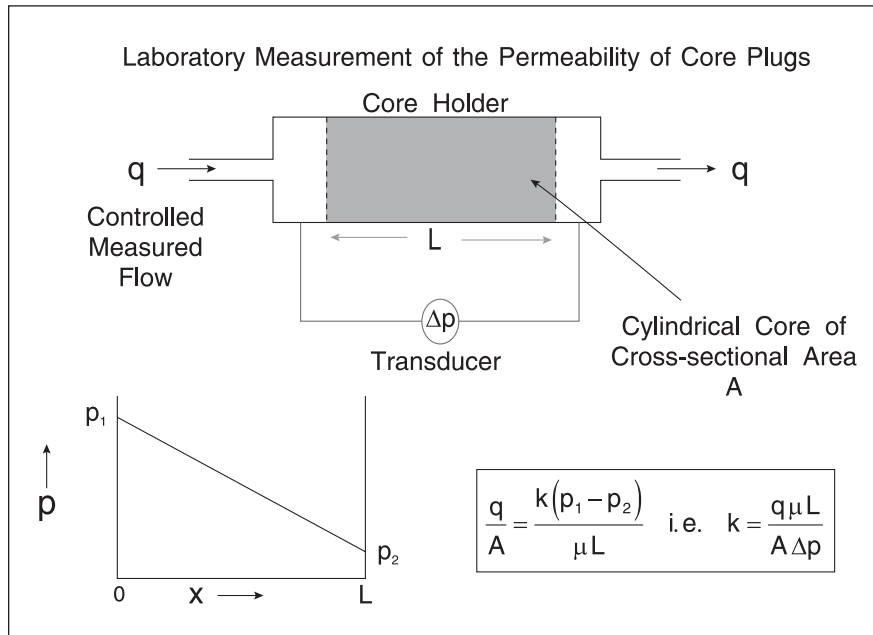


Fig. 1-6. Linear incompressible flow in a core plug

Hence, integrating Eq. (1-12) between the limits

$$l = 0, \quad p = p_1 \quad \text{and} \quad l = L, \quad p = p_2$$

gives

$$\frac{q}{A} \int_0^L dl = - \frac{k}{\mu} \int_{p_1}^{p_2} dp \quad (1-13)$$

i.e.,

$$q = \frac{kA}{\mu} \frac{(p_1 - p_2)}{L} \quad (1-14)$$

This equation is used, for example, to calculate the permeability of a core plug from the measured pressure differential on injecting liquid of viscosity  $\mu$  at a constant rate  $q$ . Note that the pressure profile is linear between the extreme values.

In an unconsolidated porous medium, such as a sandpack illustrated in figure 1-7, the theory of laminar flow in packed beds developed in chemical engineering can be used to show how the permeability is related to the average size of the particles comprising the bed  $D_{vs}$  and the bed porosity or voidage  $\phi$ . Here,  $D_{vs}$  is the volume-surface (Sauter) mean particle diameter defined as

$$D_{vs} = \frac{6(1 - \phi)}{a} \quad (1-15)$$

where  $a$  is the specific surface area of the bed (wetted surface/unit volume of bed  $m^2/m^3$ ).

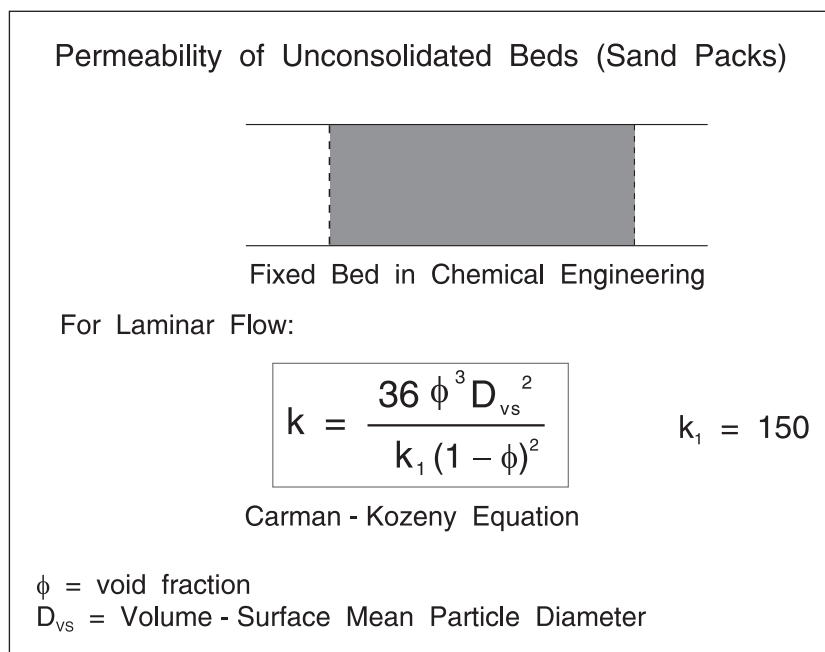


Fig. 1-7. Permeability of a sand pack (unconsolidated porous medium)

The following equation, based on the Carman–Kozeny model of laminar flow in packed beds, gives the permeability as a function of  $\phi$  and  $D_{vs}$ :

$$k = \frac{36\phi^3 D_{vs}^2}{k_1(1-\phi)^2} \tag{1-16}$$

where  $k_1 = 150$  is the Kozeny constant

This equation shows that in unconsolidated porous media the porosity and average grain size are the key determinants of permeability; note that permeability varies approximately with the fifth power of the porosity. An empirical equation for the permeability of well-sorted detrital rocks with porosities down to 10% has been developed by Berg,<sup>3</sup> which takes the following form:

$$k = 5.1 \times 10^{-6} \phi^{5.1} (MD)^2 e^{-1.385PD_s} \tag{1-17}$$

where

- $k$  = permeability (darcy)
- $\phi$  = porosity
- MD = weight median grain size (mm)
- $PD_s$  = PHI percentile deviation (a measure of sorting).

The weight median grain size is obtained by sieve analysis of the disaggregated sandstone rock, and  $PD_s$  is the standard deviation of a plot of weight percentage versus the quantity PHI defined through the equation

$$D = \left( \frac{1}{2} \right)^{PHI} \quad \text{and} \quad D = \text{grain size (mm)}$$

This transformation produces an approximately normal distribution for which a standard deviation can be computed. The important point about the Berg correlation is that it clearly demonstrates that in real sandstone rocks (albeit of low clay content) the permeability is indeed a function of the square of the average grain size and the porosity to the fifth power. The degree of sorting, i.e., the distribution of particle sizes, also has an effect on the permeability.

The question of predicting permeability from open-hole logs was addressed by Timur of Chevron, who produced a much used correlation of the form

$$k_{TIMUR} = \frac{A\phi^B}{S_{w,irr}^C} \quad (1-18)$$

where  $S_{w,irr}$  is the irreducible water saturation which is used as a grain size indicator. The currently used version of the Timur predictor is

$$k_{TIMUR} = 10000 \frac{\phi^{4.5}}{S_{w,irr}^2} \quad (1-19)$$

Modified versions of the Timur equation have recently been used in connection with nuclear magnetic resonance (NMR) logging.

Since permeability varies with the fifth power of porosity, any change in the latter will have a large effect on the former. As a reservoir is depleted in (pore) pressure, the grain pressure or effective stress increases, as illustrated in figure 1-8, and compaction, i.e., reduction in porosity, takes place; this can have a significant effect on permeability in an unconsolidated formation. In figure 1-9 the effect of confining pressure on the pore volume of Berea sandstone is shown; here the fractional change in pore volume, i.e.,  $(V_{pa} - V_p)/V_{pa}$ , is plotted against the grain pressure  $p_c - p_p$  where

- $V_{pa}$  = pore volume at zero confining pressure,
- $V_p$  = pore volume under confining pressure,
- $p_c$  = confining pressure, and
- $p_p$  = pore pressure.

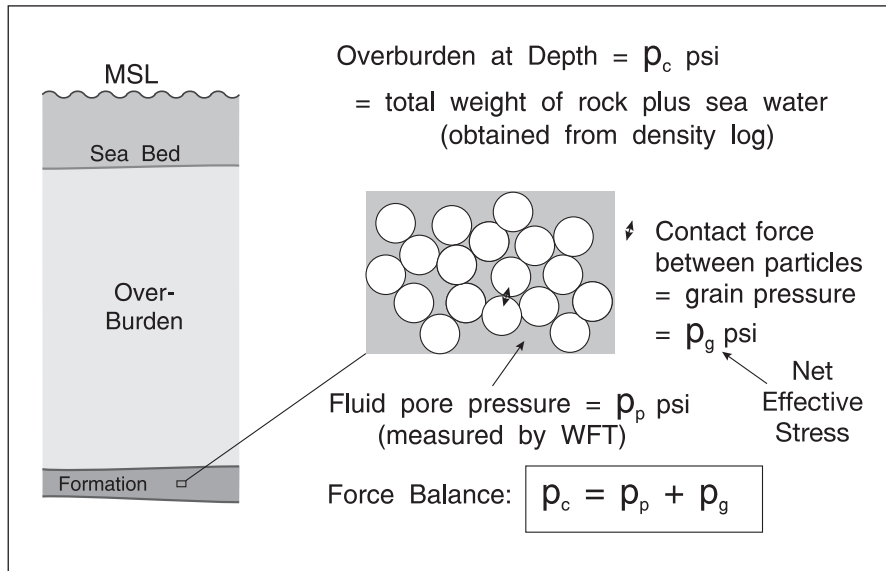


Fig. 1-8. Basic rock mechanics

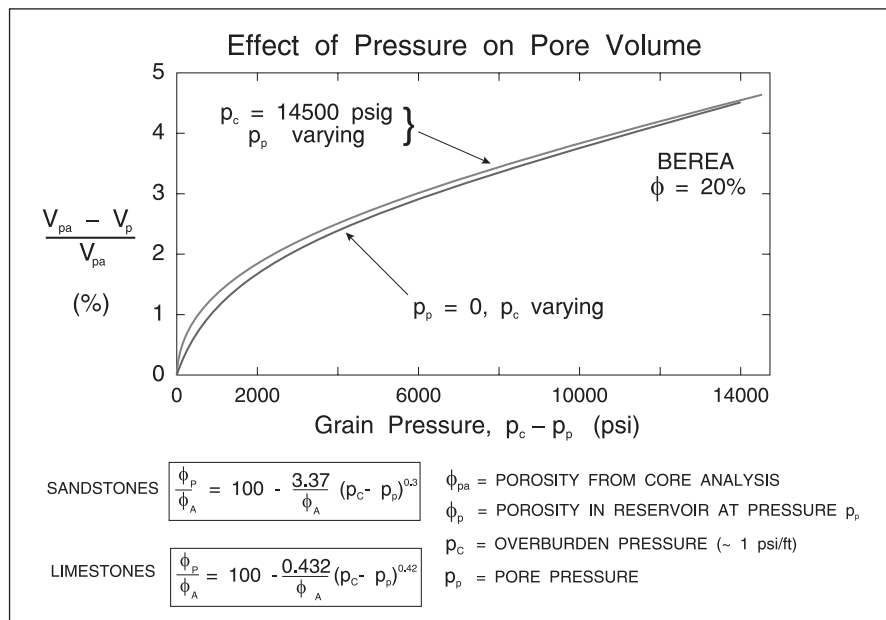


Fig. 1-9. Effect of overburden pressure on pore volume

Since small changes in porosity imply large changes in permeability, the latter may be expected to be a function of the grain pressure, i.e.,  $p_c - p_p$ . The phenomenon of rock compressibility or compaction is of great importance in reservoir engineering and the definition of  $c_f$  will be discussed later in this chapter. The effect of confining pressure on the permeability of various sandstones from the Stanford rock physics project is shown in figure 1-10; the lower the permeability level—which correlates with the clay content—the greater the sensitivity of permeability to grain pressure. In figure 1-11 the normalized permeability as a function of pore pressure at constant effective pressure (overburden) is shown, again demonstrating the importance of measuring rock properties at in situ conditions.

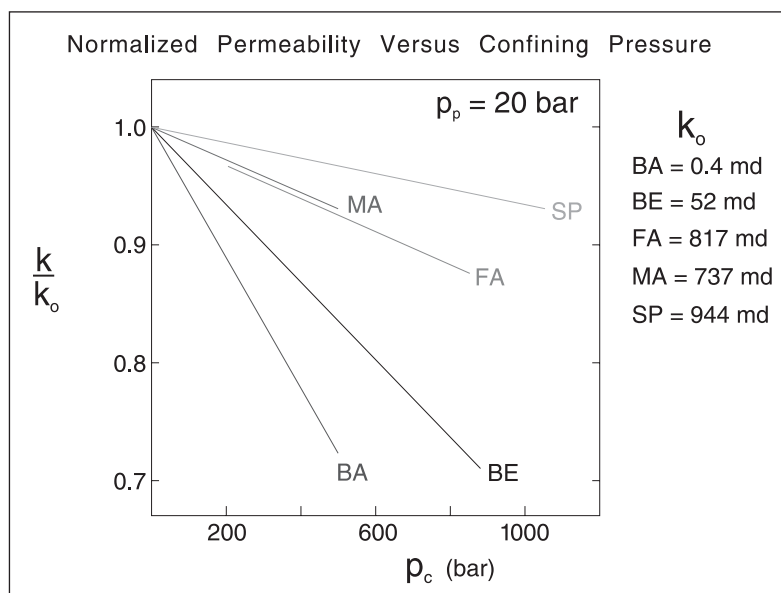


Fig. 1–10. Effect of confining pressure on rock permeability

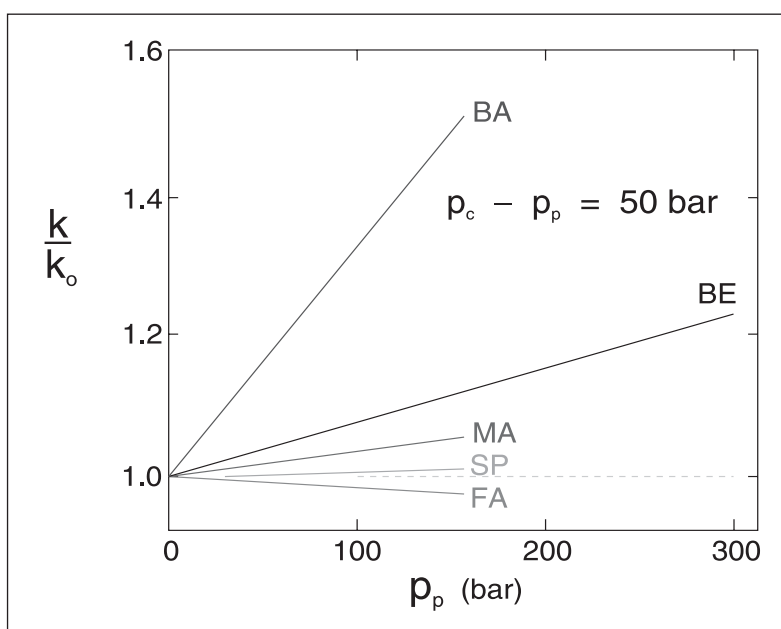


Fig. 1–11. Normalized rock permeability versus pore pressure at fixed grain pressure

In the deep water fields in the Gulf of Mexico (GOM), the formations are highly unconsolidated due to a “ballooning” effect of the very high pore pressure (ca 18,000 psia since the formations are at great depth and overpressured). If the pressure were allowed to fall by depletion, there would be a significant reduction in permeability partially compensated by a decrease in viscosity. However, the effect of pore pressure on oil viscosity is less than that on permeability, and the decision has been made to initiate pressure maintenance by water injection early in the field development. The operating companies are using the highest discharge pressure pumps which are currently available to keep the pressure as close to the initial values as possible.



## Steady-state Radial Flow

### Basic well model

In its simplest form, an oil reservoir consists of a single, homogeneous layer of porous rock of uniform thickness  $h$  and permeability  $k$  bounded above and below by horizontal impermeable barriers. Each producing well in the reservoir is surrounded by a drainage area from which oil flows to the well in question. Initially, it is assumed that this region is circular in shape with an external radius  $r_e$  and that the well of radius  $r_w$  is centrally located as illustrated in figure 1–12. The pressure at the outer limit of the circular region is designated  $p_e$  and this quantity can be measured by a wireline formation tester survey in an observation well roughly equidistant from the producers. In figure 1–12,  $p_{wf}$  is the well bottom-hole flowing pressure. Flow to the well is essentially radial in character and most of the pressure drop occurs quite close to the wellbore.

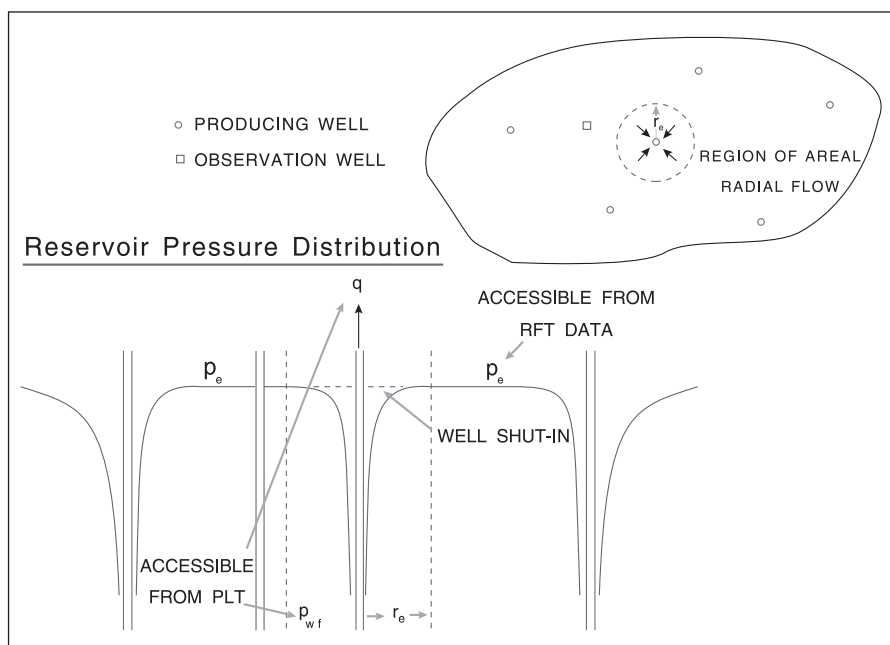


Fig. 1–12. Radial flow single well model

The pore space is completely filled with oil of viscosity  $\mu$ , except for connate water which does not flow under reservoir conditions. The oil is everywhere above its bubble pressure (undersaturated) and hence no free gas phase exists. Such a prototype reservoir is illustrated in figure 1–13. If the well is open to flow over the whole interval  $h$ , and is produced at a flow-rate  $q$ , the symmetry of the system results in radial flow in the direction of the well, i.e., there are no vertical or tangential velocity components. In the succeeding treatment, the permeability  $k$  will be identified with the permeability to oil at the connate water saturation  $S_{wc}$ . Also, the oil flow rate  $q$  is the volumetric flow of oil at reservoir conditions; note that  $q$  is positive for production at the well.

The formulae to be developed are known as well models, since they describe reservoir flow in the vicinity of an individual well, i.e., radial near-well-bore flow.

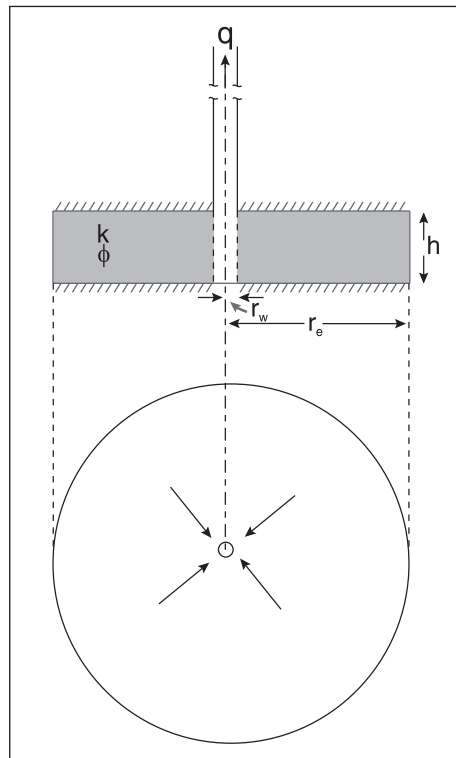


Fig. 1–13. Model cylindrical reservoir with central well

## Boundary conditions

In all reservoir flow problems of this type, it is necessary to specify the boundary conditions determining pressure and flow at the inner face ( $r = r_w$ ) and the external face ( $r = r_e$ ) of the flow system. Steady-state flow can occur only if fluid is injected over the outer boundary at the same rate  $q$  as it is produced at the well. The pressure at the wellbore  $r = r_w$  is denoted  $p_w$ , while that at the external radius  $r = r_e$  is denoted  $p_e$ . The simple steady-state model is useful in analyzing reservoirs in which produced oil is replaced by another fluid, usually water, which is either introduced through injection wells (pressure maintenance or water-flooding) or derived from an aquifer communicating with the oil reservoir. The choice of the appropriate value of  $r_e$  for a particular well and the physical significance of  $p_e$  will be discussed later. Suffice it to say at the moment that  $r_e$  in a pattern water-flood, for example, is governed by the half-distance between injection and producing wells and that  $p_e$  is identified with the reservoir pressure at the mid-point between the producer in question and the surrounding injectors.

## Steady-state radial flow of an incompressible fluid

In the steady-state radial flow of an incompressible fluid, the volumetric flow rate passing through any cross-section is the same as shown in figure 1–14. Hence the main feature of radial flow is that the superficial fluid velocity given by

$$u_r = - \frac{q}{2\pi rh} \quad (1-20)$$

increases rapidly in absolute value as the well bore is approached. For laminar flow, Darcy's law in the form

$$u_r = - \frac{k}{\mu} \frac{dp}{dr} \tag{1-21}$$

relates the local pressure gradient and fluid velocity. Combining Eqs. (1-20) and (1-21) and separating the variables, since  $q$ ,  $k$ , and  $\mu$  are constants, results in

$$\frac{q\mu}{2\pi kh} \cdot \frac{dr}{r} = dp \tag{1-22}$$

which can be integrated between the limits

$$r = r_w, p = p_w \quad \text{and} \quad r = r_e, p = p_e$$

to give

$$\frac{q\mu}{2\pi kh} \int_{r_w}^{r_e} \frac{dr}{r} = \int_{p_w}^{p_e} dp \tag{1-23}$$

i.e.,

$$\frac{q\mu}{2\pi kh} \ln \frac{r_e}{r_w} = (p_e - p_w) \tag{1-24}$$

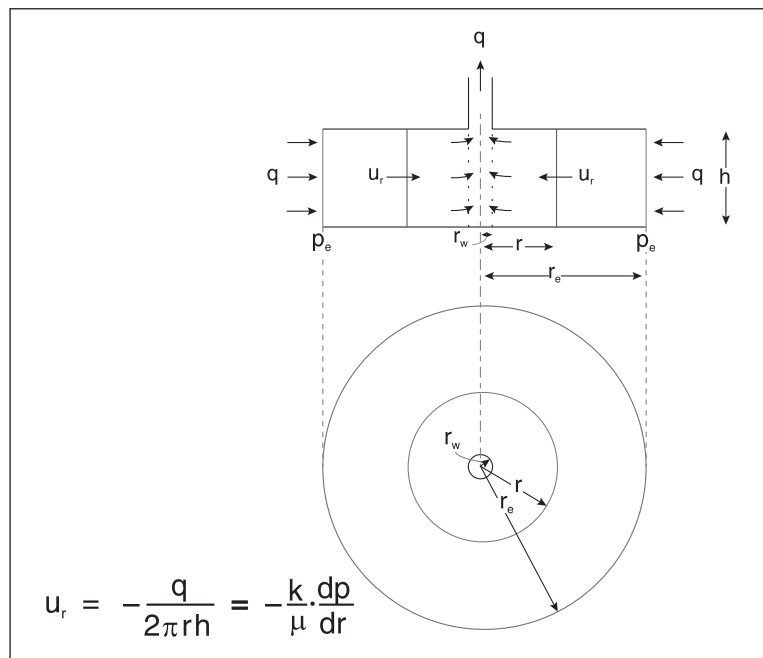


Fig. 1-14. Steady-state radial incompressible flow

This may be written explicitly for the flow rate as

$$q = \frac{2\pi kh}{\mu \ln \frac{r_e}{r_w}} (p_e - p_w) \quad (1-25a)$$

or explicitly for the pressure difference

$$p_e - p_w = \frac{q\mu}{2\pi kh} \ln \frac{r_e}{r_w} \quad (1-25b)$$

The difference between the external pressure  $p_e$  and the well bottom hole pressure  $p_w$  is known as the *drawdown* in petroleum engineering and Eq. (1-24) is the important relation between well production rate  $q$ , drawdown, and reservoir properties. Such an equation is known as a *well inflow model*. The radial flow integration and the pressure distribution are illustrated in figure 1-15. The drawdown is directly proportional to the production rate  $q$  and the oil viscosity  $\mu$  and is inversely proportional to the reservoir permeability thickness product  $kh$ . Note that both  $q$  and  $\mu$  refer to in situ reservoir conditions. The invariance of these relationships is embodied in the definition of the dimensionless overall pressure drop or drawdown  $p_{De}$  given by

$$p_{De} = \frac{p_e - p_w}{\frac{q\mu}{2\pi kh}} \quad (1-26)$$

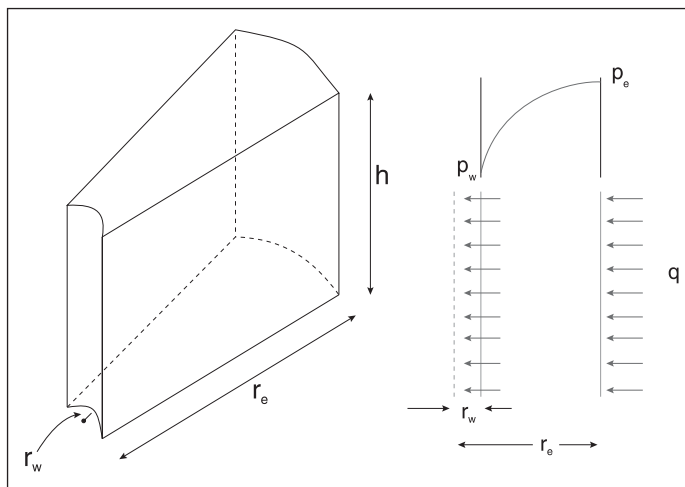


Fig. 1-15. Steady-state radial laminar flow

This is a much used quantity in the analysis of well behavior which, in the steady state, depends only on the geometry of the drainage area, i.e., the ratio of the external to well-bore radius  $r_e/r_w$ , which is known as the *dimensionless external radius*  $r_{De}$ . Thus the steady-state radial flow equation may simply be written as

$$p_{De} = \ln r_{De} \quad (1-27)$$

The pressure  $p$  at any radius  $r$  intermediate between  $r_w$  and  $r_e$  is given by

$$p - p_w = \frac{q\mu}{2\pi kh} \ln \frac{r}{r_w} \quad (1-28)$$

which follows from (1-23) on changing the upper integration limit. Again, defining dimensionless pressure drop and radius by

$$p_D = \frac{p - p_w}{\frac{q\mu}{2\pi kh}} \quad \text{and} \quad r_D = \frac{r}{r_w}$$

the pressure profile in the vicinity of a producing well may be written as

$$p_D = \ln r_D \quad (1-29)$$

This relation is shown in figure 1-16, which demonstrates very clearly how the pressure decreases rapidly as the well-bore is approached. This is associated with the increase in fluid velocity as the area for flow  $2\pi rh$  diminishes. The most significant proportion of the total drawdown occurs in the near-well-bore region. For example, if  $r_e/r_w$  is 1,000, which is representative of actual reservoir conditions, and the total dimensionless drawdown  $p_{De}$  from Eq. (1-27) is 6.91, then 66.6% of this is accounted for within a region extending only to  $100r_w$  from the well-bore. Hence,  $r_e$  need be known only very approximately to get a good estimate of drawdown for a given production rate.

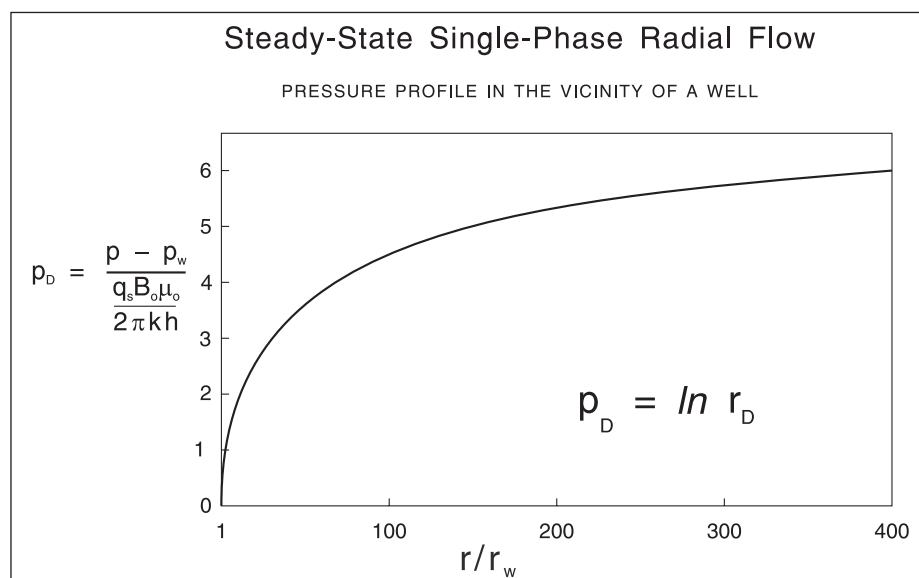


Fig. 1-16. Dimensionless pressure distribution

## Well productivity

The steady-state radial flow equation shows how the permeability–thickness product  $kh$  influences the rate at which oil can be produced from a well. This quantity is an extremely important reservoir parameter which crucially affects the decision as to whether an oil field is commercially viable. The productivity of an oil well is quantified by the PI  $J_{sse}$  which has the following definition:

$$J_{sse} = \frac{q_s}{(p_e - p_w)} \quad (1-30)$$

where  $q_s$  is the oil flow rate at stock tank conditions; thus the PI is the rate at which stock tank oil can be produced per unit pressure drawdown. The productivity is usually expressed in oil field units, viz., bbl/d/psi, and in these units the steady-state radial flow equation becomes

$$q_s B = \frac{1.1273 \times 10^{-3} 2\pi kh}{\mu \ln \frac{r_e}{r_w}} (p_e - p_w) \quad (1-31)$$

where  $q_s$  is the flow rate at stock tank conditions and  $B$  is the oil formation volume factor. The units of the quantities in Eq. (1–31) are as follows:

$q_s$ : bbl/day	$\mu$ : cp	$k$ : md
$h$ : ft	$p_e, p_w$ : psi	$r_e, r_w$ : ft

In field units, the dimensionless drawdown or pressure drop is given by

$$P_D = \frac{(p - p_w)}{\frac{887.2 q_s B \mu}{2\pi kh}} \quad (1-32)$$

and Eq. (1–31) may be written as

$$P_{De} = \ln r_{De} \quad (1-33)$$

as before, but remembering the correct definition of  $p_{De}$ . Comparing Eqs. (1–30) and (1–31) shows that for steady-state radial flow the productivity index of the well in field units is given by

$$J_{sse} = \frac{1.127 \times 10^{-3} 2\pi kh}{B\mu \ln \frac{r_e}{r_w}} \text{ bbl/d/psi}$$

The productivity index of a well is the most commonly used measure of its ability to deliver oil and is one of the most important concepts in petroleum engineering. PIs range from values much less than unity to nearly 100,000 in extremely prolific wells in Iran. The best wells in the North Sea have PIs of about 500.

## Well inflow performance

The steady-state radial flow equation defines the relation between well production rate  $q_s$ , bottom hole pressure  $p_w$ , and reservoir pressure which is identified with  $p_e$ . It is often convenient to represent this three-variable interaction graphically in the form of a plot of flowing bottom hole pressure as a function of production rate for several values of the reservoir pressure as shown in figure 1–17. Normally,  $q$  is on a stock tank basis and the inflow equation is

$$p_e - p_w = \frac{B\mu \ln \frac{r_e}{r_w}}{2\pi kh} q_s \quad (1-34)$$

Hence a plot of  $p_w$  versus  $q_s$  is a straight line of slope  $-1/J_{sse}$  and intercept  $p_e$ . Such diagrams are very useful for matching well inflow and vertical lift performances; this aspect will be treated in detail later.

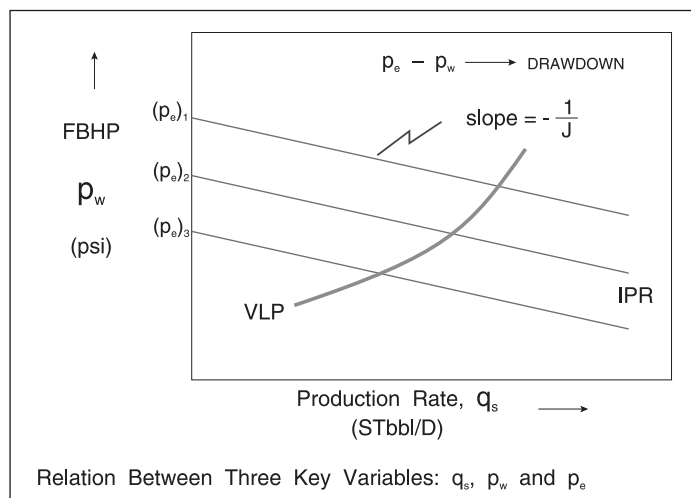


Fig. 1–17. IPR on a well inflow performance diagram

## Volume average pressure in steady-state flow

The pressure profile in a cylindrical steady-state flow system between  $r = r_w$  and  $r = r_e$ , shown in figure 1–16, is given by

$$p = p_w + \frac{q\mu}{2\pi kh} \ln \frac{r}{r_w} \quad (1-35)$$

In some circumstances, it is useful to know the volume-averaged pressure within the system, defined by

$$\bar{p} = \frac{\int p dV}{V} = \frac{\int_{r_w}^{r_e} p 2\pi r h dr}{\pi r_e^2 h} \quad (1-36)$$

Substituting Eq. (1-35) into Eq. (1-36) and carrying out the necessary integration gives the following result:

$$\bar{p} = p_w + \frac{q\mu}{2\pi kh} \left( \ln \frac{r_e}{r_w} - \frac{1}{2} \right) \quad (1-37)$$

Thus in steady-state radial flow, the difference between the mean pressure  $\bar{p}$  and the external pressure  $p_e$  is small and is given by

$$p_e - \bar{p} = \frac{1}{2} \cdot \frac{q\mu}{2\pi kh} \quad (1-38)$$

i.e., a dimensionless pressure difference of one half. The concept of average pressure in steady-state radial flow is illustrated in figure 1-18.

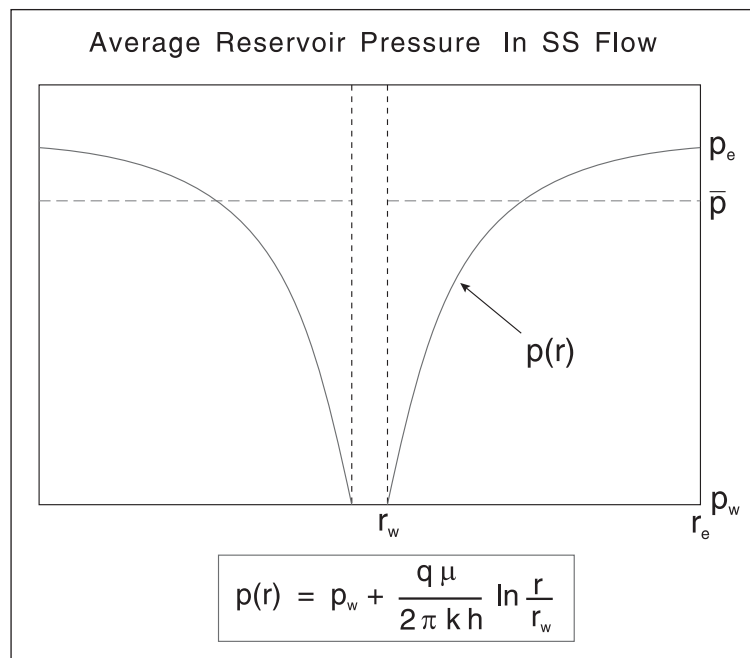


Fig. 1-18. Average pressure in steady-state flow



A steady-state PI based on the average pressure in the drainage area has the form

$$q_s = J_{ssa} (\bar{p} - p_w) \quad (1-39a)$$

$$J_{ssa} = \frac{1.127 \times 10^{-3} 2\pi kh}{B\mu \left( \ln \frac{r_e}{r_w} - \frac{1}{2} \right)} \text{ bbl/d/psi} \quad (1-39b)$$

## Semi-steady-state Radial Flow

### Introduction

In the preceding section, the concept of steady-state radial flow in the region around a well was introduced and the attainment of this condition was shown to be a consequence of fluid being injected over the external face at the same rate as production at the well-bore. The outer boundary condition for steady-state flow may be written in the form

$$r = r_e, \quad \left. \frac{dp}{dr} \right|_{r_e} = \frac{q\mu}{2\pi khr_e} \quad (1-40)$$

which follows from Darcy's law and the uniform imposed flux. Thus the pressure gradient at  $r_e$  is specified through a fixed flow condition. This form of external boundary condition is relevant when produced oil is replaced in the reservoir by another fluid such as water. In the steady-state model, there is no depletion of fluid within the radial zone.

However, in many reservoir situations there is no natural water influx or gas-cap expansion and, in the absence of artificial fluid injection, oil production results solely from expansion of the oil in place as the reservoir pressure is reduced. In this case, the most appropriate form of external boundary condition is the no-flow condition, i.e.,

$$r = r_e, \quad \left. \frac{dp}{dr} \right|_{r_e} = 0 \quad (1-41)$$

In such a bounded drainage region, sustained production of oil is accompanied by a continuous decline in pressure throughout the system. Thus the pressure is a function of time and the mass of oil within the radial zone decreases; this is basically an unsteady-state process. However, when an undersaturated, bounded reservoir is produced at a constant rate, after an initial start-up period, the rate of pressure decline at all points in the system becomes constant and uniform. The pressure distribution in a closed circular reservoir with a central well is shown as a function

of time in figure 1–19. The initial period when a pressure disturbance propagates out from the well is known as *transient* or *infinite-acting* flow; this regime is studied in detail in *Well Test Design and Analysis* since it is the basis of well testing. When the disturbance reaches the outer boundary, the shape of the distribution stabilizes and the pressure changes linearly with time. In reservoir engineering, this situation is referred to as *semi-steady-state flow* because the time derivative of pressure is constant; this regime is also known as *stabilized flow* since the pressure profile in the depletion zone, although declining, maintains the same shape. The solution technique for semi-steady-state (SSS) flow will be set out in some detail since the method is a perfectly general one which can be applied to a variety of flow problems. SSS depletion is an important reservoir drive mechanism in the early life of an undersaturated reservoir.

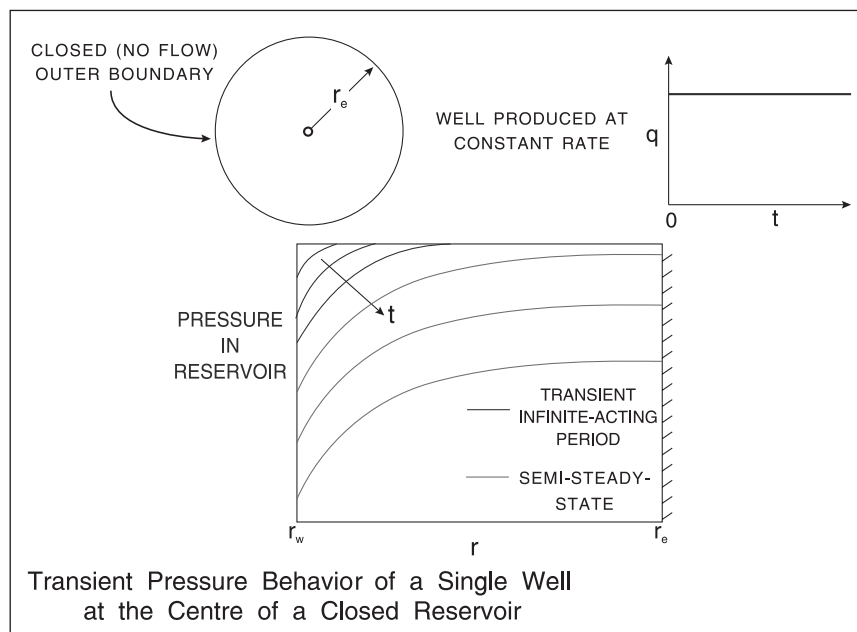


Fig. 1–19. Pressure distribution in transient and semi-steady-state flow

## Semi-steady-state solution

The physical situation again concerns a cylindrical, homogeneous region of constant thickness  $h$  and external radius  $r_e$ , with a centrally located vertical well of radius  $r_w$ . However, in the SSS analysis no flow is allowed across the external face and oil production from the cell occurs solely as a result of the expansion of the oil in place due to a reduction in pressure. In SSS flow, the local oil flow rate varies from a maximum value  $q$  at the production face to zero at the external face. Hence the instantaneous pressure profile will not be the same as in the steady-state case. In the SSS model, it will be taken that the central well is produced continuously at a constant rate  $q$ . The instantaneous pressure profile in the cylindrical drainage region is shown in figure 1–20 and it will be tacitly assumed that this profile does not change in shape and the pressure is declining everywhere at the same rate, i.e.,

$$\frac{dp}{dt} = \text{constant} \quad (1-42)$$

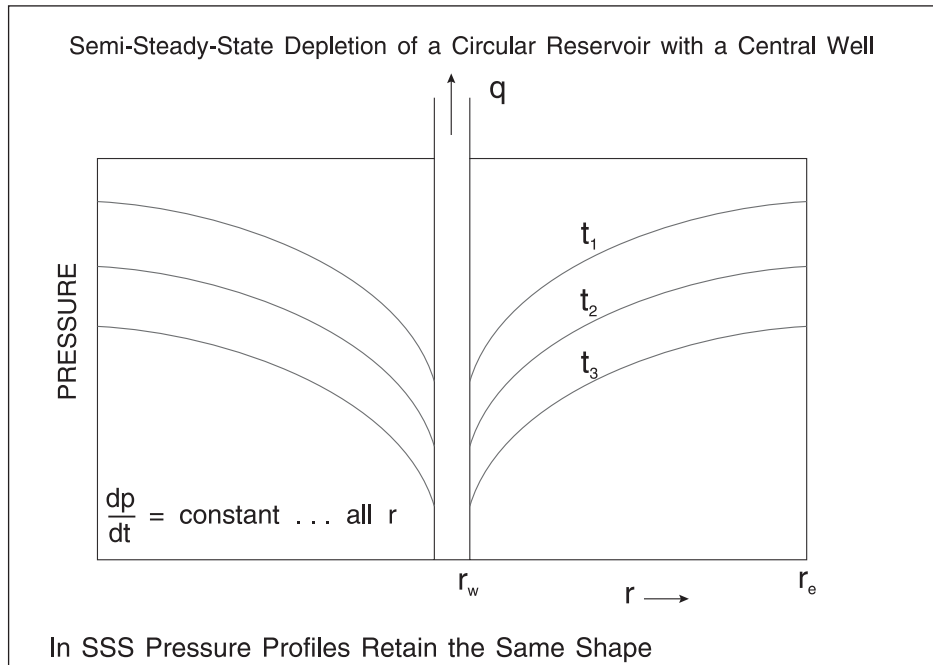


Fig. 1–20. Semi-steady-state depletion of a circular closed reservoir

It should be emphasized that this type of stabilized flow is attained only after a transient period during which the pressure in the region changes from the initial uniform value to a profile characteristic of SSS flow. The transient period is very important in connection with the testing of wells and has been treated at length in *Well Test Design and Analysis*. In the meantime, the concept of uniform pressure decline will be accepted, and the demonstration of the validity of this behavior referred to the mathematical analysis of transient flow is in *Well Test Design and Analysis*. At any point in time, the instantaneous pressure distribution has a volume average value  $\bar{p}$ , defined by Eq. (1–36); this is illustrated in figure 1–21.

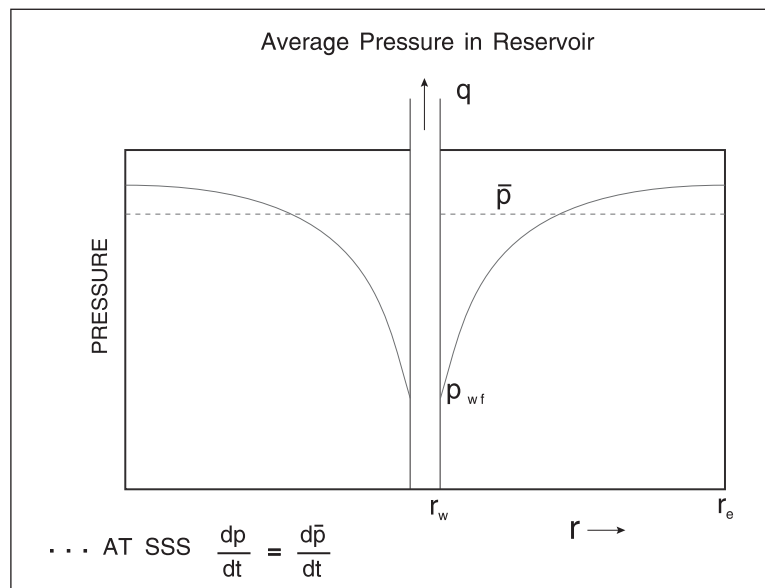


Fig. 1–21. Average pressure during SSS depletion

In Eq. (1–42), an ordinary rather than a partial derivative has been employed since the rate of pressure change is independent of position. If each point in the reservoir is declining in pressure at the same rate, then the fluid is uniformly expanding provided the compressibility is constant everywhere in the system. The fluid compressibility  $c$  is defined as the fractional change in volume per unit change in pressure, i.e.,

$$c = -\frac{1}{V} \frac{\partial V}{\partial p} \quad (1-43)$$

and for liquids this quantity is very nearly constant, i.e., independent of pressure level. The compressibility of a liquid is also very small and small changes in volume result in large changes in pressure and vice versa; this is the basic reason for the inefficiency of depletion drive.

The rate of pressure decline in depletion drive is easily obtained by equating the oil production rate at the well to the overall volume rate of fluid expansion within the drainage region; this is the simplest form of the material balance. Considering a time interval  $dt$  over which the in situ fluid expands by an amount  $dV_p$  due to a pressure change  $dp$ , then using the definition of compressibility

$$q = \frac{dV_p}{dt} = -cV_p \frac{dp}{dt} \quad (1-44)$$

Note that  $dp/dt$  is negative for oil production. Putting the pore volume  $V_p = \pi r_e^2 h \phi$ , where  $\phi$  is the porosity, gives

$$\frac{dp}{dt} = -\frac{q}{c\pi r_e^2 h \phi} \quad (1-45)$$

which is a simple expression for the rate of pressure decline. Equation (1–45) is applicable to any pressure in the distribution since its shape is constant and, in particular, it applies to the average pressure  $\bar{p}$ . In figure 1–22, this quantity is plotted versus time on a Cartesian graph where a straight line of slope  $m^* = -q/(c\pi r_e^2 h \phi)$  is present; this illustrates the primary depletion of an undersaturated reservoir block with no aquifer support. The key point about SSS depletion is the linear decline of the average pressure with time according to Eq. (1–45). If the volume  $V_p$  drained by a particular well is relatively small due to reservoir compartmentalization, then this rate of pressure change can be rapid which will have an adverse effect on the well's production rate.

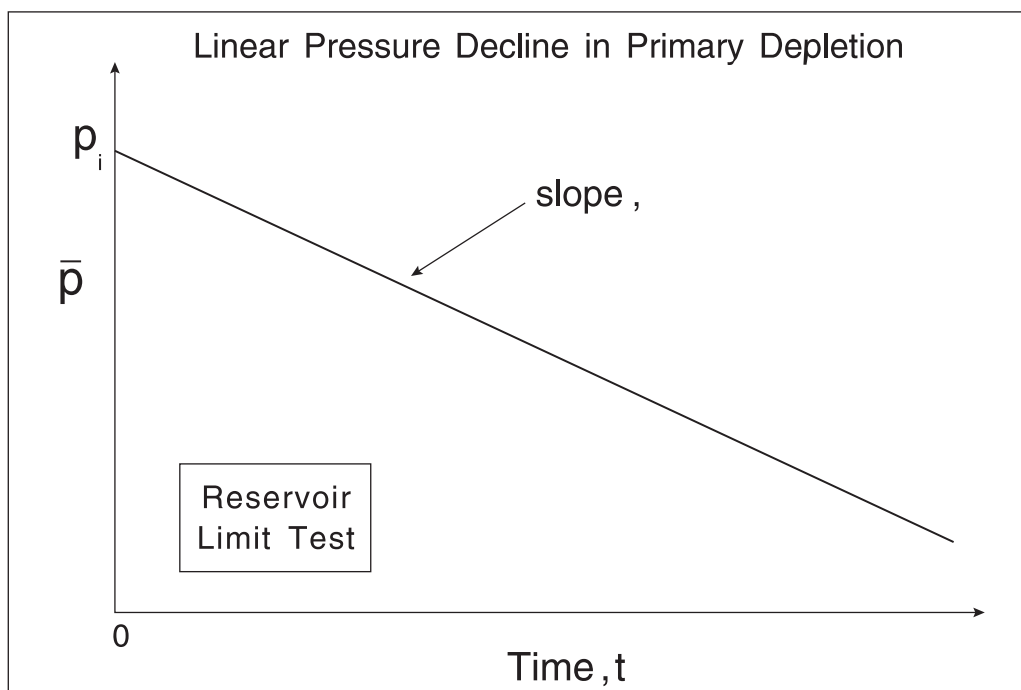


Fig. 1-22. Cartesian plot of average pressure in SSS depletion

The compressibility used in equation (1-45) should also account for the expansion of connate water and porosity reduction due to formation compression as the pore pressure reduces. It was shown in *Well Test Design and Analysis* on transient pressure behavior that the appropriate compressibility in (1-45) is actually

$$c_t = S_{wc}c_w + (1 - S_{wc})c_o + c_f \quad (1-46)$$

where  $S_{wc}$  = connate water saturation,  
 $c_w$  = compressibility of water,  
 $c_o$  = compressibility of oil, and  
 $c_f$  = formation compressibility.

Equation (1-45) should therefore be written in the form

$$\left. \frac{dp}{dt} \right|_{SSS} = - \frac{q_s B}{\pi \phi c_t r_e^2 h} \quad (1-47)$$

The hydrocarbon pore volume (HCPV) is now given by

$$HCPV = (1 - S_{wc}) V_p = (1 - S_{wc}) \pi r_e^2 h \phi \quad (1-48)$$

This quantity is often referred to as the *original-oil-in-place* or OOIP.

## Formation compaction

The formation compressibility  $c_f$  is defined as

$$c_f = - \frac{1}{V_p} \frac{\partial V_p}{\partial p_g} \quad (1-49)$$

Here,  $p_g$  is the grain pressure given as

$$p_g = p_c - p_p \quad (1-50)$$

where  $p_c$  = overburden or confining pressure and  
 $p_p$  = fluid or pore pressure.

Any increase in the grain pressure will lead to some degree of formation compaction, i.e., reduction in pore volume, and in unconsolidated rocks this effect can be quite strong. The formation compressibility at reservoir conditions is a rock property which can be determined by enclosing core samples in a special porosimeter capable of measuring pore volume at different confining pressures.

A dramatic illustration of the effect of formation compaction was seen in the Ekofisk reservoir in the Norwegian sector of the North Sea. The formation comprises high-porosity ( $\phi \approx 0.42$ ) chalk as shown in figure 1–23, where the Danian (Paleocene) chalk approximately 400 ft thick is separated from the 600-ft-thick Cretaceous chalk by a tight zone. The reservoir originally contained 6.1 billion barrels of oil in place and is one of the largest in the North Sea. The initial pressure was 7,000 psia and the field was produced without pressure maintenance (water injection) because it was originally thought to be oil wet. The overburden stress in the reservoir is 9,000 psia and at the initial pore pressure the net effective stress is 2,000 psia. At the end of 1985, after several years of production, the pore (reservoir) pressure had declined to 4,000 psia giving a grain pressure or net effective stress of 5,000 psia. This is a very large increase in the grain pressure for a soft, porous chalk and, with hindsight, it is to be expected that considerable compaction of the formation would occur. The compaction of the reservoir was transmitted to the surface and subsidence of the seabed occurred to such an extent that the topsides of the platform had to be raised by several metres—an enormous engineering undertaking. The extent of the subsidence is plotted in figure 1–24, where an elliptical bowl can be seen to have formed with a maximum depression of 2.5 m. It is ironic that, just as the severity of the subsidence was becoming apparent, a water flood pilot was showing that the fractured reservoir responded well to water injection, contrary to earlier belief. The field is now under pressure maintenance to arrest the formation compaction.

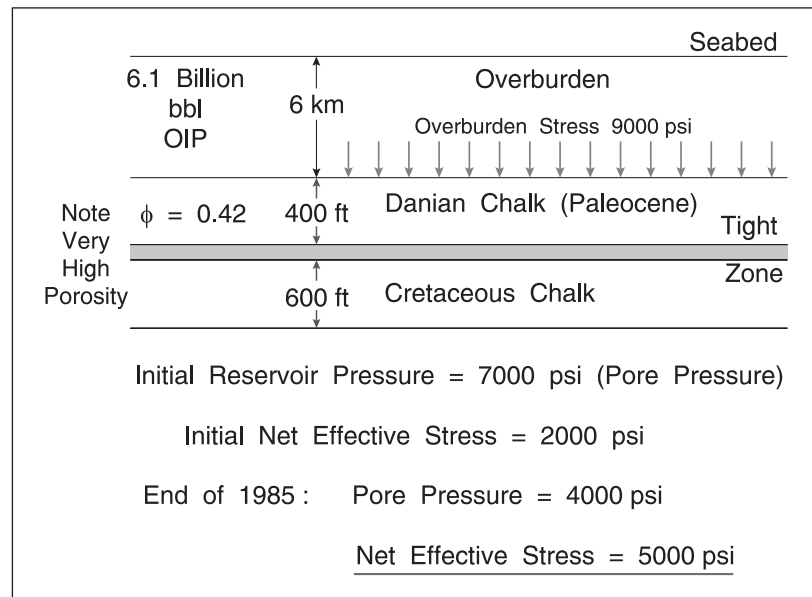


Fig. 1-23. Ekofisk reservoir

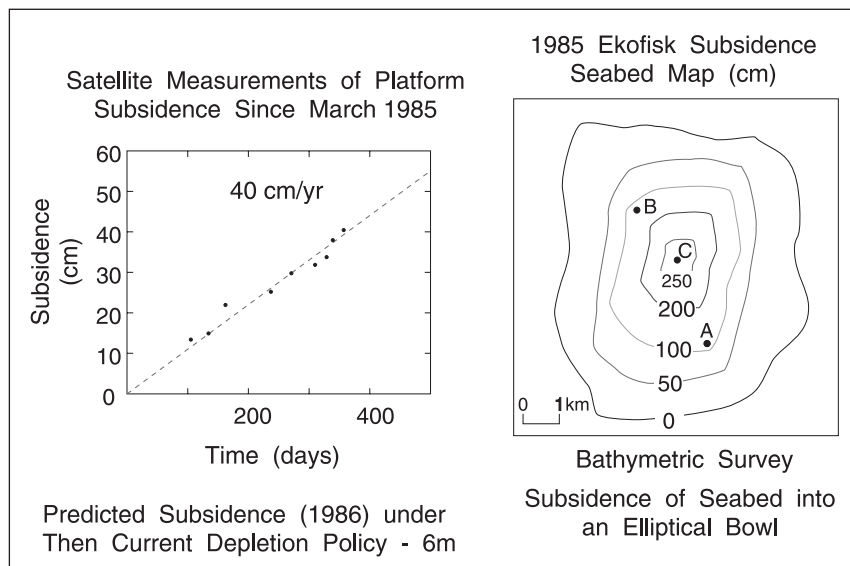


Fig. 1-24. Ekofisk seabed subsidence map (1985)

Recently, Cook and Jewel<sup>4</sup> have given an interesting account of the effect of rock compaction on the Valhall field, again in the Norwegian sector of the North Sea. This is also a high-porosity chalk reservoir undergoing primary pressure depletion, and the authors identified the single most important and unique feature influencing long-term production performance to be reservoir rock compaction. The simulation studies indicate that over half the oil produced from the Valhall reservoir is a direct result of the rock compressibility mechanism. In the crest area, formation compressibilities can be as high as  $150 \times 10^{-6} \text{ psi}^{-1}$  and it is estimated that compaction contributes over 70% of hydrocarbon recovery. Reservoir compaction was first identified in 1986 when subsidence of the surface facilities was detected, consistent with that experienced in the neighboring Ekofisk field.

There has been a considerable amount of work conducted in the area of rock compaction for chalk fields both in Norway and Denmark.<sup>5</sup> With the extraction of reservoir fluids, the reservoir pore pressure decreases and the net stress (overburden weight less reservoir pore pressure) increases to the point where the rock deforms. This compression of the rock provides a massive energy source, which contributes significantly toward oil recovery in the field. Rock compaction tables were used in the simulation studies to allow for the effect. At the outset of history, matching existing published compaction curves were used.<sup>6</sup> However, a satisfactory history match was obtained only by increasing the original rock curves by a factor of 1.5, and the final set of compaction curves are shown in figure 1–25 (after Cook and Jewel). Note the different yield point pressures for the various porosity classes; the yield point defines where the rock goes from elastic to plastic deformation.

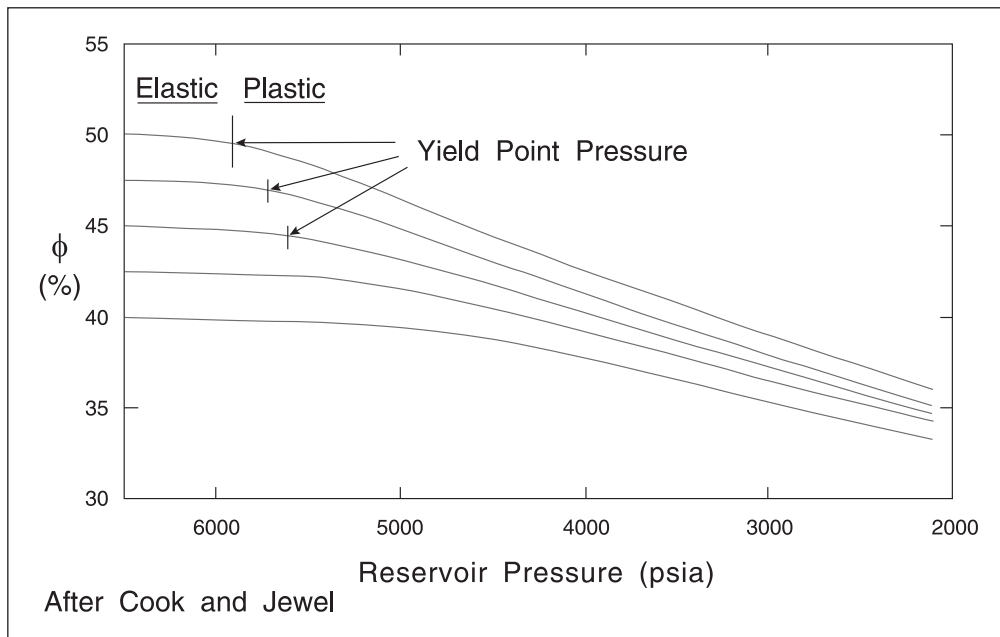


Fig. 1–25. Valhall porosity versus reservoir pressure

A rock compaction hysteresis model is used to account for reservoir pressure increases. For increasing reservoir pressure, rock compressibility is reversed, characterized by a constant  $c_f$  of  $5 \times 10^{-6} \text{ psi}^{-1}$ . This slope represents the elastic compaction region of the rock, consistent for all porosity classes.

The new rock compaction curves were compared to those published for the Ekofisk field<sup>7</sup> and it was found that the slopes of the curves in the plastic region were quite similar. The original rock curves were based on core which had undergone significant net stress prior to extraction from the reservoir. This net stress exposure had hardened the core, resulting in stronger matrix rock which was later used for analysis in the laboratory.

Rock compaction is known to affect permeability, and indeed a permeability decline has been seen in well test analysis results from the Valhall field. In the most extreme case, on the reservoir crest, a measured pressure transient analysis (PTA) permeability of 120 md was corrected to an original value of 300 md.



## Drainage areas and virtual no-flow boundaries

One important feature of this stabilized type of solution when applied to a whole reservoir has been pointed out by Matthews, Brons, and Hazebrook and is illustrated in figure 1–26. This is the fact that once the reservoir is producing under SSS flow conditions, each well will drain from within its own no-flow boundary quite independently of the other wells.

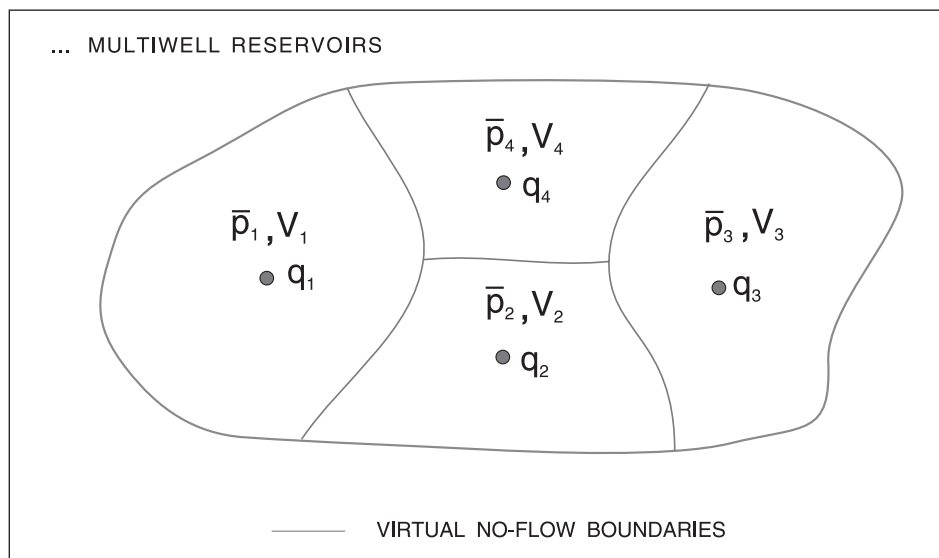


Fig. 1–26. Concept of drainage areas and virtual no-flow boundaries

For this condition,  $dp/dt$  must be constant throughout the entire reservoir; otherwise, flow would occur across the boundaries causing a readjustment in their positions until stability is eventually achieved. In this case, a simple technique can be applied to determine the volume averaged reservoir pressure

$$\bar{p}_{\text{res}} = \frac{\sum_i \bar{p}_i V_i}{\sum_i V_i} \quad (1-51)$$

in which  $V_i$  = the pore volume of the  $i^{\text{th}}$  drainage volume and

$\bar{p}_i$  = the average pressure within the  $i^{\text{th}}$  drainage volume.

Equation (1–45) implies that, since  $dp/dt$  is constant for the reservoir, then if the variation in compressibility is small,

$$q_i \propto V_i \quad (1-52)$$

and hence the volume average in Eq. (1-46) can be replaced by the rate average as follows:

$$\bar{p}_{\text{res}} = \frac{\sum_i \bar{p}_i q_i}{\sum_i q_i} \quad (1-53)$$

Whereas the  $V_i$  are difficult to determine in practice, the  $q_i$  are measured on a routine basis throughout the lifetime of the field thus facilitating the calculation of  $\bar{p}_{\text{res}}$  which is the pressure at which the reservoir material balance is evaluated. Methods for determining the individual  $\bar{p}_i$  are given in the companion volume, *Well Test Design and Analysis*.

Under SSS conditions, the reservoir pore volume drained by a well is proportional to that well's production rate, i.e.,

$$V_i = \frac{V_t q_i}{q_t} \quad (1-54)$$

This concept is based on pore volume and not on area; variations in thickness, porosity, and fluid saturation must be considered when changing drainage volumes estimated from (1-54) to drainage areas. In the assignment of drainage areas, any physical no-flow boundaries must be recognized before virtual boundaries are set on the basis of Eq. (1-54). This is illustrated in figure 1-27, where well 1 is located in a separate fault block and wells 2, 3, and 4 establish drainage areas according to prescription (1-54) within their fault block. This methodology applies to a single phase, constant-compressibility systems only, and an idealized cylindrical reservoir or drainage area with a closed outer boundary is shown in figure 1-28.

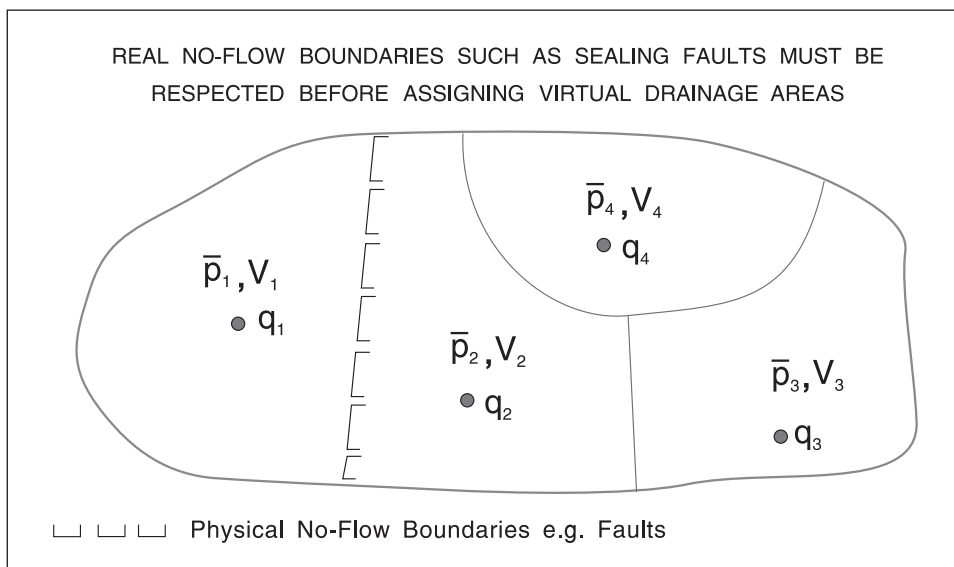


Fig. 1-27. Effect of real no-flow boundaries on the assignment of drainage areas

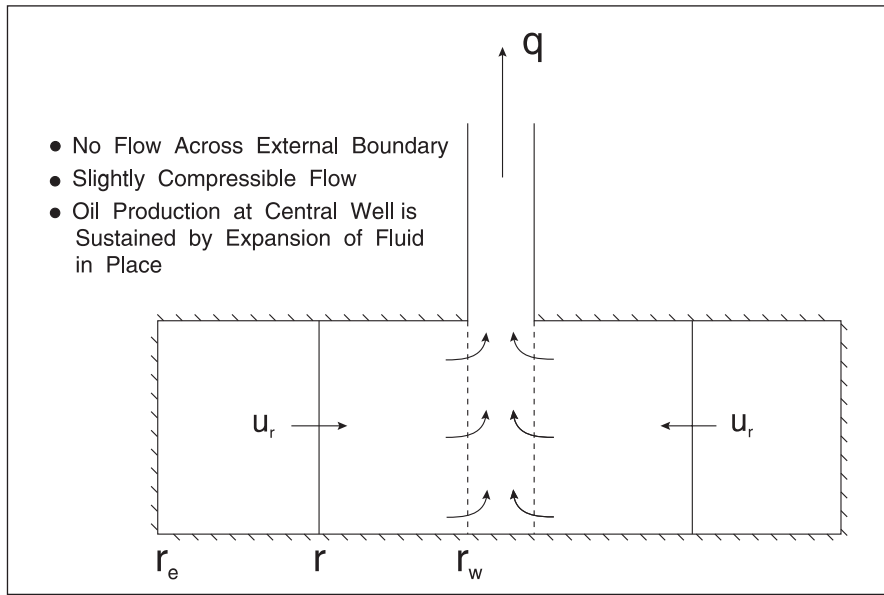


Fig. 1–28. Semi-steady-state (SSS) radial flow in a closed cylindrical reservoir

Equation (1–45) shows how the pressure at any point varies with time. The instantaneous pressure profile in the radial zone can be determined by realizing that the oil flow crossing any circumference at radius  $r$  will be proportional to the fluid volume between  $r$  and  $r_e$ ; this is illustrated in figure 1–29. Thus the oil flow at  $r$ , denoted  $q_r$ , is given by

$$q_r = -c_t \pi(r_e^2 - r^2)h\phi \frac{dp}{dt} \tag{1-55}$$

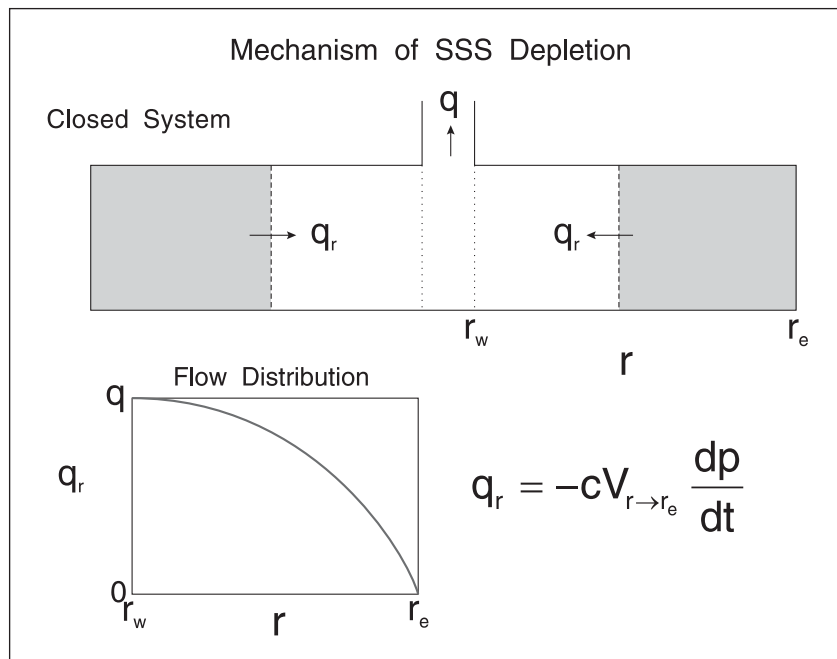


Fig. 1–29. Mechanism of SSS flow

At the well-bore,

$$q = - c_t \pi r_e^2 h \phi \frac{dp}{dt} \quad (1-56)$$

and hence from Eqs. (1-55) and (1-56), there results

$$q_r = q \left( 1 - \frac{r^2}{r_e^2} \right) \quad (1-57)$$

This equation shows how the oil flow at radius  $r$  is determined by the cumulative expansion of all the fluid contained within the rock volume between  $r$  and the external boundary. Naturally,  $q_r$  increases progressively as the wellbore is approached, where it attains the maximum value of  $q$ , which is the well production rate. The local pressure gradient is given by Darcy's law:

$$\frac{q_r}{2\pi r h} = \frac{k}{\mu} \frac{dp}{dr} \quad (1-58)$$

and substituting (1-57) gives

$$q \left( 1 - \frac{r^2}{r_e^2} \right) = \frac{2\pi r h k}{\mu} \frac{dp}{dr} \quad (1-59)$$

in which  $q$  is, of course, constant. Separating the variables and integrating between the limits,

$$r = r_w, \quad p = p_w \quad \text{and} \quad r = r_e, \quad p = p_e$$

results in

$$\int_{r_w}^{r_e} \left( 1 - \frac{r^2}{r_e^2} \right) \frac{dr}{r} = \frac{2\pi k h}{q\mu} \int_{p_w}^{p_e} dp \quad (1-60)$$

The analytical solution to (1-60) takes the form

$$q = \frac{2\pi k h (p_e - p_w)}{\mu \left( \ln \frac{r_e}{r_w} - \frac{1}{2} + \frac{r_w^2}{2r_e^2} \right)} \quad (1-61)$$

and the pressure at radius  $r$  is given by the equivalent formula

$$q = \frac{2\pi kh(p - p_w)}{\mu \left( \ln \frac{r}{r_w} - \frac{r^2}{2r_e^2} + \frac{r_w^2}{2r_e^2} \right)} \quad (1-62)$$

For  $r_e \gg r_w$ , which is the usual case, then (1-61) may be written as

$$q = \frac{2\pi kh(p_e - p_w)}{\mu \left( \ln \frac{r_e}{r_w} - \frac{1}{2} \right)} \quad (1-63)$$

This is the well inflow equation under SSS conditions. The pressure profile and flow distribution for SSS flow are shown in figure 1-30. In terms of dimensionless overall drawdown, Eq. (1-63) may be written as

$$\frac{p_e - p_w}{\frac{q\mu}{2\pi kh}} = p_{De} = \ln r_{De} - \frac{1}{2} \quad (1-64)$$

Surprisingly, the difference between the pressure profile in SS and SSS flow is not great. Considering Eq. (1-62), it is obvious that for  $r$  close to  $r_w$  the term  $r^2 / 2r_e^2 - r_w^2 / 2r_e^2$  is very small indeed and the two profiles are indistinguishable. The overall drawdown is greater for SS flow because the well production  $q$  passes unchanged through the whole radial zone; quantitatively, Eq. (1-64) shows that the dimensionless overall drawdown in SS flow exceeds that in SSS flow by one half, which is not much when  $\ln r_{De}$  is of the order of 8, say.

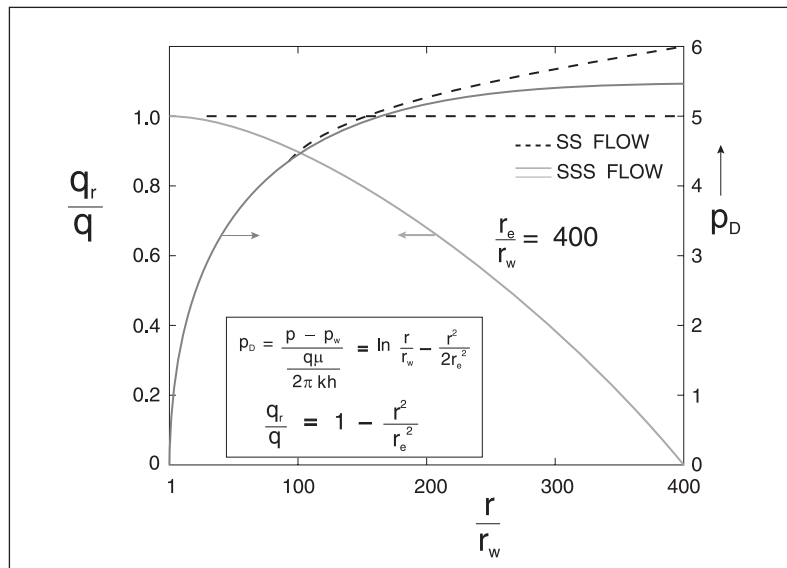


Fig. 1-30. Dimensionless pressure profile and flow distribution in SSS radial flow

## Well Inflow in terms of average pressure

The particular inflow equation represented by (1-63) is not of much use practically since the pressure at the external boundary cannot be measured directly. It is therefore more common to express the pressure drawdown in terms of  $\bar{p} - p_w$  instead of  $p_e - p_w$  since  $\bar{p}$ , which is the average pressure within the drainage volume, can be readily determined from a well test as shown in *Well Test Design and Analysis*. To express the inflow equation in terms of the average pressure, it is first necessary to derive an expression for  $\bar{p}$  as

$$\bar{p} = \frac{\int_{r_w}^{r_e} p dv}{\int_{r_w}^{r_e} dv} \quad (1-65)$$

and since  $dV = 2\pi r h \phi dr$ , this becomes

$$\bar{p} = \frac{2\pi h \phi \int_{r_w}^{r_e} p r dr}{\pi (r_e^2 - r_w^2) h \phi} \quad \text{i.e.} \quad \bar{p} = \frac{2}{r_e^2} \int_{r_w}^{r_e} p r dr \quad (1-66)$$

since  $r_e^2 - r_w^2 = r_e^2$ . Hence, substituting Eq. (1-62) for  $p$  results in

$$\begin{aligned} \bar{p} &= \frac{2}{r_e^2} \int_{r_w}^{r_e} \left[ p_w + \frac{q\mu}{2\pi kh} \left( \ln \frac{r}{r_w} - \frac{r^2}{2r_e^2} \right) \right] r dr \\ &= p_w + \frac{2}{r_e^2} \cdot \frac{q\mu}{2\pi kh} \int_{r_w}^{r_e} r \left( \ln \frac{r}{r_w} - \frac{r}{2r_e^2} \right) dr \end{aligned} \quad (1-67)$$

The first term of the integrand can be evaluated by integration by parts, i.e.,

$$\begin{aligned} \int_{r_w}^{r_e} r \ln \frac{r}{r_w} dr &= \left[ \frac{r^2}{2} \ln \frac{r}{r_w} \right]_{r_w}^{r_e} - \int_{r_w}^{r_e} \frac{1}{r} \frac{r^2}{2} dr \\ &= \left[ \frac{r^2}{2} \ln \frac{r}{r_w} \right]_{r_w}^{r_e} - \left[ \frac{r^2}{4} \right]_{r_w}^{r_e} \end{aligned}$$

$$= \frac{r_e^2}{2} \ln \frac{r_e}{r_w} - \frac{r_e^2}{4}$$

again assuming  $r_e \gg r_w$ .

Integration of the second term gives

$$\int_{r_w}^{r_e} -\frac{r^3}{2r_e^2} dr = -\left[\frac{r^4}{8r_e^2}\right]_{r_w}^{r_e} = -\frac{r_e^2}{8}$$

The complete integral is then

$$= \frac{r_e^2}{2} \ln \frac{r_e}{r_w} - \frac{r_e^2}{4} - \frac{r_e^2}{8} = \frac{r_e^2}{2} \ln \frac{r_e}{r_w} - \frac{3r_e^2}{8} \quad (1-68)$$

Accordingly, Eq. (1-67) becomes

$$\bar{p} = p_w + \frac{q\mu}{2\pi kh} \left[ \ln \frac{r_e}{r_w} - \frac{3}{4} \right] \quad (1-69)$$

Comparison of Eqs. (1-69) and (1-63) shows that the cell extremity pressure exceeds the average cell pressure by an amount

$$\Delta p = p_e - \bar{p} = \frac{q\mu}{2\pi kh} \cdot \frac{1}{4} \quad (1-70)$$

At the beginning of this section it was stated that a SSS PI based on boundary pressure was not practical. However in chapter 4 of *Well Test Design and Analysis* it is demonstrated that pressure transient analysis yields boundary pressures more directly than average pressures. The use of the average pressure PI is really a consequence of the application of material balance methods.

## Well Productivity in a Bounded Drainage Area

The productivity of a well in a bounded drainage area is normally defined in terms of the average pressure  $\bar{p}$ , since this quantity is observable from a well test. Hence the productivity index of the well is given by the equation

$$J_{SSS} = \frac{q_s}{\bar{p} - p_w} = \frac{q}{B(\bar{p} - p_w)} \quad (1-71)$$

The SSS well inflow equation is

$$q = \frac{2\pi kh(\bar{p} - p_w)}{\mu \left( \ln \frac{r_e}{r_w} - \frac{3}{4} \right)} \quad (1-72)$$

Hence, on substituting (1-72) in (1-71), the PI  $J_{SSS}$  is given by

$$J_{SSS} = \frac{2\pi kh}{B\mu \left( \ln \frac{r_e}{r_w} - \frac{3}{4} \right)} \quad (1-73)$$

provided stabilized flow has been achieved. In field units, Eq. (1-73) becomes

$$J_{SSS} = \frac{1.127 \times 10^{-3} 2\pi kh}{B\mu \left( \ln \frac{r_e}{r_w} - \frac{3}{4} \right)} \text{ bbl/d/psi} \quad (1-74)$$

For true single-phase SSS flow, the productivity index is constant, independent of flow rate or drawdown as shown by Eq. (1-74). However, in practice the linearity between flow rate and drawdown is not preserved and the PI declines somewhat. The cause of this decrease may be due to

- inertial effects near the well-bore at high flow rates;
- decrease in the permeability to oil due to the presence of free gas caused by the pressure falling below the bubble point;
- increase in oil viscosity associated with liberation of gas or simply reduced pressure;
- reduction in formation permeability due to rock compressibility.

In situations where the near-well-bore pressure falls below the bubble point or dew point and two-phase flow occurs, it is necessary to employ a two-phase pseudo-pressure to express well productivity; this topic is treated in chapter 3.

## Generalized form of the semi-steady-state inflow equation

The SSS inflow equation developed in the previous section is a little restrictive in that it only applies to a well producing from the center of a circularly shaped drainage area. When a whole reservoir is producing under SSS conditions, each well will develop its own fixed drainage boundary as shown in figure 1-27 and the shapes of these may be far from circular. In particular, a given



well may not be symmetrically located in the drainage region and this has a pronounced effect on SSS drawdown. However noncircular, nonsymmetric systems do indeed eventually reach SSS conditions although it may take much longer for the flow to stabilize than in the case of a circular, central well system. Not unexpectedly, the average flow paths are longer for unsymmetrically placed wells and a greater drawdown is experienced than in a symmetric system of the same overall area. The problem of areal flow convergence and bunching of the streamlines because the well lies in the proximity of a no-flow boundary (real or virtual) is illustrated in figure 1–31.

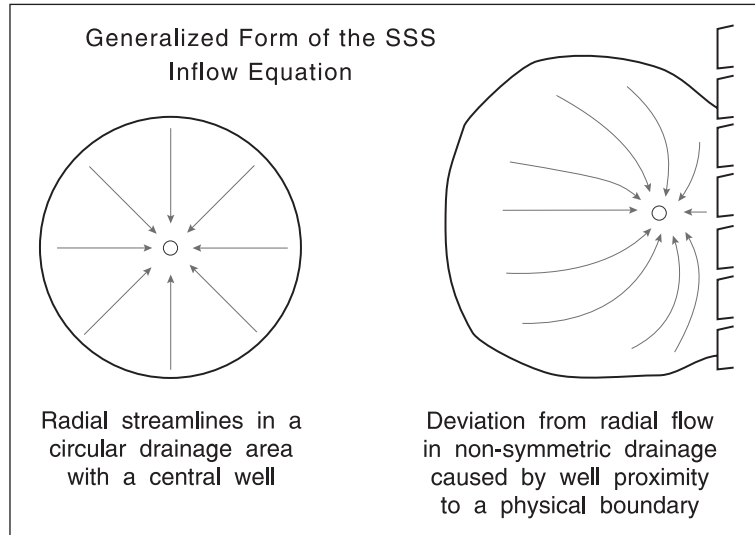


Fig. 1–31. Deviation from pure radial flow in nonsymmetric drainage area

**Selection of Dietz Shape Factors**


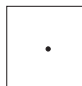
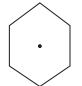

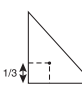
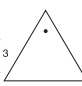
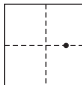
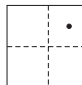
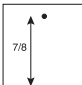


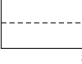
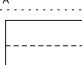
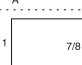
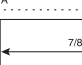
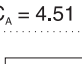
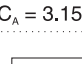
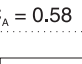
	$C_A$ 31.62 $t_{DA_{SSS}}$ 0.1		$C_A$ 30.88 $t_{DA_{SSS}}$ 0.1		$C_A$ 31.6 $t_{DA_{SSS}}$ 0.1
	$C_A$ 27.6 $t_{DA_{SSS}}$ 0.2		$C_A$ 21.9 $t_{DA_{SSS}}$ 0.4		$C_A$ 0.098 $t_{DA_{SSS}}$ 0.9
	$C_A$ 12.98 $t_{DA_{SSS}}$ 0.7		$C_A$ 4.51 $t_{DA_{SSS}}$ 0.6		$C_A$ 3.34 $t_{DA_{SSS}}$ 0.7
	$C_A = 21.8$ $t_{DA_{SSS}} = 0.3$		$C_A = 10.8$ $t_{DA_{SSS}} = 0.4$		$C_A = 2.08$ $t_{DA_{SSS}} = 1.7$
	$C_A = 4.51$ $t_{DA_{SSS}} = 1.5$		$C_A = 3.15$ $t_{DA_{SSS}} = 0.4$		$C_A = 0.58$ $t_{DA_{SSS}} = 2.0$
	$C_A = 5.38$ $t_{DA_{SSS}} = 0.8$		$C_A = 2.70$ $t_{DA_{SSS}} = 0.8$		$C_A = 0.23$ $t_{DA_{SSS}} = 4.0$

Fig. 1–32. Shape factors for various closed single well drainage areas

The inflow equation is generalized by introducing the so-called Dietz shape factors, denoted by  $C_A$ , which are presented for a variety of different geometrical configurations in figure 1–32. The basic inflow equation for a radial system at the SSS is

$$\bar{p} - p_w = \frac{q\mu}{2\pi kh} \left( \ln \frac{r_e}{r_w} - \frac{3}{4} \right) \quad (1-75)$$

This may be written in the alternative form

$$\bar{p} - p_w = \frac{q\mu}{2\pi kh} \cdot \ln \frac{\pi r_e^2}{\pi r_w^2 e^{3/2}} \quad (1-76)$$

in which the natural log can alternatively be expressed as

$$\frac{4\pi r_e^2}{4\pi e^{3/2} r_w^2} = \frac{4\bar{A}}{56.32 r_w^2} = \frac{4\bar{A}}{\gamma 31.6 r_w^2} \quad (1-77)$$

where  $\bar{A}$  is the area being drained,  $\gamma$  is the exponential of Eulers constant equal to 1.781, and 31.6 is the Dietz shape factor  $C_A$  for circular geometry. The quantity  $\gamma$  arises naturally in the analysis of transient pressure behavior and the reason for its inclusion in (1–77) will become clear later. The generalized form of the SSS inflow equation is written therefore as

$$\bar{p} - p_w = \frac{q\mu}{2\pi kh} \cdot \frac{1}{2} \ln \frac{4\bar{A}}{\gamma C_A r_w^2} \quad (1-78)$$

which states that the SSS drawdown depends both on the overall area and the geometric configuration of the drainage region. The shape factors  $C_A$  have been established for very many configurations by Dietz, and those for highly unsymmetric systems fall considerably below the value of 31.6 for true radial flow. Thus the drawdown is affected by the location of the well within its drainage area. The procedure for allocating drainage areas has already been described in section “Semi-steady-state Solution”. Naturally, it is never possible to obtain the exact shape of the drainage volume, but a reasonable approximation can usually be made which can considerably improve the accuracy of calculations made using the inflow equation. Note that the shape factor is in fact a correction for deviation from true radial flow.

Some authors in Norway prefer to express the effect of well location and drainage area shape in terms of a pseudo-skin factor  $S_A$ , defined through the identity

$$\frac{1}{2} \ln \frac{4\bar{A}}{\gamma C_A r_w^2} = \ln \frac{r_e}{r_w} - \frac{3}{4} + S_A \quad \text{where} \quad r_e = \sqrt{\frac{\bar{A}}{\pi}} \quad (1-79)$$

Solving Eq. (1-79) for  $S_A$  yields

$$S_A = \frac{1}{2} \ln \frac{4\pi}{\gamma C_A} + \frac{3}{4} \quad (1-80)$$

and the generalized well inflow equation may be written in the alternative form

$$\bar{p} - p_w = \frac{q\mu}{2\pi kh} \left( \ln \frac{r_e}{r_w} - \frac{3}{4} + S_A \right) \quad (1-81)$$

where  $S_A$  is a pseudo-skin representing the additional pressure drop due to deviation from pure radial flow given by (1-80). It is a matter of preference whether Eq. (1-78) or (1-81) is used to express the effect of drainage area shape on well productivity index. Dietz shape factors for a wide variety of shapes and well locations are given in figure 1-32.

Also listed in figure 1-32 is a dimensionless time  $(t_{DA})_{SSS}$  defined as

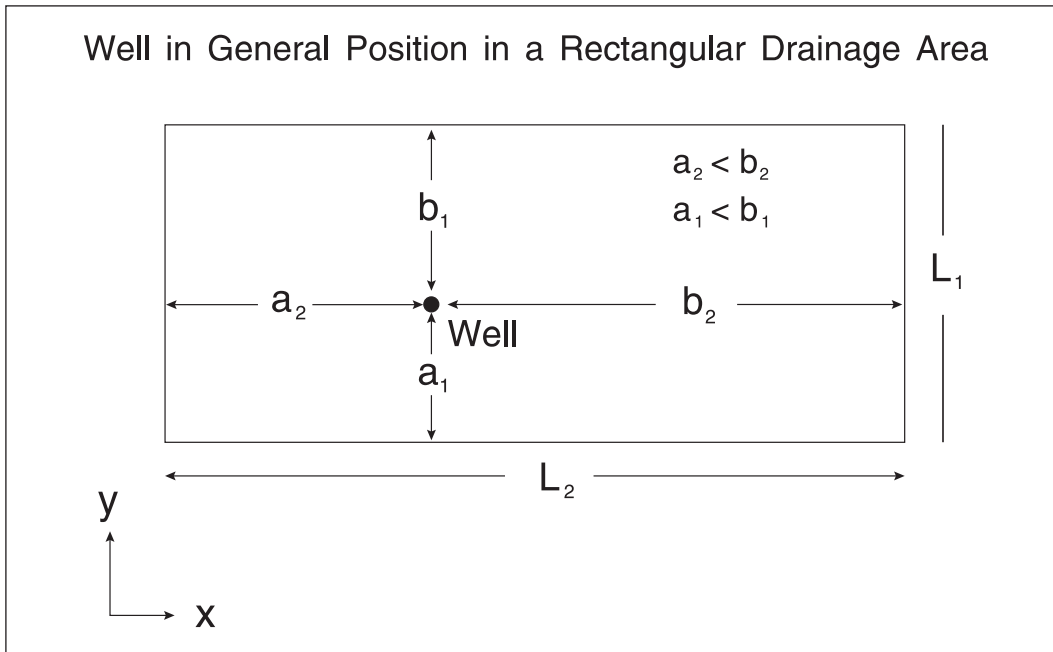
$$(t_{DA})_{SSS} = \frac{kt_{SSS}}{\phi\mu c_t \bar{A}} \quad (1-82)$$

in which  $t_{SSS}$  is the time for the well, which has been producing at a reasonably steady rate of production, to reach the SSS condition. Unless the calculated value of  $t_{DA}$  exceeds the figure quoted for each geometrical configuration, then the well pressure distribution has not stabilized in shape and is not producing under SSS conditions and the Dietz shape factors cannot be used.

## Analytical formulae for Dietz shape factors

In many cases, a rectangular drainage area is sufficient to describe the physical situation; this is especially true in the case of long, narrow reservoirs like channel sands. Yaxley<sup>8</sup> has given a very convenient approximate formula for computing  $C_A$  in this geometry, which is illustrated in figure 1-33. The overall dimensions of the rectangle are denoted  $L_1$  and  $L_2$ , where  $L_1 < L_2$ , i.e.,  $L_1$  is the width of the reservoir and  $L_2$  is the length. The shape of the rectangular reservoir is characterized by the ratio  $L_2/L_1$ . The well location within the rectangle is defined by the distances  $a_2$ ,  $b_2$  and  $a_1$ ,  $b_1$  as shown in the diagram and the dimensionless location parameters:

$$x_D = a_D = \frac{a_2}{L_2} \quad b_D = \frac{b_2}{L_2} = 1 - a_D \quad \text{and} \quad y_D = c_D = \frac{a_1}{L_1} \quad (1-83)$$



**Fig. 1-33.** Well in an arbitrary position in a closed rectangle

For a well in the center of the rectangle,  $x_D = y_D = 0.5$ . The explicit formula for  $C_A$  in this geometry is

$$C_A = \frac{4\bar{A}}{\gamma r_w^2 \exp \left[ \frac{4\pi L_2}{L_1} \left( \frac{a_D^3}{3} + \frac{b_D^3}{3} \right) + 2 \ln \left( \frac{L_1}{2\pi r_w \sin(\pi c_D)} \right) \right]} \quad (1-84)$$

where  $\gamma = 1.781$  is the exponential of Euler's constant. This equation is very useful for quickly predicting Dietz shape factors for a well in arbitrary position in any rectangle. As an example, for a well in the center of a 5:1 rectangle, i.e.,  $L_2/L_1 = 5$  and  $x_D = y_D = 0.5$ , it gives  $C_A = 2.359$ , which is identical to the value quoted by Dietz. However, it should be pointed out that this equation is not valid as  $c_D$  tends to zero and the well approaches one boundary of the rectangle as illustrated in figure 1-34. In this case, the behavior can be computed from that of a double rate well at the center of a rectangle of twice the width as shown in the diagram; by equating the two results it can be demonstrated that the minimum value of  $c_D$  which should be used in Eq. (1-84) is given by

$$c_D = \frac{1}{\pi} \sin^{-1} \left( \frac{\pi r_w}{2L_1} \right) \quad (1-85)$$

This modification allows formula (1–84) to be used when the well is very close to one boundary. However, if the well is located in the corner of the rectangle, Eq. (1–84) (even with the modification) will still fail to give a good result and the alternative formulation in terms of a wedge-shaped drainage area is preferable; this is described shortly.

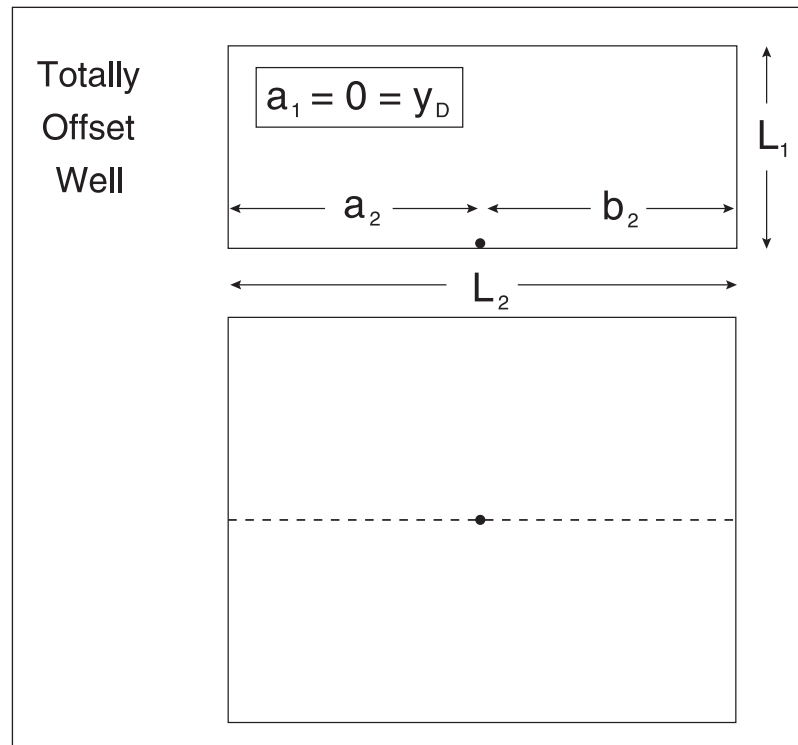


Fig. 1–34. Well very close to one boundary of the rectangle

An interesting application of the Dietz shape factor concept arises in connection with well clusters as illustrated in figure 1–35, where a group of four wells drilled from a common location is located quite close together in the reservoir. In the giant Gronigen gas field in Holland, for example, such well clusters are a significant feature of the development, since it is very convenient for both operational and environmental reasons to have groups of wells drilled from one location and tied into a common manifold. In figure 1–35, the four wells, presumed to be of roughly equal rate, are located at the center of a large reservoir block at some average pressure  $\bar{p}$ . By symmetry, each well will drain a quarter of the total system, and individual rectangular drainage areas with a well situated in the corner will develop as indicated. If the spacing of the well cluster is small compared to the dimensions of the block in which the pod is located, then the Dietz shape factors will be quite small and the individual productivity indices will be affected by the proximity of the virtual no-flow boundaries. Thus the Dietz shape factor concept allows the effect of interference between the closely spaced wells to be evaluated. Suppose that the cluster spacing is chosen such that  $x_D = y_D = 0.1$  for each of the individual wells drainage area. Then  $C_A$  from (1–85) is 0.4 and the pseudo-skin  $S_A$  due to well interference is given by Eq. (1–80); the value turns out to be 2.2, which is not very significant. The conclusion is that unless the wells in the cluster are very close together indeed, then the well interference effect is quite small and the cluster concept is, in fact, a sensible arrangement. If the cluster is increased to five wells, as shown in figure 1–36, the drainage areas take on a more complicated shape.

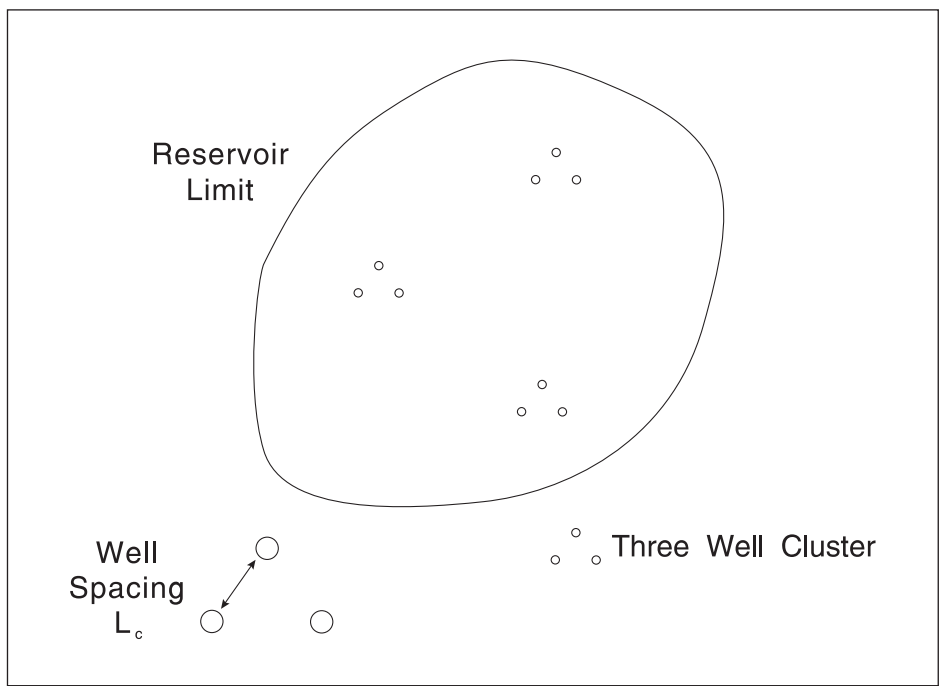


Fig. 1-35. Well cluster

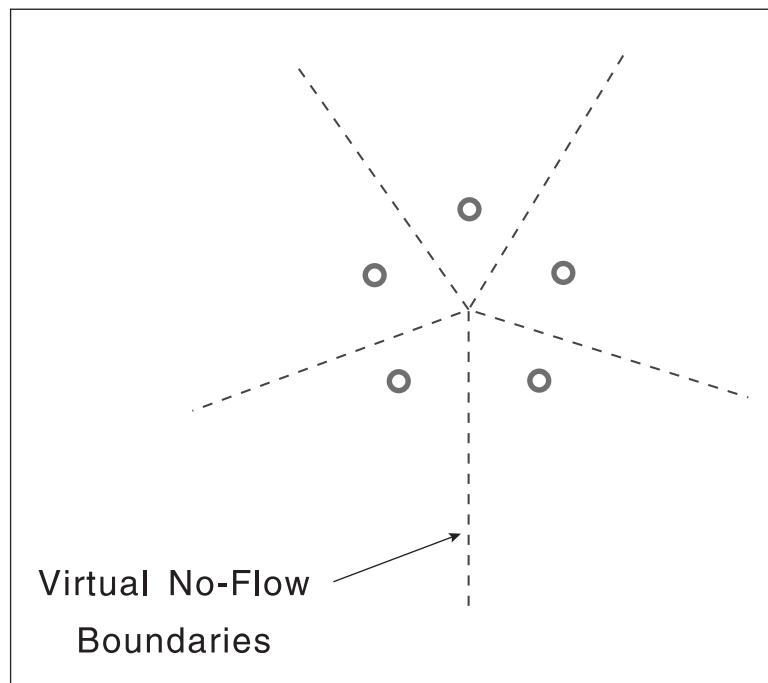


Fig. 1-36. Five-well cluster

The formula (1-85) given above for the Dietz shape factor for a well in general position in a rectangle will cover a wide variety of practical situations. However, in some circumstances the drainage area is better approximated by a triangular or wedge form as illustrated in figure 1-37. Again, Yaxley has given a convenient formula for calculating the shape factor in this geometry, viz.,

$$C_A = \frac{4\bar{A}}{\gamma r_w^2 \exp \left[ \frac{4\pi}{\theta} \left( \ln \frac{r_e}{r_w} - \frac{3}{4} \right) + 2 \ln \frac{\theta r_o}{2\pi r_w \sin \left( \frac{\pi\theta_o}{\theta} \right)} \right]} \tag{1-86}$$

where 
$$\bar{A} = \frac{\theta}{2\pi} \pi r_e^2 = \frac{\theta}{2} r_e^2$$

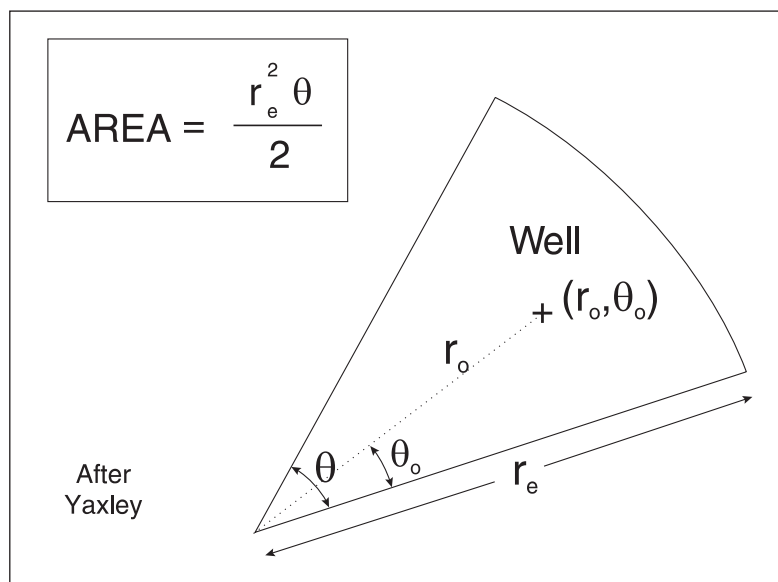


Fig. 1-37. Triangular or wedge-shaped drainage area

Although the shape factors are often quoted for the well located in various positions in a closed triangle, this formula for a wedge shaped drainage area is just as useful and has the advantage of being quite general.

The application of Eq. (1-86) can be demonstrated by considering a well on the bisector of two faults at an angle of 60°; thus  $\theta = \pi/3$  and  $\theta_o = \pi/6$ . For the purposes of computation, the external radius of the wedge  $r_e$  is taken to be 1,000 and the wellbore radius 1.0. In table 1-1, the Dietz shape factor for various values of  $r_o$  are tabulated, and it can be seen that as  $r_o$  approaches  $r_w$ , the shape factor becomes very small indeed. In the limiting case of  $r_o = r_w$ , the well is located at the apex and  $C_A$  is given by the condition

$$p_D = \frac{2\pi}{\theta} \left( \ln \frac{r_e}{r_o} - \frac{3}{4} \right) = \frac{1}{2} \ln \frac{4\bar{A}}{\gamma C_A r_w^2} \tag{1-87}$$

It is this condition that gives rise to the extremely small values of  $C_A$  as the well position becomes coincident with the intersection point. The conclusion from this analysis is that wells should not be located very close to intersecting barriers whether they be physical in nature or virtual no-flow boundaries in multiple well situations. It is really Eq. (1–86) that determines how close wells in a cluster can be before serious deterioration in performance sets in, i.e., even when the angle of intersection is  $90^\circ$ , this form is preferable in corner geometry. Note that the term

$$\ln \frac{\theta_o r_o}{2\pi r_w \sin(\pi\theta_o/\theta)}$$

in Eq. (1–86) is analogous to the Hantush flow convergence term

$$\ln \frac{L_1}{2\pi r_w \sin(\pi c_D)}$$

in the rectangle formulation (1–84); thus  $\theta_o r_o$  is analogous to the channel width  $L_1$ , and  $\theta_o/\theta$  corresponds to the geometric location of the well in the channel  $c_D$ . The formulation of these wedge equations by Yaxley presents a powerful yet simple method of handling a difficult problem.

**Table 1–1.** Dietz shape factors for a well on the bisector of intersecting faults ( $r_e = 1,000$ ,  $r_w = 1$ )

Intersection angle	$\theta = 60^\circ$	$\theta = 90^\circ$	
	Well distance from apex, $r_o$	Dietz shape factor, $C_A$	Dietz shape factor, $C_A$
	1	$9.52895 \times 10^{-27}$	$7.1163 \times 10^{-16}$
	5	$2.3264 \times 10^{-18}$	$1.77907 \times 10^{-10}$
	10	$3.4304 \times 10^{-15}$	$1.1386 \times 10^{-8}$
	20	$3.51275 \times 10^{-12}$	$7.2871 \times 10^{-7}$
	50	$3.3500 \times 10^{-8}$	$1.77907 \times 10^{-4}$
	100	$3.4304 \times 10^{-5}$	$1.1386 \times 10^{-2}$
	200	$3.51275 \times 10^{-2}$	0.7287
	300	2.0256	8.3004
	350	9.46298	20.9305
	400	35.9706	46.6372

In this example, it is evident that the wedge formula is valid provided the well distance from the apex  $r_o$  is less than about one-third of the external radius  $r_e$ ; if Eq. (1–86) predicts a Dietz shape factor value greater than the upper limit of 31.62, then obviously the actual predicted quantity should be replaced by this theoretical limit. The very small values of  $C_A$  listed in table 1–10 show how much well productivity index will be diminished if the well is located near the apex of intersecting faults.



# Wellbore Damage and Improvement Effects

## Introduction

In the preceding treatment of steady-state and SSS radial flow, the porous medium has been assumed to be of uniform permeability to oil right up to the well-bore or sandface at  $r = r_w$ . The dominant influence of the near-well-bore region in determining drawdown has been pointed out and it has been tacitly assumed that the wellbore radius  $r_w$  is constant over the producing zone and accurately known. Any variations in the formation permeability in the vicinity of the wellbore or in the actual wellbore radius will seriously invalidate the simple radial flow models. In practice, both these effects occur to a greater or lesser extent in a real well and the basic radial flow models must be modified to include an allowance for such phenomena. This is achieved by including a correction term known as the *skin factor*, which represents the difference between the bottom-hole pressure predicted by the homogeneous radial flow model and the proper value allowing for permeability or well-bore radius variation.

In many wells, the formation near the wellbore is damaged during the drilling phase especially if the completion and drilling fluids have not been well selected and controlled in quality. In producing wells, permeability impairment can result from

- mud solids invasion and plugging;
- clay swelling on contact with mud filtrate;
- chemical precipitation or scaling, e.g., calcium carbonate or barium sulfate;
- particle tilting;
- movement of sand fines towards the wellbore;
- sand consolidation treatment; and
- formation compaction.

Injection wells are also prone to formation damage associated with

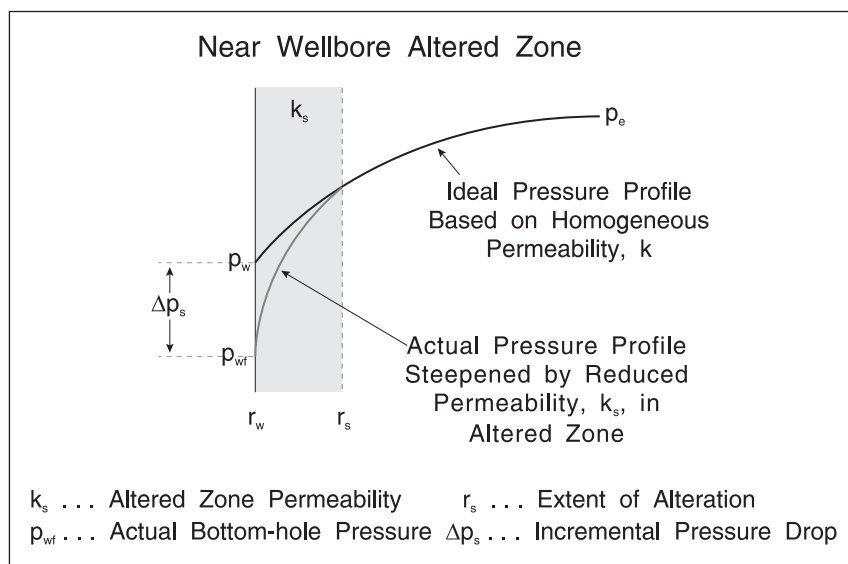
- plugging due to particulate matter in the injection fluid;
- clay alteration on contact with injected fluid, e.g., sea water; and
- water incompatibility.

Of course, it is always possible to increase the permeability in the vicinity of a well by various stimulation techniques such as acidizing and fracturing, so both damage and improvement can occur. In the case of sea water injection wells, the process of thermal fracturing due to the development of a cold ring around the wellbore can lead to significant improvement in well performance. Such methods are very important in maintaining well productivity.

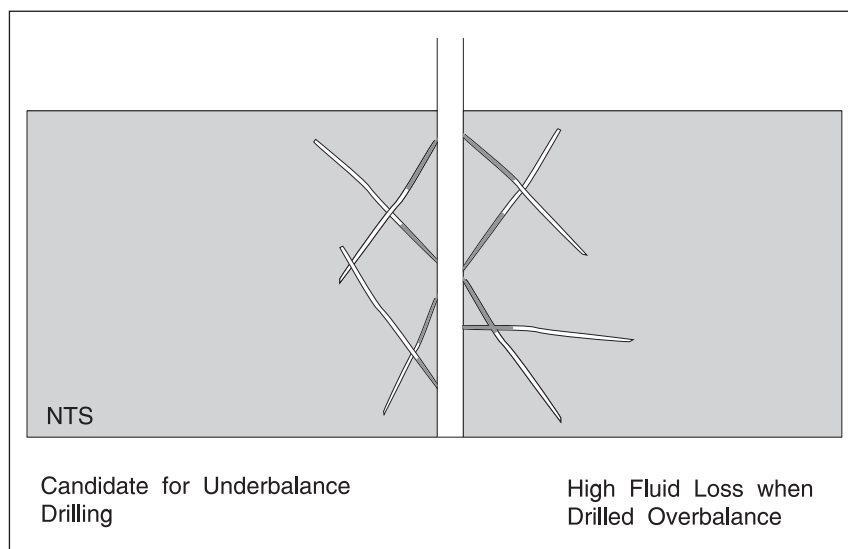
## Near-wellbore altered zone

In many situations, the phenomenon of formation damage is associated with a radial altered region around the wellbore as illustrated in figure 1–38a; here, the permeability within the cylindrical altered region, which extends out to a radius  $r_a$ , is  $k_a$ . When  $k_a < k$ , the pressure profile

is steepened by the reduced permeability. The difference between the predicted wellbore pressure assuming no damage  $p_w$  and the actual bottom-hole pressure allowing for alteration  $p_{wf}$  is known as the *skin pressure drop*  $\Delta p_s$ . This is the incremental pressure drop due to the near-wellbore formation damage. One of the main physical origins of an altered zone is the occurrence of mud filtrate invasion during drilling. In non-fractured formations, the invasion of mud solids is not usually a problem since the internal filter cake is of small extent and will be bypassed by perforation tunnels. However, in the Elephant field in Libya, the pore size of the rock was large enough to allow the deep invasion of small particles from the mud. These fines were associated with wind-blown desert dust and the remedy was to cover the mud units to prevent dust contamination. In formations that exhibit natural fracturing, the fracture width is large enough to allow mud solids invasion as illustrated in figure 1–38b. In this case, the connection with the fracture network is damaged and such formations are candidates for underbalance drilling. Note that the presence of fractured zones is indicated by high mud fluid losses during drilling.



**Fig. 1–38a.** Near-wellbore altered zone



**Fig. 1–38b.** Invasion of Natural Fractures by Mud Solids

In figure 1–39, the borehole condition is represented with the mud hydrostatic pressure at a certain measured depth designated  $p_m$  and the formation pore pressure at the same depth labeled  $p_f$ . The difference  $p_m - p_f$  is known as the *overbalance*. The mud system is designed to form an impermeable filter cake which minimizes the leak-off of mud filtrate into the formation. However, the filter cake has a finite permeability and there is always some fluid loss occurring. In the case of water-based mud, the salinity of the mud filtrate is usually less than that of formation water and this invasion of a different fluid causes alteration of dispersed clay in the formation. The greatest loss of fluid occurs immediately behind the bit before a filter cake has formed; this is known as *spurt loss*. During the period when mud is circulating, the rate of fluid loss attains an approximately constant value since the filter cake thickness reaches an equilibrium due to a balance between cake erosion and cake deposition. When mud circulation is stopped, the filter cake gradually increases in thickness and the mud fluid loss rate slowly decreases during this period of static filtration. The time dependence of the mud fluid loss is also illustrated diagrammatically in figure 1–39. Note that in exploration wells the overbalance will be large due to lack of knowledge of formation pressure and therefore fluid loss will be much more severe than in a development well where the mud weight can be balanced closely to the known formation pressure. In addition, exploration wells will often be drilled with water-based mud, whereas development wells will more likely use less damaging oil-based mud. Thus, severe formation damage is most likely in exploration/appraisal wells.

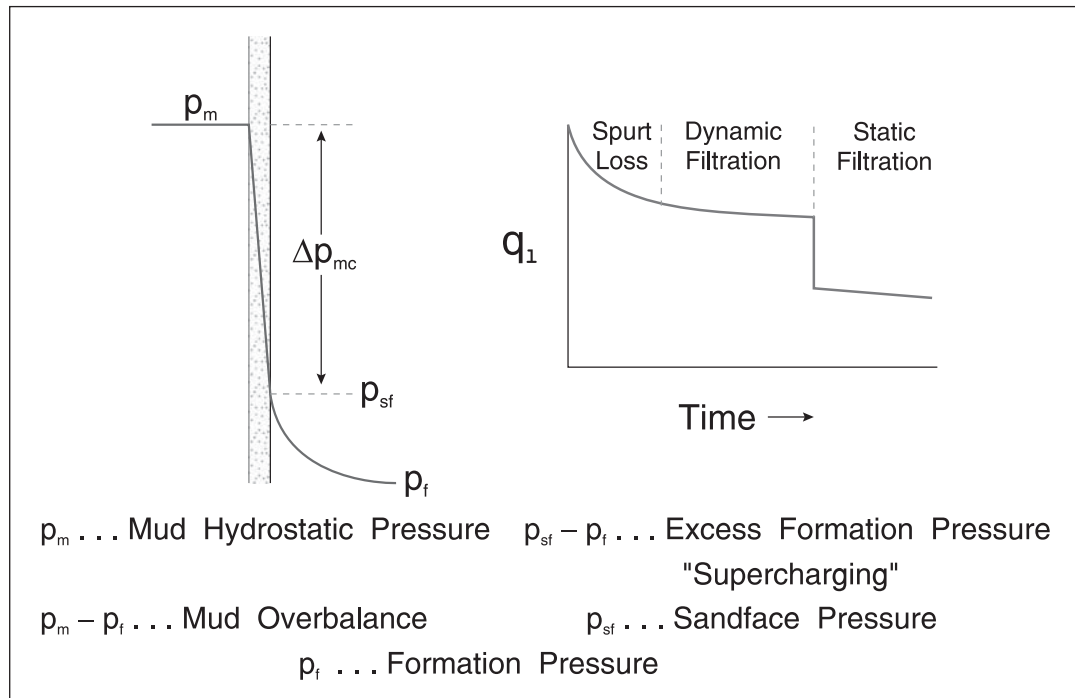


Fig. 1–39. Mechanics of mud filtrate invasion

Assuming a piston-like invasion process as illustrated in figure 1–40, the depth of mud filtrate invasion  $r_{inv}$  is a function of the cumulative fluid loss during the three phases of drilling;  $r_{inv}$  is given by the material balance equation

$$r_{inv} = \sqrt{\frac{Q_1}{\pi\phi(1 - S_{or} - S_{wc})}} \quad (1-88)$$

where  $Q_1$  = cumulative fluid loss per unit measured length of wellbore,  
 $\phi$  = porosity,  
 $S_{or}$  = residual oil saturation in the swept (invaded) zone, and  
 $S_{wc}$  = initial (connate) water saturation.

The important point is that the quantity  $r_{inv}$  is often synonymous with the extent of the altered zone responsible for formation damage. Modern resistivity logging tools with shallow and deep depth of investigation measurements can yield estimates of  $r_{inv}$ , which may be useful in assessing the penetration of formation damage associated with alteration due to mud filtrate invasion.

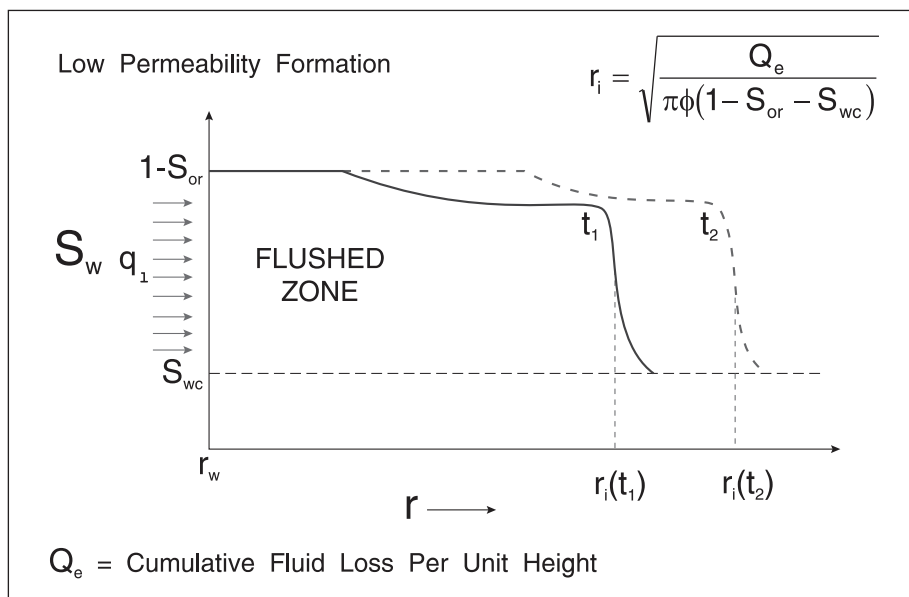


Fig. 1–40. Saturation profile due to mud filtrate invasion in a low-permeability formation

## Water-sensitive authigenic clays

The main interaction of mud filtrate with the formation is due to authigenic (dispersed) clays present in the porous medium. Three main types of clay mineral occur; these are

- Kaolinite (Kandite group)
- Illite (Mica group)
- Montmorillonite (Smectite group).

Clay minerals are complex aluminosilicates which are deposited in the pore space before oil accumulation occurs. Clay-water sensitivity takes place according to two main mechanisms:

Interlayer interactions—Swelling of lattice volume due to hydration.

This is characteristic of the smectite group and causes static permeability reduction with no actual movement of clay. Swelling alone is not felt to be an important mechanism for formation damage.

Interparticle interactions—Emerge from behavior of clay surfaces which are negatively charged as a result of substitution.

Electrical charge causes clay particles to separate, i.e., swelling occurs. The influx of less saline water gives rise to clay instability and breaking away of clay platelets. Entrapment or bridging of these dislodged clay particles at pore throats causes dynamic permeability change. This is the most important mechanism of permeability reduction. Lattice expansion is the main cause of clay instability and dispersion.

Clay minerals occur as pore linings and loose pore fill as illustrated in figure 1-41 and their surface area is a major factor in the effect of clay content on rock permeability; specific surface areas of some clay minerals are given below:

quartz	0.15 cm <sup>2</sup> /g
kaolinite	22 m <sup>2</sup> /g
smectite	82 m <sup>2</sup> /g
illite	113 m <sup>2</sup> /g

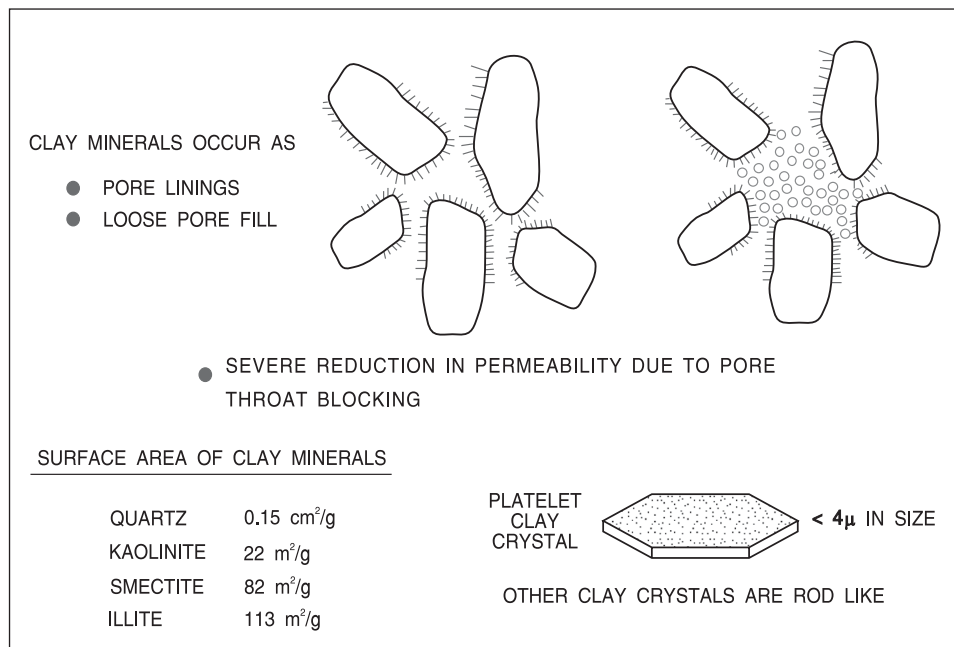


Fig. 1-41. Pore lining and loose pore fill with clay minerals

The smectite crystal is in the form of a platelet, whereas illite has a wispy structure like candy floss. The principal clay types are the following:

**Kaolinite**—hydrated alumino silicate

Kaolinite crystals exist in the form of relatively large size individual particles which have a loose attachment to sand grains. The principal engineering problem is the migration of fines loosened by high flow rate near the wellbore; this can be cured by clay stabilization treatment, e.g., polyhydroxy aluminium.

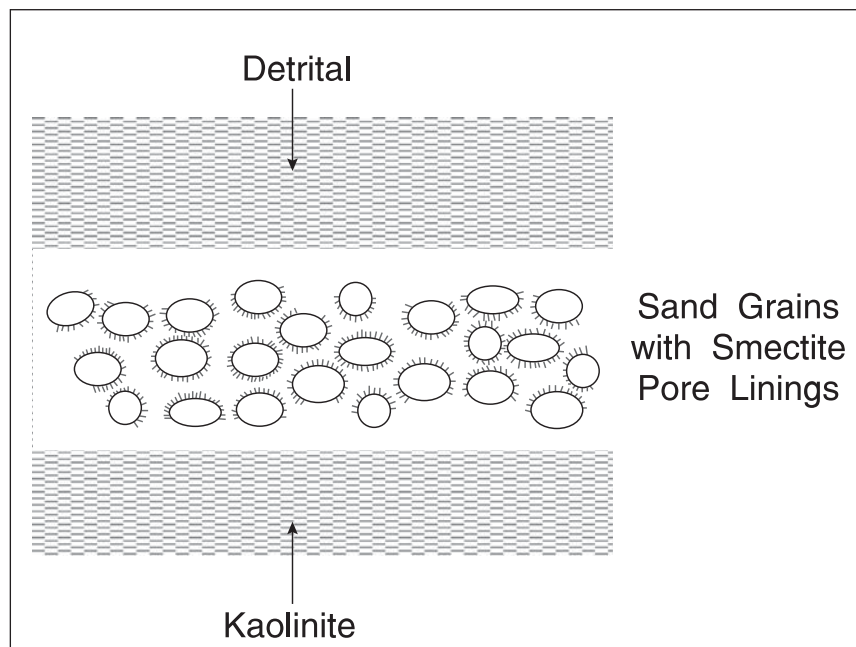
**Smectite**—hydrated alumino silicate also containing Mg, Na, and Fe.

This comprises a whole group of clays whose water sensitivity depends on the Na content. The main engineering problems are extreme water sensitivity and a high irreducible water saturation; the problems may be alleviated by using oil or KCl-based mud.

**Illite**—hydrated silicate which contains K and Al.

This also gives high, irreducible water saturations and grows in pores as masses of long hair-like crystals. It may be dissolved using an acid mixture of HCl and HF.

The scanning electron microscope (SEM) coupled with energy dispersive X-ray diffraction (EDAX) has been a major contributor to the understanding of the behavior of clay minerals. It can analyze pore lining and pore fill material directly. It is also possible to use bulk X-ray diffraction analysis on fine-grained fractions ( $<5\ \mu\text{m}$ ). However, bulk analysis, e.g., log measurements, is dominated by kaolinite present as interlaminated clay, illustrated in figure 1–42.



**Fig. 1–42.** Detrital and authigenic (dispersed) clay

## Dimensionless skin factor

One way of quantifying damage to operating wells represents the wellbore condition by an incremental pressure drop at the wellbore in addition to the normal pressure profile due to radial flow in the formation; this is illustrated in figure 1–43. The superposed pressure drop called the *skin effect* is presumed to occur over an infinitesimally thin skin zone in which the permeability impairment is confined. Accordingly, the bottom-hole flowing pressure of a real well is given by

$$p_{wf} = p_w - \Delta p_s \quad (1-89)$$

where the skin pressure drop  $\Delta p_s$  is a function of the well flow rate  $q_s B$ , the fluid viscosity  $\mu$ , and the characteristics of the physical damaged zone, i.e., its average radial thickness and permeability. In Eq. (1–89),  $p_w$  represents the well-face pressure predicted by homogeneous radial flow without permeability modification.

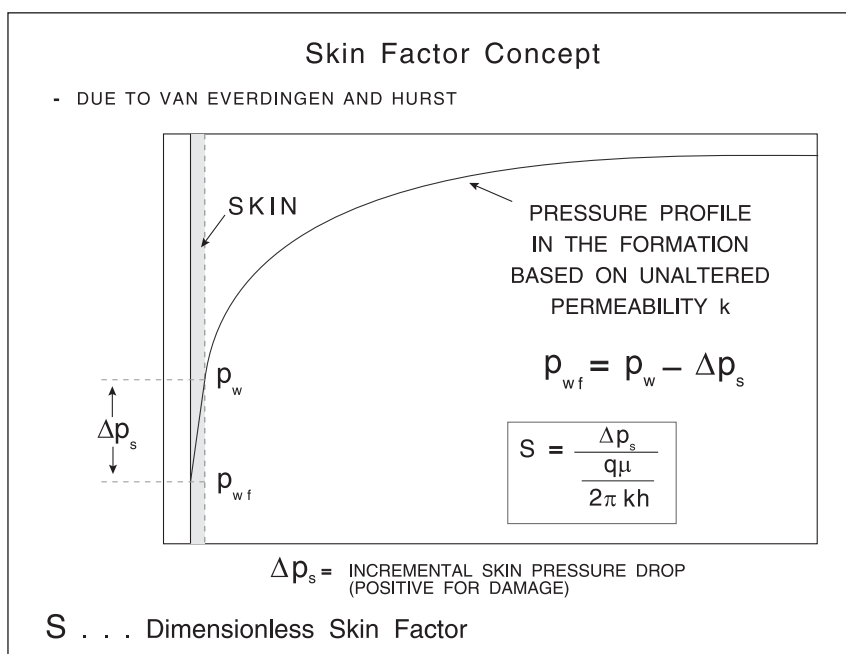


Fig. 1–43. Van Everdigen and Hurst infinitesimal skin concept

The dimensionless skin pressure drop is denoted  $S$  and is defined by the equation

$$S = \frac{\Delta p_s}{\frac{q_s B \mu}{2\pi k h}} \quad (1-90)$$

Since the pressure drop over the damaged zone, assuming laminar flow, should be proportional to  $q_s B \mu$ , the dimensionless skin effect  $S$  depends only on the nature of the impairment. The quantity

$S$  was called the *skin factor* by van Everdingen and Hurst who first proposed the skin concept and is a quantitative measure of any damage to the well.

According to the definition, the skin pressure drop  $\Delta p_s$  and the skin factor  $S$  are both positive for localized permeability reduction in the neighborhood of a producing well. However, in this region, it is also possible to achieve an increase in permeability (or effective permeability) relative to the value in the remainder of the formation as a result of well stimulation treatments such as acidizing or fracturing. In this case, pressure gradients in the vicinity of the well are less (in absolute value) than those that would exist if the formation permeability were completely uniform. This situation is illustrated in figure 1–44, where the actual profile and a negative skin pressure drop is depicted. Thus a negative skin factor is possible, and it indicates that permeability enhancement has occurred. Although the negative skin concept is perhaps physically unrealistic, it does provide a valuable quantitative measure of near-well-bore improvement; values of  $S$  down to  $-5$  have been observed. It is important to appreciate that radial flow is highly sensitive to conditions near the well where superficial velocities are at their highest.

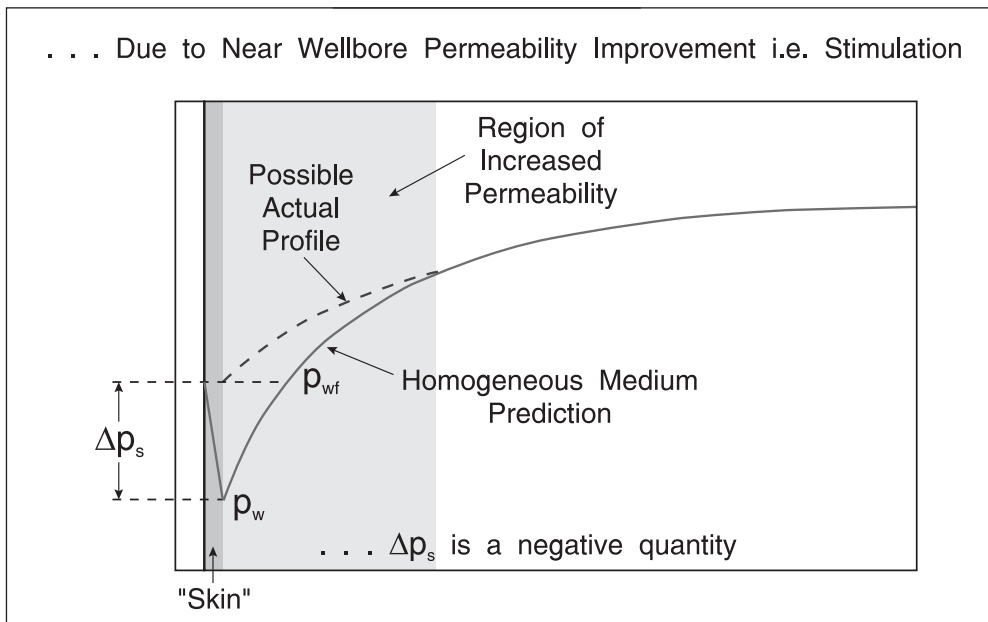


Fig. 1–44. Negative skin effect

## Analytical skin formulae

The dimensionless skin factor  $S$  accounts for any deviation from homogeneous, radial flow in the near-wellbore region. The skin effect due to formation damage cannot usually be predicted *a priori*, and the actual measurement of this quantity is one of the major objectives of the transient pressure testing of wells. However, in certain circumstances it is possible to make an estimate of the incremental pressure drop in the damaged zone and calculate the skin factor. The best example of this is a sand consolidation treatment where the permeability and extent of the altered zone can be predicted. The physical situation is shown in figure 1–45, where an altered zone of radius  $r_s$  and permeability  $k_s$  surrounds the wellbore; the formation itself is of permeability  $k$  and thickness  $h$ . The altered zone can be a result of mud invasion, clay swelling,



or a resin–sand consolidation treatment; for all these,  $k_s < k$ . In the case of an altered zone due to an acid stimulation then, often  $k_s > k$ .

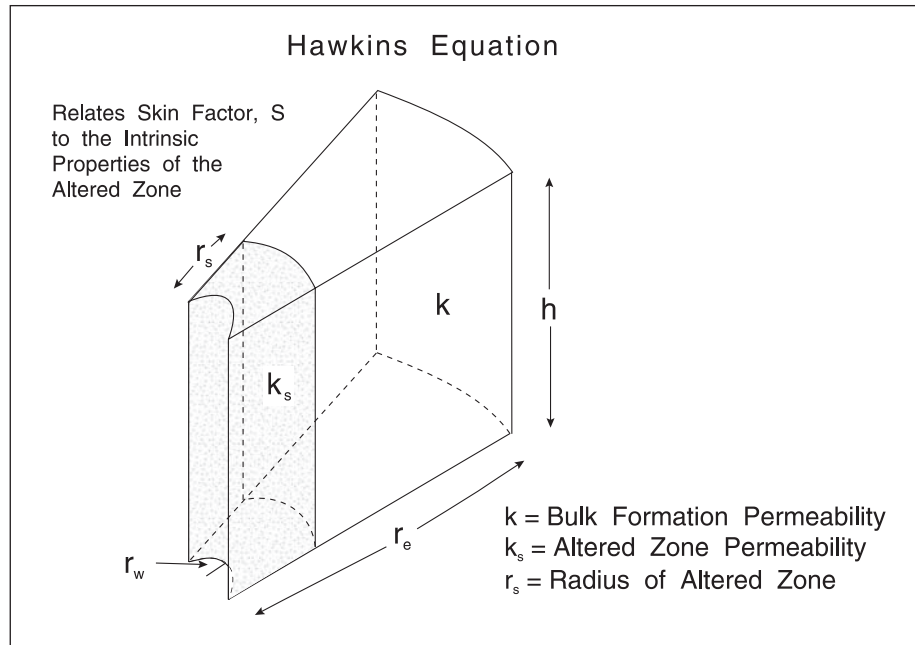


Fig. 1–45. Hawkins formulation of the skin effect

One of the major assumptions in the treatment of skin effects is that the altered zone is relatively small in extent, i.e.,  $r_s \ll r_e$ , and that, even if the flow is in the SSS regime, throughout the skin region

$$q_r = q \left( 1 - \left( \frac{r}{r_e} \right)^2 \right) = q \quad (1-91)$$

Thus the flow through the altered zone is always modeled on a steady-state basis according to the instantaneous well production rate  $q$ . The error resulting from assuming a constant flow through the finite skin is negligible. The skin pressure drop  $\Delta p_s$  is the difference between the actual steady-state pressure drop over the altered zone and that which would exist if the damaged zone permeability were equal to the formation permeability,  $k$ ; this is illustrated on a dimensionless basis in figure 1–46. Thus

$$\Delta p_s = \frac{q\mu}{2\pi k_s h} \ln \frac{r_s}{r_w} - \frac{q\mu}{2\pi k h} \ln \frac{r_s}{r_w}$$

i.e.,

$$\Delta p_s = \frac{q\mu}{2\pi k h} \left( \frac{k}{k_s} - 1 \right) \ln \frac{r_s}{r_w} \quad (1-92)$$

Hence the dimensionless skin factor  $S$  is given by

$$S = \frac{\Delta p_s}{\frac{q\mu}{2\pi kh}} = \left( \frac{k}{k_s} - 1 \right) \ln \frac{r_s}{r_w} \quad (1-93)$$

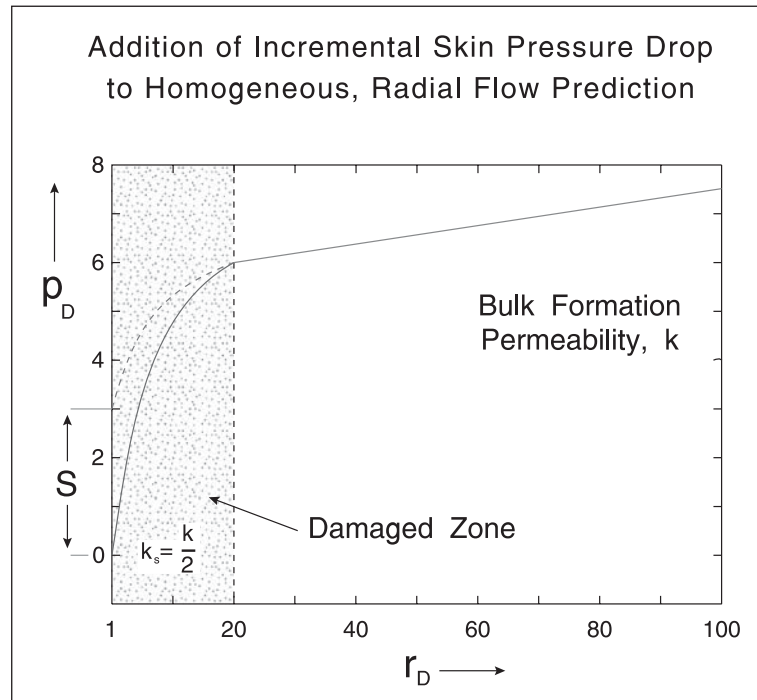


Fig. 1-46. Radial composite skin effect on a dimensionless basis

Note that both the radius and permeability of the altered zone must be specified in order to determine  $S$ . Equation (1-93) is due to Hawkins<sup>9</sup> and implies that the well is open to flow along the total length of the production interval.

In practice,  $S$  and  $k$  are measured in a well test and, in an open hole,  $r_w$  is obtained from a calliper survey. However, knowing these three quantities it is not possible to calculate both  $k_s$  and  $r_s$  from Eq. (1-93). It is possible to get around this difficulty by defining an effective wellbore radius  $r_{w,eff}$  which makes the calculated pressure drop in an ideal reservoir equal to that in an actual reservoir with skin. Thus

$$\ln \frac{r_e}{r_{w,eff}} = \ln \frac{r_e}{r_w} + S \quad (1-94)$$

or

$$r_{w,eff} = r_w e^{-S} \quad (1-95)$$

The direct application of the Hawkins equation requires knowledge of both the altered zone permeability  $k_s$  and its radial extent  $r_s$ ; in a few circumstances, this full information is available. For example, sand consolidation treatments are used to cause sand grains in an unconsolidated formation to adhere and therefore reduce the problem of sand production. In one form of treatment, a resin is employed to physically glue the particles together. The reduction in permeability engendered by the coating of resin can be measured in the laboratory, and the depth of penetration of the treatment, i.e.,  $r_s$  can be estimated from the volume of the batch pumped into the formation. Hence the skin due to the resin treatment can be calculated using the Hawkins equation.

In the development of under saturated reservoirs, it is preferable to implement pressure maintenance by water injection before the bottom-hole pressure of the producing wells falls below the bubble point. The phenomenon of gas block occurs when a free gas saturation  $S_{gc}$  is allowed to develop in the region around the wellbore as illustrated in figure 1–47. The extent of the gas-affected region depends on how much  $p_{wf}$  is below the bubble-point pressure  $p_b$ , and the oil permeability in the two-phase inner zone must be written as  $k_o = kk_{ro}(S_{gc}, S_{wc})$  where  $k_{ro}(S_{gc}, S_{wc})$  is the relative permeability to oil at the critical gas saturation in the presence of connate water. The important point is that  $k_{ro}(S_{gc}, S_{wc})$  is less than unity and the oil permeability in the gas-invaded region is reduced below the permeability to oil at connate water saturation. Again, the Hawkins equation can be used to compute the skin effect due to two-phase flow if an estimate of  $k_{ro}(S_{gc}, S_{wc})$  is available from laboratory data on relative permeability; the extent of the inner region is given by the condition that  $p = p_b$  at  $r = r_s$ . Large skin effects can arise if the bottom-hole pressure is substantially below the bubble point, which will lead to a deterioration in the well PI, and hence it is better to maintain the reservoir pressure by water injection such that gas block does not occur.

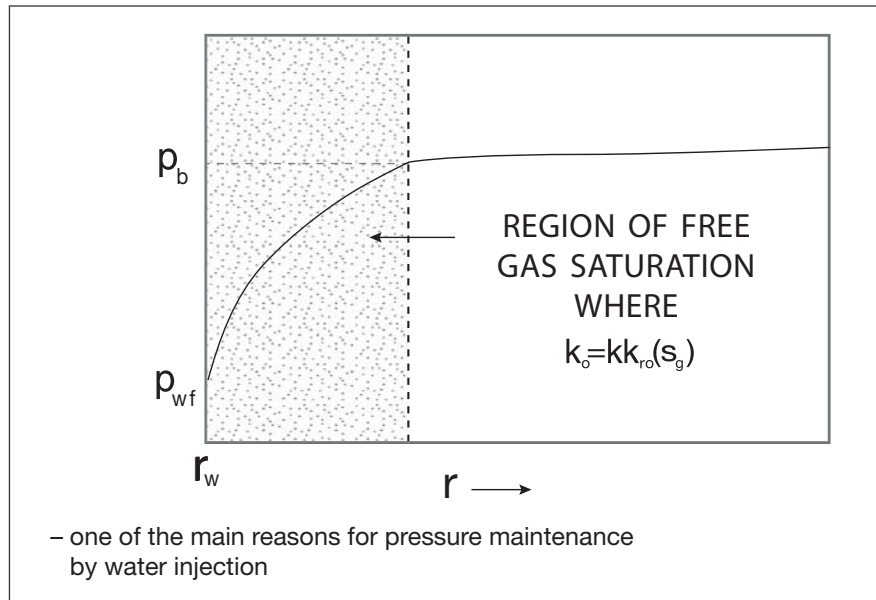


Fig. 1–47. Phenomenon of gas block

An interesting situation with regard to formation damage arises in connection with fines migration illustrated in figure 1–48. Formation fines are presumed to be water-wet and retained in the immobile (connate) water film during the period of primary recovery and single-phase oil

production. However, after water breakthrough, the water phase is in flow and the fines become mobile. The radially convergent flow causes the fines to migrate towards the producing wells and in the near-wellbore region bridging of fines particles at pore throats results in severe damage and a progressively higher skin factor. This mechanism was identified in connection with a field in Alaska (McKenzie River) and the only remedy was to sidetrack the wells to new locations once the damage became severe. Note that it is only after water breakthrough that the problem occurs.

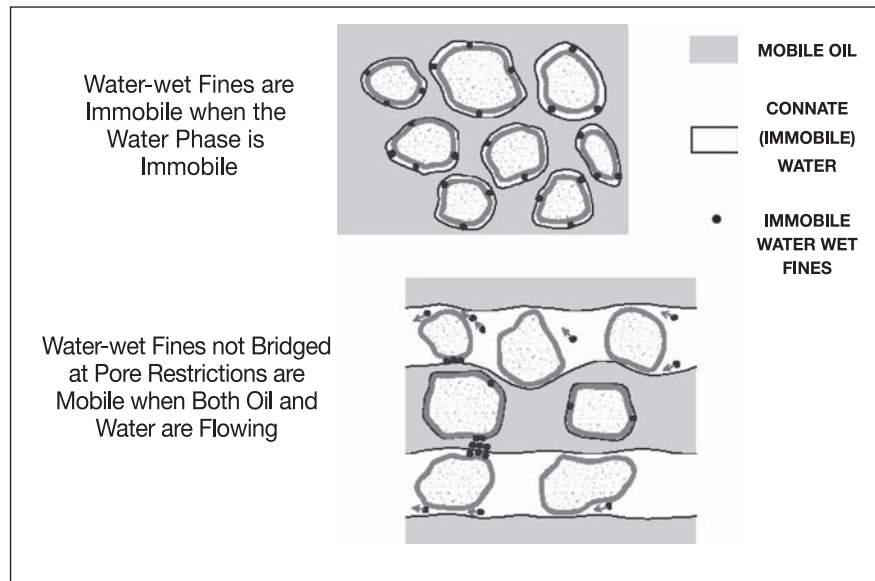
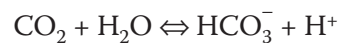
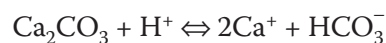


Fig. 1-48. Movement of formation fines

In many Middle East limestone reservoirs, the main production problem is calcium carbonate scale formation which develops after the reservoir goes below the bubble point. In limestone territory, any intrusion of basalt into the carbonate formations can produce large amounts of carbon dioxide which dissolves in brine to form carbonic acid:



The total  $\text{CO}_2$  in the water phase is the sum of physically dissolved  $\text{CO}_2$  and bicarbonate ion. At high temperature and pressure, the above reaction equilibrium is displaced to the right and the hydrogen ion then reacts with solid calcium carbonate according to the equation



Thus the amount of carbonate,  $\text{Ca}_2\text{CO}_3$ , in solution depends on the quantity of  $\text{CO}_2$  present. Above the bubble point, any free  $\text{CO}_2$  in the reservoir will distribute between the oil and brine phases with a large proportion in the aqueous phase as  $\text{HCO}_3^-$  ion. When the reservoir pressure falls below the bubble point and a free gas phase forms (as shown previously in figure 1-47),  $\text{CO}_2$  now distributes between oil, gas, and brine phases with a significant proportion in the gas. Hence the amount of  $\text{CO}_2$  present in the brine phase is reduced and  $\text{Ca}_2\text{CO}_3$  precipitates out.

# 2

## **Skin Factor in Fractured and Perforated Wells**

---

### **The Effect of Perforations on Well Productivity**

#### **Introduction**

In the treatment in the preceding chapter, it has been tacitly assumed that the well has an open-hole completion. However, in most producing areas, certainly in the North Sea, all wells are cased through the producing interval and then selectively perforated. A notable exception to this policy are the fractured limestone reservoirs in Iran where the wells are always completed open-hole and then fitted with gas exclusion liners or plugs if necessary, to reduce gas or water coning, respectively. Only the permeable zones of the reservoir are perforated and the perforations will normally cease some distance above the original water–oil contact (if it exists) in order to minimize the possibility of water coning. Likewise, a well will not be perforated in the oil column in the immediate vicinity of the gas cap to prevent gas coning. These are, of course, the major reasons for the partial completions previously mentioned.

In perforated completions, fluids enter the wellbore through tunnels made by bullets or jets that penetrate the casing, cement sheath, and part of the producing formation. The productivity of such completions depends on the flow properties of the perforations with shot density, i.e., number of perforations per foot, and shot penetration depth being crucial. A cased, perforated completion results in nonradial flow near the wellbore as flow lines converge on individual perforations and it is natural to express the effect of perforation as a contribution to the skin effect.

#### **Perforating systems**

Jet perforating is based on explosive shaped charges that pierce a hole through casing and cement and establish connection between the wellbore and the formation. A typical shaped

charge is shown in figure 2–1 and the following five main components can be discerned:

- primer
- steel case
- explosive charge
- liner
- cavity

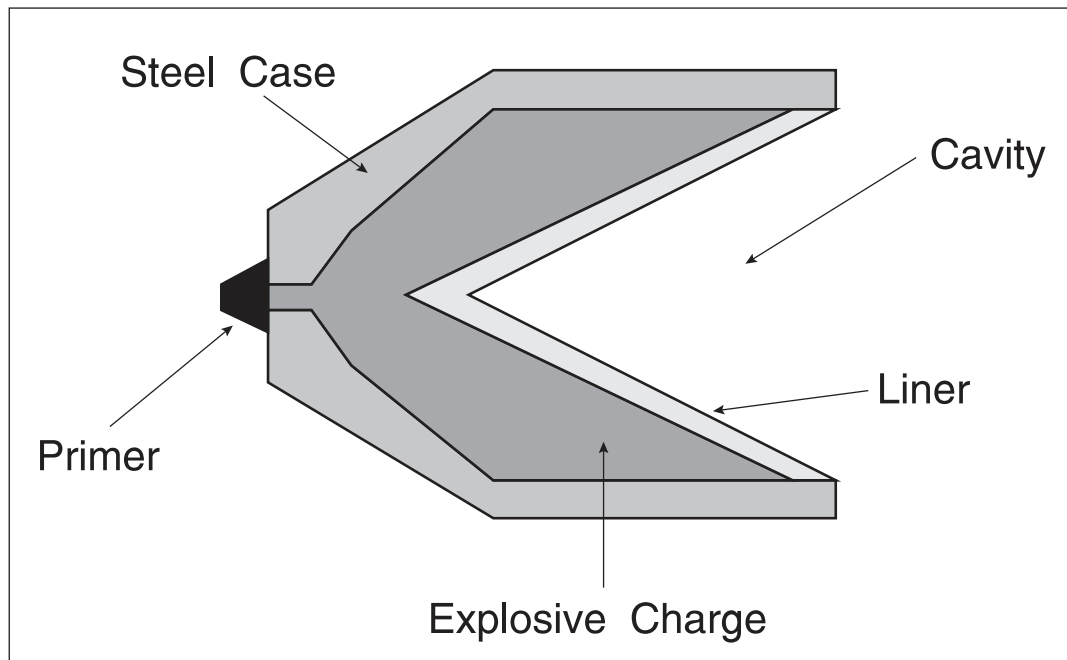


Fig. 2–1. Shaped charge design

Shaped charges come in a wide variety of designs, and the symmetry must be very carefully controlled to ensure the optimal jet effect. Cone axis offset, liner thickness variation, and charge density variation all cause performance deterioration. Quality control during manufacture is therefore crucial to efficient operation. The mechanism of jet perforation is illustrated in figure 2–2, where, after detonation, the liner is now moving towards the target as a liquid jet of approximately 1/16" diameter and a forward velocity of the order of 20,000 ft/s. The pressure exerted on the target is around  $5 \times 10^6$  psi and a tunnel is driven through casing and cement into the rock by the passage of the slug of liquid like material. The performance of shaped charges is measured in the API—American Petroleum Institute—test denoted RP 43. Here, the charge is fired into a target consisting of a cylinder of Berea sandstone encapsulated by cement in a steel canister as shown in figure 2–3. In order to simulate overbalanced perforation, a 1,500-psi differential towards the target is established, and after perforation a core backpressure of 1,000 psi allows salt water to flow into the system at a pressure differential of 500 psi. The core is then backflushed with kerosene at a differential of 200 psi until stabilization. Since most modern perforation of wells is carried out with underbalance conditions, a reverse flow version of the API test is also carried out; this is illustrated in figure 2–4. In this case, there is a differential of 200 psi towards the “well” side of the target, i.e., the perforation entry face, and after perforation the system is again backflushed with kerosene.

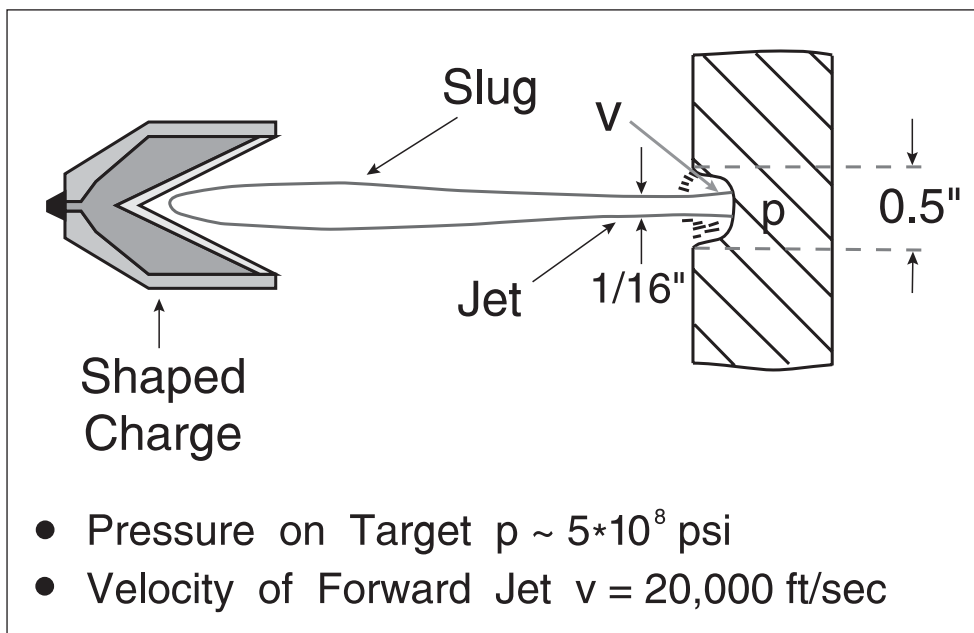


Fig. 2-2. Jet perforation

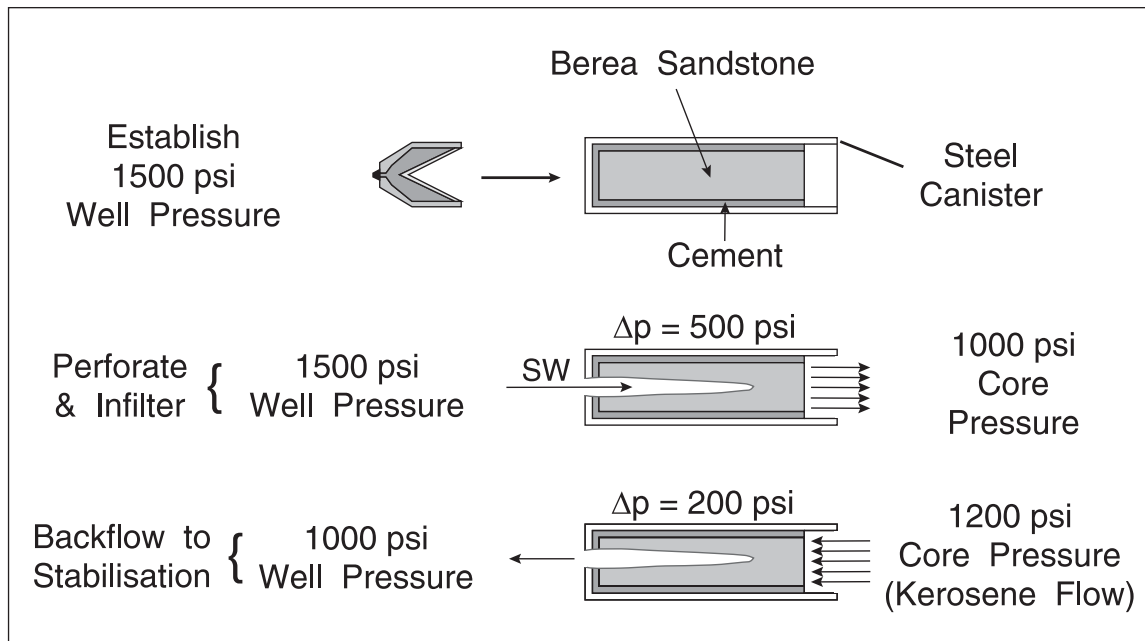


Fig. 2-3. API test with positive pressure

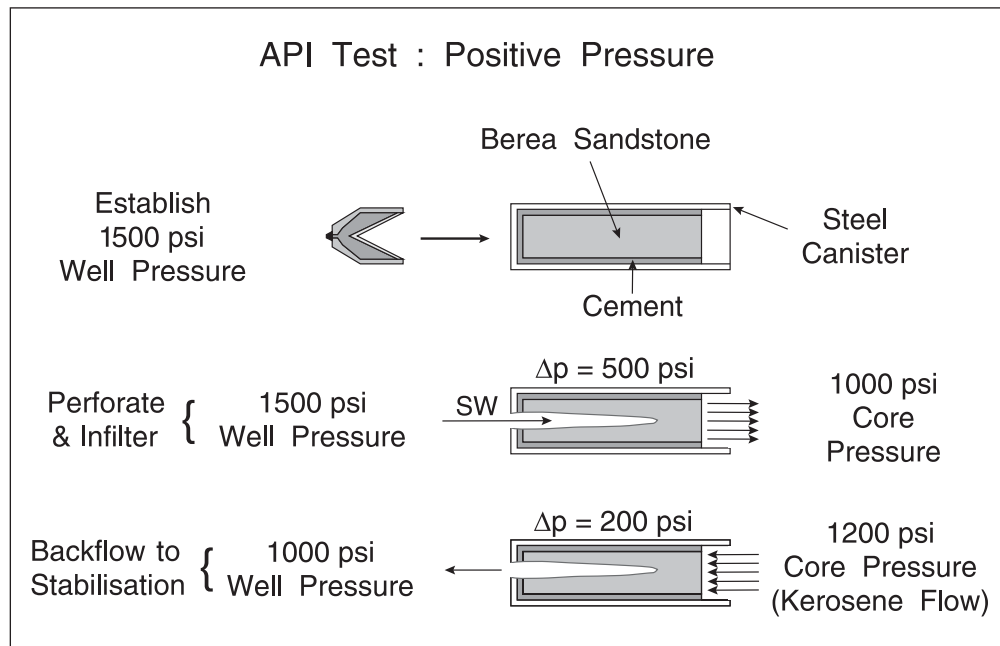


Fig. 2-4. API test with reverse pressure flow

The effectiveness of the perforation is calculated by comparing the flowing pressure drop after backflushing with that of an ideal tunnel in rock of the same permeability. The result of this test is expressed as core flow efficiency (CFE) and the procedure is shown in figure 2-5. The following steps are involved in the determination of CFE:

1. The intrinsic permeability of the Berea core before perforation is determined in a Hassler core holder using kerosene of viscosity  $\mu_o$  as the fluid:

$$k_o = \frac{q_o \mu_o L_o}{A \Delta p_o}$$

2. The core is then mounted in the canister and perforated. The apparent permeability  $k_p$  is then found by again flowing kerosene of viscosity  $\mu_p$ :

$$k_p = \frac{q_p \mu_p L_o}{A \Delta p_p}$$

3. The effective permeability  $k_i$  of the target with an "ideal" perforation of the measured length of the actual tunnel is found from the correlation shown in figure 2-5.

4. 
$$CFE = \frac{k_p}{k_i}$$



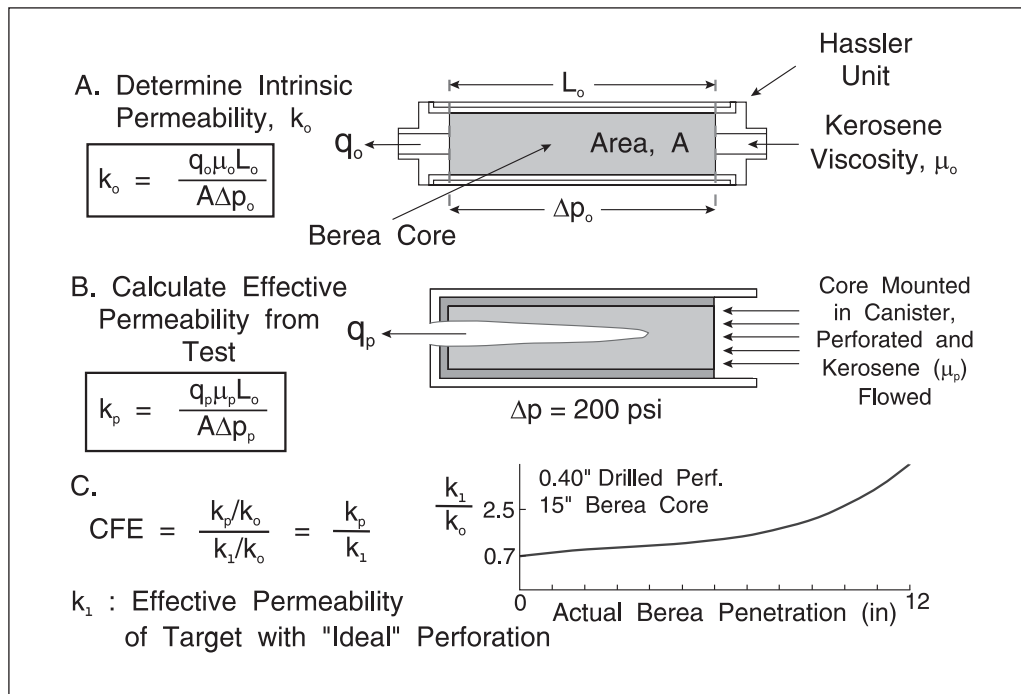


Fig. 2-5. Core flow efficiency

Unfortunately, the basis of the calculation of the ideal permeability  $k_1$  is now known to be significantly in error and this method produces CFEs which are much too small; this aspect will be treated in detail later. In addition to determining CFE, the penetration of the tunnel into the Bera target is also measured as shown in figure 2-6. The entry hole diameter is designated E.H. and the total core and total target penetrations are designated TCP and TTP, respectively; these are all illustrated in figure 2-6. In order to explain the low core flow efficiencies obtained in typical laboratory tests, the existence of a crushed zone around the tunnel was postulated as indicated in the diagram. In field conditions, the backflushing of debris from the perforation tunnel and the residual compacted zone are illustrated in figure 2-7. As the high-velocity jet penetrates or punches its way through the target, formation material is forced laterally or radially outward from the axis of the perforation. This results in the creation of a compacted zone around the tunnel as shown in figure 2-7. Immediately after penetration, the perforation is found to be filled with debris and it is only after a certain amount of fluid has been flowed from the perforation that it will liberate its debris and appear clean. However, even when the perforation is clean, the damaged or compacted zone remains as illustrated in figure 2-7. This is characterized by substantially reduced permeability of the order of 20% of that in the original formation. The lateral extent of the zone varies from about 1/2 in. at the tip of the perforation to 1 in. at the face plate for a typical large Hollow Carrier gun charge. Zones are smaller for shallow penetrating charges. The effect of the compacted zone is that it reduces the flow efficiency of the perforation as compared, for example, to an ideal hole of the same depth and diameter.

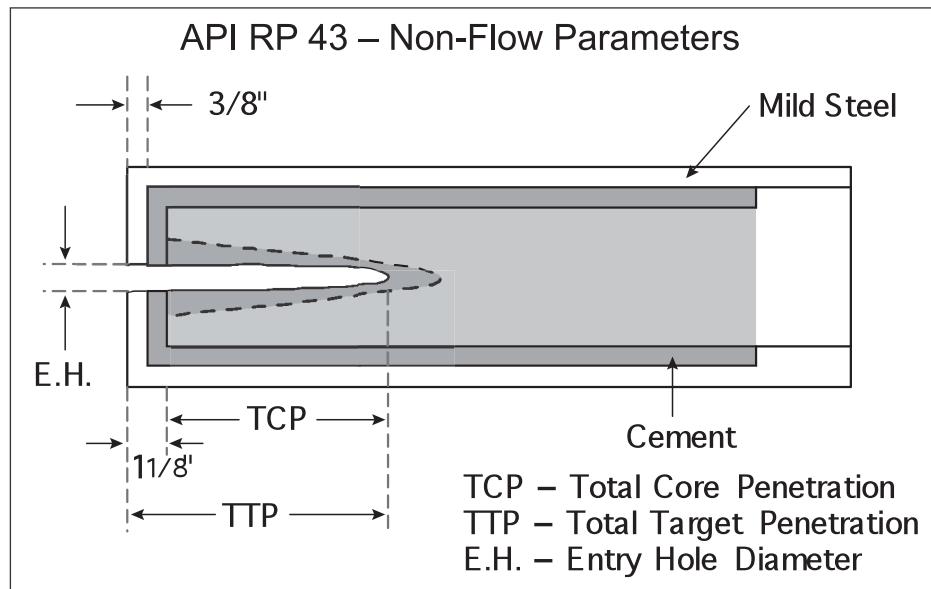


Fig. 2-6. Target penetration

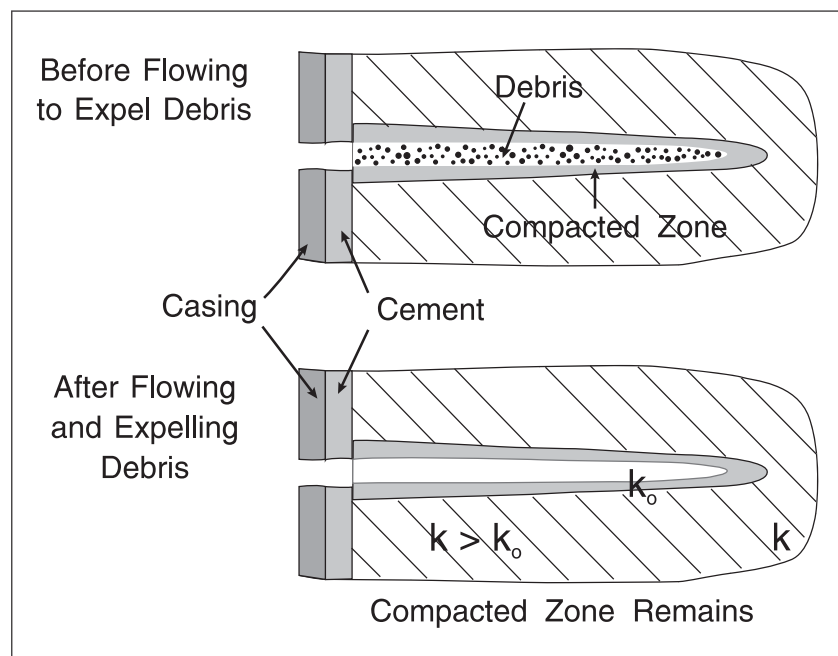


Fig. 2-7. Compacted zone

The relation between CFE and crushed zone thickness has been examined by Locke, who quotes the results shown in figure 2-8. The effects of crushed zone thickness and permeability ratio  $k_c/k_0$  on core flow efficiency have been calculated using a very fine mesh finite method (FEM) element simulation of the cylindrical, perforated core experiment. Figure 2-8 refers to the situation of a 9" perforation of 0.5" diameter, which is the base case for many perforation studies.

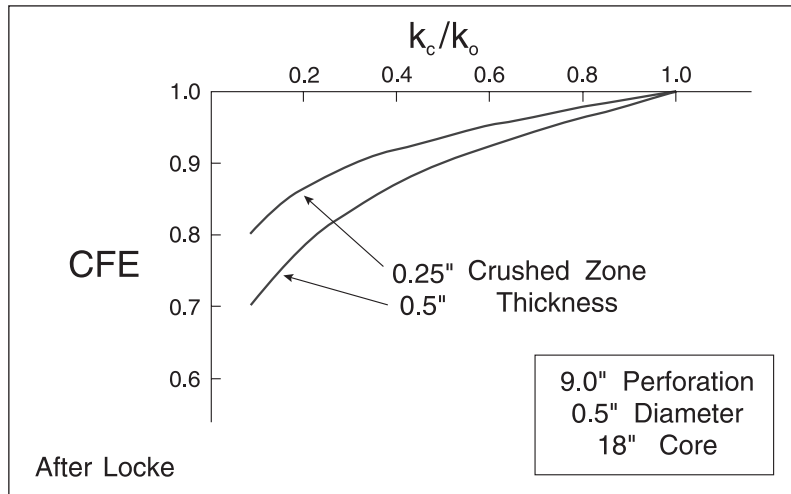


Fig. 2-8. Relation between CFE and crushed zone properties

The two key quantities that control the behavior of a perforated completion are the number of shots per foot and the depth of penetration of the perforation tunnels, denoted  $l_p$ . The penetration into a Berea target in the confined geometry of the API test must be corrected to downhole conditions of rock strength and in-situ stress, and a Berea penetration multiplier (BPM) is used to represent this transform. Figure 2-9 shows the effect of effective stress and rock type on BPM values as predicted by the Schlumberger SPAN (Perforating Analysis) program. The importance of penetration depth is illustrated in figure 2-10, where the interaction of formation damage and perforation is indicated; the biggest single barrier to understanding perforation efficiency is the lack of knowledge of the actual extent of formation damage following drilling. The quantity  $r_s$  which characterizes the thickness of the damaged region is probably related to the depth of mud filtrate invasion, but no method of measuring  $r_s$  is currently available. Well testing, in open hole prior to casing and perforating, could in principle determine the skin factor  $S$  but further decomposition into the separate components  $k_s$  and  $r_s$  is not possible.

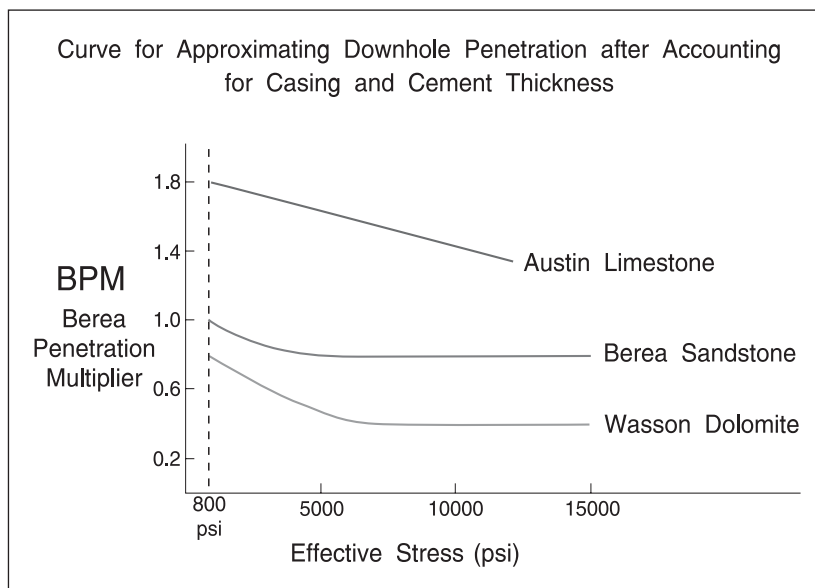


Fig. 2-9. Berea penetration multiplier

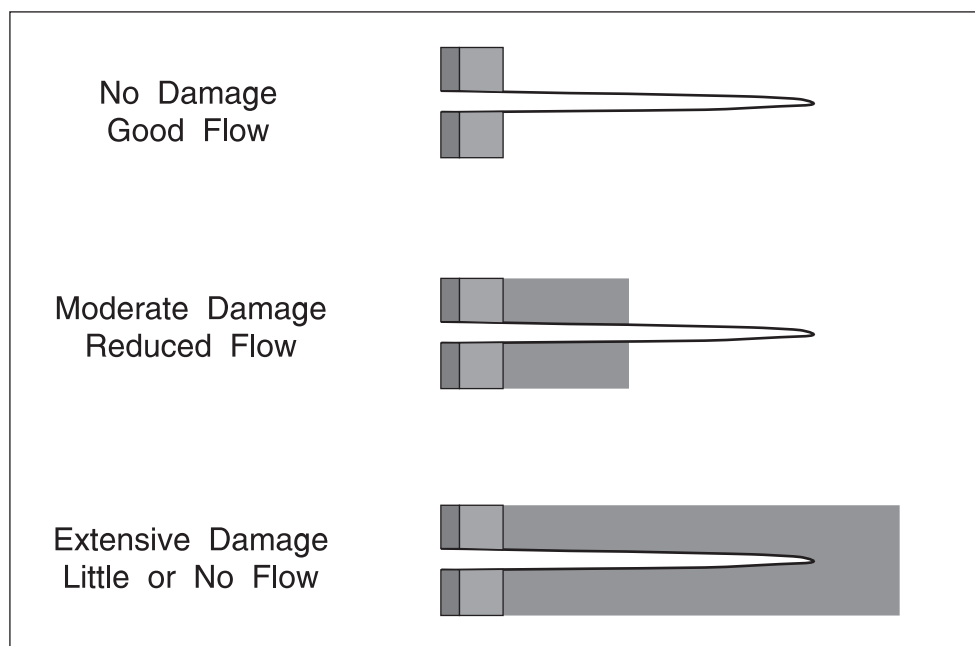


Fig. 2–10. Interaction of formation damage and perforation

## Perforated completions

Depth of penetration has received inordinate emphasis over the years as the factor most important to test well deliverability. Yet, field results often contradict this in reports of small guns providing better production results than large ones—when the small guns (shooting one third to one-half as deep) are fired with differential pressure towards the wellbore. Well completion conditions are of equal or even greater importance than penetration in terms of achieving best well deliverability, and this aspect will be considered in detail later. In addition to shots per foot and depth of penetration, the phase angle of the perforations also has an effect on well deliverability. Modern perforating guns allow spiral type geometry as shown in figure 2–11. Reference to the work of Harris<sup>1</sup> helps place penetration in its proper perspective. Figure 2–12 shows how the steady-state (SS) productivity ratio varies with perforation penetration taking into account the number of shots per foot (or shot density); the results are for ideal perforations with no compacted zone. It can be seen that four perforations per foot, 5–6 in. deep, would yield the same theoretical flow capacity as the uncased hole. Evidently, if there is no formation damage, the first few inches of penetration are very important, but beyond about 6 in. the productivity ratio increases only slowly. This result was published in 1966 and the accuracy with which perforation performance could be modeled was limited. Nevertheless, the industry standard became four shots per foot with 9" penetration, since this essentially gave the same performance as open hole. The productivity ratio was defined by the equation

$$PR = \frac{\ln \frac{r_e}{r_w}}{\ln \frac{r_e}{r_w} + S} \quad (2-1)$$

where  $S$  is the skin factor for a perforated completion given by

$$S = \frac{\Delta p_p}{\frac{q\mu}{2\pi kh}} \quad (2-2)$$

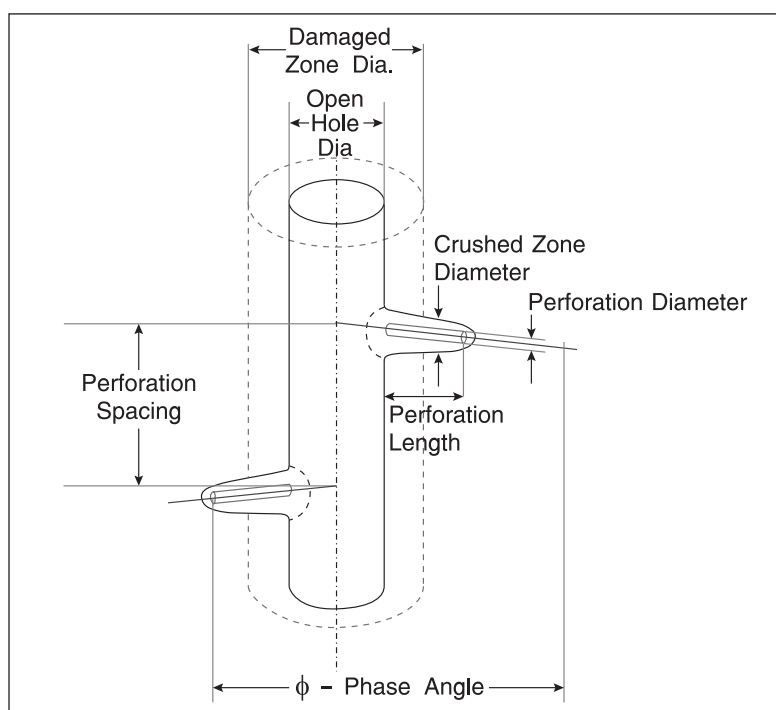


Fig. 2-11. Perforation geometry

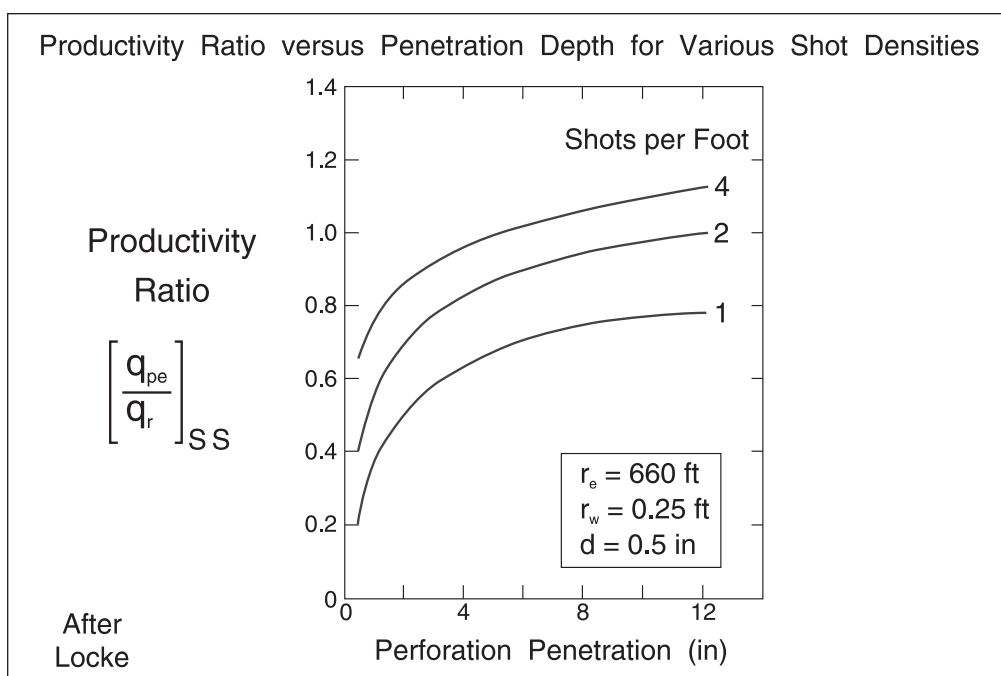


Fig. 2-12. Productivity ratio from the work of Harris

In simulations of perforated completions, a finite difference or finite element model of the detailed flow in the near-wellbore region is carried out, which describes the local flow convergence into the perforation tunnels that are assumed to be of infinite conductivity. SS flow from a radius  $r_e$  yields a drawdown  $(p_e - p_{wf})_{pc}$  in the perforated case and a drawdown  $(p_e - p_{wf})_{oh}$  where

$$(p_e - p_{wf})_{oh} = \frac{q\mu \ln \frac{r_e}{r_w}}{2\pi kh} \quad (2-3)$$

The extra pressure drop  $\Delta p_p$  due to the perforations is given by

$$\Delta p_p = (p_e - p_{wf})_{pc} - (p_e - p_{wf})_{oh} \quad (2-4)$$

In terms of the capacity of the well to produce, shot density would appear to be of greater importance than penetration depth. As pointed out by Harris, the perforation pattern has a noticeable effect on productivity. Strip shooting (all the perforations in a vertical line on the same side of the hole) gives lower productivity than staggered arrangements.

The above would tend to de-emphasize the importance of perforation depth. However, the data of Harris neglects formation and perforation damage. Figure 2–10 illustrates the problem and advances a convincing argument for emphasis on maximum penetration. Basically, the objective is to penetrate at least 5–6 in. beyond the region of reduced permeability, when shooting at four shots per foot. Further, the reduced perforation efficiency resulting from the compacted zone can be compensated for by increased penetration. In an undamaged formation, a perforation density of four shots per foot and penetration depths of 6 in. or more will yield productivities in excess of that from an open hole. In a damaged formation, considerably deeper penetrations are necessary to achieve this.

Since the pioneering work of Harris, many studies have been made on the productivity of perforated completions. Papers by Hong,<sup>4</sup> Klotz et al., and Locke<sup>9</sup> have improved understanding of the process, and with increased sophistication in the grids used to model the localized flow convergence into the perforations, more accurate results have been achieved. In figure 2–13, the productivity ratio as a function of perforation length for the base case of four shots per foot and 90° phasing with no crushed or damaged zone according to different studies is presented. The most recent work of Locke using a highly refined finite element mesh has become the standard reference on this topic. One of the main contributions of this work has been to demonstrate the importance of phase angle as illustrated in figure 2–14. There is a clear advantage in moving away from in-line perforating guns, and modern practice concentrates on spiral orientation of the perforations. Figure 2–15—also from the work of Locke—shows the effect of perforation diameter and crushed zone permeability on productivity ratio. The general conclusion is that, except in the case of gravel packed completions, for a given mass of explosive it is better to produce a long, thin tunnel since depth of penetration is much more significant than perforation diameter.

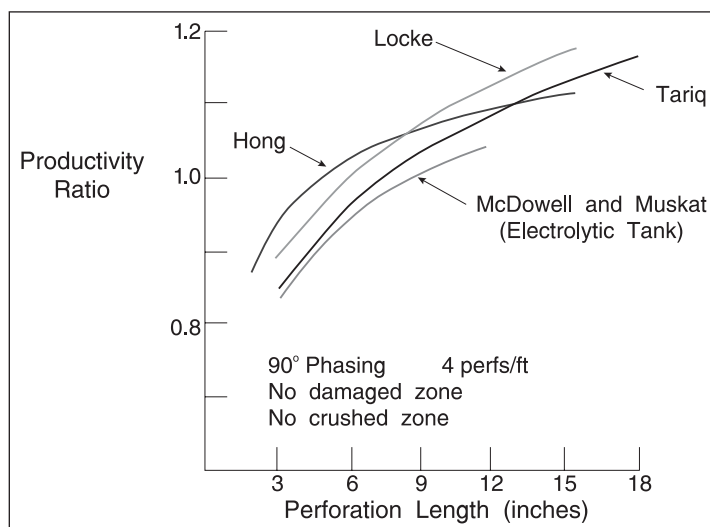


Fig. 2-13. Results of Hong, Klotz et al., and Locke

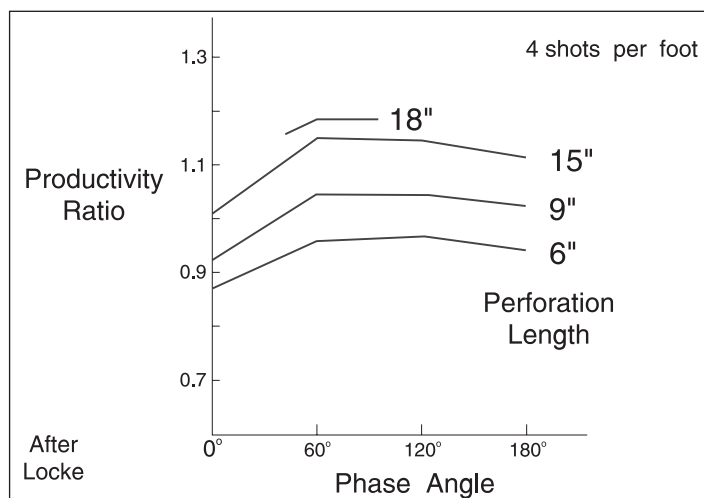


Fig. 2-14. Productivity ratio as a function of phase angle

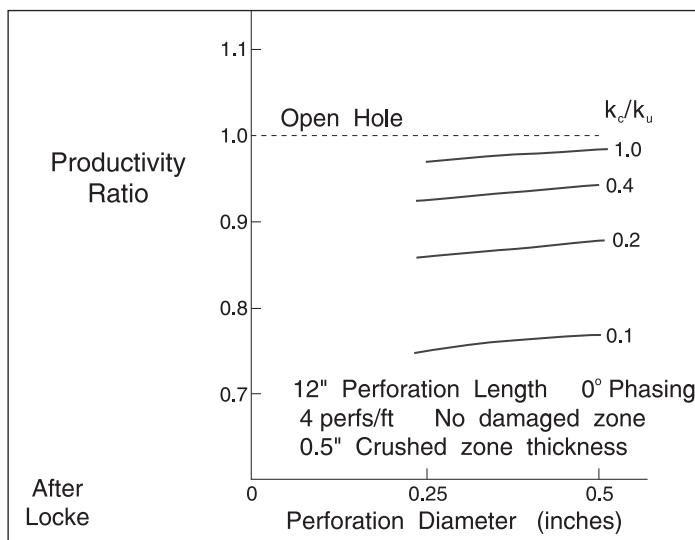


Fig. 2-15. Effect of perforation diameter on productivity ratio

## Fluid mechanics of the API test

Since much of the perception of the nature of the flow into perforations is gathered from API test results, it is useful to consider the detailed nature of the flow process in this confined geometry. As a prelude to this, it is useful to first treat spherical flow since the flow into the tip of the perforation is approximately hemispherical in nature. The Forcheimer equation for flow in porous media takes the form

$$\frac{dp}{dr} = \frac{\mu}{k} u_r + \beta \rho u_r^2 \quad (2-5)$$

and for the spherical geometry shown in figure 2-16, the flux or superficial velocity  $u_r$  at radius  $r$  is given by

$$u_r = \frac{q}{4\pi r^2} \quad (2-6)$$

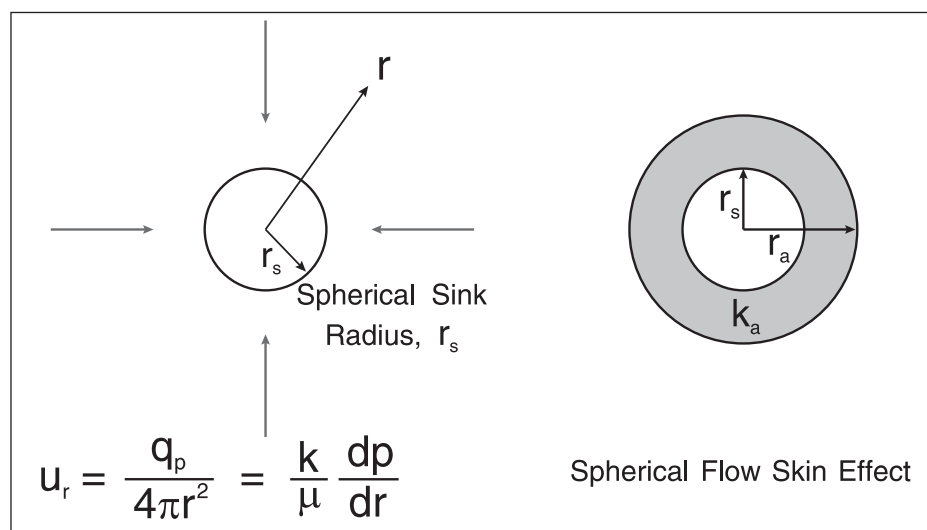


Fig. 2-16. Spherical flow

The integration of the Forcheimer equation in spherical geometry is given in the later section on spherical flow and the result for the total pressure drop is quoted here

$$p_e - p_w = \frac{q\mu}{4\pi k} \left( \frac{1}{r_s} \right) + \frac{\beta \rho q^2}{(4\pi)^2 3} \left( \frac{1}{r_s^3} \right) \quad (2-7)$$

In oil field units, the equations take the form

$$\Delta p = \Delta p_D + \Delta p_{ND} \quad (2-8a)$$



where

$$\Delta p_D = \frac{887.2 q \mu}{4 \pi k r_s} \quad (2-8b)$$

and

$$\Delta p_{ND} = \frac{5.6901 \times 10^{-11} \beta \rho q^2}{(4\pi)^2 3 r_s^3} \quad (2-8c)$$

where the density  $\rho$  is in g/cc (not lb/ft<sup>3</sup>). A fluid density in g/cc is akin to a gravity and it is imperative to get the correct units conversion factors especially for the non-Darcy term

The flow pattern in the API test is of the form shown in figure 2–17, where the flow into the perforation is seen to be localized near the tip of the tunnel. Detailed finite element simulations of this flow system have been carried out by Egan<sup>7</sup> who modeled SS combined Darcy and non-Darcy flow, i.e., the Forcheimer equation was employed. With regard to the non-Darcy component, the perforation tip effect causes spherical-like behavior and the results of the detailed simulation studies could be expressed by the result

$$\Delta p_{ND} = \frac{\beta \rho q_p^2}{(4\pi)^2 3 r_s^3} \quad (2-9)$$

where

$$r_s = 1.37 r_p \quad (2-10)$$

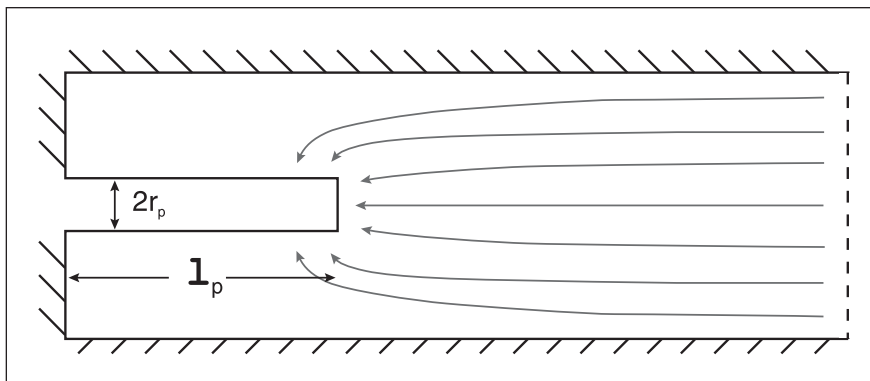


Fig. 2–17. Finite element simulation of flow to a confined perforation

Here,  $r_s$  is the equivalent spherical radius which is related to the perforation radius  $r_p$  by Eq. (2–10). The constant 1.37 in this equation was derived from the FEM simulations with a very small mesh size, particularly around the tip. This very simple result shows the importance of localized flow convergence into the tip of the perforation in the mechanics of non-Darcy flow.  $\Delta p_{ND}$  was found to be independent of  $l_p$  but very sensitive to  $q_p$ —the flow rate per perforation—and  $r_p$ . When the non-Darcy flow effect is appreciable (i.e., high permeability), the

API test will be sensitive to perforation tip radius as illustrated in figure 2–18. In field units, Eq. (2–9) becomes

$$\Delta p_{ND} = \frac{5.6901 \times 10^{-11} \beta \rho q_p^2}{(4\pi)^2 3 r_s^3} \quad (2-11)$$

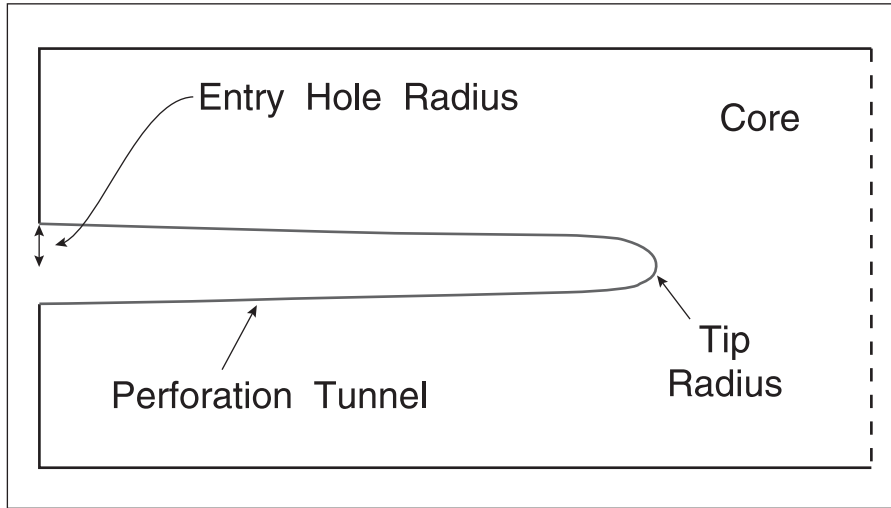


Fig. 2–18. Tip radius of perforation tunnel

Note that the non-Darcy pressure drop takes place very close to the tip of the perforation due to the  $1/r^3$  variation with radius implicit in Eq. (2–7).

The Darcy flow component of the pressure drop in a perforated, confined core exhibits the same characteristics of localized flow convergence into the tip of the tunnel. The total pressure drop observed in numerical simulations can be partitioned into a linear flow contribution based on the length  $L_c - l_p$  and a spherical flow contribution into the tip based on  $r_{sd}$ . Thus

$$\Delta p_D = \frac{q_p \mu (L_c - l_p)}{Ak} + \frac{q_p \mu}{4\pi k} \left( \frac{1}{r_{sd}} - \frac{1}{r_c} \right) \quad (2-12)$$

↑	↑
Linear flow along core	Spherical flow convergence into tip

Again, calibrating this model with the detailed FESs shows that for the spherical flow component

$$r_{sd} = 1.26 r_p \quad (2-13)$$

The Darcy pressure drop in the API test is influenced by  $l_p$  and  $r_p$ .

The effective permeability of an ideal, perforated core is defined by the relation

$$k_i = \frac{q_p \mu L_c}{\pi r_c^2 \Delta p} \quad (2-14)$$

From Eq. (2-12)

$$\Delta p = \frac{q_p \mu}{k} \left( \frac{L_c - l_p}{\pi r_c^2} + \frac{1}{4\pi} \left( \frac{1}{r_{sd}} - \frac{1}{r_c} \right) \right) \quad (2-15)$$

and comparing (2-15) with (2-14) yields the result

$$\frac{k_i}{k} = \frac{L_c}{(L_c - l_p) + \frac{r_c^2}{4} \left( \frac{1}{r_{sd}} - \frac{1}{r_c} \right)} \quad (2-16)$$

Equation (2-16) can be used to calculate the effective permeability as defined in the API test procedure and represents the results of detailed FEM simulations of an ideal perforation; in this equation,  $r_{sd}$  is taken as  $1.26r_p$ .

For the special case—corresponding to a typical API test—of

$$L_c = 15" \quad r_c = 3.5625" \quad \text{and} \quad r_p = 0.2"$$

Eq. (2-16) reduces to

$$\frac{k_i}{k} = \frac{15}{(15 - l_p) + 11.7} \quad (2-17)$$

In figure 2-19, the result of the present work, i.e., Eq. (2-17), is presented as a plot of  $k_i/k$  versus  $l_p$ . On the same graph, the calibrations of Taylor, based on crude finite difference techniques carried out before 1967, are also plotted. As can be seen from the figure, there is a very large difference between the two curves and the Taylor result considerably overpredicts the ideal permeability. As a consequence, when actual data are analyzed using this as a calibration of ideal performance, it appears that the perforation is underperforming relative to an ideal tunnel of the same length. This basic error in the interpretation of the API test led to the belief that the crushed zone effect was significant, because only by introducing such a correction could actual data be reconciled with the theoretical model.

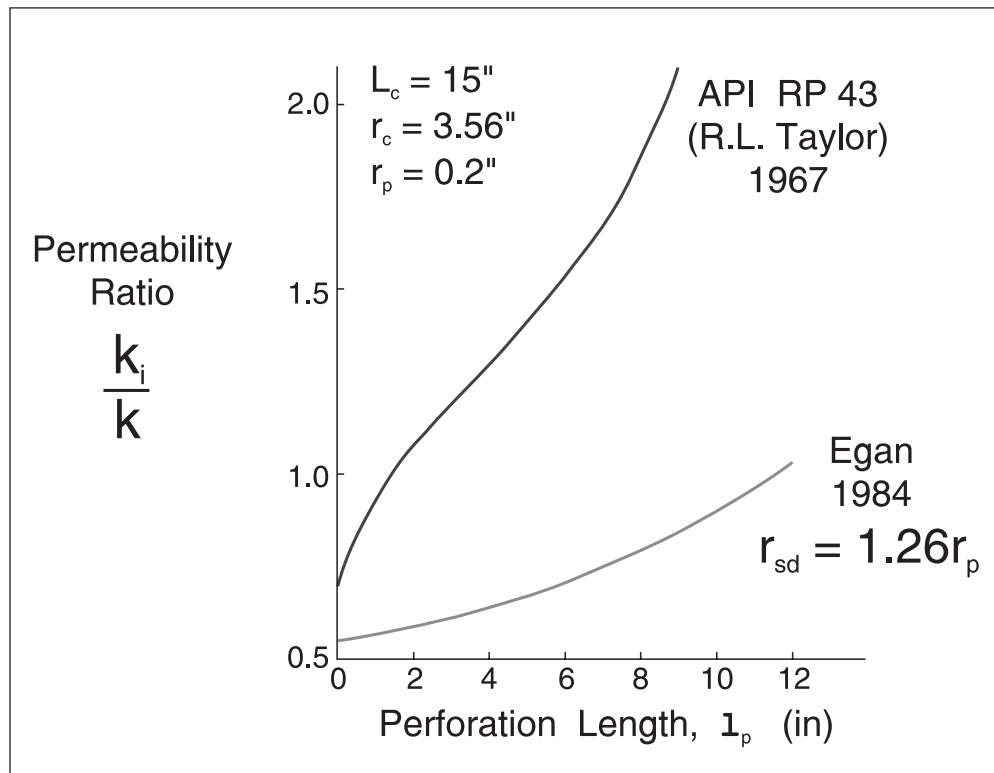


Fig. 2-19. API RP 43 test calibrations

It was essentially the work of Zimmerman<sup>28</sup> on the simulation of the pressure response of the wireline formation tester (WFT) probe that demonstrated the need for a highly refined mesh in the vicinity of a spherical source. The early finite difference simulation of Taylor simply had far too few grid points to guarantee any accuracy in the results, and the pressure drop to flow the perforation is grossly underestimated. Modern finite element techniques use optimized meshes to secure high accuracy in modeling the detailed nature of the flow, and the work of Egan paid much attention to this aspect. It is now understood that the so-called crushed zone has a much lower significance than previously thought and CFEs are much higher than the standard API test—based on the Taylor calibration—would indicate.

Since spherical flow convergence plays an important part in perforation performance, it is useful to consider the concept of spherical flow skin as illustrated in figure 2-16. Here, an altered region of permeability  $k_a$  extends out to a radius  $r_a$  over which the incremental pressure drop is given by

$$\Delta p_s = \frac{q\mu}{4\pi kr_s} \left( 1 - \frac{r_s}{r_a} \right) \left( \frac{k}{k_a} - 1 \right) \quad (2-18)$$

i.e.,

$$S_s = \frac{\Delta p_s}{\frac{q\mu}{4\pi k r_s}} = \left(1 - \frac{r_s}{r_a}\right) \left(\frac{k}{k_a} - 1\right) \quad (2-19)$$

This is the spherical flow analog of the Hawkins equation and it shows that spherical flow is highly sensitive to any permeability reduction near the sink; here  $r_s$  is the spherical sink radius and  $q$  the sink flow rate.

In the context of Darcy flow in a confined core illustrated in figure 2–20, where an altered region around the tunnel is depicted, the pressure drop is now given by

$$\Delta p = \frac{q\mu}{k} \left( \frac{L_c - l_p}{\pi r_c^2} + \frac{1}{4\pi r_{sd}} \left( \left(1 - \frac{r_{sd}}{r_c}\right) + S_s \right) \right) \quad (2-20)$$

where  $r_{sd} = 1.26 r_p$

$$\therefore S_s = \left( \left( \frac{k\Delta p}{q\mu} - \frac{L_c - l_p}{\pi r_c^2} \right) 4\pi r_{sd} - \left(1 - \frac{r_{sd}}{r_c}\right) \right)$$

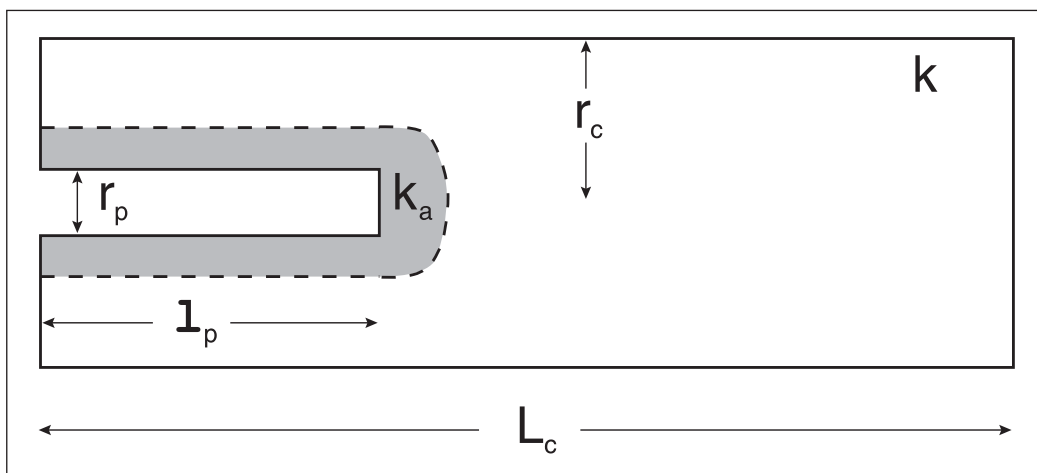


Fig. 2–20. Darcy flow in a confined core with alteration

All the quantities on the right-hand side of this equation are measured in the API test and interpretation in terms of a spherical flow skin factor may be an attractive alternative to that of a crushed zone.  $S_s$  is the perforation spherical skin relevant to confined flow. In principle,  $r_p$  is the radius near the tip; however, this is difficult to measure and may be replaced by the entrance radius. It is possible to define a perforation efficiency through the equation

$$PE = \frac{\frac{L_c - l_p}{\pi r_c^2} + \frac{1}{4\pi r_{sd}} \left(1 - \frac{r_{sd}}{r_c}\right)}{\frac{L_c - l_p}{\pi r_c^2} + \frac{1}{4\pi r_{sd}} \left( \left(1 - \frac{r_{sd}}{r_c}\right) + S_s \right)} \quad (2-21)$$

i.e., the ratio of flow with damage  $S_s$  to flow without damage. Note that all the preceding theory is relevant only to confined flow in the canister geometry of the API test.

## Effects of underbalance on perforation flow

Depth of penetration has received much emphasis over the years as the factor most important to benefit well deliverability. Yet, field results often contradict this in reports of small guns providing better production results than large ones when the small guns (shooting one-third to one-half as deep) are fired with differential pressure towards the wellbore. Well completion conditions are of equal or even greater importance than penetration in terms of achieving best well deliverability. The effect of underbalance has been studied in the laboratory by Halleck and Deo,<sup>2</sup> who reached the following conclusions:

- Underbalance between 500 and 1,000 psi is needed to obtain optimum flow efficiency;
- Perforation cleanup is due initially to transient pressure gradients followed by post-shot SS flow;
- Perforations with low initial flow efficiencies could be improved by washing, but not to optimum levels;
- The amount of rock debris washed from the perforations correlated directly with the shooting underbalance applied;
- The presence of brine improved cleanup.

The practical benefit of underbalance was demonstrated by the pioneering work of King et al.<sup>3</sup> who conducted a study of 90 wells perforated with the tubing conveyed system and showed a correlation between underbalance pressure and formation permeability that can be used to obtain clean perforations. The data, based on oil and gas producers in clean sandstone, are from wells that were perforated, tested, acidized, and then retested. There is a clear minimum underbalance line, shown in figures 2-21 and 2-22, separating the datasets of wells that had clean perforations (unassisted by acidizing) from those wells that showed a significant productivity increase after acidizing. This correlation has been widely used in the industry to design TCP jobs and achieve a maximum effective shots per foot.

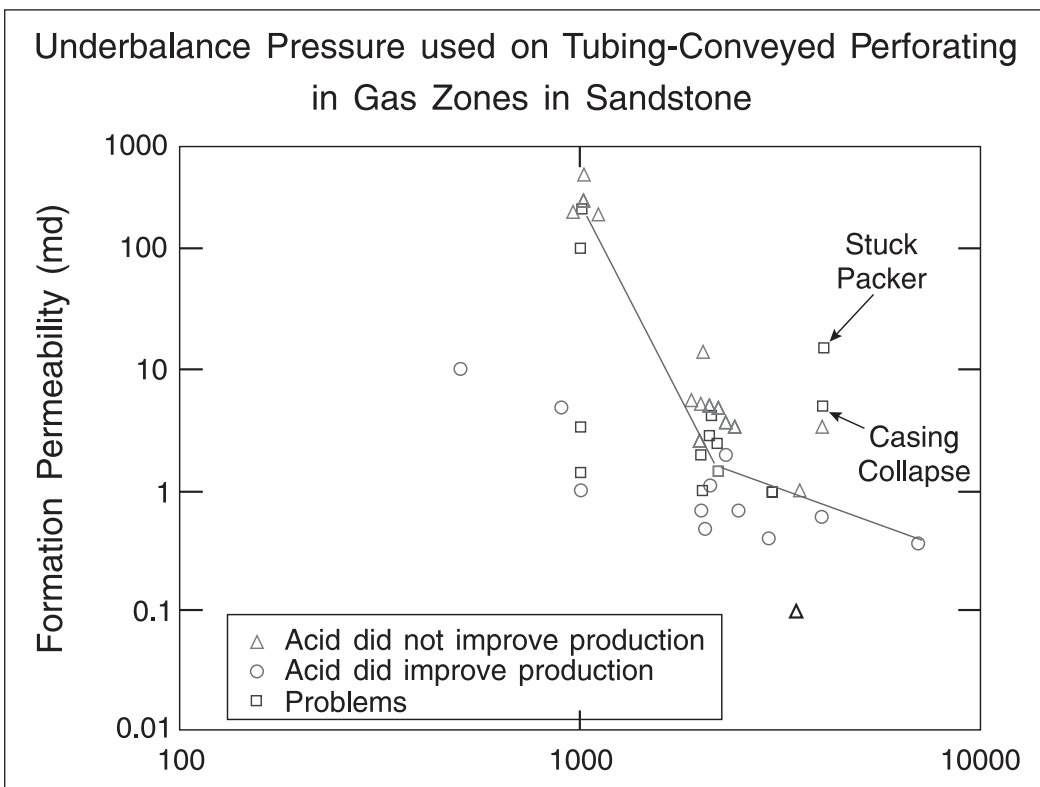


Fig. 2–21. King correlation for gas zones

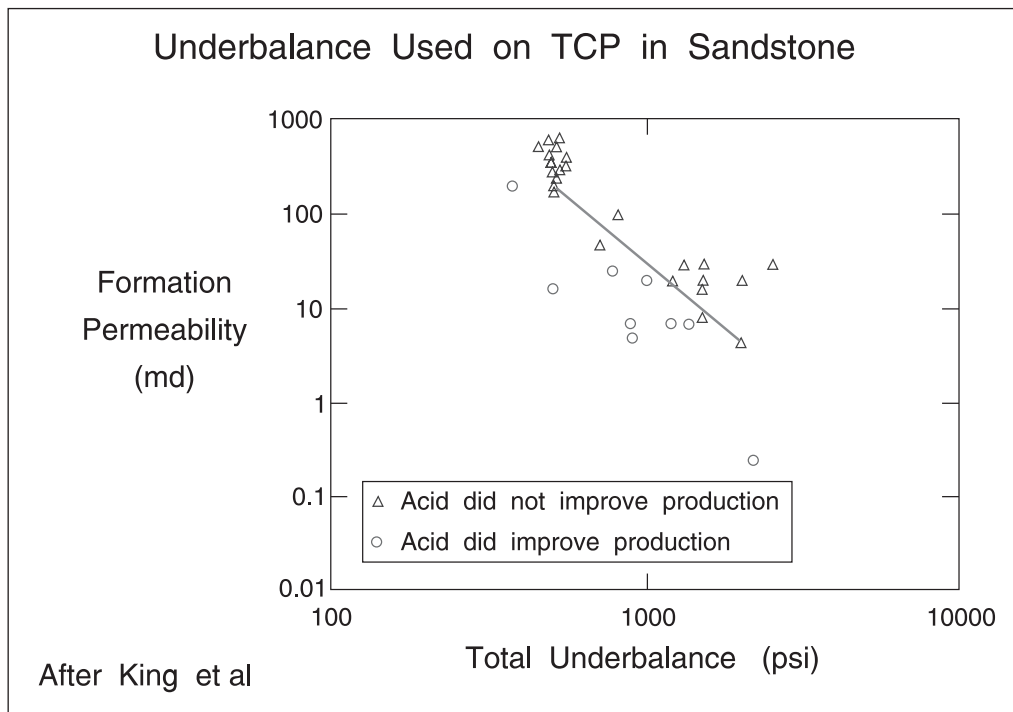


Fig. 2–22. King correlation for oil zones

## Perforation characteristics

As the high-velocity jet penetrates or punches its way through the target, formation material is forced laterally or radially outward from the axis of the perforation. This results in the creation of a compacted zone around the tunnel as shown in figure 2–7. Immediately after penetration, the perforation is found to be filled with debris and it is only after a certain amount of fluid has been flowed from the perforation that it will liberate its debris and appear clean. However, even when the perforation is clean, the damaged or compacted zone remains as illustrated in figure 2–7. This is characterized by substantially reduced permeability of the order of 20% of that in the original formation. The lateral extent of the zone varies from about ½ in. at the tip of the perforation to 1 in. at the face plate for a typical large Hollow Carrier gun charge. Zones are smaller for shallow penetrating charges. The effect of the compacted zone is that it reduces the flow efficiency of the perforation as compared, for example, to an ideal hole of the same depth and diameter.

In terms of the capacity of the well to produce, shot density would appear to be of greater importance than penetration depth. In the past, it was often inadvisable to exceed four shots per foot because of the limitation on the mechanical strength of the formation. However modern practice indicates that there is no mechanical problem with high shot density perforating. As pointed out by Harris, the perforation pattern has a noticeable effect on productivity. Strip shooting (all the perforations in a vertical line on the same side of the hole) gives lower productivity than staggered arrangements.

## Perforation skin factor $S_{pe}$

The ideal skin factor  $S_{pe}$ , is used to represent the pressure drop caused by flow convergence into the perforations and is a function of the cement sheath radius  $r_w$ , the perforation diameter  $2r_p$ , the penetration beyond the cement sheath  $l_p$ , the vertical perforation spacing interval  $h_{pe}$ , the number of perforations per plane  $m$  or the phasing  $\theta$ , and the ratio of horizontal to vertical permeability  $k_r/k_z$ . The controlling dimensionless groups based on these variables are as follows:

$$d_D = \frac{d}{r_w} \sqrt{\frac{k_r}{k_z}} \quad (\text{dimensionless hole diameter})$$

$$a_D = \frac{l_p}{r_w} \quad (\text{dimensionless penetration})$$

$$h_D = \frac{h_{pe}}{r_w} \sqrt{\frac{k_r}{k_z}} \quad (\text{dimensionless spacing interval})$$

$$m = 360/\theta \quad (\text{number of perforations per plane})$$



Harris and, more recently, Hong<sup>4</sup> have obtained numerical solutions to the problem of converging flow into a cased and perforated well. These solutions pertain to patterns of ideal perforations and do not allow for the effect of a compacted zone. The ideal perforation skin  $S_{pe}$  refers to a situation modelled by FEM simulation with all perforations flowing in a homogeneous medium. The computed results on drawdown in SS flow are presented in the form of an apparent skin effect  $S_{pe}$  from which well productivity without formation damage (according to SS or semi-steady-state (SSS) operation) can be rapidly calculated. The dimensionless skin effect for an idealized perforation pattern is a function of the dimensionless groups just defined, and Harris presents the functional dependence on a series of graphs. Hong extended the work of Harris to larger well diameters and also analyzed the interaction between perforations and a well-defined altered zone of the Hawkins type. Thus in the open-hole condition before perforating a drilling damaged region of reduced permeability  $k_a$  and radial extent  $r_a$  has been created in which a set of perforations will be embedded. The open-hole skin i.e. pre-perforation skin will be given by the Hawkins equation.

$$S_{oh} = \left( \frac{k}{k_a} - 1 \right) \ln \frac{r_a}{r_w} \quad (2-22)$$

Hong presented his results in the form of a nomograph and this form of presentation was later adopted by Locke as shown in figure 2-31.

In the previous chapter the Hawkins formula for the skin effect due to a well-defined altered zone in the immediate vicinity of the wellbore was derived and this was identified with the true skin  $S_{tr}$  associated with formation damage or improvement. In the case of a perforated well, it is not easy to distinguish between the combined effects of an existent altered region and subsequent perforation because of the unpredictable nature of the compacted zone around each tunnel. Hence,  $S_{tr}$  as used later in equation (1-93) refers to the dual influence of both effects viz formation damage and subsequent perforation. Note that the flow convergence associated with perforations occurs much nearer to the wellbore than that due to partial completion or penetration and, over a radial distance scale, comparable to the thickness of the altered zone. Thus, the skin effect due to perforation is subject to the Rowland correction when the well is partially penetrating.

If the compacted zone is lumped with any incipient altered zone, then it would be convenient if the true skin  $S_{tr}$  could be written as an arithmetic sum of individual components of the form

$$S_{tr} = S_{pe} + S_d \quad (2-22a)$$

where the factor  $S_{pe}$  is the skin effect associated with ideal perforations as given by the analysis of Harris or Hong. However the interacting nature of a perforation bank embedded in a damaged zone created during drilling implies that only a combined effect can be entertained and the equation should be written in the following way

$$S_{tr} = S_c = \overline{S_{pe} + S_d} \quad (2-22b)$$

i.e. the effects of perforation and damage do not occur in series and must be described through a combined (true) skin  $S_c$ ; a model predicting  $S_c$  values will be developed later.

Substituting Eq. (2–22b) into Eq. (1–117) in chapter 1 results in

$$S_a = \overline{S_{pe}} + S_d/b + S_p + S_{swp} = S_c/b + S_p + S_{swp} \quad (2-23)$$

which is a generalized equation for the total apparent skin  $S_a$  in a perforated, damaged, partially completed, deviated well. As before, the contributions due to combined perforation and damage  $S_c$ , partial completion  $S_p$ , and well deviation  $S_{swp}$  can be estimated from the appropriate theoretical relation (assuming that the perforation depth and diameter are known). If the total apparent skin has been measured in a transient well test, then an appropriate model can be used, in principle, to find the drilling damage parameters  $k_s$  and  $r_s$ . The motivation for this is that a justification for stimulation, e.g., acidizing, can only be made on the basis of the change that can be obtained by utilizing the estimate of the combined skin  $S_c$  after stimulation (hopefully negative) in Eq. (2–23) to find the modified apparent skin and then using the appropriate inflow relation for the productivity. The most important attribute of Eq. (2–23) is that it demonstrates the sensitivity of the total skin effect to the contribution from damage through the division of the true skin  $S_c$  by the penetration ratio  $b$ . Assessing the effect of stimulation on a perforated completion is not easy and an exercise in pre- and post-acid skin determination is required.

When the altered zone is well defined, i.e.,  $k_s$  and  $r_s$  known, such as in sand consolidation, and the compacted zone can be neglected, it is possible to predict the damage skin  $S_d$ . However, the analysis of Hawkins (or of Jones and Watts for a partially completed well) is no longer applicable when perforations penetrate the altered zone. This problem has been examined by Hong, who present nomograms for estimating the damage effect in this situation. Two cases arise: one when the perforation lies wholly inside the altered region and one when it extends right through into the formation proper. As one might expect, the damage effect is much less in the latter situation.

## Approximate Model of the Skin Factor in a Perforated Completion

### Introduction

The concept of a well skin factor  $S$  was introduced by Van Everdingen and Hurst to explain the effect of formation damage on well productivity. For an openhole completion with a cylindrical altered region of radius  $r_a$  and reduced permeability  $k_a$  as illustrated in figure 2–23, the theoretical skin  $S_{oh}$  is given by the familiar Hawkins equation:

$$S_{oh} = \frac{\Delta p_s 2\pi kh}{q\mu} = \left( \frac{k}{k_a} - 1 \right) \ln \frac{r_a}{r_w} \quad (2-24)$$

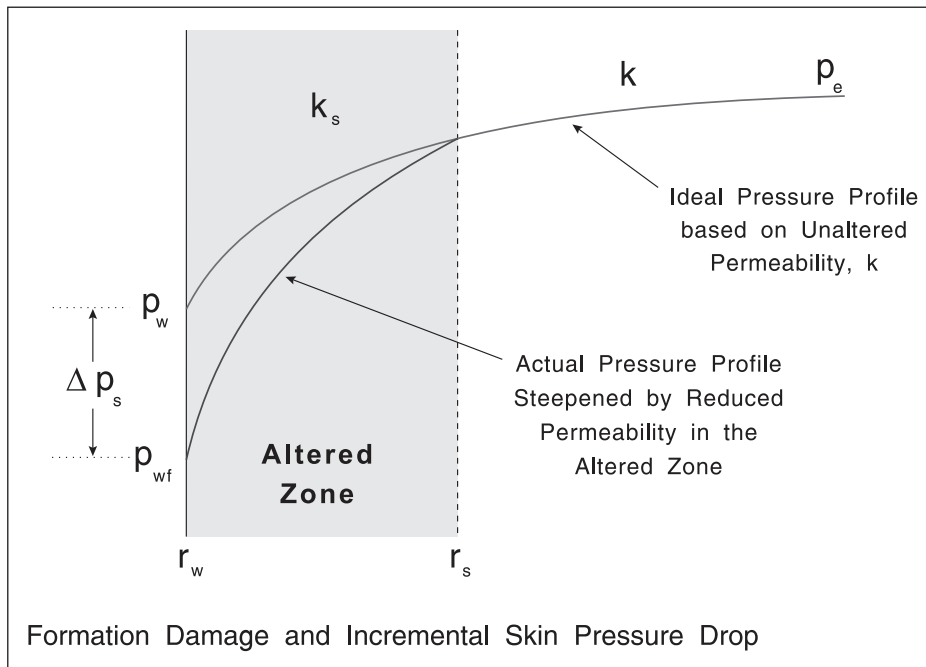


Fig. 2–23. Altered zone in an openhole completion

Here,  $\Delta p_s$  is the incremental pressure drop occurring in the near-wellbore region due to the changed permeability. The key point is that the skin factor is used as a device to represent any deviation from pure radial flow at formation permeability  $k$  in the vicinity of the sandface. Well skin factors can be determined in the field from transient pressure testing, but this does not allow the independent calculation of  $k_a$  and  $r_a$  from Eq. (2–24). Presuming  $r_a$  to be associated with the depth of invasion of mud filtrate, an estimate of this quantity is possible via resistivity logs and hence  $k_a$ —the damaged zone permeability—can be computed in principle from (2–24) if  $S_{oh}$  has been determined from a well test. When a well is cased and perforated as illustrated in figure 2–24, the skin factor  $S_c$  represents the combined effect of perforation and formation damage. Obviously, there is a complicated three-dimensional flow distribution in the vicinity of the wellbore with localized flow concentration into the individual perforations. It is interesting that the first study of the detailed nature of the flow into a perforated well was carried out by Muskat<sup>5</sup> in 1950 using an electrolytic tank analog model. In more recent investigations, sophisticated finite element numerical simulations have been employed to model the flow behavior. The original results of Muskat, plotted in figure 2–13, are surprisingly close to the most recent numerical results with very fine grids; this is a real tribute to the 1950 analog study. An approximate analytical model will be developed here which can be used to correlate the results of such studies and provide physical insight into the flow mechanism. In general, the inflow behavior of a perforated completion depends on the following key factors:

- perforation density, i.e., number of shots per unit length  $n_s$ ;
- perforation length, i.e., depth of penetration  $l_p$ ;
- geometry of perforation pattern, i.e., phasing  $\theta$ ;
- permeability anisotropy  $A = k_v/k$ ;
- formation heterogeneity;
- extent and magnitude of any formation damage  $r_a$  and  $k_a$ ;

- presence of a compacted zone around the perforation tunnel;
- perforation tunnel radius  $r_p$ ;
- wellbore radius  $r_w$ .

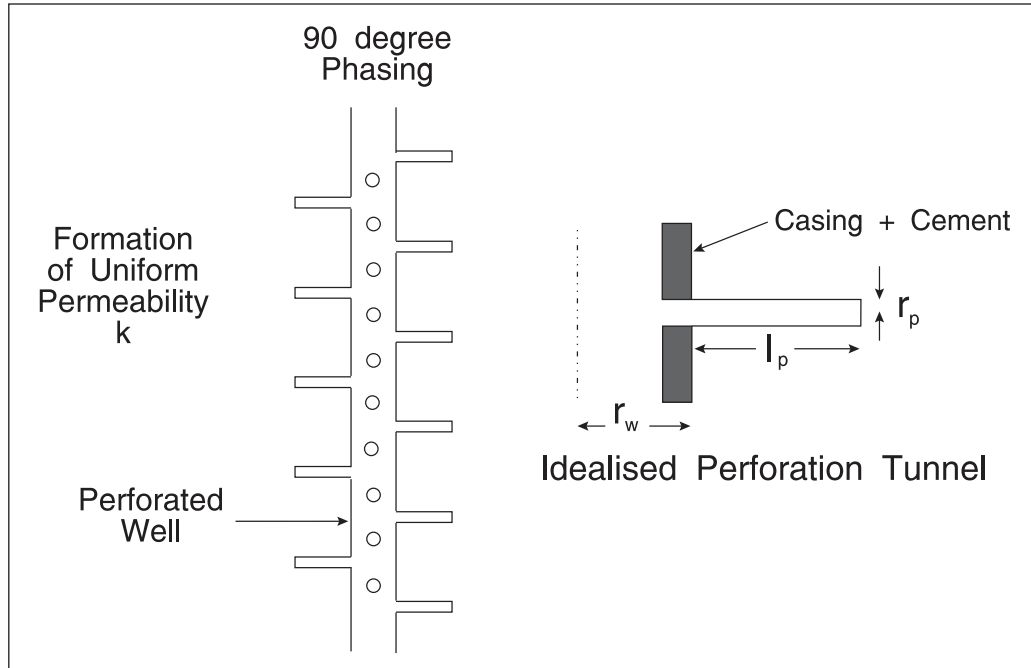


Fig. 2–24. Perforated completion

Supposing an FEM simulation of a perforated completion has been set up, which can model the detailed nature of SS flow into the well, i.e., predict the well bottom-hole flowing pressure  $p_w$  for a given flow rate  $q$ , then the results can always be expressed in terms of a combined perforation/damage skin factor  $S_c$  through the defining equation

$$p_{Dss} = \frac{(p_e - p_w)2\pi kh}{q\mu} = \ln \frac{r_e}{r_w} + S_c \quad (2-25)$$

Thus for a specified well rate  $q$  and uniform external pressure  $p_e$  at radius  $r_e$  (where  $r_e \gg r_w + l_p$ ), the simulator computes a perforation pressure  $p_w$  assuming infinite conductivity tunnels, from which  $S_c$  can be computed using (2–25). Following the accepted practice of using the skin factor to account for deviations from pure radial flow, this is a useful way of expressing the results of such studies. The problem is to correlate the skin factor  $S_c$  with the determining variables in the list given above. It is also possible to define a SS productivity index (PI)  $J_{ss}$  through an equation relating surface flow rate to drawdown, viz.,

$$q_s = J_{ss}(p_e - p_w) \quad (2-26)$$

which on comparison with (2–25) gives

$$J_{ss} = \frac{2\pi kh}{B\mu \left( \ln \frac{r_e}{r_w} + S_c \right)} \quad (2-27)$$

Finite element methods (FEM) allow great sophistication in the complexity of the grid setup in the numerical simulation, and the results of such investigations are quite sensitive to the grid system employed. There is considerable localized flow concentration into the perforation tips, and very fine elements are required in this vicinity. Much of the early work has now been shown to have significant error due to inadequate grid refinement; however, more recent investigations have employed highly optimized grids and the results of different authors are converging to similar conclusions. It should be remembered that the FEM simulations are all for a homogeneous porous medium of uniform, horizontal permeability  $k$  in which the perforated completion is embedded. Real formations are heterogeneous and individual perforation tunnels will lie in varying permeability. Indeed, one of the attractions of tubing conveyed perforation (TCP)—besides the advantage of underbalance—is that a large number of shots per foot increases the statistical chance of individual tunnels landing in localized high permeability. Another problem, especially in deviated wells, is that the perforating guns may not lie symmetrically in the well and hence perforations will have different penetrations on opposite sides of the hole. Simulations of idealized perforation patterns in a homogeneous formation do not account for such effects and hence it is not necessary to be ultrasophisticated in the question of grid refinement.

The objective is to develop an understanding of the mechanism of the skin effect in a perforated well that will assist in the interpretation of skin factors measured in actual well tests and allow realistic assessments to be made of the likely origin of reduced productivity. An accurate FEM simulation of a perforated well with no altered zone or compacted zone will give an ideal skin factor  $S_{pe}$  for a homogeneous, undamaged formation; this simply accounts for the deviation from pure radial flow near the wellbore due to the presence of infinite conductivity tunnels. Skin factors determined from well tests can be compared to ideal values, and the flow efficiency of a well can be defined as the ratio of the actual PI to that which would occur with  $S_c$  taking on the ideal value; thus

$$\frac{\text{FLOW}}{\text{EFFICIENCY}} = \frac{\ln \frac{r_e}{r_w} + (S_c)_{\text{ideal}}}{\ln \frac{r_e}{r_w} + (S_c)_{\text{measured}}} \quad (2-28)$$

Some authors have used the concept of a productivity ratio (PR) to quantify the effect of ideal perforation on well performance where

$$\text{PR} = \frac{\ln \frac{r_e}{r_w}}{\ln \frac{r_e}{r_w} + (S_c)_{\text{ideal}}} \quad (2-29)$$

In the approach adopted here, ideal perforation behavior will be characterized by a skin factor and Eq. (2–29) can always be used to compute productivity ratios where required. Note that in modern TCP with deep penetration and many shots per foot, it is quite easy for ideal perforation skins to be negative, i.e., a perforated well without damage can produce more than open hole. Here  $(S_c)_{ideal}$  is synonymous with  $S_{pe}$ .

The approximate model for perforated well productivity described here is a development of the idea due to McLeod,<sup>6</sup> which is illustrated in figure 2–25; McLeod assumed that the actual three-dimensional flow pattern could be approximated by pure radial flow up to the perforation tips at  $r_w + l_p$  followed by local radial vertical flow convergence into individual tunnels. This model was the first to show how non-Darcy flow affected perforated completions and illustrated the crucial importance of shots per foot in gas well completion design. Examination of FEM simulation results shows that the flow distribution in the vicinity of individual perforations is much more spherical in character than radial vertical with significant flow concentration into the perforation tip. The McLeod model assumes uniform flux along the tunnel length, whereas in practise most of the entry occurs near the tip whenever the phasing is greater than 0 degrees; this is important in the modeling of gravel pack completions.

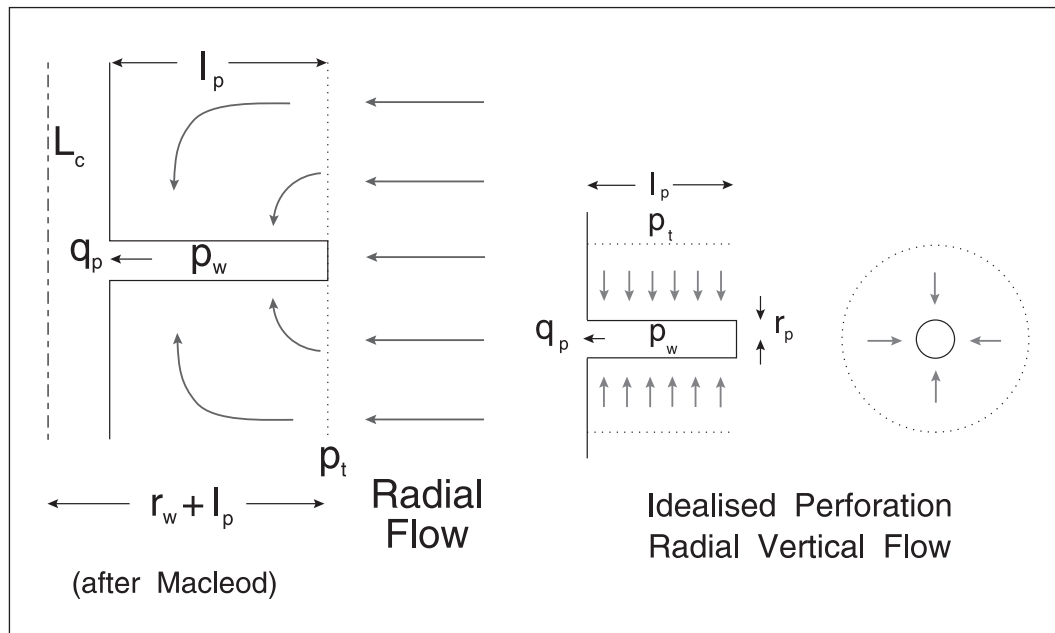


Fig. 2–25. Radial vertical flow model for perforation inflow

The skin factor  $S_c$  due to perforation and formation damage will be referred to as the *true skin* since it reflects the near-wellbore condition of the well. However, in the context of well productivity, it is useful to model other phenomena—such as limited entry and well deviation—through the use of pseudo-skin factors; for example, in the case of a limited entry with a penetration ratio  $b = h_p/h$ , the SS well inflow is described by the equation

$$P_{Dss} = \frac{(p_e - p_w)2\pi kh}{q\mu} = \ln \frac{r_e}{r_w} + S_a \quad (2-30)$$

where

$$S_a = \frac{S_c}{b} + S_p \quad (2-31)$$

$S_a$  is called the *total apparent skin* and is the sum of contributions from different effects; here,  $S_p$  is the pseudo-skin due to limited entry (described in the section “Geometric or completion skin factors”). When a well is tested under transient conditions, the pressure behavior in the middle time region is described by an equation of the form

$$p_D = \frac{(p_i - p_w)2\pi kh}{q\mu} = \frac{1}{2} \ln \frac{4t_D}{\gamma} + S_a \quad (2-32)$$

The important point is that well testing usually determines the quantity  $S_a$ —the total apparent skin—and interpretation of the well test often involves determining  $S_c$  from the measured total effect. In the detailed discussion of the various skin contributions, emphasis will be placed on deriving formulae for  $S_a$  in different conditions.

It is useful to express equations in terms of practical units, and the following oil field units have been adopted here:

$p$ : psi	$q_{sp}$ : bbl/d	$k$ : md
$\mu$ : cp	$\beta$ : ft <sup>-1</sup>	$\rho$ : g/cc
$r$ : ft	$h$ : ft	$l$ : ft

For this system, the dimensionless pressure  $p_D$  is given by

$$p_D = \frac{\Delta p 2\pi kh}{887.2 q\mu} \quad \text{and} \quad J_{ss} = \frac{2\pi kh}{887.2 B\mu \left( \ln \frac{r_e}{r_w} + S_c \right)} \quad (2-33)$$

When field units are used in equations, for clarity and ease of conversion to other units systems the theoretical constants like  $2\pi$  entering the fundamental version in strict scientific units will be left in place.

## Spherical steady-state flow

In the development of an approximate model for inflow into a perforated completion, the local flow convergence into individual perforations is described by spherical flow theory and it is useful at this point to consider the integration of the Forcheimer equation in SS spherical conditions as shown in figure 2–26. For SS, incompressible flow the Forcheimer equation takes the form

$$\frac{dp}{dr} = \frac{\mu}{k} u_r + \beta \rho u_r^2 \quad (2-34)$$

where the flux at radius  $r$  is  $u_r = \frac{q_{sp}}{4\pi r^2}$ ; here  $\beta$  is the inertial resistance coefficient,  $\rho$  is the fluid density, and  $q_{sp}$  is the volumetric (in situ) flow rate into the spherical sink. Substituting for  $u_r$  gives

$$\frac{dp}{dr} = \frac{q_{sp}\mu}{4\pi k r^2} + \frac{\beta\rho q_{sp}^2}{(4\pi)^2 r^4} \quad (2-35)$$

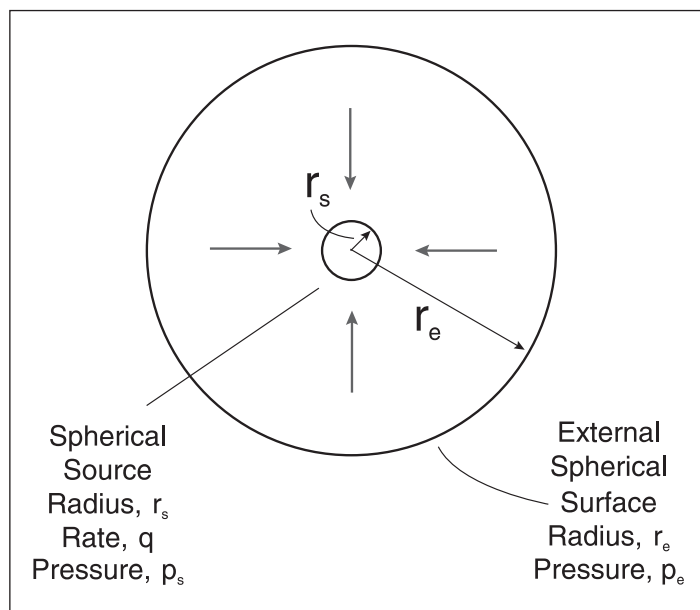


Fig. 2-26. Ideal spherical flow geometry

Integrating between the limits of external radius  $r_e$  and source radius  $r_s$  gives

$$\int_{p_s}^{p_e} dp = \frac{q_{sp}\mu}{4\pi k} \int_{r_s}^{r_e} \frac{dr}{r^2} + \frac{\beta\rho q_{sp}^2}{(4\pi)^2} \int_{r_s}^{r_e} \frac{dr}{r^4} \quad (2-36)$$

$$p_e - p_s = \frac{q_{sp}\mu}{4\pi k} \left( \frac{1}{r_s} - \frac{1}{r_e} \right) + \frac{\beta\rho q_{sp}^2}{3(4\pi)^2} \left( \frac{1}{r_s^3} - \frac{1}{r_e^3} \right) \quad (2-37)$$

The maximum pressure gradient occurs at the sink, i.e.,  $r = r_s$ , and is given by

$$\left. \frac{dp}{dr} \right|_{r_s} = \frac{q_{sp}\mu}{4\pi k r_s^2} + \frac{\beta\rho q_{sp}^2}{(4\pi)^2 r_s^4} \quad (2-38)$$



When the sink radius is identified with a perforation tip, this equation for maximum stress on the formation is important in sanding calculations. On the basis of (2-43), it is possible to define a Reynold's number for perforation tip flow as

$$\text{Re} = \frac{\left(\frac{dp}{dr}\right)_{\text{ND}}}{\left(\frac{dp}{dr}\right)_{\text{DA}}} = \frac{\beta\rho q_{\text{sp}}^2}{(4\pi)^2 r_s^4} \frac{4\pi k r_s^2}{q_{\text{sp}} \mu} = \frac{\beta\rho k q_{\text{sp}}}{4\pi r_s^2 \mu} \quad (2-39a)$$

When Re as defined above is greater than about 0.1, then non-Darcy flow is important. Practical application of the equations in oil field units requires the insertion of units conversion factors. In oil field units, Eq. (2-39a) becomes

$$\text{Re} = \frac{\left(\frac{dp}{dr}\right)_{\text{ND}}}{\left(\frac{dp}{dr}\right)_{\text{DA}}} = \frac{6.4135 \times 10^{-14} \beta\rho k q_{\text{sp}}}{4\pi r_s^2 \mu} \quad (2-39b)$$

Typically, the flow rate through an individual perforation has to be above about 30 bbl/day for the perforation liquid Reynold's number to exceed a value of 0.1 for an oil of viscosity  $\mu$  of 1 cp.

In Eq. (2-37),  $r_e$  is usually large compared to  $r_s$  and the following simplified form, independent of  $r_e$ , may be employed, i.e.,

$$p_e - p_s = \frac{q_{\text{sp}} \mu}{4\pi k r_s} + \frac{\beta\rho q_{\text{sp}}^2}{3(4\pi)^2 r_s^3} \quad r_e \gg r_s \quad (2-40)$$

In oil field units, this becomes

$$p_e - p_s = \frac{887.2 q_{\text{sp}} \mu}{4\pi k r_s} + \frac{5.6901 \times 10^{-11} \beta\rho q_{\text{sp}}^2}{3(4\pi)^2 r_s^3} \quad (2-41)$$

The total pressure drop  $\Delta p = p_e - p_s$  is composed of two components: one due to laminar or Darcy flow and the other due to inertial or non-Darcy flow, i.e.,

$$\Delta p = p_e - p_s = \Delta p_{\text{DA}} + \Delta p_{\text{ND}} \quad (2-42)$$

where  $\Delta p_{\text{DA}} = \frac{q_{\text{sp}} \mu}{4\pi k r_s}$  or  $\frac{887.2 q_{\text{sp}} \mu}{4\pi k r_s}$  and  $\Delta p_{\text{ND}} = \frac{\beta\rho q_{\text{sp}}^2}{3(4\pi)^2 r_s^3}$  or  $\frac{5.6901 \times 10^{-11} \beta\rho q_{\text{sp}}^2}{3(4\pi)^2 r_s^3}$

The approximate model to be developed in the succeeding section is based on the premise that non-Darcy flow effects are localized near the perforation tips; thus the spherical sink flow rate  $q_{sp}$  used here will become identified with the flow to an individual perforation denoted  $q_p$ .

### Steady-state radial and linear flow

It is useful at this point to derive the radial and linear flow integrations of the Forcheimer equation which arise, for example, in the McLeod model and in the analysis of gravel pack completions, respectively. In the case of radial flow illustrated in figure 2–27, the flux at cylindrical radius  $r$  is given by

$$u_r = \frac{q}{2\pi hr} \tag{2-43}$$

where  $h$  is the height of the system. Integration of (2–34) in conjunction with (2–43) gives the familiar result

$$p_e - p_s = \frac{q\mu}{2\pi kh} \ln \frac{r_e}{r_s} + \frac{\beta\rho q^2}{(2\pi h)^2} \left( \frac{1}{r_s} - \frac{1}{r_e} \right) \tag{2-44}$$

In the case of an openhole well,  $h$  is the formation thickness and the source radius  $r_s$  is the wellbore radius  $r_w$ .

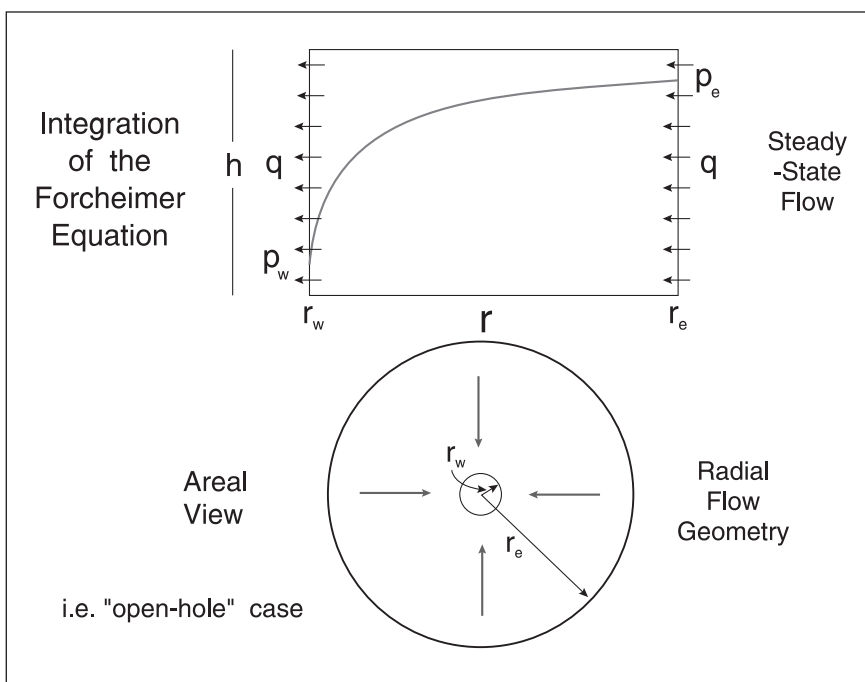


Fig. 2–27. Radial flow geometry

For linear flow along a channel of constant cross-sectional area  $A_c$  and length  $l$ , then

$$u = \frac{q}{A_c} \quad (2-45)$$

and the integrated form of (2-34) is

$$p_e - p_s = \frac{q\mu l}{kA_c} + \frac{\beta\rho q^2 l}{A_c^2} \quad (2-46)$$

This equation will be used later to model the pressure drop in a gravel-packed perforation tunnel.

## Perforated completion

The inflow behavior of a perforated completion can be studied by setting up a detailed FEM simulation of a well in a homogeneous formation of permeability  $k$ . The perforation pattern is characterized by the total number of shots  $N_p$ , the perforation length  $l_p$ , and radius  $r_p$  as well as the geometry of the system, e.g., in-line, spiral, or 90 degree phasing. In order to model the local flow convergence into individual perforations, very fine elements are required especially around the perforation tips. In this treatment, an approximate model will be developed that can be used to express the results of such detailed simulations of SS inflow and provide physical insight into the mechanism of the process. Examination of simulation results shows that the flow distribution is characterized by concentration at the tip of the perforation with an approximately hemispherical flow taking place in this region. The local flow distribution is illustrated diagrammatically in figure 2-28, and the idea is to represent the tunnel by a hemispherical sink of equivalent radius  $r_s$  where

$$r_s = \sqrt{r_p l_p} \quad (2-47)$$

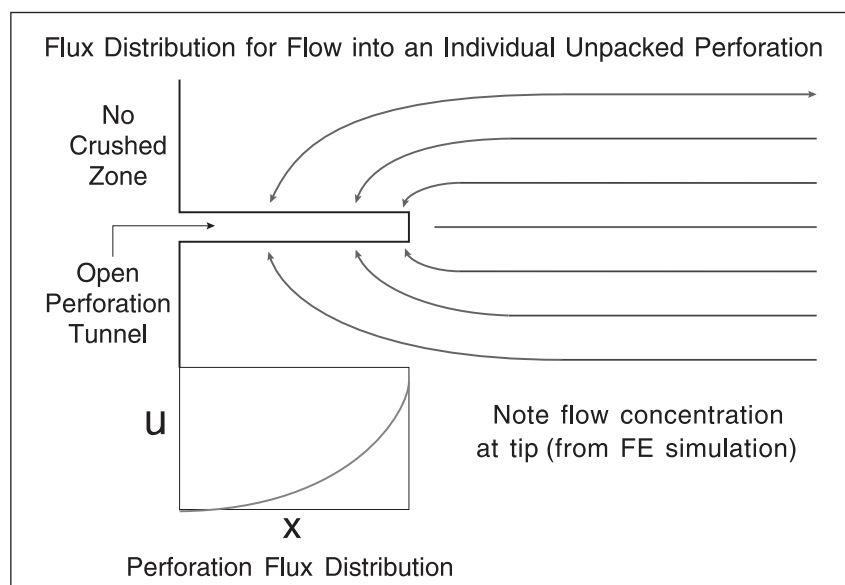


Fig. 2-28. Flow concentration into an individual perforation

This definition of an equivalent spherical radius is based on equating the surface area of the perforation with the surface area of a hemisphere of radius  $r_s$ , i.e.,

$$2\pi r_p l_p = 2\pi r_s^2 \quad \text{giving} \quad r_s = \sqrt{r_p l_p}$$

The approximate model is based on radial flow up to the perforation tip followed by local spherical flow convergence into individual perforations as shown in figure 2–29. Denoting the intermediate pressure at the perforation tip (at cylindrical radius  $r = r_w + l_p$ ) by  $p_t$ , the classical radial flow theory gives

$$p_e - p_t = \frac{q\mu}{2\pi kh} \ln \frac{r_e}{r_w + l_p} \quad (2-48)$$

where  $q$  is the well rate and  $h$  the formation thickness, i.e.,  $q/h$  is the flow rate per unit height. In this discussion of perforated completions, it will be assumed that  $r_w$  is the open-hole radius given by the calliper survey and  $l_p$  is the active perforation length (not including cement and casing). The bottom-hole pressure  $p_w$  is now assumed to be given by

$$p_t - p_w = f_D^s \frac{q_p \mu}{4\pi k_s r_s} \quad (2-49)$$

where  $q_p = q/N_p$  is the flow rate per perforation. Equation (2–49) along with (2–48) is simply the definition of the flow shape factor  $f_D^s$  that allows the results of FEM simulations to be expressed in a convenient form;  $k_s$  is the spherical permeability given by

$$k_s = \sqrt[3]{k^2 k_v} = k \sqrt[3]{A} \quad (2-50)$$

where  $A$  is the formation vertical to horizontal permeability anisotropy, i.e.,  $A = k_v/k$ . Thus the drawdown for a perforated completion may be written as

$$p_e - p_w = \frac{q\mu}{2\pi kh} \ln \frac{r_e}{r_w + l_p} + f_D^s \frac{q_p \mu}{4\pi k_s r_s}$$

i.e.,

$$p_e - p_w = \frac{q\mu}{2\pi kh} \left( \ln \frac{r_e}{r_w + l_p} + \frac{f_D^s h}{2N_p r_s \sqrt[3]{A}} \right) \quad (2-51)$$

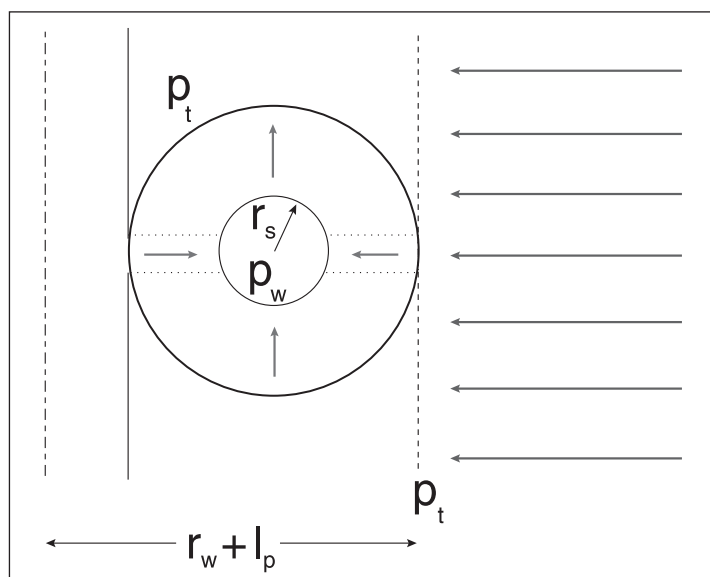


Fig. 2–29. Approximate inflow model

Anticipating that the flow shape factors  $f_D^s$  are of the order of unity, this model shows very clearly how the inflow into a perforated completion is crucially controlled by the following parameters:

- $N_p$  – Number of perforations
- $l_p$  – Perforation depth of penetration
- $A$  – Formation anisotropy

A perforated completion is usually described by the number of shots per unit length, denoted  $n_s$ , and the number of perforations  $N_p$  is given by  $N_p = n_s h$  for a full completion.

The pressure drop for pure radial (open-hole) flow is given by

$$p_e - p_w = \frac{q\mu}{2\pi kh} \ln \frac{r_e}{r_w} \quad (2-52)$$

and the difference between the actual  $\Delta p$  and this quantity is

$$\Delta p_s = \frac{q\mu}{2\pi kh} \left( \ln \frac{r_e}{r_w + l_p} + \frac{f_D^s h}{2N_p r_s^3 \sqrt{A}} - \ln \frac{r_e}{r_w} \right) \quad (2-53)$$

This is the incremental skin pressure drop relative to open-hole conditions, and the skin factor  $S_c$  due to perforation becomes

$$S_c = \frac{\Delta p_s 2\pi kh}{q\mu} = \ln \frac{r_w}{r_w + l_p} + \frac{f_D^s h}{2N_p r_s^3 \sqrt{A}} \quad (2-54a)$$

$$\text{or} \quad S_c = \ln \frac{r_w}{r_w + l_p} + \frac{f_D^s}{2n_s r_s \sqrt[3]{A}} \quad (2-54b)$$

Hence, for radial SS Darcy flow into a perforated well with a full entry and no altered zone, the inflow equation may be written as

$$p_{Dss} = \frac{(p_e - p_w)2\pi kh}{q\mu} = \ln \frac{r_e}{r_w} + S_c \quad (2-55)$$

The perforation skin factor is principally controlled by the number of perforations  $N_p$  and the depth of penetration  $l_p$ , but the perforation radius  $r_p$ , the formation anisotropy  $A = k_v/k$ , and the flow shape factor  $f_D^s$  which is a function of shooting pattern also affect  $S_c$ . In the formulation of the model, it is presumed that all perforations are flowing equally, i.e.,  $q_p = q/N_p$ , and that the rock permeabilities  $k$  and  $k_v$  are uniform; this is a major assumption that will not be satisfied in heterogeneous formations. However, the homogeneous model does provide an initial basis for modeling perforation behavior. Note that the local flow convergence into a perforation tip is affected by the formation anisotropy  $A$  since it is spherical permeability that enters Eq. (2-49). Since no altered region has yet been introduced into the model, Eq. (2-54a,b) represent the ideal perforation skin in the absence of damage of any sort.

As  $N_p$  becomes large, the second term in Eq. (2-54a,b) is negligible and  $S_c$  attains a minimum negative value given by

$$(S_c)_{\min} = \ln \frac{r_w}{r_w + l_p} = -\ln \frac{r_w + l_p}{r_w} \quad (2-56)$$

i.e., an effective well-bore radius of  $r_w + l_p$ ; this imposes a lower limit of negative skin due to high shot density perforation.

## Darcy flow shape factors

The Darcy flow shape factor  $f_D^s$  as defined by Eq. (2-51) is simply a way of presenting the results of exact FEM simulations in a useful form that is easy to apply. Egan<sup>7</sup> has carried out a careful study using an advanced code developed by Campbell, which has a powerful finite element generation facility. In agreement with the conclusions of Tariq,<sup>8</sup> it was shown that the earlier simulations of Locke,<sup>9</sup> Hong,<sup>10</sup> and Harris<sup>11</sup> were optimistic due to insufficient grid dimension. Interestingly, the most recent FEM results are quite close to the original data of Muskat obtained from electrolytic tank experiments. Egan studied the following three perforation geometries:

- strip, i.e., 0 degree phasing with all perforations in line
- plane, i.e., 90 degree phasing
- spiral

Egan's data were converted to spherical flow shape factors using the rearranged form of (2-54b), i.e.,

$$f_D^s = \left( S_c - \ln \frac{r_w}{r_w + l_p} \right) 2n_s \sqrt{r_p l_p} \sqrt[3]{A} \quad (2-57)$$

and the results are plotted in figure 2-30 for the three perforation geometries. In the case of a spiral pattern that involves the least interaction between adjacent perforations, the flow shape factors are remarkably close to unity indicating the applicability of the spherical flow approximation. The results for in-line (strip) shooting are least well represented by spherical flow theory as would be expected, given the nature of the flow pattern; the anomalous nature of in-line perforation has been pointed out by Karakas and Tariq.<sup>12</sup> However, the importance of phasing has been recognized in modern perforation practice and in-line perforation is currently not often carried out. The spherical flow shape factor  $f_D^s$  for staggered phasing does not differ substantially from unity and the ideal skin factor can be predicted with very little error by assuming  $f_D^s = 1$  in Eq. (2-54b). Very accurate predictions of  $S_c$  require the information on flow shape factor from FEM studies—such as figure 2-30—to be stored in a database.

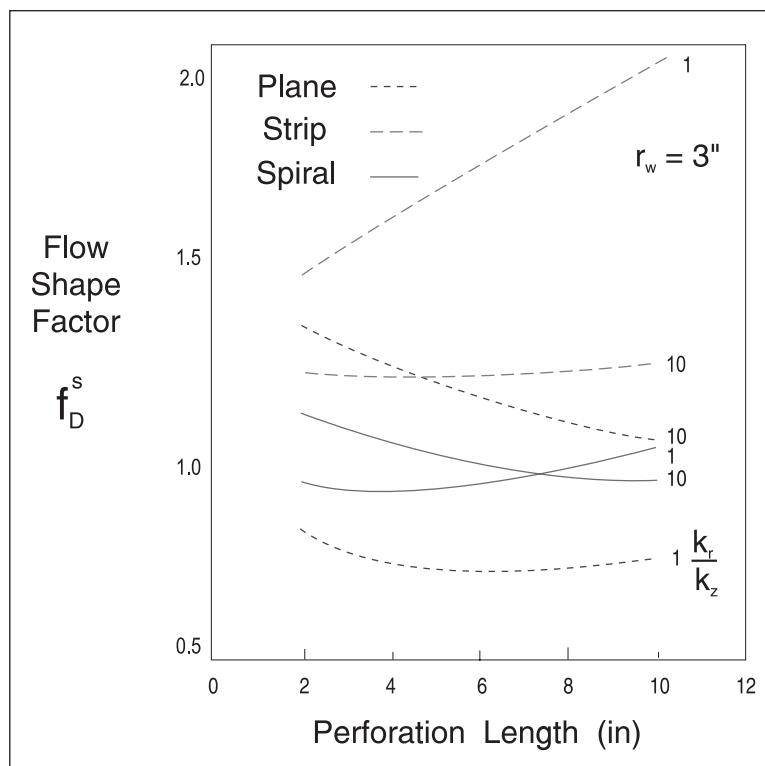


Fig. 2-30. Perforation flow shape factors for Darcy flow

The flow shape factors computed from the results of Locke<sup>9</sup> are given in table 2-1 and Locke's nomogram is shown in figure 2-31.

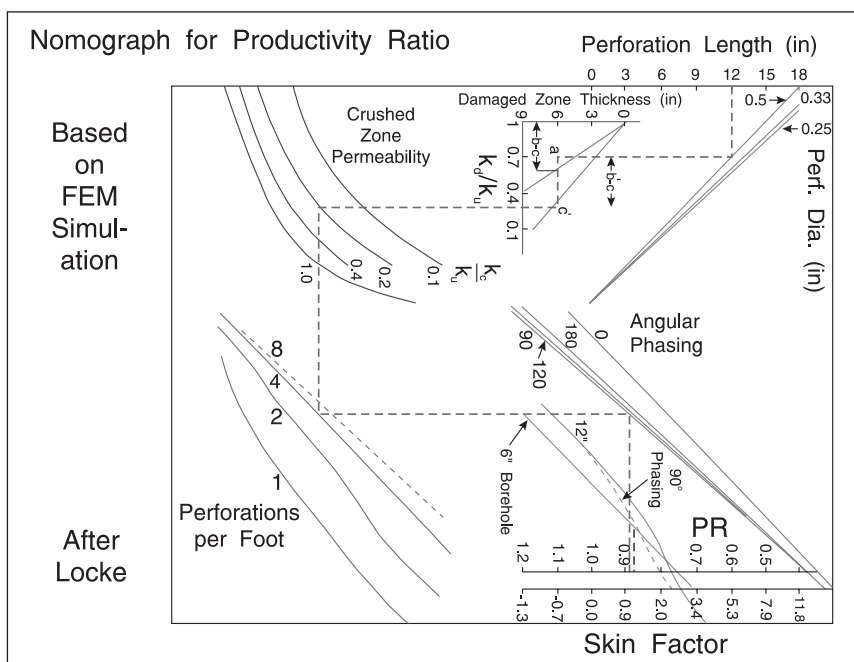


Fig. 2–31. Locke Nomogram for perforation skin factors

Table 2–1. Flow shape factors extracted from Locke’s FEM data

Shots per Foot	2	2	2	2	4	4	4	4	8	8	8	8
$\theta_p$ (°)	0	180	120	90	0	180	120	90	0	180	120	90
$l_p$ (in)												
3	1.317	1.055	0.918	0.913	1.699	1.174	1.047	1.035	2.879	1.320	1.020	0.916
6	1.265	0.906	0.816	0.779	1.803	1.158	0.963	0.897	3.084	1.222	0.847	0.667
9	1.253	0.853	0.783	0.693	1.906	1.136	0.856	0.766	3.413	1.413	1.103	0.952
12	1.264	0.808	0.623	0.583	2.043	1.108	0.923	0.842	3.717	1.477	1.130	0.946
15	1.253	0.737	0.627	0.589	2.081	1.138	0.893	0.828	3.955	1.631	1.270	0.934
18	1.316	0.782	0.669	0.612	2.229	1.253	0.942	0.899	4.203	2.110	1.516	1.289

## Perforation damage

The original work by Bell<sup>13</sup> on core flow efficiency postulated a crushed zone round the perforation tunnel, as illustrated in figure 2–32, which would reduce perforation performance. Here, the cylindrical, modified zone around the perforation tunnel has a radius  $r_{ps}$  and thickness  $\delta r_s = r_{ps} - r_p$  where  $r_p$  is the perforation tunnel radius. The existence of such a crushed zone due to the effect of the entry of the shaped charge has been put in serious doubt because the prediction of ideal perforation performance in the original API test is known to be in error. Again, not nearly a fine enough grid was used in the finite difference simulation of SS flow in the confined geometry of the API test, and the correlation for ideal pressure drop underpredicts  $\Delta p_{ideal}$  considerably. Hence, a crushed zone has to be invoked to allow real data to match an optimistic model. However, the concept of a damage envelope is in fact very relevant to the problem of



scale deposition that occurs in many reservoirs. In the North Sea province, for example, the most serious production problem is the precipitation of barium sulfate due to the mixing of injected sea water, rich in sulfate ion, with formation water, rich in barium and strontium ions. When mixing occurs in the vicinity of a producer after water breakthrough, the precipitate is swept towards the perforations where it forms bridges around the tunnel creating a damage envelope as illustrated in figure 2–32. Field experience has shown that, after scale buildup, reperforation will immediately restore well productivity demonstrating that the problem lies very close to the perforations and the damage does not take the form of an extended radial altered region. The solution to the barium sulfate scale problem is to inject inhibitor—organic phosphonate—as a slug, which will adsorb on the rock and produce back slowly over a long period of time. This prevents the buildup of scale and keeps the perforations clean. The treatment must be repeated when analysis of produced water shows that the inhibitor concentration has fallen below a critical level. Successful scale inhibition also means that electrical submerged pumps (ESPs) can be used to boost production as an alternative to gas lift.

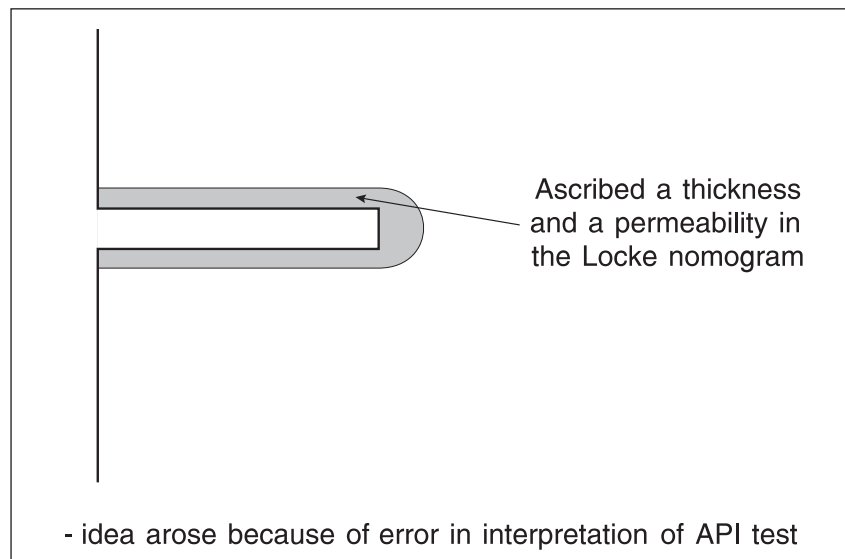


Fig. 2–32. Damaged envelope or crushed zone around a perforation tunnel

Localized damage to the formation around a perforation tunnel can be modeled using the concept of a spherical flow skin factor as shown in figure 2–33, where a modified region of permeability  $k_{cz}$  extends out to a spherical radius  $r_{sa}$ . The incremental pressure drop  $\Delta p_{ss}$  due to this damaged shell is given by the equation

$$\Delta p_{ss} = \frac{q_{sp}\mu}{4\pi kr_s} \left( 1 - \frac{r_s}{r_{sa}} \right) \left( \frac{k}{k_{cz}} - 1 \right) \quad (2-58)$$

and the dimensionless skin factor for spherical flow is defined as

$$S_s = \frac{\Delta p_{ss}}{q_{sp}\mu} = \left( 1 - \frac{r_s}{r_{sa}} \right) \left( \frac{k}{k_{cz}} - 1 \right) \quad (2-59)$$

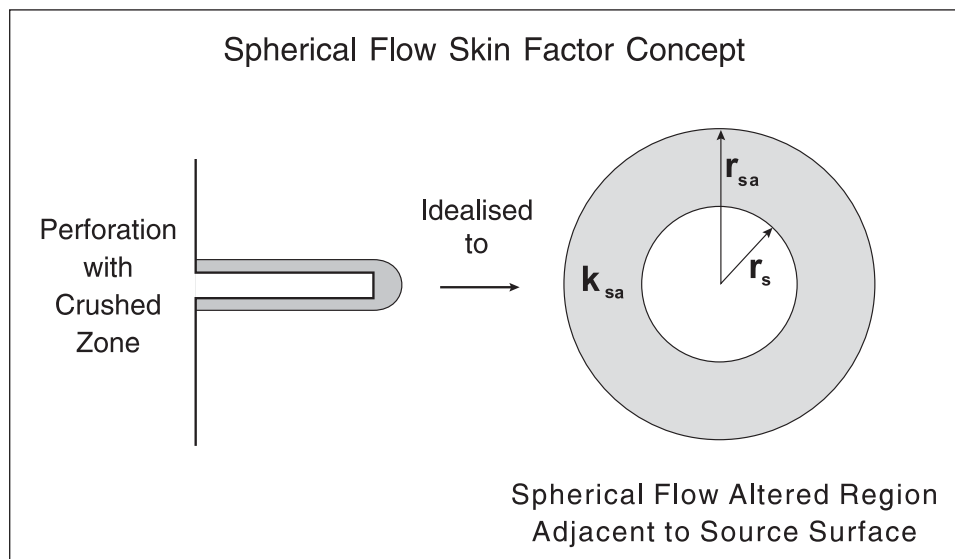


Fig. 2-33. Spherical flow skin factor

This is the spherical flow equivalent of the Hawkins equation and demonstrates the effect of near-perforation damage. Equation (2-59) was first derived in connection with SS flow into the probe of a wireline formation tester.

In order to use this equation, it is useful to express the term  $1 - r_s/r_{sa}$  in terms of the thickness  $\delta r_s$  of a cylindrical envelope of damage around a tunnel of length  $l_p$  as illustrated in figure 2-32. Noting that  $r_s = \sqrt{r_p l_p}$ , it follows that

$$1 - \frac{r_s}{r_{sa}} = 1 - \frac{1}{\sqrt{1 + \frac{\delta r_s}{r_p}}} \quad (2-60)$$

and Eq. (2-59) may be written in the alternative form

$$S_s = \frac{\Delta p_{ss} 4\pi k r_s}{q_{sp} \mu} = \left( 1 - \frac{1}{\sqrt{1 + \frac{\delta r_s}{r_p}}} \right) \left( \frac{k}{k_{cz}} - 1 \right) \quad (2-61)$$

Equation (2-49) for the spherical flow component of the pressure drop now takes the form

$$p_t - p_w = \left( f_D^s + S_s \right) \frac{q_p \mu}{4\pi k_s r_s} \quad (2-62)$$

and the overall skin factor due to perforation becomes

$$S_c = \ln \frac{r_w}{r_w + l_p} + \frac{(f_D^s + S_s)}{2n_s r_s \sqrt[3]{A}} \quad (2-63)$$

The spherical flow skin factor  $S_s$  is a convenient way of allowing for the effect of localized, near-tunnel damage, which is quite different in concept from the damage associated with a radial altered zone discussed in the next section.

The most recent experimental work on perforation damage in underbalanced conditions by Behrmann et al.<sup>14</sup> has suggested that the tunnel-altered zone is of the order of 0.5 in. in thickness with a permeability reduction ratio  $k_{cz}/k$  of the order of 0.7. This confirms that the crushed zone is much less important than previously thought, but it does exist and in principle should be accounted for. Substituting these numbers in Eq. (2-59) gives a spherical perforation damage skin  $S_s$  of 0.1, which is almost negligible compared to the flow shape factor of the order of unity. Note that McLeod also concluded from field results (well B in his paper) that underbalanced perforating resulted in negligible perforation damage. The effect of the so-called crushed zone, as measured in laboratory experiments such as the new API procedure, can be quantified through  $S_s$  and hence introduced into the model of a perforated completion.

## Effect of a radial, uniform altered region

The classical model of formation damage due to filtrate invasion postulates a radial altered region of modified permeability  $k_a$  extending to a cylindrical radius  $r_a$  as shown in figure 2-34. The assumption is now made that the depth of damage, i.e., mud filtrate invasion  $r_a$ , is greater than the perforation length  $l_p$ , and the approximate model can now be written as

$$\Delta p = p_e - p_w = \frac{q\mu}{2\pi kh} \ln \frac{r_e}{r_a} + \frac{q\mu}{2\pi k_a h} \ln \frac{r_a}{r_w + l_p} + (f_D^s + S_s) \frac{q\mu}{4\pi k_{sa} r_s N_p} \quad (2-64)$$

where the radial component of the pressure drop has been computed in two stages, i.e., in unaltered formation up to  $r_a$  and in altered permeability between  $r_a$  and  $r_w + l_p$ . Forming the incremental pressure drop due to perforation and damage by subtracting the pure radial  $\Delta p$  gives

$$\Delta p_s = \frac{q\mu}{2\pi kh} \ln \frac{r_e}{r_a} + \frac{q\mu}{2\pi k_a h} \ln \frac{r_a}{r_w + l_p} - \frac{q\mu}{2\pi kh} \ln \frac{r_e}{r_w} + (f_D^s + S_s) \frac{q\mu}{4\pi k_{sa} r_s N_p}$$

and

$$S_{ca} = \frac{\Delta p_s 2\pi kh}{q\mu} = \ln \frac{r_w}{r_a} + \frac{k}{k_a} \ln \frac{r_a}{r_w + l_p} + \frac{(f_D^s + S_s) kh}{2N_p r_s \sqrt[3]{A} k_a}$$

i.e.,

$$S_{ca} = \ln \frac{r_w}{r_a} + \frac{k}{k_a} \ln \frac{r_a}{r_w + l_p} + \frac{(f_D^s + S_s)k}{2n_s r_s \sqrt[3]{Ak_a}} \quad (2-65)$$

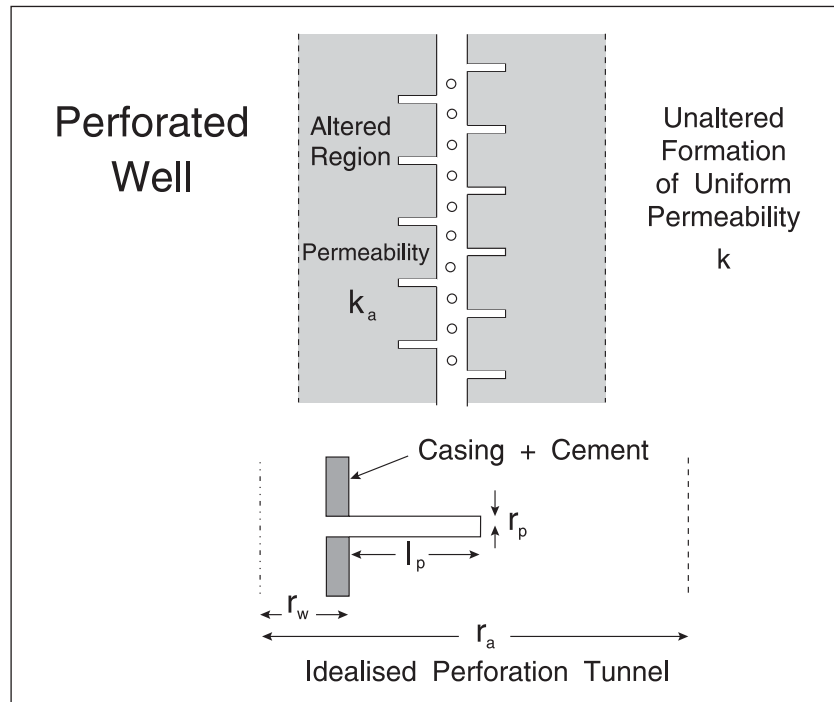


Fig. 2-34. Perforation within an altered region

This equation for  $S_{ca}$ —usually termed the *mechanical skin*—allows for the combined effect of formation damage or stimulation and perforation (assuming  $r_a > r_w + l_p$ ) and is a generalization of the familiar Hawkins equation for the open-hole case, i.e.,

$$S_{oh} = \left( \frac{k}{k_a} - 1 \right) \ln \frac{r_a}{r_w} \quad (2-66)$$

The application of Eq. (2-65) presents a certain amount of difficulty (like (2-66)) since it is very difficult to obtain independent estimates of both  $r_a$  and  $k_a$ ; the combined skin factor depends on how much the perforations penetrate the damaged region, i.e., the magnitude of  $r_a$  relative to  $r_w + l_p$ . If the combined skin  $S_c$  and the formation permeability  $k$  are measured in a well test and  $r_a$  is assumed known from depth of mud filtrate invasion estimates (obtained from resistivity logs), then Eq. (2-65) may in principle be solved for  $k_a$ .

In the case where the depth of alteration  $r_a$  is less than the perforation tip radius  $r_w + l_p$ , i.e., the perforation tunnels penetrate through the altered zone, it is suggested that the effect of alteration be ignored and the skin factor is simply computed using Eq. (2-63). This is consistent with the premise that flow is concentrated into the tip of the perforation tunnels and if the altered zone is

smaller in radius than the tip, it is effectively bypassed. However, this introduces a discontinuity into the model and an alternative approach based on interpolation is given later.

The concept of an altered region is also applicable when the permeability  $k_a$  is greater than the undisturbed formation permeability  $k$ ; in this case, the open-hole formula (2–66) will predict a negative skin factor indicating that the well has been stimulated. The process of matrix acidization yields an improved permeability  $k_a$  in the near-wellbore region out to a radius  $r_a$  that is controlled by the volume of acid injected. Matrix acidizing is usually carried out in carbonate reservoirs which react favorably to a hydrochloric acid treatment. However, an interesting example, where successful stimulation with HCl can be achieved, occurs when a sandstone reservoir contains a significant amount of calcite. If the calcite has been deposited in the pores by diagenesis, it can be leached out by acid treatment and the formation permeability significantly increased. For example, in the Claymore field the presence of calcite in the pore space has led to poor permeability in certain parts of the reservoir and the wells in question have been very successfully stimulated at relatively low cost by HCl treatment. The rock sensitivity to acid and the possible permeability improvement are usually established by special core analysis. The mechanics of the stimulation is not straightforward since acid injection is essentially an unstable process in which the acid follows local high-permeability streaks that are then made more permeable causing them in turn to accept more acid. This leads to the phenomenon of “worm-holing” in which extended channels of small dimension propagate out through the rock making it difficult to predict the extent of the altered region  $r_a$ . Empirical relations linking  $k_a$  and  $r_a$  to acid volumes and strength must be established. However, the altered region model allows such phenomena to be described quantitatively, and Eq. (2–65) may be used to predict the (negative) skin factor of a perforated, stimulated well. Note that acid injection will probably commence at the perforation tips as illustrated in figure 2–35 and this should be accounted for in the assessment of  $r_a$ .

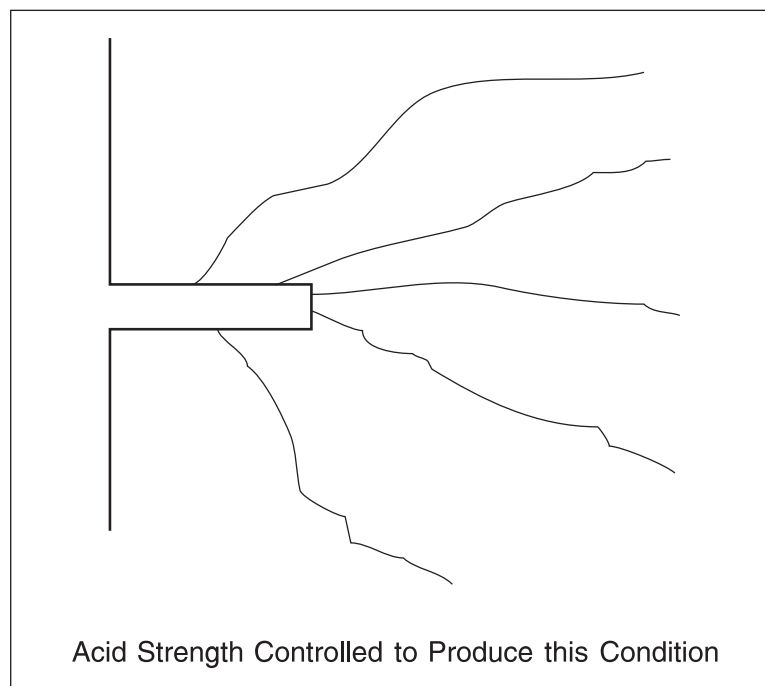


Fig. 2–35. Phenomenon of worm-holing in an acidized, perforated well

In well test analysis, the presence of an extensive cylindrical altered region is referred to as a *radial composite model* (described in detail in chapter 12 of *Well Test Design and Analysis*) and it is widely used in connection with water injection wells where an inner and outer region develop as oil is displaced by water. In particular, the cold ring where water is flowing at injection temperature, i.e., cold water viscosity can be modeled as an altered region using the type of formulation developed here, the permeability ratio  $k/k_a$  would simply be replaced by the viscosity ratio  $\mu_{w,IT}/\mu_{w,RT}$ , i.e.,  $k_a = k/M$ , and  $r_a$  by the distance to the temperature front  $r_T$ ; here IT refers to injection temperature, RT to reservoir temperature, and  $M$  is the mobility ratio of outer to inner region. However, the modeling of the skin effect in water injection wells is complicated by the phenomenon of thermal fracturing, which is rate dependent, and will not be treated here. In a transient well test, the total apparent skin  $S_a$  in the case of a radial composite refers to the intercept of the second straight line corresponding to the properties of the outer region. In the special case of an extensive altered zone, i.e.,  $r_a \gg r_w + l_p$ , the combined alteration/perforation skin  $S_{ca}$  can be decomposed, if desired, into the constituent components as follows:

$$S_{ca} = MS_c + S_{rc} \quad (2-67)$$

where

$$M = \frac{k}{k_a} \quad \text{and} \quad S_{rc} = (M-1) \ln \frac{r_a}{r_w + l_p}$$

Here, the nomenclature used in chapter 12 of *Well Test Design and Analysis* for radial composite systems has been employed; the quantity  $S_{rc}$  is the skin effect due to the altered zone (Hawkins equation for large shot density) and  $S_c$  is the true perforation skin given by Eq. (2-63); this discrimination is possible only when the outer radius of the altered region is large compared to the perforation length measured from the well centerline. For formation damage with  $r_a$  relatively small, only the combined form (2-65) is relevant.

If the extent of the altered region is less than the depth of penetration of the perforations ( $r_a < r_w + l_p$ ), then the combined skin factor  $S_{ca}$  is simply presumed to be given by Eq. (2-63), i.e., the effect of the altered zone is ignored if the perforations pass through it completely. This assumption is valid if most of the flow enters the perforation in the vicinity of the tip. However, this approach will lead to a discontinuity in the modeling of perforation performance and an alternative strategy is illustrated in figure 2-36 where an empirical interpolation process is used to estimate the effect of the altered region. Suppose the skin for zero radius of damage is designated  $S_{ca}(r_a = r_w)$  and the skin where the damaged region extends to twice the perforation length is designated  $S_{ca}(r_a = r_w + 2l_p)$ , then for intermediate values of  $r_a$  the skin is computed as

$$S_{ca}(r_a) = S_{ca}(r_a = r_w) + \left[ S_{ca}(r_a = r_w + 2l_p) - S_{ca}(r_a = r_w) \right] \left( \frac{r_a - r_w}{2l_p} - \frac{1}{2\pi} \sin \left( \frac{\pi(r_a - r_w)}{l_p} \right) \right) \quad (2-68)$$

$$r_w < r_a < 2l_p + r_w$$

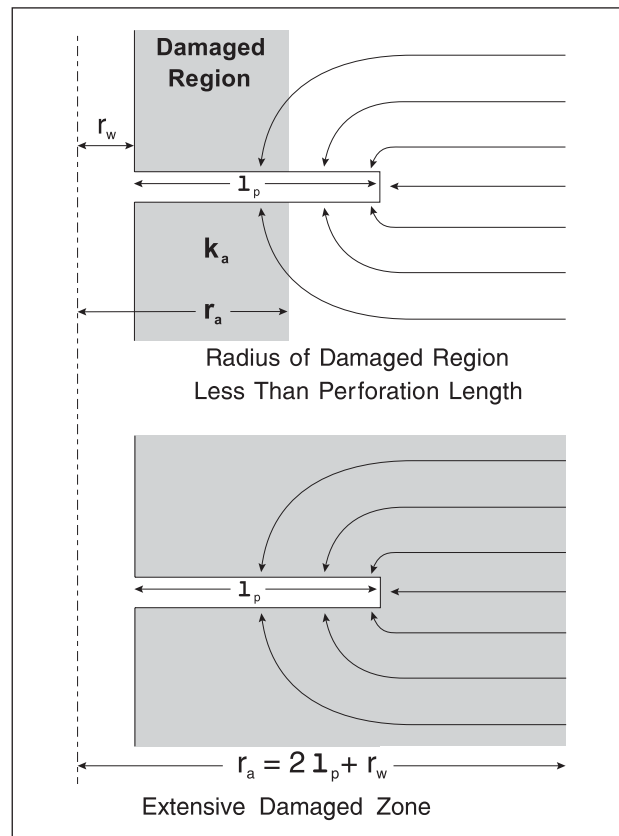


Fig. 2–36. Empirical interpolation procedure to handle inner damaged zone

This totally empirical interpolation function has the property that the skin changes sharply as the perforation tip approaches and then extends through the damaged region. In most cases, it is felt that perforation length is considerably less than the damage radius, i.e.,  $r_a > 2l_p + r_w$ , but in the cases where this condition is not satisfied, a smooth transition is predicted by the proposed interpolation. In practice, the formation damage does not conform to the radial composite model (step change from  $k_a$  to  $k$  at  $r_a$ ) and the transition predicted by Eq. (2–68) is felt to be quite satisfactory.

## Non-Darcy flow

For Darcy (laminar) flow, the concept of the spherical flow shape factor  $f_D^s$  has been shown to be a good mechanistic approach to correlating and extending the results of detailed simulations of the flow process in the vicinity of perforations. In the section “Spherical steady-state flow,” the theory of spherical flow including the non-Darcy component was derived and, in the context of a perforated completion, it is logical to extend the approximate model to allow for non-Darcy flow. It is evident that the flow concentration into the tip of a perforation will result in the non-Darcy effect being confined to this region. Equation (2–42) can be modified to include a non-Darcy flow shape factor which models the flow into an actual perforation; thus

$$\Delta p_{ND} = f_{ND}^s \frac{\beta \rho q_p^2}{3(4\pi)^2 r_s^3} \quad \text{and} \quad r_s = \sqrt{r_p l_p} \quad (2-69a)$$

Again, the equivalent spherical radius  $r_s$  has been employed in the definition of the non-Darcy flow shape factor  $f_{ND}^s$ ; detailed simulations of nonlinear flow into perforation patterns based on the Forcheimer equation will be used to determine  $f_{ND}^s$  values. In oil field units, Eq. (2-69a) becomes

$$\Delta p_{ND} = f_{ND}^s \frac{5.6901 \times 10^{-11} \beta \rho q_p^2}{3(4\pi)^2 r_s^3} \quad (2-69b)$$

Since the two components of the pressure drop are additive (for incompressible flow), the total pressure drop may be written as

$$\begin{aligned} p_e - p_w &= \frac{q\mu}{2\pi kh} \ln \frac{r_e}{r_w + l_p} + f_D^s \frac{q_p \mu}{4\pi k_s r_s} + f_{ND}^s \frac{\beta \rho q_p^2}{3(4\pi)^2 r_s^3} \\ &= \frac{q\mu}{2\pi kh} \left( \ln \frac{r_e}{r_w} + S_c \right) + f_{ND}^s \frac{\beta \rho q^2}{3(4\pi)^2 r_s^3 N_p^2} \end{aligned} \quad (2-70)$$

giving

$$p_{Dss} = \frac{(p_e - p_w) 2\pi kh}{q\mu} = \ln \frac{r_e}{r_w} + S_c + f_{ND}^s \frac{\beta \rho q kh}{24\pi \mu r_s^3 N_p^2} \quad (2-71a)$$

In oil field units, Eq. (2-71a) becomes

$$p_{Dss} = \frac{(p_e - p_w) 2\pi kh}{887.2 q \mu} = \ln \frac{r_e}{r_w} + S_c + f_{ND}^s \frac{6.414 \times 10^{-14} \beta \rho q kh}{24\pi \mu r_s^3 N_p^2} \quad (2-71b)$$

or alternatively

$$p_{Dss} = \ln \frac{r_e}{r_w} + S_c + D_c q \quad (2-72a)$$

where

$$D_c = f_{ND}^s \frac{6.414 \times 10^{-14} \beta \rho kh}{24\pi \mu r_s^3 N_p^2} = f_{ND}^s \frac{6.414 \times 10^{-14} \beta \rho k}{24\pi \mu r_s^3 n_s^2 h} \quad (2-72b)$$

Thus, the rate-dependent contribution to the total skin has been related to the inertial resistance coefficient  $\beta$  and the number of perforations  $N_p$ . Note that the rate-dependent skin coefficient  $D_c$  is inversely proportional to  $N_p^2$ , indicating that shots per foot is the key parameter controlling non-Darcy flow effects. The use of a radial (open-hole) formula for the non-Darcy flow



contribution in a perforated well is completely erroneous. When an altered region is present, Eqs. (2–72a,b) are still applicable with  $S_c$  now given by (2–65) and  $\beta$  replaced with the value representative of the altered region.

In the MacLeod model, the non-Darcy pressure drop is given by the radial vertical approximation

$$\Delta p_{ND} = \frac{\beta \rho q_p^2}{4\pi^2 l_p^2 r_p} \quad (2-73)$$

Comparing the spherical flow Eqs. (2–69a,b) for  $\Delta p_{ND}$  with MacLeod's model (2–73) shows that the spherical flow model places more importance on the tunnel radius  $r_p$  because of the stronger effect of tip flow convergence.

The choice between the two approaches depends on whether  $l_p^2 r_p$  (radial) or  $(l_p r_p)^{3/2}$  (spherical) gives flow shape factors that are more constant as the perforation length and diameter change. It is interesting to compare the predictions of the two models for a typical perforation tunnel of length 0.75 ft (9 in.) and radius 0.020833ft (1/4 in.) assuming  $f_{ND}^s$  equal to unity, i.e., with the spherical model uncalibrated. Thus, in Eq. (2–73),  $4\pi^2 l_p^2 r_p = 0.463$ , while in Eqs. (2–69a,b),  $3(4\pi)^2 (l_p r_p)^{3/2} = 0.925$ ; for this perforation size, the uncalibrated spherical model predicts about half the non-Darcy pressure drop of the radial model. However, the two models are not dissimilar in their estimates and both give a realistic estimate of the non-Darcy effect which is sensitive to perforation length and perforation diameter, with the spherical flow model placing a slightly greater emphasis on the latter. In his original paper, MacLeod suggests that the inertial resistance coefficient  $\beta$  in Eq. (2–73) be evaluated using the so-called crushed zone permeability  $k_{dp}$  in a correlation of the form

$$\beta = \frac{2.6 \times 10^{10}}{k^{1.2}} \quad (\beta : \text{ft}^{-1} \text{ k} : \text{md}) \quad (2-74)$$

For example, MacLeod suggests that with overbalance,  $k_{dp}$  may be as low as 2.5–3.0% of the undamaged formation permeability assuming all perforations were flowing; this enormously increases the value of  $\beta$  used in Eq. (2–73) and may lead to a gross overestimate of the non-Darcy effect. Recent work has shown that the apparent existence of the crushed zone is due to misinterpretation of the API core flow efficiency test and it is not recommended to use a reduced permeability in Eq. (2–74) when estimating  $\beta$  values. The problem with well A in MacLeod's paper is much more likely to be few perforations flowing as illustrated in figure 2–37, i.e., effective shots per foot  $n_{s,eff}$  rather than a uniform damage to all perforations. Production logging in wells completed with a large overbalance (500 psi for well A) clearly indicates how few perforations actually flow. Thus, the large non-Darcy effect present in well A can be better explained by utilizing a low value of  $n_s$  in Eq. (2–72b); this is a physically more consistent explanation than that proposed by MacLeod. The fact remains that overbalanced perforation has resulted in a poorly performing well and this example shows the problem in interpreting field results where either the effective shots per foot or the perforation damage zone can be used to account for deviation from ideal behavior.

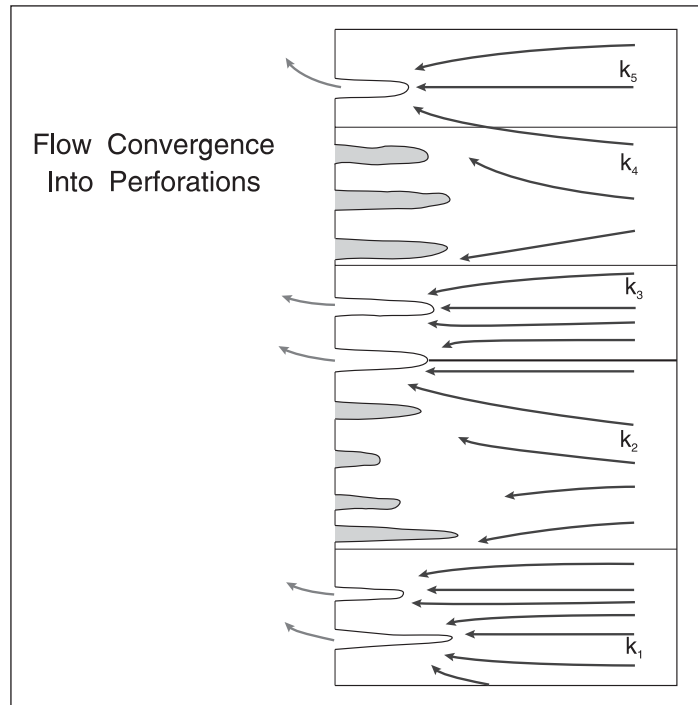


Fig. 2-37. Problem of plugged perforations associated with overbalanced perforating

Although the existence of a crushed zone as a result of perforation is now not thought to be a serious problem, post-perforation damage to tunnels can occur, particularly in gravel-pack completions. The physical origin of this type of perforation alteration is treated in the section “Linear flow in a gravel-packed perforation tunnel,” and the effect of a damaged zone on the non-Darcy component of the total pressure drop will now be considered on the basis of the spherical model. Referring to figure 2-33, the incremental non-Darcy pressure drop over the region between  $r_s$  and  $r_{sa}$  is given by Eq. (2-37), i.e.,

$$\Delta p_{ND,SS} = \frac{\beta_{sa} \rho q_p^2}{3(4\pi)^2} \left( \frac{1}{r_s^3} - \frac{1}{r_{sa}^3} \right) - \frac{\beta \rho q_p^2}{3(4\pi)^2} \left( \frac{1}{r_s^3} - \frac{1}{r_{sa}^3} \right)$$

i.e.,

$$\Delta p_{ND,SS} = \frac{\beta \rho q_p^2}{3(4\pi)^2 r_s^3} \left( \frac{\beta_{sa}}{\beta} - 1 \right) \left( 1 - \frac{r_s^3}{r_{sa}^3} \right) = S_{ND}^s \frac{\beta \rho q_p^2}{3(4\pi)^2 r_s^3} \quad (2-75)$$

where  $S_{ND}^s$  is a non Darcy spherical skin factor defined as

$$S_{ND}^s = \left( \frac{\beta_{sa}}{\beta} - 1 \right) \left( 1 - \frac{r_s^3}{r_{sa}^3} \right) \quad (2-76)$$

The assumption is now made that the inertial resistance coefficient  $\beta$  is inversely proportional to permeability to the power 1.2, and Eq. (2-76) may be written as

$$S_{ND}^s = \left( \left( \frac{k}{k_{sa}} \right)^{1.2} - 1 \right) \left( 1 - \frac{r_s^3}{r_{sa}^3} \right) \quad (2-77)$$

Equation (2-77) indicates that the effect of a tunnel-altered envelope of reduced permeability  $k_{sa}$  has an even stronger effect on the non-Darcy component of the skin than on the Darcy term  $S_s$  represented by Eq. (2-59). The inclusion of a spherical non Darcy component of the skin is now possible and Eqs. (2-71a,b) may now be written in the form

$$p_{Dss} = \frac{(p_e - p_w)2\pi kh}{q\mu} = \ln \frac{r_e}{r_w} + S_c + \left( f_{ND}^s + S_{ND}^s \right) \frac{\beta\rho qkh}{24\pi\mu r_s^3 N_p^2} \quad (2-78)$$

Thus, the spherical non-Darcy perforation damage skin  $S_{ND}^s$  simply adds to the non-Darcy flow shape factor  $f_{ND}^s$  exactly as in the Darcy case represented by Eq. (2-62). Note that the expression (2-77) for  $S_{ND}^s$  and the corresponding expression for  $S_s$ , i.e., (2-59), are not all that different in form and the value of either spherical skin depends heavily on the permeability ratio  $k/k_{sa}$ . As a first approximation, it would be quite realistic to assume  $S_{ND}^s$  equal to  $S_s$  and apply the same dimensionless spherical skin factor to both the Darcy and non-Darcy terms. The important point is that a damage envelope around perforation tunnels causing a high Darcy skin will also lead to an equivalent increase in the non-Darcy coefficient  $D_c$ ; such an effect has been seen in high-permeability North Sea oil reservoirs where a large Darcy skin is accompanied by a significant rate-dependent skin determined from a multirate test.

## Spherical non-Darcy flow shape factors

Modeling the detailed behavior of a perforated completion with non-Darcy flow involves solving the Forcheimer equation over the finite element grid constructed to simulate the pattern. This is a nonlinear problem that is considerably more difficult than Darcy flow case, and only two studies of this case have been reported, i.e., those of Egan and Tariq. Again, the results of nonlinear FEM simulations can be solved for non-Darcy flow shape factors using Eqs. (2-69a,b) written in the form

$$f_{ND}^s = \frac{\Delta p_{ND} 2\pi kh}{q\mu} \frac{24\pi\mu r_s^3 n_s^2 h}{\beta\rho qk} = \frac{\Delta p_{ND} 48\pi^2 r_s^3 N_p^2}{\beta\rho q^2} \quad (2-79)$$

where  $\Delta p_{ND}$  is the difference between the total pressure drop in the Darcy plus non-Darcy case and the Darcy flow alone case. The data of Egan were analyzed in this fashion and the results for  $f_{ND}^s$  are shown in figure 2-38 for the three perforation geometries. Once again, the flow shape factors for a spiral pattern are very close to being constant at a value of around 1.3, and Eqs. (2-71a,b) give a very good prediction of the non-Darcy or rate-dependent contribution to the total skin. Note that it would be equally valid to define flow shape factors for the MacLeod radial model and to use these as a basis for correlating FEM results.

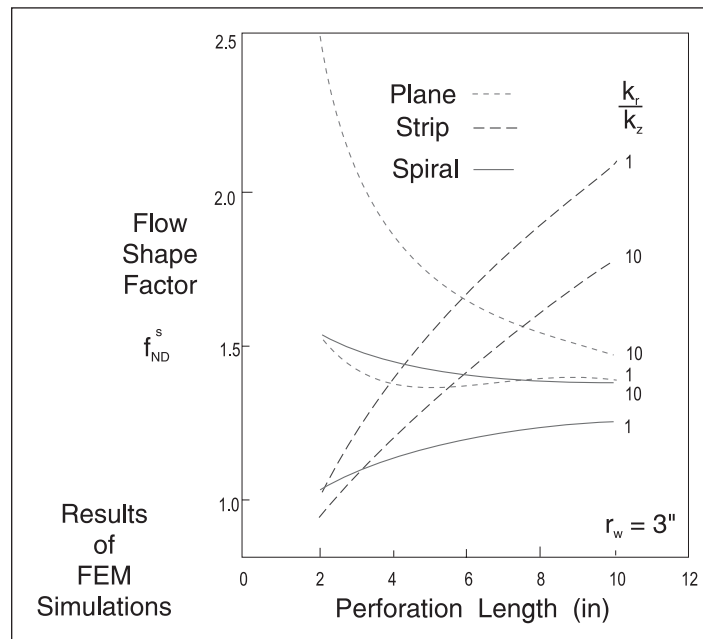


Fig. 2–38. Flow shape factors for non-Darcy flow

The effect of shots-per-foot on gas well deliverability is illustrated in figure 2–39 for a low-permeability formation ( $k = 2$  md) where it is evident that the classic four shots per foot is perfectly adequate. In a high-permeability formation, shown in figure 2–40, the sensitivity to shots-per-foot is much greater and a larger shot density would seem appropriate; however, such a well will be tubing-controlled and will not operate at anything like the high flow rates depicted in figure 2–40. At an operating rate of 200 MMscf/d, typical of 5½" tubing capability, again  $n_s = 4$  appears adequate. These calculations were made with the WELLFLO software using the Katz and Firoozabadi correlation to relate the inertial resistance coefficient  $b$  to the permeability  $k$ . The values of the skin factor components are listed in the tables 2–2 and 2–3.

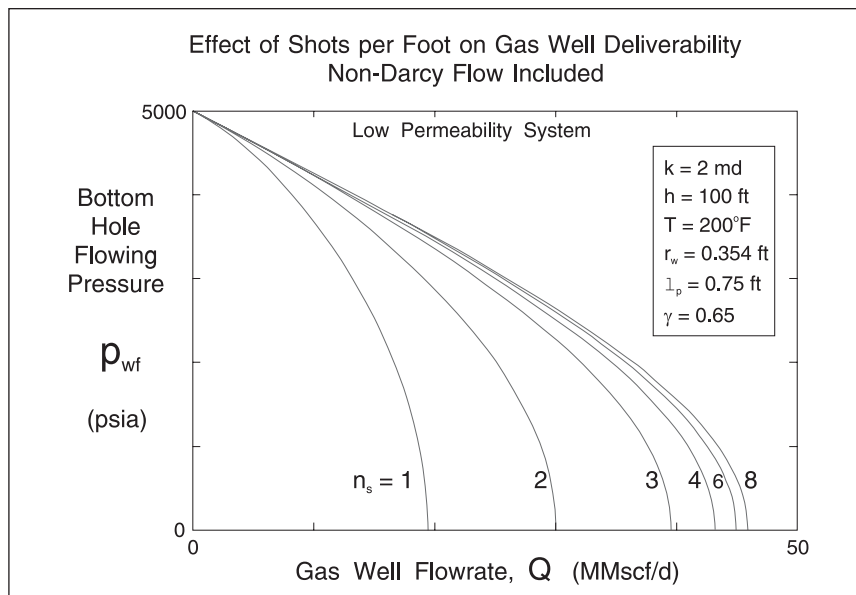


Fig. 2–39. Effect of shots per foot on well deliverability—low permeability

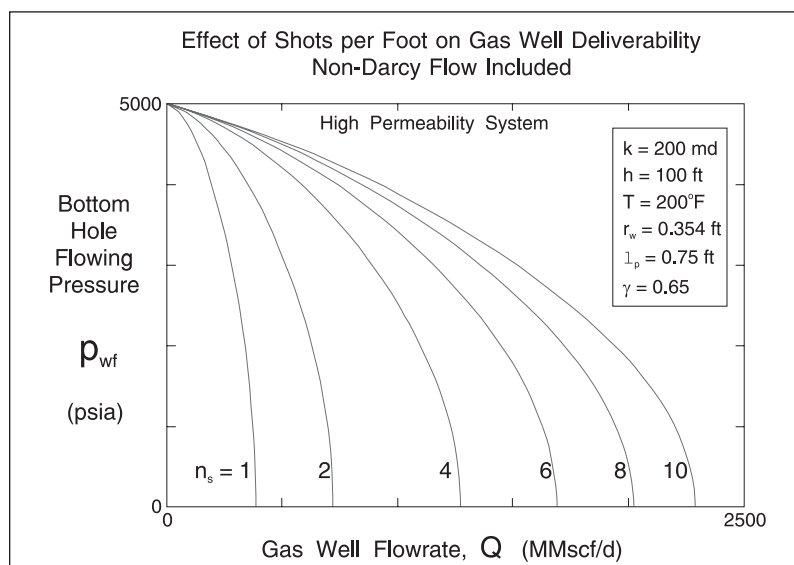


Fig. 2-40. Effect of shots per foot on well deliverability—high permeability

Table 2-2. Effect of shots per foot on gas well deliverability—low permeability

Shots per foot, $n_s$	Darcy skin, $S$	Non-Darcy coefficient, $D$ (MMscf/d) <sup>-1</sup>	$DQ$ ( $Q = 20$ MMscf/d)
1	1.541	0.449	8.98
2	0.276	0.119	2.37
4	-0.356	0.0328	0.656
6	-0.553	0.0163	0.326
8	-0.652	0.0102	0.204
10	-0.711	0.0071	0.142
$k = 2$ md $h = 100$ ft $r_w = 0.354$ ft $l_p = 0.75$ ft $r_g = 0.65$ $T = 200$ °F			

Table 2-3. Effect of shots per foot on gas well deliverability—high permeability

Shots per foot, $n_s$	Darcy skin, $S$	Non-Darcy coefficient, $D$ (MMscf/d) <sup>-1</sup>	$DQ$ ( $Q = 200$ MMscf/d)
1	1.541	0.1788	35.76
2	0.276	0.0472	9.44
4	-0.356	0.013	2.60
6	-0.553	0.0065	1.30
8	-0.652	0.0041	0.82
10	-0.711	0.0028	0.56
$k = 200$ md $h = 100$ ft $r_w = 0.354$ ft $l_p = 0.75$ ft $r_g = 0.65$ $T = 200$ °F			

These rate-dependent coefficients  $D$  calculated theoretically are at least one order of magnitude smaller than typical values observed in the field from gas well testing. There are two reasons for this serious discrepancy. The first relates to the number of perforations that are actually flowing. With modern tubing-conveyed perforation at close to optimum underbalance, the problem of plugged perforations is much reduced compared to the old situation when

overbalanced perforating with mud in the well was common. However, in a heterogeneous formation, perforations located in high permeability will obviously flow at much higher rates than tunnels embedded in locally tight rock. In figure 2–41, a typical plot of core data from a well is presented (using a logarithmic scale), and a set of perforations is then set into the formation. Given the wide variation in permeability on a foot-by-foot basis, it is evident that some perforation tunnels will flow at a much higher rate than others; this is the geostatistical aspect of perforation. Current estimates suggest that only one-third of perforations should be treated as flowing, and it is significant that at one shot-per-foot (active) the rate-dependent coefficient  $D$  in table 2–3 is  $0.2 \text{ (MMscf/d)}^{-1}$  which is typical of gas wells throughout the world.

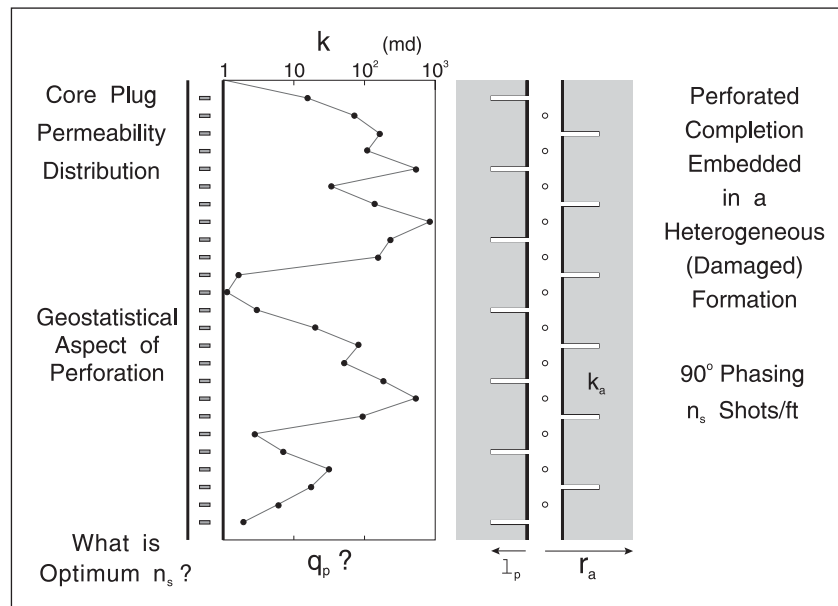


Fig. 2–41. Perforated completion embedded in a heterogeneous formation

## Non-Darcy flow into an open-hole completion

The preceding discussion has concentrated on the non-Darcy effect in perforated completions in order to demonstrate the importance of the effective shots per foot in controlling the laminar-inertial component of the pressure drop in cased wells. It is of interest to compute the non-Darcy effect in an open-hole completion exhibiting pure radial flow to a well of radius  $r_w$ . In this case, the non-Darcy pressure drop from Eq. (2–44) is given by

$$\Delta p_{ND} = \frac{\beta \rho q^2}{(2\pi h)^2 r_w} \quad (2-80a)$$

where  $1/r_e$  has been assumed to be negligible. In oil field units this becomes

$$\Delta p_{ND} = \frac{5.6901 \times 10^{-11} \beta \rho q^2}{(2\pi h)^2 r_w} \quad (2-80b)$$

Alternatively, the non-Darcy contribution to the skin effect takes the form

$$D_c = \frac{\beta \rho k}{2\pi h r_w \mu} \quad (2-81a)$$

or in oil field units

$$D_c = \frac{6.414 \times 10^{-14} \beta \rho k}{2\pi h r_w \mu} \quad (2-81b)$$

It is worthwhile to re-emphasize that these equations for the non-Darcy effect are strictly limited to open-hole conditions and are not applicable to perforated completions. However, this approach is still advocated in some literature sources for the treatment of non-Darcy flow even in cased hole; the proper analysis of inertial effects in perforated completions has been treated at length in the preceding sections.

Equation (2-44) may be written in the form

$$p_e - p_w = \frac{1}{J_{ss}} q_s + F q_s^2 \quad (2-82)$$

where

$$F = \frac{\beta \rho B^2}{(2\pi h)^2 r_w} \quad \text{or in field units} \quad F = \frac{5.6901 \times 10^{-11} \beta \rho B^2}{(2\pi h)^2 r_w} \quad (2-83)$$

and

$$J_{ss} = \frac{2\pi k h}{B\mu \left( \ln \frac{r_e}{r_w} + S_d \right)} \quad \text{or in field units} \quad J_{ss} = \frac{2\pi k h}{887.2 B\mu \left( \ln \frac{r_e}{r_w} + S_d \right)}$$

(here, in field units,  $\rho$  is expressed in g/cc).

The formulation given above for an open-hole situation is referred to in the literature as the *Jones equation* following a paper by Jones, Blount, and Glaze<sup>15</sup> in 1976.

## Correlations for the inertial resistance coefficient

Practical application of the formulae for the non-Darcy contribution to the total skin effect requires information on the inertial resistance coefficient  $\beta$ . The utility of accurate predictions of the spherical flow shape factor  $f_{ND}^s$  from FEM simulations is limited by the experimental difficulties encountered in measuring  $\beta$  in the laboratory. The inertial resistance coefficient is a rock property that depends particularly on pore size distribution and porosity. Theoretical expressions—analogueous to the Berg correlation for permeability—for the inertial resistance

coefficient of unconsolidated porous media such as fracture proppant and gravel pack sand do exist, but they are not applicable to reservoir rock. In principle,  $\beta$  should be measured directly as part of the core analysis program, but the experimental procedure is difficult and prone to error. Therefore, it is usually the case that recourse is made to empirical correlations relating  $\beta$  to permeability. These correlations take the form

$$\beta = \frac{a}{k^c} \quad (2-84)$$

where  $a$  and  $c$  are constants. The best known correlation of this type is that due to Firoozabadi and Katz,<sup>16</sup> who proposed the form

$$\beta = \frac{2.33 \times 10^{10}}{k^{1.201}} \quad \text{where } \beta: \text{ft}^{-1} \quad \text{and } k: \text{md} \quad (2-85)$$

However, it was pointed out by Firoozabadi and Katz that a generalized correlation like this can only predict  $\beta$  to within an order of magnitude; thus, it is extremely difficult to estimate non-Darcy pressure drops with any real accuracy unless field specific data on  $\beta$  are available. For example, Morrison and Duggan<sup>17</sup> have described the problems associated with laboratory measurement of  $\beta$  and given a specific correlation for data from the Morecambe Bay field; their version is

$$\beta = \frac{1.56 \times 10^{11}}{k^{1.84}} \quad \text{where again } \beta: \text{ft}^{-1} \quad \text{and } k: \text{md} \quad (2-86)$$

Another form also involving porosity has been suggested by Noman and Archer<sup>18</sup>:

$$\beta = \frac{2.48 \times 10^9}{\left( \frac{k}{\phi S_g} \right)^{1.22}} \quad (2-87)$$

This list of correlations is by no means exhaustive and simply serves to indicate the wide range of methods available and the limitations of a generalized approach. When high-rate gas wells are under consideration, then it is advisable to commission a special core analysis program for the direct measurement of inertial resistance coefficient on core plugs from the reservoir. The constants  $a$  and  $c$  in Eq. (2-84) can then be determined for the rock type involved; this will allow much greater confidence in the prediction of possible non-Darcy pressure drop. Perhaps, more significantly, if the quantity  $F$  is determined from a step-rate well test, its interpretation in terms of effective shots per foot will be more valid if  $\beta$  is known with some degree of accuracy.



## Linear flow in a gravel-packed perforation tunnel

The flow of fluid through a bed of unconsolidated particles has been studied in chemical engineering, and the usual starting point for the prediction of pressure drop in a packed bed is the Ergun equation which takes the form

$$\frac{dp}{dx} = \frac{150\mu u(1-\phi)^2}{D_p^2\phi^3} + \frac{1.75\rho u^2(1-\phi)}{D_p\phi^3} \quad (2-88)$$

where  $D_p$  is the volume-surface (Sauter) mean particle size,  $\phi$  is the porosity of the bed, and  $u = q/A$  is the superficial velocity. This equation is written in any consistent scientific units and may be compared with the generic (Forcheimer) form

$$\frac{dp}{dx} = \frac{\mu}{k_p} u + \beta_p \rho u^2 \quad (2-89)$$

defining the permeability  $k_p$  and the inertial resistance coefficient  $\beta_p$  of the particulate bed. Thus, in terms of the grain size and porosity (or voidage)

$$k_p = \frac{D_p^2\phi^3}{150(1-\phi)^2} \quad (2-90)$$

and

$$\beta_p = \frac{1.75(1-\phi)}{D_p\phi^3} \quad (2-91)$$

In strict SI units, permeability has the dimensions of  $L^2$  (i.e.,  $m^2$ ) and inertial resistance coefficient has dimension of  $L^{-1}$  (i.e.,  $m^{-1}$ ). In oil field units with  $k_p$  in md,  $\beta_p$  in  $ft^{-1}$ , and  $D_p$  in mm, these equations become

$$k_p = \frac{1.01325 \times 10^9 D_p^2 \phi^3}{150(1-\phi)^2} \text{ md} \quad (2-92)$$

and

$$\beta_p = \frac{3.048 \times 10^2 \times 1.75(1-\phi)}{D_p\phi^3} \text{ ft}^{-1} \quad (2-93)$$

Given the average particle size in millimeters and the bed porosity, these equations may be used to predict the permeability and inertial resistance coefficient of unconsolidated porous media. Note how sensitive  $k_p$  and  $\beta_p$  are to bed porosity in particular.

In the case of an internal gravel-packed completion, additional pressure drop occurs in the perforation tunnel now filled with sand of permeability  $k_p$  as illustrated in figure 2-42. The approximate model is based on the conservative assumption that flow into the perforation is concentrated at the tip and therefore the flow rate along the tunnel may be taken to be  $q_p = q/N_p$ . The flux or superficial velocity in the tunnel is given by

$$u = \frac{q_p}{A_p} = \frac{q}{N_p \pi r_p^2} = \frac{q}{n_s h \pi r_p^2} \quad (2-94)$$

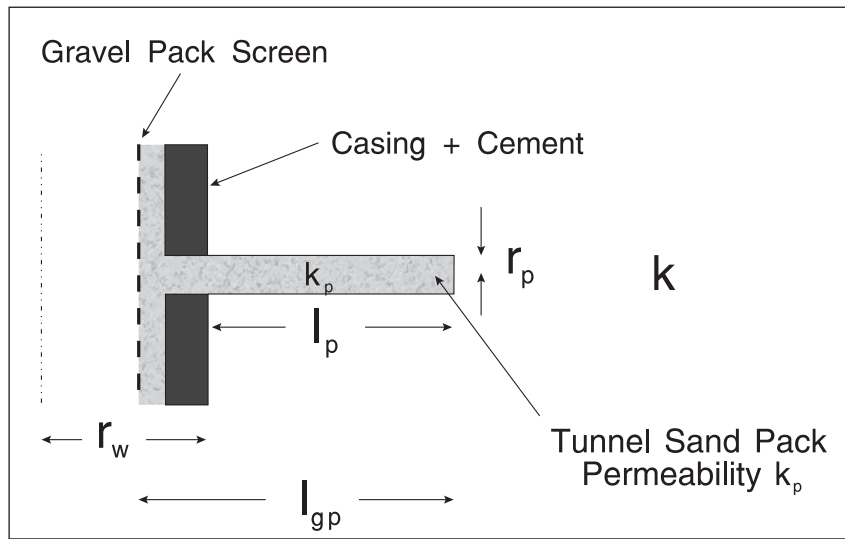


Fig. 2-42. Gravel-packed perforation tunnel

The Forcheimer equation for linear incompressible flow along the tunnel of length  $l_{gp}$  is

$$\frac{dp}{dx} = \frac{\mu}{k_p} u + \beta_p \rho u^2 \quad (2-95)$$

where the superficial velocity  $u$  is given by (2-94); Eq. (2-95) is readily integrated—since  $u$  is constant—giving

$$\Delta p_p = \frac{q \mu l_{gp}}{k_p N_p A_p} + \frac{\beta_p \rho q^2 l_{gp}}{N_p^2 A_p^2} \quad (2-96)$$

Here,  $\Delta p_p$  is the additional pressure drop due to the gravel pack,  $k_p$  is the permeability of the gravel packing sand, and  $\beta_p$  is its inertial resistance coefficient. The length  $l_{gp}$  is the total length of gravel-packed tunnel from the screen to the perforation tip, which is somewhat greater than the length of perforation  $l_p$  penetrating permeable formation. The pressure drop in an actual

gravel-pack completion may be greater or less than this ideal value. If flow into the perforation followed the uniform flux model, then the pressure drop would be given by a formula of the form

$$\Delta p_p \approx \frac{q\mu l_{gp}}{2k_p N_p A_p} + \frac{\beta_p \rho q^2 l_{gp}}{3N_p^2 A_p^2} \quad (2-97)$$

i.e., the effective length is roughly one-half of the value for concentrated tip flow. On the other hand, if the sand permeability is degraded below the laboratory measured value  $k_p$ , the pressure drop will be greater than that predicted by (2-96). Influx of fines from the formation and/or residual gel can cause the effective gravel-pack permeability to be drastically reduced. In order to account for such effects, it is convenient to introduce a gravel-pack factor denoted  $f_{gp}$  such that

$$(l_{gp})_{eff} = f_{gp} l_{gp} \quad (2-98)$$

Thus, a multiplier giving effective length is used to quantify deviations from the ideal pressure drop predicted by (2-96) and the expression for  $\Delta p_{gp}$  becomes

$$\Delta p_{gp} = \frac{q\mu f_{gp} l_{gp}}{k_p N_p A_p} + \frac{\beta_p \rho q^2 f_{gp} l_{gp}}{N_p^2 A_p^2} \quad (2-99)$$

Note that the same efficiency factor is introduced into the Darcy and non-Darcy terms; this is not strictly valid, but correcting the two terms identically reduces complexity of the model.

The dimensionless additional pressure drop  $(\Delta p_{gp})_D$  is given by

$$(\Delta p_{gp})_D = \frac{\Delta p_{gp} 2\pi kh}{q\mu} = \frac{2\pi f_{gp} l_{gp} kh}{k_p N_p A_p} + \frac{2\pi f_{gp} l_{gp} kh \beta_p \rho q}{\mu N_p^2 A_p^2} \quad (2-100)$$

This can be written in the form of a gravel-pack contribution to the total skin, i.e.,

$$S'_{gp} = S_{gp} + D_{gp} q = \frac{2\pi f_{gp} l_{gp} kh}{k_p N_p A_p} + \frac{2\pi f_{gp} l_{gp} kh \beta_p \rho}{\mu N_p^2 A_p^2} q \quad (2-101)$$

i.e.,

$$S_{gp} = \frac{2\pi f_{gp} l_{gp} kh}{k_p N_p A_p} = \frac{2\pi f_{gp} l_{gp} k}{k_p n_s A_p} \quad (2-102)$$

and

$$D_{gp} = \frac{2\pi f_{gp} l_{gp} kh \beta_p \rho}{\mu N_p^2 A_p^2} = \frac{2\pi f_{gp} l_{gp} k \beta_p \rho}{\mu n_s^2 h A_p^2} \quad (2-103a)$$

In oil field units, Eq. (2-103a) for  $D_{gp}$  becomes

$$D_{gp} = \frac{2\pi \times 6.414 \times 10^{-14} f_{gp} l_{gp} k \beta_p \rho}{\mu n_s^2 h A_p^2} \quad (2-103b)$$

In oil wells, again the non-Darcy contribution will often be negligible and it has been included in the analysis mainly for completeness. However, field experience of gravel-pack completions in high-permeability, unconsolidated formations has shown the existence of significant non-Darcy skin effect and hence Eq. (2-103b) is important. If a well is tested before and after gravel packing, the additional skin due to the pack  $S'_{gp}$  can be obtained directly by difference, i.e.,

$$S'_{gp} = (S_a)_{post} - (S_a)_{pre} \quad (2-104)$$

and the gravel-pack factor determined as

$$f_{gp} = \frac{S'_{gp}}{\frac{2\pi l_{gp} k}{k_p n_s A_p} + \frac{2\pi 6.414 \times 10^{-14} l_{gp} k \beta_p \rho}{\mu n_s^2 h A_p^2} q} = \frac{S'_{gp}}{(S'_{gp})_{ideal}} \quad (2-105)$$

The concept of a pre- and post-gravel-pack well test to determine the pack contribution to the total skin is similar to the situation with fractured wells where the pre- and post-fracture well tests are used to determine the finite conductivity and wing length of the fracture. A high post-gravel-pack skin usually indicates problems with gel plugging of the pack and  $S'_{gp}$  values as high as 80 have been recorded in gravel-packed wells in Malaysia compared to design values of around 8. The value of  $S_{gp}$  as a function of the permeability ratio  $k_p/k$  for  $n_s$  equal to four shots per foot is shown in table 2-4.

**Table 2-4.** Ideal gravel-pack Darcy skin factor as a function of permeability ratio

Permeability Ratio $\frac{k_p}{k}$	$S_{gp}$ ( $r_p = 0.25$ in., $l_p = 10$ in.)
1,000	0.96
500	1.92
100	9.6
36	26.7
10	96.0

$S_{gp}$  depends crucially on the permeability ratio and the shots per foot. The value of  $k_p/k = 36$  quoted in table 2-4 corresponds to the Saucier<sup>22</sup> particle size ratio of 6 and the assumption that the permeability is proportional to  $\bar{D}^2$ , i.e., presuming the formation permeability is given by the unconsolidated media formula; this assumption is conservative and the actual  $k_p/k$  ratio will normally be greater than this. Hence, a gravel-pack skin of 27 very much represents an upper limit to

the ideal value. An  $S_{gp}$  of 8 ( $k_p/k \approx 100$ ) implies approximately a halving of the well PI due to gravel packing, which is an acceptable reduction in productivity. Gravel-pack skins of, say, 80 imply a very large decrease in well PI and indicate a very unsuccessful operation and very large multiplier  $f_{gp}$ .

A particular problem arises in connection with the non-Darcy component of the skin modeled by Eq. (2-103b); normally, the inertial resistance coefficient  $\beta$  will simply be related to permeability through an equation of the form of (2-74) or (2-84) given previously. However, when a high-gravel pack skin is present, it is likely that this may take the form of a damage envelope as described in the section “Perforation damage,” which for the Darcy component can be modeled with the tunnel damage skin factor  $S_s$ . Hence, there may be an extra non-Darcy pressure drop caused by forcing fluid through this tunnel lining as illustrated in figure 2-43. This effect is modeled by the tunnel non-Darcy spherical skin factor  $S_{ND}^s$  discussed in the section “Spherical non-Darcy flow shape factors.”

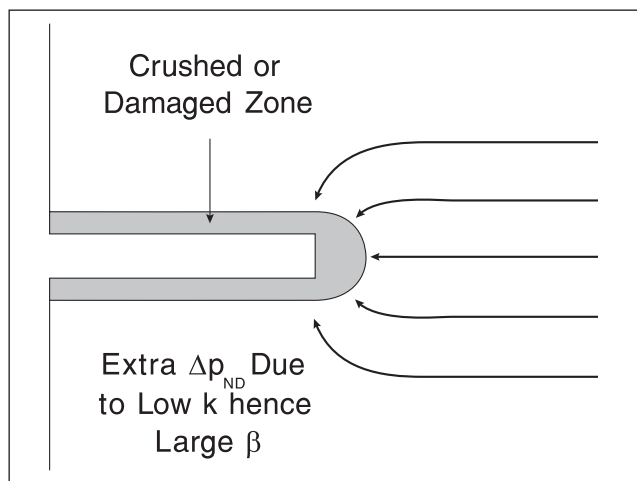


Fig. 2-43. Additional non-Darcy pressure drop in perforation tunnel lining

The problem of the invasion of fines from the formation will not show up immediately on the post-packing well test but the well apparent skin  $S_a$  will increase with time as mixing of gravel and formation sand progressively occurs. This is a good example of the need for time-lapse monitoring of the well performance through pressure build-up testing and analysis. The understanding of internal gravel-pack completions is very much tied to the ideas of perforation behavior developed here and the realization that tip flow is a predominant mechanism. The spherical model allows a calculation of the formation stress (pressure gradient) in the vicinity of the tunnel, which is necessary for the formulation of rock mechanics models of formation breakdown leading to fines invasion. It is interesting that Statoil have been able to avoid the need for gravel-packing wells in the Gullfaks field—which has an unconsolidated formation—by employing high-shot density perforation that reduces stress to such an extent that gravel packing is not required. For an offshore field with highly deviated wells, this is of considerable benefit and it illustrates what can be achieved when the physics of the problem is well understood. A simple criterion based on the sonic log is not sufficient to base decisions on whether or not to gravel-pack. In connection with well testing, it is now possible to monitor very accurately fines production (using an acoustic probe) as a function of well rate; this type of information is most useful in analyzing sanding tendency.



not all perforations are flowing. The ideal permeability of gravel-pack sand can be estimated using the Berg<sup>19</sup> correlation which takes the form

$$k_p = 5.1 \times 10^{-6} \phi^{5.1} \bar{D}^2 e^{-1.385PD} \quad (2-108)$$

where

- $k_p$  = gravel permeability (md)
- $\bar{D}$  = median grain size,  $D_{50}$  (mm)
- $P_D$  = phi percentile deviation =  $(D_{10} - D_{90})/2$
- $D_{10}$  = 10 percentile gravel size on the cumulative sieve analysis curve (mm)
- $D_{90}$  = 90 percentile gravel size (mm)
- $\phi$  = porosity (percent)

For an unconsolidated sand pack, the Berg correlation shows the importance of the following factors on the permeability:

- porosity
- median particle size
- particle size distribution

Data on gravel permeability as a function of grain size has also been presented by Gurley,<sup>20</sup> which have the advantage of not requiring porosity information:

Sieve size (US mesh)	$k_p$ (md)
10–20	$5.0 \times 10^5$
16–30	$2.5 \times 10^5$
20–40	$1.2 \times 10^5$
40–60	$4.0 \times 10^4$

The gravel inertial resistance coefficient  $\beta_p$  can be obtained from the correlation quoted by Oyeneyin<sup>21</sup> with permeability  $k_p$  in md:

$$\beta_p = \frac{2.239 \times 10^9}{k_p^{0.95}} \text{ (ft}^{-1}\text{)} \quad (2-109)$$

Pucknell and Mason<sup>30</sup> quote a different form, viz.,

$$\beta_p = \frac{2.73 \times 10^{10}}{k_p^{1.1045}} \text{ (ft}^{-1}\text{)} \quad (2-110)$$

# 3

## Well Inflow Performance Relations

---

### Oil Well Inflow Performance Relation

#### Single layer IPR for semi-steady-state conditions

The inflow performance of oil wells is usually modeled on the basis that the non-Darcy flow effect is negligible and the steady-state (SS) behavior is represented by the radial flow equation with the non-Darcy skin terms set to zero; thus in oil field units

$$\frac{(p_e - p_w)2\pi kh}{887.2q\mu} = \ln \frac{r_e}{r_w} + S_a \quad (3-1)$$

If there is a severe limited entry in a high-rate oil well with very few perforations flowing, then the non-Darcy term may, in fact, be significant and should be included in the analysis; however, in most situations it is quite in order to neglect the non-Darcy term in oil well description. The non-Darcy effect has been included in the formulation in the preceding chapter because the results are required for the gas well case to be considered later. It is much easier to derive gas well deliverability models if the incompressible flow results are already known. When discussing the productivity of wells, it is usually more appropriate to consider semi-steady-state (SSS) inflow rather than SS and to base the model on the drainage region average pressure  $\bar{p}$ . Introducing the Dietz shape factor  $C_A$  to account for the areal flow convergence effect due to well location within the drainage area of specified geometry, the SSS well inflow equation takes the form

$$(p_D)_{SSS} = \frac{(\bar{p} - p_w)2\pi kh}{887.2q\mu} = \frac{1}{2} \ln \frac{4\bar{A}}{\gamma C_A r_w^2} + S_a \quad (3-2)$$

where  $S_a$  is the total skin due all possible effects and  $\gamma = 1.781$ . The Dietz shape factors are tabulated in many textbooks, e.g., Earlougher<sup>1</sup>, and for a well in the center of a circular drainage area  $C_A$  takes on the upper limiting value of 31.62 as shown in figure 3-1. The average pressure



of the drainage area is usually determined from the extrapolated pressure on a Horner buildup plot, denoted  $p^*$ , through the Miller, Brons, and Hazebroek (MBH) correction:

$$P_{D,MBH} = \frac{(p^* - \bar{p})2\pi kh}{887.2q\mu} = \frac{1}{2} \ln(C_A t_{pDA}) \tag{3-3}$$

where  $t_p$  is the production time used in the Horner function and  $t_{pDA}$  is the dimensionless producing time based on drainage area, given by

$$t_{pDA} = \frac{0.0002636kt_p}{\phi\mu c_t \bar{A}} \tag{3-4}$$

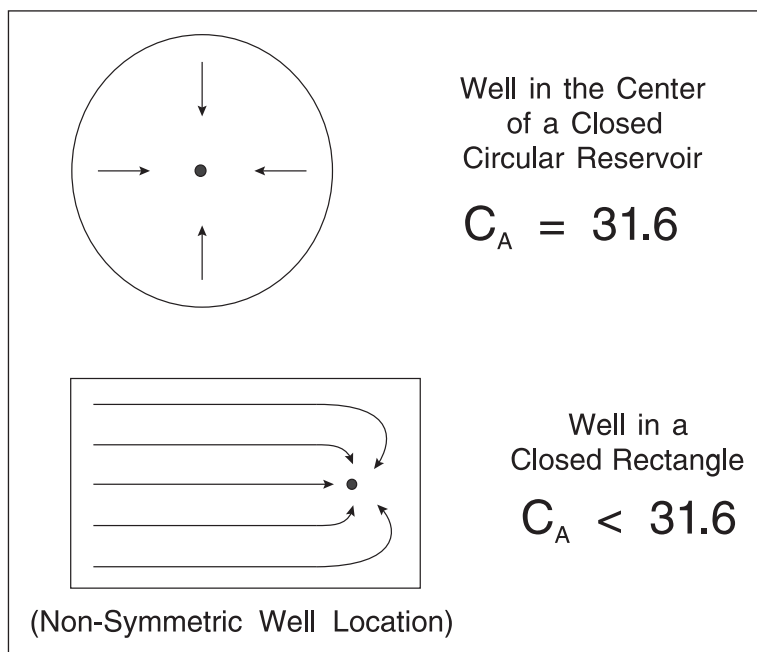


Fig. 3-1. Areal flow convergence accounted for by Dietz shape factors

The SSS expressions for the productivity index (PI) assume that production in the reservoir has been of sufficient duration for stabilized drainage areas to develop. During the preceding transient period, the initial pressure  $p_i$  is more relevant than  $\bar{p}$ , and expressions for the transient productivity index—which is time dependent—will be given later. The problem of transient deliverability is important in low-permeability reservoirs.

The drainage area  $\bar{A}$  and corresponding Dietz shape factor  $C_A$  are usually determined by inspection of the reservoir structure map and areas are assigned to wells in proportion to their rate according to the prescription

$$\frac{V_i}{V_t} = \frac{q_i}{\sum_{i=1}^N q_i} \quad (3-5)$$

where  $V_t$  = total pore volume of fault block or reservoir compartment

$V_i$  = pore volume of drainage area assigned to well  $i$

$q_i$  = production rate of well  $i$

$N$  = number of wells in physical compartment.

The process of selecting drainage areas by inspection of a reservoir map is illustrated in Figure 1.27 (chapter 1) where the physical no-flow boundaries (reservoir limits and sealing faults) are first used to define compartments and then the virtual no-flow boundaries are allocated according to Eq. (3-5) and the number of wells in the block. Traditionally, this exercise was referred to as *planimetry*. It is important to note that no-flow boundaries near to the wells will always be physical in nature and the virtual no-flow interfaces will constitute the far boundaries of the drainage area.

The SSS PI of an oil well is defined as

$$q_s = J_{SSS}(\bar{p} - p_w) \quad (3-6)$$

and comparing (3-6) with (3-2) shows that in oil field units

$$J_{SSS} = \frac{2\pi kh}{887.2B\mu \left( \frac{1}{2} \ln \frac{4\bar{A}}{\gamma C_A r_w^2} + S_a \right)} \quad (3-7)$$

The PI is probably the single most important quantity regarding well behavior, and values of  $J_{SSS}$  range from an upper limit of around 10,000 bbl/d/psi for extremely productive wells with a large  $kh$  product down to values less than 0.001 which are below the economic minimum for oil production. The inflow performance relation (IPR) is a plot of well flow rate  $q_s$  versus flowing bottom hole pressure  $p_w$ ; hence, rearranging (3-6) gives

$$p_w = \bar{p} - \frac{1}{J_{SSS}} q_s \quad (3-8)$$

i.e., the IPR is a straight line of intercept  $\bar{p}$  and slope  $-1/J_{SSS}$ , as illustrated in figure 1-3 (chapter 1). Knowledge of the average reservoir pressure  $\bar{p}$  and the well productivity index  $J_{SSS}$  allows the IPR to be plotted on the well performance diagram. The intersection of the IPR with the vertical lift performance (VLP) curve gives the well operating point and the production rate.

Fetkovich<sup>2</sup> has quoted field examples of oil wells in undersaturated reservoirs with the flowing bottom-hole pressure above the bubble point, i.e., single-phase conditions where non-Darcy effects are definitely occurring, and he makes a strong case for multirate testing of oil wells. Fetkovich has also suggested that the productivity of oil wells be modeled by an empirical equation of the form

$$q_s = c(\bar{p}^2 - p_w^2)^n \quad (3-9)$$

where  $c$  and  $n$  are constants which fit field measurements of well flowing pressure at various oil rates. The fact that the exponent  $n$  is not unity and  $p^2$  is used in the formulation indicates that either oil wells are affected by laminar-inertia effects or some other nonlinearity is present; the Fetkovich method is treated in detail in a later section. For example, in an unconsolidated formation the permeability is, in fact, a function of drawdown due to increasing formation compaction as the pore pressure falls. A value of  $n$  in Eq. (3-9) which is different from unity allows it to model any nonlinear behavior in the inflow relation. Stress (pore pressure) dependent permeability is treated in detail in chapter 17 of *Well Test Design and Analysis* (addendum) on coal bed methane wells.

The concept of PI of an oil well has traditionally been based on the volumetric flow rate at standard (surface, i.e., stock tank) conditions  $q_s$ . It is also useful to define a PI in terms of mass flow rate in lb/day  $m_o$ , where

$$m_o = 5.614 q \rho_o \quad \rho_o = \text{density of in situ oil in lb/ft}^3$$

The definition of  $J_m$  in terms of mass flow rate is

$$m_o = J_m (\bar{p} - p_w) \quad (3-10)$$

giving

$$J_m = \frac{2\pi k h \rho_o}{158.02 \mu \left( \frac{1}{2} \ln \frac{4\bar{A}}{\gamma C_A r_w^2} + S_a \right)} \quad (3-11)$$

where  $J_m$  has units of lb/day/psi. The formulae due to Yaxley for predicting  $C_A$  values in rectangular and wedge-shaped reservoirs were given in chapter 1. Note that the formation volume factor  $B$  has disappeared, and the in situ mass flow rate  $m_o$  is given by

$$m_o = (5.614 \times q_s \rho_{so} + \text{GOR} \times q_s \gamma_g \times 0.07645) \text{ lb/day} \quad (3-12)$$

where GOR = surface gas–oil ratio (SCF/bbl)

$\gamma_g$  = gravity of produced gas

$\rho_{so}$  = density of stock tank oil (lb/ft<sup>3</sup>).

Alternatively, if the in situ mass flow rate is predicted from Eq. (3–10), then the stock tank oil volumetric flow rate is given by

$$q_s = \frac{m_o}{5.614 \times \rho_{so} + \text{GOR} \times \gamma_g \times 0.07645} \text{ STbbl/day} \quad (3-13)$$

These equations facilitate a description either on a total mass  $m_o$  or a stock tank oil  $q_s$  basis and allow interchange between the two approaches to be made; when multiphase systems are involved, there is considerable attraction in working on in terms of total mass.

## Transient IPR

When a new well is set in flow for the first time (or an existing well is flowed again after an extended shutin), there is a period of transient flow during which the pressure disturbance is propagating out in an infinite-acting or semi-infinite-acting fashion. For a given drainage area—determined by the well pattern and sealing fault locations—the time to reach an SSS condition is denoted  $(t_{DA})_{SSS}$ , where

$$(t_{DA})_{SSS} = \frac{kt_{SSS}}{\phi\mu c_t A} \quad (3-14)$$

This quantity is listed for different drainage area shapes and well positions as companion information to the table of the Dietz shape factors  $C_A$ ; for example, in the case of a well in the center of a circular or square drainage area,  $(t_{DA})_{SSS} = 0.1$ . Further insight into the time to attain SSS, i.e.,  $t_{SSS}$ , may be obtained by observing that in most situations the quantity  $(t_{DLF})_{SSS}$  defined as

$$(t_{DLF})_{SSS} = \frac{kt_{SSS}}{\phi\mu c_t L_f^2} \quad (3-15)$$

where  $L_f$  is the distance from the well to the furthest boundary is equal to 0.25, i.e., the time to attain SSS is practically synonymous with the time for the depth of investigation to reach the far boundary. The propagation of a pressure disturbance in a channel reservoir is illustrated in figure 3–2. The infinite-acting time  $t_{ia}$  up to the point where the disturbance reaches the nearest boundary at a distance  $L$  from the well is given by the radial flow depth of investigation formula

$$r_i = L = \sqrt{\frac{4kt_{ia}}{\phi\mu c_t}} \quad \text{i.e.} \quad \frac{kt_{ia}}{\phi\mu c_t L^2} = 0.25 \quad (3-16)$$

while the time to essentially reach SSS ( $t_{sia}$ ) is predicted by the length of investigation formula for linear flow based on the distance to the far boundary  $L_f$ , viz.,

$$l_i = L_f = \sqrt{\frac{5kt_{sia}}{\phi\mu c_t}} \quad \text{i.e.,} \quad \frac{kt_{sia}}{\phi\mu c_t L_f^2} = 0.2 \quad (3-17)$$

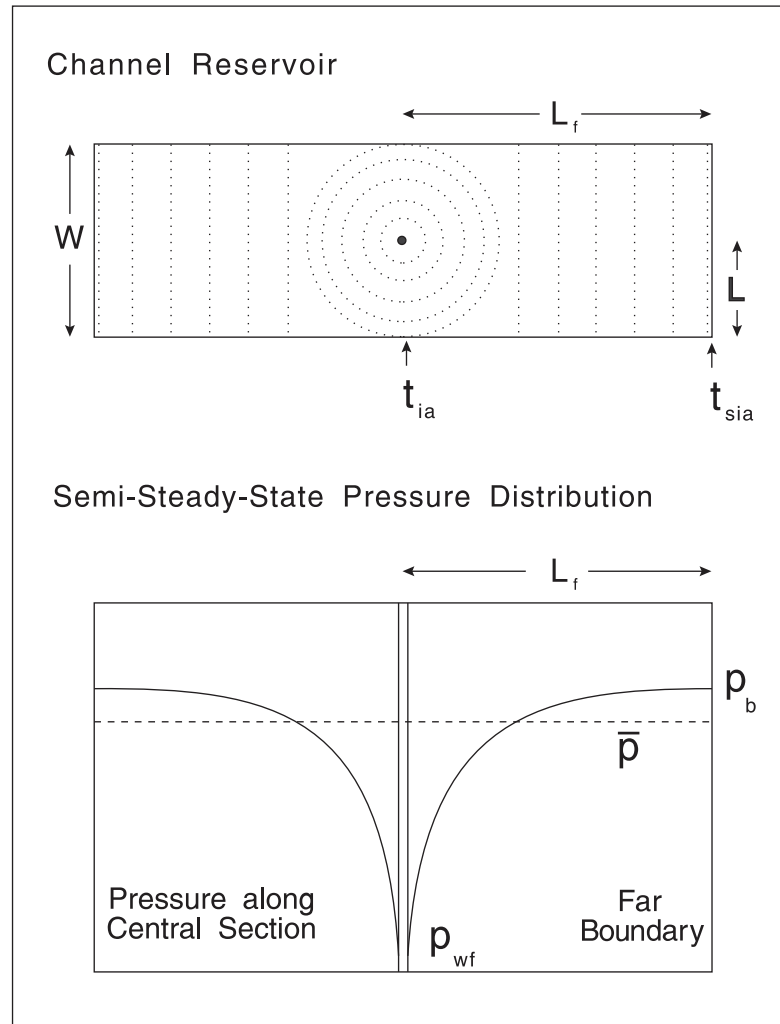


Fig. 3-2. Propagation of transient pressure disturbance in a channel reservoir

For a well in the center of a square reservoir,  $t_{ia}$  and  $t_{sia}$  are, of course, identical and there is no late transient period.

The important point is that in low-permeability reservoirs a considerable period of transient or late transient production will occur; indeed, it may be of the order of a year or more before a stabilized production regime is established. When a well is produced at constant rate (CRD), the flowing bottomhole pressure  $p_{wf}$  may be presented on a Cartesian graph as shown in figure 3-3 and three distinct regimes are denoted:

- Transient or infinite-acting —  $t < t_{ia}$
- Late transient or semi-infinite-acting —  $t_{ia} < t < t_{sia}$
- Semi-steady-state depletion —  $t > t_{sia}$ .

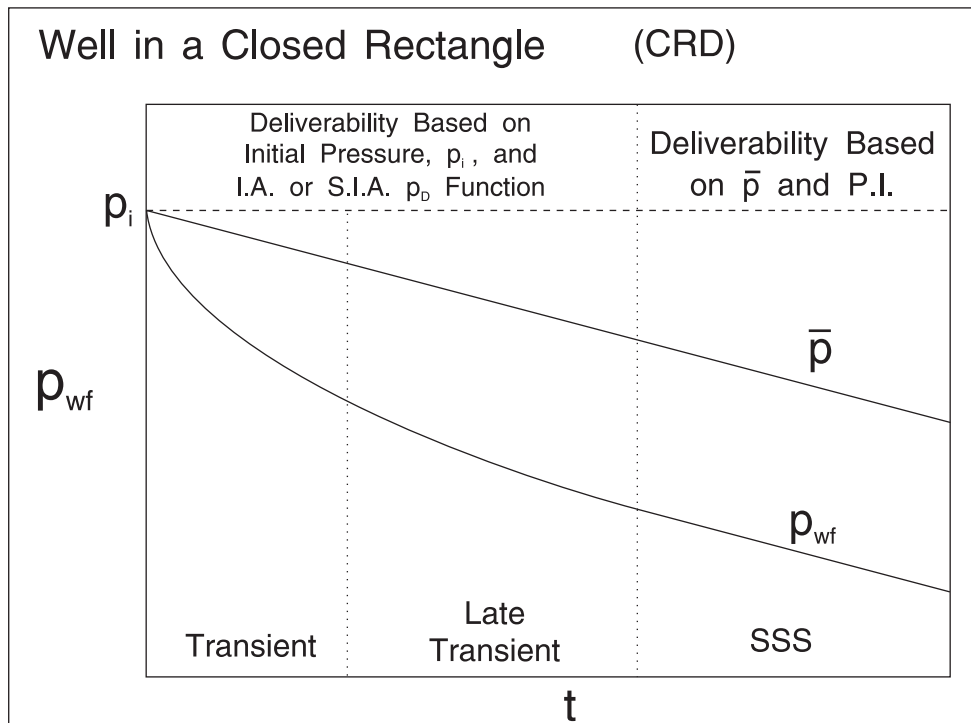


Fig. 3–3. Production regimes in primary depletion

During the first two phases, where the pressure disturbance is propagating out from the well as illustrated in figure 3–4, the transient productivity index—denoted  $J_{tr}$ —is decreasing until eventually a stabilized final value  $J_{SSS}$  is attained. In figure 3–4, the well is produced at essentially constant bottom-hole pressure (production scenario) and the rate declines as the sandface pressure gradient decreases, with the transient pressure disturbance moving out according to the depth-of-investigation equation. The time-dependent transient PI defined through the relation

$$q_s = J_{tr}(p_i - p_{wf}) \quad (3-18)$$

is, in fact, identified with the familiar infinite-acting (or semi-infinite-acting)  $p_D$  functions used in well test analysis. The essential point is that a constant rate  $p_D$  function can be used with very little error even when the rate is, in fact, changing; thus the approximation is made that

$$\frac{(p_i - \tilde{p}_{wf})2\pi kh}{\tilde{q}_s B\mu} = p_D(t_D) \text{ i.e., } J_{tr} = \frac{2\pi kh}{B\mu(p_D(t_D))} \quad (3-19)$$

where the notations  $\tilde{p}_{wf}$  and  $\tilde{q}_s$  imply that the instantaneous values of the bottom-hole flowing pressure and the well surface rate are related by Eq. (3–19) with  $t_D$  based on the total flowing time. Equation (3–19) is known as the *Fetkovich approximation*. The  $p_D$  function  $p_D(t_D)$  employed in (3–19) is the constant-rate solution to the diffusivity equation for any semi-infinite system model. Henceforth, the superscript  $\sim$  will be dropped but, whenever transient inflow is being discussed, the implication is that the quasi-constant-rate approximation is being made.

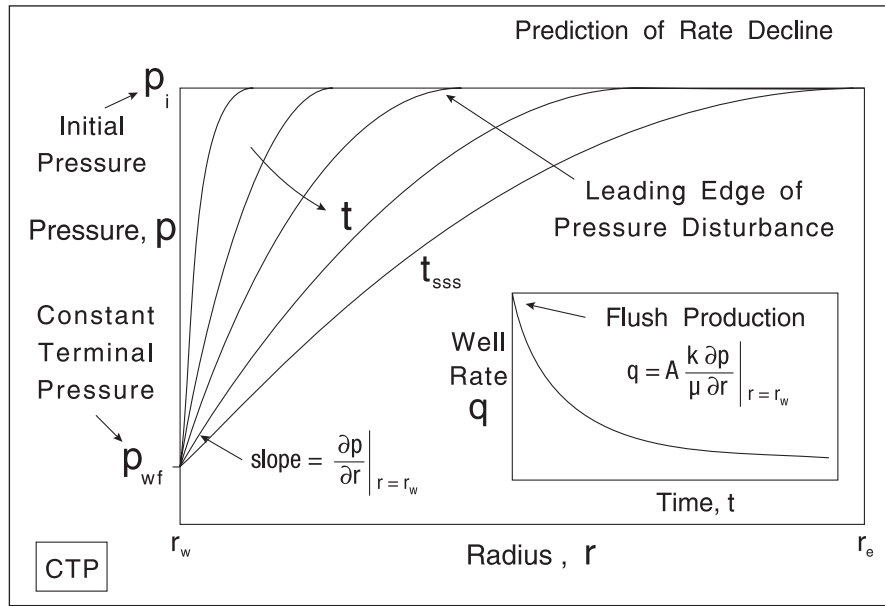


Fig. 3-4. Transient production

a) Radial flow

Thus for infinite-acting radial flow to a vertical well

$$p_D = \frac{(p_i - p_{wf})2\pi kh}{q_s B\mu} = \frac{1}{2} \left( \ln \frac{4t_D}{\gamma} + 2S_a \right) \quad (3-20)$$

and comparison of Eqs. (3-18) and (3-20) shows that

$$J_{tr} = \frac{2\pi kh}{B\mu \left( \frac{1}{2} \ln \frac{4kt}{\gamma\phi\mu c_t r_w^2} + S_a \right)} \quad (3-21)$$

The transient productivity index  $J_{tr}$  shows continual decrease as time goes by and the temporal dependence of the IPR may be represented on a well performance diagram as shown in figure 3-5; the operating point indicates the well production at the selected times. This decline in well rate due to transient inflow behavior is very important in properly assessing the economics of wells in tight reservoirs. At the point where the well enters SSS behavior, a switch can be made to using  $J_{SSS}$  and  $\bar{p}$  as shown in figure 3-6; note that  $J_{SSS}$  at the changeover is larger than  $J_{tr}$  just prior to the switch since the former is based on  $\bar{p}$  and the latter on  $p_i$ .

In chapter 1, a generalized form for the SSS Dietz shape factor for a well in a closed rectangle was given. This geometry is particularly flexible and allows typical fault blocks to be adequately modeled. In the late transient period, the well response is affected by the nearest no-flow boundaries and the corollary of the closed rectangle in SSS is the right-angle pair of faults illustrated in figure 3-7; for this situation, the semi-infinite  $p_D$  function is given by

$$p_D = \frac{(p_i - p_{wf})2\pi kh}{q_s B\mu} = \left( \frac{1}{2} \ln \frac{4t_D}{\gamma} + \sigma + S_a \right) \quad (3-22)$$

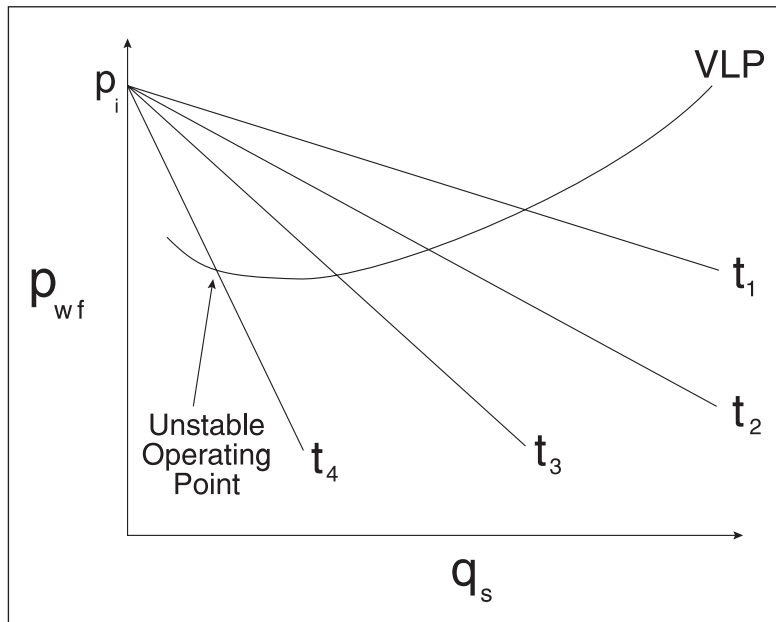


Fig. 3-5. Transient IPR on a well performance diagram

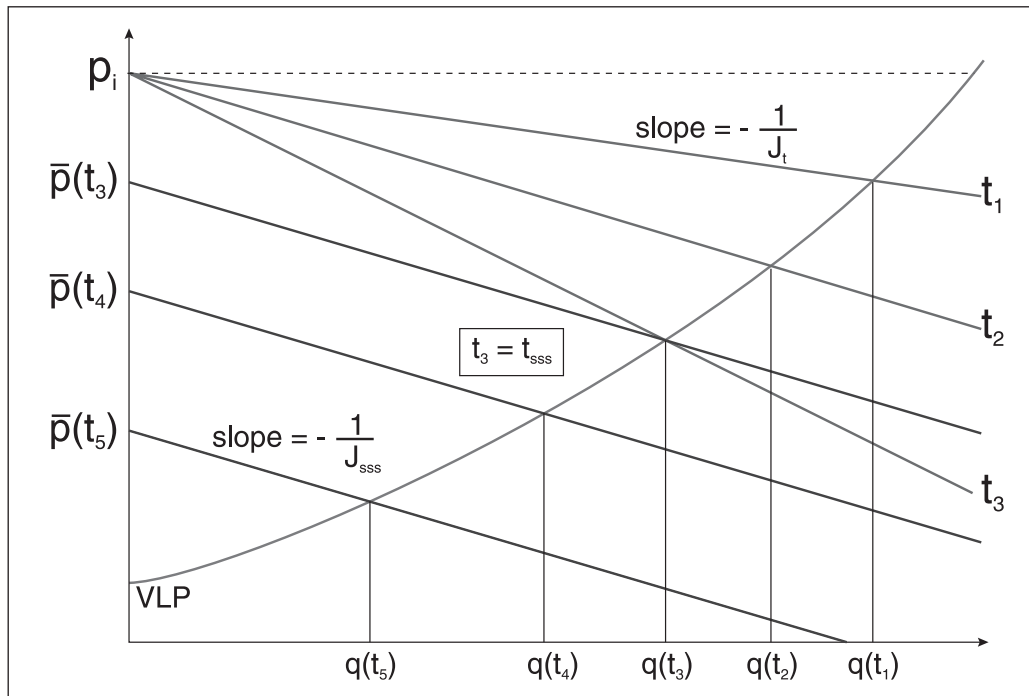


Fig. 3-6. Transient and SSS production on a well performance diagram



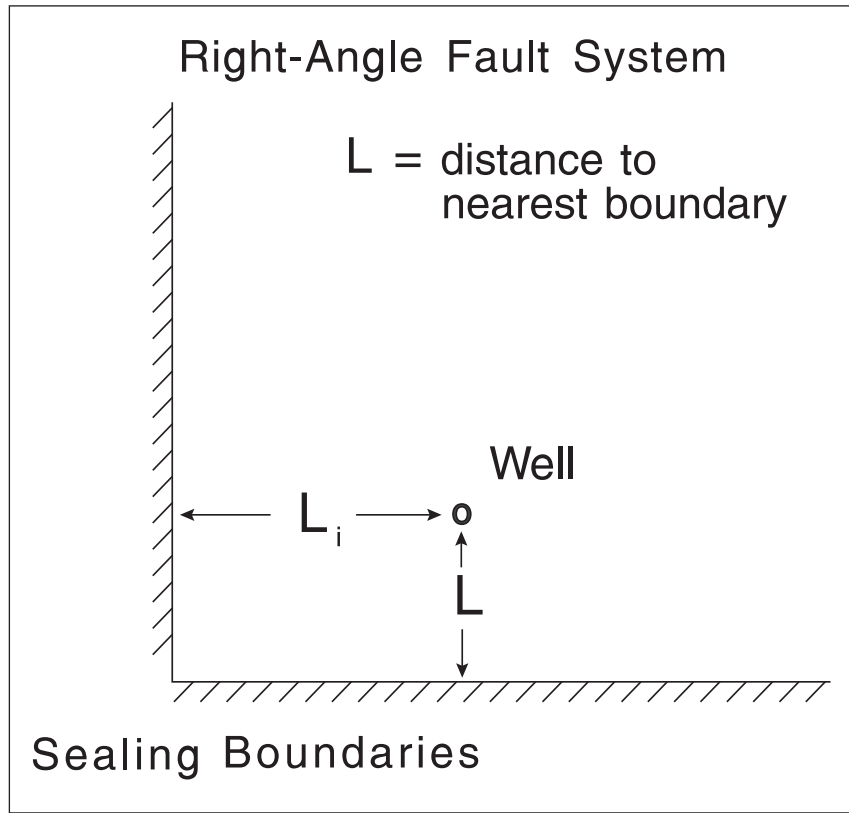


Fig. 3-7. S-l. system comprising a vertical well and a pair of right-angle sealing faults

Here  $\sigma$  represents the effect of the image wells modeling fault behavior, i.e., the additional dimensionless pressure drop due to the near boundaries, and is given by

$$\sigma = \frac{1}{2} \sum_{j=1}^3 E_i \frac{\phi \mu c_t r_j^2}{4kt} \quad (3-23)$$

The transient PI accordingly becomes

$$J_{tr} = \frac{2\pi kh}{B\mu \left( \frac{1}{2} \ln \frac{4kt}{\gamma \phi \mu c_t r_w^2} + \sigma + S_a \right)} \quad (3-24)$$

in which  $\sigma$  is a time dependent-quantity given by Eq. (3-23). This model allows for the affect of nearby faults on the late transient productivity of the well; when the far boundaries begin to influence the inflow behavior, i.e.,  $t > t_{SSS}$ , the SSS model for a closed rectangle becomes appropriate with the Dietz shape factor corresponding to the well location in the drainage area. Well productivity in all three flow regimes—transient, late transient, and SSS—can therefore be handled in a unified treatment.

## b) Linear flow in a channel reservoir

Many pressure build-up tests indicate that the well is located between approximately parallel boundaries due either to fluvial deposition or terrace faulting. It was shown in chapter 6 of *Well Test Design and Analysis* that the semi-infinite  $p_D$  function for linear flow in a channel reservoir with localized flow convergence into a vertical well is given by the equation

$$p_D = \frac{(p_i - p_{wf})2\pi kh}{q_s B\mu} = 2\sqrt{\pi t_{Dw}} + \sigma + S_a \quad (3-25)$$

where

$$t_{Dw} = \frac{kt}{\phi\mu c_t W^2} \quad \text{and} \quad \sigma = \ln \frac{W}{2\pi r_w \sin(\pi c_D)}$$

Here  $W$  is the width of the channel and  $c_D = L/W$  is the relative location of the well within the channel; for example, for a centrally located well  $c_D = 0.5$ . The late transient PI is now given by

$$J_{tr} = \frac{2\pi kh}{B\mu \left( \sqrt{\frac{4\pi kt}{\phi\mu c_t W^2}} + \ln \frac{W}{2\pi r_w \sin(\pi c_D)} + S_a \right)} \quad (3-26)$$

Linear flow exhibits a square root of time dependence which is considerably stronger than the logarithmic variation of  $J_{tr}$  with time characteristic of radial flow. Hence it is particularly important in channel reservoir geometry to recognize that a decline in well rate may be expected as the pressure disturbance linearly propagates along the system.

## c) Fractured and horizontal wells

As already mentioned, the transient aspect of productivity is most important in low-permeability systems where the time to reach SSS conditions  $t_{SSS}$  can be extremely long. In a tight reservoir, it is often necessary to boost production either by hydraulically fracturing the well or by drilling horizontally. These are the two main options for ensuring economic well rates. However, it is still necessary to recognize that transient production will occur with a declining well rate; in particular, the rates measured immediately on putting the well into production are not representative of the average rate that can be sustained over the period used to compute the economic viability of the stimulation job or horizontal well drilling. In order to properly assess the benefits of these options, the flow rate—as fixed by the operating point on the well performance diagram—must be determined as a function of time.

A constant rate  $p_D$  function may be written in generalized form as

$$p_D = p_D(t_{Dc}, \Pi_1, \Pi_2, \dots) \quad (3-27)$$

where  $t_{Dc}$  is a characteristic dimensionless time and  $\Pi_j$  are dimensionless parameter groups entering the model. For example, in chapter 8 of *Well Test Design and Analysis* the fundamental  $p_D$  function for a finite conductivity fracture is given in the form

$$p_D = \frac{(p_i - p_{wf})2\pi kh}{q_s B\mu} = p_D(t_{Dxf}, F_{CD}) \quad (3-28)$$

while in chapter 12, the  $p_D$  function for a horizontal well takes the form:

$$p_D = \frac{(p_i - p_{wf})2\pi kh}{q_s B\mu} = p_D(t_{DL/2}, z_{wD}, A, L_D, Z_D) \quad (3-29)$$

The transient PI for these situations may therefore be written as

$$J_{tr} = \frac{2\pi kh}{B\mu(p_D(t_{DC}, \Pi_1, \Pi_2, \dots) + S_a)} \quad (3-30)$$

with the dimensionless parameter groups specified and the dimensionless characteristic time  $t_{Dc}$  evaluated from the real times  $t$  at which it is desired to determine  $J_{tr}$ . Equation (3-30) illustrates how the constant-rate  $p_D$  function for any relevant model can be used in the prediction of well deliverability in the transient or late transient period. This approach presumes that all the requisite parameters have been properly identified through well test interpretation and shows how advanced methods carry over into the reliable prediction of deliverability.

## Composite IPR of a stratified system

The treatment of well inflow in section “Single Layer IPR for Semi-steady-state Conditions” refers to a single-layer reservoir at vertical pressure equilibrium, in which case the concept of drainage area average pressure  $\bar{p}$  is valid. However, wireline formation tester (WFT) measurements in new wells in produced fields have shown that often adjacent layers are depleted (or supported) to quite different average pressures. Suppose that a WFT survey has indicated the presence of a stratified system, i.e., layers that are essentially noncommunicating in the reservoir but are produced into a common wellbore. The situation is illustrated in figure 3-8, where a system of  $N$  layers is shown each having its own value of pressure, permeability–thickness product, and skin factor. The production from an individual layer is given by

$$q_{s,j} = J_{SSS,j}(\bar{p}_j - p_w) \quad (3-31)$$

where

$$J_{SSS,j} = \frac{2\pi k_j h_j}{887.2B\mu \left( \frac{1}{2} \ln \frac{4\bar{A}}{\gamma C_A r_w^2} + S_{a,j} \right)} \quad (3-32)$$

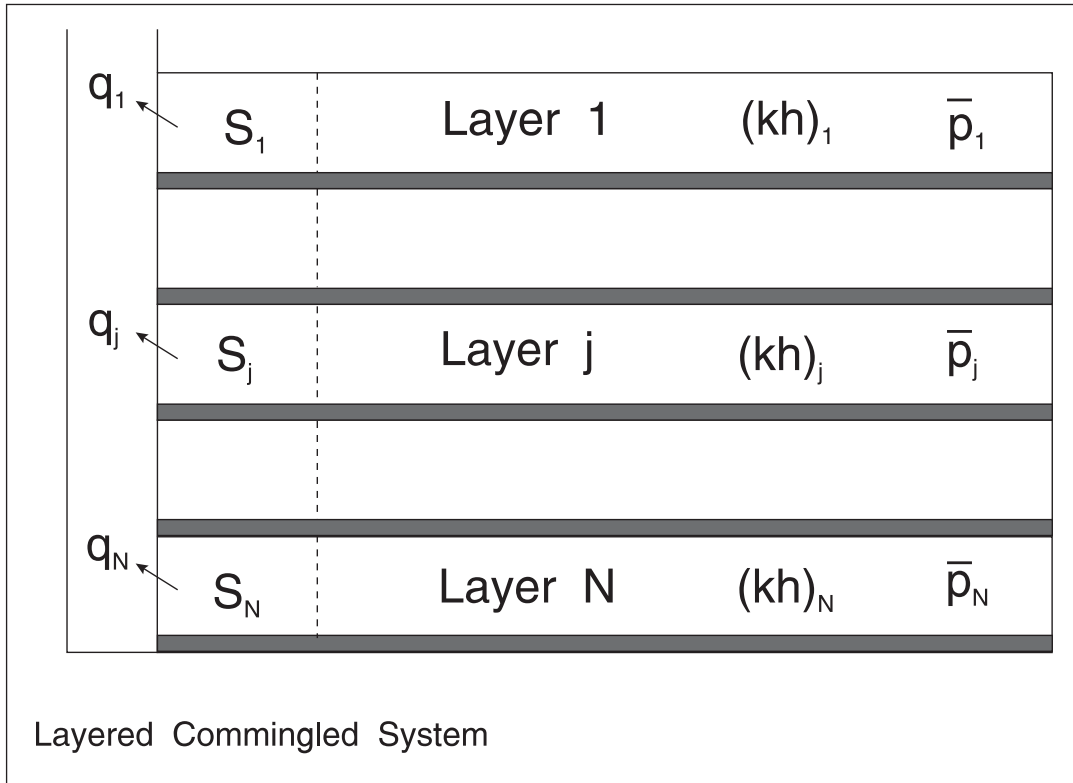


Fig. 3–8. Commingled production from a stratified reservoir

The commingled condition is that the sum of the individual layer rates is the total surface rate  $q_s$ , i.e.,

$$q_s = \sum_{j=1}^N q_{s,j} \quad (3-33)$$

The individual layer inflow performance relations are shown diagrammatically in figure 3–9, and it can be seen that the well total rate  $q_s$  is predicted by a straight line composite IPR of the form

$$q_s = J_{SSS}(\bar{p}^* - p_w) \quad (3-34a)$$

where

$$\bar{p}^* = \frac{\sum_{j=1}^N J_{SSS,j} \bar{p}_j}{J_{SSS}} \quad \text{and} \quad J_{SSS} = \sum_{j=1}^N J_{SSS,j} \quad (3-34b)$$

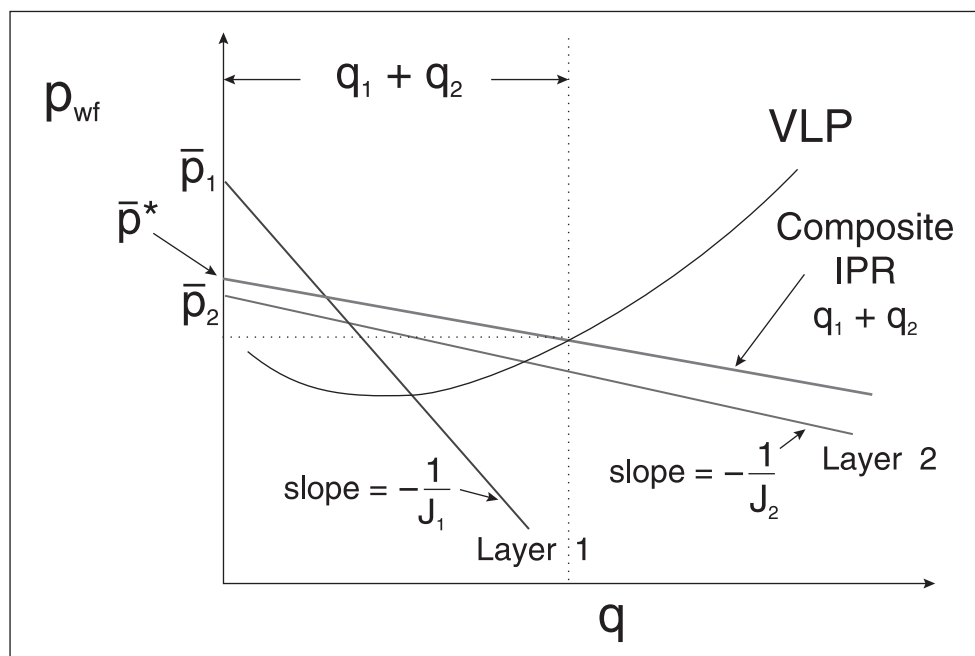


Fig. 3-9. Individual and composite IPR relations in a commingled system

Here,  $\bar{p}^*$  is the PI weighted mean layer pressure and  $J_{SSS}$  is the sum of the individual productivity indices; the composite IPR may be written as

$$p_w = \bar{p}^* - \frac{1}{J_{SSS}} q_s \quad (3-35)$$

Again, this is a straight line relationship between bottom-hole pressure  $p_w$  and surface rate  $q_s$ . However, Eq. (3-34a and b) is only valid when single-phase (oil) flow is occurring in each layer. Once one or more layers breakthrough to water, the situation becomes more complex and differences in layer pressure cause quite complex variation in the total water-cut; this aspect of multiphase flow will be treated later.

## Horizontal wells with vertical fractures

The theory discussed in the preceding section for commingled production in a layered system applies equally well to a horizontal well producing from different compartments of a reservoir. In particular, the situation where a horizontal well is repeatedly hydraulically fractured at successive locations along its length, resulting in multiple vertical fractures, can be modeled as a commingled system. In this case, the  $J_{SSS,j}$  values refer to the individual fractures and the  $S_{a,j}$

in Eq. (3–32) are the pseudoradial skin factors pertinent to a vertical fracture which depend on fracture half length  $x_f$ , fracture conductivity  $k_f b_f$ , and fracture skin  $S_{fr}$ , as discussed in chapter 2.  $N$  is now the number of hydraulic fractures, and in most cases the reservoir pressure,  $\bar{p}_j$ , will be the same for each. Determining the parameters of the individual fractures is not an easy task, but in the design case—where the parameters will be estimated—the effect of multiple vertical fractures along a horizontal well can be calculated. This technique has been very successfully used in the Dan field offshore Denmark and combines the advantages of vertical fractures and horizontal wells particularly when the effective vertical permeability is very low. Horizontal wells with multiple vertical fractures are treated in detail in chapter 17 of *Well Test Design and Analysis* (addendum).

## Extension to Gas Well Inflow Performance

### Concept of pseudopressure

Steady-state inflow into a gas well is complicated by the expansion of the gas as the pressure falls and the variation of viscosity  $\mu$  with pressure. The flow rate of a gas well is conventionally expressed in volumetric rate at standard conditions, denoted  $Q$ . When a gas well is flowed at constant rate, it is actually the mass flow rate  $m_g$  that is fundamental and the volume at standard conditions per unit time is really a measure of mass flow. The relation between mass flow rate  $m_g$  and standard volumetric rate  $Q$  is

$$m_g = \rho_{sc} Q \quad \text{where} \quad \rho_{sc} = \frac{p_{sc} M_w}{z_{sc} R T_{sc}} \quad (3-36)$$

For the special case of gas field units with  $Q$  in MSCFD,  $m_g$  in lb/day, and the gas gravity relative to air denoted  $\gamma_g$ , the conversion is

$$m_g = 76.45 \gamma_g Q \quad (3-37)$$

In the succeeding treatment, attention will be focussed on  $m_g$  rather than  $Q$  (which is the conventional choice) since the extension to two-phase flow, e.g., gas condensate, is much clearer if total mass flow rate is employed. Consider now SS radial flow of a real gas to a vertical well produced at constant mass rate  $m_g$  as illustrated in figure 3–10; the flow equation based on Darcy's law takes the form

$$\frac{dp}{dr} = \frac{\mu}{k} u_r = \frac{\mu}{k} \frac{m_g}{\rho 2\pi r h} \quad (3-38)$$

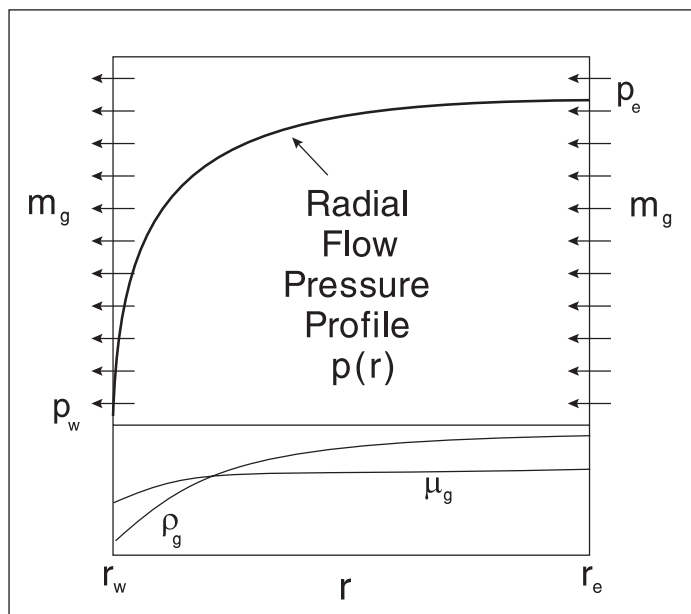


Fig. 3–10. Steady-state radial compressible flow

In this equation, both the gas density  $\rho$  and its viscosity  $\mu$  are pressure dependent; separating the variables and integrating gives

$$\int_{p_w}^{p_e} \frac{\rho}{\mu} dp = \frac{m_g}{2\pi kh} \int_{r_w}^{r_e} \frac{dr}{r} = \frac{m_g}{2\pi kh} \ln \frac{r_e}{r_w} \quad (3-39)$$

Multiplying both sides of Eq. (3–39) by the quantity  $\frac{\mu_i}{\rho_i}$ , where  $\mu_i$  and  $\rho_i$  are the gas viscosity and density, respectively, at the reservoir temperature and initial pressure, gives

$$\frac{\mu_i}{\rho_i} \int_{p_w}^{p_e} \frac{\rho}{\mu} dp = \frac{m_g \mu_i}{2\pi kh \rho_i} \ln \frac{r_e}{r_w} \quad (3-40)$$

On the basis of Eq. (3–40), now define a normalized pseudopressure function  $\psi(p)$  as

$$\psi(p) = \frac{\mu_i}{\rho_i} \int_{p_b}^p \frac{\rho}{\mu} dp' \quad (3-41)$$

where  $p_b$  is some low base pressure; in terms of pseudopressure, Eq. (3–40) may now be written in the convenient form

$$\Delta\psi = \psi(p_e) - \psi(p_w) = \frac{m_g \mu_i}{2\pi kh \rho_i} \ln \frac{r_e}{r_w} \quad (3-42)$$

The important point is that the pseudopressure function can be computed in advance and stored as a table for subsequent use via interpolation. The variation of gas density and viscosity with pressure (at reservoir temperature) are implicitly held in  $\psi(p)$  which is computed by quadrature, e.g., Simpson's rule, as illustrated in figure 3-11.

$$\psi(p) = \frac{\mu_i}{\rho_i} \int_{p_b}^p \frac{\rho(p')}{\mu(p')} dp' \quad \text{where} \quad \rho(p) = \frac{pM_w}{z(p)RT} \quad (3-43)$$

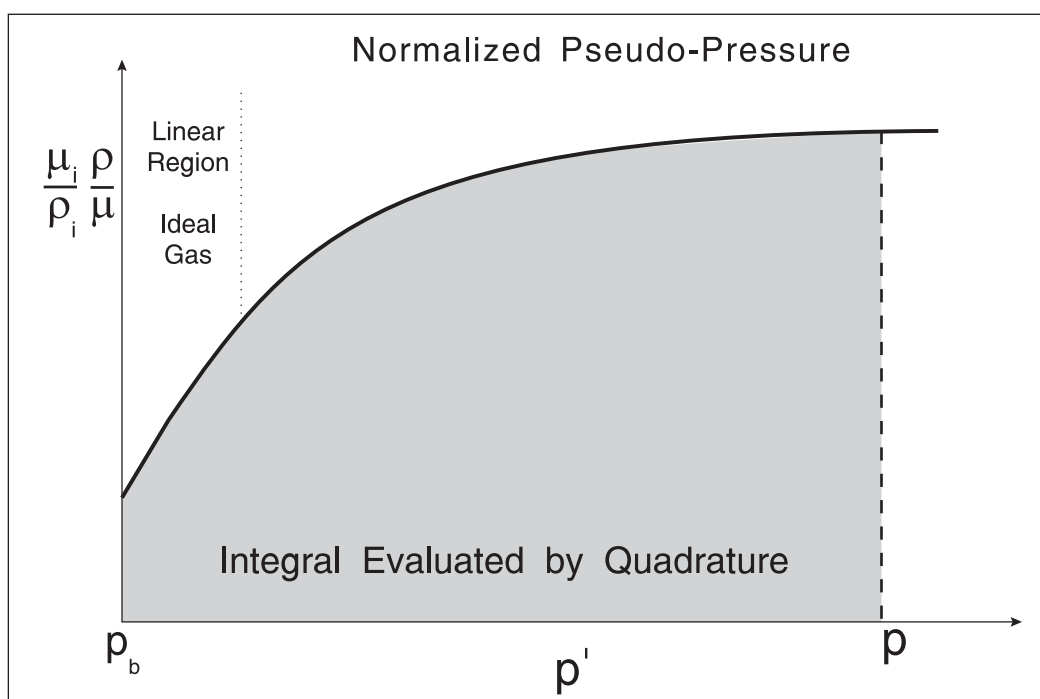


Fig. 3-11. Computation of the real gas pseudopressure by quadrature

Here  $\mu(p)$  represents some accurate correlation or prediction method for the gas viscosity as a function of pressure, and  $z(p)$ —the variation of compressibility factor with pressure—is obtained from an equation of state. The choice of the reservoir initial pressure  $p_i$  at which the reference viscosity  $\mu_i$  and the reference density  $\rho_i$  are computed is arbitrary. The advantage of normalizing the pseudopressure by multiplying by the constant  $\mu_i/\rho_i$  is that  $\psi(p)$  so defined simply has the units of pressure. The quantity  $m_g/\rho_i$  is the gas volumetric flow rate at initial reservoir pressure, i.e., the in situ flow rate  $q$ , at  $p_i$ , and Eq. (3-42) may be written as

$$\Delta\psi = \psi(p_e) - \psi(p_w) = \frac{q\mu_i}{2\pi kh} \ln \frac{r_e}{r_w} \quad (3-44)$$

$$\text{where } q = QB_{gi} \text{ and } B_{gi} = \frac{p_{sc}}{p_i} \frac{z_i}{z_{sc}} \frac{T}{T_{sc}} \text{ or } B_{gi} = \frac{\rho_{sc}}{\rho_i}$$



Here  $B_{gi}$  is the gas formation volume factor based on the reservoir initial pressure, and the determination of  $\Delta\psi$  as the difference between two pseudopressures is illustrated in figure 3–12. Thus the use of normalized pseudopressure allows the compressible flow equation to be written in a form identical to the oil (incompressible flow) equation. Equation (3–44) may also be rearranged in dimensionless form as

$$\psi_D = \frac{\psi(p_e) - \psi(p_w)}{\frac{QB_{gi}\mu_i}{2\pi kh}} = \frac{\psi(p_e) - \psi(p_w)}{\frac{q\mu_i}{2\pi kh}} = \frac{\psi(p_e) - \psi(p_w)}{\frac{m_g\mu_i}{2\pi kh\rho_i}} = \ln \frac{r_e}{r_w} = \ln r_{De} \quad (3-45)$$

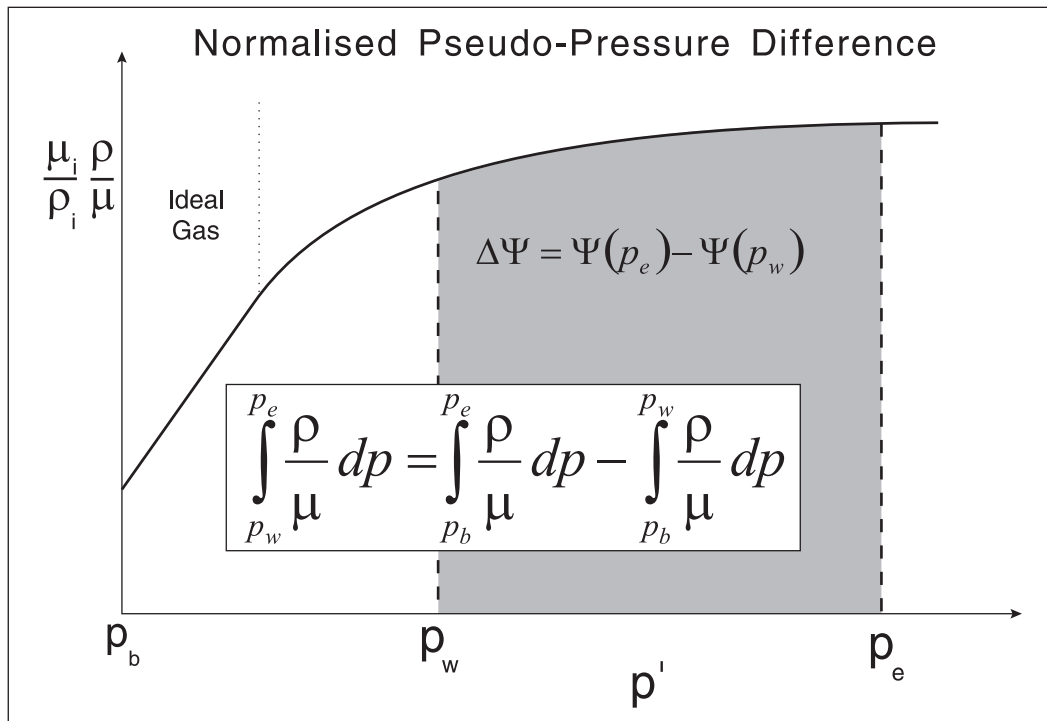


Fig. 3–12. Reservoir integral as the difference between two pseudopressures

A normalized pseudo-pressure function  $\psi(p)$  computed by numerical integration using the Schmidt–Wenzel equation of state and the correlation for gas viscosity is shown in figure 3–13; the reference viscosity and density ( $\mu_i$  and  $\rho_i$ ) for this example are 0.02791 cp and 15.978 lb/ft<sup>3</sup>, respectively, corresponding to an initial pressure of 5,000 psia. At high pressure—above about 2,500 psia—the slope of this graph is unity, i.e.,

$$\frac{d\psi(p)}{dp} = 1 \quad (3-46)$$

indicating that in these conditions the effects of gas expansion and viscosity change are, in fact, negligible; this is the basis of what is known as the *p approach* in gas well analysis, i.e., treat the gas phase as a liquid.

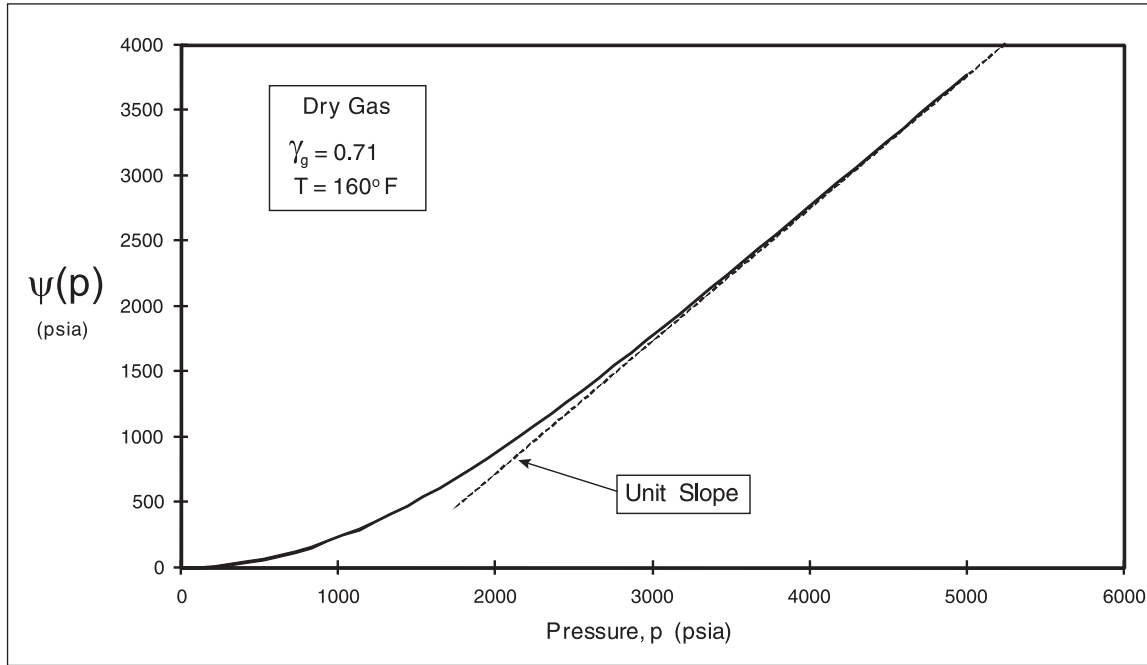


Fig. 3-13. Normalized pseudo-pressure function

In the preceding treatment, it is assumed that the gas density  $\rho$  is computed from an equation of state given the composition of the mixture or the gas gravity; calculations based on gas gravity imply only small amounts of  $\text{CO}_2$  and  $\text{N}_2$  present in the system. For a dry gas reservoir, the PVT information may be presented simply as graphs of the gas formation volume factor  $B_g$  and the gas viscosity  $\mu_g$  as a function of pressure at reservoir temperature; the units of  $B_g$  are simply volume of gas at standard conditions per unit volume at reservoir conditions, i.e.,

$$B_g = \frac{P_{sc}}{p} \frac{z}{z_{sc}} \frac{T}{T_{sc}} = \frac{\rho_{sc}}{\rho} \quad (3-47)$$

In terms of formation volume factor, the normalized dry gas pseudopressure is given by

$$\psi(p) = B_{gi} \mu_i \int_{p_b}^p \frac{1}{B_g \mu} dp \quad (3-48)$$

For a given reservoir pressure  $p_e$  and corresponding pseudopressure  $\psi(p_e)$ , the well pseudopressure is computed as

$$\psi(p_w) = \psi(p_e) - \Delta\psi = \psi(p_e) - \frac{q\mu_i}{2\pi kh} \ln \frac{r_e}{r_w} \quad (3-49)$$

and the pressure  $p_w$  corresponding to the computed  $\psi(p_w)$  is obtained by using the transform in reverse which may be written formally as

$$p_w = \psi^{-1}(\psi_w) \quad (3-50)$$

This process is illustrated in figure 3–14. The pseudopressure function is a convenient method of handling the nonlinearity introduced into the problem by gas expansion and pressure-dependent viscosity. In transient gas well test analysis, it has been the practice to use a pseudopressure  $m(p)$ , defined as

$$m(p) = 2 \int_{p_b}^p \frac{p dp}{\mu z} \tag{3-51}$$

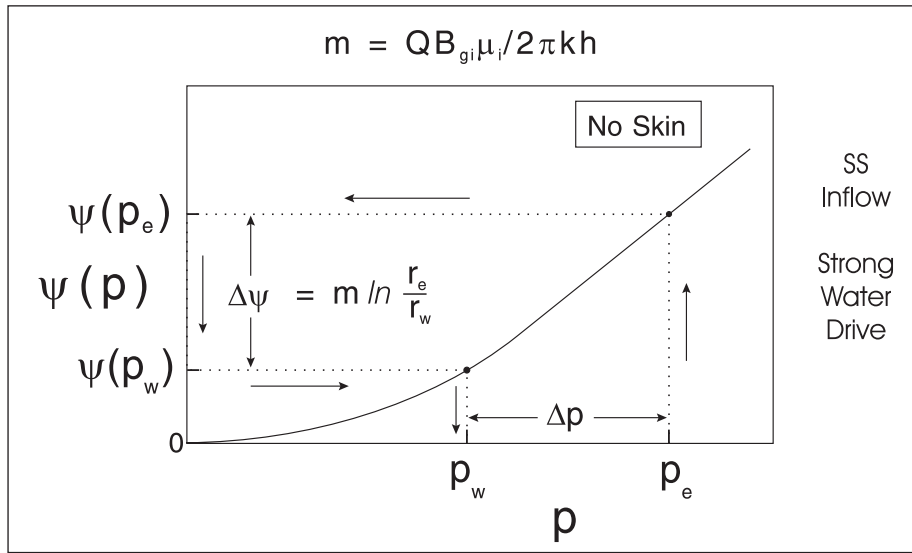


Fig. 3–14. Gas well drawdown form normalized pseudopressure function

This will be termed here the *conventional pseudopressure*, which was introduced by Al-Hussainy *et al.*<sup>3</sup> in 1966. The two alternative forms of real gas pseudopressure differ only by a constant factor and it is straightforward to switch from one to the other using the relation

$$\psi(p) = \frac{\mu_i z_i}{2p_i} m(p) \tag{3-52}$$

The advantage of the normalized form is that the gas equations preserve similarity to the oil equations and in transient well test analysis the plots involve a quantity  $\psi(p)$  whose units are in fact pressure.

The integrand of the pseudopressure function  $m(p)$  is  $\frac{2p}{\mu z}$  or of the normalized form  $\psi(p)$ , it is  $\frac{\mu_i \rho}{\rho_i \mu}$ . At low pressures, up to about 1,500 psia, the integrand is a linear function of pressure as illustrated in figure 3–11; this is the ideal gas region where the  $\mu z$  product is essentially constant. In this situation, the real gas pseudopressure difference, i.e.,  $m(p_e) - m(p_w)$ , has the simple form

$$m(p_e) - m(p_w) = 2 \int_{p_w}^{p_e} \frac{p dp}{\bar{\mu}z} = \frac{p_e^2 - p_w^2}{\bar{\mu}z} \quad (3-53)$$

Here the bar above the  $\mu z$  product indicates that this quantity has been treated as a constant; note, however, that  $\mu_i z_i$  is not a suitable value for  $\bar{\mu}z$  and that Eq. (3-53) is valid only provided  $p_e$  is less than, say, 1,500 psia. This, of course, is the basis of the “pressure squared approach” for analyzing gas wells, but in the modern context, based on computer application, the use of pseudopressure is correct under all conditions and there is really no need to use the pressure squared form. Again, referring to figure 3-11, it is apparent that at high pressure, i.e., above about 3,000 psia, the integrand is nearly constant, or decreasing slightly, and the  $m(p) - p$  relation is a straight line; in this situation, the “gas” phase in the reservoir is behaving like a liquid or “dense” phase. The pressure level at which dense phase behavior begins is dependent on the reservoir temperature (high reservoir temperature results in a higher pressure threshold for the beginning of the straight line section of the pseudopressure function).

The pseudopressure has been derived on the basis of pure SS radial flow but the formulation can simply be extended to cover Darcy total skin and SSS influx from an arbitrary drainage area by writing Eq. (3-42) in the form

$$\Delta\psi = \psi(\bar{p}) - \psi(p_w) = \frac{m_g \mu_i}{2\pi k h \rho_i} \left( \ln \frac{r_e}{r_w} - \frac{3}{4} + S_a \right) \quad (3-54a)$$

or

$$\Delta\psi = \psi(\bar{p}) - \psi(p_w) = \frac{m_g \mu_i}{2\pi k h \rho_i} \left( \frac{1}{2} \ln \frac{4\bar{A}}{\gamma C_A r_w^2} + S_a \right) \quad (3-54b)$$

and all the concepts relating to  $S_a$  in the previous chapter are immediately applicable to gas well deliverability prediction. The average pressure,  $\bar{p}$ , of the closed reservoir compartment of drainage area,  $\bar{A}$ , is controlled by gas reservoir material balance and Eq. (3-54a and b) represents a “snapshot” at a given point in time. In the case of a cylindrical altered zone of radius  $r_a$  and permeability  $k_a$ , the actual pseudopressure drop in the skin zone, from Eq. (3-42), is given by

$$\left( \psi(p_a) - \psi(p_{wf}) \right)_{\text{actual}} = \frac{m_g \mu_i}{2\pi k_a h \rho_i} \ln \frac{r_a}{r_w} \quad (3-55)$$

whereas the pseudopressure drop which would occur over this region if the permeability were unaltered is

$$\left( \psi(p_a) - \psi(p_{wf}) \right)_{\text{unaltered}} = \frac{m_g \mu_i}{2\pi k h \rho_i} \ln \frac{r_a}{r_w} \quad (3-56)$$

Thus, defining an incremental skin pseudopressure drop as

$$\Delta\psi_s = \left( \psi(p_a) - \psi(p_{wf}) \right)_{\text{actual}} - \left( \psi(p_a) - \psi(p_{wf}) \right)_{\text{unaltered}}$$

then from Eqs. (3–55) and (3–56),  $\Delta\psi_s$  is given by

$$\Delta\psi_s = \frac{m_g \mu_i}{2\pi k h \rho_i} \left( \left( \frac{k}{k_a} - 1 \right) \ln \frac{r_a}{r_w} \right)$$

i.e.,

$$S = \frac{\Delta\psi_s}{\frac{m_g \mu_i}{2\pi k h \rho_i}} = \left( \left( \frac{k}{k_a} - 1 \right) \ln \frac{r_a}{r_w} \right) \quad (3-57)$$

This is simply a rederivation of the Hawkins equation in terms of pseudopressure, which serves to demonstrate the theoretical basis for Eq. (3–54a and b); in gas wells with a high skin factor and a low bottom-hole flowing pressure, the pseudopressure formulation allows for the expansion and change in viscosity of the gas as it flows through the altered region. According to Eq. (3–57), the dimensionless pseudopressure drop over the skin zone is determined by the alteration parameters  $k/k_a$  and  $r_a/r_w$  and is a constant. However, the actual skin pressure drop  $\Delta p_s$  depends on where the pseudopressure function is entered to evaluate  $\psi^{-1}(p_{wf})$ , as illustrated in figure 3–15; if the bottom-hole flowing pressure is low and the initial flat region of the pseudopressure curve is entered, then the skin pressure drop for fixed  $S$  can become very large. High skin factors in tight gas reservoirs can therefore be extremely detrimental to deliverability, and, conversely, the effect of stimulation, i.e., negative skin, can be much stronger than in oil wells. The pseudopressure method allows proper handling of skin effect in gas reservoirs and all modeling of gas well IPR should be made on this basis.

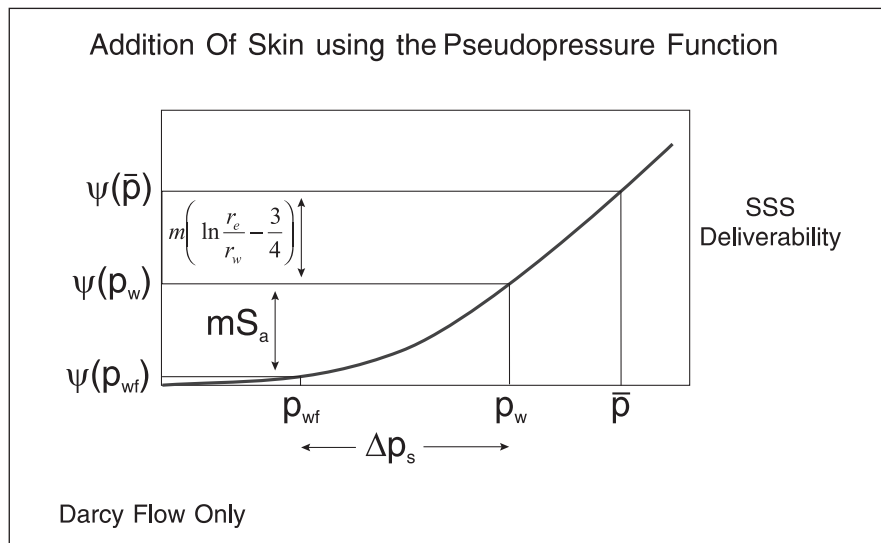


Fig. 3–15. Effect of bottom-hole pressure on the actual skin pressure drop

In terms of standard volumetric rate, Eq. (3-54a and b) becomes

$$\Delta\psi = \psi(\bar{p}) - \psi(p_w) = \frac{QB_{gi}\mu_i}{2\pi kh} \left( \frac{1}{2} \ln \frac{4\bar{A}}{\gamma C_A r_w^2} + S_a \right) \quad (3-58a)$$

or in gas field units, i.e.,

$$Q : \text{MSCF/D} \quad k : \text{md}$$

$$h : \text{ft} \quad \mu_i : \text{cp}$$

$$\psi : \text{psia} \quad r_w : \text{ft}$$

$$\Delta\psi = \psi(\bar{p}) - \psi(p_w) = \frac{1.5802 \times 10^5 QB_{gi}\mu_i}{2\pi kh} \left( \frac{1}{2} \ln \frac{4\bar{A}}{\gamma C_A r_w^2} + S_a \right) \quad (3-58b)$$

On replacing  $B_{gi}$  by the expression

$$B_{gi} = \frac{p_{sc} z_i T}{p_i z_{sc} T_{sc}} = \frac{14.696 z_i T}{520 p_i}$$

this may be written as

$$\Delta\psi = \psi(\bar{p}) - \psi(p_w) = \frac{4465.9 Q z_i T \mu_i}{2\pi k h p_i} \left( \frac{1}{2} \ln \frac{4\bar{A}}{\gamma C_A r_w^2} + S_a \right) \quad (3-59)$$

Thus the PI of a gas well in Darcy flow and at high pressure may be defined as

$$Q = J_g (\bar{p} - p_{wf}) \quad (3-60)$$

$$\text{where } J_g = \frac{2\pi k h p_i}{4465.9 z_i T \mu_i \left( \frac{1}{2} \ln \frac{4\bar{A}}{\gamma C_A r_w^2} + S_a \right)} = \frac{2\pi k h}{1.5802 \times 10^5 B_{gi} \mu_i \left( \frac{1}{2} \ln \frac{4\bar{A}}{\gamma C_A r_w^2} + S_a \right)}$$

Here  $J_g$  has units of MSCF/D/psi with  $B_{gi}$  in  $\text{ft}^3/\text{SCF}$ . The inflow performance relation of a gas well is simply a plot of gas well flow rate (in MSCF/D) versus bottom-hole flowing pressure (in psia), as shown in figure 3-16. The results of the process illustrated in figure 3-15, i.e., the bottomhole flowing pressure for a range of flow-rate values for a specified reservoir pressure, are presented on such a plot and the slope of the straight line section of the gas well IPR at high pressure is  $-1/J_g$ . Note that the IPR curve (in the absence of non-Darcy flow) is simply a linear translation of the pseudopressure function.

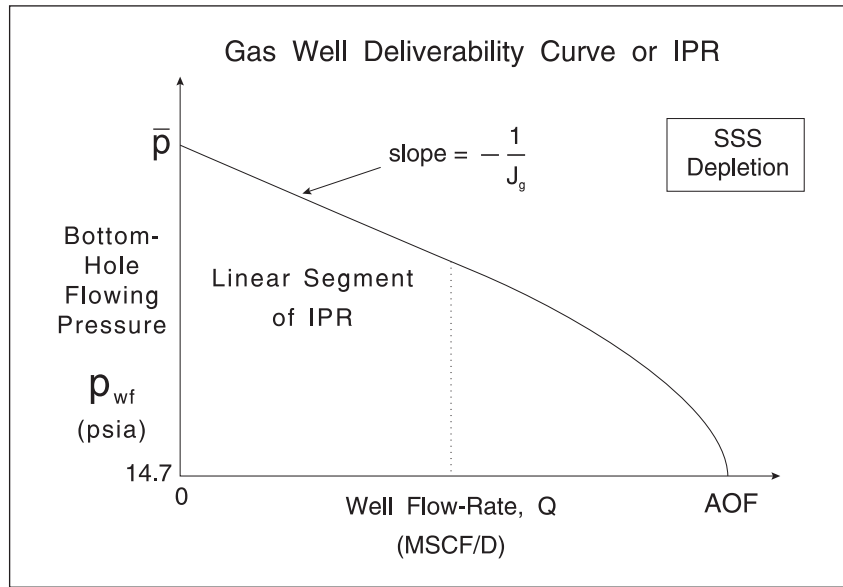


Fig. 3-16. Gas well inflow performance relation (IPR)

In terms of mass flow rate  $m_g$  in lb/day, this becomes

$$\Delta\psi = \psi(\bar{p}) - \psi(p_{wf}) = \frac{158.02m_g\mu_i}{2\pi kh\rho_i} \left( \frac{1}{2} \ln \frac{4\bar{A}}{\gamma C_A r_w^2} + S_a \right) \quad (3-61)$$

This latter equation can be written in the form

$$\Delta\psi = \psi(\bar{p}) - \psi(p_{wf}) = \frac{1}{J_m} m_g \quad (3-62)$$

where

$$J_m = \frac{2\pi kh\rho_i}{158.02\mu_i \left( \frac{1}{2} \ln \frac{4\bar{A}}{\gamma C_A r_w^2} + S_a \right)} \quad \text{lb/day/psi}$$

Here,  $J_m$  is the PI of a gas well on a mass basis and referred to pseudopressure.

Equation (3-59) in terms of normalized pseudopressure and volumetric flow rate at standard conditions is the preferred form of the gas well deliverability equation (after the addition of Non-Darcy skin treated in the next section). However, it is also possible to define an inflow equation in terms of  $m(p)$ , which is still widely used especially in pressure transient analysis. The relation between  $m(p)$  and  $\psi(p)$  is

$$m(p) = \frac{2p_i}{\mu_i Z_i} \psi(p) \quad (3-63)$$

and Eq. (3.61) may be written in the alternative form

$$\Delta m = m(\bar{p}) - m(p_w) = \frac{1421.5QT}{kh} \left( \frac{1}{2} \ln \frac{4\bar{A}}{\gamma C_A r_w^2} + S_a \right) \quad (3-64)$$

which is the version appearing in most references.

## Treatment of non-Darcy flow

In the previous chapter, an analysis of non-Darcy flow for perforated oil wells was carried out; however, it is rare for the non-Darcy effect to be significant in an oil well unless very few perforations are active. The phenomenon of rate-dependent skin is mainly associated with gas wells, and in this section the results already derived for oil will be extended to cover the compressible flow case. Again, commencing with pure radial flow to a vertical well, the flow equation based on the Forcheimer model is

$$\frac{dp}{dr} = \frac{\mu}{k} u_r + \beta \rho u_r^2 = \frac{\mu}{k} \frac{m_g}{\rho 2\pi r h} + \beta \rho \left( \frac{m_g}{\rho 2\pi r h} \right)^2 \quad (3-65)$$

Here,  $\beta$  is a rock property known as the *inertial resistance coefficient* which has units of  $L^{-1}$ . Inertial resistance in a porous medium occurs when the Reynolds number based on a pore dimension becomes greater than approximately unity and the inertial terms in the Navier–Stokes equation become important. In a fluid mechanical sense, Darcy flow is classified as a creeping flow, whereas non-Darcy flow, while still laminar in the sense that turbulence certainly does not exist, is non-creeping flow. The inertial resistance is dominated by the tortuosity of the porous medium and it is changes in flow direction, rather than expansion and contraction of the pores, that lead to significant inertial resistance. The parameter  $\beta$  can be measured on rock samples as part of a special core analysis exercise. In the unsteady-state core analysis experiments carried out in modern laboratories, both the parameters  $k$  and  $\beta$  are found by nonlinear regression; however, care must be taken that the velocities in the core have been high enough to allow a satisfactory determination of  $\beta$ . The physics of non-Darcy flow has been investigated in depth by Sketne<sup>4</sup> in an outstanding piece of research. In a porous medium with changing cross-section, as illustrated in figure 3–17, and when the Reynolds number based on pore dimension exceeds unity, there is an appreciable inertial component in the solution of the Navier–Stokes equation for laminar flow. This is the origin of inertial resistance characterized by the coefficient  $\beta$ .

In principle, the nonlinear Eq. (3–65), in which both  $\mu$  and  $\rho$  are dependent on pressure, can be integrated only numerically; however, recognizing that non-Darcy effect is concentrated near the outlet face, an almost exact integration is possible. Multiplying through by  $\rho/\mu$  gives

$$\frac{\rho}{\mu} \frac{dp}{dr} = \frac{m_g}{2\pi k h} \frac{1}{r} + \frac{\beta m_g^2}{\mu (2\pi h)^2} \frac{1}{r^2} \quad (3-66)$$



which may be integrated analytically by assuming that the viscosity in the non-Darcy term can be taken as constant; thus

$$\int_{p_w}^{p_e} \frac{\rho}{\mu} dp = \frac{m_g}{2\pi kh} \int_{r_w}^{r_e} \frac{dr}{r} + \frac{\beta m_g^2}{\mu (2\pi h)^2} \int_{r_w}^{r_e} \frac{dr}{r^2}$$

i.e.,

$$\frac{\mu_i}{\rho_i} \int_{p_w}^{p_e} \frac{\rho}{\mu} dp = \frac{m_g \mu_i}{2\pi kh \rho_i} \ln \frac{r_e}{r_w} + \frac{\mu_i \beta m_g^2}{\bar{\mu} \rho_i (2\pi h)^2} \left( \frac{1}{r_w} - \frac{1}{r_e} \right)$$

or

$$\psi(p_e) - \psi(p_w) = \frac{m_g \mu_i}{2\pi kh \rho_i} \ln \frac{r_e}{r_w} + \frac{\mu_i \beta m_g^2}{\bar{\mu} \rho_i (2\pi h)^2} \left( \frac{1}{r_w} - \frac{1}{r_e} \right) \quad (3-67a)$$

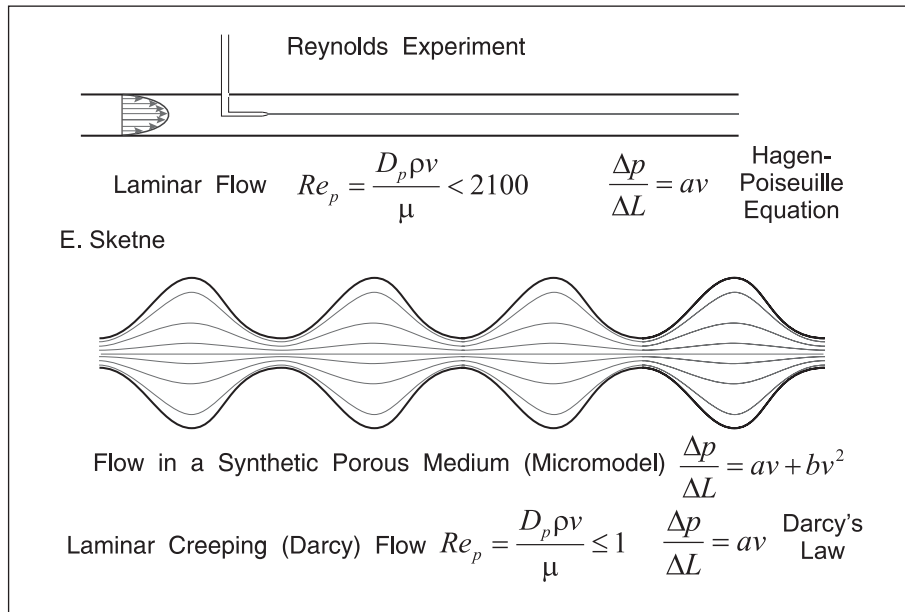


Fig. 3-17. Laminar inertial flow in a synthetic porous medium

Thus the pseudopressure concept can be used when non-Darcy flow occurs, but the formulation is not exact and the viscosity  $\bar{\mu}$  in the inertial term must be evaluated at some pressure. Comparison of exact integrations of (3-65) using a Runge-Kutta method and the results of (3-67a and b) show that if  $\bar{\mu}$  is evaluated at the average pressure, i.e.,  $(p_w + p_e)/2$ , then very little error occurs. Equation (3-67a, b, and c) is, of course, the classical radial flow integration of the Forcheimer equation applicable only to open-hole conditions; usually,  $r_e \gg r_w$  and (3-67a) reduces to

$$\Delta\psi = \psi(p_e) - \psi(p_w) = \frac{m_g \mu_i}{2\pi kh \rho_i} \ln \frac{r_e}{r_w} + \frac{\mu_i \beta m_g^2}{\bar{\mu} \rho_i (2\pi h)^2 r_w} \quad (3-67b)$$

In principle, the determination of the bottomhole pressure  $p_w$  for a given reservoir pressure  $p_e$  and well flow rate requires some iteration since  $\bar{\mu} = \mu((p_w + p_e)/2)$  is initially unknown. Unless the drawdown is large, i.e., a low permeability reservoir, then it will be quite adequate to assume  $\mu_i \approx \bar{\mu}$ , giving the direct equation

$$\Delta\psi = \psi(p_e) - \psi(p_w) = \frac{m_g \mu_i}{2\pi k h \rho_i} \ln \frac{r_e}{r_w} + \frac{\beta m_g^2}{\rho_i (2\pi h)^2 r_w} \quad (3-67c)$$

Note that if the permeability is low, it will be unlikely that non-Darcy effects will be important anyway. This equation may be put in the more convenient form

$$\frac{\psi(p_e) - \psi(p_w)}{\frac{m_g \mu_i}{2\pi k h \rho_i}} = \ln \frac{r_e}{r_w} + D_m m_g \quad (3-68)$$

where

$$D_m = \frac{\beta k}{2\pi h r_w \mu_i}$$

The product  $D_m m_g$  is the rate-dependent component of the skin in the case of open-hole conditions. In nearly all applications of this type of equation, the inertial resistance coefficient  $\beta$  will be related to permeability through an empirical correlation of the form (in field units)

$$\beta = \frac{2.6 \times 10^{10}}{k^{1.2}} \quad (\beta : \text{ft}^{-1}, k : \text{md}) \quad (3-69)$$

i.e.,  $\beta k$  is approximately constant, and the product  $D_m m_g$  depends mainly on the well flow rate per unit height  $m_g/h$ . Thus it is only in high-rate wells that non-Darcy flow need be considered where  $D_m m_g$  is comparable to  $\ln \frac{r_e}{r_w}$  which is typically of the order 7–8.

In terms of the volumetric rate at standard conditions, the open-hole inflow equation may be written as

$$\frac{\psi(p_e) - \psi(p_w)}{\frac{QB_{gi}\mu_i}{2\pi k h}} = \ln \frac{r_e}{r_w} + S + \frac{\beta k \rho_{sc}}{2\pi h r_w \mu_i} Q \quad (3-70)$$

where a conventional Darcy (mechanical) skin  $S$  has been added to the formulation. Suppose now that the well has a limited entry as shown in figure 3–18, where the completed height is  $h_p$ . The non-Darcy pseudopressure drop is concentrated in the region close to the completed sandface of height  $h_p$  and is given by

$$\Delta\psi_{ND} = \frac{\beta m_g^2}{\rho_i (2\pi h_p)^2 r_w} = \frac{\beta \rho_{sc} B_{gi}}{(2\pi h_p)^2 r_w} Q^2 \tag{3-71}$$

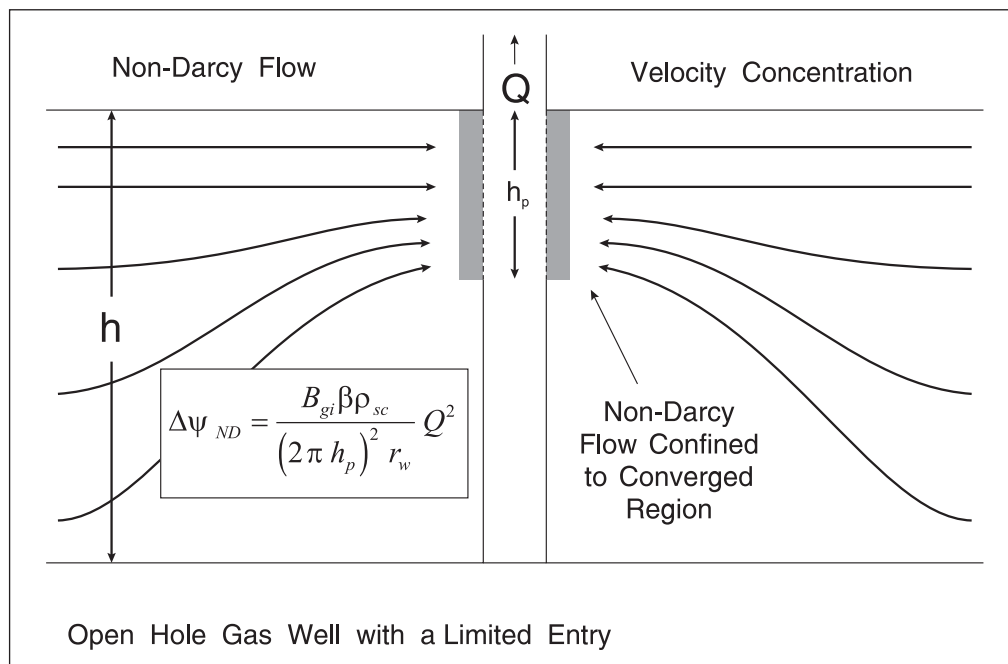


Fig. 3-18. Open-hole gas well with a limited entry

Referring to figure 3-18, it is assumed that Darcy flow alone occurs in the flow convergence region giving rise to a conventional, limited entry, incremental pressure drop; non-Darcy flow is present only after the flow convergence has occurred and the flow lines are again essentially straight.

In this case, the inflow equation now takes the form

$$\frac{\psi(p_e) - \psi(p_w)}{\frac{QB_{gi}\mu_i}{2\pi kh}} = \ln \frac{r_e}{r_w} + \frac{S_{tr}}{b} + S_p + \frac{\beta k \rho_{sc}}{2\pi h b^2 r_w \mu_i} Q \tag{3-72}$$

where  $b = \frac{h_p}{h}$  is the completion ratio and  $S_p$  is the familiar Brons and Marting geometric skin due to limited entry. For an open-hole completion, the true or intrinsic skin  $S_{tr}$  is given by the Hawkins equation:

$$S_{tr} = \left( \frac{k}{k_s} - 1 \right) \ln \frac{r_s}{r_w} \tag{3-73}$$

Equation (3-72) may be written in the form

$$\frac{\psi(p_e) - \psi(p_w)}{\frac{QB_{gi}\mu_i}{2\pi kh}} = \ln \frac{r_e}{r_w} + S_a + D_a Q \quad (3-74)$$

where  $S_a = \frac{S_{tr}}{b} + S_p$  is the apparent (total) Darcy skin and  $D_a = \frac{\beta k \rho_{sc}}{2\pi h b^2 r_w \mu_i}$  is the rate-dependent coefficient. This analysis shows that the apparent rate-dependent skin coefficient  $D_a$  is proportional to  $1/b^2$  and limited entry causing flow concentration can lead to serious downgrading of the deliverability of a gas well. Another situation that leads to an augmented non-Darcy pressure drop is illustrated in figure 3-19, where a high-permeability lens straddles the wellbore; this phenomenon has been given the name “geoskin” and gives rise to a negative mechanical skin in wells which have not been stimulated by acidizing or fracturing. It is principally in fluvial depositional environment where the effect has been seen in field examples. The high-permeability lens causes flow concentration and this will result in a large non-Darcy pressure drop. The paradoxical situation arises where the mechanical skin is negative, but this is counteracted by a large rate-dependent skin. It was a source of concern to the author that the interpretation of some gas well tests gave a large  $D$  and a negative  $S$ ; however, figure 3-19 shows how such a situation is, in fact, quite easily explained.

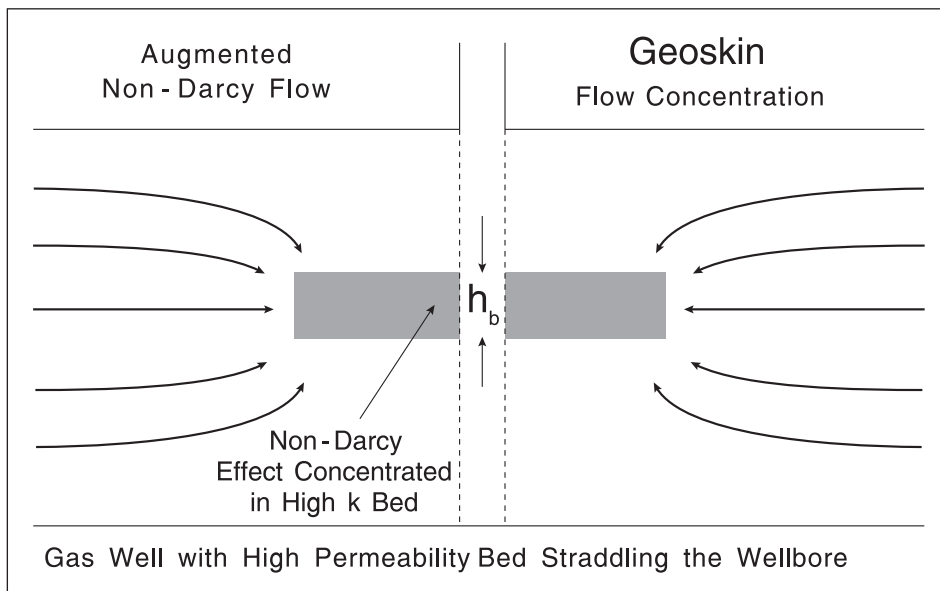


Fig. 3-19. Augmentation of non-Darcy flow by a high-permeability lens straddling the wellbore

Supposing the two components of the skin  $S_a$  and  $D_a$ , the  $kh$  product, and the average reservoir pressure  $\bar{p}$ , have been determined in a well test, the SSS deliverability curve (IPR) can be synthesized as illustrated in figure 3-20. The loop is traversed for a range of values of the flow rate up to the absolute open-hole flow (AOF) corresponding to a bottom-hole flowing pressure equal to  $p_{sc}$ , and the computed IPR plotted as shown in figure 3-21.

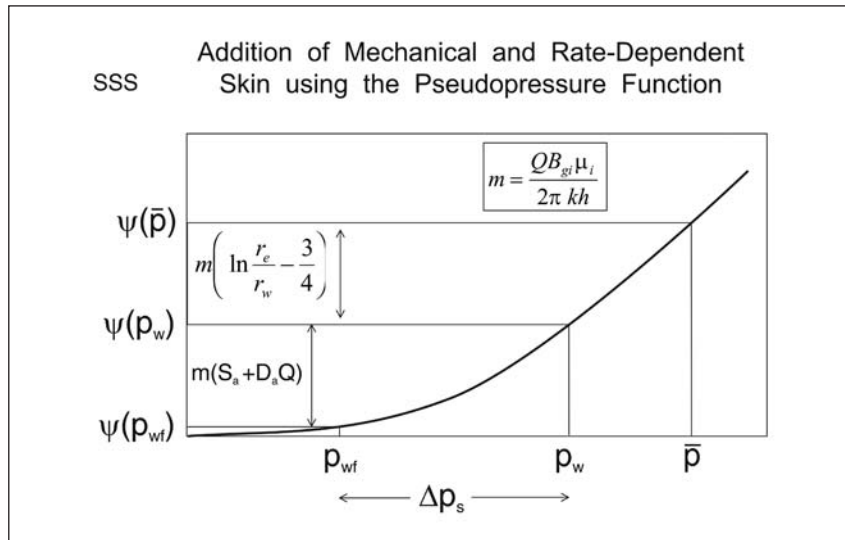


Fig. 3–20. Synthesis of gas well SSS deliverability curve (IPR) including rate-dependent skin

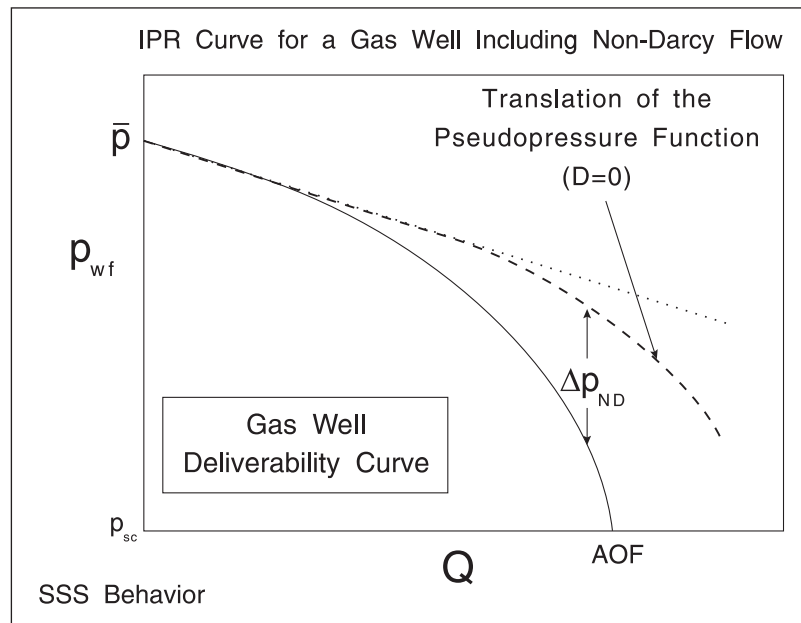


Fig. 3–21. Gas well deliverability curve showing non-Darcy pressure drop

Turning now to the more realistic case of a perforated completion and adopting the approximate model based on local spherical flow convergence into individual perforations, the spherical coordinates version of the SS Forcheimer equation is:

$$\frac{dp}{dr} = \frac{\mu}{k_s} u_r + \beta \rho u_r^2 = \frac{\mu}{k_s} \frac{m_g}{\rho 4\pi r^2} + \beta \rho \left( \frac{m_g}{\rho 4\pi r^2} \right)^2 \quad (3-75)$$

which, on integration between the limits of the inner or source radius  $r_s$  at pressure  $p_s$  and the external or outer radius  $r_o$  at pressure  $p_o$  (where  $r$  is now spherical radius) and applying the same simplification with regard to  $\bar{\mu}$  as in the radial flow case, becomes

$$\psi(p_o) - \psi(p_s) = \frac{m_g \mu_i}{4\pi \rho_i k_s} \left( \frac{1}{r_s} - \frac{1}{r_o} \right) + \frac{\mu_i}{\bar{\mu}} \frac{\beta m_g^2}{3(4\pi)^2 \rho_i} \left( \frac{1}{r_s^3} - \frac{1}{r_o^3} \right) \quad (3-76)$$

or

$$\Delta\psi = \psi(p_o) - \psi(p_s) = \frac{m_g \mu_i}{4\pi \rho_i k_s r_s} + \frac{\mu_i}{\bar{\mu}} \frac{\beta m_g^2}{3(4\pi)^2 \rho_i r_s^3} \quad r_o \gg r_s \quad (3-77)$$

In the approximate model of a perforated completion, the flow shape factors are introduced while  $m_g$  in the above equation becomes identified with  $m_{gp} = m_g/N_p$ ,  $p_o$  becomes  $p_t$  and  $p_s$  is replaced by  $p_w$ ; thus

$$\Delta\psi = \psi(p_t) - \psi(p_w) = f_D^s \frac{m_g \mu_i}{4\pi \rho_i k r_s \sqrt[3]{AN_p}} + f_{ND}^s \frac{\mu_i}{\bar{\mu}} \frac{\beta m_g^2}{3(4\pi)^2 \rho_i r_s^3 N_p^2} \quad (3-78a)$$

where  $r_s = \sqrt{r_p I_p}$  and  $A = k/k_v$ ; the viscosity  $\bar{\mu}$  is again evaluated at the average pressure  $(p_t + p_w)/2$ . In gas field units, with  $m_g$  in lb/day, this becomes

$$\Delta\psi = \psi(p_t) - \psi(p_w) = f_D^s \frac{158.02 \times m_g \mu_i}{4\pi \rho_i k r_s \sqrt[3]{AN_p}} + f_{ND}^s \frac{\mu_i}{\bar{\mu}} \frac{2.89137 \times 10^{-14} \beta m_g^2}{3(4\pi)^2 \rho_i r_s^3 N_p^2} \quad (3-78b)$$

Equation (3-78a and b) predicts the pseudopressure drop due to spherical-like flow convergence into the individual perforations. On a dimensionless basis, (3-78a and b) becomes

$$\frac{\psi(p_t) - \psi(p_w)}{\frac{m_g \mu_i}{2\pi k h \rho_i}} = f_D^s \frac{h}{2N_p r_s \sqrt[3]{A}} + f_{ND}^s \frac{\beta k h}{24 \rho_i \bar{\mu} r_s^3 N_p^2} m_g \quad (3-79a)$$

or in gas field units

$$\frac{\psi(p_t) - \psi(p_w)}{\frac{158.02 m_g \mu_i}{2\pi k h \rho_i}} = f_D^s \frac{h}{2N_p r_s \sqrt[3]{A}} + f_{ND}^s \frac{1.82974 \times 10^{-16} \beta k h}{24 \rho_i \bar{\mu} r_s^3 N_p^2} m_g \quad (3-79b)$$

which in terms of standard volumetric rate  $Q$  may be written as

$$\frac{\psi(p_t) - \psi(p_w)}{\frac{QB_{gi}\mu_i}{2\pi kh}} = f_D^s \frac{h}{2N_p r_s^3 \sqrt{A}} + f_{ND}^s \frac{\beta kh \rho_{sc}}{24\pi \bar{\mu} r_s^3 N_p^2} Q \quad (3-80a)$$

or again in gas field units

$$\frac{\psi(p_t) - \psi(p_w)}{\frac{1.5802 \times 10^5 QB_{gi}\mu_i}{2\pi kh}} = f_D^s \frac{h}{2N_p r_s^3 \sqrt{A}} + f_{ND}^s \frac{1.3972 \times 10^{-14} \beta kh \gamma}{24\pi \bar{\mu} r_s^3 N_p^2} Q \quad (3-80b)$$

where  $\gamma$  is the gas gravity relative to air. Expression (3–80a and b) gives the dimensionless pseudopressure drop due to localized perforation flow convergence.

## Steady-state gas well inflow performance

Following the development of the incompressible flow case, the approximate model for gas well inflow may now be formulated on a dimensionless basis. Again, radial flow up to  $r_w + l_p$  is assumed and an altered region can be incorporated as before, giving

$$\frac{\psi(\bar{p}) - \psi(p_w)}{\frac{m_g \mu_i}{2\pi kh \rho_i}} = \frac{1}{2} \ln \frac{4\bar{A}}{\gamma C_A r_w^2} + S'_a \quad (3-81)$$

where

$$S'_a = S_{psw} + \frac{S_c}{b} + \frac{\hat{D}_c}{b^2} m_g + \frac{S_{gp}}{b} + \frac{\hat{D}_{gp}}{b^2} m_g$$

In this formulation, the total skin  $S'_a$  includes both Darcy and non-Darcy effects and it is common to write this as

$$S'_a = S_a + \hat{D}_a m_g \quad (3-82)$$

where

$$S_a = S_{psw} + \frac{S_c}{b} + \frac{S_{gp}}{b} \quad (3-83)$$

and

$$\hat{D}_a = \frac{\hat{D}_c + \hat{D}_{gp}}{b^2} \quad (3-84)$$

In terms of volumetric flow rate at standard conditions, the corresponding inflow model is

$$\frac{\psi(\bar{p}) - \psi(p_w)}{\frac{QB_{gi}\mu_i}{2\pi kh}} = \frac{1}{2} \ln \frac{4\bar{A}}{\gamma C_A r_w^2} + S'_a \quad (3-85)$$

where

$$S'_a = S_a + D_a Q = S_{psw} + \frac{S_c}{b} + \frac{D_c}{b^2} Q + \frac{S_{gp}}{b} + \frac{D_{gp}}{b^2} Q \quad (3-86)$$

with

$$D_c = f_{ND}^s \frac{\beta k \rho_{sc}}{24\pi \bar{\mu} r_s^3 n_s^2 h} \quad D_{gp} = \frac{2\pi f_{gp} l_{gp} k \beta_p \rho_{sc}}{\bar{\mu} n_s^2 h A_p^2}$$

or in gas field units

$$D_c = f_{ND}^s \frac{1.3972 \times 10^{-14} \beta k \gamma}{24\pi \bar{\mu} r_s^3 n_s^2 h} \quad \text{and} \quad D_{gp} = \frac{1.3972 \times 10^{-14} 2\pi f_{gp} l_{gp} k \beta_p \rho_{sc}}{\bar{\mu} n_s^2 h A_p^2}$$

The objective of step-rate gas well transient testing is to determine the  $kh$  product of the well and the two components of the skin  $S_a$  and  $D_a$ . Knowledge of the size and shape of the well's drainage area allow  $\bar{A}$  and  $C_A$  to be calculated.

## $p^2$ form of the normalized pseudopressure function

The definition of the normalized pseudopressure  $\psi(p)$  given in Eq. (3-41) allows for the variation of gas viscosity  $\mu$  and compressibility factor  $z$  with pressure. However, if these two quantities are presumed constant at the values corresponding to the reference pressure  $p_i$ , then the normalized pseudopressure assumes the simple form

$$\psi(p) = \frac{p^2}{2p_i} \quad (3-87)$$

and the dimensionless normalized pseudopressure drop may be written as

$$\psi_D = \frac{\psi(\bar{p}) - \psi(p_w)}{\frac{QB_{gi}\mu_i}{2\pi kh}} = \frac{\bar{p}^2 - p_w^2}{2p_i QB_{gi}\mu_i} = \frac{\bar{p}^2 - p_w^2}{\frac{Qp_{sc} z_i T \mu_i}{\pi T_{sc} kh}} \quad (3-88)$$



Figure 3–22 shows the variation of  $\mu z$  with pressure for a gas of gravity  $\gamma = 0.65$  at a reservoir temperature of  $T = 200^\circ\text{F}$ . In the range 14.7–1,500 psia, the  $\mu z$  product lies in the range 0.0125–0.0134 and at the mid-point (reference) pressure of 750 psia the  $\mu z$  value of 0.0128 gives a maximum error of 5%. Thus the pressure squared approach is certainly reasonable at reservoir pressures less than about 1,500 psia; however, if a slightly larger error bar is accepted, the  $p_2$  method can be used up to, say, 2,000 psia, as suggested by some authors, with the reference pressure  $p_i$  chosen as 1,000 psia. In gas field units, the SSS inflow equation then assumes the familiar form

$$\psi_D = \frac{\bar{p}^2 - \bar{p}_w^2}{\frac{1421.5Qz_i T \mu_i}{kh}} = \frac{1}{2} \ln \frac{4\bar{A}}{\gamma C_A r_w^2} + S'_a \tag{3-89}$$

which may be written as

$$\bar{p}^2 - p_w^2 = EQ + FQ^2 \tag{3-90}$$

where

$$E = \frac{1421.5z_i T \mu_i}{kh} \left( \frac{1}{2} \ln \frac{4\bar{A}}{\gamma C_A r_w^2} \right) + S'_a \tag{3-91}$$

and

$$F = \frac{1421.5z_i T \mu_i D_a}{kh} \tag{3-92}$$

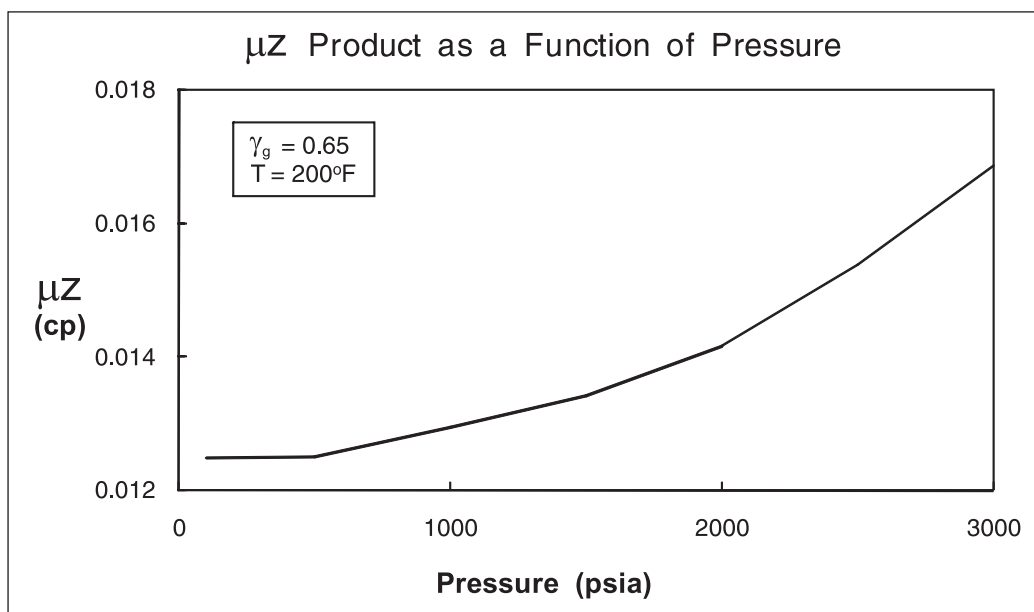


Fig. 3–22. Variation of  $\mu z$  product with pressure for a dry gas

In this formulation, the quantity  $p_i$  ceases to be identified with the original initial reservoir pressure and simply becomes a reference pressure for the evaluation of the  $\mu_i$  and  $z_i$  values. The value of  $p_i$  in this case must lie in the region where  $\mu$  and  $z$  are, indeed, constant (less than 1,500 psia, say) and the average of  $\bar{p}$  and  $p_{sc}$  is suggested since the deliverability curve will be used over this range of pressures. Equation (3-90) is the simplified form of the gas well deliverability equation which is presented as a plot of bottom-hole flowing pressure  $p_w$  versus gas standard volumetric rate  $Q$  for a specified reservoir pressure  $\bar{p}$ . In this approximate version of the inflow relation, the quantity  $\bar{\mu}$  implicit in  $D_a$  will simply be taken as  $\mu_i$  since the model is based on constant viscosity. The AOF potential of a gas well is defined as the well rate for a bottom-hole flowing pressure of 14.7 psia, and solving Eq. (3-90) for  $Q$  at  $p_w = 14.7$  psia gives

$$\text{AOF} = \frac{-E + \sqrt{E^2 + 4F(\bar{p}^2 - 216)}}{2F} \quad (3-93)$$

Thus the gas well inflow performance relation is not a straight line, and the deliverability according to (3-90) is plotted as a curve on the well performance diagram as shown in figure 3-23; the intersection of the non-linear IPR with the gas VLP curve as usual gives the well operating point.

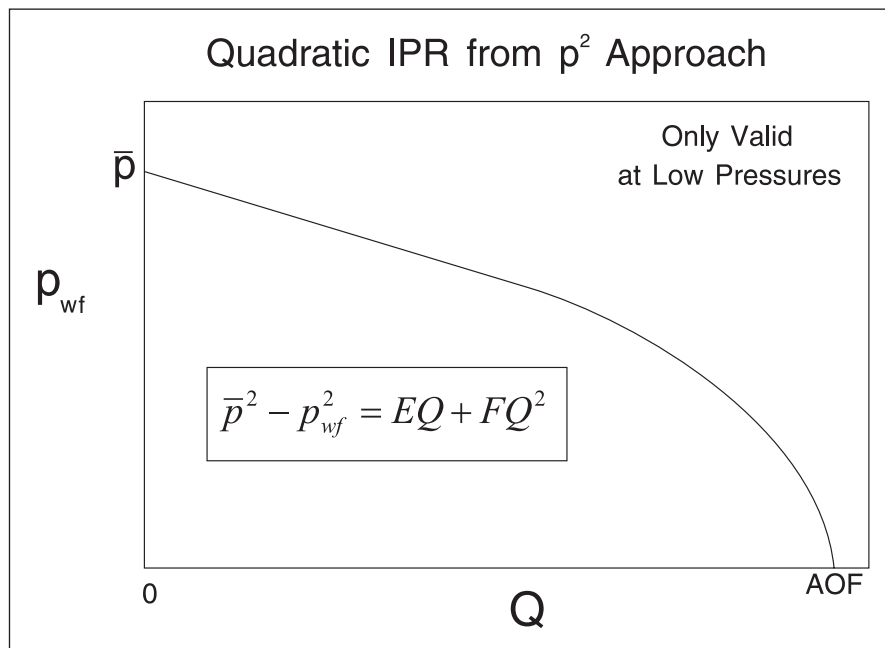


Fig. 3-23. Gas well deliverability on the well performance diagram

The  $p^2$  approach essentially assumes that the gas is ideal in behavior, i.e.,  $\rho_g \propto p$ , which is valid only at low pressures, and therefore this method is not recommended for the prediction of gas well deliverability. Inspection of pseudopressure functions show that at pressures in excess of about 3,000 psia the  $\psi(p)$  versus  $p$  relation is, in fact, linear and not quadratic as suggested by Eq. (3-87).

For an open-hole completion the non-Darcy coefficient in the equations above (in gas field units) is given by

$$D_a = \frac{1.3972 \times 10^{-14} \beta k \gamma}{2\pi h r_w \mu_i} \quad (3-94)$$

which results in

$$F = \frac{1.9861 \times 10^{-11} \beta \gamma z_i T}{2\pi h^2 r_w} \quad (3-95)$$

When a limited entry is present,  $h$  in Eq. (3-95) should be replaced by  $h_p$ . In the literature, this combination of the  $p^2$  approximation and the open-hole formula for the non-Darcy effect is known as the *Jones equation* for gas wells. Note that both the  $p^2$  method and the assumption of pure radial (open-hole) inflow are not recommended in the light of modern understanding of gas well behavior; the real gas pseudopressure and the relation of the inertial effect to perforation parameters is a much more scientifically based approach.

The coefficients  $E$  and  $F$  in the deliverability Eq. (3-90) can also be obtained directly by plotting data from a step-rate or isochronal test in the form  $\frac{\bar{P}^2 - P_w^2}{Q}$  versus  $Q$  to give  $F$  from

the slope and  $E$  from the intercept; this is known as *LIT analysis* and is fully covered in chapter 13 of *Well Test Design and Analysis*. For the present purpose, it is sufficient to appreciate that a direct entry of  $E$  and  $F$  values into Eq. (3-90) is often required.

## High-pressure gas well inflow

For bottom-hole pressures above about 2,500 psia, the pseudopressure function is essentially a straight line of the form

$$m(p) = ap + b \quad (3-96)$$

This is illustrated in figure 3-24, where  $m(p)$  for a gas of gravity 0.756 and a reservoir temperature of 197 °F is plotted and a straight line of slope  $a = 0.3804 \times 10^6$  has been fitted to the points at  $p > 2,500$  psia. The inflow expression in terms of  $m(p)$  and field units takes the form

$$\Delta m = m(\bar{p}) - m(p_w) = \frac{1421.5QT}{kh} \left( \frac{1}{2} \ln \frac{4\bar{A}}{\gamma C_A r_w^2} + S + DQ \right) \quad (3-97)$$

And, if the substitution  $\Delta m = a\Delta p$  from (3-96) is made, there follows

$$Q = \frac{akh}{1421.5T \left( \frac{1}{2} \ln \frac{4\bar{A}}{\gamma C_A r_w^2} + S + DQ \right)} (\bar{p} - p_w) \quad (3-98)$$

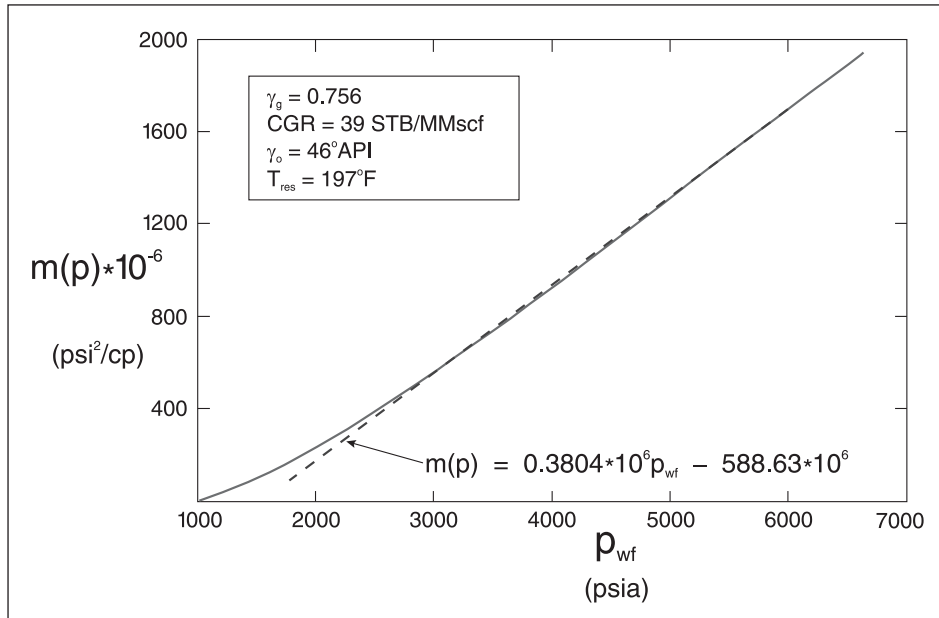


Fig. 3-24. Linear portion of the pseudopressure function at high pressure

This expression is of the form

$$Q = \frac{(\bar{p} - p_w)}{E + FQ} \quad (3-99)$$

where

$$E = \frac{1421.5T}{akh} \left( \frac{1}{2} \ln \frac{4\bar{A}}{\gamma C_A r_w^2} + S \right)$$

and

$$F = \frac{1421.5TD}{akh}$$

In the case where the inertial term  $D$  is negligible, the gas well inflow model takes the simple form

$$Q = J_{SSS,g} (\bar{p} - p_w) \quad (3-100)$$

where

$$J_{SSS,g} = \frac{1}{E} = \frac{akh}{1421.5T \left( \frac{1}{2} \ln \frac{4\bar{A}}{\gamma C_A r_w^2} + S \right)}$$

This gas well PI in terms of pressure is a very useful concept especially in high-permeability reservoirs where the drawdown is not large and the flowing bottom-hole pressure remains above 2,500 psia. The IPR is easily computed from (3-99) and plotted in the usual way; note that the IPR is quadratic because of the rate-dependent skin term. If the gas flow rate is expressed in MMscf/d (rather than the SPE recommended field unit of Mscf/d), the constant 1,421.5 should be replaced by  $1.4215 \times 10^6$ .

### Summary of gas well non-Darcy skin analysis

The theoretical analysis of the non-Darcy effect in a perforated gas well, including the contribution of a gravel pack, can be summarized as follows:

$$D_a = \frac{D_c + D_{gp}}{b^2} \quad (3-101)$$

where  $D_c$  = perforation non-Darcy skin coefficient

i.e.,

$$D_c = f_{ND}^s \frac{1.3972 \times 10^{-14} \beta k \gamma}{24\pi \bar{\mu} r_s^3 n_s^2 h} \text{ MSCF/D}$$

and  $D_{gp}$  = gravel pack non-Darcy skin coefficient

i.e.,

$$D_{gp} = \frac{2\pi \times 1.3972 \times 10^{-14} f_{gp}^s l_{gp} k \beta_p \gamma}{\bar{\mu} n_s^2 h A_p^2} \text{ MSCF/D}$$

The preceding equations give  $D$  in units of MSCF/D; the corresponding equations in terms of mass flow rate  $m_g$  in lb/day are

$$D_c = f_{ND}^s \frac{1.82974 \times 10^{-16} \beta k}{24\pi \bar{\mu} r_s^3 n_s^2 h} \text{ lb/day}$$

$$D_{gp} = \frac{2\pi \times 1.82974 \times 10^{-16} f_{gp}^s l_{gp} k \beta_p}{\bar{\mu} n_s^2 h A_p^2} \text{ lb/day}$$

## Generation of the gas well deliverability curve

The  $p^2$  approach gives a direct method of computing the gas well deliverability curve ( $p_{wf}$  versus  $Q$ ) and the AOF. However, it is much better to use the pseudopressure function to generate the relation from the deliverability equation (3–102a and b) by finding the bottom-hole pressure  $p_{wf}$  corresponding to various values of  $Q$  for a specified reservoir pressure  $\bar{p}$ ; in terms of  $m(p)$ , this may be written formally as

$$m(p_{wf}) = m(\bar{p}) - \frac{QP_{sc}T}{z_{sc}T_{sc}\pi kh} \left( \frac{1}{2} \ln \frac{4\bar{A}}{\gamma C_A r_w^2} + S'_a \right) \quad (3-102a)$$

or in gas field units

$$m(p_{wf}) = m(\bar{p}) - \frac{1421.5QT}{kh} \left( \frac{1}{2} \ln \frac{4\bar{A}}{\gamma C_A r_w^2} + S'_a \right) \quad (3-102b)$$

i.e.,

$$m(p_{wf}) = m(\bar{p}) - \frac{1421.5QT}{kh} \left( \frac{1}{2} \ln \frac{4\bar{A}}{\gamma C_A r_w^2} + S'_a + D_a Q \right)$$

$$p_{wf} = m^{-1}(p_{wf}) \quad (3-103)$$

Equation (3–102a and b) may be written in the form

$$\Delta m(p) = m(\bar{p}) - m(p_{wf}) = \Delta m(p)_D + \Delta m(p)_{ND} \quad (3-104)$$

where

$$\Delta m(p)_D = \frac{1421.5QT}{kh} \left( \frac{1}{2} \ln \frac{4\bar{A}}{\gamma C_A r_w^2} + S'_a \right) = E'Q$$

and

$$\Delta m(p)_{ND} = \frac{1421.5TD_a Q^2}{kh} = F'Q^2$$

It is presumed that  $kh$ ,  $S'_a$ , and  $D_a$  are known from well testing, and knowledge of the well's drainage area allows  $A$  and  $C_A$  to be estimated. Alternatively, in a design situation, these quantities are simply specified directly. The mechanics of the deliverability curve construction process are illustrated in figure 3–25, where for any flow rate  $Q$ ,  $\Delta m(p)$  is formed as the sum  $E'Q + F'Q^2$  and the pseudopressure function is used to calculate  $p_{wf}$  from  $\bar{p}$ . A typical gas well deliverability curve, i.e., a plot of  $p_{wf}$  versus  $Q$ , has been shown in figure 3–21 with the two

contributions to the pressure drop identified; this relationship will be stored as a table or fitted polynomial for use in conjunction with the VLP curve on the well performance diagram.

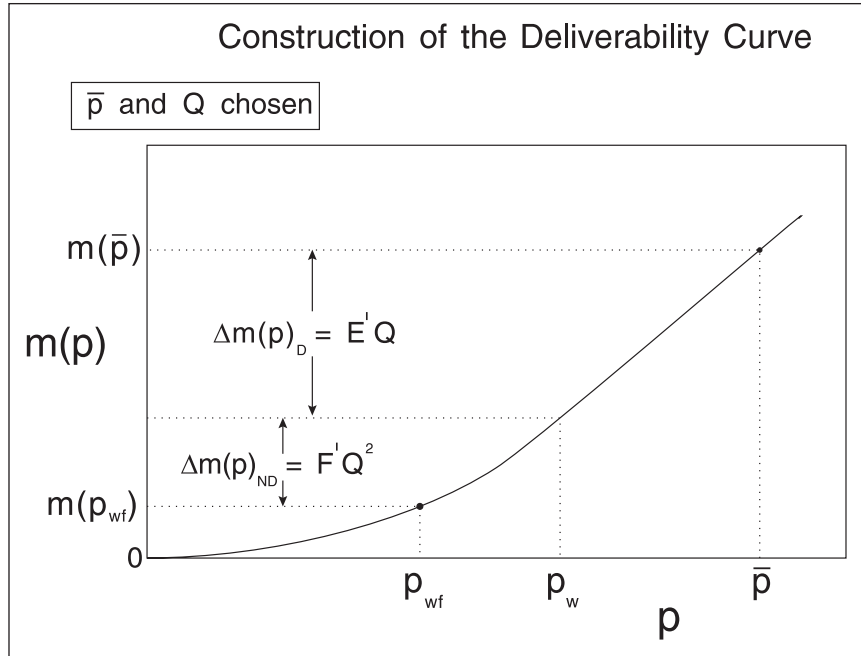


Fig. 3-25. Use of  $m(p)$  function to generate gas well deliverability curve

The preceding treatment is the classical derivation of gas well deliverability on the basis of  $m(p)$  and volumetric rate at standard conditions  $Q$ , and the equations given above correspond to those quoted in most standard texts on gas reservoir engineering. In terms of normalized pseudopressure and mass flow rate  $m_g$ , the deliverability equation takes the form

$$\psi(p_{wf}) = \psi(\bar{p}) - \frac{158.02m_g\mu_{gi}}{2\pi kh\rho_{gi}} \left( \frac{1}{2} \ln \frac{4\bar{A}}{\gamma C_A r_w^2} + S_a + \hat{D}_a m_g \right) \quad (3-105)$$

$$p_{wf} = \psi^{-1} - (p_{wf})$$

This may be written more conveniently as

$$\psi(p_{wf}) = \psi(\bar{p}) - \frac{1}{J_m} m_g - F_m m_g^2 \quad (3-106)$$

where

$$J_m = \frac{2\pi kh\rho_{gi}}{158.02\mu_{gi} \left( \frac{1}{2} \ln \frac{4\bar{A}}{\gamma C_A r_w^2} + S_a \right)} \quad (3-107)$$

and

$$F_m = \frac{158.02 \mu_{gi} \hat{D}_a}{2\pi k h \rho_{gi}} \quad (3-108)$$

This is the generalized form of the gas well deliverability equation which is identical in form to the multiphase flow versions to be developed later.

The gas well IPR models only flow in the reservoir to the wellbore and it is also necessary to model the tubing performance in order to predict the rate at which a well will flow for a specified wellhead pressure. In figure 3–26, some gas well IPRs for different reservoir pressures and two VLPs for different wellhead pressures are plotted; the appropriate intersection depends on the reservoir and wellhead pressures at the time in question.

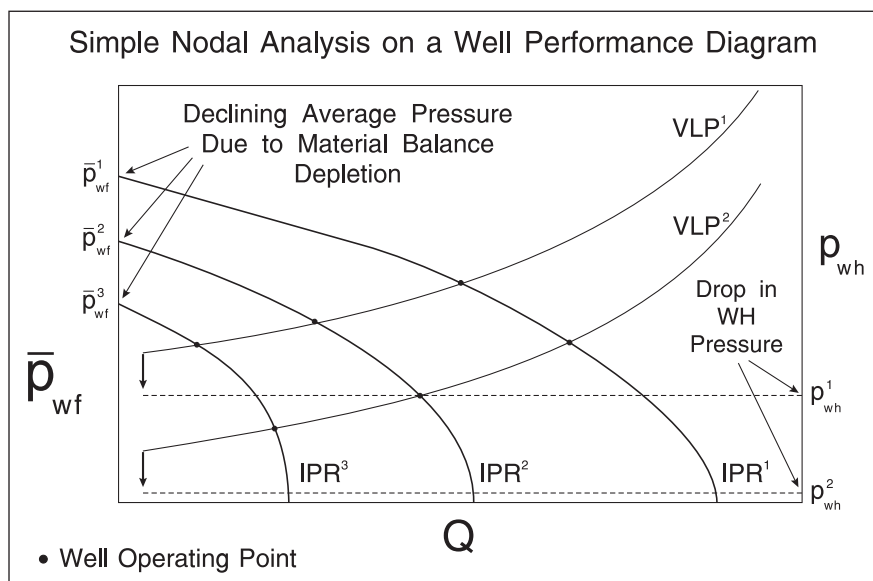


Fig. 3–26. Gas well deliverability for ranges of reservoir and wellhead pressures

## Backpressure equation

In the early days of gas reservoir engineering, the inflow performance of a gas well with laminar-inertial effects was modeled by an empirical equation of the form

$$Q = c(\bar{p}^2 - p_{wf}^2)^n \quad (3-109)$$

This was introduced by Rawlins and Schnellhardt<sup>5</sup> after interpreting several hundred multirate gas well tests. Originally, the proposed equation was based on empirical observation without suggestion as to why pressure squared should be used or why the exponent  $n$  had to be in the range 0.5–1. It is now known that the “pressure squared” behavior in the backpressure equation accounts for the pressure dependence of the reservoir integral, while the exponent  $n$  accounts for varying degrees of non-Darcy flow. The latter quantity can be obtained from stabilized test



data where  $\bar{p}^2 - p_{wf}^2$  is plotted versus  $Q$  on a log–log scale. The exponent is determined from the inverse slope of the line and is a measure of the inertial condition of the well; the constant  $c$  is determined from a known test point. As mentioned, non-Darcy flow yields values of  $n$  between 0.5 and 1.0. In terms of mass flow rate, Eq. (3–109) becomes

$$m_g = \rho_{sc} c (\bar{p}^2 - p_{wf}^2)^n \quad (3-110a)$$

or in gas field units

$$m_g = 76.45 \gamma_g c (\bar{p}^2 - p_{wf}^2)^n \text{ lb/day} \quad (3-110b)$$

where the coefficient  $c$  has been quoted in MSCFD/(psi)<sup>2n</sup>.

## Two-phase incompressible flow

When the reservoir is undersaturated and pressure maintenance by water injection has been employed to keep the bottom-hole flowing pressure above the bubble point, then eventually water breakthrough occurs at the producers. The well now produces two immiscible fluids—oil and water—at in situ volumetric rates  $q_o$  and  $q_w$ , respectively, which can be measured. Again, considering SS radial flow to the well, the equations describing the separate phases can be written as

$$\text{oil phase} \quad \frac{q_o}{2\pi hr} = \frac{k k_{ro}}{\mu_o} \frac{dp}{dr} \quad (3-111a)$$

$$\text{water phase} \quad \frac{q_w}{2\pi hr} = \frac{k k_{rw}}{\mu_w} \frac{dp}{dr} \quad (3-111b)$$

where  $k_{ro}$  and  $k_{rw}$  are the relative permeabilities to oil and water, respectively, which depend on saturation as shown in figure 3–27. This model of the simultaneous flow of oil and water using the so-called rock curves assumes diffuse flow conditions, i.e., no gravity segregation of the phases. The flowing water-cut  $f_w$ , defined on an in situ basis as

$$f_w = \frac{q_w}{q_w + q_o} \quad (3-112)$$

is controlled by the reservoir and in the model it is taken as a specified quantity. If it is the surface rates that have been measured and expressed as a water–oil ratio  $WOR = q_{ws}/q_{os}$ , the relation between the in situ water-cut  $f_w$  and the surface water–oil ratio  $WOR$  is

$$f_w = \frac{\text{WOR} \frac{B_w}{B_o}}{1 + \text{WOR} \frac{B_w}{B_o}} \quad (3-113)$$

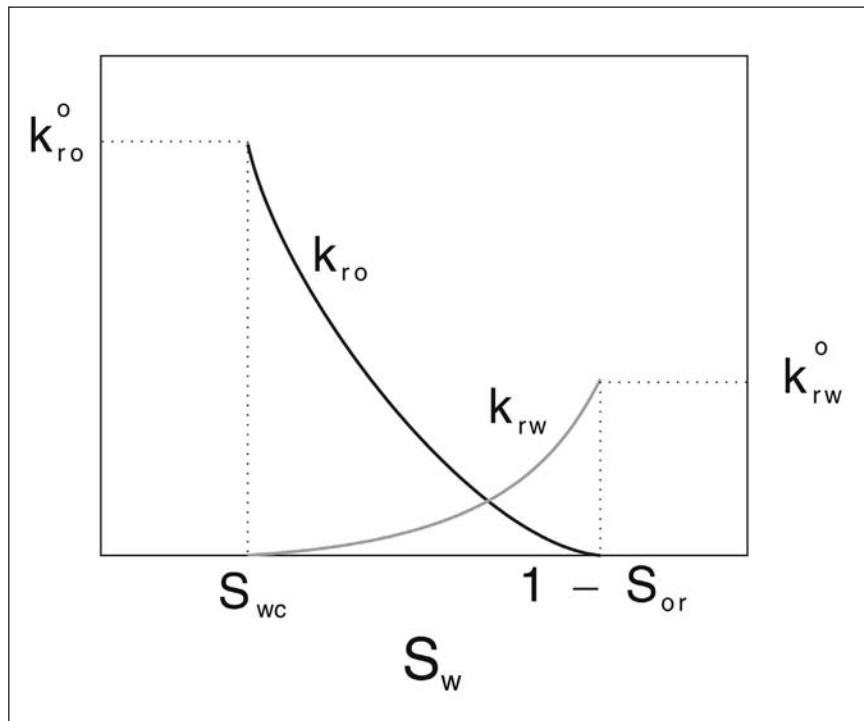


Fig. 3-27. Relative permeability curves

Later, the model of completely segregated flow based on straight line relative permeability curves will be also be described. Neither the diffuse nor fully segregated flow models allow the water-cut to be a function of rate which is a characteristic of coning situations. In the theory that follows, it will always be assumed that the down-hole water-cut or the surface water–oil ratio is known.

It is useful to utilize the following parametric form of the relative permeability curves based on the work of Corey:

$$k_{row}(S_w) = k_{row}^o \left( \frac{1 - S_w - S_{orw}}{1 - S_{orw} - S_{wc}} \right)^m \quad (3-114a)$$

$$k_{rwo}(S_w) = k_{rwo}^o \left( \frac{S_w - S_{wc}}{1 - S_{orw} - S_{wc}} \right)^n \quad (3-114b)$$

which involve the end-point relative permeabilities,  $k_{row}^o$  and  $k_{rwo}^o$  the exponents  $m$  and  $n$  which control the shape of the predicted curves and depend on wettability and the irreducible saturations  $S_{wc}$  and  $S_{orw}$ . These parameters can be established by fitting laboratory relative permeability data to the functional form (3–114a and b), which is an easy way of inputting information into a model.

In a recent study, Tjolsen *et al.*<sup>6</sup> have correlated the parameters of the Corey form to formation permeability for different depositional environments including mouthbars, distributory channels, and tidal bays. Examination of their extensive dataset (83 core plugs from a single North Sea well) on relative permeability indicates that, for general purposes, the following values may be used:

$$k_{row}^o = 1.0 \quad m = 3.5 \quad n = 2.0 \quad S_{orw} = 0.3$$

with  $S_{wc}$  and  $k_{rwo}^o$  related to absolute permeability through the approximate correlations

$$S_{wc} = 0.475 - 0.11 \log_{10}(k) \quad 1 \leq k \leq 10000 \quad (k : \text{md})$$

$$k_{rwo}^o = 0.35 + 0.08 \times \log_{10}(k) \quad 1 \leq k \leq 10000 \quad (k : \text{md})$$

The latter correlations reflect the fact that  $S_{wc}$  decreases with increasing absolute permeability, while the end-point permeability to water  $k_{rwo}^o$  increases as the absolute permeability becomes larger; this latter conclusion was one of the main results of the Tjolsen *et al.* study. The variation of  $k_{rwo}^o$  with absolute permeability, in fact, depended on depositional environment, and the result quoted here is an “average” estimate; the original reference should be consulted for more precise information on the Corey parameters. Note that this formulation, with  $k_{row}^o$  equal to unity, implies that the permeability, denoted here as  $k$ , is in fact the permeability to oil at connate water saturation; this is now accepted as an industry standard when quoting permeability values.

Water–oil imbibition relative permeability curves are dominated and controlled by the reservoir wettability. Consequently, the Corey exponents  $n$  and  $m$  depend on the rock wettability. Most reservoirs are not strongly water-wet or oil-wet but exhibit intermediate wetting behavior. Experience-based relative permeability functions, which lie within the middle of broadly acceptable ranges, are recommended for neutrally wet rock as default values. Should the reservoir be more oil-wet than represented by the base case, poorer reservoir performance would result and this is termed the “downside” case. Conversely, the “upside” case corresponds to a more water-wet reservoir.

Suggested default values for Corey exponents and residual saturations, representing typical values for weakly water-wet to weakly oil-wet, i.e. neutral, are given in table 3–1 along with the “upside” and “downside” cases.

**Table 3–1.** Representative values of the Corey parameters

Parameter	Default	Upside case (more water-wet)	Downside case (more oil-wet)
m	4.0	2.0	6.0
n	4.0	6.0	2.0
$S_{wc}$	0.15	0.25	0.10
Land C coeff.	4	1.5	3
$S_{orw}$	0.19	0.35	0.24
$k_{row}^o$	1.0	1.0	1.0
$k_{rwo}^o$	0.50	0.20	0.80

In formulating the simultaneous flow equation (3–111a and b), the phase pressure gradients are assumed equal, i.e. capillary pressure is neglected, and it follows that

$$\frac{q_w \mu_w}{k_{rw}} = \frac{q_o \mu_o}{k_{ro}} \quad \text{i.e.} \quad \frac{k_{rw}}{k_{ro}} = \frac{q_w \mu_w}{q_o \mu_o} = \frac{f_w}{1-f_w} \frac{\mu_w}{\mu_o} = \text{WOR} \frac{B_w}{B_o} \frac{\mu_w}{\mu_o} \quad (3-115)$$

This is the condition that the phases have the same pressure gradient and the saturation will adjust itself so that (3–115) is satisfied. As already mentioned, the in situ water-cut  $f_w = q_w / (q_w + q_o)$  is governed by the reservoir fractional flow of water in the well vicinity at the time in question. Thus, presuming the phase viscosities are known and the producing water oil ratio ( $\text{WOR} = q_{sw} / q_{so}$ ) has been measured, then  $k_{rw} / k_{ro}$  can be determined from (3–115); there is only one saturation that yields a specified relative permeability ratio  $k_{rw} / k_{ro}$  and hence, once this has been determined by inspection of the relative permeability curves, the individual  $k_{rw}$  and  $k_{ro}$  values follow. In order to carry out this calculation, it is useful to prepare a graph of  $k_{rw} / k_{ro}$  versus saturation  $S_w$ , as shown in figure 3–28. When parametric relative permeability curves are employed, the determination of saturation from a known value of  $k_{rw} / k_{ro}$  can be written as a root-finding exercise, viz.,

$$\mathbf{f}_{\text{rpr}}(S_w) = \frac{f_w \mu_w}{(1 - f_w) \mu_o} - (1 - S_{or} - S_{wc})^{m/n} \frac{k_{rw}^o (S_w - S_{wc})^n}{k_{ro}^o (1 - S_w - S_{or})^m} = 0 \quad (3-116a)$$

Alternatively, in terms of the flowing mass fraction of water  $y$ , Eq. (3–116a) may be written in the form

$$\mathbf{f}_{\text{rpr}}(S_w) = \frac{k_{ro} \rho_o}{\mu_o} - \frac{1 - y}{y} \frac{k_{rw} \rho_w}{\mu_w} = 0 \quad (3-116b)$$

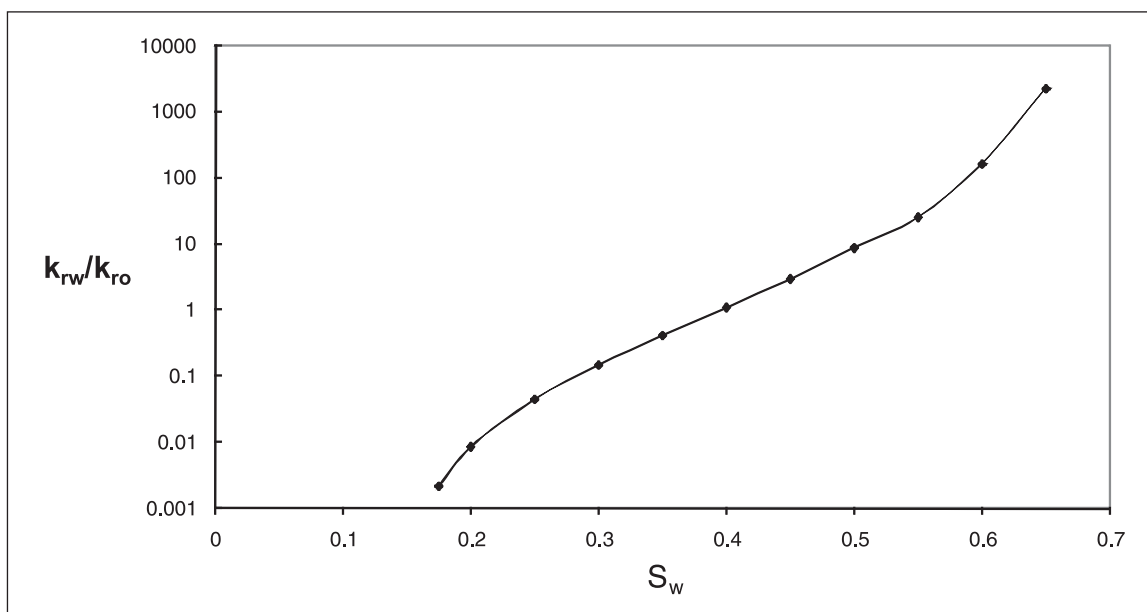


Fig. 3-28. Relative permeability ratio as a function of saturation

The flowing mass fraction water  $y$  is given by

$$y = \frac{q_w \rho_w}{q_w \rho_w + q_o \rho_o} = \frac{f_w \rho_w}{f_w \rho_w + (1 - f_w) \rho_o} \quad (3-117)$$

The saturation that satisfies the preceding nonlinear algebraic equation (either form (a) or (b) as convenient) results in relative permeabilities  $k_{rw}$  and  $k_{ro}$  that allow the phases to flow simultaneously with the same pressure gradient. Naturally, the water saturation in the radial flow region around the well depends on the water-cut, the viscosity ratio  $\mu_w/\mu_o$ , and the nature of the relative permeability curves. Addition of (3-111a) and (3-111b) gives

$$q_t = q_o + q_w = 2\pi kh r \left( \frac{k_{ro}}{\mu_o} + \frac{k_{rw}}{\mu_w} \right) \frac{dp}{dr} \quad (3-118)$$

which on integration yields

$$\Delta p = p_e - p_w = \frac{q_t}{2\pi kh \left( \frac{k_{ro}}{\mu_o} + \frac{k_{rw}}{\mu_w} \right)} \ln \frac{r_e}{r_w} \quad (3-119a)$$

or

$$\Delta p = p_e - p_w = \frac{q_t \mu_o}{2\pi kh \left( k_{ro} + \frac{k_{rw} \mu_o}{\mu_w} \right)} \ln \frac{r_e}{r_w} \quad (3-119b)$$

In Eq. (3–119a and b), the quantity  $\left(\frac{k k_{ro}}{\mu_o} + \frac{k k_{rw}}{\mu_w}\right)$  is known as the total mobility  $\left(\frac{k}{\mu}\right)_t$  and this is measured directly in a transient well test carried out under two-phase conditions. The well PI is given by the expression

$$q_{st} = q_{so} + q_{sw} = J_{ss}(p_e - p_w) \quad (3-120)$$

where

$$J_{ss} = \frac{2\pi kh \left(\frac{k_{ro}}{\mu_o} + \frac{k_{rw}}{\mu_w}\right)}{B_t \left(\ln \frac{r_e}{r_w} + S_a\right)} = \frac{2\pi kh \left(k_{ro} + \frac{k_{rw}\mu_o}{\mu_w}\right)}{B_t \mu_o \left(\ln \frac{r_e}{r_w} + S_a\right)} = \frac{2\pi h \left(\frac{k}{\mu}\right)_t}{B_t \left(\ln \frac{r_e}{r_w} + S_a\right)} \quad (3-121)$$

in which a total apparent skin  $S_a$  has been introduced and  $B_t$ —the total formation volume factor—is given by

$$B_t = \frac{q_{so} B_o + q_{sw} B_w}{q_{so} + q_{sw}} \quad (3-122)$$

For SSS conditions, Eq. (3–121) would take on the form

$$J_{SSS} = \frac{2\pi kh \left(\frac{k_{ro}}{\mu_o} + \frac{k_{rw}}{\mu_w}\right)}{B_t \left(\frac{1}{2} \ln \frac{4\bar{A}}{\gamma C_A r_w^2} + S_a\right)} = \frac{2\pi kh \left(k_{ro} + \frac{k_{rw}\mu_o}{\mu_w}\right)}{B_t \mu_o \left(\frac{1}{2} \ln \frac{4\bar{A}}{\gamma C_A r_w^2} + S_a\right)} = \frac{2\pi h \left(\frac{k}{\mu}\right)_t}{B_t \left(\frac{1}{2} \ln \frac{4\bar{A}}{\gamma C_A r_w^2} + S_a\right)} \quad (3-123)$$

The PI in two-phase flow refers to the total liquid production,  $q_{st} = q_{so} + q_{sw}$ , and is affected by the factor  $\left(k_{ro} + \frac{k_{rw}\mu_o}{\mu_w}\right)$  which can be greater or less than unity depending on the viscosity ratio of the phases, i.e.,  $\mu_o/\mu_w$ . If the water viscosity is less than that of oil, this will tend to increase the PI to total liquid and vice versa. The relative permeability effect always tends to reduce the productivity since the sum of the two relative permeabilities is always less than unity; this is especially true at high water-cut in a water-wet system. As the water-cut in a well increases with time, the PI will change even when  $kh$  and  $S_a$  remain constant. The ratio of the two-phase PI to the single phase oil PI—a productivity ratio—is

$$\frac{(J_{ss})_t}{(J_{ss})_o} = \frac{B_o}{B_t} \left(k_{ro} + \frac{k_{rw}\mu_o}{\mu_w}\right) = \frac{1 + \text{WOR}}{1 + \text{WOR} \frac{B_w}{B_o}} \left(k_{ro} + \frac{k_{rw}\mu_o}{\mu_w}\right) \quad (3-124)$$

Note that in Eq. (3–124) the relative permeabilities are a function of saturation and hence depend on water-cut. Knowledge of the relative permeability curves and phase viscosity ratio allows this productivity ratio to be predicted for any producing WOR. If the PI has been measured in single-phase oil conditions, this ratio may be used as a multiplier to predict the change in well behavior as a water-cut develops. However, it should be remembered that changes in the total skin factor  $S_a$  may occur after water breakthrough due to such problems as scale deposition, fines movement, or clay swelling. Thus as a zone develops a water-cut, its continuing ability to produce total liquid, as measured by the two-phase PI, is affected by the following:

- The nature of the relative permeability curve which is determined by the residual saturations  $S_{wc}$  and  $S_{or}$ , the end-point relative permeabilities  $k_{ro}^o$  and  $k_{rw}^o$ , and the Corey exponents  $m$  and  $n$ . For a water-wet system, the overall relative permeability  $k_{ro} + k_{rw}$  will decrease as the water-cut increases.
- The viscosity ratio between water and oil, i.e.,  $\mu_w/\mu_o$ . When  $\mu_w < \mu_o$ , the well's ability to produce liquid is increased, and vice versa.
- If the zone skin factor  $S_a$  increases after water breakthrough due to scaling, fines migration, or clay swelling, this will reduce the well PI.

The two-phase inflow model derived above refers to diffuse flow in the zone, i.e., the water saturation is uniform with depth and there is no tendency for the water to segregate downwards. In high-permeability formations, it can arise that complete segregation of oil and water occur with the water flowing as a Dietz tongue underneath the oil. The theory of two-phase flow shows that this segregated flow can simply be modeled by using straight line relative permeability curves ( $m = n = 1$ ) between the end points as shown in figure 3–29; hence the two limiting cases of diffuse and segregated flow can be handled in a convenient manner. Note that the SS theory can be applied only if the water-cut is known from field measurements. For incompressible two-phase flow, the inflow performance relation is still a straight line of the form

$$p_w = \bar{p} - \frac{1}{J_{SSS}} q_{st} \quad (3-125)$$

and two methods are again available for determining the IPR:

- Carry out a transient well test which identifies  $\left(\frac{k}{\mu}\right)_t$ ,  $S_a$ , and  $\bar{p}$  using the Perrine–Martin method and calculate  $J_{SSS}$  from Eq. (3–123);
- Flow the well in a production test at two different rates and establish two points on the IPR line; care must be taken that SSS conditions are attained at the end of each flow period.

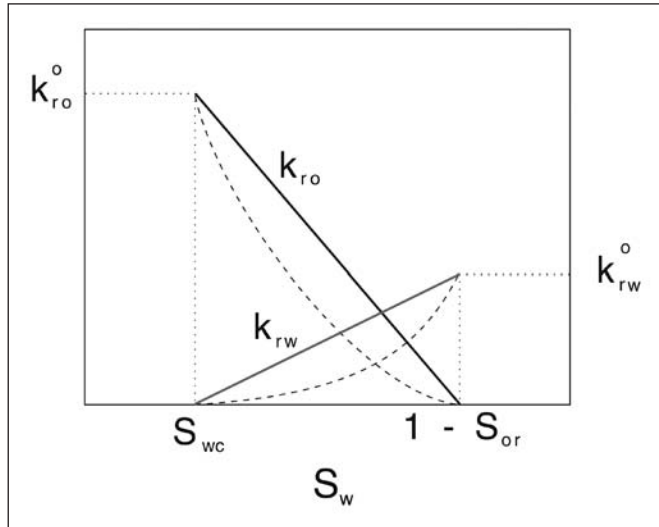


Fig. 3–29. Straight line relative permeability curves for segregated flow

## Two-phase incompressible flow pseudopressure function

In order to maintain compatibility with the generalized approach to the prediction of multiphase inflow performance on a mass basis, Eq. (3–118) may be posed in terms of total mass flow rate as

$$m_t = m_o + m_w = q_o \rho_o + q_w \rho_w = \left( \frac{k_{ro} \rho_o}{\mu_o} + \frac{k_{rw} \rho_w}{\mu_w} \right) 2\pi k h r \frac{dp}{dr} \quad (3-126)$$

which leads to the following definition of a pseudopressure for two-phase incompressible flow:

$$\psi(p) = \frac{\mu_r}{\rho_r} \int_{p_b}^p \left( \frac{k_{ro} \rho_o}{\mu_o} + \frac{k_{rw} \rho_w}{\mu_w} \right) dp' \quad (3-127)$$

and the steady-state radial inflow equation

$$\psi(p_e) - \psi(p_w) = \frac{m_t \mu_r}{2\pi k h \rho_r} \ln \frac{r_e}{r_w} \quad (3-128)$$

In the computation of the integral (3–127), the water saturation  $S_w$  is obtained as the root of (3–116b) and the relative permeabilities then follow from (3–114a and b); in fact, this water saturation is independent of pressure and Eq. (3–127) may be written as

$$\psi(p) = \frac{\mu_r}{\rho_r} \left( \frac{k_{ro} \rho_o}{\mu_o} + \frac{k_{rw} \rho_w}{\mu_w} \right) \int_{p_b}^p dp' = \frac{\mu_r}{\rho_r} \left( \frac{k_{ro} \rho_o}{\mu_o} + \frac{k_{rw} \rho_w}{\mu_w} \right) (p - p_b)$$



$$\text{i.e.,} \quad \psi(p) = M'(p - p_b) \quad (3-129)$$

where  $M' = \frac{\mu_r}{\rho_r} \left( \frac{k_{ro}\rho_o}{\mu_o} + \frac{k_{rw}\rho_w}{\mu_w} \right)$  is a density-weighted mobility ratio. The choice of reference density  $\rho_r$  and viscosity  $\mu_r$  is arbitrary, but the most convenient one is the single-phase oil properties  $\rho_o$  and  $\mu_o$ . In this case, the quantity  $M'$  is the ratio of the density weighted mobility of the two-phase flowing mixture to that of oil given by

$$M' = \left( k_{ro} + k_{rw} \frac{\rho_w \mu_o}{\rho_o \mu_w} \right) \quad (3-130)$$

Depending on the viscosity ratio and the nature of the relative permeability curves,  $M'$  can be greater or less than unity. Thus for incompressible flow, the pseudopressure  $\psi(p)$  is a linear function of pressure, and quadrature is not required for its evaluation. Given the total mass flow rate  $m_t$  from (3-128) the individual phase mass flow rates at in situ conditions follow as

$$m_o = (1 - y)m_t \quad m_w = ym_t \quad (3-131)$$

while the in situ volumetric rates are given by

$$q_o = \frac{m_o}{\rho_o} \quad q_w = \frac{m_w}{\rho_w} \quad (3-132)$$

The productivity of the well on a mass basis is predicted by the equation

$$m_t = J_m (\psi(\bar{p}) - \psi(p_w)) \quad (3-133)$$

where for SSS inflow the PI on a mass basis, in scientific units, is given by the formula

$$J_m = \frac{2\pi k h \rho_r}{\mu_r \left( \frac{1}{2} \ln \frac{4\bar{A}}{\gamma C_A r_w^2} + S_a \right)} \quad (3-134a)$$

The field units version is

$$J_m = \frac{2\pi k h \rho_o}{158.02 \mu_o \left( \frac{1}{2} \ln \frac{4\bar{A}}{\gamma C_A r_w^2} + S_a \right)} \text{ lb/day/psi} \quad (3-134b)$$

where the reference density and viscosity are referred to the oil phase.

In the general case of the immiscible flow of oil and water, the densities and viscosities are weak functions of pressure and the two-phase pseudopressure given by (3–127) will be computed by quadrature in the usual way. The PI on a mass basis  $J_m$ , defined by (3–134a and b), is constant and uniquely characterizes the deliverability. However, it is also useful to define a characteristic PI based on pressure difference and total volumetric flow rate of liquid at surface conditions through Eq. (3–120). The relation between the PI on a mass basis and a volumetric basis is obtained by comparing Eqs. (3–123) and (3–134); the result, in scientific units, is

$$J_{SSS} = J_m \frac{k_{ro} + \frac{k_{rw}\mu_o}{\mu_w}}{\rho_o} \quad (3-135)$$

Note, however, that  $J_m$  is based on pseudopressure, whereas  $J_{SSS}$  is based on actual pressure. In field units, the relation becomes

$$J_{SSS} = J_m \frac{k_{ro} + \frac{k_{rw}\mu_o}{\mu_w}}{\rho_o} \frac{158.0}{887.2} \quad (3-136)$$

Thus the PI on a mass basis is directly related to the classical volumetric PI in the case of incompressible liquid systems. The pseudopressure method has been derived to maintain a common basis with compressible systems undergoing mass transfer but, in this case, it is exactly equivalent to the more classical approach based on volumetrics derived in the preceding section.

## Two-Phase Compositional Flow

When the formation pressure falls below the bubble point in an oil reservoir or below the dew point in a gas reservoir, two-phase compositional flow occurs in the near-wellbore region. In oil or volatile oil situations, below the bubble point, gas is liberated as the pressure falls and the flashing process is loosely referred to as *solution gas drive*. The permeability to oil is reduced by the presence of free gas and the well PI decreases as the gas saturation develops. In the case of a gas reservoir, retrograde condensation of liquid may occur and the presence of a more viscous phase again impairs well productivity. The SS inflow is now also affected by the compositional behavior of the fluids, and relative permeability phenomena play an important role. In the development of the two-phase pseudopressure concept, it will be assumed that a compositional phase behavior model is available that can predict the flash curve of the mixture as it falls below the bubble or dew point. A flash curve is a table of the following PVT variables as a function of pressure at reservoir temperature:

$x$  – mass fraction liquid (oil or condensate)

$\rho_g$  – gas phase density

$\rho_o$  – oil or condensate phase density

$\mu_g$  – gas phase viscosity

$\mu_o$  – oil or condensate phase viscosity

Presuming that the reservoir fluid has been characterized, the equation of state compositional model can be run in advance to compute the phase behavior and store the flash curve of the mixture which can be accessed by interpolation. Thus it will be assumed that the quantities listed above are known functions of pressure alone; above the bubble or dew point, single-phase conditions exist and  $x = 1$  or  $0$ , respectively.

## Radial steady-state Darcy flow

The treatment of two-phase SS radial flow into a well was first considered by Evinger and Muskat,<sup>7</sup> who introduced the concept of two-phase pseudopressure in connection with solution gas drive illustrated in figure 3–30a. Muskat<sup>8</sup> also addressed the problem of condensate blockage in discussions on gas cycling, and Fetkovich<sup>9</sup> used Muskat's results to derive a rate- and time-dependent blockage skin for use in the standard gas deliverability equation. Figure 3–30b shows a condensate system where the reservoir pressure denoted  $p_e$  is above the dew point and accordingly there is a zone of single-phase flow from  $r_e$  to  $r_{dew}$  and two-phase flow between  $r_{dew}$  and  $r_w$ . At any radius  $r$  less than  $r_{dew}$ , the simultaneous flow of liquid and vapor (at thermodynamic equilibrium) is described by the equations

$$\frac{q_g}{2\pi rh} = \frac{m_g}{2\pi rh\rho_g} = \frac{kk_{rg}}{\mu_g} \frac{dp}{dr} \quad (3-137)$$

$$\frac{q_o}{2\pi rh} = \frac{m_o}{2\pi rh\rho_o} = \frac{kk_{ro}}{\mu_o} \frac{dp}{dr} \quad (3-138)$$

where  $q_g$  and  $q_o$  are local in situ flow rates and  $k_{rg}$  and  $k_{ro}$  are the relative permeabilities of the phases, which depend on saturation; it is therefore assumed that a set of relative permeability curves are available as illustrated in figure 3–31. For convenience, it is again useful to assume parametric forms for the gas–oil relative permeability relations, i.e.,

$$k_{ro} = k_{ro}^o \left( \frac{1 - S_g - S_{or}}{1 - S_{gr} - S_{or}} \right)^{m'} \quad (3-139a)$$

$$k_{rg} = k_{rg}^o \left( \frac{S_g - S_{gr}}{1 - S_{gr} - S_{or}} \right)^{n'} \quad (3-139b)$$

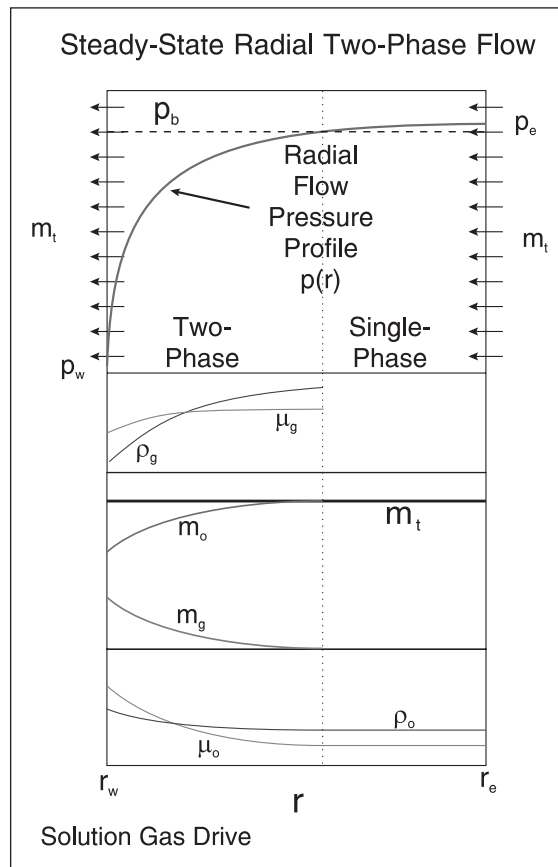


Fig. 3–30a. Two phase radial flow—solution gas drive

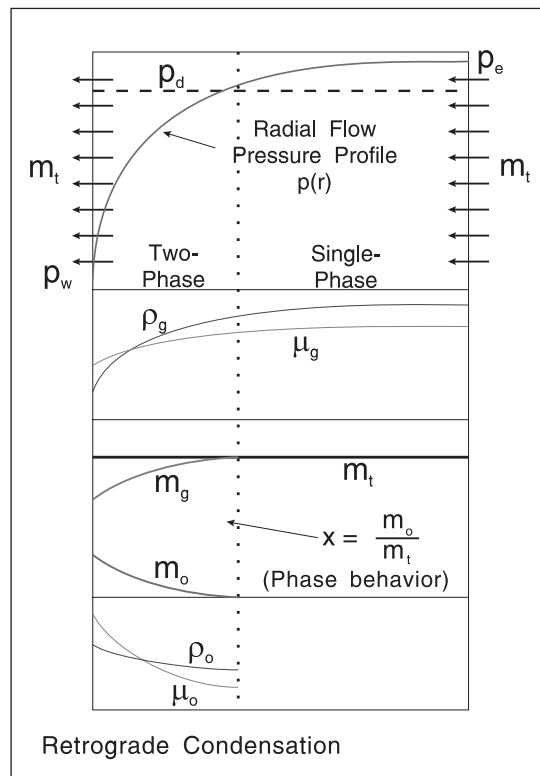


Fig. 3–30b. Two phase radial flow—gas condensate

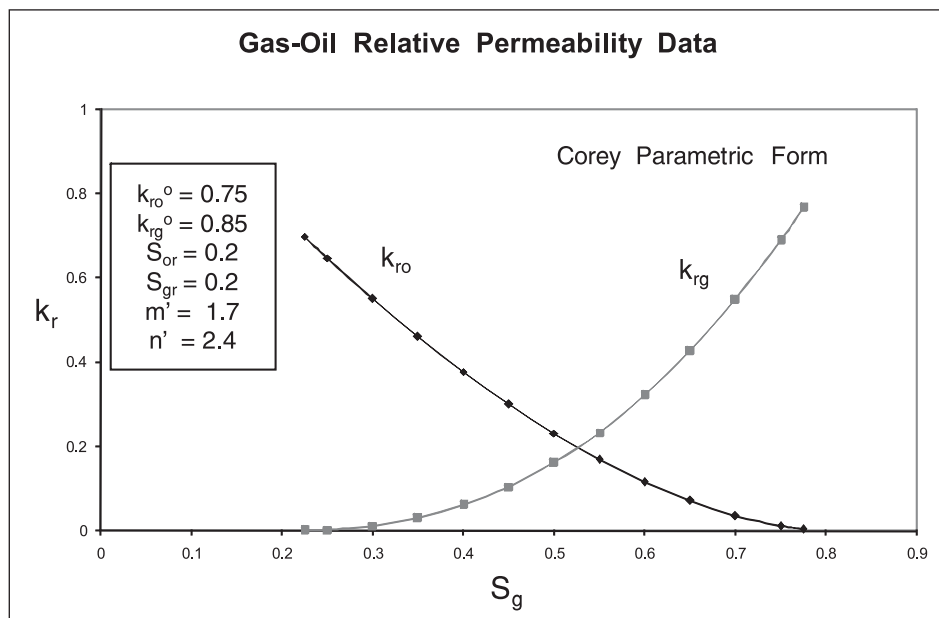


Fig. 3–31. Gas–oil relative permeability curves

Typical values for the parameters of the Corey approximation for gas–oil systems (at connate water saturation in the range 15–25%) taken from the data quoted by Honarpour *et al.*<sup>10</sup> are as follows:

$$k_{ro}^o = 0.75 \quad m' = 1.7 \quad S_{or} = 0.2$$

$$k_{rg}^o = 0.85 \quad n' = 2.4 \quad S_{gr} = 0.2$$

Whitson and Fevang<sup>11</sup> assume parametric relations of the form

$$k_{ro} = k_r(S_{wi})(S_o^*)^2 \left[ \frac{S_o}{1 - S_{wi}} \right]^{\frac{2+\lambda}{\lambda}} \tag{3-140a}$$

$$k_{rg} = k_r(S_{wi})(S_g^*)^2 \left[ 1 - (1 - S_g^*)^{\frac{2+\lambda}{\lambda}} \right] \tag{3-140b}$$

where

$$S_o^* = \frac{S_o - S_{or}}{1 - S_{wi} - S_{or}} \quad S_g^* = \frac{S_g}{1 - S_{wi}}$$

$$\lambda = 2 S_{wi} = 0.25 \quad k_r(S_{wi}) = 0.8 \quad S_{or} = 0.1$$

The relative permeability curves for the Corey parameters above are shown in figure 3–31c.

In Eqs. (3–140a and b), the saturations refer to the hydrocarbon pore space. Modern practice in reporting relative permeability data prefers to use conventional saturations based on total pore volume and includes the presence of connate water as  $S_{wi}$ . The Corey expressions then take the alternative form

$$k_{ro} = k_{ro}^o \left[ \frac{1 - S_g - S_{wi} - S_{org}}{1 - S_{wi} - S_{org} - S_{gc}} \right]^{m'} \quad (3-141a)$$

$$k_{rg} = k_{rg}^o \left[ \frac{S_g - S_{gc}}{1 - S_{wi} - S_{org} - S_{gc}} \right]^{n'} \quad (3-141b)$$

where the end-point values  $k_{ro}^o$  and  $k_{rg}^o$  are set to unity by some authors. The appropriate value of critical gas saturation  $S_{gc}$  is related to pore size distribution, with lower values attributed to rocks with larger porosity and permeability. It is considered to be higher for pressure depletion than for gas injection since, during pressure depletion, i.e., solution gas drive, the gas saturation develops in all pores, whereas, during gas injection, only the larger pores are initially saturated by gas.

Equation (3–141b) is valid only in the range of gas saturations  $S_{gc} < S_g < 1 - S_{wi} - S_{org}$ , i.e., the region where both phases are mobile. In the context of reservoir simulation, where a region of immobile condensate at a saturation less the  $S_{gc}$  develops, it is necessary to allow for the variation of  $k_{rg}$  in the range  $S_{gc} < S_g < 1 - S_{wi}$ . In order to handle this effect, Eq. (3–141b) is written alternatively as

$$k_{rg} = k_{rg}^o \left[ \frac{S_g - S_{gc}}{1 - S_{wi} - S_{gc}} \right]^{n'} \quad (3-141c)$$

This allows the gas phase relative permeability function to be fitted over the entire range of allowable gas saturations. In the interval  $1 - S_{wi} - S_{org} < S_g < 1 - S_{wi}$ , the oil (condensate) relative permeability is zero because  $S_o < S_{org}$ .

The values of residual oil saturation in gas drive  $S_{org}$  are controlled by gravity and interfacial tension forces. In the reservoir gravity forces become more significant so that  $S_{org}$  values with gravity drainage are often much lower than the values of  $S_{orw}$  in a water-flood process. Conditions favorable to drainage to low oil saturations include the following:

- Significant formation dip
- A thick oil column
- Good vertical permeability
- Low oil viscosity
- Significant oil–gas density difference
- Low gas–oil interfacial tension

In gas–oil drainage, oil nearly always acts as the wetting phase with respect to gas.

Gas–oil relative permeability functions that lie within the middle range of experience are used by McPhee<sup>12</sup> for the default or base case. Sensitivity is considered by allowing for “upside” and “downside” cases. The upside case represents a relatively high-permeability rock with good gas flood performance (lower relative permeability to gas and higher oil relative permeability). The downside case represents a lower permeability rock with comparatively poorer gas flood performance (higher relative permeability to gas and lower oil relative permeability). Typical Corey values for each case are given in table 3–2.

**Table 3–2.** Corey parameter values for gas–oil drainage relative permeability curves

Parameter	Base case	Upside case	Downside case
$n'$	6	4	8
$m'$	2	4	2
$S_{gc}$	0.05	0.075	0.02
$S_{org}$	0.1	0.1	0.1
$k_{ro}^o$	1	1	1
$k_{rg}^o$	1	1	1

Unfortunately, all this data refers to gas flooding processes in core where it is difficult to measure the critical gas saturation. Hence, these  $S_{org}$  values are probably low in the context of solution gas drive.

As the pressure falls through the radial region, the local mass fraction of liquid changes according to the flash curve, assuming that the phases are at local thermodynamic equilibrium. At SS conditions, the sum of liquid and vapor mass flow rates is constant, i.e.,

$$m_t = m_g + m_o \quad (3-142)$$

The mass ratio of liquid to vapor is given by the relation

$$\frac{m_o}{m_o + m_g} = x \quad \text{i.e.} \quad \frac{m_o}{m_g} = \frac{x}{1-x} \quad (3-143)$$

and dividing Eq. (3–138) by (3–137) results in

$$\frac{m_o}{m_g} = \frac{x}{1-x} = \frac{\rho_o k_{ro} \mu_g}{\rho_g k_{rg} \mu_o}$$

i.e.,

$$\frac{k_{ro}}{k_{rg}}(S_g) = \frac{x}{1-x} \frac{\rho_g \mu_o}{\rho_o \mu_g} \quad (3-144a)$$

$$\text{or} \quad f_{\text{rpr}}(S_g) = \frac{k_{\text{ro}}\rho_o}{\mu_o x} - \frac{k_{\text{rg}}\rho_g}{(1-x)\mu_g} = 0 \quad (3-144b)$$

The saturation  $S_g$  at radius  $r$  is determined by finding the value that satisfies Eq. (3-144a and b); thus for any given pressure  $p$ , the mass fraction liquid  $x$ , the phase densities  $\rho_g$  and  $\rho_o$ , and the phase viscosities  $\mu_g$  and  $\mu_o$  are determined by interpolation in the flash table, and then the saturation  $S_g$  that satisfies Eq. (3-144a and b) is found. In order to solve this equation, a graph of  $k_{\text{ro}}/k_{\text{rg}}$  versus saturation  $S_g$  can be constructed as illustrated in figure 3-32; if the relative permeability ratio is known from (3-144a), then the corresponding saturation is immediately available. Alternatively, a root-finding algorithm can be used on Eq. (3-144b) to find the value of the gas saturation that satisfies the simultaneous flow condition. The individual relative permeabilities can then be obtained from the specified relative permeability curves.

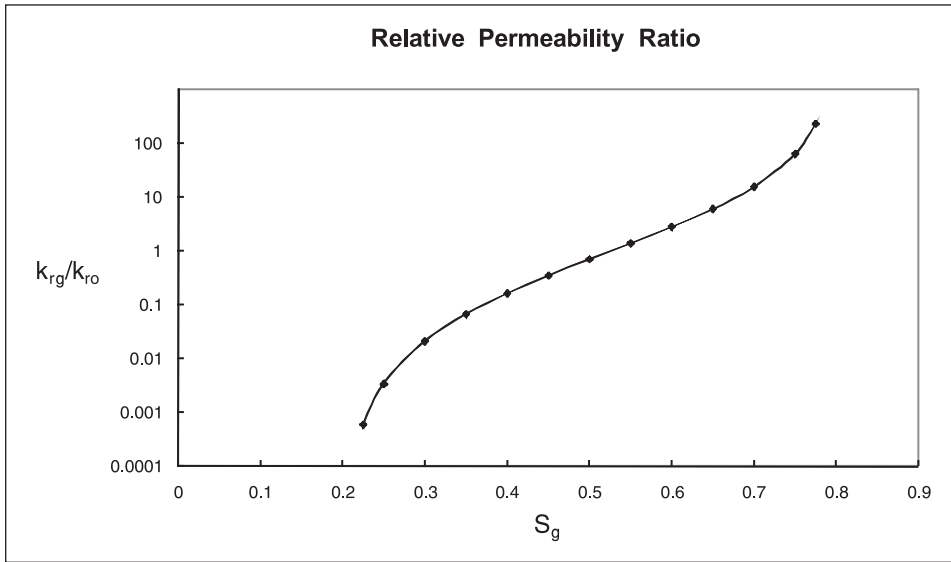


Fig. 3-32. Relative permeability ratio as a function of saturation

Substituting Eqs. (3-137) and (3-138) into (3-142) shows that the total mass flow of mixture is given by

$$m_t = m_o + m_g = 2\pi r k h \left( \frac{k_{\text{ro}}\rho_o}{\mu_o} + \frac{k_{\text{rg}}\rho_g}{\mu_g} \right) \frac{dp}{dr} \quad (3-145)$$

which can be integrated as follows:

$$\int_{P_w}^{P_e} \left( \frac{k_{\text{ro}}\rho_o}{\mu_o} + \frac{k_{\text{rg}}\rho_g}{\mu_g} \right) dp = \frac{m_t}{2\pi k h} \int_{r_w}^{r_e} \frac{dr}{r} \quad (3-146)$$



On multiplying by a reference viscosity  $\mu_r$  and dividing by a reference density  $\rho_r$ , Eq. (3–146) may be written as

$$\frac{\mu_r}{\rho_r} \int_{p_w}^{p_e} \left( \frac{k_{ro}\rho_o}{\mu_o} + \frac{k_{rg}\rho_g}{\mu_g} \right) dp = \frac{m_t\mu_r}{2\pi kh\rho_r} \int_{r_w}^{r_e} \frac{dr}{r} \quad (3-147)$$

and a two-phase normalized pseudopressure can now be defined as

$$\psi(p) = \frac{\mu_r}{\rho_r} \int_{p_b}^p \left( \frac{k_{ro}\rho_o}{\mu_o} + \frac{k_{rg}\rho_g}{\mu_g} \right) dp' \quad (3-148)$$

The radial flow equation on a mass basis takes the familiar form

$$\Delta\psi = \psi(p_e) - \psi(p_w) = \frac{m_t\mu_r}{2\pi kh\rho_r} \ln \frac{r_e}{r_w} \quad (3-149)$$

or in dimensionless terms

$$\psi_D = \frac{\psi(p_e) - \psi(p_w)}{\frac{m_t\mu_r}{2\pi kh\rho_r}} = \ln \frac{r_e}{r_w} \quad (3-150)$$

Thus the effect of phase change, i.e. vaporisation or condensation, can be accounted for by the use of a two-phase pseudopressure which can be computed in advance and stored as a function. The two-phase pseudopressure is computed by quadrature in the usual way, i.e.,

$$\psi(p) = \frac{\mu_r}{\rho_r} \int_{p_b}^p \left( \frac{k_{ro}(S_g)\rho_o(p)}{\mu_o(p)} + \frac{k_{rg}(S_g)\rho_g(p)}{\mu_g(p)} \right) dp' \quad (3-151)$$

where

$$S_g = \mathbf{f}_{rpr}^{-1} \left( \frac{x(p)}{1-x(p)} \frac{\rho_g(p)\mu_o(p)}{\rho_o(p)\mu_g(p)} \right)$$

as illustrated in figure 3–33; here the notation  $\mathbf{f}_{rpr}^{-1}$  (relative permeability ratio) indicates that the saturation is found as the root of Eq. (3–144a and b). The definition of pseudopressure extends into the single-phase region, i.e.,  $p > p_{dew}$ , simply by assigning  $x = k_{ro} = S_o = 0$  and  $k_{rg} = 1$  when the pressure is above the dew point. Correspondingly, in solution gas drive  $k_{rg} = S_g = 0$  and  $k_{ro} = x = 1$  when  $p > p_{bubble}$ . All the information pertaining to phase behavior, physical properties, and

relative permeability is implicit in the pseudopressure function, which allows two-phase flow to be treated by the same methods applicable to single-phase flow. However, the model based on pseudopressure is only as accurate as the data that is used in the computation of  $\psi(p)$ ; in particular, the validity of the relative permeability curves employed to generate  $\psi(p)$  may be questionable. Modern equation of state (EOS) compositional models are capable of predicting phase behavior and physical property data with good reliability and the pseudopressure approach allows this important data to be easily incorporated into well inflow models.

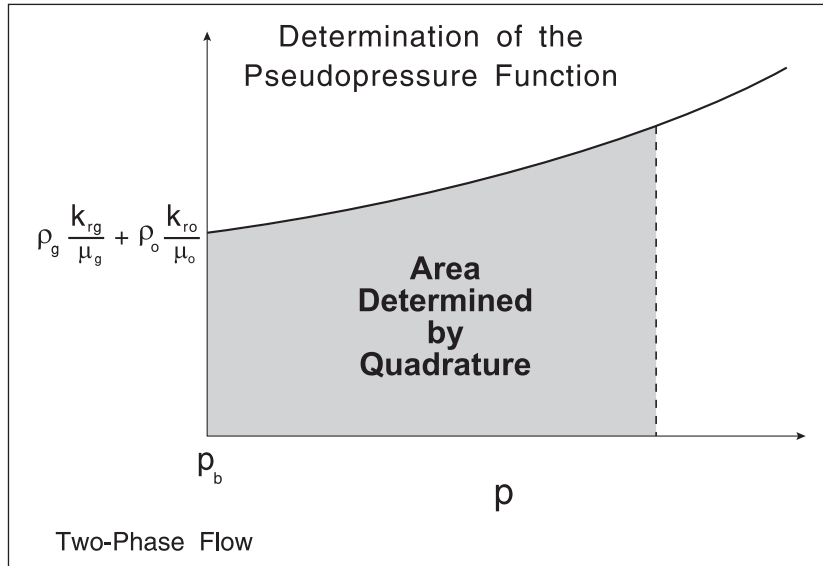


Fig. 3-33. Computation of the two phase pseudopressure by quadrature

The choice of the reference viscosity and density in the definition of  $\psi(p)$  is different depending on the state of the reservoir fluid. In the case of a gas-condensate reservoir, when the reservoir fluid is single-phase gas above the dew point, the reference condition is the gas viscosity and density at initial pressure,  $\mu_{gi}$  and  $\rho_{gi}$ , respectively. Conversely in an oil reservoir, where the reservoir fluid is oil at or above the bubble point (solution gas drive), the reference condition is the oil viscosity and density at reservoir initial pressure. Thus the following cases can be stated:

Gas condensate:

$$\psi(p) = \frac{\mu_{gi}}{\rho_{gi}} \int_{p_b}^p \left( \frac{k_{ro}\rho_o}{\mu_o} + \frac{k_{rg}\rho_g}{\mu_g} \right) dp' \quad (3-152)$$

$$\psi_D = \frac{\psi(p_e) - \psi(p_w)}{\frac{m_t \mu_{gi}}{2\pi k h \rho_{gi}}} = \ln \frac{r_e}{r_w} \quad (3-153)$$

Solution gas drive:

$$\psi(p) = \frac{\mu_{oi}}{\rho_{oi}} \int_{p_b}^p \left( \frac{k_{ro}\rho_o}{\mu_o} + \frac{k_{rg}\rho_g}{\mu_g} \right) dp' \quad (3-154)$$

$$\psi_D = \frac{\psi(p_e) - \psi(p_w)}{\frac{m_t \mu_{oi}}{2\pi k h \rho_{oi}}} = \ln \frac{r_e}{r_w} \quad (3-155)$$

The two-phase compositional well inflow model, which has been derived for SS radial flow, can now be generalized for SSS conditions and the total skin factor  $S_a$  introduced to handle all the complicating effects previously discussed; thus

$$\psi_D = \frac{\psi(\bar{p}) - \psi(p_w)}{\frac{m_t \mu_{gi}}{2\pi k h \rho_{gi}}} = \frac{1}{2} \ln \frac{4\bar{A}}{\gamma C_A r_w^2} + S_a \quad (3-156a)$$

for a gas-condensate well, or for solution gas drive

$$\psi_D = \frac{\psi(\bar{p}) - \psi(p_w)}{\frac{m_t \mu_{oi}}{2\pi k h \rho_{oi}}} = \frac{1}{2} \ln \frac{4\bar{A}}{\gamma C_A r_w^2} + S_a \quad (3-156b)$$

The concept of two-phase pseudopressure allows the results from single-phase liquid flow to be used directly in the two-phase case. The only major problem is the incorporation of a non-Darcy term into the inflow model; this issue is treated in the next section.

## Spherical steady-state non-Darcy flow

In gas-condensate wells, there is an interaction between the influence of liquid dropout, i.e., retrograde condensation, and the non-Darcy flow effect in the vicinity of the perforation tips. The total apparent skin  $S'_a$  is a complicated combination of mechanical skin, two-phase flow effect, and the non-Darcy contribution. It is therefore necessary to develop a model for gas-condensate well inflow that incorporates all these phenomena and provides a basis for analyzing measured skin factors in condensate wells. Since non-Darcy flow is confined to the region near perforation tips, a spherical flow model will be derived that can be applied in conjunction with the flow shape factors already introduced in the preceding chapter. The basis of this model is that non-Darcy flow is limited to the gas phase for which the Forchheimer equation may be written as

$$\frac{dp}{dr} = \frac{\mu_g}{kk_{rg}} \frac{m_g}{4\pi r^2 \rho_g} + \beta \rho_g \left( \frac{m_g}{4\pi r^2 \rho_g} \right)^2 \quad (3-157)$$

The flow of the condensate (liquid) phase is described by the Darcy-flow-only expression

$$\frac{dp}{dr} = \frac{\mu_o}{kk_{ro}} \frac{m_o}{4\pi r^2 \rho_o} \quad (3-158)$$

The local saturation is now given by the condition that the pressure gradient is the same in both phases, i.e., capillary pressure is neglected; thus at radius  $r$ , where the pressure is  $p$ , the saturation is given by the condition

$$\mathbf{f}_{\text{rnd}}(S_o) = \frac{\mu_g}{kk_{rg}} \frac{m_g}{4\pi r^2 \rho_g} + \beta \rho_g \left( \frac{m_g}{4\pi r^2 \rho_g} \right)^2 - \frac{\mu_o}{kk_{ro}} \frac{m_o}{4\pi r^2 \rho_o} = 0 \quad (3-159)$$

The spherical flow equation (3-157) with the saturation given by nonlinear relation (3-159) can be integrated using a standard numerical integration technique such as the Runga–Kutta method between the limits of  $r_s$ —the spherical source radius—and  $r_e$ . The nonlinear equation (3-159) is solved using a root-finding algorithm such as the secant method. Note that the local saturation is affected by the non-Darcy component of the pressure gradient, i.e., the saturation is driven to a smaller value at small  $r$  to accommodate the increased gradient in the gas phase due to inertial effects. In the case where  $\beta$  is zero, Eq. (3-159) reduces to

$$\mathbf{f}_{\text{rpr}}(S_o) = \frac{\mu_g}{k_{rg}} \frac{m_g}{\rho_g} - \frac{\mu_o}{k_{ro}} \frac{m_o}{\rho_o} = 0 \quad (3-160)$$

which is identical to (3-144a and b). In order to introduce the two-phase pseudopressure, Eqs. (3-157) and (3-158) are written in the form

$$\frac{\rho_g k_{rg}}{\mu_g} dp = \left( \frac{m_g}{4\pi r^2 k} + \frac{k_{rg} \beta}{\mu_g} \left( \frac{m_g}{4\pi r^2} \right)^2 \right) dr \quad (3-161)$$

$$\frac{\rho_o k_{ro}}{\mu_o} dp = \frac{m_o}{4\pi r^2 k} dr \quad (3-162)$$

which on addition yields

$$\left( \frac{\rho_g k_{rg}}{\mu_g} + \frac{\rho_o k_{ro}}{\mu_o} \right) dp = \left( \left( \frac{m_g}{4\pi r^2 k} + \frac{m_o}{4\pi r^2 k} \right) + \frac{k_{rg} \beta}{\mu_g} \left( \frac{m_g}{4\pi r^2} \right)^2 \right) dr$$

$$\text{i.e.,} \quad \frac{\mu_{gi}}{\rho_{gi}} \left( \frac{\rho_g k_{rg}}{\mu_g} + \frac{\rho_o k_{ro}}{\mu_o} \right) dp = \left( \left( \frac{m_t \mu_{gi}}{4\pi r^2 k \rho_{gi}} \right) + \frac{k_{rg} \beta \mu_{gi}}{\mu_g \rho_{gi}} \left( \frac{m_g}{4\pi r^2} \right)^2 \right) dr \quad (3-163)$$

which can be integrated between the limits of  $r_s$  and  $r_e$  where the corresponding pressures are  $p_w$  and  $p_t$ , i.e.,

$$\int_{p_w}^{p_t} \frac{\mu_{gi}}{\rho_{gi}} \left( \frac{\rho_g k_{rg}}{\mu_g} + \frac{\rho_o k_{ro}}{\mu_o} \right) dp = \int_{r_e}^{r_s} \frac{m_t \mu_{gi}}{4\pi k \rho_{gi}} \frac{dr}{r^2} + \int_{r_s}^{r_e} \frac{k_{rg} \beta \mu_{gi}}{\mu_g \rho_{gi}} \left( \frac{m_g}{4\pi} \right)^2 \frac{dr}{r^4} \quad (3-164)$$

An approximate integration of this formula can be achieved if  $k_{rg}$ ,  $\mu_g$ , and  $m_g$  can be treated as constants at some representative conditions; once again, the average pressure  $(p_t + p_w)/2$  seems a reasonable choice. Thus Eq. (3-164) is written in integrated form as

$$\psi(p_t) - \psi(p_w) = \frac{m_t \mu_{gi}}{4\pi k \rho_{gi} r_s} + \frac{\bar{k}_{rg} \beta \mu_{gi} \bar{m}_g^2}{3(4\pi)^2 \bar{\mu}_g \rho_{gi} r_s^3} \quad (3-165)$$

To determine whether this approximate formula is valid over a wide range of conditions requires a comparison of the results of (3-165) and the exact integration of the differential form (3-157) in conjunction with (3-159). The most difficult issue is the saturation at which  $\bar{k}_{rg}$  is to be evaluated.

In the context of a perforated completion, Eq. (3-165) can be applied with  $m_t$  replaced by the mass flow rate per perforation  $m_{pt} = m_t/N_p$  as before; the non-Darcy pseudopressure drop therefore becomes on introducing the flow shape factor

$$\Delta\psi_{ND} = f_{ND}^s \frac{\bar{k}_{rg} \beta \mu_{gi} \bar{m}_g^2}{3(4\pi)^2 \bar{\mu}_g \rho_{gi} r_s^3 N_p^2} \quad (3-166)$$

or in dimensionless terms

$$\frac{\Delta\psi_{ND}}{2\pi k h \rho_{gi}} = f_{ND}^s \frac{kh \bar{k}_{rg} \beta \bar{m}_g^2}{24\pi \bar{\mu}_g r_s^3 N_p^2 m_t^2} m_t \quad (3-167a)$$

In gas field units with  $m_t$  in lb/day

$$\frac{\Delta\psi_{ND}}{158.02m_t\mu_{gi}} = f_{ND}^s \frac{1.82974 \times 10^{-16} kh\bar{k}_{rg} \beta \bar{m}_g^2}{24\pi\bar{\mu}_g r_s^3 N_p^2 m_t^2} m_t \quad (3-167b)$$

The inertial resistance coefficient  $\beta$  is a fundamental rock property which can be measured directly by special core analysis. However, it is common practice to estimate the inertial resistance coefficient from a correlations of the form

$$\beta = \frac{2.6 \times 10^{10}}{k^{1.2}} \quad (3-168)$$

where  $\beta$  is in  $ft^{-1}$  and  $k$  is in md. When a liquid saturation exists in the core, it is recommended that  $k$  be replaced by the product  $kk_{rg}$ , i.e., for two-phase flow

$$\beta = \frac{2.6 \times 10^{10}}{(kk_{rg})^{1.2}} \quad (3-169)$$

Thus the inertial resistance coefficient is increased by the presence of a liquid saturation; however, the term  $(\bar{m}_g/m_t)^2$  in Eq. (3-167a and b) will reduce the non-Darcy term because the mass flow of gas is less than the total mass flow  $m_t$ . The net result is that the two-phase non-Darcy effect is very little different from that in dry gas. The formulation (3-169) is included in the model for the two-phase non-Darcy pseudopressure drop.

## Behavior of the pseudopressure function

In order to examine the inflow behavior of a two-phase compositional system, it is useful to consider a typical gas-condensate reservoir fluid and construct the normalized pseudopressure function  $\psi(p)$ . The most important information regarding a gas condensate system is the liquid dropout curve shown in figure 3-34 based on the mass fraction condensate  $x$ . The main feature of retrograde condensation is that below the dew point pressure the liquid fraction rises sharply and then stabilizes at an approximately constant value over quite a wide pressure range before revaporization occurs at relatively low pressure and the amount of liquid phase decreases again. The phase densities and viscosities are shown in figure 3-35a and b, where the vapor-liquid equilibrium (VLE) package has used the Patel and Teja equation of state to compute densities and the corresponding states method to estimate phase viscosities. It should be emphasized that there is very little laboratory data on retrograde condensate viscosity and the predicted values cannot be usually be checked against any direct measurements. However, it is useful to observe that the condensate liquid (or more properly dense phase) is about 10 times more viscous than the gas phase; note that this particular condensate is not near critical conditions where phase densities and viscosities become almost identical. In order to calculate  $\psi(p)$ , it is also necessary to have available a set of relative permeability curves. Again, it is very difficult to find good experimental

measurements of gas-condensate relative permeability and the curves shown in figure 3–36a represent one of the few sets to be found in the literature. Proper understanding of condensate inflow behavior is limited by the accuracy of the liquid dropout, density, viscosity, and relative permeability data that are available; this is the main difficulty with the pseudopressure approach which requires this information for the generation of the appropriate  $\psi(p)$  function (fig. 2–36b).

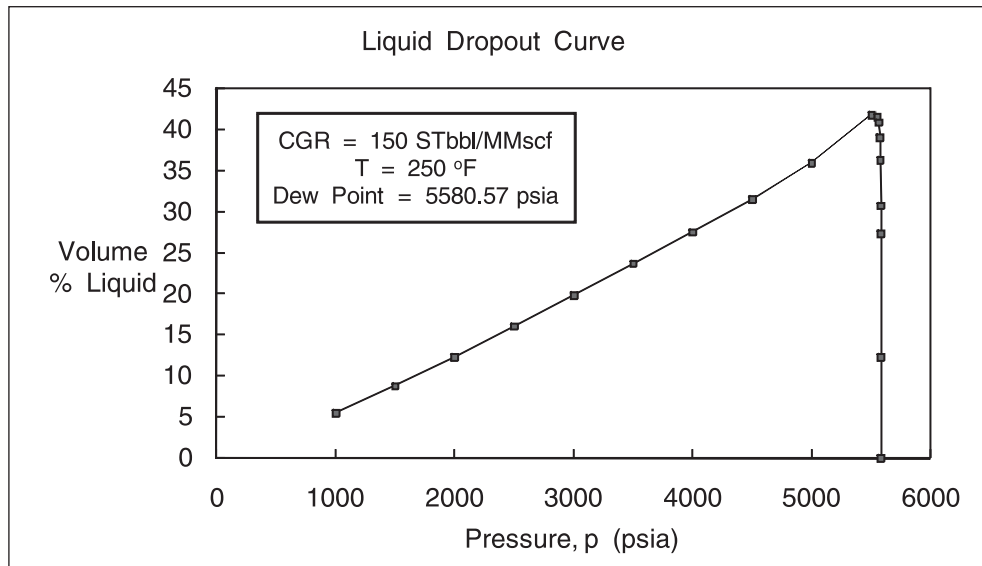


Fig. 3–34. Typical condensate liquid drop-out curve

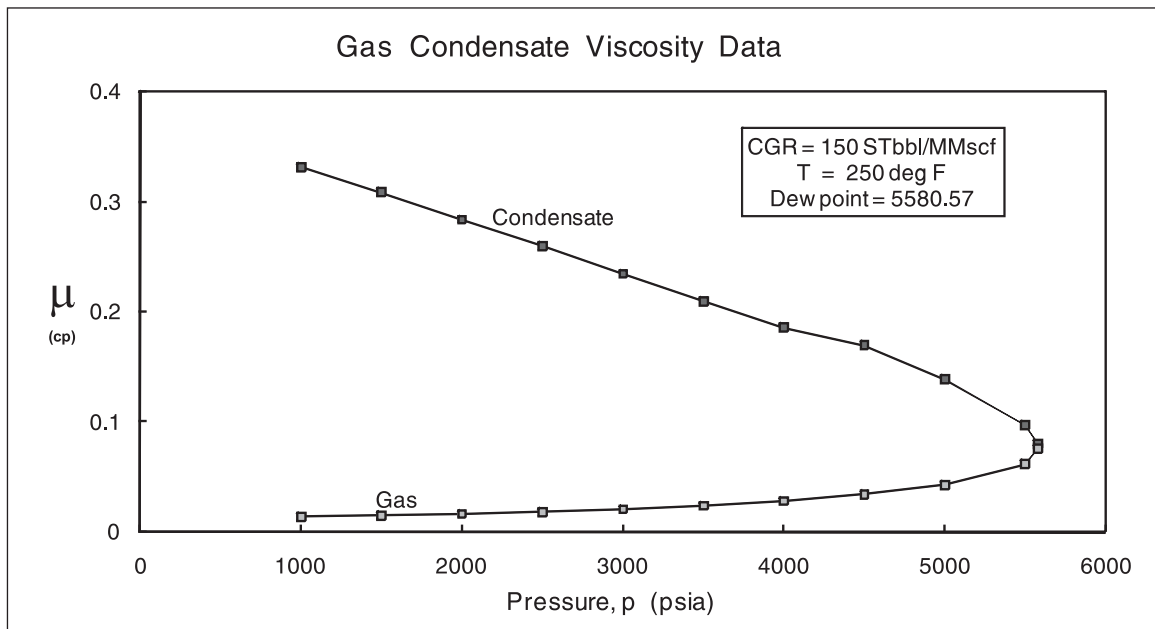


Fig. 3–35a. Phase viscosity information

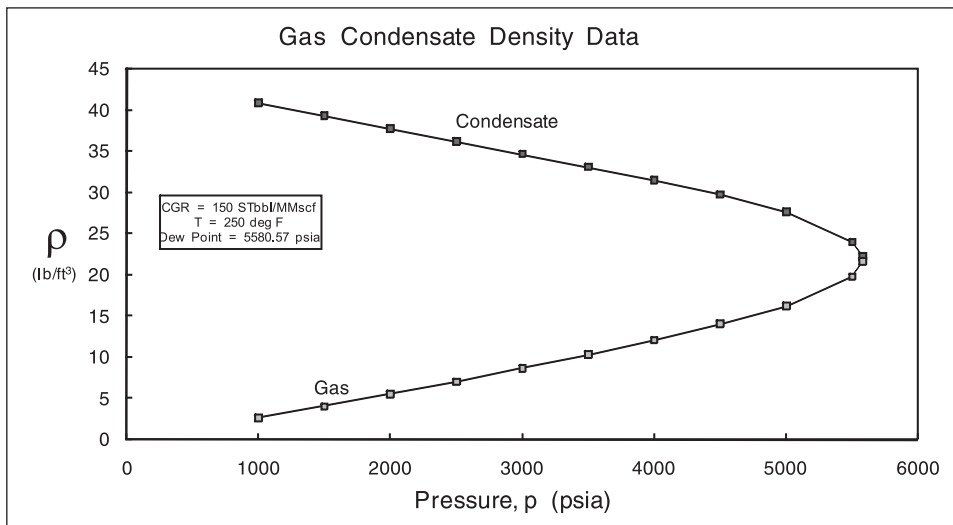


Fig. 3–35b. Phase density information

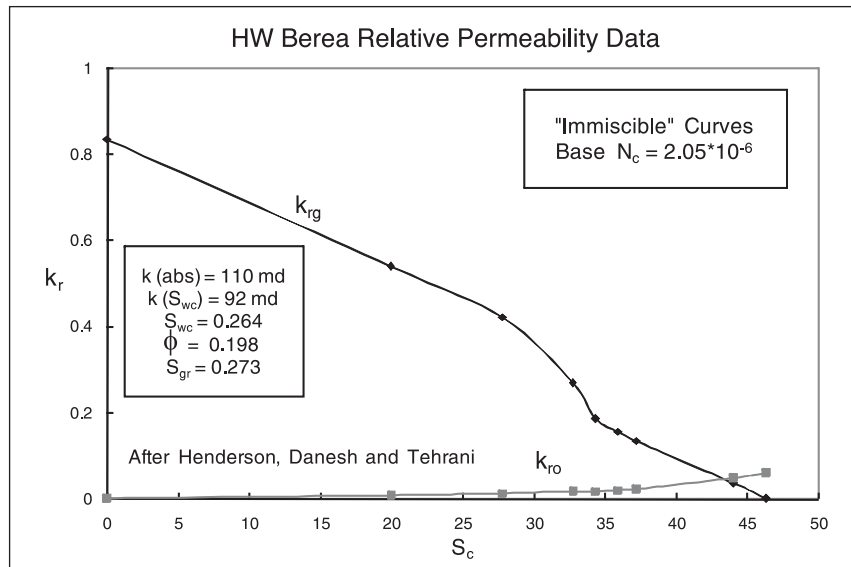


Fig. 3–36a. Measured gas-condensate relative permeability curves

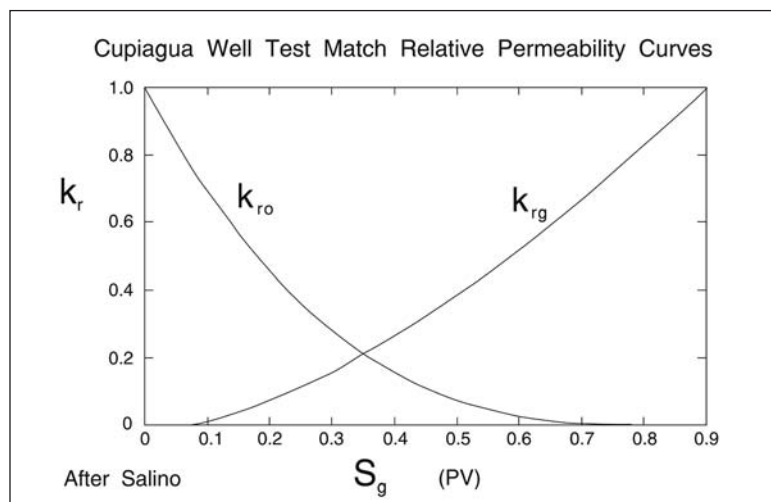


Fig. 3–36b. Gas-condensate relative permeability curves from matching field pressure data



Given then the relative permeability curves of figure 3–36b and the liquid dropout curve of figure 3–34, the pseudopressure may be computed by quadrature using Simpson’s rule as shown diagrammatically in figure 3–33; the resultant  $\psi(p)$  function versus  $p$  is shown in figure 3–37. As can be seen, the pseudopressure function for a gas-condensate system exhibits two straight line sections. Above the dew point pressure, the two phase pseudopressure has the property

$$\frac{d\psi(p)}{dp} = 1 \quad (3-170)$$

i.e., the single-phase gas is behaving essentially as an incompressible fluid. The single-phase gas pseudopressure defined as

$$\psi_g(p) = \frac{\mu_{gi}}{\rho_{gi}} \int_{p_b}^p \frac{\rho_g}{\mu_g} dp \quad (3-171)$$

is also plotted on figure 3–37 from which it is evident that, at high pressure, the gas pseudopressure is given by a relation of the form

$$\psi(p) = p + c \quad (3-172)$$

implying that the ratio  $\frac{\rho_g}{\mu_g}$  is constant and equal to  $\frac{\rho_{gi}}{\mu_{gi}}$ . The surprising feature of the two-phase pseudopressure function is the appearance of the second straight line below the dew point pressure which extends down to about 1,000 psia. The slope of this line is given by

$$\left. \frac{d(\psi)}{dp} \right|_{tp} = M' = \overline{\frac{\rho_g k_{rg} \mu_{gi}}{\mu_g \rho_{gi}} + \frac{\rho_o k_{ro} \mu_{gi}}{\mu_o \rho_{gi}}} \quad (3-173)$$

which for the example case is about 0.25, i.e., roughly four times less than the single-phase gas value of unity. The fact that the pseudopressure function is linear over a substantial pressure range implies that the argument of the pseudopressure integral, i.e.,

$$\overline{\frac{\rho_g k_{rg} \mu_{gi}}{\mu_g \rho_{gi}} + \frac{\rho_o k_{ro} \mu_{gi}}{\mu_o \rho_{gi}}} \quad (3-174)$$

is constant and the overbar indicates that the quantity  $\frac{\rho_g k_{rg}}{\mu_g} + \frac{\rho_o k_{ro}}{\mu_o}$  is virtually independent of pressure in the specified range. Inspection of the liquid dropout curve of figure 3–44 shows that in a gas-condensate system the liquid mass fraction is approximately constant over a wide pressure range below the dew point, as are the phase densities and viscosities. Hence, the liquid saturation predicted by Eq. (3–144a and b) does not vary very much and the argument (3–174) is essentially

constant; note that both terms in Eq. (3–174) are less than unity. The pseudopressure function therefore exhibits two straight line sections with a slope ratio  $M'$  determined by the mobility of single-phase gas relative to that of the two phase mixture which exists below the dew point. The effective mobility of the two-phase mixture is affected by the high viscosity of the condensate phase but this is compensated to some extent by its higher density. For the condensate system chosen as an example, the mobility of the two-phase mixture is approximately one-quarter of the gas mobility. This is the liquid dropout effect which increases the pressure gradient required for the simultaneous flow of a two-phase mixture. It is interesting to observe that the system behaves as a constant liquid fraction mixture of specific mobility. Below a pressure of around 1,000 psia, the pseudopressure function exhibits nonlinearity due to the variation in gas density  $\rho_g$  and the revaporization of condensate at low pressure as shown in the liquid dropout curve.

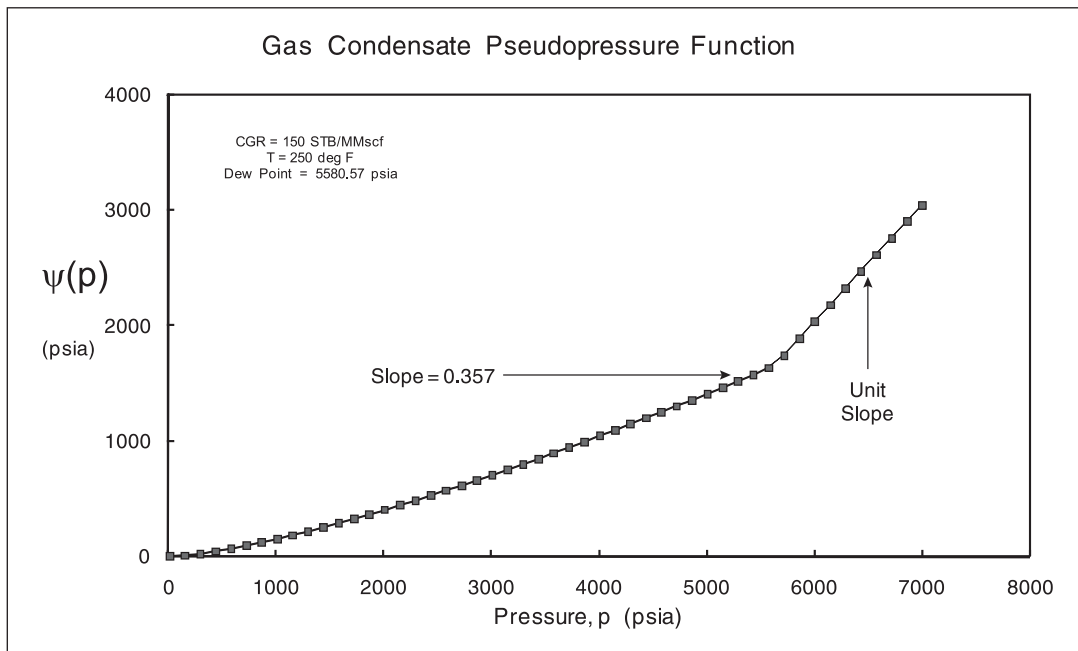


Fig. 3–37. Typical condensate pseudopressure function

In the single-phase region, Darcy's law takes the form

$$\frac{m_t}{A} = \frac{k\rho_{gi}}{\mu_{gi}} \frac{dp}{dr} \quad (3-175)$$

while in the two-phase region, assuming a mixture of constant vapour–liquid ratio, Darcy's law becomes

$$\frac{m_t}{A} = \frac{m_g + m_o}{A} = \left( \frac{kk_{rg}\rho_g}{\mu_g} + \frac{kk_{ro}\rho_o}{\mu_o} \right) \frac{dp}{dr} \quad (3-176)$$

Hence the quantity  $M'$  defined as

$$M' = \frac{\rho_g k_{rg} \mu_{gi}}{\mu_g \rho_{gi}} + \frac{\rho_o k_{ro} \mu_{gi}}{\mu_o \rho_{gi}} \quad (3-177)$$

is the ratio of the density-weighted mobility of the two-phase mixture to that of single-phase gas, and Eq. (3-176) may be written as

$$\frac{m_t}{A} = \frac{m_g + m_o}{A} = \frac{k_{gi} M' dp}{\mu_{gi} dr} \quad (3-178)$$

In a compositional model, it is recognized that the mass flows of gas and liquid sum to a constant total, i.e.,  $m_t = m_g + m_o$ , and, although the liquid is more viscous than gas, it is also denser and the superficial velocity of the mixture may decrease as retrograde condensation occurs. Thus the mobility ratio  $M'$  depends on

- the liquid dropout  $x$ , which helps to fix the saturations  $S_o$  and  $S_g$ ;
- the combined density–viscosity ratio  $\frac{\mu_o \rho_g}{\mu_g \rho_o}$ ;
- the relative permeability curves  $k_{rg}$  and  $k_{ro}$ .

The closer a condensate system is to the critical point, the closer the phase properties become, and  $M'$  approaches unity (remembering that the relative permeability curves tend to straight lines as the interfacial tension tends to zero). Thus if conditions are near critical, the effect of two-phase flow is negligible since the two-phase mixture is extremely close to single-phase gas in its properties.

In order to estimate the magnitude of the blocking effect of two-phase flow, the mass fraction gas corresponding to the maximum in the liquid dropout curve can be determined from the PVT model; let this quantity be denoted  $x^{MLD}$ . The gas saturation corresponding to  $x^{MLD}$ , found by solving Eq. (3-144a and b), is similarly denoted  $S_g^{MLD}$  and the mobility of this two-phase mixture is

$$\left[ \frac{\rho_g k_{rg}}{\mu_g} + \frac{\rho_o k_{ro}}{\mu_o} \right]^{MLD} \quad (3-179)$$

This is close to the average mobility in the two-phase region and the ratio

$$\frac{\left[ \frac{\rho_g k_{rg}}{\mu_g} + \frac{\rho_o k_{ro}}{\mu_o} \right]^{MLD}}{\frac{\rho_{gi}}{\mu_{gi}}} \quad (3-180)$$

# 4

## Gas Reservoir Material Balance

---

### Introduction

An important topic in gas reservoir engineering is the problem of water influx from an aquifer. In general, the influx of water is undesirable since gas is trapped as a residual saturation at high pressure and the inflow performance of the gas-producing wells deteriorates as a water-cut develops. It is therefore essential to try and detect any aquifer movement as early as possible. The material balance approach using pressure depletion data is the first reservoir monitoring exercise that can give a clue to natural water drive. Gas reservoirs vary in nature from straightforward volumetric depletion to strong water drive situations. The prediction of water influx is uncertain because of the difficulty of assessing the degree of communication between the aquifer and the gas reservoir. There may be continuous barriers present near the gas–water contact which inhibit the influx of water, and faulting may also impose restrictions to fluid flow in the aquifer–reservoir system. Aquifer influx will be aided by any high-permeability layers extending down into the water leg. Obviously, the first stage in assessing water movement is to appraise the geological model and examine the scope for influx. Frequently, permeabilities are much less in the aquifer than in the gas column due to diagenesis continuing there after it has stopped at accumulation in the hydrocarbon zone. In the appraisal of a gas field, it is important to try and obtain some information on permeabilities in the aquifer from core analysis. If water influx eventually becomes a problem, it will be necessary to run a reservoir simulation to see how to best control the problem and data will be required to carry out such studies. Even at the field development stage, it is necessary to try and anticipate water production since facilities will have to be provided to handle the situation. Water influx has a very large impact on the ultimate gas recovery and hence on producible reserves—many mistakes have been made in overestimating gas reserves in fields which have turned out to have strong water drive contrary to expectation. Much experience of water drive gas reservoirs has been obtained in the Gulf of Mexico, and the ultimate recovery factor of many exhausted fields provides good insight into the effects of water influx and how it can be detected. The methods that will be described here have been developed in part from studies of these fields.

## Volumetric reserves calculation

The first calculation of the reserves of a gas reservoir occurs at the field appraisal stage when the hydrocarbon pore volume  $V_{gi}$  is computed by an integration of the form

$$V_{gi} = \int \phi(1 - S_{wc})dV \quad (4-1)$$

This integral is computed from maps of the reservoir thickness, porosity, and water saturation across the field based on geophysical (seismic), log, and core data; sophisticated mapping packages are used to carry out this volumetric determination of the initial hydrocarbon in place. However, knowledge of the full extent of the field may be limited, and the process of interpolation of parameters between the measuring points (wells) is subject to uncertainty. Also, the extent to which different sand bodies are in communication is not known at this stage, and some form of cutoff will usually have been employed to designate nonproductive pay. Hence it is necessary to confirm the reserves estimate by monitoring the depletion rate of the field once production starts. In some cases, the reservoir turns out to be much larger than originally thought, and in other situations it proves to be smaller in the sense that the compartments communicating with the wells are not extensive. Reservoir limit testing is therefore a very important part of gas reservoir engineering.

The mass of gas in place (GIP)  $m_{gi}$  is given by

$$m_{gi} = V_{gi}\rho_i \quad \text{where} \quad \rho_i = \frac{M_w p_i}{z_i RT} \quad (4-2)$$

and  $p_i$  is the initial reservoir pressure determined from wireline formation tester surveys or well tests in the appraisal wells. The equation of state for a real gas, i.e., the definition of the compressibility factor  $z$ , plays a key role in understanding depletion, and figure 4–1 shows the variation of compressibility factor with pressure for a typical reservoir gas at reservoir temperature. The compressibility  $c_g$  of a real gas is given by

$$c_g = \frac{1}{p} - \frac{1}{z} \frac{dz}{dp} \quad (4-3)$$

and this also may be obtained from the equation of state as shown in figure 4–2, where it can be seen that at high pressure the compressibility becomes almost constant, i.e., the fluid “gas” is behaving as a liquid.

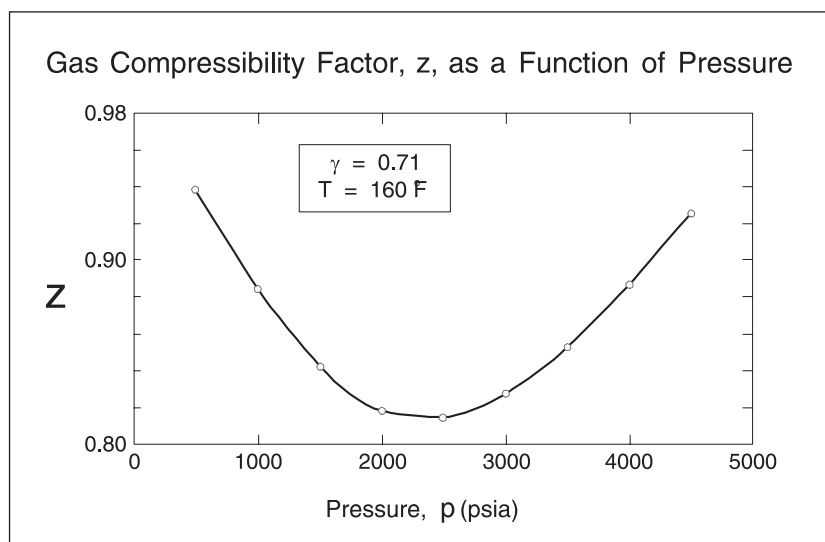
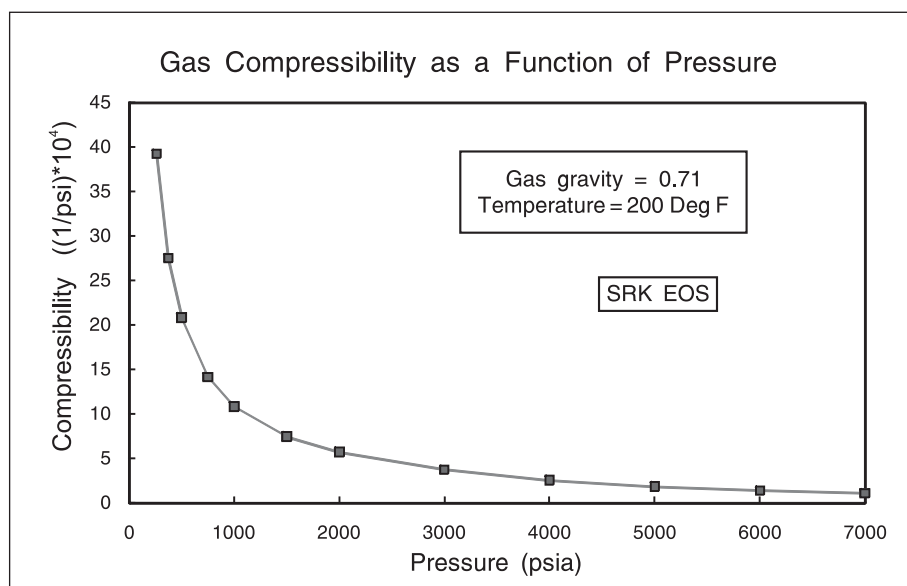


Fig. 4-1. Variation of compressibility factor with pressure

Fig. 4-2. Variation of the compressibility  $c_g$  with pressure

## Gas Material Balance

The material balance method is a fundamental reservoir engineering tool for the evaluation of past and future overall reservoir performance. It is based on the law of conservation of mass applied to the total system. Applied to past performance, a material balance analysis provides insight into the prevailing production mechanism and allows the estimation of the hydrocarbons initially in place. In its predictive mode, the material balance can be used to generate future reservoir performance and to estimate potential recovery. The simplest gas material balance treats the gas reservoir as a tank at a uniform pressure  $p$ ; this is justified in many cases because of the low viscosity of gas which tends to minimize pressure differences in the reservoir. However,

the possibility of compartmentalization is always present—an issue which will be mentioned later. Thus the pressure is associated with the average pressure of the whole reservoir and it is assumed that this can be measured by pressure buildups in the wells: an important part of the material balance approach is to regularly measure the reservoir pressure. Indeed, in the early days of reservoir engineering, the reason for carrying out pressure build-up surveys was for material balance studies. The zero-dimensional material balance for a gas accumulation takes the form

$$m_g = m_{gi} - m_{gp} \quad (4-4)$$

where  $m_g$  = mass of gas presently in reservoir,

$m_{gi}$  = mass of gas initially present in reservoir, and

$m_{gp}$  = cumulative mass of gas produced from the system.

Normally, a precise record of the cumulative gas production will be available from field off-take monitoring. The in situ volume of gas remaining in the reservoir  $V_g$  is given by the equation of state for a real gas, i.e.,

$$V_g = \frac{m_g zRT}{M_w p} = \frac{(m_{gi} - m_{gp})zRT}{M_w p} \quad (4-5)$$

The mass of gas  $m_g$  is related to the volume at standard conditions  $G$  by the equation

$$G = \frac{m_g}{\rho_{sc}} \quad \text{where} \quad \rho_{sc} = \frac{M_w p_{sc}}{RT_{sc}} \quad (4-6)$$

Hence the material balance in terms of standard volumes may be written as

$$V_g = \frac{(G_i - G_p)zT p_{sc}}{p T_{sc}} \quad (4-7)$$

This equation simply predicts the actual volume  $V_g$  of the gas remaining in the reservoir after a cumulative production  $G_p$  from an initial GIP of  $G_i$ . The real gas compressibility factor  $z$  is a function of pressure  $p$ , and hence this equation is nonlinear; an equation of state, e.g. the cubic, three-parameter Schmidt–Wenzel equation, can be used to obtain accurate  $z$  factors. In field units with  $p_{sc} = 14.7$  psia and  $T_{sc} = 520^\circ\text{R}$ , this becomes

$$V_g = \frac{(G_i - G_p)zT}{35.37p} \quad (4-8)$$

which is a working equation for in situ gas volume.

## Case 1—No water influx

In the case where there is no water influx, i.e.,  $W_e = 0$  and changes in connate water and pore volume can be neglected, the present gas volume  $V_g$  is, in fact, identical to the initial gas filled pore volume  $V_{gi}$  which is related to the initial GIP  $G_i$  through the equation

$$\frac{V_{gi}P_i}{z_i T} = \frac{G_i P_{sc}}{T_{sc}} \quad (4-9a)$$

i.e., 
$$V_{gi} = G_i \frac{z_i T P_{sc}}{T_{sc} P_i} = \frac{G_i}{E_i} \quad \text{where} \quad E_i = \frac{T_{sc} P_i}{z_i T P_{sc}} \quad (4-9b)$$

The quantity  $E$  is known as the *gas expansion factor* since it represents the ratio of the volume of a mass of gas at standard conditions to the volume at in situ conditions.

Putting  $V_g = V_{gi} = G_i \frac{z_i T P_{sc}}{T_{sc} P_i} = \frac{G_i}{E_i}$  in the gas material balance (4-7) gives, after rearrangement

$$\frac{P}{z} = \frac{P_i}{z_i} - \frac{P_i}{z_i G_i} G_p \quad (4-10)$$

Thus when  $\frac{P}{z}$  is plotted against  $G_p$ , a straight line of slope  $-\frac{P_i}{z_i G_i}$  should result: this is the basis of the well known  $\frac{p}{z}$  plot of gas reservoir engineering illustrated in figure 4-3.

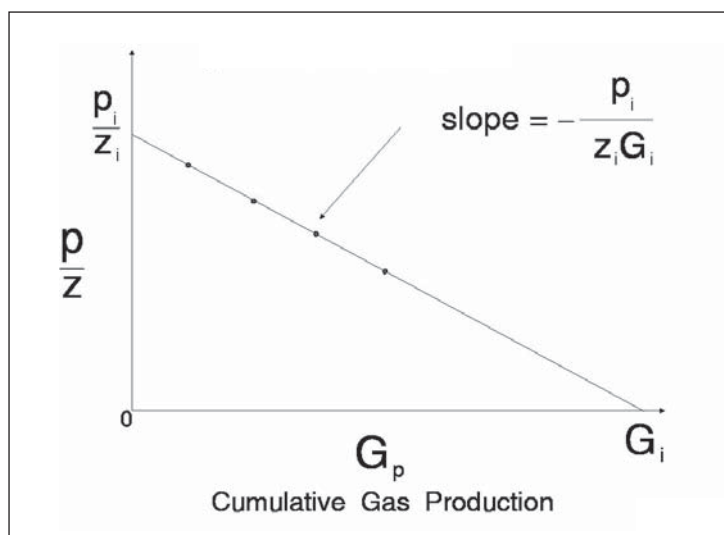


Fig. 4-3.  $p/z$  Plot for a volumetric depletion gas reservoir

The initial GIP  $G_i$  is determined from the intercept of the straight line with the  $G_p$  axis at  $p/z = 0$  as shown in the diagram. Thus the GIP can be estimated from the pressure depletion data; if this is substantially different from the value obtained by integration, then the discrepancy should be investigated as discussed below.



For volumetric depletion, the recovery efficiency  $E_{rg}$ —defined as the fractional recovery at abandonment—is given by

$$E_{rg} = \frac{G_{pa}}{G_i} = \left( 1 - \frac{p_a z_i}{p_i z_a} \right) \quad (4-11)$$

where  $p_a$  is the abandonment pressure and  $z_a$  is the corresponding compressibility factor. The eventual abandonment pressure is an economic decision based on the costs of gas compression and delivery to gas customers.

However, such a calculation of the original GIP, i.e. reserves, should be treated with caution since it is based on several simplifying assumptions:

- no water influx;
- single compartment (tank) gas reservoir;
- negligible formation and connate water compressibility.

In practice, the phenomena of water influx, compartmentalization, and high formation compressibility (in abnormally pressured reservoirs) are frequently of importance and the simple material balance approach can give quite wrong estimates of reserves. The  $p/z$  plot is a very useful indicator of reservoir behavior, but it is dangerous to automatically interpret the slope or intercept in terms of  $G_i$ . In the following sections, the effects of these other phenomena will be considered.

An example of a  $p/z$  plot for a Middle East gas reservoir is shown in figure 4–4a, where a very nice straight line is obtained extrapolating to nearly 130 bcm; there is always an issue whether or not the initial reservoir pressure should be used. In principle, it should be included in the fit but, if the measured value is subject to error, then it is better to omit  $p_i$  from the regression points. The initial reservoir pressure  $p_i$  is a true average pressure since there is no pressure variation through the reservoir at the time  $t = 0$ . Subsequent pressures may not be true averages but simply the extrapolation of Horner plots to infinite shut-in time  $p^*$  or  $p^{**}$ . In this case, the  $p/z$  plot will have the form shown in figure 4–4b, where the anomaly between  $p_i$  and later pressures is apparent. The correct GIP is obtained by maintaining the slope of the later points and shifting the line to coincide with the initial pressure. Only in the case where the Matthews, Brons, and Hazebroek (MBH) method using Dietz shape factors is employed are the pressures genuine average quantities. Suppose the extrapolated pressures differ from true average pressure by an amount  $\delta p$ , then the material balance equation becomes

$$\frac{\bar{p}}{z} = \frac{p^* + \delta p}{z} = \frac{p_i}{z_i} - \frac{p_i}{z_i G_i} G_p \quad (4-12a)$$

i.e.,

$$\frac{p^*}{z} = \frac{p_i}{z_i} - \frac{\delta p}{z} - \frac{p_i}{z_i G_i} G_p \quad (4-12b)$$

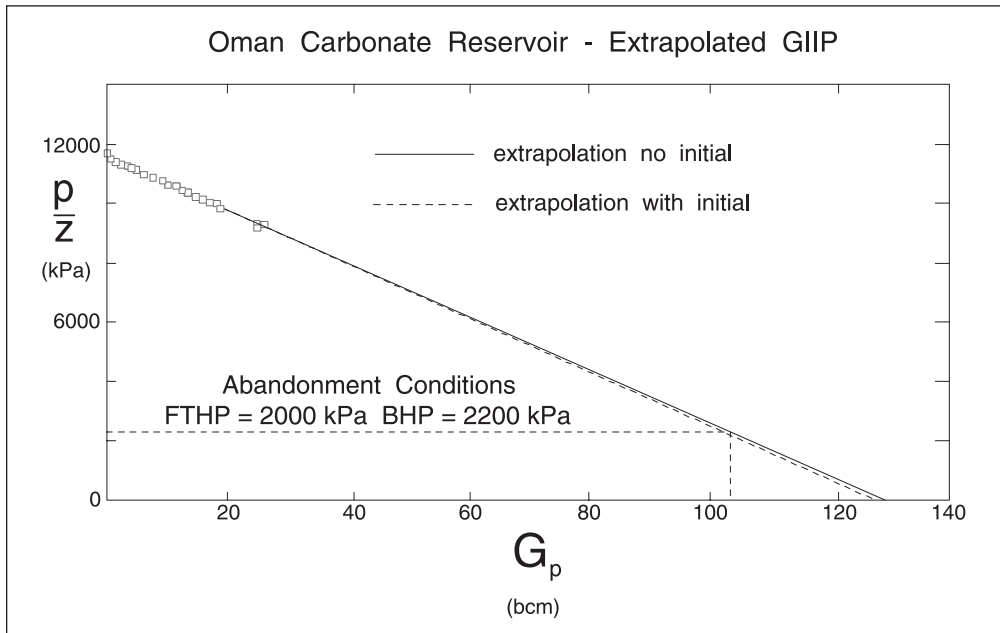
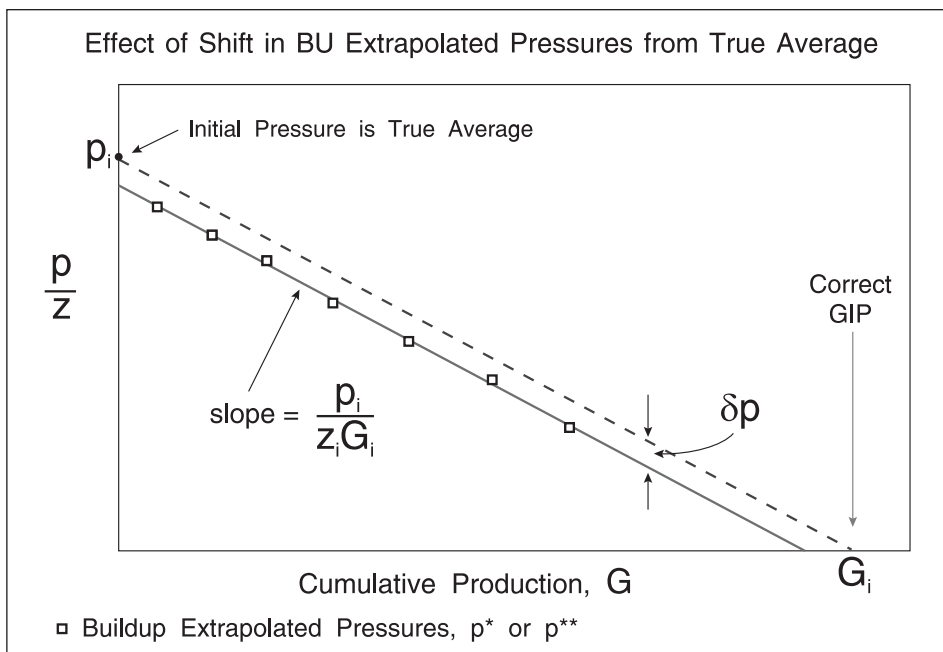
Fig. 4-4a.  $p/z$  Plot for Omani Reservoir

Fig. 4-4b. Effect of shift in BU extrapolated pressure

This suggests that the slope of the  $\bar{p}/z$  plot, i.e.,  $p_i/(z_i G_i)$  is a better indicator of gas-in-place than the intercept; this corresponds to the situation in oil where semi-steady-state (SSS) depletion is analyzed on the basis of the slope of a straight line on the Cartesian graph.

For a fixed pore volume, i.e.,  $V_g = V_{gi}$  the material balance may be written in differential form over a time interval  $\delta t$  as

$$V_g \rho(p) - V_g \left\{ \rho(p) + \frac{\partial \rho}{\partial p} \delta p \right\} = m \delta t \quad (4-13)$$

Here  $m$  is the mass flow rate at which the tank reservoir of pore volume  $V_g$  is produced. The compressibility of a fluid  $c$  is defined as

$$c = \frac{1}{\rho} \frac{\partial \rho}{\partial p} \quad \text{i.e.} \quad \frac{\partial \rho}{\partial p} = c\rho \quad (4-14)$$

and substituting (4-14) into (4-13), on taking the limit, gives

$$V_g c \frac{dp}{dt} = -\frac{m}{\rho} \quad (4-15)$$

In the treatment that follows, the forward integration of differential equations based on (4-15) will be used as the basis for material balance calculations. For a gas, both  $c$  and  $\rho$  are pressure dependent but—in the case of fixed gas pore volume—Eq. (4-15) is an exact expression, albeit nonlinear, of the material balance.

## Abnormally pressured gas reservoirs

In some situations, notably in geopressured reservoirs, the gas compressibility during the early stages of depletion may be of the same order of magnitude as the water and reservoir compressibility and these effects have to be included in the material balance equation. This problem has been addressed by Hammerlindl,<sup>1</sup> and the methodology described here follows the treatment in his paper. Any reservoir whose pressure exceeds the hydrostatic pressure of brine is an abnormally pressured system; a typical hydrostatic gradient is 0.465 psi/ft. The overburden corresponds to a gradient of approximately 1.0 psi/ft and the geostatic ratio is defined as

$$\text{Geostatic Ratio} = \frac{\text{observed fluid pressure in reservoir}}{\text{pressure due to the weight of overlying deposits}}$$

Any subsurface fluid pressure for which the geostatic ratio is between 0.465 and 1.0 is therefore an abnormally pressured reservoir. One major characteristic of abnormally pressured gas reservoirs is a high formation compressibility  $c_f$ . The compressibility of gas, which is given by

$$c_g = \frac{1}{p} - \frac{1}{z} \frac{\partial z}{\partial p} \quad (4-16)$$

becomes quite small at high pressure and therefore comparable with the formation compressibility which may be as high as  $20\text{--}50 \times 10^{-6} \text{ psi}^{-1}$  in a geopressured system. The high formation compressibility should accordingly be taken into account in estimating gas reserves. The variation of gas compressibility with pressure for a typical reservoir gas is shown in figure 4-5, and it can be seen that at high pressure  $c_g$  is of the order of  $30 \times 10^{-6} \text{ psi}^{-1}$ . Formation compressibility  $c_f$  in normally pressured sandstone is of the order of 3–6 microsip. Note that

Hammerlindl defines a unit of compressibility called the microsip which is an abbreviation for  $10^{-6} \text{ psi}^{-1}$  (with sip referring to square inches per pound).

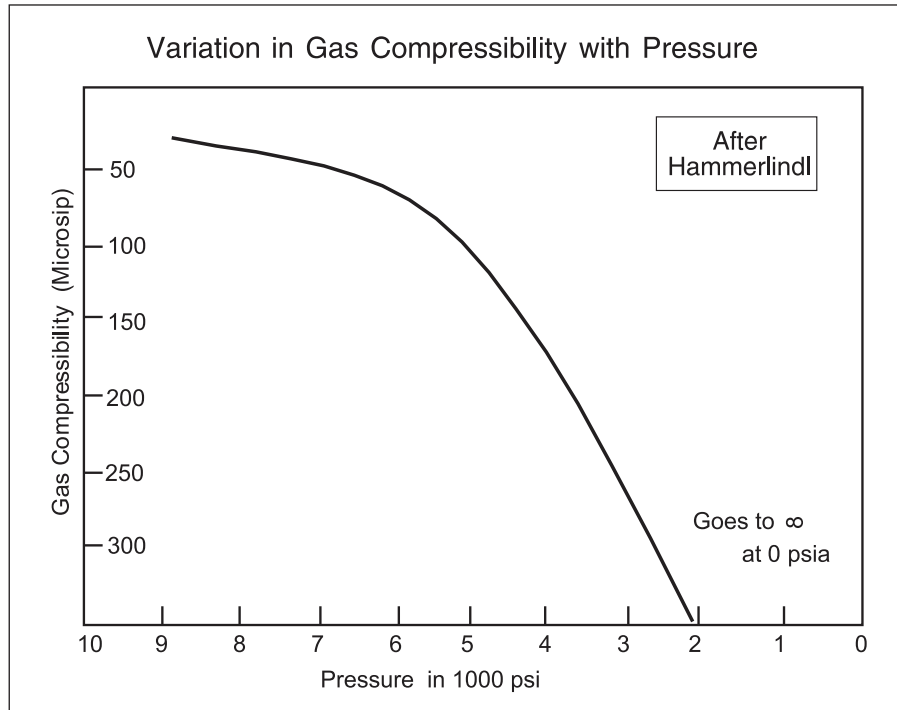


Fig. 4-5. Gas compressibility data for the North Ossum field

Hammerlindl gives empirical data on formation compressibility from three over pressured reservoirs, including the North Ossum field, which is reproduced here in figure 4-6; the formation compressibility is plotted against depth in the abnormally pressured segments of the reservoirs. Good data was limited, and no consideration was given to the effect of porosity which was fairly uniform in the reservoirs examined at around 25%. In an overpressured reservoir, the sand grains are not supporting as great a portion of the overburden pressure as they would in a normally pressured system. When the pressure is reduced, three simultaneous reactions take place to reduce the hydrocarbon pore space:

- the reservoir contracts, i.e., compaction drive occurs
- the sand grains expand
- connate water expands

This reduction in gas pore volume acts as a drive mechanism, and reserve estimates using early life pressures on the classical  $p/z$  plot (which ignores formation and water compressibility) indicate errors, which have been shown to approach 100%.

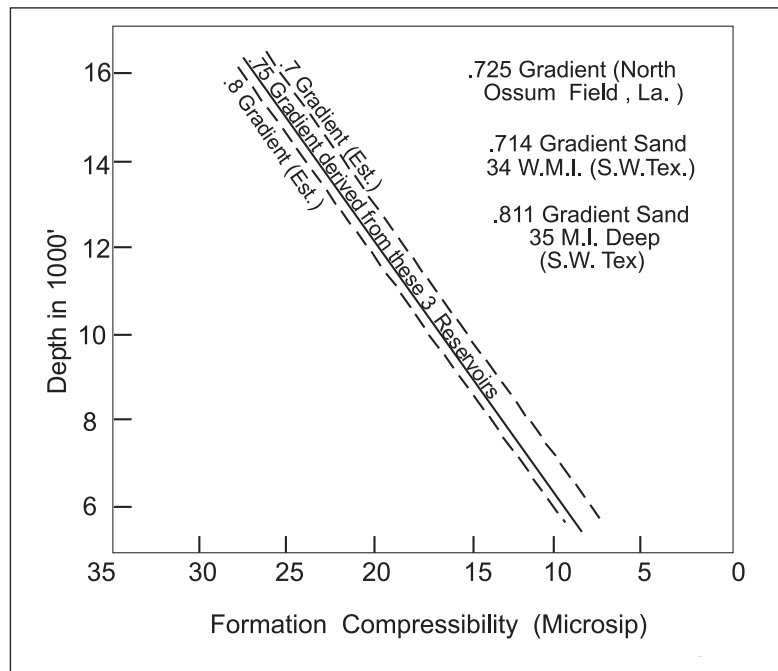


Fig. 4-6. Formation compressibility data for the North Ossum field

In such abnormally high pressured depletion-type gas reservoirs, two distinct slopes are evident when a plot of shut-in bottom-hole pressures versus cumulative production is used to predict reserves. The final slope of the  $p/z$  plot is steeper than the initial slope as illustrated in figure 4-7 taken from Hammerlindl's paper; consequently, reserve estimates based on the early life portion of the curve are highly erroneous. At approximately a normal gradient, the reservoir characteristics change to the same as a normally pressured reservoir where the effect of formation compressibility virtually ceases.

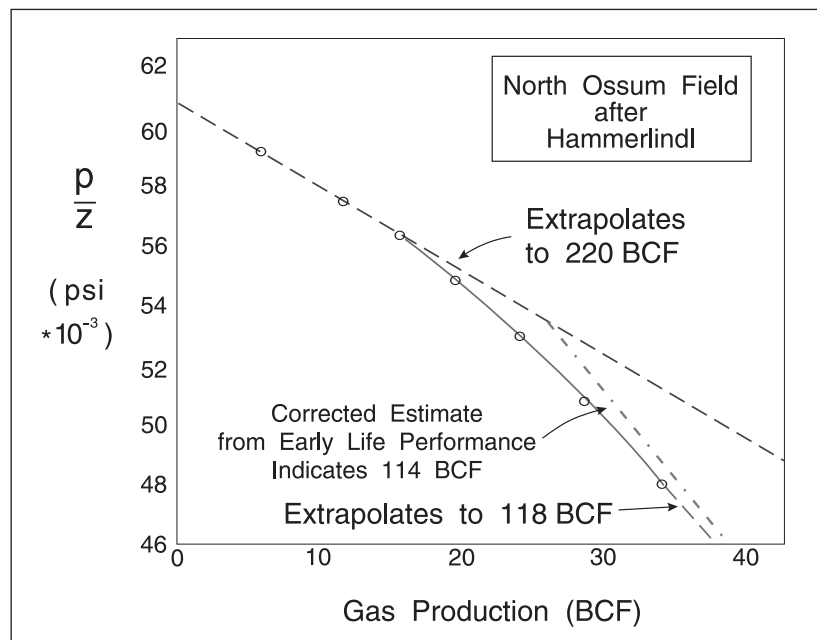


Fig. 4-7.  $p/z$  versus cumulative production for the North Ossum field

Allowing for the change in porosity due to compaction and the expansion of connate water leads to the modified volume balance

$$V_g = V_{gi} - \Delta V_g \quad (4-17)$$

where  $\Delta V_g =$  change in connate water volume + change in pore volume

$$= V_{pi} S_{wc} c_w \Delta p + V_{pi} c_f \Delta p \quad \text{where} \quad \Delta p = p_i - \bar{p}$$

assuming that the formation compressibility  $c_f$  is constant. Hence putting  $V_{gi} = V_{pi}(1 - S_{wc})$  gives

$$V_g = V_{pi} \left( (1 - S_{wc}) - \Delta p (c_f + S_{wc} c_w) \right) \quad (4-18a)$$

or

$$V_g = V_{gi} \left( 1 - \frac{\Delta p}{1 - S_{wc}} (c_f + c_w S_{wc}) \right) \quad (4-18b)$$

The term  $\frac{\Delta p}{1 - S_{wc}} (c_f + c_w S_{wc})$  is the correction for the effect of water and formation compressibility.

Putting

$$V_g = \frac{(G_i - G_p) z T p_{sc}}{T_{sc} p} \quad \text{and} \quad V_{gi} = \frac{G_i z_i T p_{sc}}{T_{sc} p_i}$$

gives after substitution and rearrangement

$$\frac{p}{z} \left( 1 - \frac{\Delta p}{1 - S_{wc}} (c_f + c_w S_{wc}) \right) = \frac{p_i}{z_i} - \frac{p_i}{z_i G_i} G_p \quad (4-19)$$

Thus, in an abnormally pressured reservoir, a plot of  $\frac{p}{z} \left( 1 - \frac{\Delta p}{1 - S_{wc}} (c_f + c_w S_{wc}) \right)$  versus  $G_p$  should give a straight line whose slope is  $\frac{p_i}{z_i G_i}$  from which the reserves can be determined. The problem here is knowing what value of  $c_f$  to use, since in practice  $c_f$  might change with pressure: indeed, there is field evidence that  $c_f$  does change quite substantially as the field depletes. When the reservoir pressure is above hydrostatic, the  $c_f$  value is high but below hydrostatic it becomes small. This point is illustrated in figure 4-8.

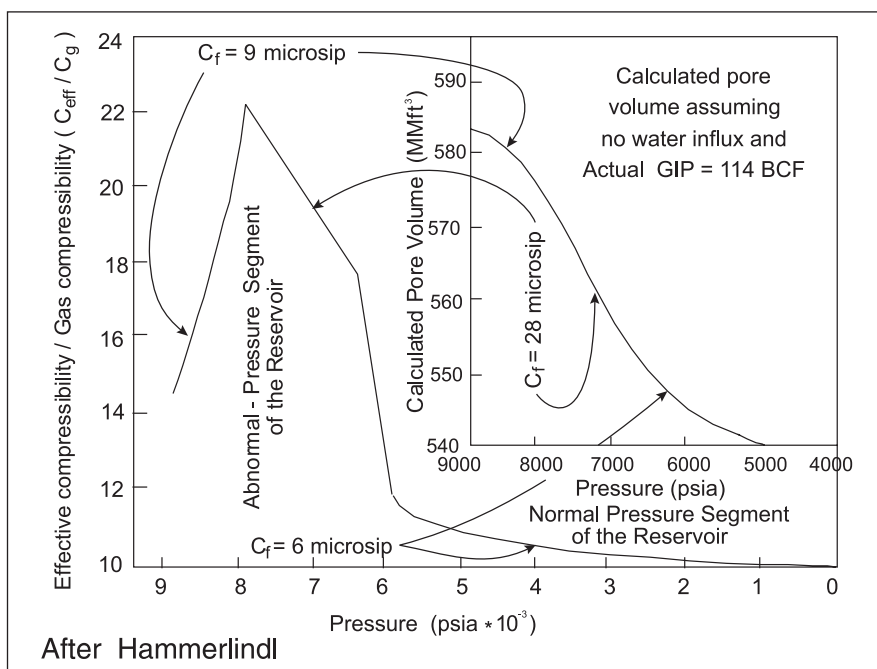


Fig. 4-8. North Ossum field, Louisiana

## Differential form of the material balance

The material balance for a single-compartment gas reservoir can also be written in differential form based on the initial pore volume of the reservoir; by analogy with a liquid system, the equation may be written as

$$c_t V \frac{d\bar{p}}{dt} = QB_g \tag{4-20}$$

where  $V$  = reservoir pore volume at the initial pressure  $p_i$ ,

$$c_t = c_w S_w + (1.0 - S_w)c_g + c_f,$$

$Q$  = gas rate at standard conditions, and

$B_g$  = gas formation volume factor.

In this equation, the gas compressibility  $c_g$  and the formation volume factor  $B_g$  are pressure-dependent quantities; in the circumstances discussed in the previous section the formation compressibility  $c_f$  may also have to be regarded as pressure dependent. This is a nonlinear ordinary differential equation (ODE) which can be integrated forward in time from the specified initial pressure  $p_i$ . In standard form, the ODE becomes

$$\frac{d\bar{p}}{dt} = \frac{QB_g}{c_t V} \tag{4-21}$$

i.e.,

$$\frac{dy}{dx} = f(x, y) \tag{4-22}$$

In systems engineering, the nonlinear equation is written in the alternative form

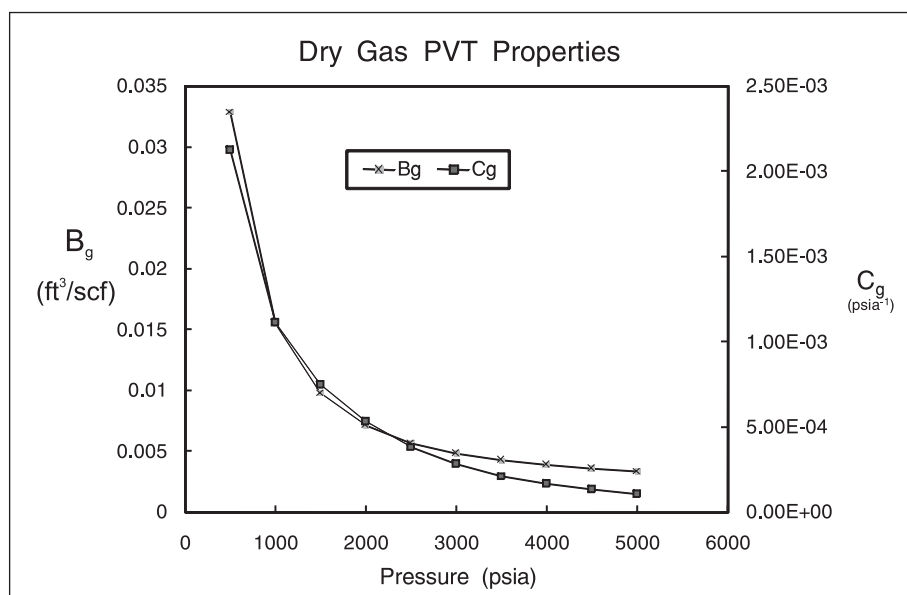
$$\frac{dx}{dt} = f(t, x, u) \quad (4-23)$$

where the forcing function  $u(t)$  is identified with the well rate  $Q$ , which in the general case is time dependent. In order to carry out an integration of this equation using a standard numerical method, the pressure-dependent quantities  $c_g$  and  $B_g$  must be tabulated as shown in table 4–1.

**Table 4–1.** Dry gas properties as a function of pressure ( $\gamma = 0.71, T = 160^\circ\text{F}$ )

Pressure $p$ (psi)	Formation volume factor $B_g$ (ft <sup>3</sup> /scf)	Gas compressibility $c_g$ (psi <sup>-1</sup> )	Compressibility factor $z$
5,000	0.003392	$1.0835 \times 10^{-4}$	0.96807
4,500	0.0036031	$1.3301 \times 10^{-4}$	0.92516
4,000	0.003882	$1.6716 \times 10^{-4}$	0.88602
3,500	0.0042687	$2.1549 \times 10^{-4}$	0.85249
3,000	0.0048326	$2.8519 \times 10^{-4}$	0.82724
2,500	0.0057074	$3.8659 \times 10^{-4}$	0.814146
2,000	0.0071669	$5.3302 \times 10^{-4}$	0.817866
1,500	0.0098330	$7.4670 \times 10^{-4}$	0.841592
1,000	0.0154886	$11.122 \times 10^{-4}$	0.883757
500	0.0328981	$21.257 \times 10^{-4}$	0.938558

For the purposes of integration, linear interpolation in this table is quite sufficient to render  $c_g$  and  $B_g$  continuous functions of the dependent variable, i.e., pressure; the physical property data of table 4–1 are plotted in figure 4–9. Note that the ratio  $\frac{B_g}{c_g}$  is approximately constant and Eq. (4–21) is only mildly nonlinear.



**Fig. 4–9.** Dry gas properties as a function of pressure



The well rate is also represented by a table of flow rates and times that are shown as knot points in figure 4–10; in the integration process, the rate can either be linearly interpolated as chords or taken in steps. Thus the function  $u(t)$  can either be piecewise linear or step form as desired. In principle, a continuously varying rate is much better approximated by piecewise linear segments, but the error in rate measurement may not warrant anything more than the simple step-rate form. However, the idea of representing a continuous function by chords as shown in figure 4–10 is an important one and the solution of a differential equation for such a time-dependent forcing function  $u(t)$  is known in mathematics as *convolution*.

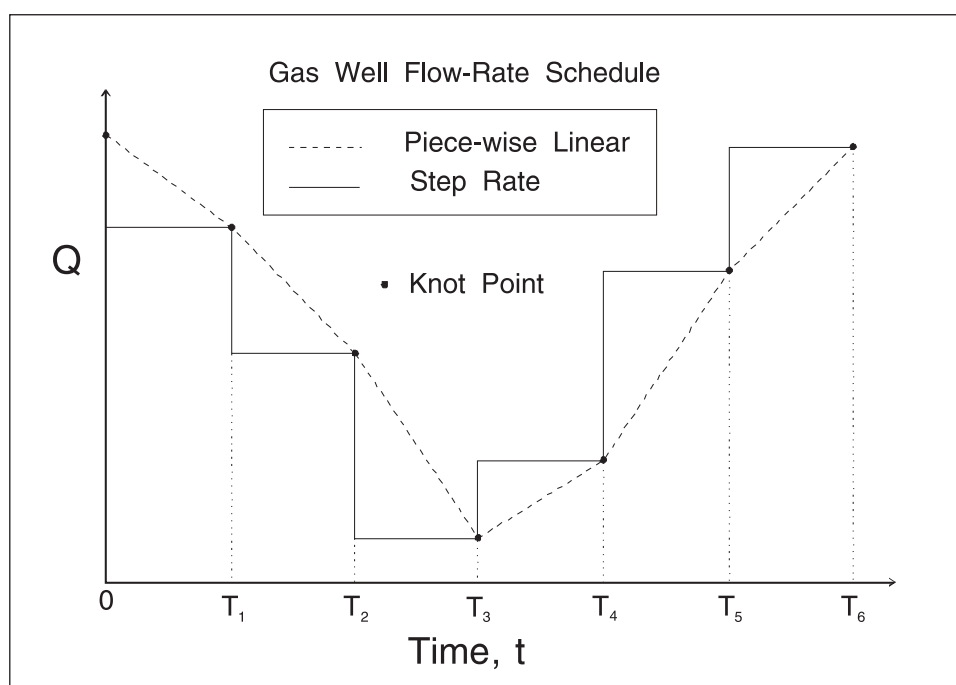


Fig. 4–10. Gas well rate as a function of time

The forward integration of the nonlinear ODE can be carried out using a standard numerical integration algorithm such as the Runge–Kutta method with adaptive stepsize control. These techniques are extremely fast and well suited to the present problem. For the PVT data in table 4–1, a forward integration for the parameter set shown in table 4–2 has been carried out and is plotted in figure 4–11.

**Table 4–2.** Test problem parameters for gas reservoir simulation using differential material balance (DMB)

$c_w = 3.0 \times 10^{-6} \text{ (psi}^{-1}\text{)}$	$S_w = 0.25$	$c_f = 4.0 \times 10^{-6} \text{ (psi}^{-1}\text{)}$
$V = 1.0 \times 10^8 \text{ ft}^3$	$Q = 50 \text{ MMscf/d}$	$p_i = 5,000 \text{ psi}$

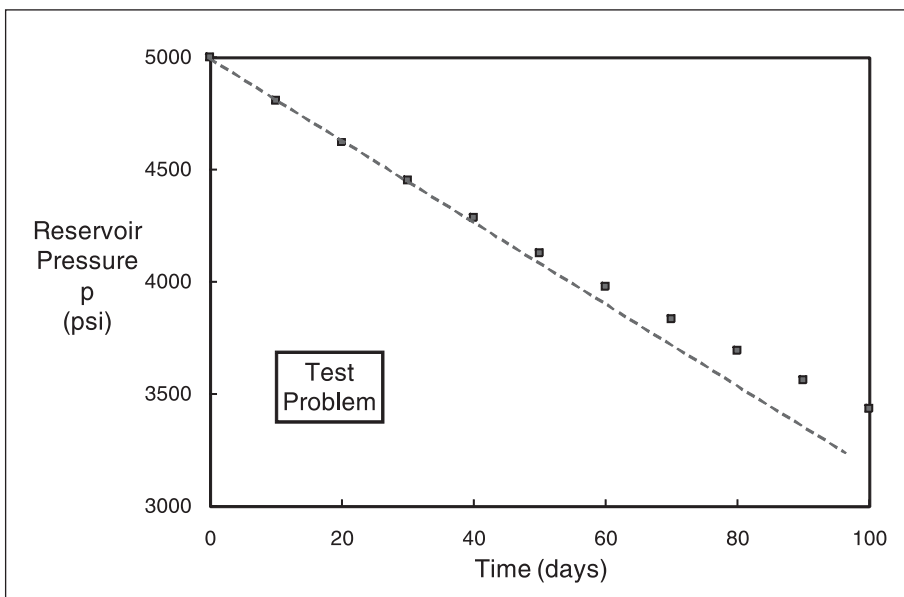


Fig. 4-11. Cartesian plot of reservoir pressure versus time for the test problem

The results from the Runge–Kutta integration of the single-compartment model can be presented in the form of a plot of  $p/z$  versus cumulative production; this is shown in figure 4-12. A straight line is obtained on this graph which has the following parameters:

$$\text{Slope} = -0.22394 \text{ psi/MMscf} \quad \text{Intercept} = 5166.4 \text{ psi}$$

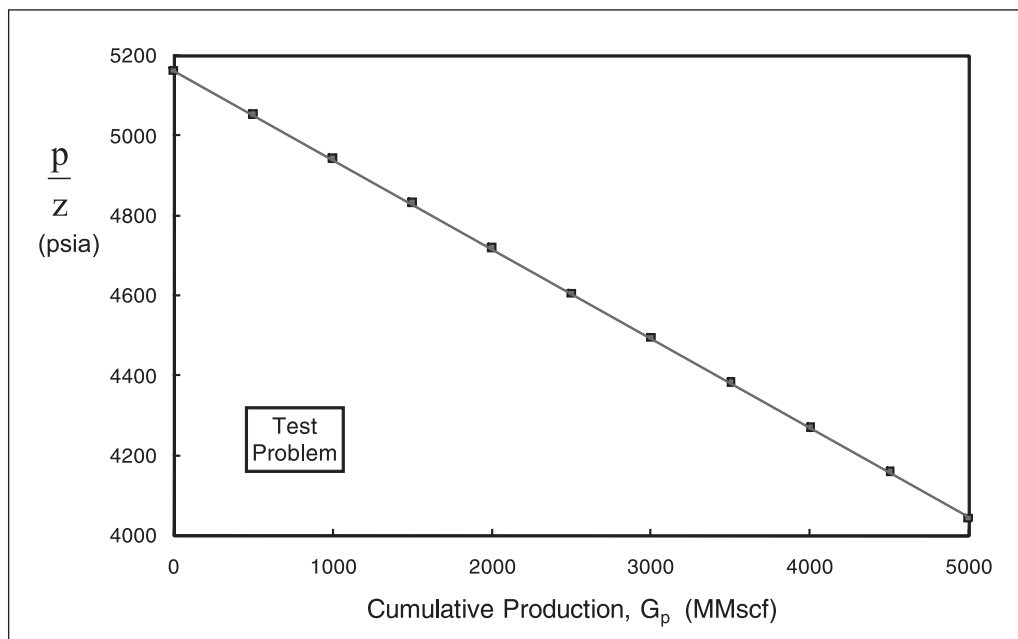


Fig. 4-12.  $p/z$  Plot for test problem

The initial volume of gas at in situ conditions is given by

$$V_i = V(1 - S_{wc}) = 10.0 \times 10^8 \times 0.75 = 0.75 \times 10^8 \text{ ft}^3$$

and the initial GIP at standard conditions is

$$G_i = \frac{0.75 \times 10^8}{B_{gi}} = \frac{0.75 \times 10^8}{0.003392} = 2.211 \times 10^{10} \text{ scf}$$

From the  $p/z$  plot, the value of  $G_p$  at  $p/z = 0$  is

$$G_p \Big|_{p/z=0} = G_i = \frac{5166.4}{0.22394} = 2.307 \times 10^4 \text{ MMscf}$$

Thus the basic  $p/z$  plot overestimates the GIP because it has not been corrected for the effect of connate water and formation compressibility; the error in this case is of the order 5%. A revised plot of

$$\frac{p}{z} \left( 1 - \frac{\Delta p}{1 - S_{wc}} (c_f + c_w S_{wc}) \right) \quad \text{versus} \quad G_p$$

would give the exact answer of  $G_i = 2.211 \times 10^4$  MMscf.

Note that the calculation of gas reserves in this fashion requires good information on the compressibility factor  $z$  as a function of pressure. The use of a generalized correlation utilizing only gravity may not be sufficiently accurate and introduce an error comparable to that ensuing from neglecting water and formation compressibility. Wherever possible, the detailed composition of the gas phase should be utilized in conjunction with a reliable three-parameter equation of state, e.g., Soave–Redlich–Kwong (SRK) or preferably Schmidt–Wenzel (SW), to generate satisfactory compressibility information.

In the formulation above, the well rate has been expressed in terms of volumetric rate at standard conditions, i.e.,  $Q$ . It is also useful to formulate the material balance in terms of mass flow rate  $m$ , and Eq. (4–21) takes the alternative form

$$\frac{d\bar{p}}{dt} = \frac{m}{\rho c_t V} \quad (4-24)$$

where  $\rho$  is the gas density which is also a function of pressure calculated from the equation of state.

In the preceding formulation, the total compressibility  $c_t$  was employed following the standard practice in well test analysis. This approach leads to a small material balance error when the

formation compressibility is nonzero (typically of the order of 0.5%) and a more rigorous formulation models the change in gas pore volume due to the expansion of connate water and the reduction in porosity due to compaction. Let  $V_g$  represent the actual gas occupied pore volume and  $\delta V_g$  the change in gas occupied volume due to water and rock compressibility; thus

$$\delta V_g = V(S_{wc}c_w + c_f)\delta p \quad (4-25)$$

Hence the differential equation tracking the gas occupied pore volume may be written as

$$\frac{dV_g}{dt} = V(S_{wc}c_w + c_f)\frac{d\bar{p}}{dt} \quad (4-26)$$

At time  $t = 0$ ,

$$V_{gi} = V(1 - S_{wc}) \quad (4-27)$$

The material balance for the gas phase now takes the form

$$V_g\rho = (V_g + \delta V_g)(\rho + \delta\rho) + m\delta t \quad (4-28)$$

which on taking the limit and putting  $\delta\rho = c_g\rho\delta p$  becomes

$$V_g c_g \frac{d\bar{p}}{dt} = -\frac{m}{\rho} - \frac{dV_g}{dt} \quad (4-29)$$

Substituting Eq. (4-26) into (4-29) gives the equivalent, nonimplicit form

$$\frac{d\bar{p}}{dt} = -\frac{1}{V_g c_g + V(S_{wc}c_w + c_f)} \frac{m}{\rho} \quad (4-30)$$

The differential material balance model now comprises two simultaneous equations (4-26) and (4-30) in the variables  $V_g$  and  $\bar{p}$ .

## Nonlinear regression

The traditional material balance approach has been dominated by the desire to formulate the problem such that a straight line on a plot can be obtained. However, this restriction is quite unnecessary in a modern context and it is possible to carry out general parameter estimation on nonlinear models. The differential form of the gas reservoir material balance derived in the preceding section allows the forward, viz., simulation, problem to be solved in an efficient manner. Thus if the reservoir initial pore volume  $V_p$  is assumed known and the well productions have been measured, the material balance model in differential form can be integrated forward in

time to yield a predicted pressure response as illustrated in figure 4–13. Note that the assumption of a value for  $V_p$  is equivalent to assuming a value for the initial GIP  $G_i$ . In a material balance study, the objective is simply to adjust the initial pore volume, i.e. gas reserves, until the predicted pressures come as close as possible to the measured pressures. In mathematical terminology, it is desired to minimize a sum of squares objective function of the form

$$\chi^2 = \sum_{i=1}^N \left( \frac{p_i^{\text{obs}} - p_i^{\text{calc}}}{\sigma_i} \right)^2 \quad (4-31)$$

where  $\sigma_i$  is an estimate of the error in the particular measurement. Nonlinear optimization algorithms exist that can efficiently carry out the search for the best value of the unknown parameter(s)—in this case  $V_p$ —that minimizes the difference between measured and predicted pressures. In figure 4–13, the double-headed arrow represents the difference ( $p^{\text{obs}} - p^{\text{calc}}$ ) for each data point. The individual measurements of (average) reservoir pressure correspond to extrapolated buildups in wells penetrating the particular compartment, e.g., fault block, that is being analyzed. Hence the term  $\sigma$  represents the error in the extrapolation process and the correction to datum as much as the physical error in the detection of pressure itself. Once the nonlinear regression algorithm has converged, the predicted and measured pressures should overlay as shown in figure 4–14; of course, there is no reason why the fitted results should not be presented in the form of a  $p/z$  plot in order to maintain a link with the basic model. The automatic regression approach, most importantly, allows time to be introduced into the material balance model; also the effects of formation and water compressibility as well as detailed PVT properties enter quite naturally into the problem.

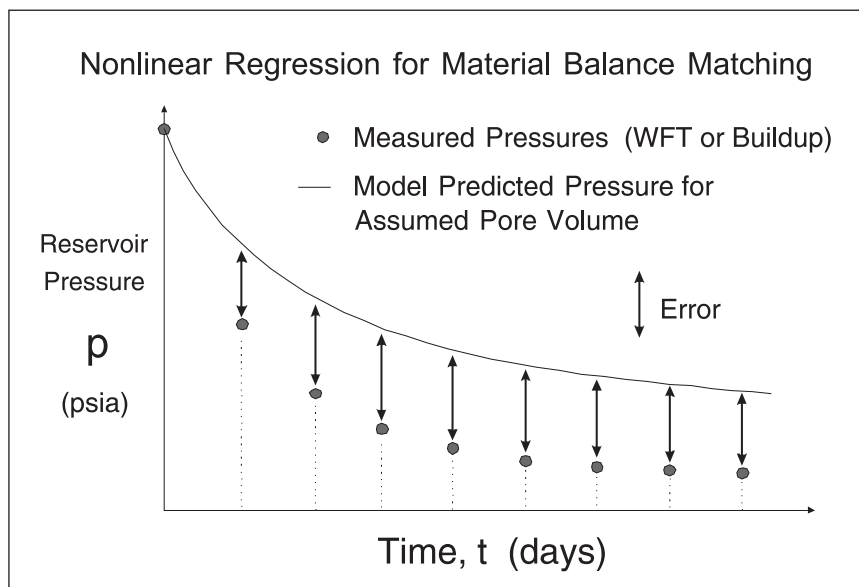


Fig. 4–13. Measured and model predicted pressure response for a tank reservoir

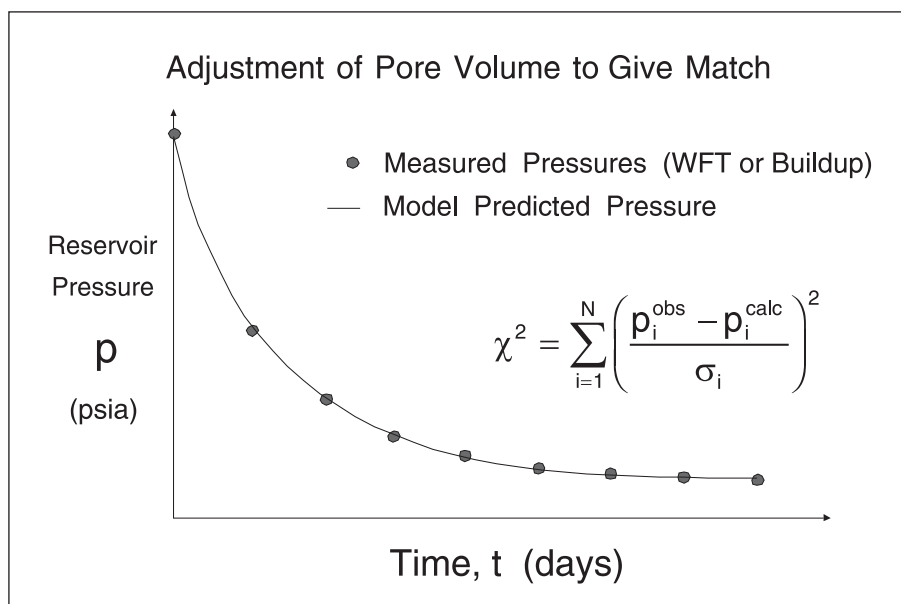


Fig. 4-14. Optimized value of the unknown parameter, i.e., pore volume

## Error in rate measurement and allocation

In the regression method, the forward problem assumes that the well rates are known and have been aggregated to give the total production history of the block under consideration; this total rate schedule is used in the simulation process and, of course, the model predictions are sensitive to error in the measurement of well rates. Hence the computed gas reserves will be affected by rate measurement error, which is usually much greater than that involved in the determination of pressure. In many fields, particularly those offshore, the rates of individual wells are measured only infrequently and the total separator rate has to be allocated on the basis of historical ratios determined, say, 1 year previously. Inaccuracies in allocation can obviously lead to significant error in the reserves associated with reservoir compartments such as individual fault blocks.

## Case 2—Natural water influx

Nearly all gas reservoirs will be in contact with an aquifer and, as the reservoir is depleted by production, water will tend to flow into the system. It is simply a question of how much influx will occur and whether this will seriously affect performance. Fortunately, in many cases the influx is small and the gas reservoir essentially behaves as a volumetric system. A serious effort should be made at the field appraisal stage to examine the possibility of water influx occurring and to gather data which will help to quantify the effect. A gas reservoir in communication with an aquifer is illustrated in figure 4-15; again the gas accumulation will be treated as a single tank of uniform pressure  $p$ .

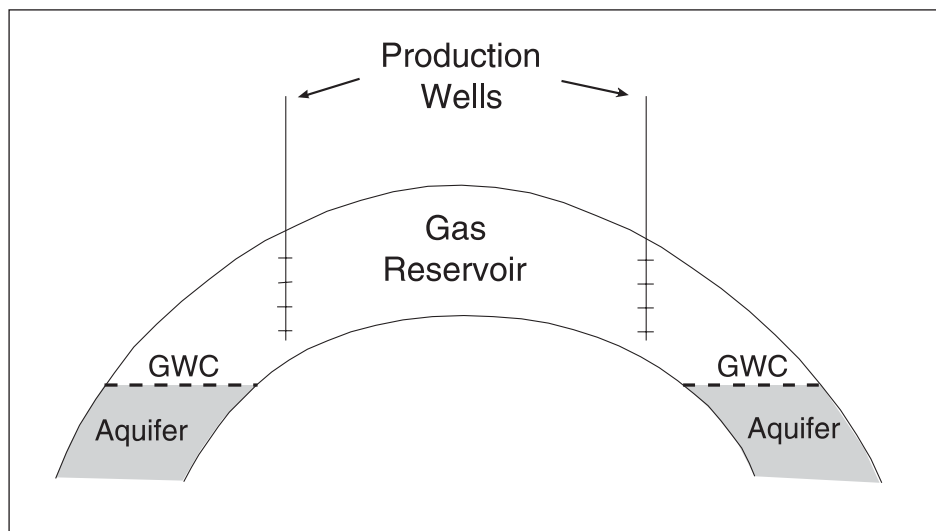


Fig. 4-15. Gas reservoir in communication with an aquifer

The cumulative water influx from the aquifer at time  $t$  will be denoted  $W_e$ . The recovery factor of a gas reservoir is very much influenced by the extent of water influx (because of the consequent trapping of gas) and the deterioration in gas well performance at increasing water-cut may adversely affect the ability to meet gas sales contracts. Coning underneath gas producers is an obvious danger if wells are produced at high rate.

When water influx occurs, the material balance in terms of in situ volumes (neglecting formation compaction) can be written as

$$V_{gi} = V_g + W_e \tag{4-32}$$

where  $V_{gi}$  = initial gas filled pore volume,

$V_g$  = remaining gas volume, and

$W_e$  = cumulative water influx.

In terms of  $p/z$ , this may be written in the form

$$\frac{p}{z} = \frac{\frac{p_i}{z_i} \left( 1 - \frac{G_p}{G_i} \right)}{1 - \frac{W_e E_i}{G_i}} \tag{4-33}$$

where

$$E_i = \frac{T_{sc} p_i}{z_i T p_{sc}}$$

The effect of aquifer influx is to upset the linearity of the  $p/z$  plot and to cause the slope to become smaller; note that  $W_e$  is a time-dependent quantity. When influx is appreciable, the reserves  $G_i$  cannot be determined from the slope or intercept of a  $p/z$  plot as illustrated in figure 4–16.

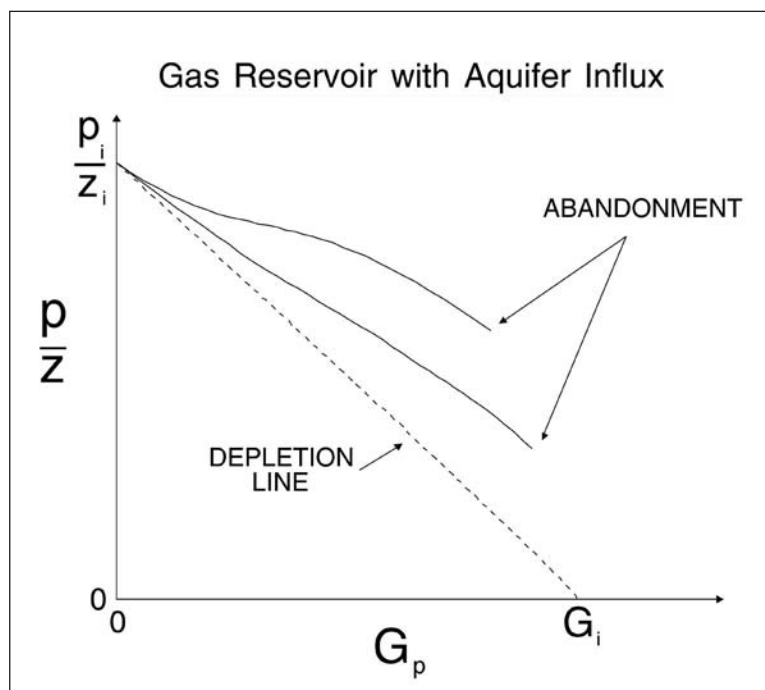


Fig. 4–16.  $p/z$  plot with natural water influx

Suppose that field data on the decline of reservoir pressure  $p$  as a function of cumulative gas production  $G_p$  has been gathered; this implies that pressure build-up surveys have periodically been carried out to obtain reservoir average pressures. This data is presented as a table of time, pressure, and cumulative gas production as shown in table 4–3. The listed times  $T_i$  in the table correspond to the availability of a build-up pressure  $p$ , while the cumulative gas production from all wells will usually be recorded very accurately for management purposes.

The gas phase material balance can now be used in the form

$$W_e = V_{g_i} - V_g = \frac{G_i}{E_i} - \frac{(G_i - G_p)zTp_{sc}}{T_{sc}p} = \frac{G_i}{E_i} - \frac{(G_i - G_p)}{E} \quad (4-34a)$$

to calculate the cumulative influx at time  $T$  when the pressure is  $p$  and total production  $G_p$ . It is convenient to use an alternative symbol for the initial GIP which will now be denoted  $G_o$  rather than  $G_i$ ; Eq. (4–33a) in the altered nomenclature becomes

$$W_e = V_{g_o} - V_g = \frac{G_o}{E_o} - \frac{(G_o - G_p)zTp_{sc}}{T_{sc}p} = \frac{G_o}{E_o} - \frac{(G_o - G_p)}{E} \quad (4-34b)$$



Thus the table of time, pressure, and cumulative production may be augmented by the cumulative water influx for an assumed value of  $G_o$ : it is important to appreciate that the influx can be computed only if the GIP is assumed known. Once  $W_e$  has been obtained, the water inflow in the form of a step rate schedule can be generated by taking differences in the table, i.e.,

$$w^i = \frac{W_e^i - W_e^{i-1}}{T^i - T^{i-1}} \tag{4-35}$$

Here  $w$  is the water flow rate in appropriate units, e.g., bbl/day.

Equation (4-34b) is the integral form of the material balance in terms of reservoir volumes neglecting the effects of formation compressibility, expansion of connate water, and trapping of gas by the advancing water front. Suppose that a dataset of pressure and cumulative production versus time is available and a table of compressibility factor  $z$ , versus pressure (at reservoir temperature) has been prepared from the appropriate equation of state (EOS). Let the data points be indexed as  $i = 1, \dots, N$  where the field data has the tabular form shown in table 4-4.

**Table 4-3.** Time, pressure, and cumulative gas production

Time $T$	Pressure $p$	Cumulative production $G_p$
$T^0$	$p^0 = p_i$	0
...	...	...
$T^i$	$p^i$	$G_p^i$
...	...	...
$T^N$	$p^N$	$G_p^N$

**Table 4-4.** Compressibility factor versus pressure

Pressure $p$	Compressibility factor, $z$
$p^0 = p_i$	$z^0$
...	...
$p^i$	$z^i$
...	...
$p^N$	$z^N$

The aquifer model allows the cumulative influx at time  $T^i$  to be computed if the parameters are assumed known. The aquifer is essentially characterized by its permeability  $k_a$  and its size  $V_{pa}$ , and it is convenient to define an unknown parameter vector  $\mathbf{a}$  as

$$\mathbf{a} = (G_o, k_a, V_{pa})^T \tag{4-36}$$

Equation (4–34b) may be written at each point  $i$  in the form

$$r^i = r^i[\mathbf{a}] = W_e^i - \frac{G_o}{E_o} + \left[ \frac{(G_o - G_p)}{E} \right]^i \quad (4-37)$$

Here the superscript  $i$  indicates that the terms are evaluated at the  $i$ -th point, i.e. time  $T^i$  and corresponding pressure  $p^i$  and cumulative production  $G_p^i$ .

## Areal pressure variation

The material balance in the form of a  $p/z$  plot requires average pressure data from pressure build-up (PBU) surveys. In a multiwell reservoir, areal variations in pressure will exist as a result of permeability variations and the presence of partially communicating barriers. However, individual wells will establish their own drainage areas and the reservoir will deplete at a joint SSS. A buildup in a specific well will yield the average pressure of its drainage area when the MBH correction is applied. The average pressure of different drainage areas will vary as illustrated in figure 4–17. and it is sufficient to employ the volume weighted average of the averages in an overall  $p/z$  plot. In fig. 4–17 the physical barriers are designated as no-flow but the instance of leaky barriers can be treated in this way provided build-ups are interpreted for well cell average pressures. In the case of multiple wells in a compartment with internally good communication the well rates are simply summed for a compartment material balance.

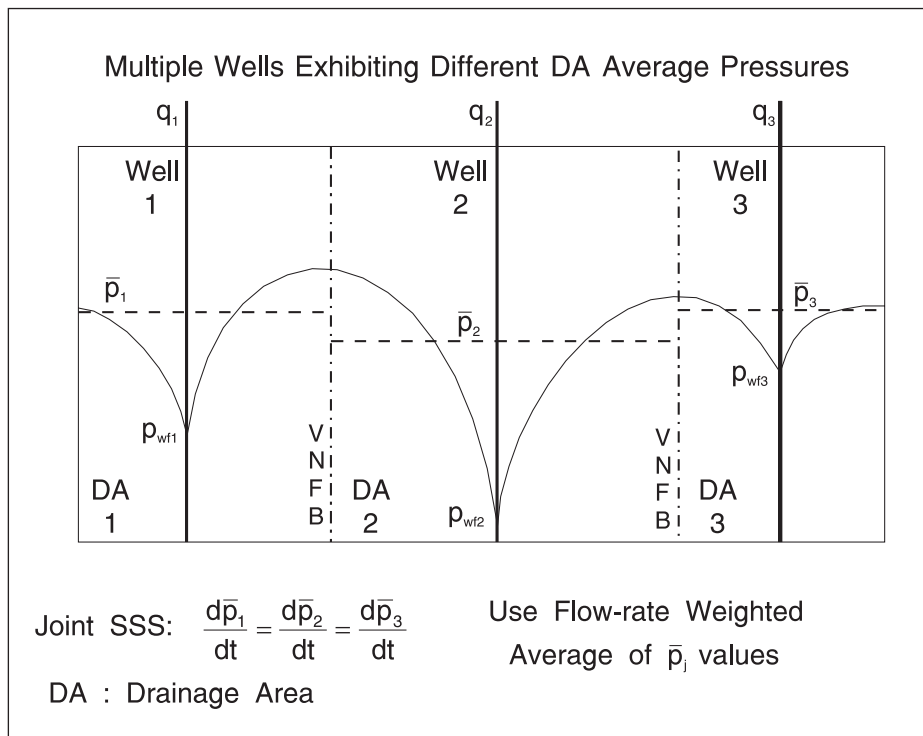


Fig. 4–17. Areal pressure variation

## Variable Rate Draw-down Analysis for Aquifer Influx

The result of these calculations is to give a time—pressure and step rate schedule—illustrated in figure 4–18—for the inflow (on the basis of an assumed  $G_i$ ), and the problem of characterizing the aquifer is identical to analyzing a variable rate draw-down (VRD) which may reach an SSS condition.

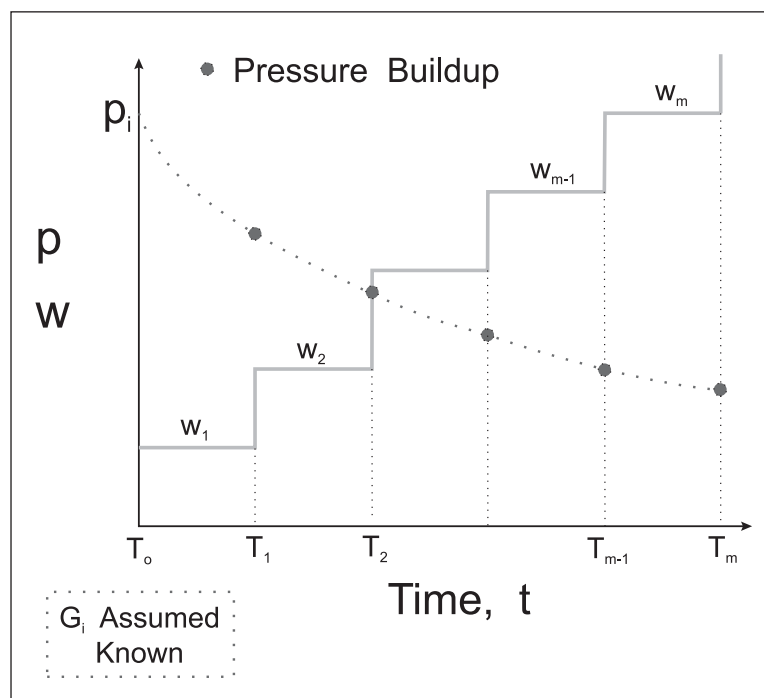


Fig. 4–18. Variable pressure and step rate data

The aquifer face rate  $w$  replaces the well (sand face) rate  $q$ , and the analogue of a constant rate well  $p_D$  function is sought that models the aquifer inflow; such functions will be denoted  $w_D$ , defined as

$$w_D = \frac{\Delta p 2\pi kh}{w\mu} \quad (4-38)$$

where  $\Delta p = p_i - p_f(t)$  and  $p_f(t)$  is the aquifer face pressure (synonymous with the reservoir pressure  $p$  for a single compartment or tank gas field). The treatment of VRD analysis will be given in terms of aquifer identification but exactly the same methodology is applicable to the extended draw-down test of a well. In general, the constant rate  $w_D$  function depends on the aquifer geometry and properties and may be written symbolically as

$$w_D = w_D(t_{DL}, \Pi_1, \Pi_2, \dots) \quad (4-39)$$

Here  $t_{DL}$  is a dimensionless time based on a characteristic aquifer dimension, i.e.,  $t_{DL} = \frac{kt}{\phi\mu c_t L^2}$  (for example  $L$  may be the inner radius  $r_b$  of an annular system) and  $\Pi_1, \Pi_2, \dots$  are dimensionless parameter groups necessary to fully define the system. The pressure drop for a constant inflow rate  $w$  is given by

$$\Delta p = p_i - p_f(t) = \frac{w\mu}{2\pi kh} w_D(t_{DL}, \Pi_1, \Pi_2, \dots) = wF(t) \quad (4-40)$$

where 
$$F(t) = \frac{\Delta p}{w} = \frac{\mu}{2\pi kh} w_D(t_{DL}, \Pi_1, \Pi_2, \dots)(t_{DL}, \Pi_1, \Pi_2, \dots)$$

is known as the *aquifer influence function* which is the rate-normalized pressure drop for constant rate. The aquifer influence function is an important quantity since deconvolution applied to measured pressure and rate signals yields  $F(t)$  directly.

## Interpretation methodology

The interpretation of VRDs where the underlying model (fundamental  $p_D$  or  $w_D$  function) is based on a closed system and exhibits a late time SSS regime is not straightforward. The classical VRD specialized plots for radial or linear flow do not apply when depletion effects are present in the data. In general, two approaches are available for VRD analysis in such situations; these are:

- Deconvolution followed by analysis using classical constant rate methods;
- Automatic matching of a selected model using generalized superposition.

In the deconvolution method, information in the signal is used to convert the pressure response to what it would have been had the rate been constant; this process does not assume any model and in principle is the best way of analyzing VRD data. Once the constant rate response has been revealed, model selection based on pattern recognition and constant rate drawdown (CRD) methods can be used for interpretation. Deconvolution techniques (which are treated at length in chapter 20 of *Well Test Design and Analysis* (addendum)) are unfortunately sensitive to noise in the data and may not yield good results: however, one area where they have been employed with success is in aquifer identification. In the automatic matching method, a model is chosen from knowledge of the geological situation and the parameters of the model are determined by nonlinear regression. This approach is more robust and is the one that will be treated first.

## Principle of superposition

The fundamental  $w_D$  function applies to constant aquifer face rate and superposition is required to generate a pressure response for a given rate history. In the approach to be adopted here, specific aquifer models, i.e.,  $w_D$  functions, will be used to generate pressure responses for the assumed known rate histories and the aquifer parameters will be adjusted to give a match to the measured data. The automatic matching algorithm (e.g. Levenberg–Marquardt) is the

vehicle for carrying out this process. The predicted pressure response is given by the familiar superposition formula for a step rate schedule, illustrated in figure 4–19, viz.,

$$\Delta p = p_i - p_f = \frac{\mu}{2\pi kh} \left( w_1 w_D(t - T_o)_{DL} + (w_2 - w_1) w_D(t - T_1)_{DL} + \dots \right) \left( + (w_m - w_{m-1}) w_D(t - T_{m-1})_{DL} + w_m S_{af} \right) \quad (4-41)$$

where an aquifer face skin factor  $S_{af}$  has been introduced to allow for a semipermeable barrier between the aquifer and gas reservoir; this imposes an additional pressure drop  $\Delta p_{fs}$  given by

$$\Delta p_{fs} = S_{af} \frac{w(t)\mu}{2\pi kh} \quad (4-42)$$

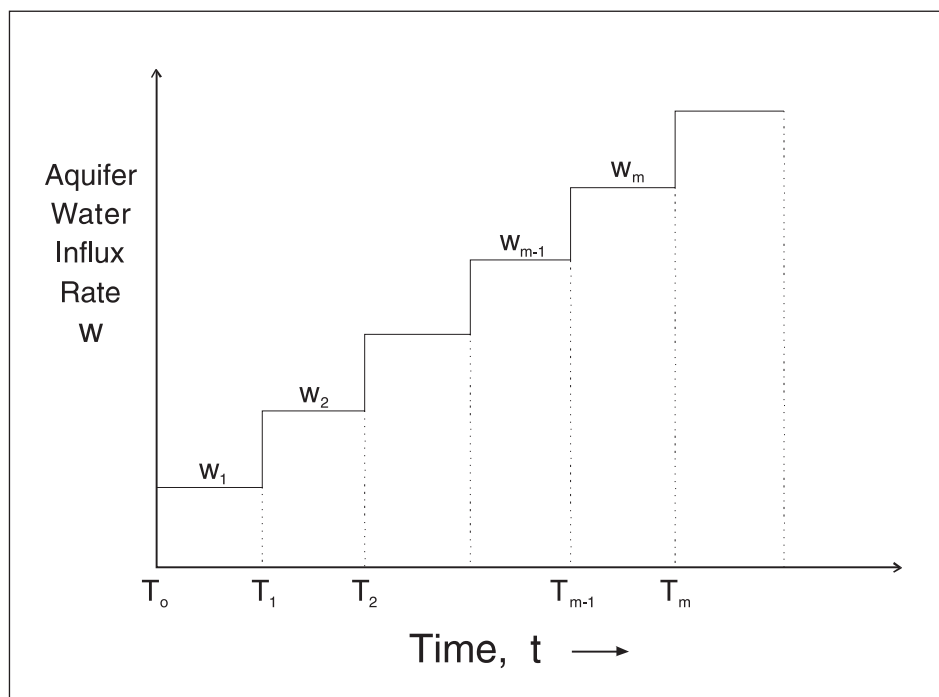


Fig. 4–19. Aquifer step-rate flow schedule for superposition

This additional resistance is important since it can account for a thin tight layer present near the gas–water contact (GWC) which delays and inhibits the aquifer influx into the reservoir as illustrated in figure 4–20.

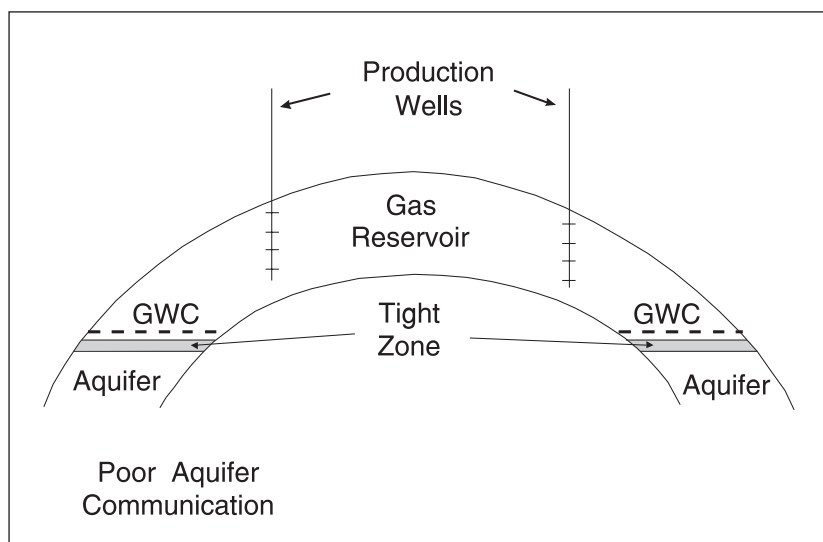


Fig. 4–20. Aquifer face skin, i.e., tight zone, near the GWC

In terms of the aquifer influence function, the superposition principle may also be written as

$$\Delta p = p_i - p_f(t) = w_1 F(t - T_0) + (w_2 - w_1) F(t - T_1) + \dots + (w_m - w_{m-1}) F(t - T_{m-1}) \quad (4-43)$$

Note that the aquifer influence function includes the effect of skin, i.e.,

$$F(t) = \frac{\mu}{2\pi k h} \left( w_D(t_{DL}, \Pi_1, \Pi_2, \dots) + S_{af} \right) \quad (4-44)$$

Implicit in the definition of  $F(t)$  is a conversion from dimensionless to real time. Knowledge of  $F(t)$ —the pressure response of the aquifer to a (constant) unit rate imposed at the active face—allows the variable rate response to be calculated by superposition.

## Radial Aquifer Models

### Aquifer influence functions

Flow in the aquifer is described by the diffusivity equation since a liquid of small compressibility is present and the hydraulic diffusivity  $k/(\phi\mu c_l)$  will control the dynamics of the aquifer response along with the skin factor modeling any semipermeable barrier which may be located near the GWC. Two elementary models will be described first which have been much used in the definition of aquifer behavior; these are the radial and the linear geometries for which analytical  $w_D$  functions are available. More complex models better related to real geology will be treated later. A radial aquifer is illustrated in figures 4–21 and 4–22, where the gas reservoir is

assumed to be circular with an external radius  $r_b$ ; the aquifer is consequently annular in shape with an internal radius  $r_b$  and it is presumed to be of finite extent of external radius  $r_e$ .

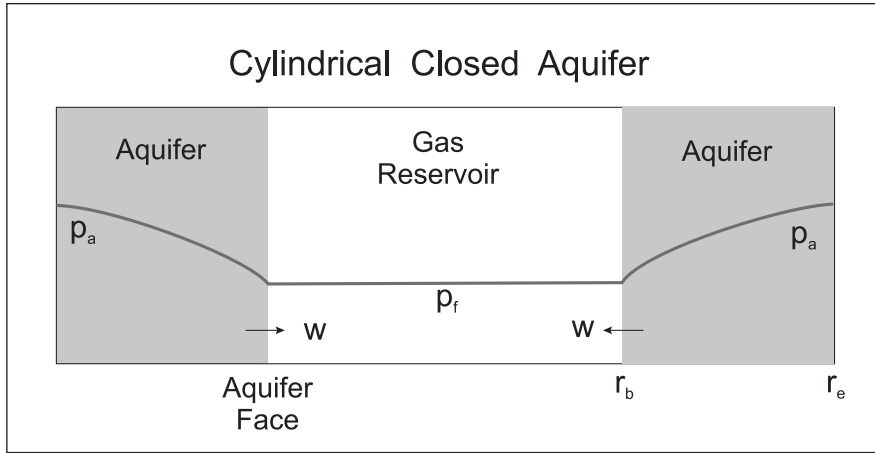


Fig. 4-21. Radial (annular) aquifer of finite extent

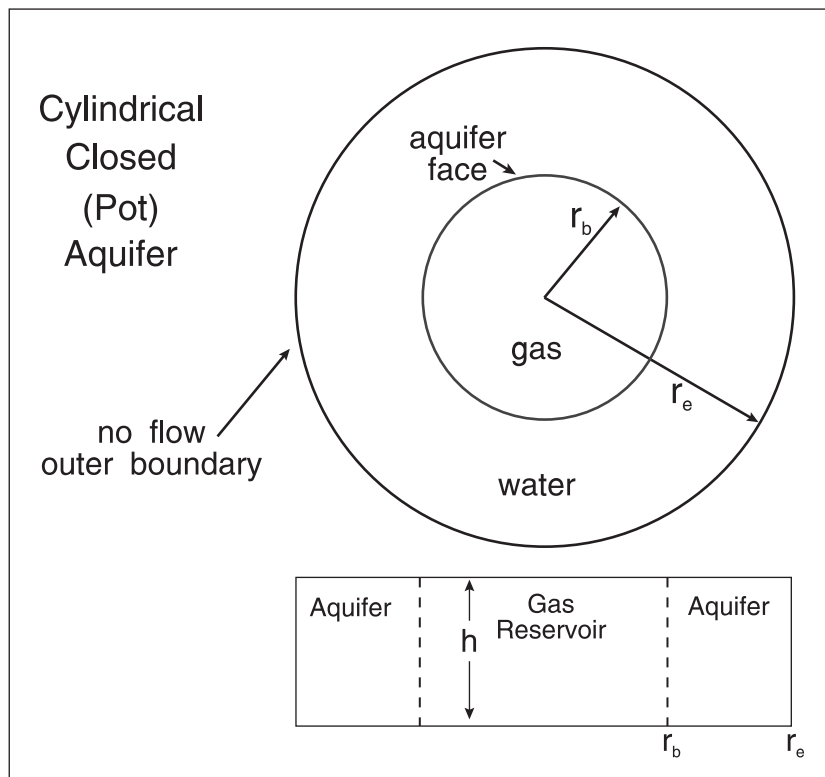


Fig. 4-22. Areal view of cylindrical closed aquifer

The inner boundary condition for the aquifer is a radial source at  $r_b$  where the flux is given by

$$u_r = \frac{w}{2\pi r_b h} = \frac{k}{\mu} \frac{dp}{dr} \tag{4-45}$$

while the outer boundary condition corresponds to no flow, i.e.  $dp/dr = 0$ , at  $r_e$ . The initial condition is that the aquifer commences at a uniform pressure  $p_i$ , and in a constant terminal (inner) rate model it is assumed that the total influx rate  $w$  is constant. The  $w_D$  function for this annular aquifer is, in fact, identical to the  $p_D$  function for a well of finite radius in a closed circular reservoir with  $r_w$  replaced by  $r_b$ . The only difference is that  $r_b$  in the case of an aquifer will normally be a large quantity whereas  $r_w$  for a well is small. The geometry of the aquifer is described by the ratio  $R$ , where

$$R = \frac{r_e}{r_b} \left( R = r_{De} = \frac{r_e}{r_w} \text{ in the case of a well} \right)$$

and the dimensionless time for the aquifer is denoted  $t_{DL}$  where  $t_{DL} = \frac{kt}{\phi\mu c_t r_b^2}$ : note that  $\mu$  is the water viscosity and  $c_t$  is the total aquifer compressibility given by  $c_t = c_w + c_f$ .

The analytical solution to the diffusivity equation for these boundary conditions is readily available (following the pioneering work of van Everdingen and Hurst<sup>2</sup> and the  $w_D$  function in real time is given by

$$w_D = \left( \frac{2}{R^2 - 1} \left( \frac{1}{4} + t_{DL} \right) - \frac{(3R^4 - 4R^4 \ln R - 2R^2 - 1)}{4(R^2 - 1)^2} \right) + \frac{1}{\pi} \sum_{n=1}^{\infty} \frac{\exp(-\beta_n^2 t_{DL}) J_1(\beta_n R)}{\beta_n^2 (J_1^2(\beta_n R) - J_1^2(\beta_n))} \quad (4-46)$$

where  $\beta_n$  are the roots of

$$\{J_1(\beta_n R)Y_1(\beta_n) - J_1(\beta_n)Y_1(\beta_n R)\} = 0$$

This  $w_D$  function is of the form  $w_D = w_D(t_{DL}, R)$  where  $L$  is associated with  $r_b$ ; the annular aquifer has only one shape parameter, i.e.,  $\Pi_1 = R = r_e/r_b$ . When  $r_b$  is large, this constant rate  $w_D$  function predicts linear flow at early time and the pressure disturbance propagates into the aquifer with a depth of investigation given by

$$r_i = r_b + \sqrt{\frac{5kt}{\phi\mu c_t}} \quad (4-47)$$

When the depth of investigation reaches the aquifer outer boundary at  $r_e$ , the Bessel function summation becomes negligible and the aquifer attains SSS behavior, i.e.,

$$w_D = \left( \frac{2}{R^2 - 1} \left( \frac{1}{4} + t_{DL} \right) - \frac{(3R^4 - 4R^4 \ln R - 2R^2 - 1)}{4(R^2 - 1)^2} \right) \quad (4-48)$$



In the case where  $R$  is large, this reduces to

$$w_D = \left( \frac{2t_{DL}}{R^2} + \ln R - \frac{3}{4} \right) \quad (4-49)$$

which is the classical SSS expression for a closed circular reservoir with a “well” of finite radius  $r_b$ . Thus finite aquifers will eventually attain SSS behavior when produced at constant face rate, i.e., the face pressure will vary linearly with time. In practice, of course, aquifers are not produced at constant rate; however, even when  $w$  is time dependent, the instantaneous dimensionless pressure difference based on the average pressure of the aquifer  $\bar{p}$  and its inner face pressure  $p_{wf}$  i.e.,

$$\hat{w}_D = \frac{(\bar{p}(t) - p_f(t))2\pi kh}{w(t)\mu} \quad (4-50)$$

reaches a quasi-steady-state (QSSS) condition where

$$\frac{(\bar{p}(t) - p_f(t))2\pi kh}{w(t)\mu} = \left( \frac{2}{R^2 - 1} \left( \frac{1}{4} \right) - \frac{(3R^4 - 4R^4 \ln R - 2R^2 - 1)}{4(R^2 - 1)^2} \right) \quad (4-51)$$

or, again when  $R$  is large

$$\frac{(\bar{p}(t) - p_f(t))2\pi kh}{w(t)\mu} = \left( \ln R - \frac{3}{4} \right) \quad (4-52)$$

This QSSS condition is the basis of the Fetkovich aquifer model to be discussed later and also is used in the development of the complex material balance which allows for more realistic geology.

The analytical real-time solution given above, i.e., Eq. (4-46), is difficult to evaluate and an alternative approach is to utilize its precursor in Laplace space which takes the form

$$\tilde{w}_D(s) = \frac{K_1(\sqrt{s} r_{De}) I_0(\sqrt{s}) + I_1(\sqrt{s} r_{De}) K_0(\sqrt{s})}{s^{3/2} \left( I_1(\sqrt{s} r_{De}) K_1(\sqrt{s}) - K_1(\sqrt{s} r_{De}) I_1(\sqrt{s}) \right)} \quad s \rightarrow t_{DL} \quad (4-53)$$

This Laplace space solution can be numerically inverted using the Stehfest algorithm to yield the dimensionless drawdown  $w_D$  at any required time  $t_D$ . When the inner radius  $r_b$  is identified with a wellbore, this becomes the Laplace space solution for a finite wellbore radius well in a closed circular reservoir. The fundamental constant rate solution is referred to as the *constant terminal*

*rate case* in the aquifer literature. It is also possible to obtain a constant terminal pressure solution which predicts the cumulative production for a fixed inner face pressure; this takes the form

$$\tilde{W}_D(s) = \frac{I_1(\sqrt{s} r_{De}) K_1(\sqrt{s}) - K_1(\sqrt{s} r_{De}) I_1(\sqrt{s})}{s^{3/2} (K_1(\sqrt{s} r_{De}) I_0(\sqrt{s}) + I_1(\sqrt{s} r_{De}) K_0(\sqrt{s}))} \quad s \rightarrow t_{DL} \quad (4-54)$$

It was pointed out by Van Everdingen and Hurst that the constant rate and the constant terminal pressure cumulative influx solutions in Laplace space are related by the identity

$$\frac{1}{s^2} = \tilde{w}_D(s) \tilde{W}_D(s) \quad (4-55)$$

Alternatively, the constant terminal pressure (CTP) rate solution denoted  $\tilde{q}_D(s)$  is given by

$$\tilde{q}_D(s) = \frac{I_1(\sqrt{s} r_{De}) K_1(\sqrt{s}) - K_1(\sqrt{s} r_{De}) I_1(\sqrt{s})}{s^{1/2} (K_1(\sqrt{s} r_{De}) I_0(\sqrt{s}) + I_1(\sqrt{s} r_{De}) K_0(\sqrt{s}))} \quad s \rightarrow t_{DL} \quad (4-56)$$

which corresponds to the identity

$$\frac{1}{s} = s \tilde{w}_D(s) \tilde{q}_D(s) \quad (4-57)$$

In these equations,  $q_D = \frac{w(t)\mu}{\Delta p 2\pi kh}$ ,  $W_D = \frac{W\mu}{\Delta p 2\pi kh}$  and  $W = \int_0^t q dt$

## Aquifer material balance

When the aquifer is finite, it is useful to consider its average pressure as defined by an aquifer material balance written as

$$W_e = c_t V_a (p_i - p_a) \quad \text{where} \quad V_a = \phi h \pi (r_e^2 - r_b^2) \quad (4-58)$$

For the special case of constant rate,  $W_e = wt$  and this becomes

$$wt = c_t \phi h \pi (r_e^2 - r_b^2) (p_i - p_a) = c_t \phi h \pi (r_e^2 - r_b^2) \Delta p_a$$

where  $\Delta p_a = p_i - p_a$

i.e., 
$$\frac{\Delta p_a 2\pi kh}{w\mu} = \frac{2kt}{c_t \phi \mu (r_e^2 - r_b^2)} = \left( \frac{2t_{DL}}{(R^2 - 1)} \right)$$

Here  $\Delta p_a$  is the decline in material balance average pressure from the initial value and the term  $\left( \frac{2t_{DL}}{(R^2 - 1)} \right)$  represents the change in average pressure on a dimensionless basis. Similarly, the term

$$\frac{\Delta p_b 2\pi kh}{w\mu} = \left( \frac{2}{R^2 - 1} \left( \frac{1}{4} \right) - \frac{(3R^4 - 4R^4 \ln R - 2R^2 - 1)}{4(R^2 - 1)^2} \right) \tag{4-59}$$

is the difference between the average and face pressures again on a dimensionless basis where  $\Delta p_b = p_a - p_f$ ; thus  $\Delta p_b$  reaches a constant value in the SSS condition. These pressures are illustrated in figure 4-23.

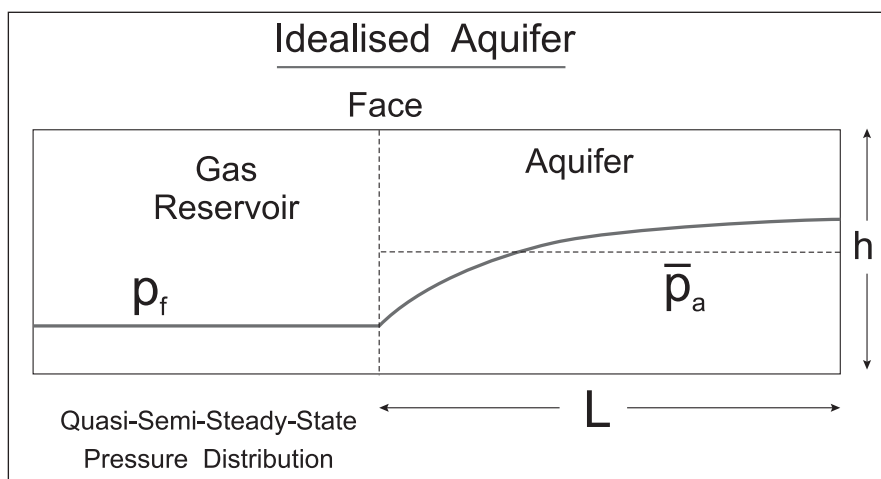


Fig. 4-23. Pressure distribution in an annular aquifer at SSS

### Infinite-acting behavior

When  $R$  is large and radial flow occurs in the system, the depth of investigation follows the familiar equation

$$r_i - r_b = \sqrt{\frac{4kt}{\phi \mu c_t}} \tag{4-60}$$

In the period during which the depth of investigation  $r_i$ , as given by (4-60), is less than the external radius  $r_e$ , the aquifer is essentially infinite-acting and its fundamental (constant rate) response is given by the familiar equation in Laplace space:

$$\tilde{w}_D(s) = \frac{K_0(\sqrt{s})}{s^{3/2}K_1(\sqrt{s})} \quad (4-61)$$

At very early time, the finite inner radius model predicts infinite-acting linear flow where the pressure drop varies with the square root of time, i.e.,

$$w_D = \frac{\Delta p 2\pi kh}{w\mu} = \sqrt{\frac{4t_{DL}}{\pi}} \quad (4-62)$$

Thus a log-log plot of  $w_D$  versus  $t_{DL}$  should exhibit a half slope at very early time (provided  $S_{af}$  is zero).

Equation (4-62) refers to a constant inner face rate situation in infinite-acting conditions and it predicts that the pressure drop ( $p_i - p_{wf}(t)$ ) will vary with the square root of time rather than the logarithmic variation encountered when the inner radius is small; this is a feature of the finite wellbore radius model. It has been demonstrated by Fetkovich that in the case where the rate is varying, then Eq. (4-62) can still be employed in the form

$$\hat{w}_D = \frac{(p_i - p_f(t))2\pi kh}{w(t)\mu} = \sqrt{\frac{4t_{DL}}{\pi}} \quad (4-63)$$

where  $t$  is the total flowing time. Fetkovich argues that the rate normalization implicit in Eq. (4-63) is the most important issue in predicting variable rate behavior, and a transient productivity index  $J_t$  can be used to describe the process; thus

$$w(t) = J_t (p_i - p_f(t)) \quad (4-64)$$

where

$$J_t = \frac{2\pi kh}{\mu \sqrt{\frac{4kt}{\pi\phi\mu c_t r_b^2}}} = 2\pi h \sqrt{\frac{\pi\phi c_t r_b^2 k}{4\mu t}} \quad (4-65)$$

This approach can be used to predict the instantaneous rate  $w(t)$  when the boundary pressure  $p_{wf}(t)$  is a monotonic function of time. Alternatively, Eq. (4-63) may be written in the form

$$w(t) = \frac{b\Delta p}{\sqrt{t}} \quad (4-66)$$

where

$$b = 2\pi h \sqrt{\frac{\pi \phi c_t r_b^2 k}{4\mu}}$$

Suppose now that the pressure drawdown at the inner face is varying linearly with time, i.e.,

$$\Delta p = (p_i - p_f(t)) = at \quad (4-67)$$

Then for this simple prescription of the time dependence of the inner boundary pressure—a single chord approximation—Eq. (4-65) becomes

$$w(t) = \frac{bat}{\sqrt{t}} = ba\sqrt{t} \quad (4-68)$$

and the cumulative influx up to time  $t$  is given by

$$W \approx \int_0^t b \sqrt{t} dt = \frac{2}{3} b (t)^{3/2} \quad (4-69)$$

This formula is valid only in the infinite-acting period of fully transient aquifer influx and requires that the boundary pressure be varying linearly with time. However, this approach gives a reasonably accurate method of calculating, in a simple fashion, the early transient influx from the aquifer. In field units, with time in days, the constant  $b$  becomes

$$b = \frac{2\pi h}{887.2} \sqrt{\frac{\pi \phi c_t r_b^2 k}{4 \times 0.006326\mu}} \quad (4-70a)$$

And, if an encroachment angle  $\theta$  is included, this becomes

$$b = \frac{2\pi h \theta}{887.2 \times 360} \sqrt{\frac{\pi \phi c_t r_b^2 k}{4 \times 0.006326\mu}} \quad (4-70b)$$

Note that the constant  $a$  has units of reciprocal days in this formulation.

## Classical cumulative influx superposition

In the original work by Van Everdingen and Hurst, the dimensionless cumulative influx function  $W_D(t_D)$  was presented in the form of graphs and tables listing  $W_D$  as a function of  $t_D$  for various values of  $R$ ; such a plot is shown in figure 4-24. The general problem of estimating aquifer influx corresponds to the case where the pressure at the aquifer inner

face, i.e., the WGC, is time dependent as shown in figure 4–25. Here the gas reservoir has been represented as a tank with a uniform pressure which is declining due to production.

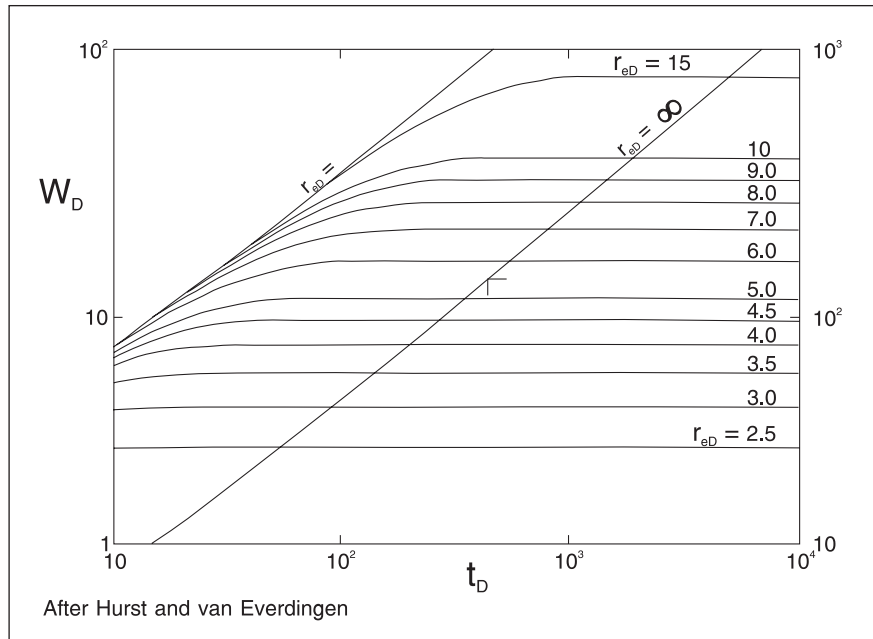


Fig. 4–24. Dimensionless water influx for constant terminal pressure case

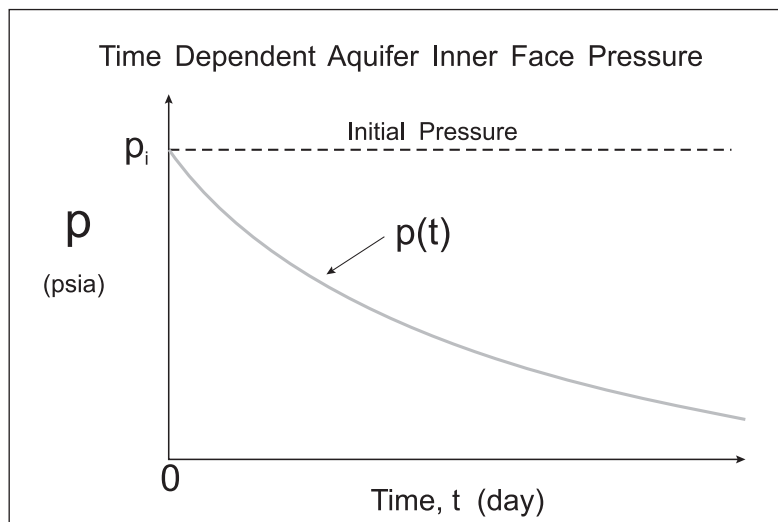


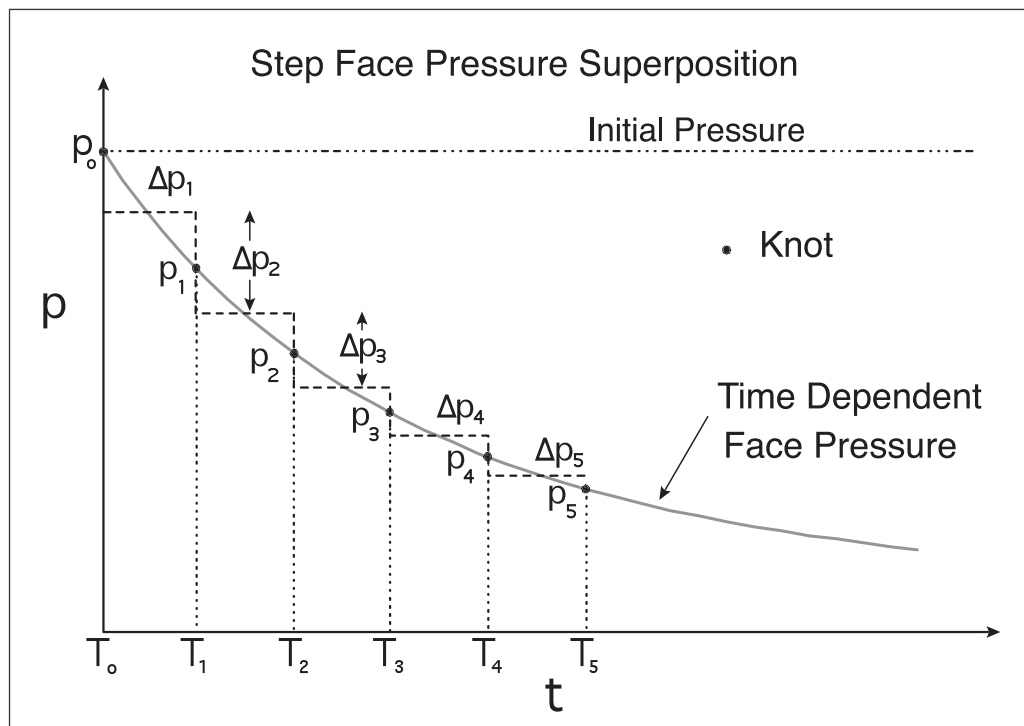
Fig. 4–25. Time-dependent aquifer face pressure

The aquifer therefore experiences a gradually decreasing pressure at its interface with the hydrocarbon system. Neither the face pressure nor the face rate is constant and the problem is to calculate the aquifer influx due to the time dependent boundary condition. Note that the aquifer problem is posed in terms of boundary pressure rather than the flux quantity which occurs in well testing applications. In most textbooks, the basic principle of superposition formulated by Van Everdingen and Hurst, based on the constant terminal pressure solution in cumulative influx form, is used to obtain an answer.

In order to calculate the cumulative influx for a specified inner face pressure, the continuous function is replaced by a series of constant pressure segments as shown in figure 4–26. Here the face pressures  $p_i$  at times  $T_i$  are denoted by the solid points (knots). Thus the continuous pressure schedule is specified as in table 4–5:

**Table 4–5.** Specification of boundary pressure data

Time	Pressure
$T_1$	$p_1$
..	..
$T_i$	$p_i$
..	..
$T_N$	$p_N$



**Fig. 4–26.** Step boundary pressure approximation

The initial boundary pressure is designated  $p_0$  and the start time is  $T_0$ ; in the calculation of influx, it is assumed that at  $T_0$  the aquifer is everywhere at uniform initial pressure  $p_0$ . The average face pressures (indicated by the dotted lines in the diagram) during each segment are given by

$$\bar{p}_i = \frac{p_{i-1} + p_i}{2} \tag{4-71}$$

and the incremental pressure drops are

$$\Delta p_1 = p_o - \bar{p}_1 = p_o - \frac{p_o + p_1}{2} = \frac{p_o - p_1}{2}$$

$$\Delta p_2 = \bar{p}_1 - \bar{p}_2 = \frac{p_o + p_1}{2} - \frac{p_1 + p_2}{2} = \frac{p_o - p_2}{2}$$

$$\Delta p_3 = \bar{p}_2 - \bar{p}_3 = \frac{p_1 + p_2}{2} - \frac{p_2 + p_3}{2} = \frac{p_1 - p_3}{2}$$

·  
·  
·

$$\Delta p_i = \bar{p}_{i-1} - \bar{p}_i = \frac{p_{i-2} + p_{i-1}}{2} - \frac{p_{i-1} + p_i}{2} = \frac{p_{i-2} - p_i}{2}$$

The cumulative water influx at some time  $t$  in the  $N$ -th time interval is obtained as a superposition of the individual terms, i.e.,

$$W_e(t) = U \left[ \Delta p_1 W_e(t_D) + \Delta p_2 W_e(t_D - T_{1,D}) + \dots + \Delta p_i W_e(t_D - T_{i-1,D}) + \dots + \Delta p_N W_e(t_D - T_{N-1,D}) \right] \quad (4-72)$$

where  $U = 2\pi f h c_t r_b^2$  and  $f = \frac{\theta}{360}$

The geometric factor  $f$  allows the aquifer to assume the form of a segment as shown in figure 4-27.



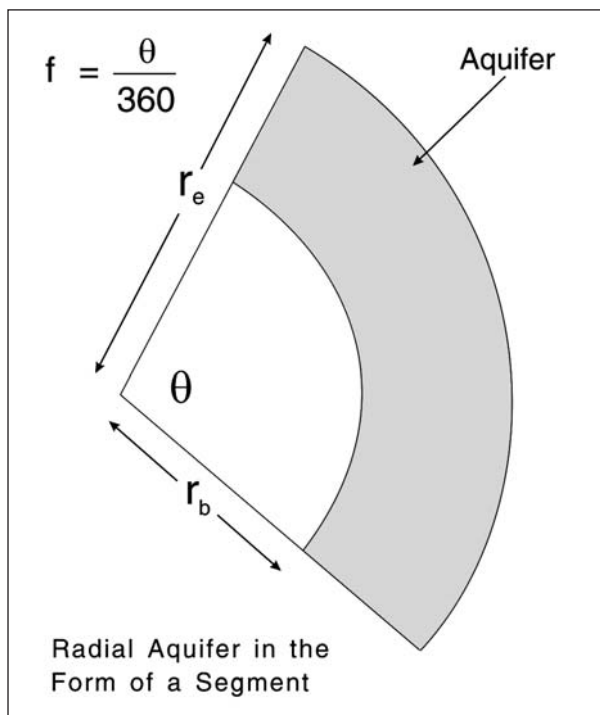


Fig. 4-27. Segmental aquifer geometry and the geometric factor  $f$

### Laplace space convolution

It is possible to proceed in a quite different way and use convolution in Laplace space to generate the variable boundary pressure response. In layered well test analysis, it is necessary to predict the rate response of a system for a measured wellbore pressure response; this is identical to the aquifer influx problem and the same methodology is applicable. Convolution in Laplace space may be written succinctly as

$$\tilde{p}_D(s) = s \tilde{q}_D(s) \tilde{\Pi}_D(s) \quad s \rightarrow t_D \tag{4-73}$$

Here  $\Pi_D(t_D)$  is a fundamental (constant rate) analytical model whose Laplace transform is  $\tilde{\Pi}_D(s)$  and

$$q_D(t_D) = \frac{q(t)}{q_r} \tag{4-74}$$

is a normalized variable rate schedule for which the pressure response  $p_D(t_D)$  is to be generated, where

$$p_D = \frac{(p_i - p_f(t)) 2\pi kh}{q_r \mu} \tag{4-75}$$

In the present case, it is the rate response that has to be generated and the convolution takes the complementary form

$$\tilde{q}_D(s) = \frac{\tilde{p}_D(s)}{s\tilde{\Pi}_D(s)} \quad (4-76)$$

In order to carry out this process, the known pressure signal must be Laplace-transformed numerically using the algorithm of Stewart and Rouboutsos.<sup>3</sup> In this approach, the continuous time-dependent face pressure is represented by piecewise linear segments as shown in figure 4–28; in the case of a time-dependent aquifer face pressure, this form of representation is very efficient since the variation is smooth and does not exhibit discontinuities. Given the table of knots, the Laplace transform of the given pressure function  $\tilde{p}(s)$  can be evaluated using the Stewart and Rouboutsos formula

$$L[f(t)] = \tilde{f}(s) = \frac{\dot{f}_0}{s^2}(1 - e^{-sT_1}) + \sum_{i=2}^{N-2} \frac{\dot{f}_i}{s^2}(e^{-sT_i} - e^{-sT_{i+1}}) + \frac{\dot{f}_N}{s^2}e^{-sT_{N-1}} \quad (4-77)$$

where

$$\dot{f}_{i-1} = \frac{f_i - f_{i-1}}{T_i - T_{i-1}}$$

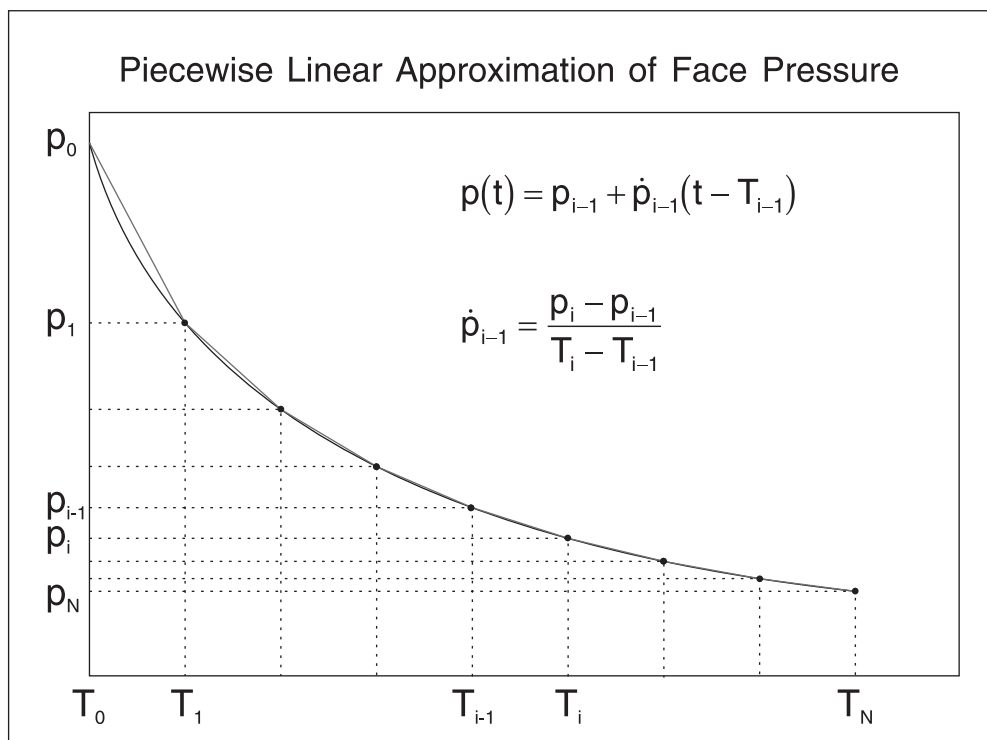


Fig. 4–28. Piecewise linear approximation of the continuous boundary pressure

The analytical model  $\tilde{\Pi}_D(s)$  corresponds to Eq. (4-53) in the case of a cylindrical closed aquifer. Equation (4-76) demonstrates how the constant terminal rate solution can be used to determine the aquifer influx rate for a known pressure history at its active face. Since the Stehfest algorithm is used to invert the convolution Eq. (4-76), only one Stehfest inversion is required to generate a point in the response. This is in stark contrast to the superposition method which requires a Stehfest inversion for every term in the summation! Hence the Laplace space convolution, with numerical transformation of the boundary pressure, is a fast process and gives excellent results.

## Fetkovich model

In order to avoid the complication of superposition or convolution, Fetkovich<sup>4</sup> proposed a simplified aquifer influx model based on the assumption of QSSS behavior as expressed by Eq. (4-78), i.e.,

$$\frac{(\bar{p}(t) - p_f(t))2\pi kh}{w(t)\mu} = \left( \ln R - \frac{3}{4} \right) \quad (4-78)$$

which states that the instantaneous influx  $w(t)$  depends only on the current aquifer average pressure  $\bar{p}(t)$  and the current face pressure  $p_f(t)$ . The influx is therefore described by the simple equation

$$w(t) = J_a (\bar{p}(t) - p_f(t)) \quad (4-79)$$

where

$$J_a = \frac{2\pi kh}{\mu_w \left( \ln R - \frac{3}{4} \right)} \quad (4-80)$$

This form is applicable only when  $R$  is large, and for small  $R$  the correct form is

$$J_a = \frac{2\pi kh}{\mu_w \left( \left( \frac{2}{R^2 - 1} \left( \frac{1}{4} \right) - \frac{(3R^4 - 4R^4 \ln R - 2R^2 - 1)}{4(R^2 - 1)^2} \right) \right)} \quad (4-81)$$

For example, for  $R=5$ , the simple expression  $\ln R - 0.75$  gives the numerical value of 0.8594, whereas the exact expression comes to 0.9755; hence in aquifer calculations, where  $R$  is relatively small, care should be taken to use the appropriate formula for  $J_a$ . In the Fetkovich method, the effect of history is ignored by assuming a sequence of QSSSs.

The material balance for the aquifer is now written in differential form as

$$c_t V \frac{d\bar{p}}{dt} = -w = -J_a (\bar{p} - p_f(t)) \quad (4-82)$$

i.e.,

$$\frac{d\bar{p}}{dt} = - \frac{J_a (\bar{p} - p_f(t))}{c_t V} \quad (4-83)$$

where

$$V = \pi \phi h (r_e^2 - r_b^2) \quad (4-84)$$

Thus the aquifer influx problem has been expressed as an ordinary differential equation (4-83), which can be integrated forward in time provided the boundary pressure  $p_f(t)$  is a specified time function. Again, linear interpolation of the boundary pressure (LIBP) can be used in the integration process using, for example, a Runge–Kutta method. The initial condition at  $t = 0$  corresponds to a known initial (face) pressure  $p_i$ . The prescribed inner boundary pressure is the forcing function for the lumped parameter aquifer influx model. In the special case where the face pressure  $p_f$  is constant, there is an analytical result for the integration from  $t = 0$  to  $t = T$ , viz.,

$$\bar{p}(T) - p_f = (p_i - p_f) \exp \left( - \frac{J_a T}{c_t V} \right) \quad (4-85)$$

or

$$W_e = c_t V (p_i - p_f) \left( 1 - \exp \left( - \frac{J_a T}{c_t V} \right) \right) \quad (4-86)$$

Note that in the original Fetkovich paper a simple step-rate superposition was proposed; however, the addition of linear interpolation of the boundary pressure considerably improves the method. The numerical solution of the system (4-83) using a Runge–Kutta algorithm is preferred to an analytical approach since it has been found that, for the case of compartmentalized systems involving multiple cells, the numerical method is much faster to compute.

## Test problem

In order to demonstrate the behavior of these aquifer models, it is useful to consider the test problem defined by Dake<sup>5</sup> in his textbook on reservoir engineering; this case was also considered in detail by Leung<sup>6</sup> in his work on aquifer influx. The example refers to a closed cylindrical aquifer with the properties listed in table 4-6.

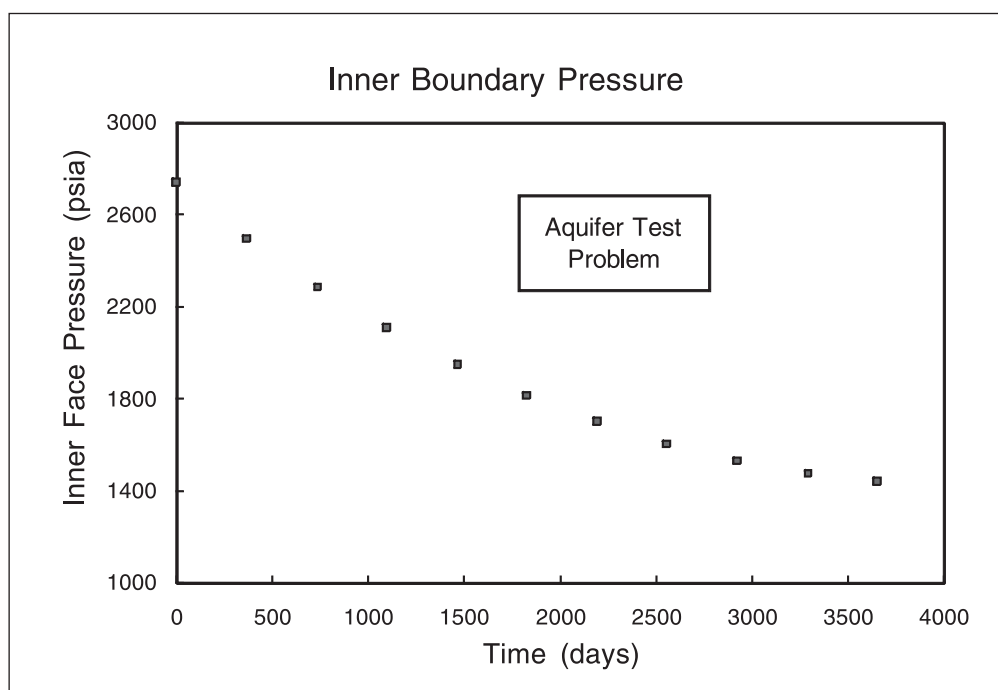
**Table 4-6.** Reservoir parameters for radial aquifer test problem

$h = 100$ ft	$k = 200$ md	$\mu_w = 0.55$ cp
$\phi = 0.25$	$c_w = 3.0 \times 10^{-6}$ psi <sup>-1</sup>	$c_f = 4.0 \times 10^{-6}$ psi <sup>-1</sup>
$r_b = 9,200$ ft	$\theta = 140^\circ$	$R = 5$

The aquifer is subjected to the inner boundary pressure history listed in table 4–7 and shown in figure 4–29.

**Table 4–7.** Radial aquifer specified inner boundary pressure

Time (years)	Pressure (psia)	Time (years)	Pressure (psia)	Time (years)	Pressure (psia)
0	2,740	4	1,949	8	1,535
1	2,500	5	1,818	9	1,480
2	2,290	6	1,702	10	1,440
3	2,109	7	1,608		



**Fig. 4–29.** Aquifer inner boundary pressure history for test problem

If this radial system was flowed at constant rate, it would take 1.3 years, i.e. 475 days, to reach an SSS condition; hence the first year of the overall 10-year period is in transient (infinite-acting) flow. The outer radius of the aquifer corresponds to an  $r_e$  of  $5 \times 9,200 = 46,000$  ft, i.e., an aquifer whose outer dimension is of the order of 9 miles.

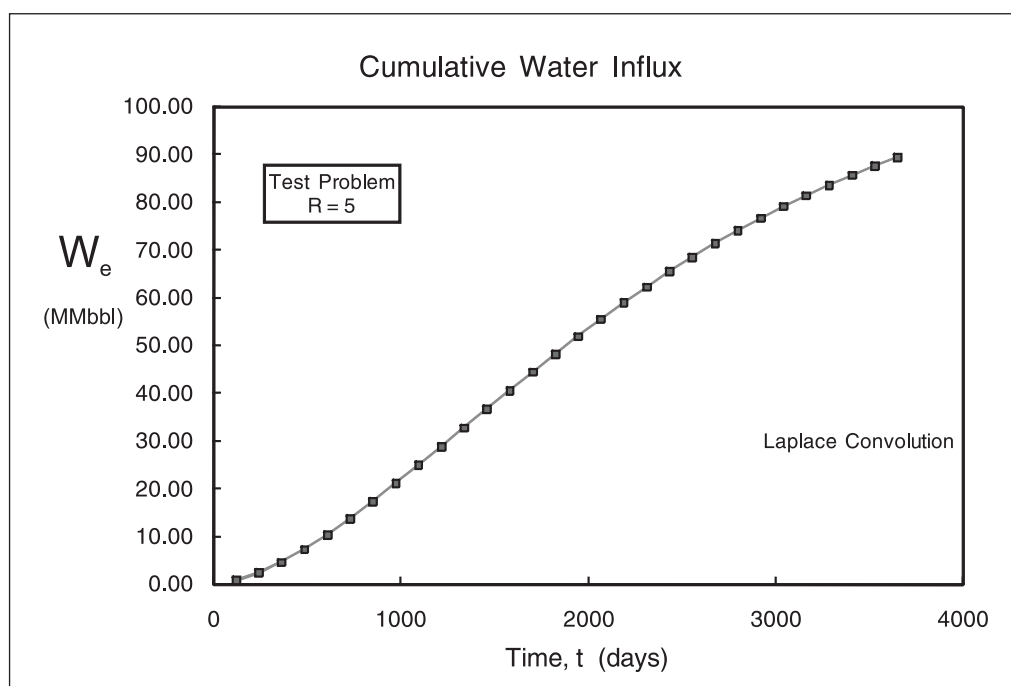
The aquifer influx calculated by superposition of the  $w_D$  function is listed in table 4–8; the details of these calculations are described by Dake and essentially 1-year periods have been adopted for the superposition according to the prescription described in section “Radial Aquifer Models” and illustrated in figure 4–29. Increasing the number of steps makes very little difference to the results and the integrated (cumulative) formulation of Van Everdingen and Hurst gives sufficiently accurate simulation with only 10 steps.

Also listed in table 4–8 are the results of Laplace space convolution using the Stehfest algorithm ( $N = 12$ ) and a piecewise linear approximation to the pressure history; these results are

virtually identical to those obtained by classical superposition but the computation time is about an order of magnitude less. Superposition is very inefficient when many steps are employed and the convolution in Laplace space is much faster in terms of computation time. The results of the aquifer influx calculations are shown in figure 4–30.

**Table 4–8.** Aquifer influx results for test problem

Time (days)	Laplace convolution W (MMbbl)	Classical superposition W (MMbbl)	Fetkovich (psss) W (MMbbl)
36.525	1.39E-01	8.55E-02	2.36E-01
365.25	4.260725	3.911757	4.17034
730.5	13.22139	12.93382	12.93352
1,095.75	24.28546	24.11856	24.24273
1,461	35.98236	35.93648	36.2243
1,826.25	47.45877	47.44653	47.84958
2,191.5	58.15819	58.15299	58.7064
2,556.75	67.67988	67.84524	68.49142
2,922	75.87602	76.28386	76.97159
3,287.25	82.80932	83.38869	84.04322
3,652.5	88.65728	89.19522	89.89316



**Fig. 4–30.** Cumulative aquifer influx as a function of time by convolution

The results of the modified Fetkovich method are also given in table 4–8 and for this case ( $R = 5$ ) the difference from the exact methods is negligible; note that Eq. (4–81) has been used

to compute  $J_a$  although in the original method Fetkovich used only the less exact (4–80). These runs illustrate the validity of the Fetkovich aquifer model (in continuous form) and it can safely be used as a basis for modeling aquifer influx. It was pointed out by Leung that when the time constant of the aquifer, i.e., the time to reach SSS, is short compared to the timescale of the forcing pressure variation, then the influx can be regarded as a succession of SSS conditions; this is the case in the present example.

In the first year of influx, a detailed calculation using 30 steps—either in Laplace space or by classical superposition—shows that the cumulative influx in this transient period is 4.56 MMbbl and the result of this calculation is shown, for interest, in figure 4–31.

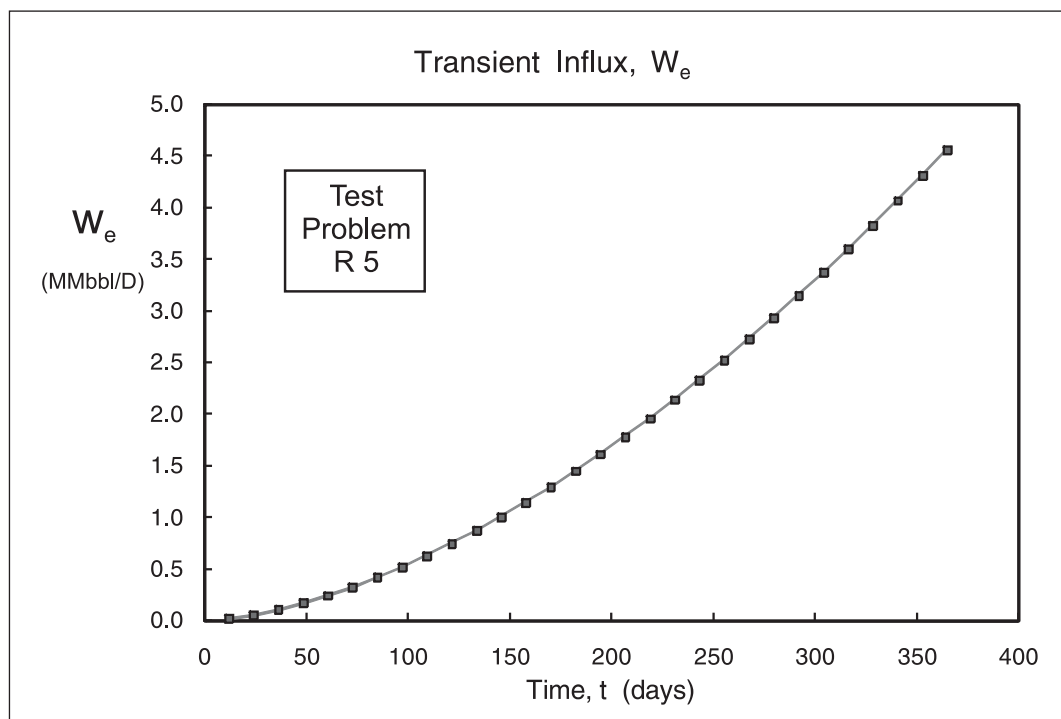


Fig. 4–31. Detailed Laplace convolution for the transient (I–A) period

## Effect of the invaded zone

In the section “Principle of Superposition” the concept of an aquifer skin was introduced which allowed the modeling of a tight zone located near the WGC and the additional pressure drop over the barrier reduces the rate of aquifer influx. In 1977, Lutes *et al.*<sup>7</sup> suggested that a modified material balance was necessary to account for the pressure gradient in the reservoir in order to allow prediction of the trapped gas volume which is strongly dependent on pressure. Pressure gradients play an important role in overall reservoir performance and the shape of  $p/z$  curves. This work was extended by Hower and Jones,<sup>8</sup> who validated a modified material balance by comparison with a numerical simulation model. In the context of a radial aquifer, the water influx creates an invaded zone as illustrated in figure 4–32; in this region, gas is trapped at a residual saturation  $S_{gr}$ . Suppose a cumulative water influx (in situ volume)  $W_e$  has occurred; then the pore volume of the invaded region  $V_i$  is given by

$$V_i = \frac{W_e}{1 - S_{gr} - S_{wc}} \quad (4-87)$$

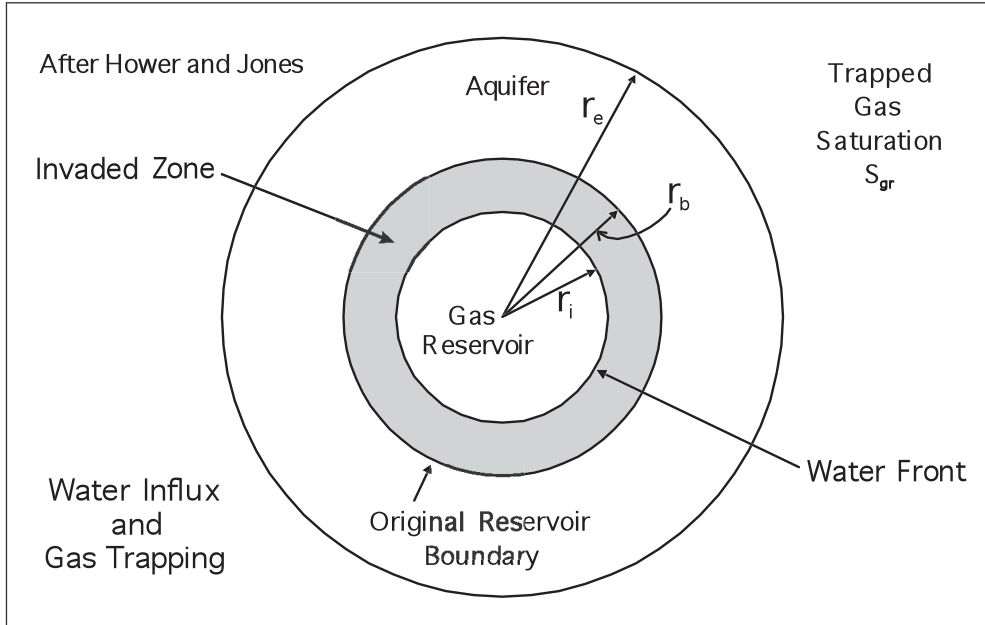


Fig. 4-32. Development of an invaded zone

Here  $S_{gr}$  is the trapped gas saturation which is of the order of 0.35 in sandstone reservoirs and 0.25 in chalk; a detailed discussion of the mechanism of gas trapping is given later in the section "Residual Gas Saturation in Water-Drive Gas Reservoirs." Note that the connate water saturation originally in the gas zone, i.e.,  $S_{wc}$ , and the trapped gas saturation, i.e.,  $S_{gr}$ , both affect how far the invading water penetrates into the reservoir. For a radial (annular) geometry, the location of the water front—assuming piston displacement—is given by

$$\pi(r_b^2 - r_i^2)\phi h = V_i = \frac{W_e}{1 - S_{gr} - S_{wc}} \quad (4-88)$$

i.e.,

$$r_i^2 = \left( r_b^2 - \frac{W_e}{(1 - S_{gr} - S_{wc})\pi\phi h} \right)^{1/2}$$

The flow of water in the invaded region is impeded by the presence of the residual gas saturation, and the pressure drop, following Hower and Jones, can be calculated approximately as

$$\Delta p_{inv} = p_f - \bar{p}_g = \frac{w\mu_w}{2\pi k k_{rw}^o h} \ln \frac{r_b}{r_i} \quad (4-89)$$



where  $w = \frac{dW_e}{dt}$

This is equivalent to defining a time-dependent aquifer face skin  $S_{af}$  equal to

$$S_{af} = \frac{\ln \frac{r_b}{r_i}}{k_{rw}^o} \quad (4-90)$$

where  $k_{rw}^o$  is an effective end-point relative permeability of water at residual gas saturation. This quantity can be quite small (0.05–0.20) and hence the pressure drop over the invaded zone can be significant. The average volumetric pressure in the invaded zone, assuming SS radial flow, is given by the equation

$$\bar{p}_{inv} = p_f - \frac{w\mu_w}{\pi k_{rw}^o kh} \left( \frac{1}{4} - \frac{r_b^2 \ln \frac{r_b}{r_i}}{2(r_b^2 - r_i^2)} \right) \quad (4-91)$$

where  $p_f$  is the aquifer face pressure at  $r_b$ .

In the preceding treatment, the aquifer face pressure  $p_f$  is employed and it is necessary to compute this quantity to evaluate the average pressure in the invaded region  $\bar{p}_{inv}$ . Since the Fetkovich aquifer model has been shown to be more than adequate for practical purposes, this procedure will be modified to allow the inclusion of the hydraulic resistance of the developing invaded region. Letting the gas reservoir pressure be denoted  $\bar{p}_g$  the Fetkovich model may now be written as

$$c_t V \frac{d\bar{p}}{dt} = -w = -J_a (\bar{p} - p_f(t)) = -J_a (\bar{p} - (\bar{p}_g + \Delta p_{inv})) \quad (4-92)$$

where  $\Delta p_{inv}$  is given by Eq. (4-89). The basic Fetkovich aquifer deliverability index  $J_a$  may be expressed as

$$J_a = \frac{2\pi kh}{\mu_w f(R)} \quad \text{where} \quad f(R) = \left( \left( \frac{2}{R^2 - 1} \left( \frac{1}{4} \right) - \frac{(3R^4 - 4R^4 \ln R - 2R^2 - 1)}{4(R^2 - 1)^2} \right) \right)$$

where the dimensionless function  $f(R)$  expresses the influence of aquifer shape. When an aquifer face skin is present, the index is modified to take the form

$$J_a^m = \frac{2\pi kh}{\mu_w (f(R) + S_{af})} \quad (4-93)$$

and Eq. (4-92) can be written in the equivalent form

$$c_t V \frac{d\bar{p}}{dt} = -w = -J_a^m (\bar{p} - \bar{p}_g) \quad (4-94)$$

with  $S_{af}$  given dynamically by (4-90). In this model, the aquifer index is composed of the single-phase flow mobility term  $2\pi kh/\mu_w$  and the dimensionless geometry term  $f(R)$ , and  $S_{af}$  representing the reduced water mobility in the invaded region because of gas trapping.

The Fetkovich model in this mode operates in terms of the average pressure  $\bar{p}$  in the aquifer region and the gas reservoir pressure  $\bar{p}_g$  but it is possible to compute the aquifer face pressure  $p_f$  from the basic expression

$$p_f = \bar{p} - \frac{w}{J_a} \quad (4-95)$$

where  $J_a$  is the basic aquifer index without the inclusion of a skin effect. Equations (4-95) and (4-91) allow the average pressure in the invaded region to be determined in the context of an aquifer influx calculation.

The distribution of pressure in the system is illustrated in figure 4-33, where the importance of determining  $\bar{p}_{inv}$  arises from the premise that, over a time interval  $\Delta t$  in which the invaded zone grows from  $r_i$  to  $r_i + \Delta r_i$ , the incremental mass of trapped gas  $\Delta m_T$  is given by

$$\Delta m_T = \Delta V_i \rho_g(\bar{p}_{inv}) S_{gr} \quad (4-96)$$

where  $\rho_g(\bar{p}_{inv})$  is the gas density evaluated from an EOS using the current invaded zone average pressure  $\bar{p}_{inv}$  and  $\Delta V_i = \frac{\Delta W_e}{1 - S_{gr} - S_{wc}}$

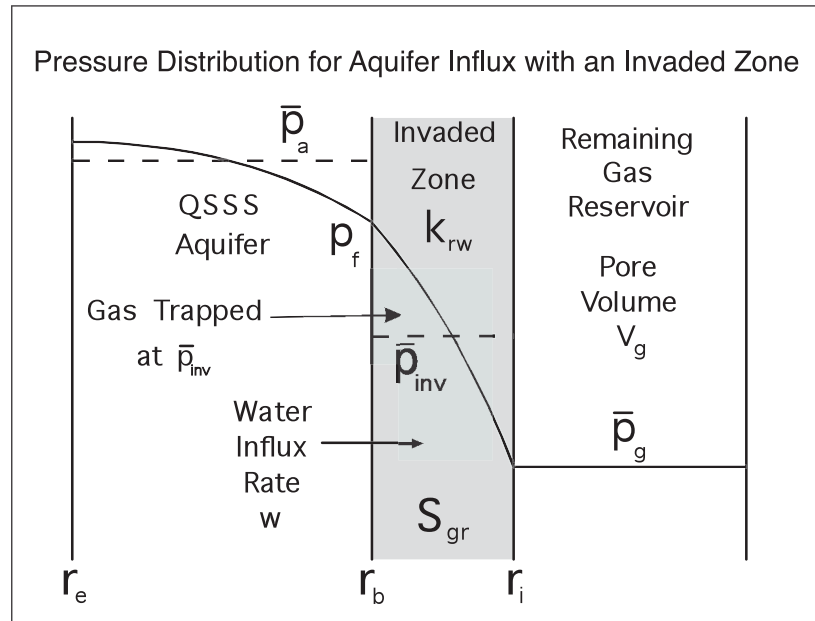


Fig. 4-33. Pressure distribution for aquifer influx

The effect of including a dynamic skin to account for the evolving invaded region is to slow down the rate of aquifer encroachment because of the additional hydraulic resistance due principally to the low relative permeability to water as a result of trapped gas. Thus it is capillary forces that induce this effect and, when the pressure drop is incorporated into the material balance calculation, a higher pressure at the original boundary  $p_f$  is predicted and a lower water influx is obtained. In addition, the mass of trapped gas is evaluated at the appropriate pressure and the quantity  $\Delta m_T$  can be integrated to yield the cumulative trapped gas as the water invades the gas reservoir. The current view is that this gas is largely not recovered with continuing blowdown because of the low relative permeability to gas  $k_{rg}$  also present in the invaded region.

In this analysis, the rock permeability  $k$  is assumed to be the same in the aquifer and the invaded region. However, in many cases the aquifer rock has been affected by continuing diagenesis after hydrocarbon accumulation has effectively terminated further change in the gas zone. Hence the reduction in water mobility due to residual gas may be offset, to some extent, by a larger absolute permeability in the invaded region  $k_{inv}$ . The aquifer face skin factor should therefore be written as

$$S_{af} = \frac{k_a \ln \frac{r_b}{r_i}}{k_{inv} k_{rw}^o} \quad (4-97)$$

Such a contrast in permeability would be shown up by core analysis of plugs taken from the original water and gas zones, respectively. A modified water relative permeability  $k'_{rw}$ , defined as

$$k'_{rw} = \frac{k_{rw}^o k_{inv}}{k_a} \quad (4-98)$$

would constitute an easy way of including this effect where necessary; here  $k_a$  is the absolute permeability of the aquifer rock.

## Further Aquifer Types

### Outcropping radial aquifers

In the preceding treatment, the radial aquifer is of the closed type and the outer boundary condition at the external radius  $r_e$  is a no-flow specification, i.e.,  $dp/dr = 0$  at  $r = r_e$ . In certain circumstances, aquifers are replenished from the surface and maintained at constant pressure at their outer boundary; this case is referred to as an *outcropping aquifer*. For example, in the Bass Straits in Australia, there is an extremely strong water drive through an aquifer which is fed from the Snowy Mountains, and one oil reservoir—the Kingfish field operated by Exxon—has produced throughout its life (in the absence of water injection) with essentially negligible pressure decline, i.e., complete pressure maintenance by natural water influx. The reservoirs in Papua New Guinea are also fed by very active aquifers which are in a dynamic state even without hydrocarbon production from reservoirs; this is evidenced by the tilted hydrocarbon contact in the unproduced field. The mathematical model of such systems—which are quite rare—is the constant-pressure outer boundary given by

$$p = p_e \quad \text{at} \quad r = r_e \quad (4-99)$$

The analytical solution for this case in real time is given by

$$w_D = \ln R - 2 \sum_{n=1}^{\infty} \frac{\exp(-\beta_n^2 t_{DL}) J_0^2(\beta_n R)}{\beta_n^2 (J_1^2(\beta_n) - J_0^2(\beta_n R))} \quad (4-100)$$

where  $\beta_n$  are the roots of

$$J_1(\beta_n) Y_0(\beta_n r_{De}) - Y_1(\beta_n) J_0(\beta_n r_{De}) = 0$$

The precursor Laplace space solution takes the form

$$\tilde{w}_D(s) = \frac{I_0(\sqrt{s} r_{De}) K_0(\sqrt{s}) - K_0(\sqrt{s} r_{De}) I_0(\sqrt{s})}{s^{3/2} (K_0(\sqrt{s} r_{De}) I_1(\sqrt{s}) + I_0(\sqrt{s} r_{De}) K_1(\sqrt{s}))} \quad (4-101)$$

For a constant inner (terminal) boundary pressure  $p_i$ , the outcropping aquifer reaches an SS condition where

$$w_D = \frac{\Delta p 2\pi kh}{w\mu} = \frac{(p_e - p_i) 2\pi kh}{w\mu} = \ln \frac{r_e}{r_b} \quad (4-102)$$

In this formulation  $p_e$  is not, of course, the actual surface pressure but rather the surface pressure corrected to reservoir depth using an appropriate water gradient. The time to reach an SS condition is given approximately by

$$r_e - r_b = \sqrt{\frac{4kt}{\phi\mu c_t}} \quad \text{if } R \text{ is large (radial flow)}$$

or

$$r_e - r_b = \sqrt{\frac{5kt}{\phi\mu c_t}} \quad \text{if } R \text{ is small (linear flow)}$$

### Linear Aquifer

In areas where faulting fixes reservoir boundaries, the fault block reservoir may have an aquifer of limited extent whose geometry is best approximated by a linear system as illustrated in figure 4–34.

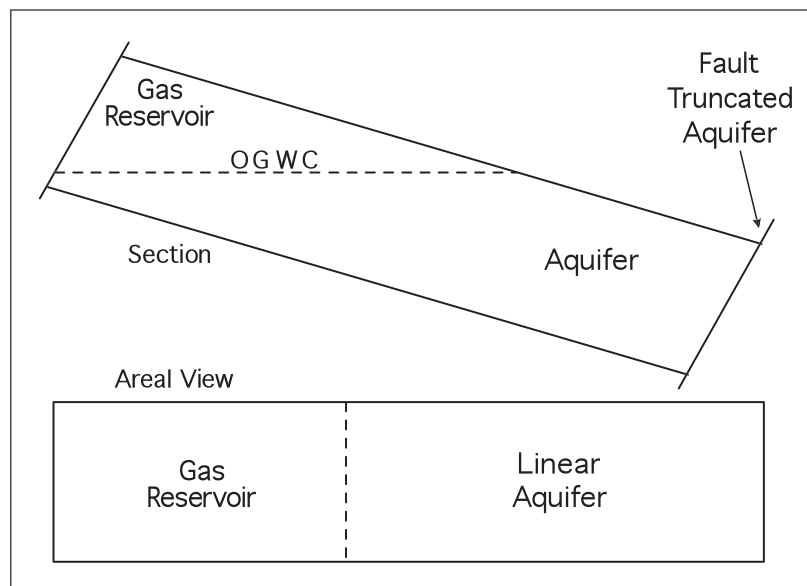


Fig. 4–34. Fault block reservoir with linear aquifer of limited extent

A linear aquifer can occur as a regional feature whenever water movement through the aquifer member is constrained to one direction. Such constraints can arise from major faults, facies change, or pinchout of the member. The constant face rate  $w_D$  function for the linear aquifer of finite length  $L$  and width  $b$  is given by

$$w_D = \frac{\Delta p 2\pi kh}{w\mu} = \frac{2\pi L}{b} \left( \left( \frac{1}{3} + t_{DL} \right) - \frac{2}{\pi^2} \sum_{n=1}^{\infty} \left( \frac{1}{n^2} \right) \exp(-n^2 \pi^2 t_{DL}) \right) \quad (4-103)$$

where 
$$t_{DL} = \frac{kt}{\phi\mu c_t L^2}$$

The  $w_D$  function for a linear aquifer has the form

$$w_D = w_D(t_{DL}, R) \quad \text{where} \quad R = \Pi_1 = L/b$$

Again, when the depth of investigation reaches the far boundary of the aquifer (or more precisely  $t_{DL} > 2.5$ ), this  $w_D$  function also exhibits SSS behavior, i.e.,

$$w_D = \frac{\Delta p 2\pi kh}{w\mu} = \frac{2\pi L}{3b} \quad (4-104)$$

where  $\Delta p_b = p_a - p_f$  and  $\Delta p_a = p_i - p_a$  with  $p_a$  the average pressure in the aquifer. The length of investigation in linear flow is give by

$$l_i = \sqrt{\frac{5k}{\phi\mu c_t}} \quad (4-105)$$

When  $l_i$  is less than  $L$ , the aquifer is infinite-acting and the fundamental  $w_D$  function reduces to the simple form

$$w_D = \frac{\Delta p 2\pi kh}{w\mu} = \sqrt{16\pi t_{Db}} \quad (4-106)$$

where 
$$t_{Db} = \frac{kt}{\phi\mu c_t b^2}$$

In the case of a linear aquifer, it is instructive to examine the concept of aquifer face skin in detail; suppose that there is a semipermeable tight zone of thickness  $l_b$  and permeability  $k_b$  at the active face, i.e., the GWC. The additional pressure drop due to this linear skin zone is given by

$$\Delta p_s = \frac{w\mu l_b}{bhk_b} = \frac{w}{T} \quad \text{where} \quad T = \frac{bhk_b}{\mu l_b}$$

Here  $T$  is the barrier conductivity, i.e., the proportionality constant between flow rate and pressure drop. Although it is never possible to individually identify the permeability and thickness of such a tight zone, the idea of an additional barrier to communication between

aquifer and reservoir is crucial to properly understand real aquifer responses. The barrier can be characterized by its conductivity  $T$  or by the aquifer face skin factor  $S_{af}$ , defined by the relation

$$S_{af} = \frac{\Delta p_s 2\pi kh}{w\mu} = \frac{2\pi kl_b}{k_b b} = \frac{2\pi kh}{\mu T} \tag{4-107}$$

Since it is convenient even in linear flow to retain the factor of  $2\pi$  in the definition of the dimensionless pressure drop  $w_D$ , the aquifer face skin  $S_{af}$  reflects this choice. Strictly speaking, the  $2\pi$  should not be used in linear flow situations, but maintaining a single definition of  $w_D$  identical to that of  $p_D$  helps to promote interchangeability between well testing and aquifer influx studies.

### Fetkovich linear aquifer

The original theory of the QSSS aquifer influx model was based on radial cylindrical geometry. However, it is straightforward to derive an analogous expression for the case of a linear aquifer illustrated in figure 4–35. Thus, from Eq. (4–104), the aquifer influx is given by

$$w(t) = J_a (p_a(t) - p_f(t)) \tag{4-108a}$$

where

$$J_a = \frac{3kbh}{\mu_w L} \tag{4-108b}$$

This is the Fetkovich model for a linear aquifer and the only difference from the treatment given previously is the changed definition of the aquifer index  $J_a$ .

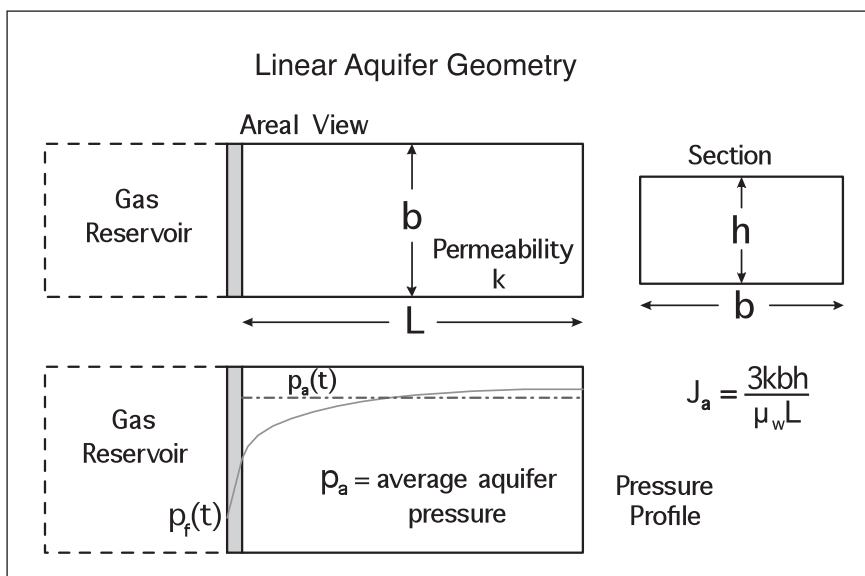


Fig. 4–35. Linear aquifer geometry

## Determination of aquifer parameters

The aquifer response for a prescribed pressure history at its face is principally controlled by

- permeability  $k$
- inner radius  $r_b$  or width  $b$
- size governed by  $R$
- porosity  $\phi$
- aquifer face skin  $S_{af}$

given that the water viscosity  $\mu$  and total compressibility  $c_t$  are fixed. As previously mentioned, any semipermeable barrier inhibiting communication between aquifer and gas body is handled through a skin factor  $S_{af}$ . In an automatic matching exercise, the aquifer porosity  $\phi$  and the length of contact with the reservoir  $r_b$  or  $b$  will hopefully be known, and the key aquifer parameters to be determined are

- permeability
- size
- face skin

Note that when  $r_e/r_b$  is not large, say less than 2, there is little difference between the annular and linear aquifer models and either one could be used.

Given a set of pressure observations, i.e., the build-up pressures at times  $T_i$ , and an assumed rate history, the automatic matching method can be used to determine parameter values which best match predicted pressures to the measurements. This fit is characterized by a value of  $\chi^2$ : if  $G_i$  has been well chosen, the fit will be good but if  $G_i$  has been badly selected giving ridiculous water influx estimates, the aquifer model will not be able to fit the data. Hence  $G_i$  is varied and a graph of  $\chi_{\min}^2$  versus  $G_i$  is plotted as shown in figure 4–36; the best estimate of the reserves  $G_i$  is the value which gives the lowest value of  $\chi_{\min}^2$ . This procedure requires the selection of an aquifer model and then proceeds to find the optimal values of both  $G_i$  and the aquifer parameters that best match the pressure observations. The technique is closely allied to well-proven methods in pressure transient testing and uses the powerful Levenberg–Marquardt algorithm to solve the aquifer influx problem. Sufficient pressure points, i.e. buildups must be available to fix the number of unknown parameters in the model: unfortunately, it is often possible to obtain build-up data only in the summer months when demand for gas is low. Such practical considerations may limit the ability to properly characterize the aquifer model. The approach described here allows methodology developed for well testing to be used in aquifer influx studies. Once the aquifer parameters have been identified, the model can be used in simulation mode to predict future behavior.



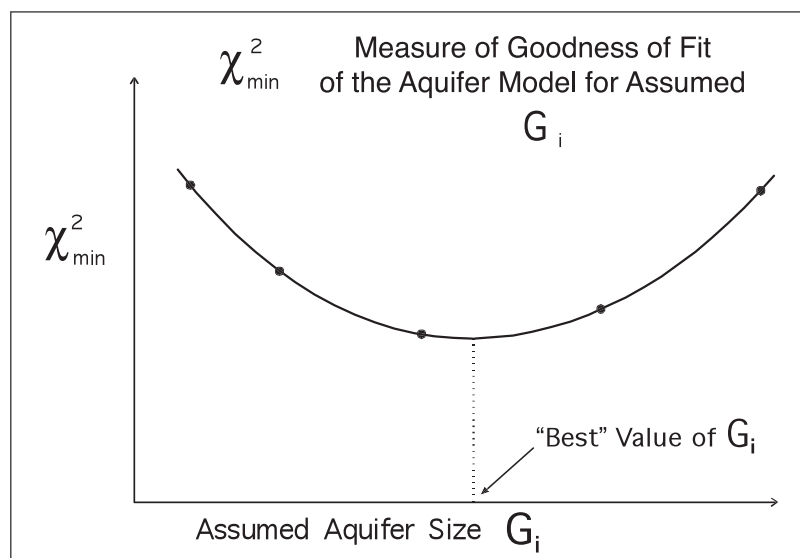


Fig. 4–36. Objective function at the minimum versus gas in place

## Deconvolution method

The second approach to resolving the problem of aquifer influx is the deconvolution method, which aims to convert the measured variable rate response to the constant rate equivalent using desuperposition. The process of deconvolution is not straightforward and it is adversely affected by noise in the data. The problem in aquifer influx identification is that the face rate is not measured directly but is deduced from the gas material balance assuming a value for  $G_i$ . Hence the whole deconvolution process may be upset by completely wrong flow information. In essence, given a measured pressure response  $\Delta p(t)$  and the corresponding rate schedule  $w(t)$ , a deconvolution algorithm will return the influence function  $F(t)$  as illustrated in figure 4–37. A powerful deconvolution algorithm based on numerical Laplace transformation is described elsewhere (chapter 20 of *Well Test Design and Analysis*) which has been found to work well even when noise is present. For the moment, it will be assumed that the data has been deconvolved and that  $F(t)$  has been generated. This function—apart from an initial step caused by skin—should be smooth, reflecting that the system is described by the diffusivity equation. If the correct influx rates have been inferred,  $F(t)$  will be well behaved and a constant-rate aquifer model can be fitted to it. In particular, if the aquifer is bounded, the  $F(t)$  function will be a straight line at late time whose slope gives the aquifer pore volume. Conversely, if the aquifer is essentially infinite, the  $F(t)$  function will exhibit  $\ln t$  or  $\sqrt{t}$  behavior depending on whether the aquifer geometry is radial or linear. An aquifer with a constant pressure boundary, i.e., replenished at surface, will show a flattening at late time. All these cases have been observed in the field and analysis of  $F(t)$  is classical CRD methodology.

The problem is to decide which the best estimate of  $G_i$  is; obviously the value that results in the best fitting aquifer model should be chosen. Hence the goodness of fit of a model to the constant rate data is a possible criterion for optimal selection of  $G_i$ . The benefit of deconvolution is that the nature of the  $F(t)$  function may help to give an idea of an appropriate aquifer model, e.g. infinite or bounded, radial or linear. If good-quality data in sufficient quantity is available, deconvolution should certainly be tried as a first step in analyzing the information. However, a

fairly detailed pressure–rate history is required and there may not have been enough buildups to give an adequate number of points for the deconvolution algorithm to function.

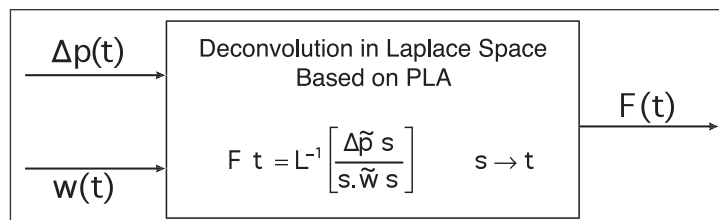


Fig. 4–37. Process of deconvolution

## Extended buildups

The work on aquifer influx into gas reservoirs in the Gulf Coast has used the data from fairly frequent buildups to provide the aquifer face pressure points for analysis; emphasis was placed on monthly monitoring of production and pressure. Certainly, production data is available on a monthly basis but buildups are not carried out so commonly and often interpolation was used to fill in pressure points. In many gas reservoirs, an extended buildup is carried out during the summer months when gas is not required. Thus rather than frequent short buildups, one long buildup is all that is available. However, in such an extended buildup, the well becomes an observation well for the reservoir pressure which may be increasing due to continuing aquifer influx. This will occur particularly when the aquifer is screened by a tight zone and the aquifer average pressure is significantly higher than that of the reservoir. In these circumstances, continuous data on the reservoir pressure is available and the gas material balance may still be used to compute the influx even although  $G_p$  is not changing during the extended buildup. The change in reservoir pressure is due to water inflow continuing as a result of the pressure differential. Continuous pressure monitoring during the summer shutin provides an excellent opportunity to gather data which can be used to detect aquifer influx. Note, however, that such long-term pressure changes can also be caused by gas compartments similarly screened by barriers supporting the well compartment during the extended shutin.

## Reservoir limit testing

The problem of identifying aquifer parameters from a set of pressure and rate data is, in fact, a case of reservoir limit testing in a variable-rate situation. The underlying fundamental  $p_D$  function chosen for automatic matching via superposition refers to a closed system and has the property that it reaches an SSS condition at late time. Hence it is possible to determine the size of the system in the matching process provided the time of testing is long enough. Most importantly, this can be done even though the rate is not constant and there is no straight line on a Cartesian plot of pressure versus time. The Levenberg–Marquardt algorithm is therefore the key to variable-rate extended draw-down testing given that closed system  $p_D$  functions can be matched just as easily as infinite-acting models. In this treatment of the aquifer influx problem, only one analytical model relevant to well testing has been considered—the circular closed reservoir with a central well of finite wellbore radius. However, other closed system models are available and could be used for matching purposes. Real extended drawdown tests

are not constant rate and show a combination of material balance depletion with superimposed transients due to rate changes; superposition of a closed system  $p_D$  function can exactly simulate these effects and hence an automatic matching process based on this approach is quite rigorous.

## Aquifer complicating features

In the preceding treatment, the aquifer has been treated as a uniform body of water and the influx has also been taken to be uniform in nature. Unfortunately, real geology does not usually lead to such idealized behavior and it is necessary to anticipate more complicated situations. For example, the aquifer may be compartmentalized as illustrated in figure 4–38; here a system of partially communicating faults has divided the aquifer into blocks separated by tight zones. The Fetkovich aquifer refers to a single, closed aquifer block and the theory of compartmentalized systems can be developed to model such discontinuous aquifers.

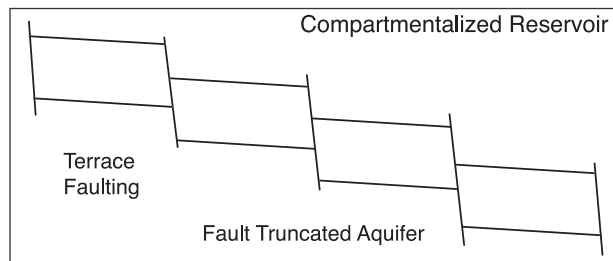


Fig. 4–38. Fault truncated aquifer

The gas reservoirs in the North Sea have experienced water breakthrough to producers because of the presence of thief zones which conduct water from the aquifer to the wells. This is illustrated in figure 4–39, which shows it is necessary for the high-permeability streak to be enveloped by low-permeability barriers, otherwise the advancing water would fall back due to the action of gravity. This mechanism was deduced from the pulsed neutron capture (PNC) logs monitoring water entry into gas wells in the Southern North Sea province as shown in figures 4–40, 4–41, and 4–42.

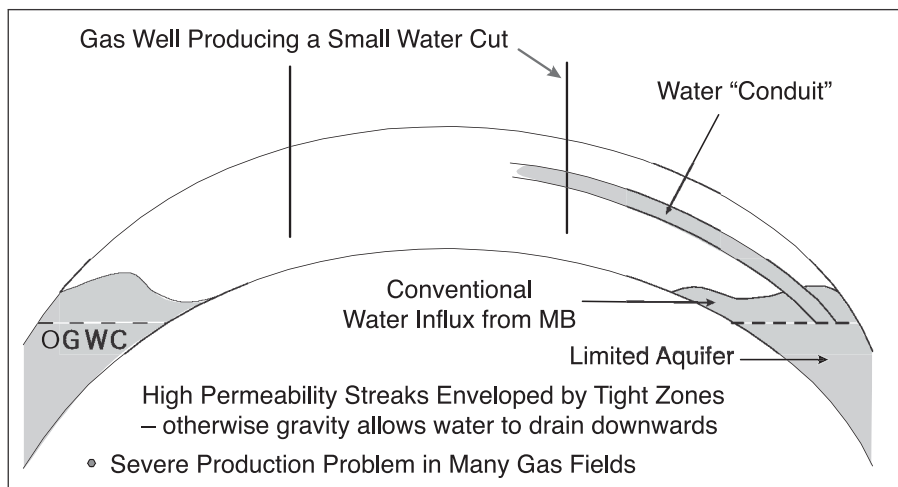


Fig. 4–39. Enveloped high permeability streaks

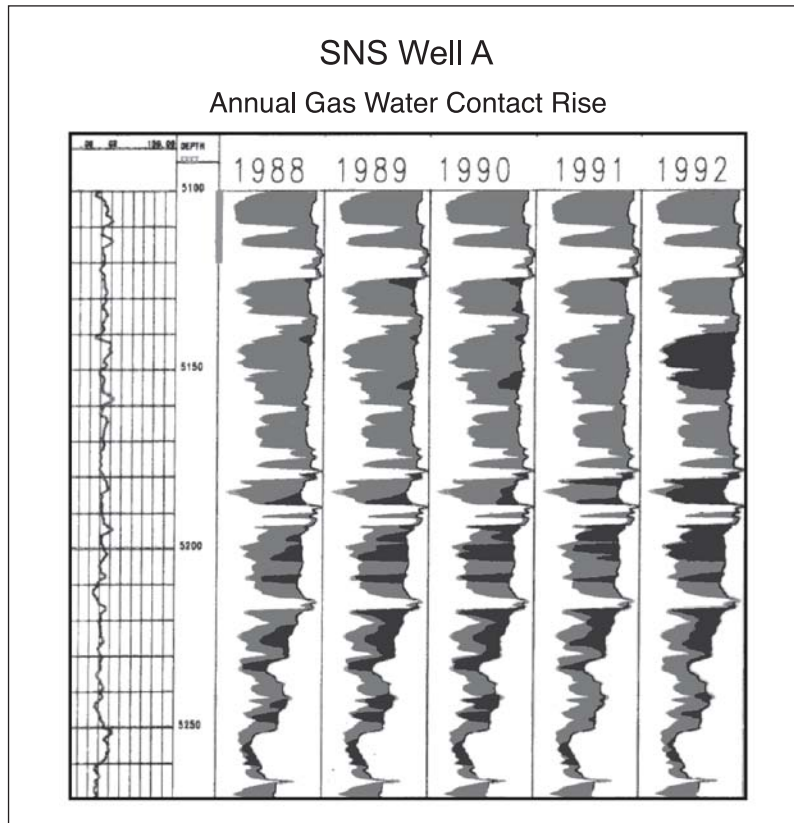


Fig. 4-40. Pulsed neutron capture log A

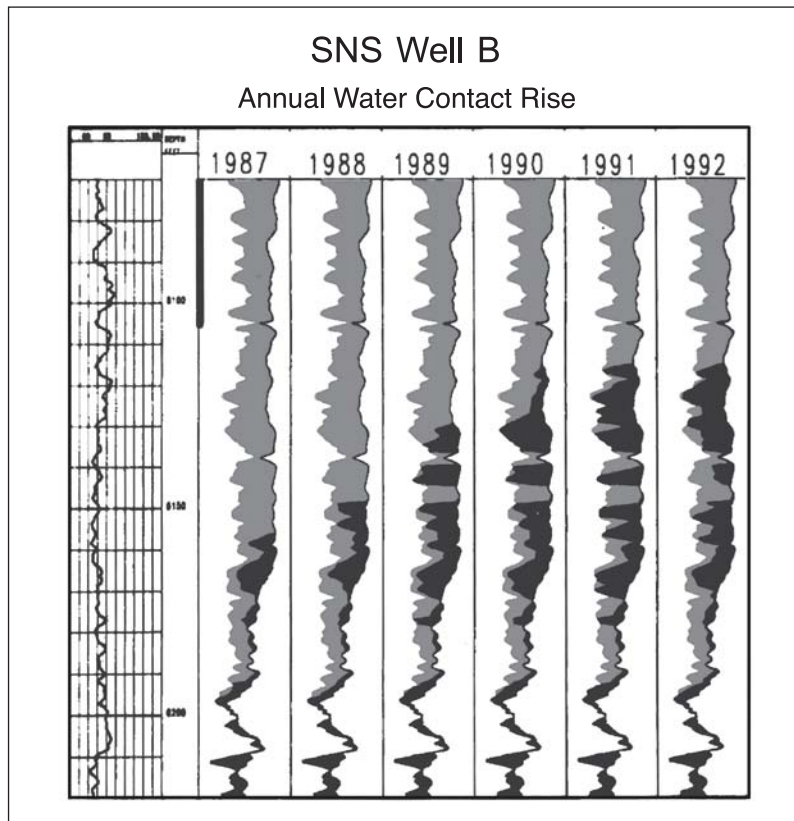


Fig. 4-41. Pulsed neutron capture log B

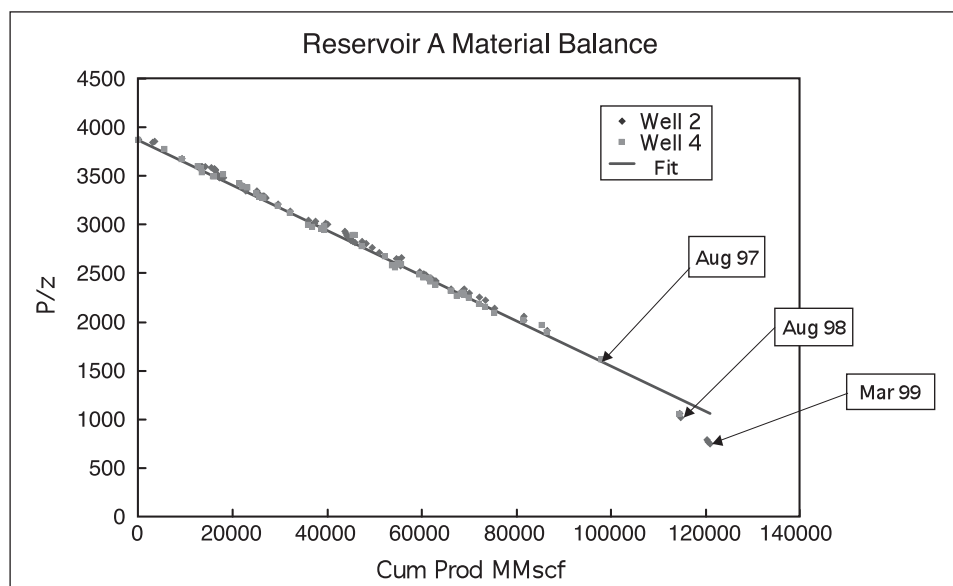


Fig. 4-42. Reservoir a p/z plot

## Case Studies

### Field example 1—Duck Lake field (D-1)

Cason<sup>9</sup> has described an interesting field example of a Louisiana gas field exhibiting an active waterdrive; this is the Duck Lake field 75 miles west of New Orleans discovered in 1949. The p/z plot for the reservoir is shown in figure 4-43, where a straight line can be fitted to the data up to a cumulative production of around 300 Bcf corresponding to approximately 45% of the actual GIP. This line extrapolates to show an OGIP of 850 Bcf. Later data, however, plot concave downward contrary to conventional expectation for a water drive situation. A material balance based on regression, modified to account for pressure gradient across the invaded region, with unsteady-state aquifer influx as developed by Lutes et al.,<sup>10</sup> was used to match the pressure and production data. The match calculated an OGIP of 681 Bcf and an aquifer–reservoir ratio R, of 6:1. The solid line in figure 4-43 shows the fitted match between model and data. It is interesting to observe that the first indication of water influx was when the first wells watered out after 200 Bcf was produced, i.e., before the end of the straight line on the p/z plot. Reservoir pressure declined continually as shown in figure 4-44. The reservoir and fluid data for the system are given in the table 4-9, and it can be seen that the reservoir permeability is very high.

Table 4-9. Duck lake field—reservoir and fluid data

Productive area = 6,100 acre	Porosity = 0.25
Permeability = 1,750 md	Initial water saturation = 0.18
Temperature = 240° F	Original gas FVF = 0.67RB/Mscf
Wet gas gravity = 0.65	Initial yield = 14bbl/MMscf
Average formation Dip = 2.5°	Aquifer–reservoir radius ratio = 6
Net sand thickness = 40–90 ft	Initial pressure = 5,800 psia

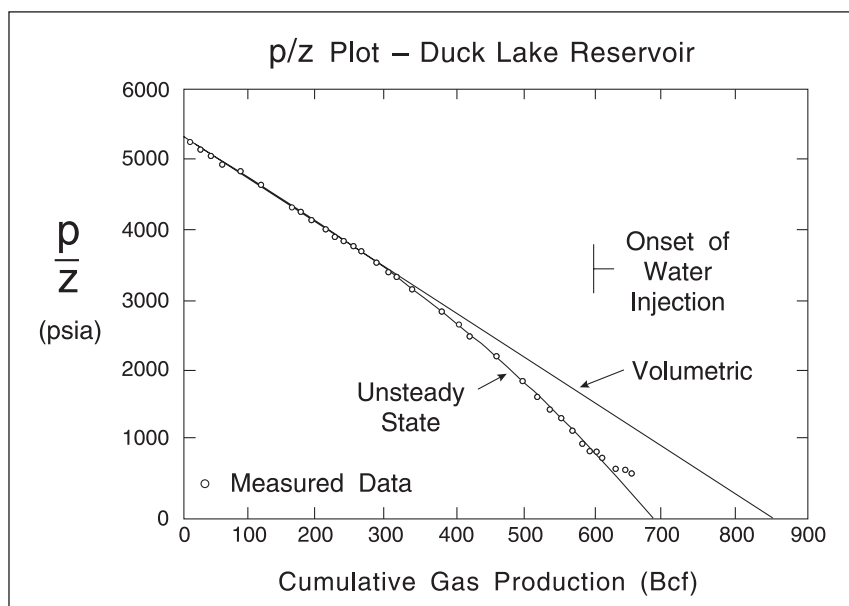


Fig. 4–43. Duck field p/z plot (after Cason)

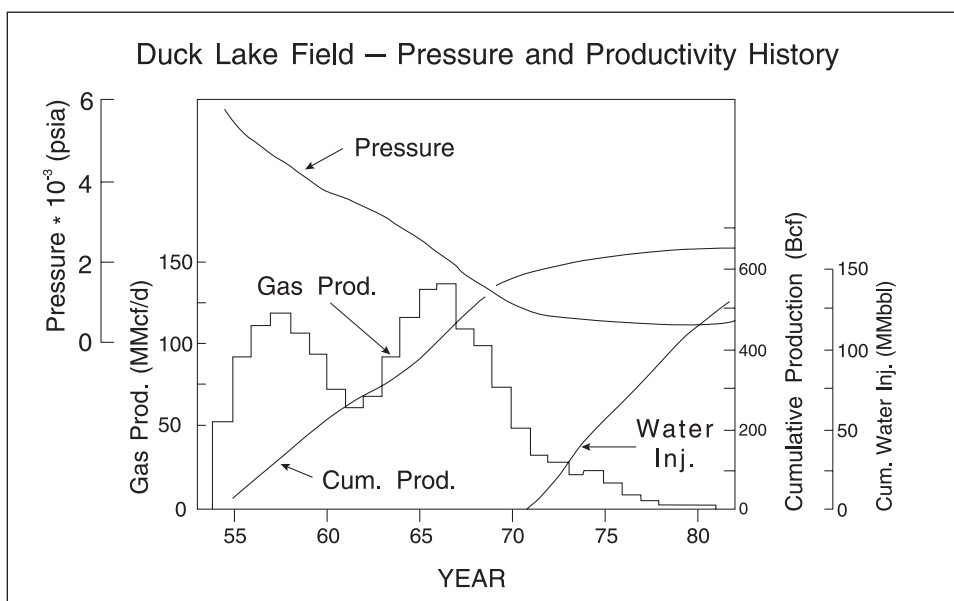


Fig. 4–44. Pressure and production history of the D–1 reservoir (after Cason)

The possibility of a concave downward p/z plot for a water drive had been previously reported. Bruns et al.,<sup>11</sup> simulated production of a theoretical reservoir for 38 combinations of aquifer size and influx properties. Several cases showed a concave-downward performance with some remaining straight throughout the production life. Once the aquifer size and influx constants became large enough, the typical concave-upward behavior was exhibited. Dumore also reported a gas reservoir in Germany for which a concave-downward p/z plot was predicted. Figure 4–45 from Cason's paper overlays run 20 of Bruns et al., the Dumore prediction, and the actual data from the D-1 reservoir; an early time straight line p/z can persist until 40%–50% of the original GIP (OGIP) is produced and can result in an overprediction of the reserves by 25%–50%. The reservoir cross-section indicating the GWC is shown in figure 4–46.

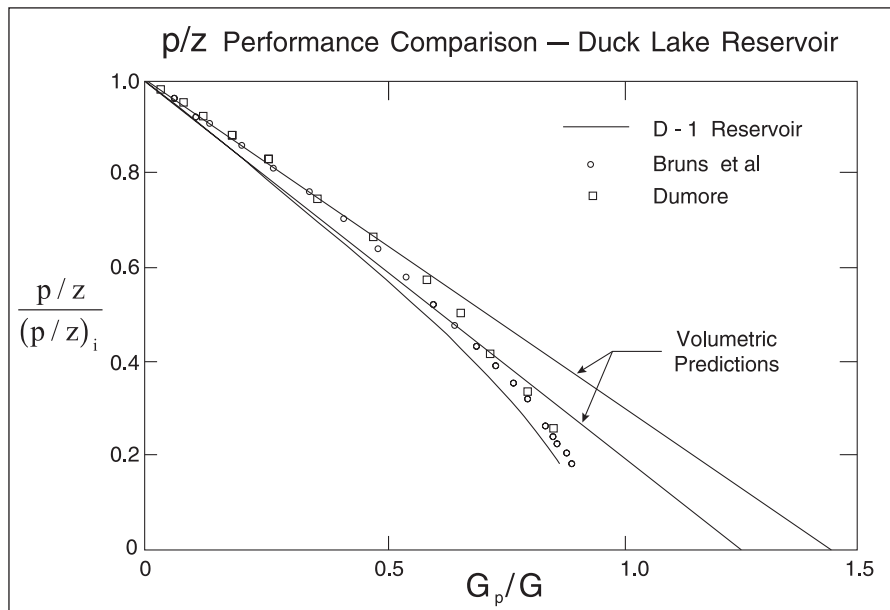


Fig. 4-45.  $p/z$  performance comparison (after Cason)

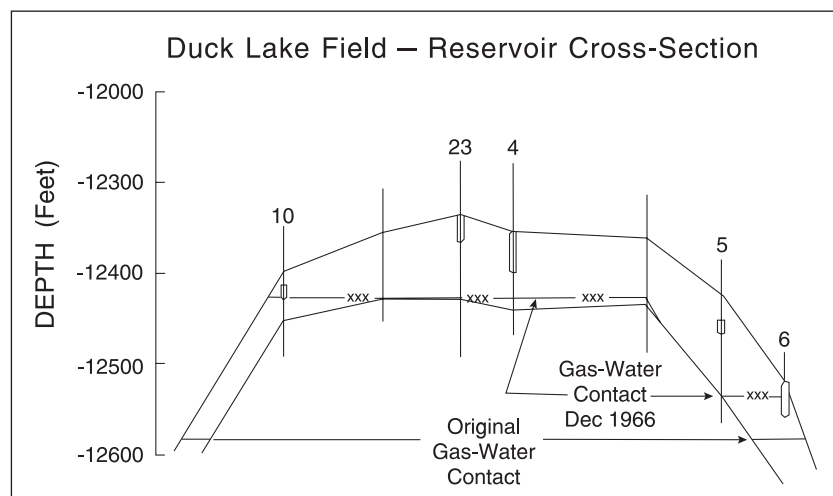


Fig. 4-46. Cross-section and gas-water contacts of the D-1 reservoir (after Cason)

## Field example 2—South Wilburton Field

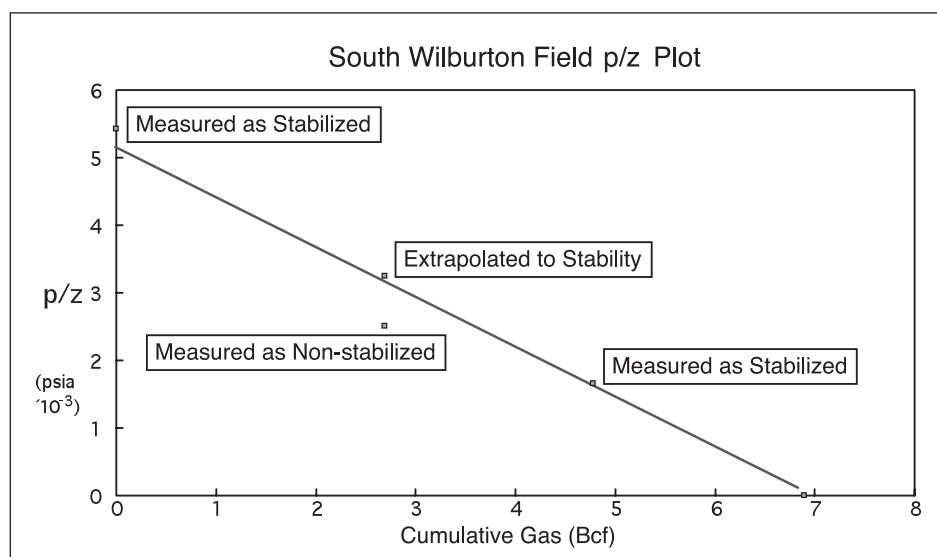
Another interesting example of reserves estimation has been presented by Guardia and Hackney<sup>12</sup> in connection with the South Wilburton field in eastern Oklahoma. This is a dry-gas reservoir in which the seismic interpretation indicates severe faulting with multiple noncontinuous thrust sheets. Formations appear to be recumbently thrust, with the same formation appearing up to nine times in a single well. Secondary porosity is apparent in the form of natural fractures and vugs; fracture networks have been identified with borehole imaging logs. They outline an approach to OGIP estimation during early development which integrates material balance and Fetkovich decline curve analysis. The use of volumetric estimation was impractical due to unpredictable discontinuities between offsets in terms of pay interval, porosity, vertical thrust segments, and facies changes.



In the study of Guardia and Hackney, the accessible reserves to each well were determined by two methods, i.e., material balance  $p/z$  plot and Fetkovich decline curve analysis. In the  $p/z$  approach, an empirical extrapolation method akin to the rectangular hyperbola technique used by Mead and Kabir was developed. Routine buildups were limited to 24–48 h, and in the low-permeability conditions it was essential to develop a proper extrapolation process to yield compartment average pressure. A  $p/z$  plot for well A-1 is shown in figure 4–47, where both stabilized and extrapolated pressures give an excellent straight line with an OGIP of 6.9 Bcf. The danger of not extrapolating the pressure to drainage area average is apparent from the uncorrected data point shown in the diagram. Although Guardia and Hackney used an empirical approach for build-up extrapolation, the method of Matthews, Brons, and Hazebroek using time to SSS, i.e.,  $t_{SSS}$ , in the Horner time function could equally well have been employed since the decline curve analysis had given this quantity; the appropriate Dietz shape factor requires knowledge of any near faults from transient analysis. The buildups were usually conducted with high resolution bottom-hole gauges but in some cases only the wellhead pressure was measured and the down-hole pressure calculated. However, in the shut-in situation there is considerable uncertainty in the wellbore temperature as transient cooling occurs and it is better to employ direct down-hole pressure measurement for a buildup. If surface pressures are used, it is also necessary to ensure that the wellbore has been evacuated of all liquids. The material balance reserve estimates for other wells in the reservoir are shown in the table 4–10.

**Table 4–10.** South Wilburton field—OGIP estimates

Well	Material balance OGIP (Bcf)	Decline curve OGIP (Bcf)	% Variance
A-1	6.8	8.4	19
B-1	0.8	0.7	(14)
C-1	2.1	2.5	16
C-2	5.3	5.8	9
D-1	2.1	2.6	19
D-2	2.9	3.9	26



**Fig. 4–47.** South Wilburton  $p/z$  plot for well A-1



This field is a classical compartmentalized system in which the accessible GIP (AGIP) for each well can be determined only by depletion analysis. The most important issue in making a good  $p/z$  plot is the proper extrapolation of buildups to material-balance average pressure. Note that the wells took from 1 to 4 months to reach a SSS condition and the rate declined dramatically in this period; some wells had flush production of around 62 MMscf/d.

In addition to the analysis of extrapolated buildups on the  $p/z$  plot, the flowing bottom-hole pressures were also analyzed using the Fetkovich type curve based on constant terminal pressure behavior in the transient and QSSS regimes. In the South Wilburton field, Exxon implemented a comprehensive data gathering program in which wellhead flowing pressures and rates were recorded daily. A special device, similar to the “Spida” system, which records and analyzes wellhead pressures (absolute and meter differential) was employed in the data collection. The wellhead pressures were corrected to bottomhole (BHFP) utilizing a modified Cullender and Smith relationship. In order to use the Fetkovich type curve, the measured rate and calculated BHFP must be transformed to constant bottom-hole pressure equivalent. Normalization was achieved by using a well inflow performance relation of the form

$$Q = a(p_e^2 - p_{wf}^2)^n \quad (4-109)$$

where  $n$  lay in the range 0.5 to 1; the user had to specify the back pressure  $p_e$  and the exponent  $n$ . It is obviously better to use a properly formulated gas well inflow performance relation (IPR) curve, based on the results of a step-rate gas well test and employing pseudopressure, to carry out the pressure normalization of the rate data. However, in each case the current reservoir (drainage area average) pressure must be estimated in order to implement the normalization. The Fetkovich type curve match yields the time to SSS and the drainage area volume provided information on the QSSS region is present in the data, i.e., the pressure disturbance has reached the far boundary. The results of decline curve analysis are also given in table 4–10 and it can be seen that analysis of the normalized rate (via calculated BHFP) gives good reserve estimation. The results from Fetkovich type curve matching are summarized in table 4–11.

**Table 4–11.** South Wilburton Field—type curve derived parameters

Well	k (md)	S	$r_e$ (ft)	$r'_w$	b (hyperbolic exponent)	$A_d$ (acre)	GIP (Bcf)
A-1	7.9	0.5	1,985	0.20	0.2	284	7.6
B-1	0.17	1.7	595	0.003	0	26	0.5
C-1	0.5	–5.1	1,364	57	0	134	2.5
C-2	0.6	–3.4	1,605	8.0	0.1	186	5.8
D-1	0.5	–2.3	2,803	2.8	0	567	2.6
D-2	6.1	0.7	1,993	0.2	0.1	286	3.7

Although Guardia and Hackney used the Fetkovich type curve, the data could have been analyzed using the approximate deconvolution method described in chapter 5 of *Well Test Design and Analysis*. This is an alternative approach which has a more advanced normalization procedure and has given excellent results in other gas reservoir studies.

## Residual Gas Saturation in Water-Drive Gas Reservoirs

One of the most important factors in predicting the production performance and recovery factor of water-drive gas reservoirs is the residual gas saturation that occurs as the invading water moves into the system; this phenomenon is illustrated in figure 4–48. Laboratory experiments, logging data, and material balance calculations have demonstrated that the trapped gas saturation in the water-invaded region of a gas reservoir could be as high as 50% of pore volume. Until recently, it was assumed that, as the reservoir was blown down, this gas saturation remained constant which implies that much of the gas trapped at high pressure early in the process can in fact be recovered later. More recent results clearly show two distinct values of residual gas saturation. The lower value corresponds to the initial gas entrapment saturation and the higher value relates to the gas saturation being mobilized under expansion. This phenomenon has been investigated by Fishlock<sup>24</sup> and Firoozabadi<sup>25</sup>; the discussion of the topic given here is a summary of the paper of Firoozabadi which gives an excellent review of present knowledge.

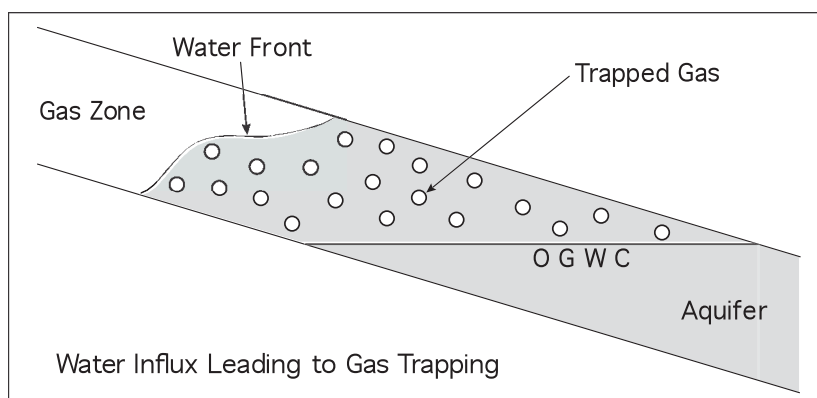


Fig. 4–48. Gas trapping with water influx

The experimental study of Geffen et al.<sup>26</sup> in 1952 on core plugs revealed that the trapped gas saturation varied from 15 to 50% of the pore space for various porous media. They also measured the trapped gas saturation in a watered-out gas reservoir by the use of a pressure core barrel and by logging and found that high trapped gas saturation is not only a laboratory phenomenon. In the experiments conducted by Geffen et al., unconsolidated sand showed a trapped saturation of about 16%, consolidated sandstones of various formations showed values of 25%–38%, while the highest value of 50% occurred in the limestone rock of Canyon Reef. In 1963, Chierici et al.<sup>27</sup> reported trapped gas saturation measurements on both unconsolidated and consolidated core samples. For consolidated sandstone the following results were given as shown in table 4–12:

Table 4–12. Trapped gas saturations due to Chierici

Sample	$\phi$	k	$S_{gr}$
A	0.207	160	0.438
B	0.189	63	0.387
C	0.221	113	0.389
D	0.212	91	0.348

Keelan and Pugh<sup>28</sup> published measurements for various carbonate rocks in 1975 and observed residual saturations from 23% to values as high as 69%; they concluded that the complexities of carbonates necessitate determination for the specific reservoir in question, i.e., correlation of  $S_{gr}$  with porosity and permeability was not possible.

The early references assume that the initial trapped gas saturation is identical to the mobilized gas saturation when pressure decreases. In other words, it is assumed that the residual gas saturation is constant and independent of pressure. Recently, Fishlock et al.<sup>24</sup> studied the water flood residual gas saturation of two long sandstone cores with permeabilities of 1,280 and 240 md, respectively. The measured trapped gas saturation for the higher permeability core was about 35% and for the lower permeability core it was 41.5%. During the blowdown of these two cores, the mobilized gas saturation was determined to be about 49% for the higher permeability and 45.5% for the lower permeability. Gas saturations were determined by nucleonic techniques and material balance. This important experimental result showed that the mobilized gas saturation was higher than the initial value. This finding was confirmed by Firoozabadi,<sup>25</sup> who also made measurements on high-permeability (around 2,000 md) sandstone core; the results are given in the table 4–13:

**Table 4–13.** Measurements of Residual Gas Saturation by Firoozabadi

Sample	Initial $S_{gr}$	Mobilized $S_{gr}$
A	0.295	0.377
B	0.311	0.41
C	0.28	0.411

An important consequence of this difference between the initial entrapped and final mobilized gas saturations is the delay of entrapped gas migration from the water-invaded region to the gas zone. Both classic material balance and reservoir simulation have to account for this. Note also that the higher remaining gas saturation in the water-invaded region at abandonment will have an adverse effect on recovery factor. Obviously, reservoir simulation is needed to determine the rate at which gas, for example, will segregate upward due to the density difference.

Realizing that gas recovery from a water-drive reservoir may be poor because of high trapped gas saturation, Agarwal, Al-Hussainy, and Ramey<sup>29</sup> showed that gas recovery from water-drive gas reservoirs are sensitive to the gas production rate. They concluded that water-drive gas reservoirs should be produced at high rate to take advantage of transient aquifer behavior. Later, Lutes et al.<sup>7</sup> observed that accelerated gas production improves gas recovery but that the magnitude of the increase was less than expected. Chesney, Lewis, and Trice<sup>30</sup> discussed the benefit of handling a large amount of water production for a gas reservoir from which the recovery under an accelerated production scheme was 64%. A trapped gas of some 44 BSCF provided the incentive for a coproduction of water and gas. Boyd et al.<sup>31</sup> reported the results of depressurizing a watered-out gas reservoir in a 4-year field test: the simulator prediction was more than double the highest actual gas production rate which was measured. This simulation was made before knowledge of the mobilized gas saturation effect was available, providing evidence of the importance of incorporating such information into simulation studies.

# Simultaneous Equation Differential Material Balance

## Theoretical treatment

Consider the situation illustrated in figure 4–49, where a gas reservoir block with aquifer influx is depicted. The initial gas region pore volume is denoted  $V_{pg,i}$ , while the initial aquifer pore volume is  $V_{a,i}$ . The connate water saturation in the gas region is denoted  $S_{wc}$  and the OGIP, on a mass basis, is given by

$$M_{g,i} = V_{pg,i} (1 - S_{wc}) \rho_{g,i} \quad (4-110)$$

where  $\rho_{g,i}$  is the gas density at initial reservoir pressure  $p_i$ . This ignores any gas which is dissolved in the formation water, and in some circumstances an allowance must be made for gas in solution. On a standard volume basis, the IGIP  $G_i$  is

$$G_i = \frac{M_{g,i}}{\rho_{sc}} \quad (4-111)$$

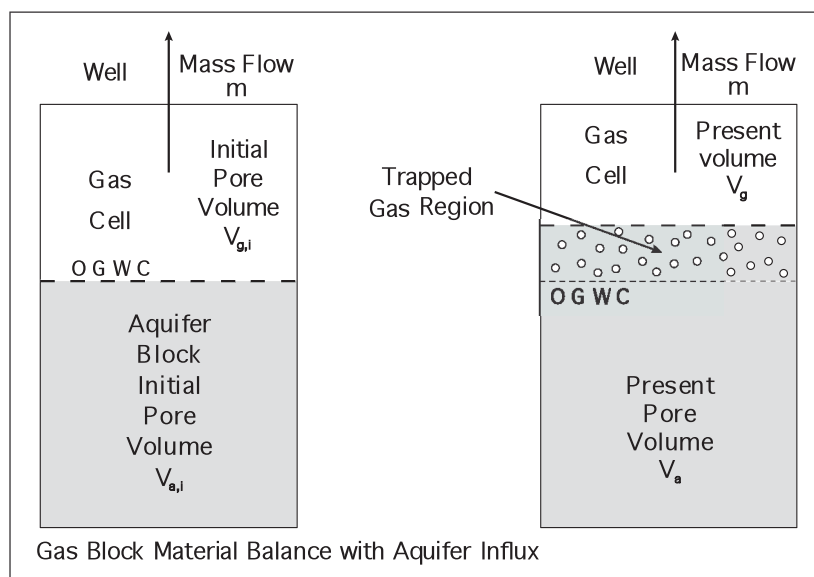


Fig. 4–49. Gas reservoir block with aquifer influx

As the aquifer expands into the original gas block, a zone at trapped gas saturation  $S_{gr}$  is formed and the continuous gas region shrinks in size with a pore volume denoted  $V_{pg}$ . Correspondingly, the aquifer volume increases and its evolving value is denoted  $V_{pa}$ . Consider a time interval  $\delta t$

over which an injection of water of volume  $\delta W_e$  occurs and the pore volume of invaded region increases by an amount  $\delta V_a$ , where

$$\delta V_a = \frac{\delta W_e}{1 - S_{gr} - S_{wc}} \quad (4-112)$$

The decrease in the gas occupied pore volume, denoted  $V_{gg}$ , is given by the equation

$$\delta V_{gg} = \frac{V_{gg}}{1 - S_{wc}} (S_{wc} c_w + c_f) \delta \bar{p}_g - \frac{1 - S_{wc}}{1 - S_{wc} - S_{gr}} \delta W_e \quad (4-113)$$

which, on taking limits, may be written in differential form as

$$\frac{dV_{gg}}{dt} = \frac{V_{gg}}{1 - S_{wc}} (S_{wc} c_w + c_f) \frac{d\bar{p}_g}{dt} - \frac{1 - S_{wc}}{1 - S_{wc} - S_{gr}} \frac{dW_e}{dt} \quad (4-114)$$

The first term accounts for the effect of compaction (rock compressibility) and expansion of connate water, while the second allows for the water influx reducing the gas “bubble” size.

This invasion results in the trapping of a mass of gas  $\delta M_T$ , where

$$\delta M_t = \rho_g S_{gr} \delta V_a \quad (4-115)$$

The rate of trapping of gas on a mass basis may therefore be obtained as  $\delta t$  tends to zero, i.e.,

$$m_T = \frac{dM_T}{dt} = \rho_g S_{gr} \frac{dV_a}{dt} \quad (4-116)$$

The differential material balance equation for the continuous gas volume is based on the mass conservation expression

$$\rho_g V_{gg} = (\rho_g + \delta \rho_g)(V_{gg} + \delta V_{pg}) + m_g \delta t + m_T \delta t \quad (4-117a)$$

which on taking the limit as  $\delta t \rightarrow 0$  and putting  $\delta \rho_g = c_{gg} \rho_g \delta \bar{p}_g$  results in

$$c_{gg} V_{gg} \frac{d\bar{p}_g}{dt} = - \frac{m_g}{\rho_g} - \frac{m_T}{\rho_g} - \frac{dV_{gg}}{dt} \quad (4-117b)$$

The third term represents the effect of shrinkage of the gas region due to the advancing water and the second term the loss of mass due to trapping which occurs in addition to the loss of mass due

to production represented by the first term  $-\frac{m_g}{\rho_g}$ . Here  $m_g$  is the instantaneous well mass flow rate, and the cumulative mass of gas produced  $W_g$  is given by the differential equation

$$\frac{dW_g}{dt} = m_g \quad (4-118)$$

The well mass flow rate  $m_g$  is the forcing function driving the block material balance system and may be a time-dependent quantity. The material balance equation for the aquifer in Fetkovich form can be written as

$$\frac{d\bar{p}_a}{dt} = -\frac{1}{c_{a,t} V_a} J_a (\bar{p}_a - \bar{p}_g) \quad (4-119)$$

with the cumulative water influx on an in situ volume basis  $W_e$ , given by the differential equation

$$\frac{dW_e}{dt} = J_a (\bar{p}_a - \bar{p}_g) \quad (4-120)$$

If the mass of trapped gas in the invaded region is denoted  $M_T$ , then this variable may also be computed from the differential equation

$$\frac{dM_T}{dt} = \frac{\rho_g S_{gr}}{1 - S_{gr} - S_{wc}} J_a (\bar{p}_a - \bar{p}_g) \quad (4-121)$$

Here the gas density  $\rho_g$  is evaluated at the current gas region pressure  $\bar{p}_g$  and gas trapped at high pressure is retained in the advancing water zone. The instantaneous volume of the water region  $V_a$  is fixed by the algebraic equation

$$V_a = V_{a,i} + \frac{W_e}{1 - S_{gr} - S_{wc}} \quad (4-122)$$

while the total compressibility for the aquifer region follows as

$$c_{a,t} = S_w c_w + (1 - S_w) c_{ga} + c_{fa} \quad (4-123)$$

with

$$\bar{S}_w = \frac{V_{a,i} + (V_a - V_{a,i})(1 - S_{gr})}{V_a} \quad (4-124)$$

In these equations,  $S_{wc}$  is the connate water saturation in the gas region and  $c_{fa}$  is the rock compressibilities in the water region. The quantity  $c_{gg}$  is the gas compressibility at the pressure  $\bar{p}_g$ , while  $c_{ga}$  is the gas compressibility at the aquifer pressure  $\bar{p}_a$ ; water compressibility  $c_w$  is treated as a constant. The gas density,  $\rho_g = \rho(\bar{p}_g)$ , and compressibility,  $c_g = c_g(p)$ , are computed using the SRK equation of state. Thus the trapped gas contributes to the total compressibility of the aquifer region but is held in place and not allowed to percolate upwards. If the aquifer pressure is substantially different from the gas region pressure, the effect of trapped gas on depletion is strong. Equation (4–117b) can be written in an alternative form which directly involves the state variables, viz.,

$$\frac{d\bar{p}_g}{dt} = \frac{1}{c_{tot} V_{gg}} \left\{ -\frac{m_g}{\rho_g} - \frac{m_T}{\rho_g} + \frac{1 - S_{wc}}{1 - S_{wc} - S_{gr}} J_a (\bar{p} - \bar{p}) \right\} \quad (4-125)$$

where

$$c_{tot} = c_g + \frac{1}{1 - S_{wc}} (S_{wc} c_w + c_f)$$

The differential system (4–114) and (4–125) to (4–121) constitutes a set of six nonlinear ODEs in six state variables, namely  $\mathbf{x} = (V_{gg}, \bar{p}_g, W_g, \bar{p}_a, W_e, M_T)^T$ , which can be forward integrated using the Runga–Kutta method, for example. The system has the form

$$\dot{\mathbf{x}} = \mathbf{f}(\mathbf{x}, \mathbf{u}, \mathbf{y}, t) \quad (4-126)$$

where the nonlinear functions  $\mathbf{f}$  are as defined above and the forcing function  $\mathbf{u}$  has only one component, i.e., the well mass flow rate,  $m_g$ . The variables in the vector  $\mathbf{y}$  represent the additional quantities entering the associated algebraic equations. The initial values of the state variables,  $\mathbf{x}^0 = (V_{gg}^0, \bar{p}_g^0, 0, \bar{p}_a^0, 0, 0)^T$ , must be specified where the initial reservoir pressures are both  $p_i$  at  $t = 0$ . In this formulation of the material balance in a gas reservoir block with water influx, the interface between the gas region and invading water has been regarded as a moving boundary whose movement is tracked by computing the influx  $W_e$  from the Fetkovich model. Note that the material balance simulation can be run up to a specified time and the state variables  $\mathbf{x}$  saved at the end of the period. It is then possible to simply restart the process and continue the forward integration for another time interval. In this situation, all elements of the starting vector  $\mathbf{x}^0$  have nonzero values.

The formulation of the material balance as a set of nonlinear simultaneous ODEs which can be integrated using a standard algorithm (e.g., Runga–Kutta with adaptive step size control) allows the direct introduction of the time dimension into the problem. In addition the cumulative gas production, water influx and trapped gas are easily computed, which allows comparison with traditional methods. The results of a lumped parameter (tank) simulation run, i.e. integration of the initial value problem, can be plotted as  $\bar{p}_g/z$  versus cumulative gas production  $G_p$  in the usual way; here,  $G_p = W_g/\rho_{sc}$ .

## Synthetic test problem

In order to illustrate the performance of the material balance model including the effect of gas trapping, a synthetic test problem was run for the data set listed in table 4–14. For this example metric units have been employed and the aquifer pore volume is 10 times the original gas pore volume. The material balance simulation was run for a time period of 486 days ( $0.42 \times 10^8 \text{ s} = 42 \text{ Ms}$ ), which corresponds to an abandonment pressure of 1.433 MPa (208 psia).

**Table 4–14.** Reservoir parameters for synthetic test problem ( $\tilde{M} = 10^3$ )

$p_i = 20 \text{ Mpa}$ (2,900.8 psia)	$T = 373 \text{ }^\circ\text{K}$	$M_w = 16.0$	$V_{pg,i} = 5 \times 10^6 \text{ m}^3$	$S_{wc} = 0.20$
$z_i = 0.9018$	$M_g = 458.9 \text{ Mkg}$	$G_i = 677.7 \times 10^6 \text{ sm}^3$ (23.93 BSCF)	$\rho_{g,i} = 114.7 \text{ kg/m}^3$	$\tilde{m}_g = 10.0 \text{ kg/s}$ (45.1 MM SCFD)
$V_{a,i} = 50 \times 10^6 \text{ m}^3$	$J_a = 10^{-8} \text{ m}^3/\text{s}/\text{Pa}$	$S_{gr} = 0.30$	$\rho_{sc} = 0.6772 \text{ kg/m}^3$	$c_f = c_w = 4.35 \times 10^{-10} \text{ Pa}^{-1}$

The material balance simulation pressure results are shown in figure 4–50, where the depletion of both gas and aquifer regions is apparent. The aquifer lags behind the gas reservoir and the rate of influx continually increases. The simulation was continued until the shrinking gas region was depleted to a very low (abandonment) pressure; the well rate was kept constant over the whole period. In figure 4–51, the cumulative water influx  $W_e$  and mass of trapped gas  $T_g$  are plotted against time, and at the end of the time period a total influx of  $1.229 \times 10^6 \text{ m}^3$  has occurred; in consequence, 15.8 Mkg of gas has been trapped in the advancing water. The data is presented in the form of a  $p/z$  plot in figure 4–52, where two effects are apparent. At intermediate time, the water influx causes a flattening of the  $p/z$  plot which would result in an overestimation of reserves if the volumetric straight line construction was imposed. There is a period at very early time where the correct slope is present (first three points) but, given the problem of obtaining average reservoir pressure from buildups, it is unlikely that GIP could be determined from real data when the depletion is so small. The behavior of the reservoir in the absence of water influx is shown for comparison and a straight line fitted to this data which gives a GIP estimate as  $683 \times 10^6 \text{ sm}^3$ ; the discrepancy between this figure and the true GIP of  $678 \times 10^6 \text{ sm}^3$  is the small effect of connate water and rock compressibility on the depletion process. The interesting feature of the  $p/z$  plot is the effect of gas trapping causing the late time concave-downward appearance of the data. The loss of 15.8 Mkg of gas to encroachment results in an accelerated depletion as the abandonment pressure is approached. The influx of  $1.23 \times 10^6 \text{ m}^3$  of water results in the gas zone being diminished by double this figure since  $1 - S_{gr} - S_{wc}$  is equal to 0.5; thus at abandonment,  $V_{pg}$  is about half  $V_{pg,i}$ . In the model, trapped gas has a compressibility calculated at the aquifer average pressure and this value will be considerably smaller than the gas compressibility in the gas region itself.



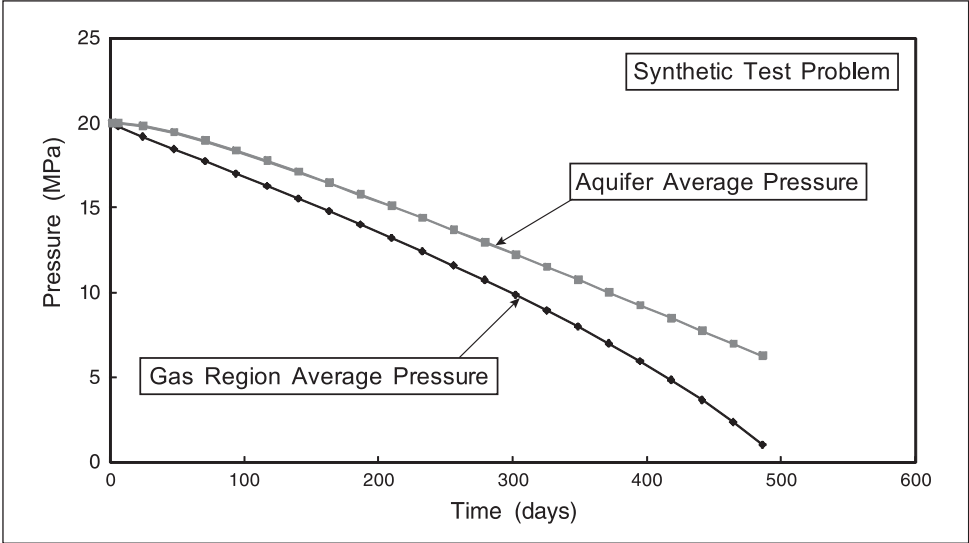


Fig. 4-50. Pressure versus time data for synthetic problem

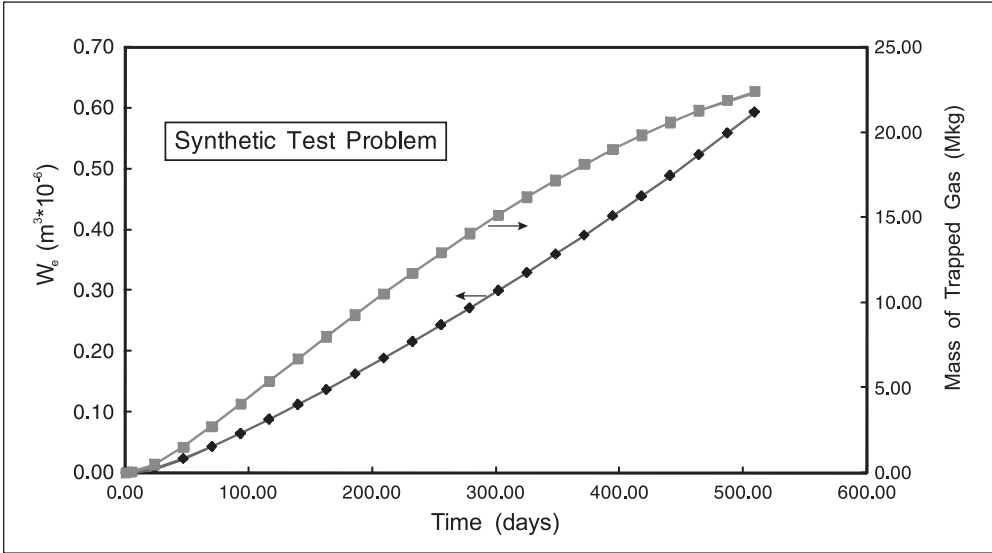


Fig. 4-51. Cumulative water influx and mass of trapped gas

# 5

## General Mechanistic Reservoir Material Balance

### Introduction

In the preceding chapter, an extensive treatment of the gas reservoir material balance was presented and the application to reserve estimation through  $p/z$  plots was described. It is now appropriate to derive the material balance equation for the case of an oil reservoir in a form analogous to the time domain formulation of the gas reservoir. In figure 5–1, a diagrammatic representation of an oil reservoir with bottom water and a gas cap is given. In this model, both injection and production wells are depicted and the oil producers may be in a coning situation. In the context of a material balance situation, the physical situation is simplified as shown in figure 5–2 where the reservoir is represented as uniform tanks comprising, in the general case, a gas cap, an oil zone (OZ), and an aquifer.

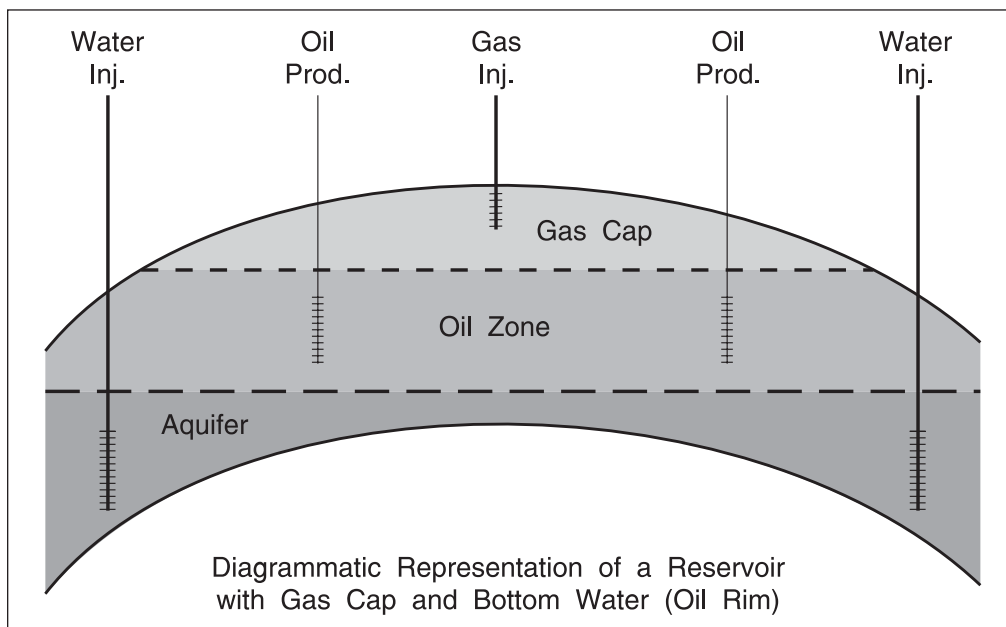


Fig. 5–1. Diagrammatic representation of an oil reservoir with bottom water and a gas cap

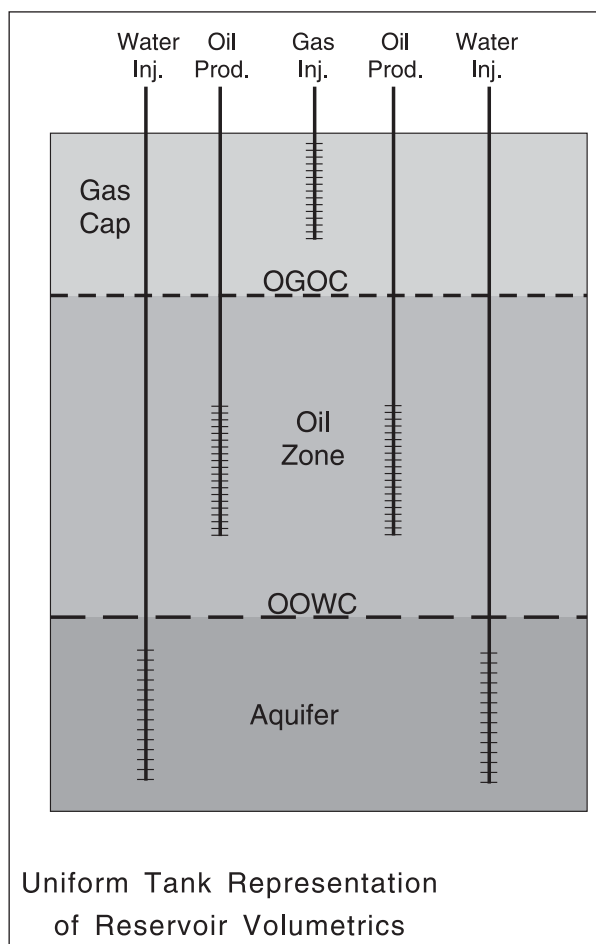


Fig. 5-2. Idealized material balance formulation of an oil reservoir

## Black Oil Model

Consider a reservoir with no gas cap or aquifer where the pressure falls below the bubble point and gas comes out of solution. In a material balance study, a black oil pressure-volume-temperature (PVT) model will normally be adequate to represent the effect of solution gas drive on the pressure depletion as the reservoir is produced. For volatile oil situations, a more detailed equation of state (EOS) model of phase behavior will probably be necessary. However, for low volatility oil systems, consisting mainly of methane and heavy components, the simplified “black oil” or two-component model for describing hydrocarbon equilibrium can be used employing data from a conventional differential vaporization test on a reservoir oil sample. In this formulation, it is assumed that no mass transfer occurs between the water phase and the other two phases and in the hydrocarbon (oil–gas) system only two components are considered. The “oil” component (also called stock tank oil) is the residual liquid at atmospheric pressure left after a differential vaporization, while the “gas” component is the remaining fluid. In order to reduce confusion, it is necessary to carefully distinguish between gas component and gas phase, and between oil component and oil phase. Numerical subscripts will be used to identify components, i.e., 1 refers to the gas component and 2 to the heavier oil component and lower case letter subscripts are employed to identify phases; further the subscript “s” will be used for standard conditions.

Consider a sample of reservoir oil containing mass  $W_2$  of oil component and  $W_{1,D}$  of (dissolved) gas component. Let  $\rho_{os}$  be the density of the pure oil component and  $\rho_{gs}$  the density of the pure gas component, both measured at standard conditions. The gas solubility  $R_s$  (also called the *dissolved gas ratio*) is defined as the volume of gas (measured at standard conditions) dissolved at a given pressure and reservoir temperature in a unit volume of stock tank oil; thus

$$R_s(p) = \frac{V_{DGs}}{V_{os}} \quad (5-1)$$

Since

$$V_{DGs} = \frac{W_{1,D}}{\rho_{gs}} \quad \text{and} \quad V_{os} = \frac{W_2}{\rho_{os}} \quad (5-2)$$

$$R_s = \frac{W_{1,D} \rho_{os}}{W_2 \rho_{gs}} \quad (5-3)$$

The volume of the oil phase at reservoir temperature and pressure is not  $V_{os}$  but somewhat larger since the dissolved gas causes some swelling of the hydrocarbon liquid. The formation volume factor for oil  $B_o$  is defined as the ratio of the volume of oil phase including its dissolved gas (measured at reservoir conditions) to the volume of oil component measured at standard conditions, i.e.,

$$B_o(p) = \frac{V_o(p)}{V_{os}} \quad (5-4)$$

However,

$$V_o(p) = \frac{W_2 + W_{1,D}}{\rho_o} \quad (5-5)$$

and combining Eqs. (5-2), (5-4) and (5-5) yields

$$B_o = \frac{(W_2 + W_{1,D})\rho_{os}}{W_2 \rho_o} \quad (5-6)$$

The gas formation volume factor  $B_g$  is the ratio of the volume of free gas (all of which is gas component), measured at reservoir conditions, to the volume of the same gas at standard conditions; thus

$$B_g(p) = \frac{V_{Fg}(p)}{V_{FGs}} \quad (5-7)$$

$$\text{Letting} \quad W_{1,F} = W_1 - W_{1,D} \quad (5-8)$$

be the mass of free gas, then

$$V_{Fg}(p) = \frac{W_{1,F}}{\rho_g} \quad V_{FGs} = \frac{W_{1,F}}{\rho_{gs}} \quad (5-9)$$

$$\text{i.e.,} \quad B_g(p) = \frac{\rho_{gs}}{\rho_g} \quad (5-10)$$

The PVT parameters for a typical black oil model are shown in figures 5-3 and 5-4 and the data are tabulated in table 5-1; this is the example used in the textbook by Dake.<sup>2</sup>

**Table 5-1.** The PVT parameters for a typical black oil model

Pressure (psia)	$B_o$ (rb/stb)	$R_s$ (scf/stb)	$B_g$ (rb/scf)
4,000 ( $p_i$ )	1.2417	510	—
3,500	1.2480	510	—
3,330 ( $p_b$ )	1.2511	510	0.00087
3,000	1.2222	450	0.00096
2,700	1.2022	401	0.00107
2,400	1.1822	352	0.00119
2,100	1.1633	304	0.00137
1,800	1.1450	257	0.00161
1,500	1.1287	214	0.00196
1,200	1.1115	167	0.00249
900	1.0940	122	0.00339
600	1.0763	78	0.00519
300	1.0583	35	0.01066

$$\begin{aligned} \gamma_g &= 0.67 \\ \rho_{os} &= 52.8 \text{ lb/ft}^3 \\ c_o &= 1.1256 \times 10^{-5} \text{ psi}^{-1} \end{aligned}$$

It is of interest to determine the gas saturation in a reservoir if the fluid composition remains unchanged; this is termed a *constant composition expansion* (CCE). The gas saturation in this process is given by

$$S_g = \frac{(R_{si} - R_s)B_g}{B_o + (R_{si} - R_s)B_g} \quad (5-11)$$

For the system described in the table 5-1, a plot of  $S_g$  versus pressure is shown in figure 5-5. The gas phase will not flow in the reservoir until the critical gas saturation  $S_{gr}$  is attained and it may require a substantial pressure drop below the bubble point before free gas starts to move.

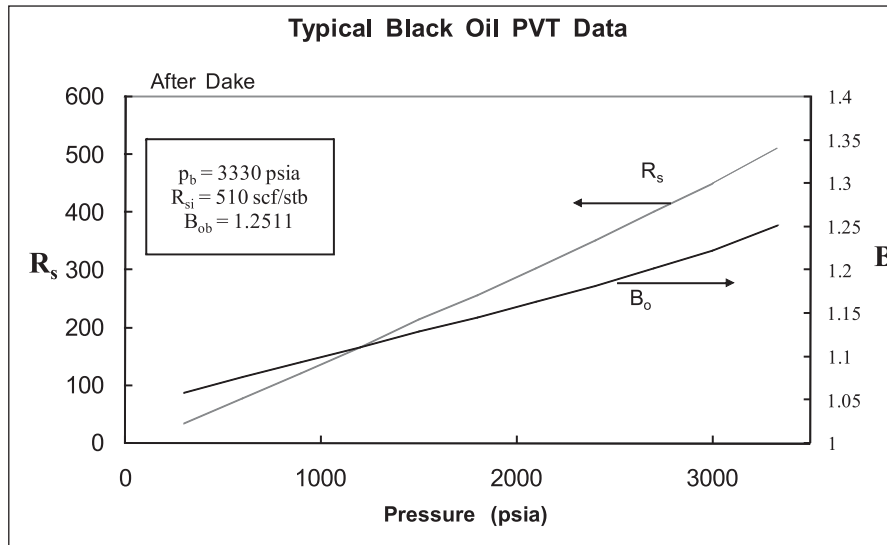


Fig. 5-3. Solution gas-oil ratio and oil formation volume factor plots

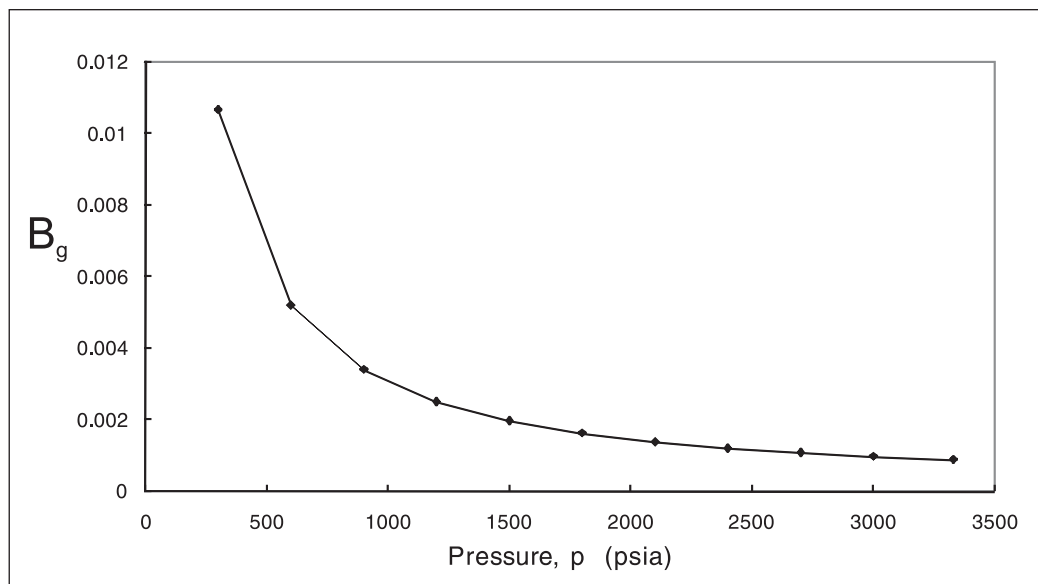


Fig. 5-4. Gas formation volume factor plot

In addition to the density and gas solubility information, the PVT data should include measurements of the phase viscosities. For the system described by Dake, viscosity data were not given and black oil correlations have been used to generate the data given below and plotted in figure 5-6.

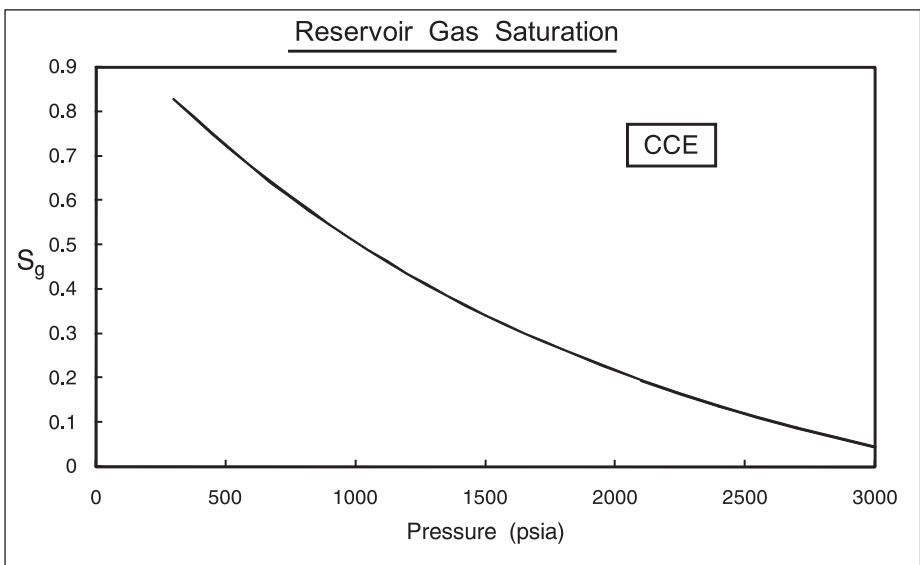


Fig. 5-5. Gas saturation as a function of pressure (CCE)

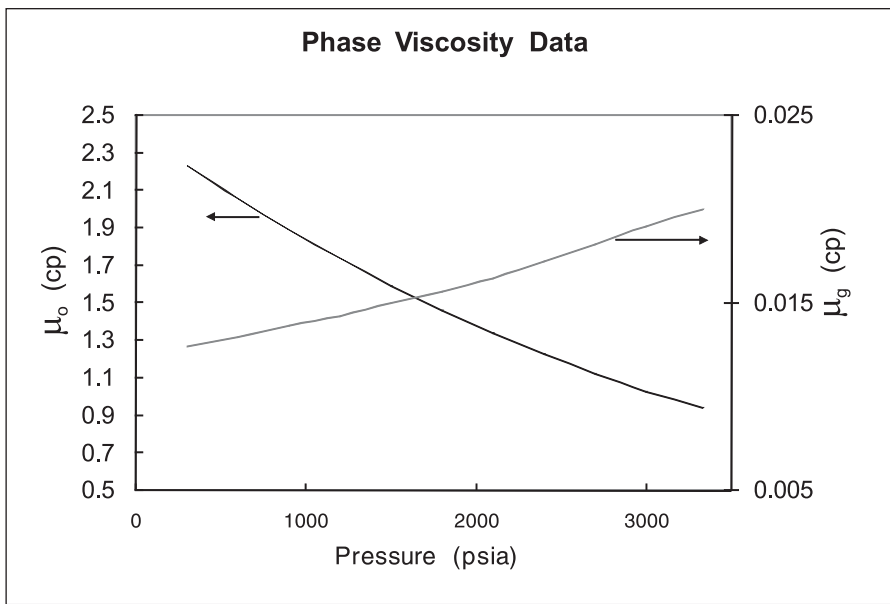


Fig. 5-6. Phase viscosities as a function of pressure

### Classical Schilthuis Material Balance

The classical material balance equation for an oil reservoir with a gas cap was first presented by Schilthuis<sup>1</sup> in 1936. The formulation is based on a volume balance which equates the cumulative observed production, expressed as in situ quantities, to the expansion of the fluids in the reservoir resulting from a pressure drop  $\Delta p$  from the initial reservoir pressure  $p_i$ . The pressure change is referred to the material balance average pressure  $\bar{p}$ ; thus

$$\Delta p = p_i - \bar{p} \tag{5-12}$$

The material balance equation defines this average pressure by treating the reservoir as a “tank” of uniform properties. Measurement of the average pressure through build-up surveys in wells allows the material balance equation to be used in the estimation of oil and gas in place. Obviously, the assumption of “tank” behavior is a major simplification, but it has been demonstrated that material balance studies are certainly worthwhile as a precursor to detailed modeling of a field using a reservoir simulator. The general form of the volumetric balance equation has been described in detail by Dake<sup>2</sup> and Chierici,<sup>3</sup> for example, and Dake’s notation will be followed here.

The concept of fluid expansion is illustrated in figure 5–7 due to Dake; here, diagram (a) represents the state of the fluids at the initial pressure assuming the oil and gas are at equilibrium, i.e., the oil is at its bubble point pressure throughout the oil bearing section. The total hydrocarbon pore volume comprises the oil zone (OZ) and the gas cap, i.e.,

$$\text{HCPV} = \text{PV}_o + \text{PV}_g \quad (5-13)$$

These pore volumes are initially estimated from volumetric calculations based on seismic maps and logs. Diagram (b) in figure 5–7 illustrates the effect of dropping the reservoir pressure by an amount  $\Delta p$  and allowing the fluids to expand. Volume A is the increase due to the expansion of oil plus dissolved gas while volume B is the increase due to the expansion of the gas cap. The combined effects of expansion of the connate water (which does not produce) and rock compaction are depicted by volume C.

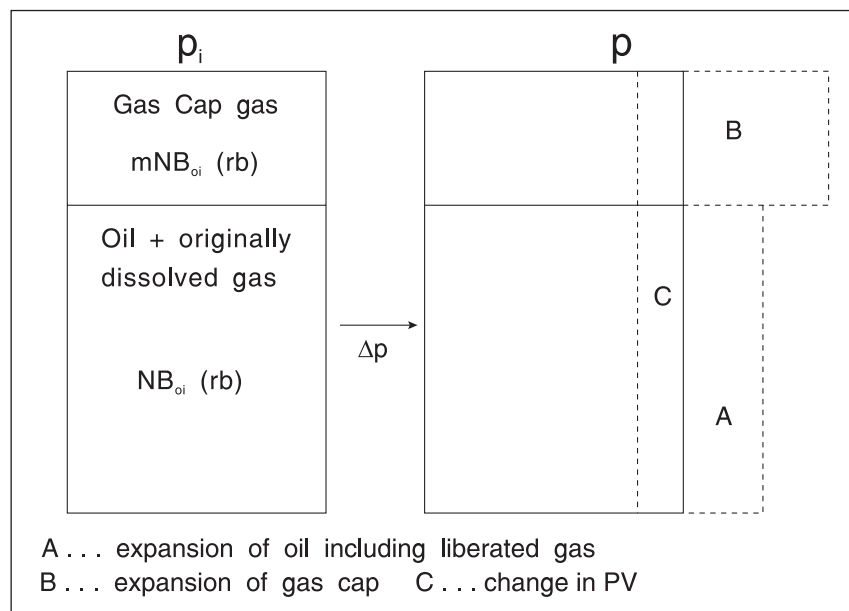


Fig. 5–7. Volume changes in a reservoir for combined solution gas and gas cap drive



The final form of the volume-based material balance equation takes the form

$$N_p [B_o + (R_p - R_s)B_g] = NB_{oi} \left[ \frac{(B_o - B_{oi}) + (R_{si} - R_s)B_g}{B_{oi}} + m \left( \frac{B_g}{B_{gi}} - 1 \right) + (1 + m) \left( \frac{c_w S_{wc} + c_f}{1 - S_{wc}} \right) \Delta p \right] \quad (5-14)$$

In this equation, the PVT quantities are functions of the average pressure, i.e.,

$$B_o = B_o(\bar{p}) \quad R_s = R_s(\bar{p}) \quad B_g = B_g(\bar{p}) \quad (5-15)$$

Given the amount the reservoir has produced on a cumulative basis and the amounts of hydrocarbon initially in place, the Schilthuis material balance can be regarded as a nonlinear equation for determining the average pressure  $\bar{p}$ . In functional form, Eq. (5-14) may be written as

$$f(\bar{p}) = N_p [B_o + (R_p - R_s)B_g] - NB_{oi} \left[ \frac{(B_o - B_{oi}) + (R_{si} - R_s)B_g}{B_{oi}} + m \left( \frac{B_g}{B_{gi}} - 1 \right) + (1 + m) \left( \frac{c_w S_{wc} + c_f}{1 - S_{wc}} \right) \Delta p \right] = 0 \quad (5-16)$$

This may be solved iteratively for the average pressure using a one-dimensional quasi-Newton method, and the depletion of the reservoir, i.e., the change in pressure from  $p_i$  may be calculated as a function of the cumulative withdrawal. In order to solve the material balance equation for reservoir pressure, a PVT model, in the form of a table representing the functions (5-15), must be supplied.

## Compositional Material Balance

### Solution gas-drive cell

The classical material balance equations are based on a black oil or modified black oil representation of the PVT behavior. An alternative approach is to develop a material balance formulation that makes direct calls to a compositional PVT module illustrated diagrammatically in figure 5-8. In the isothermal flash calculation, the overall composition of the hydrocarbon mixture  $z$  and the pressure and temperature are specified and the routine returns the mole fraction vapor  $\beta$ , the compositions of the vapor and liquid phases  $y$  and  $x$ , respectively, and the

densities of the phases  $\rho_g$  and  $\rho_o$ . The volume occupied by the hydrocarbon mixture per mole of feed is given by

$$v = v_g + v_o = \frac{\beta M_g}{\rho_g} + \frac{(1 - \beta)M_o}{\rho_o} \quad (5-17)$$

where  $M_g$  and  $M_o$  are the molecular weights of the gas and oil phases respectively. The fraction of the hydrocarbon volume occupied by the gas phase, here denoted  $\tilde{S}_g$ , is given by

$$\tilde{S}_g = \frac{v_g}{v} \quad (5-18)$$

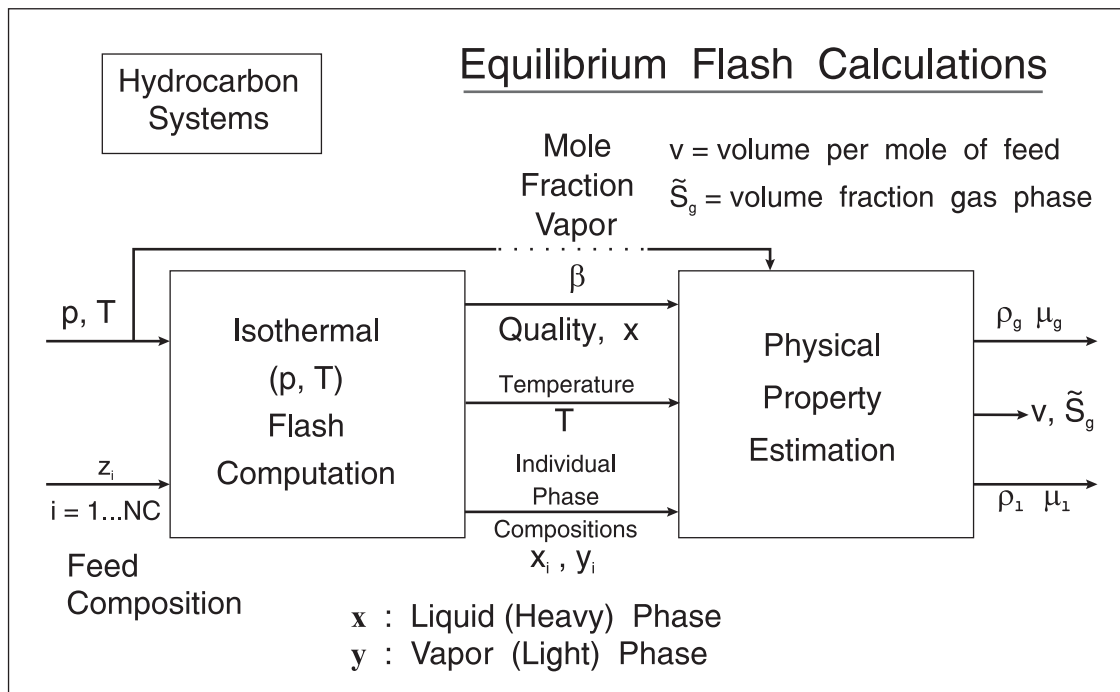


Fig. 5-8. Isothermal flash calculation

In an isochoric flash calculation, the volume is specified as  $v^{\text{spec}}$  along with the composition  $z$  and the temperature  $T$ , and the problem is to determine the pressure  $p$ . Thus, an outer loop must be incorporated that solves the problem

$$f(p) = v - v^{\text{spec}} = 0 \quad (5-19)$$

The isochoric flash problem is similar in mathematical structure to the isenthalpic flash where it is the temperature that must be determined; the isochoric flash calculation is illustrated in figure 5-9. The outer loop problem, i.e., the functional Eq. (5-19), is easily solved using a one-dimensional quasi-Newton (secant) method.

A material balance cell is shown diagrammatically in figure 5–10, where the pressure has fallen below the bubble point and two-phase conditions exist throughout the region; the assumption in the material balance approach is that the pressure and fluid saturations are uniform. Consider a reservoir of fixed hydrocarbon pore volume  $\tilde{V}_p = V_p(1 - S_{wc})$  which is filled with hydrocarbon of overall composition  $z^0$  and suppose a well is produced at a total mass rate  $m_t$  where

$$m_t = m_o + m_g \tag{5-20}$$

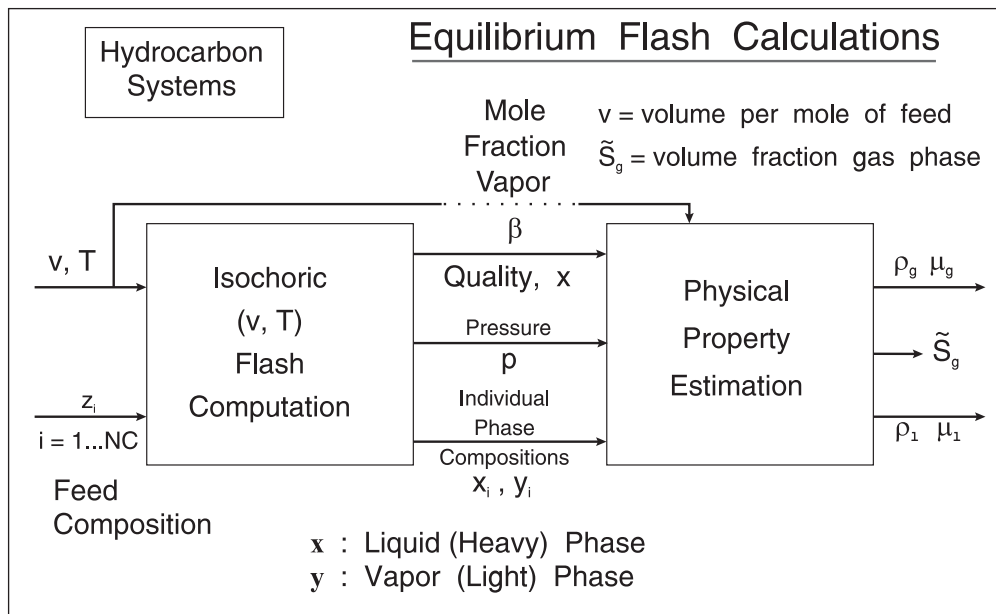


Fig. 5–9. Isochoric flash calculation

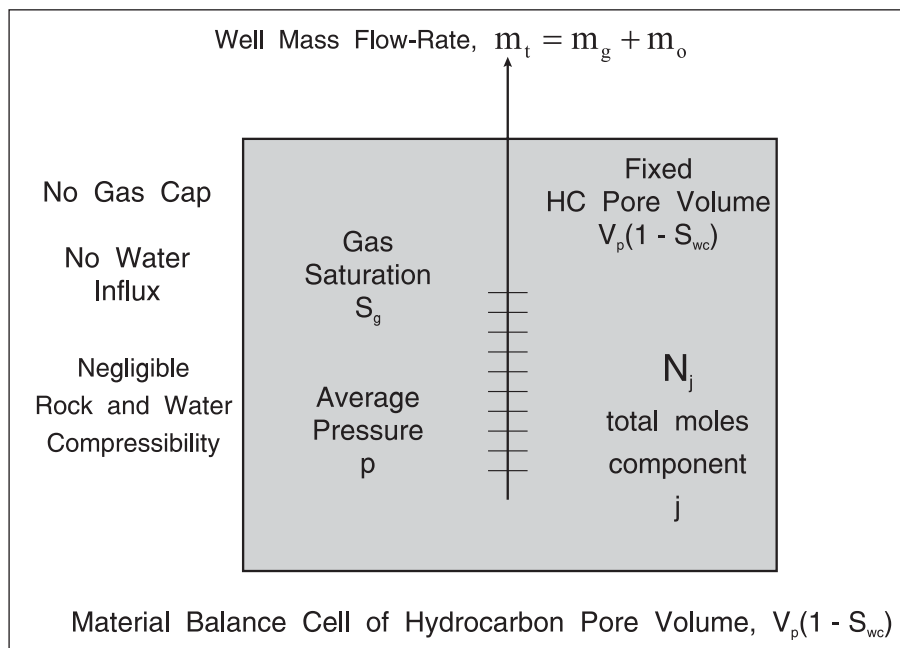


Fig. 5–10. Material balance compartment for a solution gas-drive situation

Here,  $m_o$  and  $m_g$  are individual mass flow rates of oil and gas phase from the two-phase region in the reservoir. Note that only the overall rate  $m_t$  is fixed. The volumetric flow rates of oil and gas leaving the material balance cell are fixed by the saturations of the gas and oil phase denoted  $S_g$  and  $S_o$ , respectively; thus flow to wells is controlled by expressions of the form

$$\bar{q}_g = \frac{A_r k k_{rg}}{\mu_g} \frac{dp}{dr} \quad \bar{q}_o = \frac{A_r k k_{ro}}{\mu_o} \frac{dp}{dr} \quad (5-21)$$

where the bar indicates average conditions for saturation in the cell. The ratio of the mass flow rates is therefore given by

$$\frac{m_g}{m_o} = \frac{\rho_g k_{rg} \mu_o}{\rho_o k_{ro} \mu_g} \quad (5-22)$$

Here, the relative permeability ratio  $k_{rg}/k_{ro}$  is a function of gas saturation  $S_g$ , and simultaneous solution of Eqs. (5-21) and (5-22) yields the individual rates  $m_g$  and  $m_o$ . Defining the mobility ratio as

$$M = \frac{k_{rg} \mu_o}{k_{ro} \mu_g} \quad (5-23)$$

the individual mass flowrates of oil and gas are given by

$$m_o = \frac{m_t}{\frac{\rho_g}{\rho_o} M + 1} \quad (5-24a)$$

$$m_g = m_t - m_o \quad (5-24b)$$

Note that the phase densities and the mobility ratio (which depends on saturation through the relative permeability curves) are changing as conditions in the cell, i.e., pressure and saturation, evolve.

For convenience, it is useful to assume parametric forms for the gas–oil relative permeability relations, i.e.,

$$k_{ro} = k_{ro}^o \left( \frac{1 - S_g - S_{or}}{1 - S_{gr} - S_{or}} \right)^{m'} \quad (5-25a)$$

and

$$k_{rg} = k_{rg}^o \left( \frac{S_g - S_{gr}}{1 - S_{gr} - S_{or}} \right)^{n'} \quad (5-25b)$$

Typical values for the parameters of the Corey approximation for gas–oil systems (at connate water saturation in the range 15%–25 %) taken from the data quoted by Honarpour et al.<sup>4</sup> are as follows:

$$\begin{aligned} k_{ro}^o &= 0.75 & m' &= 1.7 & S_{or} &= 0.2 \\ k_{rg}^o &= 0.85 & n' &= 2.4 & S_{gr} &= 0.2 \end{aligned}$$

The gas phase has composition  $\mathbf{y}$  and the oil phase has composition  $\mathbf{x}$ . Letting  $N_j$  represent the total moles of component  $j$  in the reservoir cell, the component material balances may be written as

$$\frac{dN_j}{dt} = - \left( \frac{m_g}{M_g} y_j + \frac{m_o}{M_o} x_j \right) \quad (5-26)$$

The quantity  $v^{\text{spec}}$  is given by

$$v^{\text{spec}} = \frac{V_p(1 - S_{wc})}{N} \quad \text{where} \quad N = \sum_{j=1}^{NC} N_j \quad (5-27)$$

This formulation does not allow for the change in hydrocarbon pore volume due to expansion of connate water and rock compaction. To allow for these effects, Eq. (5–27) has to be written in the modified form

$$v^{\text{spec}} = \frac{V_p \left( (1 - S_{wc}) - \Delta p (c_f + c_w S_{wc}) \right)}{N} \quad (5-28)$$

where  $c_w$  is the compressibility of water  $c_f$  is the rock compressibility and  $\Delta p = p_i - p$ .

The overall composition of the mixture contained in the pore space is represented by  $\mathbf{z}$  where

$$z_j = \frac{N_j}{N} \quad (5-29)$$

Supposing  $\mathbf{z}$  and  $V_p$  are specified, the isochoric flash routine will determine the pressure  $p$  which satisfies the functional equation

$$f(p) = v - v^{\text{spec}} = 0 \quad (5-30)$$

At the solution, the mole fraction vapour  $\beta$ , the gas and oil phase compositions  $\mathbf{y}$  and  $\mathbf{x}$ , the individual phase densities  $\rho_g$  and  $\rho_o$ , and the phase molecular weights  $M_g$  and  $M_o$  are all determined. The computed pressure  $p$  is, of course, the material balance average pressure of the compartment. Note that the modern EOS-based flash calculation routine is capable of returning good values of both the oil and gas phase densities and the isochoric form can determine the system pressure since the volumetrics are reliable provided adequate characterization of the reservoir fluid has been carried out.

The volume occupied by the gas and oil phases per mole of hydrocarbon feed is given by

$$v_g = \frac{\beta M_g}{\rho_g} \quad v_o = \frac{(1 - \beta)M_o}{\rho_o} \quad (5-31)$$

The fraction of the hydrocarbon pore volume occupied by gas denoted  $\tilde{S}_g$  is given by

$$\tilde{S}_g = \frac{v_g}{v} \quad (5-32)$$

Similarly, the fraction of the hydrocarbon pore volume occupied by oil  $\tilde{S}_o = 1 - \tilde{S}_g$ . The conventional saturations with respect to total void space are given by

$$S_g = (1 - S_{wc,corr})\tilde{S}_g \quad \text{and} \quad S_o = (1 - S_{wc,corr})\tilde{S}_o \quad (5-33)$$

Here, the connate water saturation has been corrected to allow for the expansion of the water phase and the compaction of the reservoir pore space, i.e.,

$$S_{wc,corr} = S_{wc} \frac{1 + c_w \Delta p}{1 - c_f \Delta p} \quad (5-34)$$

where

$$\Delta p = p_i - p$$

The material balance model has the mathematical form

$$\dot{\mathbf{v}} = \mathbf{f}(\mathbf{v}, \mathbf{w}, \mathbf{u}) \quad (5-35a)$$

$$\mathbf{g}(\mathbf{v}, \mathbf{w}, \mathbf{u}) = \mathbf{0} \quad (5-35b)$$

$$\mathbf{u} = \mathbf{u}(t) \quad \mathbf{v}(t = 0) = \mathbf{v}^0 \quad (5-35c)$$

i.e., a nonlinear system of simultaneous ordinary differential equations (ODE) and algebraic equations. The state vector  $\mathbf{v}$  of dimension  $NC$  represents the component mole numbers  $N_j$  and the subsidiary variable vector  $\mathbf{w}$  represents all the other quantities entering the equation set. The system of algebraic equations includes the isochoric flash calculation depicted in figure 5–11. The forcing function  $\mathbf{u}(t)$  is the specified well total mass flow rate  $m_t$ ; in many cases, the well rate is specified as a step-rate function as shown diagrammatically in figure 5–12.

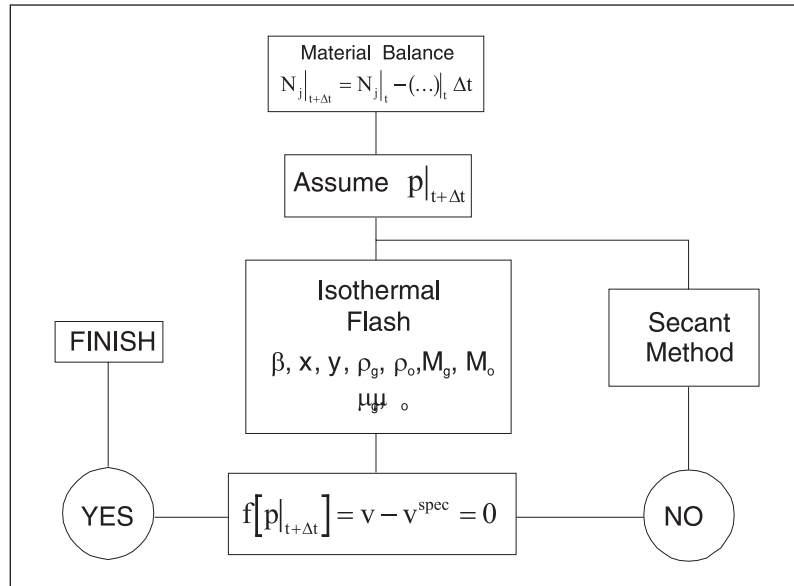


Fig. 5–11. Isochoric flash in solution gas drive

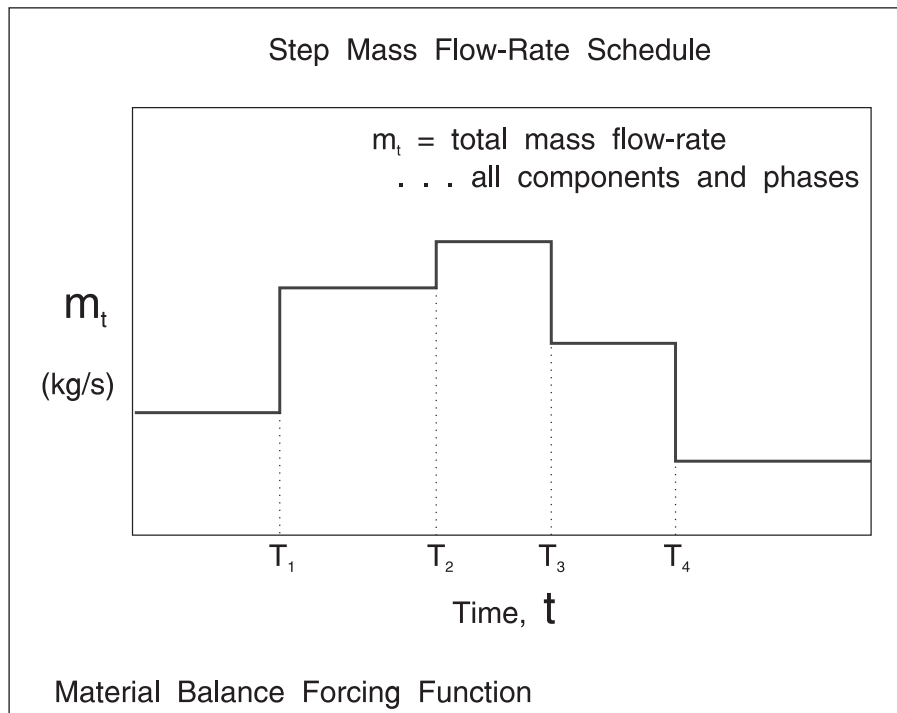


Fig. 5–12. Well mass flow rate expressed as a step-rate function

The initial condition for this model is the liquid-filled reservoir at the bubble point pressure with a single-phase reservoir fluid of composition  $\mathbf{z}^c$  and density  $\rho_{ob}$ ; the initial value for the total moles of component  $j$  is given by

$$N_j^0 = \frac{V_p(1 - S_{wc})\rho_{ob} z_j^c}{M_o^i} \quad (5-36)$$

The stability check in the PVT module will indicate when the pressure has fallen below the bubble-point.

### Black oil model as an isochoric flash

Suppose that the black oil pressure functions  $R_s$ ,  $B_o$ , and  $B_g$  are available, either as tables or explicit functions from correlations. In a compositional frame, component 1 is the gas and component 2 is oil. In the context of the material balance, the moles of components 1 and 2, i.e.,  $N_1$  and  $N_2$ , are fixed and the volume must be determined. The mass of each component follows as

$$W_1 = N_1 M_{w,1} \quad \text{and} \quad W_2 = N_2 M_{w,2} \quad (5-37)$$

Here,  $W_1$  is the total amount of gas component present and the amount of dissolved gas is given as

$$W_{1,D} = \frac{W_2 \rho_{gs} R_s}{\rho_{os}} \quad (5-38)$$

Hence the free gas becomes

$$W_{1,F} = W_1 - W_{1,D} \quad (5-39)$$

The volume occupied by the mixture is now given by

$$V^{\text{mix}} = \frac{B_o W_2}{\rho_{os}} + \frac{W_{1,F} B_g}{\rho_{gs}} \quad (5-40)$$

The specific volume per mole of feed  $v$  follows as

$$v = \frac{V^{\text{mix}}}{N} \quad \text{where} \quad N = N_1 + N_2 \quad (5-41)$$

This formulation of the black oil model allows compatibility with the compositional approach to the material balance advocated here. The material balance calculations can be carried out on



a compositional or black oil basis as desired. The isochoric flash embodied in equation (5-30) allows the specific molar volume  $v$  to be determined by either approach and the secant method will be used in both cases to find the pressure satisfying the functional form (5-30). Densities at reservoir conditions are given by

$$\rho_o = \frac{\rho_{os} + R_s \rho_{gs}}{B_o} \quad \rho_g = \frac{\rho_{gs}}{B_g} \quad (5-42)$$

## Integration of the Material Balance Equation

The simplest approach to integrating the material balance equations is to use the basic Euler method which can be written as

$$N_j|_{t+\Delta t} = N_j|_t + \left. \frac{dN_j}{dt} \right|_t \Delta t \quad (5-43a)$$

where

$$\left. \frac{dN_j}{dt} \right|_t = \left( -\frac{m_g}{M_g} y_j - \frac{m_o}{M_o} x_j \right) \Big|_t \Delta t \quad (5-43b)$$

and

$$m_o = \frac{m_t}{\frac{\rho_g}{\rho_o} M + 1} \quad m_g = m_t - m_o$$

In this explicit method, the phase compositions  $x$  and  $y$  are evaluated at the beginning of the time step and held constant over the time step. Similarly the phase densities and mobility ratio are known at the beginning of the time step and also held constant; the total mass flow rate  $m_t$  is obtained from the step rate schedule (forcing function). Thus, the total moles of each component in the cell at the new time level can be computed as

$$N|_{t+\Delta t} = \sum_{j=1}^{NC} N_j|_{t+\Delta t} \quad (5-44)$$

and the corresponding specific volume, i.e.,  $v|_{t+\Delta t}$ , follows as

$$v|_{t+\Delta t} = \frac{V_p(1 - S_{wc})}{N|_{t+\Delta t}} \quad (5-45)$$

The overall composition of the mixture at the new time level, i.e.,  $\mathbf{z}|_{t+\Delta t}$  can be obtained as

$$z_j|_{t+\Delta t} = \frac{N_j|_{t+\Delta t}}{N|_{t+\Delta t}} \quad (5-46)$$

and the isochoric flash routine can be called to return the pressure, phase compositions, and phase specific volumes at the new time level. Thus, the quantities

$$P|_{t+\Delta t} \quad \mathbf{y}|_{t+\Delta t} \quad \mathbf{x}|_{t+\Delta t} \quad \mathbf{v}_g|_{t+\Delta t} \quad \mathbf{v}_o|_{t+\Delta t}$$

are now known and the phase saturations follow as

$$S_g|_{t+\Delta t} = (1 - S_{wc}) \frac{v_g}{v} |_{t+\Delta t} \quad (5-47a)$$

$$S_o|_{t+\Delta t} = 1 - S_g|_{t+\Delta t} - S_{wc} \quad (5-47b)$$

This sequence completes one step in the integration process and the material balance solution progresses forward by successive application of the algorithm. The main output is the evolution of the reservoir pressure in response to production and the producing gas–oil ratio (GOR) of the system.

Given the mass flow rates  $m_g$  and  $m_o$  and compositions  $\mathbf{y}$  and  $\mathbf{x}$  of these streams, it is then necessary to convert to surface conditions by emulating the separation process as illustrated in figure 5–13. Three calls of an isothermal ( $p, T$ ) flash routine are required to bring the general well stream to stock tank conditions. The pressure and temperature of each of the three flashes must be specified and the process yields a flow rate of gas at standard conditions  $Q$  and an oil flow rate at stock tank conditions  $q_s$ . In addition, the compositions and densities of the surface streams will be calculated as  $\mathbf{y}^s$  and  $\mathbf{x}^s$ , and  $\rho_g^s$  and  $\rho_o^s$ . The producing GOR is defined as

$$\text{GOR} = \frac{Q}{q_s} \quad (5-48)$$

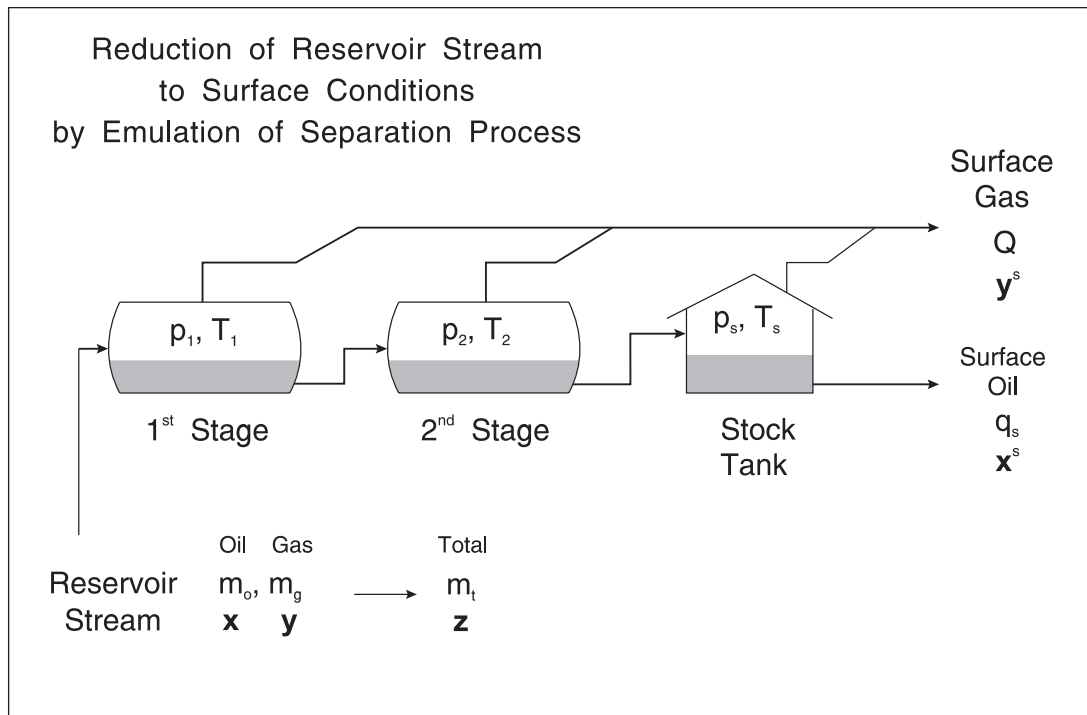


Fig. 5-13. Reduction of compositional streams to surface conditions

For a reservoir producing by solution gas drive, the producing GOR varies with time in the manner illustrated in figure 5-14.

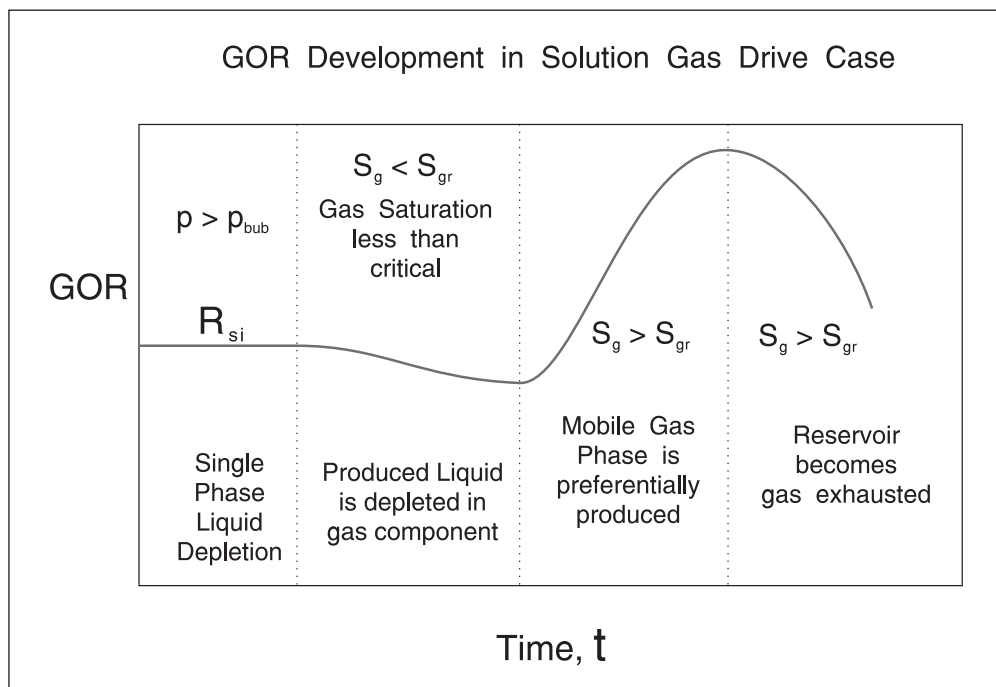


Fig. 5-14. Producing GOR for a field in solution gas drive

## Undersaturated liquid behavior

Above the bubble point, the well produces only an oil phase with the initial reservoir fluid composition  $z^c$ , and the density  $\rho_o$  is predicted by the EOS solved for the fluid composition  $z^c$  and the pressure at the new time level  $p|_{t+\Delta t}$ . Thus, formally

$$\rho_o = f_{RL}\left(p|_{t+\Delta t}\right) \quad (5-49)$$

since the fluid composition and temperature are known; here, the function  $f_{RL}$  designates the liquid density calculated from the cubic EOS. The apparent liquid density may be written as

$$\rho_{o,app} = \frac{N|_{t+\Delta t} M_o^i}{V_p(1 - S_{wc})} \quad (5-50)$$

and the pressure at the new time level must satisfy the equation

$$f_{LC}\left(p|_{t+\Delta t}\right) = \frac{\rho_o - \rho_{o,app}}{\rho_{o,app}} = 0 \quad (5-51)$$

This functional equation for the new pressure can readily be solved using the secant method. In this approach, the liquid density is modeled by the cubic EOS taking the liquid root for the evaluation of  $\rho_o$ . Traditionally, the weakest element of EOS modeling has been the prediction of liquid phase density, and basing the liquid expansion on the cubic EOS is somewhat risky. It has been presumed that the tuning process has included the laboratory PVT data on the liquid phase above the bubble point pressure and the matched EOS satisfactorily reproduces the change in liquid density with pressure. Note that the liquid compressibility over a depletion step is given by

$$c_o = \frac{1}{\bar{\rho}} \frac{\Delta\rho}{\Delta p} \quad (5-52)$$

where  $\Delta\rho = \rho_o(p|_t) - \rho_o(p|_{t+\Delta t})$      $\Delta p = p|_t - p|_{t+\Delta t}$

and  $\bar{\rho} = \frac{\rho_o(p|_t) + \rho_o(p|_{t+\Delta t})}{2}$

The liquid compressibility determined from the VPT equation of state for the (untuned) 10-component crude oil system is shown in figure 5-15.

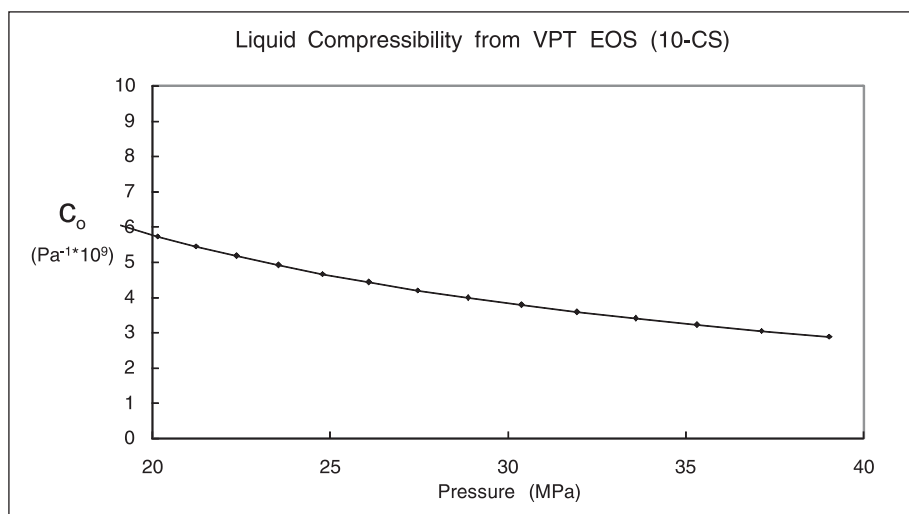


Fig. 5–15. Liquid phase compressibility above the bubble-point for the 10-CS

## Well models in the material balance cell

In the material balance model, the forcing function is the total mass flow rate of all wells producing from the block; this is designated  $m_t$  and is given by the summation

$$m_t = \sum_{i=1}^{NWB} m_{t,i} \quad (5-53)$$

where  $m_{t,i}$  is the mass flow rate of well  $i$  of which there are  $NWB$  penetrating the material balance cell. The individual total rates of oil and gas  $q_o$  and  $q_g$  are controlled by the current saturation in the reservoir. Each well has an associated inflow model that allows the bottom-hole flowing pressure of the well to be determined using steady-state (SS) radial flow theory as described in chapter 3 where the two-phase pseudopressure was introduced. The overall (flowing) composition of the producing fluid is denoted  $\tilde{z}$ , where

$$\tilde{z}_i = \frac{\frac{m_g y_i}{M_g} + \frac{m_o x_i}{M_o}}{\sum_{i=1}^{NC} \left( \frac{m_g y_i}{M_g} + \frac{m_o x_i}{M_o} \right)} \quad (5-54)$$

Here,  $x$  and  $y$  are the current compositions of the gas and liquid phases present in the tank, and the flowing composition is dependent on the ratio of the mass flow rates controlled by relative permeability. In the compositional material balance, the composition of the produced fluid is changing and the pseudopressure function—which applies for a specific value of  $\tilde{z}$ —must be continually updated to allow for this variation. In figure 5–16, a semi-steady-state (SSS) radial flow region around an individual well is shown with streams  $\bar{q}_{g,i}$  and  $\bar{q}_{o,i}$ , where the bar indicates

that the flow rates are based on material balance average pressure and saturation. The volumetric flow rates must satisfy the relation

$$m_{t,i} = \bar{q}_{g,i}\rho_g + \bar{q}_{o,i}\rho_o \quad (5-55)$$

where the total mass flow rate  $m_t$  is specified as constant. In Eq. (5-55), the densities depend on the compositions  $x$  and  $y$  and pressure  $p$  of the flowing phases.

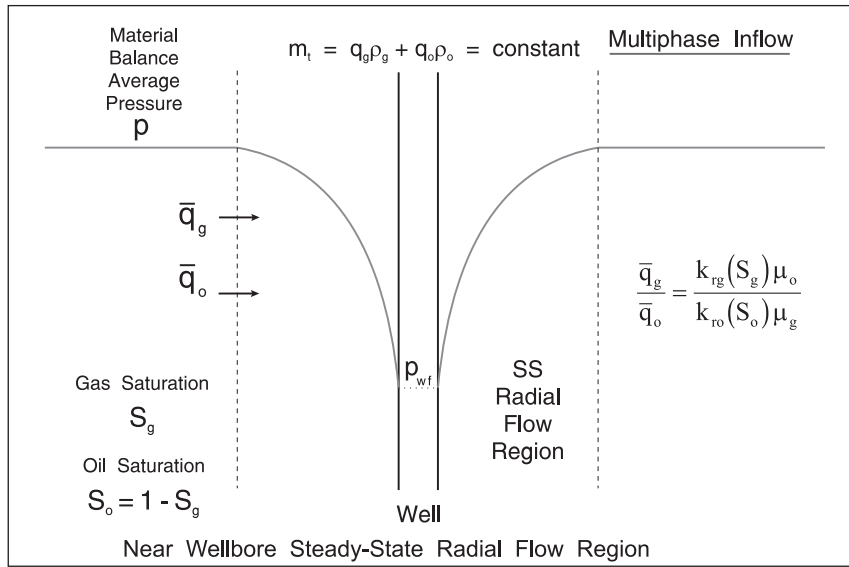


Fig. 5-16. Near-wellbore semi-steady-state radial flow region

In the near-wellbore region, further flashing of the mixture occurs and the sandface streams, denoted  $q_{g,i}|_w$  and  $q_{o,i}|_w$ , are different in composition and rate; however, the total rate and overall composition remain constant throughout the SS region, i.e.,

$$m_{t,i} = \left( q_{g,i}\rho_g + q_{o,i}\rho_o \right) \Big|_w \quad (5-56)$$

In the computation of the well inflow performance relation, the overall composition of the flowing mixture is held at  $\tilde{z}$ ; in the context of a time-stepping material balance model, the overall composition of the produced fluid is changing continuously, but it is still useful to generate a two-phase pseudopressure function based on the instantaneous flowing composition  $\tilde{z}$ .

For SSS conditions, the inflow performance relation (IPR) is written in the form

$$m_{t,i} = J_{ss,i} (\psi(p) - \psi(p_{wf})) \quad (5-57)$$

where  $p$  is identified with the (material balance) average pressure of the cell and the SSS productivity index (PI) is given by

$$J_{SSS,i} = \frac{2\pi kh\rho_r}{\mu_r \left( \ln \frac{r_e}{r_w} - \frac{3}{4} + S_a \right)} \quad (5-58)$$

In the case where the well is located in a noncircular drainage area, then  $J_{SSS,i}$  is written alternatively as

$$J_{SSS,i} = \frac{2\pi kh\rho_r}{\mu_r \left( \frac{1}{2} \ln \frac{4\bar{A}}{\gamma C_A r_w^2} + S_a \right)} \quad (5-59)$$

where  $C_A$  is the Dietz shape factor corresponding to the well position and the drainage area shape. In the case of fractured or horizontal wells, the total apparent skin  $S_a$  in Eq. (5-59) is simply replaced by the pseudoradial skin  $S_{pr}$ , i.e.,

$$J_{SSS,i} = \frac{2\pi kh\rho_r}{\mu_r \left( \frac{1}{2} \ln \frac{4\bar{A}}{\gamma C_A r_w^2} + S_{pr} \right)} \quad (5-60)$$

Formulae relating  $S_{pr}$  to horizontal well length  $L$ , anisotropy  $A$ , and damage skin  $S_d$  are given in chapter 12 of *Well Test Design and Analysis*. In situations where the horizontal or fractured well SSS deliverability is better represented by the pseudolinear model, also described in chapter 12, the well PI  $J_{SSS,i}$  should be specified directly.

A material balance cell may have multiple producing wells each characterized by individual  $kh$  products, Dietz shape factors, and skin factors. Since saturation conditions in a material balance cell are uniform, the pseudopressure function is the same for all wells in the block.

The well models are necessary in the tuning process (described in the section “Tuning of Material Balance Model”) when bottom-hole flowing pressures are measured with permanent gauges.

## Synthetic test problem

In order to demonstrate the operation of the general material balance, a crude oil represented by 10 pure hydrocarbon components was selected; the composition of the reservoir fluid is given in table 5-2.

**Table 5-2.** Composition of initial reservoir fluid

Mole fraction of pure hydrocarbon component in reservoir fluid				
$C_1 : 0.4604$	$C_2 : 0.0426$	$C_3 : 0.0090$	$C_4 : 0.0109$	$C_5 : 0.0095$
$C_6 : 0.0103$	$C_7 : 0.0292$	$C_8 : 0.0417$	$C_9 : 0.0337$	$C_{10} : 0.3527$

A small reservoir of pore volume  $V_p$  equal to  $10^6 \text{ m}^3$  was selected and the single well was produced at a constant mass flow rate of  $1.0 \text{ kg/s}$ ; the reservoir parameters are listed in table 5–3.

**Table 5–3.** Reservoir parameters for synthetic test problem

$V_p = 10^6 \text{ m}^3$	$S_{wc} = 0.2$	$\tilde{v} = 0.8 \times 10^6 \text{ m}^3$	$T = 400 \text{ K}$
$p_i = 25 \text{ MPa}$	$P_{bub} = 18.09 \text{ MPa}$	$c_w = 4.35 \times 10^{-10} \text{ Pa}^{-1}$	$c_f = 8.7 \times 10^{-10} \text{ Pa}^{-1}$

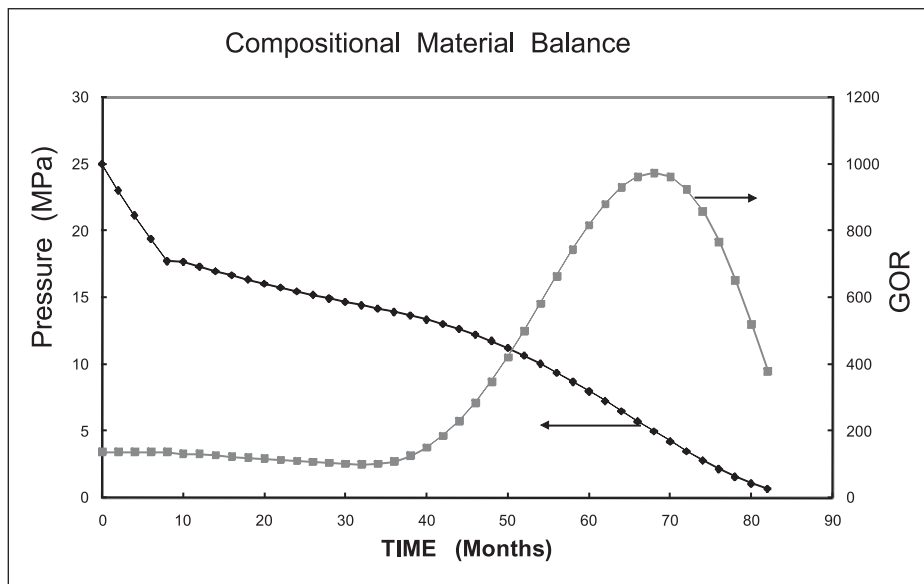
The relative permeability data was input as Corey coefficients as given in table 5–4.

**Table 5–4.** Relative permeability data

$k_{ro}^o = 0.75$	$m' = 1.7$	$\tilde{S}_{or} = 0.2$
$k_{rg}^o = 0.85$	$n' = 2.4$	$\tilde{S}_{gr} = 0.2$

The reservoir behavior in terms of pressure and producing GOR is shown in figure 5–17, where an initial period of liquid only depletion is present until the reservoir pressure falls below the bubble-point. In this region, the GOR is constant (solution GOR) and the pressure falls according to the equation

$$\frac{dp}{dt} = -\frac{q}{c_t V_p} = -\frac{m_t}{\rho_o c_t V_p} \quad (5-61)$$



**Fig. 5–17.** Pressure and GOR for solution gas-drive reservoir—test problem results

In the present formulation, the oil compressibility is not constant but changes with pressure according to the cubic EOS used in the model; in this case the Valderrama–Patel–Teja (VPT) three-parameter EOS was used. Once the pressure has fallen below the bubble point, the gas



saturation in the cell starts to increase as shown in figure 5–18; in this region, it is the two-phase compressibility that controls the pressure decline rate. As long as the gas saturation is below the critical value, only an oil phase is produced. In the simulation data, the critical gas saturation is given by  $S_{gr} = \tilde{S}_{gr}(1 - S_{wc}) = 0.2 \times 0.8 = 0.16$  and it takes approximately 29 months for the gas to become mobile in the reservoir. Once  $S_g > S_{gr}$ , the production of a free gas phase commences and the GOR rapidly increases as shown in figure 5–17; this is the main characteristic of a solution gas-drive reservoir. However, it must be pointed out that it takes a considerable time to bring the gas saturation up to the critical value. In a material balance model, with uniform conditions throughout the block, the time to reach the period of increasing GOR may be exaggerated since localized upward migration of gas may occur. Note that the liquid depletion rate above the bubble point is 0.91 MPa/month, whereas in the solution gas-drive period below the critical gas saturation it is only 0.15 MPa/month, i.e., the effective two-phase compressibility is six times greater than the liquid compressibility. Once the critical gas saturation is attained and free gas production commences after 28 months, the pressure declines more rapidly due to loss of gas from the reservoir.

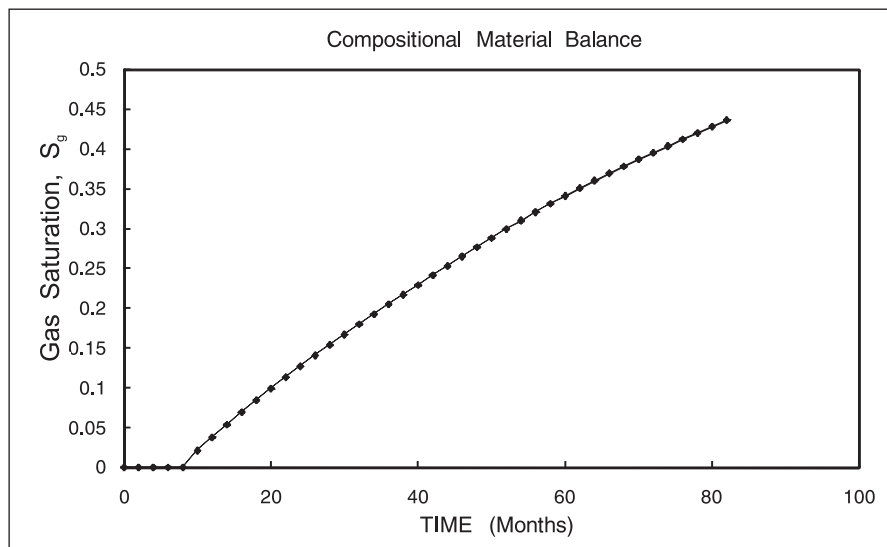


Fig. 5–18. Evolution of gas saturation in solution gas drive—test problem results

The maximum in the GOR response at 68 months is due to the changing gas formation volume factor  $B_g$ , defined as

$$B_g = \frac{\bar{q}_g}{\bar{q}_{sg}} \quad (5-62)$$

Here,  $\bar{q}_g$  is the in situ volume (rate) of gas produced into the well at reservoir conditions and  $\bar{q}_{sg}$  is the volume (rate) of the same gas at standard conditions. As the reservoir pressure falls,  $B_g$  becomes closer to unity, i.e., larger, and the volume of gas at standard conditions reduces substantially even though  $\bar{q}_g$  is maintained. Note that the well is produced at constant total mass rate  $m_t$  and the in situ mass ratio of oil to gas is controlled by the factor  $\rho_g M / \rho_o$  which is pressure dependent. The simulation was terminated at a cut-off reservoir pressure of 0.5 MPa after 82

months of production. The same problem was run with the black oil PVT model defined in the section “Black Oil Model” and the pressure and GOR behavior are shown in figure 5–19.

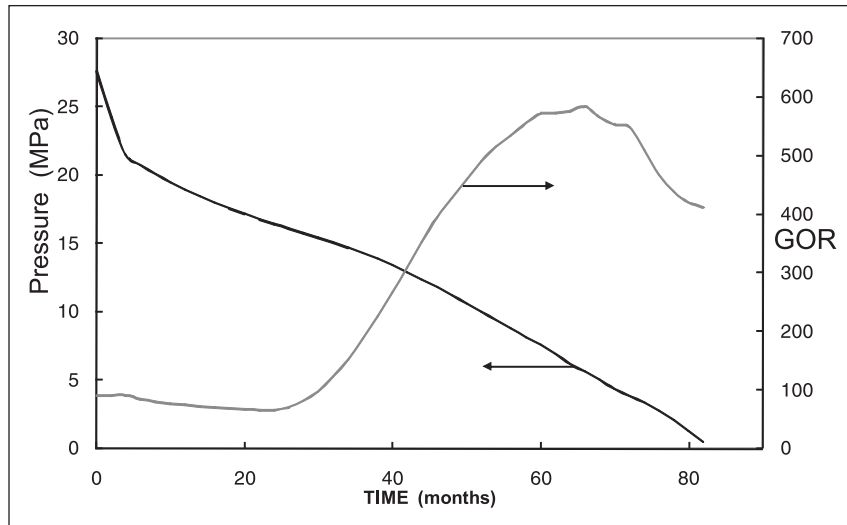


Fig. 5–19. Pressure and GOR for solution gas-drive reservoir—black oil PVT

A two-phase inflow model used to calculate the bottom-hole flowing pressure of a well whose PI in single-phase liquid flow (for a liquid viscosity  $\mu_{\text{ref}} = 10^{-3} \text{ Nsm}^{-2}$ ) was  $J_{\text{SSS}} = 9.327 \times 10^{-10} \text{ m}^3\text{s}^{-1}\text{Pa}^{-1}$ . The plot of  $\bar{p}$  and  $p_{\text{wf}}$  versus time is shown in figure 5–20, where the well PI in single-phase flow is about 1.5 times higher than that in two-phase flow. Hence, the gas block effect, for the relative permeability curves used, is not very serious in this case. Note that, although the reservoir is forced to flow to a low abandonment pressure, the well bottom-hole pressure will have fallen to atmospheric pressure after 2,190 days. In figure 5–21, the produced fluid gravities (ex final separator) are plotted indicating very little change over the life of the field, i.e., it is a typical black oil system although it has been modeled compositionally.

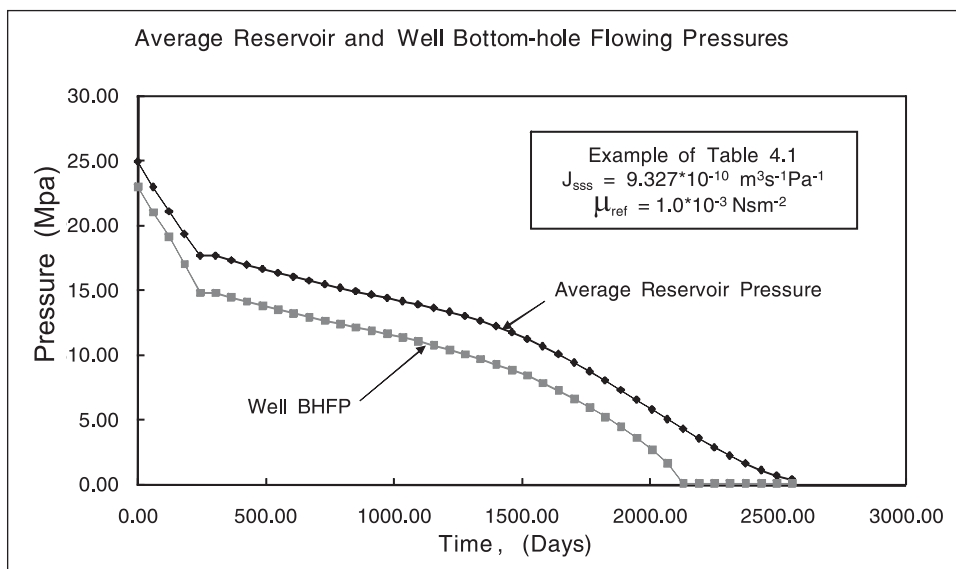


Fig. 5–20. Well BHFP versus time plot

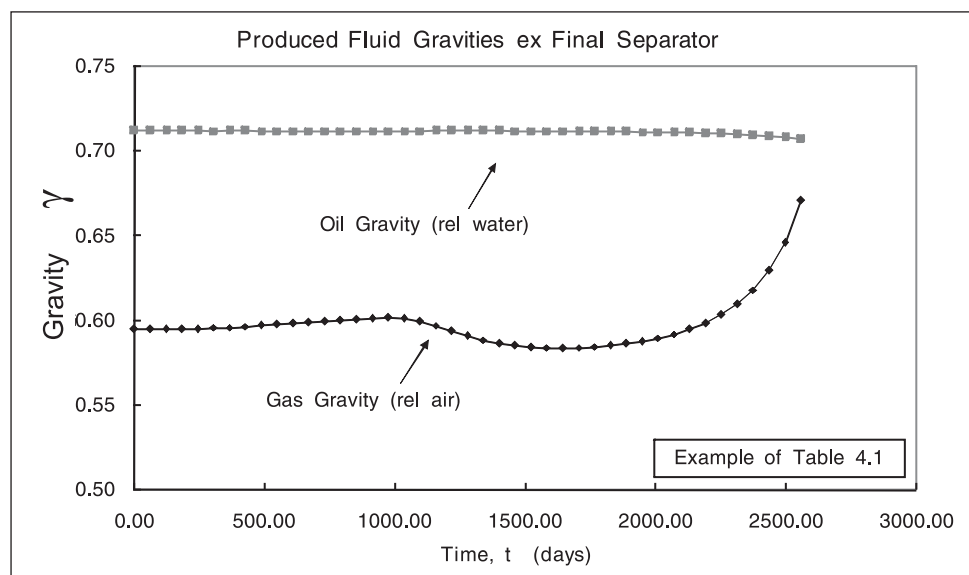


Fig. 5-21. Produced fluid gravity versus time plot

## Critical gas saturation $S_{gc}$

In a material balance program, where the well production is controlled by gas–oil drainage relative permeability curves, the critical gas saturation is a crucial parameter since this controls when the producing GOR begins to deviate from the solution GOR. The process of upward gas percolation giving rise to a secondary gas cap (described in the succeeding section) also begins when the gas saturation in the reservoir reaches the critical value. The value of  $S_{gr} = 0.16$ , i.e.,  $\tilde{S}_{gr} = 0.2$ , is quite high and in the synthetic example in the preceding section the pressure falls to 14.7 MPa before gas starts to flow, whereas the bubble point is 18.1 MPa. The critical gas saturation is defined as the minimum gas saturation at which gas phase flow can occur. Its value is often established from the extrapolation of the gas relative permeability for an external gas-drive process. Another approach used less frequently is the measurement of gas saturation at the point where the gas phase becomes mobile under an internal gas expansion condition. These two methods are fundamentally different and critical gas saturation is of a different nature for external and internal gas-drive processes. The appearance of the gas phase in an internal expansion process is a heterogeneous bubble nucleation phenomenon where the formation of a new phase requires work supplied by the environment surrounding the site where the nucleus will appear. Also, thermodynamic considerations require supersaturation for the initiation of nucleation. The growth of the initial nucleus, caused by diffusion and expansion, agglomeration of various nuclei, and mobilization of the connected bubbles, in an internal gas expansion process is entirely different from the gas-phase mobilization in external gas-drive systems.

Knowledge of critical gas saturation is important for estimating recovery in a solution gas-drive reservoir and methane production from geopressured aquifers. Measured values of the critical gas saturation in the literature range from 2% to 27% PV. For solution gas-drive systems, and particularly for fractured reservoirs, high values of critical gas saturation mean high oil recoveries, e.g., a 15% critical gas saturation could imply greater than 15% oil recovery. On the other hand, for geopressured aquifers, only low values of critical gas saturation, i.e., <0.5%, could give substantial gas recovery.

Madaoui<sup>5</sup> reported an extensive set of critical gas saturations for several rock and fluid samples measured on a vertical core of length 14–16 in. Critical gas saturations varied from 4.4% to 26.4% on a residual water free basis. Abgrall and Iffly<sup>6</sup> measured critical gas saturations for both vugular and intergranular rocks using reservoir crudes and simple fluids. Like the Madaoui study, their experiments were conducted on vertical core and assumed zero supersaturation. Their data varied from 1.7% to 6.3% for the intergranular porosity cores and from 17.4% to 26.4% for the vugular cores. The most recent experimental study has been carried out by Firoozabadi et al.,<sup>7</sup> who demonstrated that supersaturation in real porous media is probably negligible; this is reassuring since the material balance model is based on the assumption of phase equilibrium. The critical gas saturations reported by Firoozabadi et al. were in the range 0.5%–2.0%, much lower than the French studies. On a chalk sample, for example, the critical gas saturation was 0.5%. These low values are supported by Saidi,<sup>8</sup> who discusses field evidence of such small values for  $S_{gr}$  in fractured reservoirs. Firoozabadi et al. indicate that a material balance error in the evaluation of the experiments of Madaoui and Abgrall and Iffly significantly overestimates the critical gas saturation. It is interesting to observe that this controversy regarding  $S_{gr}$  is exactly analogous to the controversy relating to critical liquid saturation  $S_{or}$  in gas condensate reservoirs discussed in chapter 17 of *Well Test Design and Analysis*. Note that liquid dropout by retrograde condensation is similar in nature to internal gas drive. It is not enough to discuss only critical gas saturation, and relative permeability at low gas saturations must also be considered. This is illustrated in figure 5–22 where figure 17–23 in chapter 17 of *Well Test Design and Analysis* has simply been reproduced with “oil” changed to “gas”. The implication of Firoozabadi’s experiments is that, while  $S_{gc}$  may be small, the relative permeability at saturations near  $S_{gc}$  is so tiny that flow will be negligible. If a Corey functional form is used to represent the relative permeability over a wide range of saturation, it will be necessary to use the “apparent” critical saturation depicted in figure 5–22 since a simple power relation cannot reproduce the tail end of the curve. In the case of condensate, the centrifuge can be used to measure very low relative permeabilities to liquid in the vicinity of  $S_{oc}$ ; unfortunately, no equivalent experiment has been devised for internal solution gas drive in the vicinity of  $S_{gc}$ . In practice,  $S_{gc}$  will be adjusted using nonlinear regression to give a match to producing GOR data from the field.

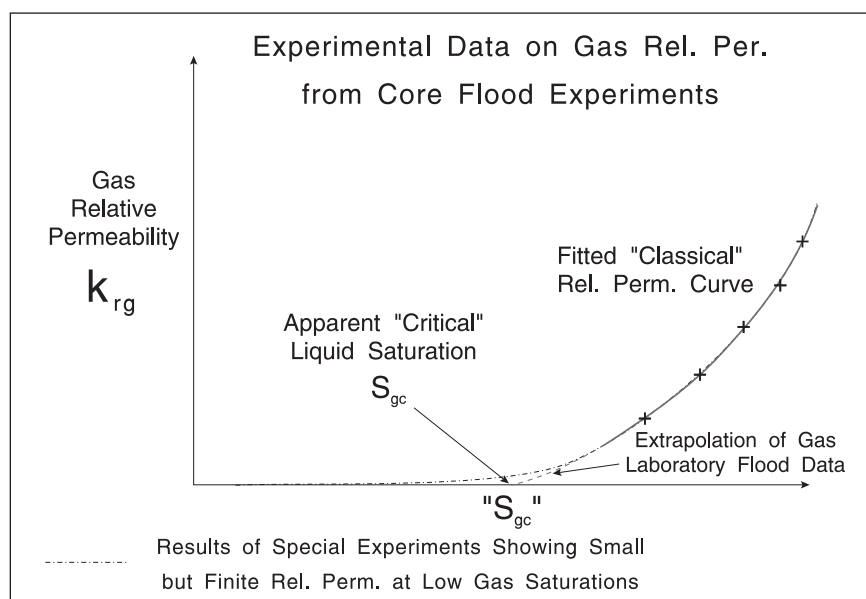


Fig. 5–22. Experimental difficulty of determining critical gas saturation

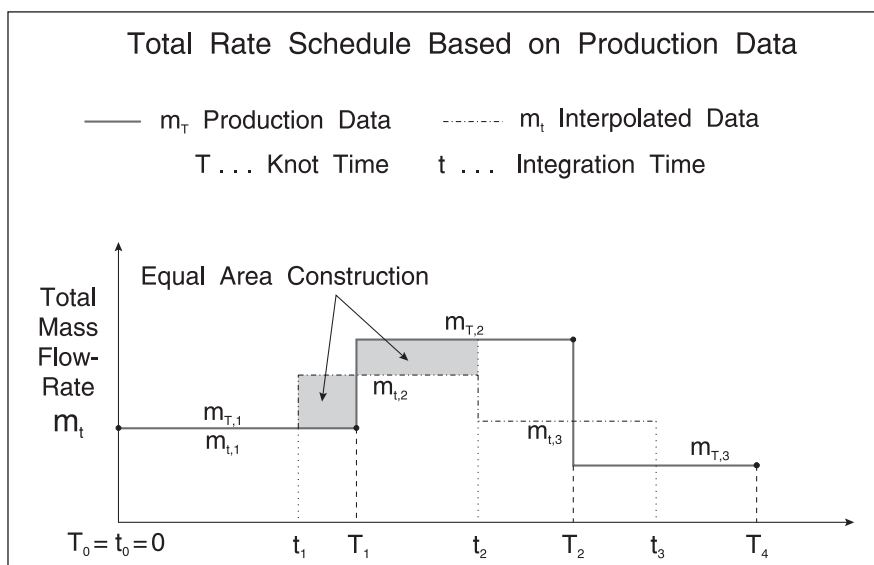


Fig. 5-23. Storage of the rate schedule information

### Variable rate production data

In the preceding treatment of the material balance integration, it was tacitly assumed that the total mass flow rate  $m_t$  (summed over all wells) was constant over the time step  $\Delta t$ . In practice, the rate data from the production database will be stored in the form of a table as illustrated in figure 5-23; here, the total mass flow rate is given as a schedule with rates specified at various knot times with backward referencing as indicated. This form of time-rate table is used in well testing, for example, and volumetric production data can be put in this form provided density (gravity) information on the fluids is available. In addition to the total rate information, the fraction of the total flow associated with each well can be stored as an allocation; thus, the rate schedule table has the form shown in table 5-5.

Table 5-5. Storage of rate and allocation information

Time	Total rate, $m_t$	Well 1 fraction	Well i fraction	Well nw fraction
0	$m_{T,1}$	$f_{m,1}^1$	$f_{m,1}^i$	$f_{m,1}^{NW}$
$T_1$	$m_{T,1}$	$f_{m,1}^1$	$f_{m,1}^i$	$f_{m,1}^{NW}$
$T_2$	$m_{T,2}$	$f_{m,2}^1$	$f_{m,2}^i$	$f_{m,2}^{NW}$
—	—	—	—	—

It is not necessary for the knot times  $T_i$ —typically monthly intervals—to coincide with the timesteps  $t_i$  for integration and therefore the correct average mass rate over a particular timestep must be calculated using an equal area principle, as shown graphically in the figure 5-23. This device ensures that variable rate data, stored as a table, can be correctly handled in a material balance correct fashion.

## Nonlinear regression

In the simulation mode, the parameters of the material balance model are specified and the forward integration predicts the pressure, i.e., material balance (MB) average pressure of the system, and producing GOR. In the history matching mode, measurements are made of pressure and producing GOR and the model parameters are adjusted until a match is obtained, i.e., the difference between predicted and measured values is minimized. The process of nonlinear regression or automatch was discussed in detail in chapter 14 of *Well Test Design and Analysis*, in connection with well test interpretation. Exactly the same algorithm can be used for the material balance problem with the modification that the objective function must be extended to include GOR in addition to pressure data. In figure 5–24, measured data is represented by crosses and the MB model prediction by circles. The  $\chi^2$  objective function takes the form

$$\chi^2 = \sum_{i=1}^{NP} \left( \frac{p_i^c(\mathbf{a}) - p_i^m}{\sigma_{p,i}} \right)^2 + \sum_{i=1}^{NP} \left( \frac{GOR_i^c(\mathbf{a}) - GOR_i^m}{\sigma_{GOR,i}} \right)^2 \quad (5-63)$$

where the superscript “c” indicates the predicted value from the model with the current  $\mathbf{a}$  values, and the superscript “m” refers to the measured values. Using the nomenclature of chapter 14 of *Well Test Design and Analysis*, the parameters of the material balance model are represented by the vector  $\mathbf{a}$ . For example,  $\mathbf{a}$  may take the form

$$\mathbf{a} = [V_p; k_{ro}^o; m'; \tilde{S}_{or}; k_{rg}^o; n'; \tilde{S}_{gr}]^T \quad (5-64)$$

implying that the parameters  $S_{wc}$ ,  $c_w$ ,  $c_f$ , and  $T$  are known. The pressure behavior is primarily controlled by the pore volume  $V_p$ , while the GOR development is predominantly determined by the relative permeability curves. Finding seven variables by regression might be dangerous and it could be advisable, for example, to force certain relative permeability parameters to specified values, leaving only the key quantities to be determined by matching. The most important relative permeability parameter in solution gas-drive is the critical gas saturation  $S_{gr}$  and the problem can be reformulated as

$$\mathbf{a} = (V_p; S_{gr})^T \quad (5-65)$$

$$S_{wc}, c_w, c_f, T, k_{ro}^o, m', \tilde{S}_{or}, k_{rg}^o, n' \quad \text{fixed}$$

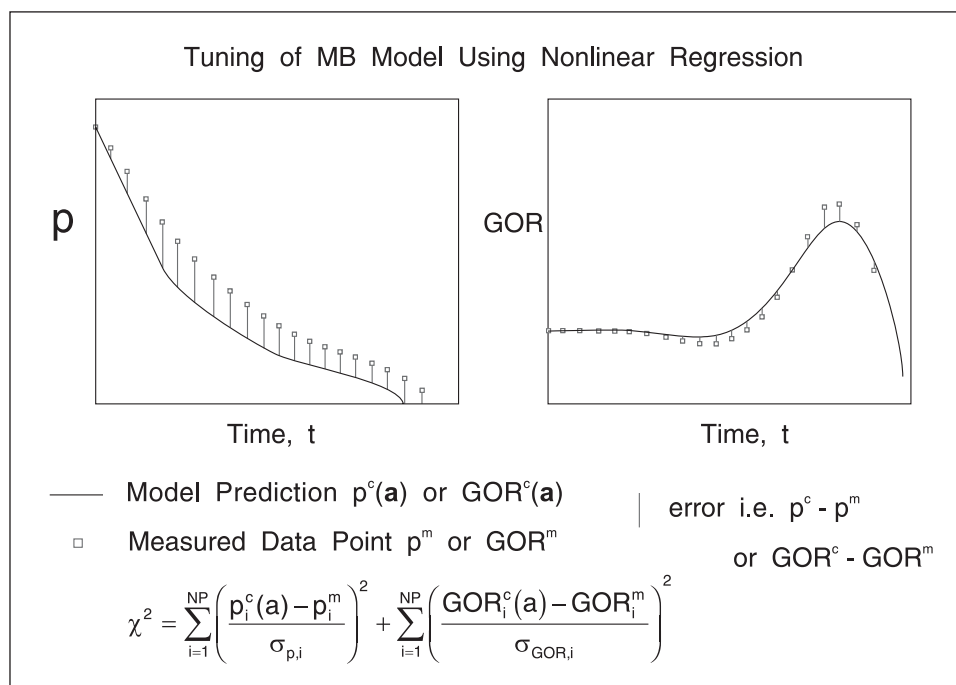


Fig. 5-24. Nonlinear regression objective function

## Integration with a Production Network Model

In the preceding formulation of the material balance model, it has been assumed that the total mass flow rate  $m_t$  of all wells producing from the block is constant over the integration time step  $\Delta t$ . In the general case, there are multiple material balance cells and the wells form part of a production system as illustrated in figure 4-77 in chapter 4.

## Evolution of a Secondary Gas Cap

### Upward percolation of free gas

The model given above does not allow for the evolution of a secondary gas cap due to the upward movement of free gas in the reservoir, as depicted in figure 5-25. In this situation, free gas percolates upward because of buoyancy and liquid drains down counter currently in the gassing zone. Percolation cannot occur until the gas saturation in the OZ exceeds the critical saturation  $S_{gr}$ , and here “free” gas refers to any gas present in excess of the critical saturation. For the purposes of the development of a material balance model, the gassing zone will be assumed to be thin and the reservoir is partitioned into a secondary gas cap (SC) and an OZ. As gas migrates upward at a rate controlled by vertical permeability, relative permeability and phase density difference the secondary gas cap grow in size. A moving boundary between the SC and the oil column propagates downward and simultaneous material balance equations for both regions have to be formulated. The problem is similar in nature to that of the gas reservoir with water

influx treated in the preceding chapter. An estimate of the upward flow of gas can be obtained from the equation

$$q_g^p = \frac{k_z k_{rg} \bar{A} \Delta \rho g}{\mu_g} \quad (5-66)$$

where  $k_z$  is an effective vertical permeability,  $\bar{A}$  is the cross-sectional area available for vertical flow, and  $\Delta \rho = \rho_o - \rho_g$  is the phase density difference. The relative permeability to gas  $k_{rg}$  is based on the current OZ gas saturation  $S_g$ . The key feature of the SC is that a residual oil saturation  $S_{or}$  remains in this region that may later be partially recovered in a blow-down phase.

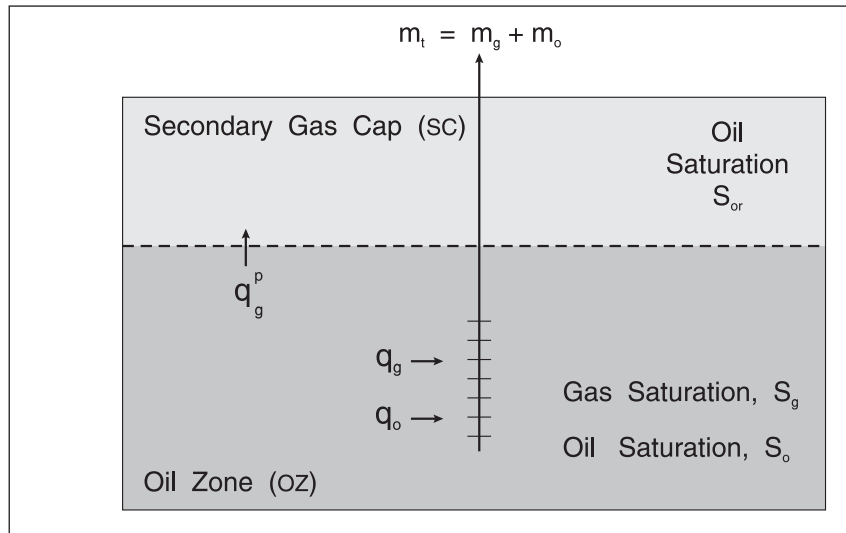


Fig. 5-25. Formation of a secondary gas cap

Referring to figure 5-26, the upward flow of gas is denoted  $q_g^p$ , and in a time interval  $dt$  the SC augments in size by an amount  $d\hat{V}^{SC}$ ; here, the cap symbol indicates a first estimate of the increase in pore volume of the SC. Initially, the region  $d\hat{V}^{SC}$  contains gas at composition  $y^{OZ}$  and saturation  $S_g^{OZ}$ , and at the end of the time step this region has become part of the SC with a residual oil saturation  $S_{or}$ , i.e., the gas saturation has increased to a value  $1 - S_{or} - S_{wc}$ . The change in gas saturation is therefore  $S_g^{OZ} - (1 - S_{or} - S_{wc})$  and a volume balance on the region  $d\hat{V}^{SC}$  gives

$$q_g^p dt = d\hat{V}^{SC} \left( S_g^{OZ} - (1 - S_{or} - S_{wc}) \right) \quad (5-67a)$$

i.e.,

$$\frac{d\hat{V}^{SC}}{dt} = \frac{q_g^p}{\left( S_g^{OZ} - (1 - S_{or} - S_{wc}) \right)} \quad (5-67b)$$

This volume balance, based on incompressible theory, gives an initial prediction of the rate of growth of the SC and the volume of additional liquid retained in the SC as a residual phase is  $d\hat{V}^{SC} S_{or}$ .



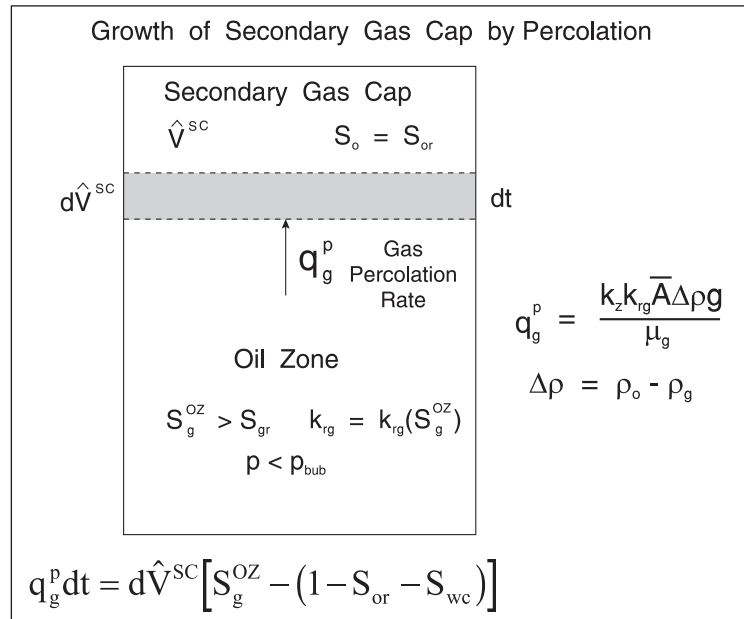


Fig. 5–26. Incremental growth of the secondary gas cap (SC)

A component material balance for the moles of component  $j$  contained in the SC takes the form

$$\frac{dN_j^{SC}}{dt} = \frac{q_g^p \rho_g^{OZ} y_j^{OZ}}{M_{wg}^{OZ}} + \frac{d\hat{V}^{SC}}{dt} \left( \frac{S_{or} x_j^{OZ} \rho_o^{OZ}}{M_{wo}^{OZ}} \right) \quad (5-68a)$$

The first term in the material balance expression is the input into the SC due to upward percolation where it is presumed that the entering gas composition is that of the OZ vapor phase. The second term is the trapping of liquid at the residual saturation  $S_{or}$  and having a composition of the OZ liquid phase. This is the theory of the “leaky” piston, which leaves some oil behind as the SC grows in size. Since the rate of SC growth, i.e.,  $d\hat{V}^{SC}/dt$ , is given by Eq.(5–67b), the rate of addition of moles of component  $j$  to the SC can be calculated on the basis of compositions at the old time level  $t$ ; thus, the composition is treated explicitly in this formulation, and Eq. (5–68a) can be written properly as

$$\frac{dN_j^{SC}}{dt} = \left( \frac{q_g^p \rho_g^{OZ} y_j^{OZ}}{M_{wg}^{OZ}} + \frac{d\hat{V}^{SC}}{dt} \left( \frac{S_{or} x_j^{OZ} \rho_o^{OZ}}{M_{wo}^{OZ}} \right) \right) \Bigg|_t \quad (5-68b)$$

The basis of Eq. (5–68b) is the condition that, at the end of the time step, the volume  $d\hat{V}^{SC}$  is filled with residual oil of composition  $x$  and gas of composition  $y$  and saturation  $(1 - S_{or} - S_{wc})$ . This is a mechanistic model of the evolution of the SC based on the presumption that the remaining liquid is at an irreducible saturation ( $S_{or}$ ); the compositions of the remaining gas and oil are held, for the moment, explicitly at the OZ compositions at the beginning of the time step. Thus, the quantities  $y$ ,  $x$ ,  $\rho_g$ ,  $\rho_o$ ,  $M_g$ , and  $M_o$  refer to the OZ and hence are superscripted “OZ”.

The overall component material balances for component  $j$  takes the form

$$\frac{dN_j}{dt} = - \left( \frac{m_g}{M_g} y_j + \frac{m_o}{M_o} x_j \right) \quad (5-69)$$

In integrated form the component material balance expressions are

$$N_j^{SC} \Big|_{t+dt} = N_j^{SC} \Big|_t + \left( \frac{q_g^p \rho_g^{OZ} y_j^{OZ}}{M_{wg}^{OZ}} + \frac{dV^{SC}}{dt} \left( \frac{S_{or} x_j^{OZ} \rho_o^{OZ}}{M_{wo}^{OZ}} \right) \right) \Big|_t \Delta t \quad (5-70)$$

$$N_j \Big|_{t+dt} = N_j \Big|_t - \left( \frac{m_g}{M_g} y_j + \frac{m_o}{M_o} x_j \right) \Big|_t \Delta t \quad (5-71)$$

Note that initially the moles of component  $j$  present if the SC is zero, i.e.,

$$N_j^{SC} \Big|_0 = 0 \quad (5-72)$$

The component material balances for the OZ follow as

$$N_j^{OZ} \Big|_{t+dt} = N_j \Big|_{t+dt} - N_j^{SC} \Big|_{t+dt} \quad (5-73)$$

The total moles present in the two regions are given by the summations

$$N^{OZ} = \sum_{j=1}^{NC} N_j^{OZ} \quad N^{SC} = \sum_{j=1}^{NC} N_j^{SC} \quad (5-74)$$

and the overall compositions follow as

$$z_j^{OZ} = \frac{N_j^{OZ}}{N^{OZ}} \quad z_j^{SC} = \frac{N_j^{SC}}{N^{SC}} \quad (5-75)$$

In this case, the material balance over the time step requires two flash calculations—one for the OZ and one for the SC. Since the total moles in each region can be established from the integrated form of the component balances, i.e.,  $N_j^{SC}|_{t+\Delta t}$ ,  $N_j|_{t+\Delta t}$ ,  $N_j^{OZ}|_{t+\Delta t}$  are obtained from Eqs. (5–70), (5–71), and (5–73), respectively.

The corresponding regional overall compositions  $z^{OZ}|_{t+\Delta t}$  and  $z^{SC}|_{t+\Delta t}$  then become known. An isothermal flash on the OZ will yield its specific volume, i.e.,  $v^{OZ}$ , and an isothermal flash on the SC will yield its specific volume, i.e.,  $v^{SC}$ , and the calculated total volume of the hydrocarbon mixture becomes

$$\tilde{V}_p = N^{OZ}v^{OZ} + N^{SC}v^{SC} \tag{5-76}$$

A pressure is sought that yields the sum of the two regional volumes equal to the actual hydrocarbon volume, i.e.,

$$f(p) = \tilde{V}_p - \tilde{V}_p^{spec} = 0 \tag{5-77}$$

where  $\tilde{V}_p^{spec}$  is the known (specified) hydrocarbon pore volume equal to  $V_p((1 - S_{wc}) - \Delta p(c_f + c_w S_{wc}))$ . This is the outer loop of an isochoric flash, which again can be solved by a one-dimensional quasi-Newton method. In the present situation, the inner loop comprises two (p, T) flash calculations, one for each region as depicted in figure 5–27. Note that the model of the SC allows for revaporization of the residual oil as the pressure falls since the total moles  $N^{SC}$  includes both phases. The progressive enlargement of the SC is driven by expansion of the gas already accumulated and addition of more gas by percolation.

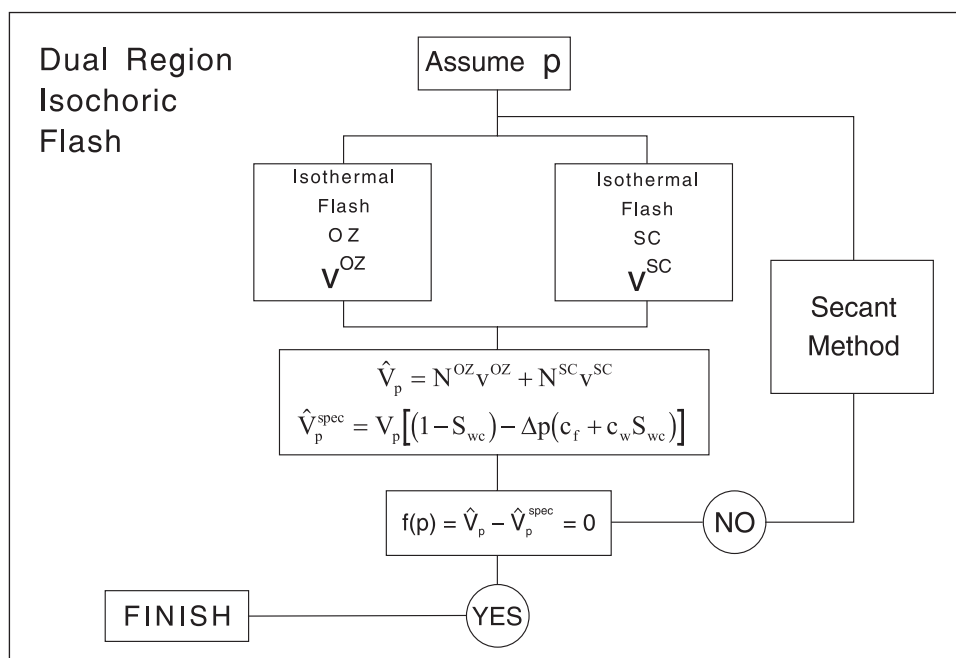


Fig. 5–27. Special isochoric flash for a two region problem

## Synthetic example

The example considered previously was run with percolation allowed to form a SC; the quantity  $k_z \bar{A}$  was set to the value  $1.0 \times 10^{-8} \text{ m}^4$ , and the simulation results are shown in figure 5–28. The formation of a SC is highly beneficial for oil recovery since gas is kept in the reservoir to provide pressure support. In this case, the producing GOR shows a momentary increase as the critical gas saturation is reached in the OZ, but then decreases as gas migrates upward to form the SC. The oil is produced at a much lower GOR than in the basic solution gas-drive case and oil production is terminated when the SC occupies the original OZ. This allows 124 months of production with 78.6% oil recovery efficiency for this high solution GOR crude. Although this degree of recovery cannot be achieved in practice due to gas coning or cusping, the present simulation shows how important gravity segregation of gas is to the recovery process. The formation of a SC is particularly important in a fractured reservoir where the degree of vertical communication is high leading to a large value of  $k_z$ . Supposing  $\bar{A}$  is  $10^5 \text{ m}^2$  (corresponding to  $h = 50 \text{ m}$ ), then  $k_z$  would have to be  $10^{-13} \text{ m}^2$ , i.e., 100 md, to yield the value of  $k_z \bar{A}$  quoted above.

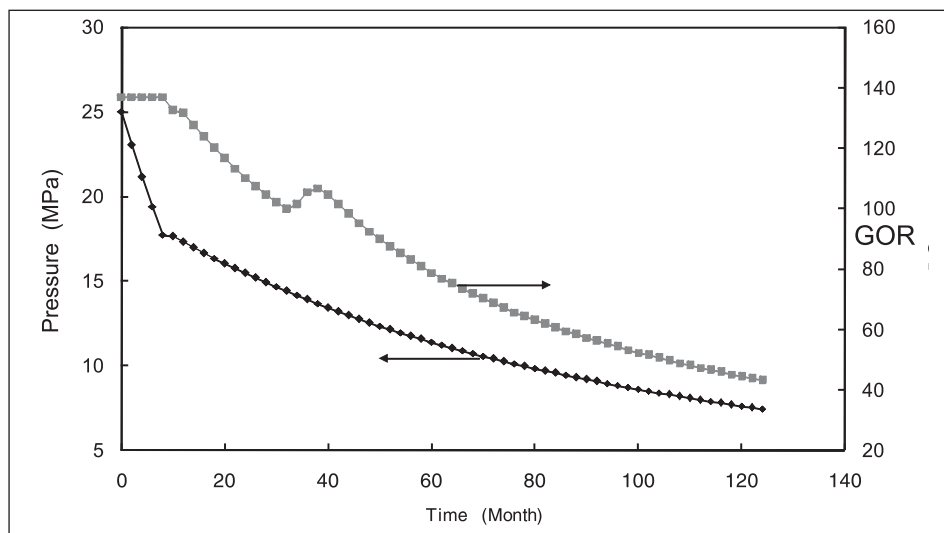


Fig. 5–28. Solution gas drive with gas percolation

## Inclusion of a primary gas cap

A saturated reservoir with a primary gas cap (PC) is shown in figure 5–29, where the initial pore volume of the gas cap is denoted  $V_p^{PC}$ ; the initial gas-phase hydrocarbon pore volume follows as  $\tilde{V}_p^{PC} = V_p^{PC}(1 - S_{wc})$ . The initial composition of the PC gas is denoted  $z^p$  and it is assumed that this gas is in thermodynamic equilibrium with the oil phase of initial composition  $z^c$ . The gas cap can accommodate an injection well in which gas can be introduced into the reservoir at a mass flow rate  $m_g^{inj}$  with the sign convention that the rate is negative for injection. The ratio of gas cap pore volume to oil column pore volume is denoted “m” in the black oil material balance formulation. As the reservoir pressure falls, the SC develops as a result of the downward expansion of the gas in the PC and upward percolation of gas from the two-phase OZ; this is illustrated in figure 5–30. The expansion of the PC causes an injection of gas into the SC region, which exhibits a residual oil saturation  $S_{or}$ .

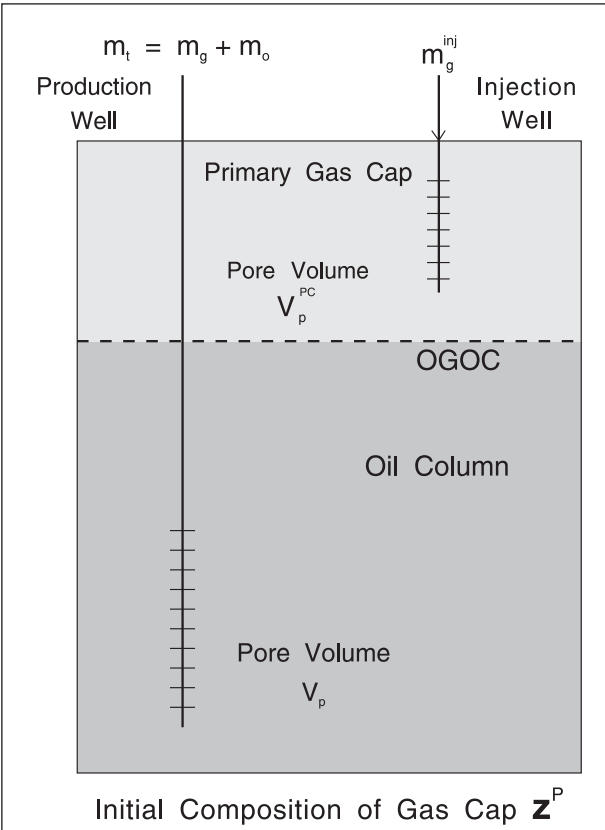


Fig. 5-29. Reservoir compartment with a primary gas cap

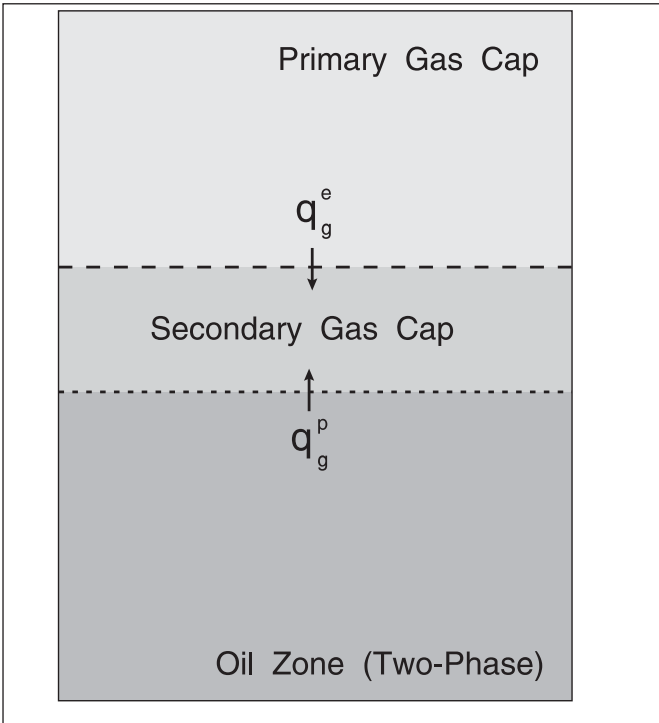


Fig. 5-30. Evolution of the secondary gas cap in the presence of a primary gas cap

In the formulation of models of gas cap drive, it is convenient to first consider the case where the primary gas cap expands with downward “piston” displacement of the contact as illustrated in figure 5–31. The hydrocarbon volume of the gas cap will be denoted  $\tilde{V}_p^{PC}$  and that of the OZ will be denoted  $\tilde{V}_p^{OZ}$ ; the sum of these two is the total reservoir HC pore volume, i.e.,

$$\tilde{V}_p = V_p \left( (1 - S_{wc}) - \Delta p (c_f + c_w S_{wc}) \right) = \tilde{V}_p^{PC} + \tilde{V}_p^{OZ} \quad (5-78)$$

where  $\Delta p = p_i - p$

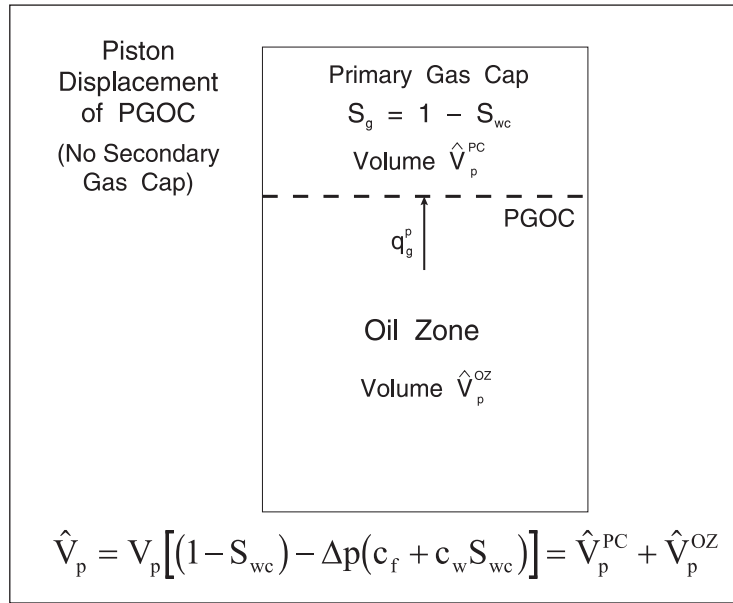


Fig. 5–31. Piston displacement of oil by gas cap expansion

Suppose now that gas is percolating upward at an in situ volumetric rate  $q_{gp}$  and the moles of component  $j$  in the primary (expanding) gas cap is denoted  $N_j^{PC}$ . The component material balances for the PC then take the form

$$\frac{dN_j^{PC}}{dt} = \frac{q_g^p \rho_g^{OZ} y_j^{OZ}}{M_{wg}^{OZ}} - \frac{m_g^{inj} y_j^{inj}}{M_{wg}^{inj}} \quad (5-79)$$

Here,  $y^{inj}$  is the specified composition of the injected gas and  $y^{OZ}$  is the current composition of the free gas in the OZ at equilibrium with the oil composition. Again,  $q_g^p$  is given by the approximation

$$q_g^p = \frac{k_z k_{rg} \bar{A} \Delta \rho g}{\mu_g} \quad (5-80)$$

where  $\Delta\rho = \rho_o^{OZ} - \rho_o^{PC}$  and  $k_{rg}$  is based on the current OZ gas saturation  $S_g^{OZ}$ . Gas will not migrate upwards until the critical gas saturation is exceeded in the OZ. Note that in the case of gas production from the gas cap (blowdown), the component material balance takes the alternative form

$$\frac{dN_j^{PC}}{dt} = \frac{q_g^p \rho_g^{OZ} y_j^{OZ}}{M_{wg}^{OZ}} - \frac{m_g^{inj} y_j^{PC}}{M_{wg}^{inj}} \quad (5-81)$$

i.e., produced gas has the composition of the PC. Over a time step  $\Delta t$ , Eq. (5-79) can be written as

$$N_j^{PC} \Big|_{t+\Delta t} = N_j^{PC} \Big|_t + \left( \frac{q_g^p \rho_g^{OZ} y_j^{OZ}}{M_{wg}^{OZ}} - \frac{m_g^{inj} y_j^{inj}}{M_{wg}^{inj}} \right) \Big|_t \Delta t \quad (5-82)$$

where a simple explicit (Euler) integration has been employed. For the OZ, the component material balances take the form

$$\frac{dN_j^{OZ}}{dt} = - \left( \frac{m_g y_j^{OZ}}{M_{wg}^{OZ}} + \frac{m_o x_j^{OZ}}{M_{wo}^{OZ}} + \frac{q_g^p \rho_g^{OZ} y_j^{OZ}}{M_{wg}^{OZ}} \right) \quad (5-83)$$

which in integrated form becomes

$$N_j^{OZ} \Big|_{t+\Delta t} = N_j^{OZ} \Big|_t - \left( \frac{m_g y_j^{OZ}}{M_{wg}^{OZ}} + \frac{m_o x_j^{OZ}}{M_{wo}^{OZ}} + \frac{q_g^p \rho_g^{OZ} y_j^{OZ}}{M_{wg}^{OZ}} \right) \Big|_t \Delta t \quad (5-84)$$

The mass in the OZ decreases as a consequence of well production and percolation into the gas cap. Given the moles of each component in the OZ and the PC at the end of the time step using the integrated material balance expressions (5-82) and (5-84), the problem is to find the pressure and PC HC pore volume at the new time level. Assuming the new pressure  $P|_{t+\Delta t}$ , the density of the gas in the PC  $\rho_g^{PC}$  is found from the single-phase EOS routine. The hydrocarbon volume of the PC is then given by

$$\tilde{V}_p^{PC} \Big|_{t+\Delta t} = \frac{N^{PC} M_{wg}^{PC}}{\rho_g^{PC}} \Big|_{t+\Delta t} \quad (5-85)$$

The two-phase mixture in the OZ of overall composition  $\mathbf{z}^{OZ}|_{t+\Delta t}$  is then flashed at the assumed pressure  $P|_{t+\Delta t}$ , yielding the mole fraction vapor  $\beta$ , the vapor and liquid compositions  $\mathbf{y}^{OZ}$  and  $\mathbf{x}^{OZ}$ , and the phase densities  $\rho_g^{OZ}$  and  $\rho_o^{OZ}$ , all at the new time level  $t + \Delta t$ . The specific molar volume follows as

$$v_m^{OZ} \Big|_{t+\Delta t} = \left( \frac{\beta M_{wg}^{OZ}}{\rho_g^{OZ}} + \frac{(1-\beta)M_{wo}^{OZ}}{\rho_o^{OZ}} \right) \Big|_{t+\Delta t} \quad (5-86)$$

and the hydrocarbon volume of the OZ at the new time level is given by

$$\tilde{V}_p^{OZ} \Big|_{t+\Delta t} = \left( N^{OZ} v_m^{OZ} \right) \Big|_{t+\Delta t} \quad (5-87)$$

The isochoric flash problem in this case involves finding the assumed pressure at the new time level  $p \Big|_{t+\Delta t}$  that satisfies the functional equation

$$f \left( p \Big|_{t+\Delta t} \right) = \left( V_p \left( (1 - S_{wc}) - \Delta p (c_f + c_w S_{wc}) \right) - \tilde{V}_p^{PC} - \tilde{V}_p^{OZ} \right) \Big|_{t+\Delta t} = 0 \quad (5-88)$$

Again, the one-dimensional secant method, in an outer loop, will solve this problem very effectively for the pressure at the new time level.

In figure 5–32, the performance of a reservoir with a PC is shown.

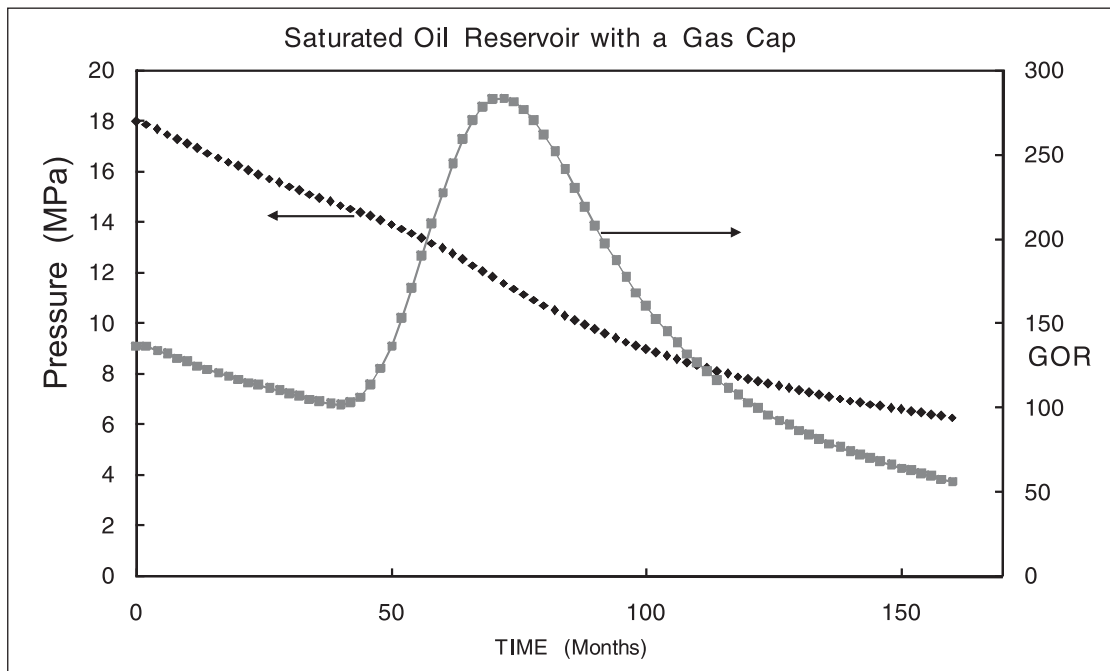


Fig. 5–32. Saturated reservoir with a primary gas cap (piston drive)



In practice, ideal piston displacement does not occur and, as the gas–oil contact moves down, a residual oil saturation is left in the SC. In figure 5–31, the PC is of fixed pore volume  $V_p^{PC}$  and due to expansion there is a flow of gas into the SC, which is denoted  $q_g^e$ . This flow can be modeled by the expression

$$q_g^e = c_g \tilde{V}_p^{PC} \frac{dp}{dt} \quad (5-89)$$

The rate of change of gas cap pressure may be approximated as

$$\frac{dp}{dt} = \frac{p|_t - p|_{t+\Delta t}}{\Delta t} \quad (5-90)$$

Hence, if the final pressure is assumed known, the support, i.e.,  $q_g^e$ , can be calculated from Eq. (5–89). The gas compressibility  $c_g$  is computed from the EOS using conditions at the beginning of the time step, i.e.,  $c_g|_t$ . The material balance expression for the PC (without gas injection) takes the form

$$\frac{dN_j^{PC}}{dt} = - \frac{q_g^e \rho_g^{PC} y_j^{PC}}{M_{wg}^{PC}} \quad (5-91a)$$

which in the integrated form becomes

$$N_j^{PC}|_{t+\Delta t} = N_j^{PC}|_t - \left. \frac{q_g^e \rho_g^{PC} y_j^{PC}}{M_{wg}^{PC}} \right|_t \Delta t \quad (5-91b)$$

The overall material balance equation for the total moles of component  $j$  is

$$\frac{dN_j}{dt} = - \left( \frac{m_g y_j^{OZ}}{M_{wg}^{OZ}} + \frac{m_o x_j^{OZ}}{M_{wo}^{OZ}} \right) \quad (5-92a)$$

or in integrated form

$$N_j|_{t+\Delta t} = N_j|_t - \left. \left( \frac{m_g y_j^{OZ}}{M_{wg}^{OZ}} + \frac{m_o x_j^{OZ}}{M_{wo}^{OZ}} \right) \right|_t \Delta t \quad (5-92b)$$

The rate of expansion of the SC is now given by

$$\frac{d\hat{V}^{SC}}{dt} = \frac{q_g^p + q_g^e}{\left(S_g^{OZ} - (1 - S_{or} - S_{wc})\right)} \quad (5-93)$$

The material balance on the SC can be written in the form

$$\frac{dN_j^{SC}}{dt} = \frac{q_g^e \rho_g^{PC} y_j^{PC}}{M_{wg}^{PC}} + \frac{q_g^p \rho_g^{OZ} y_j^{OZ}}{M_{wg}^{OZ}} + \frac{d\hat{V}^{SC}}{dt} \left( \frac{S_{or} \rho_o^{OZ} x_j^{OZ}}{M_{wo}^{OZ}} \right) \quad (5-94a)$$

$$\text{i.e.,} \quad N_j^{SC} \Big|_{t+\Delta t} = N_j^{SC} \Big|_t + \left( \frac{q_g^e \rho_g^{PC} y_j^{PC}}{M_{wg}^{PC}} + \frac{q_g^p \rho_g^{OZ} y_j^{OZ}}{M_{wg}^{OZ}} + \frac{d\hat{V}^{SC}}{dt} \left( \frac{S_{or} \rho_o^{OZ} x_j^{OZ}}{M_{wo}^{OZ}} \right) \right) \Big|_t \Delta t \quad (5-94b)$$

## Addition of a coning model

The phenomenon of gas coning is treated in detail in the following chapter and for the moment the coning process will be represented as a “short-circuit” allowing gas to flow directly from the gas cap to wells producing from the oil column; this idea is illustrated in figure 5–33. For the moment, it will simply be assumed that the total well mass flow rate  $m_t$  is given by

$$m_t = m_H + m_g^c \quad (5-95)$$

where  $m_g^c$  is the bypassing mass flow rate of gas direct from the gas cap and  $m_H$  is the mass flow of hydrocarbon from the OZ. If the gas saturation in the OZ is less than critical, then  $m_H = m_o$  and Eq. (5–95) becomes

$$m_t = m_o + m_g^c \quad (5-96)$$

The in situ volumetric flow rates of oil and gas are

$$q_o = \frac{m_o}{\rho_o} \quad q_g^c = \frac{m_g^c}{\rho_g} \quad (5-97)$$

and the in situ GOR may be written as

$$GOR_{is} = \frac{q_g^c}{q_o} \tag{5-98}$$

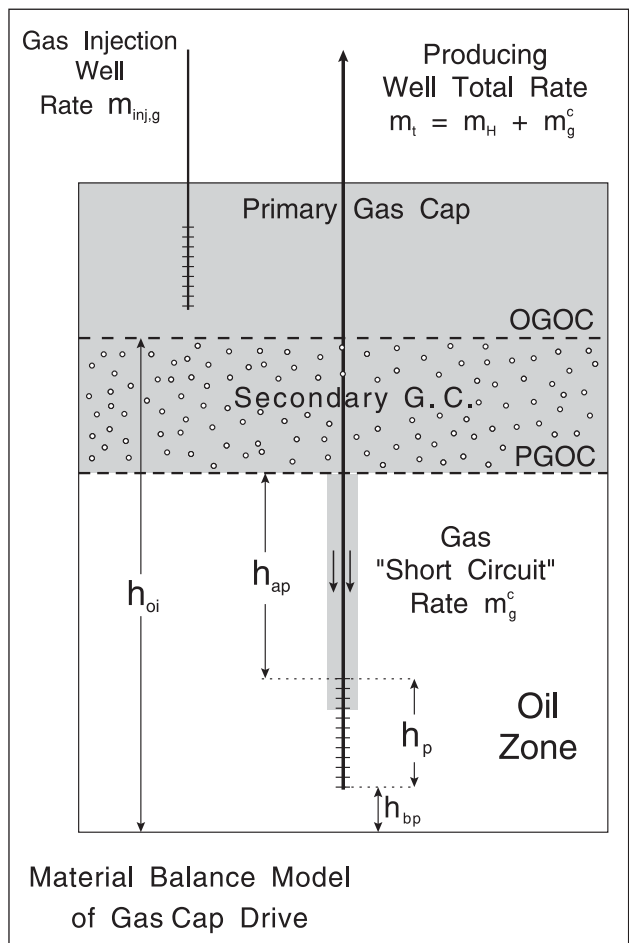


Fig. 5-33. Gas coning as a bypassing phenomenon

A coning model simply defines the  $GOR_{is}$  as a function of time as shown in figure 5-34, and for the moment it will be assumed that the function represented in figure 5-35 has been quantified and may be written symbolically as

$$GOR_{is} = f_C(t) \tag{5-99}$$

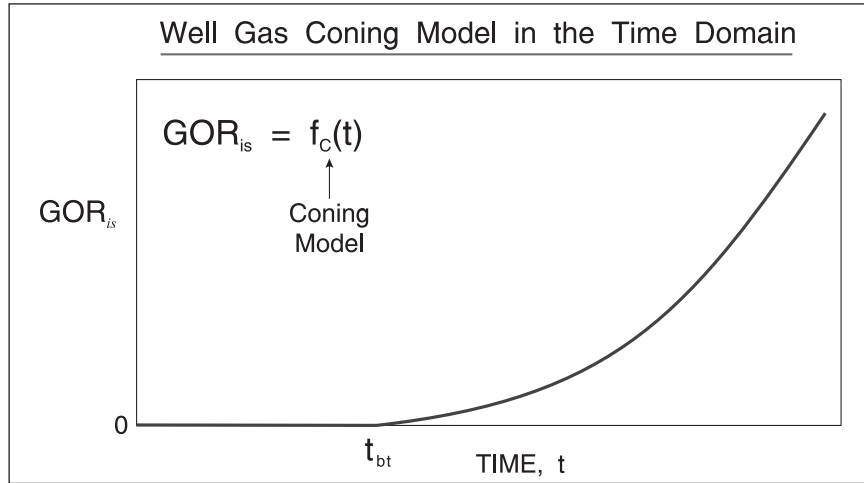


Fig. 5-34.  $GOR_{is}$  time dependence specified through a coning model

Note that up until time  $t_{bt}$ —the time to breakthrough—the in situ GOR is zero, after which it steadily increases. Quantitative forms for the coning function  $f_c(t)$  will be given in the succeeding chapter; the coning model developed by Addington<sup>9</sup> was specifically designed to run in conjunction with a material balance model of gas cap drive.

In the coning situation, the total mass flow  $m_t$  is specified and the in situ GOR is fixed by the coning model. The ratio of the mass flows constituting the OZ stream, designated  $r_m$ , is given by

$$\frac{m_g}{m_o} = \frac{\rho_g}{\rho_o} M = r_m \quad \text{where} \quad M = \frac{k_{rg}\mu_o}{k_{ro}\mu_g} \quad (5-100)$$

Thus, 
$$m^t = m_g^c + m_o + m_g = m_g^c + m_o(1 + r_m) \quad (5-101)$$

Similarly, the in situ GOR is given by

$$GOR_{is} = \frac{q_g^c}{q_o + q_g} = \frac{m_g^c}{\rho_g^{pc} m_o \left( \frac{1}{\rho_o} + \frac{r_m}{\rho_g} \right)} \quad (5-102)$$

Solving Eqs. (5-101) and (5-102) for  $m_g^c$  and  $m_o$  gives

$$m_g^c = \frac{GOR_{is} \rho_g^{pc} m_t \left( \frac{1}{\rho_o} + \frac{r_m}{\rho_g} \right)}{1 + r_m + GOR_{is} \rho_g^{pc} \left( \frac{1}{\rho_o} + \frac{r_m}{\rho_g} \right)} \quad (5-103a)$$

$$m_o = \frac{m_t - m_g^c}{1 + r_m} \quad \text{and} \quad m_g = m_o r_m \quad (5-103b)$$

This is the inflow model when coning is taking place; if the in situ GOR is zero, this reduces to

$$m_o = \frac{m_t}{1 + r_m} \quad \text{and} \quad m_g = m_o r_m \quad (5-104)$$

Note that the coning stream of rate, i.e.,  $m_g^c$ , has the composition of the PC, whereas streams of rate  $m_o$  and  $m_g$  have oil and gas compositions, respectively, of the OZ.

When coning is occurring, the growth of the SC is governed by the modified equation

$$\frac{d\hat{V}^{SC}}{dt} = \frac{q_g^p + q_g^e - q_g^c}{\left( S_g^{OZ} - (1 - S_{or} - S_{wc}) \right)} \quad (5-105)$$

The material balance on the SC is modified as follows:

$$\frac{dN_j^{SC}}{dt} = \frac{q_g^e \rho_g^{PC} y_j^{PC}}{M_{wg}^{PC}} + \frac{q_g^p \rho_g^{OZ} y_j^{OZ}}{M_{wg}^{OZ}} - \frac{q_g^c \rho_g^{SC} y_j^{SC}}{M_{wg}^{SC}} + \frac{d\hat{V}^{SC}}{dt} \left( \frac{S_{or} \rho_o^{OZ} x_j^{OZ}}{M_{wo}^{OZ}} \right) \quad (5-106a)$$

$$\text{i.e., } N_j^{SC} \Big|_{t+\Delta t} = N_j^{SC} \Big|_t + \left( \frac{q_g^e \rho_g^{PC} y_j^{PC}}{M_{wg}^{PC}} + \frac{q_g^p \rho_g^{OZ} y_j^{OZ}}{M_{wg}^{OZ}} - \frac{q_g^c \rho_g^{SC} y_j^{SC}}{M_{wg}^{SC}} + \frac{d\hat{V}^{SC}}{dt} \left( \frac{S_{or} x_j^{OZ}}{M_{wo}^{OZ}} \right) \right) \Big|_t \Delta t \quad (5-106b)$$

The overall material balance equation for the total moles of component  $j$  is

$$\frac{dN_j}{dt} = - \left( \frac{m_g y_j^{OZ}}{M_{wg}^{OZ}} + \frac{m_o x_j^{OZ}}{M_{wo}^{OZ}} + \frac{m_g^c y_j^{SC}}{M_{wg}^{SC}} \right) \quad (5-107a)$$

or in integrated form

$$N_j \Big|_{t+\Delta t} = N_j \Big|_t - \left( \frac{m_g y_j^{OZ}}{M_{wg}^{OZ}} + \frac{m_o x_j^{OZ}}{M_{wo}^{OZ}} + \frac{m_g^c y_j^{SC}}{M_{wg}^{SC}} \right) \Big|_t \Delta t \quad (5-107b)$$

## Nonlinear regression

The model matching option using nonlinear regression now has an extended list of tuning variables of the form

$$\mathbf{a} = (V_p, S_{gr}, k_z \bar{A})^T \quad (5-108a)$$

or

$$\mathbf{a} = (V_p, V_p^{PC}, S_{gr}, k_z \bar{A})^T \quad (5-108b)$$

$$S_{wc}, c_w, c_f, T, k_{ro}^o, m', S_{or}, k_{rg}^o, n' \quad \text{fixed}$$

In this case, the development of the producing GOR is very much controlled by the degree of vertical communication characterized by  $k_z \bar{A}$ , and again the objective function  $\chi^2$  will involve both pressure and GOR. The inclusion of percolation into the model gives a much greater flexibility in matching observed GOR development in solution gas-drive situations.

## Gas and Gas-condensate Reservoirs

### Depletion above the dew point

In the case of a gas reservoir whose initial condition lies to the right of the critical point, the first task is to determine the dew point pressure  $p_{dew}$ . Above the dew point, the well produces only an in situ gas phase with the initial reservoir fluid composition  $z^c$ , and the density  $\rho_g$  is predicted by the EOS solved for the fluid composition  $z^c$  and the pressure at the new time level  $p|_{t+\Delta t}$ . Thus, formally

$$\rho_g = f_{RG}(p|_{t+\Delta t}) \quad (5-109)$$

since the fluid composition and temperature are known; here, the function  $f_{RG}$  designates the gas-phase density calculated from the cubic EOS. The apparent gas density may be written as

$$\rho_{g,app} = \frac{N|_{t+\Delta t} M_o^i}{V_p (1 - S_{wc})} \quad (5-110)$$

and the pressure at the new time level must satisfy the equation

$$f_{GC}(p|_{t+\Delta t}) = \frac{\rho_g - \rho_{g,app}}{\rho_{g,app}} = 0 \quad (5-111)$$

This functional equation for the new pressure can readily be solved using the secant method. In this approach, the gas density is modeled by the cubic EOS taking the gas root for the evaluation of  $\rho_g$ . Note that the gas compressibility over a depletion step is given by

$$c_g = \frac{1}{\bar{\rho}} \frac{\Delta \rho}{\Delta p} \quad (5-112)$$

where  $\Delta \rho = \rho_g(p|_t) - \rho_g(p|_{t+\Delta t})$   $\Delta p = p|_t - p|_{t+\Delta t}$

and  $\bar{\rho} = \frac{\rho_g(p|_t) + \rho_g(p|_{t+\Delta t})}{2}$

## Retrograde condensation without gravity segregation

Once the pressure falls below the dew-point pressure, the system may be treated as a two-phase cell using the theory previously developed; thus, the solution gas-drive formulation can be carried over to the problem of retrograde condensation without changing the nomenclature. The “oil” phase is now the condensate and it is assumed initially that no gravity segregation occurs. The two-phase flash calculations are carried out in exactly the same fashion although the feed compositions will obviously be richer in light components. The well modeling will now allow for the liquid dropout effect in the near-wellbore region.

The performance of a gas-condensate reservoir (GCR) whose parameters are listed in table 5-6 is shown in figure 5-35; the field is produced at a constant mass flow rate of 1 kg/s. The composition of the initial reservoir fluid is given in table 5-7 and the conversion of this fluid to standard conditions (using the three stage separator parameters listed in table 5-6) is listed in table 5-8. Above the dew point, the pressure depletes in the single-phase gas region and a  $p/z$  plot will be a straight line. As the pressure falls below the dew point, condensate dropout occurs and the liquid saturation rises. However, the amount of retrograde liquid—controlled by the liquid dropout curve—is not sufficient to allow the liquid saturation to rise above the critical value of 0.2. The liquid saturation ( $S_o = 1 - S_{wc} - S_g$ ) soon reaches a maximum when vaporization starts to reduce it again. As the dew point is crossed, the pressure depletes less rapidly since the two-phase compressibility is greater than that of single-phase gas; this accounts for the flattening of the pressure graph. In figure 5-36, the producing CGR is plotted as a function of time and above the dew point it is constant at  $0.0005406 \text{ sm}^3/\text{sm}^3$ . As the reservoir pressure falls below the dew point, the producing CGR decreases quite rapidly and becomes zero after

4 years of production. This is a result of the small number of components in the compositional description and the absence altogether of a heavy “tail”. Thus, the producing stream after 4 years is single phase according to the stability criterion and the reservoir produces dry gas although a liquid phase is present in the reservoir. Note that the liquid saturation in the reservoir does not reach the critical value and only the resident vapor phase actually produces. The densities of the produced fluids (stock tank) are plotted in figure 5–37 where the effect of vaporization is shown by the increasing densities towards the end of the process.

**Table 5–6.** Synthetic reservoir parameters

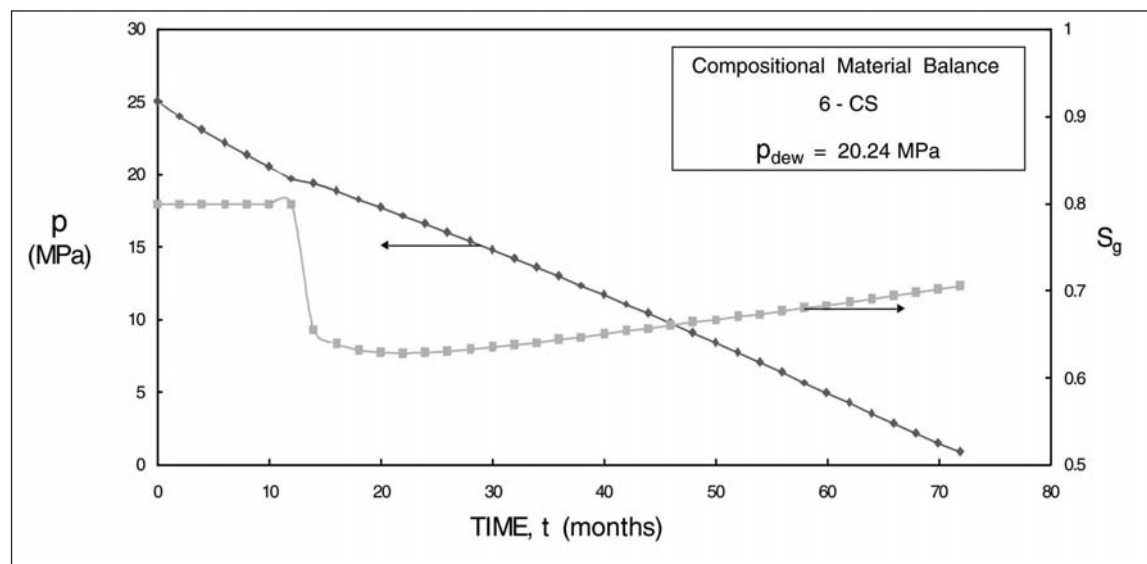
$p_i$ : 25 MPa	$T$ : 350 °K	$V_p$ : $10^6$ m <sup>3</sup>	$S_{wc}$ : 0.2	$c_w$ : $4.25 \times 10^{-10}$ Pa <sup>-1</sup>
$c_f$ : $8.7 \times 10^{-10}$ Pa <sup>-1</sup>	$p_1$ : 3 MPa	$T_1$ : 350 °K	$p_2$ : 1 MPa	$T_2$ : 310 °K
$p_s$ : $1.013 \times 10^5$ Pa	$T_s$ : 293.13 °K	$\rho_{gi}$ : 313.4 kg/m <sup>3</sup>	$z_{ci}$ : 0.8011	$M_{wi}$ : 29.22
$k_{ro}^o$ : 0.75	$m'$ : 1.7	$S_{or}$ : 0.2	Mass HC : $2.5077 \times 10^8$ kg	$P_{dew}$ : 20.239 MPa
$k_{rg}^o$ : 0.85	$n'$ : 2.4	$S_{gr}$ : 0.2		

**Table 5–7.** Composition of initial reservoir fluid (mole fraction)

$C_1$	$C_2$	$C_3$	$C_5$	$C_7$	$C_{10}$
0.71	0.10	0.06	0.06	0.05	0.02

**Table 5–8.** Conversion of reservoir fluid to standard conditions

Properties of separated gas phase at standard conditions			
Volume	$M_w$	Mass	Density, $\rho_{g,sc}$
$1.8947 \times 10^8$ m <sup>3</sup>	22.91	$1.8043 \times 10^8$ kg	0.9523 kg/m <sup>3</sup>
Properties of separated liquid phase at stock tank conditions			
Volume	Gravity	Mass	Density, $\rho_{1,st}$
102,428 m <sup>3</sup>		$0.70322 \times 10^8$ kg	686.7 kg/m <sup>3</sup>

**Fig. 5–35.** Performance of a gas condensate reservoir



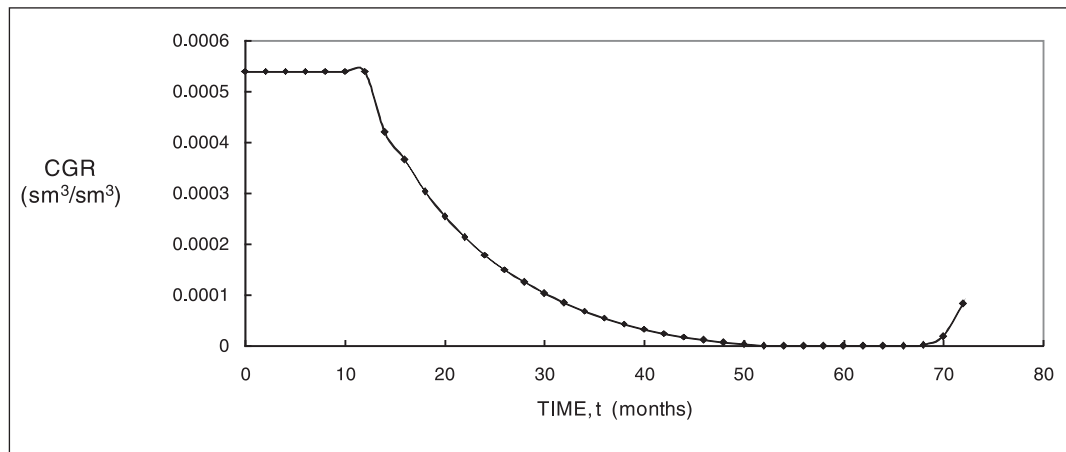


Fig. 5–36. CGR evolution of a gas condensate reservoir

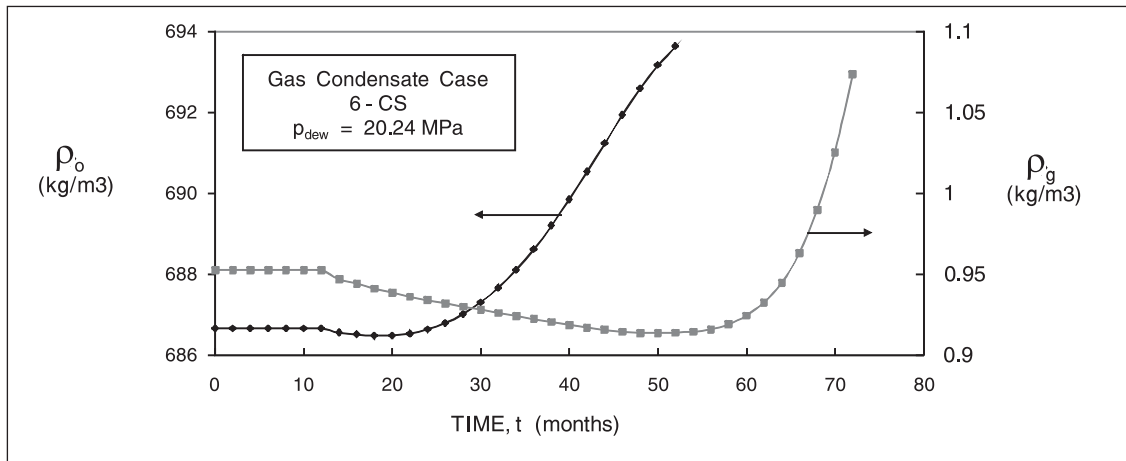


Fig. 5–37. Produced fluid densities

In planning the development of a retrograde gas condensate field, it is often required to be able to forecast the future rates of gas and liquid production. After the reservoir pressure falls below the dew point, the amount of condensate in the flowing well stream declines as a function of the decrease in pressure. This is illustrated in figure 5–38 which shows actual measured data on four U.S. reservoirs. The data have been converted to a common, dimensionless ratio basis comparing the current liquids production divided by the value at the dew-point against the ratio of the current reservoir pressure to the dew point pressure. Figure 5–39 is a similar plot for six Eocene Wilcox sand reservoirs in the Sheridan field, Colorado County, Texas. Inspection of these figures shows that most or the entire retrograde liquid decline in each of the reservoirs occurs during the period when the reservoir pressure is declining to 40%–50% of the dew point pressure. Thereafter, the liquid content remained relatively constant (or theoretically increasing slightly as revaporization occurs) until reservoir depletion was complete. Further field data from Nigeria due to Vrij are shown in figure 5–40 confirming these conclusions. Another empirical correlation for liquid recovery below the dew point has been presented by Garb<sup>10</sup> assuming that the liquid yield would decline according to a set of hyperbolic equations whose parameters were a function only of the liquid content at the dew point. Figure 5–41 shows Garb's prediction in

dimensionless form. In a review of the empirical methods, Miller pointed out that the Garb correlation appeared to be pessimistic, particularly at high CGR, with respect to actual field data such as that of Vrij.

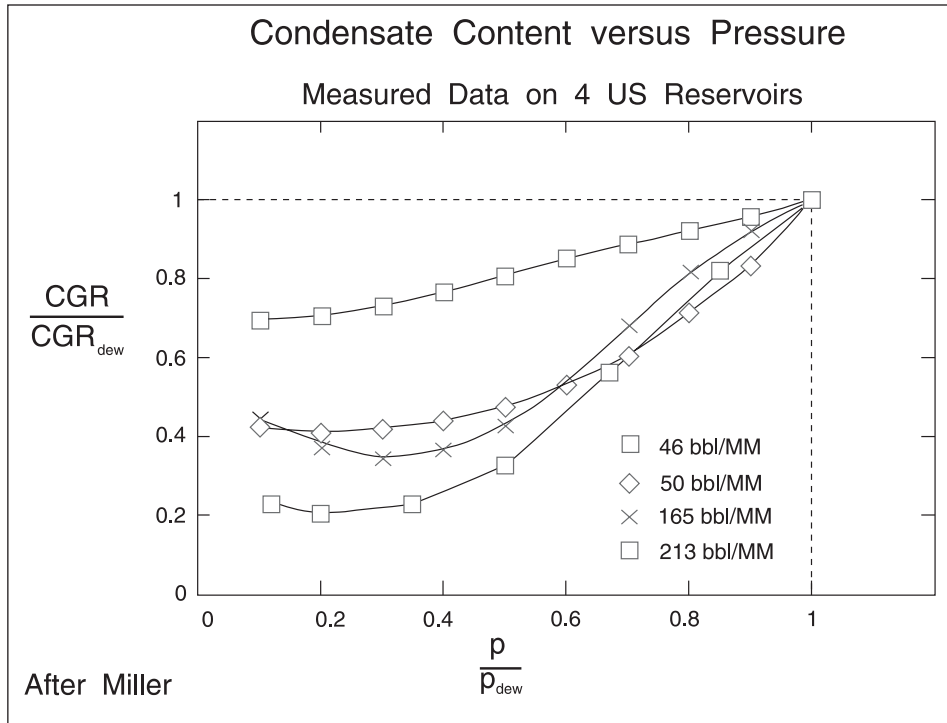


Fig. 5-38. Measured CGR data on four U.S. reservoirs

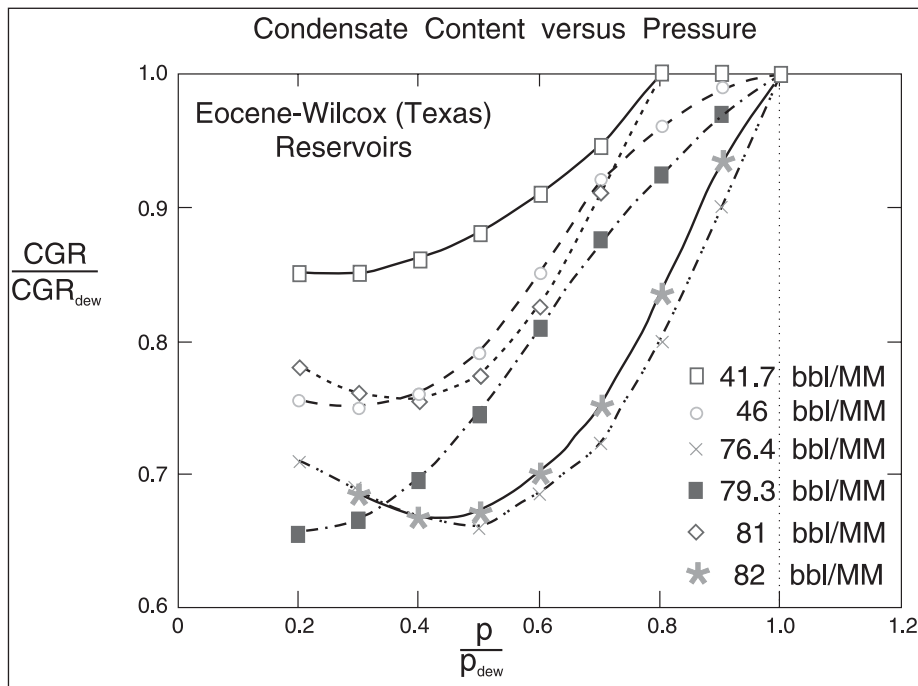


Fig. 5-39. Measured CGR data on six Eocene reservoirs

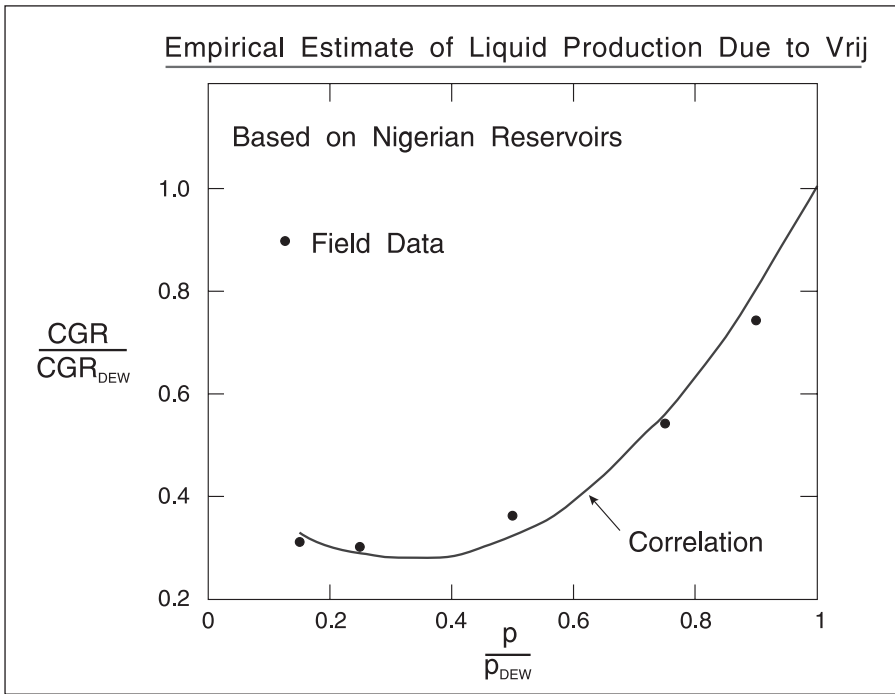


Fig. 5-40. Measured CGR data from Nigeria

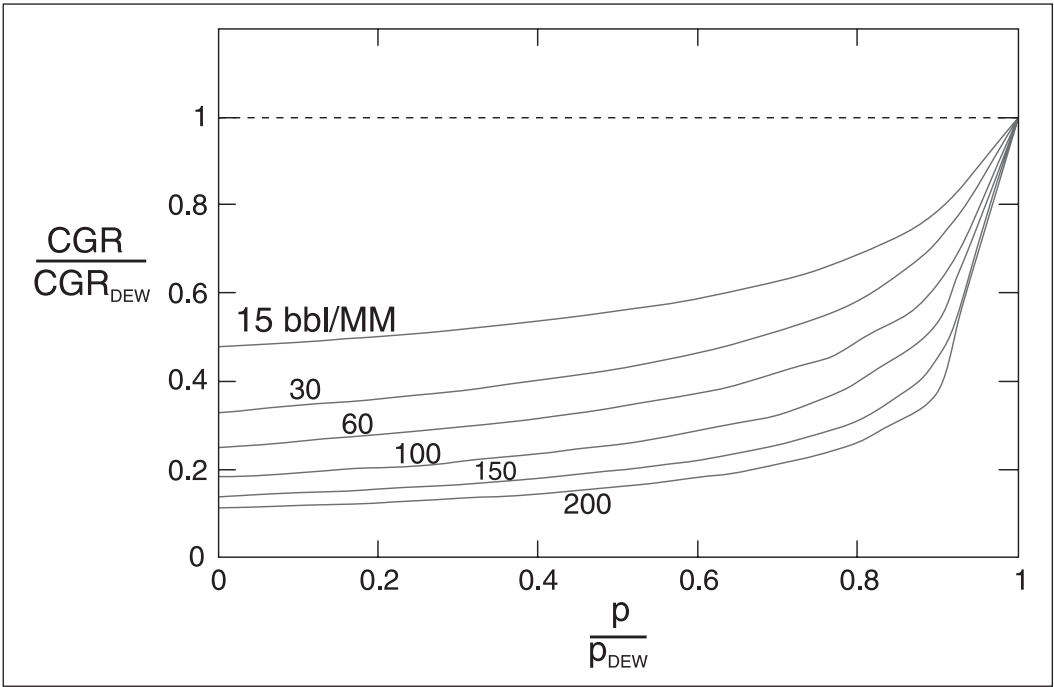


Fig. 5-41. Garb empirical correlation for liquid yield

The synthetic example on which figures 5–36 to 5–38 are based used Corey relative permeability curves with the parameter values listed in table 5–6. It is evident, on comparison with the field data shown in figures 5–38 to 5–41, that the material balance model with basic rock curves does not predict the evolution of the producing CGR in actual fields. The CGR, in practice, does not fall to essentially zero as depicted in figure 5–36; this is due to a more complex, overall reservoir flow process. The situation is analogous to the one in solution gas drive where the relative permeability curves that are required can be classified as pseudo curves representing the reservoir overall production response. It is necessary to tune the pseudo-relative-permeability curves to production data gathered after the pressure has fallen below the dew-point.

## Gravity segregation of condensate

In the case of a gas condensate field, there is a tendency for the liquid phase to form a secondary oil rim at the base of the cell; this gravity drainage is the inverse process to that of percolation treated previously and is illustrated in figure 5–42. The gravity drainage rate depends on the density difference between gas and condensate and is given by

$$q_o^d = \frac{k_z k_{ro} \bar{A} \Delta \rho g}{\mu_o} \quad (5-113)$$

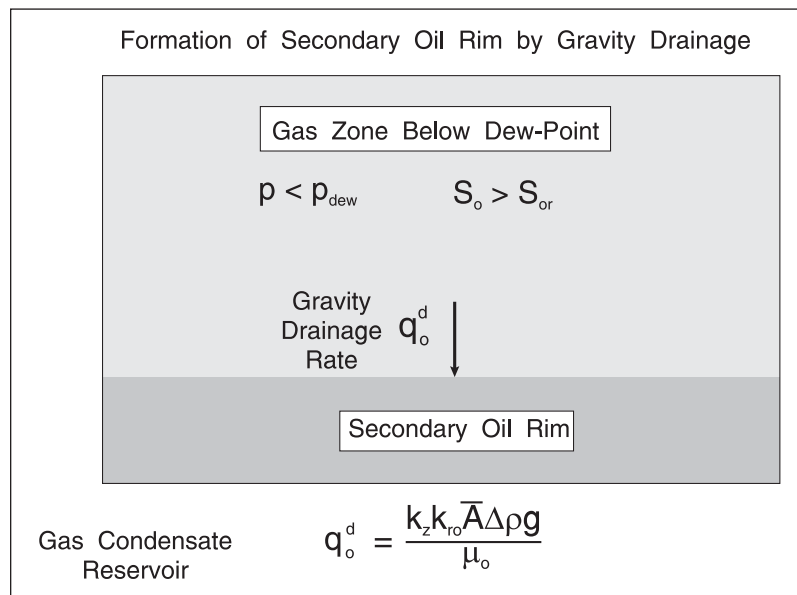


Fig. 5–42. Gravity drainage of condensate and the formation of a secondary oil rim

The growth of the secondary oil rim that contains only liquid phases, i.e., condensate and connate water, is governed by the volume balance

$$\frac{d \hat{V}_p^{SR}}{dt} = \frac{q_o^d}{1 - S_{wc}^{corr}} \quad (5-114)$$

The component material balance for the secondary oil rim, designated "SR", is given by

$$\frac{dN_j^{SR}}{dt} = \frac{Q_o^d \rho_o^{RG} X_j^{RG}}{M_{wo}^{RG}} \quad (5-115)$$

or in integrated form

$$N_j^{SR} \Big|_{t+dt} = N_j^{SR} \Big|_t + \left( \frac{Q_o^d \rho_o^{RG} X_j^{RG}}{M_{wo}^{RG}} \right) \Big|_t dt$$

The density of this liquid phase will depend on its composition and is designated  $\rho_o^{SR}$ , and the hydrocarbon pore volume occupied by the secondary oil rim becomes

$$\tilde{V}_p^{SR} = \frac{N^{SR} M_{wo}^{SR}}{\rho_o^{SR}} \quad (5-116)$$

Hence, the total pore volume of the secondary rim is given by

$$V_p^{SR} = \frac{\tilde{V}_p^{SR}}{1 - S_{wc}^{corr}} \quad (5-117)$$

The isochoric flash problem posed by the two-region case takes the form

$$f(p|_{t+\Delta t}) = \left( V_p \left( (1 - S_{wc}) - \Delta p (c_f + c_w S_{wc}) \right) - \tilde{V}_p^{RG} - \tilde{V}_p^{SR} \right) \Big|_{t+\Delta t} = 0 \quad (5-118)$$

The secant method may be used to find the pressure at the new time level which satisfies this equation.

## Dry gas injection (recycling)

The injection of dry gas into a gas condensate reservoir is known as recycling and in this situation a lean gas zone (GZ) develops as illustrated in figure 5-43. In a one-dimensional material balance model, it is assumed that the injected dry gas displaces rich gas in a piston fashion along streamlines and breakthrough of injected gas to the producing wells is modeled by the bypass flow rate  $m_g^b$ ; the theory of the miscible displacement is given in chapter 6. Dry gas is injected at a rate  $m_g^{inj}$ , and the composition of this injected gas is denoted  $y^{inj}$ . The injected gas displaces rich gas, but any liquid saturation present in the rich GZ is transferred to the lean

GZ as the interface moves downward. This liquid will then partially revaporize as it contacts the lean gas; this is an important part of the eventual recovery process in the blowdown phase.

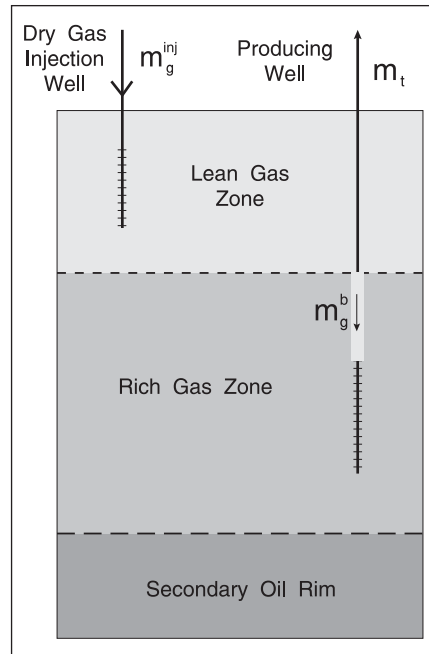


Fig. 5-43. Dry gas injection into a gas condensate reservoir (recycling)

Consider first the period when the reservoir is above the dew point and assume piston displacement of reservoir gas by injected dry gas depicted in figure 5-44. A component material balance on the lean GZ takes the form

$$\frac{dN_j^{LG}}{dt} = \frac{m_g^{inj} y_j^{inj}}{M_{wg}^{inj}} \quad (5-119a)$$

or, in integrated form

$$N_j^{LG} \Big|_{t+dt} = N_j^{LG} \Big|_t + \left( \frac{m_g^{inj} y_j^{inj}}{M_{wg}^{inj}} \right) \Big|_t dt \quad (5-119b)$$

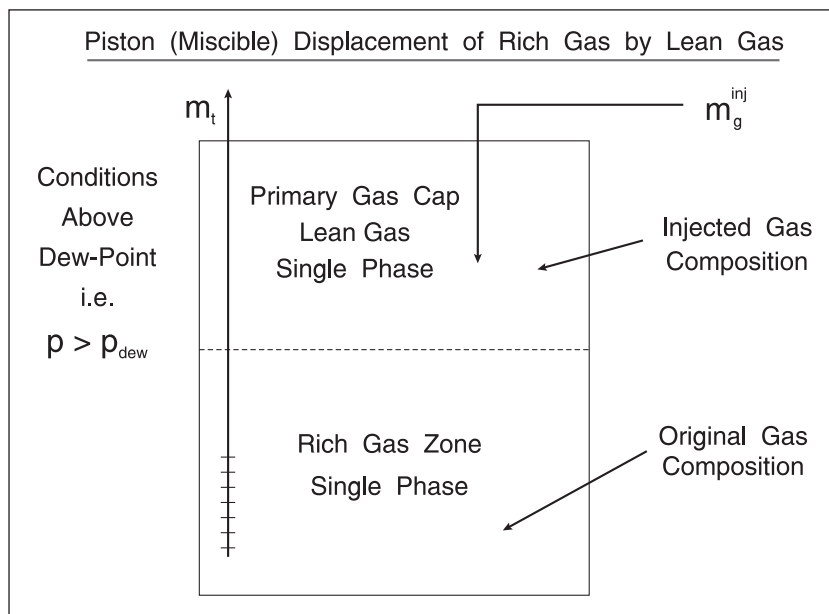


Fig. 5-44. Formation of a primary gas cap above the dew point pressure

Similarly, for the rich GZ the component balances may be written as

$$\frac{dN_j^{RG}}{dt} = - \frac{m_t z_j}{M_w} \tag{5-120a}$$

$$N_j^{RG} \Big|_{t+dt} = N_j^{RG} \Big|_t - \left( \frac{m_t z_j^c}{M_w} \right) \Big|_t dt \tag{5-120b}$$

Here,  $z^c$  is the composition of the original reservoir fluid and  $M_w$  is its molecular weight; above the dew point, the well is producing single-phase fluid from the rich gas region at a mass flow rate  $m_t$ . The volume occupied by the two regions is given by

$$\tilde{V}_p = V_p \left( (1 - S_{wc}) - \Delta p (c_f + c_w S_{wc}) \right) = \tilde{V}_p^{LG} + \tilde{V}_p^{RG} \tag{5-121}$$

A pressure at the new time level, i.e.,  $p|_{t+dt}$ , is sought which satisfies the condition

$$\left( V_p \left( (1 - S_{wc}) - \Delta p (c_f + c_w S_{wc}) \right) = \tilde{V}_p^{LG} + \tilde{V}_p^{RG} \right) \Big|_{t+dt} = 0 \tag{5-122}$$

where  $\Delta p = p_i - p|_{t+dt}$

$$\tilde{V}_p^{RG} \Big|_{t+dt} = \frac{N^{RG} M_{wg}^{RG}}{\rho_g^{RG}} \Big|_{t+\Delta t} \quad M_{wg}^{RG} = M_w$$

$$\tilde{V}_p^{LG} \Big|_{t+dt} = \frac{N^{LG} M_{wg}^{LG}}{\rho_g^{LG}} \Big|_{t+\Delta t} \quad M_{wg}^{LG} = M_{wg}^{inj}$$

The densities of the two gases (lean and rich), viz.,  $\rho_g^{RG}$  and  $\rho_g^{LG}$ , are found from the EOS using the appropriate molecular weight and the pressure at the new time level  $p|_{t+dt}$ . In this version of the gas isochoric flash, two regions with different molecular weights have been accounted for. The volume fraction of the lean gas region, denoted  $\chi$ , is given by

$$\chi = \frac{\tilde{V}_p^{LG}}{\tilde{V}_p} \quad (5-123)$$

When the pressure falls below the dew point of the rich gas region, more complicated calculations, described in the succeeding paragraphs, have to be carried out. At the moment the dew point is crossed, the situation is depicted in figure 5–45, where the injection of lean gas—perfectly displacing rich gas—has created a PC. The rich gas region has now become two phase and it is convenient to describe it as an OZ. As the pressure is reduced further and more dry gas injected, the lean gas region continues to grow. That part of it which contacts retrograde liquid and where vaporization will occur can be designated as an SC. The theory developed for solution gas-drive carries over with some modification including the simplification that upward percolation of gas does not occur.

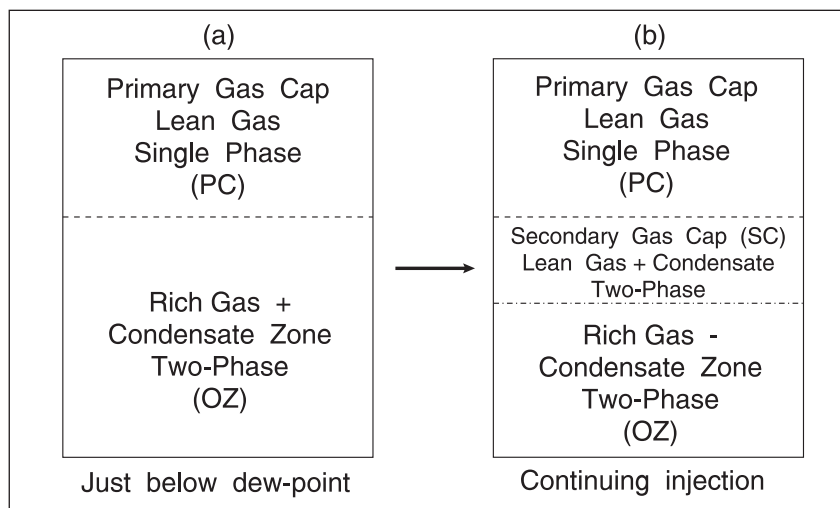


Fig. 5–45. Development of two-phase region



In the following analysis, the treatment of an OZ, an SC, and a PC will be modified to describe the behavior of a gas recycling project. The PC has been created during the period when the pressure is above the dew point of the single-phase rich gas region. Therefore, the original hydrocarbon pore volume is partitioned into the PC of HC pore volume  $\tilde{V}_p^{PC}$  and the HC pore volume of the SC and OZ zones  $\tilde{V}_p^{PC+OZ}$  which will be contracted to  $\tilde{V}_p'$ . If the volume fraction of the lean gas region when the pressure reaches the dew point is denoted  $\chi_D$ , then

$$\tilde{V}_p^{PC} = \chi_D \tilde{V}_p \quad \tilde{V}_p' = (1 - \chi_D) \tilde{V}_p \quad \tilde{V}_p = \tilde{V}_p^{PC} + \tilde{V}_p' \quad (5-124)$$

Both the vaporizing zone (SC) and the rich GZ (OZ) may have a liquid (condensate) saturation and both will have a water saturation denoted  $S_{wc}^{corr}$  where

$$S_{wc}^{corr} = S_{wc} \frac{(1 + c_w \Delta p)}{(1 - c_f \Delta p)} \quad (5-125)$$

The continuing injection of dry gas drives the further expansion of the lean gas region and it will be assumed that in the secondary cap region any retrograde liquid will not be displaced by the dry gas. However, this liquid will vaporize to some extent. The flow of gas into the SC will be denoted  $q_g^e$  as before and this is given by the expression

$$q_g^e = q_g^{inj} - c_g \tilde{V}_p^{PC} \frac{dp}{dt} \quad (5-126)$$

where

$$\frac{dp}{dt} = \frac{P|_{t+\Delta t} - P|_t}{\Delta t} \quad \text{and} \quad q_g^{inj} = \frac{m_g^{inj}}{\rho_g^{inj}}$$

The material balance for the primary gas cap takes the form

$$\frac{dN_j^{PC}}{dt} = \frac{m_g^{inj} y_j^{inj}}{M_{wg}^{inj}} - \frac{q_g^e \rho_g^{PC} y_j^{PC}}{M_{wg}^{PC}} \quad (5-127)$$

where a positive sign convention for injection has been adopted. The overall material balance for the total moles of component j is

$$\frac{dN_j}{dt} = - \left( \frac{m_g y_j^{OZ}}{M_{wg}^{OZ}} + \frac{m_o x_j^{OZ}}{M_{wo}^{OZ}} \right) + \frac{m_g^{inj} y_j^{inj}}{M_{wg}^{inj}} \quad (5-128)$$

The rate of expansion of the SC, illustrated in figure 5–46, is now given by

$$\frac{d\tilde{V}^{SC}}{dt} = \frac{q_g^e}{1 - S_o^{OZ} - S_{wc}^{corr}} \quad (5-129)$$

where  $S_o^{OZ}$  is the condensate (oil) saturation in the OZ; this assumes that rich gas is simply replaced by lean gas on an in situ volumetric basis, with the condensate that has dropped out remaining unchanged. The material balance on the SC can now be written as

$$\frac{dN_j^{SC}}{dt} = \frac{q_g^e \rho_g^{PC} y_j^{PC}}{M_{wg}^{PC}} + \frac{d\hat{V}_p^{SC}}{dt} \left( \frac{S_o^{OZ} \rho_o^{OZ} x_j^{OZ}}{M_{wo}^{OZ}} \right) \quad (5-130)$$

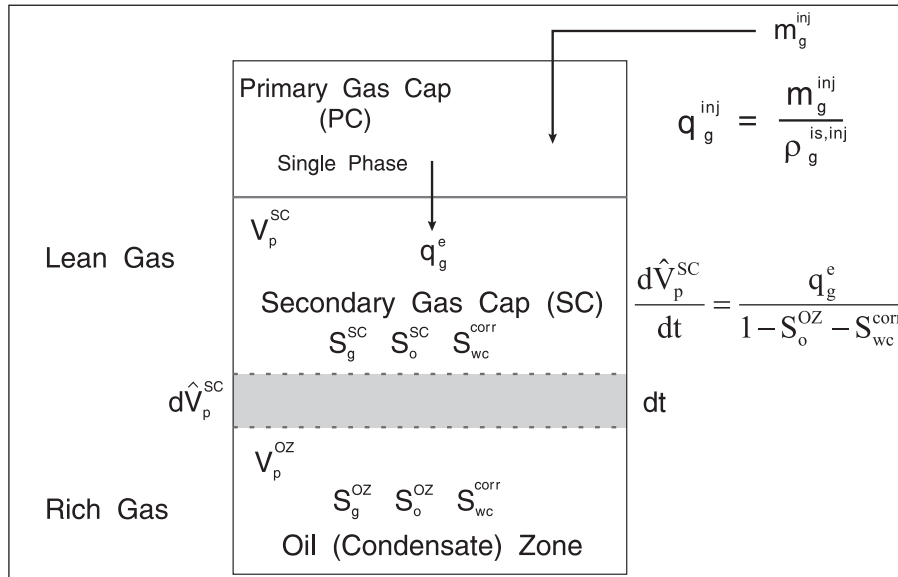


Fig. 5–46. Growth of the secondary (lean) gas cap

The material balance for the oil (condensate) zone follows by difference, i.e.,

$$\frac{dN_j^{OZ}}{dt} = \frac{dN_j}{dt} - \frac{dN_j^{PC}}{dt} - \frac{dN_j^{SC}}{dt} \quad (5-131)$$

The isochoric flash problem in this three-region situation can now be written as

$$f(p|_{t+\Delta t}) = \left( V_p \left( (1 - S_{wc}) - \Delta p (c_f + c_w S_{wc}) \right) - \tilde{V}_p^{PC} - \tilde{V}_p^{OZ} - \tilde{V}_p^{SC} \right) \Big|_{t+\Delta t} = 0 \quad (5-132)$$

where the HC volumes of the respective regions are given by

$$\tilde{V}_P^{PC} \Big|_{t+\Delta t} = \frac{N^{PC} M_{wg}^{PC}}{\rho_g^{PC}} \Big|_{t+\Delta t} \quad (5-133a)$$

$$\tilde{V}_P^{OZ} \Big|_{t+\Delta t} = \left( N^{OZ} v_m^{OZ} \right) \Big|_{t+\Delta t} = \left( N^{OZ} \left( \frac{\beta^{OZ} M_{wg}^{OZ}}{\rho_g^{OZ}} + \frac{(1 - \beta^{OZ}) M_{wo}^{OZ}}{\rho_o^{OZ}} \right) \right) \Big|_{t+\Delta t} \quad (5-133b)$$

$$\tilde{V}_P^{SC} \Big|_{t+\Delta t} = \left( N^{SC} v_m^{SC} \right) \Big|_{t+\Delta t} = \left( N^{SC} \left( \frac{\beta^{SC} M_{wg}^{SC}}{\rho_g^{SC}} + \frac{(1 - \beta^{SC}) M_{wo}^{SC}}{\rho_o^{SC}} \right) \right) \Big|_{t+\Delta t} \quad (5-133c)$$

Two flash calculations are required to equilibrate the mixtures in the OZ and the SC, and one EOS call to evaluate the density of the gas in the PC.

The gas condensate reservoir used to demonstrate the behavior of depletion drive was also used to illustrate the effect of dry gas reinjection. In this case, pure methane was injected at a rate of 0.2 kg/s with the production rate maintained at 1.0 kg/s; the reservoir parameters for the synthetic example are again shown in table 5–8. The reservoir performance is shown in figure 5–47 where the pressure is seen to fall much less rapidly than in the depletion case. Accordingly, it takes longer to reach the dew point and the CGR—shown in figure 5–48—remains at the value corresponding to the initial reservoir fluid longer. Note that this simulation was also carried out with “rock” relative permeability curves and the prediction of producing CGR below the dew point is pessimistic.

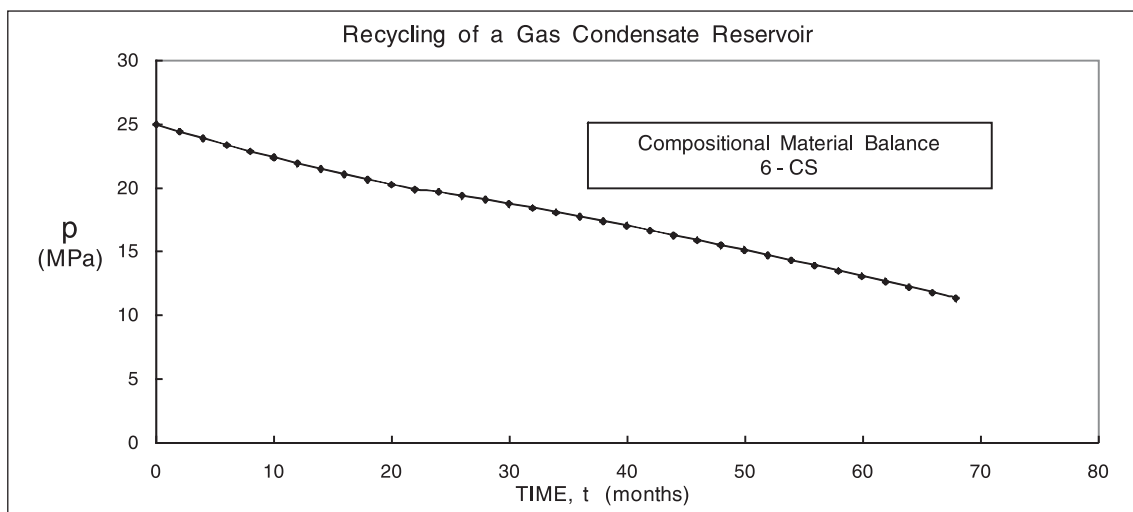


Fig. 5–47. Reservoir performance under dry gas reinjection

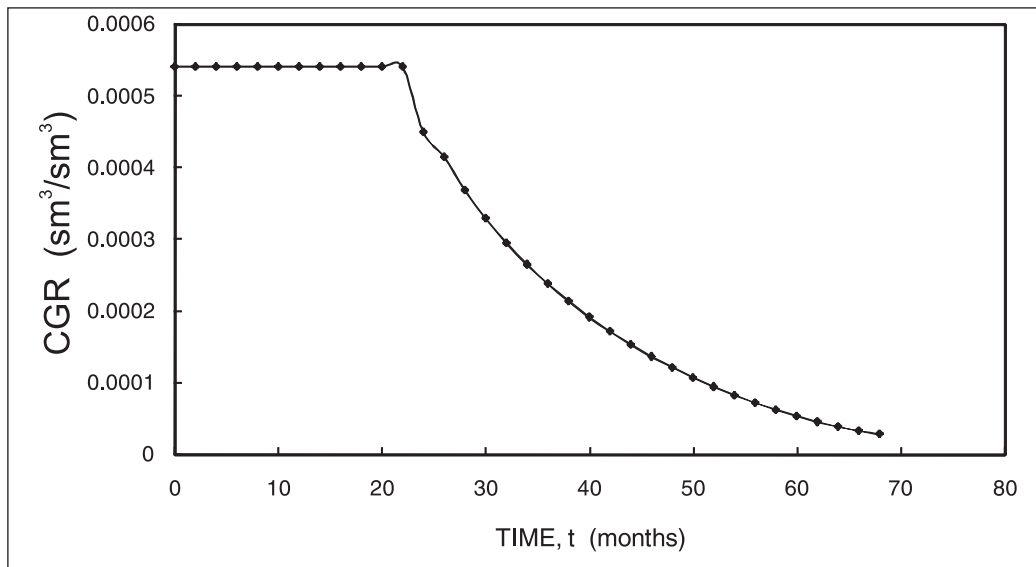


Fig. 5-48. Evolution of CGR in recycling

## Gas Recycling with a Displacement Model

In the preceding treatment, the development of the dry gas region is modeled as a piston displacement process. However, it is also possible to implement the areal displacement model, described in the next chapter, in the context of recycling. Indeed, the Banks model was based on miscible displacement along a stream tube and hence it is eminently applicable to the problem of dry gas breakthrough at the producing well. In figure 5-49 the effect of areal sweep is depicted as a direct bypassing flow from the lean gas region to the producing well. The flow rate of lean gas is denoted  $m_{gc}$ , while the flow of rich gas is labeled  $m_g$ . The composition of these two streams is different and the resultant combined stream will have an intermediate composition. The fractional flow of lean gas is denoted  $f_{LG}$ , where

$$f_{LG} = \frac{q_{gc}}{q_{gc} + q_g} = \frac{\frac{m_{gc}}{\rho_{gc}}}{\frac{m_{gc}}{\rho_{gc}} + \frac{m_g}{\rho_g}} \quad (5-134)$$

and

$$m_t = m_{gc} + m_g \quad (5-135)$$

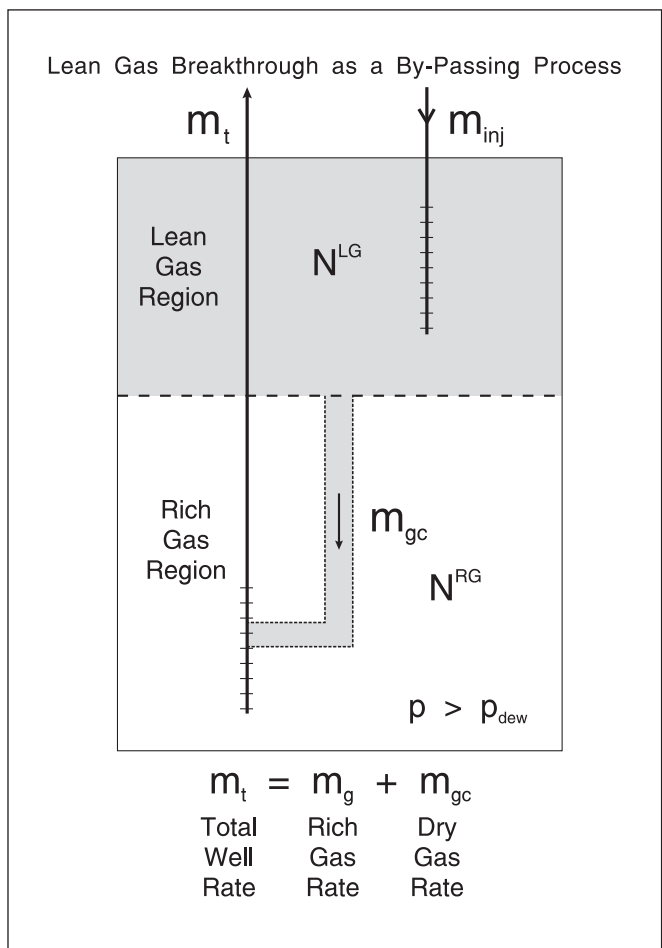


Fig. 5-49. The effect of areal displacement viewed as a bypassing process

This system of equations can be solved, for a specified  $m_t$  and  $f_{LG}$ , as follows:

$$q_g = \frac{m_t}{\frac{f_{LG}}{1 - f_{LG}} \rho_{gc} + \rho_g} \tag{5-136}$$

$$q_{gc} = \frac{f_{LG}}{1 - f_{LG}} q_g \tag{5-137a}$$

$$m_{gc} = q_{gc} \rho_{gc} \tag{5-137b}$$

$$m_g = m_t + m_{gc} \tag{5-137c}$$

The fractional flow of lean (injected) gas is obtained from the Banks correlation, i.e.,

$$f_{LG} = f_{LG} \left\{ \alpha, \frac{V_{inj}}{V_p} \right\} \quad (5-138)$$

Here,  $V_{inj}$  is the cumulative volume of injected gas at reservoir conditions, i.e., current pressure, and  $\alpha$  is the shape factor entering the Banks correlation. The component material balance equations for the two regions—lean gas and rich gas—take the form

$$\frac{dN_j^{RG}}{dt} = - \frac{m_g z_j^{RG}}{M_w^{RG}} \quad (5-139a)$$

$$\frac{dN_j^{LG}}{dt} = \frac{m_{inj} z_j^{inj}}{M_w^{inj}} - \frac{m_{gc} z_j^{LG}}{M_w^{LG}} \quad (5-139b)$$

and the isochoric flash matches the hydrocarbon volume to the HC pore space, i.e.,

$$\hat{V}_p = \frac{N^{LG} M_w^{LG}}{\rho_{LG}} + \frac{N^{RG} M_w^{RG}}{\rho_{RG}} \quad (5-140)$$

where

$$\hat{V}_p = V_p \left\{ (1 - S_{wc}) - \Delta p (c_f + S_{wc} c_w) \right\}$$

$$\Delta p = p_i - p$$

$$N^{LG} = \sum_{j=1}^{NC} N_j^{LG}$$

and

$$N^{RG} = \sum_{j=1}^{NC} N_j^{RG}$$

Equation (5–140) may be written in integrated form as

$$f(p|_{t+\Delta t}) = \left( V_p \left( (1 - S_{wc}) - \Delta p (c_f + c_w S_{wc}) \right) - \tilde{V}_p^{RG} - \tilde{V}_p^{LG} \right) \Big|_{t+\Delta t} = 0 \quad (5-141)$$

where

$$\tilde{V}_p^{RG} = \frac{N^{RG} M_w^{RG}}{\rho_{RG}} \quad \rho_{RG} = \rho_{RG} \left\{ z^{RG}, p \right\}$$

and

$$\tilde{V}_p^{LG} = \frac{N^{LG} M_w^{LG}}{\rho_{LG}} \quad \rho_{LG} = \rho_{LG} \left\{ z^{LG}, p \right\}$$

A synthetic example has been run where the injection rate of lean gas (taken to be pure methane for simplicity) was sufficient to maintain the reservoir pressure above the dew point. This is termed *full gas recycling* and make-up gas is required to achieve the balanced injection rate. Initially, the producing fluid is the original rich gas and the CGR is constant until injection gas breakthrough occurs. The value of  $\alpha$  in the Banks model was set at 1.494 and hence dry gas breakthrough occurs when 0.7 reservoir PV of gas has been injected; other reservoir parameters are given in table 5–9. Thereafter, an increasing proportion of the produced fluid is lean gas, and the variation of CGR with time is shown in figure 5–50. The pressure behavior is shown in figure 5–51, where it can be seen that the pressure increases until dry gas break through and decreases thereafter. Before breakthrough, the methane injection rate  $m_{inj}$  of 0.55 kg/s is overbalanced, i.e., the in situ volumetric flow rate of the low molecular weight injected gas is greater than the volumetric flow rate of much heavier rich gas although its mass flow rate  $m_t$  is 1.0 kg/s. At the initial reservoir pressure, the density of lean gas is 144 kg/m<sup>3</sup>, whereas the density of the rich gas is 313 kg/m<sup>3</sup>. Once breakthrough of dry gas occurs and the molecular weight of the produced gas starts to decrease, the in situ volumetric rate of produced gas is greater than that of the injected gas and the pressure decreases.

**Table 5–9.** Reservoir parameters for gas recycling synthetic example

$\alpha = 1.49411$	$V_p = 10^6 \text{ m}^3$	$S_{wc} = 0.2$	$m_{inj} = 0.55 \text{ kg/s}$
$c_w = 4.35 \times 10^{-10} \text{ Pa}^{-1}$	$c_f = 8.7 \times 10^{-10} \text{ Pa}^{-1}$	$m_t = 1.0 \text{ kg/s}$	$T = 350 \text{ K}$
$p_i = 25 \text{ MPa}$	$p_{dew} = 20.239 \text{ MPa}$	$CGR_i = 5.406 \times 10^{-4}$	$M_{w,i} = 29.23$
$M_{w,inj} = 16.04$			

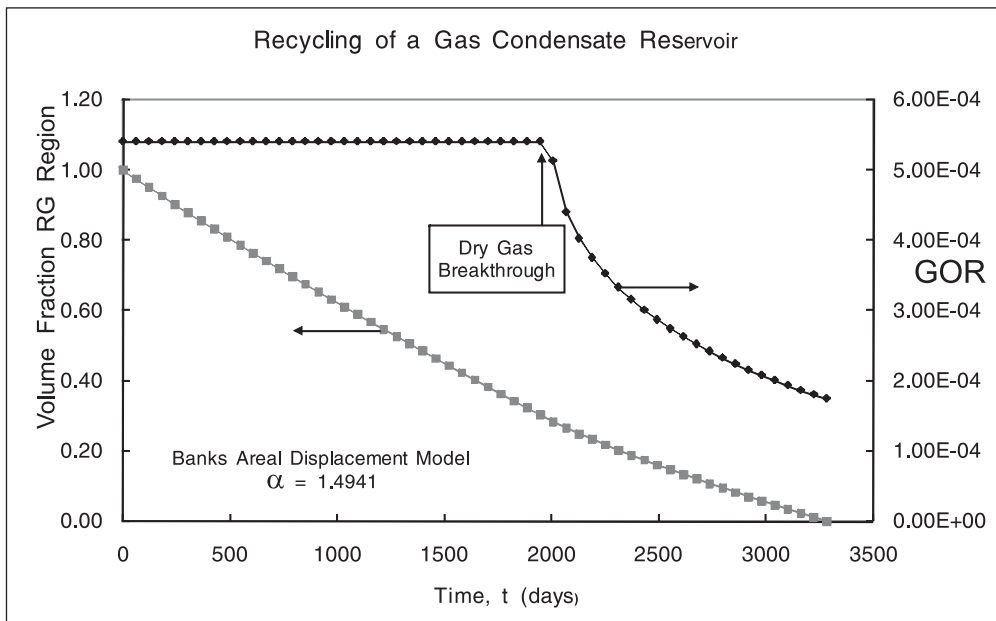


Fig. 5-50. Producing CGR with progressive dry gas breakthrough

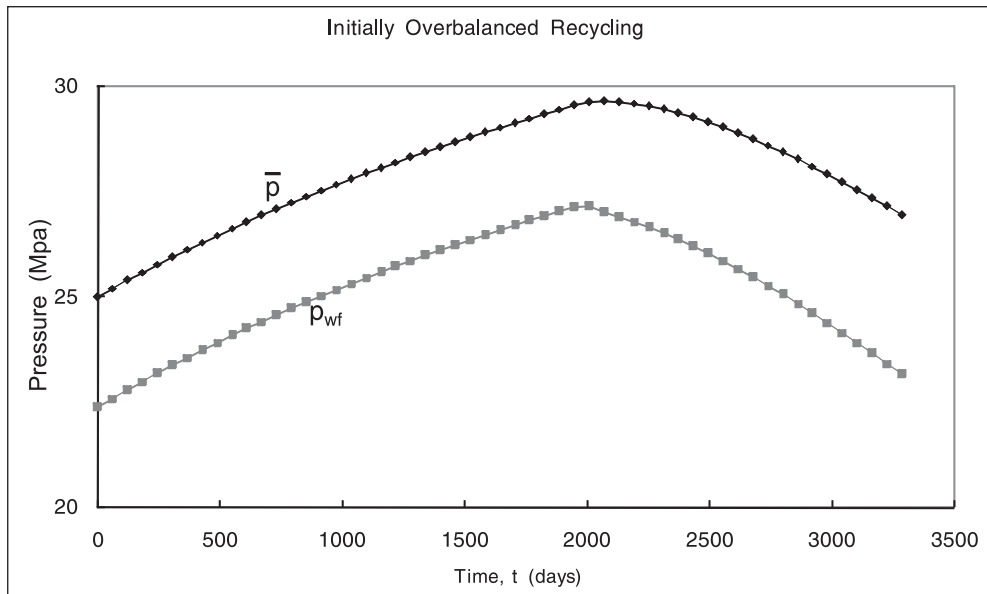


Fig. 5-51. Pressure history in an initially overbalanced injection

The preceding analysis is applicable to the case where the lean gas injection rate is sufficiently high to prevent the reservoir pressure falling below the dew point. In practice, it may not be economical to specify such high injection rates and the reservoir pressure is allowed to decline. Once two-phase conditions exist in the reservoir, a modified analysis of the producing fluid model is necessary; the two-phase situation is illustrated in figure 5-52. The in situ volumetric flow of rich gas  $q_g$  in the previous analysis is now replaced by the in situ volumetric flow of gas, i.e.,  $q_g + q_o$ , and condensate and the fractional flow of lean gas is now defined as



$$f_{LG} = \frac{q_{gc}}{q_{gc} + q_g + q_o} = \frac{\frac{m_{gc}}{\rho_{gc}}}{\frac{m_{gc}}{\rho_{gc}} + \frac{m_g}{\rho_g} + \frac{m_o}{\rho_o}} \tag{5-142}$$

where the ratio of rich gas to condensate flow is controlled by relative permeability, i.e.,

$$\frac{m_g}{m_o} = \frac{\rho_g k_{rg} \mu_o}{\rho_o k_{ro} \mu_g} = R \tag{5-143}$$

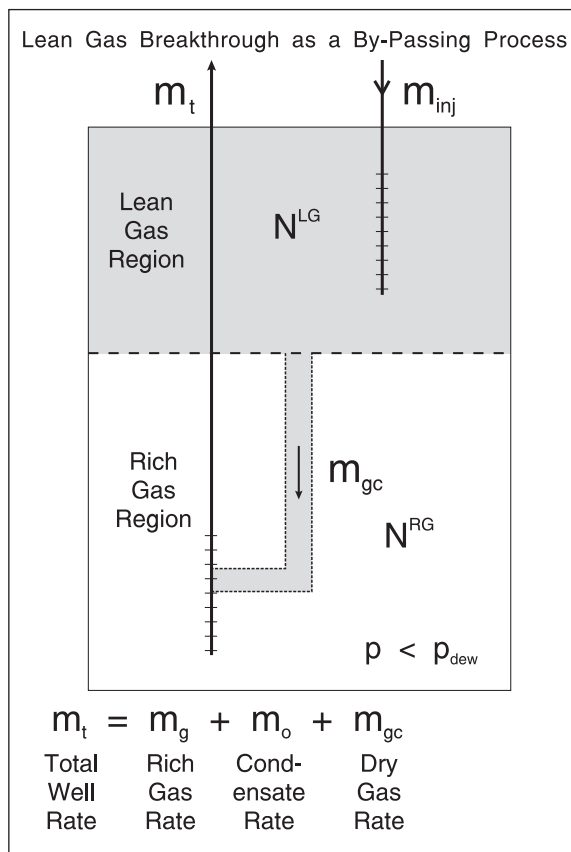


Fig. 5-52. The effect of areal displacement viewed as a bypassing process

Defining the quantity a as

$$a = \frac{\rho_{gc} \left( \frac{1}{R\rho_o} + \frac{1}{\rho_g} \right)}{\left( \frac{1}{R} + 1 \right)} \tag{5-144}$$

Eqs. (5-142) and (5-143) may be solved explicitly:

$$m_{gc} = \frac{f_{LG} a m_t}{1 - f_{LG} + a f_{LG}} \quad (5-145a)$$

$$m_g = \frac{m_t - m_{gc}}{\left(\frac{1}{R} + 1\right)} \quad (5-145b)$$

$$m_o = \frac{m_g}{R} \quad (5-145c)$$

where

$$m_t = m_{gc} + m_g + m_o$$

In figure 5-53, the result of a material balance simulation with the dry gas injection rate reduced to 0.3 kg/s is shown. The pressure now falls below the dew point and the producing CGR decreases. At the point of dry gas breakthrough, the produced fluid becomes leaner and the CGR drops even more rapidly. This level of gas reinjection was determined to be economic for the giant Karachaganak field and it is interesting to observe that the recovery efficiency for condensate in the synthetic example is 62%.

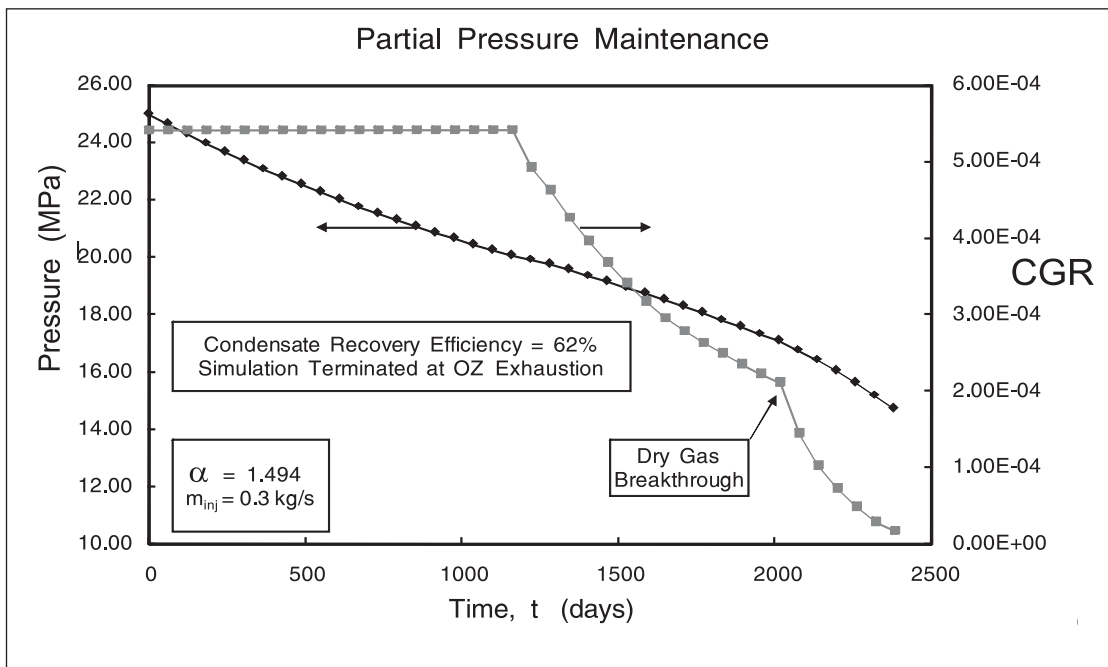


Fig. 5-53. Reduced dry gas injection rate

# Aquifer Influx

## Undersaturated reservoir case

The subject of aquifer influx was treated in depth in the preceding chapter in connection with the gas reservoir material balance. The same approach will be adopted here in the case of an oil reservoir, and following the conclusions reached in chapter 4, only the Fetkovich aquifer will be considered since this was shown to be adequate for material balance purposes. An oil reservoir with aquifer support is shown in figure 5-54, where the aquifer average pressure is designated  $p_a$ . The aquifer model takes the form

$$c_a V_{pa} \frac{dp_a}{dt} = -w = -J_a (p_a - p) \tag{5-146}$$

where

$$c_a = c_w + c_f$$

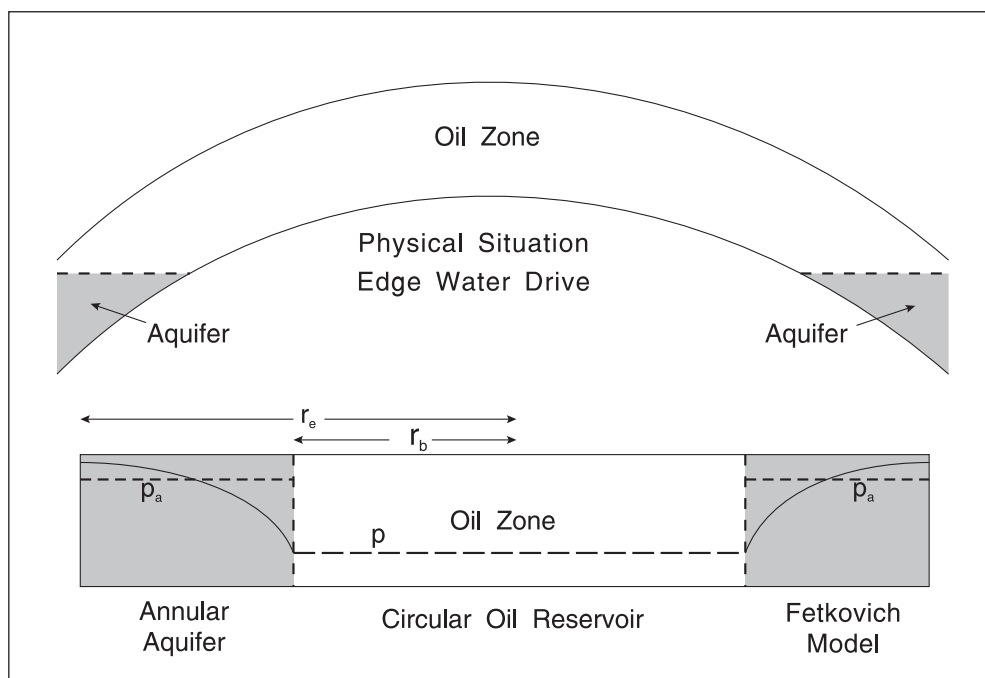


Fig. 5-54. Aquifer influx based on the Fetkovich model

In the case where water is injected into the aquifer at a mass flow rate  $m_{inj,w}$ , this becomes

$$c_a V_{pa} \frac{dp_a}{dt} = -J_a (p_a - p) + \frac{m_{inj,w}}{\rho_w} \tag{5-147a}$$

$$w = J_a (p_a - p) \quad (5-147b)$$

Here,  $J_a$  is the Fetkovich aquifer constant and  $V_{pa}$  is the pore volume of the aquifer; an analytic formula for  $J_a$  in terms of aquifer radial dimensions and permeability was given in chapter 4. The volumetric flow of water into the OZ is  $w$ , and a region of trapped hydrocarbon at residual oil saturation propagates into the reservoir; this will be termed the *invaded zone* (IZ) and another moving boundary problem presents itself. For the moment, conditions above the bubble point pressure will be considered with no free gas present.

In figure 5-54, the aquifer influx is regarded as edge water drive. However, it is equally valid to consider the case of bottom water drive as shown in figure 5-55 with the stipulation that the equation defining  $J_a$  is modified. Note that the edge water-drive model is associated with classical waterflood displacement theory, whereas bottom water drive often leads to a coning situation. In the case of bottom water drive, the water influx creates an invaded zone at residual oil saturation. The thickness of the invaded zone will increase by an amount  $dh$  for a volumetric influx  $W_e$ , where

$$W_e = \bar{A} \phi (1 - S_{wc} - S_{orw}) dh \quad (5-148)$$

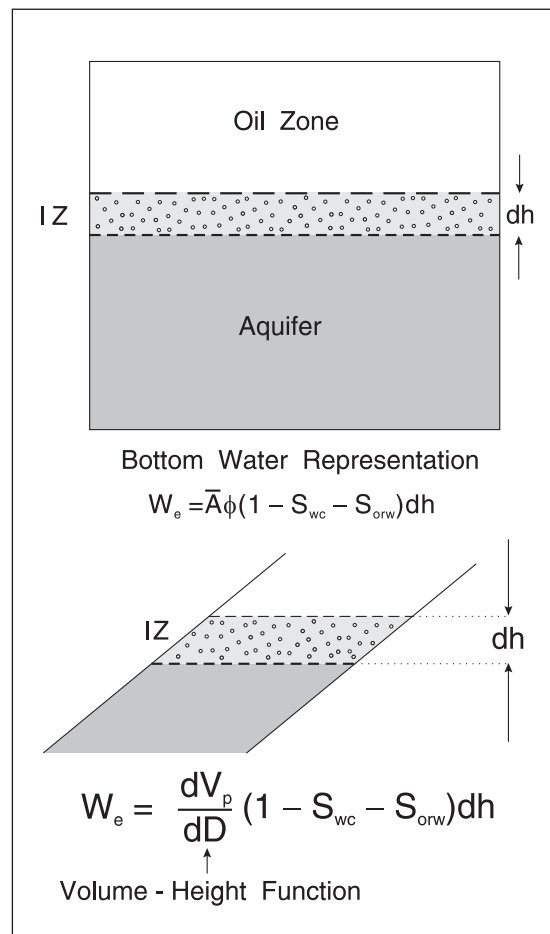


Fig. 5-55. Volume-depth function

Here, the quantity  $\bar{A}\phi$  is presumed constant. In the general case, also illustrated in figure 5–55, this quantity is variable with true vertical depth (TVD) and Eq. (5–148) is written as

$$W_e = \frac{dV_p}{dD}(1 - S_{wc} - S_{orw})dh \quad (5-149)$$

Here,  $dV_p/dD$  is a function of TVD, D, and is known as the volume–depth function. This depends on the reservoir geometry and can be input into the material balance study. In the treatment here, the case where  $\bar{A}\phi$  is constant will be considered with the proviso that this quantity may always be replaced by a more general volume–depth function.

The growth of the invaded zone is modeled by the volume balance

$$\frac{d\hat{V}^{IZ}}{dt} = \frac{w}{1 - S_{orw} - S_{wc}} \quad (5-150)$$

and the component material balance equations for the invaded zone take the form

$$\frac{dN_w^{IZ}}{dt} = \frac{w\rho_w}{M_{ww}} + \frac{d\hat{V}^{IZ}}{dt} \frac{S_{wc}\rho_w}{M_{ww}} \quad (5-151)$$

Here, water is both a component and an immiscible phase. The trapping of liquid hydrocarbon as a residual saturation leads to the material balance for component j:

$$\frac{dN_j^{IZ}}{dt} = \frac{d\hat{V}^{IZ}}{dt} \left( \frac{S_{orw}x_j^{OZ}\rho_o^{OZ}}{M_w^{OZ}} \right) \quad (5-152)$$

In integrated form, these become

$$N_w^{IZ} \Big|_{t+\Delta t} = N_w^{IZ} \Big|_t + \left( \frac{w\rho_w}{M_{ww}} \right) \Big|_t \Delta t \quad (5-153)$$

and

$$N_j^{IZ} \Big|_{t+\Delta t} = N_j^{IZ} \Big|_t + \left( \frac{d\hat{V}^{IZ}}{dt} \left( \frac{S_{orw}x_j^{OZ}\rho_o^{OZ}}{M_w^{OZ}} \right) \right) \Big|_t \Delta t \quad (5-154)$$

Above the bubble point, the composition of the trapped liquid, i.e.,  $x^{OZ}$ , is the original reservoir fluid composition  $z^c$ . The total moles of trapped hydrocarbon is given by the summation

$$N^{IZ}|_{t+\Delta t} = \sum_{j=1}^{NC} N_j^{IZ}|_{t+\Delta t} \quad (5-155)$$

The overall hydrocarbon component material balances for component  $j$  takes the form

$$\frac{dN_j}{dt} = - \left( \frac{m_g}{M_g} y_j + \frac{m_o}{M_o} x_j \right) \quad (5-156)$$

which in integrated form becomes

$$N_j|_{t+dt} = N_j|_t - \left( \frac{m_g}{M_g} y_j + \frac{m_o}{M_o} x_j \right) \Big|_t \Delta t \quad (5-157)$$

Note that initially the moles of component  $j$  present in the invaded zone is zero, i.e.,

$$N^{IZ}|_0 = 0 \quad (5-158)$$

The component material balances for the OZ follow as

$$N_j^{OZ}|_{t+dt} = N_j|_{t+dt} - N_j^{IZ}|_{t+dt} \quad (5-159)$$

The total moles present in the OZ is given by the summation

$$N^{OZ} = \sum_{j=1}^{NC} N_j^{OZ} \quad (5-160)$$

and the overall composition follows as

$$z_j^{OZ} = \frac{N_j^{OZ}}{N^{OZ}} \quad (5-161)$$

The overall water balance for the reservoir region IZ + OZ is given by

$$N_w|_{t+\Delta t} = N_w|_t + \left( \frac{w\rho_w}{M_{ww}} \right) \Big|_t \quad (5-162)$$

with the initial condition

$$N_w|_0 = \frac{V_p S_{wc} \rho_w^i}{M_{ww}} \quad (5-163)$$

The integration of the aquifer Eq. (5-146) is based on a modified Euler method to give stability to the influx prediction. In this approach, the water inflow  $w$  is evaluated at the average pressure difference over the time step, i.e.,

$$w = J_a \frac{(p_a|_{t+\Delta t} - p|_{t+\Delta t}) + (p_a|_t - p|_t)}{2} \quad (5-164)$$

and the aquifer material balance in integrated form becomes

$$\frac{c_a V_{pa} (p_a|_{t+\Delta t} - p_a|_t)}{\Delta t} = -J_a \frac{(p_a|_{t+\Delta t} - p|_{t+\Delta t}) + (p_a|_t - p|_t)}{2} \quad (5-165)$$

If the oil zone pressure at the new time level, i.e.,  $p|_{t+\Delta t}$ , is assumed known, this can be solved for the aquifer pressure at the new time level, viz.,

$$p_a|_{t+\Delta t} = \frac{c_a V_{pa} p_a|_t - J_a \frac{-p|_{t+\Delta t} + p_a|_t - p|_t}{2} \Delta t}{c_a V_{pa} + \frac{J_a \Delta t}{2}} \quad (5-166)$$

In the case where water injection into the aquifer is occurring, this becomes

$$p_a|_{t+\Delta t} = \frac{c_a V_{pa} p_a|_t - J_a \frac{-p|_{t+\Delta t} + p_a|_t - p|_t}{2} \Delta t + \frac{m_{inj,w} \Delta t}{\rho_w|_t}}{c_a V_{pa} + \frac{J_a \Delta t}{2}} \quad (5-167)$$

In order to formulate the isochoric flash calculation for the two regions (OZ and IZ), it is necessary to have an EOS for the aqueous phase. As before, an iterative (secant method) calculation is set up to find the new pressure, i.e.,  $p|_{t+\Delta t}$ , which renders the sum of the volumes of water and hydrocarbon equal to the specified pore volume. It is sufficient to assume that the compressibility of water  $c_w$  is constant, and the density is given by

$$\rho_w = \rho_w^i e^{c_w(p - p_i)} \quad (5-168)$$

Here,  $\rho_w^i$  is the density of the aqueous phase (brine) at the initial pressure  $p_i$ . It is convenient to define the actual pore volume in the reservoir (OZ plus IZ), corrected for compaction as  $\bar{V}_p$ , where

$$\bar{V}_p = V_p \left( 1 - c_f (p_i - p|_{t+\Delta t}) \right) \quad (5-169)$$

Suppose the new pressure  $p_{t+\Delta t}$  is assumed known; then the density of water at time  $t + \Delta t$  is given by

$$\rho_w|_{t+\Delta t} = \rho_w^i e^{c_w(p|_{t+\Delta t} - p_i)} \quad (5-170)$$

The oil density at the new time level is obtained from the EOS liquid root based on the composition  $z_j^{OZ}$  and the pressure  $p|_{t+\Delta t}$ ; this density is written  $\rho_o|_{t+\Delta t}$ . The isochoric flash problem is to find the pressure which satisfies the volume condition:

$$f_{if} \left( p|_{t+\Delta t} \right) = \left( \bar{V}_p - \frac{N_w|_{t+\Delta t} M_{ww}}{\rho_w|_{t+\Delta t}} - \frac{N|_{t+\Delta t} M_{wo}}{\rho_o|_{t+\Delta t}} \right) \quad (5-171)$$

Note that for pressures above the bubble point, where the oil phase is unchanged in composition from the initial state, it is immaterial whether oil is trapped in the IZ or present in the OZ; hence, the total moles of oil  $N|_{t+\Delta t}$  has been used in the volume condition. Similarly, the total moles of water  $N_w|_{t+\Delta t}$  is used and the actual location of the water (IZ or OZ) is not important in the volume condition. In this formulation water is considered to have a constant compressibility  $c_w$ , but the oil density is determined by the EOS for a liquid oil phase. The rock compressibility  $c_f$  is also treated as a constant. The model will predict the aquifer pressure  $p_a$ , the reservoir (IZ and OZ) pressure  $p$ , the water influx rate  $w$ , and the fraction of the pore volume  $\bar{V}_p$  occupied by the IZ.

## Reservoir pressure below bubble point

The theory in the preceding section is applicable as long as the pressure is above the oil bubble point and only liquids are present in the system. If the pressure falls below the bubble point,



two-phase conditions will exist in the OZ. In addition, both oil and gas will be trapped by the advancing water and held in the IZ. It will be assumed that this hydrocarbon saturation is trapped at a level  $S_{Hrw}$  and that oil and gas are retained in at individual saturations  $S_{orw}$  and  $S_{grtr}$ . Figure 5–56 (after Willhite) depicts one model of the displacement process in which the gas is trapped immiscibly at the leading edge of the oil bank, leaving a trapped gas saturation  $S_{gtr}$  of magnitude  $S_{gro}$ , i.e., it is the residual saturation to an oil rather than water displacement that is controlling. Note that although the hydrocarbon is trapped at a saturation of  $S_{Hrw}$ , as the pressure falls this hydrocarbon flashes and expands and the actual hydrocarbon (oil + gas) saturation in the invaded zone increases above  $S_{Hrw}$ . Thus, the solution gas drive occurs both in the OZ and the IZ.

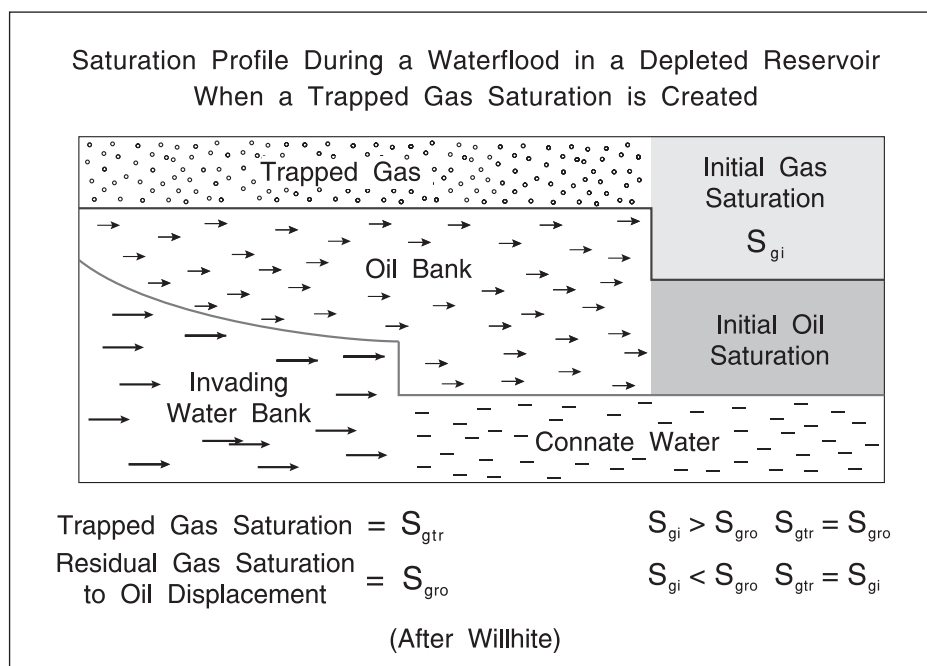


Fig. 5–57. Saturation profile during a waterflood in a depleted reservoir

The trapping of a mixture of oil and gas when the pressure is below the bubble point is modeled by the equation

$$\frac{dN_j^{IZ}}{dt} = \frac{d\hat{V}^{IZ}}{dt} \left( \frac{S_{orw} x_j^{OZ} \rho_o^{OZ}}{M_{wo}^{OZ}} + \frac{S_{grw} y_j^{OZ} \rho_g^{OZ}}{M_{wg}^{OZ}} \right) \tag{5-172}$$

where

$$\frac{d\hat{V}^{IZ}}{dt} = \frac{w}{1 - S_{Hrw} - S_{wc}}$$

The relation between the waterflood trapped oil and gas saturations  $S_{orw}$  and  $S_{grw}$  is discussed in the succeeding chapter; for the moment, they are simply defined as independent quantities.

## Inclusion of a coning or displacement model

It is possible to include in the material balance formulation a mechanistic coning model that allows water from the IZ to flow directly to the producing well as illustrated in figure 5–57. The theory of water or gas coning in vertical or horizontal wells is treated in detail in the following chapter, and for the moment it will be simply assumed that the total mass flow of fluid  $m_t$  includes an aqueous component, i.e.,

$$m_t = m_H + m_w = m_o + m_g + m_w \quad (5-173)$$

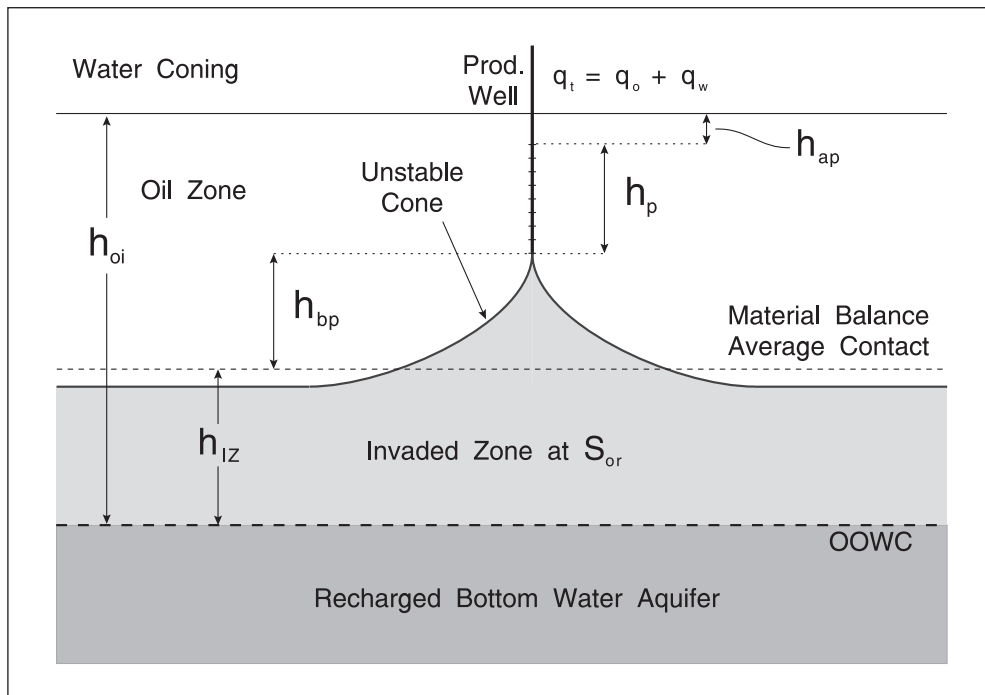


Fig. 5–57. Water coning into a vertical well

If the pressure is maintained above the bubble point, the flow of gas in situ is zero and this becomes

$$m_t = m_o + m_w \quad (5-174)$$

The volumetric flow rates of oil and gas are

$$q_o = \frac{m_o}{\rho_o} \quad \text{and} \quad q_w = \frac{m_w}{\rho_w} \quad (5-175)$$

The water–oil ratio (WOR) is defined as

$$\text{WOR} = \frac{q_w}{q_o} \quad (5-176)$$

A coning model simply defines the WOR as a function of time as shown in figure 5–58, and for the moment it will be assumed that the function represented in figure 5–58 has been quantified and may be written symbolically as

$$\text{WOR} = f_c(t) \quad (5-177)$$

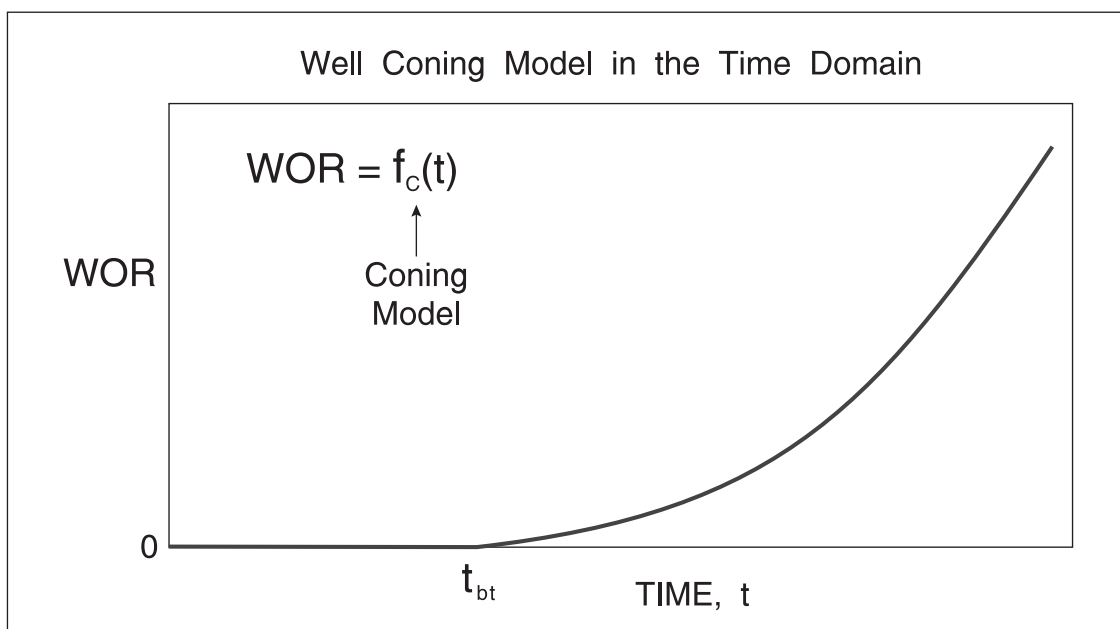


Fig. 5–58. WOR time dependence specified through a coning model

Note that up until time  $t_{bt}$ —the time to breakthrough—the WOR is zero, after which it steadily increases. Quantitative forms for the coning function  $f_c(t)$  will be given in the succeeding chapter; the coning model developed by Yang and Wattenbarger<sup>11</sup> was specifically designed to run in conjunction with a material balance model of bottom water drive. The coning situation is illustrated in figure 5–59, where the produced water at mass flow rate  $m_w$  is shown to flow directly from the IZ to the well. This “bypassing” or “short circuit” approach is a convenient method of introducing the coning phenomenon into a material balance model which predicts the dynamic evolution of the IZ. When coning is occurring, the growth of the IZ is governed by the modified equation

$$\frac{d\hat{V}^{IZ}}{dt} = \frac{w - q_w}{1 - S_{or} - S_{wc}} \quad (5-178)$$

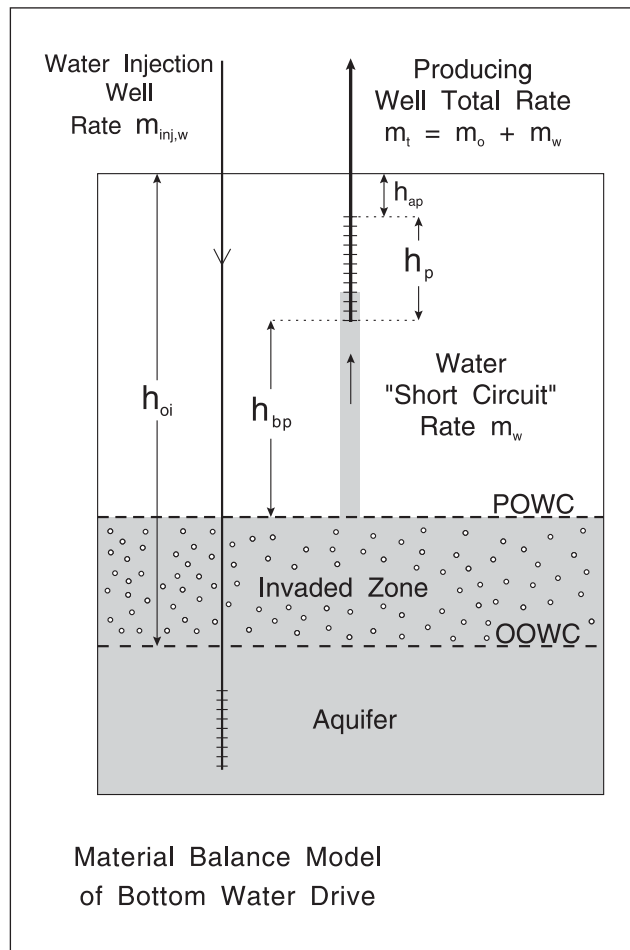


Fig. 5–59. Diagrammatic representation of coning as bypassing water

The water component balance becomes

$$\frac{dN_w^{IZ}}{dt} = \frac{(w - q_w)\rho_w}{M_{ww}} \quad (5-179)$$

Given the total producing well mass flow rate  $m_t$  and a coning model that yields instantaneous WOR, the in situ volumetric rates of oil and water production are

$$q_o = \frac{m_t}{\text{WOR}\rho_w + \rho_o} \quad q_w = \text{WOR} q_o \quad (5-180)$$

The same approach can be used to incorporate the classical water drive into the material balance. In this case, the physical situation corresponds more to edge water drive as illustrated in figure 5–60, and again a displacement function is used to relate the producing WOR to time, i.e.,

$$\text{WOR} = f_D(t) \quad (5-181)$$

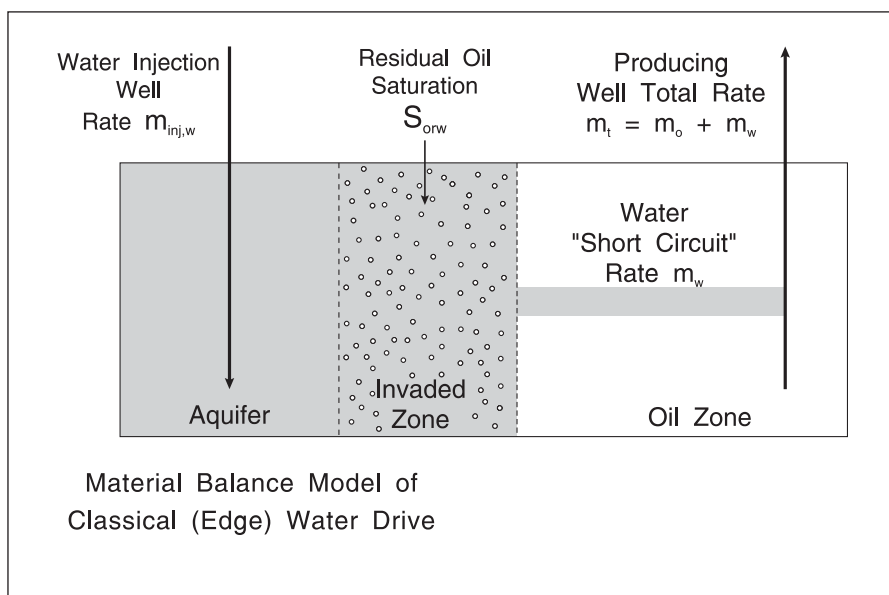


Fig. 5-60. Diagrammatic representation of displacement as bypassing water

In the following chapter, it will be shown that in the water-drive case, a more suitable form of the displacement function is

$$f_w = f^{wD}(V_{pmi}) \tag{5-182}$$

where  $f_w$  is the fractional flow of water and  $V_{pmi}$  is the movable pore volume injected into the system from the aquifer. In this case, the short-circuiting mass flow  $m_w$  represents the breakthrough of water controlled by the mechanics of the displacement process.

### Dry Gas Reservoir with Active Water Drive

In chapter 4, the theory of a gas reservoir with active water drive was formulated as a simultaneous set of ordinary differential equations. It is useful here to present this model in finite difference form similar in nature to the other models discussed in this chapter. In the case of dry gas (no liquid condensate phase present), the process is not a compositional one if the solubility of the hydrocarbon components in the aqueous phase is assumed negligible. The influx of water into the gas reservoir from the aquifer is represented in figure 5-61 as bottom water drive and the trapped gas saturation is denoted  $S_{grw}$ . Initially, it will be assumed in this model that the pressure in the IZ is identical to that in the GZ, but the original aquifer body is at a different pressure  $p_a$ . The growth of the IZ is modeled by the volume balance

$$\frac{dV^{\wedge IZ}}{dt} = \frac{w}{1 - S_{grw} - S_{wc}} \tag{5-183}$$

and the component material balance equations for the IZ take the form

$$\frac{dN_w^{IZ}}{dt} = \frac{w\rho_w}{M_{ww}} + \frac{dV^{IZ}}{dt} \frac{S_{wc}\rho_w}{M_{ww}} \quad (5-184)$$

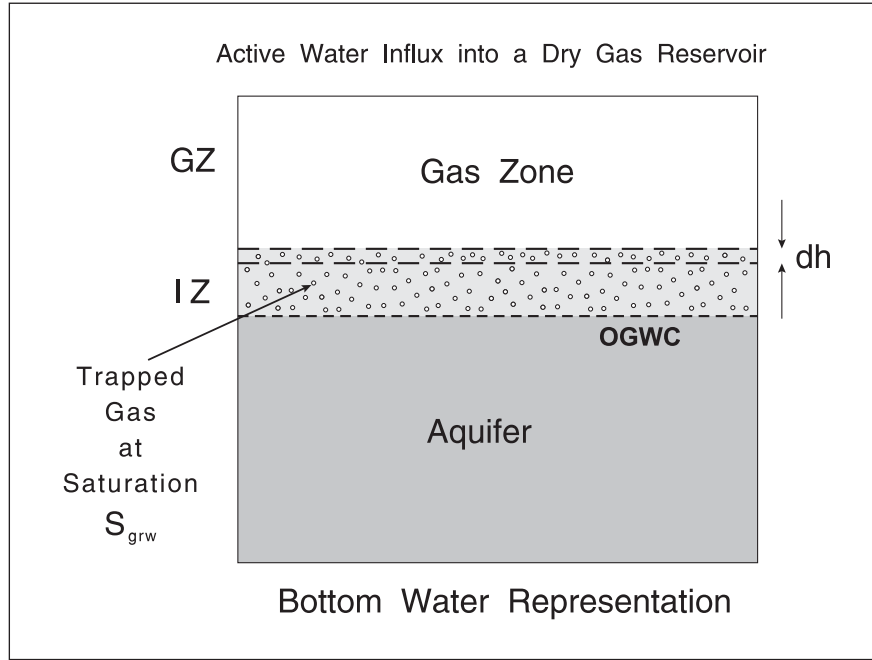


Fig. 5-61. Dry gas reservoir with active water drive

Note, however, that this equation is not used directly in the first version of the model, which employs an overall water balance on the region IZ + GZ. The trapping of gas as a residual phase leads to the material balance for component  $j$ :

$$\frac{dN_j^{IZ}}{dt} = \frac{dV^{IZ}}{dt} \left( \frac{S_{grw} y_j \rho_g^{GZ}}{M_w^{GZ}} \right) \quad (5-185)$$

Here,  $N_j^{IZ}$  refers to the actual amount of gas removed from the producible GZ by trapping. In integrated form, this becomes

$$N_j^{IZ} \Big|_{t+\Delta t} = N_j^{IZ} \Big|_t + \left( \frac{dV^{IZ}}{dt} \left( \frac{S_{grw} y_j \rho_g^{GZ}}{M_w^{GZ}} \right) \right) \Big|_t \Delta t \quad (5-186)$$

The total moles of trapped gas is given by the summation

$$N^{IZ}|_{t+\Delta t} = \sum_{j=1}^{NC} N_j^{IZ}|_{t+\Delta t} \quad (5-187)$$

The overall hydrocarbon component material balance for component  $j$  is

$$\frac{dN_j}{dt} = -\frac{m_g y_j}{M_g} \quad (5-188)$$

which in integrated form becomes

$$N_j|_{t+dt} = N_j|_t - \left( \frac{m_g}{M_g} y_j \right) \Big|_t \Delta t \quad (5-189)$$

The component material balance for the GZ follows as

$$N_j^{GZ}|_{t+dt} = N_j|_{t+dt} - N_j^{IZ}|_{t+dt} \quad (5-190)$$

with the total moles remaining in the GZ given by

$$N^{GZ}|_{t+\Delta t} = \sum_{j=1}^{NC} N_j^{GZ}|_{t+\Delta t} \quad (5-191)$$

The overall water balance in the region IZ + GZ is given by

$$N_w|_{t+dt} = N_w|_t + \left( \frac{w\rho_w}{M_{ww}} \right) \Big|_t \Delta t \quad (5-192)$$

The equations describing the aquifer are given by (5-164) to (5-170) as before.

The gas density at the new time level is obtained from the EOS based on the fixed composition  $z$  and the pressure  $p|_{t+\Delta t}$ . The isochoric flash problem is to find the pressure that satisfies the overall volume condition

$$f_{if}(p|_{t+\Delta t}) = \left( \bar{V}_p - \frac{N_w|_{t+\Delta t} M_{ww}}{\rho_w|_{t+\Delta t}} - \frac{N|_{t+\Delta t} M_{wg}}{\rho_g|_{t+\Delta t}} \right) = 0 \quad (5-193)$$

where

$$\bar{V}_p = V_p \left( 1 - c_f(p_i - p|_{t+dt}) \right) \quad (\text{actual pore volume allowing for compaction})$$

$$\text{Vol}_w = \frac{N_w|_{t+\Delta t} M_{ww}}{\rho_w|_{t+\Delta t}} \quad (\text{volume of total water in region IZ + GZ})$$

$$\rho_w|_{t+\Delta t} \quad \text{evaluated at pressure} \quad p|_{t+dt}$$

$$\text{Vol}_g = \frac{N|_{t+\Delta t} M_{wg}}{\rho_g|_{t+\Delta t}} \quad (\text{volume of total gas in region IZ + GZ})$$

$$\rho_g|_{t+\Delta t} \quad \text{evaluated at pressure} \quad p|_{t+dt}$$

This simplified form of the isochoric flash is possible because the pressure in the two regions IZ and GZ is identical and the gas composition is the same everywhere. It is also possible to derive an alternative form of the model in which the IZ is presumed to be at pressure  $p_a$ ; the main effect of this change is a slightly lower in situ volume of trapped gas because  $p_a$  is higher than  $p$ .

Accordingly, in the second form of this model—the version developed in chapter 4 in differential form—the IZ is held at the aquifer average pressure  $p_a$ ; this is physically more realistic but gives a more complicated model. The effect of trapped gas on the depletion behavior is stronger if it is held at the aquifer pressure which is higher than the GZ pressure  $p$ . The volume balance now takes the form

$$\bar{V}_p = V^{IZ} + V^{GZ} \quad (5-194)$$



where

$$V^{IZ} = \frac{N_w^{IZ}|_{t+\Delta t} M_{ww}}{\rho_{wa}|_{t+\Delta t}} + \frac{N_w^{IZ}|_{t+\Delta t} M_{wg}}{\rho_{ga}|_{t+\Delta t}} \quad (5-195)$$

(densities evaluated at  $p_a|_{t+dt}$ )

$$V^{GZ} = \frac{N_w^{GZ}|_{t+\Delta t} M_{ww}}{\rho_w|_{t+\Delta t}} + \frac{N_w^{GZ}|_{t+\Delta t} M_{wg}}{\rho_g|_{t+\Delta t}} \quad (5-196)$$

(densities evaluated at  $p|_{t+dt}$ )

Again, Eq. (5-196) may be written in functional form

$$f_{if}(p|_{t+\Delta t}) = (\bar{V}_p - V^{IZ} - V^{GZ}) = 0 \quad (5-197)$$

and the pressure at the new time level which satisfies this equation is sought. The amount of trapped gas, i.e. that present in the invaded zone, is regulated by Eqs. (5-186) and (5-187) and the remaining amount in the GZ is obtained by difference using the mass balance Eqs. (5-190) and (5-191).

The best way of handling the calculation of the amount of water in the two regions (IZ and GZ) is first to appreciate that the water saturation in the GZ changes only by water expansion and formation compaction. Thus, the saturation  $S_w^{GZ}$  is identical to the quantity  $S_{wc,corr}$  given by Eq. (5-34) i.e.,

$$S_w^{GZ} = S_{wc,corr} = S_{wc} \frac{1 + c_w \Delta p}{1 - c_f \Delta p} \quad (5-198)$$

This saturation is also predicted by the in situ volume condition

$$S_w^{GZ} = \frac{N_w^{GZ}|_{t+\Delta t} M_{ww}}{\rho_w|_{t+\Delta t} V^{GZ}} \quad (5-199)$$

If  $V^{GZ}$  is eliminated by combining (5-199) and (5-196), after some algebra, the result becomes

$$N_w^{GZ}|_{t+dt} = \left( \left( \frac{\rho_w M_{wg}}{\rho_g M_{ww}} \right) \left( \frac{S_{wc,corr}}{1 - S_{wc,corr}} N^{GZ} \right) \right) |_{t+dt} \quad (5-200)$$

Since  $N_w^{GZ}|_{t+dt}$  is known from (5-191), this allows the amount of water in the GZ to be calculated directly, and the amount of water in the IZ can be obtained by difference using the overall water balance (5-192), i.e.,

$$N_w^{IZ}|_{t+dt} = N_w|_{t+dt} - N_w^{GZ}|_{t+dt} \quad (5-201)$$

Perhaps, the key numerical point about the model is the semi-explicit determination of the gas trapping through the use of the gas density at the beginning of the step in Eq. (5-186).

## Associated water model

In terms of  $p/z$ , the material balance equation takes the modified form

$$\frac{p}{z} \left( 1 - \frac{(p_i - p)(c_w S_{wc} + c_f)}{1 - S_{wc}} \right) = \frac{p_i}{z_i} \left( 1 - \frac{G_p}{G_i} \right) \quad (5-202)$$

## Tuning of Material Balance Model

In the preceding sections, the forecasting problem has been treated in detail; here, the parameters of the model are specified and the production is predicted forward in time. In the history matching mode, measured production data are available and the problem is to estimate model parameters that match the model to the data. The key measurements for a material balance model can be listed as follows:

- Average pressure
- Producing GOR
- Producing WOR

Interpreted well tests are the source of average pressure data and the production data (stored in a database) takes the form indicated in table 5-10.

**Table 5-10.** Production data stored in database

Time	Separator oil rate (stock tank)	Oil density (gravity)	Separator gas rate (standard conditions)	Gas density (gravity)	Water flow rate	Total mass flow rate
------	------------------------------------	--------------------------	---	--------------------------	--------------------	-------------------------

In addition to the block average pressures determined from well test buildups, any wireline formation tester (WFT) pressure surveys run into the block may be identified with cell average pressures. Permanent gauges are also used to monitor the bottom-hole flowing pressure of individual wells.

## Notes

- 1 Schilthuis, R. J. "Active Oil and Reservoir Energy," *Trans. AIME* 118, (1936): 33–52.
- 2 Dake, L. P. "Fundamentals of Reservoir Engineering," chapter 3, Elsevier (1978).
- 3 Chierici, G. L. "Principles of Petroleum Reservoir Engineering" (Springer-Verlag 1994), *Well Test Design and Analysis*, chap. 10.
- 4 Honarpour, M., Koederitz, L., and Harvey, A. H. "Relative Permeability of Petroleum Reservoirs" (Boca Raton, Florida, USA: CRC Press, 1986), 91.
- 5 Madaoui, K. "Conditions de Mobilite de la Phase Gazeuse lors de la Decompression d'un Melange d'Hydrocarbures en Milieu Poreux" (Thesis, Toulouse Univ., France, 1975).
- 6 Abgrall, E., and Iffly, R. "Etude Physique des Ecoulements par Expansion des Gaz Dissous," *Rev. de L'IFP*, (Oct. 1973): 667–692.
- 7 Firoozabadi, A., Ottesen, B., and Mikkelsen, M. "Measurements of Supersaturation and Critical Gas Saturation," *SPE Formation Evaluation* 7, no. 4 (Dec. 1992): 337–344.
- 8 Saidi, A. M. "Reservoir Engineering of Fractured Reservoirs" (Total Edition Press, Paris, chap. 7, 1987).
- 9 Addington, D. V. "An Approach to Gas Coning Correlations for a Large Grid Cell Reservoir Simulator," *JPT* 33 (11), (Nov. 1981): 2267–2274.
- 10 Garb, F. A. "Empirical Estimate of Liquid Yield in Gas Condensate Reservoirs," *Petroleum Engineer International*, Oct. 1978.
- 11 Yang, W., and Wattenbarger, R. A. "Water Coning Calculations for Vertical and Horizontal Wells" SPE 22931, (SPE 66th Annual Technical Conference, Dallas, Tx, Oct. 1991).

# 6

## Coning and Displacement Models in the Material Balance Context

### Introduction

Many wells produce from oil zones underlain by “bottom water.” When the well is flowing, water moves up toward the wellbore in a cone shape. At certain conditions, water breaks through and concurrent oil and water production takes place. In the preceding chapter, a general material balance model was introduced that allowed the various producing mechanisms to be incorporated. In the initial treatment in chapter 5, a well was allowed to produce only hydrocarbon phases, i.e. gas and/or oil. However, in coning situations it is also necessary to predict the time to water breakthrough and the subsequent development of the water–oil ratio (WOR). Water influx into a well due to coning is illustrated diagrammatically in figure 6–1. In the case of oil reservoirs with a gas cap, the coning of gas downwards is a serious problem and this situation is depicted in figure 6–2.

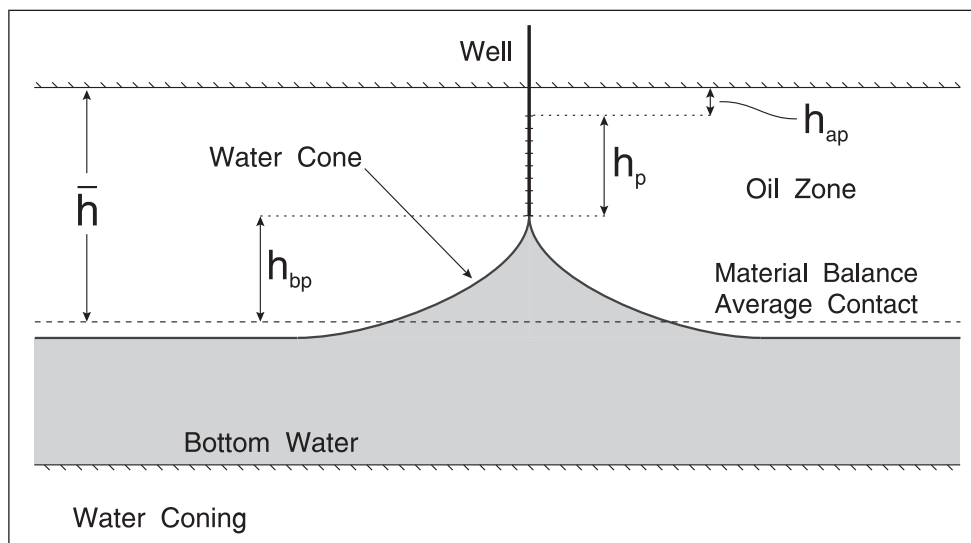


Fig. 6–1. Diagrammatic representation of water coning in an oil well

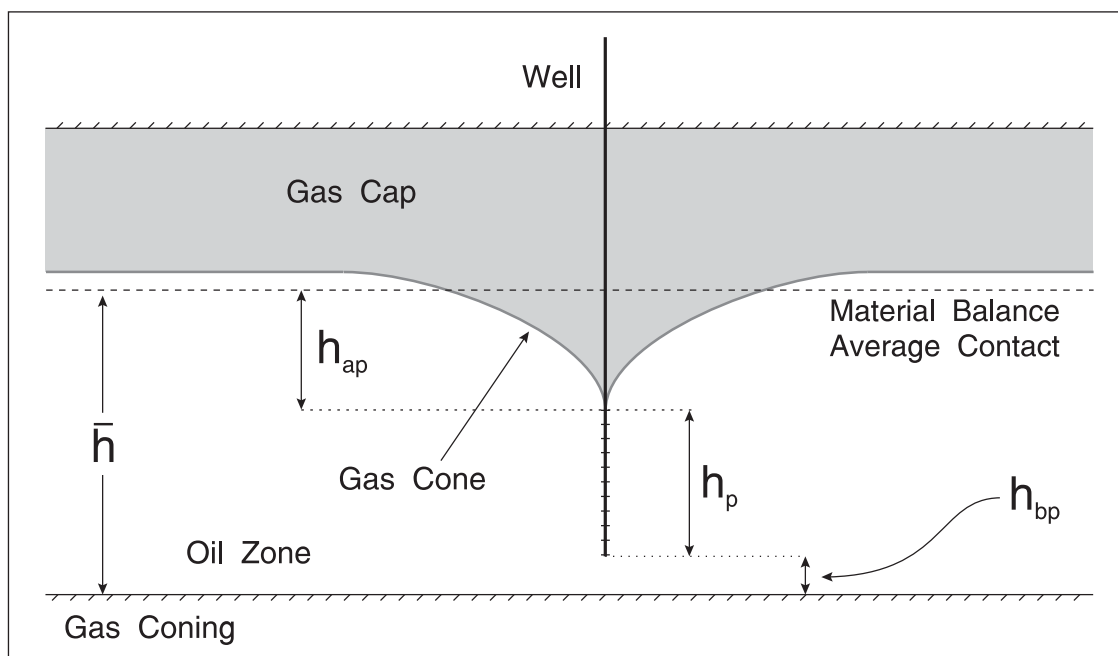


Fig. 6–2. Diagrammatic representation of gas coning in an oil well

## Addington Gas Coning Model for Vertical Wells

### Theoretical background

Addington<sup>1</sup> carried out a study of gas coning into an oil well and showed that a straight line results when the gas–oil ratio (GOR) after gas breakthrough is plotted against the average oil column height above perforations. Based on this observation, Addington performed an extensive parameter sensitivity analysis from which the slope and intercept of the straight line was correlated with various reservoir and fluid properties affecting coning performance. From this correlation, both the GOR and the critical coning rate can be calculated.

The basis of the study of gas coning was the material balance calculation of the thickness of the primary and secondary gas cap as illustrated in figure 6–3. Addington identified the key variable in gas coning to be the average oil column height above the perforations which is denoted  $h_{ap}$ . For a given completion, i.e. location of the perforated interval  $h_p$ , the material balance calculations allow the quantity  $h_{ap}$  to be monitored. Using a two-dimensional fully implicit radial simulator with fine gridding, Addington studied the gas coning behavior of wells using PVT data for the Prudhoe Bay field. In the sensitivity study, the critical coning rate was determined as a function of  $h_{ap}$ , i.e., for a given value of  $h_{ap}$  the oil rate was increased until gas coning just commenced. The value of the oil column height above perforations at the critical rate was denoted  $h_{gb}$ —the subscript gb referring to gas breakthrough. In figure 6–4 (after Addington), the height  $h_{gb}$  is plotted against a parameter group  $P$ , defined as

$$P = \frac{q(k_v/k_h)^{0.1} \mu_o F_1 F_2}{k_h \sqrt{h_p}} \quad (6-1)$$

where  $F_1$  is a geometric factor given by

$$F_1 = \frac{h_{ap} + h_p}{h_{ap} + h_p + h_{bp}} \quad (6-2)$$

and  $F_2$  is a well spacing factor equal to 1 for a standard well spacing of 160 acres; for other well spacings

$$F_2 = \left( \frac{\text{well spacing in acre}}{160} \right)^{0.1} \quad (6-3)$$

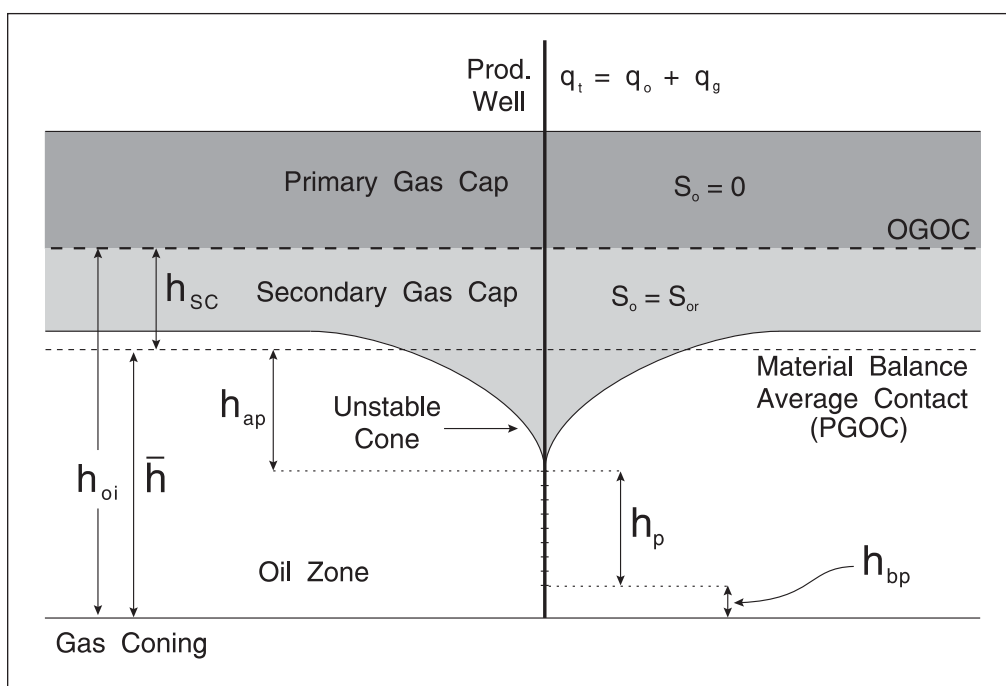


Fig. 6-3. Primary and secondary gas cap locations

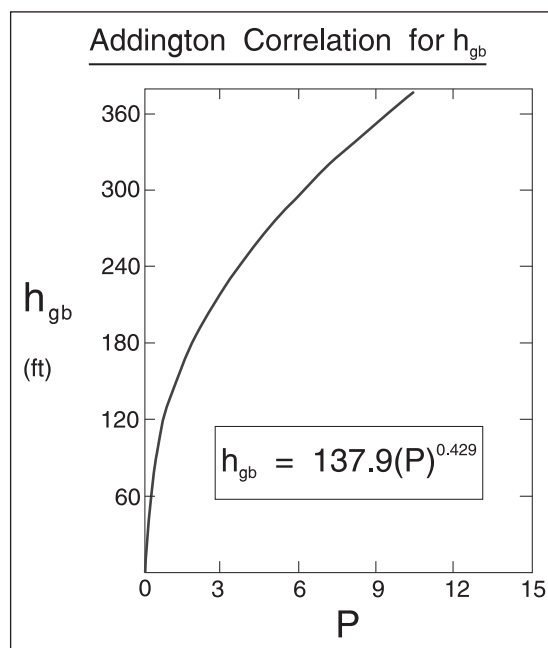


Fig. 6–4. Correlation for oil column height above perforations at inception of coning

The data shown in figure 6–4 was fitted to a power-law equation of the form

$$h_{gb} = 137.9(P)^{0.429} \quad (6-4)$$

Unfortunately, Addington did not give any information in his paper as to the actual density difference between oil and gas at reservoir conditions; the simulations were carried out using the Prudhoe Bay reservoir fluid black oil model. This means it is difficult to generalize the correlation to other conditions since the parameter group  $P$  should include the density difference  $\Delta\rho$ .

Supposing that the material balance calculations have determined the oil column height above the perforations  $h_{ap}$ ; then the generalized correlation (6–4) may be used to determine  $P$ , on the basis that  $h_{ap} \equiv h_{gb}$ . The value of  $q_c$  can therefore be calculated from  $P$  and, if this is greater than the actual well rate, then coning is not occurring and the GOR is the solution GOR.

Addington then went on to examine the producing GOR after gas breakthrough and he made the observation that the GOR increases as the oil column height above perforations, i.e.,  $h_{ap}$ , decreases. In fact, a plot of  $\log(\text{GOR})$  versus  $h_{ap}$  is a straight line as shown in figure 6–5. Here the producing GOR for different well rates is plotted and it can be seen that, after breakthrough, a straight line is present. When the rate is less than the critical, the producing GOR is equal to the solution GOR; however, once the critical rate is exceeded, the GOR increases. Many simulations runs were carried out to quantify the variation of GOR as the rate was increased from the critical. In the paper, Addington showed that straight lines were present on semilog GOR versus  $h_{ap}$  plots as other variables such as anisotropy, horizontal permeability, and perforation thickness were changed. In this study, the GOR was calculated at surface conditions, i.e., in units of Mscf/stb, rather than at reservoir conditions which are more fundamental. The slope of the semilog plot of

$\log_{10}(\text{GOR})$  versus  $h_{ap}$  is denoted “m”, and the data from simulation runs is shown in figure 6–6 (after Addington). The parameter is now written as P', where

$$P' = \frac{q_t(k_v/k_h)^{0.5}\mu_o F_1 F_3}{k_h \sqrt{h_p}} \tag{6-5}$$

and

$$q_t = q_o + q_g$$

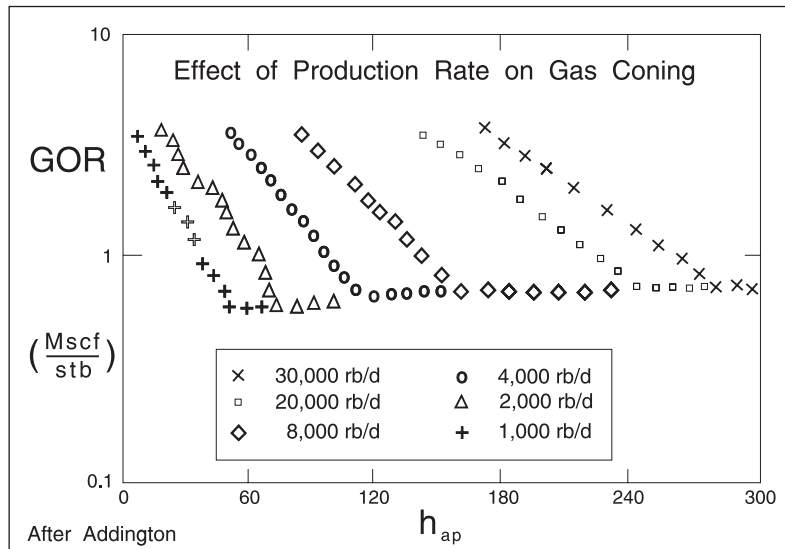


Fig. 6–5. Variation of GOR after breakthrough with  $h_{ap}$

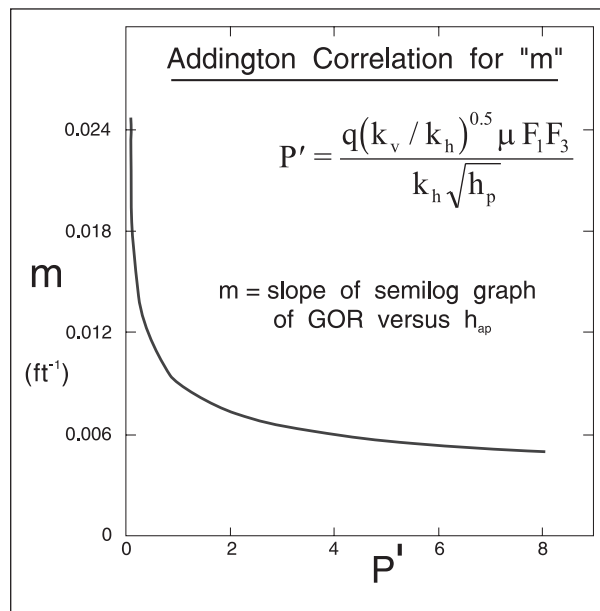


Fig. 6–6. Generalized correlation for slope of GOR curve after gas breakthrough



Here,  $q_t$  is the total well production rate in reservoir barrels per day with the other variables in SPE field units. The information contained in figure 6–6 may be summarized formally as

$$\tilde{q}_{cD} = 39.0633 \times 10^{-4} \left[ \frac{1}{r_{De}} \right]^{0.6} \frac{1}{1 + M^{0.7}} \frac{(1 - \lambda)^{1.4}}{(1 - \delta)^{0.4}} \frac{h_{bp}^2}{(h_{oi} - h_p - h_{ap})^2 - h_{bp}^2} \quad (6-6)$$

This observation of semilog variation of the GOR after breakthrough was an important step in developing empirical coning models. A polynomial regression analysis on the curve shown in figure 6–6 gives the fit

$$y = 4.2746 + 7.1851x - 2.8665x^2 + 0.66742x^3 - 0.074001x^4 + 0.0030731x^5 \quad (6-7)$$

where  $y = m \times 10^3$  and  $x = \frac{1}{p}$

On figure 6–5, each of the break points represents a critical flow situation, i.e.  $h_{ap}$  is synonymous with  $h_{bg}$  and  $q$  is the critical coning oil flow rate (at reservoir conditions). Accordingly, at rates greater than critical, the GOR may be written as

$$\text{Log}_{10}(\text{GOR}) = m(h_{ap} - h_{bg}) + \log_{10}(\text{GOR}^o) \quad (6-8)$$

In this formulation, the total well rate at in situ conditions,  $q_r$ , is entered into correlation (6–5) to determine the corresponding  $h_{bg}$ , and again it is presumed that material balance calculations have established  $h_{ap}$ . Correlation (6–6) is then used to estimate the semilog slope  $m$ , and finally Eq. (6–7) is used to determine the actual GOR.

In Eq. (6–8), the quantity  $\text{GOR}^o$  is the surface GOR of the fluid produced from the oil zone in the absence of coning, i.e., the combined stream  $m_H$ , where  $m_H = m_o + m_g$ , leading to surface rates  $q_s^o$  and  $Q^o$ . Thus

$$\text{GOR}^o = \frac{Q^o}{q_s^o} \quad (6-9)$$

Here the superscript “o” implies the absence of coning. Note that, if the gas saturation is less than critical, then the quantity  $m_g$  is zero and  $G^o = \text{GOR}_s^o = R_s$ , i.e., the solution gas content of the oil phase. The Addington correlation then allows the surface GOR of the total producing stream  $m_t$  to be determined. If the ratio of the surface GOR to the in situ GOR is continually monitored, then the surface GOR can be converted to the more fundamental quantity  $\text{GOR}_{is}^o$ . As noted earlier, it would have been better if the Addington correlation had been formulated directly in terms of  $\text{GOR}_{is}^o$ .



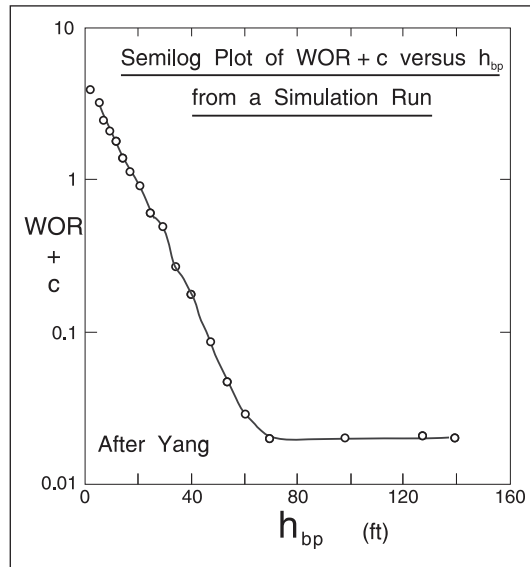


Fig. 6-8. Semilog plot of WOR versus oil column height below perforations

The height below perforations at which an unstable cone just forms is denoted  $h_{wb}$ , where the subscript “wb” refers to water breakthrough. The value of  $h_{wb}$  is controlled principally by

- Well volumetric rate  $q_t$
- Horizontal permeability  $k_h$
- Phase density difference  $\Delta\rho = \rho_w - \rho_1$

but other reservoir and fluid parameters also affect the critical height for a specified rate. From the statistical analysis of many simulation runs, the following correlation (in SPE field units) was developed:

$$\left[ \frac{h_{oi} - h_{ap} - h_p}{h_{wb}} \right]^2 = 1 + 39.0633 \times 10^{-4} \left( \frac{1}{r_{De}} \right)^{0.6} \left( \frac{1}{\tilde{q}_D} \right) \frac{1}{1 + M^{0.7}} \frac{(1 - \lambda)^{1.4}}{(1 - \delta)^{0.4}} \quad (6-11)$$

where 
$$r_{De} = \frac{r_e}{h_{oi}} \sqrt{\frac{k_v}{k_h}}$$

$$\tilde{q}_D = \frac{q_t \mu_o}{k_h k'_{ro} h_{oi}^2 \Delta\gamma} \quad \text{where} \quad \Delta\gamma = \text{difference in fluid hydrostatic gradients (psi / ft)}$$

$$\lambda = \frac{h_{ap}}{h_{oi}}$$

$$\delta = \frac{h_p}{h_{oi}}$$

$$M = \frac{\mu_o k'_{rw}}{\mu_w k'_{ro}} \quad (k'_{rw}, k'_{ro} \text{ end point relative permeabilities})$$

In the form presented by Yang, the combination of variables represented by  $\tilde{q}_D$  has to be evaluated in SPE field units. In order to make Eq. (6–11) properly dimensionless, it is necessary to define  $q_D$  in SPE units as

$$q_D = \frac{887.22 \times q_t \mu_o}{k_h k'_{ro} h_{oi}^2 \Delta\gamma} \quad (6-12)$$

where  $\Delta\gamma$  is still in psi/ft. Correlation (6–11) now takes the general form

$$\left[ \frac{h_{oi} - h_{ap} - h_p}{h_{wb}} \right]^2 = 1 + 3.46577 \left( \frac{1}{r_{De}} \right)^{0.6} \left( \frac{1}{q_D} \right) \frac{1}{1 + M^{0.7}} \frac{(1 - \lambda)^{1.4}}{(1 - \delta)^{0.4}} \quad (6-13)$$

In a consistent set of units, e.g. SI, the dimensionless group  $q_D$  simply becomes

$$q_D = \frac{q_t \mu_o}{k_h k'_{ro} h_g^2 \Delta\rho} \quad \text{where} \quad \Delta\rho = \rho_w - \rho_o$$

Suppose the material balance calculations have shown that the water–oil contact has risen by an amount  $h_{LZ}$  and the oil column height below perforations is currently  $h_{bp}$ . If the well is flowing at a rate  $q_t$ , then the question arises as to whether it is critical or subcritical. In order to evaluate cone instability, it is convenient to express correlation (6–11) in the alternative form

$$\tilde{q}_{cD} = 39.0633 \times 10^{-4} \left[ \frac{1}{r_{De}} \right]^{0.6} \frac{1}{1 + M^{0.7}} \frac{(1 - \lambda)^{1.4}}{(1 - \delta)^{0.4}} \frac{h_{bp}^2}{(h_{oi} - h_p - h_{ap})^2 - h_{bp}^2} \quad (6-14a)$$

This version applies to SPE units only and the general form is

$$q_{cD} = 3.46577 \left[ \frac{1}{r_{De}} \right]^{0.6} \frac{1}{1 + M^{0.7}} \frac{(1 - \lambda)^{1.4}}{(1 - \delta)^{0.4}} \frac{h_{bp}^2}{(h_{oi} - h_p - h_{ap})^2 - h_{bp}^2} \quad (6-14b)$$

This allows the dimensionless critical rate to be determined for the current value of  $h_{bp}$  and the critical rate follows as

$$\text{(SPE field units)} \quad q_c = \frac{k_h k'_{ro} h_{oi}^2 \Delta\gamma q_{cD}}{887.22 \times \mu_o} \quad \text{or} \quad q_c = \frac{k_h k'_{ro} h_{oi}^2 \Delta\gamma \tilde{q}_{cD}}{\mu_o}$$

$$(SI \text{ units}) \quad q_c = \frac{k_h k'_{ro} h_{oi}^2 g \Delta \rho q_{cD}}{\mu_o}$$

If the actual rate  $q_t$  is less than the critical  $q_c$ , then  $WOR = 0$  and  $q_t = q_0$ , i.e., the cone is stable. On the other hand, if  $q_t > q_c$ , then the cone is unstable and water production is occurring.

From the results of very many simulation runs, Yang and Wattenbarger developed a correlation for the slope of the semilog plot of  $(WOR + c)$  versus  $h_{bp}$ . This takes the form

$$m = -0.015 \left[ 1 + 485.7757 \left( \frac{1}{r_{De}} \right)^{0.5} \left( \frac{1}{\tilde{q}_D} \right)^{0.5} \frac{1}{1 + M^{0.03}} \frac{(1 - \delta)(1 - \lambda)}{h_{oi}^{1.7}} \right] \quad (6-15a)$$

or in alternative dimensionless form

$$m = -0.015 \left[ 1 + 1.44694 \times 10^4 \left( \frac{1}{r_{De}} \right)^{0.5} \left( \frac{1}{q_D} \right)^{0.5} \frac{1}{1 + M^{0.03}} \frac{(1 - \delta)(1 - \lambda)}{h_{oi}^{1.7}} \right] \quad (6-15b)$$

The units of “ $m$ ” in both these forms is  $ft^{-1}$  with  $h_{oi}$  also entered in feet; if heights are in meters, then the correct version is

$$m = -0.049 \left[ 1 + 1.9198 \times 10^3 \left( \frac{1}{r_{De}} \right)^{0.5} \left( \frac{1}{q_D} \right)^{0.5} \frac{1}{1 + M^{0.03}} \frac{(1 - \delta)(1 - \lambda)}{h_{oi}^{1.7}} \right] \quad (6-15c)$$

When the well is in a coning state, the producing  $WOR$  is then estimated from the relation

$$\text{Log}_{10}(WOR + 0.02) = m(h_{bp} - h_{wb}) + \text{log}_{10}(0.02) \quad (6-16)$$

Although this technique was established only for positive values of  $h_{bp}$ , the method continues to predict the  $WOR$  even when  $h_{bp}$  is negative, i.e., the invaded zone has reached the perforations.

The Yang and Wattenbarger procedure is ideally suited to fit into the framework of a material balance study of bottom water drive. In this context, the well total volumetric flow rate  $q_t$  is held constant over a time step conforming to the backward Euler integration scheme. At the end of the time step, the final pressure and invaded zone thickness are computed and the corresponding phase densities  $\rho_1$  and  $\rho_w$ . The test for coning is then made and, if positive, the  $WOR$  corresponding to the current  $q_t$  and  $h_{IZ}$  is determined according to the Yang and Wattenbarger method; this value of  $WOR$  is then used for the next time step. Thus the coning calculations are one-time step in arrears but the error introduced is small for reasonable time steps.

The correlation can also be used to predict WOR for variable rate cases. The prediction is based on the assumption that WOR has no hysteresis, i.e., WOR is a function of current height  $h_{bp}$ , and current production rate and previous production history has no influence on the current WOR. Under such an assumption, the correlations are valid for the variable rate case; only  $h_{wb}$  and slope  $m$  have to be recalculated each time the rate changes.

A sample calculation for a vertical well is shown in figure 6–9, where the solid line represents the WOR calculated from the correlation while the circles are the results from a simulator run with variable rate. The production starts at 2,500 rb/d, decreases to 1,000 rb/d at a height of 42 ft, and then increases to 4,500 rb/d at a height of 21.6 ft. The figure shows that, every time the rate changes, the correlation predicts a more abrupt jump of WOR. However, as time goes on after a rate change, correlation WOR gradually approaches simulation WOR; the difference is due to coning hysteresis.

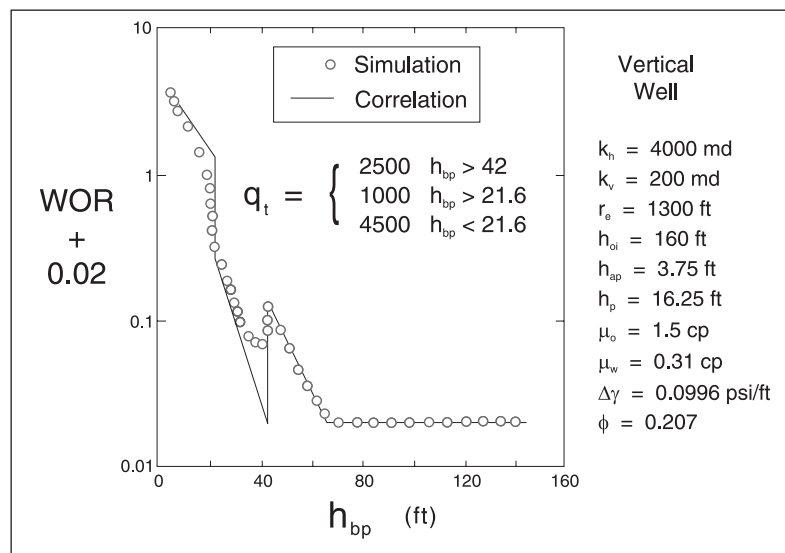


Fig. 6–9. WOR hysteresis analysis for a vertical well

## Synthetic example

A material balance simulation invoking the water coning option was carried out using the parameter values listed in figure 6–10. The initial oil column height is 50 m and the top 20 m of formation are perforated. Water injection in the aquifer was set to yield a balanced bottom water drive and the Yang correlation was employed to fix the producing WOR plotted in figure 6–10. After 65 months of injection, the thickness of the invaded zone has attained 18 m and the oil column height below perforations,  $h_{bp} = 12$  m, is less than the critical value of  $h_{wb} = 12.49$  m. Water production commences at this point and the development of the WOR as  $h_{bp}$  decreases with increase in  $h_{IZ}$  is shown in the plot. Note that the growth of the WOR is gradual, quite unlike the sharp breakthrough encountered in a displacement process. The simulation has been extended to negative values of  $h_{bp}$ , i.e., the material balance water–oil contact (POWC) has risen above the bottom of the perforated interval. In figure 6–11, the cumulative oil and water productions on a volume basis are plotted against time.

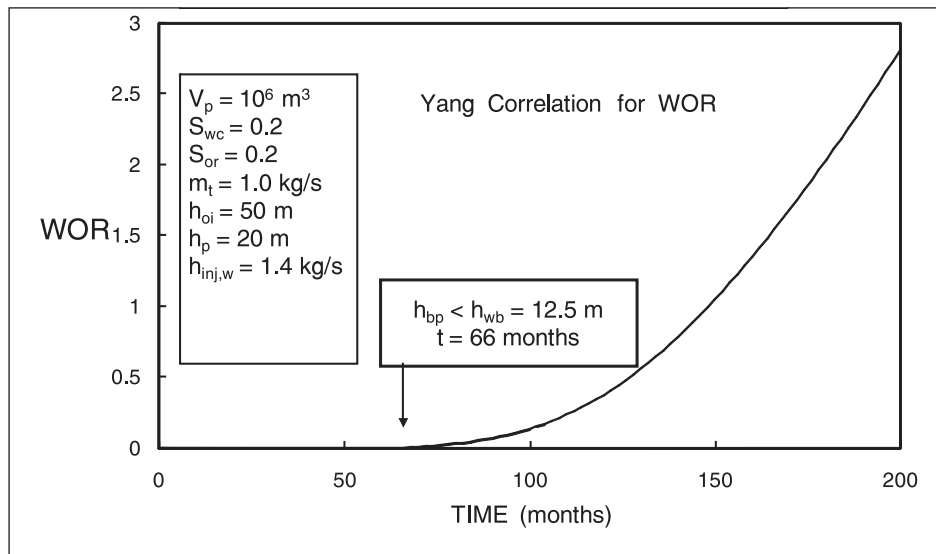


Fig. 6-10. Water-cut development in bottom water drive

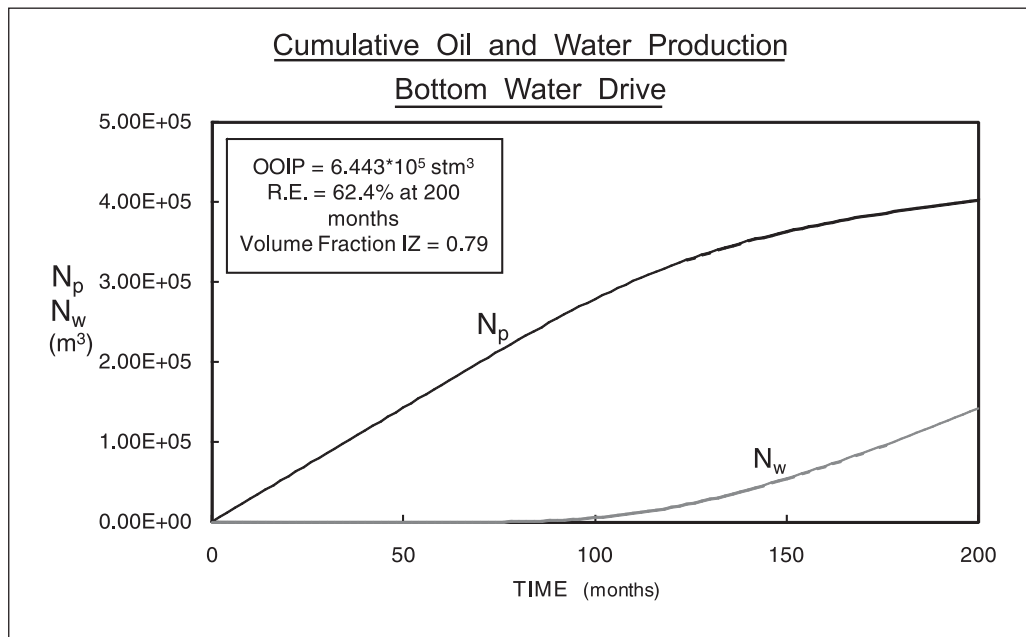


Fig. 6-11. Cumulative oil and water production

A key issue in the understanding of production is the effect of changing the total liquid rate for example by installing an ESP say. In figure 6-12 the preceding coning model was run with a doubling of rate 150 h production; the WOR goes up dramatically and very little extra oil is produced. In figure 6-13 the effect of a recompletion i.e. reducing the open interval from 20 m to 10 m is seen to decrease the water-cut substantially.

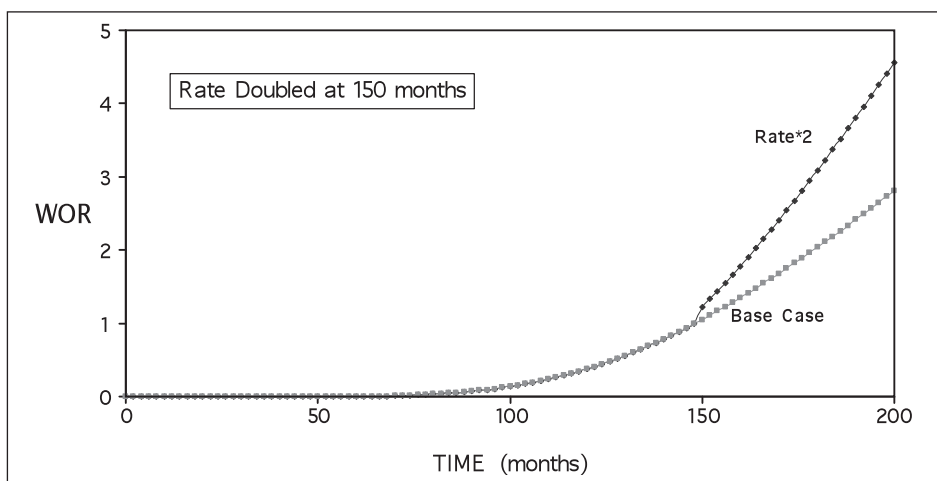


Fig. 6-12. Effect of production rate change on WOR in bottom water situation

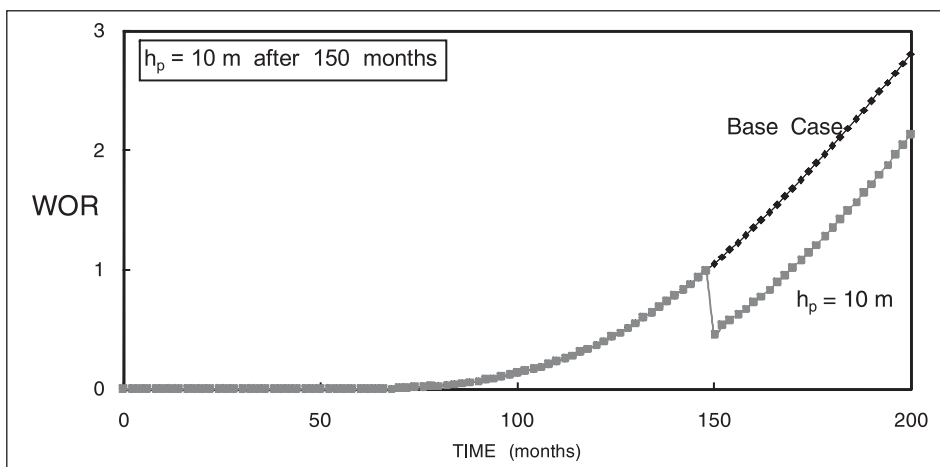


Fig. 6-13. Effect of recompletion on WOR in bottom water situation

## Empirical Displacement Model

### Unit mobility areal sweep

The simplest model of a water drive process is piston displacement in which there is a sharp front between the invading water and the swept oil; this is illustrated for linear flow in a rectangular reservoir in figure 6-14. The movable pore volume,  $V_{pmi} = V_p(1 - S_{orw} - S_{wc})$ , is based on the oil saturation change from  $(1 - S_{wc})$  to  $S_{orw}$  where  $S_{orw}$  is the water flood residual oil saturation. If the cumulative water injection is  $W_e$ , then the movable pore volume injected  $V_{pmi}$  is given by

$$V_{pmi} = \frac{W_e}{V_p(1 - S_{orw} - S_{wc})} \quad (6-17)$$



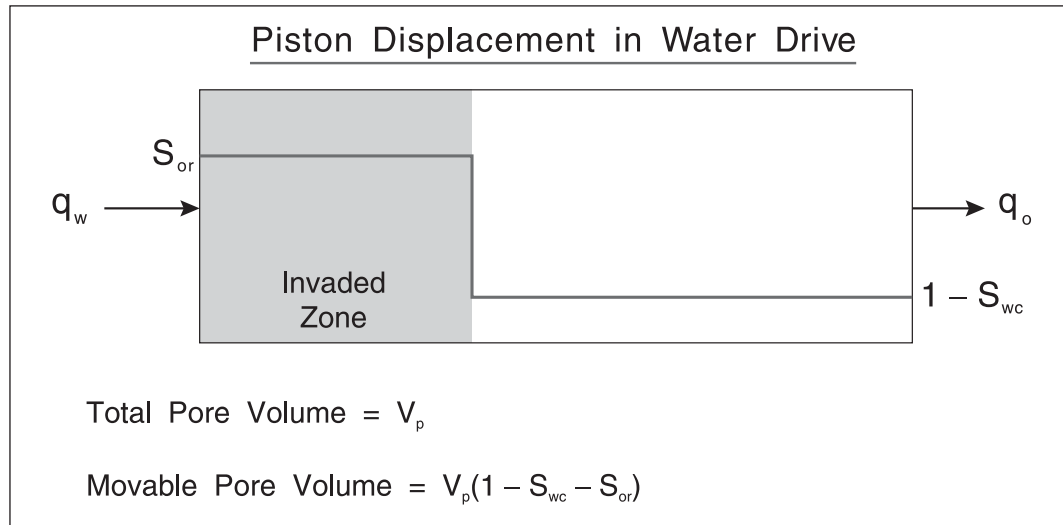


Fig. 6-14. Piston displacement in linear flow

For piston displacement in linear flow, when  $V_{pmi}$  is equal to unity, the producing water-cut jumps instantaneously from 0 to 1.

Consider now the situation shown diagrammatically in figure 6-15, in which an injection and producing well are located in a reservoir which takes the shape of a double circular arc segment of angle  $\alpha$ . Suppose that the fluid injected into the injection well is miscible with the fluid present in the reservoir and has the same viscosity, i.e., single-phase flow is occurring. However, the injected fluid is marked with a tracer such that its proportion in the produced fluid can be monitored. The streamlines for the displacement are shown in the diagram, and breakthrough of the injected fluid is determined by the velocity along the center streamline. There is an exact mathematical solution for the time of travel along each streamline and an equation can be determined relating the fractional flow of injected fluid at the outlet to the cumulative amount injected. This result was given by Banks<sup>3</sup> in 1987 and takes the form

$$V_{pmi} = \left( \frac{2\alpha \sin^2 \alpha}{\alpha - \sin \alpha \cos \alpha} \right) \cdot \left( \frac{\sin \beta - \beta \cos \beta}{\sin^3 \beta} \right) \quad (6-18)$$

where  $\beta = \alpha f_w$

The recovery efficiency in terms of movable pore volumes is given by

$$R_f = \frac{\sin^2 \alpha}{(\alpha - \sin \alpha \cos \alpha)} \left[ \frac{\beta - \sin \beta \cos \beta}{\sin^2 \beta} + \frac{2(\alpha - \beta)(\sin \beta - \beta \cos \beta)}{\sin^3 \beta} \right] \quad (6-19)$$

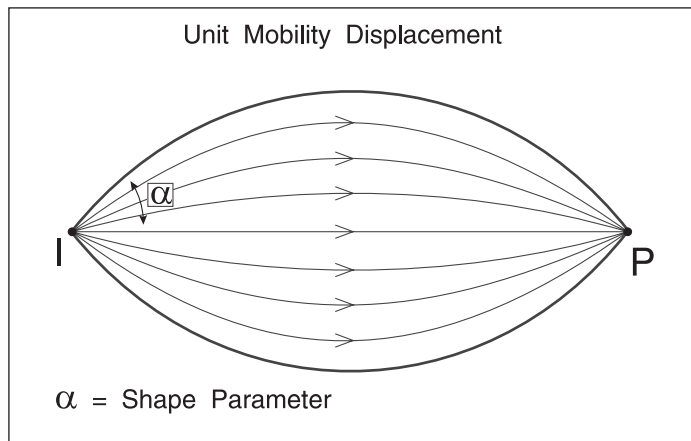


Fig. 6–15. Unit mobility areal sweep in an arc segment

Note that the expression yields  $V_{pmi}$  for a specified  $f_w$  and it is possible to generate a produced water-cut curve by selecting a series of  $f_w$  values and computing the corresponding  $V_{pmi}$  values from Eq. (6–19). Such a graph for  $\alpha = 1.49411$  is shown in figure 6–16, where the water cut is zero up to a value of  $V_{pmi} = 0.69846$  and thereafter water production occurs. The value of  $V_{pmi}$  at breakthrough is a function of  $\alpha$ , and in this case

$$V_{pmi}|_{bt} (\alpha = 1.49411) = 0.69846 \quad (6-20a)$$

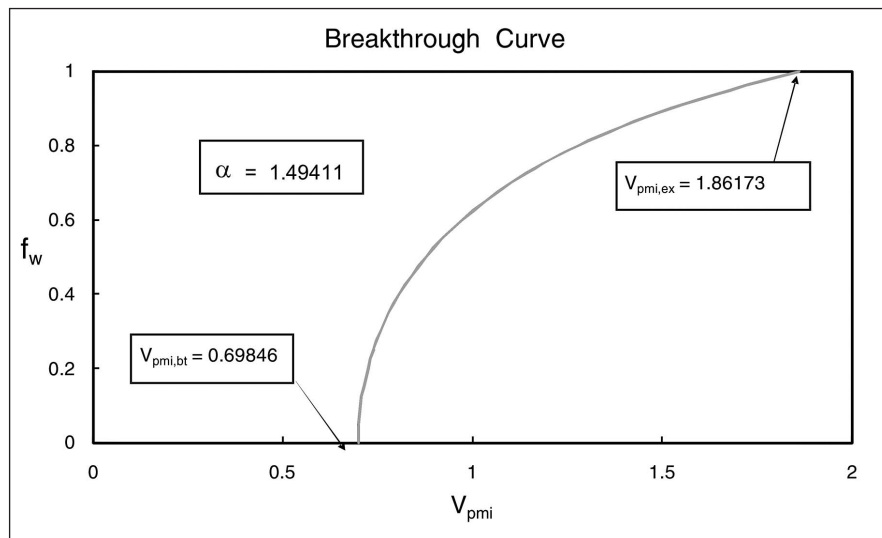


Fig. 6–16. Computed breakthrough curve for  $\alpha = 1.49411$

The quantity  $V_{pmi}|_{bt} (\alpha)$  can be determined by entering Eq. (6–18) with a small value of  $f_w$ , say 0.0001 (but not zero). Similarly, the value of  $V_{pmi}$  at exhaustion (flood out) is also a function of  $\alpha$ , e.g.,

$$V_{pmi}|_{ex} (\alpha = 1.49411) = 1.8617 \quad (6-20b)$$

Here, a value of  $f_w = 0.999$  has been used to determine the movable pore volume injected at exhaustion. The values of these quantities for different values of  $\alpha$  are given in table 6–1.

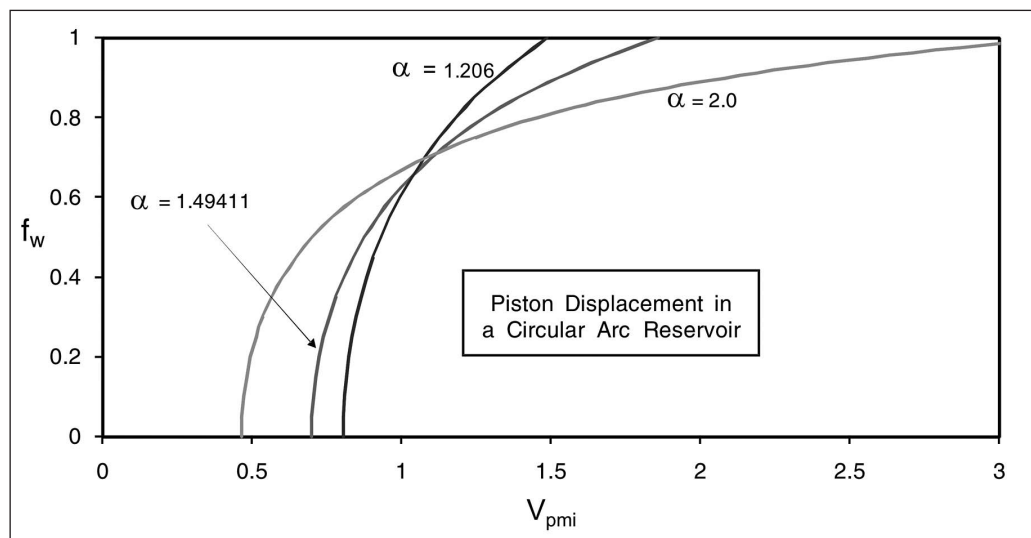
**Table 6–1.** Breakthrough and exhaustion movable pore volumes

$\alpha$	1.49411 (85.6°)	1.5708 (90°)	1.8693 (107.1°)	2.0 (114.6°)
$V_{pmi bt}$	0.69846	0.66666	0.52940	0.46352
$V_{pmi ex}$	1.8617	1.9951	2.7278	3.20566
Ratio, R	2.665	2.993	5.153	6.916

With reference to figure 6–15, the time (or  $V_{mpi}$ ) to breakthrough corresponds to the time of travel along the shortest streamline, while the time to exhaustion corresponds to the time of travel along the longest streamline. If  $\alpha$ —which is designated the shape factor—is small, there is not a large difference and the ratio R defined as

$$R = \frac{V_{pmi|ex}}{V_{pmi|bt}} \quad (6-21)$$

is also small. However, as the angle becomes larger, the contrast in streamline length increases and R becomes larger as indicated in table 6–1. Breakthrough curves for three different values of  $\alpha$  are shown in figure 6–17, where the final  $\alpha$  of 1.206 represents the narrowest reservoir; an angle  $\alpha = 1.5708$  rad (90°), corresponds to a circular reservoir.



**Fig. 6–17.** Effect of shape factor  $\alpha$  on the nature of the breakthrough curve

Displacement curves have been presented in the literature for two important water flooding situations depicted in figure 6–18, i.e., a five-spot and a line drive. The streamlines for single-phase flow in the quadrant of a five-spot are also shown in figure 6–18, and it can be seen by comparison with figure 6–15 how the double circular arc geometry is a reasonable approximation of the five-spot. Banks found that for a value of the shape factor  $\alpha = 86.5^\circ$ , i.e., 1.4941 rad, the fractional flow curve predicted by the circular arc model follows that of a five-spot to within 1% error. Similarly, a square line drive pattern is approximated by an  $\alpha$  value of  $107.1^\circ$ , i.e. 1.8963 rad. The graph of  $f_w$  versus  $V_{pmi}$  will be referred to as a *displacement function*, i.e.,

$$f_w = f^{wD}(V_{pmi}) \quad (6-22)$$

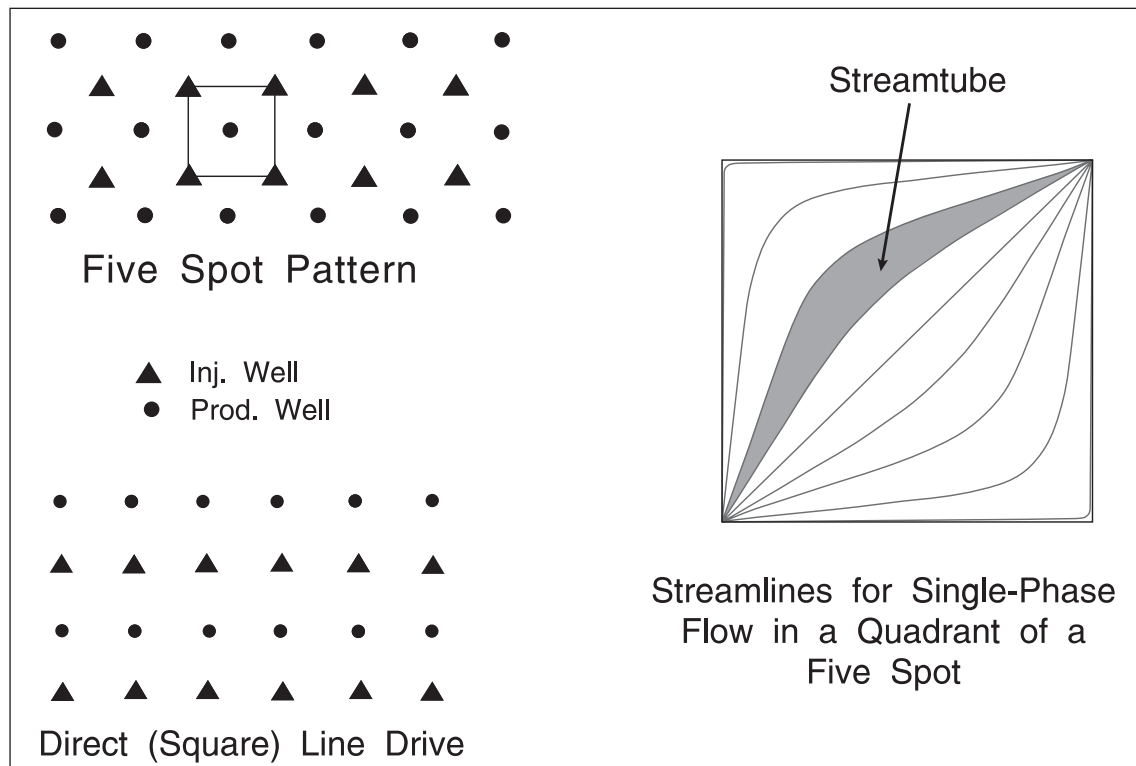


Fig. 6–18. Typical reservoir shapes in water flooding

The Banks correlation is a particular form of displacement function applicable to unit-mobility water flood processes. Since the double circular arc model, i.e., Eq. (6–18) is implicit in  $f_w$ , the function—once generated—is stored as a table which is accessed by linear interpolation.

## Synthetic examples

A balanced waterflood was simulated with a value of  $\alpha = 1.49411$ , which Banks had found to closely model the unit mobility displacement in a five-spot geometry; the reservoir parameters are given in figure 6-19. The fractional flow of water in the producing stream is shown in figure 6–19, where breakthrough occurs after 118 months of injection. The shape of the curve in figure 6–19 is obviously

the same as that in figure 6–16 since time translates directly to movable pore volume injected when the rate is constant. The key point is that the material balance model has generated the producing water-cut using a mechanistic description of the water-drive process. Since the water drive was balanced, the plot of pressure versus time is not of importance.

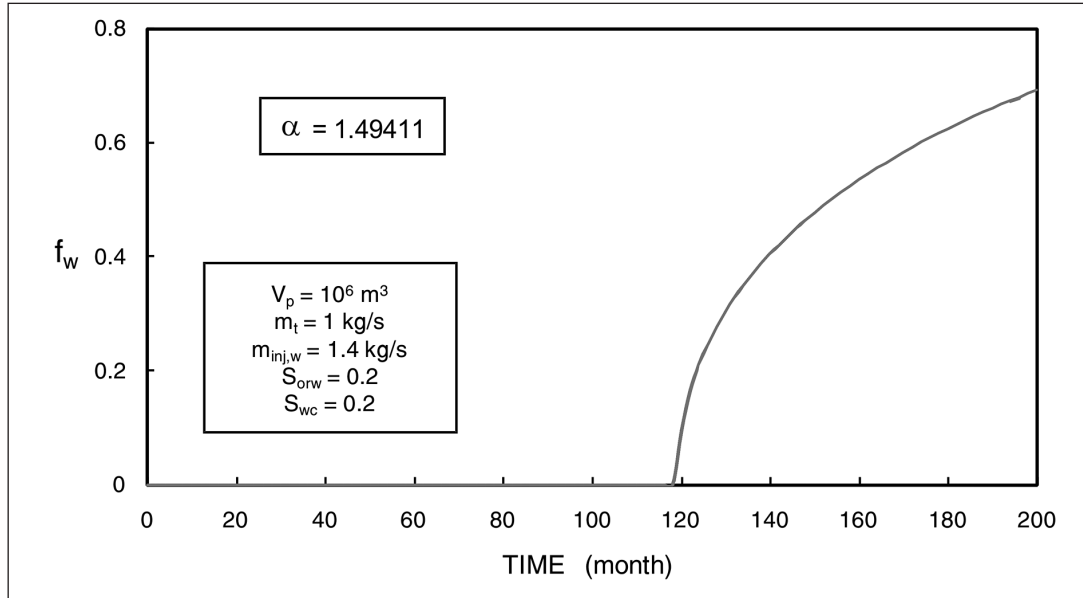


Fig. 6–19. Waterflood simulation based on Banks correlation,  $\alpha = 1.4941$

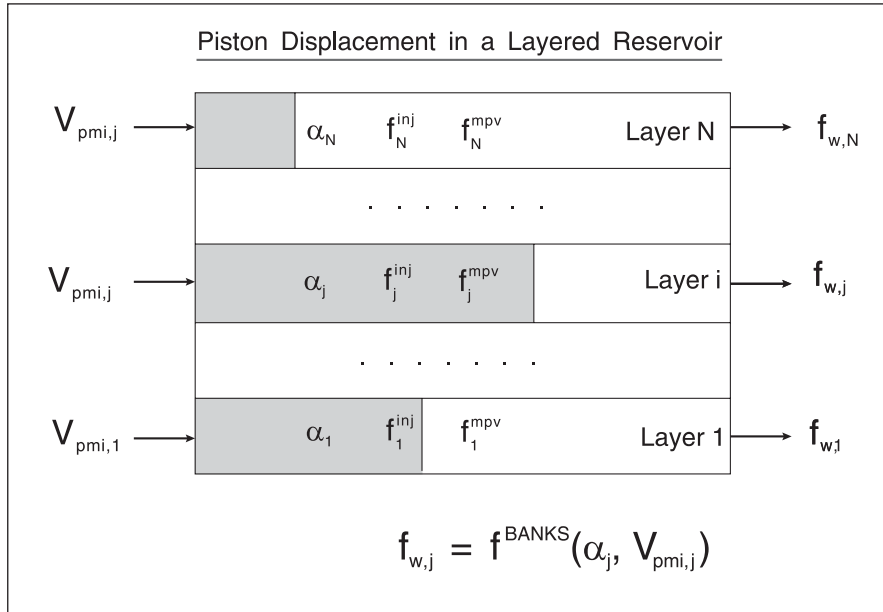
## Layered systems

The outstanding problem of water drive in the North Sea reservoirs, for example, is that of layering in which zones of different properties are flooded in parallel as illustrated in figure 6–20. If the assumption of piston displacement in each layer is made, then this model is associated with the name of Stiles. Suppose the total rate of injection of water is  $q_w$ ; then the basis of the commingled approach is to assume that the fraction of the total water injected which enters layer  $j$  is  $f_j^{\text{inj}}$ . Suppose that the total movable pore volume in the reservoir is  $V_{\text{pm}}$ , given by

$$V_{\text{pm}} = V_p(1 - \bar{S}_{\text{wc}} + \bar{S}_{\text{orw}}) \quad (6-23)$$

where the overbar indicates average value for the layered system. Now suppose that the fraction of the total movable pore volume located in layer  $j$  is  $f_j^{\text{mpv}}$  i.e.,

$$V_{\text{pm},j} = V_{p,j}(1 - S_{\text{wc},j} - S_{\text{orw},j}) = f_j^{\text{mpv}} V_{\text{pm}} \quad (6-24)$$



**Fig. 6–20.** Layered reservoir model for Stiles-type waterflood simulation

Let the total amount of water injected into the system be  $W_e$ , and hence the water injected into layer  $j$  becomes  $f_j^{\text{inj}} W_e$ . The movable pore volume injected into layer  $j$  is therefore given by

$$V_{\text{pmi},j} = \frac{f_j^{\text{inj}} W_e}{f_j^{\text{mpv}} V_{\text{pm}}} \quad (6-25)$$

The fractional flow of water in the stream emanating from layer  $j$  is denoted  $f_{w,j}$  and this is obtained by entering the Banks correlation with the layer shape factor  $\alpha_j$  and the layer movable pore volume injected, i.e.,  $V_{\text{pmi},j}$ ; thus

$$f_{w,j} = f^{\text{BANKS}}(\alpha_j, V_{\text{pmi},j}) \quad (6-26)$$

The fractional flow of water in the combined exit stream follows as

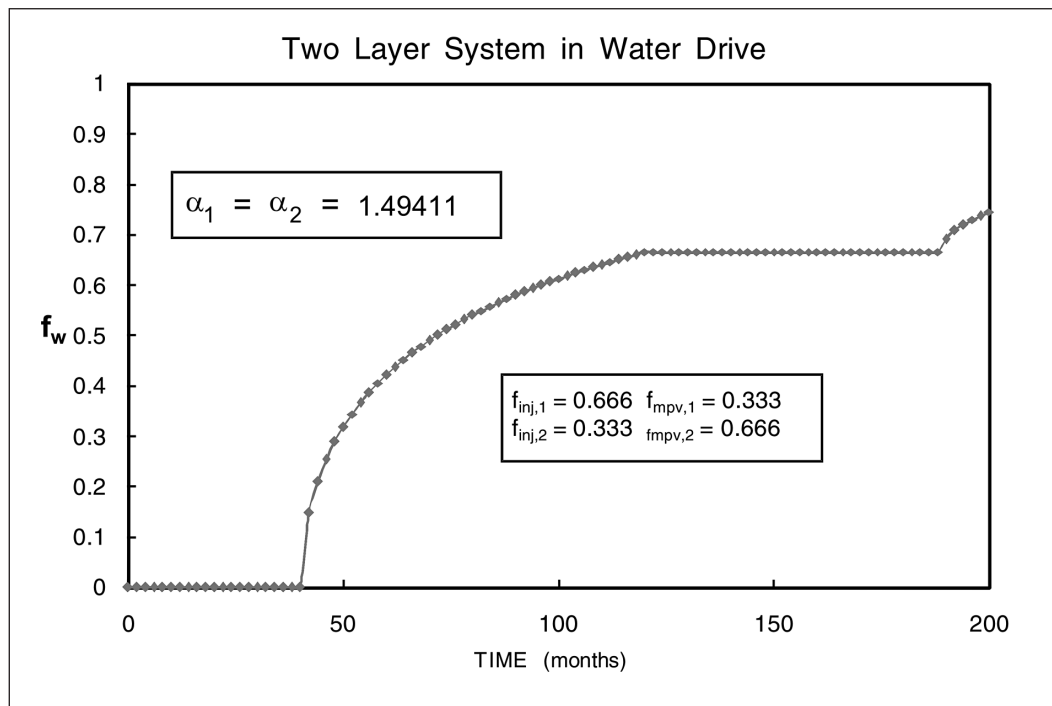
$$f_w = \sum_{j=1}^N f_{w,j}^{\text{inj}} \quad (6-27)$$

In the two-layer case, the fractional flow of water accordingly is fixed by a four-parameter model (since the sum of fractions must add to unity) if the shape factor is different between the individual layers. Note that this model allows for areal sweep efficiency in each layer through the choice of  $\alpha_j$ .

In figure 6–21, the result of a two-layer waterflood simulation is shown where the layer parameters are given in table 6–2.

**Table 6–2.** Layer parameters for two-layer waterflood simulation

Layer	Shape factor, $\alpha$	$f_j^{\text{inj}}$	$f_j^{\text{mpv}}$
1	1.49411	0.6666	0.3333
2	1.49411	0.3333	0.6666



**Fig. 6–21.** Waterflood simulation for two layer system,  $\alpha = 1.4941$

The Banks correlation is limited to unit mobility situations where the displacement is piston-like. For an unfavorable mobility ratio, the fractional flow–movable pore volume curve exhibits a different character. In linear flow, for example, the well-known Welge construction is used to develop the curve of fractional flow versus movable pore volumes injected. Figures 6–22a and b show an example of a displacement function generated by the Welge method and are taken from the textbook by Dake (exercise 10.2, table 10.5). These curves exhibit the shock front of the Buckley–Leverett problem and cannot be fitted by the Banks model which represents an areal sweep effect rather than a one-dimensional displacement. Note, however, that all real reservoirs will exhibit areal sweep effects.

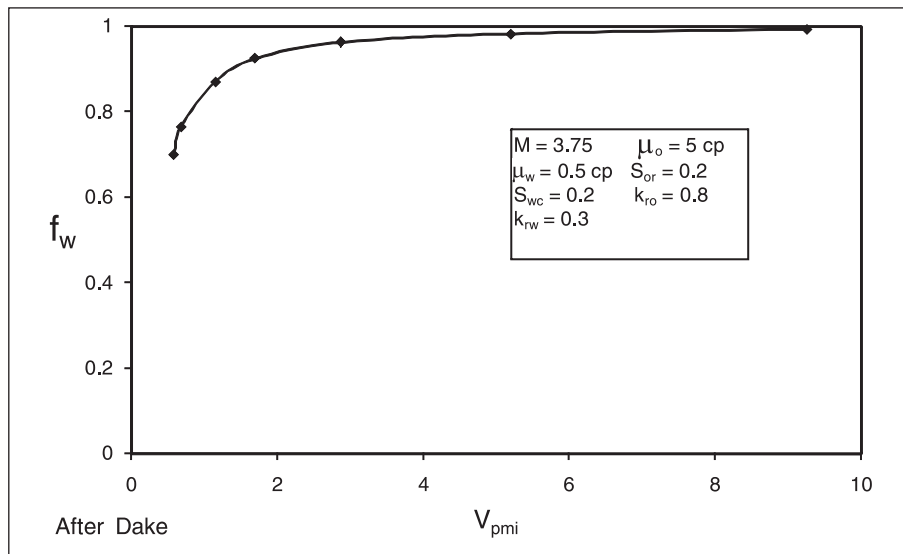


Fig. 6–22a. Linear flow displacement function from the Welge construction (Dake)

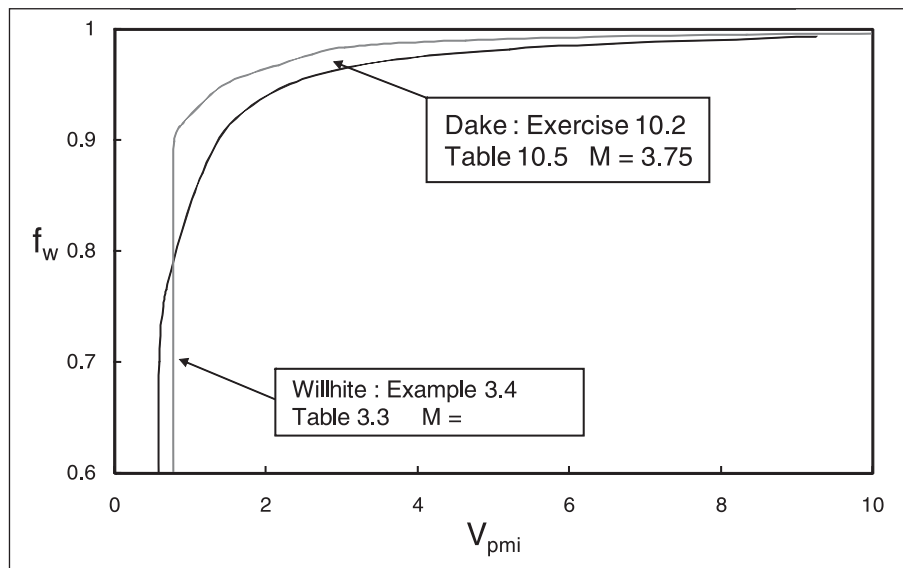


Fig. 6–22b. Linear flow displacement function from the Welge construction (Willhite)

Figure 6–18 illustrates the device of a streamtube along which an essentially one-dimensional displacement takes place; this idea was introduced by Higgins and Leighton,<sup>4</sup> who showed how the one-dimensional behavior associated with fractional flow theory can be combined with the areal sweep performance to yield the overall displacement function  $f_w^D$ . In figure 6–23, a displacement function resulting from a streamtube calculation for a five-spot is shown; this is example 4.4, table 4.7 in the textbook by Willhite.<sup>5</sup> The step in this response is due to the small number of streamtubes employed with near piston displacement in each one. The central stream tube breaks through first and then the adjacent ones break through a short time later because of their longer path.



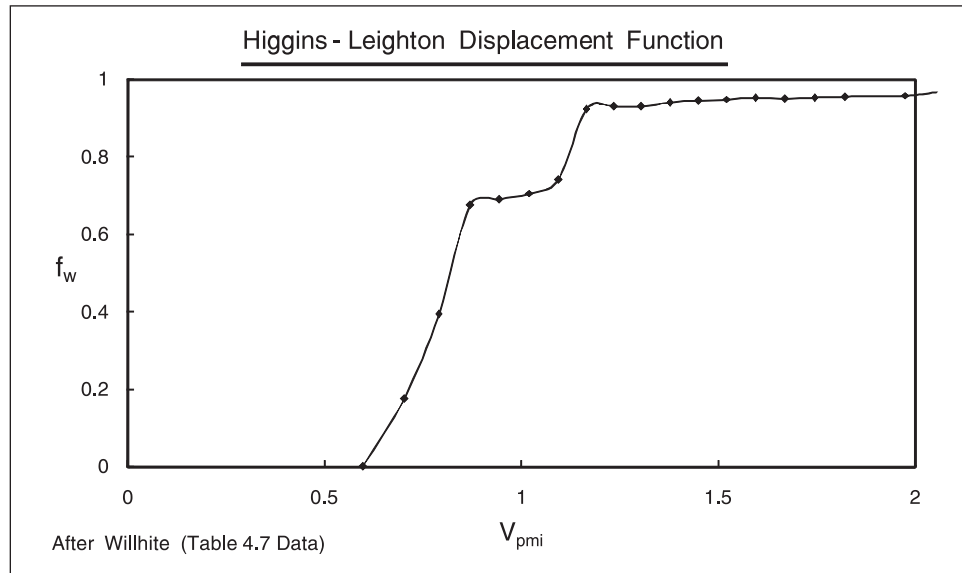


Fig. 6-23. Five-Spot areal flow displacement function from streamtube calculations

In the material balance program, the displacement function is stored as a table and linear interpolation is used as table lookup. This table can originate from the Banks correlation or it can be simply input as data. This allows the displacement function to be generated by any of the methods routinely used in waterflood design and then used in the context of a material balance study. Thus a modern streamtube simulator, such as FRONTSIM, can be used to generate a displacement function which is then utilized into the material balance program. In this way, the mechanistic behavior of the water displacement process is incorporated into the material balance model.

The displacement function  $f_w^{wD}$  has the property of an eventual approach to a limiting value of  $f_w = 1$ . A rectangular hyperbola of the form

$$(y - a)(x - b) = c \quad (6-28)$$

has this property of asymptotically approaching the limiting value  $a$ . Hence a possible approximation for the form of the displacement function is

$$(f_w - 1)(V_{pmi} - b) = c \quad (6-29)$$

where the combination  $b - c$  is associated with  $V_{pmi}|_{bt}$  and the second parameter  $c$  controls the shape of the function. Thus Eq. (6-29) is a two-parameter form which could be fitted to displacement functions generated by a streamtube simulator. Alternatively, in the history matching mode, this form may be assumed for the displacement function and the parameters  $b$  and  $c$  found by non-linear regression. This is a completely empirical approach to the tuning problem. In figure 6-24, a rectangular hyperbola has been fitted to Banks function for  $\alpha = 1.49411$ , and it can be seen that the approximation has a much more pronounced “tail” than the analytical  $f_w^{wD}$  function. However, the Banks model is for piston displacement only, and

$f^{wD}$  functions based on Buckley–Leverett theory along streamtubes exhibit more dispersion. Hence the rectangular hyperbola approximation is worth pursuing as an empirical model, the parameters of which are determined by regression.

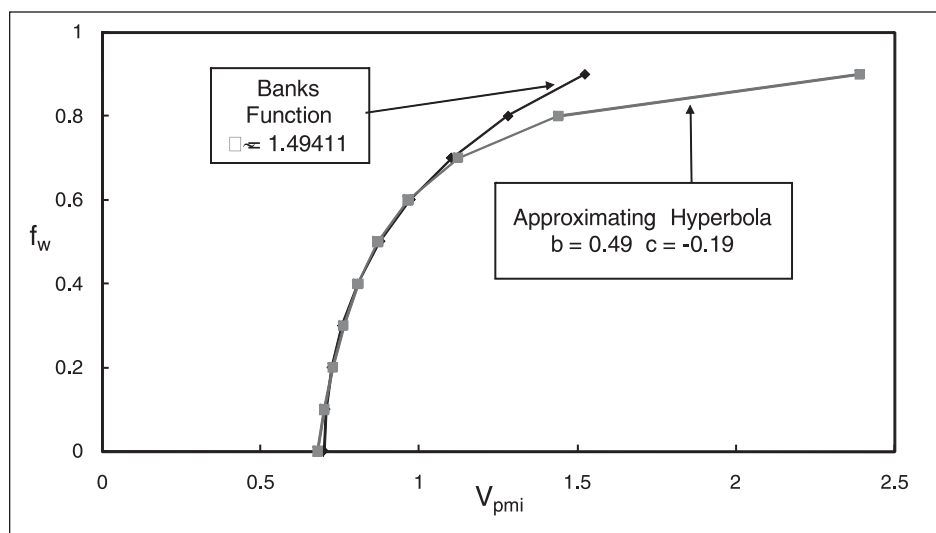


Fig. 6–24. Overlay of banks function with a rectangular hyperbola

In the water flooding literature, nearly all published displacement functions are for vertical well patterns and there is a need to develop such information for horizontal well situations. There is therefore a requirement to build up a library of dimensionless displacement functions (“ $f^{wD}$  type curves”) which can be called by the material balance program. Suppose a given reservoir situation suggests that a particular displacement curve is appropriate for the mobility ratio and well layout. However, the material balance model does not reproduce the actual field WOR data. In order to tune the displacement function to the measured water-cut behavior, some rational method of altering the form of the function would be required. An alternative approach might be a cubic spline approximation to the  $f^{wD}$  function.

## Waterflooding below the bubble point

In the synthetic example given in the section “Addington Gas Coning Model for Vertical Wells,” the water injection rate into the aquifer was balanced, i.e., the reservoir pressure was increasing slightly and the oil zone pressure did not fall below the bubble point. In this situation, the displacement is very close to incompressible flow and no free gas is present in the reservoir. However, there is no problem in handling underbalanced water drives where the pressure is allowed to fall below the bubble point. The only modification to the model is allowance for the effect of a gas saturation, by defining movable pore volume injected as

$$V_{pmi} = \frac{W_e}{V_p(1 - S_{orw} - S_{wc} - S_g^{OZ})} \quad (6-30)$$

The presence of a trapped gas saturation at the time residual oil is trapped by water has a substantial effect on the residual oil saturation in a preferentially water-wet rock.<sup>6</sup> In consolidated, water-wet rock, a trapped gas saturation reduces the residual oil saturation and the magnitude of this effect may be estimated from figure 6–25 (after Willhite). Richardson and Perkins<sup>7</sup> show much smaller effects of gas saturation on residual oil saturation in unconsolidated sand. A change of 2% saturation was detected between waterfloods conducted with no initial gas saturation and those with an initial gas saturation of 25%. Oil-wet rocks have not been studied extensively, but available data from dri-filmed alundum cores indicate no effect of trapped gas on residual oil saturations. The correlation represented by figure 6–25 can be built into the material balance program such that the input value of  $S_{orw}$  is decreased if oil is trapped with a concurrent gas saturation.

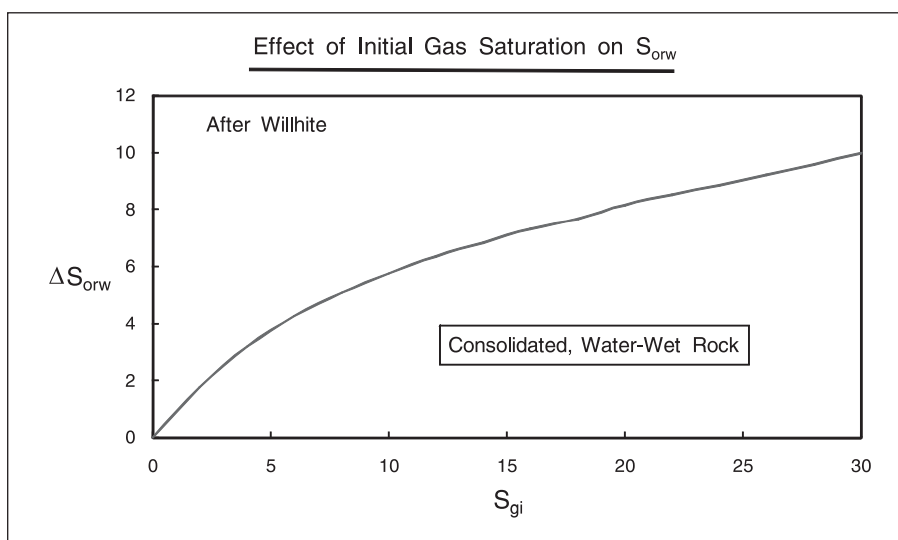


Fig. 6–25. Effect of initial gas saturation on waterflood recovery

## Multiple well situations

The preceding theory has been developed without reference to the number of wells in the reservoir and is therefore applicable to the system overall performance. In the case of the coning mechanism, it was possible to consider the behavior of individual wells since the completion, defined through  $h_p$ ,  $k_h$ , and  $k_v$ , for example, can be different in each case. Since coning is a local well phenomenon, it is possible to specify the process on a well-by-well basis. However, the material balance model only allows one present oil–water contact (POWC) which is the same for all wells; this is the limitation of a “tank” model. In the history matching mode, the production data is known on a well-by-well basis or as a field total. Note that the field total is usually measured directly as the process separator output, but individual well rates are determined by allocation. This allocation is made on the basis of well tests, i.e., periodically diverting the flow from a well through the test separator and measuring oil, gas, and water flows. Here the terminology “field total” may, in fact, refer to a reservoir compartment since the material balance may be applied to noncommunicating fault blocks. The process of allocation therefore occurs at two levels—compartment and individual wells—as illustrated in figure 6–26. The total rates from the process separator are superscripted “SEP” while the overall rates from a compartment

are superscripted “k”. Although, the volumetric rates at standard conditions are indicated on the diagram, proper combination of streams on a mass (compositional) basis is implied.

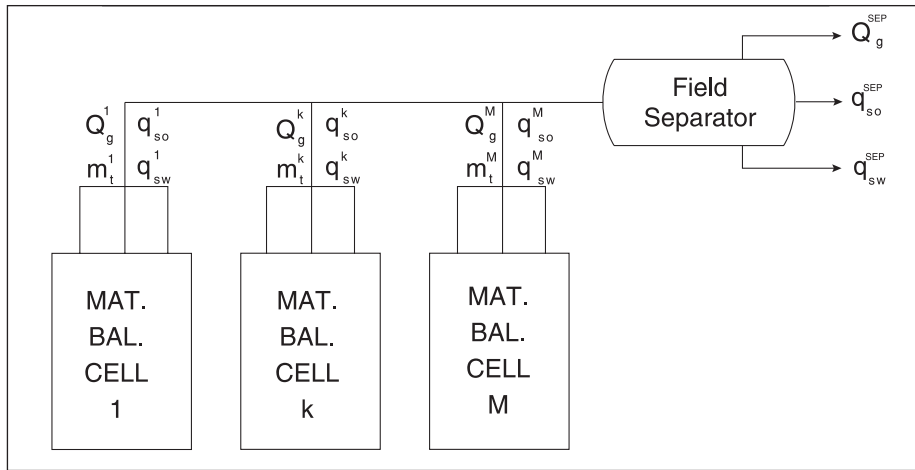


Fig. 6–26. Problem of allocation to compartments and individual wells

In the waterflood situation, some regular pattern of wells such as a five-spot or line-drive is assumed and each production well has an associated drainage area. In the history matching mode, the individual well rates can be recombined to give the block overall performance and this can be made the basis for the matching process. However, part of the tuning process is to adjust the parameters of the individual well models to allow a match to the actual well rate and flowing bottom-hole pressure. In depletion, the concept of a Dietz drainage area allows the total reservoir (fault block) to be apportioned on a well-by-well basis. In water drive, a similar apportionment of the total pore volume can be made, i.e., in proportion to the cumulative liquid production from a producing well as a fraction of the total.

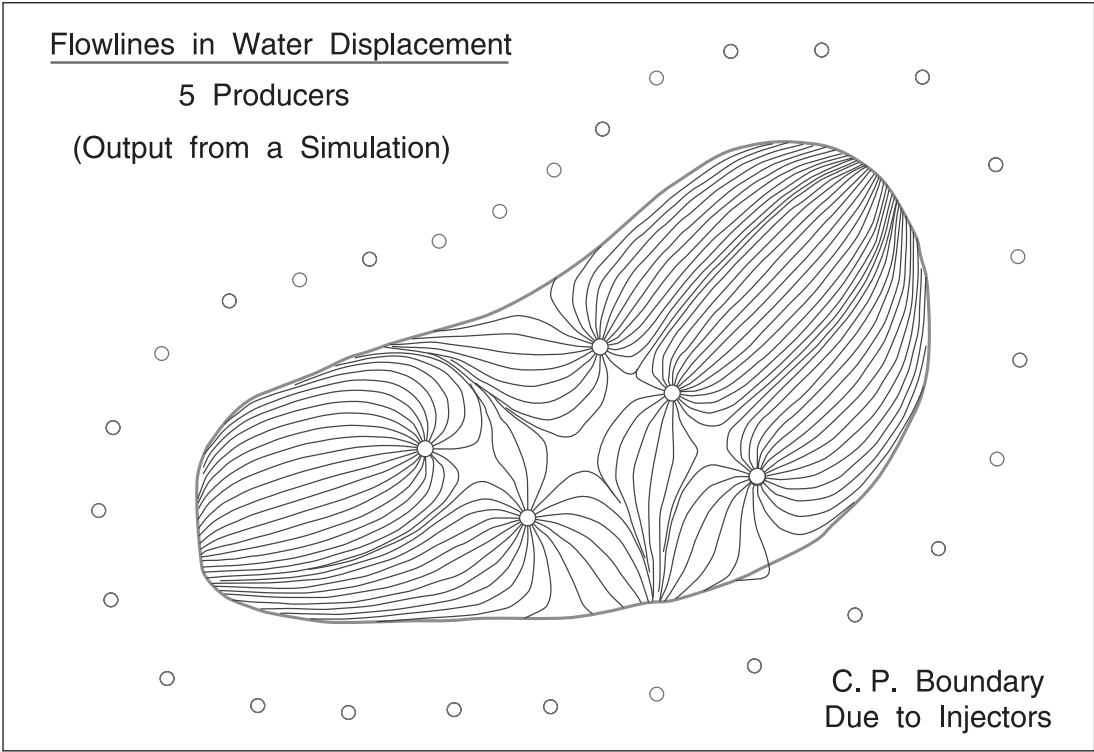
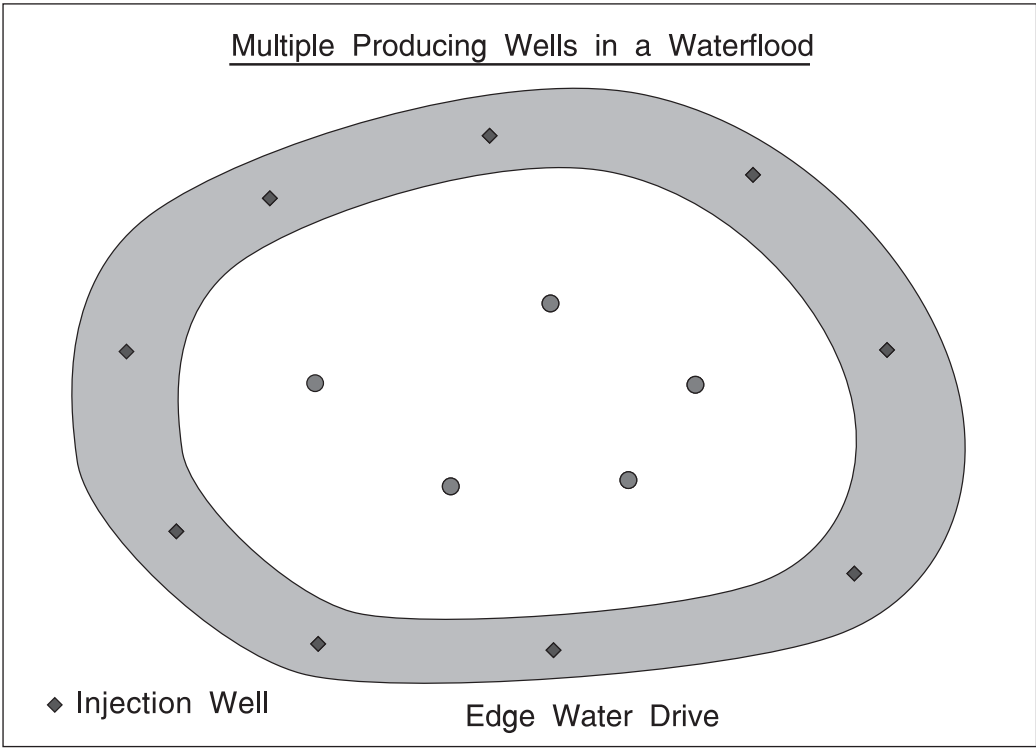
A multiple well situation is depicted in figure 6–27a, b, and c, where the swept areas associated with a well are approximately proportional to the cumulative production from a well as a fraction of the total cumulative production. Thus in a manner analogous with Dietz drainage areas in primary production, the following prescription may be made:

$$\frac{V_{pm}^k}{V_{pm}} = f_{sw}^k \quad (6-31)$$

where  $V_{pm}$  = total reservoir movable pore volume (MPV),

$V_{pm}^k$  = displacement volume associated with well k, and

$f_{sw}^k$  = fraction of total MPV swept to well k.



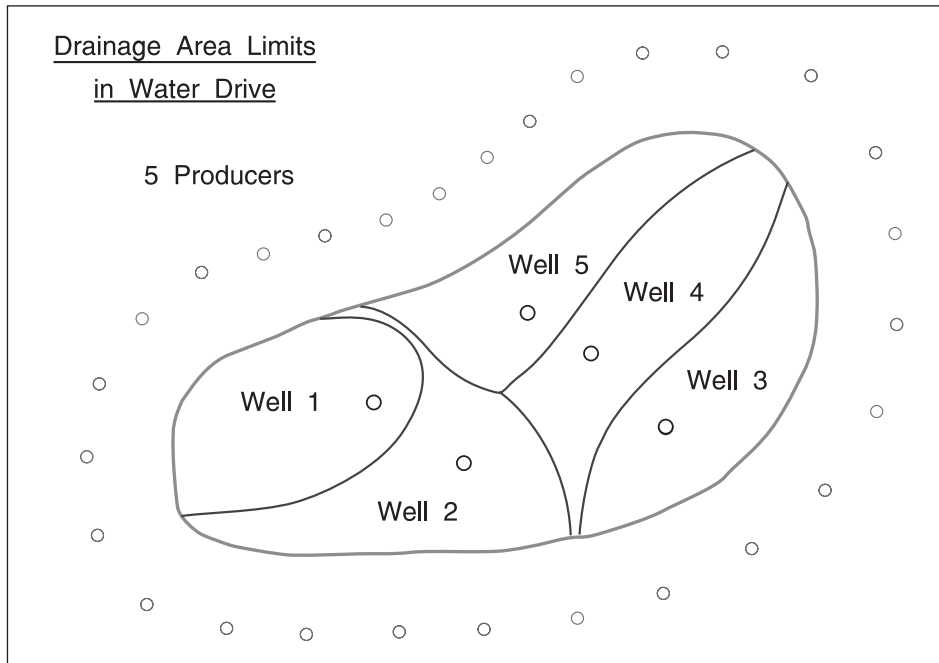


Fig. 6-27a, b, and c. Multiple producing wells in a waterflood

In a balanced waterflood situation, the volume of liquid (oil plus water) produced from the swept area will be equal to the volume of water entering and the movable pore volume produced is given by

$$V_{pmi}^k = \frac{Q_1^k}{V_{pm}^k} = \frac{Q_1^k}{f_{sw}^k V_{pm}^k} \quad (6-32)$$

where  $Q_1^k$  = cumulative production of liquid from well k.

The quantity  $V_{pmi}^k$  is used to enter the Banks correlation and the fractional water flow of well k is obtained; this is denoted  $f_w^k$ , i.e.,

$$f_w^k = f_w^k \left\{ V_{pmi}^k \right\} \quad (6-33)$$

In this mode, the water-cut development differs from well to well which results in a more realistic model of the water-flooding process. In particular, the measured water production from each well can be matched individually, which will allow a better forecast of that wells' behavior. Adjustment of the swept volume factor, i.e.,  $f_{sw}^k$ , allows the time to breakthrough of a given well to be controlled, while the shape factor, i.e.,  $\alpha^k$ , controls the water-cut development after breakthrough. Note that the layering option is still available for each well, giving more latitude in the matching of the measured water-cut data. In figure 6-28, the water-cut development of a two-well reservoir, each produced at a rate of 0.5 kg/s, is shown with the second well breaking through much earlier than the first because its fractional swept volume is smaller; in this example, only one layer is present in each well.

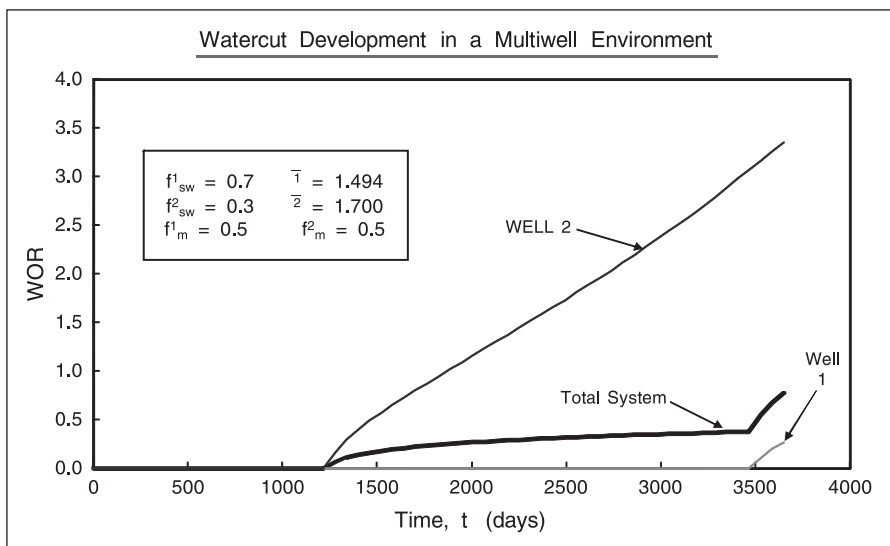


Fig. 6–28. Water-cut development in a two well system

## Matching field water-cut data

The combination of the Banks correlation and the layered reservoir formulation allows water drives to be modeled with a significant degree of flexibility. One reason for introducing the Banks model was to allow field water-cut data to be fitted in the history matching mode. For example, the two-layer version involving four parameters, i.e.,  $\alpha_1$ ,  $\alpha_2$ ,  $f_1^{inj}$  and  $f_1^{mpv}$  may be sufficient to give a fit to WOR data. In this exercise, the material balance model is driven by a nonlinear regression routine which will search for parameter values to minimize a sum-of-squares objective function.

## Notes

1. Addington, D. V. "An Approach to Gas Coning Correlations for a Large Grid Cell Reservoir Simulator," *JPT* 33 (11), (Nov. 1981): 2267–2274.
2. Yang, W., and Wattenbarger, R. A. "Water Coning Calculations for Vertical and Horizontal Wells" SPE 22931, (66th Annual Technical Conference, Dallas, Tx, 1991).
3. Banks, D. Internal Britoil Memo (1987).
4. Higgins, R.V., and Leighton, A. J. "A Computer Method of Calculating Two-Phase Flow in Any Irregularly Bounded Porous Medium," *JPT* 14 (6), *Trans.A.I.M.E.* 267, (June 1962): 679–683.
5. Willhite, G. P. "Waterflooding", SPE Textbook Series, Vol. 3 (1986).
6. Kyte, J. R. *et al.* "Mechanism of Water Flooding in the Presence of Free Gas," *Trans AIME* 207, (Sept. 1956): 215–221.
7. Richardson, J. G., and Perkins, F. M. "A Laboratory Investigation on the Effect of Rate on the Recovery of Oil by Waterflooding," *Trans AIME* 210, (April 1957): 114–121.

# 7

## Decline Curve Analysis

---

### Introduction

Rate-time decline curve extrapolation is one of the oldest and most often used tools of the petroleum engineer. The various methods used have always been regarded as strictly empirical and generally not scientific. However, the work of Fetkovich in particular has shown that there is a good theoretical basis for decline curve analysis and that there is, in fact, a strong relationship to well test interpretation particularly extended draw-down or reservoir limit testing. Well test analysis has focused on constant rate situations and various algorithms have been devised for analyzing variable rate situations. Generalized superposition can be used, for example, to allow transient data to be converted to a form that is analogous to the constant rate drawdown case. At a higher level, the process of deconvolution has also been examined, which converts variable-rate data to equivalent constant-rate form for analysis. The numerical deconvolution algorithm can also be used to convert variable-rate data to constant bottom-hole pressure equivalent where the rate is presented as a declining function of time. Decline curve analysis is closely related to constant-pressure solutions to the diffusivity equation. The production constrained convolution described in chapter 3 is a unique form of decline curve prediction that incorporates information on the formation through the parameters of a model and the tubing vertical lift performance. Note that if the model involves a closed-system outer boundary condition, then a transition between semi-infinite-acting behavior and semi-steady-state (SSS) depletion will occur. Similarly, any decline curve analysis will distinguish between the two types of behavior. Although SSS is strictly a phenomenon pertaining to constant rate conditions, a quasi-semi-steady-state (QSSS) will develop in a closed system when the rate is in monotonic decline.

Decline curve analysis is synonymous with the interpretation of production data and it is interesting to observe that it is particularly in low-permeability reservoirs that the conditions are such that the well is produced essentially at a fixed bottom-hole pressure. In such cases, any transient or depletion behavior will be manifested in the rate variation. However, the variable-rate methods already described in chapter 5 of *Well Test Design and Analysis* are entirely adequate to handle rate decline at nearly constant wellbore pressure; rate normalization with specific superposition time functions, convolution of various reservoir models, or full deconvolution can be employed to analyze data and make predictions of future performance.



In order to restrict the range of techniques used to analyze data, it is recommended here to adopt the strategy of converting variable rate situations to a form which corresponds to the constant-rate case. It is perfectly possible to implement the alternative strategy of converting models and data to constant wellbore pressure equivalent and then using specialized plots and log-log type curve matches for interpretation of rate transients. This latter approach has been proposed by Fetkovich et al.<sup>2</sup> in an excellent study of production and test data from a wide variety of wells and fields. For the reason given above, constant-pressure type curves will not be presented here, but the paper by Fetkovich et al. on this topic is certainly one of the best papers on reservoir engineering ever written. Many of the field examples cited in the paper refer to low-permeability reservoirs with fractured wells and the authors point out that the traditional decline curve analysis based on the empirical Arps form should never be applied to transient, i.e., semi-infinite-acting, data! It is ironic that the main source of constant-pressure production data is in such tight systems but that the traditional decline curve analysis for depletion is inappropriate for transient conditions. The onset of depletion is recognized by the unit slope on the logarithmic derivative diagnostic in drawdown. Fetkovich et al. emphasized that extended drawdown data are often more valuable than build-up data in low-permeability systems because the duration of a buildup is not long enough (constrained by deferred production economics) to show up late time effects. The production mechanism as affected by such phenomena as aquifer influx, reservoir compartmentalization, or support from very low permeability matrix in a fractured reservoir is best identified by interpretation of extended drawdown, i.e., production data. Buildups are still important in the determination of permeability and skin and the principle of reciprocity expounded in chapter 4 of *Well Test Design and Analysis* is important in the correct analysis of the variable rate flowing period. Fetkovich also pointed out (in 1984) that the problem of analyzing production data is the poor quality of the rate data and this remains true today. When variable rate data are analyzed, for example using the rate-normalized pressure drop  $\Delta p/\Delta q$ , it must be recognized that error in rate measurement causes considerable noise in the functioned data. It may therefore be impossible to use derivative diagnostics that have been so useful in build-up analysis; smoothing techniques are notoriously difficult to apply without losing information, but the successful analysis of production data may well be dependent on some judicious smoothing and adjustment of rate data. This problem has already been addressed in connection with slug testing which is, of course, a variable-rate situation. Improvement in pressure transducer technology now allows the deployment of permanent downhole pressure gauges, but the use of such information is crucially limited by the quality of the rate data that must also be gathered simultaneously. Much more attention has to be paid to production monitoring systems which gather and store high-quality rate data; the rate measurement ideally should be carried out downhole, but in the case where only surface rate is available, particular attention to quality should be given. Traditionally, the rate information has been expressed in volumetric terms, whereas in practice mass rate is more fundamental and useful. With the increasing application of high-performance mass flow meters for surface measurements, the use of mass flow rates will hopefully blossom.

In production engineering, decline curve analysis is also used to extrapolate the performance of wells in water flooded reservoirs. In this situation, the oil rate is decreasing with time due to the progressively increasing water-cut. This is an entirely different situation from declining oil rate due to the depletion of the average pressure of reservoir compartments, and the application of decline curve analysis to water breakthrough phenomena will not be considered here.

## Constant Wellbore Pressure Testing

The transient behavior of a well operating at constant bottom-hole pressure is analogous to that of a well flowing at constant rate. Constant bottom-hole pressure production is illustrated in figure 7–1 and the rate is seen to decline as the pressure disturbance propagates out into the system. It is difficult to produce wells at constant bottom-hole pressure, but wells under artificial lift, for example, may well flow at a condition approximating this form. Gas wells in low-permeability reservoirs also produce essentially at a fixed bottom-hole pressure and the rate exhibits time variation.

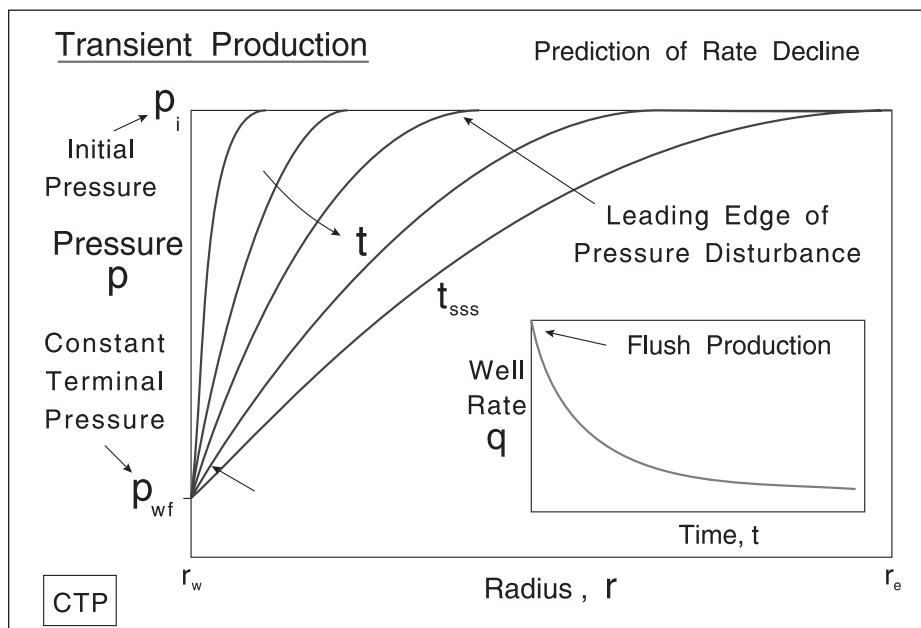


Fig. 7–1. Schematic of rate and pressure histories in a constant pressure test

For infinite-acting radial flow, the variation of the well rate with time can be expressed in dimensionless form using the groups

$$q_D = \frac{\mu q(t)}{2\pi kh(p_i - p_{wf})} \quad \text{and} \quad t_D = \frac{kt}{\phi\mu c_t r_w^2} \quad (7-1)$$

where  $p_i$  is the reservoir pressure and  $p_{wf}$  is the specified bottom-hole pressure. Jacob and Lohman<sup>1</sup> have demonstrated that the analytical solution to the diffusivity equation for the constant wellbore pressure inner boundary condition takes the following form at long times:

$$q_D = \frac{2}{\ln \frac{4t_D}{\gamma} + 2S} \quad (7-2)$$

This, of course, may be written in field units in the form

$$q_s(t) = J_t (p_i - p_{wf}) \quad (7-3)$$

where

$$J_t = \frac{2\pi kh}{887.2B\mu \left( \frac{1}{2} \ln \frac{0.0002637 \times 4kt}{\gamma\phi\mu c_t r_w^2} + S \right)}$$

which simply confirms that constant-pressure production with  $(p_i - p_{wf})$  fixed can be modeled by a transient productivity index with total time  $t$  entering the logarithmic term. The error in (7-2) is only 1% when  $t_D > 8 \times 10^4$  and the transient rate decline follows a model of the form

$$q_s(t) = \frac{a}{\ln t + b} \quad (7-4)$$

where

$$a = \frac{4\pi kh(p_i - p_{wf})}{887.2B\mu} \quad \text{and} \quad b = \ln \frac{0.0002637 \times 4k}{\gamma\phi\mu c_t r_w^2} + 2S$$

On the basis of Eq. (7-4), a specialized plot of  $\frac{1}{q_s(t)}$  versus  $\ln t$  will be a straight line of the form

$$\frac{1}{q_s(t)} = m_q \ln t + b_q \quad (7-5)$$

where

$$m_q = \frac{1}{a} = \frac{887.2 \times B\mu}{4\pi kh(p_i - p_{wf})}$$

and

$$b_q = \frac{b}{a}$$

as defined above. Permeability  $k$  may therefore be determined from the slope and the skin factor  $S$  from the intercept of such a plot.

The main point of this analysis is to point out that data in transient rate decline following a model of the form (7-4) cannot be fitted to an empirical model of the Arps-type described in the next section. This has been forcefully put by Fetkovich et al.<sup>2</sup> in their definitive study of decline curve analysis using type curves. Variable-rate data in the transient regime is probably best analyzed using the techniques developed in chapter 5 of *Well Test Design and Analysis*, where the rate-normalized pressure drop  $\Delta p/q$  is plotted versus a superposition time function  $f_t(t)$ ; this approach avoids the unnecessary duplication of type curves and specialist plots for

the constant-pressure case. Note that the deconvolution algorithm discussed in chapter 5 of *Well Test Design and Analysis* can also convert constant wellbore pressure data to constant rate equivalent. Real drawdown data are neither constant rate nor constant bottomhole pressure; these are simply two limiting cases for which theoretical results can be derived. It is convenient to base interpretation methods on the constant-rate situation because of the importance of buildups in well testing.

## Semi-infinite behavior

It is quite possible in the constant wellbore pressure model to postulate the presence of no-flow boundaries such as sealing faults and to define semi-infinite flow regimes just as in the constant-rate case. The principle of superposition is still applicable and image wells may be used to simulate the effect of simple fault systems. In the context of decline curve analysis, it is very important to ascertain when data are in an infinite or semi-infinite transient regime and should be analyzed by conventional variable-rate welltest analysis techniques. Only data that correspond to depletion should be used in decline curve analysis; this point will be emphasized in later sections. The key issue is predicting the end of semi-infinite behavior and the onset of a closed system response. A dimensionless time based on the distance to the far boundary is the basis of the condition for the effect of the closing boundary being felt; this is illustrated in figure 7–2. The end of semi-infinite-acting (SIA) flow is given by the equation

$$\frac{kt_{sia}}{\phi\mu c_t L_f^2} = 0.2 \quad (7-6)$$

In low-permeability reservoirs, the duration of this flow period may be very long indeed and decline analysis and forward prediction should be based on transient techniques as discussed in chapter 3 of *Well Test Design and Analysis*.

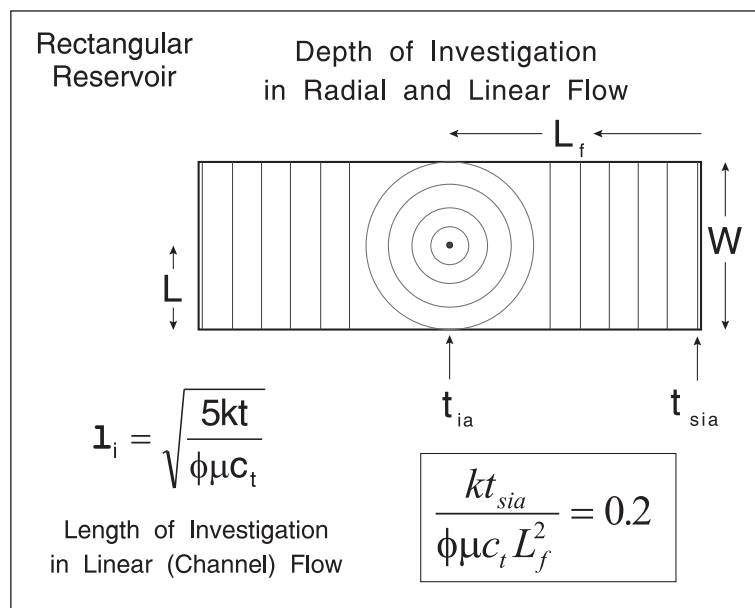


Fig. 7–2. End of semi-infinite-acting (SIA) flow

Decline curve analysis as treated here will be confined to systems produced essentially at constant wellbore pressure and in the quasi-steady-state, i.e., the equivalent of SSS depletion in the case of constant rate. In figure 7-2, a well in a closed compartment has been depicted. In the case where one or more of the boundaries is “leaky,” i.e., a semipermeable barrier, the phenomenon of compartmentalization, as discussed at length in chapters 12 and 15 of *Well Test Design and Analysis*, comes into play. The role of such compartmentalization (support from cells screened from the well cell by tight zones) on well decline rate is important and one of the main reasons for nonzero exponents in the empirical rate–time equations presented in the next section is this effect. Note that the complex material balance model (chapter 12) will predict constant wellbore pressure decline simply by specifying a flat vertical lift performance (VLP) curve in the production-constrained mode.

## Empirical Rate–Time Equations

The instantaneous rate at which the production from a well is declining, per unit production rate, is defined as

$$D(t) = - \frac{1}{q} \frac{dq}{dt} \quad (7-7)$$

Field data have shown that  $D(t)$  is a function of the  $b$ -th power of the instantaneous rate itself, i.e.,

$$D = aq^b \quad (7-8)$$

and  $b$  is generally between 0 and 1 but in some cases can exceed unity. For a given well or reservoir,  $a$  and  $b$  will not change as long as the producing conditions remain unaltered. The rate decline  $D$  varies with time according to Eq. (7-8). Combining Eqs. (7-7) and (7-8) yields

$$- \frac{dq}{q^{b+1}} = a dt \quad (7-9)$$

For  $b \neq 0$ , Eq. (7-9) can be integrated from initial conditions  $t = 0$ ,  $q = q_i$ , to general time  $t$  at which the rate is  $q_t$ :

$$\frac{1}{b} (q_t^{-b} - q_i^{-b}) = at \quad (7-10)$$

The initial decline rate  $D_i$  at  $t = 0$  is given by

$$D_i = aq_i^b \quad (7-11)$$

which on substitution into (7-10) and rearrangement gives

$$q_t = q_i (1 + bD_i t)^{-1/b} \quad (7-12)$$

This form of equation for describing the rate decline of a well was first proposed by Arps.<sup>3</sup>

For the case where  $b = 0$ , Eq. (7-8) reduces to

$$D = a = \text{const} \quad (7-13)$$

and integrating Eq. (7-9) now gives

$$\ln \frac{q_i}{q_t} = Dt \quad (7-14)$$

i.e.,

$$q_t = q_i e^{-Dt} \quad (7-15)$$

This is a special form known as *exponential decline*.

Equation (7-12) or (7-15), depending on whether  $b \neq 0$  or  $b = 0$ , allows the rate to be calculated as a function of time. The cumulative oil production  $N_p$  can be obtained by integration of the appropriate expression for  $q(t)$ . For exponential decline ( $b = 0$ ), there results

$$N_p = \int_0^t q(t') dt' = q_i \int_0^t e^{-Dt'} dt' = \frac{q_i}{D} (1 - e^{-Dt}) = \frac{q_i}{D} \left( 1 - \frac{q(t)}{q_i} \right) \quad (7-16)$$

This can be simply expressed as

$$N_p = \frac{q_i - q(t)}{D} \quad b = 0 \quad (7-17)$$

For the general case where  $b \neq 0$  and  $b \neq 1$ , the integration of (7-12) takes the form

$$N_p = \int_0^t q(t') dt' = q_i \int_0^t (1 + bD_i t')^{-1/b} dt'$$

$$= \frac{q_i}{(b-1)D_i} \left[ (1 + bD_i t)^{\frac{b-1}{b}} - 1 \right] \quad (7-18)$$

Substitution of Eq. (7-12) into (7-18) yields the alternative form

$$N_p = \frac{q_i}{(b-1)D_i} \left[ \left( \frac{q_i}{q(t)} \right)^{b-1} - 1 \right] \quad (7-19)$$

For the case of  $b = 1$ , Eq. (7-19) is indeterminate and the integral must be evaluated as follows:

$$\begin{aligned} N_p &= \int_0^t q(t') dt' = q_i \int_0^t (1 + D_i t')^{-1} dt' \\ &= \frac{q_i}{D_i} \ln(1 + D_i t) \end{aligned} \quad (7-20)$$

Alternatively, this may be written in the equivalent form

$$N_p = \frac{q_i}{D_i} \ln \left( \frac{q_i}{q(t)} \right) \quad b=1 \quad (7-21)$$

This case where  $b = 1$  is referred to as *harmonic decline*, whereas the general case ( $b \neq 0, b \neq 1$ ) is known as *hyperbolic decline*.

Nearly all conventional decline curve analyses, then, are based on the empirical rate-time equations given by Arps as

$$q_s(t) = q_i \frac{1}{[1 + bD_i t]^{1/b}} \quad (7-22)$$

In modern terms, this is a three-parameter functional expression which can be fitted to a set of corresponding rate and time values as illustrated in figure 7-3. The unknown parameters are found by a nonlinear regression algorithm that minimizes the usual objective function

$$\chi^2 = \sum \left( \frac{q_s^m - q_s^p}{\sigma_q} \right)^2$$

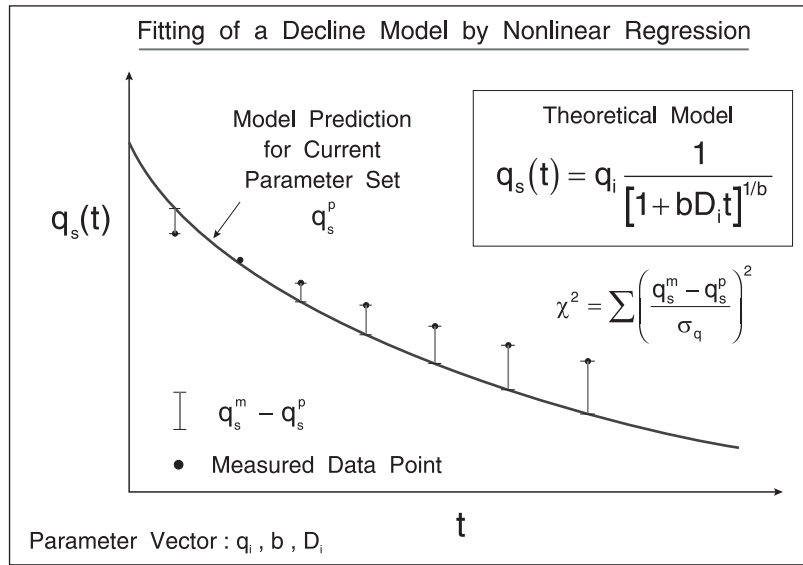


Fig. 7-3. Nonlinear regression applied to an empirical Arps hyperbolic decline function

Here  $q_s^m$  is a measured surface rate at time  $t$ , while  $q_s^p$  is the rate predicted by the empirical model at time  $t$  for some parameter set  $\mathbf{a}$ . The unknown parameters to be determined by regression are

$$\mathbf{a} = (q_i; D_i; b)^T \quad (7-23)$$

The basis of the decline curve analysis is to find the vector  $\mathbf{a}$  that minimizes the sum of squares objective function  $\chi^2$  using an appropriate optimization technique such as the Levenberg–Marquardt algorithm.

The allowable range of the decline curve exponent  $b$  will normally be restricted to  $0 \leq b \leq 1$  and starting values for the nonlinear regression will usually be obtained from the overlay and match to the Fetkovich decline type curve described later. The essential precaution in applying automatic matching to an Arps empirical model is that only data representative of depletion be selected for regression, i.e., the log–log derivative diagnostic plot of the transformed data, should exhibit a unit slope. Automatic matching should probably be regarded as a fine-tuning of the manual match on the Fetkovich decline type curve.

For the case where  $b = 0$ , Eq. (7-22) reduces to the exponential decline equation

$$q_s(t) = q_i e^{-D_i t} \quad (7-24)$$

and for the other limiting case in which  $b = 1$ —referred to as harmonic decline—there results

$$q_s(t) = q_i \frac{1}{[1 + D_i t]} \quad (7-25)$$



Thus  $b$  lies in the range  $0 \leq b \leq 1$ ; as will be seen later, there is theoretical justification for these limiting values of  $b$ .

In essence, a decline curve analysis consists of fitting the empirical model to a dataset and then using the estimated parameter values to extrapolate the well rate into the future. The cumulative production over a specified time period can be calculated from this forward prediction as illustrated in figure 7-4.

In figure 7-5, a dataset from Slider<sup>4</sup> is shown along with the fitted hyperbolic decline curve using a nonlinear regression routine; the parameter values are

$$D_i = 0.08474/\text{month} \quad b = 0.3229 \quad q_i = 2544 \text{ STB/D}$$

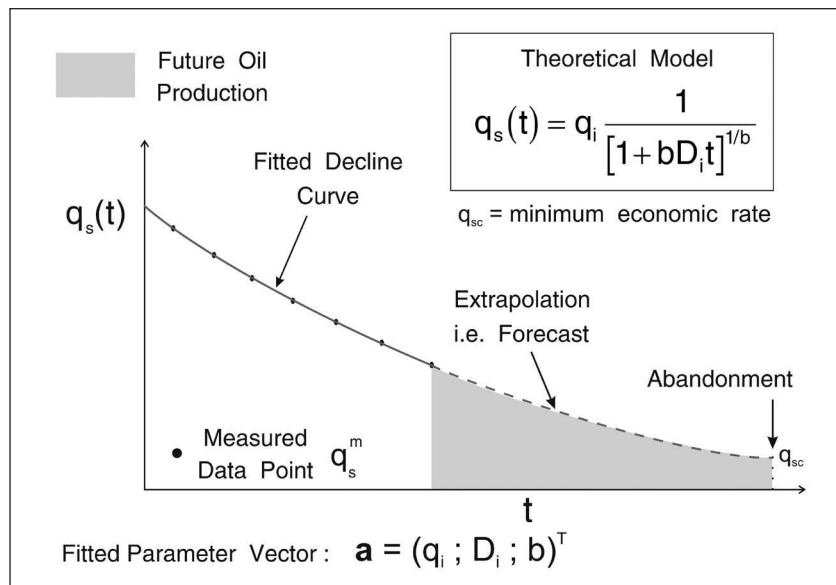


Fig. 7-4. Prediction of future production by extrapolation of the fitted decline curve

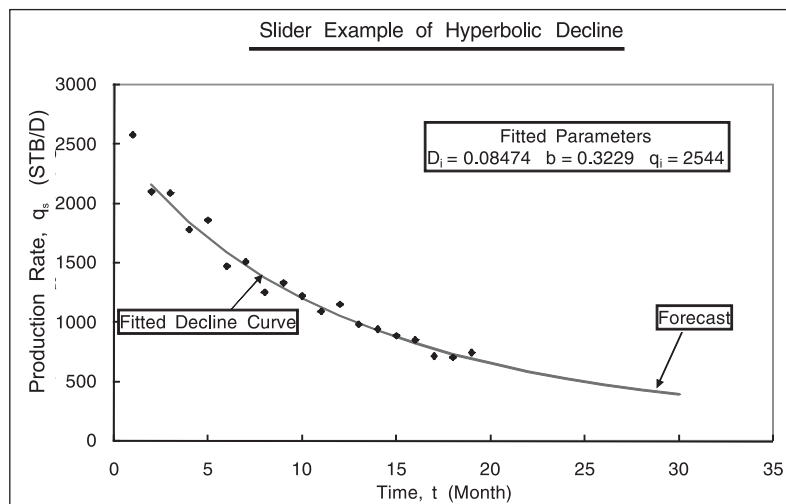


Fig. 7-5. Decline dataset due to Slider

Note that the first data point ( $t = 1$  month;  $q_s = 2,580$  STB/D) has been ignored in the formation of the sum of squares; this is an “outlier” which degrades substantially the goodness of fit to the data in that its contribution to the sum, if included, totally dominates. In the problem set by Slider, the additional reserves produced to an economic limit of 100 STB/D and 10 STB/D were found by the graphical method in which the following parameters were obtained:

$$b = 0.5 \quad D_i = 0.025$$

The results generated by nonlinear regression are compared with Slider’s values in table 7–1.

**Table 7–1.** Comparison of nonlinear regression (NLR) approach with Slider’s graphical method

Method	$q_i$ (STB/D)	$D_i$ month <sup>-1</sup>	$b$	$q_{sc}$ (STB/D)	$T_2$ (month)	$Q$ (bbl)
NLR	2,544	0.08474	0.3229	100	67.37	13,475
NLR	–	–	–	10	182	17,387
Graph		0.025	0.5	100	80	15,720
Graph	–	–	–	10	292	22,402

## Minimum economic rate $q_{sc}$

The definition of recoverable reserves is closely tied to the concept of a minimum economic rate for a well, which is denoted here  $q_{sc}$ ; below this rate, the operating cost of the well is greater than the net revenue from the oil produced. Hence, the well production will normally be terminated at this point and reserves remaining in the drainage area will not be recovered. The cut-off rate  $q_{sc}$  is marked on figure 7–4 and the shaded area of incremental cumulative production is truncated at the point where the well rate has declined to this value.

## Exponential decline for a single-compartment system

An insight into the theoretical basis for exponential decline can be gained by studying a single-compartment liquid system producing at constant bottom-hole pressure  $p_{wf}$  from a single well. The well production rate is related to the average pressure of the cell according to the expression

$$q_s = J_{SSS}(\bar{P} - p_{wf}) \quad (7-26)$$

where

$$J_{SSS} = \frac{2\pi kh}{B\mu \left( \frac{1}{2} \ln \frac{4\bar{A}}{\gamma C_A r_w^2} + S \right)}$$

The elementary material balance for the closed depleting cell is given in differential form by

$$c_t V \frac{d\bar{p}}{dt} = -q_s B = J_{sss} (\bar{p} - p_{wf}) B \quad (7-27)$$

On separating the variables, this may be written as

$$\frac{d\bar{p}}{\bar{p} - p_{wf}} = -\frac{J_{sss} B}{c_t V} dt$$

which on integration becomes

$$\bar{p} - p_{wf} = (\bar{p}_i - p_{wf}) e^{-\frac{J_{sss} B}{c_t V} t} \quad (7-28)$$

Hence, the well flow rate at time  $t$  is given by

$$q_s(t) = J_{sss} (\bar{p} - p_{wf}) = J_{sss} (\bar{p}_i - p_{wf}) e^{-\frac{J_{sss} B}{c_t V} t} \quad (7-29)$$

i.e., 
$$q_s(t) = q_{si} e^{-D_i t} \quad (7-30)$$

where 
$$q_{si} = J_{sss} (\bar{p}_i - p_{wf}) \quad \text{and} \quad D_i = \frac{J_{sss} B}{c_t V}$$

Here,  $V$  is the pore volume of the compartment, which is related to the drainage area  $\bar{A}$  by the equation

$$V = \phi \bar{A} h \quad (7-31)$$

and  $\bar{p}_i$  is the average pressure at  $t = 0$  synonymous with the time at which depletion commences. Thus, classical material balance depletion of a closed liquid system at a constant bottom-hole pressure  $p_{wf}$  will result in exponential decline of the well rate. Equation (7-30) is identical in form to (7-24) and a physical meaning can be attached to the decline coefficient  $D_i$ . Note that knowledge of the production mechanism allows the correct form of the decline curve to be assessed, in this case liquid depletion with no support from gas cap or water influx yielding  $b = 0$  in the empirical form (7-22). The key idea that decline curve analysis should be based on a combination of a rate equation and a material balance is again due to Fetkovich.<sup>7</sup> Thus, exponential decline (i.e.,  $b = 0$ ) is the fundamental liquid solution for a closed compartment produced at constant bottom-hole pressure; the process of depletion and declining rate can be conveniently represented on a well performance diagram as shown in figure 7-6.

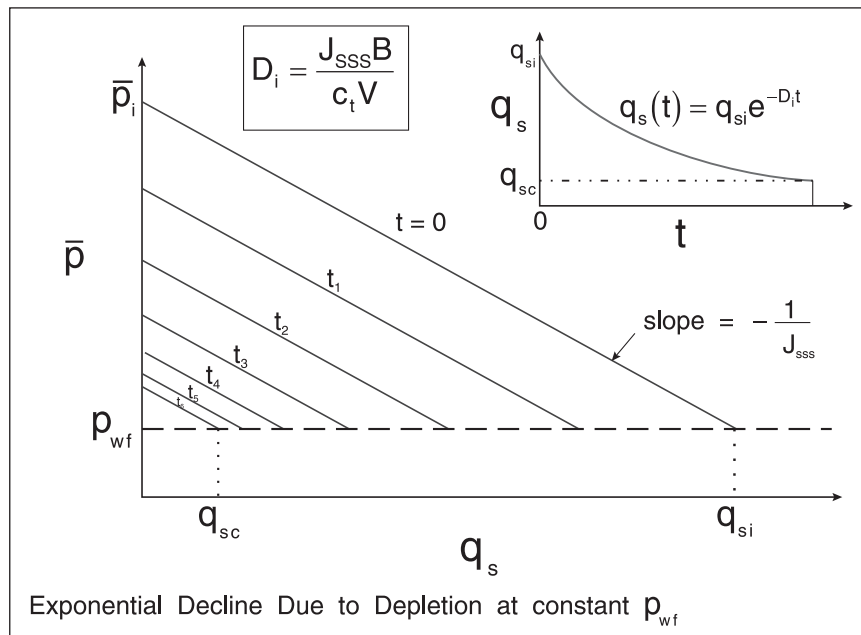


Fig. 7-6. Exponential decline on a well performance diagram

The equation describing exponential decline in rate, i.e., (7-30), shows that a semilog graph of  $q_s(t)$  versus time  $t$  will be a straight line of slope  $-D_i$  and intercept  $\ln q_{si}$ , as shown on figure 7-7. In the general case where three parameters of an Arps form are determined by nonlinear regression, it is necessary to estimate reasonable starting values for the parameter set  $\mathbf{a}_0 = (q_{si}; D_i; b)_0^T$ . It is advisable to commence the search with  $b = 0$ , i.e., exponential decline, and starting values for  $q_{si}$  and  $D_i$  determined as the slope and intercept of the specialized semilog graph of  $\ln q_s$  versus  $t$ . This procedure reliably and simply yields starting values for the unknown parameters  $\mathbf{a}$ . One of the advantages of modern optimization algorithms is that they also generate error estimates for the fitted parameters which are of use in assessing the significance of the calculated results.

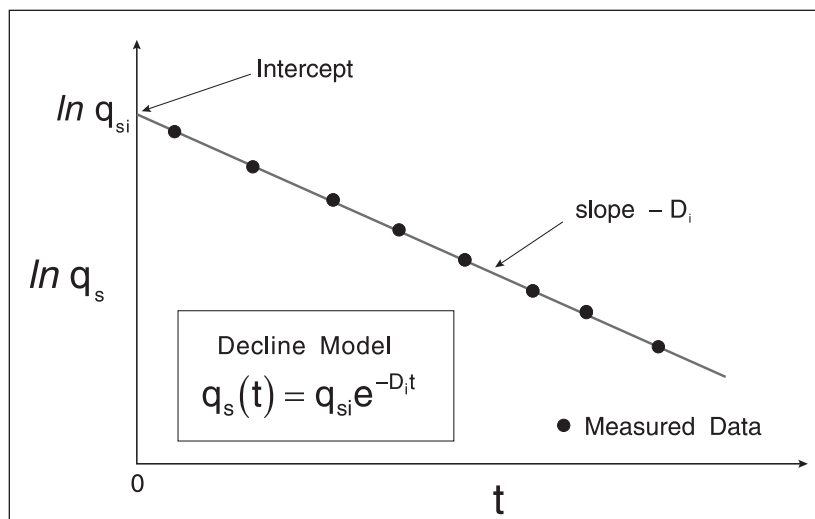


Fig. 7-7. Straight line on semilog rate plot for exponential decline

## Decline rates

The decline rate  $D$  is defined as the negative of the slope of the semilog graph of  $\ln q$  versus  $t$ , i.e.,

$$D = -\frac{d \ln q}{dt} = -\frac{\frac{dq}{q}}{dt} \quad (7-32)$$

and has units of reciprocal time. In the case of exponential decline, also referred to as *constant percentage decline*,  $D$  is constant as shown above and equal to the initial value  $D_i$ . In the general case of hyperbolic decline,  $D$  is proportional to a fractional power of the production rate, i.e.,

$$D = -\frac{\frac{dq}{q}}{dt} = aq^b \quad (7-33)$$

where  $b$  is a fraction between 0 and 1 as already stated and from the initial conditions  $a = \frac{D_i}{q_i^b}$ .

In the case of harmonic decline with  $b = 1$ , Eq. (7-33) reduces to

$$D = -\frac{\frac{dq}{q}}{dt} = aq \quad \text{where} \quad a = \frac{D_i}{q_i} \quad (7-34)$$

In some texts, this quantity is referred to as the *nominal decline rate* since it is based on  $q$  being a continuous function, whereas real production data are often discontinuous in nature, i.e., production per period is quoted.

## Transformation to cumulative production

Much of the practical application of decline curve analysis is based on plots of well rate versus cumulative production denoted  $N_p$  and defined as

$$N_p = \int_0^t q_s(t) dt \quad (7-35)$$

Obviously, the form of a graph of  $q_s(t)$  versus  $t$  will be quite different from one of  $q_s(t)$  versus  $N_p$ . The use of cumulative production helps to reduce the problem of noise in the raw data and allows periods of well shutin to be easily handled.

In the case of a single closed compartment exhibiting exponential decline on a time basis, the material balance can be expressed as

$$N_p = \int_0^t q_s(t) dt = c_t V (p_i - \bar{p}(t)) \quad (7-36)$$

and the instantaneous rate  $q_s(t)$  is given by

$$q_s(t) = J_{SSS} (\bar{p}(t) - p_{wf}) \quad (7-37)$$

i.e.,

$$q_s(t) = J_{SSS} \left( p_i - \frac{N_p}{c_t V} - p_{wf} \right) \quad (7-38)$$

which indicates that a plot of  $q_s(t)$  versus  $N_p$  should be a straight line of slope  $-\frac{J_{SSS}}{c_t V}$  as illustrated in figure 7-8. If the well is produced until the reservoir pressure reaches the fixed bottom-hole pressure  $p_{wf}$ , the total amount of oil which can be produced by expansion of oil in place, denoted  $N_{pi}$  where the subscript 'i' signifies abandonment, is given by

$$N_{pi} = c_t V (p_i - p_{wf}) \quad (7-39)$$

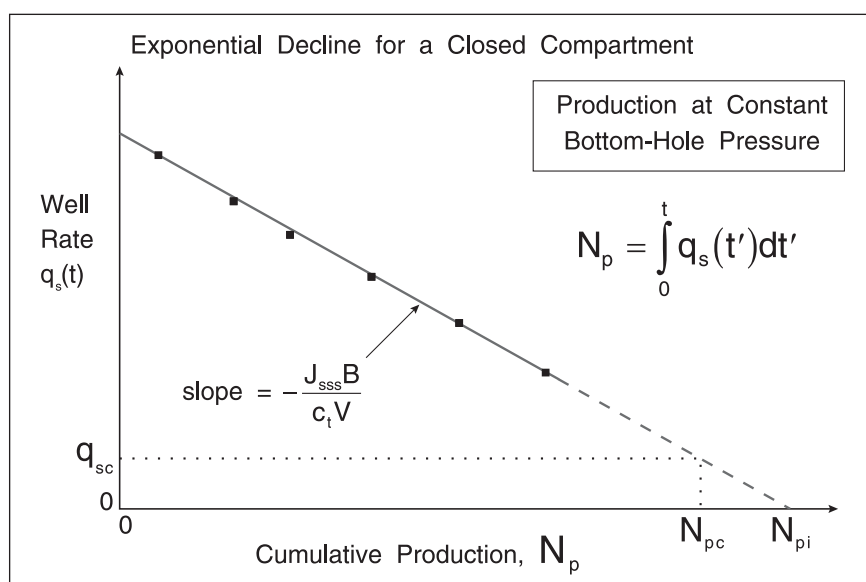


Fig. 7-8. Transformed plot of well rate versus cumulative production for depletion

Hence substituting Eq. (7-39) into (7-38) gives

$$q_s(t) = \frac{J_{SSS}}{c_t V} (N_{pi} - N_p) \quad (7-40)$$

and the intercept  $N_{pi}$  of the Cartesian graph of well rate  $q_s(t)$  versus cumulative production  $N_p$  gives the reserves recoverable by depletion to the attainable reservoir pressure  $p_{wf}$ . Alternatively, if a minimum economic rate is prescribed as  $q_{sc}$ , then the producible reserves  $N_{pc}$  may also be determined as shown in the diagram. The Cartesian plot of  $q_s$  versus  $N_p$  in the case of constant bottom-hole pressure production is the analog of the familiar Cartesian graph of  $p_{wf}$  versus  $t$  or  $N_p$  in the constant-rate case.

If the decline does not correspond to a closed liquid system and is hyperbolic in nature due to the drive mechanism, the Cartesian graph of  $q_s$  versus  $N_p$  will be concave upward as shown in figure 7–9. It would obviously be useful to be able to fit an empirical form to these data in order to make forward extrapolations and reserve estimates. In order to achieve this objective, it is convenient to define an equivalent time scale from the table of rate versus cumulative production assuming that the rate follows a piecewise linear form as illustrated in figure 7–10. Based on the integral

$$N_p = \int_0^t q_s(t) dt$$

and assuming a quadrature based on the quadrilateral rule, it can be shown that the equivalent time  $t_i$  corresponding to cumulative production  $N_{p,i}$  is given by

$$t_i = t_{i-1} + \frac{N_{p,i} - N_{p,i-1}}{q_{s,i} + \frac{q_{s,i-1} - q_{s,i}}{2}} \tag{7-41}$$

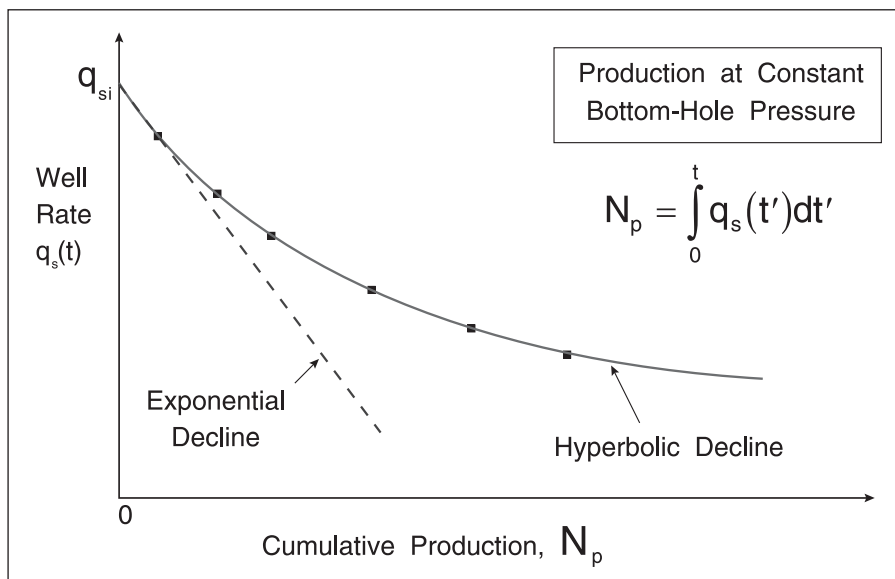


Fig. 7–9. Hyperbolic decline on a rate–cumulative production Cartesian graph

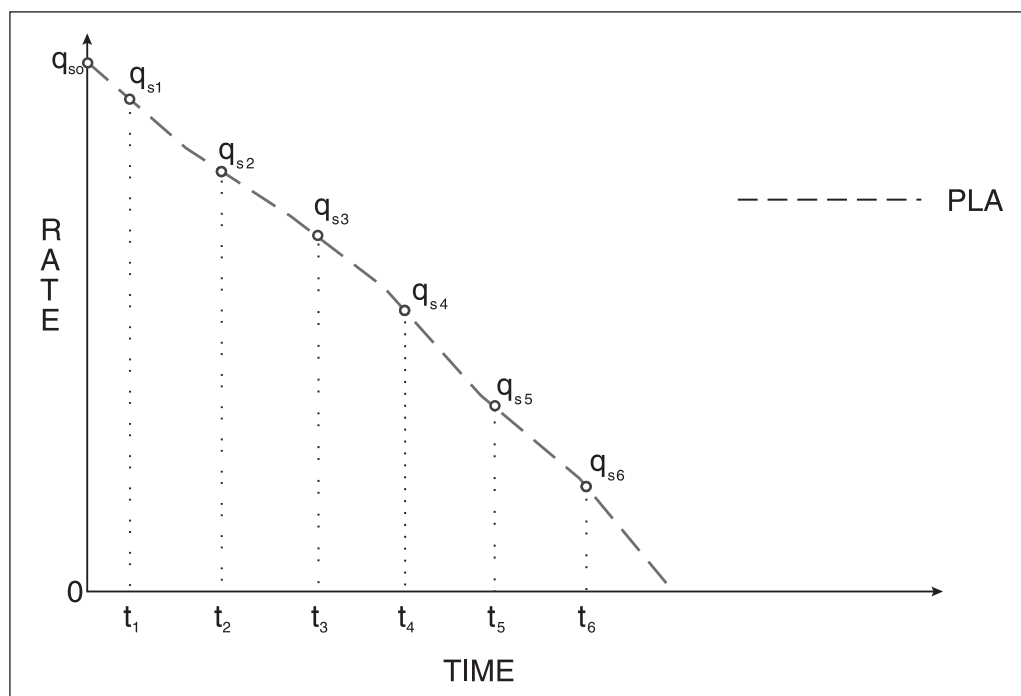


Fig. 7-10. Piecewise linear rate approximation

Starting from  $t_1 = \frac{N_{p,1}}{q_{s,1}}$ , this algorithm may be used sequentially to generate a series of times equivalent to the tabulated cumulative productions. The Arps empirical form can then be fitted to the transformed data in the usual way and the results transferred back to the Cartesian plot for cumulative production for presentation. This procedure has the advantage of preserving the nature of the nonlinear regression, i.e., a fit of the Arps form to rate–time data, and allows meaning to be attached to the parameter values. However, the results are still presented on the Cartesian plot and the time scale is fixed by the information on rate versus cumulative production. Using cumulative production reduces the effect of noise in the data and periods of well shutin can be handled although any transient draw-down data following a build-up period must be disregarded.

Since the exponential (depletion) model predicts the severest decline and gives conservative predictions, it may be the policy to use the straight line extrapolation on the rate versus cumulative production Cartesian graph. However, if curvature is apparent, then the method described here may be used to yield an improved estimate of recoverable reserves. Note that compartmentalized behavior will result in hyperbolic decline and overly pessimistic reserve calculations based on the straight line fit.

## Production database

It is useful at this juncture to examine the form of database structures for production information. The most common method of storing production data is illustrated in figure 7-11; here the cumulative production over a 24-h period obtained by integrating the continuous flow measurements is used as a basis for an average daily rate. In mathematical form



$$\bar{q}_{si} = \frac{\int_{T_{i-1}}^{T_i} q_s(t) dt}{T_i - T_{i-1}} \tag{7-42}$$

and the database for single phase flow takes the form of table 7-2.

Table 7-2. Production database

Date	Average daily rate	Time (day)
	$\bar{q}_{si}$	
d/m/y	$\bar{q}_{s1}$	$T_1$
d/m/y	$\bar{q}_{s2}$	$T_2$
	—	—
d/m/y	$\bar{q}_{s,i-1}$	$T_{i-1}$
d/m/y	$\bar{q}_{si}$	$T_i$
d/m/y	$\bar{q}_{s,i+1}$	$T_{i+1}$
	—	—

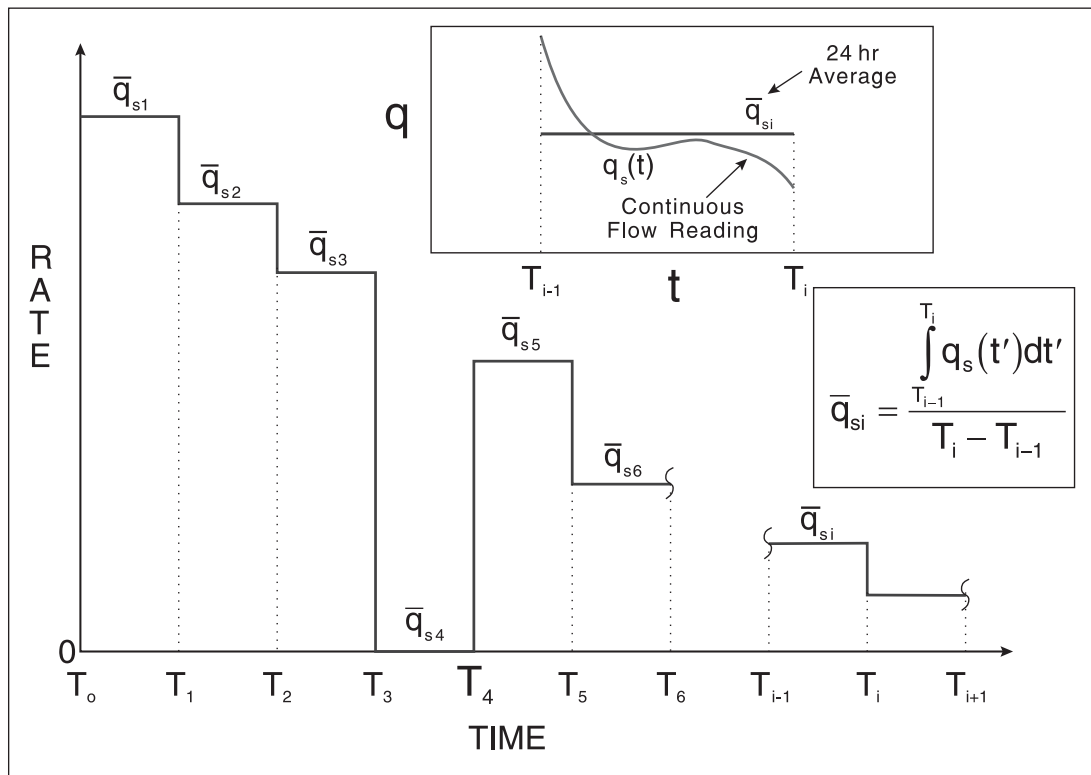


Fig. 7-11. Production database format

Thus, the database essentially stores the production on a daily basis tabulated for each day referenced by date. It is then a simple matter to augment this structure with a column of times  $T_i$  measured in days; it is this form that is most often used for decline curve analysis. In figure 7–12, the conversion to a continuous, piecewise linear rate schedule is shown where the time at the mid-point is employed. Note that for the case of equal intervals—in this case 24 h—the mid-point time maintains material balance consistency. This follows from the similarity of the shaded triangles shown in figure 7–12.

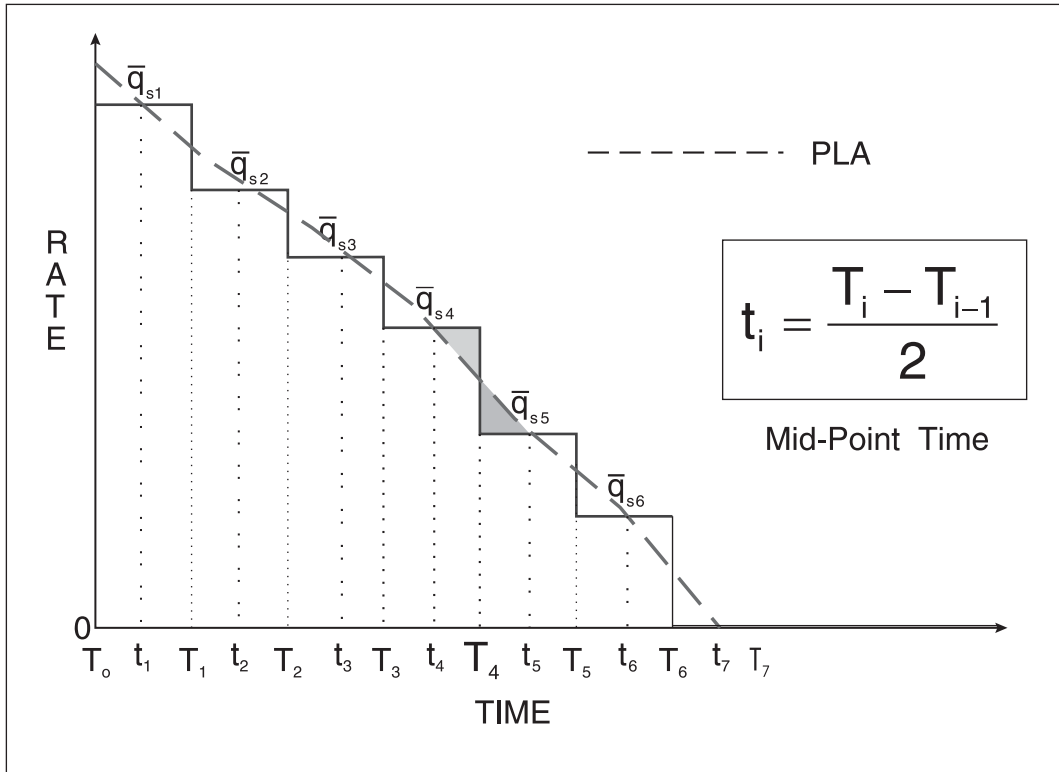


Fig. 7–12. Conversion of step-rate schedule to piecewise linear (PLA)

## Change in production conditions—stimulation

Part of the objective of decline curve analysis is to allow the performance to be predicted after some change in conditions, for example, stimulating the well. In the formulation of the depletion model, the well rate is modeled by an expression based on the SSS productivity index  $J_{SSS}$  which is related to the formation permeability and the well total apparent skin by the expression

$$J_{SSS} = \frac{2\pi kh}{B\mu \left( \frac{1}{2} \ln \frac{4\bar{A}}{\gamma C_A r_w^2} + S \right)} \quad (7-43)$$

In a stimulation or workover, it is the well total apparent skin factor  $S$  that is altered and it is interesting to determine what effect a change in  $S$  will have on the decline rate. In the case of a single closed compartment of area  $\bar{A}$ , the exponential decline model takes the form

$$q_s(t) = q_{si} e^{-D_i t} \tag{7-44}$$

where 
$$q_{si} = J_{SSS}(\bar{p}_i - p_{wfi}) \text{ and } D = \frac{J_{SSS}B}{c_t V}$$

Hence, increasing the productivity index by stimulating the well will change both  $q_{si}$  and  $D_i$  according to the prescription

$$q_{si}^{new} = q_{sf}^{old} \times \frac{J_{SSS}^{new}}{J_{SSS}^{old}} \tag{7-45a}$$

$$D_i^{new} = D_i^{old} \times \frac{J_{SSS}^{new}}{J_{SSS}^{old}} \tag{7-45b}$$

Thus, the modified decline behavior can be predicted if the change in well productivity index can be estimated from the treatment design. Note that both  $q_{si}$  and  $D_i$  are proportional to  $J_{SSS}$  and the new decline has the form shown in figure 7-13.

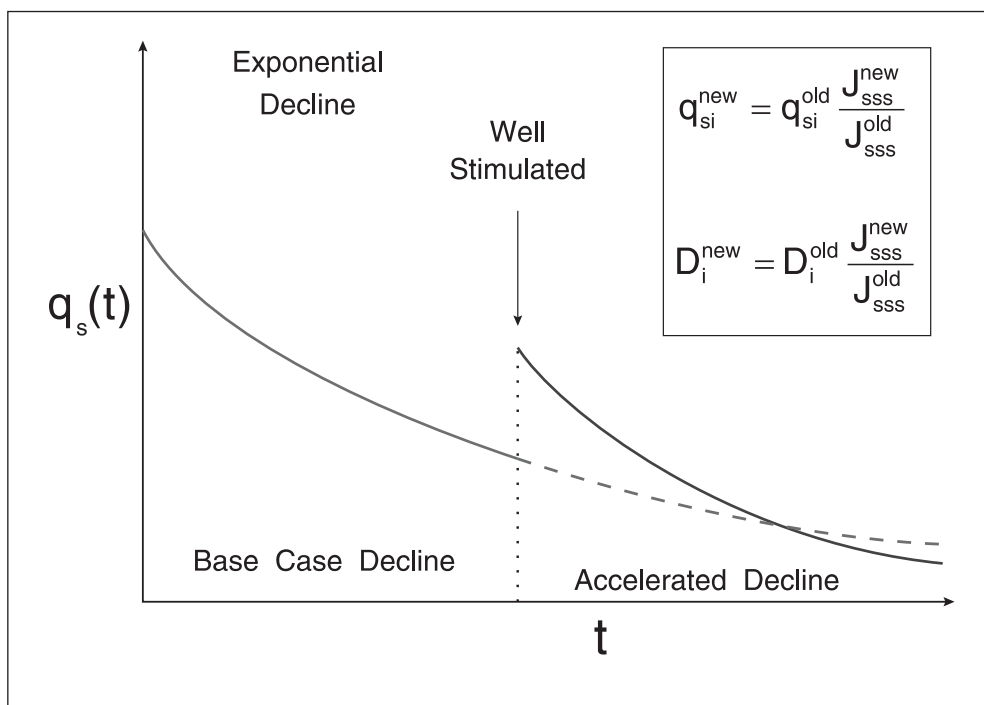


Fig. 7-13. Effect of well stimulation on decline behavior

## Field examples

Chierici has given the following field example in his text book and this will be used to demonstrate the application of the nonlinear regression approach. A reservoir denoted AX-1 has been producing oil for over 30 years from the Bartlesville (Oklahoma) sands at a depth of 300–400 m. Between 1985 and 1988, 42 wells were on production; the combined production data from this group of wells are given in table 7–3. The objective is to produce a decline curve forecast of the field rate. From January 1989, additional wells were brought in and 25 wells were stimulated; the total production data from these 50 wells are also listed. A decline curve was fitted using NLR to each dataset giving the following parameter values:

$$42 \text{ Wells } q_i = 209.7 \text{ m}^3/\text{day} \quad D_i = 0.01904 \text{ month}^{-1} \quad b = 0$$

$$50 \text{ Wells } q_i = 672.8 \text{ m}^3/\text{day} \quad D_i = 0.03130 \text{ month}^{-1} \quad b = 0$$

**Table 7–3.** Reservoir AX-1 production data

	Months	Wells on production	Oil rate (m <sup>3</sup> /day)
1985 Jan.	0	42	210
April	3	42	198
July	6	42	187
Oct.	9	42	177
1986 Jan.	12	42	167
April	15	42	157
July	18	42	149
Oct.	21	42	141
1987 Jan.	24	42	133
April	27	42	125
July	30	42	118
Oct.	33	42	112
1988 Jan.	36	42	106
April	39	42	100
July	42	42	94
Oct.	45	42	89
1989 Jan.	48	50	150
April	51	50	136
July	54	50	124
Oct.	57	50	113
Dec.	60	50	103

This dataset is plotted in figure 7–14, and the fitted decline curves are superimposed in figure 7–15. Over the period month 48 to month 72, the cumulative production  $N_p$  from the 50 wells is 2,527 m<sup>3</sup>, whereas for the original 42-well case the cumulative production would have been 1,620 m<sup>3</sup> only. Thus, the incremental oil production as a result of drilling the extra 8 wells is 907 m<sup>3</sup>. If the minimum economic rate is set at 50 m<sup>3</sup>/day for 50 wells and 42 m<sup>3</sup>/day for 42 wells, the cumulative production to abandonment are

$$50 \text{ Wells } T_2 = 83 \text{ months } N_{pa} = 3187$$

$$42 \text{ Wells } T_2 = 84.5 \text{ months } N_{pa} = 2210$$

i.e., an increase of 977 m<sup>3</sup>. For completeness, the semilog graph of  $\log_{10}(q_s)$  versus time  $t$  is shown in figure 7–16, where the slope (on a  $\log_{10}$  basis) is  $-0.00827 \log_{10}$  cycle/month. The exponential decline parameters may be found from the slope and intercept of this plot, e.g.,

$$D_i = -0.00827 \times 2.30258 = -0.01904$$

but the NLR method has been used here since the value of  $b$  is tested in this approach. It appears that the Chierici data are synthetic since a value of  $b$  exactly equal to zero is found by the regression algorithm.

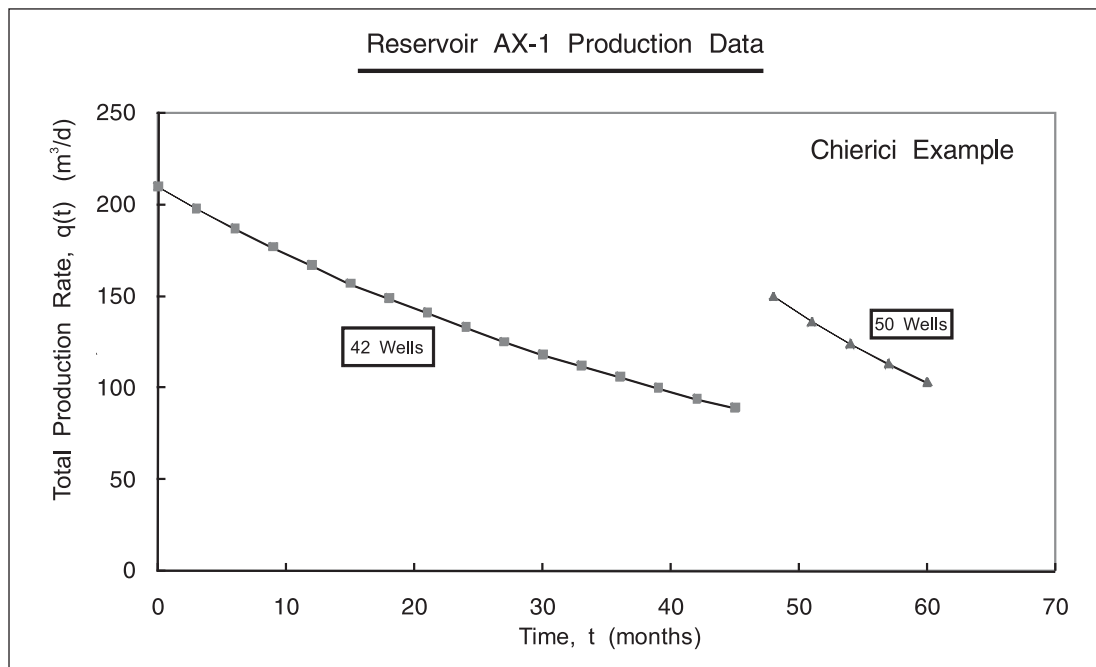


Fig. 7–14. Data for Chierici exponential decline example

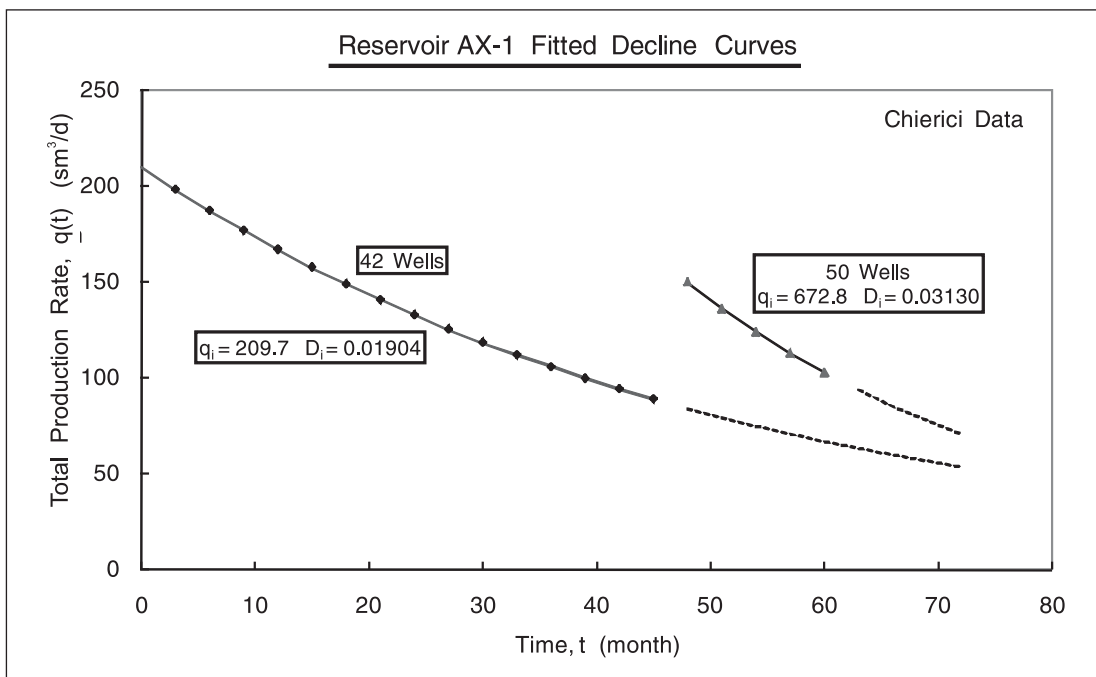


Fig. 7-15. Decline curves fitted to Chierici data

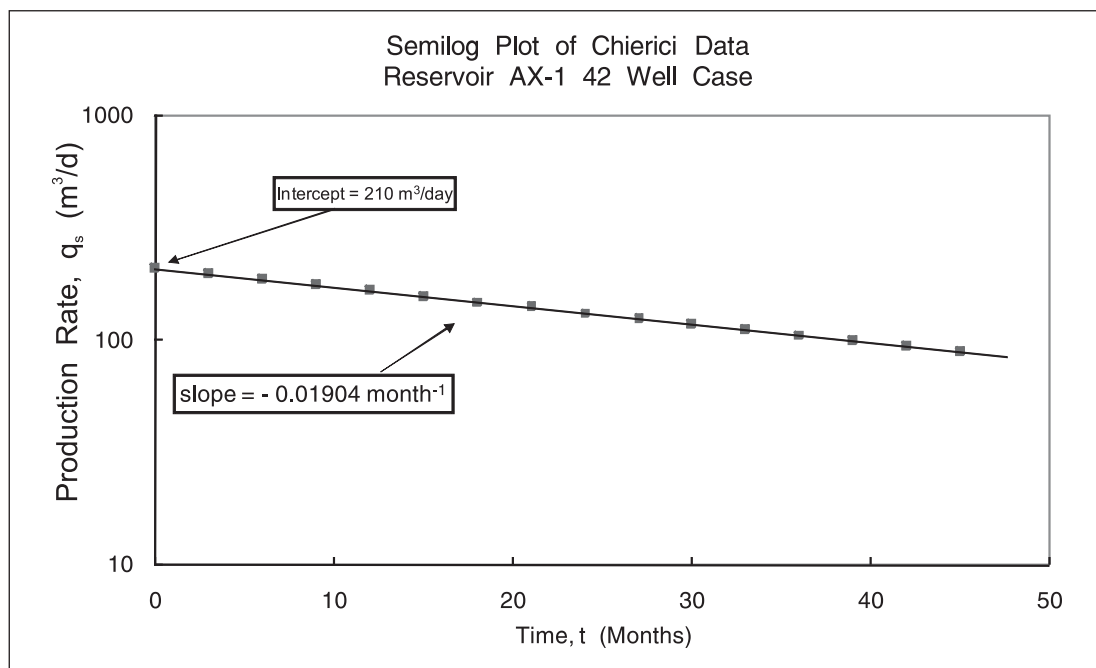


Fig. 7-16. Semilog graph of  $\log_{10}(q_s)$  versus time t

The next example concerns total production data (all wells) from a North Sea field, and an exponential decline, with the parameters determined by regression, is seen to fit the data very well as shown in figure 7-17.

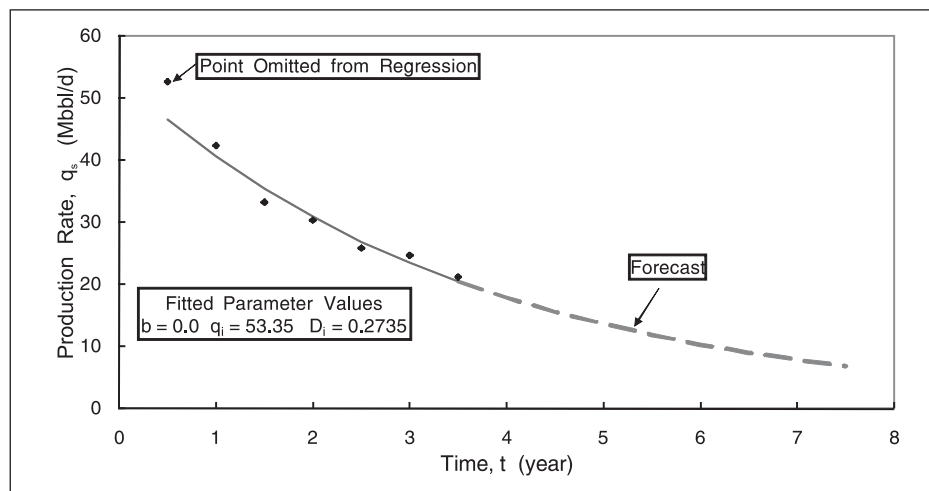


Fig. 7–17. North Sea field decline data

## Fetkovich Type Curve for Depletion

For depletion in an ideal liquid system, the empirical exponent  $b$  in the general form is zero. In the original work on decline curve analysis Arps<sup>3</sup> used data from actual fields and wells due to Cutler<sup>5</sup> and found  $b$  to lie in the range 0–0.7 with over 90% of cases having values less than 0.5; no case was found with  $b$  in excess of 0.7. Arps’s own experience, however, indicated that  $b$  values of 1 did occur but were rare. The idea of a log–log overlay in the analysis of rate decline data was due to Slider<sup>6</sup> and he should be given credit for the first application of type curve matching in the petroleum industry. This procedure was further developed by Fetkovich,<sup>7</sup> who defined decline curve dimensionless groups as

$$t_{Dd} = D_i t \quad q_{Dd} = \frac{q_s(t)}{q_i} \tag{7-46}$$

and plotted  $q_{Dd}$  versus  $t_{Dd}$  on log–log scale for various values of  $b$ ; the resultant decline data type curve is shown in figure 7–18. Note that all the curves coincide and become indistinguishable for  $t_{Dd} < 0.3$ . As pointed out by Fetkovich, any data existing before a  $t_{Dd}$  of 0.3 will *appear* to be an exponential decline and thus plot as a straight line on a semilog graph; a nonlinear regression algorithm could return any value of  $b$  between 0 and 1. In the type curve matching procedure, illustrated in figure 7–19, the actual data in the form of  $q_s(t)$  versus time  $t$  is plotted on a compatible log–log scale and overlaid on the type curve. The time match yields the coefficient  $D_i$  (initial decline rate) as

$$D_i = \frac{[t_{Dd}]_M}{[t]_M} \tag{7-47}$$

and the rate match gives the initial rate  $q_i$

$$q_i = \frac{[q_s]_M}{[q_{Dd}]_M} \quad (7-48)$$

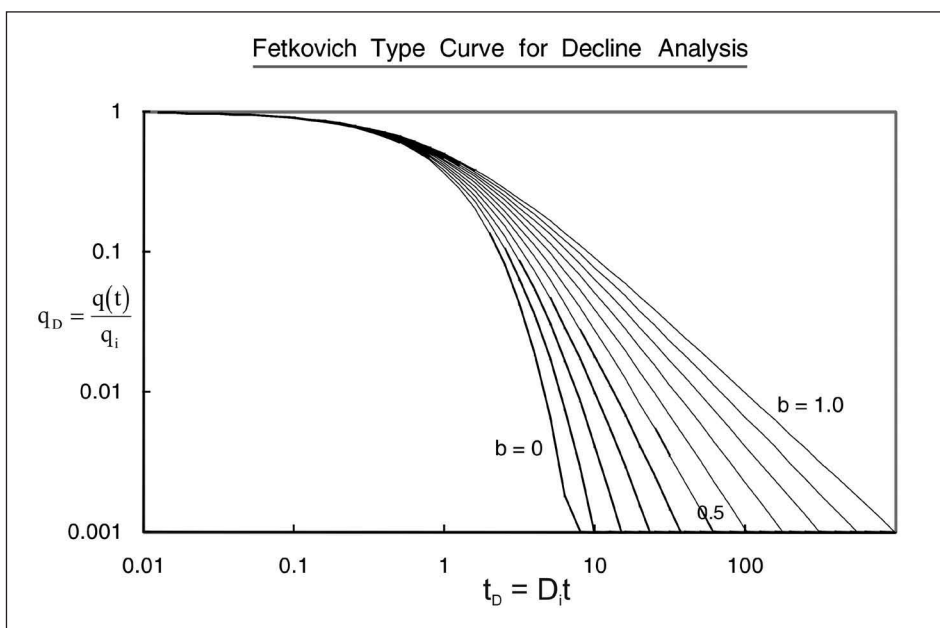


Fig. 7-18. Type curves for Arps's empirical rate-time decline equations

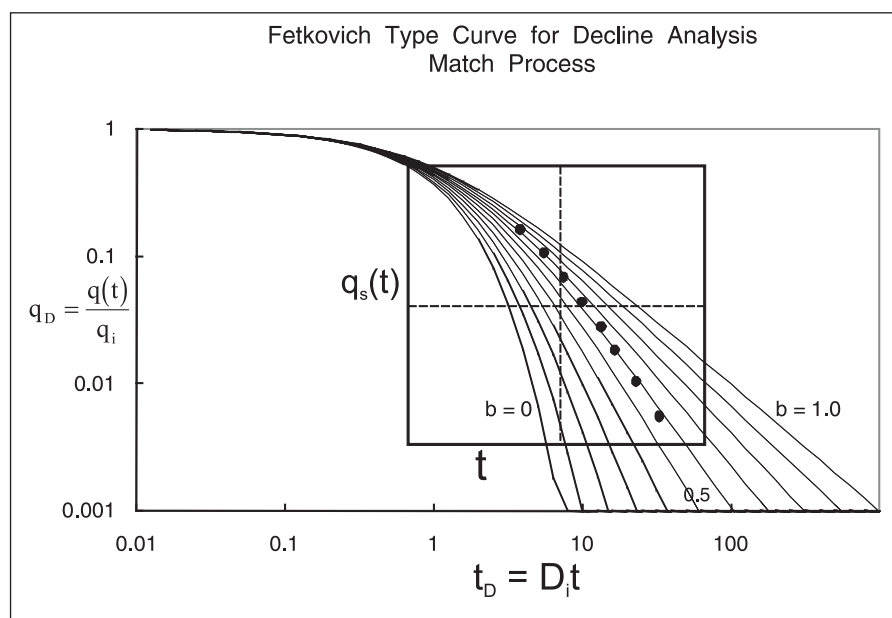


Fig. 7-19. Fetkovich type curve matching process



The parameter match gives  $b$  directly. It is important that decline curve analysis only be applied to data which correspond to depletion. Transient data can be fitted to the empirical form by automatic matching and it has been shown by Fetkovich<sup>7</sup> that this will result in a value of  $b$  which is greater than unity. However, it is very unwise to extrapolate such a fit into the period when depletion does eventually affect the behavior; this can result in a gross overestimation of future production. In the case of exponential decline, i.e., a liquid system with  $b = 0$ , it is possible to attach a physical meaning to  $D_i$ . If a closed reservoir is produced from an initial pressure  $\bar{p}_i$  down to the wellbore pressure  $p_{wf}$ , the cumulative production at stock tank conditions  $N_{pi}$  is given by

$$N_{pi} = \frac{Vc_t(\bar{p}_i - p_{wf})}{B} \quad (7-49)$$

From Eq. (7-44),  $D_i$  may be written as

$$D_i = \frac{J_{SSS}B}{c_t V} = \frac{q_i B}{(\bar{p}_i - p_{wf})c_t V} = \frac{q_i}{N_{pi}} \quad (7-50)$$

Hence, the cumulative production obtainable by depletion may be calculated as

$$N_{pi} = \frac{q_i}{D_i} \quad (7-51)$$

where  $q_i$  and  $D_i$  are determined from the match Eqs. (7-47) and (7-48), respectively.

The main objective of decline curve analysis is, of course, to make a forward prediction of production by evaluating the fitted empirical function at future values of time; this process has been illustrated in figure 7-4. For a time range  $T_1 - T_2$ , the cumulative production is given by

$$Q = \int_{T_1}^{T_2} q_s(t) dt \quad (7-52)$$

where  $q_s(t)$  is given by (7-22). The designated integral may be evaluated as

$$Q = \frac{q_i}{(b-1)D_i} \left[ \left(1 + bD_i T_2\right)^{\frac{b-1}{b}} - \left(1 + bD_i T_1\right)^{\frac{b-1}{b}} \right] \quad (7-53)$$

when  $b \neq 0$  and  $b \neq 1$ . For exponential decline with  $b = 0$ , the integral is given by the reduced form

$$Q = \frac{q_i}{D_i} \left[ e^{-D_i T_1} - e^{-D_i T_2} \right] \quad (7-54)$$

These expressions for cumulative production over specified time intervals allow the economics of declining production to be assessed once the empirical parameters of the decline curve  $b$  and  $D_i$  have been determined.

In the case where a minimum economic rate  $q_{sc}$  has been specified, the upper time limit  $T_2$  is given by the condition

$$q_{sc} = q_i \frac{1}{[1 + bD_i T_2]^{1/b}}$$

i.e.,

$$T_2 = \frac{\left( \frac{q_i}{q_{sc}} \right)^b - 1}{bD_i} \quad (7-55a)$$

or

$$T_2 = \frac{\ln \frac{q_i}{q_{sc}}}{D_i} \quad \text{for exponential decline} \quad (7-55b)$$

This allows the recoverable reserves curtailed by the well minimum economic rate to be calculated. The lower limit  $T_1$  is the present time at the end of the history-match period.

In some cases, decline curve analysis is applied to the summed production data from a group of wells and this approach is consistent with the concept of Dietz drainage areas in a multiple well reservoir compartment. If the drainage area of a particular well  $i$  is proportional to its rate following the familiar prescription

$$\frac{q_i}{V_i} = \frac{q_t}{V_t}$$

then the quantity  $D_i = q_i/N_{p_i}$  will be the same for all the wells provided they have the same bottom-hole flowing pressures  $p_{wf}$ . This implies that decline curve analysis can be applied to the total production from the compartment or fault block as illustrated in figure 7-20; conversely, lumped decline curve analysis should not be applied to data from different, i.e., noncommunicating, portions of a field.

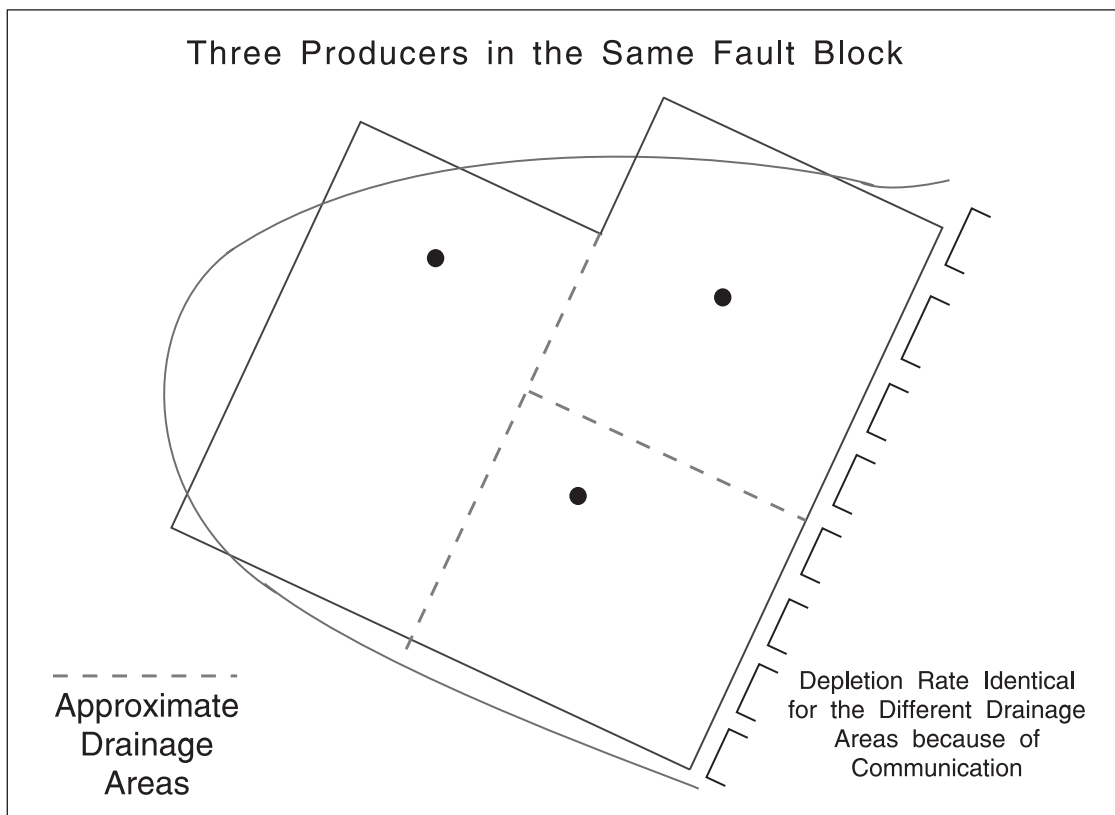


Fig. 7–20. Grouping of wells in a given reservoir compartment

Decline curve analysis is based on production data for constant bottom-hole pressure  $p_{wf}$ . Naturally in most field situations the bottomhole pressure is not exactly constant and changes with the rate. It has been pointed out by Fetkovich that pressure normalization takes the form

$$q_s^{nor} = q_s(t) \frac{\bar{p}_i - p_{wf}^{ref}}{\bar{p}_i - p_{wf}(t)} \tag{7-56}$$

where  $p_{wf}(t)$  is the time-dependent bottom-hole pressure. Given that most rate measurements are made at surface, it is possible to use a nodal analysis (vertical lift performance) package to compute the bottom-hole flowing pressure corresponding to a given surface rate and wellhead pressure, as illustrated in figure 7–21. This presumes that the VLP program has been calibrated in terms of tubing surface roughness, say, to actual well production data and illustrates a useful application of a steady-state flowing well simulator. The pressure normalization described by Eq. (7–56) is the constant-pressure analog of the rate normalization carried out when variable-rate data are converted to constant-rate equivalent.

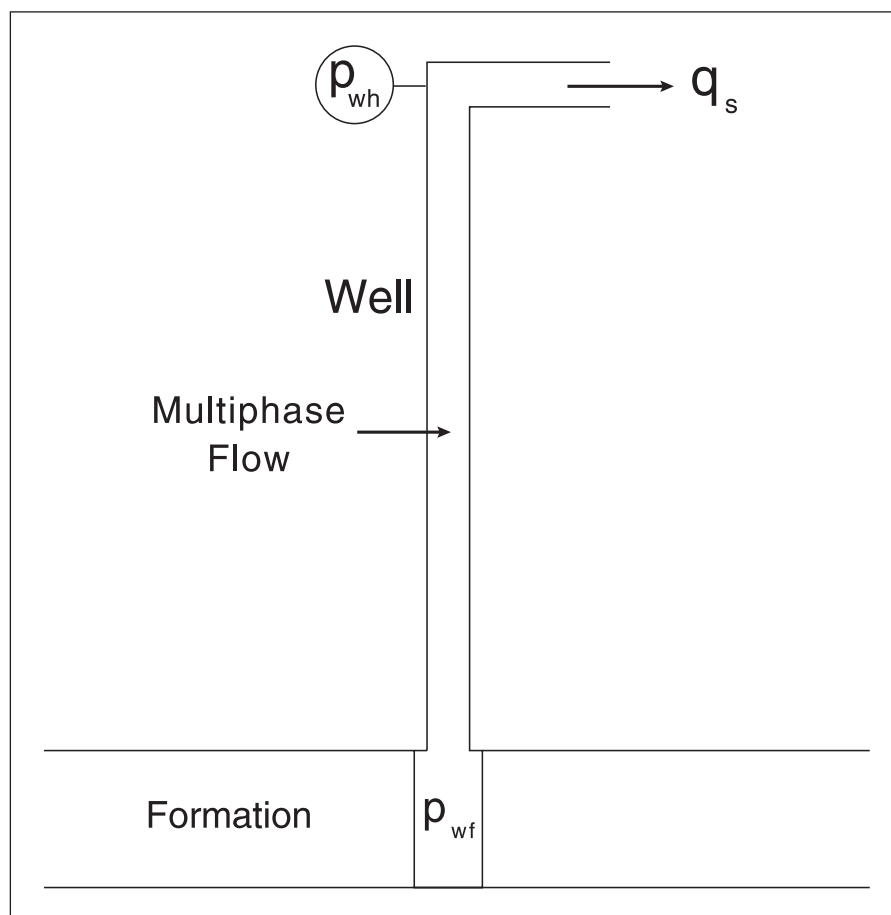


Fig. 7–21. Use of nodal analysis program to correct for variation in flowing pressure

Decline curve analysis on the basis of real time, i.e., considering  $q$  to be a direct function of actual flowing time,  $t$  is valid only provided the well is kept in continuous production and the rate is decreasing monotonically. If the well is periodically shut in for a long buildup and the production is intermittent with significant transient behavior, the sensible approach is to employ full superposition with a closed reservoir model or to utilize the approximate algorithm described in chapter 5 of *Well Test Design and Analysis* to discern material balance effects.

## Nonzero decline curve exponent

A theoretical derivation of the exponential decline with  $b = 0$  was described earlier. In practice, decline curve data often exhibit a nonzero value of the exponent  $b$ —referred to as *hyperbolic decline*—with a value close to 0.5 being quite common. This implies that the decline in production does not follow the perfectly closed, liquid filled system model. The exponential (liquid depletion) form gives the fastest decline rate and data in hyperbolic decline plot on a semilog graph with upward curvature as shown in figure 7–22.

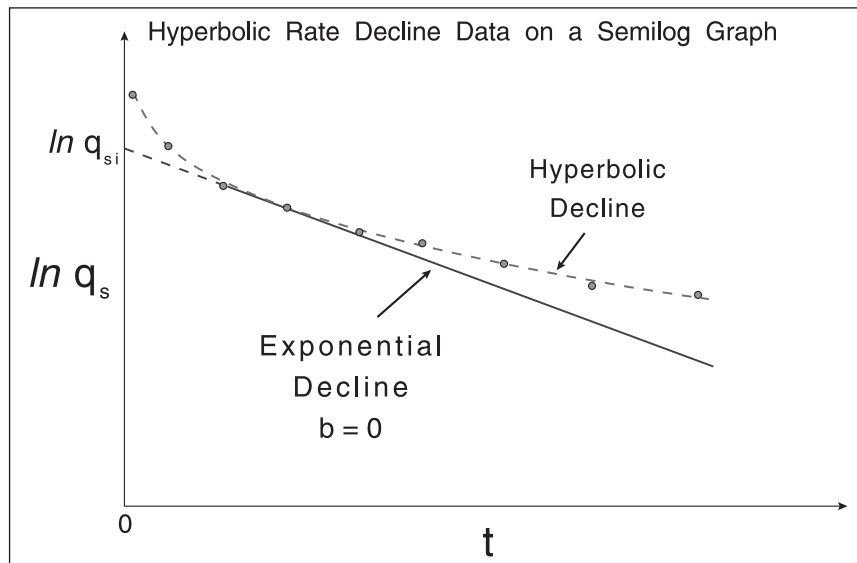


Fig. 7-22. Hyperbolic decline data on a semilog graph

Many of the decline curve datasets correspond to solution gas drive, and Fetkovich<sup>7</sup> has suggested that  $b$  should lie in the range  $0.5 < b < 0.667$  for this situation. It is possible to simulate depletion in solution gas-drive situations by running a closed reservoir model in the constrained convolution mode for specified and constant  $p_{wf}$  and employing the pseudopressure function for solution gas drive. This approach is discussed in detail in chapter 3 on multiphase flow where the use of two-phase compressibility is also advocated in generation mode.

The second major cause of nonzero exponents is pressure support either from the aquifer or from reservoir compartments screened from the well cell by tight zones. The behavior of compartmentalized systems is discussed in detail in chapter 12 and decline curve analysis for this situation is treated at length. For the moment, it is sufficient to note that the convolution algorithm for fixed bottom-hole pressure can be run with a variety of reservoir models, e.g., radial closed composite or two-cell compartmentalized, to investigate the nature of the decline curve with delayed support of various forms. Again, decline curve exponents greater than zero occur.

Decline curve analysis has been applied to gas wells and in this case the nonzero nature of the exponent is due both to the nonlinear nature of the inflow performance relation (IPR) relation and the changing compressibility of the gas in the reservoir as the average pressure decreases especially below values around 1,500 psia. By analyzing some data quoted by Carter,<sup>8</sup> Fetkovich has observed that the hyperbolic decline exponent is of the order of 0.5 in gas wells where the  $\mu c_g$  ratio, defined as

$$\frac{\mu(p_i)c_g(p_i)}{\mu c_g}$$

is approximately 0.55. When the  $\mu c_g$  ratio is close to unity and the gas well essentially obeys the liquid solution, then  $b = 0$  as expected. Depletion in gas wells is best understood using the concepts of pseudopressure and pseudotime developed in chapter 13 of *Well Test Design and Analysis*, where it is demonstrated that a straight line on the Cartesian graph of  $\psi(p)$  versus  $t_a$  will

yield the original gas-in-place. Prediction of gas well deliverability is also best carried out using production-constrained convolution on a fitted closed reservoir model.

## Semi-Steady-State Depletion

In situations where a closed system  $p_D$  function is employed, the Fetkovich approximation assumes QSSS conditions after the total time exceeds  $t_{SSS}$ ; the inflow performance relation takes the form of a straight line of slope  $-1/J_{SSS}$  as illustrated in figure 7-23. The average pressure of the drainage area  $\bar{p}(t)$  is given by the material balance equation

$$\frac{d\bar{p}}{dt} = -\frac{q}{c_t V} \quad (7-57)$$

where  $V$  is the pore volume of the drainage area equal to  $\phi h \bar{A}$ ; this equation may be written in integral form as

$$\bar{p}(t) = p_i - \frac{1}{V} \int_0^t \frac{q}{c_t} dt = p_i - \frac{q_r c_{ti}}{c_{ti} V q_r} \int_0^t \frac{q}{c_t} dt = p_i - \frac{q_r}{c_{ti} V} t_a \quad (7-58)$$

where  $t_a$  is the material balance pseudotime defined by the integral relation

$$t_a = \frac{c_{ti}}{q_r} \int_0^t \frac{q}{c_t} dt \quad (7-59)$$

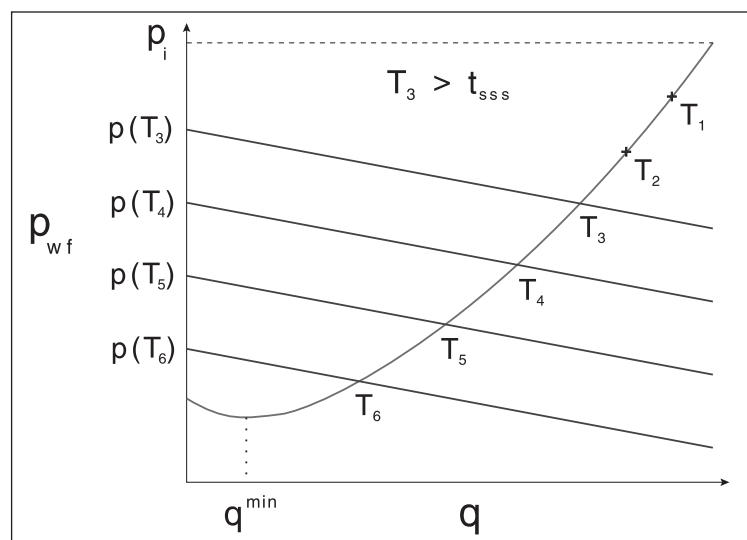


Fig. 7-23. Semi-steady-state depletion on a well performance diagram

The material balance equation (7-58) defines the drainage area average pressure at any time  $t = T_M$ , and the intersection of the straight line IPR with the VLP curve defines the well flow rate  $q_M$  at

time  $T_M$ . Note that when the rate varies with time the material balance equation must be integrated considering the time dependence of  $q$ ; the normalized pseudotime  $t_a$  is simply a convenient method in the context of well test analysis for recognizing this requirement. The pseudotime also allows any dependence of  $c_t$  on pressure to be handled. The intersections of the successive IPR lines with the appropriate VLP relation are marked on figure 7–23 and the corresponding decline curve can be drawn from this.

Examination of VLP curves computed from algorithms modeling multiphase flow in wells shows that often the relation can be represented by a straight line over a substantial range of flow rates; this is illustrated in figure 7–24. Thus, the near-linear VLP curve may be described by the approximation

$$p_{wf} = p_{wf}^{q=0} + \frac{1}{L}q \quad (7-60)$$

where  $1/L$  is the slope of the straight line segment of  $f_{VL}$ ; Eq. (7–60) derives from the inverted form

$$q = L(p_{wf} - p_{wf}^{q=0}) \quad (7-61)$$

where  $L$  is an apparent friction loss coefficient whose units are bbl/day/psi, i.e., the same as productivity index  $J_{SSS}$ . The quantity  $p_{wf}^{q=0}$  is the intercept of the straight line section of the VLP and the difference  $p_{wf}^{q=0} - p_{wh}$  is dependent on the gravity term in the two-phase flow simulation; here,  $p_{wh}$  is the wellhead pressure. Thus,  $p_{wf}^{q=0} - p_{wh}$  is controlled by such variables as the vertical depth, the fluid bubble point, the oil gravity, and the density of the two-phase flowing mixture. The vertical lift index  $L$  is essentially determined by fluid friction in the wellbore and is therefore a function of the tubing diameter, the oil viscosity, and the measured depth. A significant linear segment of the VLP will occur when accelerational effects are small, but the rate is still high enough for slip phenomena not to be important.

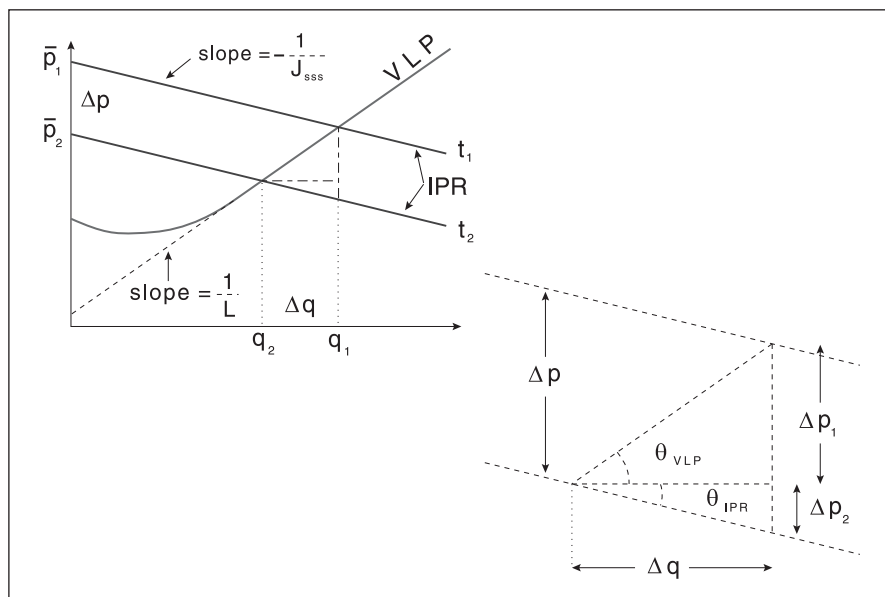


Fig. 7–24. Near-linear VLP relation

In figure 7–24, two IPR lines are drawn corresponding to times  $t_1$  and  $t_2$ , respectively. During the time interval  $\Delta t = t_2 - t_1$ , the average pressure falls by an amount  $\Delta p = \bar{p}_2 - \bar{p}_1$  where the differential material balance Eq. (7–57) shows that

$$\Delta p = \frac{q}{c_t V} \Delta t \quad (7-62)$$

Over the time interval  $\Delta t$ , the rate falls by an amount  $\Delta q = q_2 - q_1$  where the rates  $q_1$  and  $q_2$  are fixed by the intersections of the respective IPR lines with the VLP relation which has been assumed to be linear; the construction is illustrated in figure 7–24. From the geometry of the this well performance diagram, the rate change may be related to the drop in average pressure as follows:

$$\Delta p = \Delta p_1 + \Delta p_2 = \Delta q \tan(\theta_{VLP}) + \Delta q \tan(\theta_{IPR}) = \Delta q \left( \frac{1}{L} + \frac{1}{J_{SSS}} \right)$$

i.e.,

$$\Delta q = \frac{\Delta p}{\left( \frac{1}{L} + \frac{1}{J_{SSS}} \right)} \quad (7-63)$$

Thus, the decline in rate over the time interval  $\Delta t$  can be related to the change in average pressure; the slopes of both the IPR and the VLP relations influence this process. Substituting Eq. (7–62) into (7–63) to eliminate  $\Delta p$  gives the result

$$\frac{dq}{dt} = - \frac{q}{c_t V \left( \frac{1}{L} + \frac{1}{J_{SSS}} \right)} \quad (7-64)$$

This is the rate decline equation for SSS vertical lift constrained production, and defining an effective production decline index  $P$  as

$$\frac{1}{P} = \frac{1}{L} + \frac{1}{J_{SSS}} \quad (7-65)$$

Eq. (7–64) may be written, on separating the variables, as

$$\frac{dq}{q} = - \frac{P}{c_t V} dt \quad (7-66)$$



This differential rate decline equation may be integrated from time  $t = 0$  when the flow rate is designated  $q(t = 0)$ ; thus

$$\int_{q(t=0)}^{q(t)} \frac{dq}{q} = - \int_0^t \frac{P}{c_t V} dt$$

i.e.,

$$\ln \frac{q(t=0)}{q(t)} = \ln \frac{q^0}{q(t)} = \frac{Pt}{c_t V} \quad (7-67a)$$

This is the classical equation of exponential production decline in SSS depletion which takes the form

$$q(t) = q^0 e^{-\frac{Pt}{c_t V}} \quad (7-67b)$$

where  $q^0$  is the initial production defined by the first intersection corresponding to QSSS depletion ( $T_3$  in figure 7-24). The time  $t$  in the exponential decline Eq. (7-67a and b) is therefore measured from the point at which QSSS behavior commences. If the rate is declining exponentially, then

$$\ln q(t) = \ln q^0 - \frac{P}{c_t V} t \quad (7-68)$$

and a plot of  $\ln q(t)$  versus time will be a straight line of slope  $m_d$  and intercept  $b_d$ , where

$$m_d = - \frac{P}{c_t V} \quad \text{and} \quad b_d = \ln q^0 \quad (7-69)$$

Exponential decline will continue as long as the VLP curve can be approximated by a straight line, i.e., up to the time  $T_6$  in figure 7-24.

Equation (7-22) can be written in the form

$$\frac{q(t)}{q^0} = \frac{1}{e^{D^0 t}} \quad (7-70)$$

where  $D^{\circ} = \frac{P}{c_t V}$  which has units of reciprocal time ( $T^{-1}$ ) and is known as the decline rate. The exponential form (7-70) is a special case of the empirical Arps's equation

$$\frac{q(t)}{q^{\circ}} = \frac{1}{(1 + bD^{\circ}t)^{1/b}} \quad (7-71)$$

with the  $b$ —the reciprocal of the decline curve exponent—equal to zero. Thus, the combination of a simple material balance model for the block average pressure and the straight line forms for both the IPR and VLP relations demonstrates a strong theoretical basis for exponential rate decline. The rate decline of the well is controlled by the volume of the compartment in which the well is located, the total compressibility, and the production decline index  $P$ . In the case where  $L \gg J_{SSS}$  and the VLP can be taken as a straight line of zero slope as shown in figure 7-25, the well bottom-hole flowing pressure is constant, i.e., independent of rate, and the classical decline curve analysis situation exists. In this case, the decline rate is given by  $D^{\circ} = \frac{J_{SSS}}{c_t V}$  since  $P \approx J_{SSS}$ ; this is the usual expression for  $D^{\circ}$  found in exponential decline theory. The treatment here has extended the constant bottom-hole pressure result to include the effect of the slope of the VLP curve on decline analysis. Conversely, when  $J_{SSS} \gg L$ , the depletion rate decline is controlled by the slope of the VLP curve, as illustrated in figure 7-26, with  $P \approx L$  and  $D^{\circ} = \frac{L}{c_t V}$ . The characteristic dimensionless time for rate decline can be defined as

$$t_{DR} = \frac{Pt}{c_t V} = D^{\circ}t = \frac{t}{\tau_R} \quad (7-72)$$

where  $\tau_R$  is a time constant for exponential rate decline equal to  $(D^{\circ})^{-1}$ . The economics of a well are highly dependent on the magnitude of this time constant and it is evident that the effective contributing pore volume  $V$  that the well is draining is a crucial factor in its determination; the important issue of reservoir compartmentalization, which is central to the proper understanding of depletion, is discussed at length in chapter 13. Equation (7-22) can be expressed in terms of dimensionless rate  $q_D = q(t)/q^{\circ}$  and dimensionless time  $t_{DR}$  as follows:

$$q_D = e^{-(t_{DR})} \quad (7-73)$$

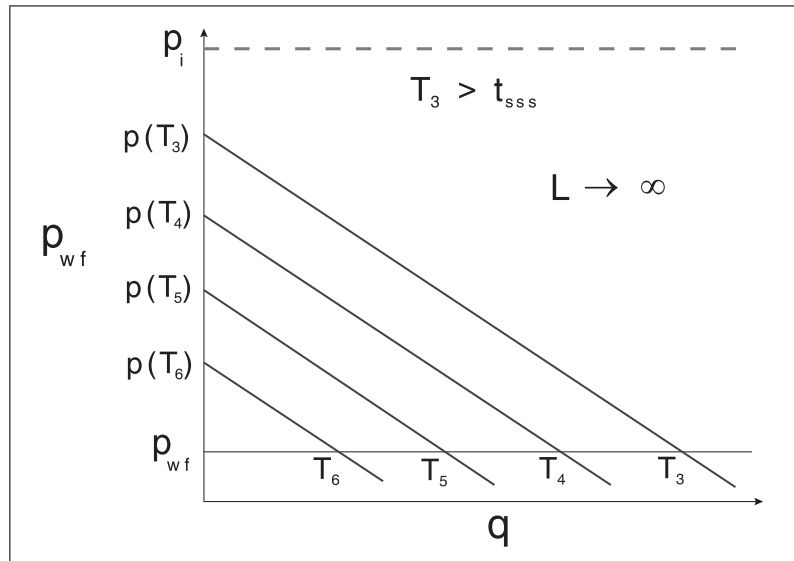


Fig. 7-25. Depletion with a constant bottom-hole flowing pressure

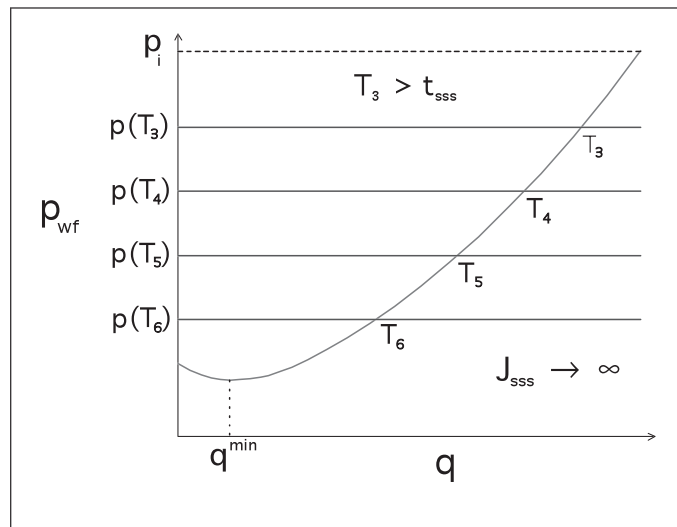


Fig. 7-26. Decline rate dominated by the VLP relation

If the well is produced for a total time  $t_p$  wholly in the exponential decline period, then the cumulative volume of oil recovered is given by

$$Q = \int_0^{t_p} q(t)dt = q^o \int_0^{t_p} e^{-D^o t} dt = \frac{q^o}{D^o} \left( 1 - e^{-D^o t_p} \right) \quad (7-74)$$

which shows that, in the limit of an infinite production time, the maximum oil which can be produced is given by  $Q^{\max} = q^o/D^o$ . Thus, the decline rate  $D^o$  has a physical significance in terms of the maximum producible oil by depletion under production constraint. However, it is much more realistic to consider production only up to the point of unstable well operation at rate  $q^{\min}$ , as indicated in figure 7-26; as previously mentioned, the minimum stable operating rate  $q^{\min}$  is

one of the most important items of information that can be obtained from the nodal analysis of vertical lift behavior. If the production time to attain a rate of  $q^{\min}$  is computed from Eq. (7-22) and the result substituted in (7-74), the cumulative production  $Q^{\lim}$  up to the cut-off flow rate  $q^{\min}$  is given by

$$Q^{\lim} = \frac{q^o - q^{\min}}{D^o} \quad (7-75)$$

## Agarwal–Gardner Decline Type Curves

### Liquid solution decline type curves for radial flow

Agarwal et al.<sup>9</sup> extended the work of Palacio and Blasinghame<sup>10</sup> in producing type curves in decline form which can be used to determine gas in place (GIP) in gas wells. The focus of this work is to examine how the constant-rate liquid solution can be used to analyze production data. The constant terminal pressure solution is taken as the variable-rate case for which an appropriate methodology has to be found. The starting point in the Agarwal et al. analysis is the constant-rate liquid solution for a well in a closed circular reservoir. The two flow regimes in this case are infinite-acting (IA) radial flow and SSS depletion. In well test analysis, a type curve is generally a log–log plot of dimensionless pressure  $p_D$  versus dimensionless time  $t_D$ , where

$$p_D = \frac{2\pi kh\Delta p}{q\mu} = \frac{2\pi kh(p_i - p_{wf})}{q\mu} \quad \text{and} \quad t_D = \frac{kt}{\phi\mu c_t r_w^2} \quad (7-76)$$

A type curve in decline form simply uses the reciprocal of  $p_D$ , i.e.,  $1/p_D$ , as ordinate and dimensionless time based on drainage area  $t_{DA}$  as abscissa; the definition of  $t_{DA}$  is

$$t_{DA} = \frac{kt}{\phi\mu c_t \bar{A}} \quad \text{where} \quad \bar{A} = \pi r_e^2 \quad (7-77)$$

It is common to write  $1/p_{wD}$  as  $q_D$ , i.e.,  $q_D = \frac{q\mu}{2\pi kh\Delta p}$  (7-78)

The constant-rate liquid solution for a closed reservoir is presented in this form in figure 7-27, where  $1/p_{wD} = q_D$  is plotted versus  $t_{DA}$  on a log–log scale. Note that the flow rate  $q$  is defined in terms of the in situ volume and the cumulative production  $Q$  used later, also at in situ conditions; for field units at stock tank conditions, the following conversions should be included:

$$q = q_s B_o \quad (7-79a)$$

$$Q = N_p B_o \quad (7-79b)$$

In the middle time region (MTR), i.e., radial flow, the dimensionless pressure is given by

$$p_D = \frac{1}{2} \ln \frac{4t_D}{\gamma} + S \tag{7-80}$$

while in the SSS depletion segment of the late time region (LTR) is

$$p_D = 2\pi t_{DA} + \frac{1}{2} \ln \frac{4\bar{A}}{\gamma C_A r_w^2} + S \quad \text{where } C_A = 31.62 \tag{7-81}$$

### Constant terminal pressure data and equivalent time

Agarwal et al, generated constant bottom-hole pressure data and overlaid the data on the constant-rate drawdown (CRD) decline type curve as shown in figure 7–28, where it can be seen that the constant BHP data do not correspond in the pseudo-semi-steady-state (PSSS), i.e., boundary dominated flow period. However, in the transient period, the constant terminal pressure (CTP) data overlays the CRD type curve exactly. It was shown by Agarwal et al. that a time transformation allows the CTP data to fit the CRD decline curve; the modified time  $t_e$  is defined as

$$t_e = \frac{\text{Cumulative Production}}{\text{Instantaneous Rate}} \tag{7-82}$$

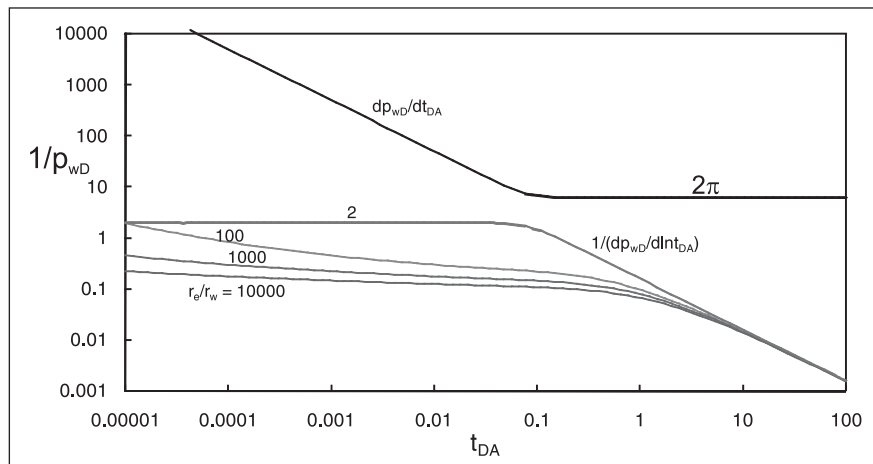


Fig. 7–27. Agarwal–Gardner decline type curve for radial systems

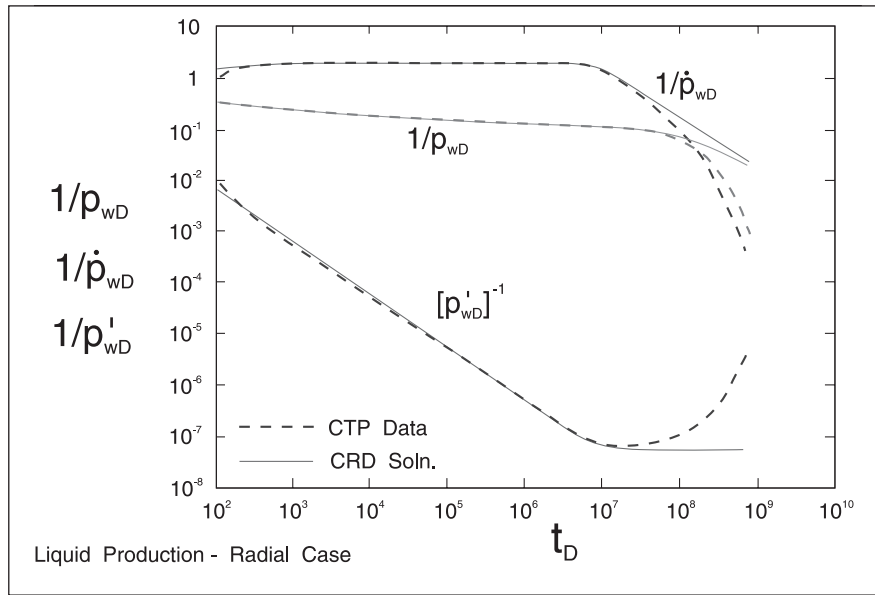


Fig. 7–28. Comparison of constant rate and constant BHP liquid production data

When the CTP data are plotted on this basis, an exact overlay is achieved throughout the whole time period as shown in figure 7–29; note that this equivalent time is the form used to determine  $t_p$  for a buildup. A type curve match implies that a log–log plot of  $\frac{q}{\Delta p}$  versus  $t_e = \frac{Q}{q}$ , on compatible scale, is overlaid on the dimensionless type curve, allowing permeability  $k$  to be determined from the rate/pressure match and reservoir drainage area,  $\bar{A}$ , from the time match. The use of  $t_e$  in the transient period, rather than  $t$ , does not affect the quality of the match in that region. The match equations in field units take the form

Pressure match: 
$$k = \frac{887.2B\mu[q/\Delta p]_M}{2\pi h[1/p_D]_M} \tag{7-83a}$$

Time match: 
$$\bar{A} = \frac{0.00026368k[t_e]_M}{\phi\mu c_t[t_{DA}]_M} \quad r_e = \sqrt{\frac{\bar{A}}{\pi}} \tag{7-83b}$$

Parameter match: 
$$r_{wa} = \frac{r_e}{[r_e/r_{wa}]_M} \quad S = \ln \frac{r_w}{r_{wa}} \tag{7-83c}$$

In CRD, the logarithmic derivative, denoted  $p' = dp_{wf}/d\ln t$ , is constant (derivative plateau) during radial IA flow. The dimensionless derivative  $p'_D$  takes on the value of 0.5 in this flow regime, while in SSS depletion in a closed system the logarithmic derivative exhibits a unit slope on a log–log diagnostic plot. In the analysis of production data, it is convenient to work with the reciprocal of  $p'$  or  $p'_D$  written as  $1/p'$  or  $1/p'_D$ ; in radial flow,  $1/p'_D$  becomes 2 while in SSS depletion a slope of  $-1$  is observed. The reciprocal logarithmic dimensionless derivative is also plotted on the decline type curve, i.e., figure 7–27, which will aid flow regime definition and permeability

determination. In the case of actual production data, the logarithmic derivative is the slope of a semilog graph of  $\Delta p/q$  versus  $\ln t_e$  and  $1/p'$  is simply the reciprocal of this quantity.

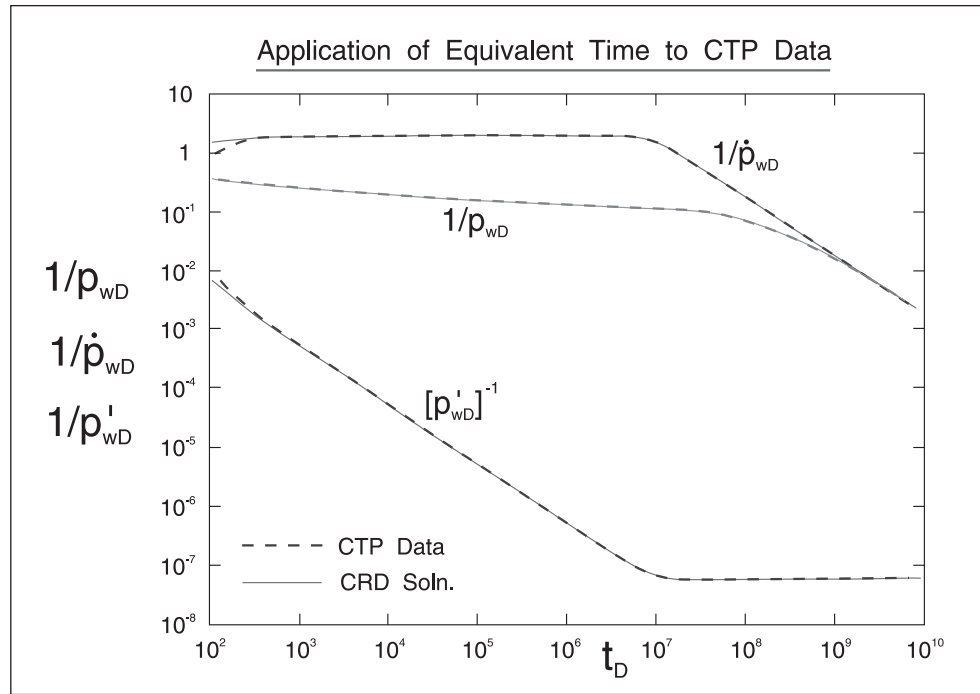


Fig. 7-29. Converting constant BHP data to an equivalent constant rate form

## Gas reservoir data

Agarwal et al. used a single-phase reservoir simulator to generate both CRD and CTP synthetic data. The overlay on the liquid decline type curve is shown in figure 7-30; this is similar to figure 7-28 in terms of plotting variables. However, the difference between the two cases during the PSSS period becomes significant; the deviation in the gas case is more severe because of the added complication of variation in gas properties. Following the approach suggested by Palacio and Blasinghame, a pseudotime is defined in terms of gas properties calculated at the material balance average pressure  $\bar{p}$ . Pseudo equivalent time  $t_a$  is defined as

$$t_a = \frac{1}{q(t)} [\mu c_g]_i \int_0^t \frac{q(t') dt'}{\mu(\bar{p}) c_g(\bar{p})} \quad (7-84)$$

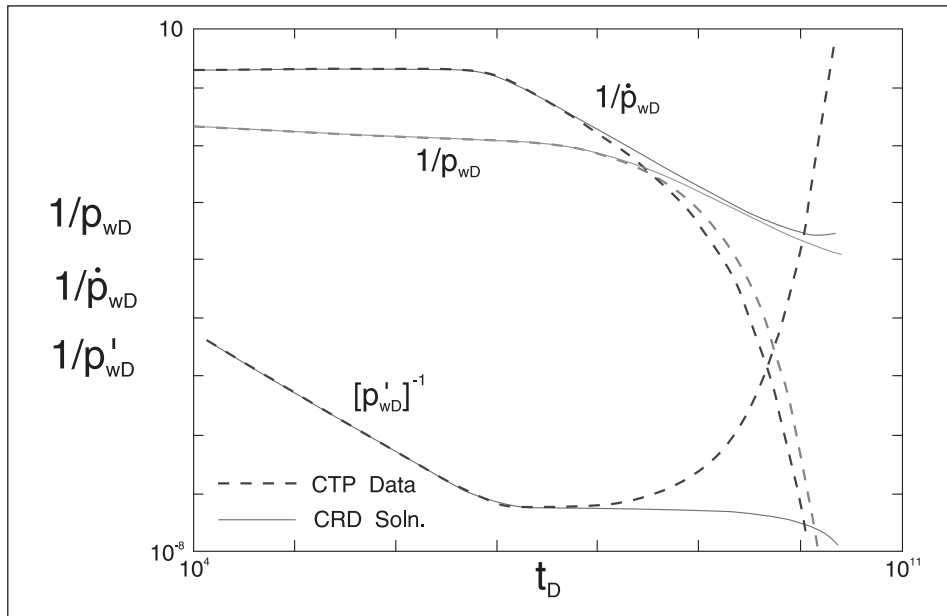


Fig. 7–30. Comparison of constant rate and constant BHP Gas production data

This definition of pseudotime has already been given in chapter 13 of *Well Test Design and Analysis*, where the issue of variable rate in gas well testing was discussed. The real gas pseudopressure  $m(p)$  is defined as

$$m(p) = 2 \int_{P_b}^p \frac{p'}{\mu z} dp' \quad (7-85)$$

The dimensionless pseudotime  $t_{aDA}$  and inverse dimensionless pseudopressure follow as

$$t_{aDA} = \frac{kt_a}{\phi[\mu c_g]_i \bar{A}} \quad 1/p_{wD} = q_D = \frac{Qp_{sc}T}{\pi khT_{sc}(m(p_i) - m(p_{wf}))}$$

In field units ( $t : h$ ) these definitions become

$$t_{aDA} = \frac{0.00026367 \times kt_a}{\phi[\mu c_g]_i \bar{A}} \quad \text{and} \quad 1/p_{wD} = q_D = \frac{1422 \times QT}{kh(m(p_i) - m(p_{wf}))}$$

Agarwal et al. in their paper suggest that time in days be used for the analysis of production data giving

$$t_{aDA} = \frac{0.0063281 \times kt_a}{\phi[\mu c_g]_i \bar{A}}$$



When synthetic gas well data at constant terminal pressure from the simulator are transformed in this fashion, they exactly overlay the liquid type curve as depicted in figure 7–29. Hence, gas well data can be analyzed using the liquid solution using the concepts of pseudotime and pseudopressure. Note, however, that a pseudotime based on average pressure requires that the size of the reservoir in terms of pore volume or GIP be known; thus, the interpretation process is iterative since the reservoir pore volume  $P_v = \phi h \bar{A}$  is determined from the time match.

## Fractured wells

In low-permeability reservoirs, the wells are often hydraulically fractured and in the case of infinite conductivity fractures a significant linear flow period will be present. The Green's function solution for a fractured well in a closed rectangular reservoir can be used to predict CRD data, and figure 7–31 has been generated using an infinite-conductivity fracture model and again is presented as  $1/p_{wD}$  versus  $t_{DA}$  supplemented by the logarithmic dimensionless derivative  $1/p'_{wD}$ . Note that linear flow is characterized by a negative half slope using this derivative function, while SSS depletion is manifested by a negative unit slope. Type curves for three fracture half lengths, viz.,  $x_e/x_f = 25, 5, 2$ , have been included and for case 1, i.e.,  $x_e/x_f = 25$ , pseudoradial flow is evident before the SSS occurs. In case 3, i.e.,  $x_e/x_f = 2$ , there is a transition from linear flow to SSS with no pseudoradial period whatsoever.

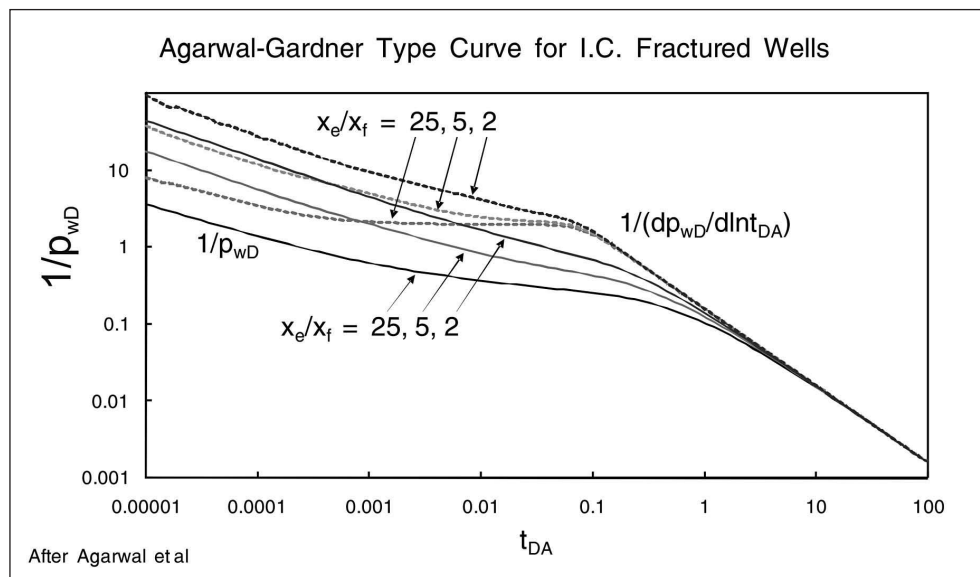


Fig. 7–31. Rate–time production decline type curve for infinite conductivity fractured wells

## Decline type curves based on cumulative production

Operations and field engineers commonly make a graph of rate  $q(t)$  or normalized rate  $q(t)/(p_i - p_{wf})$  as a function of cumulative production; a recent paper on this topic is due to Callard et al.<sup>11</sup> It is therefore useful to develop a theoretical basis for this form of decline

analysis. The basic CRD data for a closed reservoir gives  $1/p_{wD}$  versus  $t_{DA}$ ; however, the same information can be presented as a plot of  $1/p_{wD}$  versus  $t_{DA}/p_{wD}$ , where

$$t_{DA}/p_{wD} = \frac{kt}{\phi\mu c_t \bar{A}} \cdot \frac{q\mu}{2\pi kh\Delta p} = \frac{Q}{2\pi c_t P_V (p_i - p_{wf})} = Q_{DA} \quad (7-86a)$$

where  $P_V = \text{Pore volume} = \phi\bar{A}h$

$Q = \text{Cumulative liquid production} = qt$  (for constant rate).

In field units, Eq. (7-86a and b) becomes

$$t_{DA}/p_{wD} = \frac{Q \times 5.6146}{2\pi c_t P_V (p_i - p_{wf})} = Q_{DA} \quad (7-86b)$$

A log-log plot of  $1/p_{wD}$  versus  $Q_{DA}$  constitutes a decline type curve based on cumulative production and this form has an advantage when there is considerable noise in the production data. Figure 7-32 shows such a plot for the radial flow model and it is apparent that in the SSS period the data is compressed under this cumulative production presentation. The derivative  $1/(dp_{wD}/d\ln Q_{DA})$  exhibits the plateau value of 2 in the transient (MTR) period and then rolls over with an asymptote of zero. Also shown in figure 7-32 is the natural derivative  $d(1/p_{wD})/dQ_{DA}$ , which interestingly attains a plateau in the SSS period; note that the plateau value depends on  $r_e/r_w$ . The log-log form of the cumulative production type curve has not proved to be useful because of this compression, and Agarwal et al. used an alternative form where the same dimensionless data are plotted on a Cartesian scale as shown in figure 7-33. Here, the SSS regime appears as straight lines (as shown by the natural derivative becoming constant) converging to the asymptotic value of  $1/2\pi = 0.159$ ; Agarwal et al. refer to this as an anchor point.

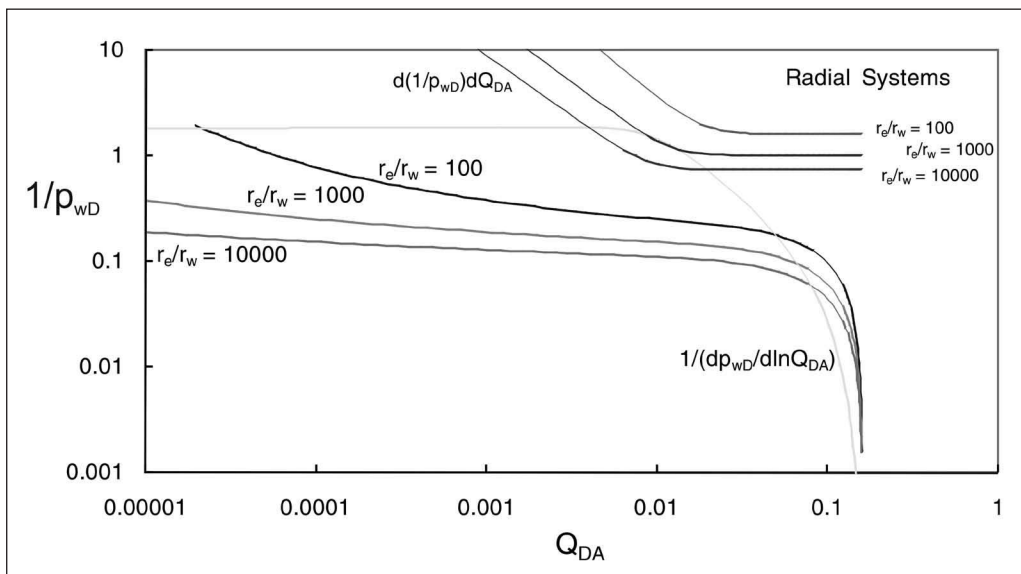


Fig. 7-32. Rate-cumulative production decline type curve for radial flow wells

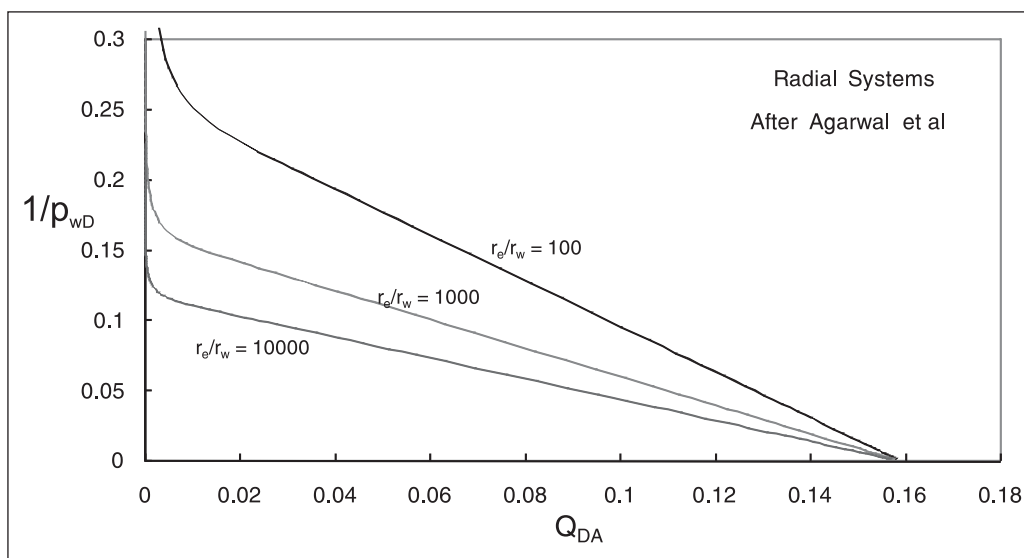


Fig. 7-33. Cartesian rate-cumulative production decline type curve for radial flow wells

The use of the Cartesian scale presentation involves a plot of the pressure-normalized rate, i.e.,  $q/(p_i - p_{wf})$ , versus pressure-normalized cumulative production, i.e.,  $Q/(p_i - p_{wf})$ . The implication of the dimensionless Cartesian graph is the existence of a straight line section in SSS of the form

$$\frac{q}{p_i - p_{wf}} = a \left( \frac{Q}{p_i - p_{wf}} \right) + b \tag{7-87}$$

At the SSS, the following relations are valid:

$$q = J_s (\bar{p} - p_{wf}) \tag{7-88}$$

and 
$$Q = c_t P_V (p_i - \bar{p}) \tag{7-89a}$$

i.e., 
$$\bar{p} = p_i - \frac{Q}{c_t P_V} \tag{7-89b}$$

Hence, using substitution, the term  $q/(p_i - p_{wf})$  may be expanded as

$$\frac{q}{p_i - p_{wf}} = \frac{J_s \left( p_i - \frac{Q}{c_t P_V} - p_{wf} \right)}{p_i - p_{wf}} = \frac{J_s (p_i - p_{wf})}{p_i - p_{wf}} - \frac{J_s Q}{c_t P_V (p_i - p_{wf})}$$

$$= J_{SSS} - \frac{J_{SSS}}{c_t P_V} \cdot \frac{Q}{p_i - p_{wf}} = b + a \left( \frac{Q}{p_i - p_{wf}} \right) \quad (7-90)$$

i.e., a straight line where  $a = -\frac{J_{SSS}}{c_t P_V}$  and  $b = J_{SSS}$

Thus the existence of the straight line follows from the SSS relations (7-88) and (7-89a and b). If  $q/(p_i - p_{wf})$  is set to zero in Eq. (7-90), there results

$$0 = J_{SSS} - \frac{J_{SSS}}{c_t P_V} \cdot \frac{Q}{p_i - p_{wf}}$$

i.e., 
$$\frac{Q}{p_i - p_{wf}} = c_t P_V \quad (7-91)$$

Thus, the x-axis intercept of the extrapolated straight line (i.e.,  $q/(p_i - p_{wf}) = 0$ ) is  $c_t P_V$ ; in field units the intercept is  $\frac{c_t P_V}{5.6146}$ . Although this is a fairly convoluted approach to the analysis of the SSS period, it is theoretically correct and the intercept does give the connected pore volume directly. This algebra is very similar to that involved in deriving the intercept of the familiar  $p/z$  plot in gas reservoir engineering. One disadvantage of the procedure is the requirement that the initial pressure  $p_i$  be known.

Since an overlay construction is valid only for a log-log type curve, in this case, the Cartesian plot of  $q(t)/(p_i - p_{wf})$  versus  $\frac{Q}{p_i - p_{wf}}$  is made directly as illustrated in figure 7-34. A straight line is fitted to the appropriate data range and the x-axis intercept yields  $c_t P_V$  allowing the pore volume  $P_V$  to be determined. The well SSS productivity index follows from the fitted slope of the line  $a$ ; thus

$$J_{SSS} = -a c_t P_V \quad (7-92a)$$

or, it can be determined directly from the y-axis intercept  $b$ ; i.e.,

$$J_{SSS} = b \quad (7-92b)$$

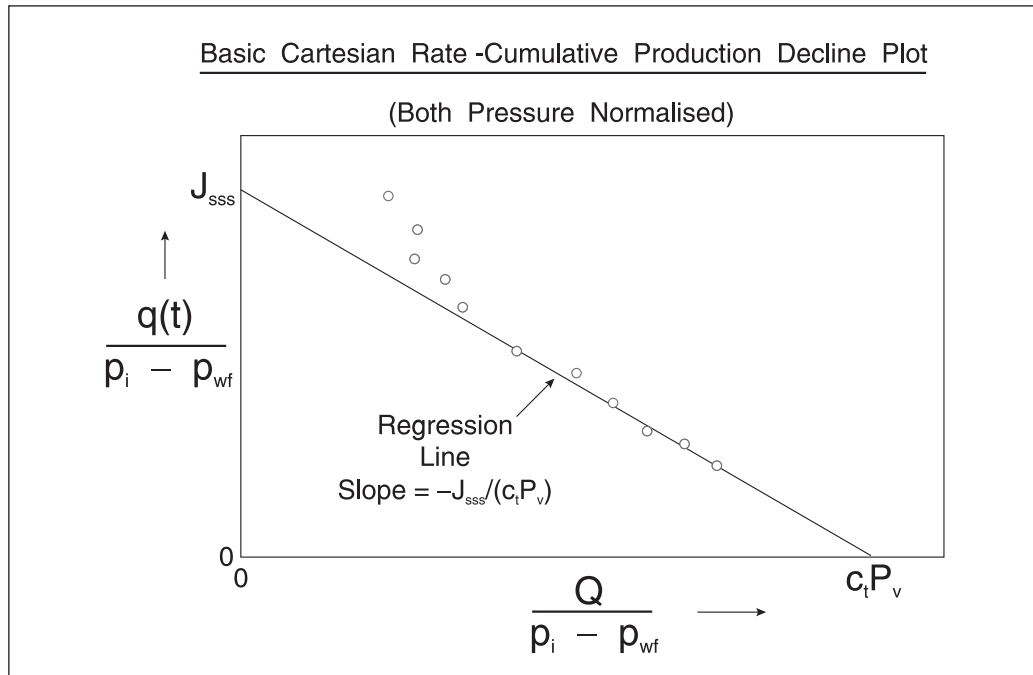


Fig. 7–34. Cartesian decline plot for radial systems (liquid flow)

If the permeability is known from log–log type curve analysis, the data can be overlaid on the dimensionless Cartesian type curve. In field units these equations become

$$J_{SSS} = -\frac{ac_t P_v}{5.6146} \quad (7-93a)$$

and

$$J_{SSS} = b \quad (7-93b)$$

## Application to gas reservoirs

The gas reservoir material balance in terms of pseudo time and pressure has been examined at length in chapter 13 of *Well Test Design and Analysis*, where it was shown that

$$\psi_i - \psi(\bar{p}) = \frac{Q_r B_{gi} \mu_i}{2\pi kh} 2\pi \frac{k}{\phi \mu_i c_{gi} A} \int_0^t \frac{\mu_i c_{gi} Q_{sc}}{\mu(\bar{p}) c_g(\bar{p}) Q_r} dt' \quad (7-94)$$

or

$$\psi_i - \psi(\bar{p}) = \frac{Q_r B_{gi} \mu_i}{2\pi kh} 2\pi \frac{k \tilde{\tau}}{\phi \mu_i c_{gi} A} \quad \text{where} \quad \tilde{\tau} = \int_0^t \frac{\mu_i c_{gi} Q_{sc}}{\mu(\bar{p}) c_g(\bar{p}) Q_r} dt' \quad (7-95)$$

where  $\psi(p)$  is the normalized pseudopressure and  $\psi_i = \psi(p_i)$ . Converting to conventional pseudopressure  $m(p)$  using the relation

$$m(p) = \frac{2p_i}{\mu_i z_i} \psi(p) \quad (7-96)$$

gives

$$m(p_i) - m(\bar{p}) = \frac{2p_{sc} T Q_r \tilde{\tau}}{T_{sc} h \phi \bar{A} \mu_i c_{gi}} \quad (7-97)$$

The quantity  $Q_r \tilde{\tau}$  is denoted  $Q_a$  in the paper by Agarwal et al., i.e.,

$$Q_a = \int_0^t \frac{\mu_i c_{gi} Q_{sc}}{\mu(\bar{p}) c_g(\bar{p})} dt' \quad (7-98)$$

and the volumetric material balance for a gas reservoir may be written as

$$m(p_i) - m(\bar{p}) = \frac{2p_{sc} T Q_a}{T_{sc} h \phi \bar{A} \mu_i c_{gi}} \quad (7-99)$$

Defining a constant  $c_{ag}$  as  $c_{ag} = \frac{\mu_i c_{gi} T_{sc}}{2p_{sc} T}$  and writing  $P_v = \phi h \bar{A}$ , Eq. (7-99) becomes

$$m(p_i) - m(\bar{p}) = \frac{Q_a}{c_{ag} P_v} \quad (7-100)$$

This is analogous to the liquid material balance expression (7-89a), i.e., the constant  $c_{ag}$  is an equivalent compressibility that can be used with pseudopressure and time. The deliverability of a gas well in SSS can be written in the form

$$Q_{sc} = J_{SSS}^{PP} (m(p_i) - m(p_{wf})) \quad (7-101)$$

and the algebra previously derived for the liquid case carries over directly to the gas situation. Thus, a plot of  $Q_{sc}/(m(p_i) - m(p_{wf}))$  versus  $Q_a/(m(p_i) - m(p_{wf}))$  will be a straight line of the form

$$\frac{Q_{sc}}{(m(p_i) - m(p_{wf}))} = J_{SSS}^{PP} - \frac{J_{SSS}^{PP}}{c_{ag} P_v} \cdot \frac{Q_a}{(m(p_i) - m(p_{wf}))} \quad (7-102)$$

Thus, in the analysis of gas wells, pseudopressure and pseudo cumulative production are used, i.e., the Cartesian plot utilizes the pseudopressure normalized rate  $Q_{sc}/\Delta m(p)$  and the pseudopressure normalized pseudo cumulative production  $Q_a/\Delta m(p)$ ; for a gas well, the Cartesian graph takes the form shown in figure 7-35 and, following the material balance terminology in gas reservoir engineering, this may conveniently be designated a rate-zQ plot.

The ratio  $t_{DA}/P_{wD} = Q_{DA} = Q/(2\pi c_t P_v(p_i - p_{wf}))$  in a liquid system at constant rate takes the form

$$t_{DA}/P_{wD} = \frac{k\tau}{\phi[\mu c_t]_i \bar{A}} \cdot \frac{Q_{sc} P_{sc} T}{\pi k h T_{sc} (m(p_i) - m(p_{wf}))} \quad (7-103)$$

while in the variable rate case it becomes

$$t_{DA}/P_{wD} = \frac{k}{\phi[\mu c_t]_i \bar{A}} \cdot \frac{Q_a P_{sc} T}{\pi k h T_{sc} (m(p_i) - m(p_{wf}))} \quad (7-104)$$

or

$$Q_{aDA} = \frac{9.0 Q_a T}{\mu_i c_{ti} \phi h \bar{A} (m(p_i) - m(p_{wf}))} \quad \text{in field units. (t : days)}$$

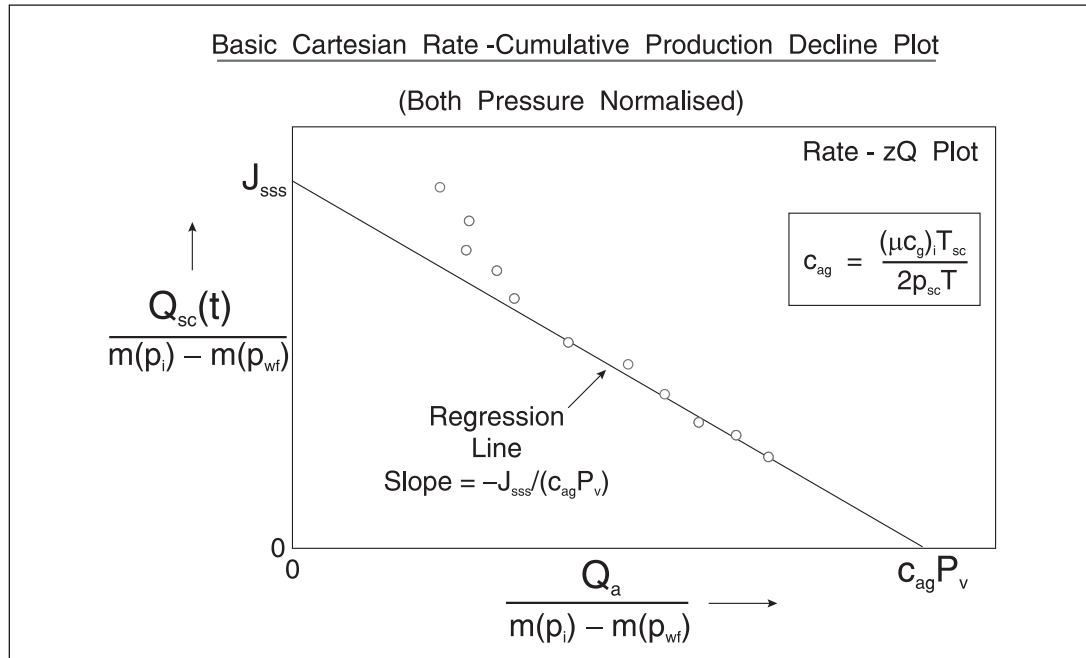


Fig. 7-35. Cartesian decline plot for radial systems (gas flow rate-Qz plot)

It is recommended by Agarwal et al. that the GIP be determined first using the Cartesian plot approach since this does not require a permeability estimate. However, the process is iterative since the determination of properties at the average pressure requires that a GIP is known. Agarwal et al. suggest that an initial value of GIP be chosen approximately half way between the gas produced  $G_p$  and the volumetric estimate of GIP denoted  $GIP_{vol}$ . The sensitivity of the Cartesian decline plot to GIP estimates is illustrated in figure 7-36 where the true GIP is 18.5 Bscf corresponding to  $r_e/r_w = 1,000$ . Initial values 20% different from this were used to calculate properties at  $\bar{p}$  and the effect on the extrapolation is clear. The iteration converges very quickly and, with the correct GIP, the data follows the trajectory of one of the  $1/p_{wD}$  rays; it does not matter which one as they all focus to the same anchor point on the  $Q_{DA}$  axis. Figure 7-37

demonstrates the use of rate–time production decline type curves and shows how the inclusion of the derivative helps to tie down the rate (vertical) match, i.e., fix the permeability. In this case, the true value is 0.1 md. Essentially, the MTR data is being analyzed for  $k$  and an effective  $r_w$  equivalent to a skin factor; the value of  $r_w$  is determined from the parameter match assuming  $r_e$  is known from the pore volume (GIP).

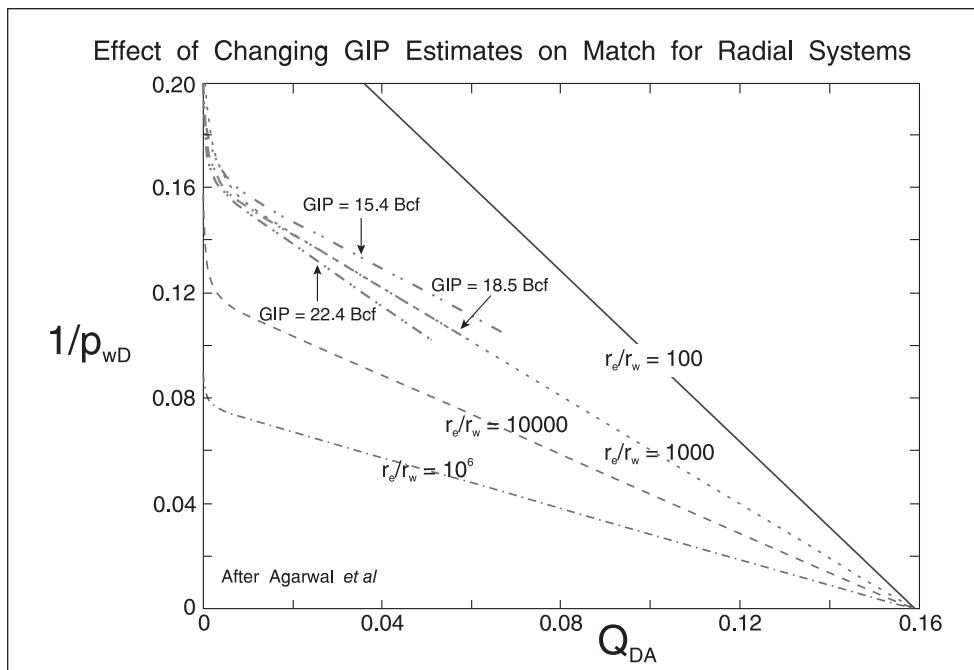


Fig. 7–36. Sensitivity of pseudopressure normalized rate– $zQ$  plot to original gas-in-place (OGIP) estimate

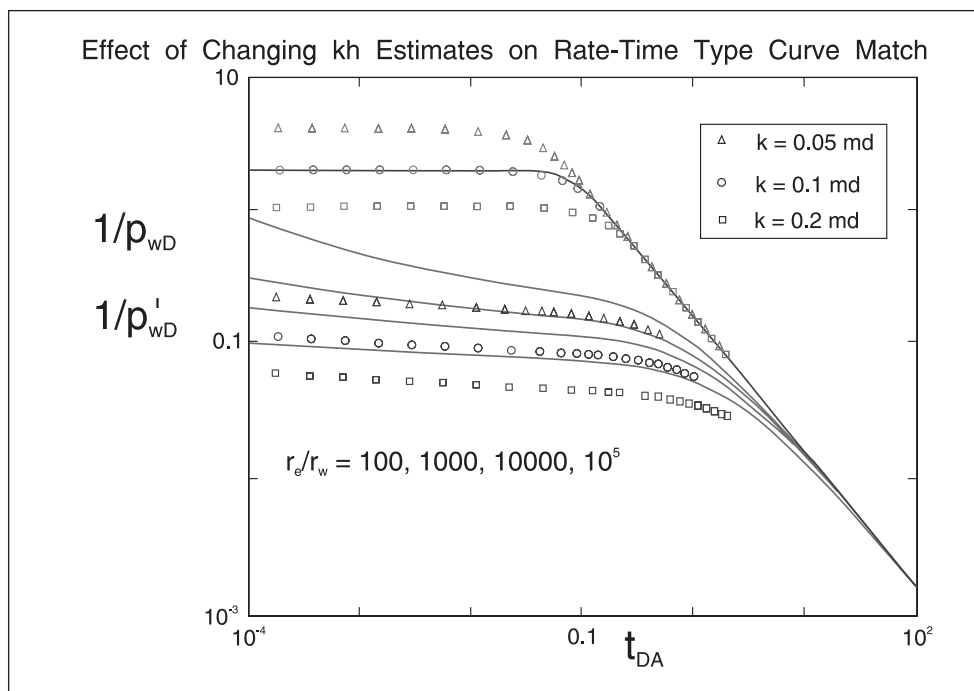


Fig. 7–37. Effect of changing  $kh$  estimates on rate–time decline type curve match



The corresponding Cartesian type curves for fractured wells are shown in figure 7–38, where it is again apparent that straight lines appear in the SSS regime.

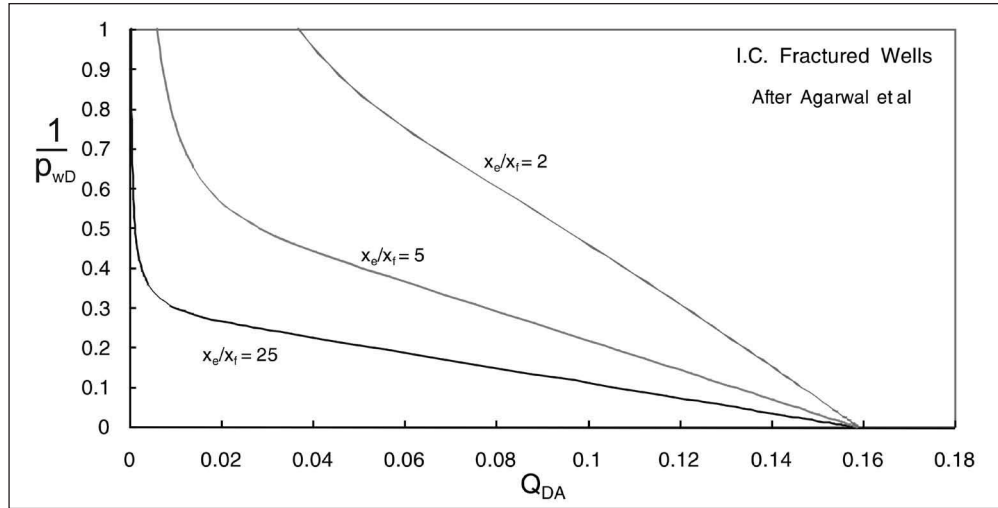


Fig. 7–38. Rate–cumulative production decline type curve for fractured wells on Cartesian scale

It is useful at this point to present the equations in SPE field units, where the material balance Eq. (7–97) becomes

$$m(p_i) - m(\bar{p}) = \frac{2.356 \times 24 T Q_r \tilde{\tau}}{h \phi \bar{A} [\mu_g c_t]_i} \quad (7-105)$$

where  $\tilde{\tau}$  is in days. The constant  $c_{ag}$  is now defined as

$$c_{ag} = \frac{[\mu_g c_t]_i}{2.356 T} \quad (7-106)$$

i.e.,

$$m(p_i) - m(\bar{p}) = \frac{Q_a}{c_{ag} P_V} \quad (7-107)$$

Here, it has been assumed that the integral  $Q_a$  includes the conversion from hours to days, i.e.,  $Q_a$  is in Mscf. The well deliverability is written as

$$Q_{sc} = J_{ss}^{pp} (m(\bar{p}) - m(p_{wf})) \quad (7-108)$$

where  $J_{ss}^{pp}$  has units of Mscf/d/(psia<sup>2</sup>/cp). At SSS conditions,  $J_{ss}^{pp}$  is given by

$$J_{ss}^{pp} = \frac{kh}{1422 T \left( \ln \frac{r_e}{r_w} + S \right)} \quad (7-109)$$

## Application to field data

Figures 7–39 and 7–40 show history-matched parameter estimates for GIP, permeability, etc. for an infill gas well in the low-permeability Red Oak sand of southeastern Oklahoma. The well was drilled in December 1991 and has slightly over 6 years of production history with a cumulative production of 1.9 Bscf. This production data are typical of that obtained from field databases and the noise or inaccuracies in measured or reported data are reflected in the dimensionless data.

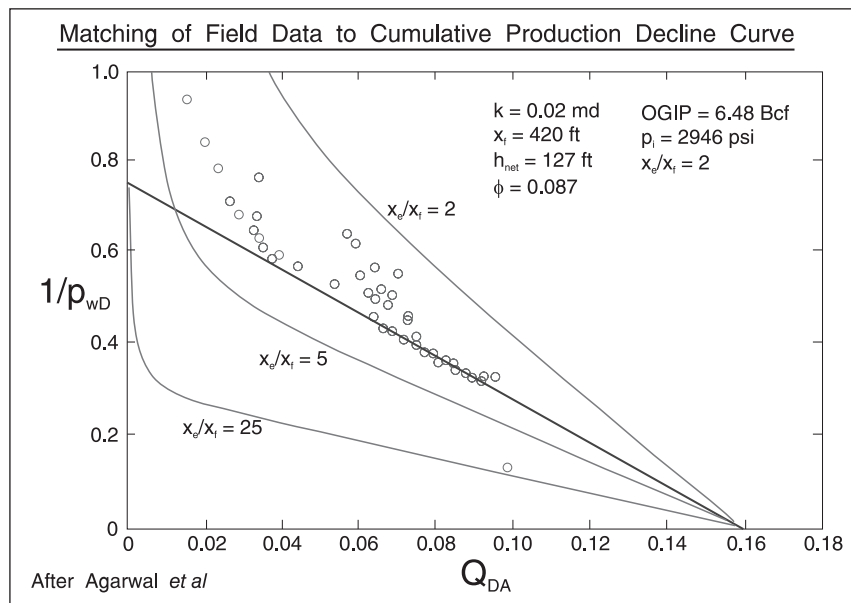


Fig. 7–39. Application to field data—estimate of GIP from rate– $zQ$  Cartesian plot

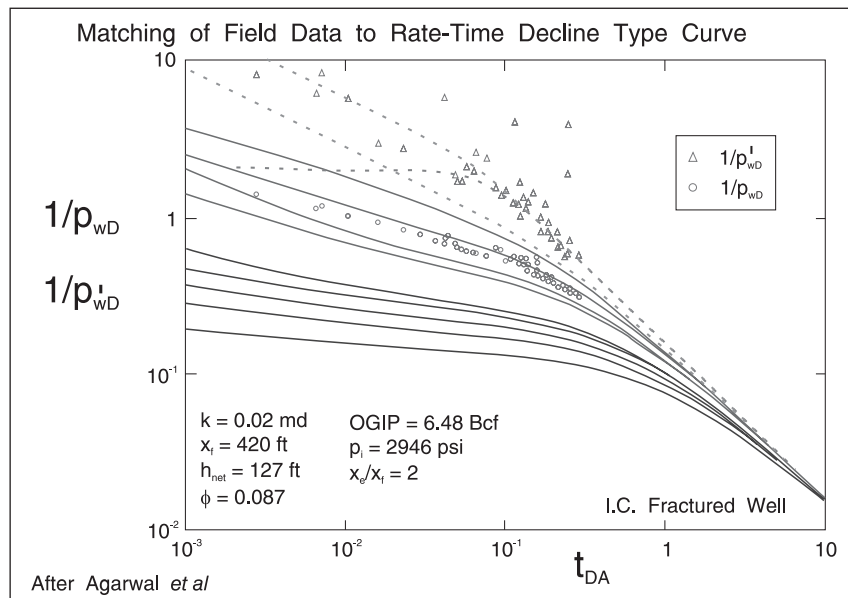


Fig. 7–40. Application to field data—estimate of  $kh$  from rate–time decline type curve match

Figure 7–40 shows that the plot of  $1/p_{wD}$  versus  $Q_{DA}$  converges nicely to the GIP anchor point and that the estimate of GIP can be used with some confidence. The character of the derivative data on the plot of  $1/p_{wD}$  versus  $t_{DA}$  (figure 7–40) clearly demonstrates that the well has attained boundary-dominated flow. This plot also illustrates a match for estimating permeability and fracture half length. Only minor modifications to the estimated parameter values were needed in order to match the well's history using a finite difference simulator.

## Notes

1. Jacob, C. E., and Lohman, S. W. "Nonsteady Flow to a Well of Constant Drawdown in an Extensive Aquifer," *Trans AGU*, (Aug. 1952): 559–569.
2. Fetkovich, M. J., Vienot, M. E., Bradley, M. D., and Kiesow, U. G. "Decline Curve Analysis Using Type Curves: Case Histories" SPE 13169, (59th Annual Technical Conference, Houston, Sept. 1984).
3. Arps, J. J. "Analysis of Decline Curves," *TRANS AIME* 160, (1945): 228–247.
4. Slider, H. C. "Worldwide Practical Petroleum Reservoir Engineering" (Pennwell, Tulsa 1983).
5. Cutler, W. W. "Estimation of Underground Oil Reserves by Oil Well Production Curves," *Bull.* 228, USBM (1924).
6. Slider, H. C. "A Simplified Method of Hyperbolic Decline Curve Analysis," *J. Pet. Tech.* 20 (3), (March 1968): 235–236.
7. Fetkovich, M. J. "Decline Curve Analysis Using Type Curves," *J. Pet. Tech.* 32 (6), (June 1980): 1065–1077.
8. Carter, R. D. "Characteristic Behaviour of Finite Radial and Linear Gas Flow Systems—Constant Terminal Pressure Case" SPE/DOE 9887, (1981 Low Permeability Symposium, Denver, Co., May 1981).
9. Agarwal, R. G., Gardner, D. C., Kleinstieber, S. W., and Fussell, D. D. "Analysing Well Production Data Using Combined Type Curve and Decline Curve Analysis Concepts," SPE 49222, (SPE Annual Tech. Conf., New Orleans, 1998).
10. Palacio, J. C., and Blasinghame, T. A. "Decline Curve Analysis Using Type Curves—Analysis of Gas Well Production Data," SPE 25909, (Low Permeability Reservoir Symposium, Denver, 1993).
11. Callard, J. G. "Reservoir Performance History Matching Using Rate/Cumulative Type Curves," SPE 30793, (1995 SPE Annual Technical Meeting, Dallas, Oct. 1995).

# 8

## Distributed Pressure Measurement

---

### Introduction

In retrospect, the introduction of the repeat formation tester (RFT) by Schlumberger in 1976 has turned out to be one of the major landmarks in reservoir engineering, comparable in importance to the advent of down-hole pressure recording in transient well testing. Distributed pressure measurement is the generic name given to a pressure–depth survey in an open-hole observation well which has just been drilled. The term wireline formation tester (WFT) will be used here to describe all devices which can make repeated measurements of local pore pressure in a borehole inactivated by drilling mud. A WFT survey is usually made after the conventional open-hole logging suite, and it is accurately depth-matched to the open-hole logs by a combined gamma ray recording. In modern logging programs, the formation microscanner (FMS) and the core log—depth-matched with a laboratory gamma ray scan and perhaps including minipermeameter data—are complementary to the WFT in the reservoir description task. It is important to distinguish between WFT surveys in unproduced reservoirs where hydrostatic (gravity–capillary) equilibrium exists and surveys in new wells in already produced fields in which differential depletion has occurred. In the former case, hydrostatic fluid gradients are observed and straight lines on a pressure–depth plot are expected. In the latter case, indications of reservoir zonation are obtained from the pattern of differential depletion or support shown up by the survey. When the first RFT surveys were carried out in a producing field in Iran in 1976, the magnitude of the measured pressure differentials between layers was a complete surprise to reservoir engineers and ideas on vertical communication in reservoirs were to undergo a profound reassessment in the following decade as the North Sea was developed. The treatment of WFT data will accordingly be separated into two categories—unproduced and produced fields. In conventional well testing, a common borehole pressure is measured as a function of time and average formation properties are deduced from the response. A WFT survey provides a detailed survey of pressure versus depth in an observation well at a particular moment in time. The main problem associated with WFT distributed pressure measurement occurs in low-permeability reservoirs and is known as *supercharging*. Long before the advent of the RFT, it was known that invasion of mud filtrate will cause an excess pressure around the wellbore, which is a function of the overbalance and the effect had been termed supercharging. Indeed, one of the objectives of the 5-min flow period in a drill stem test is to relieve any such excess pressure by producing the well and causing a drawdown. It is particularly important to understand this phenomenon since it limits our ability to detect true formation pore pressure.

The RFT was a development of a previous tool known as the formation interval tester (FIT) and originally it was intended that the (then) new RFT would essentially be used for sampling fluids from the formation. The incorporation of a pressure gauge in the device had the primary purpose of simply providing an indication of local formation permeability, i.e., whether sampling would be possible. In the event, it turned out that the ability to measure local formation pressure with a probe that penetrated the mud filter cake was by far the most important feature of the device. However, it is interesting that the new generation wireline formation tester introduced by Schlumberger—known as the *Modular Dynamic Tester* (MDT)—has much improved sampling and permeability detection capability.

## Principles of WFT Distributed Pressure Measurement

### Wireline formation tester

A schematic of the WFT device is shown in figure 8–1, and the principle of the measurement is to set a packer against the mud filter cake through which a probe emerges to make contact with the formation. In order to achieve a seal, the tool is positioned using hydraulically operated rear arms that set the packer against the formation with considerable force. Once the probe is set, a small volume of fluid is withdrawn from the formation by means of two pretest chambers equipped with pistons each of which displaces 10 cc. Chamber 1 has a lower flow rate than chamber 2 and the piston travel times result in flow rates of the order of 50 and 125 cc/min, respectively. This extraction of fluid is known as the *drawdown*, and approximately spherical flow takes place in the vicinity of the probe tip. A filter in the probe prevents sand entry into the tool and a piston cleans the filter when the tool is retracted. Naturally, the pressure falls as this fluid is withdrawn and, once the pistons stop, a buildup of pressure occurs in the formation. In a high-permeability reservoir, this build-up process is quite rapid, but in low permeability it can take a long time to occur. A sensitive transducer monitors the pressure in the flow line, which is transmitted to the surface and displayed as a log; such a pressure–time record—with both analog and digital tracks—is illustrated in figure 8–2.

Before the tool is set for a test, the transducer is registering the mud hydrostatic pressure at the present depth. As the packer is set, the pressure rises slightly because of mud cake compression and then the probe piston retracts and the pressure drops because of the resulting flow-line volume expansion and communication with the formation. The pressure drawdown during the movement of each piston is clearly visible on the log and the travel times can be measured for computation of the exact withdrawal rates denoted  $q_1$  and  $q_2$ . When the second piston reaches the end of its motion, the buildup to reservoir pressure takes place. There is a classical rise to a final stabilized pressure (except in very low permeability) which is the reservoir pressure at the setting depth. A WFT device can be reset at any number of locations in the well and a plot of reservoir pressure versus true vertical depth is the principal objective of the survey.

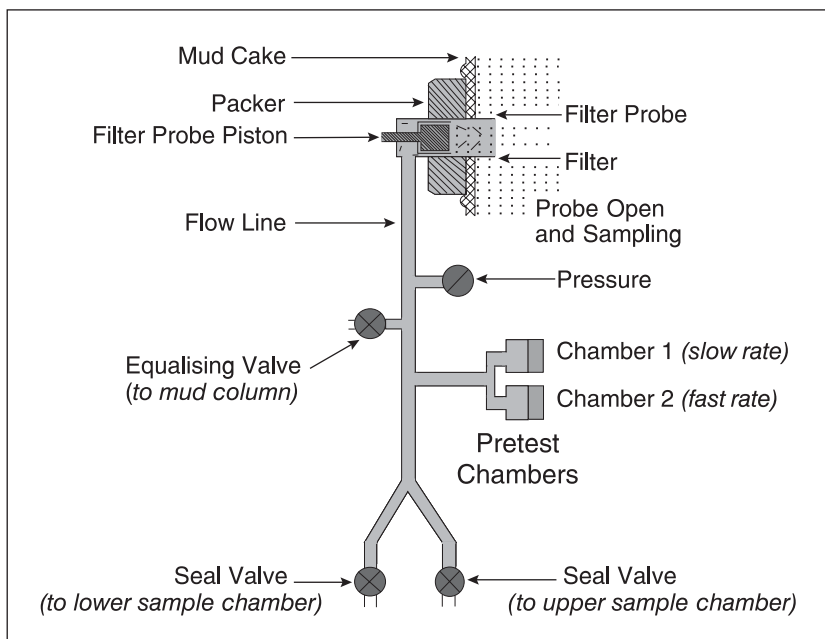


Fig. 8-1. Schematic of WFT tool

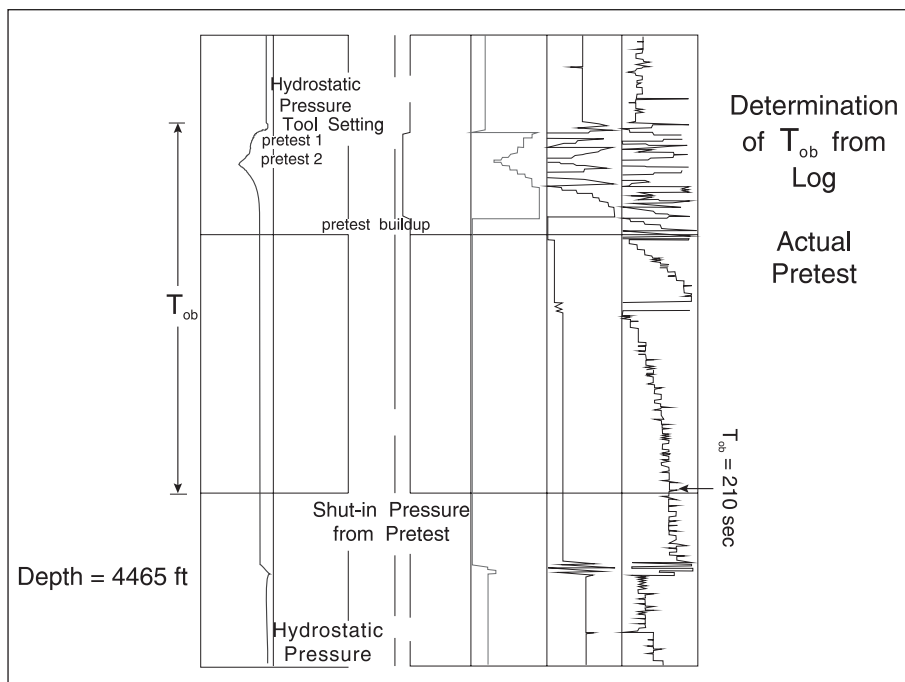


Fig. 8-2. Typical pretest pressure recording

Obviously, the correction from measured depth to true vertical depth is only as good as the well deviation survey; one of the first quality control checks on a WFT job is to verify that

- a) the WFT tool is correctly depth matched to the open-hole logs
- and b) the conversion to true vertical depth is accurately made.

Despite assurances to the contrary, it is quite surprising how often serious errors arise from lack of attention to these details.

A diagrammatic representation of the pressure–time record is shown in figure 8–3 and seven essential quantities are determined from the log; these are indicated on the figure and are as follows:

- Mud hydrostatic pressure  $p^m$
- Buildup stabilized pressure  $p^f$
- Duration of the first draw-down period  $T_1$
- Duration of the second flow period  $T_2$
- Time of observable buildup  $T_{ob}$
- First draw-down final pressure drop (referred to  $p^f$ ), i.e.,  $\Delta p_{DD,1}$
- Second draw-down final pressure drop (also referred to  $p^f$ ), i.e.,  $\Delta p_{DD,2}$

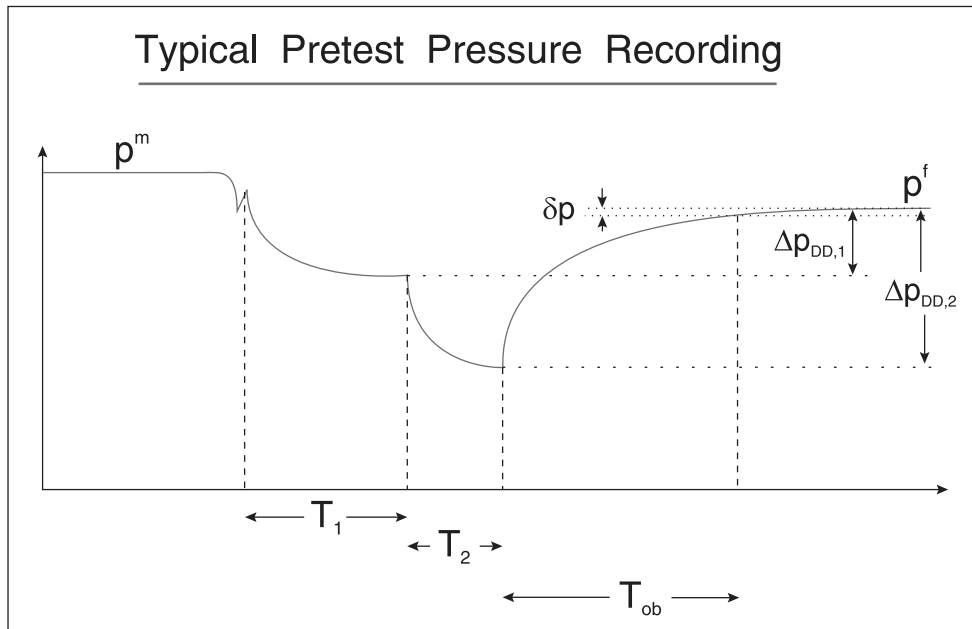


Fig. 8–3. Diagrammatic representation of a WFT test record

The two pressures  $p^m$  and  $p^f$  and the pressure differences  $\Delta p_{DD,1}$  and  $\Delta p_{DD,2}$  are directly obtained from the digital track, while the times are picked off the analog track; it is important that these values are accurately recorded. The time of observable buildup is essentially the time taken for the pressure to stabilize, which will be used as a local permeability indicator. The raw data from a WFT survey consists of a table of these quantities at a sequence of measured or true vertical depths. The most important element is the estimate of formation pressure  $p^f$ , and the other quantities are largely related to quality control. However, the permeability estimates—which will be treated in detail later in this chapter—are also valuable in their own right.

The flow rates during the two draw-down periods are given by

$$q_1 = \frac{10.0}{T_1} \text{ cc/s}$$

and

$$q_2 = \frac{10.0}{T_2} \text{ cc/s}$$

## Simplified (Single-phase) Supercharging Analysis

In essence, a WFT tool is able to isolate the probe from the mud column by means of the packer and hence detect the formation pressure immediately behind the filter cake. However, the sandface pressure may not be synonymous with the undisturbed formation pressure some distance from the wellbore. In open-hole conditions, mud filtrate loss is occurring and, in fact, the well may be considered to be under injection albeit at a very low rate. The pressure distribution in the wellbore region is illustrated in figure 8–4 where the sandface pressure  $p^s$  is intermediate between the formation pressure  $p^f$  and the mud hydrostatic pressure  $p^m$  existing in the well. In most circumstances,  $p^s$  is indistinguishable from  $p^f$ , but in low-permeability formations the excess pressure  $p^s - p^f$  due to mud filtrate injection may be appreciable. The purpose of the filter cake is to minimize the mud fluid loss rate  $q_f$ , and the higher the resistance of the cake, the closer  $p^s$  is to  $p^f$ , i.e., nearly all the pressure differential between mud hydrostatic and formation appears over the cake. It must be recognized, however, that a WFT device measures the sandface pressure which is not identical to the undisturbed formation pressure. Indeed, the biggest practical problem associated with WFT surveys is the occurrence of this supercharging phenomenon, and the most important aspect of quality control of the measurement is the assessment of the likely degree of supercharging (if any) that may be present. Again, it should be emphasized that this is a problem only in low-permeability formations.

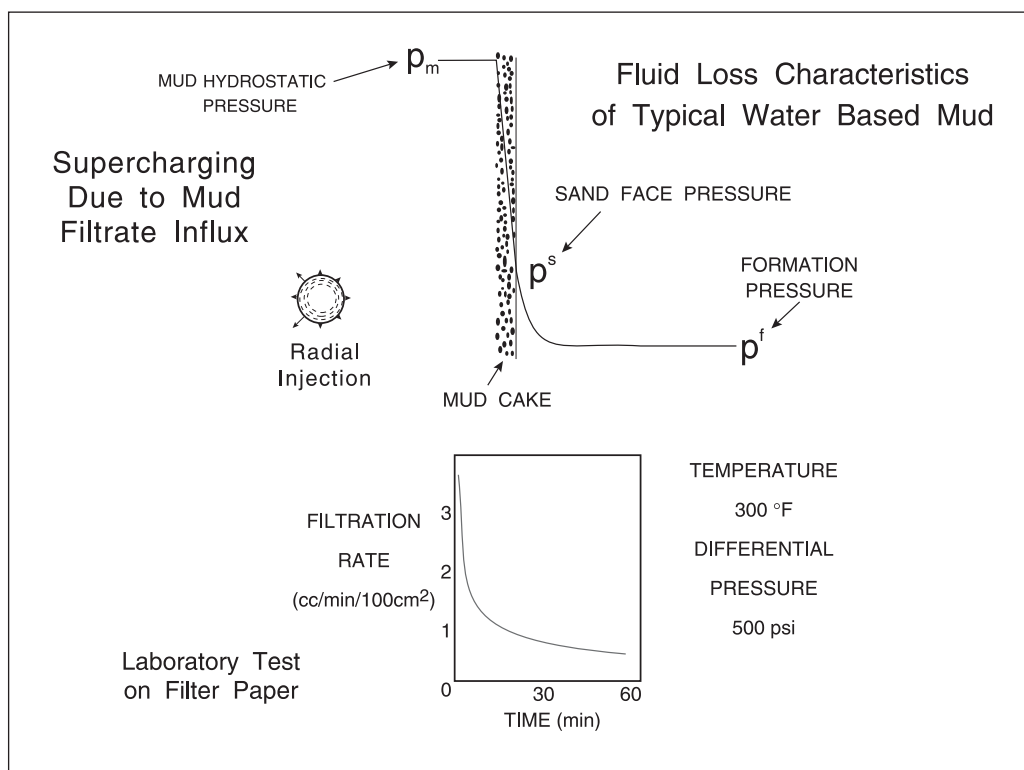


Fig. 8–4. Pressure drop over mud cake and formation due to fluid loss



The mechanics of mud filtrate invasion indicate that fluid loss takes place in three stages:

- a) the initial spurt loss leading to a rapid buildup of filter cake;
- b) dynamic filtration that occurs while mud is being circulated in the well;
- c) static filtration after circulation of mud has been arrested.

Ferguson and Klotz<sup>1</sup> have measured fluid loss rates from water-based mud in a model oil well and they showed that in dynamic filtration conditions an equilibrium is reached between cake deposition and cake erosion. The cake accordingly attains an equilibrium thickness and the filtration rate becomes constant; a typical fluid loss profile for dynamic filtration is shown in figure 8–5. When circulation is stopped and static filtration takes place, the fluid loss rate approximately becomes half and then continues to decrease with time as shown in figure 8–5. For the particular mud studied by Ferguson and Klotz, the static fluid loss was described by the equation

$$q_1 = \frac{0.217}{\sqrt{\Delta t + 15.5}} \quad (8-1)$$

where  $q_1$  is fluid loss (cc/min/100cm<sup>2</sup>) and  $\Delta t$  is time from termination of circulation (h).

Note that the standard American Petroleum Institute (API) filter loss test is not representative of down-hole conditions and cannot be used to predict actual filtration rates in a well. Following the observations of Ferguson and Klotz, the supercharging effect can be quite adequately modeled by assuming constant injection rates for both the dynamic and static filtration periods as illustrated in figure 8–6; here,  $q_{1,1}$  is the dynamic fluid loss rate over a time period  $T_d$ , and  $q_{1,2}$  is the static fluid loss rate. In order to develop a simple model of supercharging, the invasion of aqueous filtrate, i.e., from water-based mud into a water zone (aquifer), will be considered; a detailed two-phase invasion model will be developed in a subsequent chapter. The injection of water into the formation according to the rate schedule of figure 8–6 can be analyzed using the familiar superposition principle, which for a two-rate process takes the form

$$\Delta p^s = p^s - p^f = \frac{q_{1,2} \mu}{4\pi k k_r} \left( \frac{q_{1,1}}{q_{1,2}} \ln \frac{T_d + \Delta t}{\Delta t} + \ln \Delta t + \ln \frac{k k_r}{\phi \mu c_t r_w^2} + 0.80908 \right) \quad (8-2)$$

where  $\Delta t$  is the time of static filtration and  $\mu$  is the filtrate viscosity. Thus, the degree of supercharging depends mainly on

- the mud static fluid loss rate  $q_{1,2}$  and
- the local formation permeability  $k$

and is affected to a lesser extent by

- the duration of dynamic filtration  $T_d$  and the time at which the test is carried out measured from the beginning of static filtration  $\Delta t$ ;
- the ratio of static to dynamic filtration rates  $q_{1,2}/q_{1,1}$ ; and
- the mud filtrate viscosity  $\mu$  (essentially water in this case).

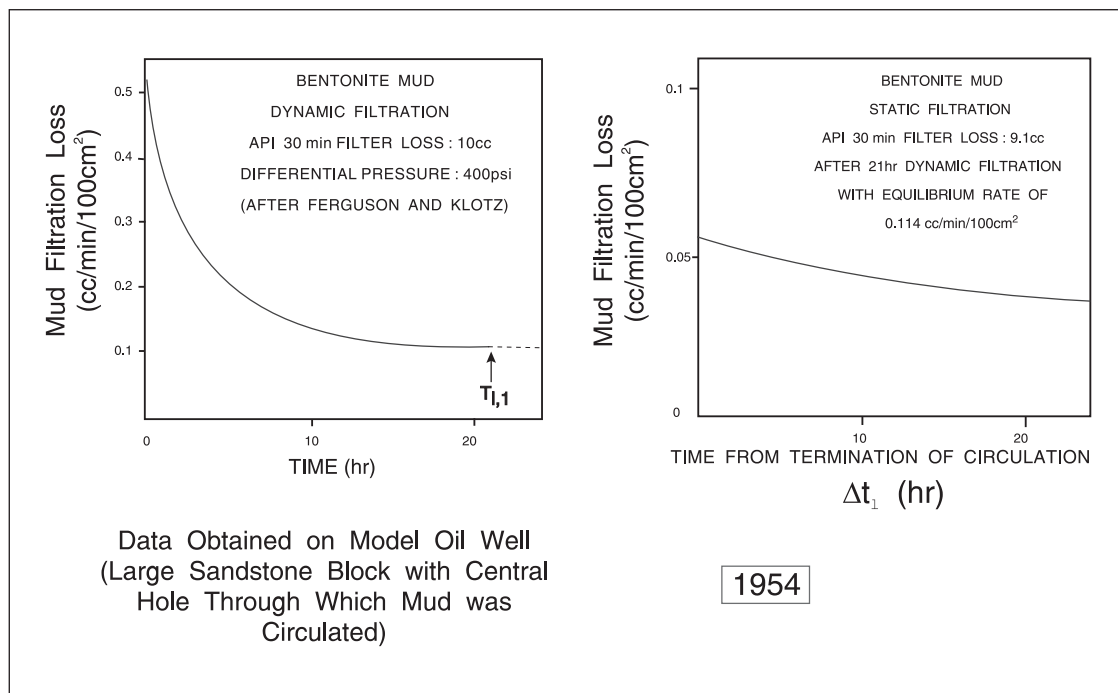


Fig. 8-5. Mud fluid loss characteristics (after Ferguson and Klotz)

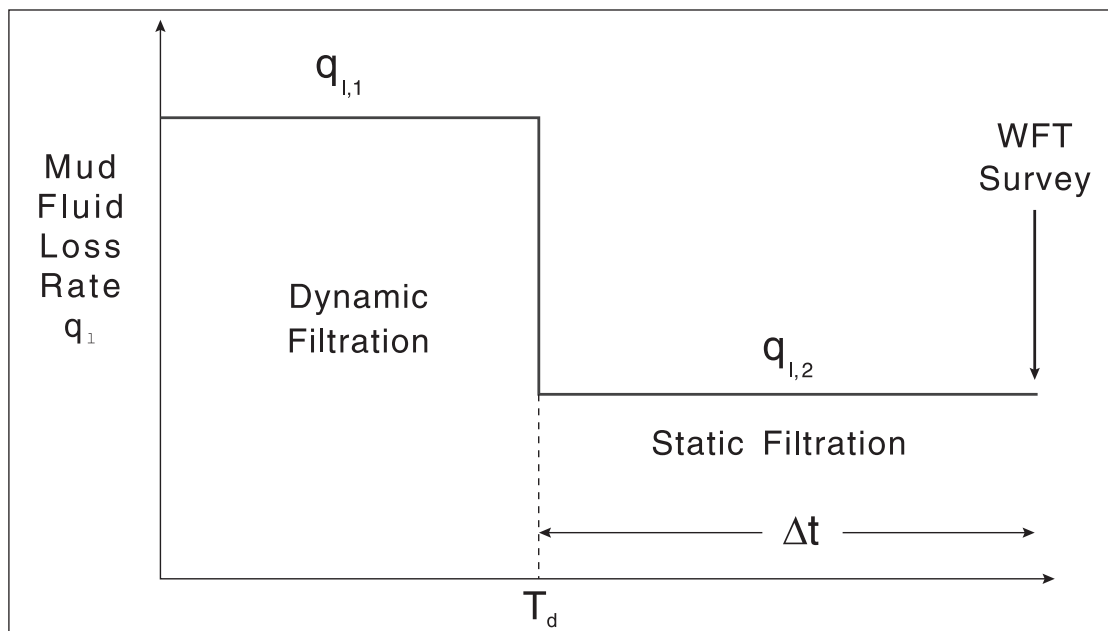


Fig. 8-6. Simplified fluid loss rate schedule

The problem with Eq. (8–2) is that both the mud fluid loss rate  $q_{1,2}$  and the local formation permeability  $k$  are very difficult to measure or predict. The experimental data of Ferguson and Klotz for water-based mud date back to 1954 and there is virtually no information on in situ fluid loss rate for oil-based mud. The variation of excess pressure  $\Delta p^s$  with formation permeability and mud static filtration rate is illustrated in figure 8–7 for typical fluid properties and filtration times ( $T_d = \Delta t = 12\text{h}$ ); the ratio of static to dynamic filtration rate was assumed to be 2. For a mud static fluid loss rate of  $0.05\text{ cc/min}/100\text{cm}^2$ , i.e., the measured value of Ferguson and Klotz at  $75^\circ\text{F}$ , the supercharging is negligible for formation permeabilities greater than  $10\text{md}$ —hence, the effect is essentially confined to low-permeability systems as previously indicated. However, even in a formation of high average permeability, the probe may land in a very low permeability streak that is supercharged and the registered pressure is anomalously high.

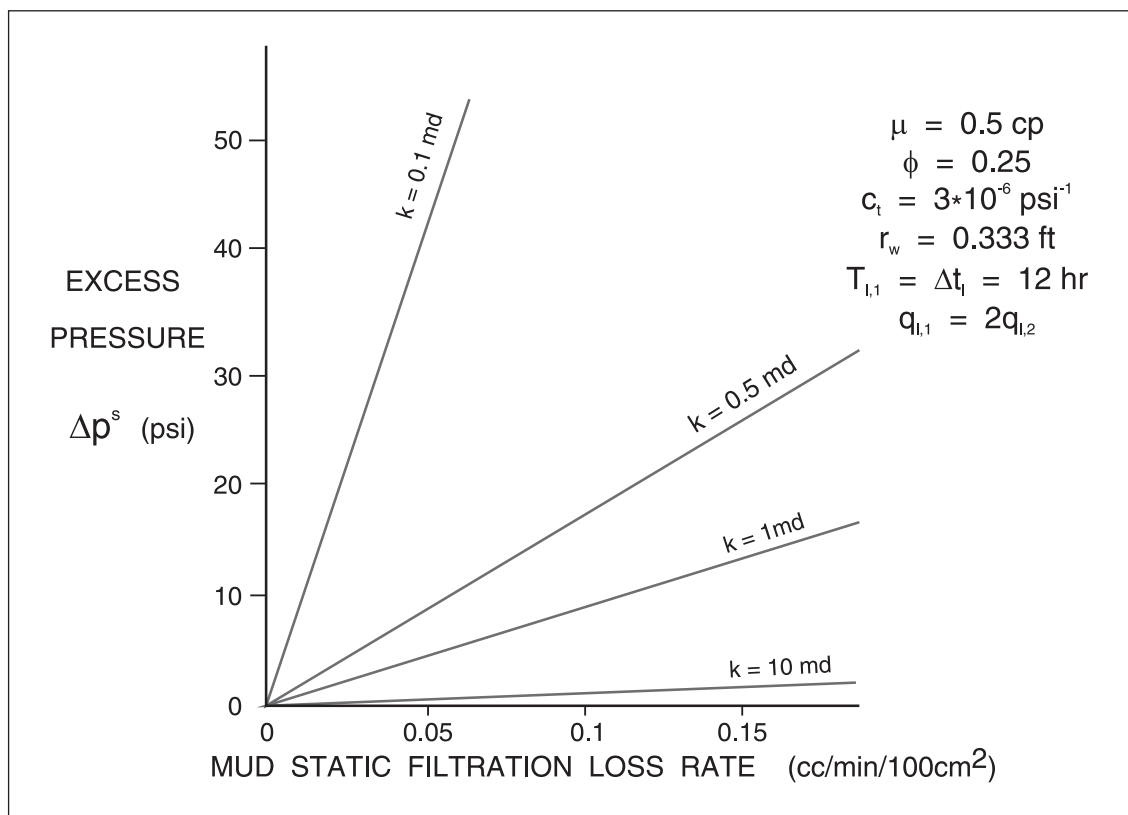


Fig. 8–7. Excess pressure due to mud filtrate influx (infinite reservoir)

The WFT survey from one of the appraisal wells in the Sleipner field in the Norwegian sector of the North Sea is shown in figure 8–8 with the actual data tabulated in table 8–1.

Table 8–1. Sleipner field WFT data

Vertical depth D (m)	Reservoir pressure $p^f$ (psia)	Draw-down permeability $k_1$ (md)	Draw-down permeability $k_2$ (md)	Average permeability $k_{1,2}$ (md)	Build-up permeability $k_s$ (md)
3,484	6,236	10.6	9.2	9.9	0.96
3,488	6,236	5.2	7.7	6.5	1.23
3,492	6,238	13.1	10.9	12.0	—
3,497	6,241	Gas			
3,505	6,242	Gas			
3,508	6,245	23.8	—	23.8	—
3,515	6,247	Gas			
3,521	6,251	9.9	—	9.9	—
3,527	6,252	Gas			
3,532	6,255	Gas			
3,537	6,257	2.7	3.4	3.1	—
3,542	6,260	6.7	—	6.7	—
3,547	6,263	5.3	5.1	5.2	—
3,550.5	6,265	29.3	74.8	52.1	—
3,554.5	6,266	25.4	12.8	19.1	—
3,559	6,267	Poor	Drawdown		
3,564	6,270	Poor	Drawdown		
3,568	6,272	21.3	24.4	22.9	—
3,578	6,276	4.8	4.5	4.7	—
3,580	6,276	6.3	5.3	5.9	—
3,585	6,279	Gas			
3,589.5	6,282	13.0	10.5	11.8	—
3,593	6,284	20.1	23.0	21.0	—
3,596.5	6,286	12.6	17.9	15.3	—
3,601	6,286	4.6	4.2	4.4	—
3,606	6,289	33.0	30.0	31.5	—
3,615.5	6,292	2.8	3.5	3.2	—
3,619	6,295	6.6	6.9	6.8	—
3,623	6,297	19.9	19.5	19.7	—
3,626	A 6,327 *	Gas			
3,630	6,300	12.5	13.5	13.0	—
3,635.5	6,303	Poor	Drawdown		
3,640.5	6,304	3.2	3.3	3.3	0.61
3,644	6,306	59.4	43.0	51.2	—
3,652	6,311	23.3	28.9	26.1	—
3,653.5	6,312	45.7	—	45.7	—
3,656	B 6,320 *	2.4	2.6	2.5	0.17

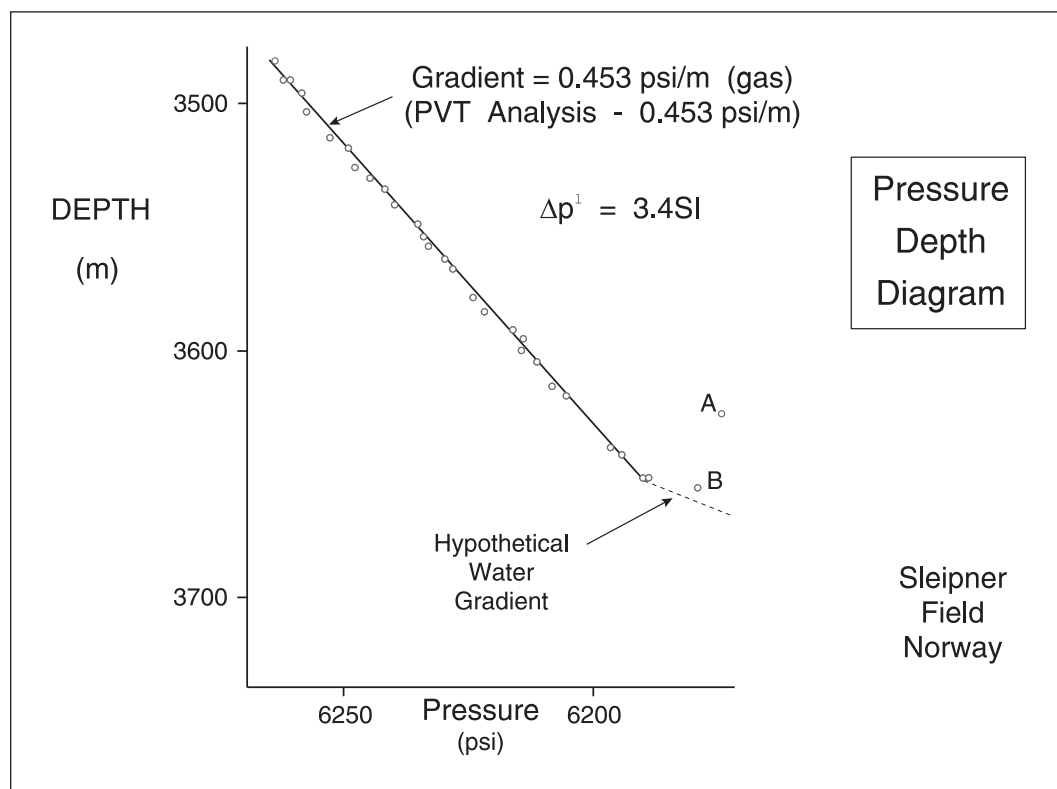


Fig. 8–8. Gas condensate field WFT survey

This survey was run around 1977 and was one of the first WFT jobs in the North Sea; its success helped to prove the validity of the then recently introduced tool. The observed pressure gradient of 0.453 psi/m derived from the slope of the pressure–depth diagram agreed exactly with the pressure-volume-temperature (PVT) information regarding in situ fluid density and the pressure points—with two exceptions—lie on the hydrostatic gas gradient. The points A and B are evidently supercharged and it is apparent that point B has the lowest permeability from spherical pretest build-up analysis. In this survey, the point at 3,640.5 m registering a build-up permeability of 0.61 md is not supercharged since it lies on the hydrostatic formation gradient; for the mud system used, this is the cut-off permeability below which supercharging becomes apparent. This RFT survey is of particular historical interest since it allowed the mechanism of supercharging to be clearly identified and showed how very good formation pressures could be obtained. One of the objectives of the survey was to confirm the gas–water contact, but due to the low permeability in the aquifer no water gradient could be obtained. However, the fact that the aquifer is tight is of crucial importance in the engineering of the gas reservoir, since it implies that little water influx will occur. It is not uncommon for the WFT survey to be the only data gathered in the water column and the estimation of permeability from pretest drawdown is an important issue which will be discussed in detail. The new version of the RFT is the MDT and one of the main applications of the improved sampling capability of this device is to obtain good formation water samples. It is interesting to note that this well was not subjected to a transient test because the drawdown and subsequent buildup that could be obtained, with the rate limited by flare capacity on an offshore rig, was less than resolution of pressure gauges available at the time.

## Rapid Local Permeability Estimation

In the preceding section, it was demonstrated that the degree of supercharging was inversely proportional to the formation permeability for a mud of given fluid loss rate. In the analysis of supercharging, it is often assumed that the mud fluid loss rate is indeed constant and does not vary from level to level. This is likely to be essentially true when the cake resistance is large compared to the formation resistance and the cake properties are not affected by the formation. In very low permeability formations, this assumption will not be valid and it may be that  $q_{1,2}$  does vary from zone to zone. However, for the moment, it will be assumed that  $q_{1,2}$  is constant over the whole interval tested and therefore supercharging is controlled by the local permeability, i.e.,

$$\Delta p^s \propto \frac{1}{k} = \frac{a}{k} = a.SI \quad (8-3)$$

where  $a$  is a proportionality constant and a supercharging index (SI) has been defined as the reciprocal of  $k$ . In principle,  $a$  is given by Eq. (8-2), viz.,

$$a = \frac{q_{1,2}\mu}{4\pi k_r} \left( \frac{q_{1,1}}{q_{1,2}} \ln \frac{T_d + \Delta t}{\Delta t} + \ln \Delta t + \ln \frac{kk_r}{\phi\mu c_t r_w^2} + 0.80908 \right) \quad (8-4)$$

but for the moment, it has been assumed that this quantity is roughly constant. The key point is that the local permeability  $k$  or its reciprocal, i.e., SI, is the main quality control for the WFT-registered pressure. Hence, it is important that a permeability estimate be obtained from the WFT pressure response. The subject of spherical flow in drawdown and buildup will be treated in detail in the following section, and for the moment only the drawdown behavior will be considered. One of the features of spherical flow is that for constant rate the probe pressure quickly attains a nearly steady-state value as indicated in figure 8-3 and the terminal pressure drops  $\Delta p_{DD,1}$  and  $\Delta p_{DD,2}$  can be analyzed for permeability. Detailed finite element computer simulations of the approximately hemispherical flow into the RFT probe were carried out by Zimmerman,<sup>2</sup> who showed that the permeability equation for the standard RFT probe-packer configuration is

$$k_d = 5660 \frac{q\mu}{\Delta p_{DD}} \quad (8-5)$$

where  $k_d$  = drawdown permeability (md),  
 $q$  = probe flow rate (cc/s),  
 $\mu$  = viscosity of flowing fluid, usually mud filtrate (cp), and  
 $\Delta p_{DD}$  = draw-down pressure difference (psi).

Thus, two estimates of draw-down permeability may be obtained, denoted  $k_{d,1}$  and  $k_{d,2}$ , respectively: one from the first drawdown where  $q_1 = 10/T_1$  and another from the second drawdown where  $q_2 = 10/T_2$ . These permeability estimates are very easy to determine from the pressure-time record.

Pressure transient testing of wells had its origin in the observation by hydrologists that the time taken for a buildup to reach the stabilized pressure was a function of formation permeability. The theory of the Theis (Horner) plot was derived to explain this behavior and provide a method for extrapolating the transient pressure response to the eventual stabilized value, thus shortening considerably the duration of a well test. The theory of transient spherical flow will be developed in the next section and it will be shown how permeability can be obtained from the slope of a spherical flow plot. For the moment, attention will be focused on the simple idea that the time taken to reach the stabilized pressure is a function of permeability. This time has been defined as the duration of observable buildup,  $T_{ob}$ , which is marked on figure 8-3; the concept of the duration of observable buildup is illustrated in figure 8-9. It is relatively straightforward to inspect the pressure record and pick off the time at which the pressure first attains a value  $p^f - \delta p$ , where  $\delta p$  is an estimate of the gauge resolution. The definition of  $T_{ob}$  is a little subjective, but it is not difficult to examine a test record and ascertain when the build-up pressure first comes within 1 psi, say, of the final stabilized value.

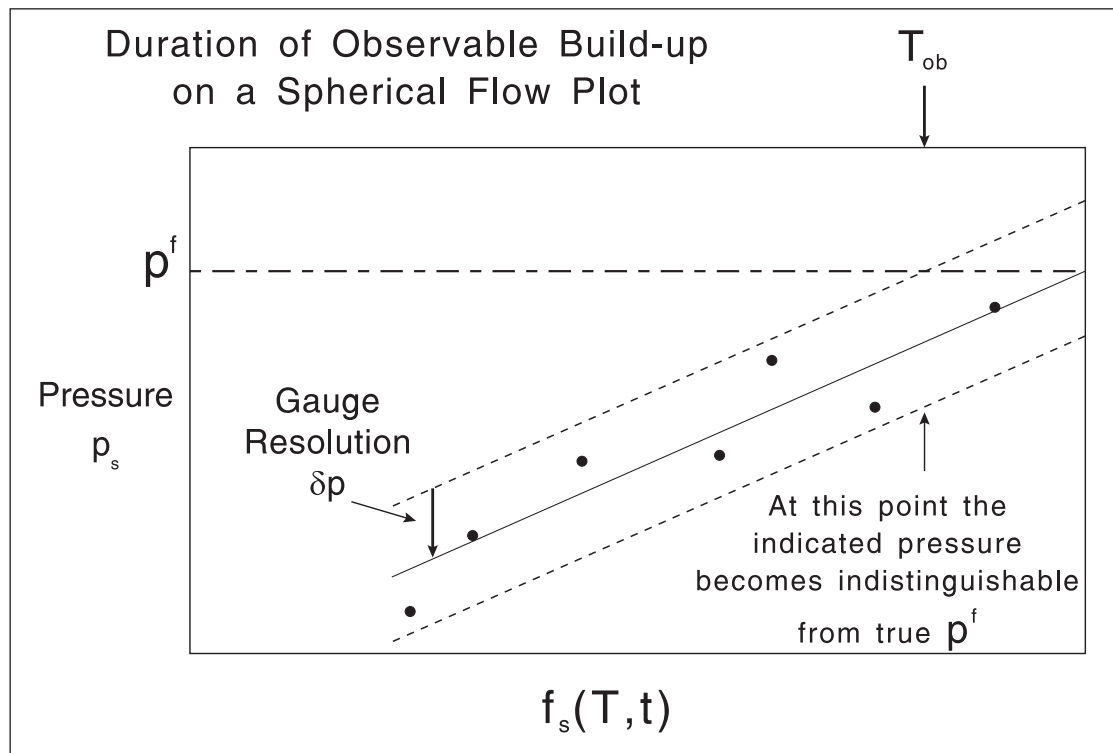


Fig. 8-9. The concept of the duration of observable buildup on a spherical flow plot

The theory of spherical flow shows that the time to reach a pressure  $p^f - \delta p$  in buildup—following a constant rate drawdown of duration  $T$ —is given by

$$\frac{1}{\sqrt{T_{ob} - T}} - \frac{1}{\sqrt{T}} = \frac{\delta p \tilde{k}_s}{8.0 \times 10^4 q \mu (\phi \mu c_t)^{1/2}} \quad (8-6)$$

where the following units have been employed: T, T<sub>ob</sub> – s

$$\begin{aligned}\delta p & - \text{psi} \\ q & - \text{cc/s} \\ \mu & - \text{cp} \\ c_t & - \text{psi}^{-1} \\ \tilde{k}_s & - \text{md}\end{aligned}$$

Here  $\tilde{k}_s$  is a spherical permeability based on the value of T<sub>ob</sub> read from the test record; thus, if  $\delta p$ —the effective gauge resolution—is chosen to be 1psi, then  $\tilde{k}_s$  is given by

$$\tilde{k}_s = \left(8.0 \times 10^4 q \mu (\phi \mu c_t)^{1/2}\right)^{2/3} \times \left(\frac{1}{\sqrt{T_{ob} - T}} - \frac{1}{\sqrt{T}}\right)^{2/3} \quad (8-7)$$

In this equation, q is taken as V<sub>d</sub>/(T<sub>1</sub> + T<sub>2</sub>) and T as T<sub>1</sub> + T<sub>2</sub>. For the following typical parameter values:

$$\begin{array}{llll} \phi = 0.25 & T_1 + T_2 = 20 \text{ s} & c_t = 3 \times 10^{-6} \text{ psi}^{-1} & V_d = 20 \text{ cc} \\ \mu = 0.5 \text{ cp} & q = 1 \text{ cc/s} & \delta p = 1 \text{ psi} & \end{array}$$

the relation between  $\tilde{k}_s$  and T<sub>ob</sub> is given in table 8–2.

**Table 8–2.** Relation between T<sub>ob</sub> and spherical permeability  $\tilde{k}_s$

T <sub>ob</sub> (s)	$\tilde{k}_s$ (md)	1/ $\tilde{k}_s$ (md <sup>-1</sup> )
30	2.20	0.45
60	0.80	1.26
120	0.36	2.80
180	0.23	4.34
240	0.17	5.87
360	0.11	8.94
600	0.066	15.07

The excess pressure due to supercharging  $\Delta p^s$  is inversely proportional to the permeability. The values of this reciprocal permeability, i.e., 1/ $\tilde{k}_s$ , are also given in Table 8–2, and a plot of 1/ $\tilde{k}_s$  (i.e., SI) against T<sub>ob</sub>, as illustrated in figure 8–10, shows that the degree of supercharging is directly proportional to the duration of observable buildup. Hence, T<sub>ob</sub> turns out to be an excellent criterion on which to assess the probability of a particular test being supercharged. The reciprocal permeability, i.e., 1/ $\tilde{k}_s$ , is referred to as SI. As a rule of thumb (developed empirically for Middle East reservoirs in the early days of RFT usage), it is rare for supercharging to be significant at values of SI less than about 3 corresponding to T<sub>ob</sub> of less than 2 min.



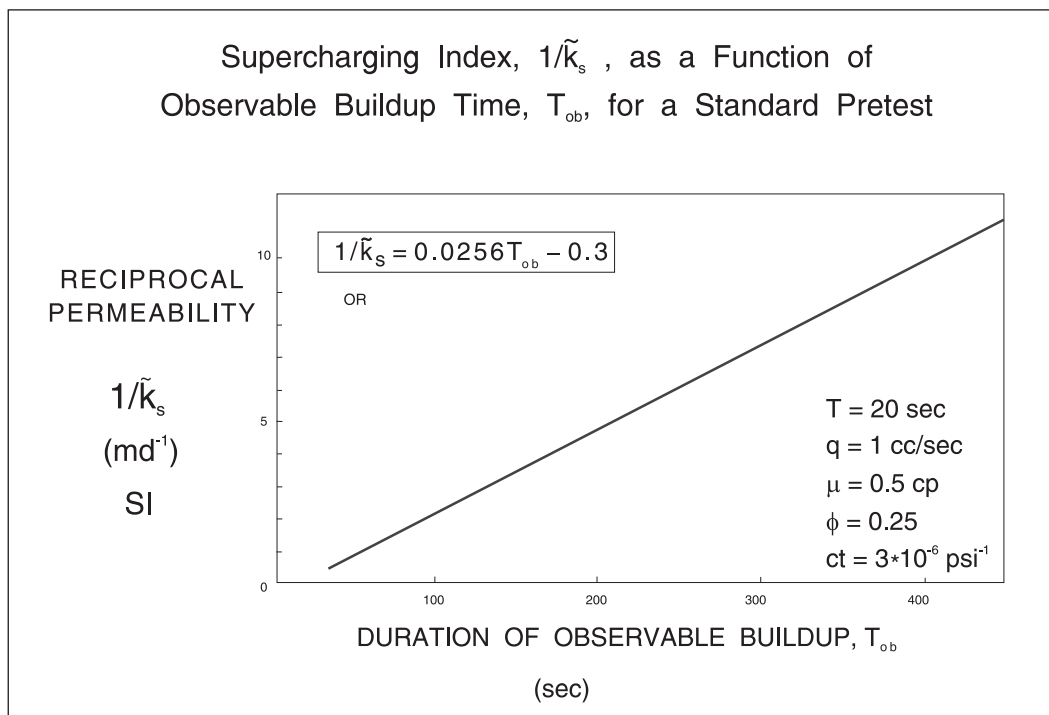


Fig. 8-10. Supercharging index as a function of observable build-up time

The linear relation between  $1/\tilde{k}_s$  and  $T_{ob}$  apparent in figure 8-10 has the form

$$\frac{1}{\tilde{k}_s} = 0.0256T_{ob} - 0.3 \tag{8-8}$$

However, for values of  $T_{ob}$  greater than 100 s, the approximate relation

$$\frac{1}{\tilde{k}_s} = \frac{T_{ob}}{40} \tag{8-9}$$

is sufficiently accurate and particularly useful for obtaining rapid estimates of spherical permeability or SI from  $T_{ob}$ . For buildups longer than 2 min,  $T_{ob}$  is inversely proportional to  $\tilde{k}_s$ .

In order to appreciate the extent of possible supercharging, the following approximate relation has been derived from examination of a limited number of supercharged tests:

$$\Delta p^s = 4 SI = \frac{4}{\tilde{k}_s} \tag{8-10}$$

It should be emphasized that this equation gives only an order of magnitude estimate of  $\Delta p^s$ . The actual value of the proportionality constant depends on the particular mud fluid loss characteristics and other factors.

The spherical permeability  $\tilde{k}_s$  derived from the build-up duration  $T_{ob}$  is closely related to the permeability obtained from the slope of the transient spherical build-up plot described in a succeeding section. It will be seen that field experience indicates that the build-up permeability  $k_s$  is in general too low—by as much as an order of magnitude—and the draw-down permeability  $k_d$  is in fact a much better estimate of the formation property. Hence, the rapid estimate  $\tilde{k}_s$  should only be used as a quality control, through its reciprocal SI, for the assessment of supercharging. It is possible to define an SI based on  $k_d$ , but historically the time of buildup has been used as a semiquantitative measure of the supercharging effect. Some analysts prefer not to use an exact number for SI but simply to define categories of pretests such as follows:

- **Very Good** : Drawdown almost invisible and buildup to final pressure in less than 1 min.
- **Good** : Drawdown around 100 psi and buildup complete after about 1 min.
- **Moderate** : Drawdown a substantial portion of total formation pressure, i.e., 1,000–3,000 psi and buildup around 2–3 min.
- **Low** : Drawdown essentially to zero psig but pretest still filled after normal cycle time. Buildup is slow and usually incomplete.
- **Very Low** : Drawdown to zero psig and pretest cylinders take a long time to fill. Very slow buildup.
- **Tight** : A dry test of no interest except as a piece of petrophysical information.

Supercharging is often significant for anything below the “Good” category.

## Background to Permeability Estimation

Open hole wireline formation pressure measurements of the type made with the RFT have been available for the past several years. The technique is well established and is widely used. The main applications include the measurement of formation pressure, identification of fluid type and fluid contacts, evaluation of reservoir structure, and the recovery of samples of reservoir fluids. WFT pressure measurements can also be used to derive formation permeability. However, this application has been viewed with some scepticism and has not generally been regarded as a proven technique. Thus the use of WFT permeability has not yet found wide acceptance in reservoir description, and WFT measurements are usually considered to be only qualitative indicators of permeability. In the early work on RFT permeability,<sup>3</sup> undue emphasis was placed on the build-up permeability because it was felt at the time that draw-down permeabilities did not have a deep enough depth of investigation and were too sensitive to local conditions very close to the probe tip. However, the excellent study by Radcliffe<sup>4</sup> on data provided by Shell Expro has shown that, in fact, draw-down permeabilities are the more reliable and build-up permeabilities are significantly low. It is interesting to observe that the current widespread use of the minipermeameter—which is based on a probe that induces a flow with spherical properties—vindicating the use of WFT permeability. Also, the new generation of WFT devices, e.g., the Schlumberger MDT, take a much larger sample than the RFT and have been designed to give better permeability estimates. The material presented here and the conclusions drawn are based on Radcliffe’s study.

There are several sources of uncertainty associated with WFT-derived permeabilities. However, the conventional sources of permeability data, i.e., well testing and core measurements, also have their limitations, and the factors affecting the accuracy of both core and WFT measurements are discussed in this section. A comparison of the three sources of permeability data (WFT, cores, and well tests) reveals that WFT devices have the following two particularly interesting features which are not available together in the other two methods:

1. A WFT tool gives an in situ measurement (as in well testing, but unlike core measurements);
2. WFT measurements are discrete, allowing permeability profiling (as is possible with core data—including minipermeameter—but not with well testing, which produces an average value of the interval). The combination of these two attributes in one technique suggests that WFT measurements could prove to be a valuable complement to conventional permeability measurements despite the uncertainties associated with the method. The present objective is therefore to assess the validity of WFT permeability measurements. The approach that has been adopted is based on the comparison of WFT-derived permeabilities with core and well test measurements.<sup>4</sup> The data were taken from four North Sea wells and include 40 usable RFT pretests and 3 suitable well tests. The selected wells and data are summarized in table 8–3.

**Table 8–3.** Summary of selected wells and field data

Well	Formation	Mud type	Res. fluid	No. of RFT tests	Quartz gauge used	Conv. core anal.	Spec. core anal.	PVT data	No. of well tests
A	Upper Jurassic	WBM	Oil	10	No	Yes	Extensive	Yes	2
A	Middle Jurassic	OBM	Cond.	16	No	Yes	Extensive	Yes	2
B	Rotlieg–Endes	WBM	Gas	4	No	Yes	Limited	No	0
C	Rotlieg–Endes	WBM	Gas	5	No	Yes	Limited	No	0
D	Rotlieg–Endes	WBM	Gas	6	Yes	Yes	No	No	0

## Review of RFT Permeability Interpretation

During an RFT pretest formation, fluid flows through the probe and into two 10-cc pretest chambers, which open sequentially. This creates a localized flow pattern in the formation which is essentially spherical in nature and the draw-down pressure depends on the effective permeability of the formation. At the end of the flowing period, a build-up period starts and the pressure measured at the probe increases until it stabilizes. The time required for this build-up is also a function of the formation permeability. Thus, there are two different approaches to derive formation permeability from RFT pretests: (1) draw-down analysis, and (2) build-up analysis.

### Drawdown analysis

The analysis of the RFT pretest drawdown is based on the theory of spherical flow of a slightly compressible fluid (usually mud filtrate) in an isotropic homogeneous medium. Because of the

spherical nature of the flow, most of the pressure drop takes place in a small volume close to the probe. Thus, during the draw-down period, steady-state conditions are usually established very quickly near the RFT probe, and the resulting pressure drop is given by

$$\Delta p_{DD} = \frac{Cq\mu}{2\pi r_{pe} k_d}$$

where

- $\Delta p_{DD}$  is the steady-state drawdown,
- $C$  is the shape factor (to account for the fact that the flow pattern is not exactly spherical, due to the presence of the borehole),
- $q$  is the flow rate,
- $\mu$  is the filtrate viscosity,
- $r_{pe}$  is the effective probe radius (i.e., the radius of the sphere which is equivalent to the actual sink, the RFT probe—which is a disc), and
- $k_d$  is the spherical isotropic draw-down permeability.

The flow shape factor  $C$  allows for the geometry of the system and takes the value of 0.5 for pure spherical flow and 1.0 for hemispherical flow. Given the presence of the borehole, whose surface is rendered a no-flow boundary by filter cake, the nearest ideal case is hemispherical flow. Finite element computer simulations of the flow process carried out by Zimmerman<sup>2</sup> give the value quoted below (0.668); the concept of flow shape factor is illustrated in figure 8–11.

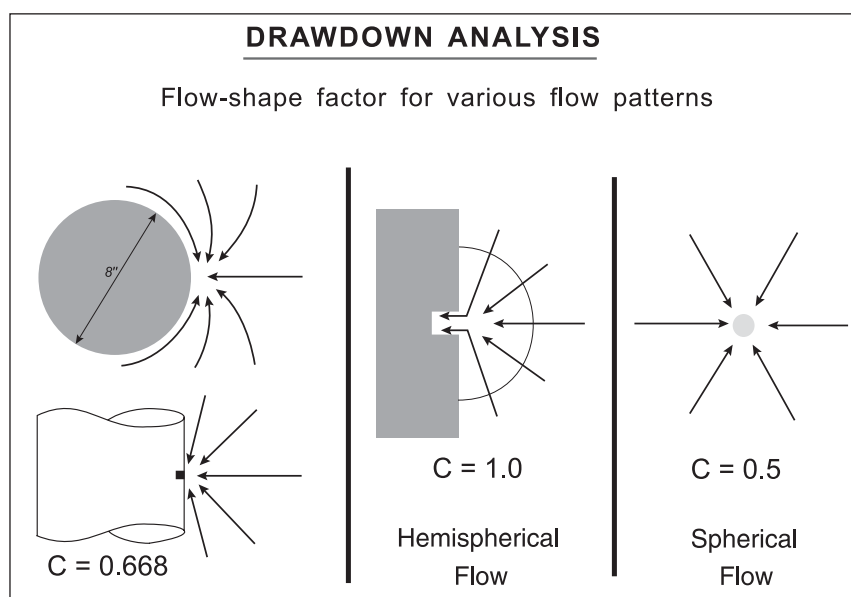


Fig. 8–11. The concept of flow shape factor

The draw-down permeability equation, in RFT units, then becomes

$$k_d = \frac{5660q\mu}{\Delta p_{DD}} \quad (8-11)$$

## Build-up analysis

During the build-up period, the pressure transient propagates spherically outwards and the build-up analysis is therefore based on spherical flow in an infinite homogeneous medium (see figure 8–12a). This approach is valid until the outwardly propagating pressure increase reaches an impermeable barrier. At this point, the spherical flow pattern starts to alter (see figure 8–12b), possibly eventually becoming radial-cylindrical.

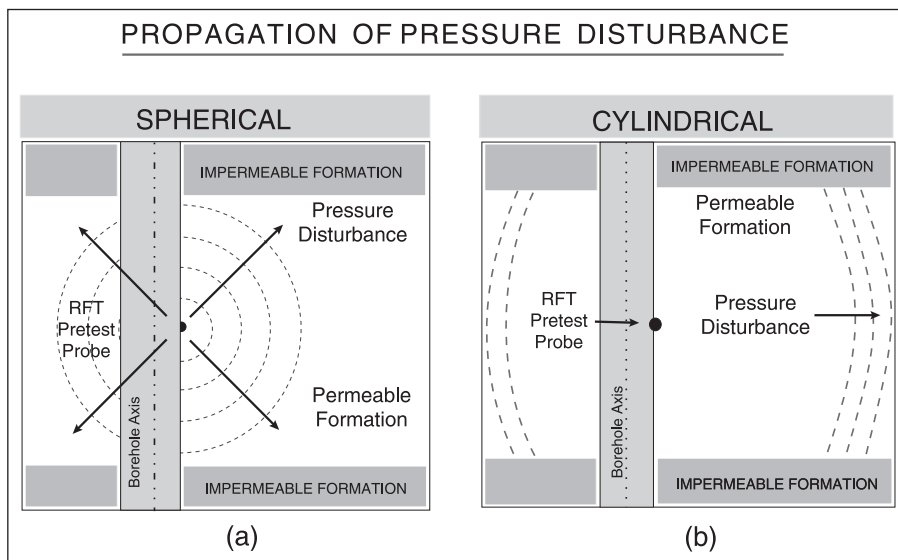


Fig. 8–12. Spherical propagation of pressure disturbance

The normal RFT pretest consists of a two-rate drawdown, as each of the two 10-cc pretest chambers has a different flow rate. The pressure response at the RFT probe during buildup is therefore obtained by superposition of the two draw-down responses. A plot of RFT probe pressure ( $p_s$ ) versus the spherical time function results in a straight line of slope  $m$ . The equation of this straight line is

$$p_s = m f_s(\Delta t) + p_i \quad (8-12)$$

where  $f_s(\Delta t)$  is the two-rate spherical time function given by

$$f_s(\Delta t) = \frac{q_2/q_1}{\sqrt{\Delta t}} - \frac{(q_2/q_1 - 1)}{\sqrt{T_2 + \Delta t}} - \frac{1}{\sqrt{T_1 + T_2 + \Delta t}}$$

The spherical build-up permeability ( $k_s$ ) can be determined from the slope using the following expression (in RFT units):

$$k_s = 1856\mu \left( \frac{q_1}{m} \right)^{2/3} (\phi c_t)^{1/3} \quad (8-13)$$

In the above,

- $q_1, q_2$  are the flow rates of the two pretests,
- $T_1, T_2$  are the flowing times of the two pretests,
- $\Delta t$  is the shut in time,
- $\phi$  is the formation porosity, and
- $c_t$  is the total compressibility.

Figure 8–13 illustrates a typical such spherical plot. Note that the initial part of the buildup deviates from a straight line because of early time effects, such as flow line storage. The plot may also deviate from a straight line at late times if boundary effects or radial variations in mobility are present.

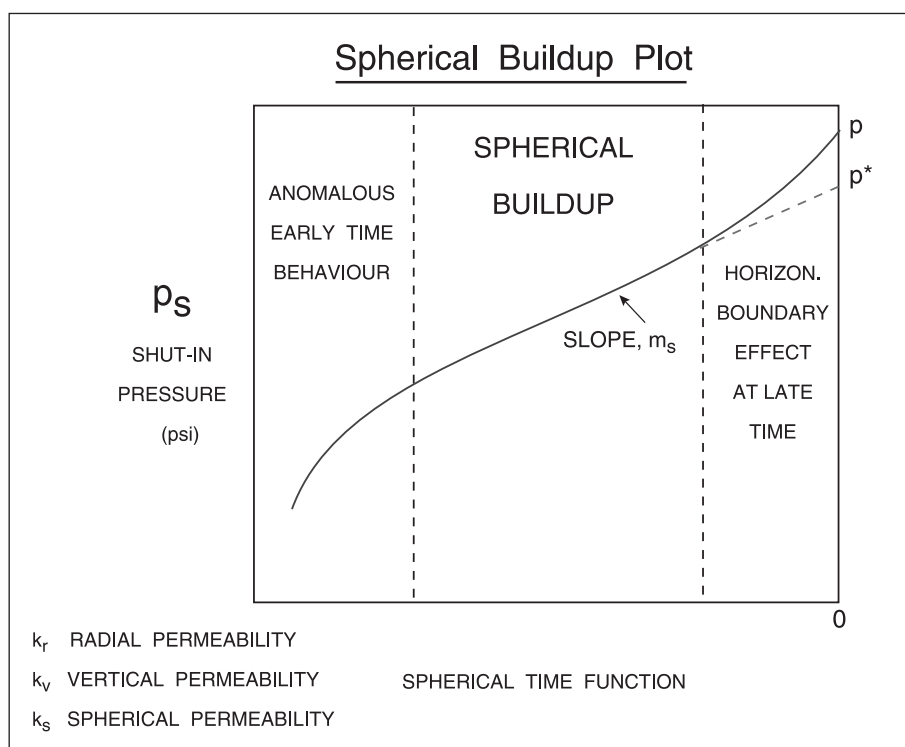


Fig. 8–13. Typical spherical plot and the different time domains

An analysis similar to that for spherical flow can also be made for cylindrical flow. Some of the RFT tests analyzed during the Radcliffe study exhibited boundary effect, but fully developed cylindrical flow was rarely observed. In addition, the derivation of permeability from a cylindrical analysis required knowledge of the bed thickness  $h$ , a parameter which can be difficult to determine. For these reasons, cylindrical build-up analysis was not used during the study and is therefore not presented here.

## Drawdown versus Buildup

Permeabilities derived from RFT measurements are influenced by several factors. These factors affect the drawdown and buildup differently, and are briefly outlined below:

**Radius of investigation:** The drawdown is influenced by the formation very close to the probe and the radius of investigation is in the order of a few centimeters. In contrast, the build-up analysis reflects the zone through which most of the flow is taking place at that time. This zone of influence occurs in that part of the formation where the pressure gradient is highest and is illustrated in figure 8–14. A simplified analysis of the buildup based on a single rate drawdown yields the following relationship<sup>3</sup>:

$$r_{i(\max)} = 0.0205 \sqrt{\frac{k_s}{\phi \mu c_t}} (T + \Delta t)^{0.2} \Delta t^{0.3} \quad (8-14)$$

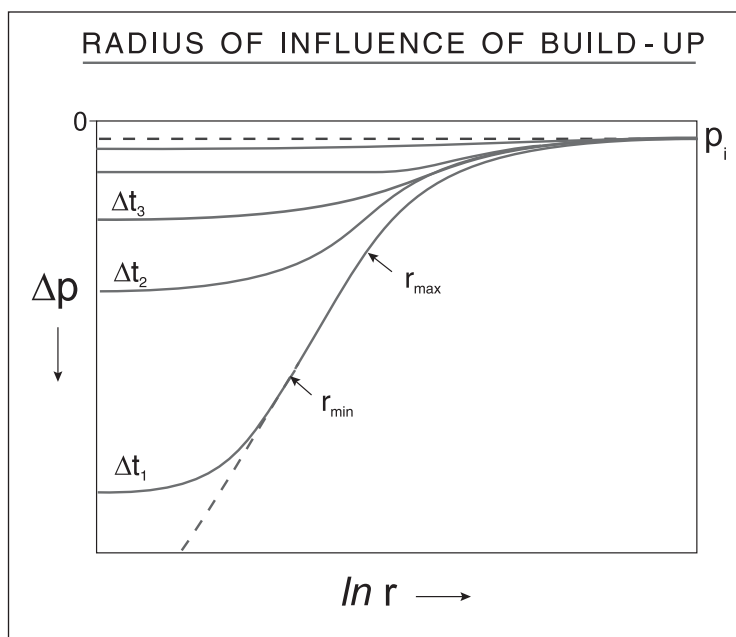


Fig. 8–14. Pressure behavior in the formation during spherical buildup

This is an important equation for the purposes of this study, as it was used to define the interval over which core data were to be averaged for comparison with  $k_s$ . Typically, values of  $r_i$  are in the range of 1–5 ft, depending on reservoir conditions. Thus, the scales of the two measurements are very different.

**Reservoir heterogeneity:** The RFT interpretation presented above assumes that the reservoir is homogeneous. Heterogeneities will affect the reliability of the analysis, particularly the buildup, where changes in slope associated with changes in formation permeability may make it difficult to detect a valid spherical straight line. Further, the build-up analysis reflects the heterogeneities of a relatively large volume of the reservoir, and could therefore be affected by both microscopic and macroscopic heterogeneities. Thus, the nature of the reservoir *seen* by the two measurements can be very different. The depth of investigation of a pretest buildup is of the order of 3 ft and the descriptor “macroscopic” lies within the confine of this limit.

**Formation damage:** A damaged zone may be present in the well as a result of particulate invasion (internal filter cake) and clay swelling. If present, the effects will reduce the permeability near the wellbore and the draw-down permeability will be pessimistic. It has also been postulated that in soft formations, the RFT probe may cause localized compaction, again leading to an underestimation of permeability from the draw-down analysis. On the other hand, in hard brittle formations, the probe might cause local fracturing leading to an optimistic draw-down permeability. The build-up analysis should not be influenced by any of the skin effects mentioned above because of its much larger radius of investigation.

**Invasion profile:** The RFT measures effective permeability to the mobile fluid (or fluids). Thus, to derive absolute permeability from a draw-down or build-up analysis, the relative permeability to the mobile fluid must be known, which, of course, is a function of saturation. This is not so much of a problem in draw-down analysis, where the radius of influence is very shallow.

The situation is not so clear, however, in the case of the build-up analysis. The radius of investigation of the buildup may or may not be larger than the diameter of invasion. In the case where it is larger, the buildup will still be influenced by the invaded zone to some extent because of the spherical nature of the flow. In the case where the radius of investigation of the buildup is within the invaded zone, saturation variations may still be encountered if the invasion profile is not steplike.<sup>5,6</sup> In either case, it can be difficult to determine which fluid is mobile (filtrate fluid, reservoir fluid, or both) and what the effective saturations are.

**Anisotropy:** In anisotropic formations, the flow pattern near the RFT probe becomes distorted<sup>7</sup> and (assuming the anisotropy is greater than 1—the usual case) the draw-down permeability lies somewhere between the spherical and the horizontal permeability. This is discussed further in the next section. The effect of anisotropy on the build-up pressure transient is much less. Here, the flow pattern remains essentially spherical and the build-up analysis still gives spherical permeability  $k_s$ , which is related to the horizontal permeability through the following expression<sup>8</sup>:

$$k_h = A^{1/3} k_s \quad (8-15)$$

where the anisotropy  $A$  is given by

$$A = \frac{k_h}{k_v} \quad (8-16)$$

It should also be pointed out that the two measurements may be affected by very different values of anisotropy. The buildup may be affected by both microscopic anisotropy due to the sedimentary texture of the rock and by macroscopic anisotropy due to layering (reservoir heterogeneity). The drawdown, however, will tend to be affected mainly by the microscopic anisotropy.

**Range of measurable permeability:** The upper limit of the build-up measurement range is determined by the resolution of the pressure gauge. In relatively high permeability formations, the pressure buildup is rapid and the variations in pressure during the straight line middle time period are less than the resolution of the pressure gauge. Stewart and Wittman<sup>2</sup> derived the



following expression for the maximum measurable permeability ( $k_s(\text{max})$ ) as a function of gauge resolution ( $\delta p$ ):

$$k_{s(\text{max})} = 390 \left( \frac{q\mu}{\delta p} \right)^{2/3} \left( \frac{\phi\mu c_t}{T} \right)^{1/3} \quad (8-17)$$

Most of the RFT surveys analyzed during this study were recorded using the strain-type pressure gauge which has a resolution of only 1 psi. The exact value of the maximum measurable permeability depends on reservoir conditions, but for this type of gauge it is typically around 10 md. This problem can be somewhat improved by using a quartz gauge which has a resolution of 0.01 psi. The practical lower limit of the build-up analysis is determined by dry tests.

For the draw-down analysis, the upper limit of the measurement range is also determined by the gauge resolution, as the drawdown decreases with increasing permeability. The actual limit again depends on the reservoir conditions but is certainly as high as several hundred millidarcies (with the strain gauge), much higher than that for the buildup. The lower limit depends on the bubble point of the fluid, as at very low permeabilities the drawdown may be so high that the pressure drops below the bubble point thereby liberating gas.

In summary, the factors discussed above tend to cause the build-up permeability to be less than the draw-down permeability, which in turn is less than the horizontal permeability, i.e., in general

$$k_s < k_d < k_h$$

The effects of these various factors on the field data analyzed during this study are discussed later.

## New developments in RFT interpretation

The conventional draw-down equation previously described was developed assuming an effective probe radius is equal to one half the actual probe radius<sup>9</sup>: i.e.,  $r_{pe} = 0.5r_p$ . When the more precise value from Carslaw and Jaeger<sup>10</sup> is used, i.e.,  $r_{pe} = 2r_p/\pi$ , then the draw-down equation for isotropic media becomes (in RFT units)

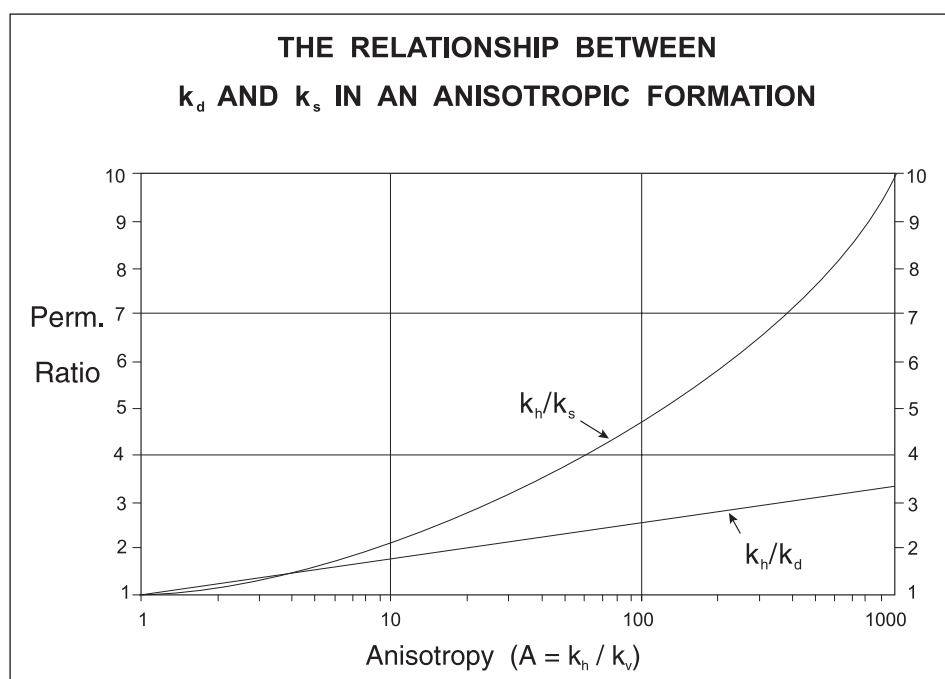
$$k_d = 6900 \frac{q\mu}{\Delta p_{DD}} \quad (8-18)$$

In an anisotropic medium, the analytical solution of the draw-down equation must be based on an ellipsoidal rather than spherical sink because of the distortion of the flow pattern. In this case, the effective probe radius varies with anisotropy, and the solution of the anisotropic draw-down equation for several values of anisotropy is given in table 8-4.

The results of Dussan and Sharma<sup>7</sup> on the effect of anisotropy on probe permeability in drawdown and buildup are shown in figure 8-15.

**Table 8-4.** Solution to the anisotropic draw-down equation<sup>7</sup>

$A = k_h/k_v$	$k_h/k_d$
1	1.000
2	1.328
3	1.462
4	1.554
5	1.626
6	1.731
7	1.773
8	1.773
9	1.810
10	1.847
100	2.571
1,000	3.303

**Fig. 8-15.** Effect of anisotropy on probe permeability

In an anisotropic medium, both draw-down and build-up permeability are a function of  $k_h$  and  $k_v$ . Thus, the two measurements can be combined to predict  $k_h$  and  $k_v$ , without prior knowledge of anisotropy. The technique therefore involves the simultaneous solution of Eq. (8-15) and the anisotropic draw-down equation. The limitation of this technique is that it is based on the assumption that the formation is homogeneous, and that the drawdown and buildup are reflecting the same reservoir characteristics. From the discussion above, it is clear that this assumption is not valid in heterogeneous formations.

## Method of Analysis of Field Data

The RFT field data (40 pretests in all) were analyzed using the conventional RFT interpretation outlined above. The build-up analysis was performed twice on each test, first using the parameters of the invaded zone and then the parameters of the uninvaded zone. Thus, two estimates of  $r_i$  were computed for each test, which were then compared with the  $d_i$  indicated by logs in order to decide which set of parameters was most appropriate for each buildup. Also, 15 of the 40 tests were found to be unsuitable for build-up analysis, either because the permeability was outside the measurable range or because the quality of the pressure data was poor. The draw-down analysis was performed using the updated draw-down equation (8–18) and, of course, the invaded zone parameters.

The values of  $k_d$  and  $k_s$  thus obtained are effective permeabilities. They were then converted to absolute permeabilities ( $k_{d(abs)}$ ,  $k_{s(abs)}$ ) assuming only one mobile phase (which may not be valid in some cases), using the appropriate end-point relative permeability.

The preparation of the routine air permeability ( $k_a$ ) core data was a three-stage process involving depth matching, conversion to in situ conditions, and averaging. The first stage was depth matching. The routine core data, consisting of porosity and horizontal air permeability measurements at approximately 1 ft intervals, were depth-matched in the area of each RFT test in order to identify the interval of core data relevant to each test. The next stage was conversion of the data to in situ conditions. Routine air permeability measurements are subject to various errors,<sup>11,12</sup> the following being the main ones:

- Gas slippage
- Overburden
- Clay swelling

The overall effect of these errors is to cause conventional air permeability measurements to be too high, particularly at lower permeabilities (i.e., in the range of interest for RFT comparison). It is therefore necessary to correct routine core measurements before they can be used. The method used to convert air permeability ( $k_a$ ) into in situ (stressed) brine permeability ( $k_b$ ) varied from well to well, depending on the type of data available. An empirical  $k_a/k_b$  relationship proposed by Juhasz<sup>11</sup> was principally used which is shown in figure 1–91 in chapter 1; this allows a correction from core air permeability to in situ brine permeability where the interstitial clay is in the equilibrium reservoir state of salinity.

The final stage was averaging. In order to compare core- and RFT-derived permeabilities, the core measurements must first be averaged in some manner to obtain an estimate of effective permeability. Warren and Price<sup>12</sup> state that for a heterogeneous system, the most probable effective permeability can be closely approximated by the geometric average of the individual permeabilities. In fact, bearing in mind the very different scales of the draw-down and build-up measurements, and the heterogeneous nature of the reservoirs, it is necessary to derive two estimates of effective permeability at each RFT test point. One value ( $k_{G(bu)}$ ) should reflect the volume of formation influencing the buildup, while the other ( $k_{G(dd)}$ ) should deflect the draw-down area close to the probe. Thus,  $k_{G(bu)}$  was taken to be the geometric average of the  $k_b$  values in an interval equal to  $2r_i$  (i.e., twice the radius of investigation of the buildup) and

centered on the RFT test depth. The arithmetic and harmonic averages were also computed for comparison. In contrast,  $k_{G(dd)}$  was typically taken to be the geometric average of only the two or three measurements nearest the RFT test depth.

The comparative procedure adopted in Radcliffe's study is based on the assumption that the core samples are representative of the formation. Although the volume of the core samples is very small compared to the volume investigated by the RFT, the horizontal permeability measurements can probably be extended to the scale of an RFT test with reasonable confidence (though the same is not true of vertical permeability measurements). However, it is felt that there is a degree of uncertainty associated with accuracy with which the core data reflects the actual permeability profile. Obviously, this uncertainty will be lower in homogeneous formations where a better correlation between core and RFT data can be expected. Thus, in order to quantify the confidence level of each correlation point, a heterogeneity indicator  $V$  was defined as follows:

$$V = \frac{k_G - k_H}{k_G}$$

Low values of  $V$  indicate homogeneous formation, while high values indicate heterogeneous formation.

Three typical pretests illustrating the nature of permeability determination are shown in figures 8-16, 8-17 and 8-18, respectively; these are labeled examples 1, 2, and 3. The depth location of these tests is shown in figure 8-19, where the extent of core averaging is also indicated.

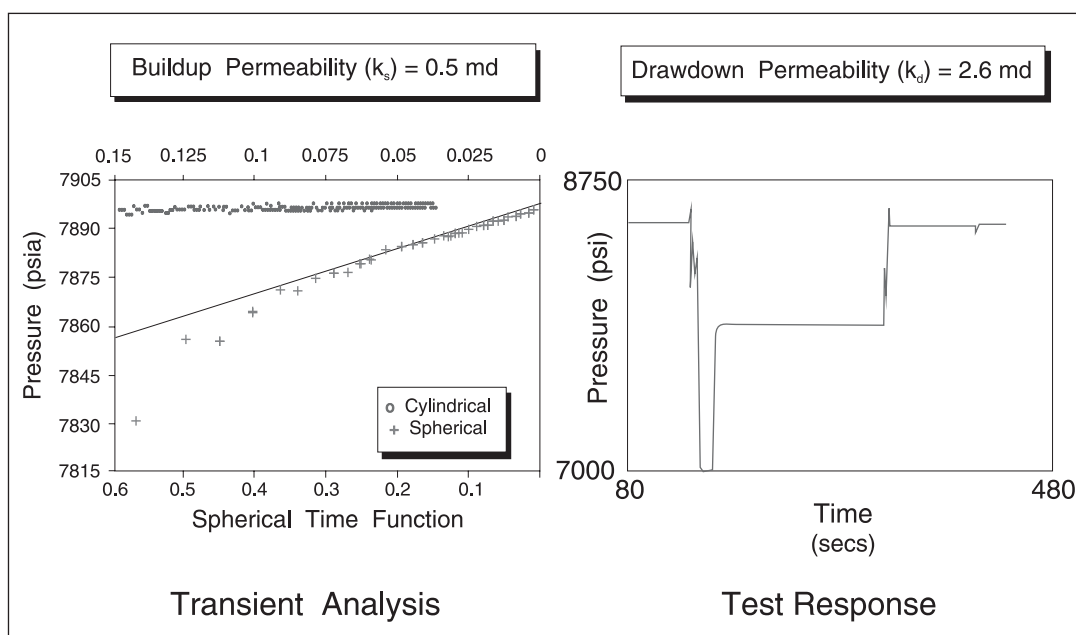


Fig. 8-16. RFT pretest example 1

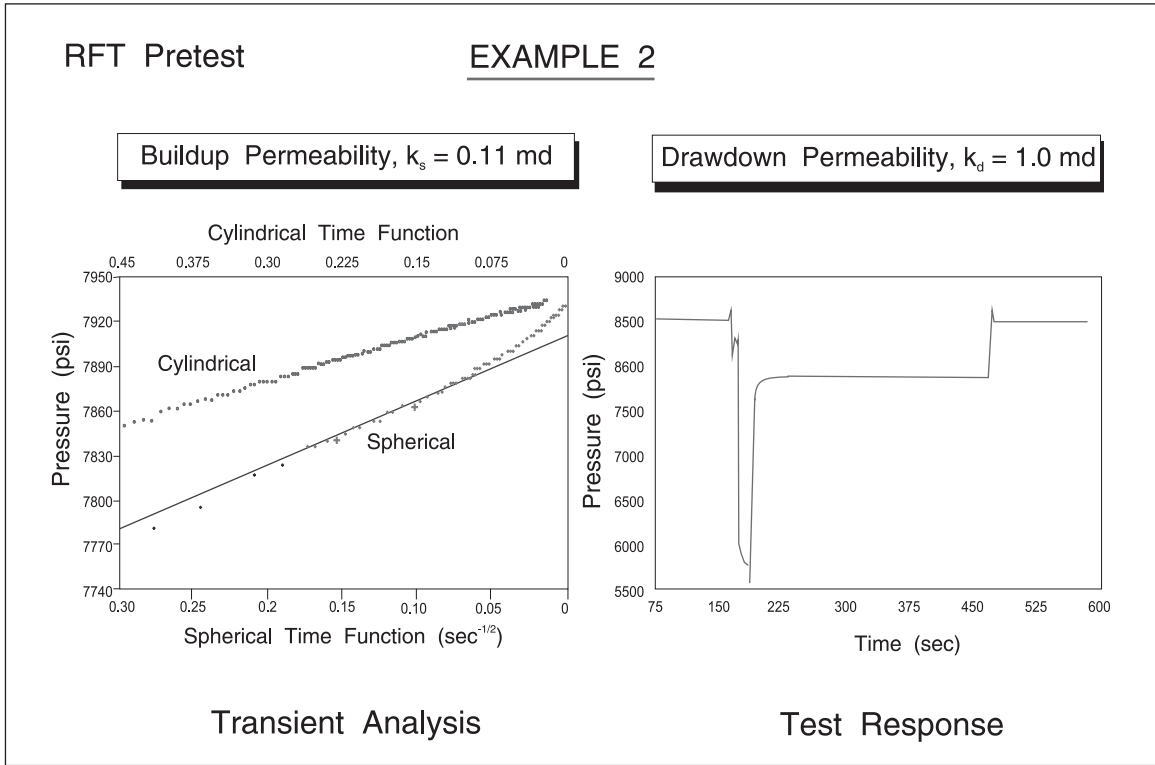


Fig. 8-17. RFT pretest example 2

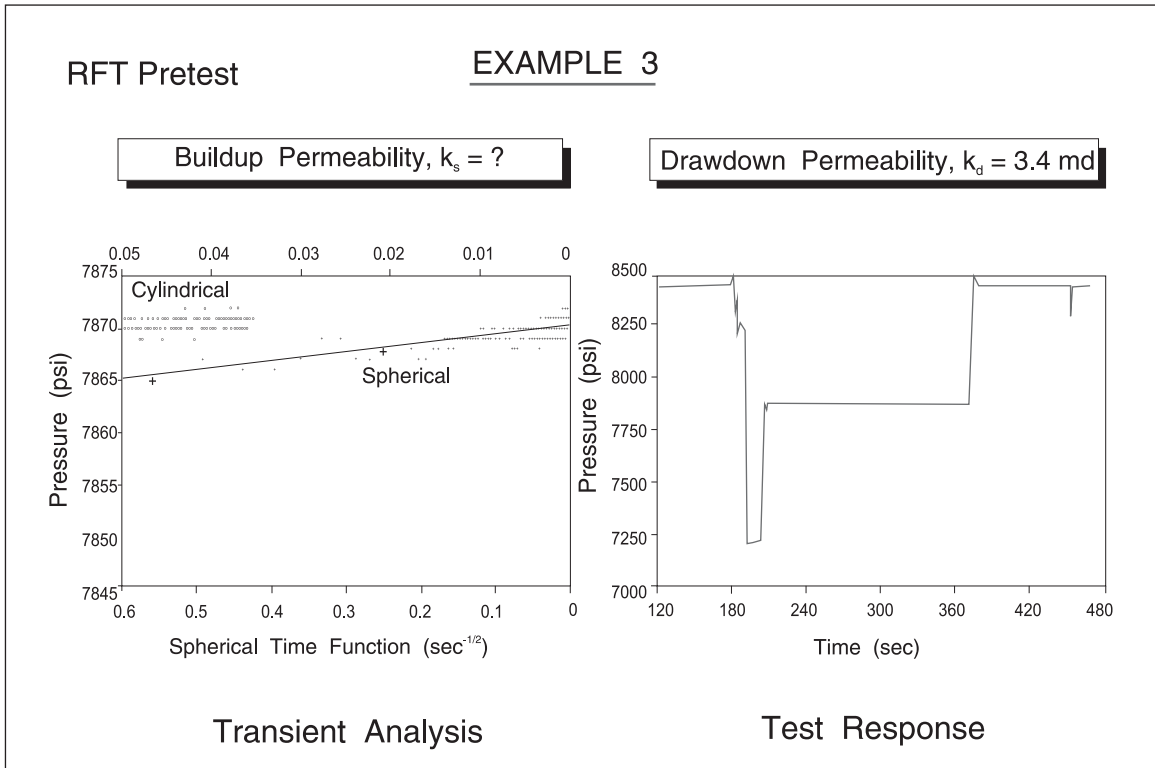


Fig. 8-18. RFT pretest example 3

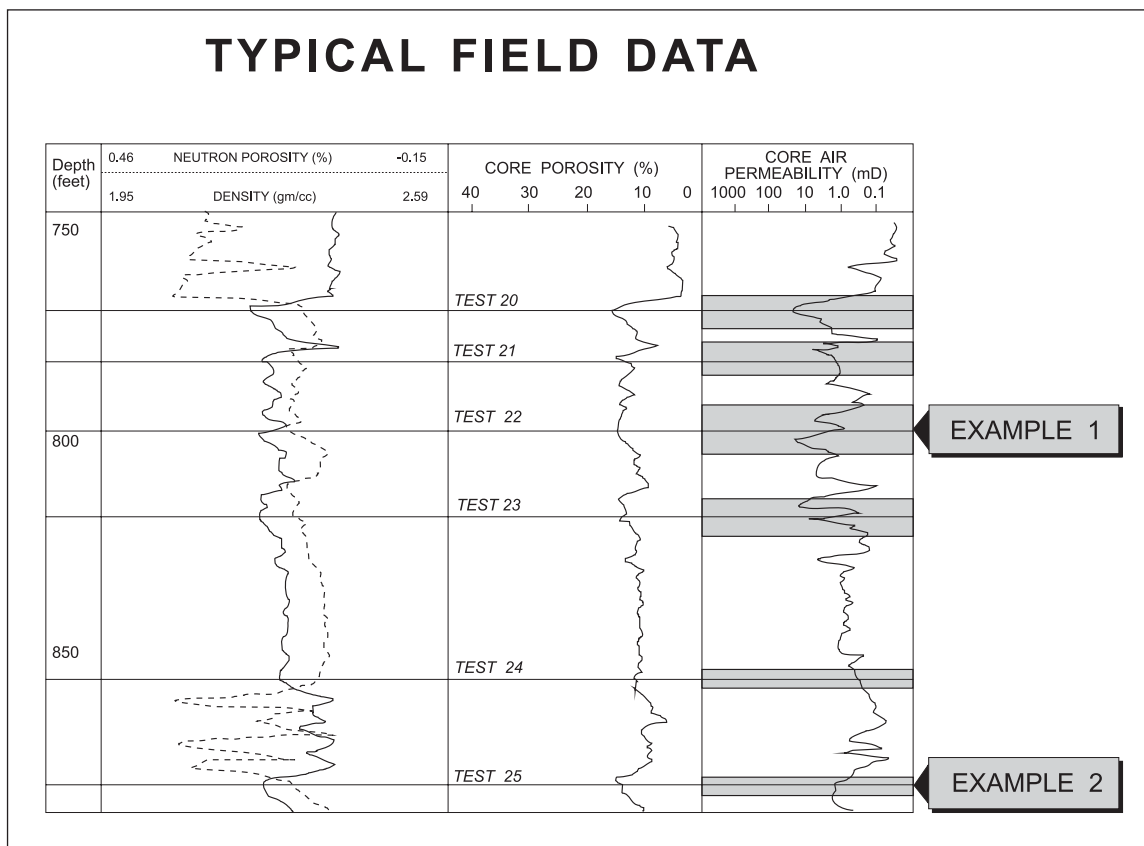


Fig. 8–19. Depth location of example pretests

## Discussion of Results

### RFT draw-down versus core permeability

Figure 8–20 shows the comparison between RFT draw-down permeability ( $k_{d(abs)}$ ) and effective permeability derived from core measurements ( $k_{G(dd)}$ ). Of the 40 data points, 53% lie within a factor of 2 of the ideal correlation, and 88% lie within a factor of 5\*. On all the figures discussed in this section, the solid lines represent the ideal correlation between the two quantities being plotted, and the dotted lines represent the limits of the error bands corresponding to discrepancies in the correlation of a factor of 2 and 5. Bearing in mind the uncertainties associated with the comparative technique, this is felt to be a reasonable correlation.

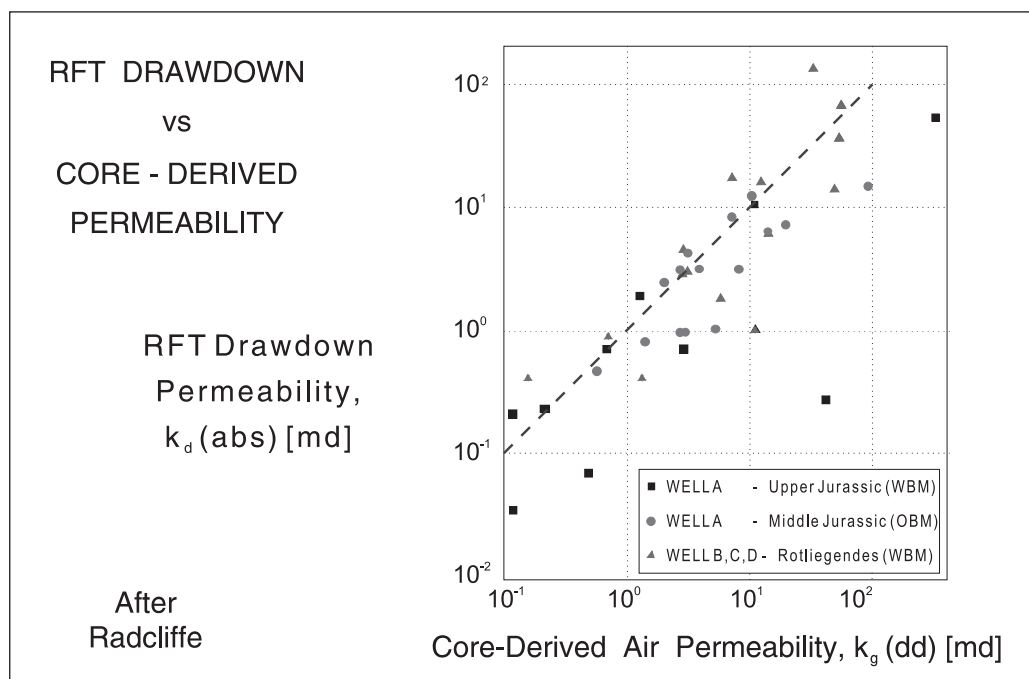


Fig. 8–20. Comparison between RFT draw-down permeability and effective permeability from core analysis

The distribution of the points shows a trend towards the bottom right. This is to be expected bearing in mind that core measurements tend to overstate permeability (despite the  $k_a/k_b$  conversion), while RFT tends to underestimate permeability. Nevertheless, almost half of the points (18 out of 40) lie above the ideal correlation line. The most likely explanations for RFT draw-down permeability being higher than core permeability are either underestimation of  $k_{G(\text{dd})}$  due to reservoir heterogeneities that are not reflected by core data and/or depth matching errors, or overestimation of  $k_{d(\text{abs})}$  due to errors in fluid mobility (too low).

The 22 points below the ideal correlation line are more widely spread than those above. The most likely explanations for the draw-down permeability being lower than the core permeability are either overestimation of  $k_{G(\text{dd})}$  due to  $k_a/k_b$  conversion errors, or underestimation of  $k_{d(\text{abs})}$  due to anisotropy or formation damage.

The effect of anisotropy was investigated further. An analysis of the core vertical permeability data showed that no reliable correlation existed between  $k_a$  and anisotropy ( $A$ ) for any of the wells. Thus, it was not possible to assign a value of anisotropy to each RFT test and correct the RFT permeabilities accordingly. However, the distribution of the anisotropy data was such that the value of  $A$  was between 0.5 and 10 for 84 out of the 91 points, with a median value close to 2.

Figure 8–21 shows the ideal correlation lines for various values of anisotropy based on the solution of the anisotropic draw-down equation. If an anisotropy of 2 is assumed, it is found that 23 points (58%) fall within a factor of 2 of the ideal correlation and 36 (90%) are within a factor of 5. Further, the points are evenly distributed about the ideal correlation line. This contrasts with the results obtained by Jensen and Mayson,<sup>13</sup> who found the RFT draw-down permeability to be consistently lower than core data. This discrepancy may be due differences in the methods used to account for the effects of anisotropy and correction of the core data.

Another contributory factor may well be well-specific skin damage. Regarding formation damage, this is difficult to quantify, but the effect should not be large since the RFT tests are mainly in relatively clean parts of the formations. In addition, the 16 tests from the Middle Jurassic in well A should have very little skin, as this section was drilled with OBM.

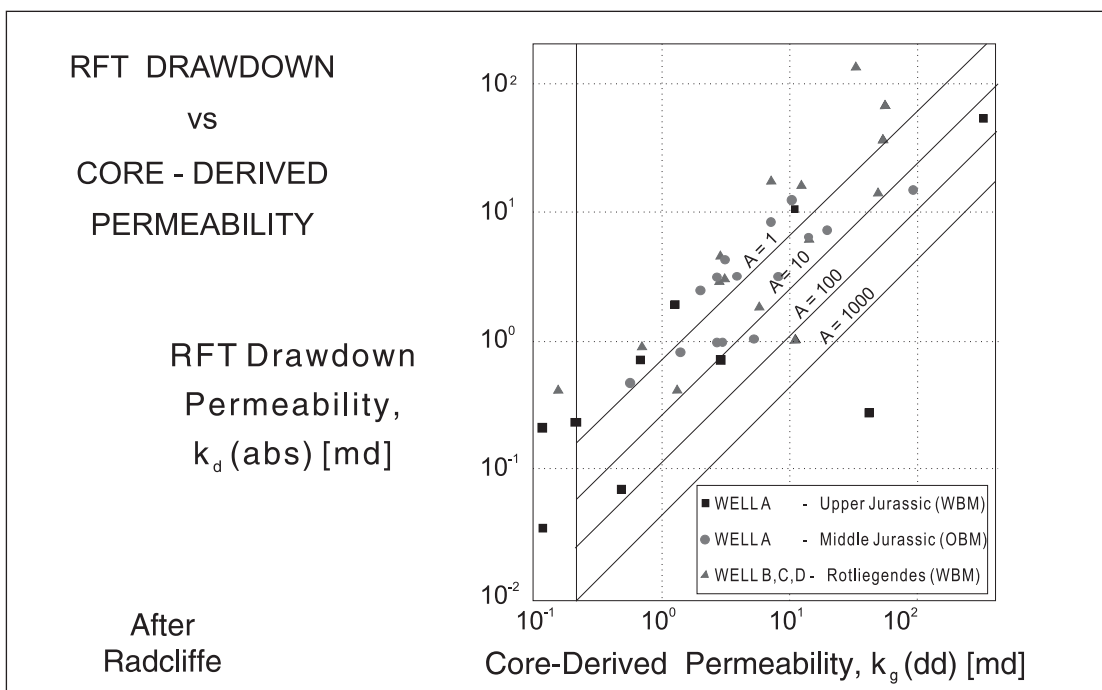


Fig. 8–21. Ideal correlation for various anisotropy values (draw-down data)

One final note: the 40 RFT tests represent several different combinations of mud filtrate and reservoir fluids; however, none of these groups shows a better correlation between  $k_{d(abs)}$  and  $k_{G(dd)}$  than any of the others.

## RFT Build-up versus core permeability

Figure 8–22 shows the comparison between the RFT build-up permeability ( $k_{s(abs)}$ ) and the effective permeability derived from core measurements ( $k_{G(bu)}$ ). Of the 25 data points, 28% lie within a factor of 2 of the ideal correlation, and 64% lie within a factor of 5. This correlation is not as good as the one achieved with the draw-down permeability. The distribution of the points shows an even more marked trend towards the bottom right than the draw-down correlation, with only 4 points above the ideal correlation line. All these points are from the Rotliegendes wells, and the most likely explanation for the build-up permeability being higher than the core permeability is an underestimation in the relative permeability (no  $k_{rw}$  data being available).



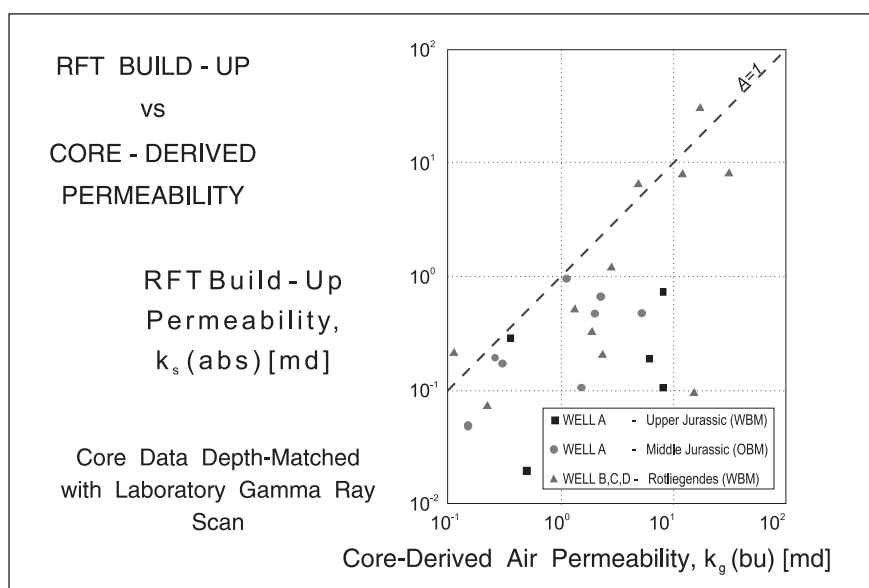


Fig. 8-22. Comparison between RFT build-up permeability and effective permeability from core analysis data

Of the 21 points below the ideal correlation line, 12 are within and 9 outside a factor of 5. The most likely explanations for the build-up permeability being lower than the core permeability are either overestimation of  $k_{G(\text{bu})}$  due to  $k_a/k_b$  conversion or depth errors, or underestimation of  $k_{s(\text{abs})}$  due to anisotropy or errors in fluid mobility (too high).

Regarding the effect of anisotropy, figure 8-23 shows the ideal correlation line for various values of anisotropy (based Table 8-4). Note that a comparison of figures 8-21 and 8-23 illustrates that  $k_d$  is a much better estimate of  $k_h$  than  $k_s$  in anisotropic formations, particularly as the build-up can be expected to exhibit anisotropy higher than indicated by measurements on core plugs, due to layering. In fact, the best correlation is obtained by assuming an anisotropy of 10, and it is found that this gives 12 points (48%) within a factor of 2, and 19 points (76%) within a factor of 5. This improves the correlation of build-up versus core, but it is still not as good as the draw-down versus core correlation.

In the case of the fluid mobility effect, the sensitivity of  $k_{s(\text{abs})}$  to fluid type was investigated by comparing the values of  $k_{s(\text{abs})}$  computed assuming invaded zone parameters to those computed assuming uninvaded zone parameters. The results show that where the mobility contrast between the invaded and uninvaded zones is low (between 0.5 and 1), the build-up permeabilities can vary by up to a factor of 2.5. However, in the gas wells where the mobility contrast is much higher (between 0.01 and 0.02), the build-up permeability can vary by over a factor of 100. Thus, the incorrect use of uninvaded zone parameters can cause a serious underestimation of build-up permeability. Further, the presence of two mobile fluids within the build-up radius of investigation can greatly reduce the total fluid mobility and thus also cause a significant underestimation of build-up permeability.

It should be pointed out that the invaded zone parameters were found to be the most appropriate for 23 out of the 25 buildups analyzed. This was fortunate because the standard build-up analysis is not valid for highly compressible fluids like gas. Note that WFT permeabilities are biased to the lower values as illustrated in figure 8-24.

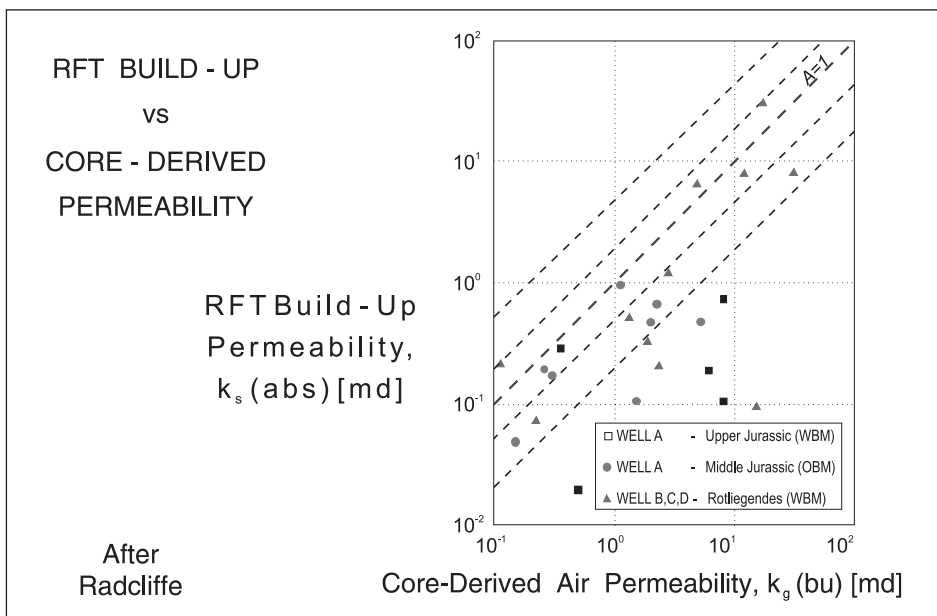


Fig. 8-23. Ideal correlation for various anisotropy values (build-up data)

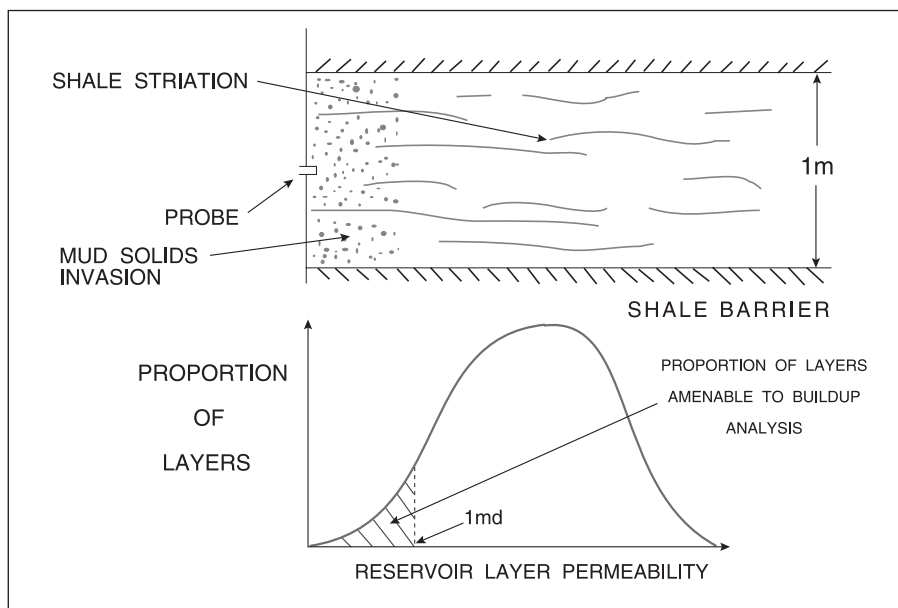


Fig. 8-24. WFT permeability in perspective

## Conclusions

1. RFT draw-down permeability agrees reasonably well with core-derived permeabilities provided core measurements are corrected to in situ brine values and the effect of anisotropy on the RFT is taken into account. Limited comparison with well-test data also shows reasonable agreement. Thus, the draw-down measurement provides a reasonable estimate of  $k_h$  provided the anisotropy is low (or known) and well damage is not excessive.

2. The RFT draw-down permeability measurement has several advantages, the main ones being that the technique is quick and simple, and the measurement is in situ and discrete and has a relatively large range (up to several hundred millidarcies).
3. A potential application of the draw-down measurement is the determination of the permeability profile. This application would, of course, require more pretests than a conventional RFT survey. However, it may be attractive when it is considered that (at least in the North Sea) a conventional RFT pressure survey is already run in most wells, while only a limited number of wells are cored.
4. The agreement between RFT build-up permeability and core-derived permeabilities is generally poor. This is due to uncertainties on the build-up measurement associated with the invasion profile and formation heterogeneities. Thus, the build-up measurement does not provide a reliable estimate of  $k_h$ .
5. The build-up measurement has several disadvantages when compared to the draw-down one, the main ones being that the interpretation technique is more involved and requires additional input parameters ( $\phi$ ,  $c_v$ ,  $d_i$ ); a valid spherical straight line can be difficult to identify (particularly in heterogeneous formations); and the measurement range is very small (up to approximately 10 md only).
6. The two RFT measurements (draw-down and build-up) are on different scales and the correlation between them is poor. Combining the two measurements to predict  $k_h$  and  $A$  may be valid in homogeneous formations but does not appear to be a very robust technique in heterogeneous formations.

## Notes

- 1 Ferguson, C. K., and Klotz, J. A. "Filtration from Mud during Drilling," *JPT* 6 (2), *Trans AIME* 210, (1954): 30–43.
- 2 Zimmerman, T. Internal Schlumberger Report.
- 3 Stewart, G., and Wittman, M. J. "Interpretation of the Pressure Response of the Repeat Formation Tester," (SPE 8362, SPE Fall Meeting, Las Vegas, 1979).
- 4 Radcliffe, D. "An Analysis of the Validity of Permeability Derived from the RFT," (M.Eng. Thesis, Heriot-Watt University, 1986).
- 5 Phelps, G., Stewart, G., and Peden, J. M. "The Effect of Filtrate Invasion and Formation Wettability on Repeat Formation Tester Measurements," (SPE 12962, Europec, London, 1984).
- 6 Phelps, G., Stewart, G., and Peden, J. M. "The Analysis of the Invaded Zone Characteristics and their Influence on Wireline Log and Well Test Interpretation" (SPE 13287, SPE Fall Meeting, Houston, 1984).
- 7 Dussan, E., and Sharma, Y. "Determination of Horizontal and Vertical Permeabilities using Measurements obtained with the Single Probe RFT" Schlumberger internal memo.
- 8 Moran, J., and Finklea, E. "Theoretical Analysis of Pressure Phenomena of the Wireline Formation Tester," *JPT* 14 (8), (Aug. 1962) 899–908.
- 9 Muskat, M. *Physical Principles of Oil Production*, (New York: McGraw-Hill Book Co.,)
- 10 Carslaw, H. S., and Jaeger, J. C. *Conduction of Heat in Solids*, (Oxford: Clarendon Press).
- 11 Juhasz, I. "Conversion of Routine Air Permeability Data into Stressed Brine Permeability Data," Shell internal report.
- 12 Warren, J. E., Skiba, F.F. and Price. H.S. "An Evaluation of the Significance of Permeability Measurement," *JPT* 13 (8), (Aug. 1961).
- 13 Jenson, C.L. and Mayson, H.J.: "Evaluation of Permeabilities Determined from Repeat Formation Tester Measurements in the Prudhoe Bay Field," SPE 14400 (SPE Ann. Tech. Mtg., Las Vegas, Sept. 1985).

# 9

## Exploration Applications of Distributed Pressure Measurement

---

### Introduction

When wireline formation tester (WFT) surveys are carried out in exploration and appraisal wells, the field is unproduced and the fluids may usually be assumed to be at hydrostatic equilibrium. Occasionally, an unproduced field may be depleted by pressure decline in the water leg due to production in nearby fields having a common aquifer. For example, the Miller field in the North Sea showed a significant decline in pressure between the discovery well and subsequent appraisal wells drilled at a later date. In this case, production from the Brae field is causing the interference. The first time such an effect was observed was in the South East Forties reservoir which has a common aquifer with the main Forties field; as the aquifer pressure declines as result of main field production, the oil zone in the satellite expands into the water leg causing the water–oil contact (WOC) to move downwards slightly. Since future development of the North Sea will largely focus on satellite fields close to existing facilities, the interpretation of WFT surveys in appraisal wells will be interesting. Another anomalous situation arises when the aquifer is in a dynamic state and the WOC exhibits tilting due to the viscous gradient which exists in the flowing aquifer. The best current example of this phenomenon can be seen in Papua New Guinea, where very active aquifers occur. Obviously, WFT pressure data from different wells will exhibit areal variation in this situation and the WOC will also be variable from well to well.

The main objectives of running WFT surveys in exploration and appraisal wells can be summarized as follows:

- determination of reservoir initial pressure;
- defining in situ fluid densities;
- estimation of fluid contacts;

- detection of hydrocarbon trapped as a residual saturation;
- permeability profiling;
- Delineating reservoir structure.

The latter activity is largely based on the comparison of WFT surveys in the various appraisal wells drilled into the field. Whenever WFT surveys in different wells are overlaid on a single pressure–depth diagram, the absolute accuracy of pressure and depth measurement immediately are a major concern. Each of the above topics will be considered in detail in this chapter.

Reservoir initial pressure can also be determined by conventional transient well testing, and the WFT survey should yield exactly the same pressure (corrected to a common datum) as the well test pressure buildup. In the event that these two estimates are different, then the cause of the anomaly should be investigated; provided the WFT survey is not degraded by excessive supercharging, it is usually assumed that the WFT gives a more reliable pressure measurement. The pressure obtained from the first buildup following the 5-minute flow period in a drill stem test (DST) requires correction to datum using a known fluid gradient, and often the exact nature of the fluid in the well at this point is not clear. One of the benefits from obtaining detailed knowledge of the reservoir pressure across a field from WFT surveys is that the mud weight in the development wells can be delicately balanced which minimizes formation damage due to mud filtrate invasion.

## Gravity–Capillary Equilibrium

WFTs make measurements of pressure as a function of depth. In an unproduced reservoir, the fluids in the system are at gravity–capillary equilibrium provided there is no movement of water in the aquifer. Pressure information is conveniently plotted on a true vertical depth versus pressure diagram on which hydrostatic fluid gradients appear. In the capillary transition zone (CTZ), where two continuous phases are present, the individual phase pressures differ by the capillary pressure  $P_c$  which may be positive (water-wet conditions) or negative (oil-wet conditions); thus

$$P_o - P_w = P_c(S_w) \quad (9-1)$$

The capillary pressure curve  $P_c(S_w)$  for a porous medium is a function of wetting properties, interfacial tension, and pore size distribution. The phase pressures in a water-wet reservoir are illustrated diagrammatically in figure 9–1.

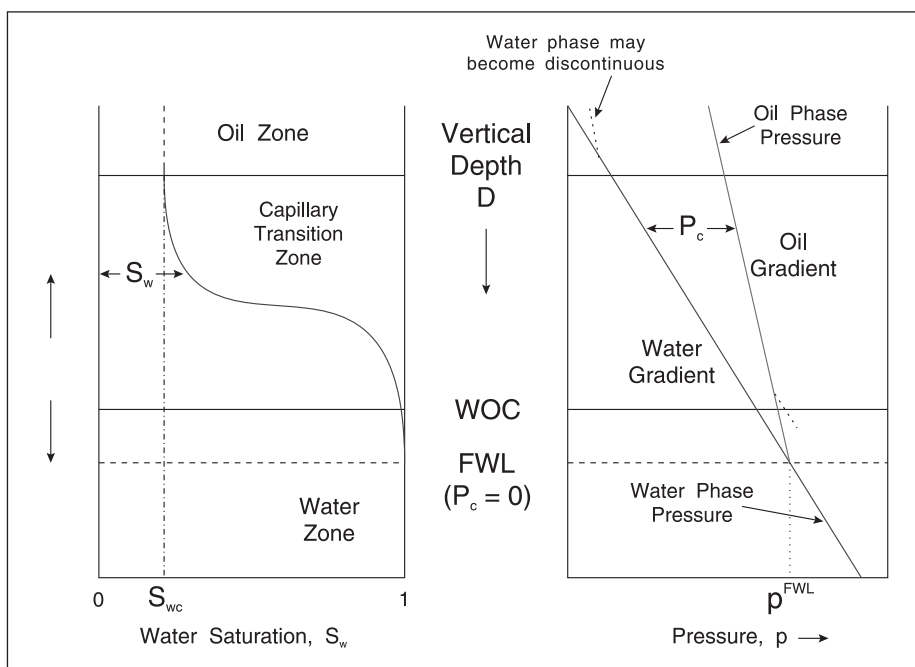


Fig. 9-1. Phase pressures at gravity-capillary equilibrium

The water-phase pressure denoted  $p_w$  is given by

$$p_w = p^{\text{FWL}} - \rho_w g h \quad (9-2a)$$

where  $p^{\text{FWL}}$  is the reference pressure at the free water level (FWL), i.e., the level of the OWC in an open borehole penetrating the formation. The quantity  $h$  is the true vertical distance measured up from the free water level. The water-phase pressure exhibits a hydrostatic gradient characteristic of the in situ formation water (brine) density  $\rho_w$ . In field units, this equation may be written as

$$p_w = p^{\text{FWL}} - 0.4335 \rho_w h \quad (9-2b)$$

$$\begin{aligned} p &: \text{psi} \\ \rho_w &: \text{g/cc} \\ h &: \text{ft} \end{aligned}$$

Similarly, the oil-phase pressure, denoted  $p_o$ , is given by

$$p_o = p^{\text{FWL}} - \rho_o g h \quad (9-3a)$$

or in field units

$$p_o = p^{\text{FWL}} - 0.4335 \rho_o h \quad (9-3b)$$

A wireline formation tester (WFT) survey from an unproduced reservoir is shown in figure 9–2, where both the formation and mud hydrostatic pressures are plotted on a pressure–depth diagram. In this case, the presence of a gas cap, oil column, and aquifer leg are all clearly apparent from the observed formation gradients and both the gas–oil contact (GOC) and the WOC can be found from the intersections of the best fit straight lines through the data. This field example has been presented since it also demonstrates that segregation in the mud column can cause the mud pressure gradient to change dramatically and a straight line is not always present. It is remarkable that gas cutting of the mud is apparently occurring even though the mud pressure (overbalance) is approximately 1,000 psi higher than the corresponding formation pressure. Contrary to the opinion of some engineers, the mud hydrostatic line need not extrapolate back to atmospheric pressure at surface since the mud gravity changes in the wellbore because of temperature variation and solids settling. A second field example from Algeria is shown in figure 9–3, which indicates the presence of a large gas zone underlain by water.

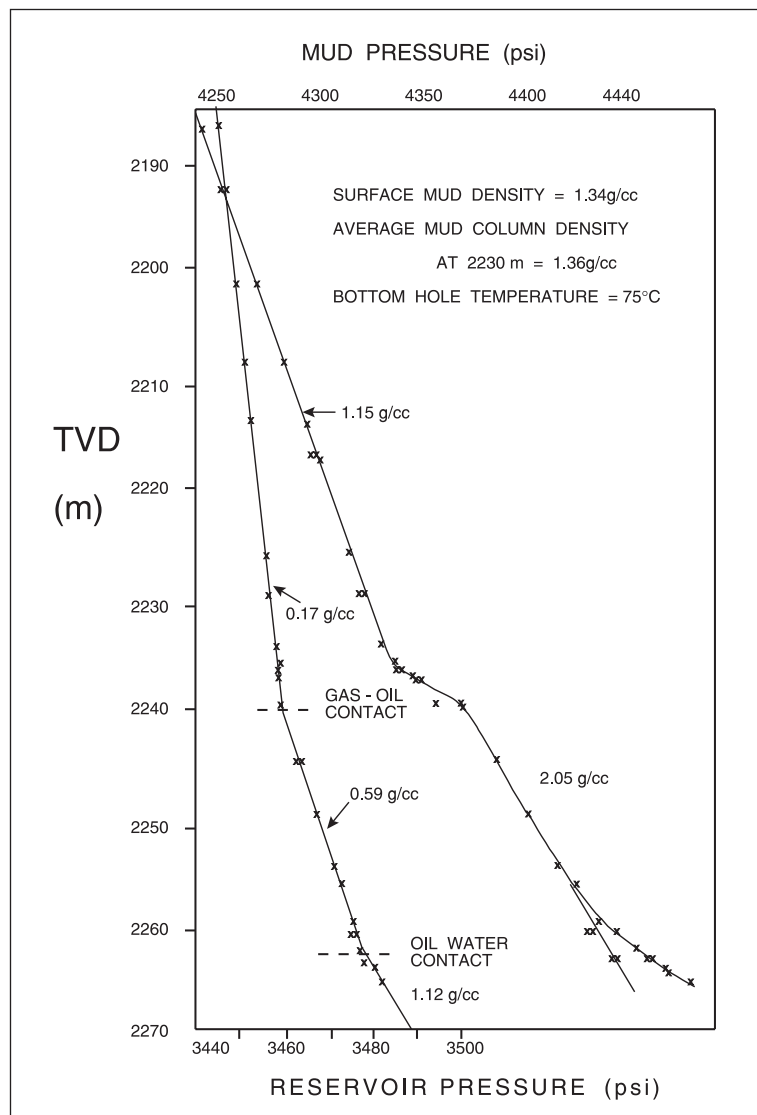


Fig. 9–2. WFT survey in an unproduced reservoir

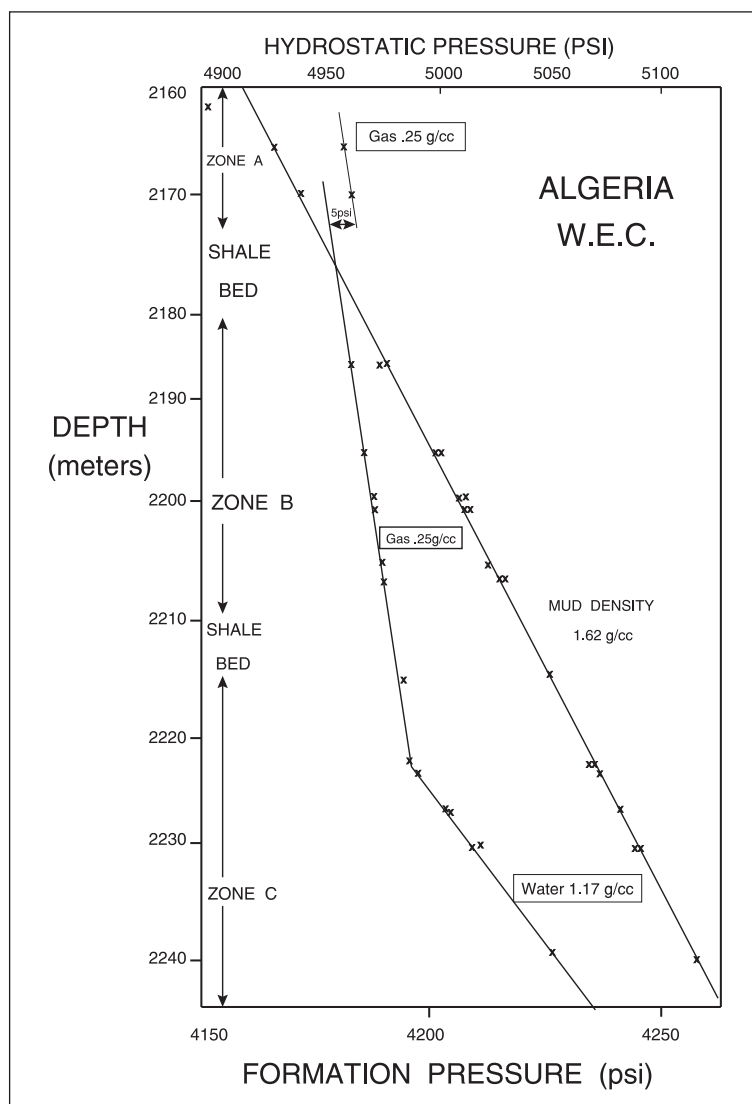


Fig. 9-3. Field example from a North African gas reservoir

Unfortunately, wireline formation testers cannot directly measure phase pressures. Mud filtrate invasion and supercharging have an important effect on the local pressure registered by a WFT device; this aspect will be considered in detail later. For the moment, it is sufficient to consider figure 9-4, which shows the pressure and saturation profiles in the vicinity of a wellbore with continuous mud filtrate invasion occurring. The results of numerical simulations of the invasion process for water-based mud (discussed in detail in a subsequent chapter) indicates that the sandface pressure in the water phase is very close to the hydrocarbon pressure at the same level far from the invaded zone. In essence, this is why the WFT works but the arguments are quite subtle and there is always the possibility of some capillary pressure effect. However, it will be tacitly assumed that the oil-phase pressure is measured in the oil column including the capillary transition zone; there are a large number of well documented field examples which prove this hypothesis. Note that the annulus around the wellbore occupied by water, i.e. mud filtrate, is in a dynamic state in the vertical sense as illustrated in figure 9-5. In the early days, the RFT was not run in Iran because a geologist stated it would see the water pressure gradient of the mud filtrate; because the potential in the falling water is imposed by the static oil in the reservoir, the formation tester “sees” the appropriate gradient.



For the moment, it is interesting to examine a concept proposed by Desbrandes and Gualdrón<sup>1</sup> and termed the *large hole observer*. In a laboratory sand pack, it is possible to install pressure tapings of relatively large diameter, say 2 mm. Suppose such an observation point is located in the capillary transition zone above the WOC as shown in figure 9–6. This very large hole will fill with oil and hence it will register the local oil-phase pressure. Thus, over the capillary transition zone a large hole observer will indicate the oil phase pressure, provided the system is water wet. This assertion was confirmed experimentally by Desbrandes and Gualdrón in a laboratory sand pack equipped with large-diameter pressure tapings. Thus, in figure 9–1 the oil phase pressure is shown as a continuous line over the capillary transition zone, implying that this quantity will be registered by the measurement system. Conversely, the water-phase pressure, which can only be detected by special tapings having semipermeable membranes, is marked by a dotted line implying it is not observable. It is well known that field data have demonstrated that WFT devices register the oil-phase pressure through capillary transition zones. However, it will be suggested later that this occurs because of the mechanics of mud filtrate invasion rather than the large hole observer effect postulated by Desbrandes and Gualdrón.

The implications of this theory are illustrated in figure 9–7. Firstly, the intersection of the measured oil gradient (in the oil zone and capillary transition zone) and the measured water gradient (in the aquifer) is synonymous with the free water level which lies below the WOC. This will be termed the *observed pressure gradient intersection (OPGI)*. The free water level lies at the OPGI and also lies below the WOC by an amount which depends on the threshold capillary pressure  $P_c^t$ ; this in turn depends on the largest pore size. In principle, there should be a discontinuity in the registered pressure as illustrated in figure 9–7. However, it is only in very tight formations that the FWL will be significantly below the WOC and in these cases the supercharging effect will considerably complicate matters.

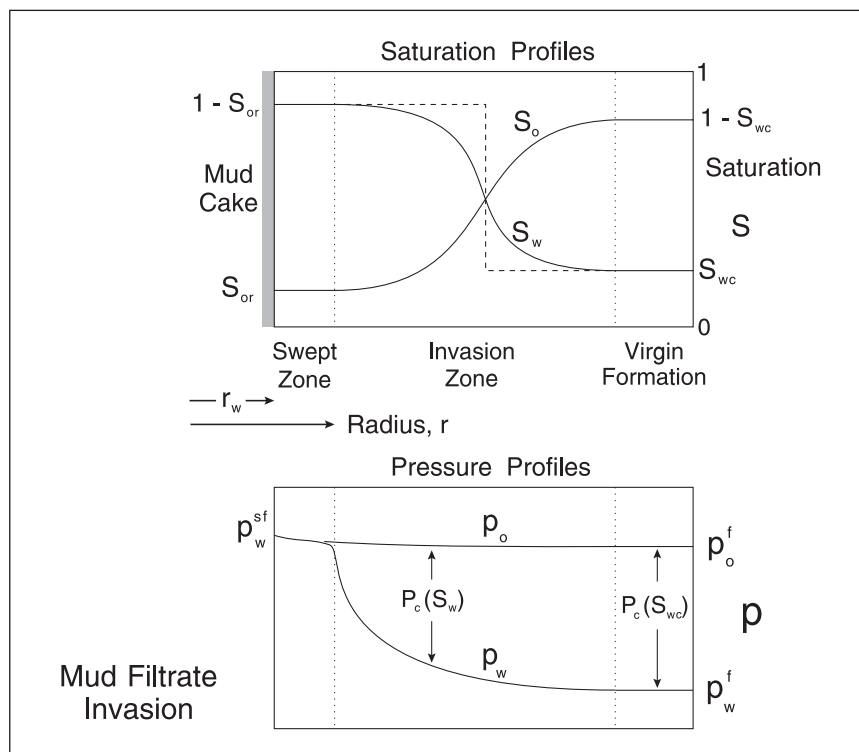


Fig. 9–4. Pressure and saturation profiles in the vicinity of a wellbore

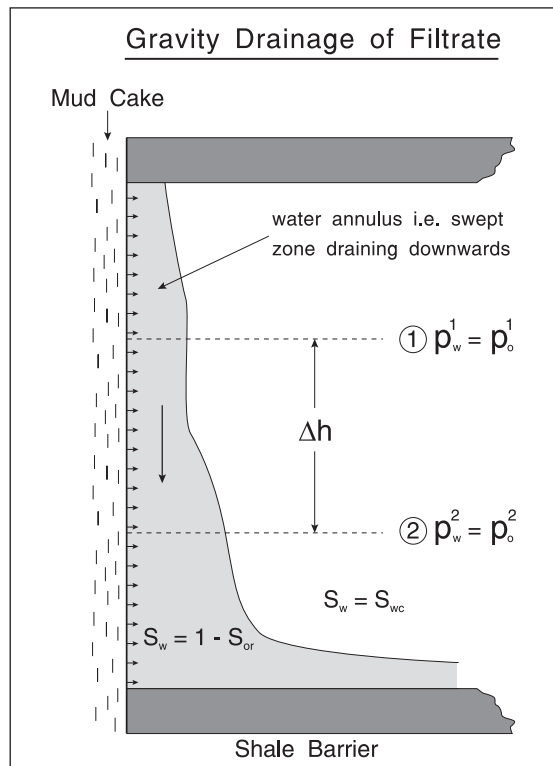


Fig. 9-5. Gravity segregation of the invaded water annulus

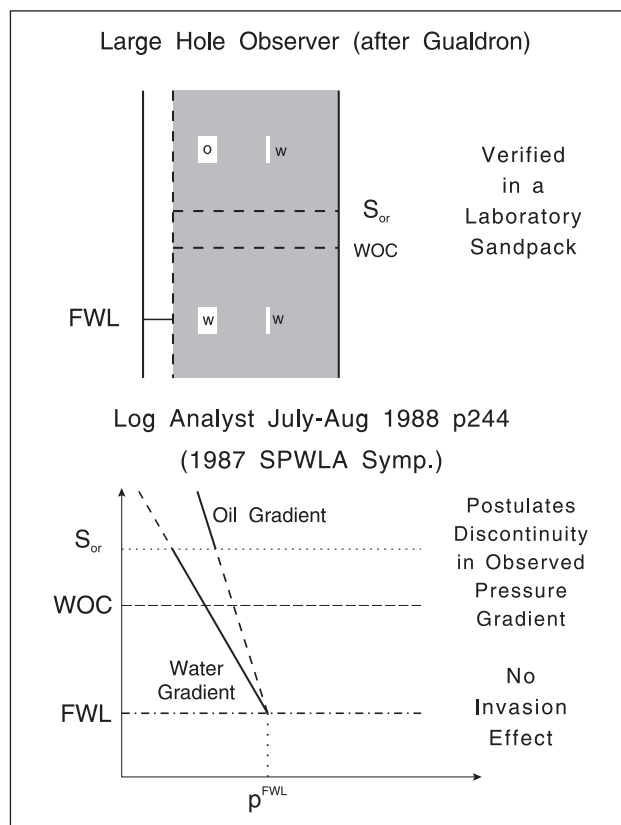


Fig. 9-6. Large hole observer

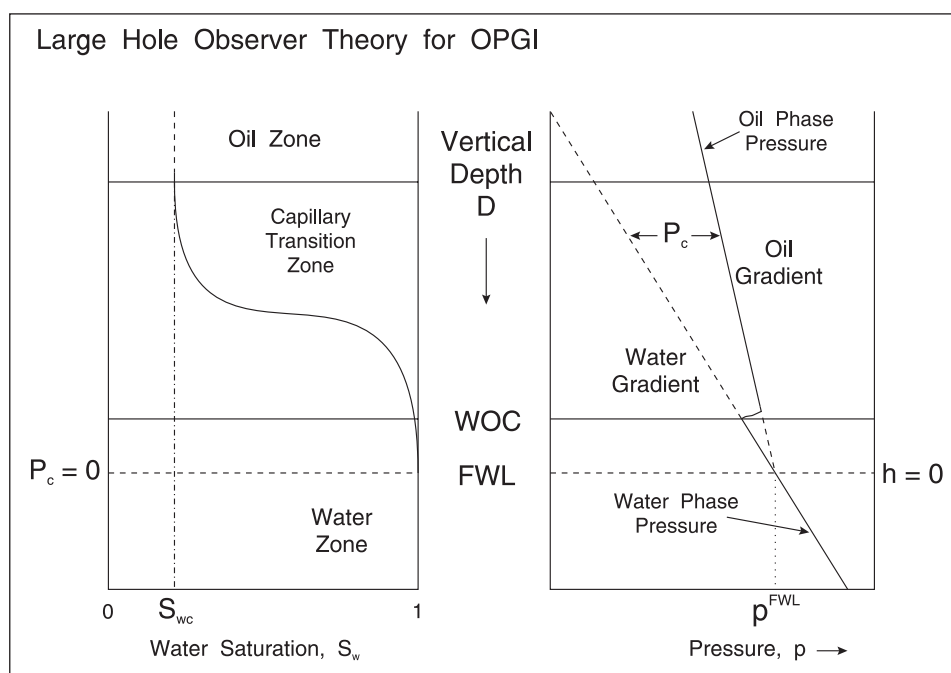


Fig. 9-7. Observed pressure gradient intersections

## Effect of a residual oil saturation $S_{or}$

The classical gravity–capillary equilibrium diagram (figure 9–1) is based on a drainage capillary pressure curve and exhibits zero oil saturation below the WOC. However, this is an oversimplification which may not adequately represent the oil accumulation process in geologic time. Hydrocarbon may exist as a trapped discontinuous phase which is completely immobile and whose pressure is unobservable. Consider, for example, the effect of faulting on the fluids disposition in a reservoir as illustrated in figure 9–8. Before tectonic movement, there is an original WOC at some level in the system as shown. If a fault block is downthrown, a redistribution of fluids will occur to establish a new flat contact. This implies that an upward displacement of oil by water has taken place in the downthrown block. The prehistoric displacement process will leave a waterflood residual oil saturation  $S_{or}$  present in the zone between the original (downthrown) contact and the new contact. This oil will exist in the form of isolated ganglia or blobs created by snap-off phenomena. However, it will be detected by resistivity logs even though it is quite immobile. In this region, only the water-phase pressure is observable and a water gradient will be registered by WFT surveys. When the oil is discontinuous, the concept of the phase pressure  $p_o$  takes on a different meaning.

It is now convenient to define the water recoverable oil contact (WROC) as the lowest level in the reservoir where oil is still continuous. Below the WROC, only a water gradient can be detected. The WOC is the lowest point at which hydrocarbon is present (whether producible or not) and it is this contact which is discernible on resistivity logs. Thus where the logs indicate a hydrocarbon saturation but a water gradient is evident from a pressure survey, the implication is that the hydrocarbon is immobile. This discrimination between mobile and immobile hydrocarbon is, in fact, one of the most important facets of distributed pressure analysis in unproduced fields.

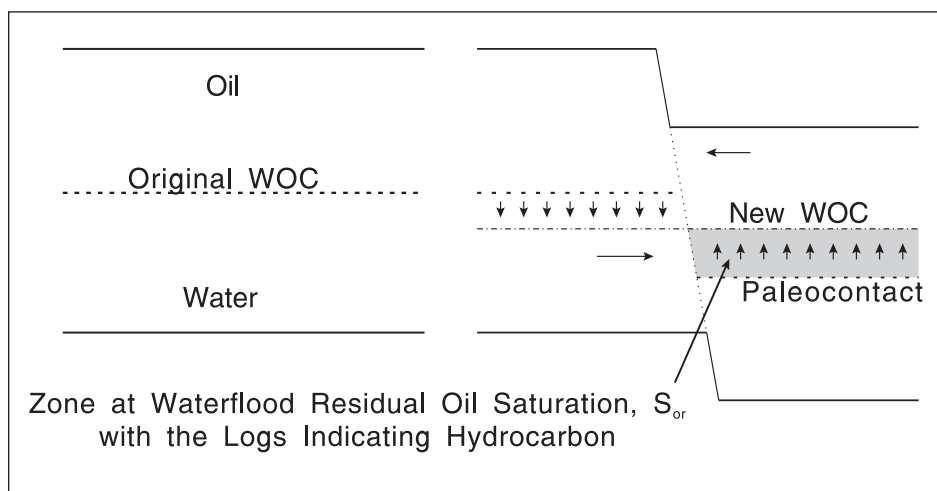


Fig. 9–8. Effect of faulting on fluid disposition in a reservoir

The concept of discontinuous oil trapped as blobs is illustrated in figure 9–9 using the capillary tube bundle as an analog. The onset of a continuous oil phase exhibiting hydrostatic pressure  $p_o$  occurs at the WROC. The free water level lies below this by an amount depending on the threshold capillary pressure  $P_c^t$  of the porous medium; this in turn is a function of the largest pore size. The important point is that the log indicated WOC may lie considerably below the FWL. The phase pressure and saturation distributions are shown in figure 9–10; note that the idea of gravity–capillary equilibrium embodied in the equation  $p_o - p_w = P_c(S_w)$  is valid only if both phases are continuous.

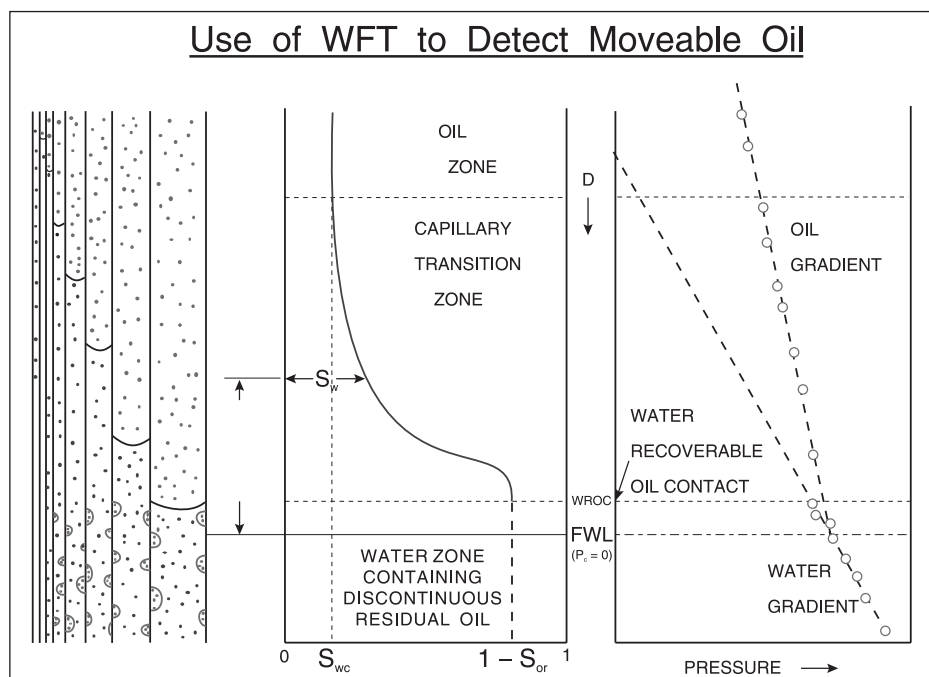


Fig. 9–9. Discontinuous trapped oil due to a paleocontact

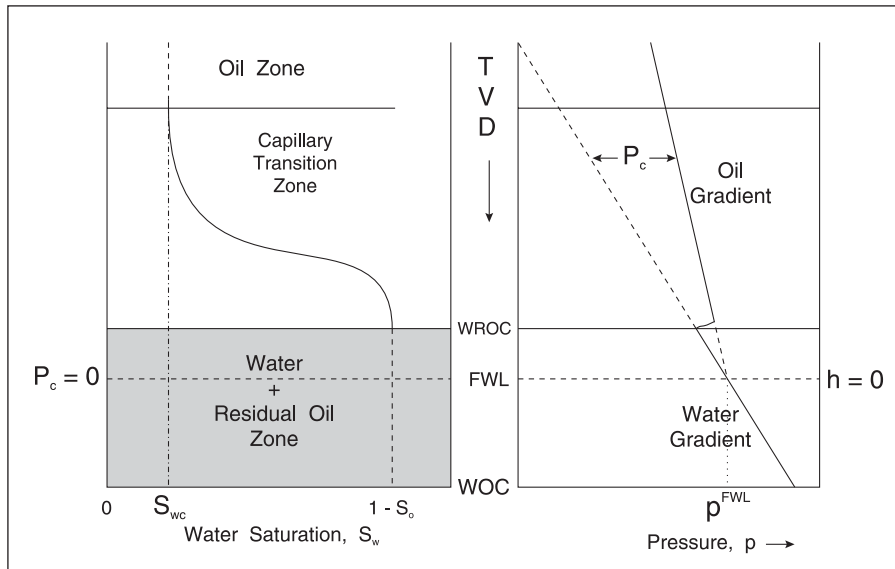


Fig. 9-10. Observed pressure gradient intersection when residual oil is present

In many cases, tectonic movement in geologic time also results in reservoir tilting, as illustrated in figure 9-11; this is another important cause of fluid redistribution in the system. It is apparent that the WOC as measured by logs, which coincides with the altered position of the original WOC after tilting, will not be flat. This is known as the *paleocontact*. However, the new WROC formed by redistribution to gravity-capillary equilibrium, which makes the level above which continuous producible oil is present, is indeed perfectly flat. Pressure gradient intersections from WFT surveys in different wells will show up the mobile hydrocarbon contact. Oil between the WROC and the WOC (paleocontact) is discontinuous and should not be included in normal reserve estimates. Note that resistivity logs should, in principle, also show this oil not to be movable (provided water-based mud has been employed).

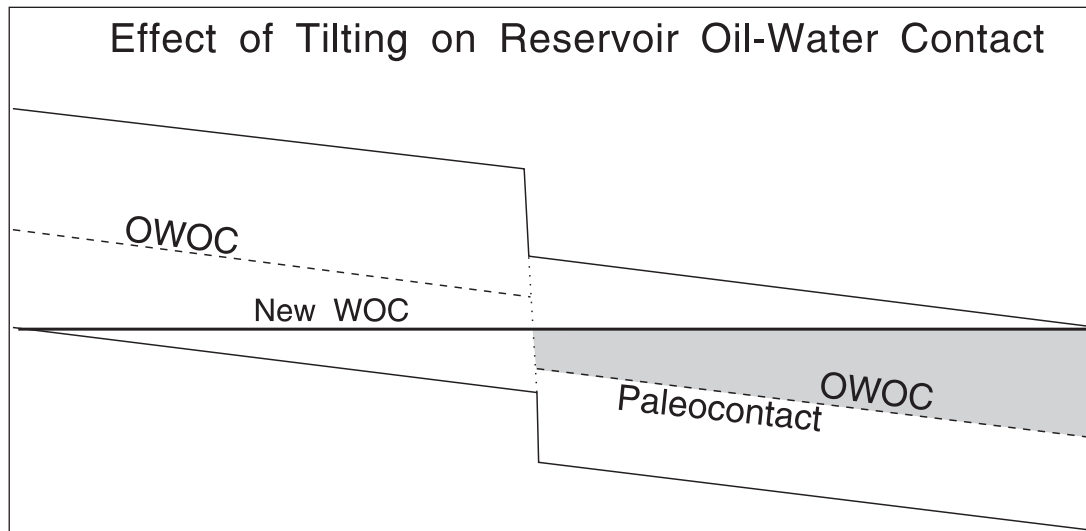


Fig. 9-11. Reservoir tilting

The first field examples of the detection of residual oil from RFT surveys originated in Abu Dhabi where there was concern about the WOC apparently varying from well to well. Figures 9–12 and 9–13 show classical WFT surveys in wells passing through the OWC with both oil and water gradients; good agreement with the open hole logs on the location of the contact is found. In figures 9–14 and 9–15, on the contrary, only a water gradient is observed even in the region where the logs indicate the presence of oil. If the zone above the log contact is tested, it will produce only water since the oil phase is discontinuous.

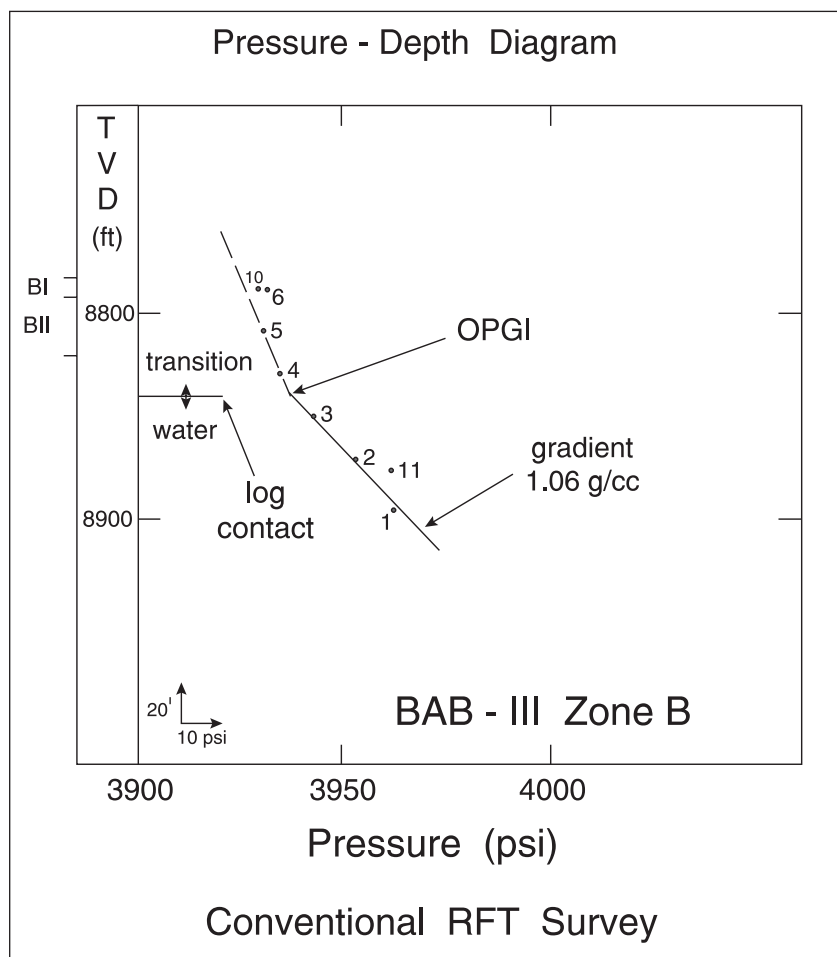


Fig. 9–12. Classical WFT survey through the water–oil contact

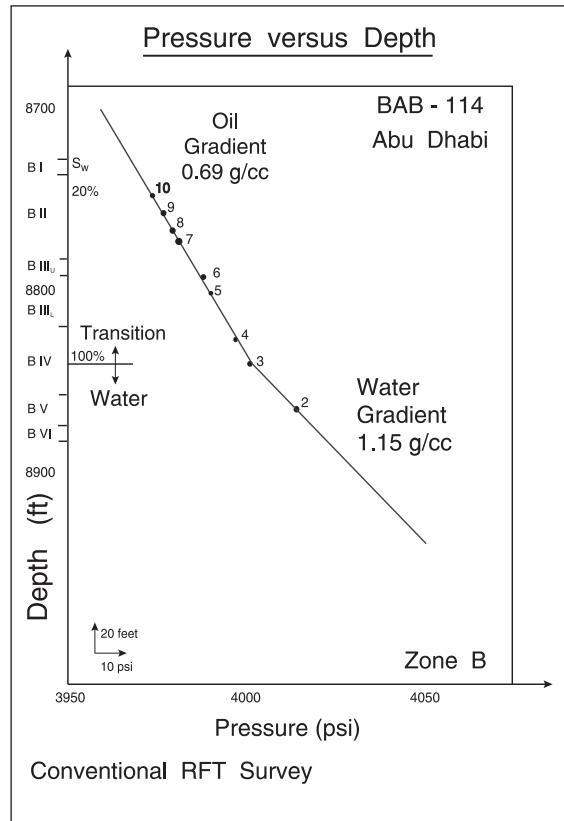


Fig. 9-13. Classical WFT survey through the water-oil contact

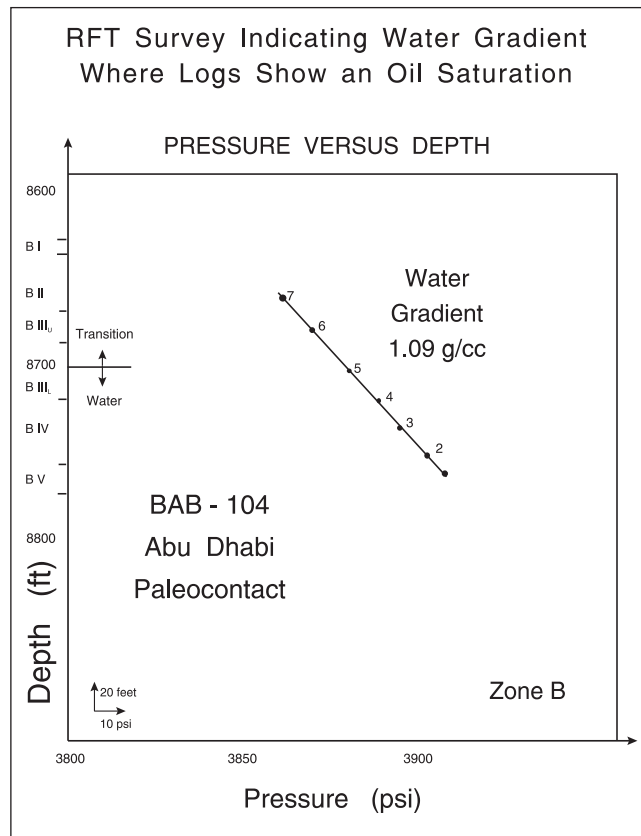


Fig. 9-14. Well showing only a water gradient where logs indicate oil

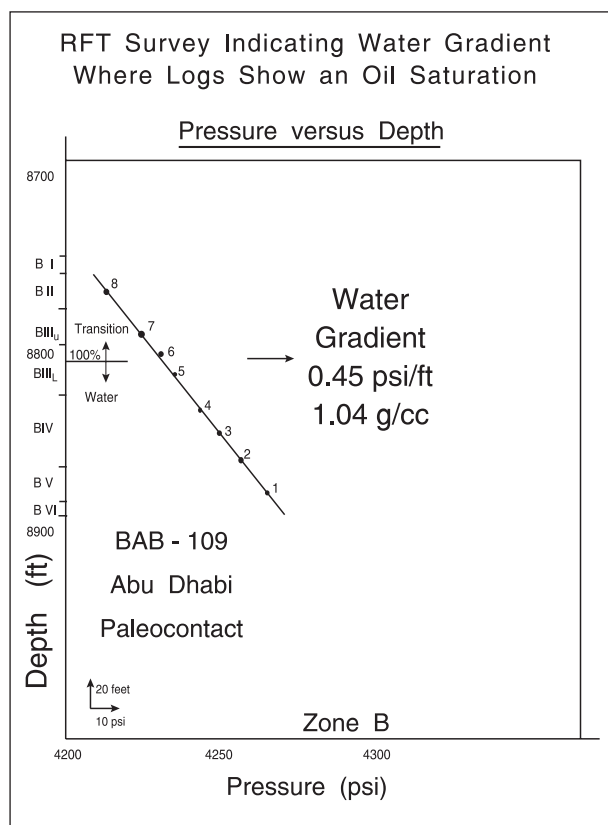


Fig. 9–15. Well showing only a water gradient where logs indicate oil

In one appraisal well in Indonesia, the WFT showed a water gradient where the logs indicated hydrocarbon. In order to confirm that the oil was nonproducing, a sample was taken with the WFT and, quite contrary to expectation, about a liter of oil was present in the chamber. Thus the result of sampling contradicted the conclusion drawn from the pressure gradient. Naturally, the well was then tested and produced 100% water. The only explanation is that surfactants in the mud system caused the mobilization of oil in the invaded region—a form of localized enhanced oil recovery. Modern oil-based muds incorporate strong surfactants which may have caused the observed effect.

It should be emphasized that the presence of discontinuous residual hydrocarbon in the water zone is probably the major reason why the WFT-observed pressure gradient intersection lies above the log-determined contact as illustrated in figure 9–10. Although other explanations for such a disparity will be advanced later (based on capillary pressure effects during invasion), the primary suspect is waterflood residual oil or gas driven by ancient fluid redistribution. The second main cause of anomalies between OPGIs and log contacts is the phenomenon of supercharging, which will be treated in detail in the section “Forced Gradient Technique.”

If there is evidence from WFT gradients and perhaps resistivity log movable oil analysis that an interval contains only residual hydrocarbon, then it is advisable to confirm this by testing the zone individually. The production of water alone will remove future doubt about the situation; this is very important in the context of reserve estimation and unitization. Hence, good WFT and openhole log interpretation should be available at the well site so that sensible decisions regarding testing can be made. Note that the new-generation of WFT tools, e.g., the Schlumberger Modular Dynamic Tester (MDT), which allow much improved sampling will help



to identify nonmovable oil or gas. The MDT device allows sampled fluids to be cycled into the mud column until the fluid analyzer indicates that reservoir fluid(s) rather than mud filtrate is being obtained. Also, development of coiled tubing systems involving packers may allow easier individual testing of intervals.

An interesting situation arises in connection with figure 9–11. In the left-hand fault block, the new WOC after redistribution is lower than the original WOC and hence all trace of the latter disappears. The open-hole logs in a well in this block will therefore detect the correct and unambiguous content. However, in the right-hand fault block, the logs will register the paleocontact which may be considerably deeper than the common new WROC. Hence there will be an apparently different log contact in the two blocks which may be used to infer a lack of communication between them. In fact, the true contact is the same in both blocks.

In general four explanations are possible for variable WOCs over a field. These are as follows:

- a) Variation in the distance between a common FWL and the WOC caused by differences in threshold capillary pressure  $P_c^t$ . This is due to changes in rock quality, particularly pore size distribution;
- b) The occurrence of residual hydrocarbon as described here;
- c) Noncommunicating fault blocks or reservoir units;
- d) Dynamic conditions in the aquifer.

Field-wide WFT surveys can be made of great help in deciding whether such phenomena are present. Note that items (a) and (d) are the possible explanations for a log contact which is variable across a field. In the case of situation (a), the FWL is at a fixed depth throughout the reservoir and it is variations in threshold capillary pressure which account for the varying log contact. This latter phenomenon has been observed in one of the world's largest gas reservoirs—the North–West dome in Qatar situated in the Khuff formation which is a classical low-permeability body. Variation of the contact across a field makes reserve estimation difficult and contentious. In principle WFT surveys which yield the FWL should indicate a field-wide common depth for the FWL even although the log contact varies; however, supercharging in such a low-permeability formation will always be a problem. In the final section of this chapter, it will be demonstrated that, in fact, the FWL varies across the North Field because of a dynamic aquifer effect.

## Detection of mobile hydrocarbon

In the preceding section, attention has been paid to the problem of identifying immobile hydrocarbon. The key pointer was the situation where the logs indicate an oil or gas saturation but the WFT exhibits a water gradient. It is interesting to observe that the reverse phenomenon is also important. In the oil zone above the capillary transition zone, water is immobile and a WFT survey shows an oil gradient. In silty, micaceous formations of very small grain size, the connate or irreducible water saturation may be as high as 70% and the porosity quite low, say 10%. In addition, the electrical conduction properties of these shaly sands are very complex. It is therefore quite possible for the log interpretation to be so much in error that a hydrocarbon saturation is completely missed as illustrated in figure 9–16. However, if a WFT survey shows an oil gradient in a zone where the logs apparently indicate only water, this is a strong clue

that producible hydrocarbon is present. Some hydrocarbon accumulations have, in fact, been discovered from oil gradients observed in WFT surveys even though the logs gave no indication.

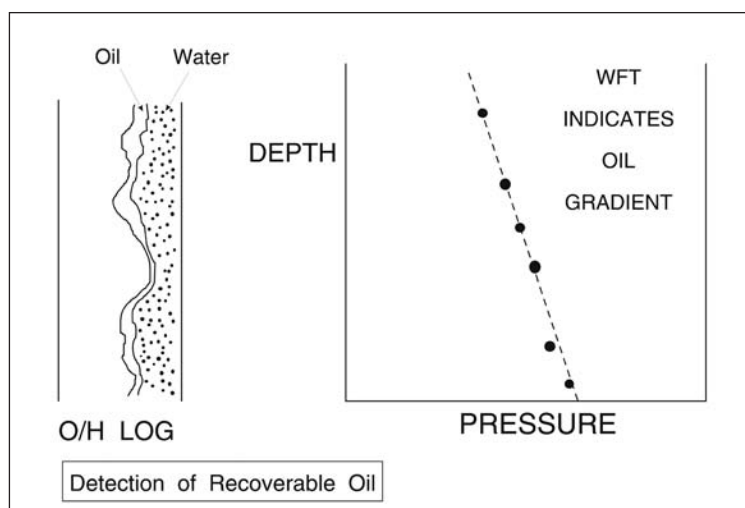


Fig. 9-16. Silty sand problem

A related problem occurs when the formation water is relatively fresh, i.e., of low salinity. Again the resistivity logs may not be able to properly distinguish between oil and water. In this case the WROC is best determined from WFT gradient intersections.

## Oil wet behavior

The classical pressure–depth diagram of figure 9-1 refers to a strongly water-wet condition in which water is imbibed upwards from the FWL into the porous medium. Thus the capillary transition zone lies above the FWL. The reverse situation is a strongly oil-wet rock where oil will be imbibed down from the FWL against buoyancy. In this case, the capillary pressure as defined by Eq. (9-1) is negative, i.e., the oil-phase pressure is less than water-phase pressure. This situation is illustrated in figure 9-17, where the capillary transition zone is now seen to lie below the FWL. The theory of Desbrandes and Gualdron suggests that in the capillary transition zone a large hole will fill with water and hence a pressure tapping will register the water phase pressure. The large hole observer is shown diagrammatically in figure 9-18. Accordingly, in figure 9-17 the water-phase pressure is shown as a continuous line through the capillary transition zone and a pressure discontinuity is postulated below the FWL. This discontinuity is a mirror image of the water-wet case. In a strongly oil-wet situation, the FWL, i.e., the pressure gradient intersection, lies above the capillary transition zone and the distance between the FWL and the WOC is now determined by the smallest pore size. Accordingly, this distance, in principle, can be quite large in contrast to the water-wet case where it is controlled by threshold capillary pressure  $P_c^t$ . Also, the large hole observer theory suggests that a water gradient should be seen over the inverted capillary transition zone. A field example from Brazil, shown in figure 9-19, exhibits the characteristic of an oil-wet system but there is no wettability data on restored native-state core to back up the pressure information.

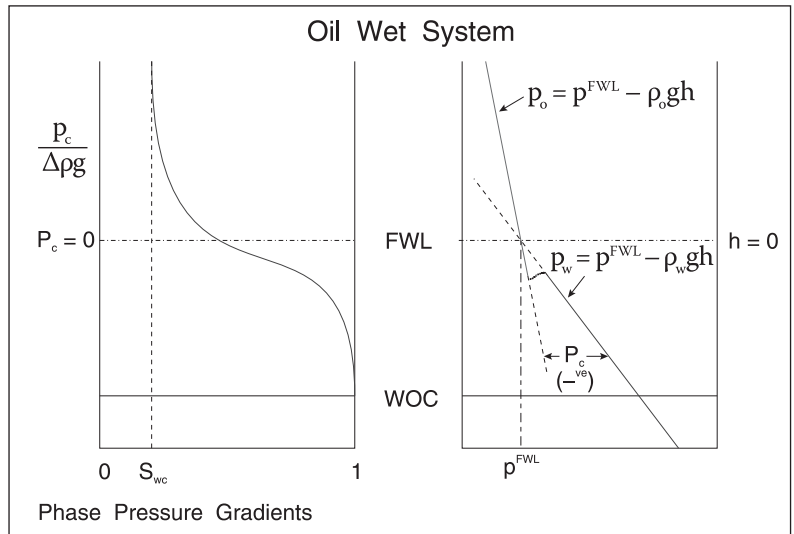


Fig. 9-17. Phase pressure gradients in oil-wet conditions

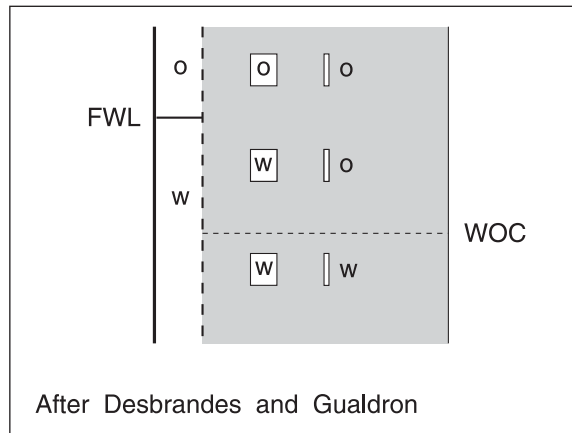


Fig. 9-18. Large hole observer in oil-wet conditions

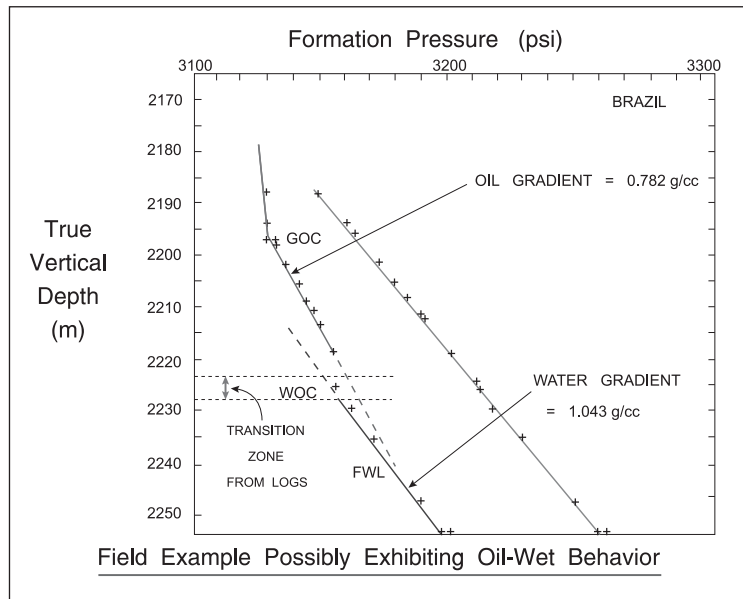


Fig. 9-19. Brazilian field example possibly demonstrating oil-wet behaviour

Thus Desbrandes and Gualdrón suggest that the simultaneous occurrence of an oil saturation and a water gradient can be explained by strongly oil-wet conditions in the capillary transition zone. They cite two field examples from Schlumberger Well Evaluation Conferences (WEC) in which the OPGI lies above the log WOC. However, a detailed examination of these examples indicates that the residual oil explanation is more likely. The important point is that both possibilities can account for the observed phenomena. Note that in the strongly oil-wet case the oil in the capillary transition zone is mobile and will produce. Hence it is important to ascertain which explanation is the valid one; obviously testing or sampling the interval exhibiting the water gradient, i.e., between the OPGI and log WOC, is a key issue.

The main argument against the strongly oil-wet hypothesis comes from the recent work on native and restored state core analysis. It is now certainly felt that oil-wet or mixed wettability conditions are far more common than was previously thought, especially in carbonate reservoirs. However, detailed studies of core wettabilities have shown that there is usually a variation of wettability with depth. Strongly oil-wet or mixed wettability conditions exist high in the oil column above the capillary transition zone where water films are thin and diffusion of asphaltenes and acid components of the crude oil to the rock surface has occurred. These absorbed hydrophobic components cause oil or mixed wettability. However, near the WOC where water saturations are high, the wettability reverts to the water-wet conditions and it is very unlikely that strongly oil-wet behavior occurs in the capillary transition zone.

Thus it is quite possible that the capillary transition zone will exhibit classical water-wet behavior while the oil zone is, in fact, oil-wet or of mixed wettability. The FWL or OPGI may well lie below the WOC—the pointer to water-wet behavior—while oil-wet conditions in practice exist over the oil zone. This anomaly has only recently become evident to reservoir engineers.

## Tar mat detection

Particularly in Middle East reservoirs, the occurrence of tar mats is common and it is necessary to be able to identify such features. In figure 9–20, an WFT survey in a Saudi Arabian well is shown with a gradient in the water zone greater than hydrostatic; here the gradient is quoted in terms of psi/ft and a gradient in excess of hydrostatic implies the psi/ft to be larger than the hydrostatic value. This is due to natural water influx into the reservoir with upward flow occurring. The system is not at gravity–capillary equilibrium although a straight line on the pressure–depth diagram is still apparent. The subject of WFT surveys in producing fields will be examined in detail in chapter 10 and for the moment it will simply be remarked that a gradient greater than hydrostatic implies upward flow in a homogeneous reservoir of uniform vertical permeability. A second WFT survey in a neighboring well is shown in figure 9–21, where a tar mat is penetrated. The existence of the tar mat is confirmed by the dry tests indicating that the pore fluid is essentially immobile, i.e., bitumen. At the time detection of a tar mat depended on visual inspection of rock core, and the ability to tie down the tar zone without the need for coring was important. Since then, tar mats have also become detectable by conventional logging.

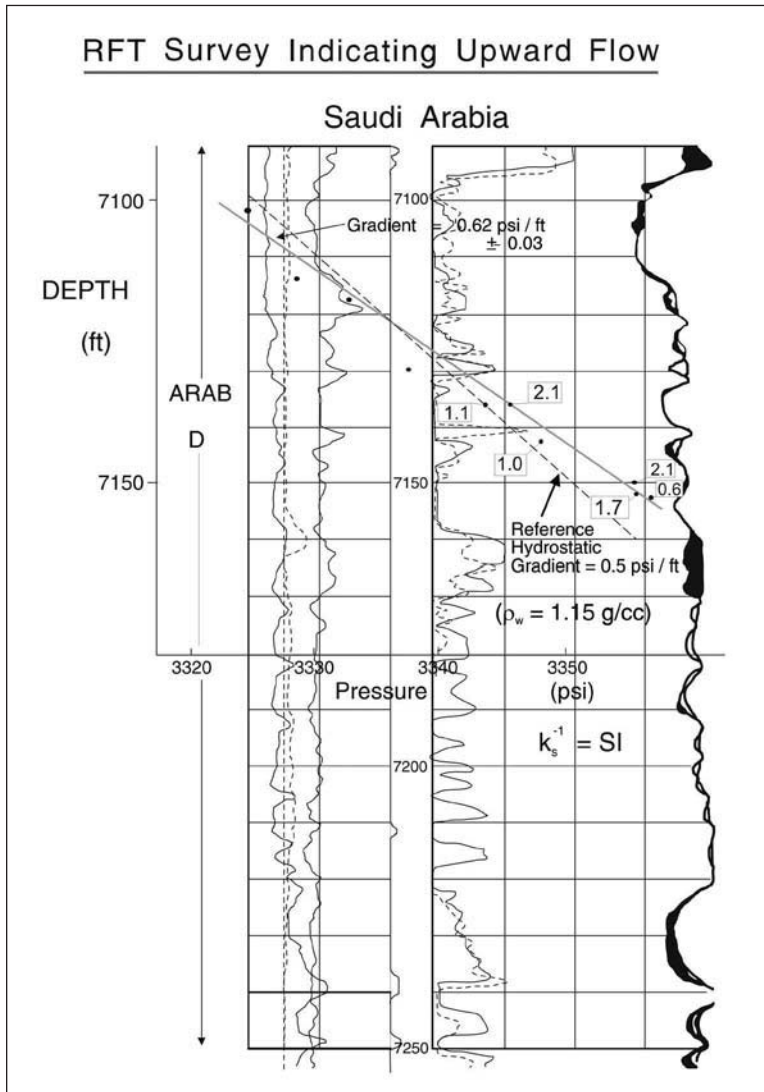


Fig. 9-20. Effect of upward natural water influx on the pressure gradient

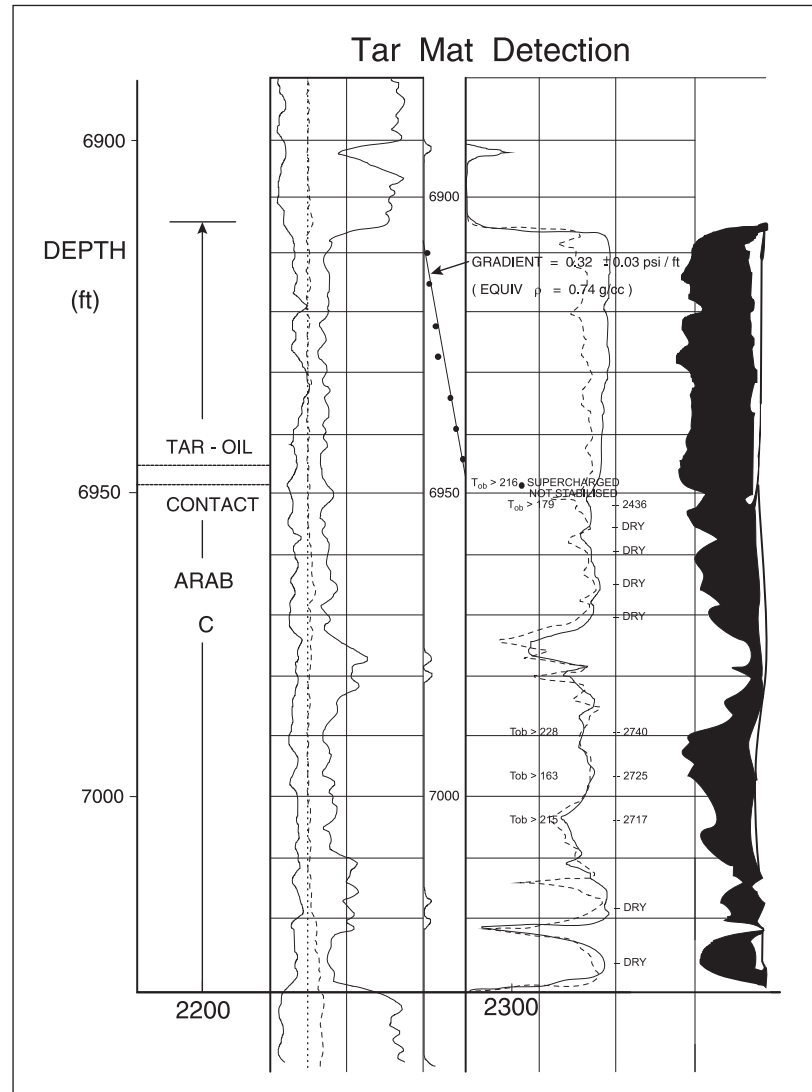


Fig. 9-21. WFT survey in well penetrating a tar mat

## Additional field examples

The detection of paleocontacts by observing water gradients where the open-hole logs indicate hydrocarbon is one of the most important applications of WFT surveys in exploration wells. In order to demonstrate that this phenomenon is, in fact, quite common, three further field examples will be described. Simplified ideas of oil accumulation histories usually depict the reservoir in a fixed position in space and being charged with hydrocarbon in one continuous stream that ends abruptly. Many examples show that these simplifications do not hold for most real reservoirs. Filling of the system in two distinct phases can produce two sets of phenomena associated with ancient and the modern hydrocarbon water contacts. These might include, for example, two asphaltene-rich zones, one within the present day oil column and one below it, as illustrated in figure 9–22.

Reservoir rocks are not fixed in space after oil emplacement. Major faulting or tilting can occur over geological time and hydrocarbons already accumulated within such tilted zones might undergo further multiple imbibition and drainage capillary equilibrium adjustments. Some mobile oil from the pretilting phase can become immobile when it occurs below the modern OWC. One of the best examples of tilting leading to a residual oil zone is the giant Prudhoe Bay field in Alaska, where the process illustrated in figure 9–23 occurred. As shown in figure 9–24, the reservoir exhibits a significant residual oil zone underneath the WOC. Interestingly, the oil in the west end of the field is present due to the tilting action and this gave substantial reserves to the owners of that part of the field.

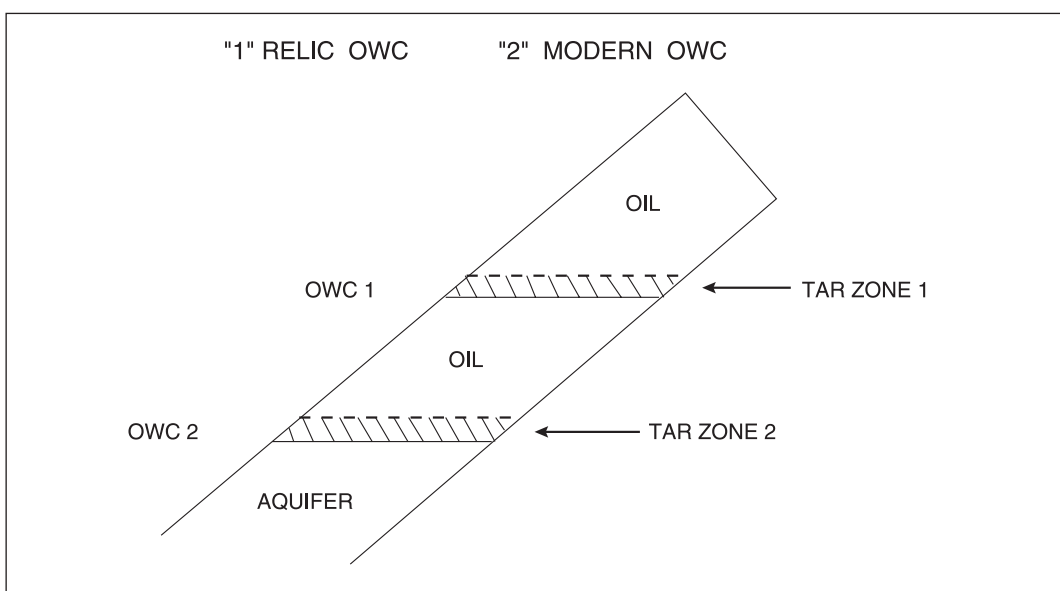


Fig. 9–22. Schematic of increased hydrocarbon accumulation

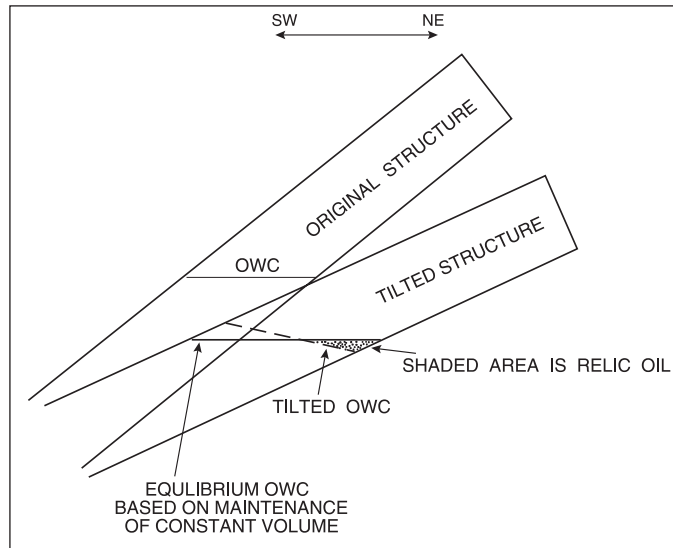


Fig. 9–23. Simplified schematic of reservoir tilting

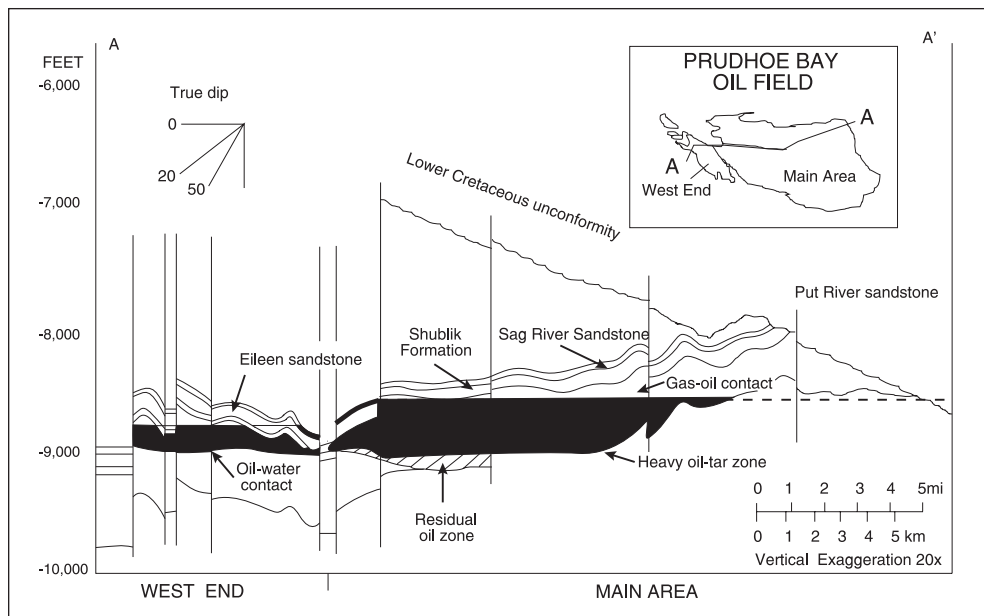


Fig. 9–24. Distribution of hydrocarbons in the Prudhoe Bay oil field

Figure 9–25 shows formation tester data from a North Sea gas well with a water gradient apparent over a gas bearing interval which was not even tested as the pressure information indicated that the gas was immobile. The field GWC at 15,360 ft lies at the top of the residual gas zone which extends down to 15,500 ft, i.e., it is 140 ft thick—a substantial amount of gas which is not included in the reserves. Interestingly, it was not possible to obtain a sample from the residual gas zone indicating that gas present is immobile. The high log-derived gas saturations below the free water level match the trapped gas saturations seen in core samples after waterflooding and are, therefore, probably the result of aquifer influx in geologic time and a rise in the field free water level. The observed trapped gas saturations are unusually high and in other wells more typical saturations are seen. In the opinion of the petrophysicist, the primary recovery of the trapped gas was likely to be low and it should not be included in the GIIP.



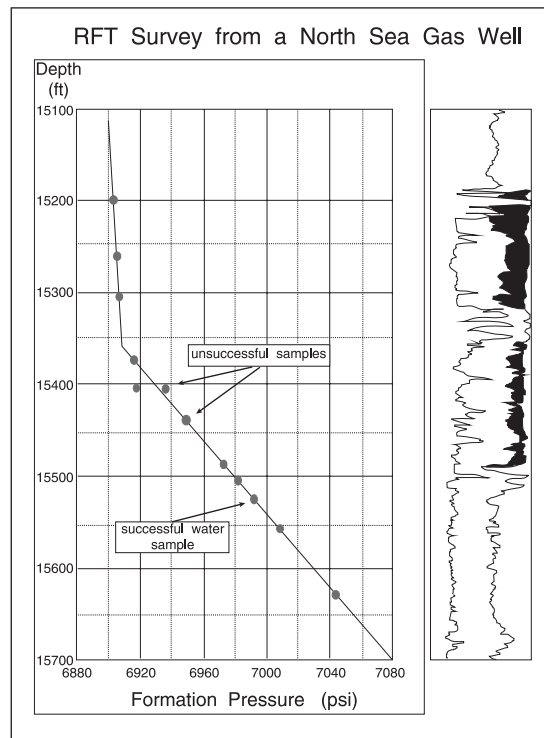


Fig. 9–25. Formation tester results from a North Sea gas well

Paleo-hydrocarbon contacts are usually detected by the presence of dead oil staining or residual hydrocarbon saturations. However, it has been pointed out by Cowan and Colley<sup>2</sup> that their presence can be inferred from diagenetic criteria.

The lower sections of many of the East Irish Sea basin (EISB) fields contain platy illite which is believed to have precipitated below a paleo-hydrocarbon water contact. The paleocontact is marked by the top of the illite-affected zone and this surface is now tilted and crosscuts depositional layering. The illite reduces the permeability by 2–3 orders of magnitude but it has no effect on porosity. It is of fundamental importance that the top platy illite surface be identified in wells and that it can be predicted for well planning, since the most productive reservoir sections are those with the thickest illite-free zones. So far the top platy illite surface has defied all attempts at identification by logging and the interface is picked using permeability–porosity relationships in cored wells and by the visual examination of sidewall cores in uncored wells.

The occurrence of residual gas is a commonly observed phenomenon within the East Irish Sea Basin (EISB) gas reservoirs such as the South Morecambe field. Residual gas is contained in partially gas-saturated rock which is located below the free water level. Effectively this means that above the FWL gas is a continuous phase while below the FWL, down to the log-derived “gas water contact,” gas is trapped as bubbles which cannot pass through pore throats. In the East Irish Sea, residual gas zones are between 100 and 275 ft thick and commonly have gas saturation of around 30% at the free water level. Apatite fission track analysis shows there has been significant cooling of the reservoir since the end of the Cretaceous which has reduced the gas volume in the system causing the FWL to migrate upwards. Thus the base of the residual zone can be considered to be a second paleocontact. The structural history of the South Morecambe field showing the evolution of multiple paleocontacts is illustrated in figure 9–26.



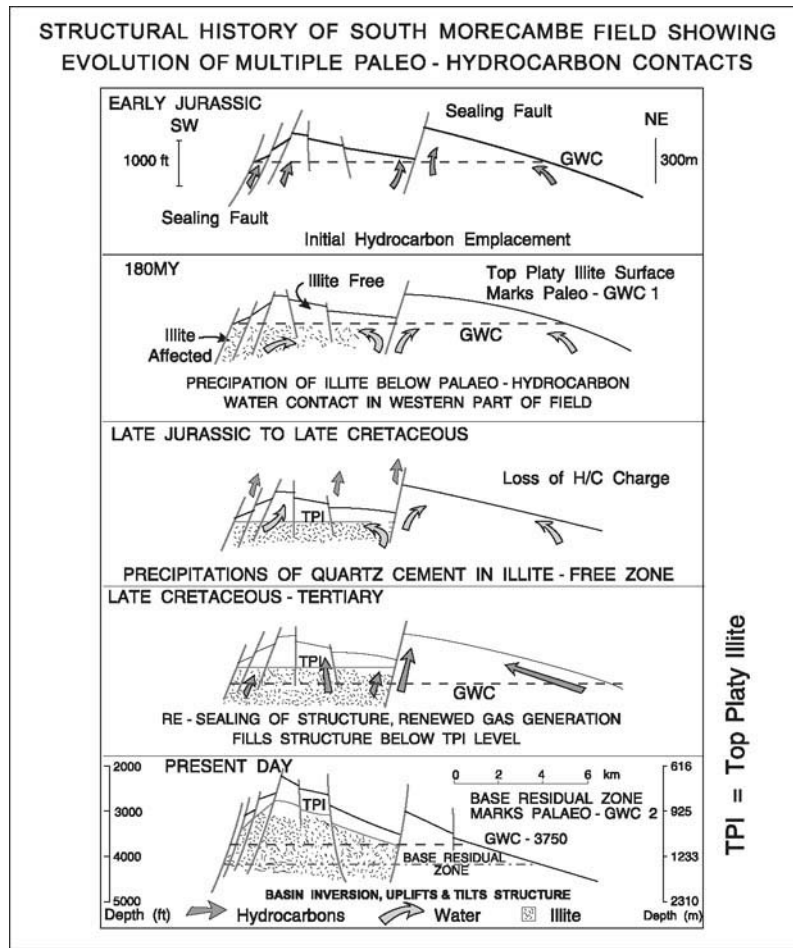


Fig. 9–26. Structural history of the South Morecambe field

In figure 9–27, WFT data from exploration wells in an Iranian field are shown. This data is unusual in that the pressure is substantially different between the reservoir units, with the upper zone higher than the lower by about 500 psi. There is apparently a geological explanation for this phenomenon.

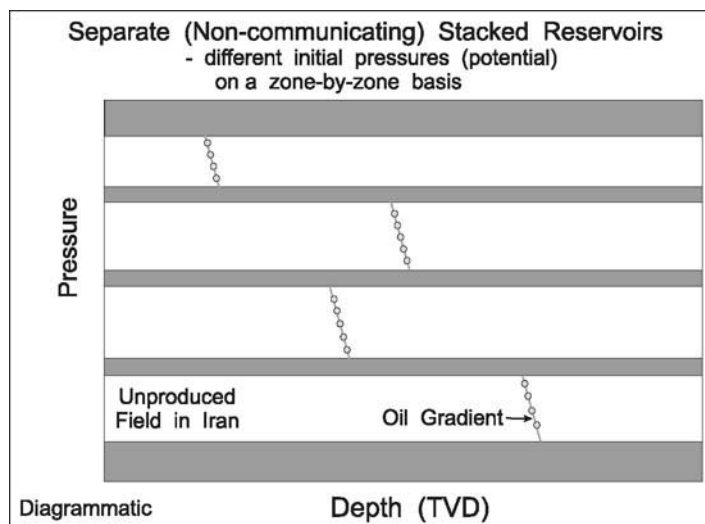


Fig. 9–27. Initial layer pressures in an Iranian reservoir

## Forced Gradient Technique

In an unproduced field, it is possible to determine the in situ fluid densities by measurement of the observed hydrostatic gradients in the gas, oil, or water zones (when present). This is illustrated in figure 9–28. The fluid regimes are identified by inspection, usually aided by overlaying lines of typical gas, oil, and water gradients on the pressure–depth data plot. Once the individual zones have been selected, a least squares best fit straight line through the appropriate range of points is computed. These regression lines have the form

$$p_g = p_g^{D=0} + m_g D \quad (\text{gas zone}) \quad (9-4a)$$

$$p_o = p_o^{D=0} + m_o D \quad (\text{oil zone}) \quad (9-4b)$$

$$p_w = p_w^{D=0} + m_w D \quad (\text{water zone}) \quad (9-4c)$$

and the slopes  $m$  and intercepts  $p^{D=0}$  of the respective best fit straight lines are given by the regression routine. Here  $D$  is true vertical depth measured from some datum  $D = 0$ . The fluid densities are obtained from the fitted slopes; in field units,

$$\rho_g = m_g / 0.4335 \quad (9-5a)$$

$$\rho_o = m_o / 0.4335 \quad (9-5b)$$

$$\rho_w = m_w / 0.4335 \quad (9-5c)$$

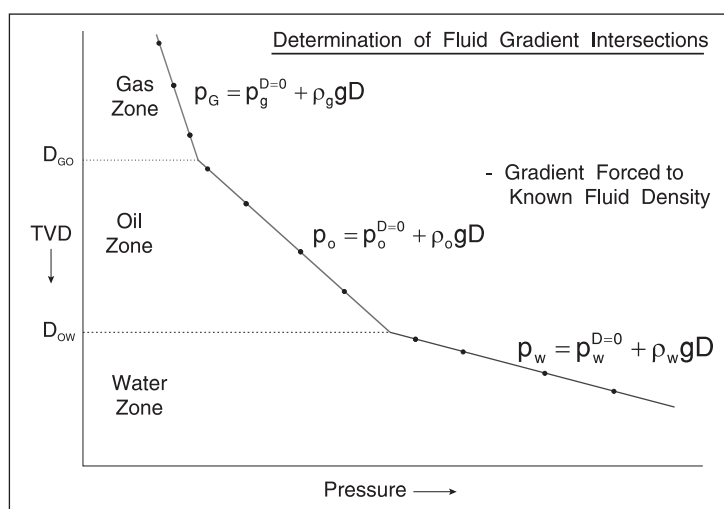


Fig. 9–28. Fluid gradients on pressure–depth diagram

The OPGI is the intersection of these fitted straight lines. Thus the gas–oil OPGI at depth  $D_{GO}$  is obtained from Eqs. (9–4a) and (9–4b) as

$$p_g^{D=0} + m_g D_{GO} = p_o^{D=0} + m_o D_{GO}$$

i.e.,

$$D_{GO} = \frac{p_g^{D=0} - p_o^{D=0}}{m_o - m_g} \quad (9-6)$$

Similarly, the oil–water OPGI at  $D_{ow}$  is

$$D_{ow} = \frac{p_o^{D=0} - p_w^{D=0}}{m_w - m_o} \quad (9-7)$$

From the point of view of understanding the reservoir, the gradient intersections  $D_{GO}$  and  $D_{OW}$  are much more important than the in situ fluid densities  $\rho_g$ ,  $\rho_o$ , and  $\rho_w$ .

In some situations, the quality of the pressure–depth information from the WFT survey is simply not sufficient to allow in situ fluid density estimation. For example, in a thin interval the effect of measurement error—both in pressure and depth—will preclude gradient determination. This is illustrated in figure 9–29, where the uncertainty in each data point is indicated by a circle. Obviously, if the depth span of the data points is not adequate, the upper and lower confidence limits of the estimated gradient are too wide. Thus the interval over which data is available must be large enough to allow a gradient to be reliably estimated. In principle, with modern pressure transducer resolution, say 0.01 psi, the minimum interval thickness for gradient determination should be quite small. If the assumption is made that the mud density is uniform, then the high resolution of the pressure transducer can be used to give very accurate depth differences between tests from the mud hydrostatic pressure readings. In this method, the mud density  $\rho_m$  is determined over the whole interval from the mud hydrostatic pressure readings, i.e., from the equation

$$p_m = p_m^{D=0} + 0.4335 \rho_m D \quad (9-8)$$

Unless mud segregation has occurred (something which is occasionally observed), the mud hydrostatic readings should fall on a very good straight line of gradient  $0.4335\rho_m$ ; this requirement is, of course, used to monitor the performance of the pressure transducer. In the short interval over which a fluid gradient is sought, the formation pressures are now plotted against an equivalent mud column depth  $D'$  rather than the measured true vertical depth  $D$ . This equivalent depth is defined from Eq. (9–8) as

$$D' = \frac{(p_m - p_m^{D=0})}{(0.4335\rho_m)} \quad (9-9)$$

where  $\rho_m$  is the mud hydrostatic for the test in question and  $p_m^{D=0}$  and  $\rho_m$  are constants. Thus the relative depth of tests in the short interval are established very accurately using the mud hydrostatic pressure measurements. This utilizes the very high resolution of modern gauges to determine depth differences: the method depends on the assumption of mud homogeneity. Over the interval of WFT testing, the mud temperature will be essentially constant; however, over the whole well, temperature variation will cause changes in the mud density and Eq. (9–8) will not predict atmospheric pressure at the well head. For the technique to succeed it is essential that mud be circulated over the well head to ensure that the mud level remains absolutely constant during the testing. It is also important that the conversion from measured depth to true vertical depth  $D$  be carried out accurately.

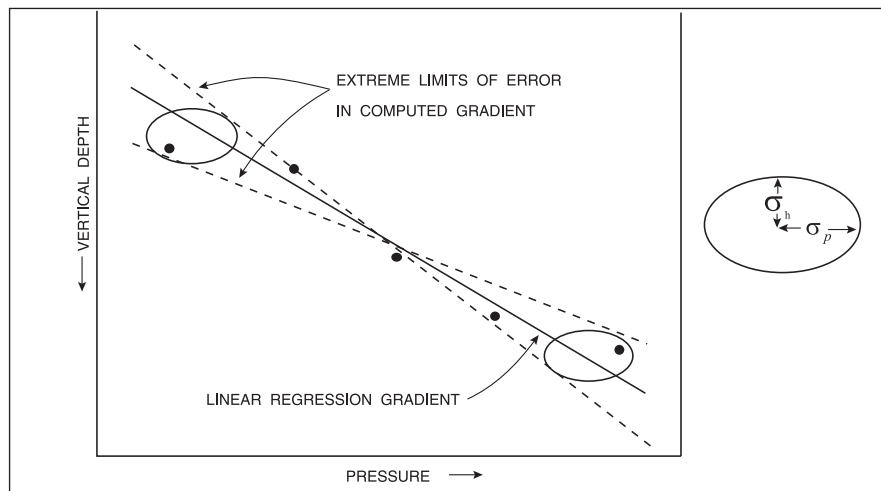


Fig. 9–29. Uncertainty in gradients on pressure–depth diagram

Unfortunately, the main problem in gradient estimation is not usually related to pressure or depth measurement error. In tight formations, the phenomenon of supercharging results in WFT-registered pressures exceeding the true formation fluid pressure; thus

$$P_{\text{WFT}} = P_{\text{true}} + \Delta p_v \quad (9-10)$$

where the excess pressure  $\Delta p_v$  varies from test to test according to the local formation permeability and mud fluid loss rate. The effect of supercharging is to shift the WFT pressure to the right of the true fluid pressure on a pressure depth diagram as shown on figure 9–30. In high-permeability formations, supercharging is very small indeed and WFT data in unproduced reservoirs exhibit very little scatter from hydrostatic fluid gradients. However, in tight reservoirs the scatter is such that gradient determination is hopeless.

Use has to be made of the fact that the density of the reservoir fluids is also determined by sampling and laboratory PVT analysis. Such information is nowadays even available at the well site. In the case of formation water, knowledge of the salinity, chemical composition, and reservoir temperature will allow the in situ density  $\rho_w$  to be predicted from correlations. Thus in practice the reservoir fluid densities are known independently. In this case, it is much preferable to fix the gradient of the fluid hydrostatic lines to the known values, viz.,

$$m_g = 0.4335 \rho_g \quad (\text{where there is a gas cap})$$

$$m_o = 0.4335 \rho_o$$

$$m_w = 0.4335 \rho_w$$

and to move these forced gradient lines over the pressure–depth plot to identify fluid regimes. In the presence of supercharging, the key concept is that the specified gradient line should define the left envelope of the data points recognizing that supercharging  $\Delta p_v$  always positive. This method is illustrated in figure 9–30. When the gradients are forced to known values in this way, much more reliance can be placed on the observed pressure gradient intersections  $D_{GO}$  and  $D_{OW}$  where applicable.

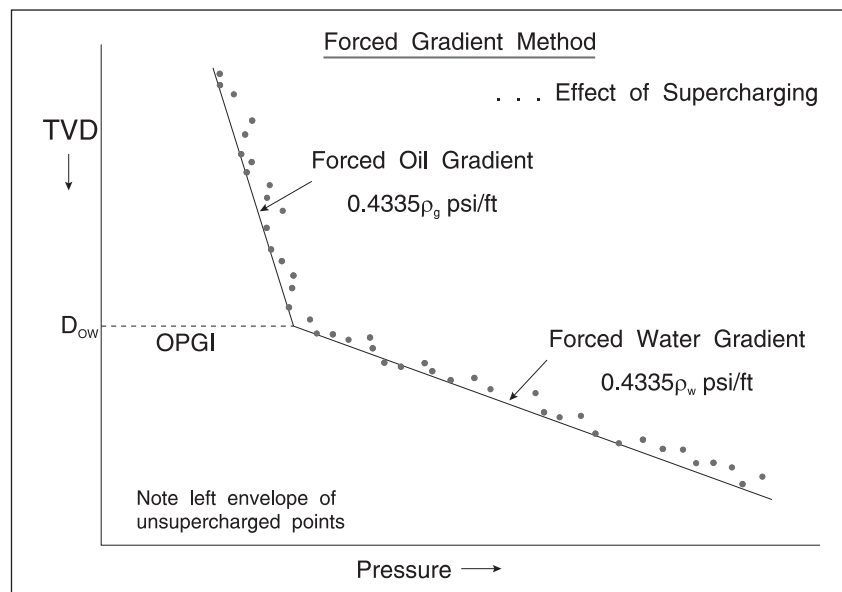


Fig. 9–30. Forced gradients on pressure–depth diagram

As an aid to recognizing the occurrence of supercharging, it is useful to make the pressure–depth diagram with each point marked by its supercharging index SI, as shown in figure 9–31. These indices can be used to indicate the reliability of data points when adjusting the position of the line of forced gradient. However, it must be recognized that in a low-permeability formation even the points of lowest SI may be supercharged to some extent and the forced line may be displaced to the right of the true gradient as illustrated in figure 9–32; this effect introduces error into the estimate of the contact position from the observed pressure gradient intersection. Such shifts in the OPGI become apparent when the WFT surveys in several wells are overlaid as discussed in the section “Statistical Analysis of Multiwell WFT Data.”

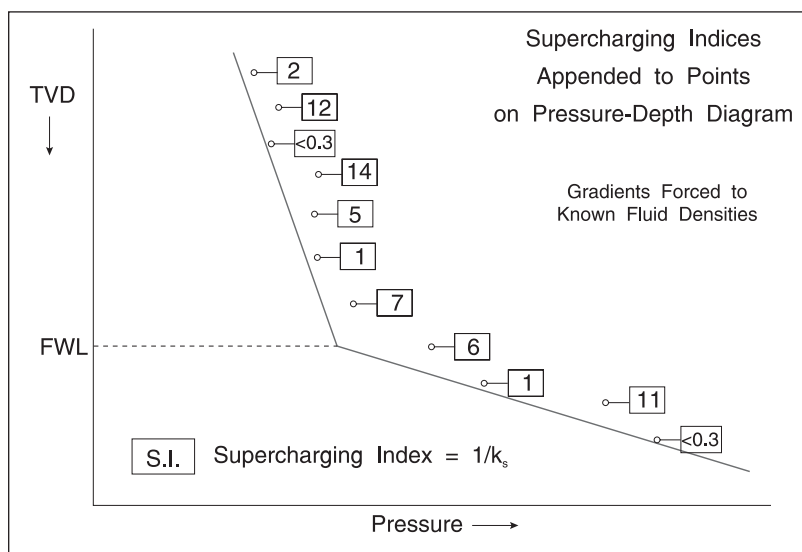


Fig. 9-31. Supercharging indices appended to points on the pressure-depth diagram

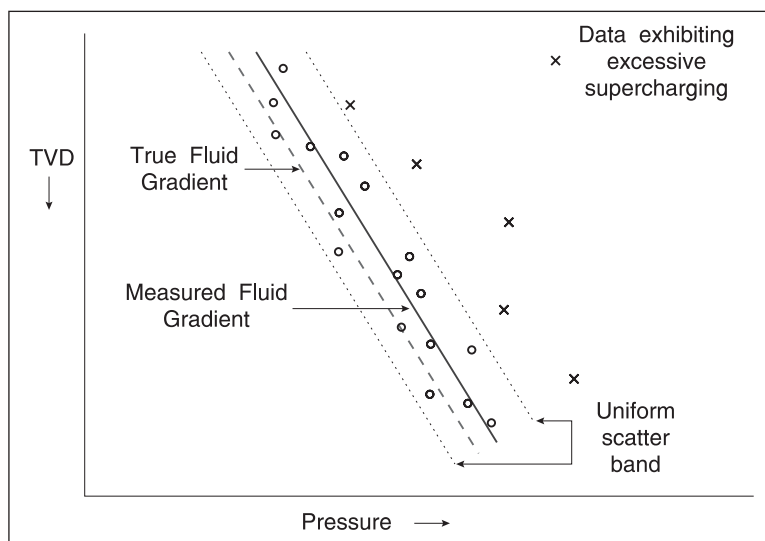


Fig. 9-32. Error in forced gradient line due to residual supercharging

A field example from Qatar using the SI to allow discrimination of supercharged points is shown in figure 9-33; this is one of the appraisal wells in the giant North field, at the time called the North West Dome (NWD). The Khuff formation is quite tight and the evidence of supercharging is apparent. It is possible to locate the gas gradient by imposing a line of slope corresponding to the known gas density, and there are two points in the aquifer through which a known water gradient can be placed. Therefore an estimate of the contact can be obtained from the intersection of these forced gradient lines. In figure 9-34, the data from a second well is superimposed and unusually a different pressure regime in the aquifer is observed. In figure 9-35, an RFT survey from an onshore Khuff well is presented, where the supercharging was so great that it was nearly impossible to obtain useful data. The tool was moved up and down to try and find streaks with sufficient permeability to give reasonable pretests but the formation was uniformly tight and the exercise was not successful in this case.

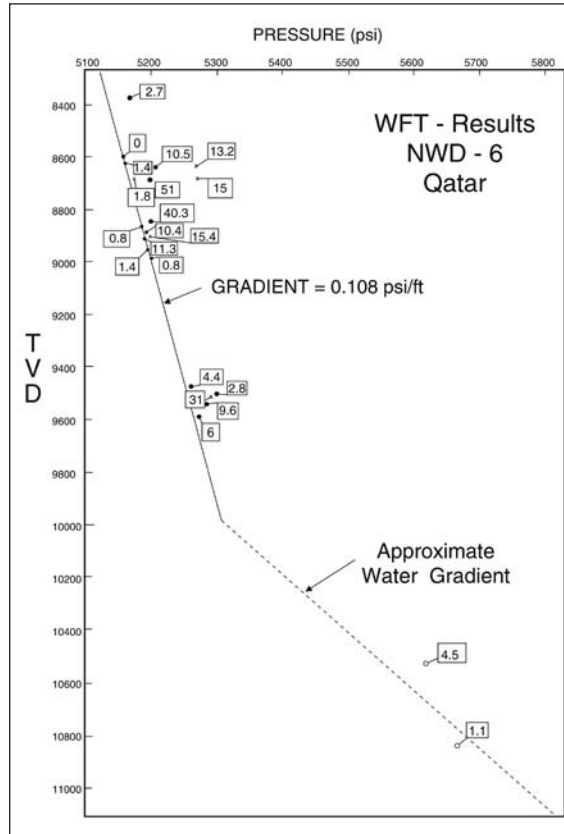


Fig. 9-33. North West Dome RFT survey

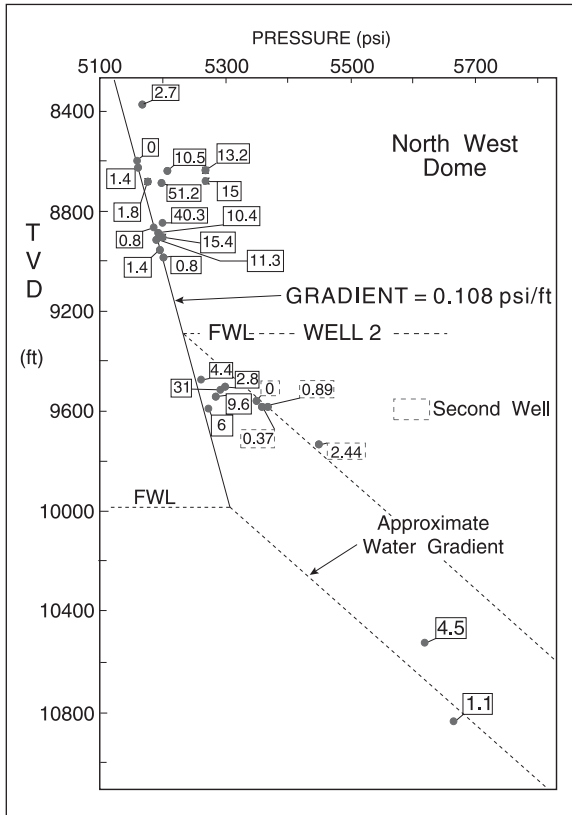


Fig. 9-34. Superimposed data from a second well

# 10

## Field Development Applications of Distributed Pressure Measurement

---

### Introduction

When a reservoir is put on production and fluid flow and depletion occur within the system, the reservoir pressure, as a function of time and position, becomes progressively different from the initial state. The application of wireline formation testers (WFTs) in reservoir engineering can be divided into two quite distinct categories, i.e., static, virgin reservoirs and dynamic, producing reservoirs. In the case of WFT surveys in exploration or appraisal wells in unproduced fields, it is known in advance that formation pressures must conform to gravity–capillary equilibrium established over geologic time. The conduct of the survey and the interpretation of the data is governed by the constraint that true formation pressures lie on straight line fluid gradients and the main objective of the testing is to delineate these gradients (water, oil, and gas where present) and their intersections.

However, when a WFT pressure survey is carried out in a new well in a field which has already been partially depleted by oil production from, and possibly affected by water injection into existing wells, the situation is quite different. The new development well is used as an observation location at which the current state of the reservoir can be determined on a vertically distributed basis. The measured pressure profile reflects the response of the reservoir to production and it is axiomatic that the pressure information cannot be interpreted in terms of reservoir structure without knowledge of the production and injection which has taken place. The advantage of WFT pressure data in observation wells is that flow between reservoir zones through the wellbore cannot occur since it is sealed with mud and genuine layer pressures are obtained provided supercharging does not take place. In development wells, the pressure profile must be analyzed both in terms of deviation from the initial state, i.e., pressure decline, and in terms of its shape.



## Introductory Field Examples in Produced Reservoirs

It is useful at this point to examine some field examples of WFT suveys in wells penetrating reservoirs not at gravity–capillary equilibrium, i.e., new wells drilled into producing fields. If the field is in a dynamic state, there is no requirement that hydrostatic fluid gradients be present. The field example from Saudi Arabia given in chapter 9 (fig. 9–20) showing a gradient steeper than hydrostatic is from a producing field with natural water influx occurring. An example from South America is shown in figure 10–1, where the problem is to determine whether the two water zones are separate or really exhibiting the same pressure regime but affected by supercharging in the lower zone. Note that all points in this region have large supercharging indices. Using the approximate formula for supercharging discussed in chapter 8, viz.,

$$\Delta p^1 = 4 \times SI \tag{10-1}$$

it was deduced that the lower zone was indeed in a different pressure regime and isolated from the upper zone.

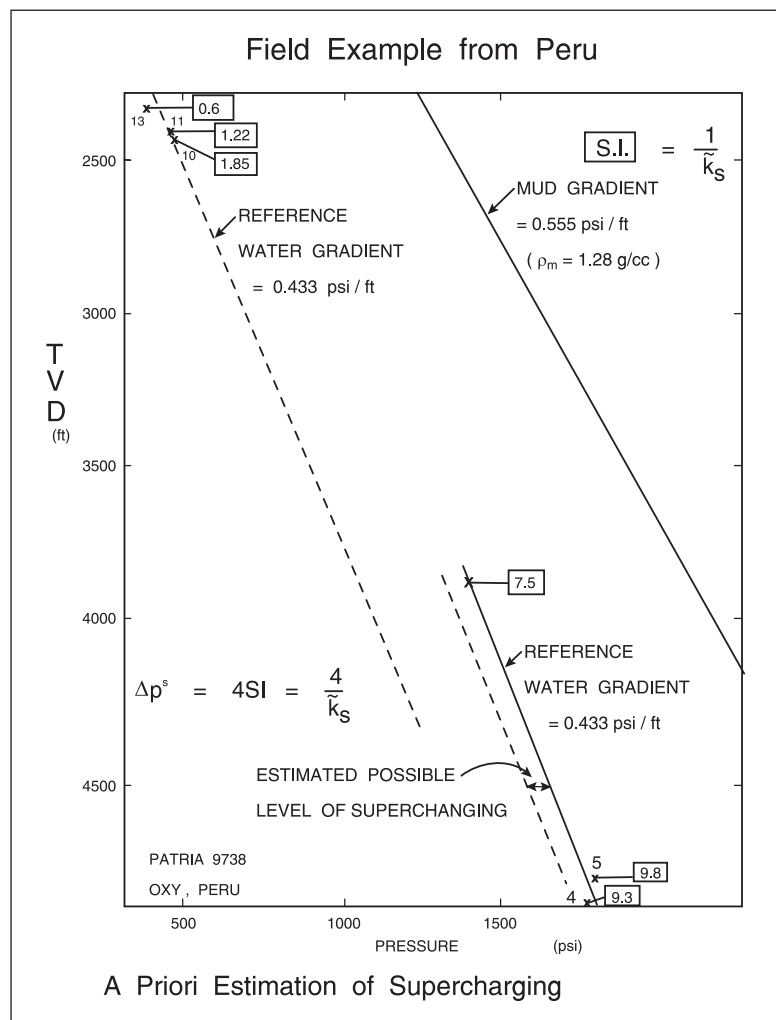


Fig. 10–1. Field example from Peru

Figure 10–2 shows a Wireline Formation Tester (WFT) survey from an offshore appraisal well in the Gulf of Campeche, Mexico; an oil gradient of 0.34 psi/ft is clearly indicated, with only two supercharged points having been eliminated from consideration. A survey in a subsequent development well drilled after significant production is shown in figure 10–3; after elimination of supercharged points using the reciprocal permeability index, it is apparent that differential depletion is taking place with pressure discontinuities over tight zones appearing. The reservoir is brecciated, with the wells only penetrating a small distance through the cap rock because of problems of lost circulation. Hence the potential for upward flow evident in the WFT survey. The presence of the barriers was not expected and, given that mud weights were balanced on well test pressures which register only the upper part of the reservoir, the importance of running distributed pressure measurement is evident. The upper zone has gone below the bubble point and the gradient is intermediate between that of oil and gas. This field example shows up one of the most applications of WFT surveys in produced fields—the unmasking of tight zones which inhibit vertical flow. Note that this field had a serious blowout preceding the use of formation tester pressure surveys.

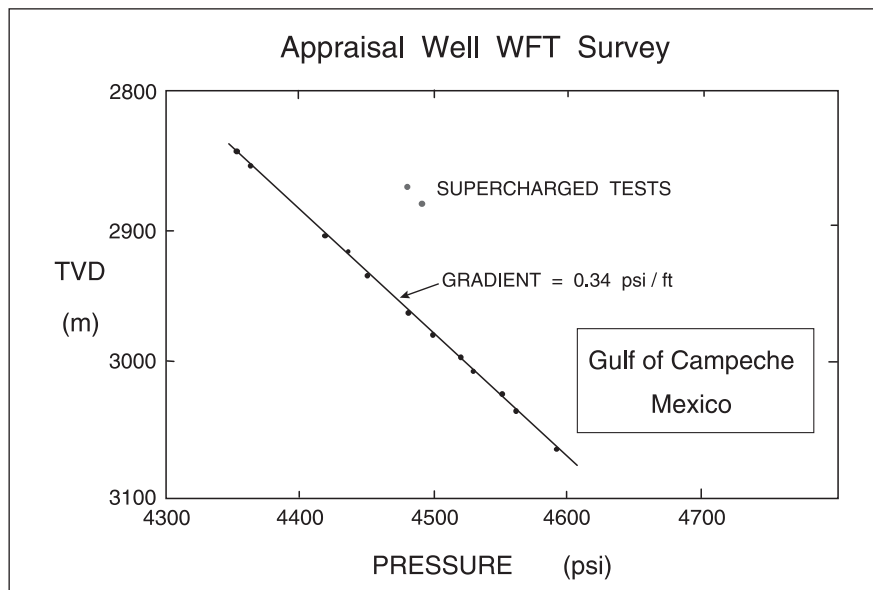


Fig. 10–2. Appraisal well WFT survey form Gulf of Campeche, Mexico

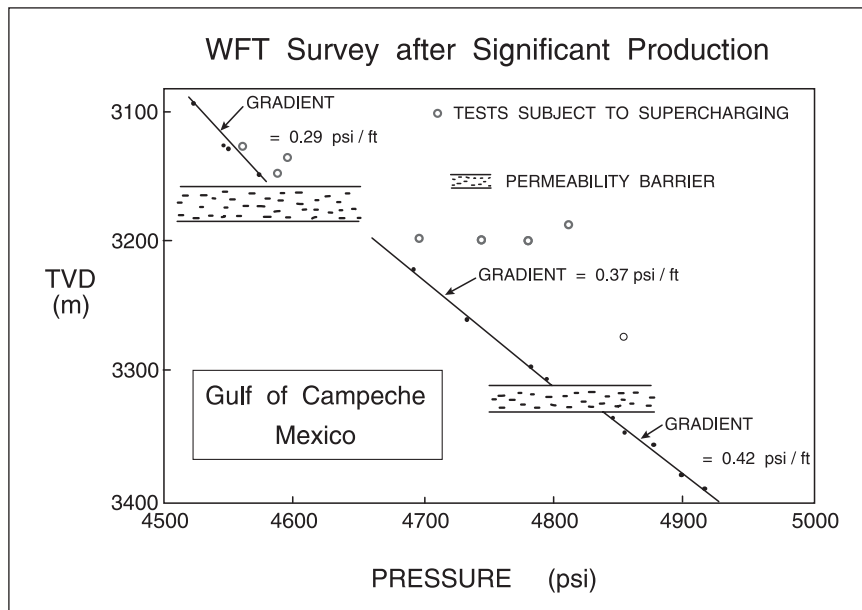


Fig. 10-3. Campeche reservoir WFT survey in the production period

An WFT survey from a long produced field in Venezuela is shown in figure 10-4, where the raw data simply comprises a cloud of points giving very little clue to the reservoir structure. The same data is presented in figure 10-5 with the shales evident on the open-hole logs inserted for comparison and supercharged points discriminated out, again based on the reciprocal permeability (supercharging) index (SI). In a produced field where there is no condition that hydrostatic gradients are present, it is only the SI—in an absolute sense—that can be used as a rejection criterion. This poses quite a problem and supercharging is always the main issue with WFT data especially in low-permeability reservoirs.

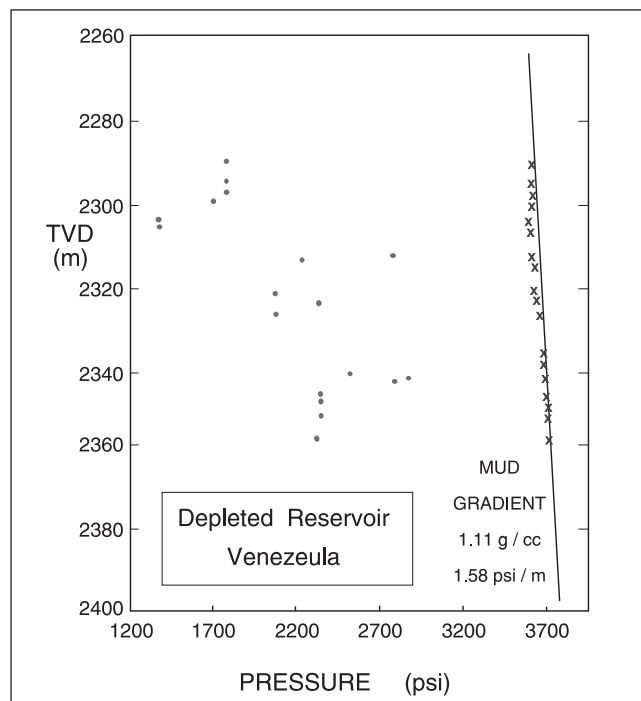


Fig. 10-4. Raw data from an WFT survey in a depleted Venezuelan reservoir

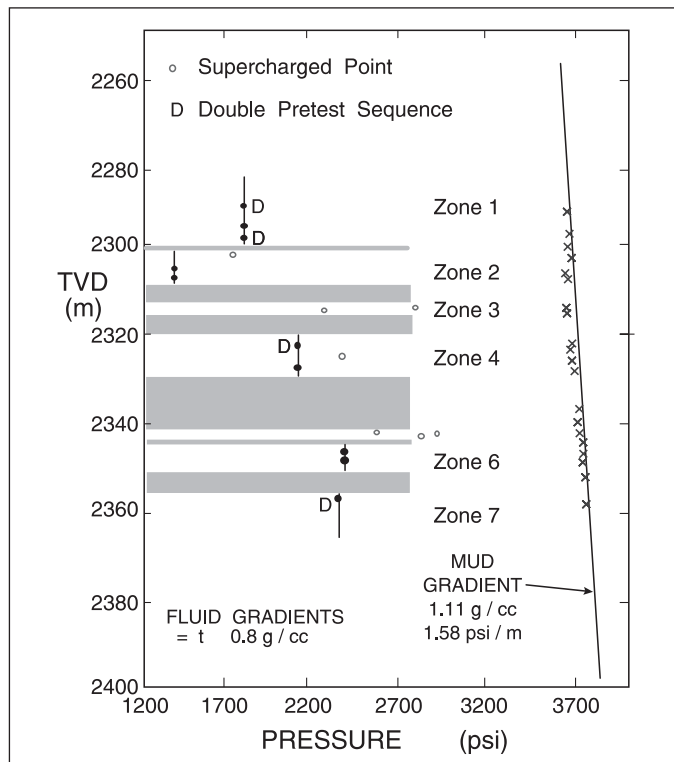


Fig. 10-5. Interpretation after elimination of supercharged points and allowance for barriers

## Single-phase Flow

### Uniform vertical permeability

In order to appreciate the significance of pressure data in developed reservoirs, it is useful to consider some relatively straightforward situations which often arise in practice. Consider first the case illustrated in figure 10-6, where a new well—to become an edge water injector—has been drilled into the aquifer of a producing field. Due to oil production from central wells and subsequent pressure depletion in the reservoir, the aquifer is expanding into the oil zone as shown, i.e., natural water drive is taking place. Thus in the vicinity of the observation well water is moving updip and the local water flux has both a vertical and a horizontal component; from the point of view of WFT pressure interpretation, it is the vertical component of the water flux, denoted  $u_{zw}$ , which is important. The vertical components of the flux and the potential gradient are related by D'Arcy's law

$$u_{zw} = \frac{q_{zw}}{A_{xy}} = \frac{k_z k_{rw}^o}{\mu_w} \cdot \frac{\partial \psi_w}{\partial D} = \frac{k_z k_{rw}^o}{\mu_w} \left[ \frac{\partial p_w}{\partial D} - \rho_w g \right] \quad (10-2)$$

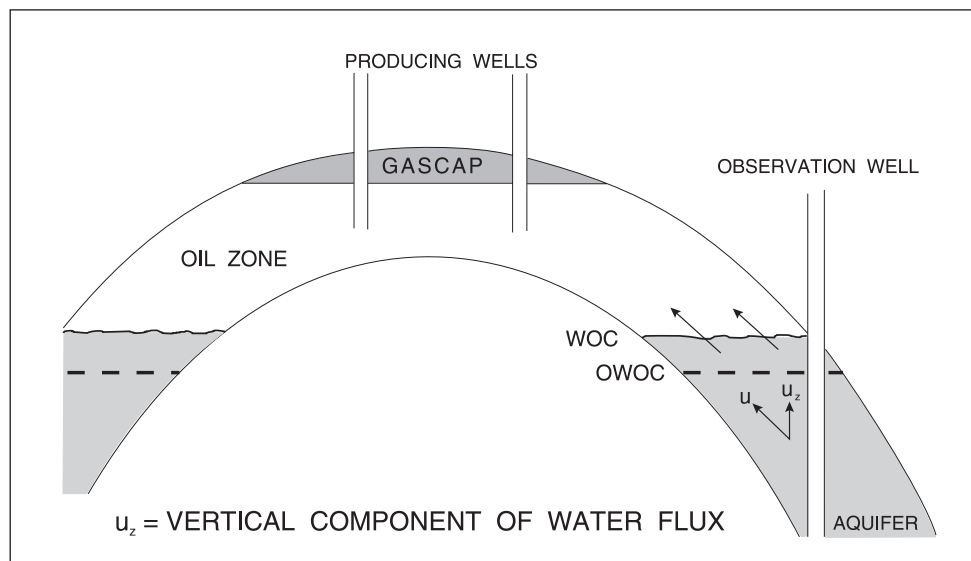


Fig. 10-6. Observation well penetrating a zone where the flow has a vertical component

Below the original water–oil contact (OWOC), only water is present and  $k_{rw}^o$  is unity. Thus in order to sustain the upward component of the water flow, a potential gradient  $\partial\psi_w/\partial D$  is required which depends principally on the flux component  $u_{zw}$  and the formation effective vertical permeability  $k_z$ . The vertical pressure gradient that will be observable from an WFT survey is therefore

$$\frac{\partial p_w}{\partial D} = \frac{u_{zw}\mu_w}{k_z k_{rw}^o} + \rho_w g = \left[ \frac{\partial p_w}{\partial D} \right]_f + \left[ \frac{\partial p_w}{\partial D} \right]_g \tag{10-3}$$

and is composed of a frictional and a gravitational component. The pressure gradient (psi/ft) in a reservoir with upward flow should be greater than the hydrostatic gradient as shown in figure 10-7. Hence, if the in situ water density is known and the actual vertical pressure gradient  $\partial p_w/\partial D$  in the flowing system is determined from a WFT survey in an observation well, the frictional gradient can be obtained as

$$\left[ \frac{\partial p_w}{\partial D} \right]_f = \frac{u_{zw}\mu_w}{k_z k_{rw}^o} = \frac{\partial p_w}{\partial D} - \rho_w g \tag{10-4}$$

provided the difference between the measured and hydrostatic gradients is significant. In a developed reservoir, it is this difference that is important and it reflects the interaction between permeability and flow. Interpretation of the quantity  $\frac{u_{zw}\mu_w}{k_z k_{rw}^o}$  for effective vertical permeability  $k_z$  requires independent knowledge of the flux  $u_{zw}$  assuming  $\mu_w$  and  $k_{rw}^o$  are known. The determination of vertical water flux in the vicinity of the observation well, at the time the WFT survey was run, is not easy since it cannot be measured directly. In general, a reservoir model of some sort is necessary to allow the prediction of in situ flow velocities in the neighborhood of new wells where WFT surveys are being carried out. For example, in the present case the

aquifer influx may be estimated from a reservoir material balance that uses pressure decline and production/injection data to infer the extent of the natural water drive. This approach can be considerably improved by actually measuring the advance of the WOC with time lapse pulse neutron capture (PNC) gamma ray spectroscopy (GST) reservoir monitoring. In developed reservoirs, one of the main reasons for making distributed pressure measurements in observation wells is to try to identify the effective vertical permeability by matching measured pressure profiles to model predictions.

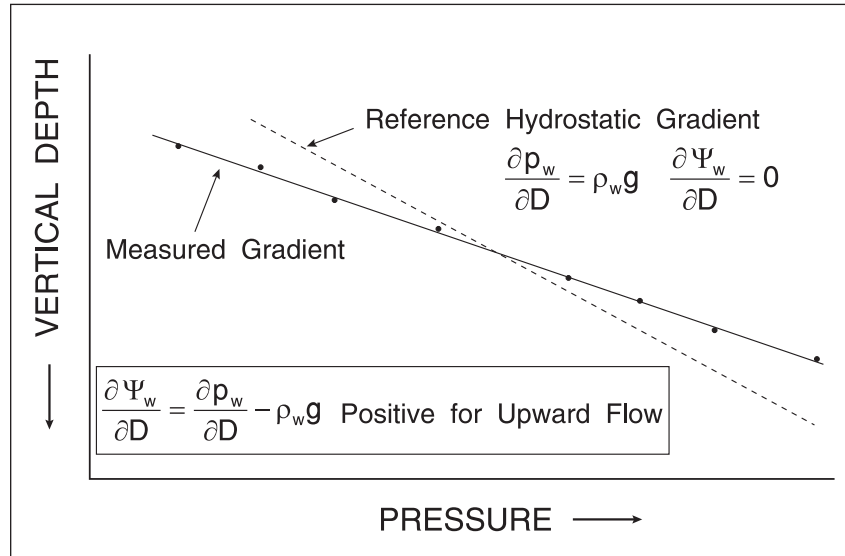


Fig. 10-7. Pressure profile in a homogeneous zone with a constant upward flow component

In the preceding treatment,  $u_{zw}$  has been taken as positive for upward flow in the reservoir. In the case where downward single-phase flow is occurring, the observed reservoir pressure gradient will be less than hydrostatic. It has been convenient to discuss the flow of water but the same analysis applies to any region in which single-phase flow with a vertical component is taking place; it is only necessary to replace the subscript “w” with “o” or “g” to obtain the corresponding expressions for oil or gas.

The general expression for the local pressure gradient in monophasic conditions is

$$\frac{\partial p}{\partial D} = \frac{u_z \mu}{k_z k_r^o} + \rho g = \left[ \frac{\partial p}{\partial D} \right]_f + \left[ \frac{\partial p}{\partial D} \right]_g \quad (10-5)$$

In a homogeneous section of reservoir over which the vertical flux component remains essentially constant, the pressure profile will be linear since both  $k_z$  and  $u_z$  do not vary. Data points obtained in an WFT survey, when plotted, will deviate from a straight line as a result of errors in the measurement of pressure and depth as illustrated in figure 10-8. The scatter due to measurement error is random and the computed slope  $m$  obtained from a least squares linear regression is

subject to some uncertainty, particularly when the data points are not sufficiently spaced in depth. The measured gradient over the zone is therefore obtained as

$$\left[ \frac{\partial p}{\partial D} \right]_{\text{measured}} = \left[ \frac{\partial p}{\partial D} \right]_{\text{true}} \pm \varepsilon_m \quad (10-6)$$

where  $\varepsilon_m$  is the error in the computed gradient and depends on the number of data points, the depth interval over which they are obtained, and the precision of pressure and depth detection.

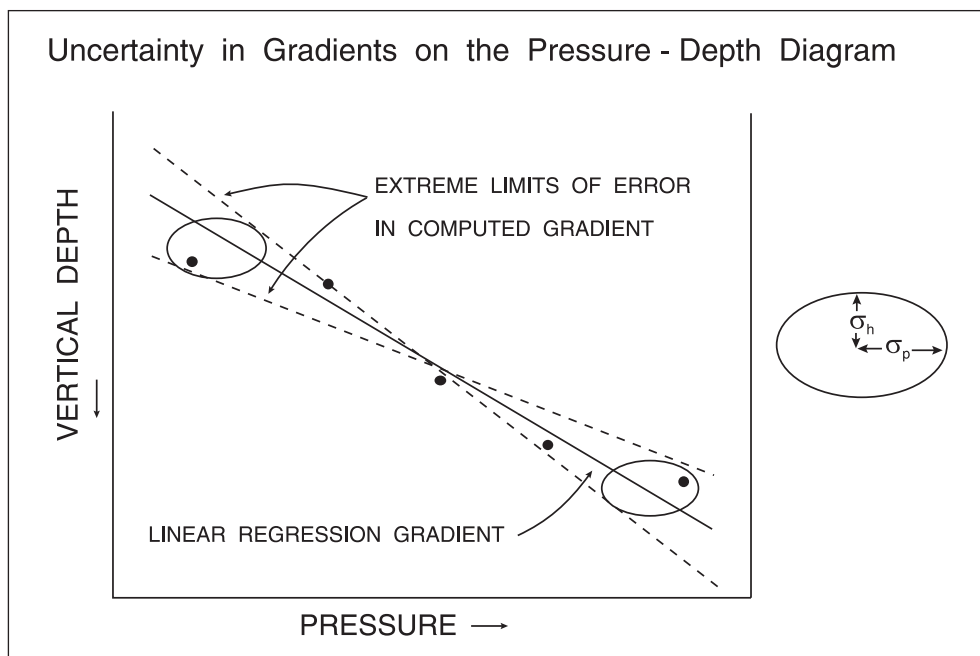


Fig. 10-8. The effect of pressure and depth measurement error on gradient determination

In many circumstances, the effective vertical permeability  $k_z$  is sufficiently high in relation to the vertical flux component  $u_z$  so that the viscous component of the true pressure gradient is less than the statistical uncertainty in the computed slope of the pressure–depth plot. In this case, the observed pressure gradient is indistinguishable from that which would occur in a static reservoir, i.e.,

$$\text{If } \frac{u_z \mu}{k_z k_r^o} < \varepsilon_m \quad \text{then} \quad \frac{\partial p}{\partial D} = \rho g \quad (10-7)$$

A zone in a developed reservoir which exhibits an essentially hydrostatic fluid gradient, even when vertical flow is occurring, is said to be in vertical pressure equilibrium. It should be emphasized that  $u_z$  values in reservoirs are very small because of the extremely large areas available for vertical flow and the frictional component of the pressure gradient is detectable only when the effective vertical permeability  $k_z$  is also very low. Figure 10-9 shows WFT surveys from the Furrial oil field in Venezuela and it can be seen that the reservoir is depleting as a “tank”

at uniform potential; this is a dramatic example of vertical pressure equilibrium and a material balance model will be very applicable as evidenced in figure 10–10.

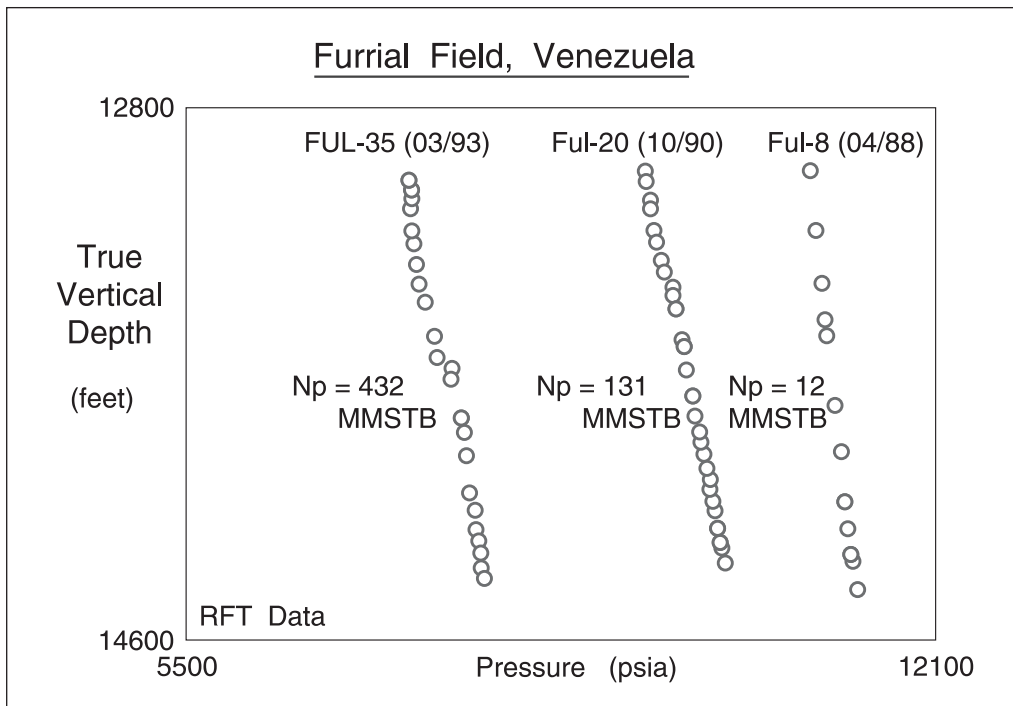


Fig. 10–9. WFT surveys in the Furrial field, Venezuela

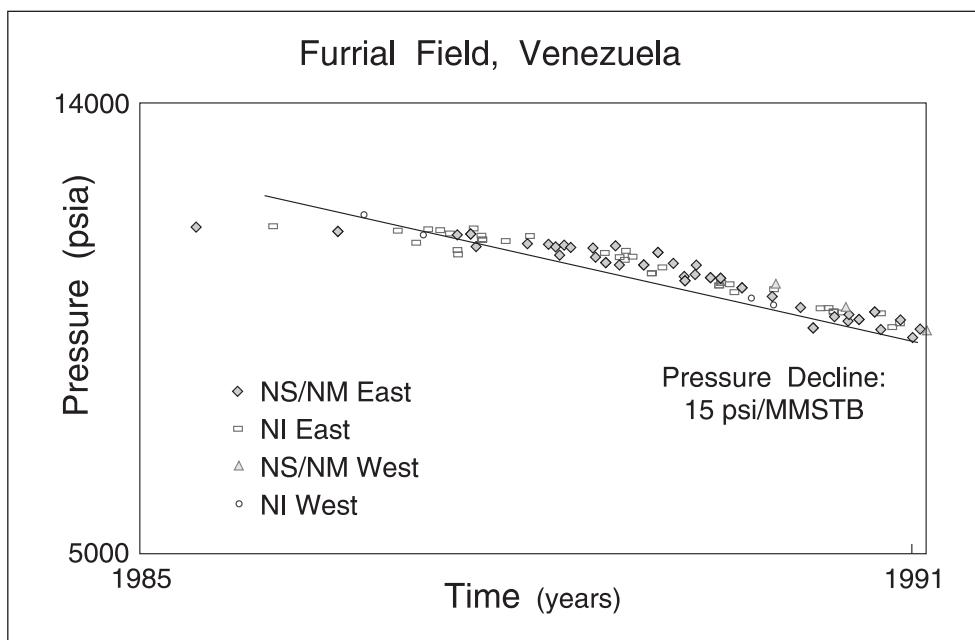


Fig. 10–10. Pressure decline in Furrial



The interpretation of a WFT survey in a developed reservoir should commence by a statistical analysis of the pressure–depth data firstly to identify zones with linear profiles and then to determine the best fit slope  $m$  and its uncertainty  $\epsilon_m$  for each linear zone. It is very important that the cumulative set of observations presented on a pressure–depth diagram be displayed at the wellsite so that testing can be continued until a statistically adequate number of data points has been obtained. The measured gradient is then compared to the hydrostatic gradient corresponding to the known in situ fluid density. When the difference is significant, the viscous component may be calculated and finally, if  $u_z$  is available from reservoir modeling, an estimate of  $k_z$  can be made. However, it should be emphasized that the demonstration of the occurrence of vertical pressure equilibrium, even though  $k_z$  cannot be obtained quantitatively, is also a useful piece of information concerning reservoir behavior.

Figure 10–11 shows the pressure depth data for a well drilled into the water zone below the OOWC. In this case, the pressure profile is linear and has a gradient quite different from hydrostatic. Before interpretation of the viscous component, it is essential to ensure that the well deviation through the formation has been accurately measured and the vertical depth scale is correct.

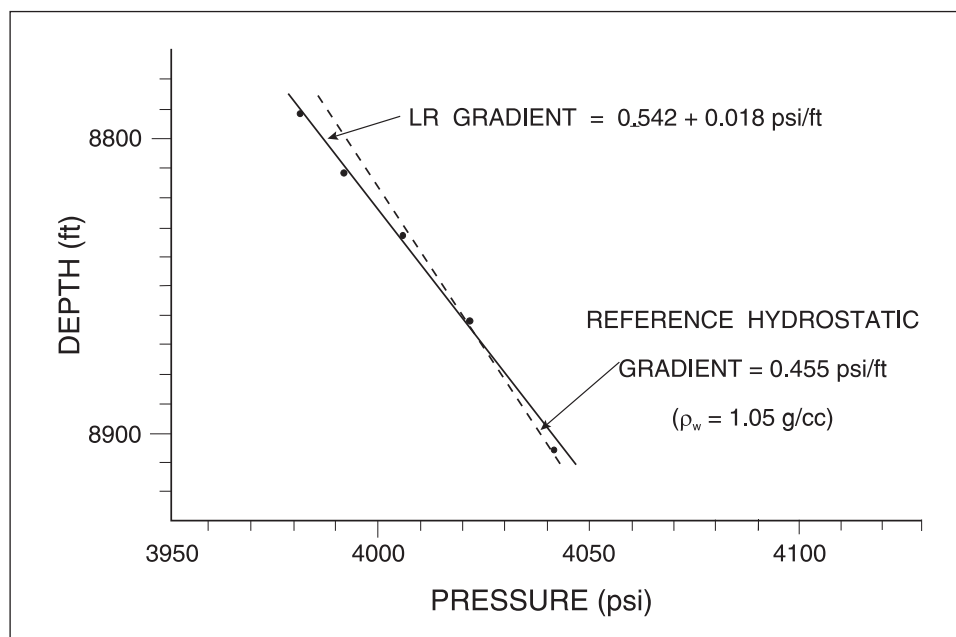


Fig. 10–11. Field example of a linear pressure profile in a water zone with significant upflow

## Identification of Permeability Barriers

In the preceding treatment of single-phase flow, it was tacitly assumed that the formation vertical permeability  $k_z$  was uniform and the pressure profile consequently linear. However, in many reservoir situations the permeability of layers corresponding to different geological facies are quite different and the observable pressure gradient, given by Eq. (10–3), will vary with depth due to changes in vertical permeability (still presuming that  $u_z$  is fixed). A common occurrence is illustrated in figure 10–12, where a thin layer of very low permeability  $k_b$  separates two zones in

each of which the vertical permeability is large enough in relation to the vertical flow component to allow vertical pressure equilibrium, i.e., uniform potential, to occur. Assuming that the permeability of the restricted zone is uniform (vertically and aurally), the potential difference over it is given by

$$\delta\psi_b = \frac{u_z \mu h_b}{k_b k_r^o} \quad (10-8)$$

Hence what is observed is the discontinuity in potential between the hydrostatic gradients that are evident in the highly permeable zones above and below. The potential difference  $\delta\psi_b$  is easily measured as shown in figure 10-12 by extrapolating the adjacent gradients and determining the separation at a fixed level. Again, if an estimate of the upflow  $u_z$  between the two permeable layers can be obtained from a reservoir model, the effective permeability of the barrier  $k_b$  can be calculated from Eq. (10-8). The thickness  $h_b$  of the low-permeability streak will normally be evident from logs.

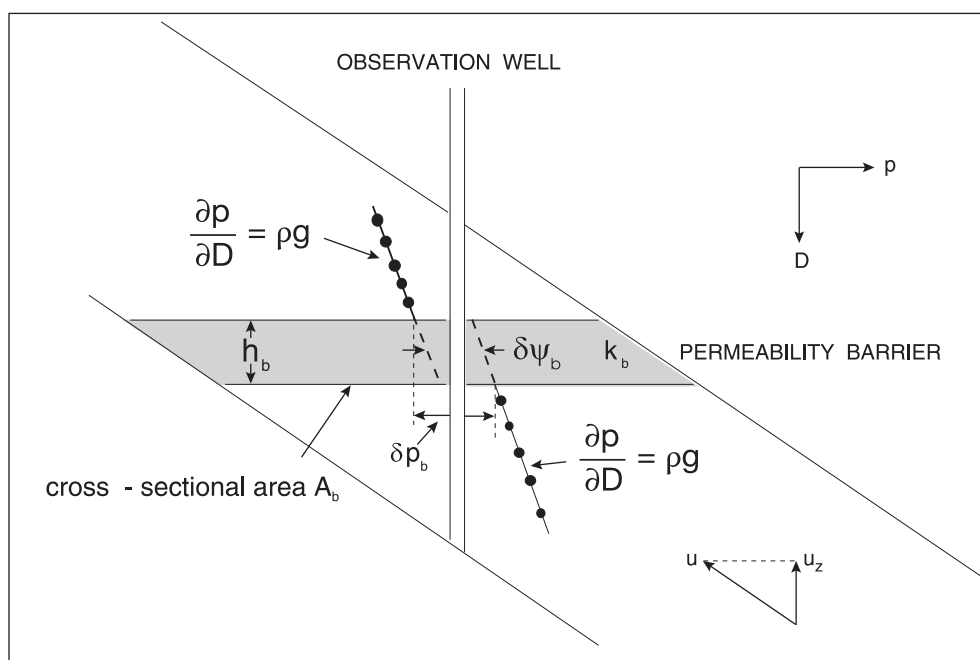


Fig. 10-12. Potential discontinuity over a barrier

Although attention has been concentrated on the quantitative estimation of the barrier effective permeability, it should be pointed out that the pressure survey has also indicated the presence of two permeable zones, which individually appear to have good internal vertical communication, separated by a barrier which is continuous over a wide area. The distributed pressure information from the producing field therefore provides a direct way of zoning the reservoir into continuous layers. Frequently, an apparent barrier which is evident on the interpreted logs, i.e., a shale, exhibits no measurable potential discontinuity on a WFT survey. This often implies that the zone is not continuous and has not presented a restriction to vertical communication. However, it should also be borne in mind that it is possible for a reservoir to be produced in such a way that very little tendency for vertical flow is induced and the component  $u_z$

is so small that the potential difference over even a strong barrier is too small to be observed. The observation of a measurable potential difference certainly confirms the existence of a low-permeability streak but the converse is not necessarily true.

### Semi-steady-state differential depletion

In order to more fully understand the process of identifying a barrier, it is useful to consider how the upflow  $u_z$  can be inferred from a simple reservoir model. The most common mechanism responsible for vertical flow is differential depletion, which again can be illustrated using the case of two permeable units, each at vertical equilibrium, separated by a low-permeability barrier as shown in figure 10–13. The individual units generally produce at different overall production rates because of differences in unit pressure and well unit productivity indices. The lower unit, denoted 1, thus has a well production rate  $q_1$  and pore volume  $PV_1$ , while the upper unit, denoted 2, produces at a well rate  $q_2$  from a total pore volume  $PV_2$ . Here the pore volume refers to a drainage area encompassing the observation well and the nearby producers, while the production rate is the total summed over all these producers. Because of the different rates of depletion, i.e., ratio of production to pore volume, the potential of each unit will initially not decline at the same rate and as time proceeds a potential difference will be established between the two units. In this simple tank (zero-dimensional) model, the unit potential is assumed uniform aerially and vertically and drawdowns near producing wells are ignored. As the potential difference develops, a concomitant crossflow from unit 1 to unit 2, denoted  $q_{12}$ , also occurs, given by

$$q_{12} = \frac{k_b A_b}{\mu h_b} (\psi_1 - \psi_2) \tag{10-9}$$

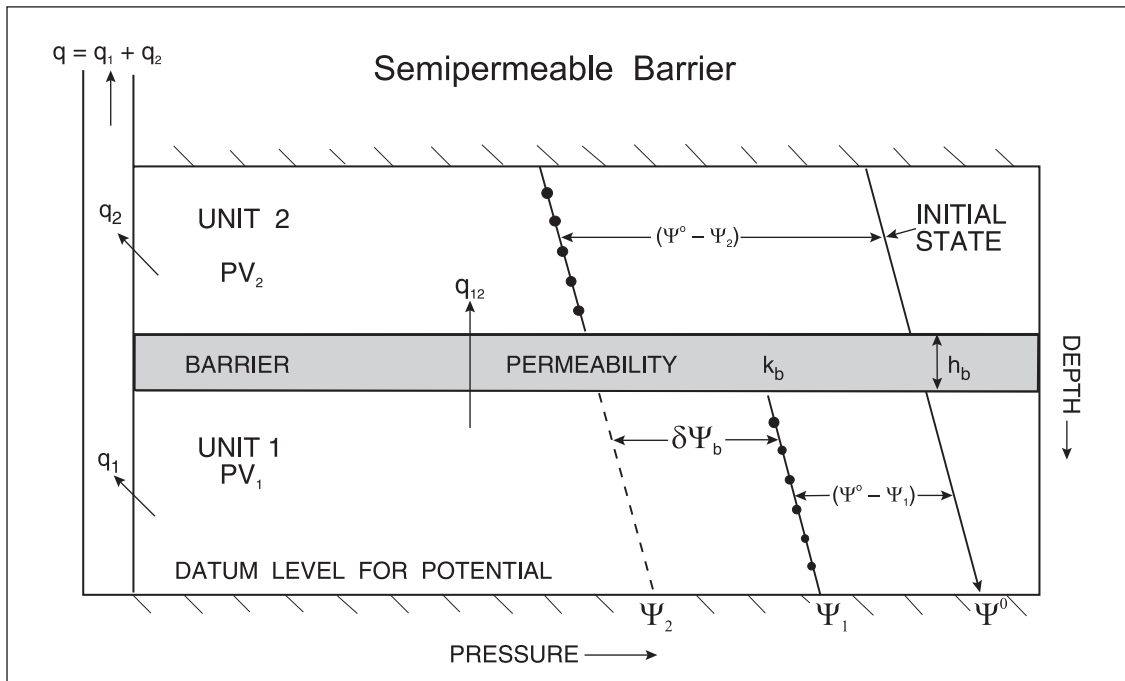


Fig. 10–13. Two permeable units at vertical equilibrium separated by a slightly permeable barrier

When reservoir crossflow takes place, the individual unit material balance equations must allow for this as follows:

$$\frac{d\psi_1}{dt} = - \frac{q_1 + q_{12}}{PV_1 c_t} \quad (10-10a)$$

$$\frac{d\psi_2}{dt} = - \frac{q_2 - q_{12}}{PV_2 c_t} \quad (10-10b)$$

where  $q_{12}$  is given by Eq. (10-9).

If the rates  $q_1$  and  $q_2$  are held constant, it can be shown that this linear differential system will eventually reach a combined, overall semi-steady-state (SSS) at which the unit potentials  $\psi_1$  and  $\psi_2$ , although different in value, decline at the same rate, i.e.,

$$\frac{d\psi_1}{dt} = \frac{d\psi_2}{dt} \quad (10-11)$$

As the unit potentials reduce from their initial (equal) value,  $\delta\psi_b = \psi_1 - \psi_2$  increases until the crossflow  $q_{12}$  reaches a level such that the net depletion rate of unit 1, i.e.,  $(q_1 + q_{12})/PV_1$ , is exactly equal to that of unit 2, i.e.,  $(q_2 - q_{12})/PV_2$ . The crossflow rate  $q_{12}$  at the combined system SSS is therefore given by

$$\frac{q_1 + q_{12}}{PV_1 c_t} = \frac{q_2 - q_{12}}{PV_2 c_t}$$

i.e.,

$$q_{12} = \frac{q_2 PV_1 - q_1 PV_2}{(PV_1 + PV_2)} \quad (10-12)$$

which follows from (10-10a), (10-10b), and (10-11). The corresponding SSS unit potential difference is obtained from Eq. (10-9), i.e.,

$$(\delta\psi_b)_{SSS} = \frac{\mu h_b (q_2 PV_1 - q_1 PV_2)}{k_b A_b (PV_1 + PV_2)} \quad (10-13)$$

as shown in figure 10-14. It is the quantity  $\delta\psi_b$  that can be measured by a distributed pressure survey in an observation well, but Eqs. (10-12) and (10-13) show that in order to identify the barrier transmissibility  $T_b = k_b/h_b$ , it is also necessary to measure the unit well production rates  $q_1$  and  $q_2$  and pore volumes  $PV_1$  and  $PV_2$ . Thus in order to interpret a distributed pressure measurement, viz.,  $\delta\psi_b$ , it is essential also to have distributed flow measurement, in this case  $q_1$  and  $q_2$ . The proportion of the total well production deriving from the individual units cannot be predicted and production logging must be employed to obtain a realistic apportionment of the total well flow. Given measured information on  $q_1$  and  $q_2$ , the reservoir model can infer the in situ

crossflow  $q_{12}$ . The impermeable barrier case ( $T_b = 0$ ), illustrated in figure 10–15, never reaches a joint SSS and the two layer pressures continue to separate indefinitely.

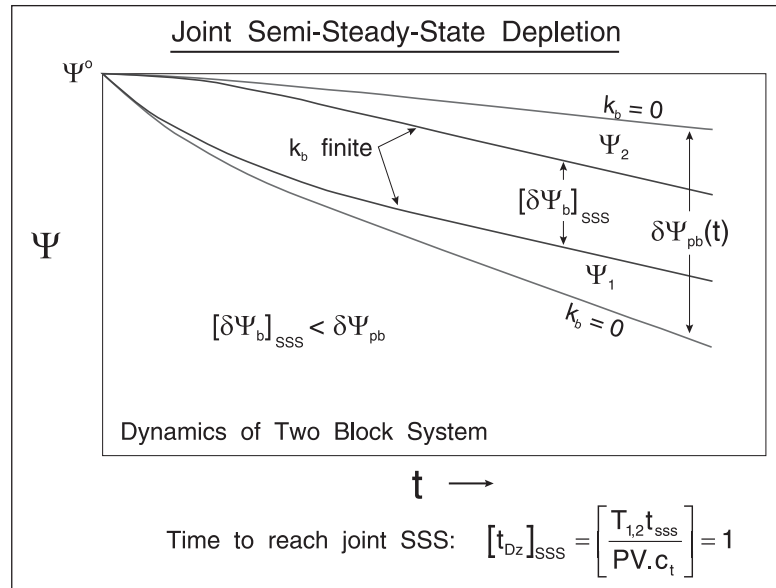


Fig. 10–14. Joint semi-steady-state

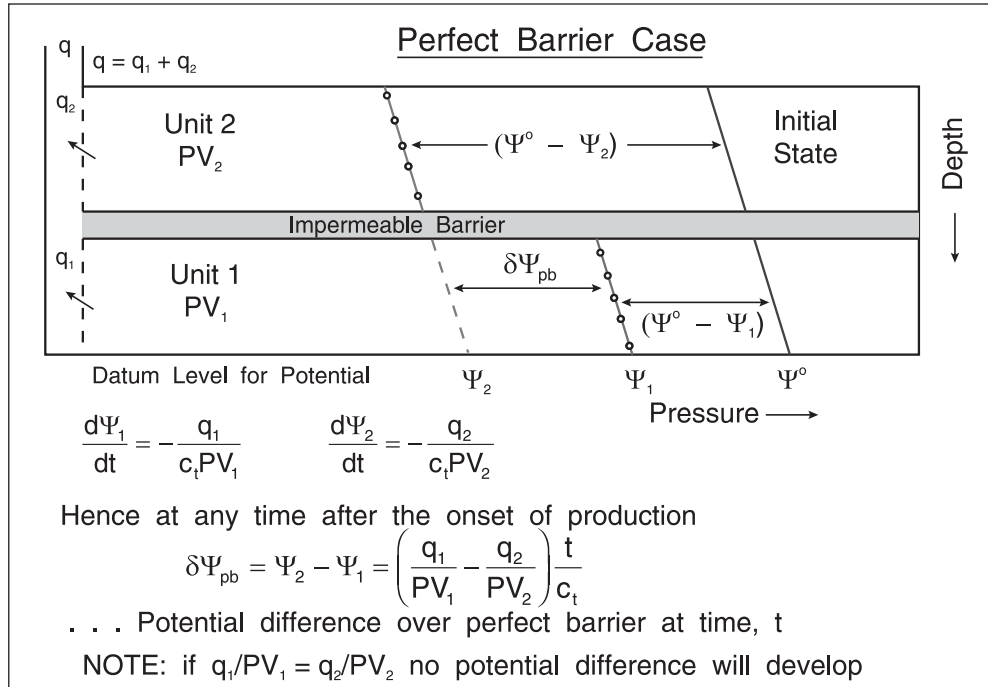


Fig. 10–15. Completely impermeable barrier case ( $T_b = 0$ )

The estimate of  $T_b$  is also dependent on knowledge of the pore volume  $PV_1$  and  $PV_2$  being drained by the producing wells. The determination of unit pore volumes by integration of porosity and sand thickness maps based on log and core data is apparently straightforward, but severe problems arise in faulted reservoirs when trying to define the aerial extent of fault

blocks. In fact, one of the most important applications of WFT pressure monitoring in produced reservoirs is the verification of drainage areas. Assuming that initially the units are at the same potential  $\psi^o$ , the integrated form of Eq. (10–10a and b) is

$$\psi_1 = \psi^o - \frac{(q_1 + q_{12})t}{PV_1 c_t} \quad (10-14a)$$

$$\psi_2 = \psi^o - \frac{(q_2 + q_{12})t}{PV_2 c_t} \quad (10-14b)$$

The potential declines from the initial value ( $\psi^o - \psi_1$ ) and ( $\psi^o - \psi_2$ ) are therefore fixed by the pore volume being drained. Hence it is possible to verify pore volumes by measuring the potential decline at specific times. This implies computing the differences ( $\psi^o - \psi_1$ ) and ( $\psi^o - \psi_2$ ) and hence it is very important that the pressure transducers used in the initial and subsequent WFT surveys have good absolute accuracy. Precise gauge calibration is the most crucial field consideration in reservoir pressure monitoring. The use of WFT pressure surveys to delineate fault blocks has been well documented by Nadir.<sup>1</sup> This paper also gives striking field examples of the zonation of a reservoir according to distributed pressure information.

The second-order linear differential system (10–10a and b) has one nonzero eigenvalue  $k_b A_b / (\mu h_b (PV_1 + PV_2) c_t)$  and the time taken for the two-unit system to reach the joint SSS is given by the condition

$$t_{Dz} = \frac{k_b A_b t}{\mu h_b (PV_1 + PV_2) c_t} > 1 \quad (10-15)$$

Thus in layered systems with an overall SSS brought about by crossflow, the vertical permeability, in this case  $k_b$ , affects the time to reach SSS. If the barrier is practically impermeable, joint SSS will never be attained.

The identification of a tight streak in a reservoir from distributed pressure surveys in observation wells is possible only if the potential difference  $\delta\psi_b$  is sufficiently large to be detectable. It is immediately apparent from Eq. (10–12) that, if the reservoir is produced in such a way that  $q_1/PV_1$  is very close to  $q_2/PV_2$ , then induced crossflow will be negligible and no potential difference will develop irrespective of whether there is a barrier or not. Also, since the quantity  $A_b$  in Eq. (10–13) is extremely large, the observable potential difference  $\delta\psi_b$  may be smaller than the pressure gauge resolution. Monitoring of the reservoir depletion will generally show up only very strong barriers, i.e., low values of  $k_b/h_b$ , in conditions where the reservoir is produced at a reasonably high rate. It is important that the reservoir does not have any wells shut in at the surface that would allow potential differences to dissipate by crossflow through wellbores. Barriers may exist that do not induce an observable potential difference during primary depletion but are certainly strong enough to severely limit the segregation of fluids according to density difference in displacement processes. A new type of interference testing based on distributed

pressure measurement at observation wells and designed specifically to reveal the existence of low vertical permeability layers which are not evident from depletion monitoring has been described by Stewart and Wittmann.<sup>2</sup>

It is also of interest to consider another common example of differential depletion that is of practical importance in which a relatively thick layer of low-permeability rock lies adjacent to a highly permeable zone (dual porosity strata). In this situation, the tight zone produces almost entirely by vertical crossflow into the adjacent permeable layer and the whole production emerges from the permeable zone. This is illustrated in figure 10–16. Flow in the low-permeability layer is essentially vertical and is described by one-dimensional linear flow theory. This is analogous to depletion in a naturally fractured reservoir where a low-permeability region produces into a high-permeability system which connects to the wells. Again if the wells are produced at near-constant rate, the combined system will also eventually attain the condition of joint SSS depletion in which the potential is declining everywhere in the same rate. The material balance equations are

$$\frac{d\psi_1}{dt} = - \frac{(q_2 - q_{21})}{PV_1 c_t} \tag{10-16a}$$

$$\frac{d\psi_2}{dt} = - \frac{q_{12}}{PV_2 c_t} \tag{10-16b}$$

and at the joint SSS where  $d\psi_1/dt$  is equal to  $d\psi_2/dt$ , the crossflow is given by

$$q_{21} = \frac{q_1 PV_2}{(PV_1 + PV_2)} \tag{10-17}$$

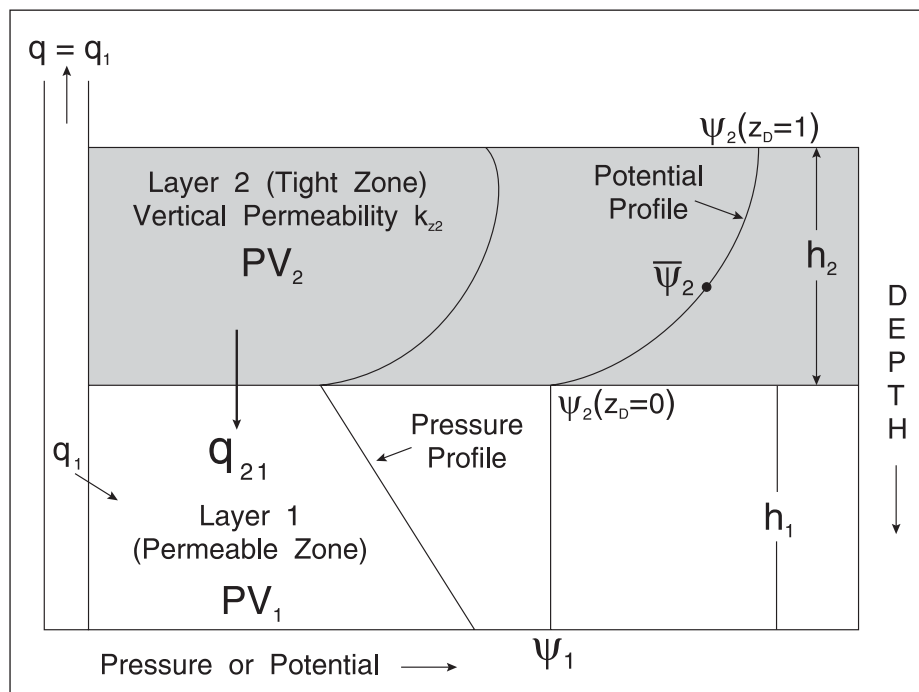


Fig. 10–16. Tight zone adjacent to a permeable layer

In order to develop a method for determining the vertical permeability of the supporting layer  $k_z$ , it is necessary to consider the form of the potential profile, which is illustrated in figure 10–16. If a layer in vertical flow is produced at a constant rate, then linear flow theory shows that, once the SSS has been attained, the potential difference over the zone is given by

$$\frac{[\psi_2(z_D = 1) - \psi_2(z_D = 0)]k_{z2}}{u_z \mu h_z} = 0.5 \quad (10-18)$$

where  $u_z$  is the constant flux at the layer boundary equal to  $q_{21}/A_{xy}$ . The shape of the potential profile is characteristic of SSS depletion by crossflow and reflects the progressive increase of the local vertical flux from zero at the upper confining no-flow boundary to a maximum value of  $u_z$  at the layer interface. The flux at any intermediate section is due to the expansion of all the fluid present between that location and the no-flow boundary. The pressure profile corresponding to this potential profile is also illustrated in figure 10–16, and it can be seen that its shape is approximately parabolic. Although there is an analytical result for linear flow potential distribution, it is sufficient to use the overall vertical permeability from Eq. (10–18). The time required to reach linear SSS depletion in the supporting layer is given by

$$\frac{k_{z2}t}{\phi \mu c_t h_z^2} > 0.5 \quad (10-19)$$

This simplified theory allows only for vertical flow in the tight zone; in some situations, it may produce by a combination of horizontal flow directly to the wells and crossflow into adjacent more permeable layers.

Figure 10–30 shows some of the first WFT pressure measurements made in a produced reservoir and the presence of two tight zones (sandstone) producing by crossflow into adjacent permeable streaks (fractured limestone) is quite clear from the parabolic nature of the pressure profile. Underneath the tight layers is a massive fractured limestone formation at vertical pressure equilibrium.

## Reservoir simulation

The characteristic pressure profile corresponding to one or other of these two canonical cases of differential depletion are often observed in WFT surveys in produced reservoirs. However, in most real situations, observed distributed pressure information cannot properly be interpreted on the basis of simple zero-dimensional SSS models. In practice, a reservoir simulator is used to predict the pressure response and the vertical permeabilities of layers are adjusted until the simulator pressure profiles, at the appropriate time and aerial position, match these observed at the observation wells; recent papers<sup>3, 4</sup> have referred to this method of assessing effective vertical permeability on a reservoir scale. Such an approach is obviously necessary to allow for complicating factors such as the presence of several layers, lack of vertical equilibrium, horizontal flow in the supporting zone, partial pressure maintenance by injection, aerial flow effects and non-SSS conditions. However, analysis of the simplified models demonstrates that a layered reservoir simulator must be matched simultaneously to distributed pressure and flow data; it is not sufficient to match pressure profiles only, and the single-well models in the simulator must



apportion total well flow according to production logging measurements as described in the literature.<sup>5</sup> Also, the simple models clearly demonstrate that reservoir depletion monitoring may show up only in very low permeability layers. The objective for identifying low vertical permeability zones early in the life of the reservoir during the primary depletion phase, or at least before water injection has become significant, is to allow the reservoir simulator to better predict the gravity segregation of phases during secondary recovery. In the North Sea, the main reason for running WFT surveys in new development wells is for history matching of layered simulators. It is axiomatic that a layered simulator is not valid unless it can reproduce historic layer pressure and flow measurements.

## Two-phase flow

The interpretation of vertical pressure profiles in producing reservoirs has been discussed for the case where only single-phase flow is occurring. However, in many situations the observation well penetrates a zone in which two flowing phases are present, e.g., gas and oil in the gassing zone of a saturated reservoir or water and oil in a region of the field under water drive. Naturally, the question arises as to what vertical pressure gradient will be observed when two mobile phases exist. In such circumstances, the vertical flow components arise partly because of the density difference between phases and the tendency of the lighter phase to move upwards and the heavier phase countercurrently downwards; this process is known, of course, as *gravity segregation*.

### Vertical saturation equilibrium

In water- or gas-drive reservoirs with very good vertical communication and low displacement rate for which the vertical equilibrium number is greater than unity, i.e.,

$$N_{VE} = N_{GV} + N_{CV} = \frac{k_z \Delta \rho g \cos \alpha A}{q_d u} + \frac{k_z \Delta p_c A}{q_d \mu h} > 1 \quad (10-20)$$

the process of phase segregation takes place to such an extent that the phases dynamically separate with the light phase lying completely above the heavy phase. This is termed *gravity or saturation vertical equilibrium* and for typical reservoir displacement velocities, the vertical permeability  $k_z$  must be very large indeed for this condition to be satisfied. When it does occur, the observable pressure gradients are exactly the same as would be seen in a static reservoir with a phase contact at the same level, i.e., an oil gradient above the current WOC and a water gradient below, as shown in figure 10–17. In water drive, the contact is the interface between moving water and oil; discontinuous residual oil in the water-swept region has no effect on the pressure gradient although it will, of course, register on logs. Hence, in these circumstances a WFT survey in a new development well can locate the phase contact if there are sufficient data points to adequately define both light and heavy phase gradients and their intersections. Stewart<sup>6</sup> has given a field example of this in the water drive case (see figure 10–24 later). The observation of such distinct oil and water gradients confirms the existence of saturation vertical equilibrium, an important piece of information about the nature of the displacement, and condition (10–20) may be used to compute a lower limit for the value of effective reservoir vertical permeability.

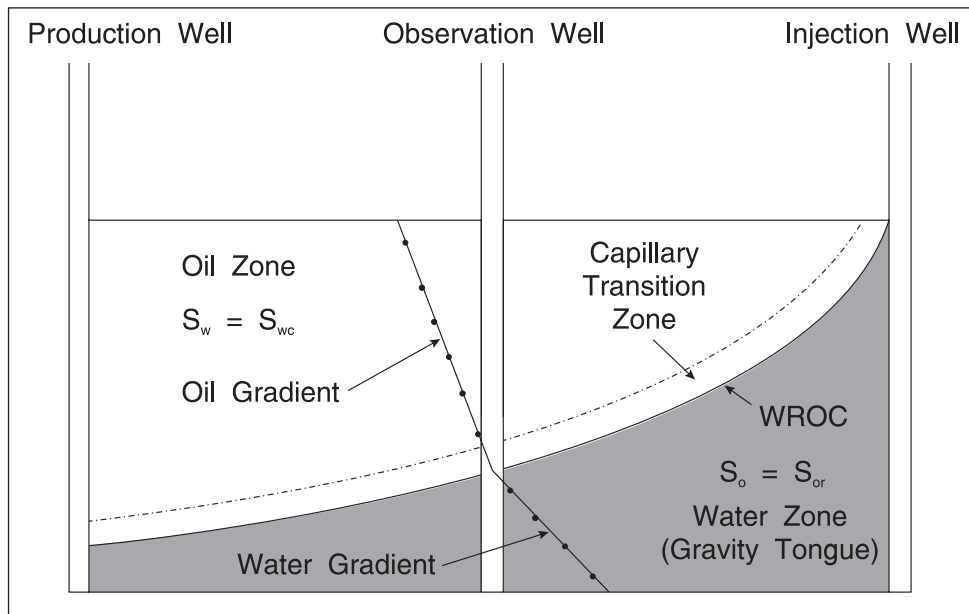


Fig. 10–17. Vertical saturation equilibrium

In the context of single-phase flow, vertical pressure equilibrium simply implies that over a zone the observed pressure gradient is indistinguishable from hydrostatic, allowing for the error in gradient determination. In two-phase flow, vertical saturation equilibrium certainly implies hydrostatic gradients in the respective phases but also the much more severe condition that the saturation distribution follows gravity–capillary equilibrium. It is important to point out that the observation of vertical pressure equilibrium during primary depletion certainly does not mean that vertical saturation equilibrium will occur in displacement. The term “good vertical communication” must be qualified by the process involved. The lack of detectable potential differences in single-phase flow does not mean that saturations in two-phase flow will be at gravity–capillary equilibrium. The only way to assess the behavior of a water or gas drive in terms of fluid segregation is through simulation with properly identified effective reservoir vertical permeabilities. Unfortunately depletion monitoring and matching of reservoir behaviour during the initial production stage can only lead to very low vertical permeability zones being revealed. This dilemma can be resolved by the new forms of interference testing described in the literature.<sup>18</sup>

## Countercurrent two-phase flow

It has been stressed that complete dynamic phase segregation is not very common and in most situations two flowing phases are present. A good example is the gassing zone of a saturated reservoir shown in figure 10–18, where gas coming out of solution tends to move upwards and oil to drain countercurrently downwards due to the phase density difference. If vertical saturation equilibrium was achieved, the gassing zone would not exist and a sharp interface between the expanding secondary gas cap and the undersaturated oil zone would be observed. In practice, such rapid segregation of gas and oil is not seen and the gassing zone is often of considerable thickness.

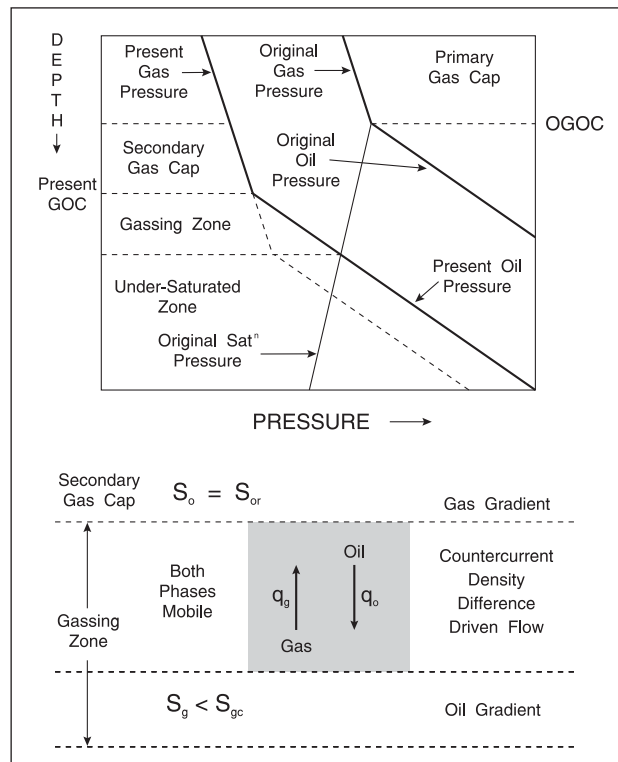


Fig. 10-18. Gassing zone in a saturated reservoir

The question is what pressure profile should be expected in an observation well penetrating the gassing zone. Assuming vertical pressure equilibrium, a gas gradient will exist in the primary and secondary gas caps, while in the saturated oil zone and in the thin region where the gas saturation is below the critical an oil gradient will be observed. Obviously, the gradient in the two (mobile) phase gassing zone can be anywhere between these two extremes as shown in figure 10-19.

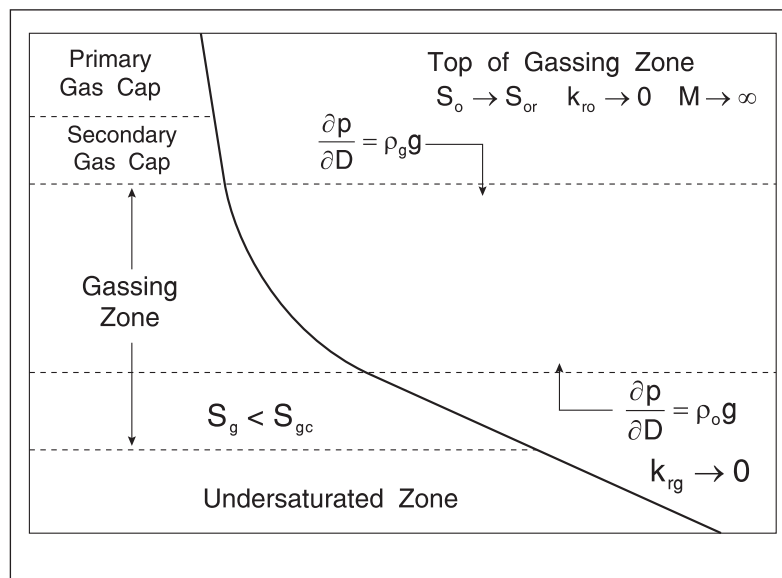


Fig. 10-19. Pressure profile for two-phase countercurrent flow

If the fluxes of gas and oil are equal and opposite, i.e.,  $q_{zo} = -q_{zg}$ , and capillary pressure is neglected, i.e.,  $p_o = p_g$ , the theory of two-phase flow shows that the local pressure gradient is given by

$$\frac{\partial p}{\partial D} = \frac{g[\rho_g + \rho_o/M]}{1 + 1/M} = \frac{g[\rho_o + M\rho_g]}{1 + M} \quad (10-21)$$

where  $M$  is the saturation-dependent mobility ratio defined as  $M = k_{rg} \mu_o / (k_{ro} \mu_g)$ . Thus the pressure gradient depends on the phase densities and the mobility ratio. If  $M$  is large, a gas gradient will be observed and this is usually called *gravity drainage of oil*. Since the viscosity of gas  $\mu_g$  is much less than that of oil  $\mu_o$ , the mobility ratio in a gassing zone is typically high except at gas saturations near the critical. If the mobility ratio is small, an oil gradient will be observed and this situation is referred to as *gas percolation*.

Thus at the bottom of the gassing zone where the gas saturation is close to the critical implying very small  $k_{rg}$  and hence small  $M$ , an oil gradient will occur. Conversely at the top, where the oil saturation approaches the residual value,  $k_{ro}$  is small and  $M$  large resulting in a gas gradient. Because of the viscosity contrast, small gas saturation just in excess of the critical will have a pronounced effect on the formation pressure gradient. Hence it will be very difficult to detect the extent of the gassing zone from pressure data.

An interesting field example of two-phase flow effects is given in figure 10–20, where a WFT survey was run in a new well located wholly in the original gas cap of a reservoir under water injection. The evident steepening of the gradient is due to oil being pushed up into the gas-cap region which leads to loss of recoverable oil as illustrated in figure 10–21.

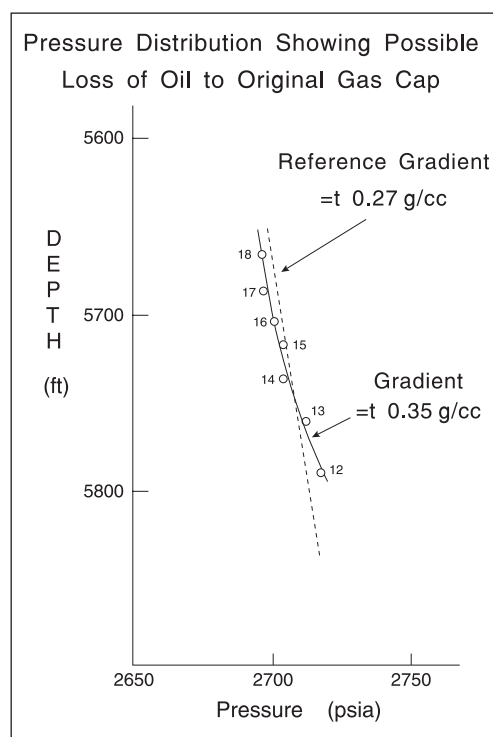


Fig. 10–20. Loss of oil to gas cap

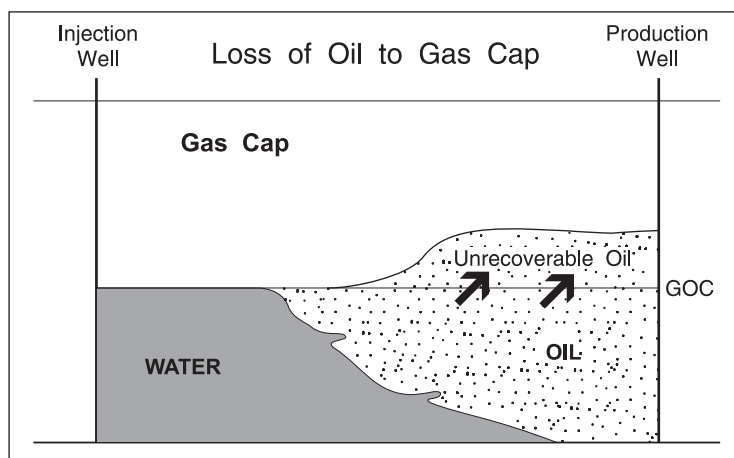


Fig. 10–21. Diagrammatic representation of loss of oil to gas cap

It has been convenient to derive the expression for the observable vertical pressure gradient under two-phase flow conditions in the context of the countercurrent gravity-driven movement of gas and oil in a gassing zone. However, exactly the same arguments apply when the flowing phases are water and oil. In most water-drive situations, phase segregation is again far from complete and there exists a substantial region in which both mobile water and oil are present. In this region between the flood front and the swept zone, countercurrent vertical flow due to phase density difference occurs. Again letting  $M$  represent the saturation-dependent mobility ratio defined by

$$M = \frac{k_{rw}\mu_o}{k_{ro}\mu_w} \quad (10-22)$$

the vertical pressure gradient for the case of zero net vertical flow, i.e.  $q_{zw} = -q_{zo}$ , is obtained from Eq. (10–21) by replacing the subscripts to give

$$\frac{\partial p}{\partial D} = \frac{g [\rho_w + \rho_o/M]}{1 + 1/M} = \frac{g [\rho_o + M\rho_g]}{1 + M} \quad (10-23)$$

Again, the gradient in the two-phase region, shown in figure 10–22, can vary between that of water and oil depending on the value of the mobility ratio  $M$  and hence the local saturation. This equation shows that neither a water gradient nor an oil gradient should be expected in observation wells situated within the two mobile phase zone of a water flood. Note that the saturation will vary both vertically and horizontally. An oil gradient will be seen ahead of the flood front and a water gradient in the swept zone provided vertical pressure equilibrium occurs. If diffuse conditions, i.e., no vertical variation of saturation, exist, the pressure profile as depicted in figure 10–23 will be linear. Figure 10–24 shows WFT pressures in a well in the Piper field in a region which has been flushed by water; in this case, gravity segregation has occurred and clear phase gradients characteristic of vertical equilibrium are evident. The waterflooding of layered reservoirs will induce fluid fronts at different locations in the various zones, as shown for Piper in figure 10–25. It was pointed out by Stewart that production logging, direct measurement of layer flow-rates is necessary to give correct modelling of the progress of the front in different layers.

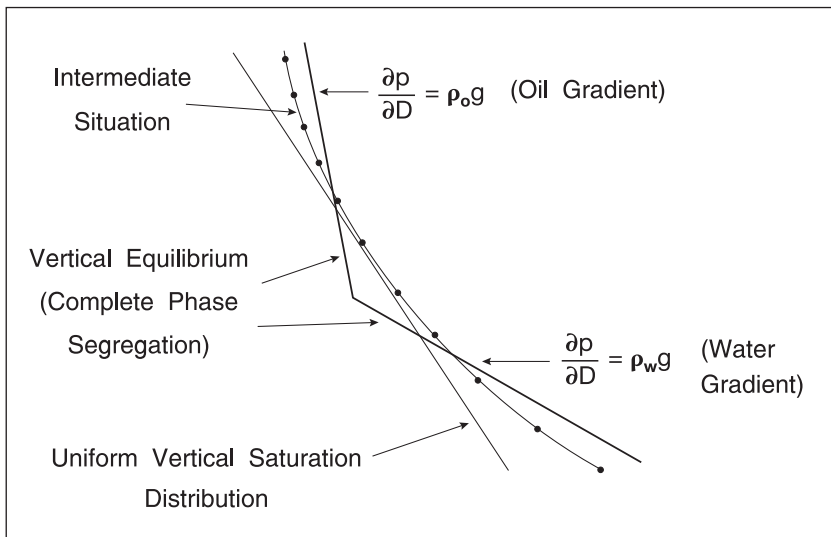


Fig. 10-22. Pressure profile in a water drive

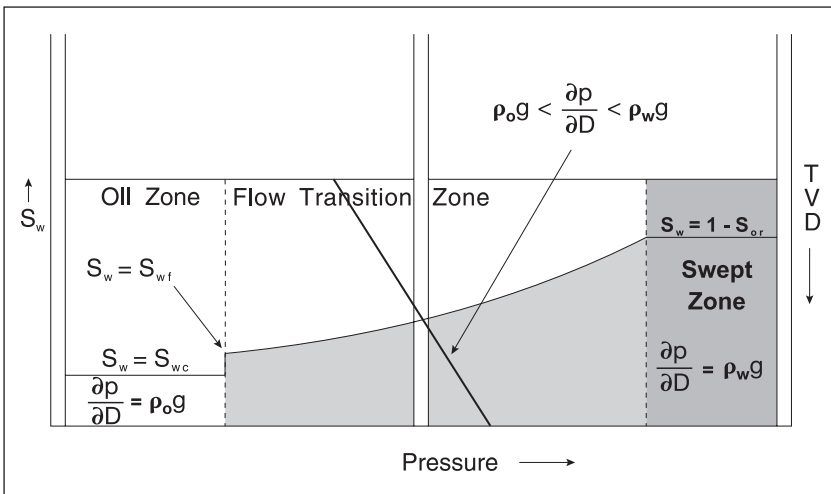


Fig. 10-23. Diffuse flow water flood

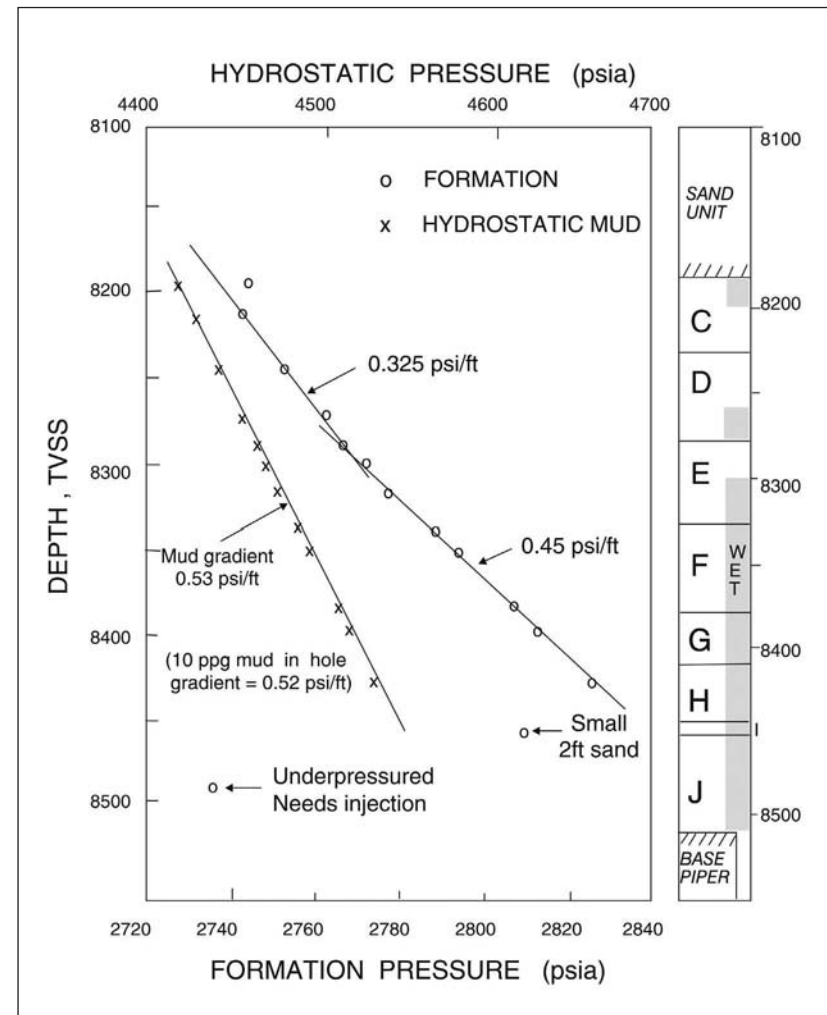


Fig. 10-24. WFT survey from a Piper well (after Stewart)

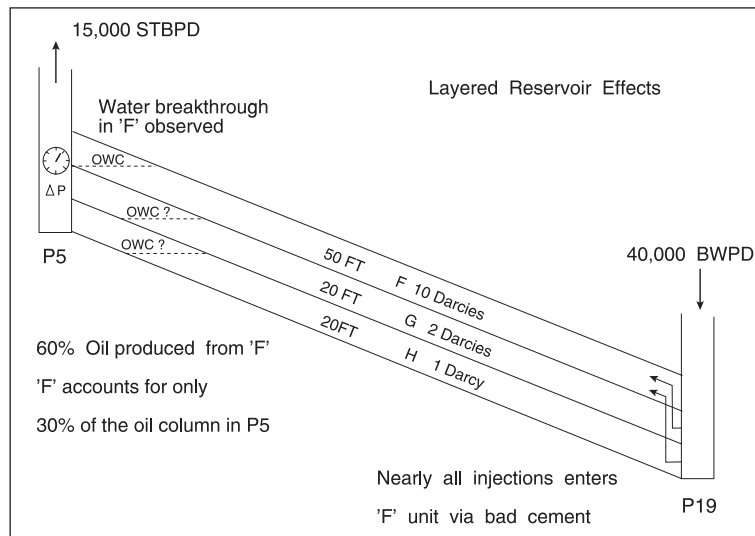


Fig. 10–25. Waterflooding the Piper field

### Cocurrent upward two-phase flow

The examination of the survey data in fig. 10–28 below indicated a gradient significantly steeper than hydrostatic ( $\rho_w g$  in scientific units) in the water zone, and this is indicative of upward flow where natural water influx is displacing gas. The theory of measured pressure gradients at new observation wells in producing fields has been addressed by Stewart and Avestaran,<sup>7</sup> but the case of upward vertical cocurrent flow with a two-phase displacement zone was not explicitly considered. Accordingly, an analysis of this situation will be given here.

Such an upward displacement is illustrated in figure 10–26, where the vertical component of the flows of water and gas at any level are denoted  $q_w$  and  $q_g$ , respectively; in an essentially incompressible displacement, the sum of the volumetric flows of water and gas is a constant, i.e.,

$$q_w + q_g = q \tag{10-24}$$

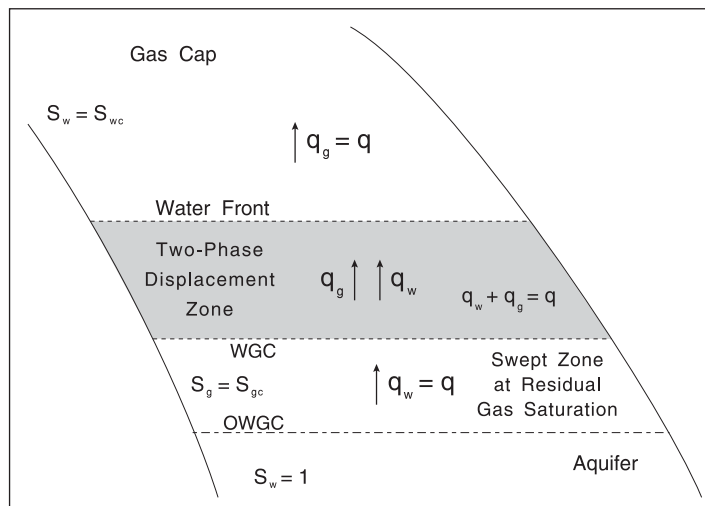


Fig. 10–26. Upward displacement of gas by water influx

Here  $q$  is the vertical component of the displacement rate which is equal to the vertical component of the water rate in the aquifer zone of zero gas saturation. A two-phase zone has developed in which both water and gas flow simultaneously, and the thickness of this region can be calculated from classical displacement theory; the region is bracketed by the present GWC and the water front. Ahead of the two-phase region, the gas flow rate is also given by  $q$  in an incompressible process. In the transition region, the flow of the individual phases are given by the equations defining relative permeability:

$$\frac{q_g}{A} = u_g = \frac{kk_{rg}}{\mu_g} \frac{\partial(p_g - \rho_g gD)}{\partial D} \quad (10-25a)$$

$$\frac{q_w}{A} = u_w = \frac{kk_{rw}}{\mu_w} \frac{\partial(p_w - \rho_w gD)}{\partial D} \quad (10-25b)$$

The upward displacement of gas by water is stabilized both by gravity and the very favorable viscosity ratio; hence the displacement region in the absence of capillary forces would not be expected to be large. Substituting Eqs. (10-25a and b) into Eq. (10-24) gives the result

$$\frac{kk_{rg}}{\mu_g} \frac{\partial(p_g - \rho_g gD)}{\partial D} + \frac{kk_{rw}}{\mu_w} \frac{\partial(p_w - \rho_w gD)}{\partial D} = \frac{q}{A} \quad (10-26)$$

In order to obtain an estimate of the local pressure gradient through the two-phase displacement region, it will be assumed for the moment that capillary effects can be neglected and the phase pressures are equal, i.e.,

$$p_g = p_w = p \quad (10-27)$$

Solving Eq. (10-26) for the local gradient  $\frac{\partial p}{\partial D}$  on this basis results in

$$\frac{\partial p}{\partial D} = \frac{\frac{q\mu_w}{Akk_{rw}} + g(M\rho_g + \rho_w)}{1 + M} \quad (10-28)$$

where

$$M = \frac{k_{rg}\mu_w}{k_{rw}\mu_g}$$

Here  $M$  is the mobility ratio which depends on saturation through the relative permeability curves. In the water zone below the two-phase region where there is no mobile gas present,  $M = 0$  and Eq. (10-28) reduces to the familiar form



$$\left. \frac{\partial p}{\partial D} \right|_w = \frac{q\mu_w}{Ak_z k_{rw}^o} + \rho_w g = \left[ \frac{\partial p}{\partial D} \right]_f + \left[ \frac{\partial p}{\partial D} \right]_{gr} \quad (10-29)$$

Here the end-point relative permeability to water  $k_{rw}^o$  recognizes that there may be a residual trapped gas saturation behind the advancing displacement region. Conversely, in the gas zone above the two-phase region where  $M = \infty$ , Eq. (10-29) assumes the other limiting form

$$\left. \frac{\partial p}{\partial D} \right|_g = \frac{q\mu_g}{Ak_z k_{rg}^o} + \rho_g g = \left[ \frac{\partial p}{\partial D} \right]_f + \left[ \frac{\partial p}{\partial D} \right]_{gr} \quad (10-30)$$

Given that the gas viscosity  $\mu_g$  is significantly less than that of water  $\mu_w$ , the frictional gradient in the gas zone will usually be negligible; here  $k_{rg}^o$  is the end-point relative permeability to gas at connate water saturation. In upward flow, both terms in the expression for the local pressure gradient are positive since friction and gravity reinforce one another. The gradients are depicted diagrammatically in figure 10-27.

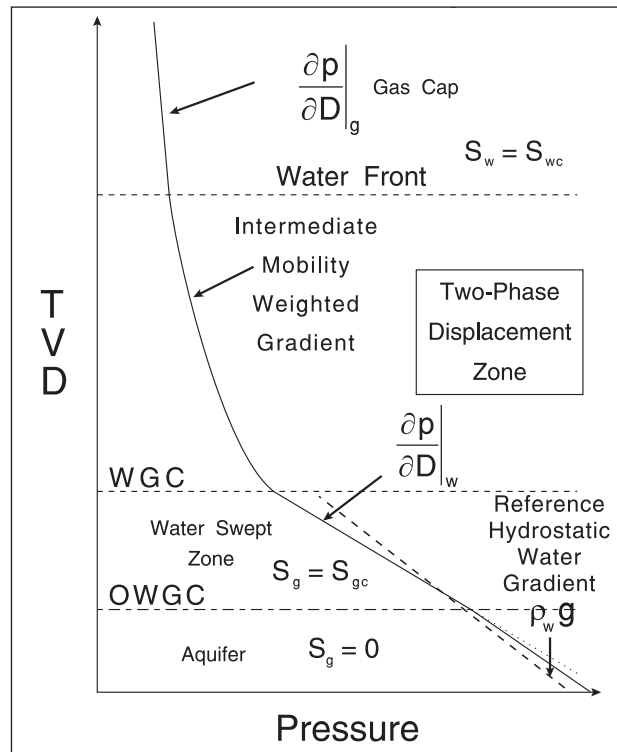


Fig. 10-27. Pressure–depth diagram for cocurrent upward displacement

In the two-phase displacement region according to Eq. (10-28), the observed pressure gradient will change from the water value  $\left. \frac{\partial p}{\partial D} \right|_w$  in the swept region to the gas value  $\left. \frac{\partial p}{\partial D} \right|_g$  ahead of the displacement zone as the saturation varies according to the flow model; this is illustrated

in figure 10–27. Note that for an intermediate gradient to exist both phases must be mobile. In the diagram, a slight change in total water gradient is indicated at the OGWC; this occurs since in the aquifer  $S_g$  is zero and  $k_{rw} = 1$ , whereas in the swept zone  $S_g = S_{gc}$  and  $k_{rw}^o < 1$ . Both gradients are steeper than the reference hydrostatic water gradient given by

$$\left[ \frac{\partial p}{\partial D} \right]_{gr} = \rho_w g \quad (10-31)$$

Although this theory neglects the effect of capillary pressure, it shows how the fluid pressure will vary through the displacement transition region penetrated by an observation well in which a WFT survey is run. Note that the thickness of the transition region will be shown up by the interval exhibiting an intermediate gradient. Field data from a North Sea gas well is shown in figure 10–28, where the different regions are clearly evident.

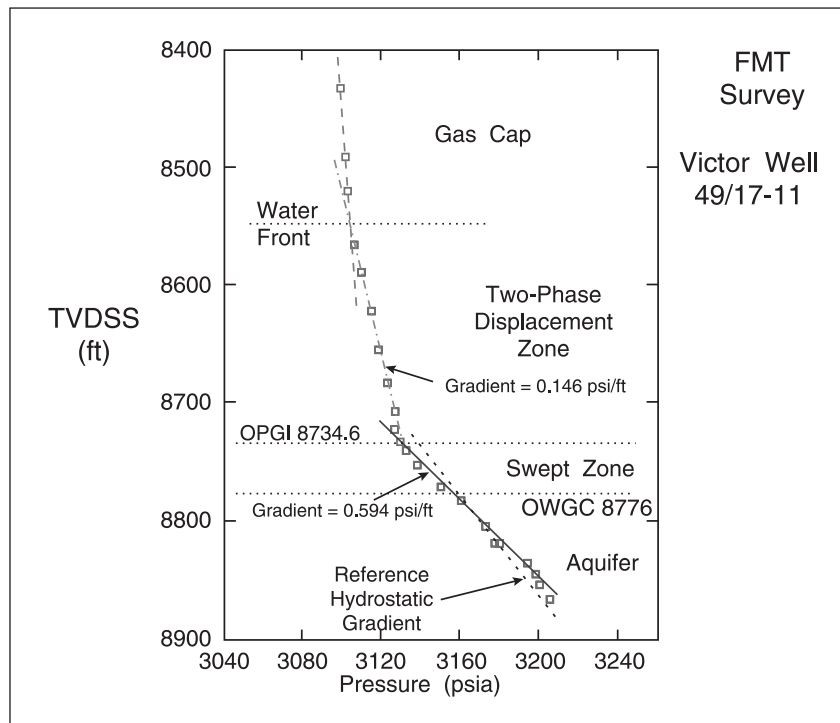


Fig. 10–28. North Sea gas well WFT survey

## Accuracy In Gradient Determination

In the preceding section it has been shown how distributed pressure information can be interpreted for vertical permeability by means of reservoir models. The resolution of the identification process is limited by the errors in pressure and depth measurement denoted  $\sigma_p$  and  $\sigma_h$ , respectively. When pressure or potential differences are formed using measurements from different transducers, e.g., in computing declines like  $(\psi^o - \psi)$  or drawdowns of the form

( $\psi - \psi_{wf}$ ), it is the absolute error that is important. However, in the determination of gradients and potential differences between layers, where all pressure readings are taken in the one trip, it is repeatability that matters and a fixed shift in the calibration is irrelevant. A carefully calibrated strain gauge has an absolute standard error of around  $\pm 13$  psi and a repeatability standard error of around  $\pm 1$  psi. A quartz crystal gauge under WFT field testing conditions, where a perfectly isothermal state cannot be achieved since the gauge is subject to repeated temperature changes, has been shown to have a practical standard error of  $\pm 0.55$  psi. In fact, the optimal solution has been found to run both a high-quality strain gauge and a quartz gauge. The WFT tool is allowed to lie stationary at the casing shoe for about three-quarters of an hour after which time a perfectly isothermal condition is guaranteed. The fixed absolute error of the strain gauge is determined and all the pressure tests are carried out with the strain gauge, which is much less sensitive to temperature changes. The strain gauge is, in fact, calibrated in situ with the quartz crystal gauge.

Given errors in pressure and depth measurement, it is evident that, when the true pressure distribution is linear, the regression slope of a set of data points with scatter will also have a standard error  $\epsilon_m$ , which depends on the number of data points  $N$  and the depth interval  $h_N$  over which they are taken as well as  $\sigma_p$  and  $\sigma_h$ . It is possible to calculate  $\epsilon_m$  by statistical methods given these quantities. The results of such a calculation giving the percentage error in the slope as a function of  $N$  and  $h_N$  is shown in figure 10–29 for  $\sigma_p = 0.55$  psi and  $\sigma_h = 0.9$  ft. These values of  $\sigma_p$  and  $\sigma_h$  represent the best that can be achieved at the present time, and it can be seen from figure 10–29 that gradient discrimination is not very practical over intervals less than about 30 ft thick. It is technically possible to reduce these measurement errors but it is also necessary to consider another source of error.

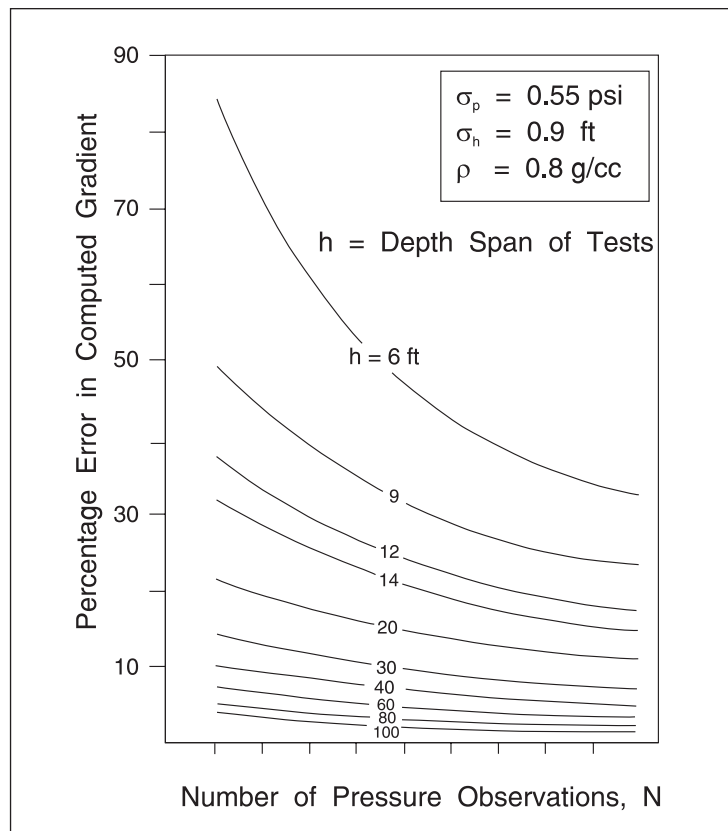


Fig. 10–29. Percentage error in gradient determination

It has been tacitly assumed that a WFT test detects the true formation pressure; in fact, what is measured is the water phase pressure at the sandface in the filtrate invaded zone. In the case of a single-phase invasion process, i.e., when testing in water bearing rock, the sample pressure  $p^s$  exceeds the undisturbed formation pressure  $p^f$  by an amount  $\Delta p_v$ :

$$p^s = p^f + \Delta p_v \quad (10-32)$$

The quantity  $\Delta p_v$  is known as the *supercharging* and is the radial flow pressure drop in the formation around the wellbore associated with the injection of mud filtrate. This has been discussed in the previous chapter. For the purposes of reservoir monitoring,  $\Delta p_v$  is an error in the measured pressure and its magnitude must be assessed.

In an unproduced reservoir where the pressure profile is known to follow hydrostatic gradients, data points having high **SI** values and exhibiting pressures greater than hydrostatic are rejected. It is essential to plot the data at the well site and to compute the spherical permeability for all test exhibiting an observable buildup. Enough tests must be made to obtain a statistically valid slope and reject any supercharged results. It is possible at this stage to determine the value of **SI** at which supercharging becomes a problem.

In a produced reservoir there is no constraint that pressure profiles are straight lines. Especially in tight zones, the formation pressure profiles are complex. Unfortunately, it is in these tight zones that supercharging will occur. It is essential that high observed pressures due to supercharging are not interpreted as reservoir effects. For this reason, a supercharging rejection criterion must be developed either in the appraisal wells or in zones of the produced reservoir known to be at vertical equilibrium. The use of the supercharging index was detailed in the preceding chapter, and this assumes great importance in produced fields where hydrostatic gradients do not occur except in special circumstances. Again, this clearly demonstrates the need for wellsite analysis and plotting of pressure tests. The WFT must be set in different locations until enough tests of low **SI** have been taken. Fortunately, in highly permeable reservoirs, supercharging, diagnosed by long pretest buildup times, is very rarely encountered.

## Use of WFT Interpretation for Reservoir Description

### Introduction

The Repeat Formation Tester was introduced into the field in 1975, and over the ensuing decade the RFT survey became established as one of the most important reservoir monitoring techniques. The operation of the device has been described in the chapter 8, and basically the RFT tool enables the vertical formation pressure distribution in an open-hole observation well to be measured. The design of the RFT has little changed since its introduction, but over the ensuing 10 years there was considerable improvement in the quality of the pressure measurement. In particular, the use of quartz crystal gauges in combination with strain gauges allowed much better absolute pressure accuracy to be achieved. Modern practice focuses exclusively on quartz gauges. Good calibration procedures at reservoir conditions are also important in maintaining measurement quality.

The WFT probe measures the pressure at the sandface of the observation well and this may be different from the undisturbed formation pressure because of the effect of mud filtrate invasion. This phenomenon is known as *supercharging* and it is significant only in very low permeability zones. The mechanism of filtrate invasion and the supercharging effect was considered in detail by Phelps.<sup>8</sup> The amount by which the sandface pressure (measured by WFT) exceeds the undisturbed formation pressure is principally controlled by the mud fluid loss rate and the local permeability; both of these quantities are extremely difficult to estimate. In the limit, the ability of the WFT to detect true formation pressure is constrained by this effect rather than by gauge accuracy. The problem of supercharging is easier to handle in the case of an unproduced reservoir where it is known that the true pressures should fall on hydrostatic gradients. In the case of a produced reservoir where no such constraint applies, the quality control parameter for each pressure observation is the measure of local permeability provided by the transient or steady-state analyses of the test buildup or drawdown. This aspect is treated in several references<sup>9, 10, 11</sup> and has been discussed at length in the previous chapters.

The application of distributed pressure measurement can be divided into two quite distinct categories—unproduced and produced fields. In exploration and appraisal wells in virgin reservoirs, the objective is to delineate the hydrostatic pressure regimes corresponding to gas, oil, and water (where present) and hence to determine the phase contacts from the intersection of the measured pressure gradients. These WFT surveys, of course, fix the initial reservoir pressure. In the case of produced fields, the objective of WFT surveys in new development wells is to measure the response of the reservoir to production. Both the pressure decline from the initial value and the pressure differences between layers are important.

In this section attention will be concentrated on the elucidation of reservoir structure from WFT distributed pressure measurements in new development wells in produced fields. The first such WFT runs were carried out in the Marun field in Iran in 1976. Two of these surveys are shown in figure 10–30, where the parabolic pressure profile of tight zones producing by crossflow into adjacent permeable zones are evident. Differences in pressure between the layers of the order of 1,000 psi were observed, and it was realized that effective vertical permeabilities were very much smaller than had been appreciated. These first WFT pressure surveys in the Marun field, in retrospect, constitute a very significant event in the development of reservoir engineering. This was the first time a distributed pressure profile through a producing reservoir had been obtained and the vertical variation in pressure was much greater than had been anticipated. A further feature of the Marun data was that the pressure profiles in the two wells 1½ km apart were virtually identical, i.e., the areal variation of pressure was small. This observation was used to infer good horizontal communication through the reservoir in the permeable layers. Already the foundation of the application of the WFT in produced fields had been established, viz., vertical pressure profiles can be used to identify horizontal permeability barriers and the areal variation of pressure is indicative of continuity between wells. However, it was not possible to infer permeabilities from the Marun data because a suitable reservoir model was not available. The quantitative interpretation of WFT pressure information requires a layered reservoir simulator whose description parameters can be adjusted until the predicted and observed pressures (at time and locations corresponding to each development well surveyed) are matched.

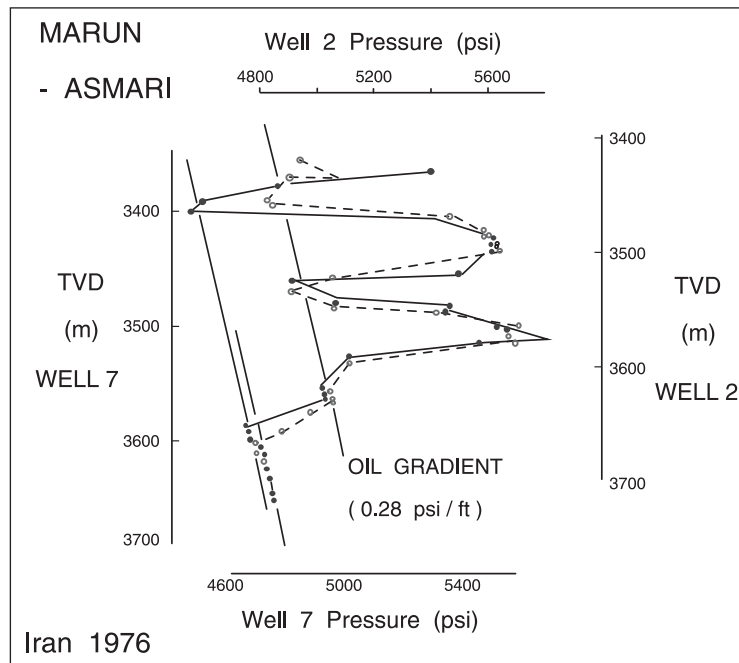


Fig. 10-30. Marun field WFT surveys

Although the pioneering WFT data from a producing field originated in Iran, it was the development of the North Sea reservoirs that demonstrated the real merit of distributed pressure measurement as a reservoir monitoring technique. The North Sea conditions were almost ideal for WFT applications. The majority of the reservoirs are highly undersaturated and the initial production mechanism is expansion of the oil in place, i.e., depletion drive. Many of the fields are overpressured and natural water drive is weak. Since the wells are very productive, it is possible to produce the fields at a high initial rate typically around 10% of recoverable reserves per annum. Consequently, the pressure declines rapidly and in heterogeneous reservoirs large pressure differences develop both vertically and areally. Pressure maintenance by water injection is eventually implemented to arrest pressure decline before the bubble point is reached. However, because of the high degree of undersaturation, a significant period of primary depletion is acceptable. During this time, producing wells are being drilled as quickly as possible and an WFT survey is made in each new development well. The observed distributed pressure data represents the response of the reservoir to production. The monitoring of reservoir response also includes the running of production logs in the producing wells so that layer flows are measured as well as the layer pressures from WFT surveys. This period of relatively simple primary depletion is the optimum time to infer reservoir structure and what is being practiced may be termed *reservoir testing*.

The development of the North Sea coincided with the advent of numerical simulation models and computers large enough to handle three-dimensional three-phase problems. It is axiomatic that a layered reservoir model requires layer flow and pressure information for realistic history matching. Reservoir testing can therefore be identified with the adjustment of reservoir description parameters so that observed layer flows and pressures match those predicted by the model. Information from other sources, particularly three-dimensional seismic surveys, special core analysis, well testing, and geological modeling, is also essential to this identification process.

## Early field examples of RFT applications in the North Sea

The important role played by the WFT in modern reservoir engineering was highlighted at the 1980 European Petroleum Conference in London where five papers were presented all emphasizing the application of distributed pressure measurement. These papers referred to different reservoirs (Piper,<sup>6</sup> Montrose,<sup>3</sup> Thistle,<sup>1</sup> Brent,<sup>12</sup> and Dunlin<sup>4</sup>) and they represent an excellent review of the early use of WFT data. Two of them were particularly significant and introduced innovative concepts into reservoir engineering. The paper by Bishlawi and Moore<sup>3</sup> on the Montrose field was the first to demonstrate how the effective vertical permeability could be found by matching a three-dimensional simulation model to the observed distributed pressure data. Fifteen development wells drilled between April 1977 and November 1979 were surveyed with the WFT, and the progressive decline in reservoir pressure and the increasing differential between the bottom water aquifer and the oil zones are shown in figures 10–31 and 10–32. In order to match simulator layer pressures (at the location and time of each survey) to the WFT measurements, the effective vertical permeability had to be in the range 0.2–0.002 md—about a factor of 100 less than the anticipated value based on core analysis.

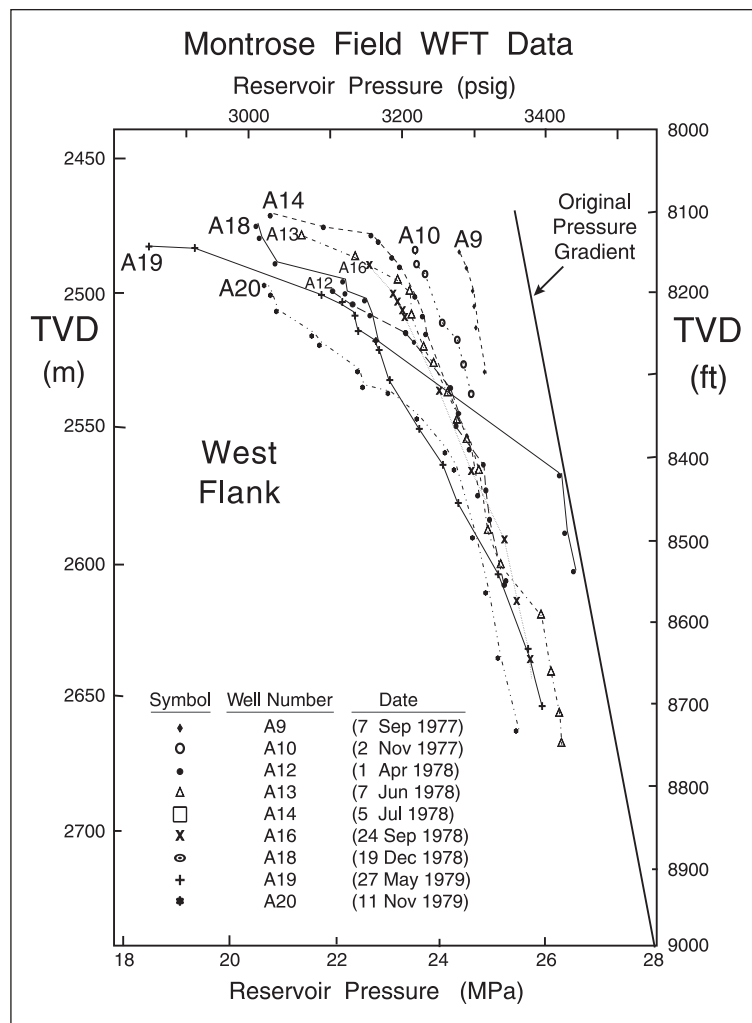


Fig. 10–31. Montrose field WFT surveys (West Flank)



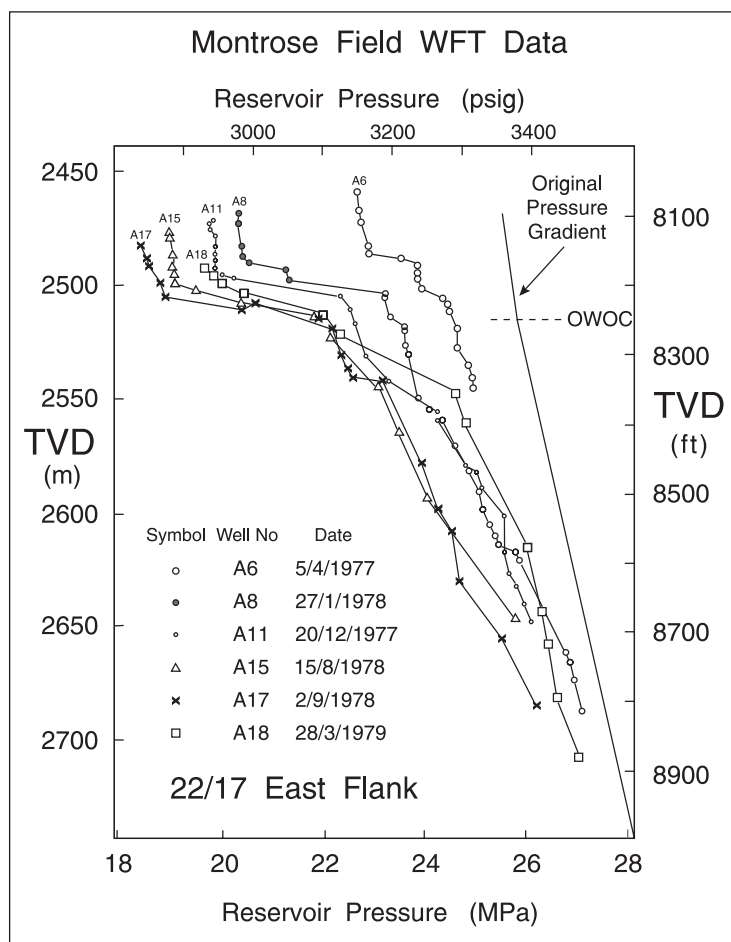


Fig. 10–32. Montrose field WFT surveys (East Flank)

It is now well established that the effective vertical permeability in a reservoir can be determined only by an in situ test; this is a result of the complicated macroscopic nature of vertical flow especially when shales are present. Core permeabilities are of very little use in assessing the average vertical permeability based on a rather large area, e.g., a typical grid block in a reservoir simulation study. Vertical permeability can also be identified by interference testing, either vertical pulse testing in one well or transient WFT interference testing between two wells, but the reservoir test as described by Bishlawi and Moore is the most widely used technique. It is currently standard practice in history matching of reservoir simulators to obtain effective vertical permeabilities in this way.

The second paper of major importance in establishing the foundation of WFT usage was the reservoir engineering study of the Thistle field published by Nadir.<sup>1</sup> The Thistle field is one of the many Jurassic reservoirs in the North Viking Graben which is the most prolific area of the North Sea both in the U.K. and Norwegian sectors. All these reservoirs have similar characteristics in that they are highly faulted and comprise the same basic sand sequence denoted Brent (Broom, Rannoch, Etive, Ness, and Tarbet). A typical fault map of a North Viking Graben reservoir is shown in figure 10–33; this refers to the Murchison field and is taken from the paper by Massie.<sup>13</sup> The various sands have widely varying properties, with the Etive constituting a very high permeability layer in all reservoirs.



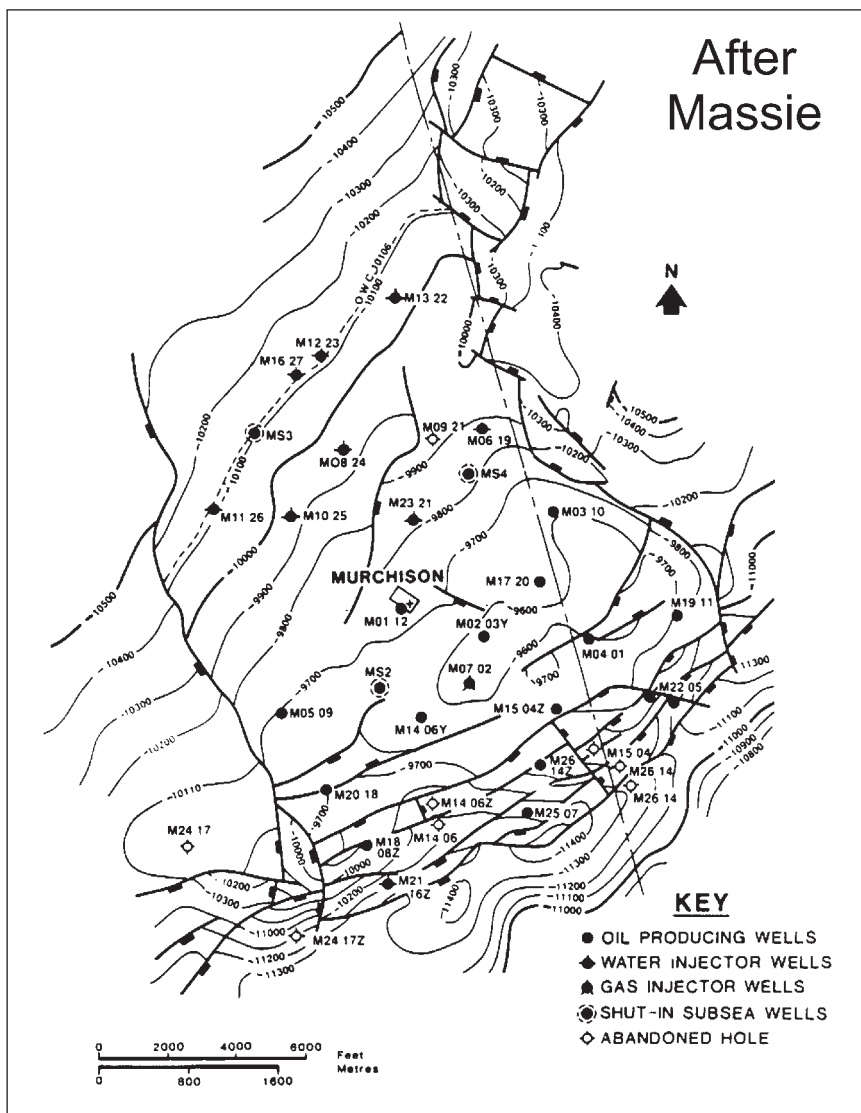


Fig. 10–33. Murchison field fault map

An WFT survey in a Thistle development well drilled after approximately 9 months of production is shown in figure 10–34 (taken from fig. 6 of Nadir’s paper referring to well 09A). The B sand (Etive/Upper Rannoch) had already depleted by 1760 psi from the initial pressure (6,060 psig) and the vertical pressure profile indicates that very large pressure differences have developed between the sand units. However, the B<sub>1</sub> B<sub>2</sub>—Upper Rannoch and Etive—sands are seen to exhibit a continuous oil hydrostatic gradient (vertical pressure equilibrium) and at the time this was presumed to imply good communication between these layer. The same phenomenon was observed in the Dunlin field [fig. 6 in reference (4) and presented here as figure 10–38], and in the paper on Dunlin by Van Rijswijk et al.<sup>4</sup> it is explicitly stated that “since the pressure measurements indicated good vertical communication between Etive and Rannoch . . .” Subsequent analysis of field performance was to prove that this assertion was erroneous and there was found to be a barrier between the Etive and Rannoch sands; this will be discussed in detail later. It was also pointed out that an WFT survey such as the one shown in figure 10–34 was a good basis for the zonation of the reservoir, and in the Dunlin field development<sup>4</sup> plan the Etive and Rannoch were lumped together at that time (1980).

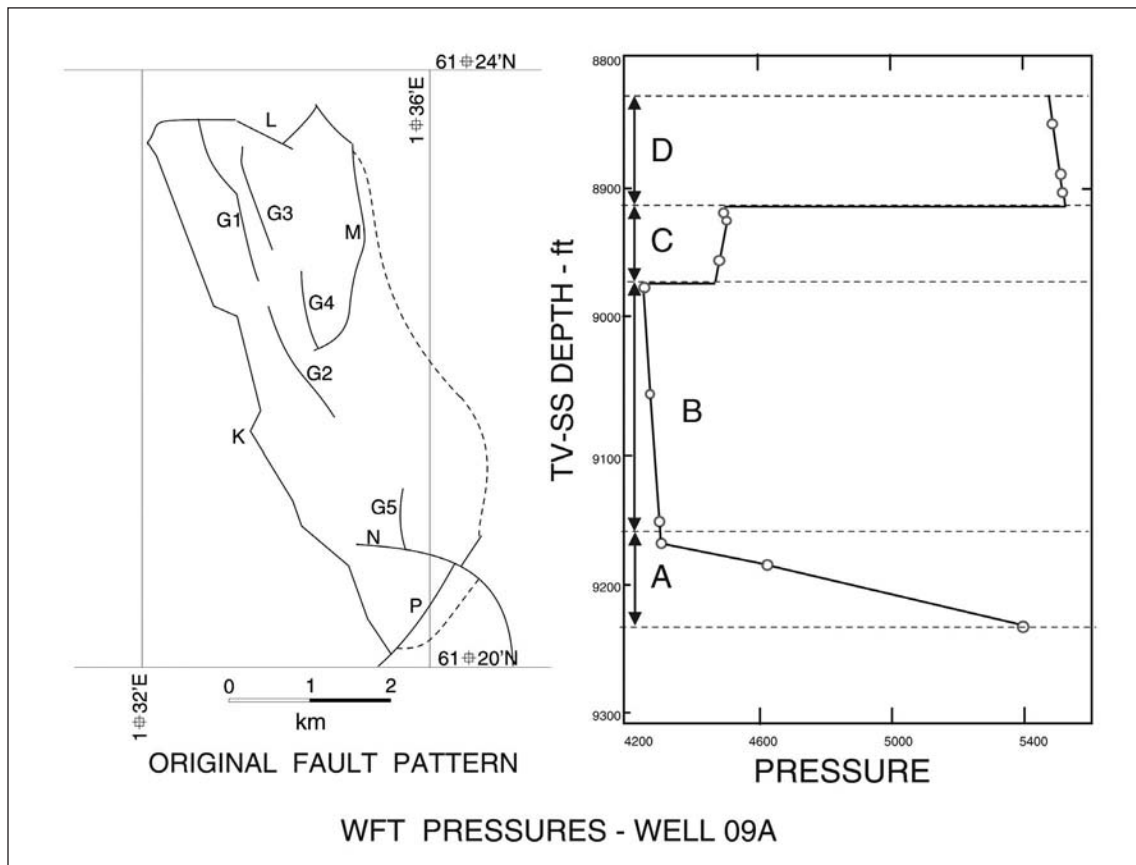


Fig. 10–34. Thistle field WFT survey (Well 09A)

The vertical pressure profile from an individual WFT survey can show up the major horizontal permeability barriers and tight zones and when the data is interpreted by history matching a layered reservoir model, quantitative estimates of vertical permeability can be obtained. This is one of the two main applications of distributed pressure measurement. However, it is not only pressure contrasts between layers at particular times and locations (corresponding to the new development wells under survey) that are important. The decline in pressure from the initial value is a good indicator of the pore volume being drained when the production mechanism is primarily expansion of oil-in-place. During the Thistle development it was found that the decline in pressure (measured with WFT surveys) of wells in the western part of the field was much greater than projected. The field is dipping towards the east where lie the WOC and the existent water injection wells. The rapid decline in pressure of the updip western section, where the producing wells were concentrated, could only be explained by the presence of a mid-field sealing fault dividing the reservoir into eastern and western fault blocks. This fault was introduced into the reservoir description, and the simulation model was then able to reproduce the areal variations of pressure over the field. In figure 10–35, the possible existence of the fault is shown as a dotted line and in figure 10–36 the fault appears as a full line on the fault map showing the acceptance by the geologists that pressure can be used to determine the presence of a (transcurrent) fault.

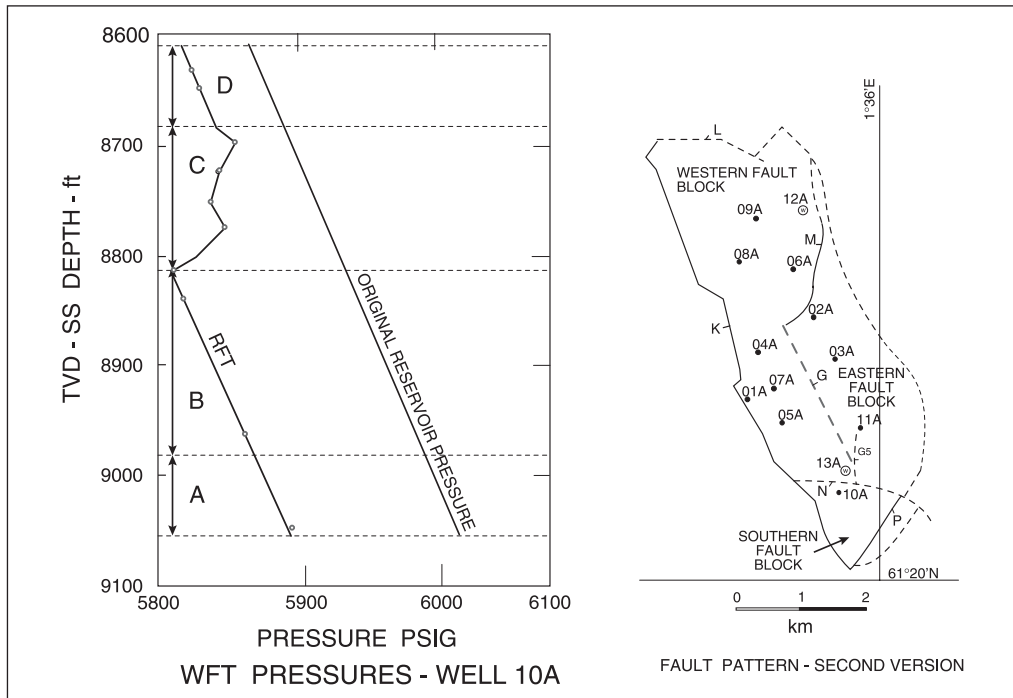


Fig. 10-35. Second Thistle field WFT with possible occurrence of central fault indicated

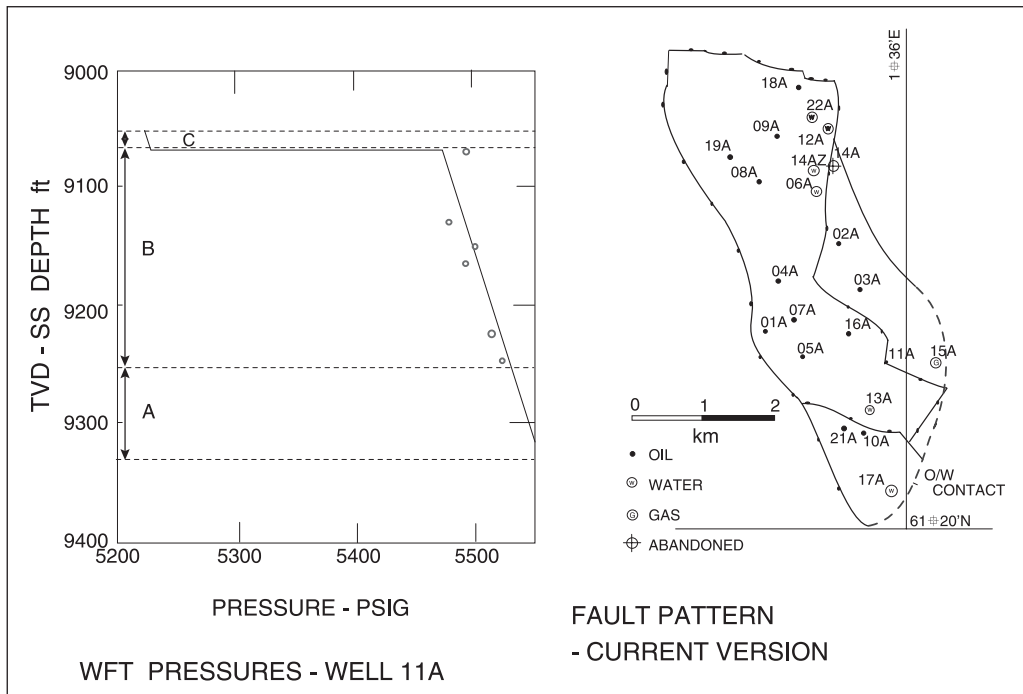


Fig. 10-36. Third Thistle WFT survey indicating acceptance of fault presence

This fault has never been detected from seismic surveys even with recent three-dimensional processing. The presence of the fault was deduced from pressure data alone, and this was a major success for reservoir pressure monitoring with the WFT. The original field development plan had envisaged peripheral edge water injectors along the WOC on the eastern flank of the field. Once the existence of the central fault had been proven, the development plan was

radically altered with new injection well locations in the western fault block. The paper by Nadir<sup>1</sup> established the second main application of distributed pressure measurement—the identification of vertical permeability barriers, i.e., faults from the areal variation of reservoir pressure. Again the quantitative method of interpretation is the reservoir simulation model and as information, including 3-D seismic, has improved more and more faults have become apparent. However, not all of these faults are sealing and often absence of areal pressure variation indicates that particular faults have good communication across them.

An interesting sequel to the discovery of the Thistle central fault has recently been reported by Bayat and Tehrani.<sup>14</sup> In April 1979, the pressure difference between the eastern and western fault blocks had increased to 2,500 psi. At this point the wells in the western block suddenly received pressure support not attributable to water injection and which could only be explained by the breakdown of the central vertical barrier. The dramatic increase in pressure of about 1,000 psi over a 3-month period was due to fault activation, although this phenomenon was not well understood at the time. From this time onwards, the barrier had to be removed from the simulator reservoir description to get a history match. The physical explanation of this event may be fracturing along the fault plane or displacement of clay particles plugging the near-fault zone.

Two further WFT surveys from Thistle wells are shown in figure 10–37, where the pattern of depletion is further confirmed with the Etive and Rannoch sands at pressure equilibrium, i.e., a hydrostatic oil gradient seen over them although the field is under production. Very similar observations were made concerning the Dunlin field with a typical WFT survey shown in figure 10–38.

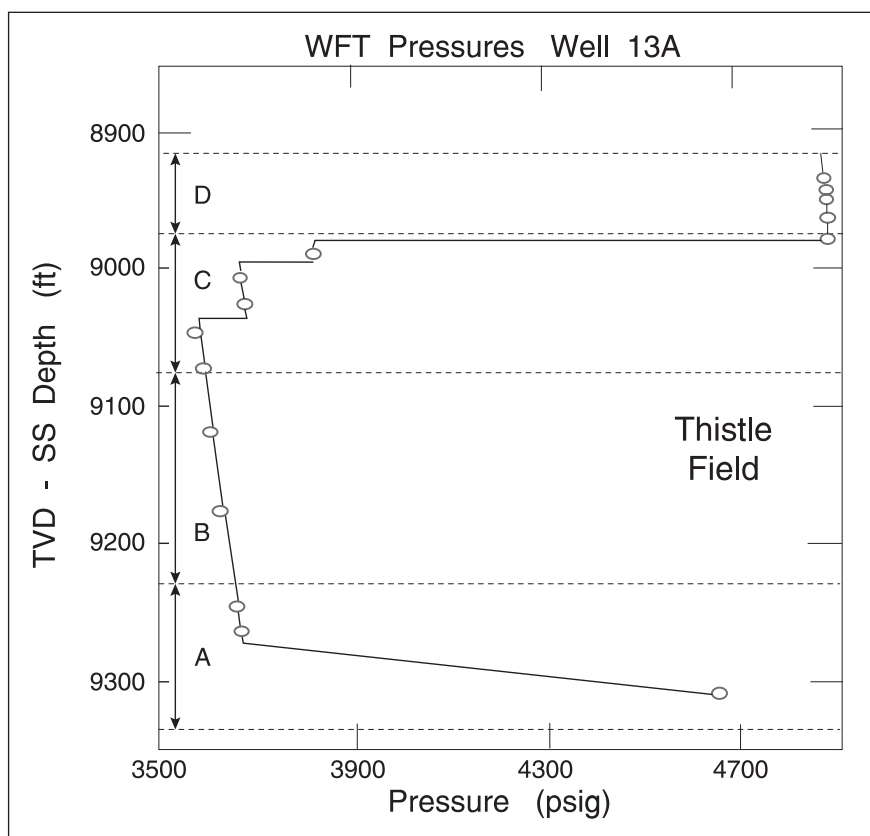


Fig. 10–37. Additional Thistle WFT surveys

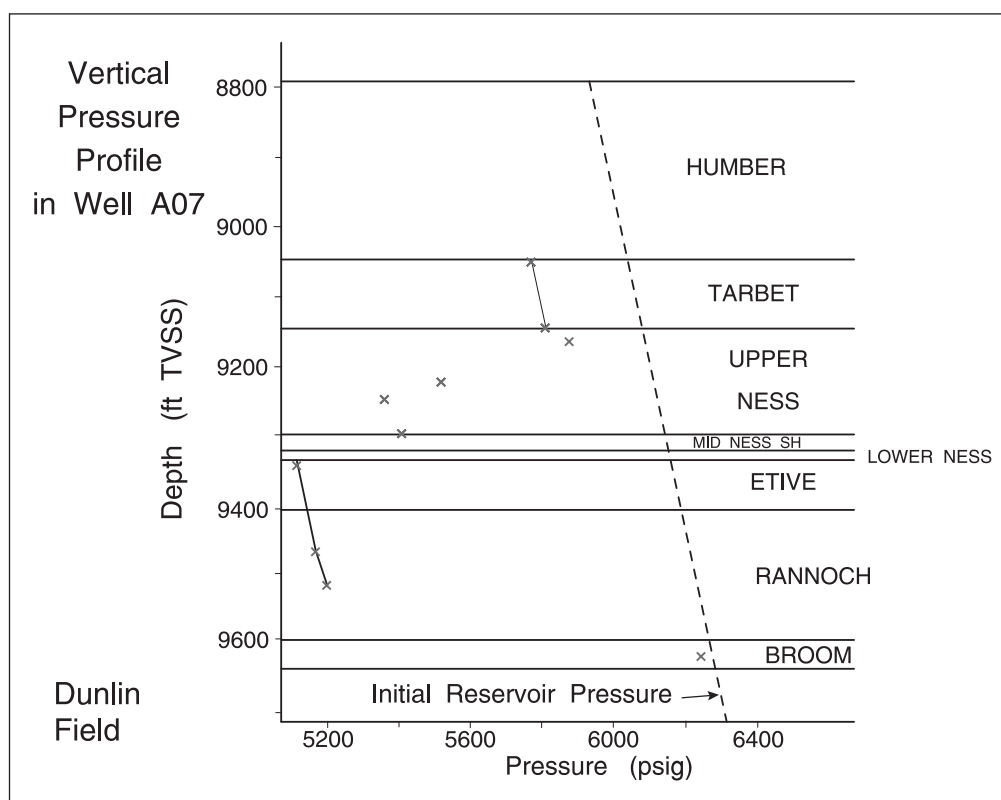


Fig. 10–38. WFT survey from the Dunlin field

The condition of vertical pressure equilibrium, where the frictional (Darcy) components of pressure gradients are negligible, is illustrated in figure 10–39, where two separate wells exhibit the same hydrostatic oil gradient; this behavior indicates good communication in the reservoir between the wells although it is not completely conclusive evidence. The situation with two separate fault blocks depleted to different pressures but still exhibiting internal vertical equilibrium is illustrated in figure 10–40. These diagrams serve to show the importance of absolute pressure accuracy in formation tester measurements, and present versions of these devices use quartz crystal transducers so that very good absolute accuracy is guaranteed.

A final field example from the North Sea will be used to highlight the way pressure information can lead to improved reservoir description. This example has not previously been published and refers to the Beryl field<sup>15</sup>—a dipping, highly permeable reservoir illustrated in figure 10–41. In fact, the permeability is so high that vertical pressure equilibrium (as discussed earlier in this chapter) should exist throughout the system, i.e., negligible deviation from a common hydrostatic gradient throughout the field. The reservoir description from the geological model is shown in figure 10–42 and an WFT survey was run in two wells 3,500 ft apart more or less at the same time. Three separate reservoirs had been postulated and, if good communication existed in each of the pressures in a given reservoir from both wells should lie on the same hydrostatic oil gradient. For the major reservoir C, this is indeed the case as shown on figure 10–43 with points 7, 8, 9, and 10 colinear with E, G, H, I, and J; this confirms communication. However, for the smaller units 4, 5 and D, E and 1, 2, 3, and A, B, C are decidedly not on the same gradient and exhibit quite different pressure regimes. The reservoir description accordingly had to be modified as shown in figure 10–44; this innovative piece of reservoir engineering was conducted by Rafi Al-Hussainy and Lou Steele.

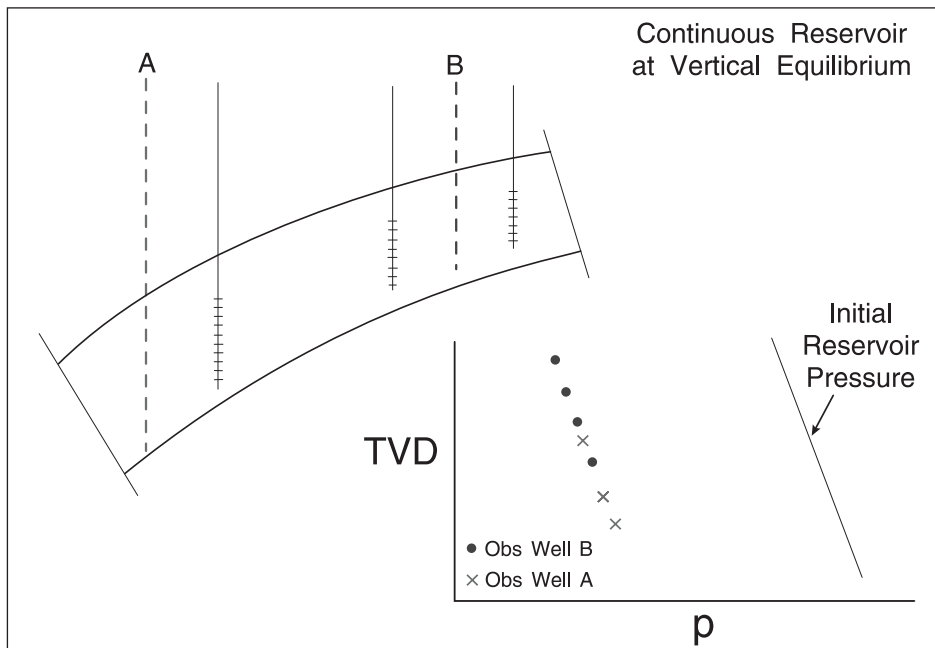


Fig. 10-39. Two wells in a field at vertical pressure equilibrium

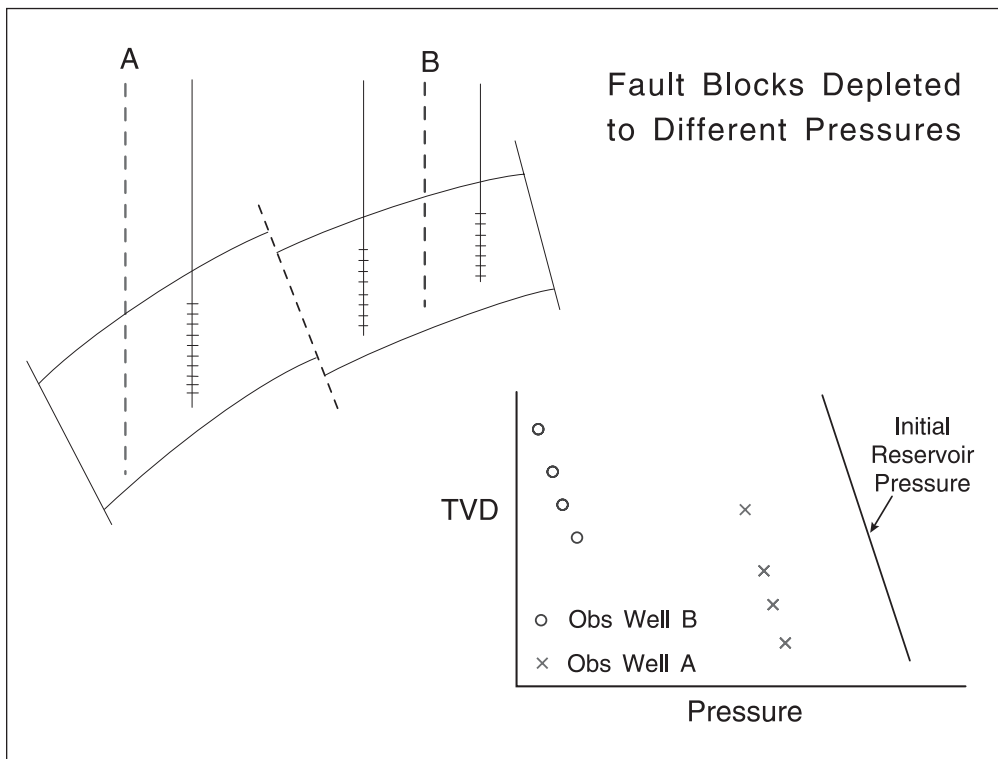


Fig. 10-40. Fault blocks depleted to different pressures but still at internal vertical equilibrium

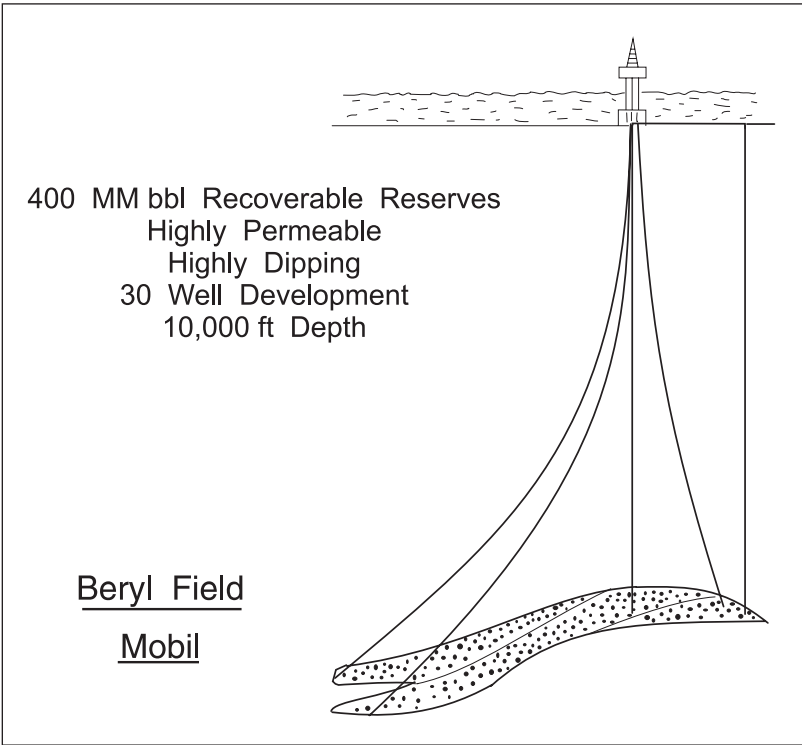


Fig. 10-41. Diagrammatic representation of the Beryl field

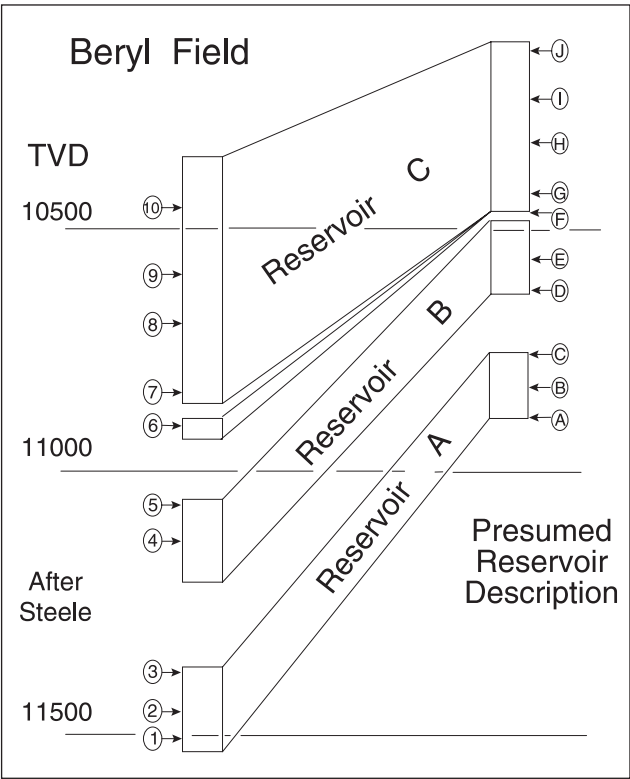


Fig. 10-42. Beryl field original reservoir description

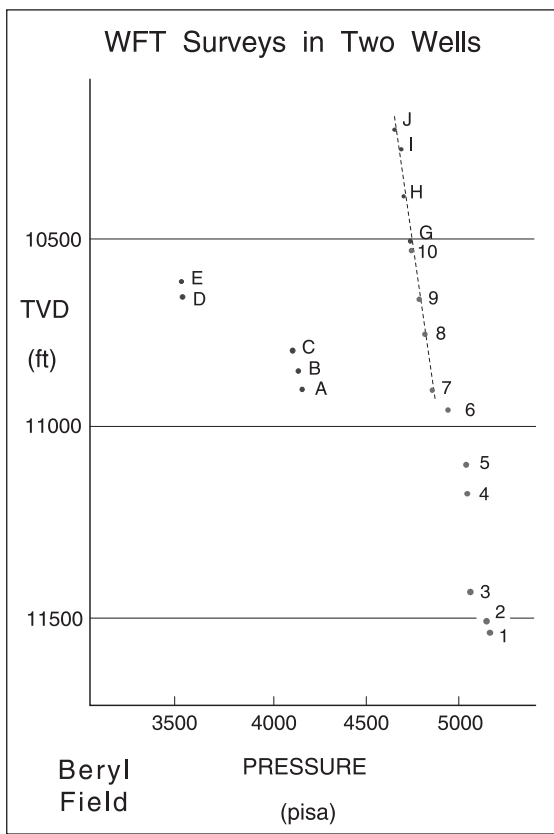


Fig. 10-43. Beryl field WFT surveys in two wells

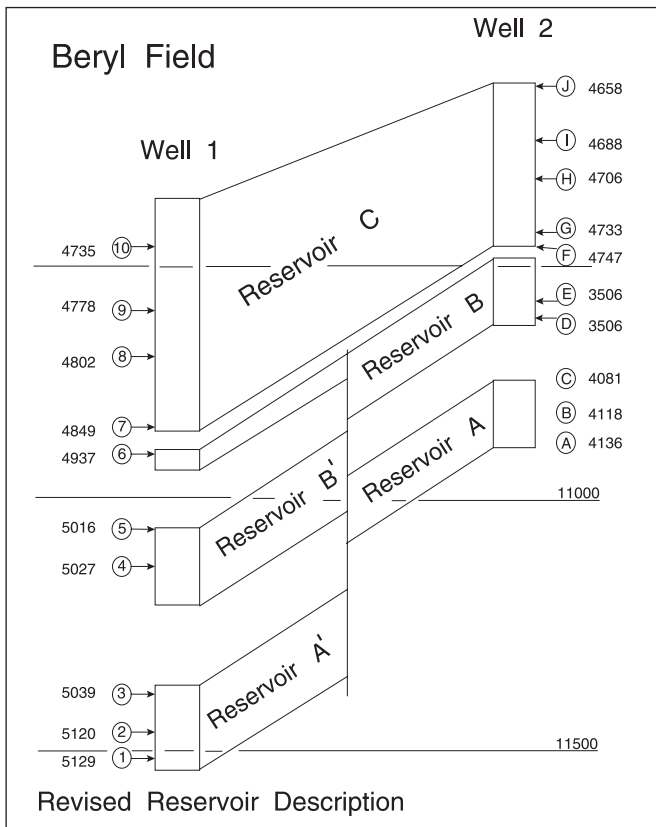


Fig. 10-44. Revised reservoir description



The major unit C is apparently thick enough that even after faulting good communication still exists. However, the smaller units have been displaced to such an extent that communication is disrupted. Although figure 10–44 implies connection between reservoirs B and A, the difference in pressure between points 4, 5 and A, B, C is evidence that this fault plane is either sealing or of very low transmissibility. Again, faulting has been detected on the basis of distributed pressure information.

This kind of information is so important for reservoir engineering purposes that in nearly every well drilled in the North Sea a distributed pressure survey is made. Figures 10–42, 10–43 and 10–44 had a huge effect on the acceptance, indeed imperative requirement, of the WFT data by reservoir engineers and these diagrams were much used by marketing personnel at the time (especially Gene Kaufman).

Thus the objective of reservoir monitoring in the early stage of field development can be stated succinctly as the identification of the effective permeability of horizontal barriers (tight zones such as micaceous streaks, shale layers, stylolites, dolomite streaks, etc.) and vertical barriers (sealing or partially communicating faults) by history matching a reservoir simulator to distributed pressure and flow measurements. Here the terms horizontal and vertical have been used loosely to distinguish between the two quite distinct types of impedance to communication. Note, however, that the area for flow across predominantly horizontal barriers is much greater than across predominantly vertical barriers. Again it should be emphasized that the inference of reservoir structure from pressure and flow behavior is best carried out early in the field like during the period when the dominant production mechanism is oil expansion. The presence of a gas cap in no way precludes this activity as witnessed by the WFT surveys in the Brent field described by Bath<sup>12</sup> and the extensive use of the device on the Prudhoe Bay reservoir. The simulation model, of course, becomes more complex and the identification process may be less definite than in the undersaturated case; in addition, the observed pressure changes may be smaller because of the high gas cap compressibility. Interestingly, one of the earliest assessments of effective permeability of horizontal barriers was the study<sup>16</sup> of the West Seminole field in Texas, where the objective was to predict the degree of loss of reserves to the gas cap caused by water injection into the oil column. In this case, the strength of a barrier separating the gas cap from the oil zone was the key factor and it was identified by very limited layer pressure data obtained by selective interval well testing. This study graphically demonstrated the need for distributed pressure measurement; if the WFT had been available from monitoring layer pressures, the problem could have been resolved with much greater precision.

The exercise of identifying reservoir structure is really part of field appraisal. Since appraisal wells are now often used as producers (with subsea completions) and the first platform development wells are used for appraisal purposes, there is little distinction between them. Up to now, information on the produced field has only been obtained after the platform has been completed and the development wells produced. Even when some wells are predrilled and connected via a manifold, production is not commenced until the platform is ready. The growing emphasis on predrilling wells for maximum early production means that well locations are chosen before any pressure depletion information is available. There is, therefore, a high risk that wells may be in the wrong place; in particular, proposed injectors may not support producers because of faulting. Hence there is a growing awareness of the importance of reservoir limit testing where an appraisal well is flowed for a considerable time through a floating production system to a tanker. The information gained from such an extended draw-down test is greatly increased if a second well can be used as an observation well for distributed pressure measurement. The future development of marginal fields will depend very much on this type of approach.

# 11

## Production Logging and Layered Systems

---

### Introduction

In chapter 10 it was pointed out that distributed pressure measurement in observation wells using wireline formation testers (WFTs) should be accompanied by distributed flow measurement in the active producers or injectors. Whether interpretation is carried out using a relatively low level model such as the complex material balance or a full reservoir simulation, it is axiomatic that layer pressure data must be complemented by layer flow data. The process of distributed flow measurement in a flowing well is, of course, known as *production logging* (PL), and the contraction PLD—production logging device—will be used as a generic descriptor for spinner type PL tools. The use of PL has increased dramatically over recent decades as reservoir engineers have come to recognize the importance of such measurements in understanding reservoir behavior. The output of a PLD survey is a flow profile that shows the proportion of the total flow emanating from each zone of the reservoir. PL is important where thick reservoirs are produced commingled into a common wellbore; a PLD survey is then the only way of assessing individual layer performance. The mechanics of running a spinner flow meter survey, the calibration of the device using up and down passes, and the computation of the flow profile will not be treated here. An excellent review by Hill<sup>1</sup> gives details of the practical aspects of PL methodology. In the context of reservoir engineering application of PL measurements, perhaps the main point to make is that the accuracy of the measurement is much better when single-phase flow conditions exist in the wellbore, i.e., gas wells, water injection wells, and oil wells, where the bottom-hole pressure is above the bubble point. In these circumstances, quantitative use can be made of the distributed flow information in terms of identifying layer properties such as productivity index (PI). When two-phase conditions exist—particularly in deviated wells—the errors in distributed flow measurement become quite severe; unfortunately, the service companies' promise to introduce new-generation PL devices has not yet been fulfilled. Pressure can be measured with great accuracy, but the determination of down-hole flow is much less precise. However, Darcy's law shows that the calculation of permeability, for example, requires knowledge of both pressure and flow rate, and at the present time the weak link in the use of distributed flow information is the poor resolution of PLDs.

In undersaturated reservoirs, the important period of primary depletion, when the reservoir is drawn down and pressure differences allowed to develop, will also coincide with single-phase conditions in the wellbores of oil producers. Hence, the WFT pressure data in new development wells are accompanied by good-quality PLD flow data from existing producers. After water breakthrough occurs, the main objective of PL is to determine in which layers water entries are occurring; this information is also extremely important in understanding reservoir internal structure. In two-phase PL interpretation, the flow profile of both phases is measured but as previously mentioned, with much less precision than the single-phase case.

Thus, distributed flow measurement is complementary to distributed pressure measurement and this information takes the form of a flow profile determined by up and down passes of the PLD. A typical single-phase flow profile is illustrated in figure 11–1. In a thick reservoir with commingled production from multiple zones or layers into a common wellbore, the flow profile is controlled by the following factors:

- permeability distribution;
- skin factor distribution;
- pressure distribution.

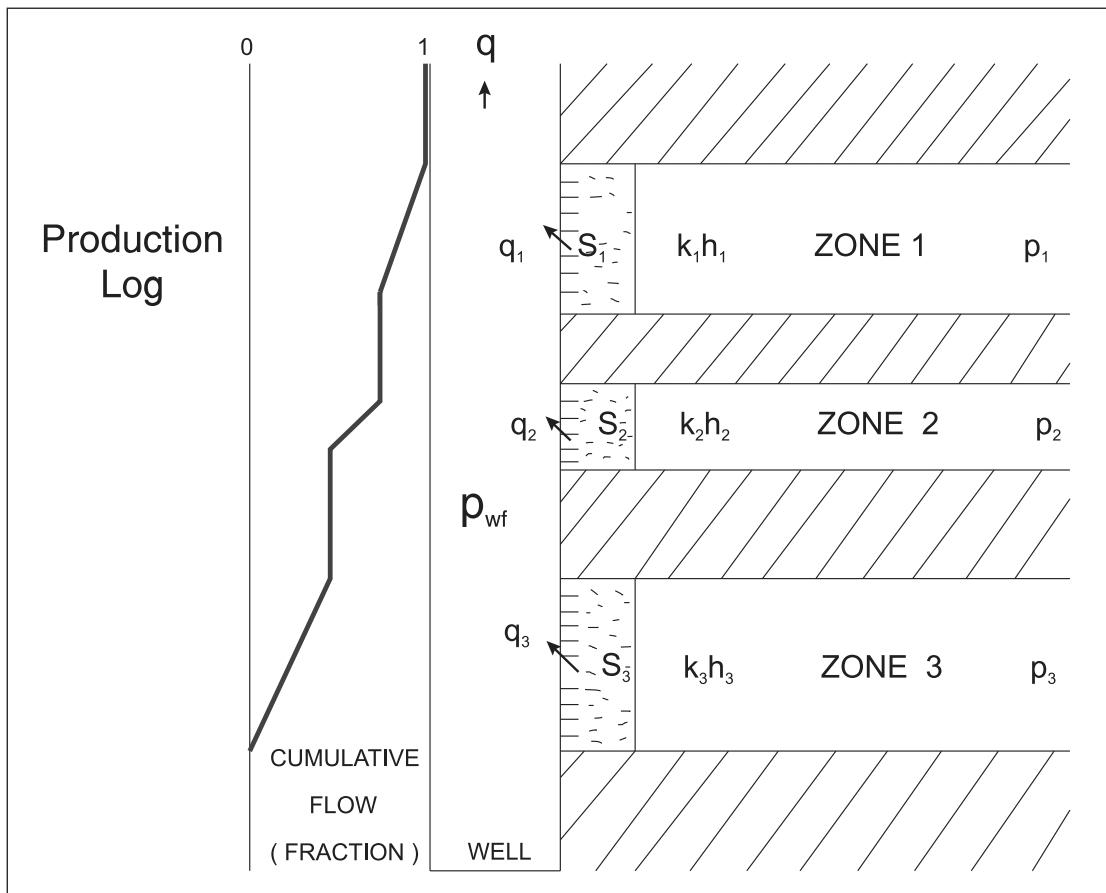


Fig. 11–1. Typical flow profile in a commingled reservoir

A schematic reservoir description for a commingled system is shown in figure 11–2 with each layer assigned its own permeability, skin factor, and pressure. The objective of layered well testing

is to determine these three quantities for a system composed of layers separated by horizontal no-flow barriers. In this chapter, the use of straightforward up and down passes of the flow meter, i.e., the flow profile, will be reviewed; the complicated subject of the design and interpretation of layered well tests involving the measurement of simultaneous rate and pressure transients is treated separately in chapter 19 of *Well Test Design and Analysis* (addendum). The problem of poor resolution of spinner flow measurement places a practical limitation on what can be achieved in terms of identifying reservoir structure, and it is necessary to restrict flow detection to the contribution of major zones only. The spinner device, in fact, registers cumulative flow and this signal has to be differentiated to obtain individual layer rates.

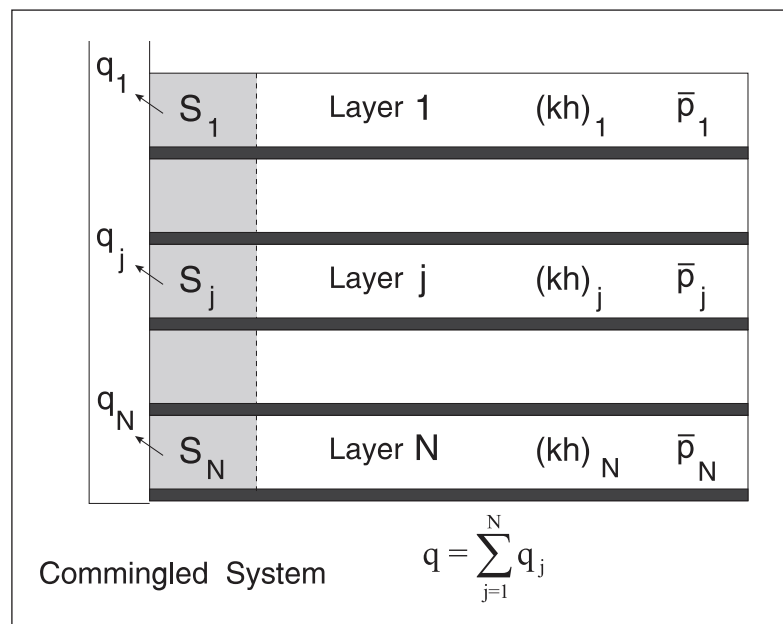


Fig. 11–2. Schematic commingled reservoir description

Some of the reasons for running production logs are to find answers for the following questions:

Decisions on workover:

- Is the well performing below its potential due to excessive skin?
- Which zones (if any) would benefit from reperforation?
- Are there any problems with the completion such as channelled cement and leaks in tubing, casing, or packers?

Reservoir management:

- Are the layers producing or accepting fluid at a rate compatible with good reservoir management (profile control)?
- Is there detection of water or gas entries?
- Is there tuning of single well models in reservoir simulators?

The extensive use of PL is the natural consequence of the decision to opt for commingled production.

An interesting reservoir situation is illustrated in figure 11–3, where the possible effect of faulting on reservoir communication is apparent. The major zone, 3, is of sufficient thickness that there is still partial juxtaposition across the fault plane and communication exists between the producing and injecting well. However, although juxtaposition is present in the two thin layers, 1 and 2, communication has been inhibited by diagenesis; this form of complexity in which the thin layers have been effectively blocked is quite a common occurrence and leads to severe problems in waterflooding the reservoir. Initially all three layers will produce according to their individual PI as shown in the well performance diagram in figure 11–4. However, as the well is produced, the layers 1 and 2 will deplete more rapidly than layer 3 which has a much larger pore volume. In addition, layers 1 and 2 are not supported by the injection well, whereas layer 3 pressure will be maintained since communication to the injector is present. PL carried out on a regular basis will show the contribution of layers 1 and 2 gradually decreasing with time. When water breaks through in layer 3, the well bottom-hole pressure will rise and layers 1 and 2 will stop producing as shown in figure 11–5.

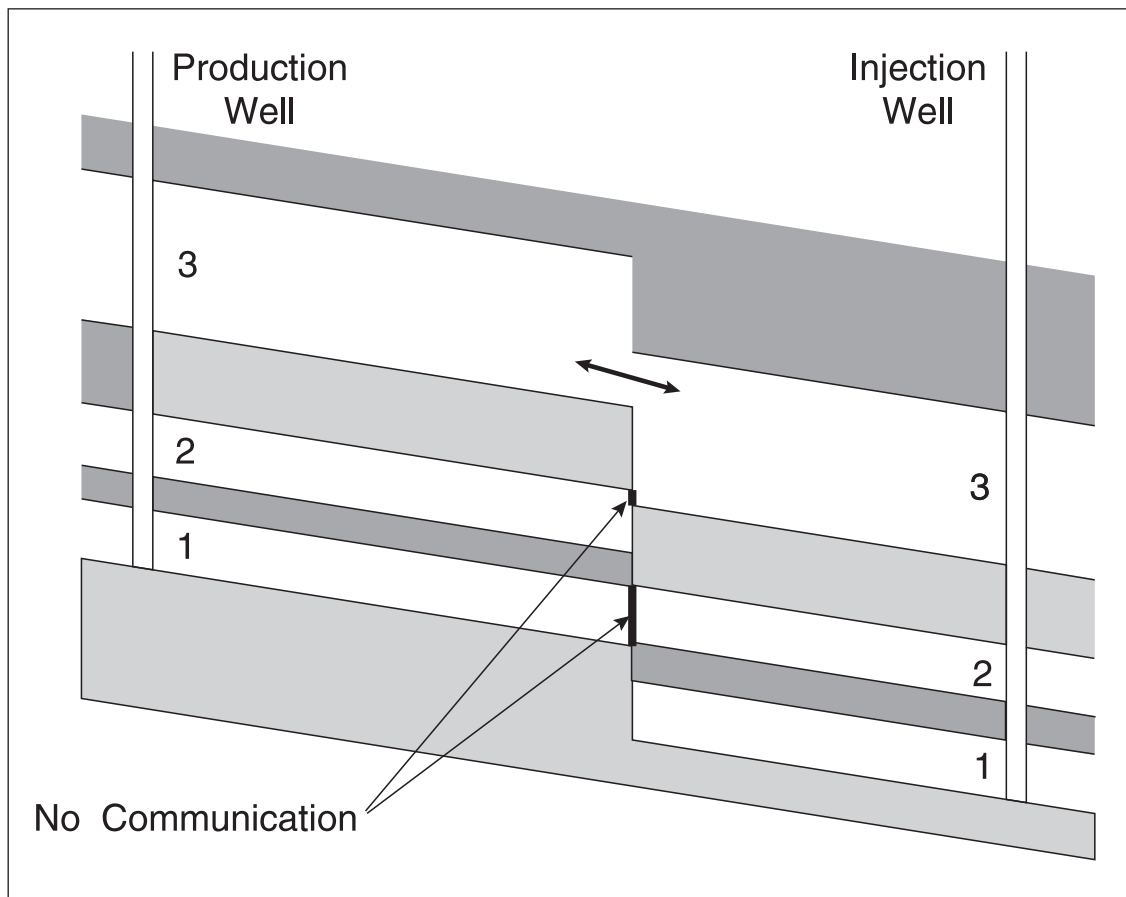


Fig. 11–3. Reservoir description illustrating lack of communication in thin layers

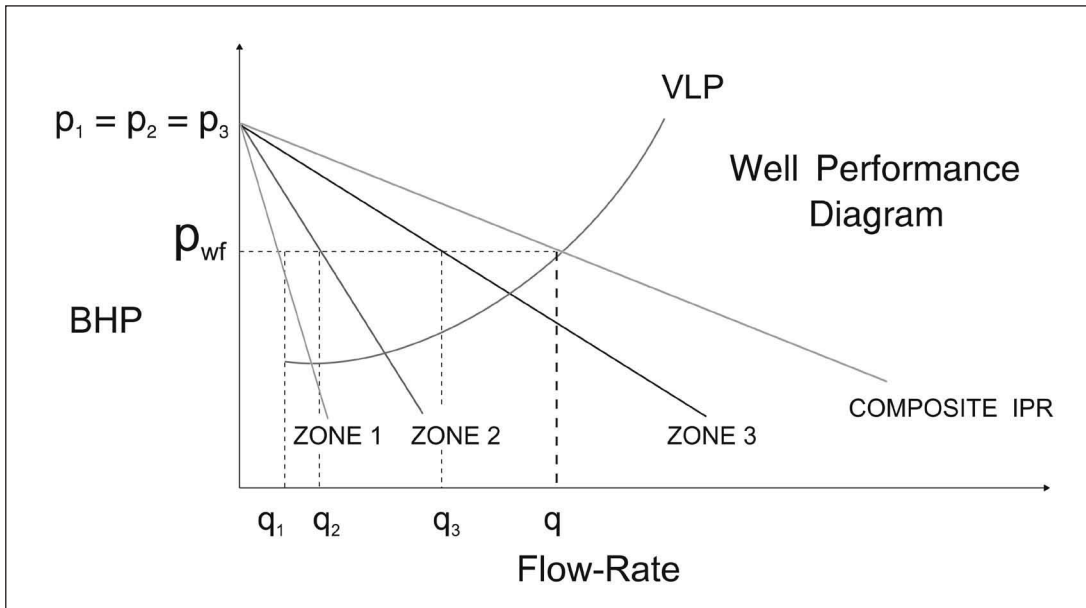


Fig. 11-4. Well performance diagram with three layers at the same initial pressure

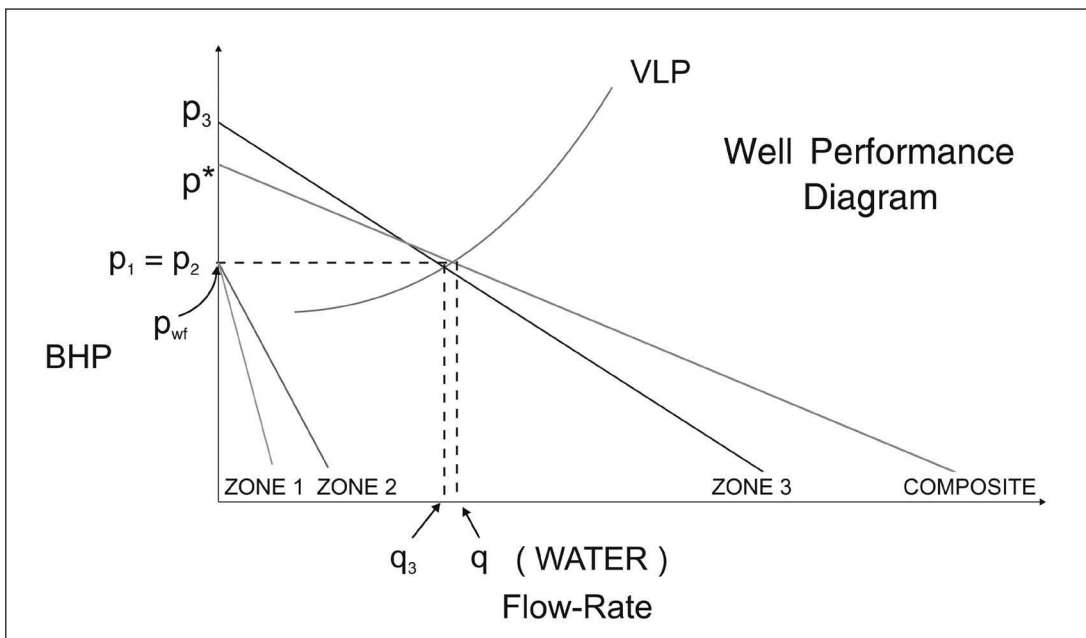


Fig. 11-5. Unsupported layers at zero flow dynamic equilibrium with bottom-hole pressure

An interpreted production log in a well producing oil and gas is shown in figure 11-6, where it is clear that the upper group of perforations is hardly flowing. With the well cut back on the small choke, it also appears that the second and third top groups of perforations are accepting fluid, i.e., wellbore crossflow is occurring. Most of the flow is entering the well from the zone at 3,700 m, and the bottom groups of perforations are also inactive; indeed, there is a standing water column up to the point (3,700 m) where the formation begins to flow. With the well rate increased at a larger choke of  $\frac{3}{4}$ " the production log changes to the form shown in figure 11-7 with negligible injection now taking place; presumably the bottom-hole flowing pressure is now less than the

lowest pressure zone. Thus the production log gives detailed insight into the mechanism, i.e., distribution of inflow. Note, however, that in two-phase flow conditions—oil and gas in this case—the relation between spinner speed and fluid volumetric rate is subject to considerable uncertainty, particularly if the well is deviated and segregated flow is occurring.

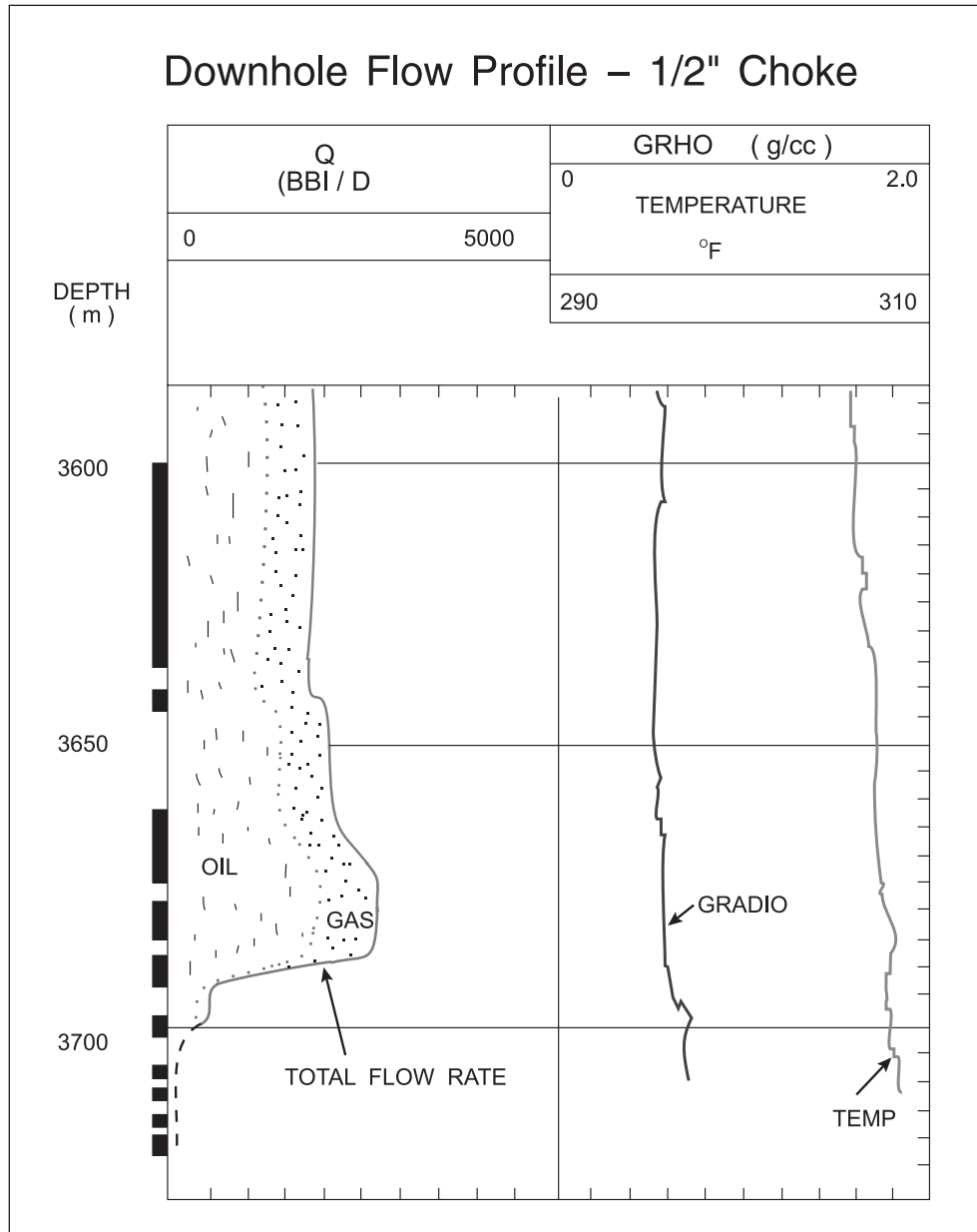


Fig. 11-6. Production log for a well producing on a 1/2" choke

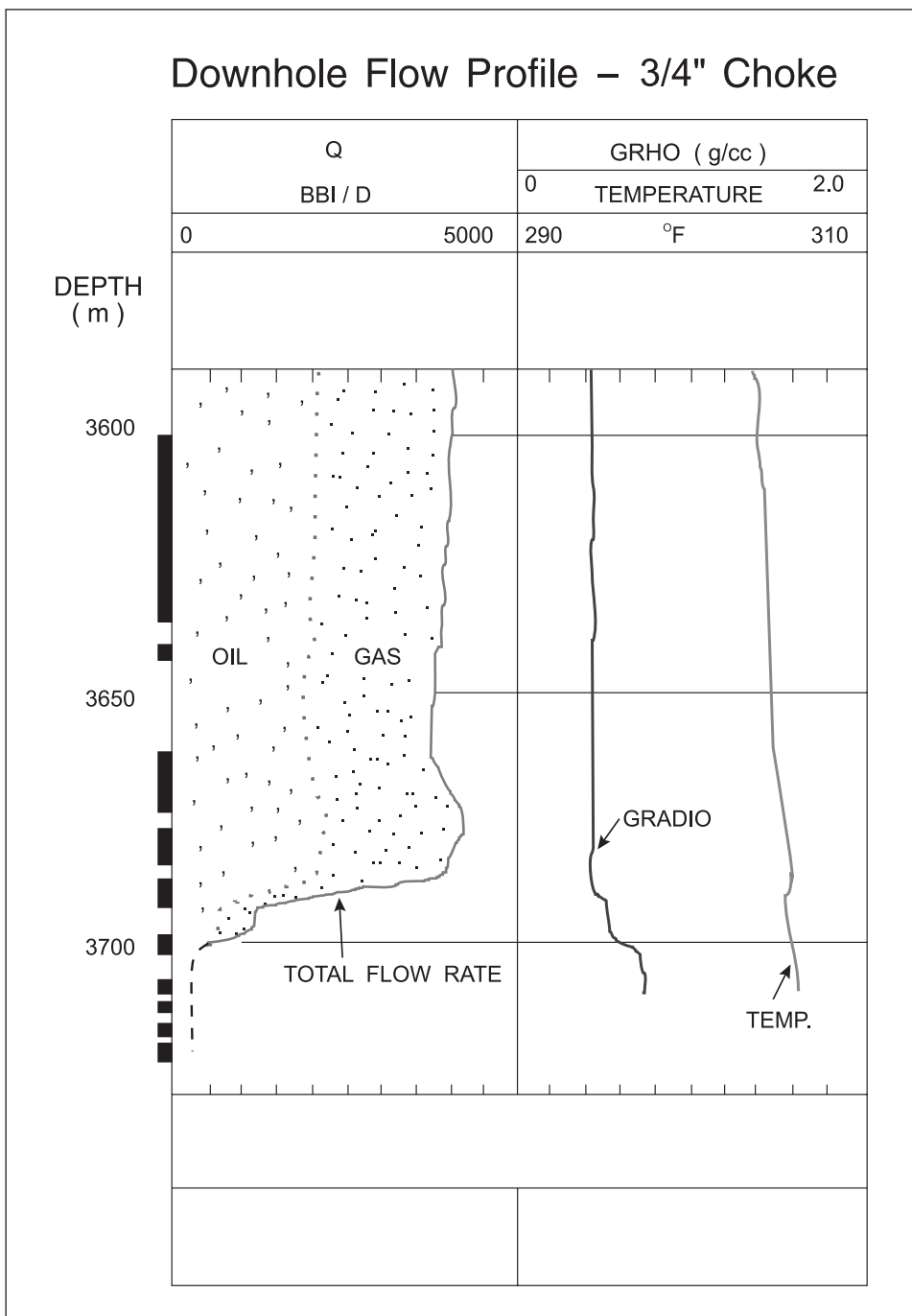


Fig. 11-7. Production log at increased rate, i.e., lower bottom-hole flowing pressure



## Some Reservoir Engineering Applications of Production Logging

In this section, some of the basic reservoir engineering applications of PL will be reviewed. In the development of the North Sea province, it was the engineers responsible for the Piper field who first appreciated the importance of PL surveys in the monitoring of a layered reservoir. In a Europec conference in 1980, Stewart<sup>2</sup> demonstrated that, in order to correctly track the waterfront movement in each layer using a reservoir simulator, it was necessary to tune the simulator well models to PL surveys. This is illustrated in figure 11–8, where it is evident that, provided no crossflow between layers is occurring, the location of the front is largely controlled by the injection rate into a layer and its cross-sectional area. Modern simulators allow the individual layer skin factors to be adjusted until the flow contributions calculated by the simulator well model match the flow profile measurements from PL surveys. This process of matching the simulator predictions to distributed flow data from producers and injectors is complementary to the parallel process of matching simulator layer pressures to WFT data in observation wells. Figures 11–9a and –b show the type of flow-profile match obtained by Bayat and Tehrani<sup>3</sup> in the Ninian field simulation study.

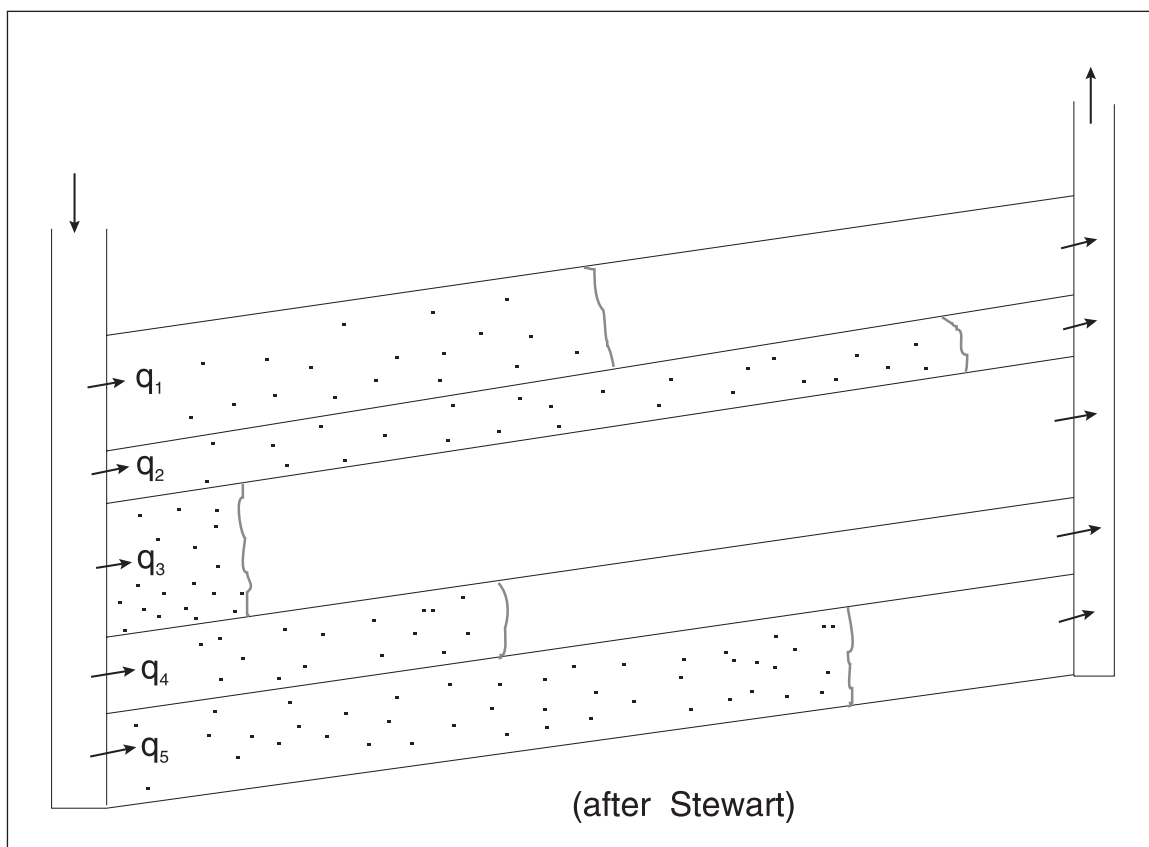


Fig. 11–8. Tracking water front locations in a reservoir simulator

The first paper to discuss the reservoir engineering applications of PL by Stewart and Wittman<sup>4</sup> showed how a single-well model can be used to interpret PL flow distribution measurements in conjunction with pressure measurements. Note that modern PL devices transmit simultaneous down-hole flow and pressure data. An important use of PL was described in this paper; figure 11–10 is a flow meter log from the giant Gawar field in Saudi Arabia, which has a superpermeability streak present over a large area of the field. This thin band—about 2 ft thick—is due to fenestral (lagoonal) deposition and, as can be seen, all the well’s production emerges from the very high permeability “thief” zone. Interestingly, the zone is embedded in low-porosity dolomite beds and, due to the shoulder effect on the logs, it is not evident at all that a thin high-porosity layer is present. Accordingly, the first production logs, run by Tom Dorran, showing the massive flow concentration were regarded with some scepticism; however, the problems of early water production soon demonstrated the adverse effect on field performance of such a thief zone. Eventually, many wells had to be shut in because facilities were not available at the time for treating salty crude.

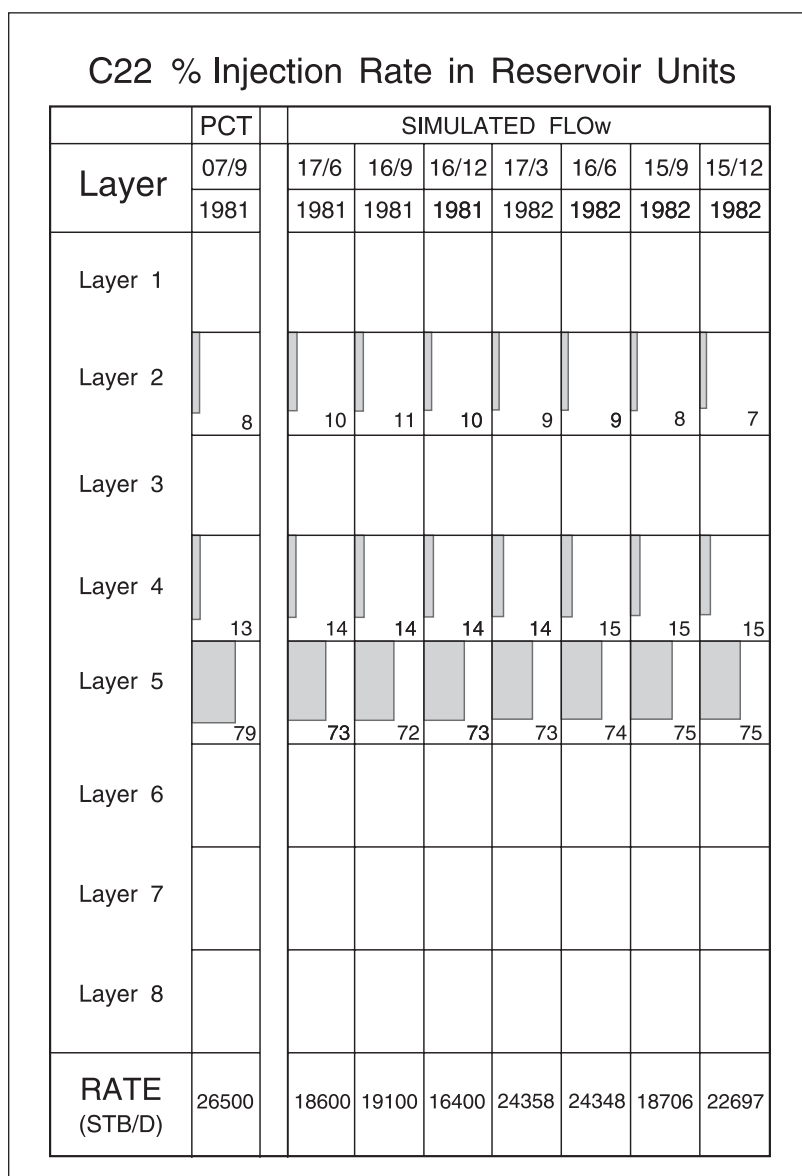


Fig. 11–9a. Ninian field flow-profile match

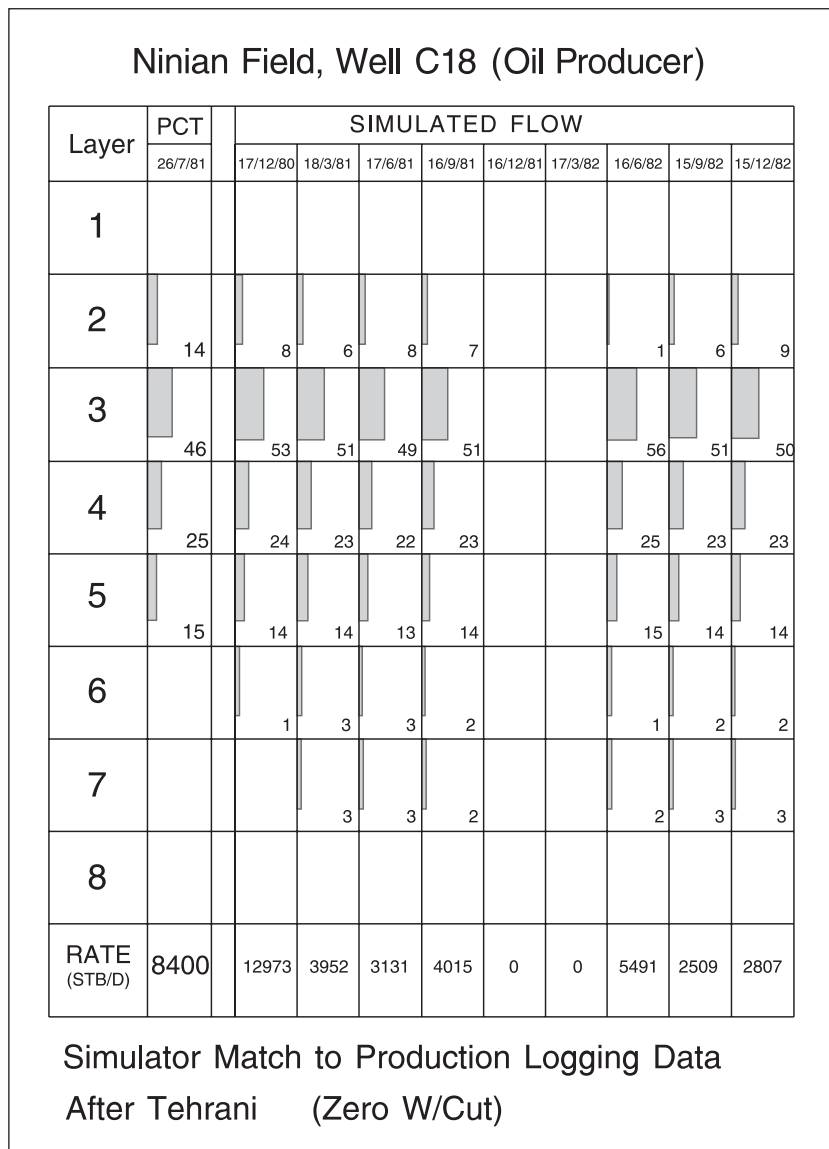


Fig. 11-9b. Ninian field flow-profile match

A related problem was mentioned in the paper by Stewart and Wittman, which had become apparent also in connection with the Piper field in the North Sea. The most permeable zone in Piper was the F sand that has a permeability of the order of 10 darcy; however, the sand is so unconsolidated that it is almost impossible to obtain any core recovery from this formation. Consequently, knowledge of the permeability of the most prolific zone is difficult to obtain and, in fact, it was PL data matched with a single-well model that tied down the F sand permeability. In the design of waterfloods, the most important information is data on permeability differences between layers and, if the most permeable zones cannot be cored, the presence of high-permeability thief zones may be missed. Hence, PL surveys are a valuable addition to core analysis work.

The problem with permeability determination from PL is that the flow profile is affected by individual layer skin factors and pressures in addition to their permeability. Thus, if there is a variation of skin from layer to layer, it will be difficult to determine permeability. As previously mentioned, the detailed treatment of transient layered well testing that allows a complete determination of layer pressures, permeabilities, and skin factors is given in chapter 19 of *Well Test Design and Analysis* (Addendum).

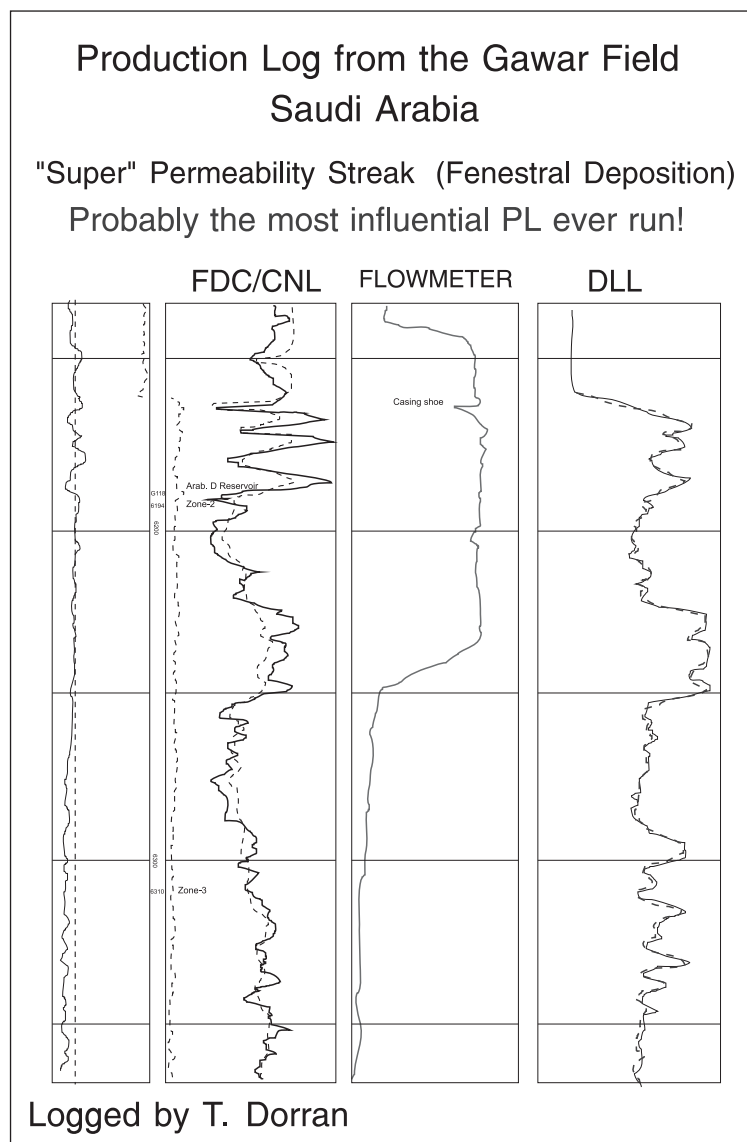


Fig. 11–10. Superpermeability streak

Figure 11–11 illustrates, in a sense, the opposite of a high-permeability continuous thief zone, i.e., an isolated sand lens of limited extent. In a short-term transient well test of such a commingled system with equal initial pressures, the slope of the semilog plot will give the total  $kh$  of the two layers. However, as described in the Introduction, the production from the sand lens will soon become negligible as its pressure quickly declines to a value very close to the flowing bottom-hole pressure. Thus, the pressure of the low capacity unit will reach a dynamic

equilibrium with the bottom-hole pressure controlled by the performance of the dominant layer as shown previously in figure 11–5. This simple situation demonstrates the benefit of time-lapse PL, since the flow profile measured at different times will show the flow contribution from layer 1 gradually declining to a negligible value. Again, the problem of reservoir storage, i.e., a two-layer system with the permeable zone bounded, is treated at length in the well testing context in chapter 19 of *Well Test Design and Analysis*.

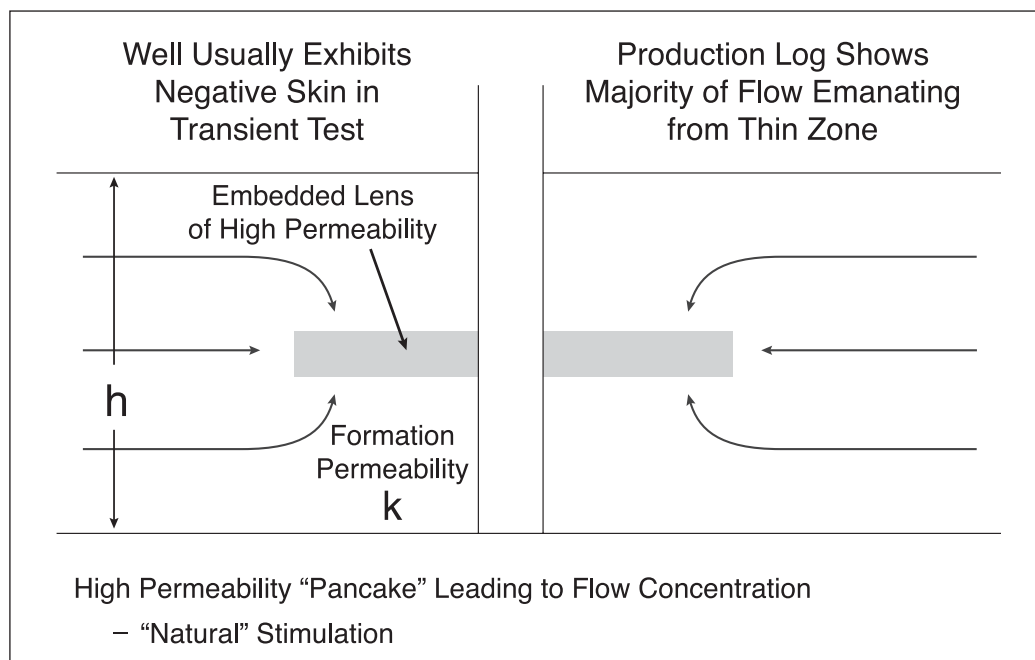


Fig. 11–11. Permeable lens of limited extent

## Layer skin distribution

It is interesting to observe how the skin factor may vary from zone to zone. From the point of view of formation damage, it is the layers that have the highest content of water-sensitive clay minerals, e.g., montmorillonite, that might be expected to suffer most formation damage when wells are drilled with water-based mud. Hence, the low-permeability layers usually being the shaliest would be expected to also exhibit the larger skin. In water injection wells, the higher permeability layers will accept more water and therefore be subject to a greater degree of cooling due to the cold sea water. Again, the thermal fracturing associated with the cold ring will probably mean that the higher permeability layers will also have smaller, i.e., more negative, skin factors than the tighter zones. In completions that are perforated and overbalanced (relatively rare in recent times with the preponderance of tubing conveyed perforation), there is a tendency for high-permeability layers to clean up first and then there is not sufficient drawdown for the perforations in the remaining layers to unplug, leading to high skin factors in the poorer zones. Thus, in general, it can be expected that the high skin zones are often those with low permeability and pose a serious problem in achieving balanced injection and production.

To summarize, the layer skin factor distribution is affected by the following:

- Perforation characteristics such as shot density and perforation depth and the problem of plugged perforations;
- Formation damage like clay swelling with some zones being more sensitive than others;
- Formation alteration such as thermal fracturing in water injection wells and scale deposition.

Profile control is the name given to the exercise of adjusting the shots per foot in individual layers to try and achieve balanced production or injection since, from a reservoir management point of view, production or injection should occur in proportion to the layers pore volume.

The problem of plugged perforations is illustrated in figure 11–12, where the additional localized flow convergence causes the skin factor to be larger than anticipated. However, it often occurs that whole groups of perforations do not produce as shown in figure 11–13 and the well exhibits a limited entry. This detection of poor well performance due to unintentional limited entry is one of the most important applications of PL and much influences decisions about workover. While on the subject of the practical application of PL, it should be mentioned that the detection of leaks is one of the most common outcomes of a survey.

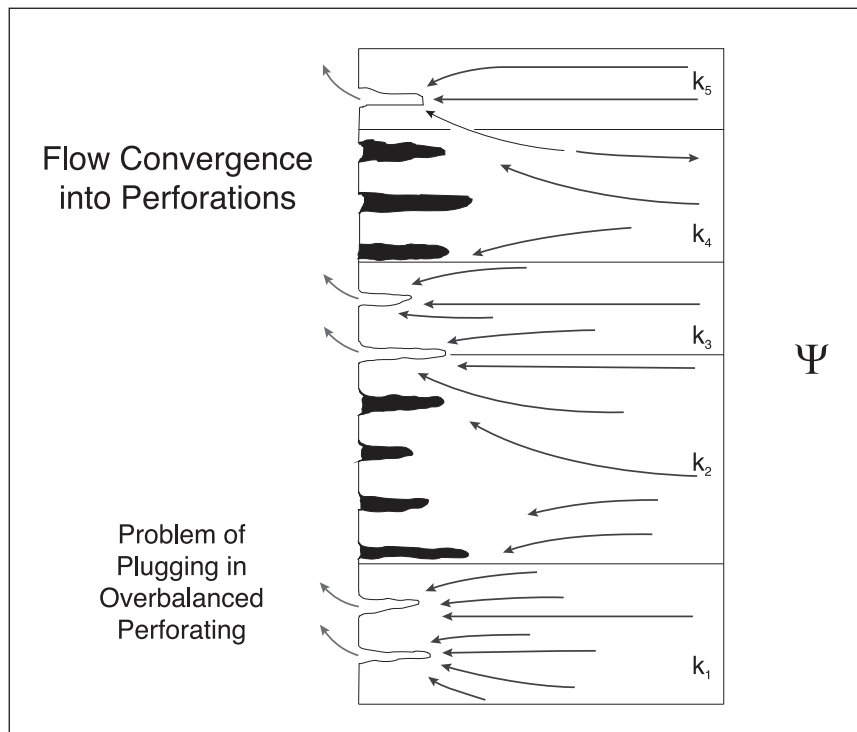


Fig. 11–12. Problem of plugged perforations and additional flow convergence

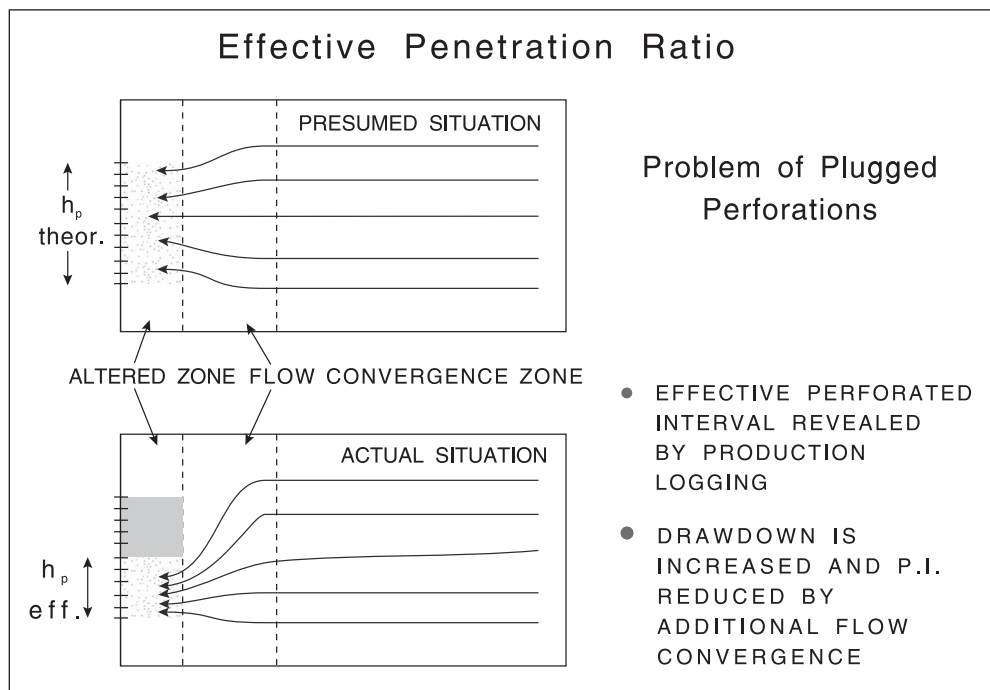


Fig. 11–13. Well limited entry as a result of a bank of perforations not flowing

In an attempt to improve understanding of perforated completions, Schlumberger developed a horizontal flow meter comprising two anemometer-type cups as illustrated in figure 11–14; the idea is to detect the jet entries associated with individual perforations. It is interesting to recount that the first attempt to measure the number of active perforations was carried out by Shell who hung off painted drillpipes in a well and counted the number of erosion marks. In this way, it was established that only about 30%–40% of perforations actually flow (in the days before underbalanced tubing conveyed perforation). The first experimental log from the horizontal flow meter, run in Abu Dhabi, is shown in figure 11–15 and the entries corresponding to individual perforations are clearly visible. It is interesting to note that the current estimate of the fraction of perforations that actually flow is still of the order of 33% despite the success of underbalanced tubing-conveyed perforation (TCP). In chapter 2, it was pointed out that the geostatistical effect of embedding perforations in a heterogeneous formation is the most likely cause—the perforations that land in locally high-permeability flow at much higher rate than those located in locally tight rock. The success of TCP must then be due to the larger number of shots-per-foot that can be achieved.

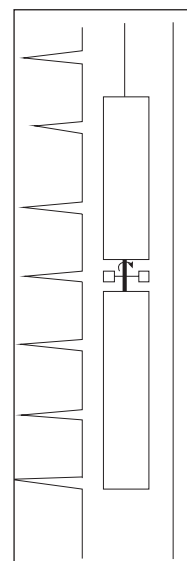


Fig. 11–14. Horizontal flow meter

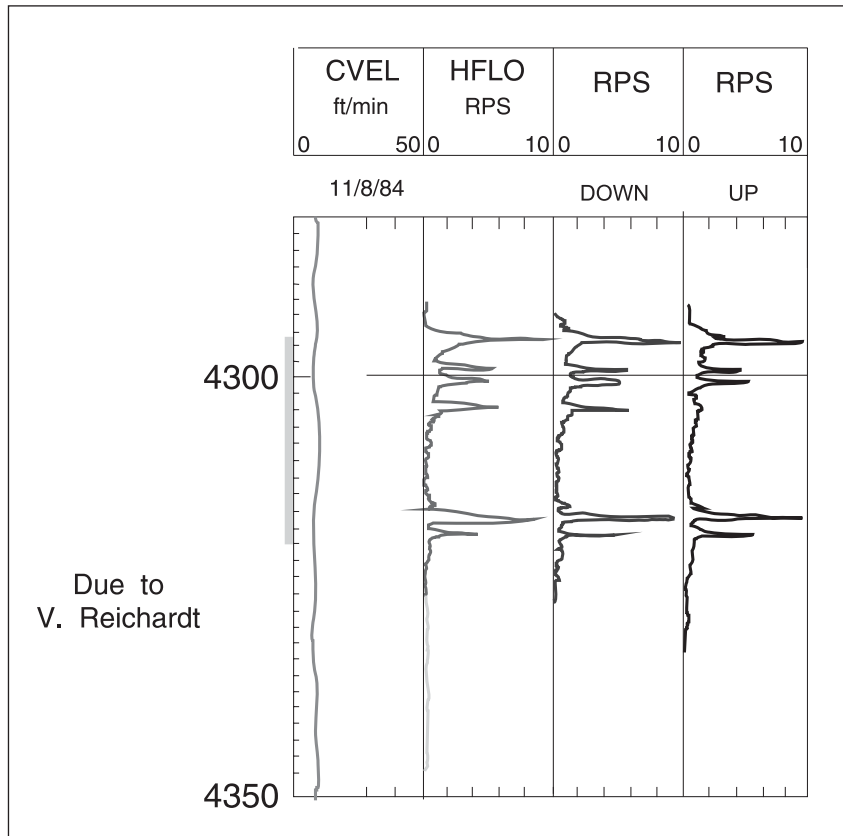


Fig. 11–15. Horizontal flow indicator (HFI) log

## Zonation

The flow distribution is obtained by differentiation of the cumulative flow profile and, as already mentioned, measurement error restricts this process to the determination of the contribution of major zones separated by barriers. Hence, the poor quality of the measurement forces a degree of zonation on the interpretation of the production log. The layered reservoir description for a commingled system recognizes these limitations, and the flow contribution from layer  $j$  can be written formally as

$$q_j = f_j(p_j^e, k_j h_j, S_j, p_{wf}) \quad (11-1)$$

with the total well flow rate given by the summation

$$q = \sum_{j=1}^N q_j \quad (11-2)$$



The distributions of flow, external pressure, permeability–thickness product, and skin factor can therefore be expressed as lists:

$$\mathbf{q} = \begin{bmatrix} q_1 \\ \dots \\ q_j \\ \dots \\ q_N \end{bmatrix} \quad \mathbf{p}^e = \begin{bmatrix} p_1^e \\ \dots \\ p_j^e \\ \dots \\ p_N^e \end{bmatrix} \quad \mathbf{kh} = \begin{bmatrix} k_1 h_1 \\ \dots \\ k_j h_j \\ \dots \\ k_N h_N \end{bmatrix} \quad \mathbf{S} = \begin{bmatrix} S_1 \\ \dots \\ S_j \\ \dots \\ S_N \end{bmatrix}$$

A typical zonation from a layered reservoir description study is shown in figure 11–16, where the zonation from logs has been presented along with the core analysis data and the flow profile. The last column is the permeability distribution which will be used in the reservoir simulation work.

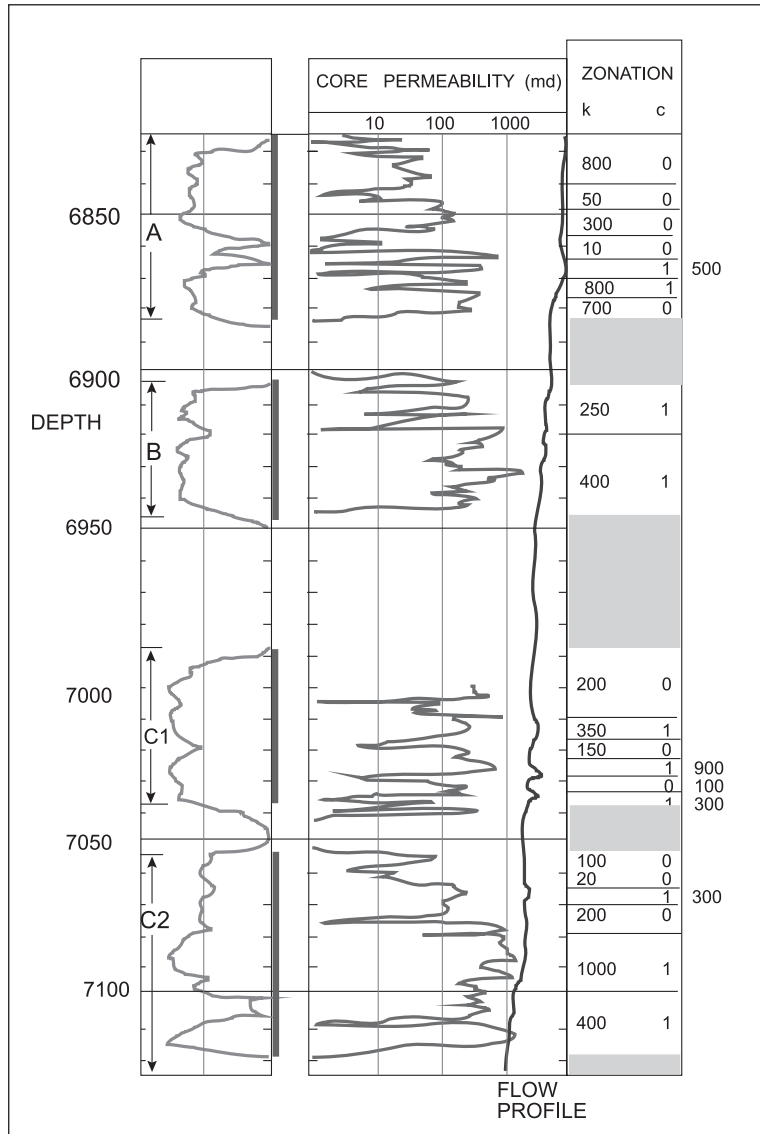


Fig. 11–16. Zonation of a commingled reservoir

## Direct measurement of layer pressures

It has already been pointed out that when a new well is drilled into a produced field, the layer initial pressures, i.e.,  $p_i^e$ , may be quite distinct due to differential depletion of the reservoir by existing producers. Whenever it is felt that differential depletion is occurring, a WFT survey will be run before the well is cased to directly measure these layer pressures; this is illustrated in figure 11–17. Here, the term initial pressure does not refer to the original reservoir pressure but rather the current layer pressures in the vicinity of the new well. If the reservoir exhibits stratified characteristics, and especially when water or gas injection will be carried out, there is a strong case for carrying out a layered well test as part of the standard appraisal procedure. In this case, the initial pressures  $p_i^e$  will already be known from the WFT survey and this information should be used in the design and analysis of the multilayer test. In addition, the WFT survey gives an excellent picture of the proper zonation and the number of layers that need to be carried in the reservoir description. Note however that a WFT survey is only possible in a new development well, i.e., as part of the initial development well test (IDT); for wells that have been producing (or injecting) for some time, the selective inflow performance (SIP) technique based on PL is available and is described later in this chapter.

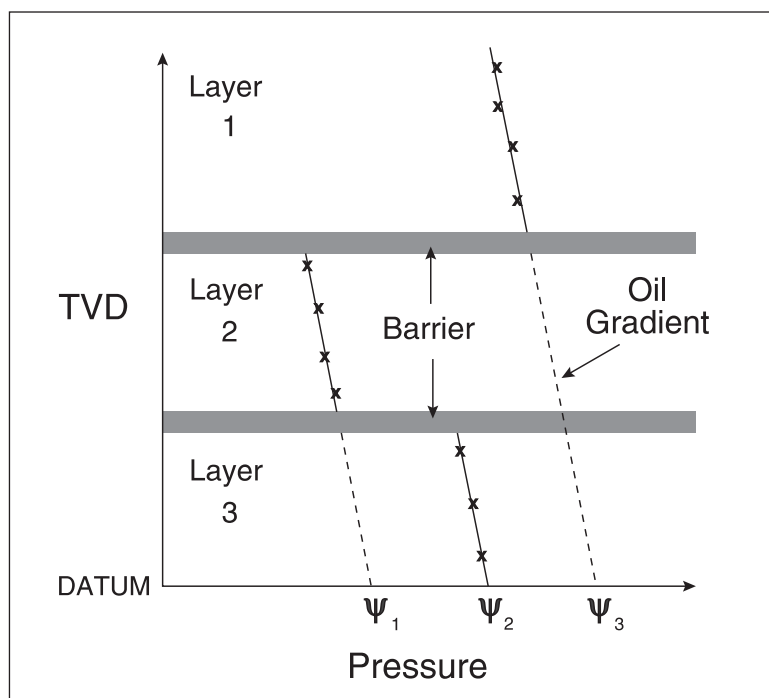


Fig. 11–17. Differential depletion on WFT survey

It is also possible to make a direct measurement of layer pressures in existing producing or injection wells using the cased hole version of the WFT. If a well is killed for a workover and is inactivated by mud, as illustrated in figure 11–18, the cased hole wireline formation tester (CHWFT) could be run to measure the layer pressure provided the well has been inactivated long enough for the buildup to essentially stabilize. The cased hole tool has the capability of shooting a single new perforation that is automatically isolated by the packer and constitutes an observation perforation for direct pressure monitoring. Note that in the workover situation, there

is no wellbore crossflow since all layers are blocked by the overbalanced mud. This technique has been used with considerable success in the Prinos field in the North Aegean Sea where an extensive reservoir monitoring campaign has allowed the development of water production to be significantly deferred. Decisions concerning workover, e.g., the setting of casing patches, bridge plugs, or exclusion liners to seal particular layers, require knowledge of both layer pressure and water cut and the cased hole WFT along with saturation monitoring has been the key to improved recovery in this field. The permeabilities of the layers are high enough that supercharging by mud filtrate invasion is not significant and pressure stabilization following shutin occurs relatively quickly.

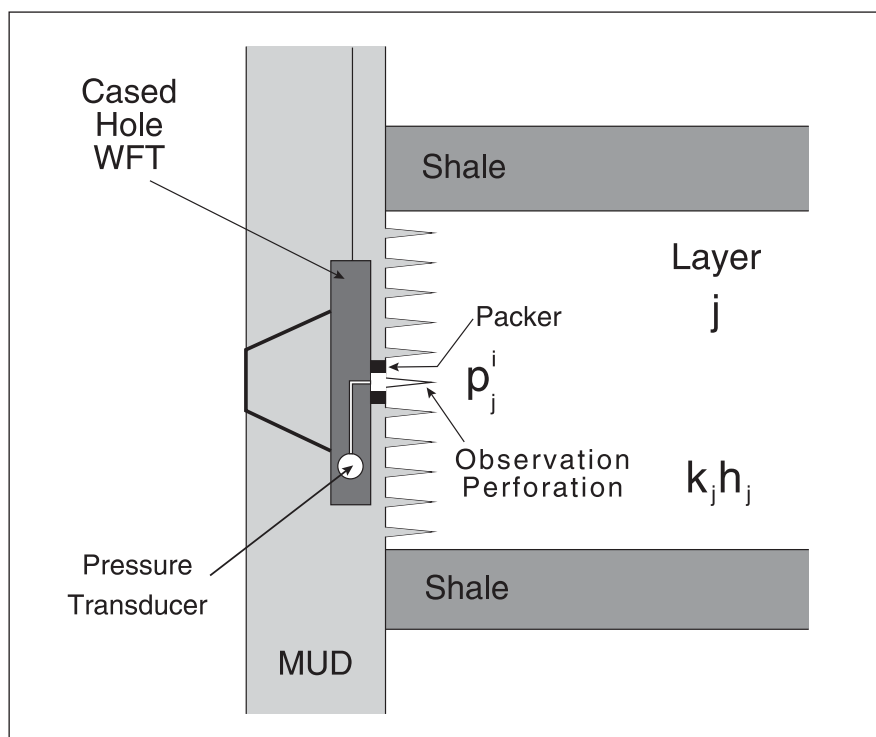


Fig. 11–18. Cased hole WFT in workover situation

A second application of the cased hole WFT is illustrated in figure 11–19, where the pressure of a zone not yet perforated has been accessed with the wireline device. It is very useful to know the pressure of such layers before they are perforated so that the effect of adding an additional zone to the commingled system can be properly considered in advance; the optimization of cumulative oil production from all layers needs to be assessed. Some operators have expressed reservations about leaving an unplugged hole in the casing if it is decided not to perforate the unproduced zone, but the ability to measure pressure in advance allows better decision making to take place. The recent cased hole WFT devices reseals the hole with resin.

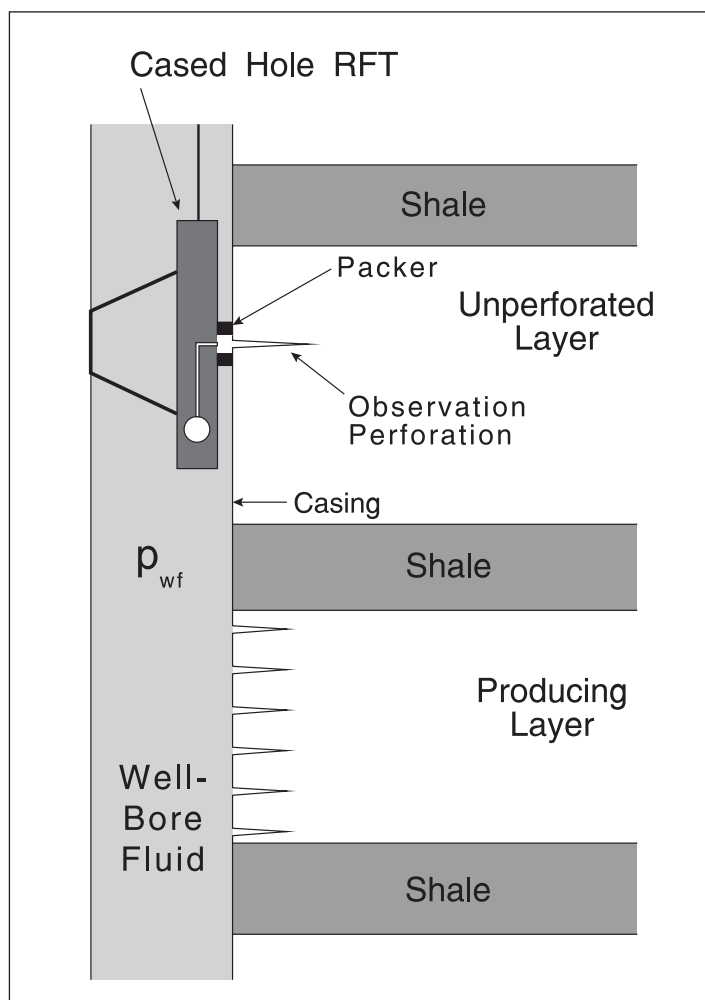


Fig. 11–19. Use of cased hole WFT to access pressure of an unperforated zone

In the treatment of layered well testing using PL tools (PLT) given in this chapter, the indirect determination of layer pressures will be addressed in detail, and an important objective of such testing is simply to allow layer pressures to be estimated using transient analysis techniques. However, it must always be remembered that cased hole WFT devices provide an alternative approach which in the correct circumstances may be advantageous. By the same token, selective interval testing, illustrated diagrammatically in figure 11–20 using packers and perhaps coiled tubing units, also offers a means of determining the same information. However, a danger associated with selective interval testing is presented in figure 11–21, where an invalid assumption concerning layer thickness and the interval being tested arises because the supposed impermeable barrier extends only a short distance from the well. Field examples have been published where the same interval was, in fact, tested twice and each of the presumed layers given much too high a permeability since the individual thickness were employed to decompose the same  $kh$  (combined layer) product. Each method must obviously be considered on its merits in a given situation.

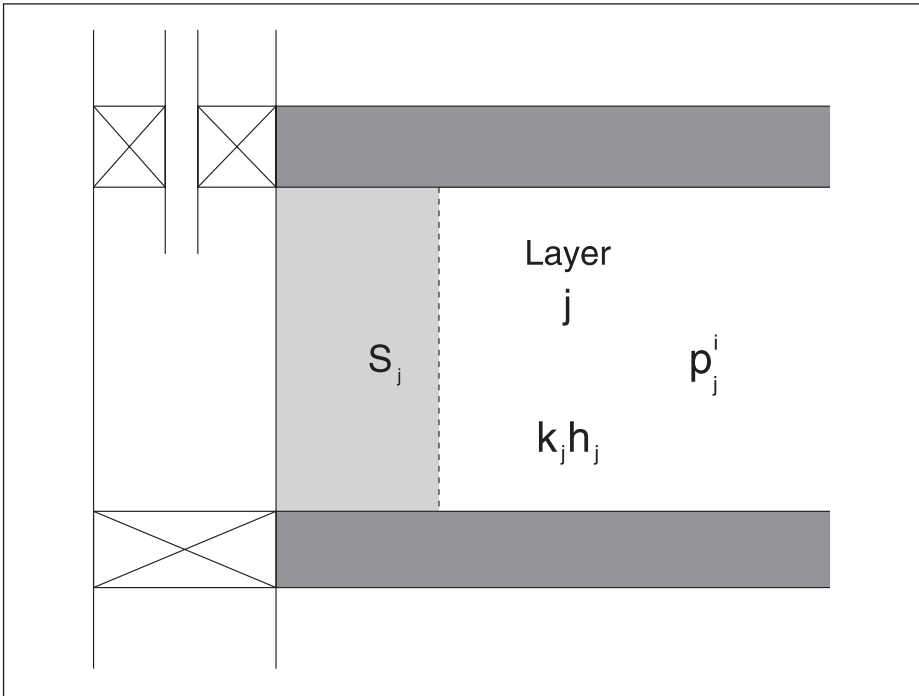


Fig. 11-20. Selective interval testing using packer technology

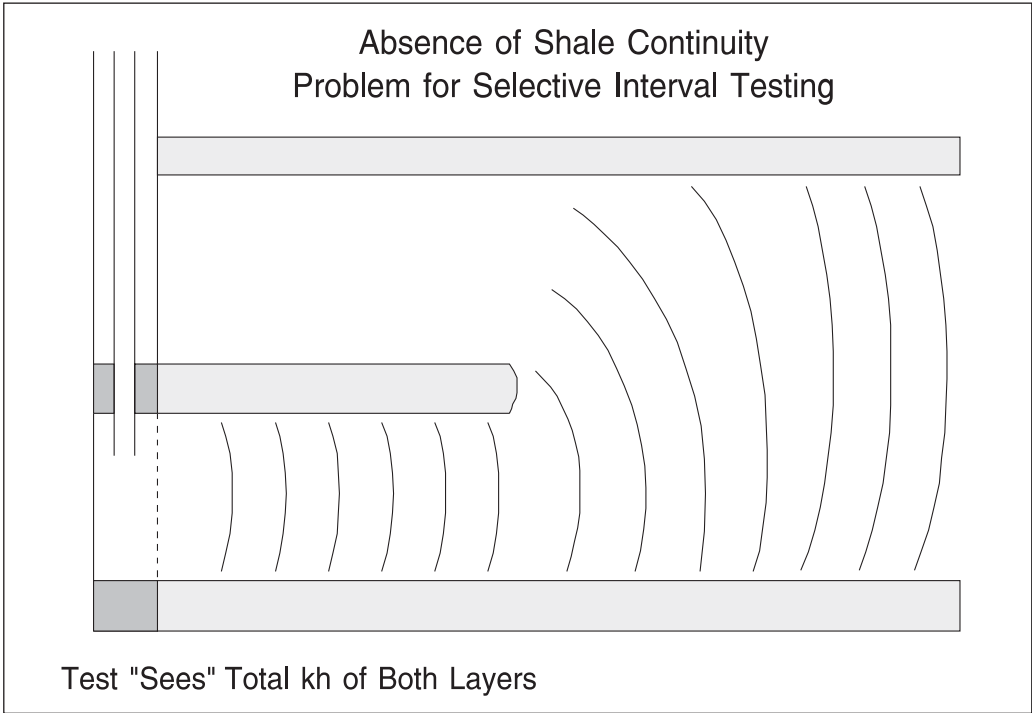


Fig. 11-21. Invalid layer identification arising from shale discontinuity

## Profile control

The term profile control refers to the situation where some well completion technique is used to try and assure the injection and production from layers which optimizes recovery. In waterflooding, for example, it may be beneficial to flood each layer at the same rate, i.e., the injection and production per zone should be roughly proportional to layer thickness. In a balanced waterflood, the injection and production rates for each layer, on an in situ basis, are equal, resulting in a stabilized, maintained pressure. Note that the concept of profile control implies a commingled system with negligible reservoir crossflow between layers.

One of the first attempts at profile control was instituted in the Brent formations of the North Viking Graben. The very permeable Etive formation was perforated at a very small shot density, while the adjacent lower permeability Rannoch sand was shot at the (then) maximum of 4 shots per foot. Unfortunately, this attempt at profile control was unsuccessful. In the Middle East, layered reservoirs horizontal laterals of length  $L$  inversely proportional to the zone permeability have allowed the balancing of production between layers.

## Flow concentration and integration of well testing with production logging

The form of the measured flow profile is affected by distribution of the three controlling variables—pressure, permeability, and skin. A high entry from a particular interval can be driven either by locally high permeability, such as the super-k layer in Gawar, or by the skin factors in other layers being very high causing flow diversion. Hence, a production log must be considered in conjunction with a transient well test; this issue is treated in detail in chapter 19 of *Well Test Design and Analysis*, on layered well testing. It is pointed out in that chapter that the determination of parameters on a layer-by-layer basis can be accomplished only if PL results are available and a dual-flow profile test is suggested as the minimum requirement. Here, a PL survey is carried out when the well is in production (or injection) and then another survey is run during a shutin to measure crossflow between zones. In chapter 19 of *Well Test Design and Analysis*, the idea of a lens of high permeability straddling the wellbore—geoskin—is shown to induce flow concentration. The diagnostic of this phenomenon is the production log indicating flow from a particular interval and the pressure transient test showing negative skin.

## Well workover

One of the justifications for running production logs is the ability to recognize that some form of workover will improve the well performance. Sadly, the industry has a history of failed workovers that did not result in any production enhancement; this topic is treated in more detail in chapter 13 (Addendum). The work of the Bennions (pere et fils) has shown clearly the type of detective work involving special core analysis and phase behavior studies required to tie down the precise mechanism of damage and accordingly identify an appropriate remedy. Again, the combination of PL and well testing is necessary to simply answer the question whether poor performance of a well is a lack of pressure or a high skin.

## Flowing gradient surveys

The basic understanding of the production of a well is the performance diagram, introduced into the industry by Gilbert, which is a plot of bottom-hole flowing pressure versus oil flow rate as illustrated in figure 11–22. In an oil well with the bottom-hole pressure above the bubble point, the inflow performance relation (IPR) is linear with a slope governed by the well productivity index  $J_{SSS}$ . The topic of well testing (pressure transient analysis (PTA)) is largely concerned with identifying the determinants of the IPR, i.e., the reservoir pressure, the zone permeability–thickness product, and the skin factor. Much of this chapter and chapter 19 of *Well Test Design and Analysis* is concerned with measuring these parameters on a layer-by-layer basis. For example, the succeeding section deals with selective inflow performance, a technique that employs PL passes to determine layer pressures and PIs. However, the well operating point is controlled by the intersection of the IPR with the vertical lift performance (VLP) curve, as shown in figure 11–22, and it is just as important to identify the parameters that control the nature of the VLP relation. Thus the effective tubing diameter necessary to match the flowing pressure survey to a two-phase pressure drop model is a key indicator of tubing performance. In the case of the formation, well testing in the reservoir monitoring mode is tracking changes in formation pressure and skin factor and consequent variation of the IPR. Note that it is absolutely essential to distinguish between production problems caused by low reservoir pressure and problems associated with formation damage such as scaling, asphaltene deposition, water sensitivity, or perforation plugging. As mentioned in the preceding section, a workover must focus on the correct target.

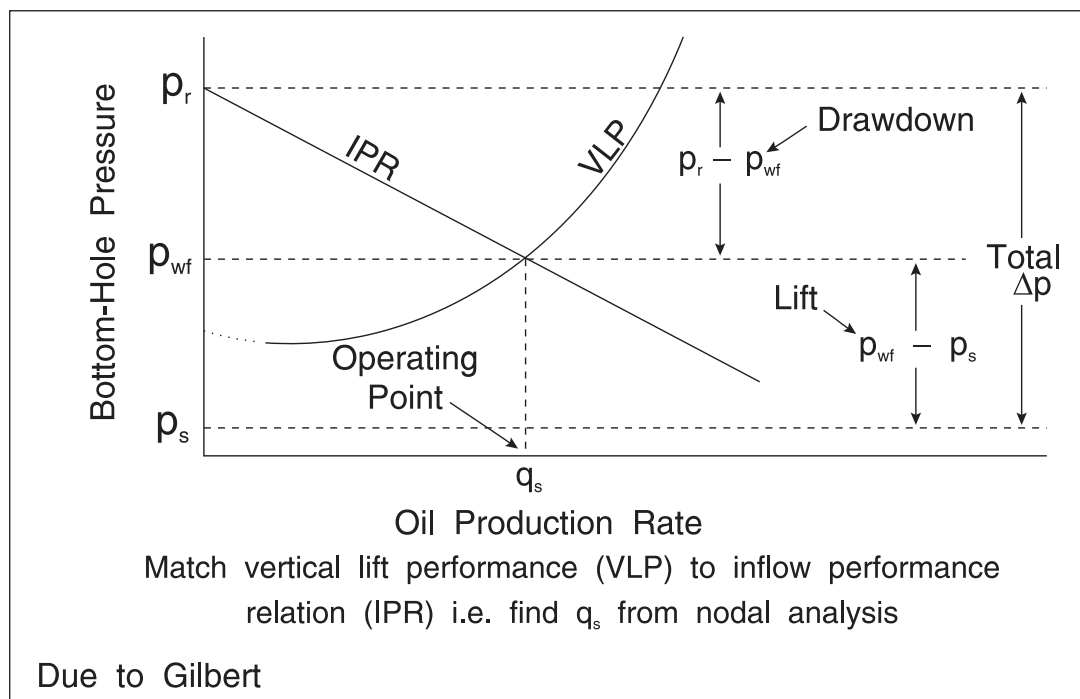


Fig. 11–22. Well performance diagram

## Selective Inflow Performance

### Single-phase flow

WFT devices have shown the importance of measuring the pressures of the various layers in a reservoir as they deplete differentially. However, a WFT survey is possible only when a new well is drilled into the field. As the development drilling program comes to an end, the opportunity to access the evolution of layer pressures is curtailed unless there is much infill drilling. From the point of view of reservoir monitoring, it is desirable to go on measuring layer pressures. It is possible to develop methods for the determination of layer pressures in active wells using PL to give information on layer flow rates. The first application of PL to layered reservoir analysis was devised for gas wells and has been called the *selective inflow performance* (SIP) technique. The idea was based on the well performance diagram for a reservoir comprising a number of isolated layers, i.e., a commingled system. Assuming semi-steady-state (SSS) conditions with each layer having its own individual external pressure  $p_j^e$  and productivity index  $J_j$ , the individual layer inflow performance relations are given by

$$q_j = J_j(p_j^e - p_{wf}) \quad (11-3)$$

This assumes that the external pressures at radius  $r_e$ —the same for all layers—are essentially constant during the test period and the well in question is at the SSS. The SSS PI is related to the layer permeability and skin factor by the familiar equation

$$J_j = \frac{2\pi k_j h_j}{\mu B \left( \ln \frac{r_e}{r_w} - \frac{3}{4} + S_j \right)} \quad (11-4)$$

These layer IPRs can be plotted on a well performance diagram, i.e., a graph of bottom-hole flowing pressure  $p_{wf}$  versus flow rate  $q_j$ , as illustrated in figure 11-23. The author presented this diagram at a seminar in Paris in 1978, and 3 weeks later a Schlumberger engineer, Simone Noik, had a patent for the SIP technique. For this purpose, Eq. (11-3) may be written as

$$p_{wf} = p_j^e - \frac{1}{J_j} q_j \quad (11-5)$$



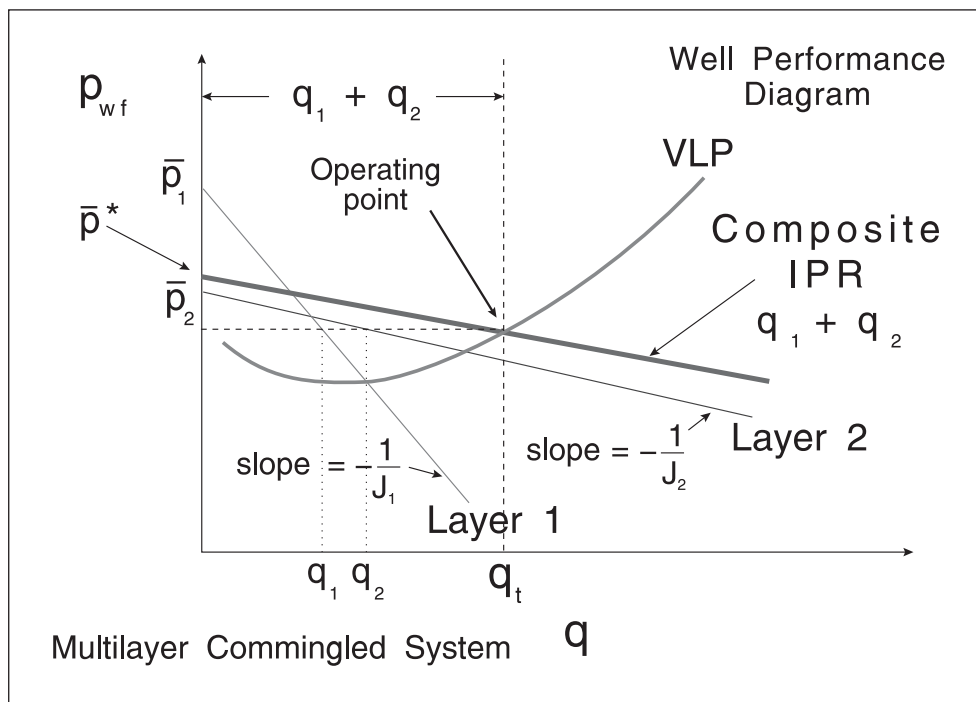


Fig. 11-23. Multilayer well performance diagram

Thus, each individual layer IPR has a slope  $-1/J_j$  and intercept  $p_j^e$ ; these are illustrated diagrammatically in figure 10-23. For a given value of  $p_{wf}$ , the total well flow  $q$  is given by

$$q = \sum q_j = \sum J_j (p_j^e - p_{wf}) \tag{11-6}$$

and prediction of the well inflow requires knowledge of the layer PIs  $J_j$  and the layer external pressures  $p_j^e$ .

The total flow rate  $q$  obtained by the summation (11-6) is also a linear function of  $p_{wf}$  of the form

$$q = J(p_w^* - p_{wf}) \tag{11-7}$$

where

$$J = \sum J_j \tag{11-8}$$

and

$$p_w^* = \frac{\sum J_j p_j^e}{\sum J_j} = \frac{\sum J_j p_j^e}{J} \tag{11-9}$$

This is the composite IPR and it is also shown in figure 11-23. Provided  $p_{wf}$  is less than  $p_w^*$ , the well will be a net producer. For all layers to flow,  $p_{wf}$  should be less than the smallest external pressure denoted  $(p_j^e)_{\min}$ . If  $p_{wf}$  is intermediate between  $p_w^*$  and  $(p_j^e)_{\min}$ , some layers will be accepting fluid. The steady-state production characteristics of a well in a commingled system

can be readily understood through the well performance diagram especially when the well VLP curve is plotted simultaneously with the composite IPR. The intersection of these two gives the well operating point. It is apparent that both layer PIs  $J_j$  and layer external pressures  $p_j^e$  must be known before well performance can be assessed.

In the SIP technique, the well is flowed at a series of total rates as shown in figure 11–24. Each flow period is presumed to be of sufficient duration that the SSS is reached, i.e., the bottom-hole flowing pressure  $p_{wf}$  and the individual layer flow rates  $q_j$  have stabilized. At the end of the flow period, a PLD is used to measure the flowing pressure  $p_{wf}(T_i)$  and the flow profile  $q_j(T_i)$ ,  $j = 1, \dots, L$  where time  $T_i$  indicates the end of the  $i$ -th flow period. The assumption is made that each individual layer rate can also be presumed to be constant as illustrated in figure 11–25. However, in practice, although the surface total rate is constant, the individual layer rates exhibit transients as shown in figure 11–26. In commingled production with both layers having the same wellbore pressure, contrast in properties manifest themselves in rate effects; this is why PL is essential. Provided each flow period is long enough for essentially SSS conditions to be attained, the data points for each layer, viz.,  $p_{wf}(T_i)$  and  $q_j(T_i)$ , can be plotted on a well performance diagram as shown in figure 11–27. The slope of the straight line for layer  $j$  gives the layer steady-state PI,  $J_j$ , while the intercept gives the layer external pressure  $p_j^e$ . This shows how a step-rate well test can yield the layer pressures using measurements of  $p_{wf}$  and layer flow rates. The SIP technique allows estimation of the layer productivity index  $J_j$ . If the layer permeability  $k_j$  is assumed known, say from core analysis, then the skin factor can be obtained from (11–4).

The SIP technique has been successfully employed in gas wells where it can also help to elucidate non-Darcy skin effects; in this case the IPRs are not straight and show curvature at high rate. It has also been employed in oil wells, a field example being shown in figure 11–28.

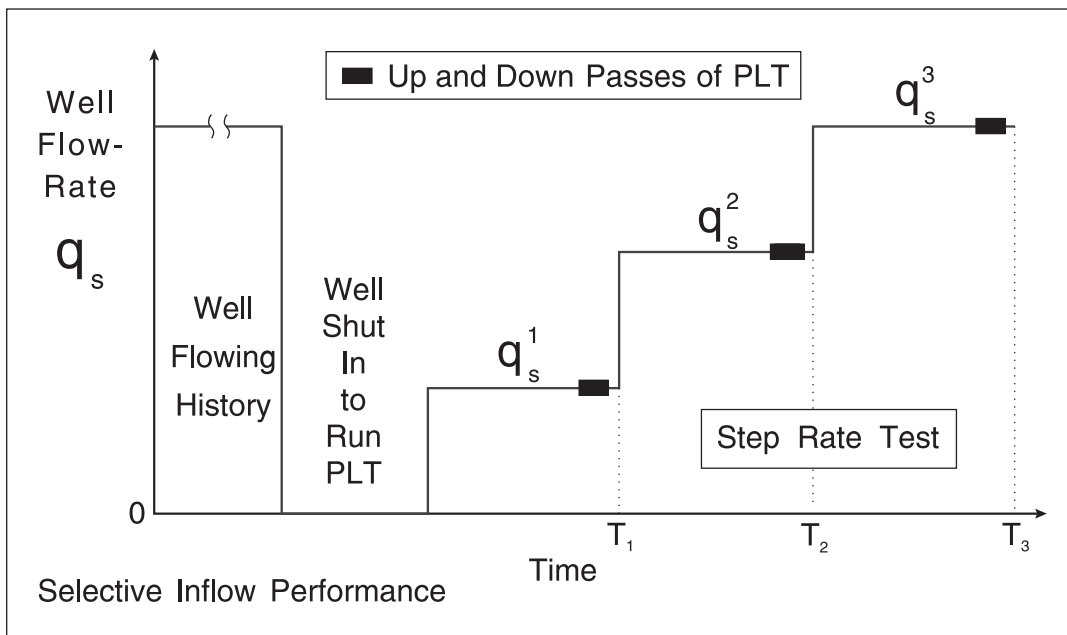


Fig. 11–24. Surface flow rate schedule for an SIP test

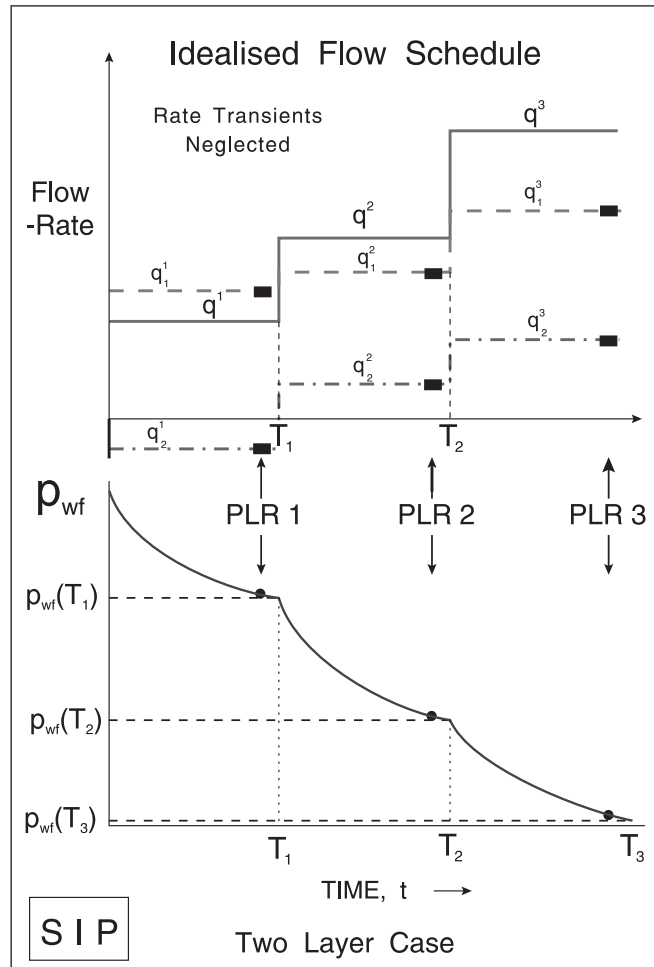


Fig. 11-25. Presumed down-hole flow schedules for an SIP test

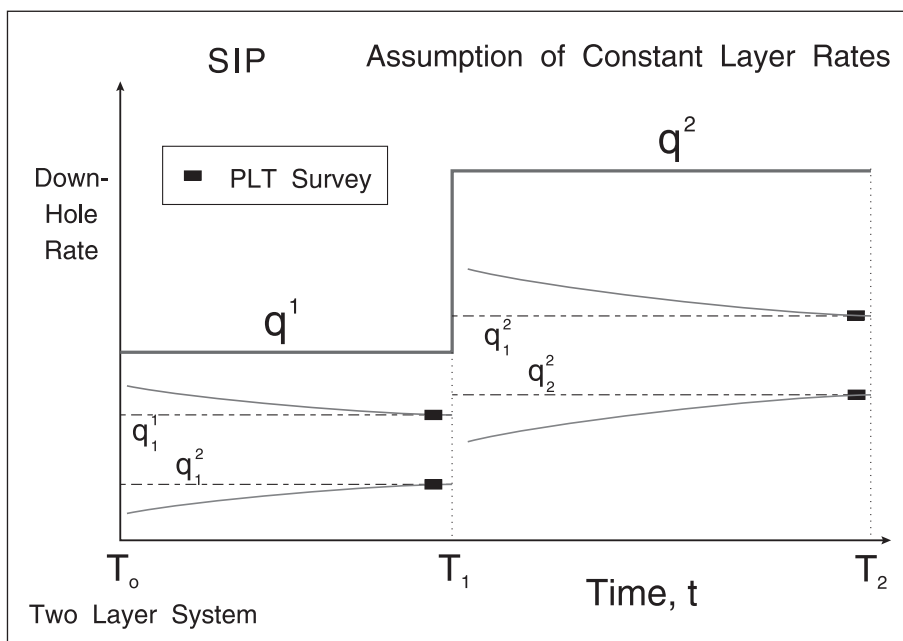


Fig. 11-26. Individual layer rate transients

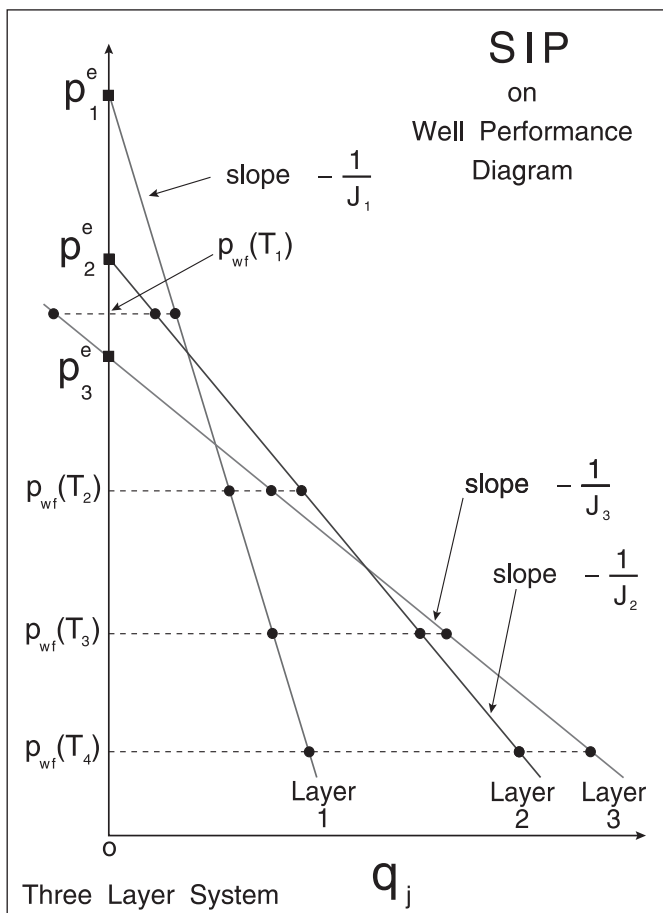


Fig. 11-27. SIP results presented on a well performance diagram

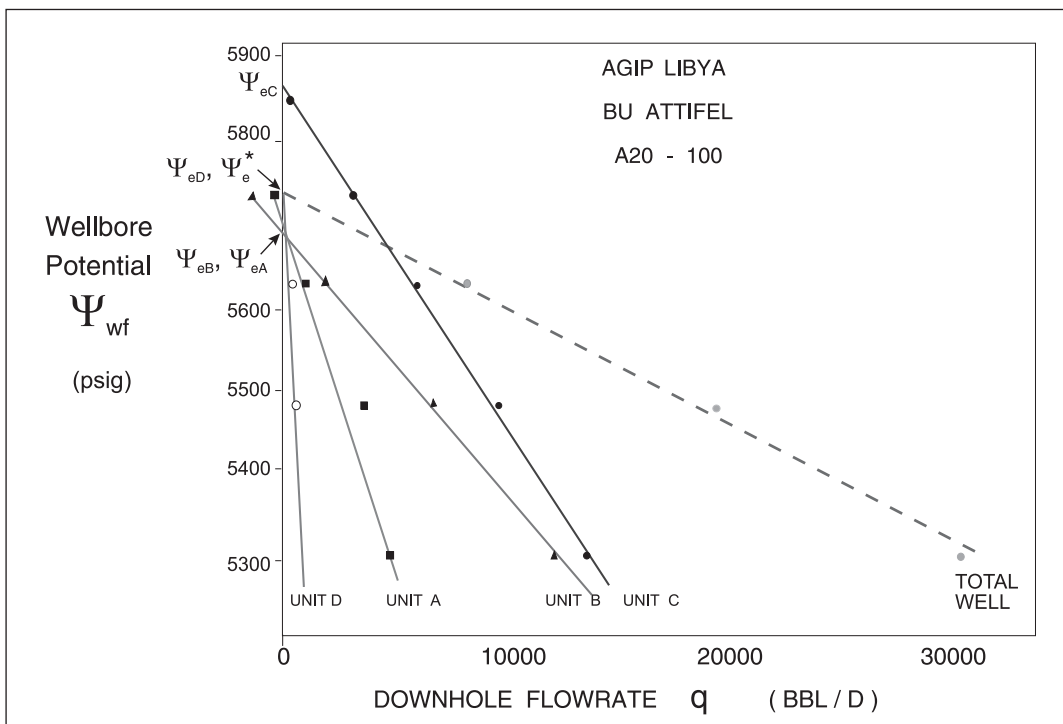


Fig. 11-28. SIP field example from Libya

However, the technique has the disadvantage that semi-steady-state conditions must be attained. This is controlled by the layer of lowest permeability ( $k_j$ ) and by the oil viscosity  $\mu$ . Note that what is implied is a quasi-semi-steady-state (QSSS) in a multiwell system. However, the main problem is the time necessary to reach such a QSSS.

In order to demonstrate the effect of flow period duration on a SIP analysis, a synthetic example was run on an analytical layered reservoir simulator using a decreasing rate schedule. The specified properties of the layers and the simulation data and results are given in table 11–1a and b. In this example, the model chosen for each layer was infinite-acting and the PI, i.e.,  $J_{ss,j}$  has to be based on the concept of drainage radius, i.e.,  $r_{d,j}$ , where

$$r_{d,j} = 0.75 \sqrt{\frac{4k_j t}{\phi \mu c_t}} \quad (11-10a)$$

and

$$J_{ss,j} = \frac{2\pi k_j h_j}{\mu B \left( \ln \frac{r_{d,j}}{r_w} + S_j \right)} \quad (11-10b)$$

The example can be termed *transient SIP* since each layer is infinite-acting and the pressure disturbance propagates out to different distances according to the layer permeability.

**Table 11–1a.** Parameter values for SIP simulation with decreasing rate

Layer number	$h_j$ (ft)	$p_j^i$ (psia)	$k_j$ (md)	$S_j$	Common layer properties $r_w = 0.33$ ft $\phi = 0.2$ $\mu = 1.0$ cp $c_t = 3.0 \times 10^{-5}$ psi <sup>-1</sup> $B_o = 1.0$
1	33	5,050	500	5	
2	33	5,000	300	3	
3	33	4,950	700	7	

**Table 11–1b.** SIP simulation results

Time (h)	$p_{wf}$ (psia)	Surface rate $q_s$ (bbl/d)	Layer 1 rate (bbl/D)	Layer 2 rate (bbl/D)	Layer 3 rate (bbl/D)
1,004	4,959.6	800	692.5	211.8	–104.3
1,008	4,966.9	600	624.1	161.8	–185.9
1,012	4,974.4	400	555.6	112.0	–267.6
1,016	4,981.9	200	487.2	62.3	–349.5

In this example, the well was flowed for 1,000 h at a constant rate of 1,000 bbl/d and then 4–h SIP flow periods were employed, and the synthetic data are plotted in figure 11–29a; the corresponding SIP plot is shown in figure 11–29b. The data appear to fall on straight lines, but the slopes are too low and the layer productivity indices are overestimated as shown in table 11–2. Correspondingly, the layer pressures are underestimated by up to 15 psi.

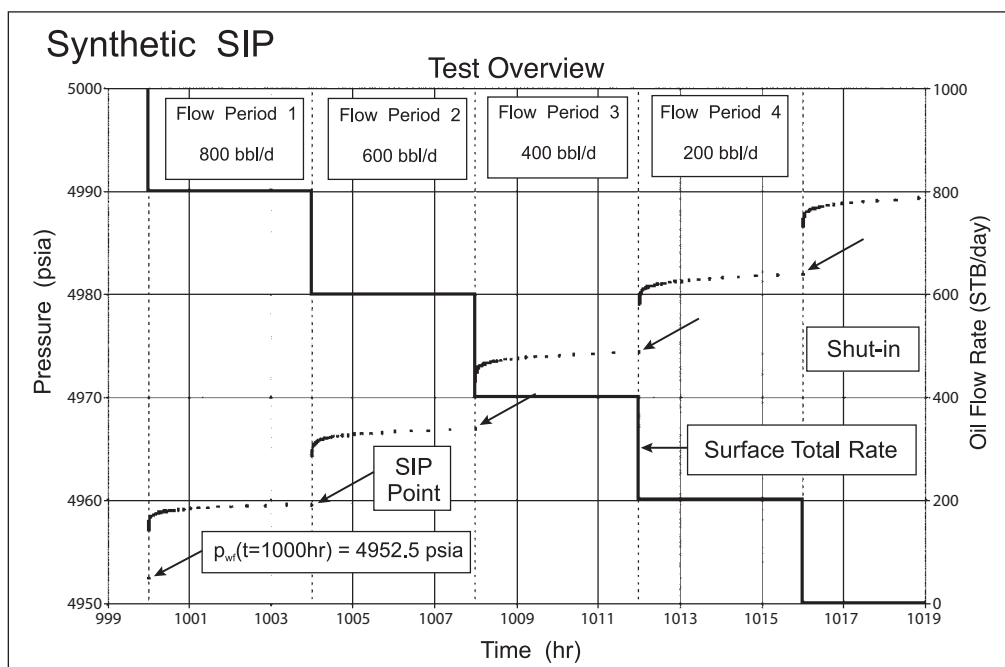


Fig. 11–29a. Synthetic field example—pressure data

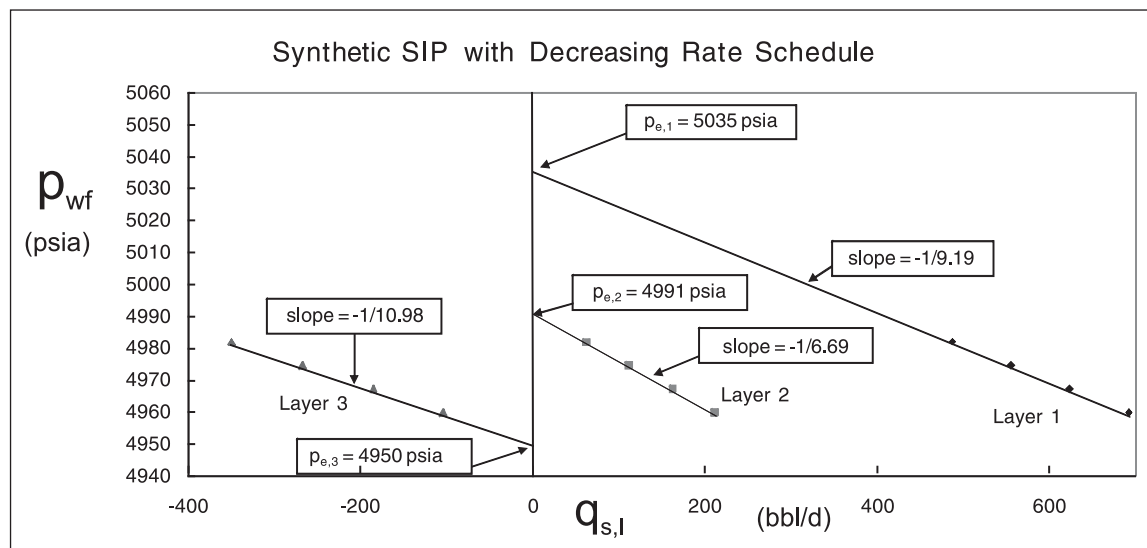


Fig. 11–29b. Synthetic field example—SIP plot

Table 11–2. Results of SIP Analysis

Layer no.	Drainage radius $r_{d,j}$ (ft)	True $p_i^j$ (psia)	SIP $p_i^j$ (psia)	True $J_{ss,j}$ (bbl/d/psi)	SIP $J_{ss,j}$ (bbl/d/psi)
1	9,373	5,050	5,035	7.69	9.19
2	7,260	5,000	4,991	5.42	6.69
3	11,091	4,950	4,950	9.43	10.98

When an increasing rate schedule is employed, the layer pressures are overestimated; thus, the estimate of pressure is a function of flow history. These effects occur because the bottom-hole flowing pressure has not stabilized. In fact the idea of stabilization is quite erroneous, even at SSS,

since the wellbore pressure follows the dynamically changing reservoir pressure. Another field example (from the North Sea) is shown in figures 11–30a and b where three layers have been identified at substantially different pressures. Although straight lines have been put through the data, they are not well defined and considerable uncertainty in the estimated pressures is present. Again, the effect of non-stabilized conditions places much doubt on the SIP technique in oil wells. There is a great incentive to reduce the duration of each flow period and to carry out an SIP analysis based on transient theory. In this situation the well is assumed to be infinite-acting throughout the step rate test; the theory of this approach is treated in chapter 19 of *Well Test Design and Analysis*, on layered well testing.

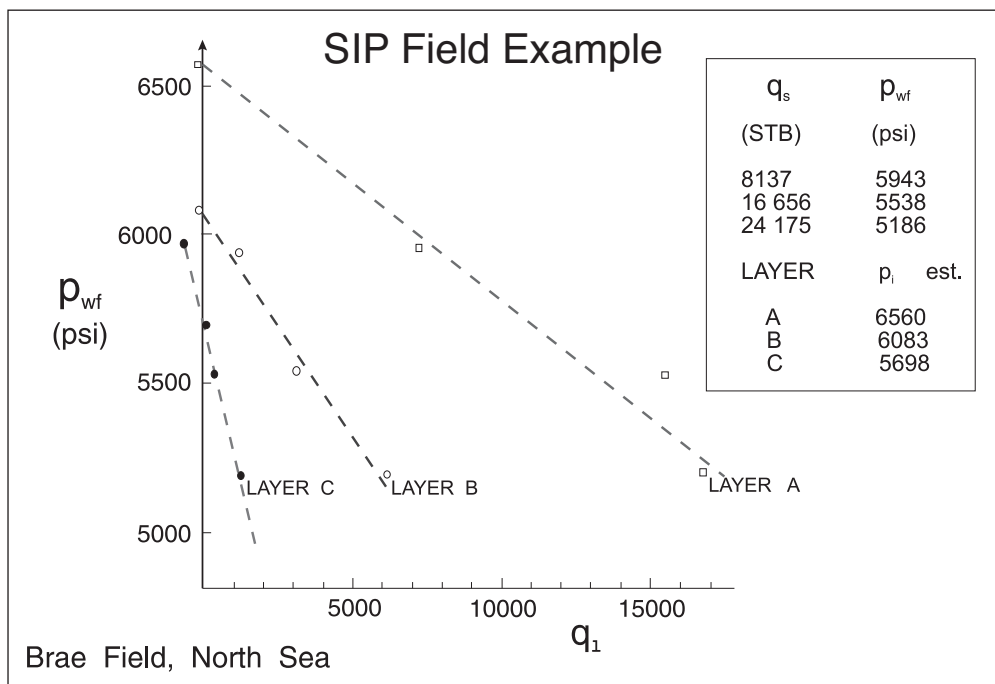
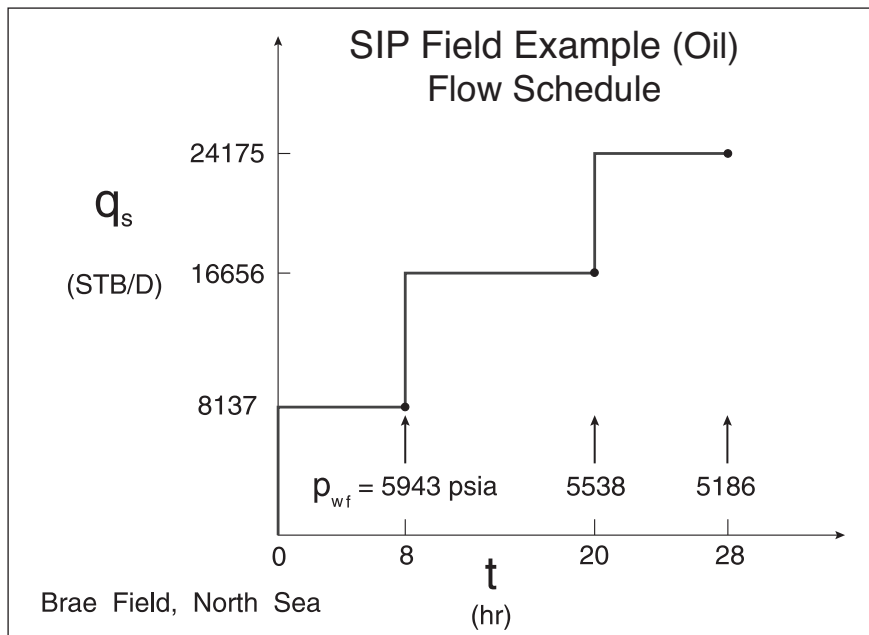


Fig. 11–30a and b. North Sea SIP example (Brae field)

## Gas well quadratic IPRs

The basic theory of the SIP procedure depends on straight line IPRs, and in the case of gas wells where non-Darcy flow is appreciable some modification is necessary. Suppose that the individual layer IPRs, in terms of pressure, are given by equations of the form

$$\bar{p}_j - p_{wf} = A_j Q_j + B_j Q_j^2 \quad (11-11a)$$

i.e.,

$$Q_j = \frac{\sqrt{A_j^2 + 4B_j(\bar{p}_j - p_{wf})} - A_j}{2B_j} \quad j = 1, \dots, N \quad (11-11b)$$

Then, for a range of assumed values of  $p_{wf}$ , the total flow can be computed from the summation

$$Q = \sum_{j=1}^N Q_j \quad (11-12)$$

Thus, the composite IPR may be readily constructed; however, it does not have a quadratic form although the underlying layer IPRs are indeed quadratic. This is illustrated in figure 11-31 for a liquid system where a composite IPR has been compiled from the individual (quadratic) IPRs of a two layer reservoir.

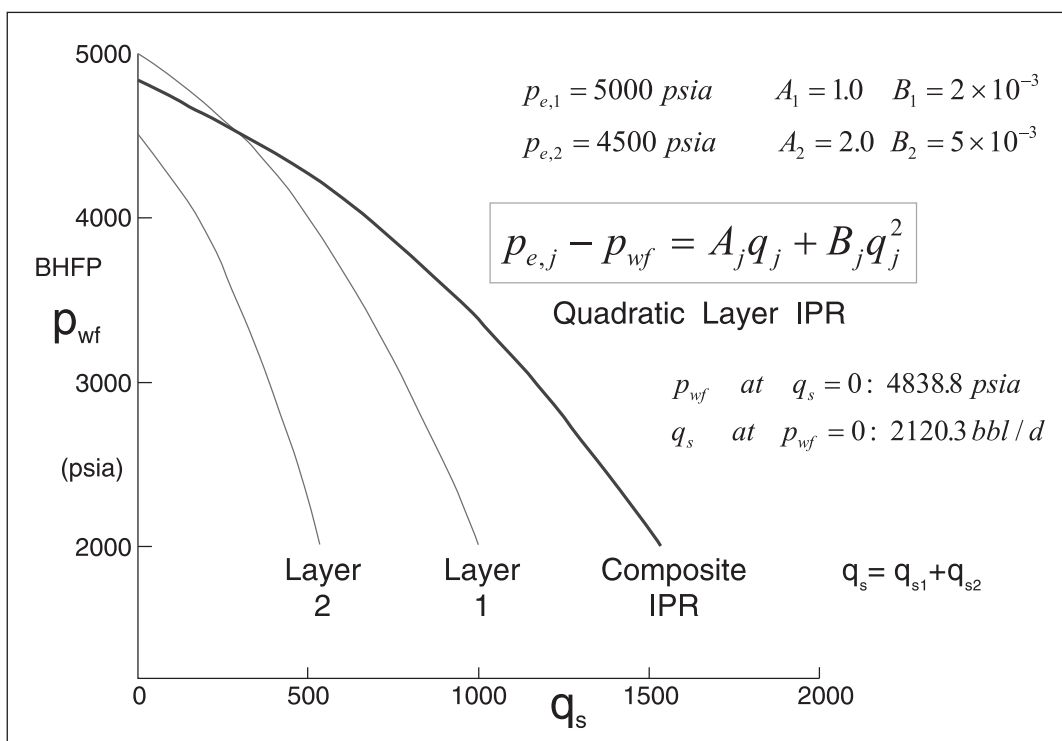


Fig. 11-31. Commingling of quadratic layer IPRs



The first extensive application of the SIP technique in gas wells was carried out in the Hassi Messaoud field in Algeria and figure 10–32 shows the plotted layer IPRs for a well labeled 3 (data provided in table 11–3). The logs were run and the interpretation carried out by C. Airlie.

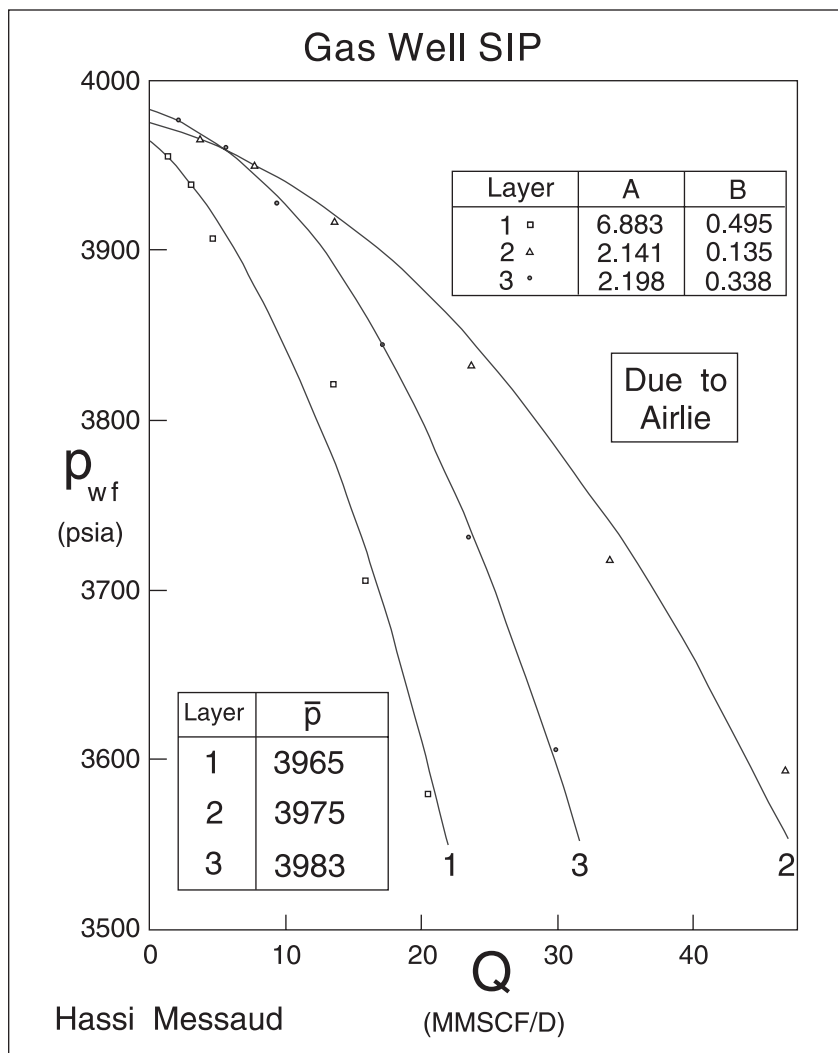


Fig. 11–32. Gas well SIP from Algeria (Hassi Messaoud)

Table 11–3. Data for Hassi Messaoud Field Example

Layer	h (ft)	h <sub>p</sub> (ft)
1	57.5	33
2	65.6	59
3	33	23

$T = 93.8^{\circ}\text{C}$        $P_c = 648.7 \text{ psia}$   
 $T_c = 392^{\circ}\text{R}$        $\gamma = 0.787$   
 $r_e = 2,300 \text{ ft}$        $r_w = 0.35 \text{ ft}$   
 $\phi = 0.2$        $\mu = 0.0245 \text{ cp}$   
 $c_t = 0.0002 \text{ psi}^{-1}$

The information on differential depletion and actual layer production rates was extensively used in the reservoir management of this giant gas-condensate field. A second example is shown in figure 11–33, where a two-layer system has been identified.

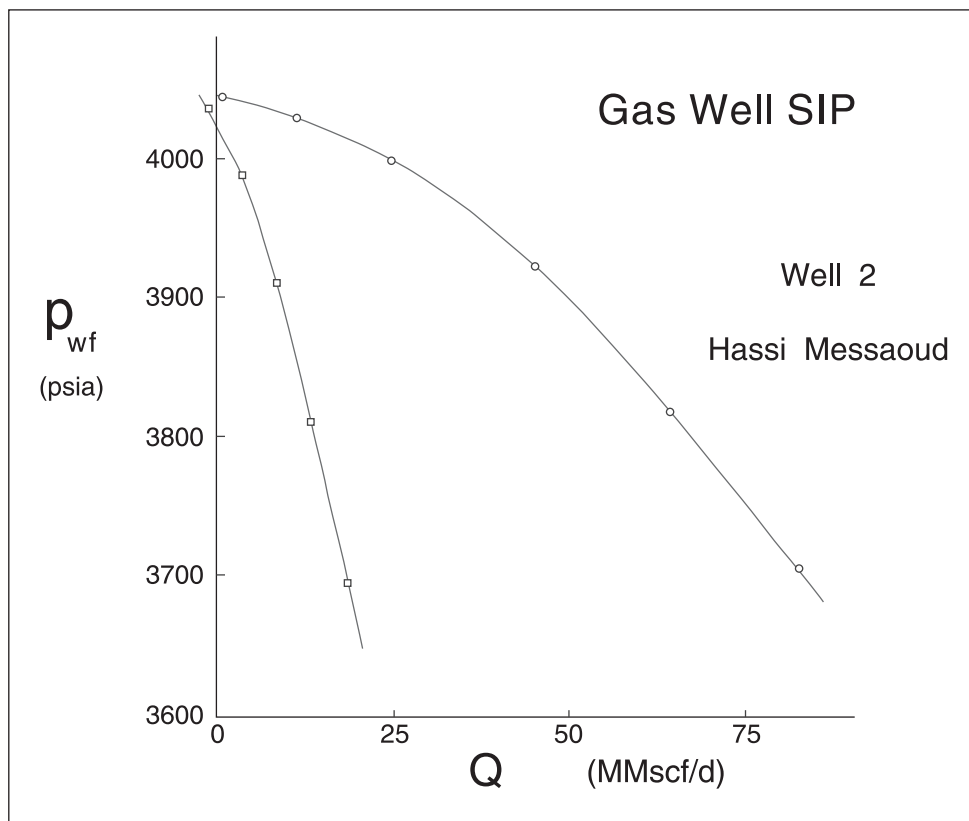


Fig. 11–33. Second gas well SIP from Algeria (Hassi Messaoud)

## Two-phase flow

For water-drive systems, the objectives of reservoir monitoring also include the detection of water breakthrough in the various layers and the subsequent periodic measurement of the developing water-cut. A diagrammatic representation of the water flooding of a stratified system is shown in figure 11–34. In layer 1, the saturation front has not yet reached the producing well and only oil flows from this layer. Layer 2 has been flooded to such an extent that water breakthrough has occurred and it produces both oil and water. Layer 3 has been completely swept to waterflood residual oil saturation  $S_{or}$  and produces only water; obviously, this layer should be closed off. In a balanced system where oil production is more or less exactly tied to water injection (on an in situ basis), reservoir pressures tend to stabilize, and in the history-matching of the reservoir simulator the main criterion is to correctly model the development of the water-cut on a layer-by-layer basis. The occurrence of water breakthrough in a well usually heralds the onset of production problems like scale deposition or fines migration, and hence the detection of the first water production is an important event. The time to breakthrough also yields information on continuity of sands between wells and sometimes provides additional evidence of the existence of thief zones.

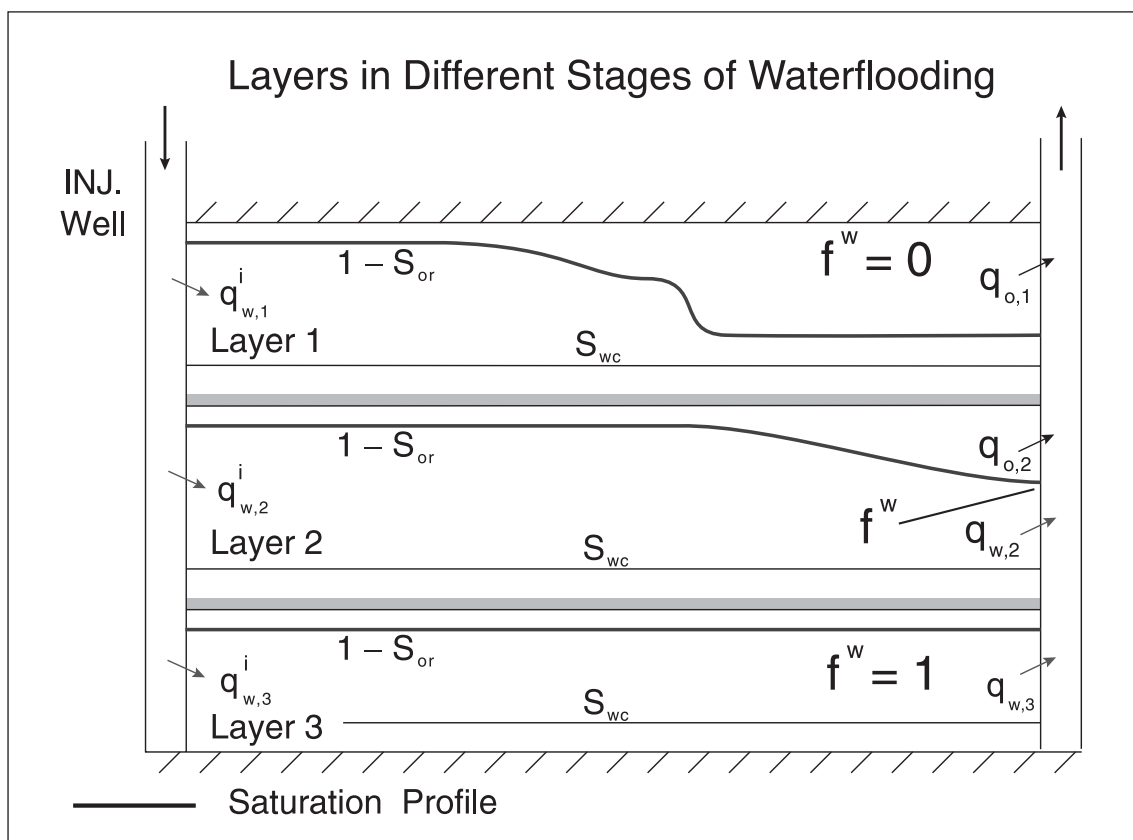


Fig. 11–34. Water flooding of a stratified system

In the two-phase situation, the interpretation of the production logs will be aimed at obtaining the water-cut (or fractional flow  $f^w$ ) of each layer. However, it must be emphasized that the resolution of the measurement is poor and the ability to accurately tie down the relative flows of oil and water from individual layers is limited. For this reason, the information from PL is complemented by pulsed neutron capture (PNC) logging which attempts to measure saturation through casing. The assignment of the total water production of the well to individual layers may be difficult, but decisions on workover depend on knowledge of the origin of the produced water. For the present purpose, it is assumed that the water-cut or fractional flow is known on a layer-by-layer basis as indicated in figure 11–34.

The stratified system illustrated in figure 11–34, with the layers separated by completely impermeable barriers, provides the opportunity to control production through dual completions and squeeze treatments. However, it is essential that the impermeable and continuous nature of the barriers has been established before such remedies are applicable. In the treatment of the two-phase production characteristics of such stratified systems, it will be assumed that no reservoir communication exists between the layers. The problem of the poor resolution of down-hole flow measurement has already been mentioned in the context of single-phase conditions; in two-phase flow, the difficulties increase dramatically and this imposes severe limitations on the implementation of two-phase SIP, for example.

A multilayer system is illustrated in figure 11–35, where commingled production from different zones to a common wellbore is taking place. Each individual layer  $j$  produces at its own watercut  $f_j^w$  which must be measured by PL surveys and is fixed by the water advance in the separate zones. The external pressures  $p_j^e$  in the layers are also variable due to differential depletion and/or support. For the moment, attention will be confined to two-phase incompressible flow of water and oil above the bubble point where a single-layer inflow performance relation of the form

$$q_{t,j} = q_{o,j} + q_{w,j} = J_j(p_j^e - p_{wf}) \quad (11-13)$$

is applicable. The individual (down-hole) phase flow rates are given by

$$q_{o,j} = (1 - f_j^w)q_{t,j} \quad q_{w,j} = f_j^w q_{t,j} \quad (11-14)$$

and the well total in situ rates are obtained by summation

$$q_w = \sum_{j=1}^N q_{w,j} \quad \text{and} \quad q_o = \sum_{j=1}^N q_{o,j} \quad (11-15)$$

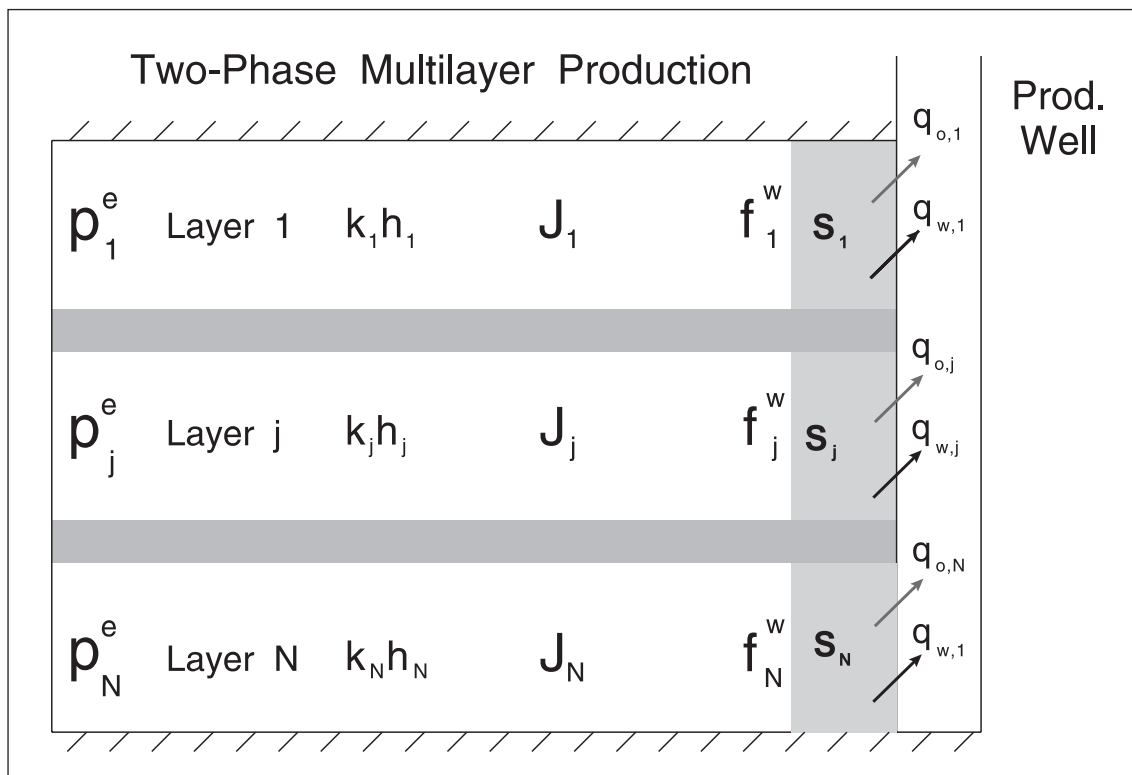


Fig. 11–35. Commingled system with layers producing at different water-cuts

The well producing water–oil ratio (WOR) then becomes

$$\text{WOR} = \frac{q_{sw}}{q_{so}} = \frac{B_o q_w}{B_w q_o} \quad (11-16)$$

The theory of two-phase incompressible flow is treated in the chapter on well performance, where the individual layer two-phase PI based on in situ total flow  $J_j$  was shown to be

$$J_j = \frac{2\pi k_j h_j \left( \frac{k_{ro}}{\mu_o} + \frac{k_{rw}}{\mu_w} \right)}{\left( \frac{1}{2} \ln \frac{4A}{\gamma C_A r_w^2} + S_{a,j} \right)} = \frac{2\pi k_j h_j \left( k_{ro} + \frac{k_{rw} \mu_o}{\mu_w} \right)}{\mu_o \left( \frac{1}{2} \ln \frac{4A}{\gamma C_A r_w^2} + S_{a,j} \right)} = \frac{2\pi h_j \left( \frac{k_j}{\mu} \right)_t}{\left( \frac{1}{2} \ln \frac{4A}{\gamma C_A r_w^2} + S_{a,j} \right)} \quad (11-17)$$

Note that in Eq. (11–17) the saturation  $S_w$  at which  $k_{ro}$  and  $k_{rw}$  are evaluated is different from layer to layer, i.e., it should be subscripted  $j$  since it depends on  $f_j^w$ . For the moment, it will be presumed that these layer two-phase PIs will be determined by the SIP technique (or full transient multilayer well testing) and it is only necessary at this stage to demonstrate that they may be treated as constants for well production analysis. In this commingled production model, it is also assumed that the individual layer water-cuts  $f_j^w$  are constant and not affected by rate—which may not be the case in a coning situation. However, the overall producing WOR is dependent on the bottom-hole flowing pressure  $p_{wf}$  which poses a problem in trying to find the well operating point on a performance diagram.

The SIP technique can be used to determine the layer pressures, water cuts, and PIs necessary for a full production analysis as illustrated in figure 11–36. A composite IPR based on total liquid rate is again valid where

$$q_t = J(p^* - p_{wf}) \quad (11-18)$$

with

$$J = \sum_{j=1}^N J_j \quad \text{and} \quad p^* = \frac{\sum_{j=1}^N J_j p_j^e}{J} \quad (11-19)$$

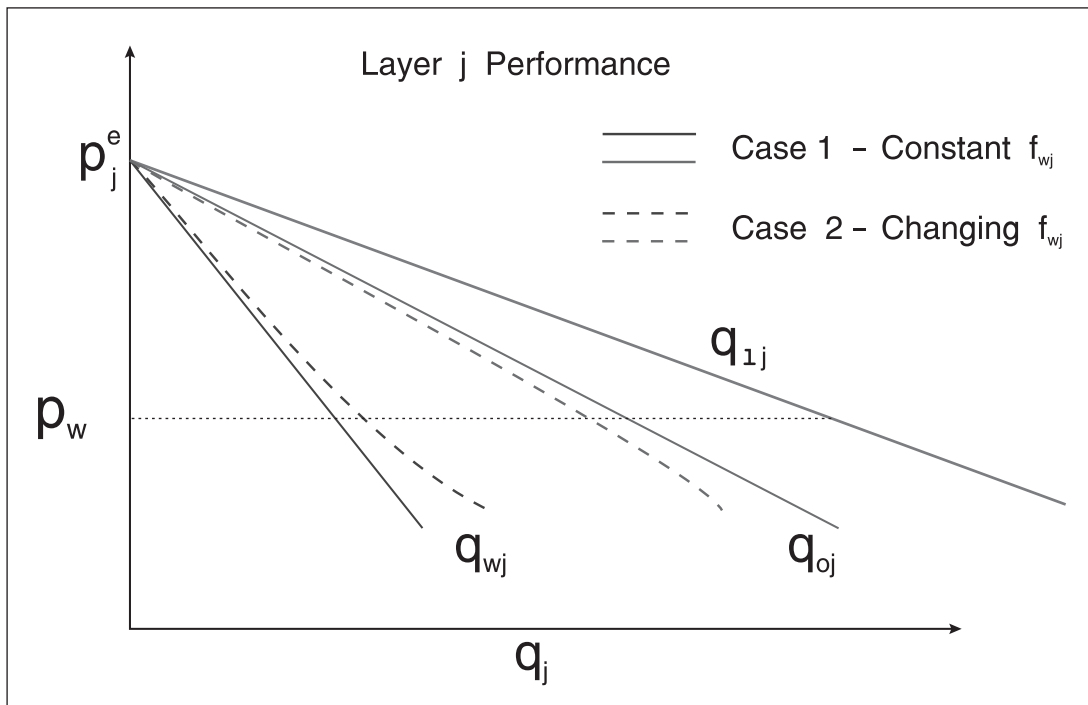


Fig. 11–36. Two-phase SIP analysis

It is also possible to derive composite IPRs for the oil and water phases as follows:

$$q_o = J_o (p_o^* - p_{wf}) \quad (11-20)$$

where

$$J_o = \sum_{j=1}^N (1 - f_j^w) J_j \quad \text{and} \quad p_o^* = \frac{\sum_{j=1}^N (1 - f_j^w) J_j p_j^e}{J_o}$$

$$q_w = J_w (p_w^* - p_{wf}) \quad (11-21)$$

where

$$J_w = \sum_{j=1}^N f_j^w J_j \quad \text{and} \quad p_w^* = \frac{\sum_{j=1}^N f_j^w J_j p_j^e}{J_w}$$

A well performance diagram showing typical composite behavior is shown in figure 11–37, where the straight line IPRs giving total liquid, total oil, and total water are plotted; this is similar in form to a two-layer system one of which produces oil and the other water. The slopes of the IPR lines are  $-1/J$ ,  $-1/J_o$ , and  $-1/J_w$ , respectively, and the intercepts are fixed by the quantities  $p^*$ ,  $p_o^*$ , and  $p_w^*$  as defined above.

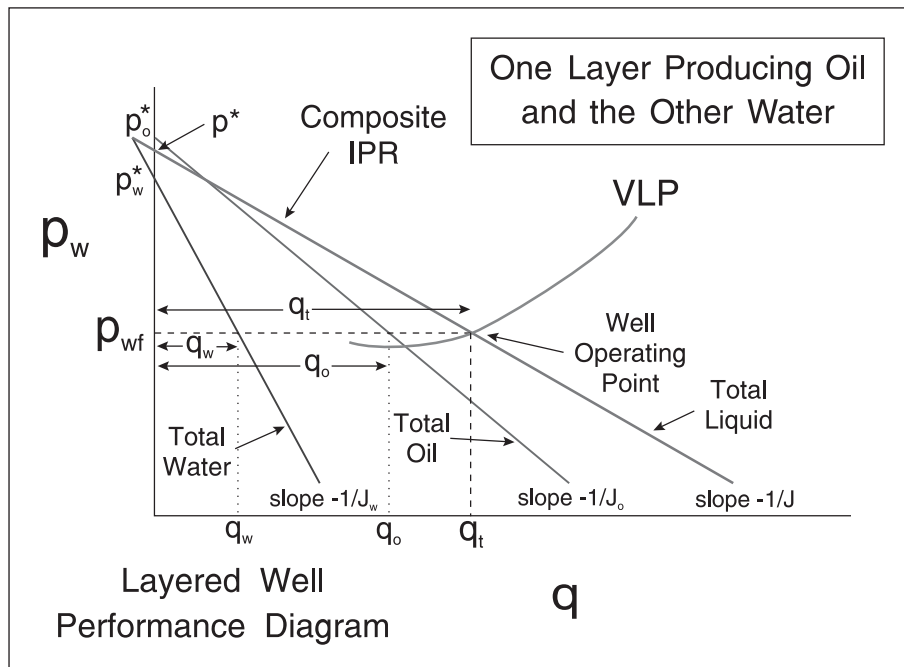


Fig. 11–37. Well performance diagram showing two-phase composites

When the layer external pressures  $p_j^e$  are different—which is generally the case—the overall water-cut denoted  $f_t^w$  and defined as

$$f_t^w = \frac{q_w}{q_w + q_o} = \frac{\sum_{j=1}^N q_{w,j}}{\sum_{j=1}^N q_{w,j} + \sum_{j=1}^N q_{o,j}} \quad (11-22)$$

depends on the well total rate  $q_t$  as illustrated in figure 11–38; this reflects the alteration in the balance of the layer contributions as the bottom-hole pressure  $p_{wf}$  changes. Thus, in a two-phase well performance diagram it is necessary to plot the total fractional flow  $f_t^w$  as a function of total liquid rate from (11–22). In order to carry out this calculation, the individual layer pressures, PIs, and fractional flows must be known. The important point is that the vertical lift performance depends strongly on the overall water-cut, and the determination of the well operating point as the intersection of the composite IPR and the VLP curve requires the appropriate function to be specified. Unfortunately, the correct value of  $f_t^w$  for the generation of the VLP relation is not known in advance and must be computed iteratively; the problem of the correct determination of the well operating point is illustrated in figure 11–39. Here, the VLP curves marked upper (u) and lower (l) have been used to bracket the actual operating curve which is determined by interpolation. When the layer pressures are all equal, as illustrated in figure 11–40, the overall water-cut  $f_t^w$  is independent of total rate and the determination of the correct value does not require iteration.

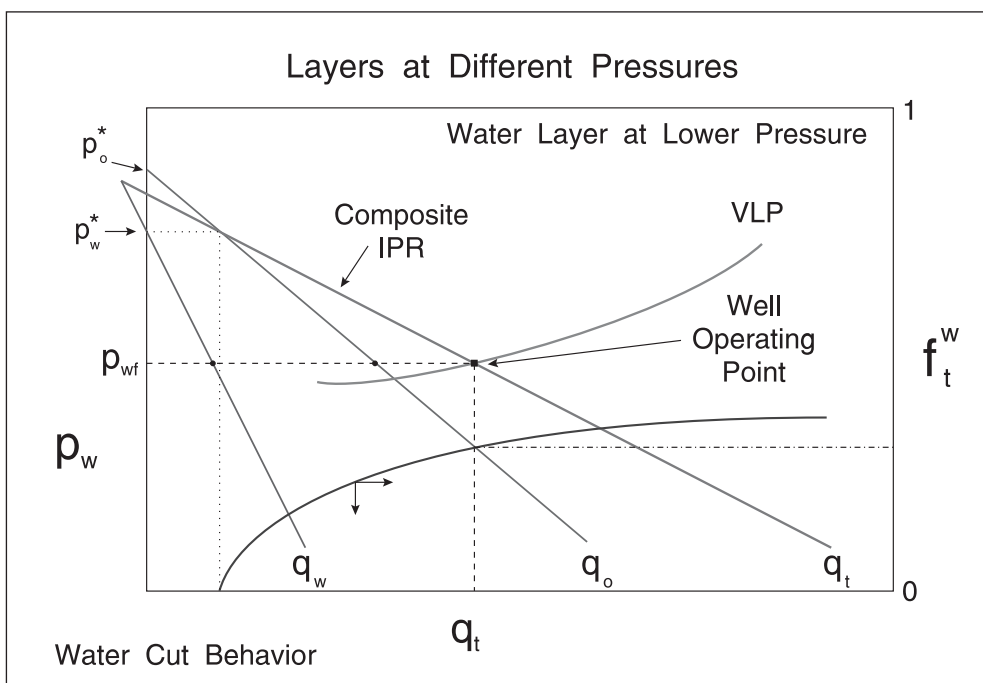


Fig. 11-38. Water-cut as a function of total rate on a well performance diagram

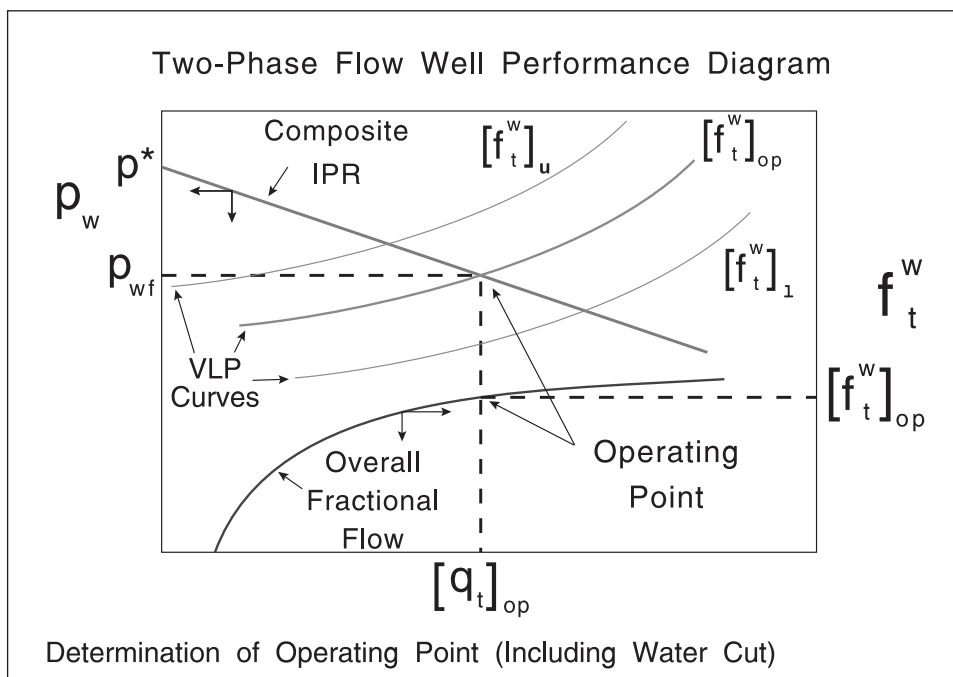


Fig. 11-39. Determination of the operating point for a well with unequal layer pressures



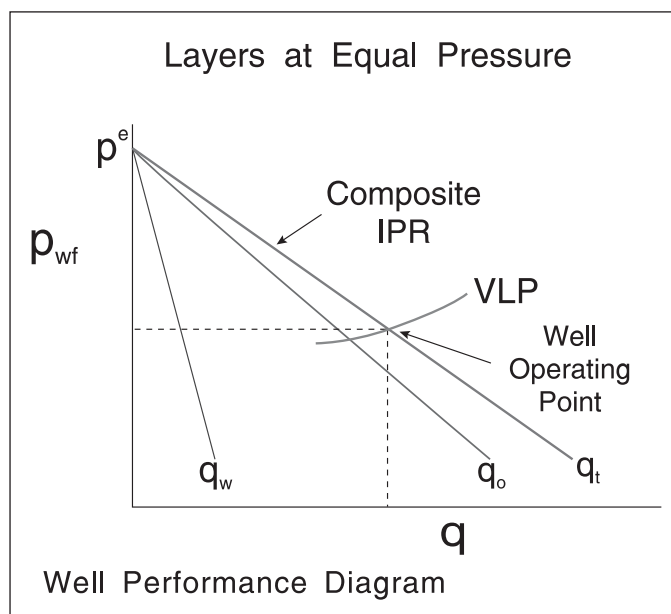


Fig. 11–40. Overall water-cut independent of total rate for equal layer pressures

The key issue in multilayer production with two-phase flow is probably the decision to workover the well and try and inhibit the water production. Recently, there have been significant advances in the technology of water shutoff, and considerable improvement to well performance can be achieved. In figure 11–41, a well performance diagram is shown for a two-layer system where layer 1 is producing both oil and water, with a high proportion of the latter. In addition, the pressure of layer 1  $p_1^e$  is high because it is well supported by the water injection. Layer 2 is at low pressure  $p_2^e$  but is still producing oil alone, i.e.,  $f_2^w = 0$ . The composite IPR and its intersection with the appropriate VLP curve give the current well operating point marked  $q_{t|op}$  with a total oil production from the two layers of  $q_{o,1} + q_{o,2}$ . If layer 1 were to be shut off, say by a casing patch or squeeze job, the VLP curve would revert to oil alone marked  $f_t^w = 0$  on the diagram. The intersection of the layer 2 IPR line with this VLP gives an oil production  $q_{o,2|alone}$  which is higher than the base case of both zones producing. This example demonstrates the importance of knowing the layer pressures in order to make intelligent workover decisions.

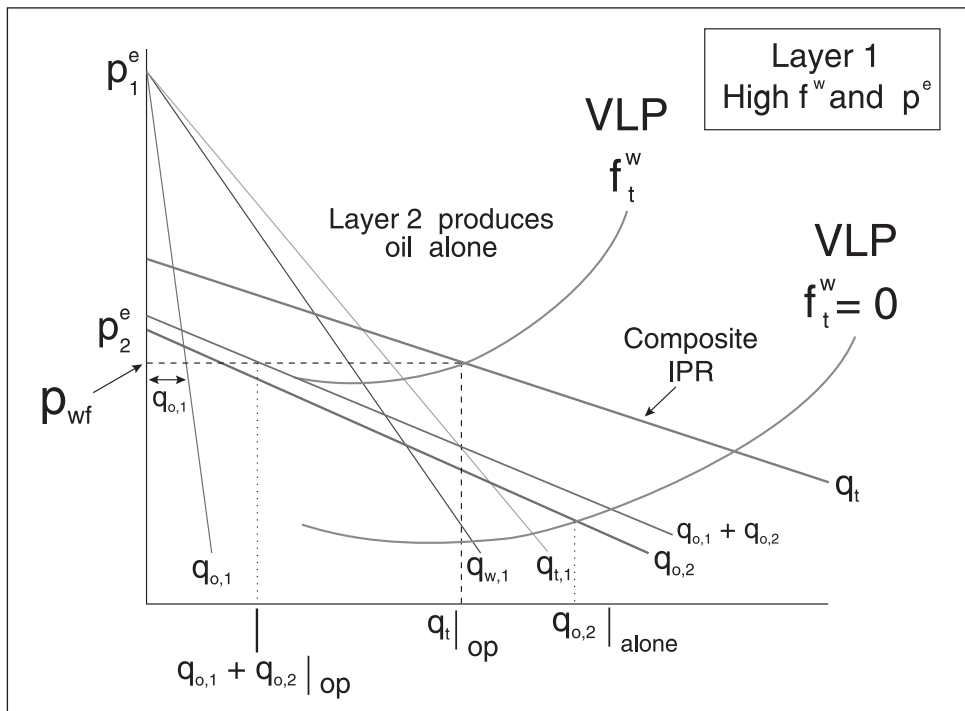


Fig. 11-41. Consequence of layer shutoff

## Integration with transient well testing and core analysis

Considering the single-phase SIP interpretation, the slope of the straight lines is associated with the inverse of the PI of the individual layers. Thus the layer PI, i.e.,  $J_{SSS,i}$ , is given by an expression of the form

$$J_{SSS,i} = \frac{2\pi\bar{k}_i h_i}{B\mu \left( \ln \frac{r_e}{r_w} - \frac{3}{4} + S_i \right)} \quad (11-23)$$

Suppose the well has been the subject of a core analysis study and the estimates of the layer permeabilities by averaging core plug data are denoted  $\hat{k}_p$ ,  $i = 1, \dots, N$  as illustrated in figure 11-42. These estimates are in error because of inadequacies in the method of averaging and alteration of the core between the in situ state in the reservoir and the modified state in the laboratory. It is difficult to say which of these effects is more important. Now, presume that in addition to the SIP PL survey in drawdown, a standard buildup has been carried out and the overall average permeability, i.e.,  $\bar{k}$ , has been determined from the semilog slope  $m$ . If the individual zone average permeabilities are written as  $\bar{k}_p$ , then for a commingled system

$$\bar{k}h = \sum_{i=1}^N \bar{k}_i h_i \quad (11-24)$$

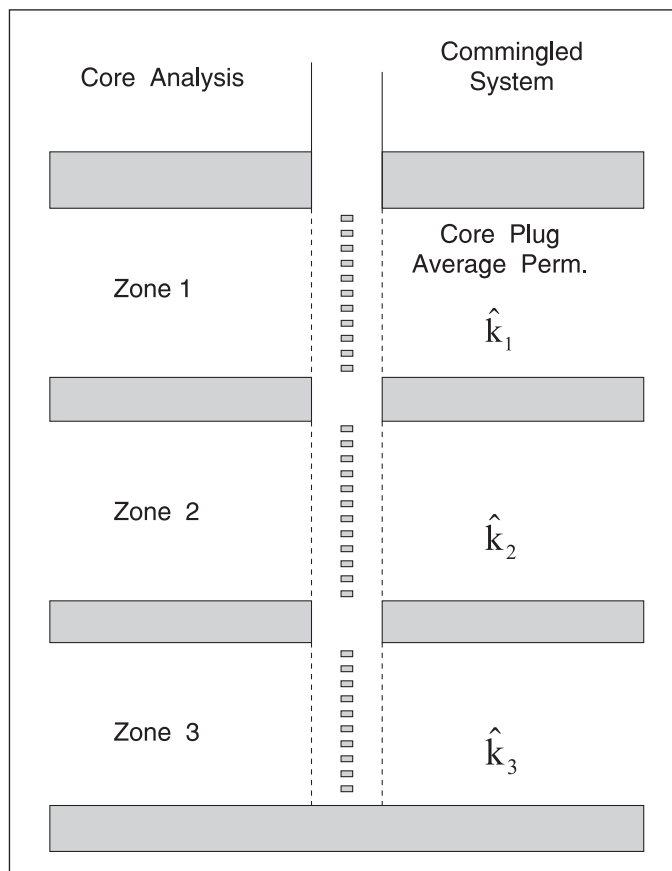


Fig. 11-42. Average zone permeabilities from core plug data

Here,  $\bar{k}_i$  is the macroscopic average permeability of flow unit  $i$  for which  $\hat{k}_i$  is an estimate. Suppose that a common correction factor  $a$  for all units can be defined through the relation

$$\bar{k}_i = a \hat{k}_i \tag{11-25}$$

Substituting (11-25) into (11-24) gives

$$\bar{k}h = \sum_{i=1}^N a \bar{k}_i h_i \tag{11-26a}$$

i.e.,

$$a = \frac{\bar{k}h}{\sum_{i=1}^N \bar{k}_i h_i} \tag{11-26b}$$

where the quantity  $\bar{k}h$  is determined from the slope of the semilog straight line (MTR) of the buildup. Here,  $a$  is simply a normalizing factor that modifies the zone average permeabilities from core analysis to agree with the overall average from a transient well test.

If the layer PI, i.e.,  $J_{SS,i}$ , is known from the SIP analysis and  $\bar{k}_i$  from corrected core data, then the layer skin factor follows from (11-23). This is a very useful extension of the SIP technique since it will allow the reservoir monitoring process to track the zone pressures and skin factors, which is the real objective of the whole procedure.

In figure 11-43, the core data from a well in the Piper Field are plotted on a logarithmic scale and a synthetic production log has been generated on the basis of cumulative  $kh$ , i.e., it has been assumed that skin is zero and the pressure is uniform. In this case, the flow profile simply follows the cumulative  $kh$  profile. The actual production log (single-phase oil flow) from the well overlays the zero-skin, uniform pressure prediction quite well, and in this case there is no evidence of plugged perforations or unusual damage in particular zones.

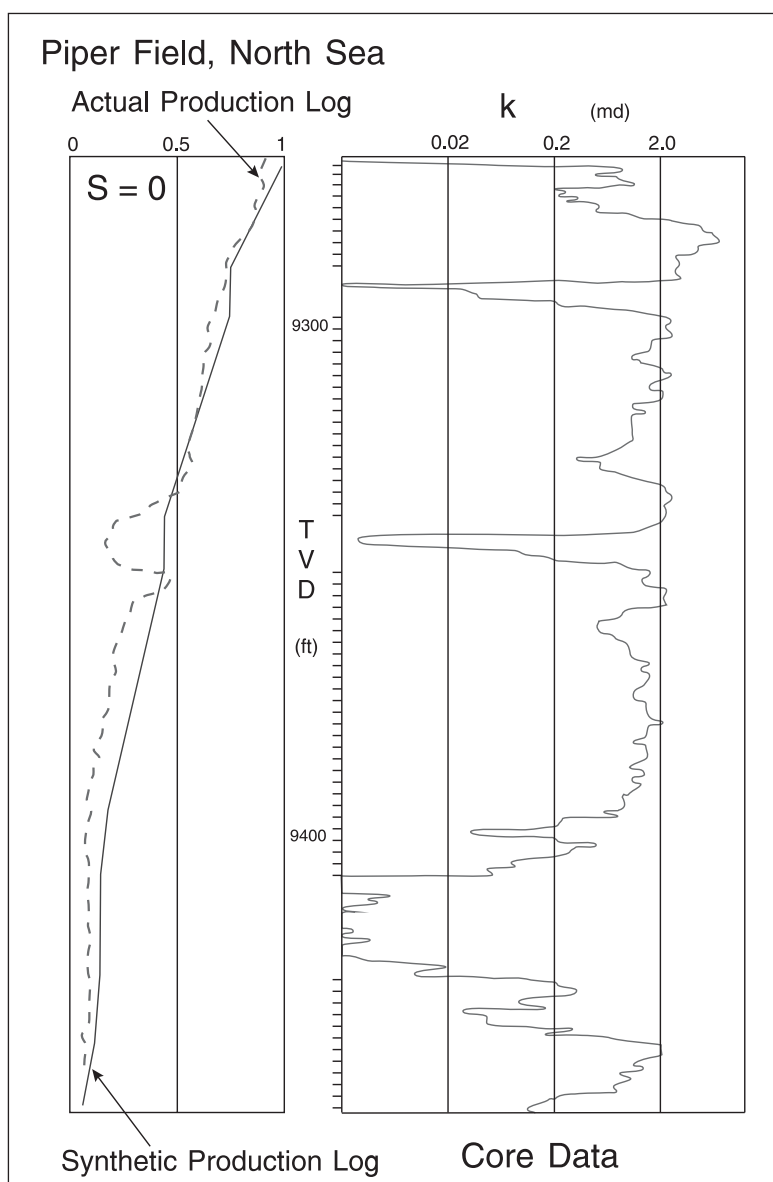


Fig. 11-43. Synthetic production log from core data

The core data here has not been normalized to a transient buildup  $\bar{k}h$ .

## Borehole video camera

The most recent innovation in PL is the use of borehole video cameras to monitor the fluids coming from perforations. The development of lenses with special wettability characteristics allow such devices to be used in oil wells in addition to gas wells where the first application was made. The video camera clearly indicates the fluids emerging from the perforations and is particularly useful in pin-pointing the zones having substantial water production. The borehole video camera is complementary to conventional PL since it is a qualitative measurement, but it holds great promise with respect to maintaining production from wells in mature fields where workover strategy is crucial.

## Notes

- 1 Hill, A. D. "Production Logging: Theoretical and Interpretive Elements," SPE Monograph 14, 1990.
- 2 Stewart, L. "Piper Field Reservoir Engineering," Paper EUR 152, European Petroleum Conference, London (Oct. 1980).
- 3 Bayat, M. G., and Tehrani, D. H. Private Communication.
- 4 Stewart, G., and Wittmann, M. J. "Well Performance Analysis: A Synergetic Approach to Dynamic Reservoir Description," (SPE 10209, 58th Annual Technical Meeting, San Antonio, Texas, Oct. 1981).

# 12

## Wireline Formation Testing (WFT) Permeability Interpretation

---

### Basic Spherical Flow Theory

The theory of pressure transient analysis applicable to wireline formation testers (WFTs) with an active probe is based on a spherical flow model. However, the actual geometry of the probe corresponds to a circular aperture on a closed-boundary cylindrical wellbore, and both hemispherical and spherical regimes occur. It is useful, first, to consider pure spherical flow and then to examine the blocking effect of the wellbore. The effect of continuing mud filtrate invasion (supercharging) is neglected in this analysis and the mudcake is assumed to be impermeable; hence it is the no-flow cylindrical boundary. The analytical solution for infinite-acting transient flow to a spherical, finite-radius source flowing at constant rate  $q$  is given in Carslaw and Jaeger and has the following form:

$$p_D = \operatorname{erfc} \sqrt{\frac{(r_D - 1)^2}{4t_D}} - \exp \left( \sqrt{\frac{(r_D - 1)^2}{t_D}} + t_D \right) \operatorname{erfc} \left( \sqrt{\frac{(r_D - 1)^2}{4t_D}} + \sqrt{t_D} \right) \quad (12-1)$$

where

$$p_D = \frac{p_i - p(r, t)}{q\mu} \quad t_D = \frac{kt}{\phi\mu c_t r_p^2} \quad r_D = \frac{r}{r_p}$$

Here,  $r_p$  is the radius of the spherical sink (called the equivalent probe radius in WFT literature) and for the flowing pressure at the sink, i.e.,  $r_D = 1$ , the expression simplifies to:

$$p_D(r_D = 1) = 1 - \exp(t_D) \operatorname{erfc}(\sqrt{t_D}) \quad (12-2)$$

This analytical solution was first quoted in the petroleum literature by Moran and Finklea<sup>1</sup> and refers to an isotropic porous medium of permeability  $k$ . The diffusion of the infinite-acting pressure disturbance is illustrated in figure 12–1, where a radius of investigation can be defined in a similar fashion to the analogous quantity in radial flow.

There is also a point sink counterpart of the finite probe radius solution and this has the following simpler form:

$$p_D r_D = \text{erfc} \left( \frac{r_D}{2\sqrt{t_D}} \right) \quad (12-3)$$

which for the sink pressure ( $r_D = 1$ ) becomes

$$p_D = \text{erfc} \left( \frac{1}{2\sqrt{t_D}} \right) \quad (12-4)$$

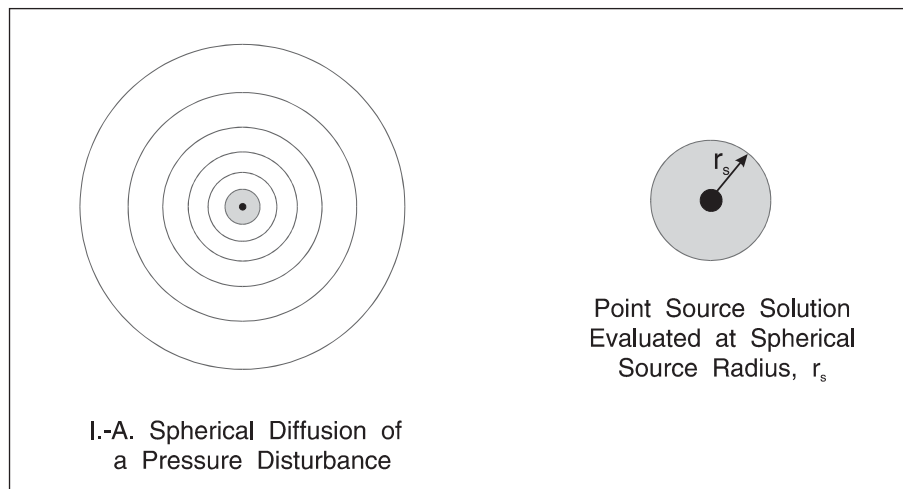


Fig. 12–1. Point source in an isotropic medium

In the same way as the exponential integral function has a log approximation, so the error function has a square-root-of-time approximation for small values of the argument. For times such that  $t_D > 8.3$ , Eq. (12–4) has the following form:

$$t_D > 8.3 \quad p_D = 1 - \frac{1}{\sqrt{\pi t_D}} \quad (12-5)$$

Thus the flowing pressure varies with the reciprocal of the square root of time and spherical flow leads to specialist plots of pressure versus  $1/\sqrt{t}$ . In terms of actual variables, the result may be written as

$$p_{pf} = p_i - \frac{q\mu}{4\pi k r_p} \left( 1 - \frac{1}{\sqrt{\pi t_D}} \right) \quad (12-6a)$$

i.e.,

$$p_{pf} = p_i - \frac{q\mu}{4\pi k r_p} + \frac{q}{4} \left( \frac{\mu}{\pi k} \right)^{3/2} \sqrt{\phi c_t} \frac{1}{\sqrt{t}} \quad (12-6b)$$

Thus a plot of flowing sink pressure  $p_{pf}$  versus  $1/\sqrt{t}$  will be a straight line of slope  $m_s$ , where

$$m_s = \frac{q}{4} \left( \frac{\mu}{\pi k} \right)^{3/2} \sqrt{\phi c_t} \quad (12-7)$$

This is the specialist plot for spherical flow, constant rate drawdown (CRD) and the slope yields the permeability  $k$  if the other parameters are known. Unlike radial flow, knowledge of the  $\phi c_t$  product is necessary for evaluation of permeability from the slope of a spherical flow plot.

The problem of formation anisotropy was also first considered by Moran and Finklea who applied the coordinate transformation suggested by Muscat; the solution to flow in an anisotropic medium can be obtained from the solution of a transformed problem which leaves vertical dimensions  $z$  unchanged and compresses the radial cylindrical coordinate  $r$  by a factor  $\sqrt{k_z/k_r}$ . Thus

$$r = \sqrt{r'^2 \frac{k_z}{k_r} + z^2} \quad (12-8)$$

A spherical source is accordingly distorted to an elliptical shape, and it was shown that the transformation also requires that the isotropic permeability  $k$  be replaced by  $k_r$  and the compressibility  $c_t$  by  $c_t k_r/k_z$ . Note that the pressure diffusion (except at very early time when pressure propagation is in the vicinity of the sink) is also elliptical (with the ellipticity orthogonal to the source shape deformation), as illustrated in figure 12-2. The dimensionless time  $t_D$  in Eqs. (12-3) and (12-5) is replaced by

$$t'_D = \frac{k_r k_z t}{\phi \mu c_t k_r r_p^2} = \frac{k_z t}{\phi \mu c_t r_p^2} \quad (12-9)$$

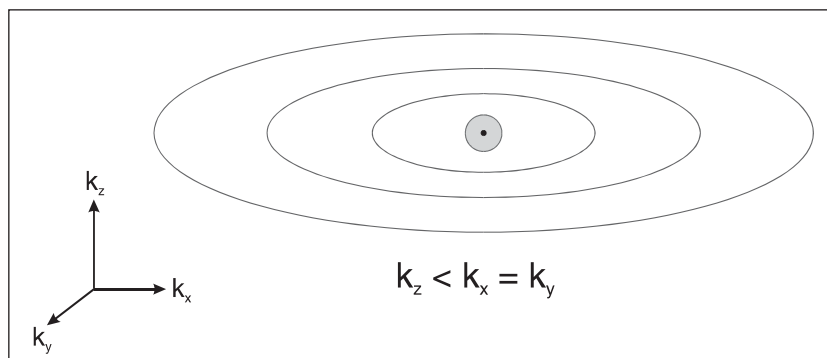


Fig. 12-2. Pressure diffusion in an anisotropic medium



The point sink solution now takes the form

$$p_D r_D = \operatorname{erfc}\left(\frac{r_D}{2\sqrt{t'_D}}\right) \quad (12-10)$$

or

$$p_D = 1 - \frac{1}{\sqrt{\pi t'_D}} \quad (12-11)$$

for  $r_D = 1$  and  $t'_D > 8.3$ . The problem is defining the radius that should be employed in the dimensionless pressure term,  $p_D$ . One way of approaching this is to use the actual radius  $r_p$  and introduce a correction term in the form of an elliptical skin  $S_{se}$ . Equation (12-11) then takes the following form:

$$p_D = 1 - \frac{1}{\sqrt{\pi t'_D}} + S_{se} \quad (12-12)$$

The spherical flow equation becomes:

$$p_{pf} = p_i - \frac{q\mu}{4\pi k_r r_p} (1 + S_{se}) + \frac{q}{4} \left(\frac{\mu}{\pi k_s}\right)^{3/2} \sqrt{\phi c_t} \frac{1}{\sqrt{t}} \quad (12-13)$$

where

$$k_s = (k_r^2 k_z)^{1/3} \quad (12-14)$$

The term  $S_{se}$  entering into Eq. (12-13) is a negative skin quantity arising from the distortion of the spherical source to an ellipsoid under the coordinate transformation which allows anisotropy to be modeled; the theory of this effect has been elucidated by Dussan and Sharma.<sup>2</sup> Spherical flow theory was first used in pressure transient analysis by Chatas,<sup>3</sup> who was concerned with an extreme limited entry in Iranian fractured reservoirs illustrated in figure 12-3.

The concept of a spherical damage skin can also be introduced into Eq. (12-12) as

$$p_D = 1 - \frac{1}{\sqrt{\pi t'_D}} + S_{se} + S_{sd} \quad (12-15)$$

where  $S_{sd}$  is a measure of rock damage in a thin spherical region around the source; this idea is illustrated in figure 12-4. The spherical flow analog of the Hawkins's equation in radial flow is

$$S_{sd} = \frac{\Delta p_s}{\frac{q\mu}{4\pi k r_s}} = \left[1 - \frac{r_s}{r_a}\right] \left[\frac{k}{k_a} - 1\right] \quad (12-16)$$

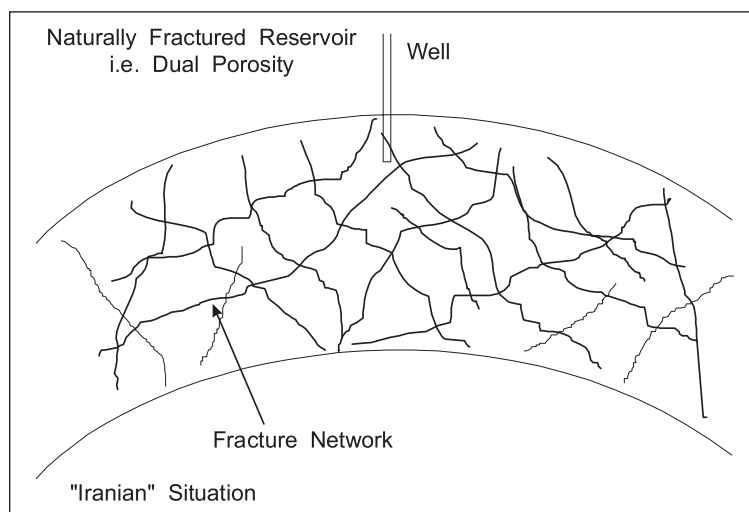


Fig. 12–3. Naturally fractured reservoir

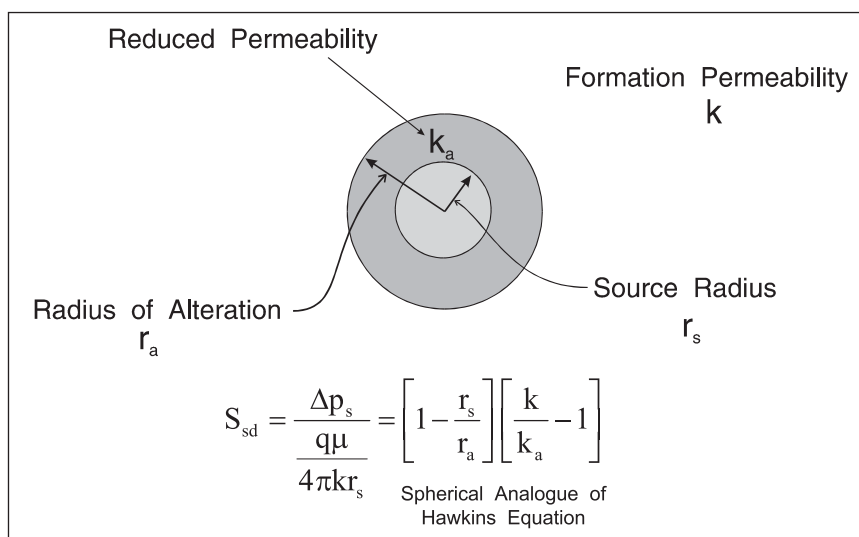


Fig. 12–4. Finite radius spherical source with formation damage

Figure 12–4 represents an idealized, perfectly spherical damaged region; in practice, the skin for a probe can be associated with the internal filter cake governed by the invasion of mud solids as depicted in figure 12–5. One issue regarding permeability from a pretest is the presence of classical formation damage in the near-wellbore region as shown in figure 12–5. The pretest pressure transient, which has a depth of investigation of the order of 3 ft, is likely to lie within the region where the permeability has been altered by mud filtrate invasion: i.e., it is the quantity  $k_a$  that will be detected.

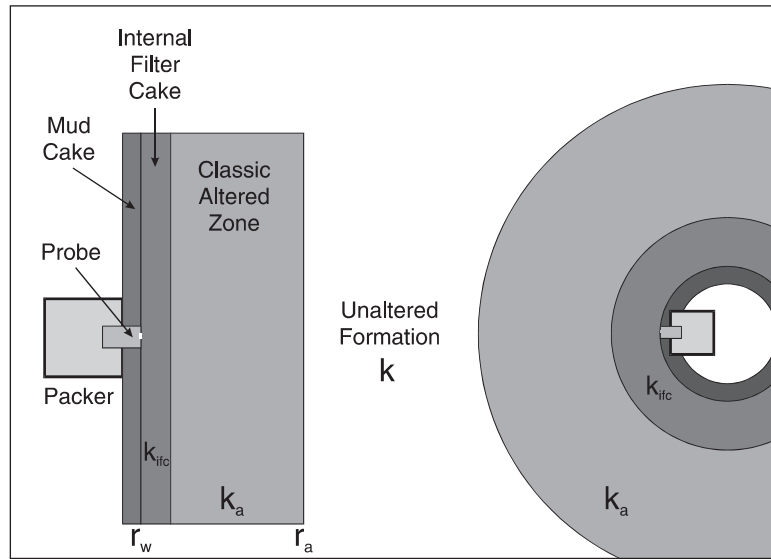


Fig. 12-5. Spherical skin concept

The spherical plot now takes the following form:

$$p_{pf} = p_i - \frac{q\mu}{4\pi k_r r_p} (1 + S_{se} + S_{sd}) + \frac{q}{4} \left( \frac{\mu}{\pi k_s} \right)^{3/2} \sqrt{\phi c_t} \frac{1}{\sqrt{t}} \quad (12-17)$$

For the purpose of conventional well test analysis, the important feature of the spherical flow plot is that the slope yields the spherical permeability  $k_s$  from the anisotropic result:

$$m_s = \frac{q}{4} \left( \frac{\mu}{\pi k_s} \right)^{3/2} \sqrt{\phi c_t} \quad (12-18a)$$

In SPE field units for oil, this becomes

$$m_s = 54637.7 \times \frac{q}{4} \left( \frac{\mu}{\pi k_s} \right)^{3/2} \sqrt{\phi c_t} \quad (12-18b)$$

and for gas, using pseudopressure  $m(p)$

$$m_s = 550206 \times \frac{QT}{4} \left( \frac{1}{\pi k_s} \right)^{3/2} \sqrt{\phi \mu c_t}$$

In the case of sandstone media with a significant degree of anisotropy, the spherical permeability  $k_s$  may be substantially lower than the radial permeability  $k_r$ .

The intercept,  $b_s$ , of the reciprocal root of time (RRT) plot based on Eq. (12-17) is given by

$$b_s = p_i - \frac{q\mu}{4\pi k_r r_p} (1 + S_{se} + S_{sd}) \quad (12-19)$$

which demonstrates that the damage skin contribution can, in principle, be determined from the intercept, provided  $S_{se}$  is known. However, it will be shown later that evaluation of this quantity requires knowledge of the anisotropy.

The spherical drawdown Eq. (12-15) has the property, theoretically, that the flowing probe pressure eventually attains a steady-state condition, i.e., becomes constant. At long flowing time, the term  $1/\sqrt{\pi t'_D}$  becomes negligible and the steady-state spherical flow equation takes the form

$$P_{pf}^{ss} = p_i - \frac{q\mu}{4\pi k_r r_p} (1 + S_{se} + S_{sd}) \quad (12-20)$$

In reality, the probe takes the form of a circular aperture located on a no-flow cylindrical boundary, i.e., the wellbore. There is a blocking effect due to the presence of the no-flow boundary and the actual flow is closer to hemispherical than spherical as illustrated in figure 12-6.

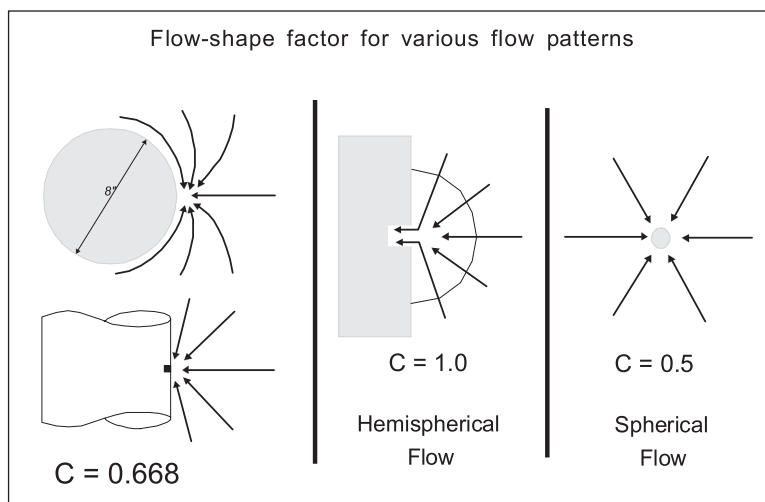


Fig. 12-6. Drawdown analysis

In the case where near-source damage  $S_{sd}$  is zero, Wittman and Stewart<sup>4</sup> wrote this in the following form:

$$P_{pf}^{ss} = p_i - \frac{C_{FE} q\mu}{2\pi k_r r_{pe}} \quad \text{where} \quad r_{pe} = \frac{r_{pa}}{2} \quad (12-21)$$

where  $C_{FE}$  is a flow shape factor that accounts for the detailed nature of the flow into the aperture located on a no-flow cylindrical wellbore. Thus there is a close correspondence between the spherical elliptical skin factor  $S_{se}$  and the flow shape factor  $C_{FE}$ . Zimmerman carried out the first

finite element simulations of flow into an aperture, showing the need for heavy grid refinement in the vicinity of the probe, and the flow shape factor in an isotropic medium was determined to be 0.668. In the analysis here, Eq. (4–20) will be written using the Dussan and Sharma effective aperture radius  $r_e = 2r_{pa}/\pi$ , which then becomes

$$p_{pf}^{ss} = p_i - \frac{q\mu}{8k_r r_{pa}}(1 + S_{se} + S_{sd}) \quad (12-22)$$

The elliptical spherical skin factor  $S_{se}$  will be determined later as a function of  $A = k_z/k_r$  and  $\epsilon = r_{pa}/r_w$  from finite element simulations of flowing probe situations. It will also be shown how the intercept of a spherical plot in transient conditions can be used to compute the damage contribution  $S_{sd}$  if a correlation for  $S_{se} = S_{se}(A, \epsilon)$  is available. The geometric skin effect  $S_{se}$  now includes the blocking effect of the wellbore on which the aperture is located and the effect of anisotropy on drawdown behavior. Note that these skin terms are based on the radial permeability  $k_r$ .

A straight line on the RRT drawdown plot will occur only if the damage skin contribution  $S_{sd}$  is constant. However, the possibility is always present that the near-probe region will be subject to a clean-up process during the flow period. In the event that  $S_{sd}$  is time dependent, then transient spherical flow analysis will fail; this is the reason why emphasis is placed on the shut-in period when zero flow (apart from a flowline storage effect) occurs at the probe. Suppose that the spherical permeability  $k_s$  and the formation pressure  $p_i$  have been determined from a buildup. The drawdown pressure record  $p_{pf}(t)$  can then be processed to evaluate the total skin  $S_s = S_{se} + S_{sd}$ , as a function of time, using Eq. (12–17). A graph of  $S_s$  versus time has the form shown in figure 12–7 and is termed a Larsen plot. This display method significantly improves the understanding of potential clean-up phenomena.

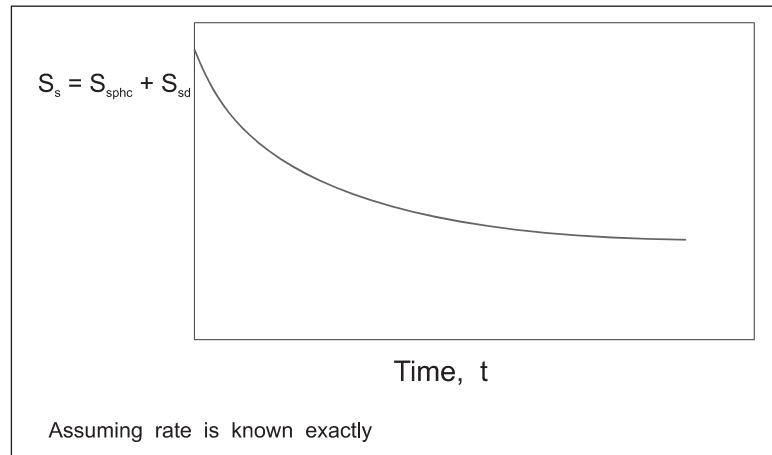


Fig. 12–7. Larsen plot of skin change during drawdown

The theory presented in the preceding section presumes that the spherical source is located in an infinitely extending porous medium. In practice, the probe may be located in a zone confined by upper and lower no-flow barriers as shown in figure 12–8. The effect of boundaries may be simulated by the use of image source terms as shown in the diagram, and the flow regime undergoes a transition from spherical to radial flow, illustrated in figure 12–9. Radial flow will

exhibit a straight line on a semilog plot of pressure versus the log of time and, if the formation thickness  $h$  is known, the radial permeability  $k_r$  can be determined from the slope.

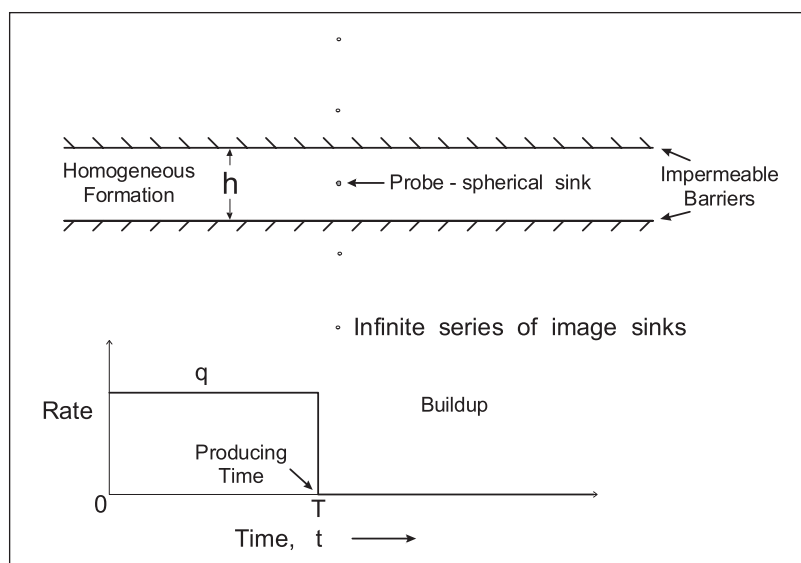


Fig. 12-8. Bounded spherical geometry

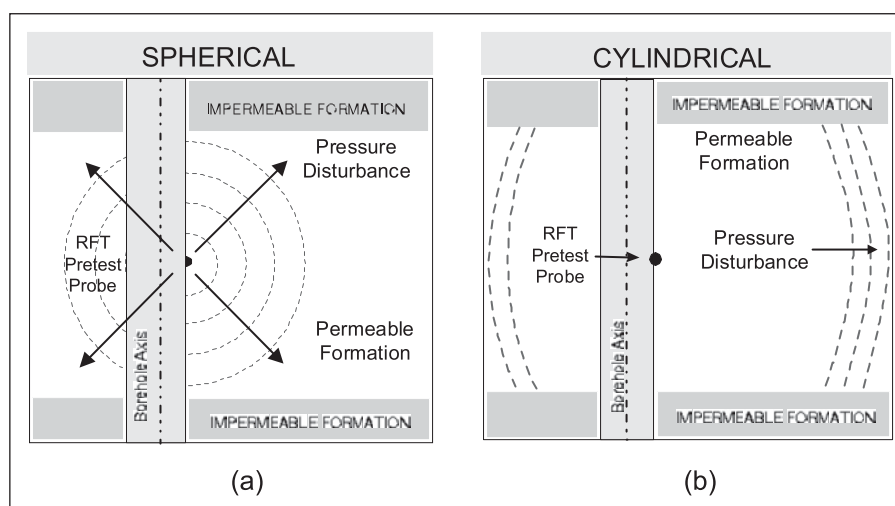


Fig. 12-9. Propagation of pressure disturbance

From a reservoir engineering point of view, it would be attractive to determine both components of the permeability, viz.,  $k_r$  and  $k_z$ . Provided the thickness  $h$  of the interval in which the formation tester tool is set is known, the radial (dip parallel) permeability can be determined from semilog analysis. However, assessment of the confining boundaries is not straightforward and much has been made of using image logs to help tie down the appropriate value of  $h$ . This is a key issue in the application of WFTs to permeability estimation.

In CRD, the specialized plot is the RRT graph which exhibits a straight line section in pure spherical flow. The terminologies early, middle, and late time regimes (ETR, MTR, and LTR) are

applicable just as in a radial flow situation. The ETR is the period when the signal is affected by flowline or wellbore storage, whereas the LTR is the period when the response is effected by local no-flow boundaries such as shales or cross-bedding. The MTR corresponds to infinite-acting spherical flow with a straight line section of ideal slope on the RRT plot. These periods are illustrated on figure 12–10.

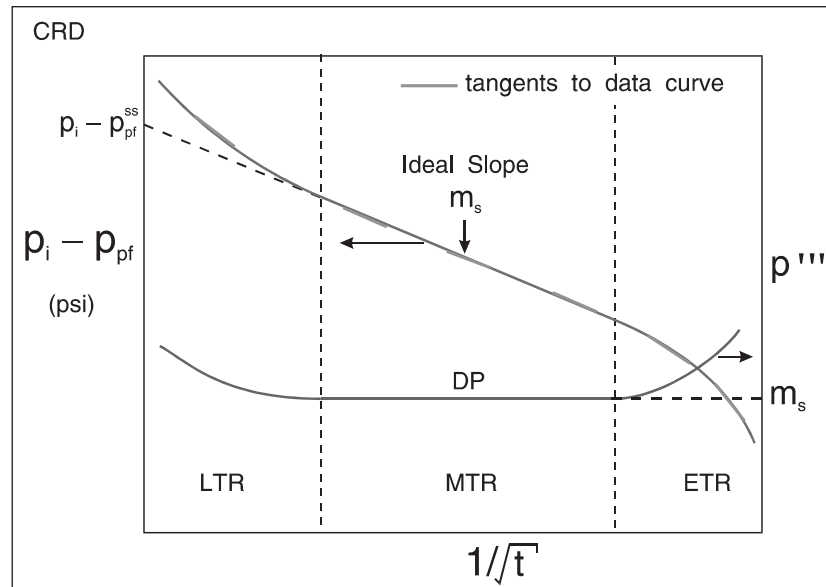


Fig. 12–10. Specialised plot for spherical flow

Following the very successful use of the logarithmic derivative in radial flow, the same approach can be extended to spherical flow. The slope of the RRT plot will be designated  $p'''$  where in CRD

$$p''' = \frac{dp_{pf}}{d\left(\frac{1}{\sqrt{t}}\right)} \quad (12-23)$$

Using the chain rule Eq., (12–23) may be expanded as

$$p''' = \frac{dp_{pf}}{dt} \cdot \frac{dt}{d\left(\frac{1}{\sqrt{t}}\right)} = -2\dot{p}t^{3/2} \quad (12-24)$$

since

$$\frac{dt^{-1/2}}{dt} = -\frac{1}{2}t^{-3/2}$$

The spherical derivative may be extracted directly from the specialized RRT plot by taking tangents to the curve as illustrated in figure 12–10. Although Eq. (12–24) suggests that the derivative of the Cartesian plot  $\dot{p}$  can be used to compute  $p'''$ , it is better to conduct the

differentiation directly on the specialized plot. It is preferable for the pressure data to be smoothed using the modern wavelet technology before the derivative  $p'''$  is extracted using numerical differentiation, for example; this is illustrated in figure 12–11 for the buildup case. The spherical derivative  $p'''$  can be overlaid on the TRRT plot as shown in figure 12–11, where the derivative plateau (DP) is a sensitive indicator of the ideal spherical flow (MTR).

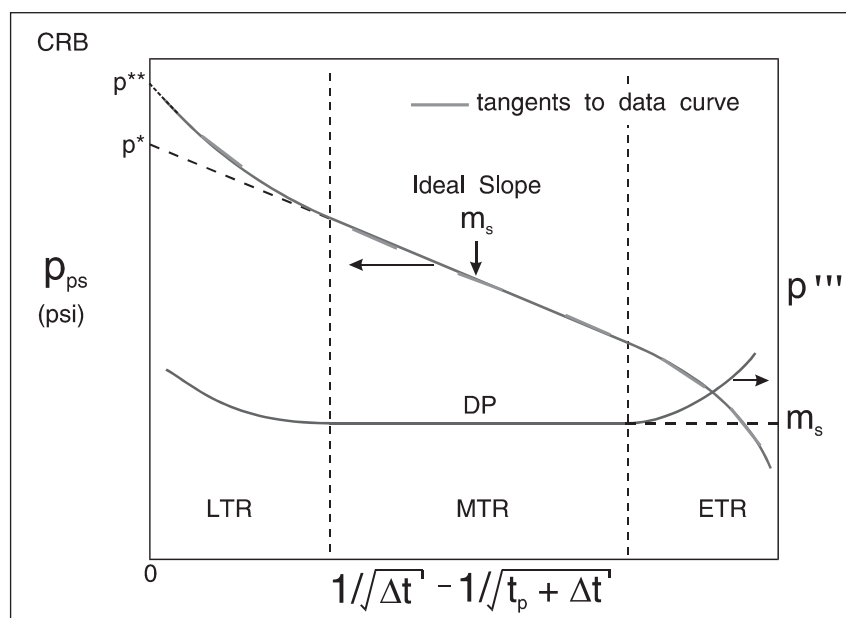


Fig. 12–11. Specialised plot for spherical flow buildup

The log–log derivative diagnostic graph for spherical flow situations takes the form of  $p'''$  plotted versus  $t$  on a log–log scale as shown in figure 12–12a and b for drawdown and buildup respectively; again, a “plateau” on the diagnostic derivative plot identifies a straight line section on the specialized RRT graph. Plotting the derivative versus time on a log–log scale allows the detection of radial flow on the diagnostic plot. Since the radial derivative follows the relation

$$p' = \dot{p}t$$

while the spherical derivative is given by

$$p''' = -2\dot{p}t^{3/2}$$

it follows that in radial flow, where  $p'$  is constant, the spherical derivative  $p'''$  will exhibit a half slope on a log–log diagnostic.



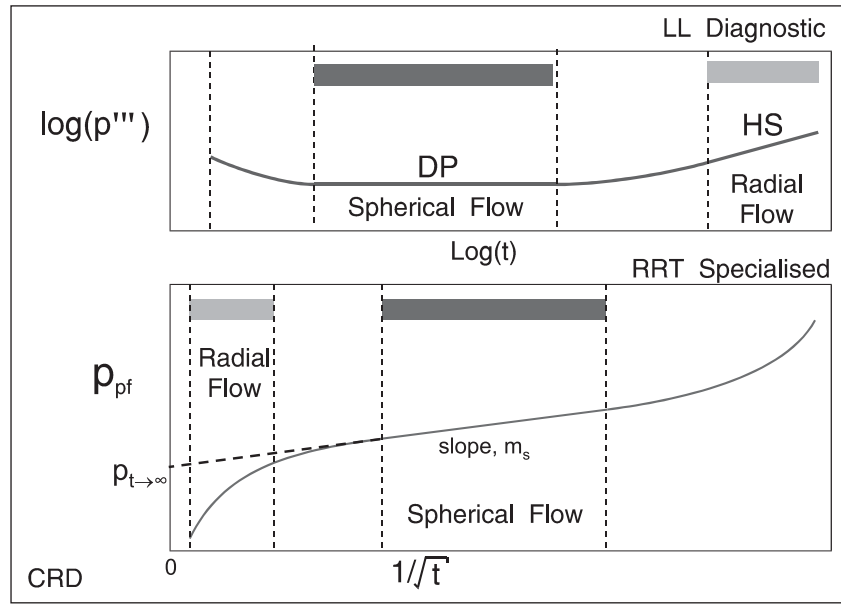


Fig. 12-12a. Overlay of LLD and RRT plots

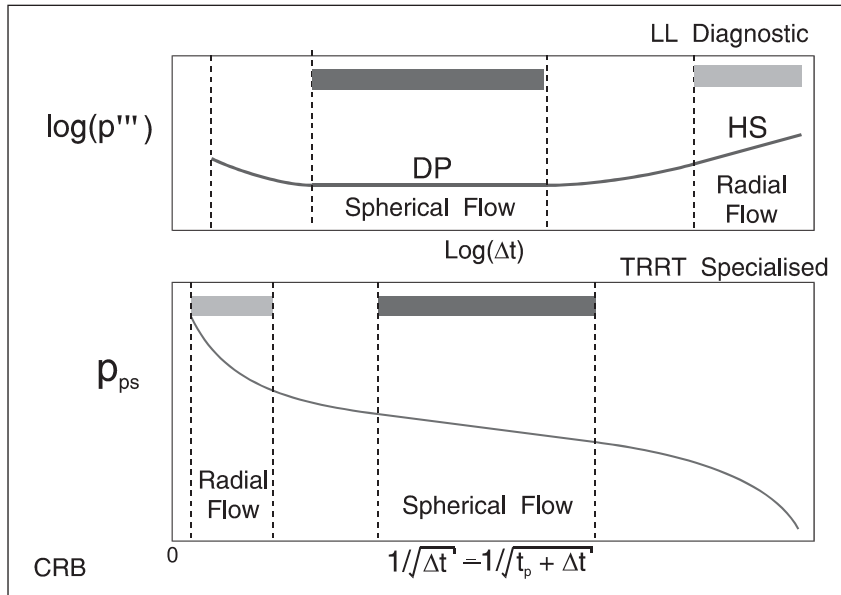


Fig. 12-12b. Overlay of LLD and TRRT plots

## Spherical flow analysis

A typical pretest on the active probe is illustrated diagrammatically in figure 12-13 for the situation where the permeability is moderate and the flowing pressure essentially reaches the steady-state condition. It has been presumed, for the moment, that the rate schedule can be represented by two constant rate periods at  $q_1$  and  $q_2$  with time end-points  $T_1$  and  $T_2$ ,

respectively. In principle, the permeability can be determined from the drawdown pressure drops, i.e.,  $\Delta p_{DD,1}$  and  $\Delta p_{DD,2}$ , as

$$\Delta p_{DD,1} = p_i - p_{sp}^{ss}(T_1) = \frac{\Omega_{ap} q_1 \mu}{4\pi k_r r_e} \quad (12-25a)$$

$$\Delta p_{DD,2} = p_i - p_{sp}^{ss}(T_2) = \frac{\Omega_{ap} q_2 \mu}{4\pi k_r r_e} \quad (12-25b)$$

i.e., 
$$k_{r,1} = \frac{\Omega_{ap} q_1 \mu}{4\pi r_e \Delta p_{DD,1}} \quad \text{and} \quad k_{r,2} = \frac{\Omega_{ap} q_2 \mu}{4\pi r_e \Delta p_{DD,2}} \quad (12-25c)$$

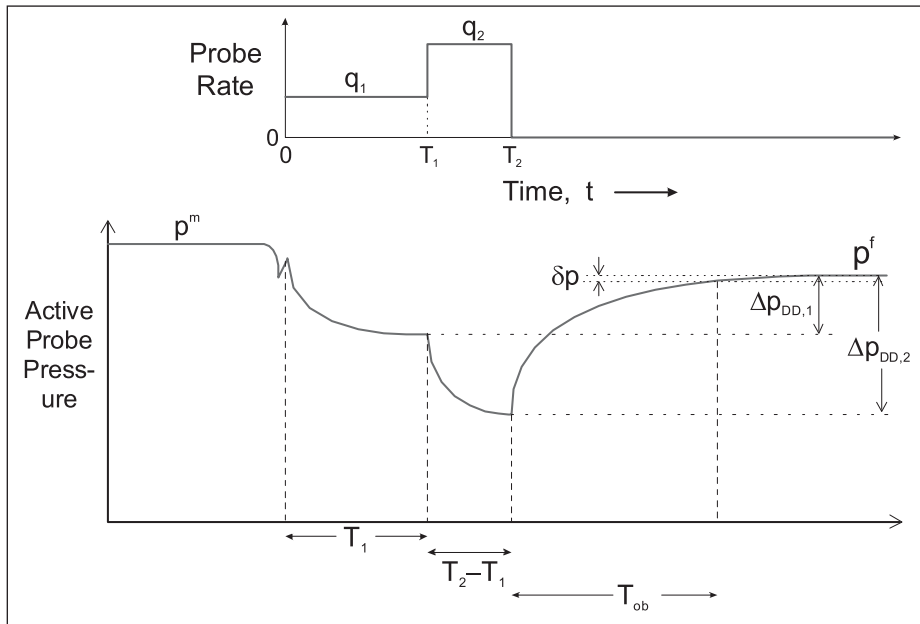


Fig. 12-13. Typical pretest pressure recording

The determination of radial permeability  $k_r$  requires knowledge of the anisotropy  $A$ , so that the aperture (active probe) shape factor  $\Omega_{ap}$  can be computed. However, the main problem with these steady-state drawdown permeability estimates is the influence of formation damage caused by internal filter cake, for example. In order to compute the pressure drops, it is necessary to know the formation pressure. In moderate and high permeability, the buildup following the period of drawdown reaches stabilization and the fluid pressure  $p^f$  can be read directly from the pretest record (Cartesian plot).

When the pretest piston stops moving, the pressure response follows shutin or buildup behavior based on the familiar superposition equation

$$p_{ps} = p_i - \frac{q\mu}{4\pi k_r r_e} \left( p_D(t_p + \Delta t)_D - p_D(\Delta t)_D \right) \quad (12-26)$$

Substituting the CRD  $p_D$  function (12–15) into the buildup superposition expression (12–26) gives:

$$p_{ps} = p_i - \frac{q\mu}{4\pi k_r r_e} \left( \sqrt{\frac{\phi\mu c_t r_e^2}{\pi k_z}} \right) \left( \frac{1}{\sqrt{\Delta t}} - \frac{1}{\sqrt{t_p + \Delta t}} \right) \quad (12-27a)$$

i.e.,

$$p_{ps} = p_i - \frac{q}{4} \left( \frac{\mu}{\pi k_s} \right)^{3/2} \sqrt{\phi c_t} \left( \frac{1}{\sqrt{\Delta t}} - \frac{1}{\sqrt{t_p + \Delta t}} \right) \quad (12-27b)$$

In low-permeability formations, the period of buildup is analyzed on a tandem reciprocal-root-of-time (TRRT) plot as illustrated in figure 12–14. Here the pressure can be extrapolated and two pressures are apparent, i.e.,  $p^*$  and  $p^f$ . Here  $p^*$  is the straight line extrapolation for spherical flow, and  $p^f$  is the extrapolation of the final trend on the spherical buildup plot. The late time upturn is the effect of horizontal barriers affecting the response. The slope of the spherical flow straight line is negative given by

$$m_s = - \frac{8 \times 10^4 q_1 \mu (\phi \mu c_t)^{1/2}}{k_s^{3/2}} \quad (12-28a)$$

(WFT field units)

or

$$m_s = - \frac{54637.7 q}{k_s^{3/2}} \left( \frac{\mu}{\pi} \right)^{3/2} (\phi c_t)^{1/2} \quad (12-28b)$$

(SPE field units)

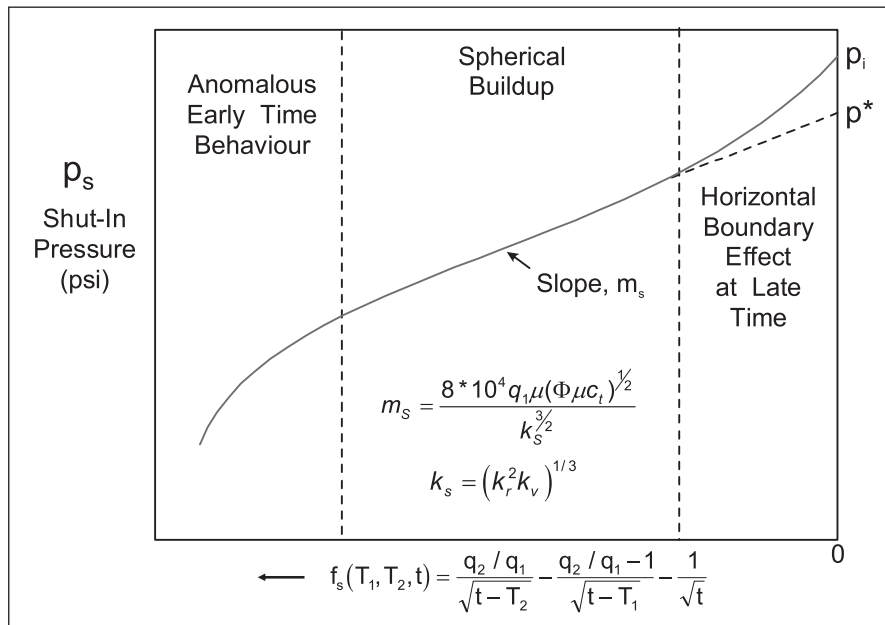


Fig. 12–14. Tandem reciprocal root of time plot for buildup

The ideal slope of the buildup plot yields the spherical permeability  $k_s$ , and again the issue of anisotropy arises.

The TRRT graph is the specialized plot for a buildup in spherical flow situations. Again, following the development of radial flow analysis, it is useful to form the derivative of the specialized plot as illustrated in figure 12–15 and to utilize the nomenclature ETR, MTR, and LTR. The derivative, denoted  $p'''$ , is therefore

$$p''' = \frac{dp_{ps}}{d\left(\frac{1}{\sqrt{\Delta t}} - \frac{1}{\sqrt{t_p + \Delta t}}\right)} \quad (12-29)$$

Using chain rule differentiation, this may be expanded as

$$p''' = \frac{dp_{ps}}{dt} \cdot \frac{dt}{d\left(\frac{1}{\sqrt{\Delta t}} - \frac{1}{\sqrt{t_p + \Delta t}}\right)} \quad (12-30a)$$

i.e.,

$$p''' = \frac{2\dot{p}}{(t_p + \Delta t)^{3/2} - \Delta t^{3/2}} \quad (12-30b)$$

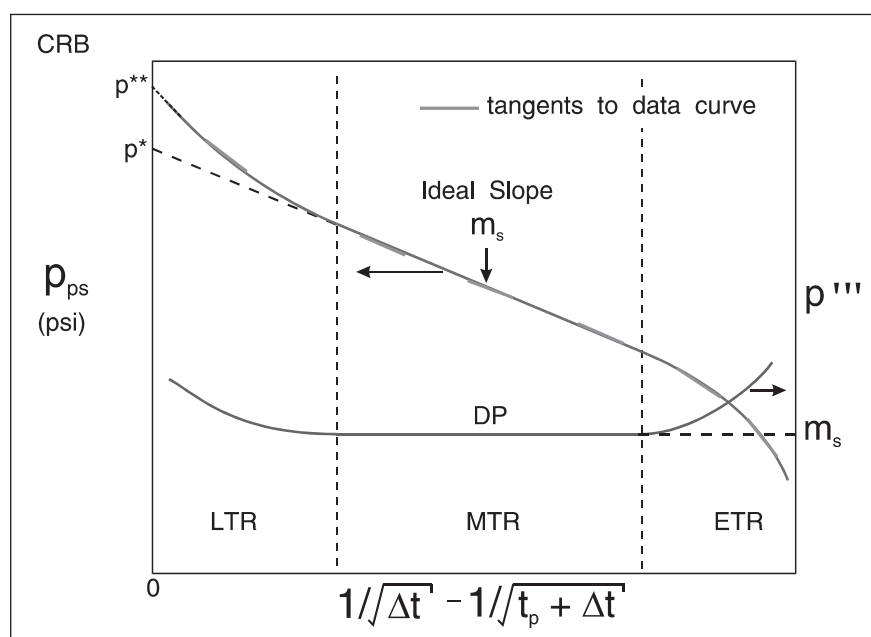


Fig. 12–15. Specialised plot for spherical flow buildup

The quantity  $1/\sqrt{\Delta t} - 1/\sqrt{t_p + \Delta t}$  is the constant rate buildup (CRB) spherical flow buildup superposition function  $f_{BS}^{sub}(\Delta t)$ , and Eq. (12-30) generalizes to

$$p''' = \frac{\dot{p}}{f_{BS}^{sup}(\Delta t)} \tag{12-31}$$

Here,  $\dot{p} = dp_{ps}/d\Delta t$  is the natural derivative of the Cartesian plot of the buildup  $p_{ps}$  versus  $\Delta t$ . In modern processing of pressure data using wavelets, the primary derivative of the data is generated after the elimination of outliers and smoothing and reduction of the data. This is the most advanced form of numerical differentiation, and Eq. (12-30) demonstrates how the reciprocal square root derivative  $p'''$  can be generated directly from the advanced  $\dot{p}$  information derived from wavelet analysis. Figure 12-16 shows the classical TRRT plot for a buildup from which the derivative is taken. The object of wavelet smoothing is to essentially remove noise and obtain data that is easier to interpret. Another attraction of the wavelet methodology is the automatic detection of break points such as the discontinuity between drawdown and buildup. Once the data has been processed in this way, it is straightforward to extract the spherical derivative directly from the specialized plot by finite differences as illustrated in figure 12-17. The process of noise removal is illustrated in figure 12-18, where random noise has been added synthetic buildup data; a smoothing algorithm should remove this, revealing the underlying signal.

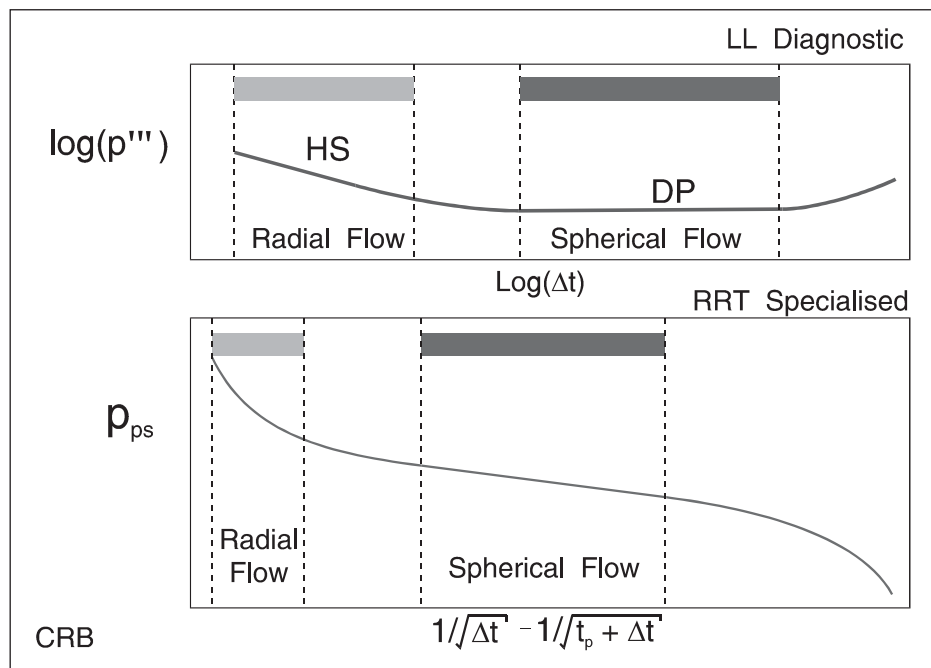


Fig. 12-16. Overlay of LLD and RRT plots

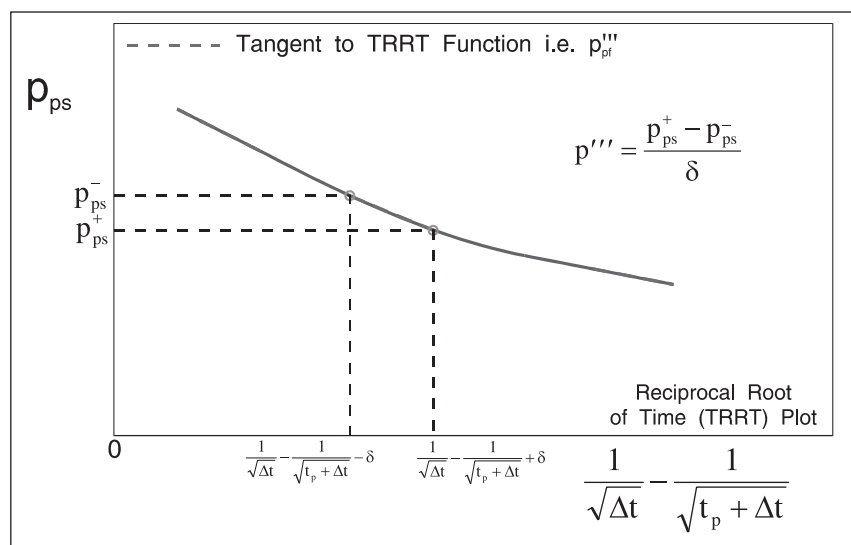
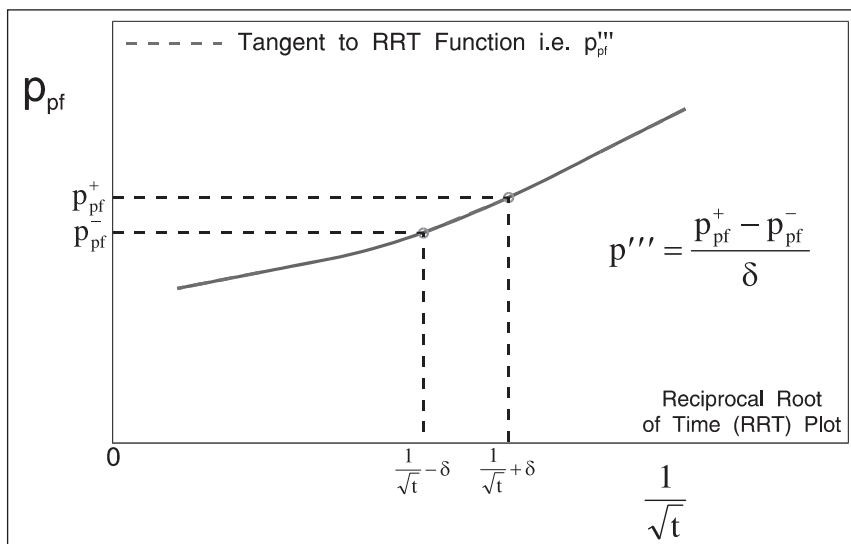


Fig. 12-17. Numerical differentiation of data for the reciprocal root derivative

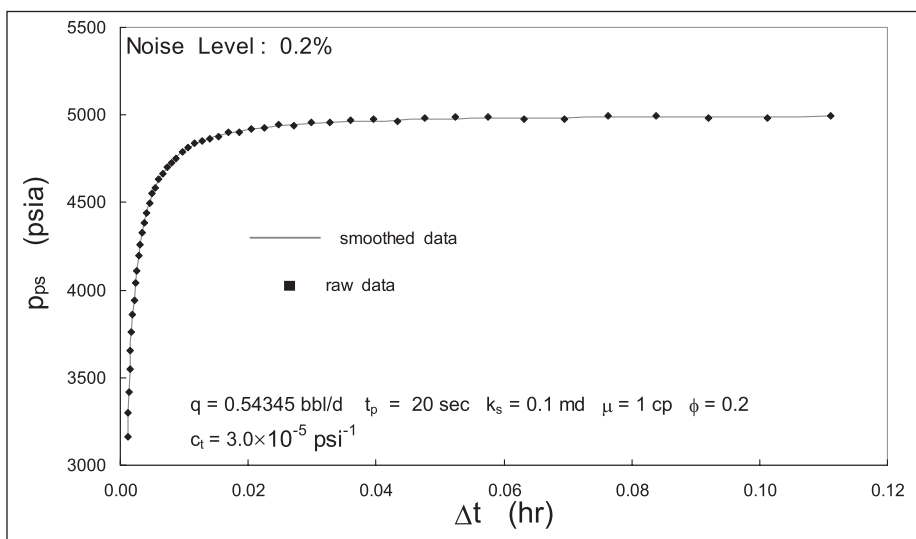


Fig. 12-18. Synthetic pretest buildup data with added random noise

The spherical flow buildup plot in standard form, i.e., Eq. (12–27), extrapolates to the initial pressure  $p_i$  as  $\Delta t \rightarrow \infty$ . It is useful to rearrange the buildup formulation into Agarwal form by writing the drawdown Eq. (12–41) at time  $t_p$  as

$$p_{pf}(t_p) = p_i + m_{sf} \frac{1}{\sqrt{t_p}} - \alpha_p (1 + S_s) \quad (12-32)$$

where 
$$m_{sf} = \frac{q}{4} \left( \frac{\mu}{\pi k_s} \right)^{3/2} \sqrt{\phi c_t}, \quad \alpha_p = \frac{q\mu}{4\pi k_r r_p} \quad \text{and} \quad S_s = S_{se} + S_{sd}$$

Subtracting Eqs. (12–27b) from (12–32) to eliminate  $p_i$  yields

$$p_{ps}(t) - p_{pf}(t_p) = -\alpha_p (1 + S_s) + m_{sf} \left( \frac{1}{\sqrt{t_p}} - \frac{1}{\sqrt{\Delta t}} + \frac{1}{\sqrt{t_p + \Delta t}} \right) \quad (12-33)$$

i.e., 
$$\Delta p_{BU} = p_{ps}(t) - p_{pf}(t_p) = -\alpha_p (1 + S_s) + m_{sf} \left( \frac{1}{\sqrt{\Delta t_{se}}} \right) \quad (12-34a)$$

or 
$$p_{ps}(t) = p_{pf}(t_p) - \alpha_p (1 + S_s) + m_{sf} \left( \frac{1}{\sqrt{\Delta t_{se}}} \right) \quad (12-34b)$$

where 
$$\frac{1}{\sqrt{\Delta t_{se}}} = \frac{1}{\sqrt{t_p}} - \frac{1}{\sqrt{\Delta t}} + \frac{1}{\sqrt{t_p + \Delta t}}$$

or 
$$\Delta t_{se} = \left[ \frac{1}{\frac{1}{\sqrt{t_p}} - \frac{1}{\sqrt{\Delta t}} + \frac{1}{\sqrt{t_p + \Delta t}}} \right]^2$$

Equation (12–34) for a buildup is in drawdown form, and the total spherical skin  $S_s$  can be calculated from the intercept in addition to the permeability  $k_s$  from the slope. The derivative diagnostics for a pretest in a thin formation are illustrated in figure 12–19, where the periods of spherical and radial flow are readily identifiable from the appropriate plateaux or half slopes (positive or negative).

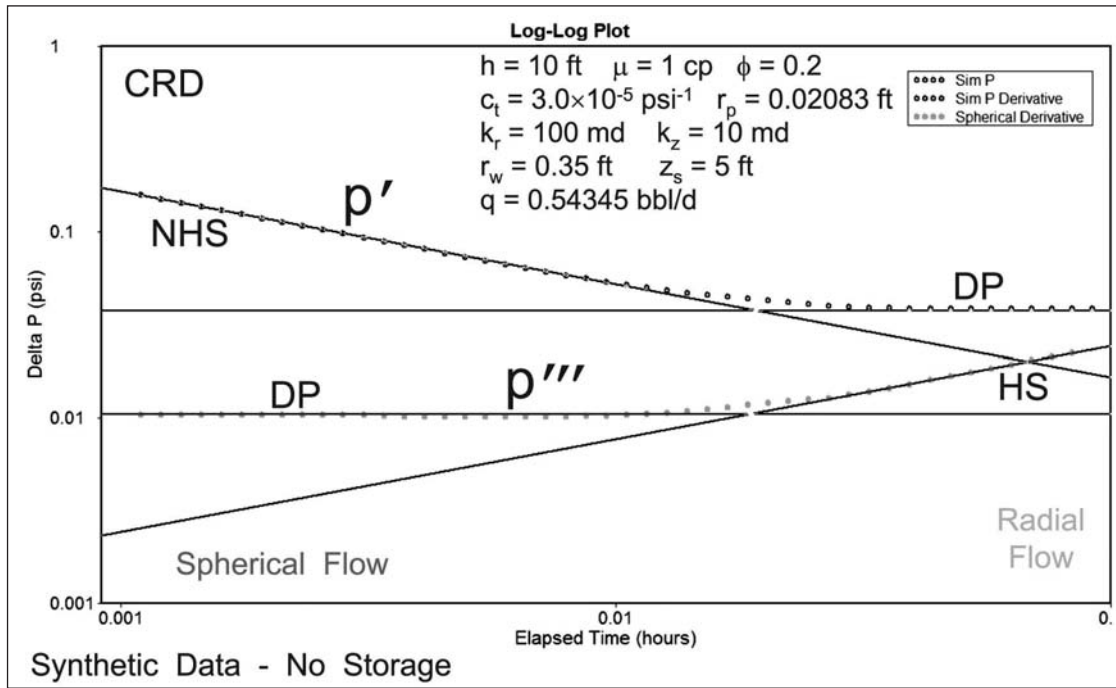


Fig. 12-19. Derivative diagnostics—pretest in a thin formation

Historically, it has been observed that the buildup (spherical) permeability computed from  $m_s$  has been nearly an order of magnitude smaller than the drawdown permeabilities computed from the original steady-state drawdown expression of Wittman and Stewart<sup>4</sup>:

$$\Delta p_{DD} = \frac{[1.1271 \times 10^{-3}] C_{q\mu}}{2\pi r_{pe} k_d} \quad (12-35)$$

where  $C$  = Wittman and Stewart flow shape factor (= 0.645 in an 8" borehole)

$r_{pe} = r_{pa}/2$  = effective probe radius

$r_{pa}$  = probe aperture radius

[ ] for SPE field units.

Thus the Wittman and Stewart<sup>4</sup> formulation was based on an isotropic medium, and the question of anisotropy was later addressed by Sharma and Dussan<sup>2</sup> who showed that the correct result for the effective probe radius in an isotropic medium  $r_e$  is

$$r_e = \frac{2r_{pa}}{\pi} \quad (12-36)$$

The steady-state drawdown in the anisotropic case was then shown to be

$$\Delta p_{DD} = p_i - p_{sp}^{ss} = \frac{q\mu}{2\pi r_{pa} k_r} F\left(\pi/2, \sqrt{1 - 1/A}\right) \quad (12-37)$$



where  $F(a,b)$  is the complete elliptic integral of the first kind; this function is tabulated in Abramowitz and Stegun, for example, and may be evaluated in Mathcad. Dussan and Sharma<sup>14</sup> have given a table (table 12–1) of the quantity

$$\Omega_{DS} = \frac{4\Delta p_{DD}^{SS} r_{pa} k_r}{q\mu} = \frac{2\pi\Delta p_{DD}^{SS} r_e k_r}{q\mu}$$

versus  $1/A = k_r/k_z$  (as defined here), and a semilog plot of the data is shown in figure 12–20.

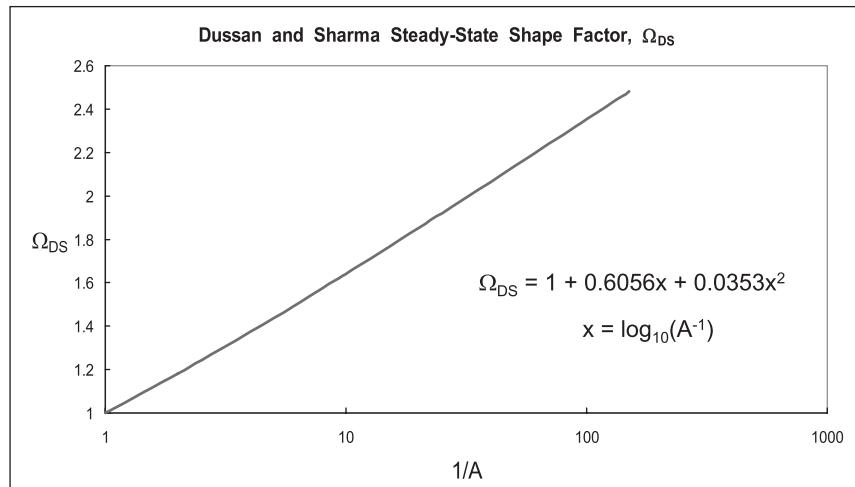


Fig. 12–20. Dussan and Sharma steady-state shape factor

Table 12–1. Steady-state shape factors of Dussan and Sharma<sup>14</sup>

1/A	$\Omega_{DS}$	1/A	$\Omega_{DS}$
1	1.0	40	2.0657
2	1.1803	50	2.1353
3	1.2917	60	2.1923
4	1.3729	70	2.2406
5	1.4370	80	2.2825
6	1.4900	90	2.3196
7	1.5353	100	2.3527
8	1.5747	110	2.3827
9	1.6098	120	2.4102
10	1.6413	130	2.4354
20	1.8515	140	2.4588
30	1.9764	150	2.4806

Note that Dussan and Sharma<sup>14</sup> considered the wellbore to be a plane, i.e.,  $r_w$  is very large compared to  $r_{pa}$ ; accordingly, in the isotropic case their result corresponds to pure hemispherical flow, i.e.,

$$\frac{2\pi\Delta p_{DD}^{SS} r_e k_r}{q\mu} = 1 \quad \text{where} \quad r_e = \frac{2r_{pa}}{\pi} \quad (12-38)$$

A quadratic regression to the data in table 12–1 gives a correlation for predicting the infinite wellbore radius shape factor  $\Omega_{DS}$ :

$$\Omega_{DS} = 1 + 0.6056 \times \log_{10}(A^{-1}) + 0.0353 \times (\log_{10}(A^{-1}))^2 \quad (12-39)$$

The theory of Dussan and Sharma<sup>14</sup> shows that Eq. (12–35) will yield radial permeability estimates which are too high since the shape factor [from Zimmerman's finite element modeling (FEM) simulations] is based on an isotropic medium. The value of  $C = 0.645$  corresponds to  $\Omega_{DS} = 0.821$ , which suggests there is a borehole effect less than hemispherical flow assumed by Dussan and Sharma.<sup>14</sup> Some new finite element simulation of an active probe needs to be carried out to resolve this discrepancy.

Dussan and Sharma<sup>14</sup> solved the problem of a disk aperture on a wellbore of essentially infinite radius. This work was considerably extended by Wilkinson and Hammond,<sup>15</sup> who gave analytical results for the finite probe radius situation defined by the parameters  $\varepsilon$  and  $\eta$ , where

$$\varepsilon = \frac{r_p}{r_w} \quad \eta = \sqrt{\frac{k_r}{k_z}} = \frac{1}{\sqrt{A}}$$

In the original repeat formation tester (RFT) tool, the quantity  $\varepsilon$  was of the order of 0.05. The results were expressed in terms of a shape factor  $C_{eff}$  where

$$C_{eff} = \frac{\Delta p(\eta, r_p, r_w)}{\Delta p(\eta, r_p, r_w = \infty)} \quad (12-40)$$

The pressure drop for an infinite wellbore radius is computed from the Dussan and Sharma theory and then this is modified for the wellbore radius effect using values of  $C_{eff}$  given by Wilkinson and Hammond listed in table 12–2 and plotted in figure 12–21a.

**Table 12–2.** Wilkinson and Hammond shape factors ( $C_{eff}$ )

$\frac{k_r}{k_z} = \frac{1}{A}$	$\varepsilon = 0.025$	$\varepsilon = 0.05$	$\varepsilon = 0.1$	$\varepsilon = 0.2$	$\varepsilon = 0.3$
$10^{-2}$	0.99	0.98	0.97	0.94	0.93
$10^{-1}$	0.99	0.98	0.96	0.93	0.90
1	0.98	0.96	0.94	0.90	0.86
10	0.97	0.95	0.91	0.86	0.82
$10^2$	0.95	0.92	0.87	0.81	0.77
$10^3$	0.91	0.87	0.82	0.76	0.72
$10^4$	0.87	0.82	0.77	0.72	0.68
$10^5$	0.82	0.78	0.73	0.68	0.65
$10^6$	0.78	0.74	0.70	0.66	0.63

The steady-state active-probe pressure drop becomes

$$\Delta p_{DD}^{SS} = \frac{q\mu\Omega_{DS}C_{eff}}{4r_{pa}k_r} \quad (12-41)$$

The data in table 12–2 is quoted only to two decimal places since Wilkinson and Hammond estimated this to be appropriate for the accuracy of the approximation in their formulation. In order to provide an algorithm for computer use, the curves of figure 12–21a, i.e., the data of table 12–2, was fitted by cubic polynomials of the form

$$C_{eff} = a_0(\varepsilon) + a_1(\varepsilon)x + a_2(\varepsilon)x^2 + a_3(\varepsilon)x^3 \quad (12-42)$$

where

$$x = \log_{10}(1/A) \quad A = k_z/k_r$$

The coefficients,  $a_j(\varepsilon)$   $j = 0, \dots, 3$ , were then fitted as quadratics in the parameter  $\varepsilon$ . The shape factors  $C_{eff}$  from this correlation are plotted in figure 12–21b, and it is probable these are more accurate than the data in table 12–2; the assumption of regularity of the underlying function of two variables  $x$  and  $\varepsilon$  allows error in the approximation to be reduced by smoothing.

For the default values of  $r_p = 0.25''$  and  $r_w = 4''$  i.e.,  $\varepsilon = 0.0625$ , the shape factor  $C_{eff}$  is 0.963 in an isotropic medium ( $A = 1$ ); for  $A = 0.01$ , it reduces to 0.903. The composite shape factors  $\Omega_{DS}C_{eff}$  and  $\Omega_{ap}$  are listed in table 12–3.

**Table 12–3.** Composite active probe shape factors ( $\Omega_{ap}$ )

A	$\Omega_{DS}$	$C_{eff}$	$\Omega_{DS}C_{eff}$	$\Omega_{ap} = 2\Omega_{DS}C_{eff}$	$\frac{k_{DD, A=1}}{k_s} = \frac{1.926}{\Omega_{ap}A^{1/3}}$
1	1	0.963	0.963	1.926	1
0.1	1.641	0.9375	1.538	3.076	1.349
0.01	2.353	0.903	2.125	4.250	2.103
0.001	3.1345	0.862	2.702	5.404	3.564

$r_p = 0.25'' r_w = 4'' \varepsilon = 0.0625$

Here,  $\Omega_{ap}$  is the quantity that should be used in Eqs. (12–25c) for evaluating steady-state drawdown pressure drops; alternatively, Eq. (12–43) given below can be used. As anisotropy becomes more severe, i.e.,  $A$  becomes smaller, the composite shape factor becomes larger. Therefore using the isotropic value will give too low a drawdown radial permeability—by approximately a factor of 2, at  $A = 0.01$ , which is modest for sandstone. In the final column of table 12–3, the ratio of naïve drawdown permeability, calculated assuming an isotropic shape factor and denoted  $k_{DD, A=1}$ , to the buildup spherical permeability  $k_s$  is listed. At a severe anisotropy of 0.001, the simplistic drawdown permeability is about 4 times larger than the spherical buildup value.

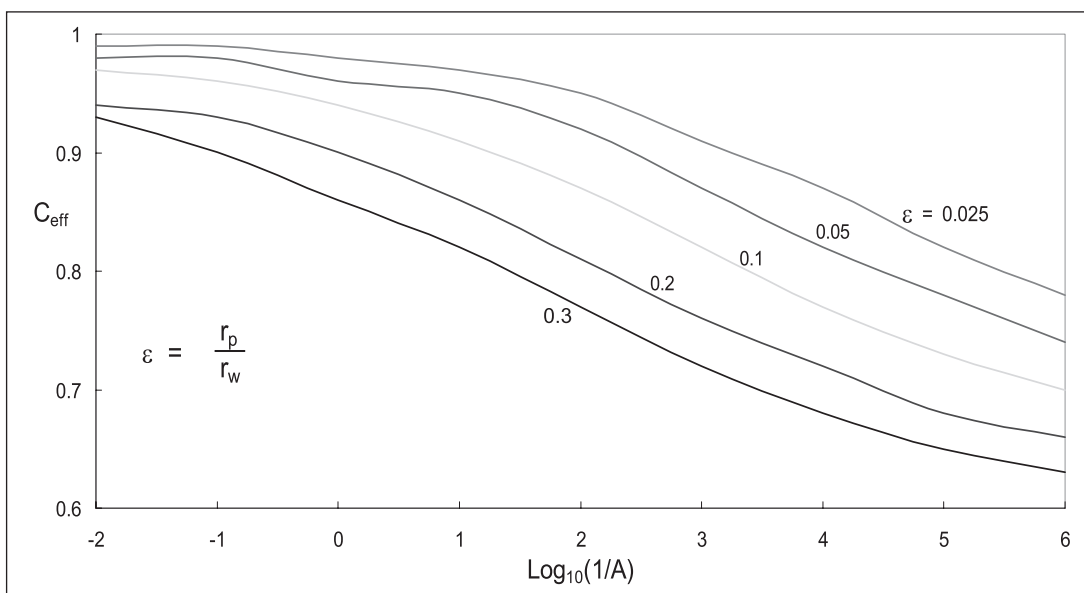


Fig. 12-21a. Wilkinson and Hammond steady-state shape factors

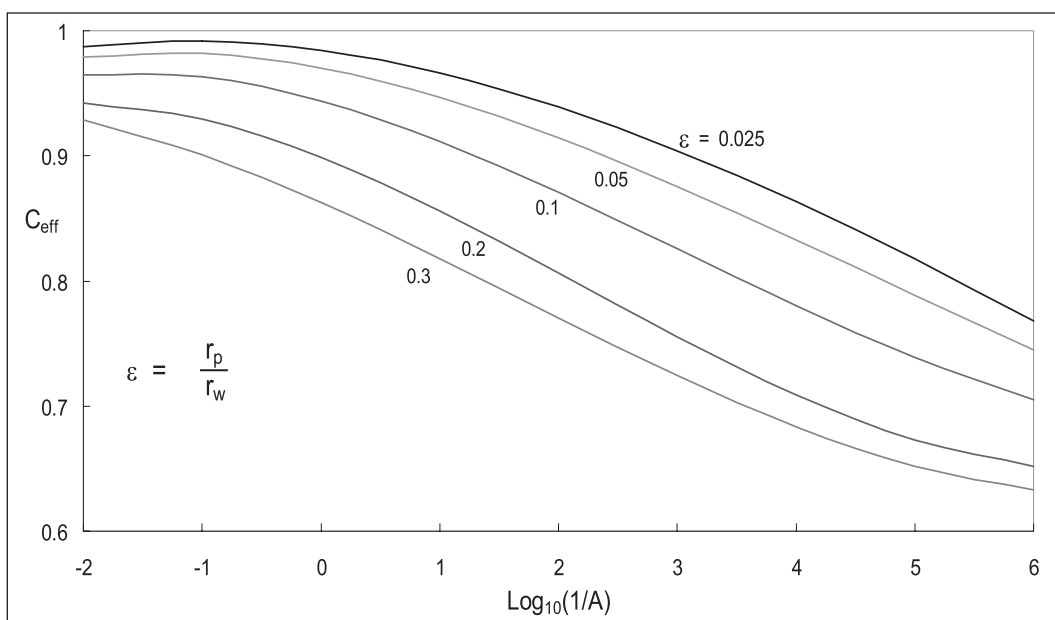


Fig. 12-21b. Wilkinson and Hammond smoothed shape factors

In a software application, the user can specify the anisotropy  $A$ , the wellbore caliper radius  $r_w$ , and the probe aperture radius  $r_{pa}$ , and the drawdown radial permeability estimates can be computed as

$$k_{r,1} = \frac{\Omega_{DS} C_{eff} q_1 \mu}{4r_{pa} \Delta p_{DD,1}} \quad \text{and} \quad k_{r,2} = \frac{\Omega_{DS} C_{eff} q_2 \mu}{4r_{pa} \Delta p_{DD,2}} \quad (12-43)$$

In an M.Eng. project at Heriot-Watt University, Radcliffe examined a large amount of Shell North Sea data and concluded that the RFT drawdown permeabilities from Eq. (12-35) were much

closer to adjacent core plug permeability (converted to in situ liquid values) than those from RFT pretest buildup slopes  $m_s$  Eq. (12–26). In this study, the whole core was depth-matched to the wireline logs using a laboratory gamma-ray scan and the core air permeability was corrected to in situ liquid permeability using an established correlation due to Juhasz. Figures 12–22–12–24 show the plots for some of the pretest analyses for permeability, and the location of examples 1 and 2 are indicated on figure 12–25. In figure 12–26, the WFT drawdown permeability is plotted versus the nearest core plug measurement and, although there is considerable scatter, overall agreement is apparent. However, the WFT buildup permeabilities computed from the slope of the TRRT plot shown in figure 12–27 are much lower than the core plug measurements. This finding has never been properly explained and more work is necessary. It has been speculated that the drawdown permeability should be lower than the buildup estimate because of fines migration or non-Darcy flow in the vicinity of the probe. It is more difficult to explain why the DD permeability is much larger than  $k_{BU}$ .

The anisotropic theory of Wilkinson and Hammond suggests that the radial drawdown permeability calculated with an isotropic shape factor will be too low; buildup transient analysis yields the spherical permeability  $k_s$ . Thus it is the ratio  $k_{DD, A=1}/k_s$  that is relevant to Radcliffe’s results. A factor of 3.5 (at  $A = 0.001$ ) does not fully explain the contrast between the two permeability estimates. One possible explanation lies in two phase flow effects. In gas condensate wells, there is a rate-dependent relative permeability effect near a flowing well; this phenomenon has been termed “viscous stripping” or “blow-through.” It could be the case that high velocity in the near-probe region reduces the capillary number and hence improves relative permeability. The DD pressure drop occurs very close to the probe, whereas the buildup process in pretest gives an average over about 3 ft. In the oil zone with water-based mud, the buildup permeability will reflect the blocking effect of two-phase (oil–water) flow. The drawdown process might reflect single-phase mud filtrate flow and hence be higher. This is very tentative, but some explanation of Radcliffe’s results must be validated. Figure 12–28 from the paper of Dussan and Sharma indicates a difference between drawdown and buildup permeabilities, which may partly explain Radcliffe’s findings.

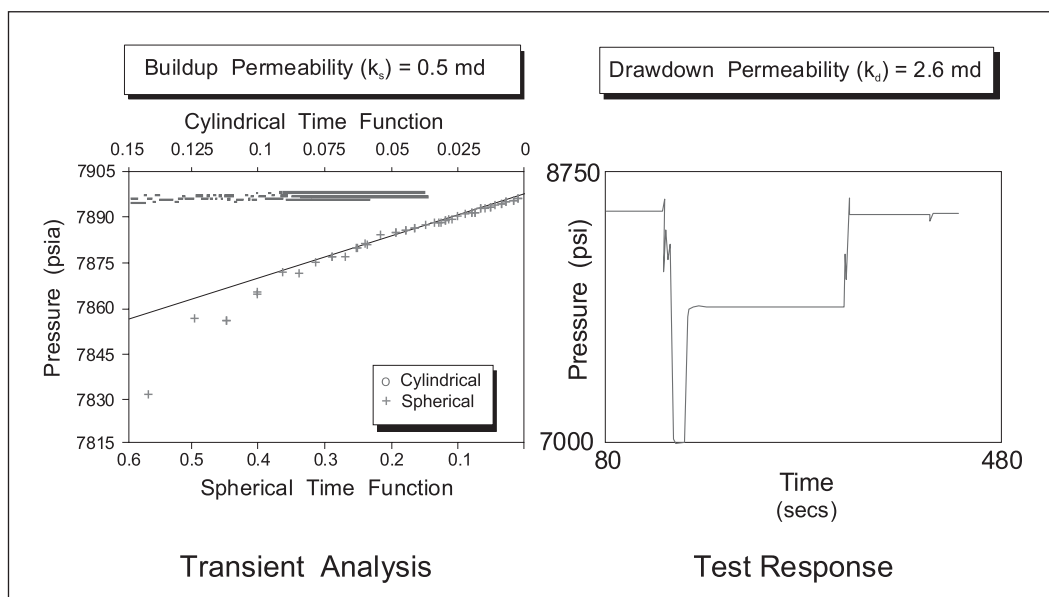


Fig. 12–22. RFT pretest example 1

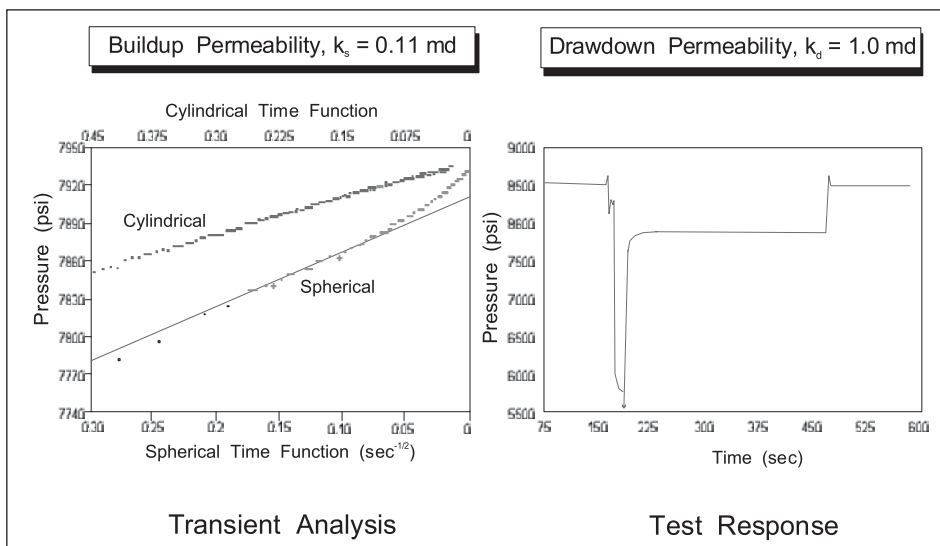


Fig. 12-23. RFT pretest example 2

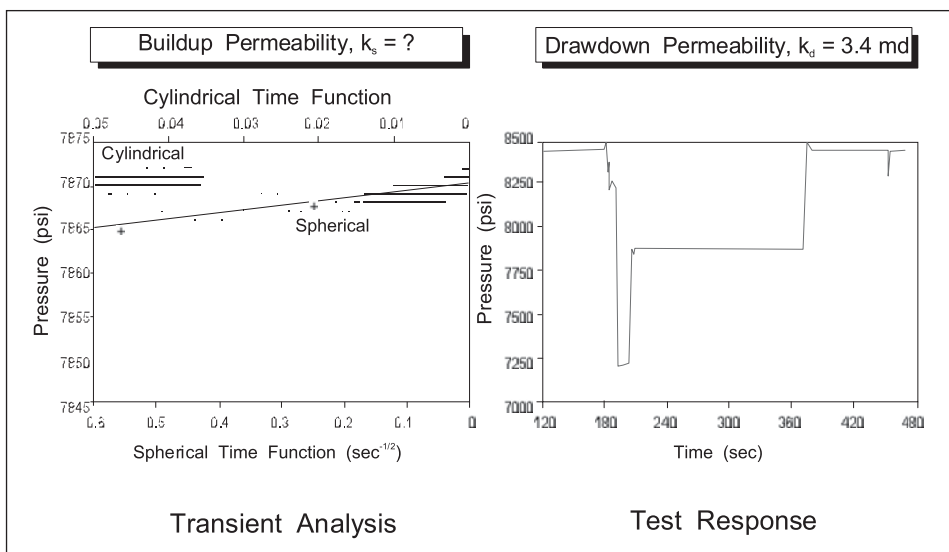


Fig. 12-24. RFT pretest example 3

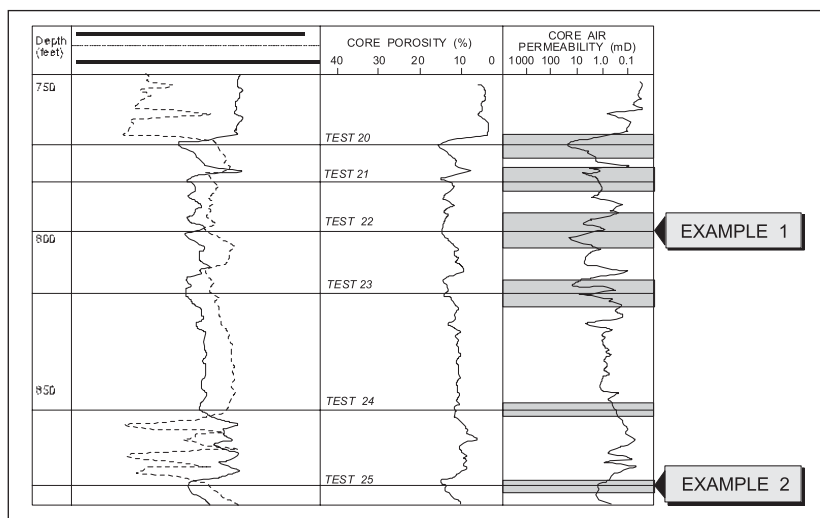


Fig. 12-25. Typical field data

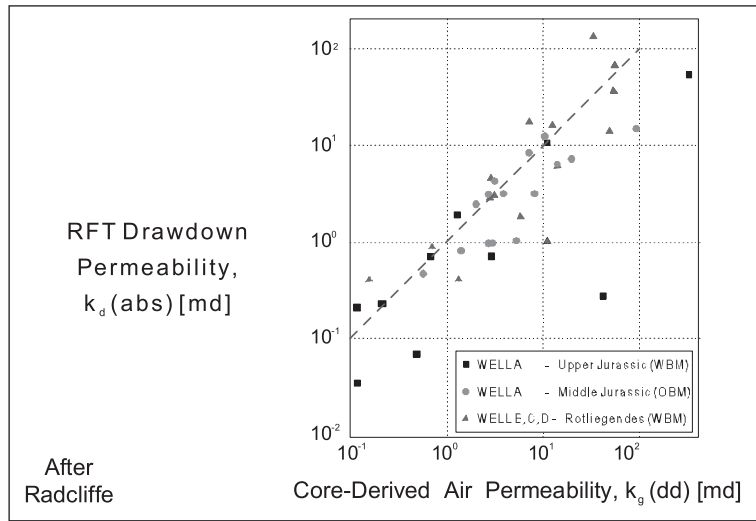


Fig. 12-26. RFT drawdown versus core derived permeability

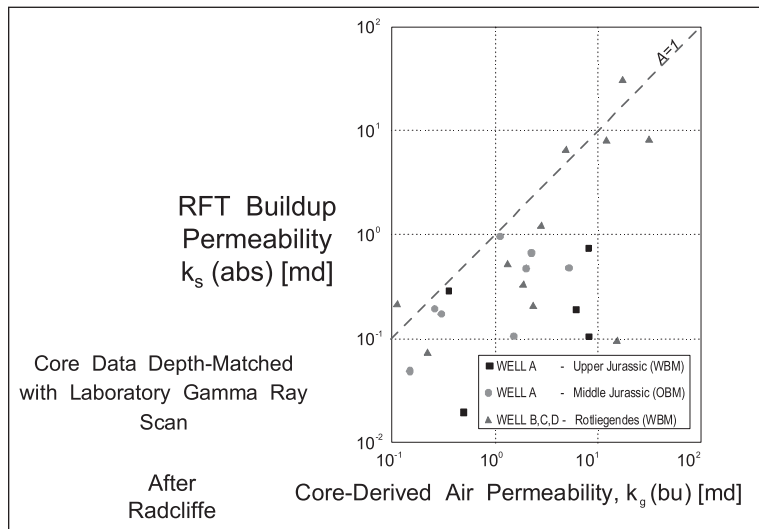


Fig. 12-27. RFT buildup versus core derived permeability

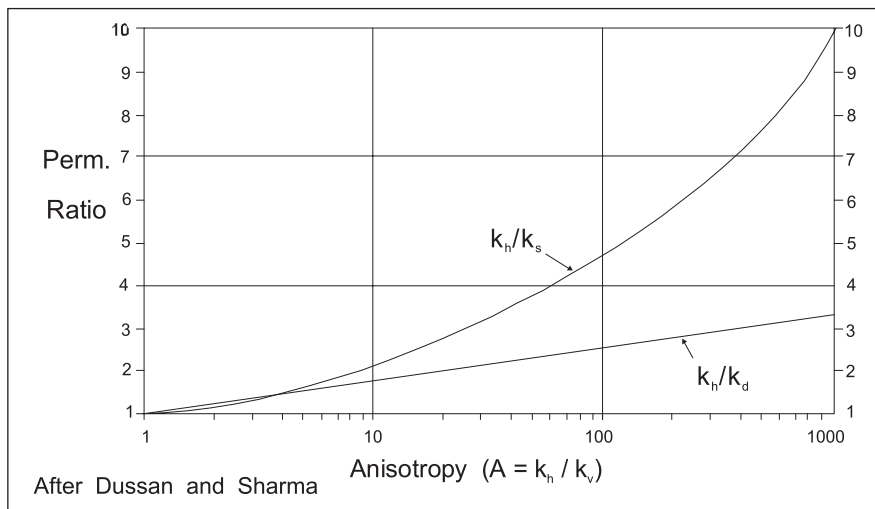


Fig. 12-28. Relationship between  $k_D$  and  $k_B$  in an anisotropic formation

The TRRT graph is a specialist buildup plot for spherical flow based on superposition and an MTR may be identified where a straight line of ideal slope  $m_s$  is present; by analogy with the semilog straight line on a Horner plot, this will be designated MTR spherical (MTRS). In order to help identify the period of spherical flow, the slope of the TRRT will be designated  $p'''$ ; in CRD, the spherical flow derivative is

$$p''' = \frac{dp_{pf}}{d\left(\frac{1}{\sqrt{t}}\right)} \quad (12-44a)$$

and in buildup it becomes

$$p''' = \frac{dp_{ps}}{d(\text{SSTF})} = \frac{dp_{ps}}{df_s(T_1, T_2, t)} \quad (12-44b)$$

where

$$\text{SSTF} = f_s(T_1, T_2, t) = \frac{q_2/q_1}{\sqrt{t - T_2}} - \frac{q_2/q_2 - 1}{\sqrt{t - T_2}} - \frac{1}{\sqrt{t}}$$

In essence tangents to the specialized plot are being taken by numerical differentiation and the spherical derivative is presented on a log-log plot of the form shown in figure 12–29. Expansion of (12–44a) by chain rule differentiation leads to:

$$p''' = -2\dot{p}t^{3/2} \quad \text{and} \quad p''' = -2p't^{1/2} \quad (12-45)$$

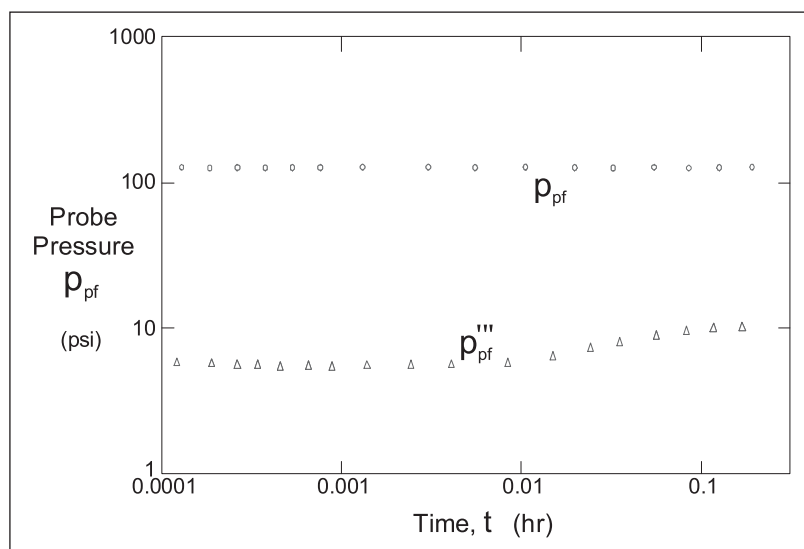


Fig. 12–29. Log–log diagnostic plot for spherical flow

In their analysis Dussan and Sharma assumed the wellbore to be an infinite vertical plane which forces the flow to be wholly hemispherical; the later Goode and Thambynayagam model



shows this assumption to be invalid and hence the shape factors of Dussan and Sharma are not exact. The fact that the Dussan and Sharma shape factor does not agree with that of Wittman and Stewart in the isotropic case is an indication of this deficiency. Since the analytic model of a disk aperture proposed by Goode and Thambynayagam (Appendix B in their paper) is so complicated the exact drawdown behavior will be determined here by FEM numerical simulation for different levels of anisotropy. The shape factors,  $\Omega_o$ , are valid for observation probe data but for active probe interpretation the composite steady-state shape factor,  $\Omega_{ap}$ , described previously has to be used. Numerical simulation has the advantage that it can be extended to cover slant and horizontal wells.

In the pretest situation the main reason for an interest in permeability is a quality check on the pressure measurement; supercharging is only serious in low permeability situations. Figure 12–30 shows an original presentation of a pretest from the first RFT run in China and it is apparent that the buildup took approximately 210 sec to reach stabilization. Spherical flow buildup theory can be used to determine the duration of observable buildup,  $T_{ob}$ , i.e. the point at which the pressure attains a stabilized value within the limit of gauge resolution illustrated in figure 12–31. Sensitivity studies revealed that  $T_{ob}$  is inversely proportional to permeability as shown in figure 12–32 and this has become the key to the diagnostic of supercharging. The reciprocal of the local permeability has been termed the supercharging index, S.I., i.e.  $S.I. = 1/k$ .

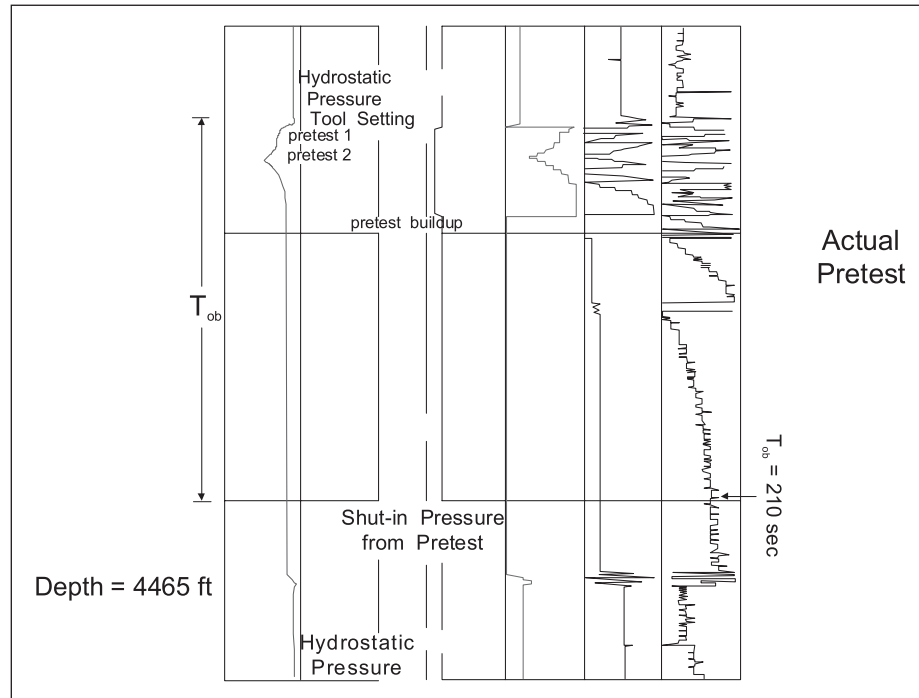


Fig. 12–30. Determination of  $T_{ob}$  from WFT log

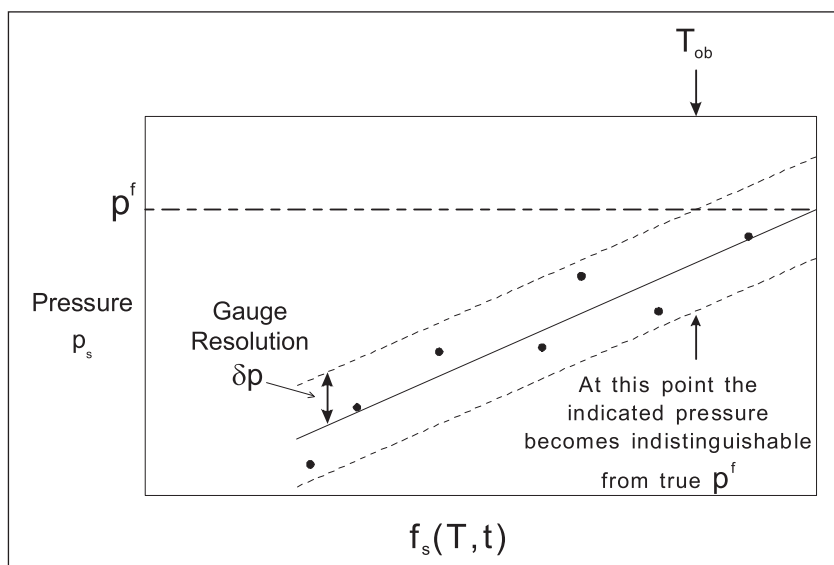
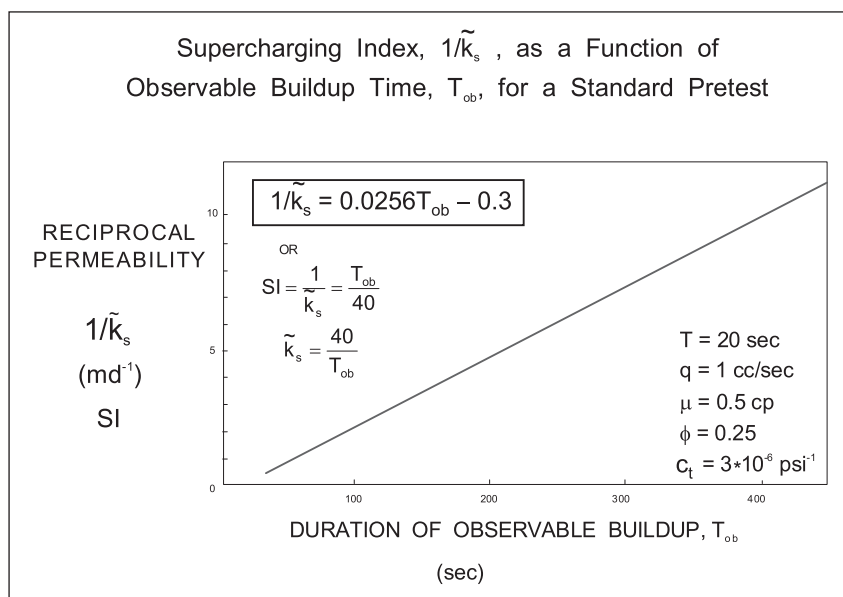


Fig. 12-31. Duration of observable buildup


 Fig. 12-32. Supercharging index as a function of  $T_{ob}$ 

The pressure in buildup from spherical flow theory is given by Eq. (12-27b) i.e.,

$$P_{ps} = P_i - \frac{q}{4} \left( \frac{m}{\pi k_s} \right)^{3/2} \sqrt{\phi c_t} \left( \frac{1}{\sqrt{\Delta t}} - \frac{1}{\sqrt{t_p + \Delta t}} \right) \quad (12-27b)$$

Thus the approach to the formation pressure, identified here by  $p_i$ , may be written as:

$$\delta_p = p_i - p_{ps} = \frac{q}{4} \left( \frac{\mu}{\pi k_s} \right)^{3/2} \sqrt{\phi c_t} \left( \frac{1}{\sqrt{\Delta t}} - \frac{1}{\sqrt{t_p + \Delta t}} \right) \quad (12-46a)$$

For a specified value of  $k_s$  and a selected  $\delta p$ , say 1 psi, the requisite value of  $\Delta t$  i.e.  $T_{ob}$  may be found by solving (12-46) using a root finding algorithm e.g. the secant method. The parameters  $q$ ,  $\mu$ ,  $\phi$ ,  $c_t$  and  $t_p$  must also be specified before the duration of observable buildup can be estimated. In SPE field units (12-46a) becomes:

$$\delta_p = \frac{54637.7 \times q}{4} \left( \frac{\mu}{\pi k_s} \right)^{3/2} \sqrt{\phi c_t} \left( \frac{1}{\sqrt{\Delta t}} - \frac{1}{\sqrt{t_p + \Delta t}} \right) \quad (12-46b)$$

This may be written in the form:

$$f(T_{ob}) = \delta p - \frac{54637.7 \times q}{4} \left( \frac{\mu}{\pi k_s} \right)^{3/2} \sqrt{\phi c_t} \left( \frac{1}{\sqrt{T_{ob}}} - \frac{1}{\sqrt{t_p + T_{ob}}} \right) = 0 \quad (12-46c)$$

In figure 12-32 the solution of (12-46c) is presented as a plot of  $1/\tilde{k}_s$  versus  $T_{ob}$  for an approach,  $\delta p$ , of 1 psi. The base case of  $t_p = 20$  sec has been presented previously and an additional case of  $t_p = 10$  sec has been computed. It has been suggested that one of the benefits of shorter piston travel times,  $t_p$ , is a faster buildup to formation pressure and Eq. (12-46) shows that this is indeed true. Thus the duration of observable buildup can be used in test design especially at low permeability. The viscosity and compressibility of mud filtrate are required for valid use of the formula.

The basic spherical flow theory for CRD and CRB has been elucidated in this section. It is straightforward to extend this to cover a general variable rate situation using a convolution based on a step-rate schedule illustrated in figure 12-33. The fundamental  $p_D$  function takes the form

$$p_D = 1 - \frac{1}{\sqrt{\pi t'_D}} + S_s \quad (12-47)$$

where

$$t'_D = \frac{k_z t}{\phi \mu c_t r_p^2} \quad \text{and} \quad p_D = \frac{p_i - p_p(t)}{4 \pi k r_p}$$

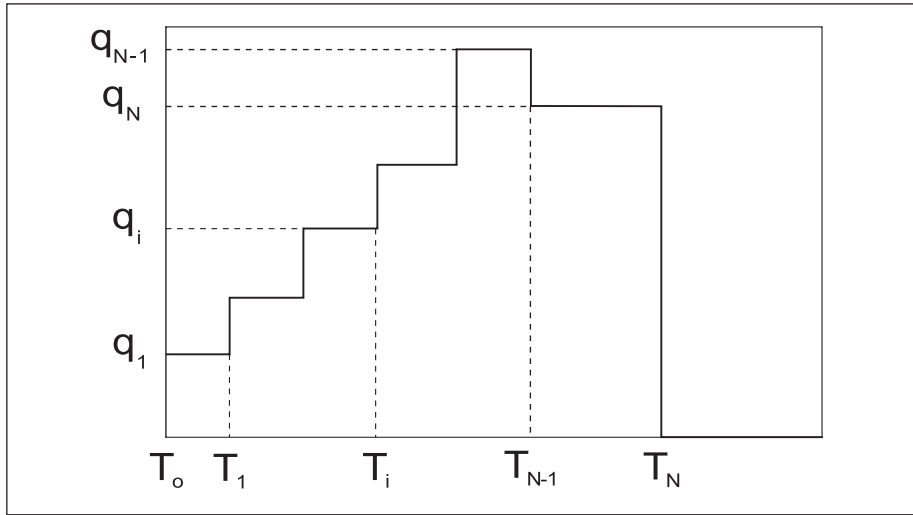


Fig. 12-33. Flow schedule represented by discrete steps

Here, the total spherical skin  $S_s = S_{se} + S_{sd}$  is the sum of the elliptical and damage contributions for a perfect spherical source of radius  $r_p$ . The superposition equation for a step-rate flow schedule may be written as

$$p_i - p_p(t) = \frac{q_r \mu}{4\pi k r_p} \left[ \sum_{i=1}^M \frac{q_i}{q_r} [p_D(t - T_{i-1})_D - p_D(t - T_i)_D] + \frac{q(t)}{q_r} p_D(t - T_M)_D \right] \quad (12-48)$$

Substitution of (12-47) into (12-48) yields the general spherical flow result:

$$p_i - p_p(t) = \frac{q_r}{4} \left( \frac{\mu}{\pi k_s} \right)^{3/2} \sqrt{\phi c_t} \left[ g_s(t, T_M) + \frac{q(t)}{q_r} \bar{S}_s \right] \quad (12-49)$$

where

$$g_s(t, T_M) = \sum_{i=1}^M \frac{q_i}{q_r} \left\{ \frac{1}{\sqrt{t - T_i}} - \frac{1}{\sqrt{t - T_{i-1}}} \right\} - \frac{q(t)}{q_r} \frac{1}{\sqrt{t - T_M}} \quad (12-50)$$

and

$$\bar{S}_s = \left( \sqrt{\frac{\pi k_z}{\phi \mu c_t}} \frac{1}{r_p} \right) (1 + S_{se} + S_{sd}) \quad (12-51)$$

Since a probe aperture on a wellbore does not represent a pure spherical source, this latter result, i.e., Eq. (12-51), may be written in the alternative form

$$\bar{S}_s = \left( \sqrt{\frac{\pi k_z}{\phi \mu c_t}} \frac{1}{r_e} \right) (1 + S_{sphc} + S_{sd}) \quad \text{where} \quad r_e = \frac{2r_{pa}}{\pi} \quad (12-52)$$

The theory behind the total geometric skin effect characterized by  $S_{\text{sphc}} = S_{\text{se}} + S_{\text{sw}}$  is given in the subsequent section "Behaviour of a Sink Probe"; this term allows for both the elliptical distortion due to anisotropy  $S_{\text{se}}$  and the blocking effect of the wellbore  $S_{\text{sw}}$ .

The function  $g_s(t, T_M)$  defined by Eq. (12-50) above is the superposition time function for spherical flow based on RRT quantities. It is the spherical flow analog of  $g_r(t, T_M)$  used in radial flow theory.

During a period of variable rate drawdown (VRD), e.g., the pump in operation, in the spherical flow situation, division of Eq. (12-49) by  $q(t)/q_r$  yields

$$\frac{p_i - p_p(t)}{q(t)/q_r} = \frac{q_r}{4} \left( \frac{\mu}{\pi k_s} \right)^{3/2} \sqrt{\phi c_t} \left[ \frac{g_s(t, T_M)}{q(t)/q_r} + \bar{S}_s \right] \quad (12-53)$$

Thus, a plot of rate normalized pressure  $\frac{p_i - p_p(t)}{q(t)/q_r}$  versus

$$f_s(t, T_M) = \frac{g_s(t, T_M)}{q(t)/q_r} = \sum_{i=1}^M \frac{q_i}{q(t)} \left\{ \frac{1}{\sqrt{t - T_i}} - \frac{1}{\sqrt{t - T_{i-1}}} \right\} - \frac{1}{\sqrt{t - T_M}} \quad (12-54)$$

will be of the following form:

$$\frac{p_i - p_p(t)}{q(t)/q_r} = m_s f_s(t, T_M) + b_s \quad (12-55)$$

where

$$m_s = \frac{q_r}{4} \left( \frac{\mu}{\pi k_s} \right)^{3/2} \sqrt{\phi c_t} \quad (12-56)$$

and

$$b_s = m_s \bar{S}_s = \frac{q_r \mu}{4\pi k_r p} S_s$$

In the case of a shutin following a period of strictly spherical flow, the variable rate buildup (VRB) method is based on the superposition equation

$$p_{\text{DS}} = \frac{[p_i - p_{\text{ps}}(t)] 4\pi k_r p}{q_r \mu} = \sum_{i=1}^N \frac{q_i}{q_r} [p_{\text{D}}(t - T_{i-1})_{\text{D}} - p_{\text{D}}(t - T_i)_{\text{D}}] \quad (12-57)$$

where  $q(t) = 0$  for  $t > T_N$ . Thus

$$p_{ps}(t) = p_i - \frac{q_r}{4} \left( \frac{\mu}{\pi k_s} \right)^{3/2} \sqrt{\phi c_t} \mathbf{h}_s(t, T_N) \quad (12-58)$$

where

$$\mathbf{h}_s(t, T_N) = \sum_{i=1}^N \frac{q_i}{q_r} \left[ \frac{1}{\sqrt{t - T_i}} - \frac{1}{\sqrt{t - T_{i-1}}} \right] \quad (12-59)$$

Provided only spherical flow has occurred during the actual drawdown period and would have continued in the extrapolated drawdown behavior

$$p_{ps}(t) = b_s + m_s \mathbf{h}_s(t, T_N) \quad (12-60)$$

and the slope and intercept of the VRB spherical flow plot will yield permeability  $k_s$  and the initial reservoir pressure  $p_i$  as in the radial flow case. Thus

$$m_s = -m_{sf} = -\frac{q_r}{4} \left( \frac{\mu}{\pi k_s} \right)^{3/2} \sqrt{\phi c_t} \quad \text{and} \quad b_s = p_i$$

This formulation of the buildup interpretation is the standard (VRRT) analysis. This can also be posed in equivalent drawdown form by writing an expression for the last flowing pressure at time  $T_N$ ; thus

$$p_{pf}(T_N) = p_i - m_{sf} \left[ \mathbf{g}_s(T_N, T_N) + \frac{q_N}{q_r} \bar{S}_s \right] \quad (12-61)$$

Subtracting this equation from Eq. (12-58) to eliminate  $p_i$  yields

$$p_{ps} = p_{pf}(T_N) + m_{sf} \left[ \mathbf{g}_s(T_N, T_N) - \mathbf{h}_s(t, T_N) + \frac{q_N}{q_r} \bar{S}_s \right] \quad (12-62)$$

This is the Agarwal form of the VRB plot where  $p_{ps}$  is graphed versus  $\mathbf{g}_s(T_N, T_N) - \mathbf{h}_s(t, T_N)$  to give a straight line of the form

$$p_{ps} = b_s + m_s \left[ \mathbf{g}_s(T_N, T_N) - \mathbf{h}_s(t, T_N) \right] \quad (12-63)$$

Where

$$m_s = \frac{q_r}{4} \left( \frac{\mu}{\pi k_s} \right)^{3/2} \sqrt{\phi c_t} \quad \text{and} \quad b_s = p_{pf}(T_N) + m_{sf} \frac{q_N}{q_r} \bar{S}_s \quad (12-64)$$

In the situation where the initial pressure  $p_i$  is not known, an ordinary VRD analysis is not possible. In this case, a fixed point at time  $T_j$  of known probe pressure  $p_p(T_j)$  and flow rate  $q(T_j)$  is chosen for differencing. These quantities are related by the drawdown equation applied at time  $T_j$ , i.e.,

$$p_i - p_p(T_j) = \frac{q_r}{4} \left( \frac{\mu}{\pi k_s} \right)^{3/2} \sqrt{\phi c_t} \left[ g_s(T_j, T_{j-1}) + \frac{q(T_j)}{q_r} \bar{S}_s \right] \quad (12-65)$$

Subtracting Eq. (12-65) from (12-49) to eliminate the initial pressure gives

$$p_p(T_j) - p_p(t) = \frac{q_r}{4} \left( \frac{\mu}{\pi k_s} \right)^{3/2} \sqrt{\phi c_t} \left[ g_s(t, T_M) - g_s(T_j, T_{j-1}) + \frac{q(t) - q(T_j)}{q_r} \bar{S}_s \right] \quad (12-66)$$

which may be rearranged as

$$\frac{p_p(T_j) - p_p(t)}{(q(t) - q(T_j))/q_r} = \frac{q_r}{4} \left( \frac{\mu}{\pi k_s} \right)^{3/2} \sqrt{\phi c_t} \left[ \frac{g_s(t, T_M) - g_s(T_j, T_{j-1})}{(q(t) - q(T_j))/q_r} + \bar{S}_s \right] \quad (12-67)$$

Hence a plot of

$$\frac{p_p(T_j) - p_p(t)}{(q(t) - q(T_j))/q_r} \quad \text{versus} \quad \frac{g_s(t, T_M) - g_s(T_j, T_{j-1})}{(q(t) - q(T_j))/q_r}$$

where  $t > T_j$  will be a straight line of slope  $m_{sf}$  and intercept  $b_{sf}$ , where

$$m_{sf} = \frac{q_r}{4} \left( \frac{\mu}{\pi k_s} \right)^{3/2} \sqrt{\phi c_t}$$

and

$$b_{sf} = m_{sf} \bar{S}_s = \frac{q_r \mu}{4 \pi k_r} \bar{S}_s \quad \text{as before}$$

This method—as in the radial flow case—allows  $k_s$  and  $S_s$  to be determined from VRD data without knowledge of the initial pressure  $p_i$ . In fact  $p_i$  is given by Eq. (12-65), which shows that the initial pressure can be determined from VRD data.

Equation (12-67) may be written in the following condensed form:

$$\frac{\Delta p}{\Delta q/q_r} = \frac{q_r}{4} \left( \frac{\mu}{\pi k_s} \right)^{3/2} \sqrt{\phi c_t} \left\{ \frac{1}{\sqrt{\Delta t_{se}}} + \bar{S}_s \right\} \quad (12-68)$$

where  $\Delta t_{se}$  is an equivalent CRD time for spherical flow given by

$$\Delta t_{se} = \left[ \frac{(q(t) - q(T_J))/q_r}{g_s(t, T_M) - g_s(T_J, T_{J-1})} \right]^2 \quad (12-69)$$

The generalized spherical flow derivative is defined as

$$p'' = \frac{\left( \frac{\Delta p}{\Delta q/q_r} \right)}{d \frac{1}{\sqrt{\Delta t_{se}}}} \quad (12-70)$$

## Vertical Observation Probe and Point Source

Multiprobe formation testers were introduced in the 1980s, and the combination of a straddle packer and an observation probe has become a frequently used combination. The pressure response of multiprobe systems was studied by Goode and Thambynayagam,<sup>6</sup> who considered a two-probe device as illustrated in figure 12-34a and b. The first study of such a device was carried out by Helga Haldorsen as a summer project at the Technical University in Trondheim, Norway; he later made an important contribution to the subject of geostatistics during his Ph.D. work with Larry Lake at the University of Texas. Here, a point source (active probe) is placed on the surface of a cylindrical wellbore and an observation probe is placed vertically above at a distance  $z_{vp}$  away. Initially, the presence of horizontal no-flow boundaries will be ignored, and later the method of images will be used to model the effect of upper and lower boundaries. In this section, the pressure response of the vertical observation probe will be modeled in the situation where the source is also a point (active probe). In the case where the active flow interval is a limited-entry wellbore as shown in figure 12-35a and b, it will be demonstrated that the observation probe response can be modeled in most circumstances by a summation of point source responses. The conditions under which this approximation is valid will be explored later using finite element numerical modeling.



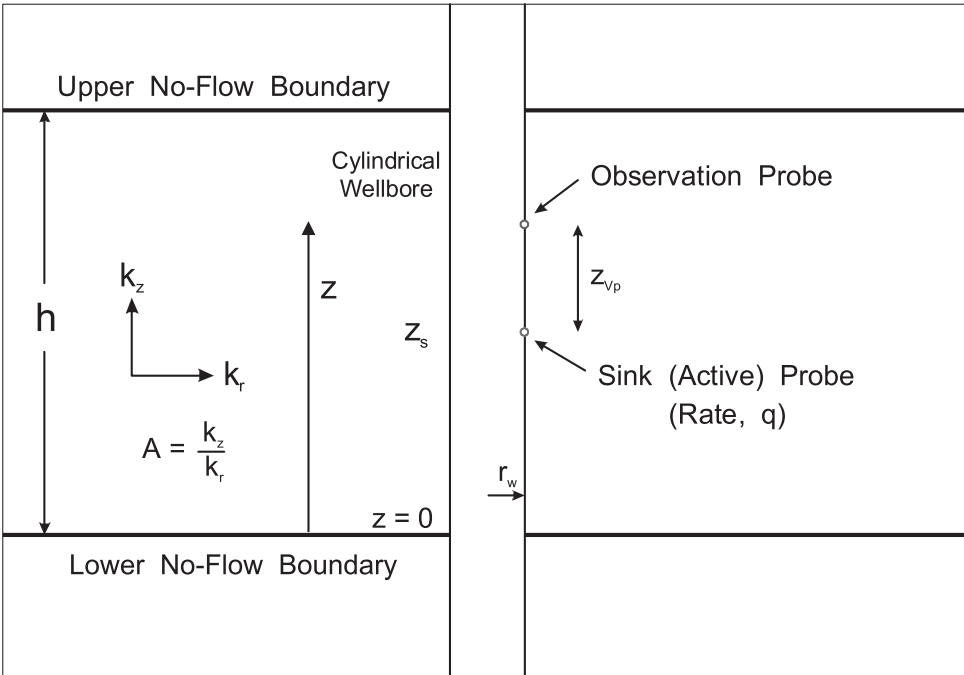


Fig. 12-34a. Geometry of a two probe WFT device

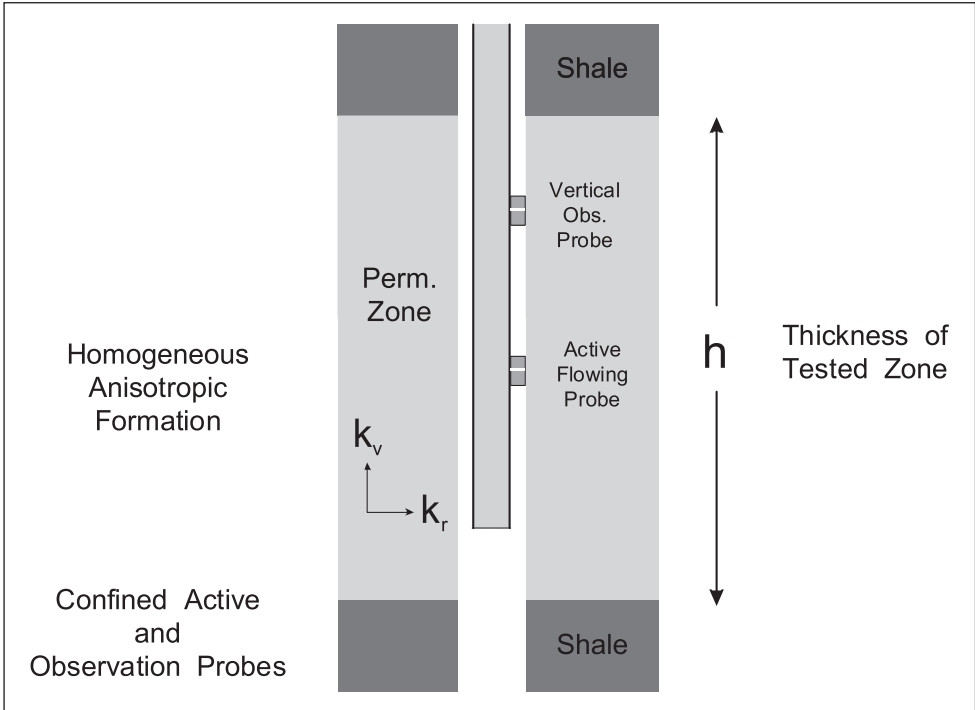


Fig. 12-34b. Diagrammatic representation of a two probe WFT device

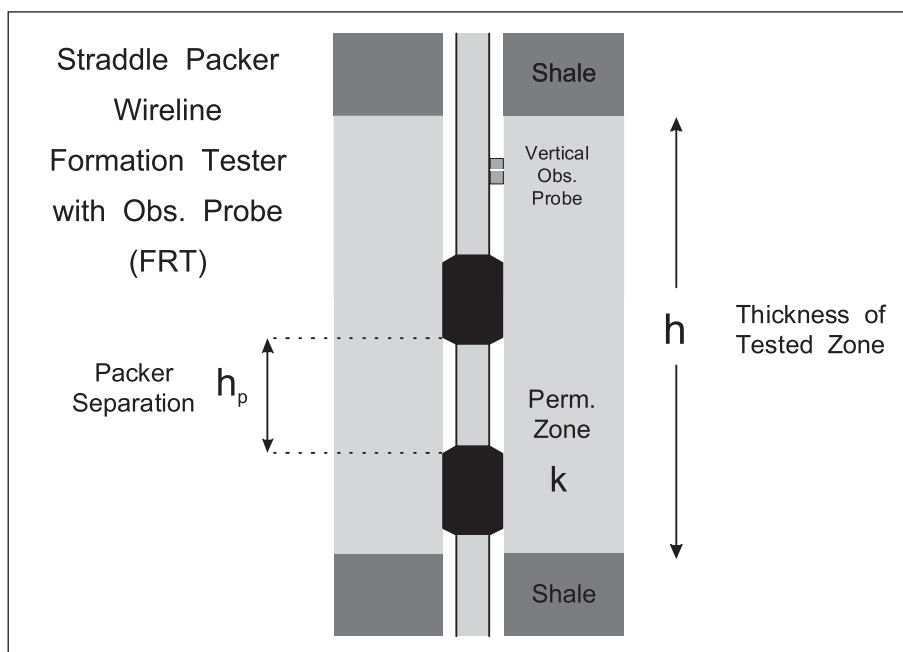


Fig. 12–35a. Straddle packer WFT device with observation probe

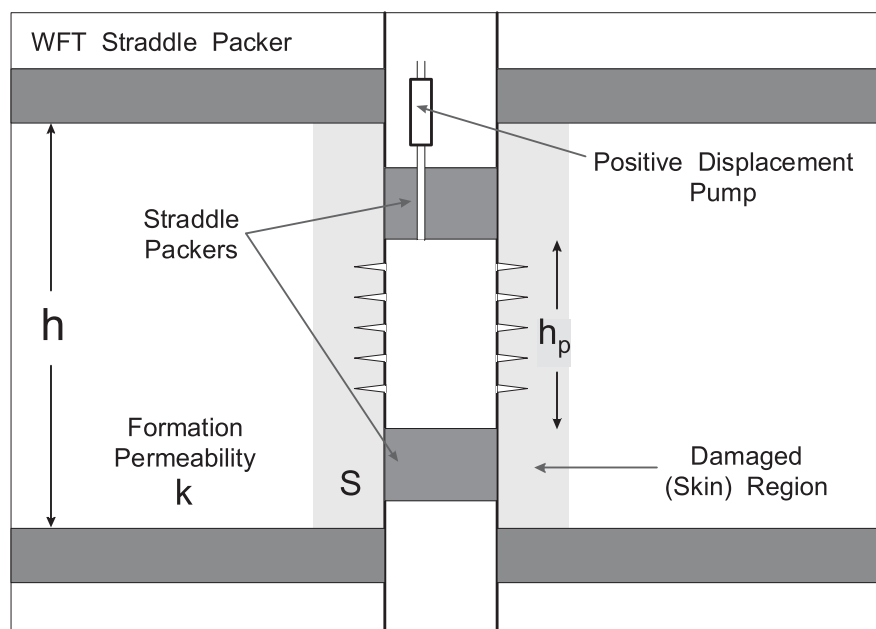


Fig. 12–35b. Straddle packer WFT device for mini DSTs

Initially, the upper and lower boundaries are excluded, and the sink probe sets up a spherical flow in an infinite region once the effect of the closed wellbore dies out. Since the formation is anisotropic, the pressure propagation is elliptical in nature. The pressure response of the observation probe has been obtained by Goode and Thambynayagam<sup>6</sup> from the solution in Carslaw and Jaeger, and takes the form

$$p_{\text{DOS}} = \frac{1}{2\sqrt{\pi}} \int_0^{t_D} \left( \frac{e^{-\frac{(z_{VP})^2}{4\beta r_w^2 A}}}{\beta^{1.5}} \right) G_o(\beta) d\beta \quad (12-71)$$

where

$$p_{\text{DOS}} = \frac{(p_i - p_{vp}(t)) 4\pi \bar{k} r_w}{q\mu}, \quad t_D = \frac{k_r t}{\phi \mu c_t r_w^2}, \quad \bar{k} = \sqrt{k_r k_z}$$

and

$$G_o(\beta) = \frac{8}{\pi^2} \sum_{n=-\infty}^{\infty} \int_0^{\infty} \frac{\beta e^{-\alpha^2 \beta}}{\alpha (J_n'(\alpha)^2 + Y_n'(\alpha)^2)} d\alpha$$

The subscript “O” on the dimensionless pressure has been used to distinguish a quantity based  $\bar{k}$  on rather than  $k_r$ ; later, a dimensionless pressure based on  $k_r$  will be denoted  $p_{\text{DS}}$ . Note that this model implies that the permeabilities in the x and y (radial) directions are equal. The subscript “S” refers to a spherical-flow dimensionless pressure based on a length quantity  $r$  ( $r_{pa}$ ,  $r_w$ ) or  $z$  and involving  $4\pi$  (rather than the  $2\pi$  in radial flow). It is convenient to evaluate the  $G_o(\beta)$  function in advance and store values in a table which can be interrogated by interpolation; such a table, computed in MathCad, is table 12–4.

**Table 12–4.** Tabulated values of  $G_o(\beta)$

$\text{Log}_{10}(\beta)$	$G_o(\beta)$
–3	1.972
–2	1.913
–1.5	1.858
–1	1.7645
–0.5	1.6272
0	1.4458
0.5	1.2371
1	1.0684
1.5	1.0036
2	0.9939
2.5	0.9963
3	0.9962

The  $G_o(\beta)$  function is also plotted in figure 12–36.

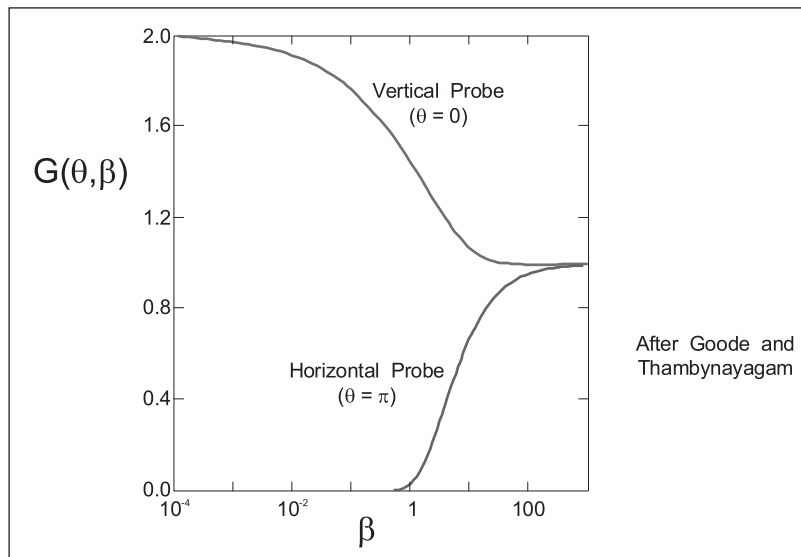


Fig. 12–36. Plot of  $G(\theta, \beta)$  versus  $\beta$

The computation of the constant (sink) rate drawdown response follows from Eq. (12–47), and the dimensionless  $p_{\text{DOS}}$  function is presented on a log–log scale in figure 12–37. Note the dimensionless pressure  $p_{\text{DOS}}$  has been defined with respect to spherical flow. The logarithmic derivative  $p'_{\text{DOS}}$  given by

$$p'_{\text{DOS}} = \frac{dp_{\text{DOS}}}{d(\ln t_D)} \quad (12-72)$$

is also plotted in figure 12–38, where the negative half slope indicates a spherical-like flow regime with probe pressure varying with the RSRT. In figure 12–38, the dimensionless spherical derivative  $p'''_{\text{DOS}}$  has been added to the data plotted later, and it is apparent that the spherical flow is diagnosed either by the negative half slope on  $p'_{\text{DOS}}$  or by a plateau on  $p'''_{\text{DOS}}$ .

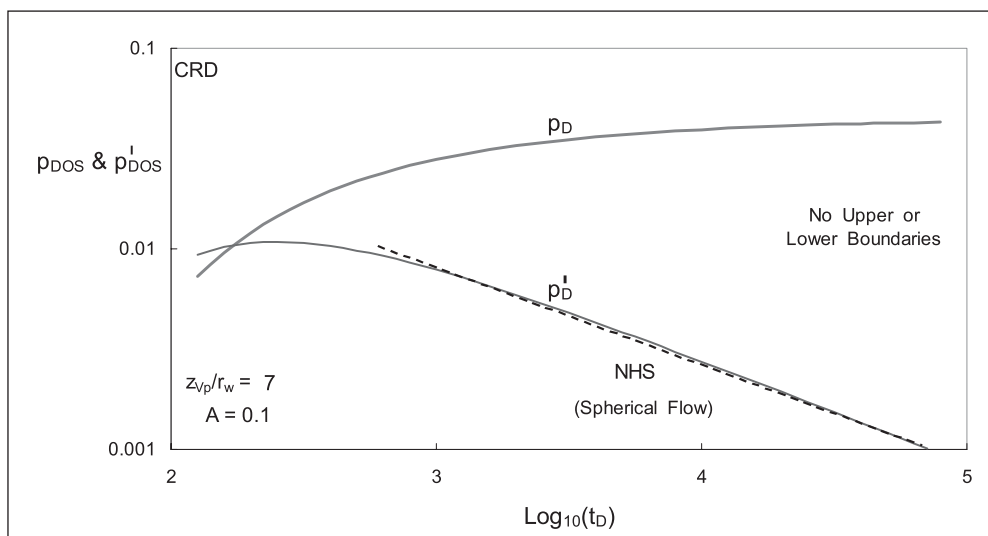


Fig. 12–37. Observation probe dimensionless response

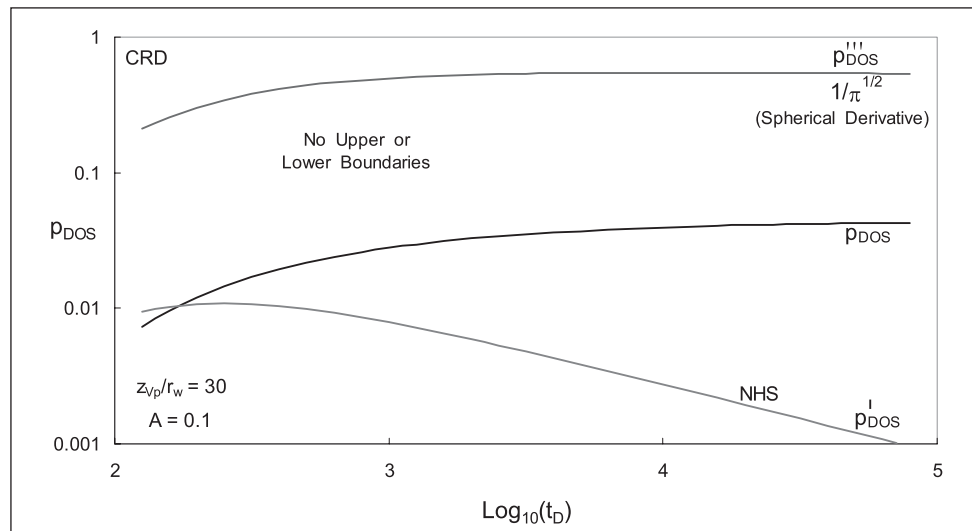


Fig. 12–38. Observation probe dimensionless response with spherical derivative

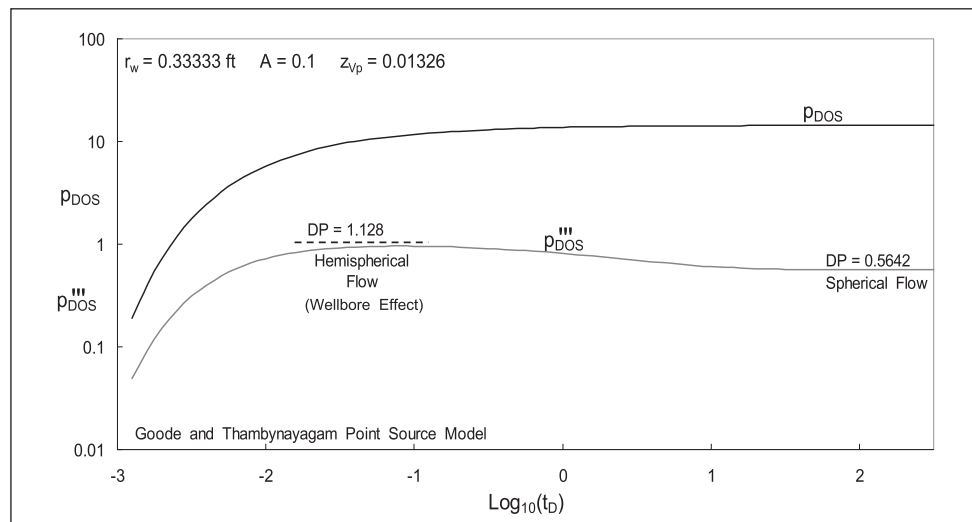


Fig. 12–39. Early time behavior of proximate observation probe

In the case illustrated in figure 12–38, the vertical observation probe is some distance from the point source on the wellbore. The Goode and Thambynayagam model cannot model the drawdown behavior of a disk aperture on the wellbore, but the response of an observation probe quite close to the point sink will give some indication of the behavior of an active probe; this will be termed a proximate probe. In figure 12–39, the ETR of a proximate probe with  $r_w = 0.33333$  ft and  $z_{vp} = 0.01326$  ft, i.e.,  $z_{vp}/r_w = 0.03978$ , is shown. The spherical derivative shows an initial plateau close to the hemispherical value of  $2/\sqrt{\pi} = 1.1284$ ; this first hemispherical flow regime is the effect of the wellbore acting as a planar no-flow boundary. At a dimensionless time  $t_D$  around 10, the flow becomes spherical in nature and the derivative  $p_{DOS}'''$  attains the plateau value of  $1/\sqrt{\pi} = 0.5642$ . The first hemispherical flow due to the wellbore is a very early time phenomenon; a  $t_D$  of 10, for example, corresponds to 1.5 min actual time for the typical parameter values listed below.

$$r_w = 0.3333\text{ft} \quad \phi = 0.2 \quad \mu = 1\text{cp} \quad c_t = 3 \times 10^{-5} \text{psi}^{-1} \quad k_r = 1\text{md}$$

At higher permeability, the duration will be even shorter, and this first hemispherical flow regime will not be apparent in real data because of storage effects.

Goode and Thambynayagam<sup>6</sup> showed that the observation probe pressure in this period is given by

$$p_i - p_{VP}(t) = \frac{q\mu}{4\pi k_r} \left( \frac{1}{z_{VP}} - \frac{1}{\sqrt{\pi t \eta_z}} \right) \quad (12-73)$$

where

$$\eta_z = \frac{k_z}{\phi \mu c_t}$$

In dimensionless form, this becomes

$$p_{DOS} = \frac{1}{\sqrt{\pi}} \left( \sqrt{\pi A} \frac{r_w}{z_{VP}} - \frac{1}{\sqrt{t_D}} \right) \quad (12-74)$$

In figure 12-40, an RRT plot in dimensionless form, i.e.,  $p_{DOS}$  versus  $1/\sqrt{t_D}$ , has a slope  $1/\sqrt{\pi}$  in the spherical flow period. In terms of actual variables, Eq. (12-73) can be written as:

$$p_{VP}(t) = p_i - \frac{q}{4} \left( \frac{\mu}{\pi k_s} \right)^{3/2} \sqrt{\phi c_t} \left( a - \frac{1}{\sqrt{t}} \right) \quad (12-75)$$

where

$$k_s = (k_r^2 k_z)^{1/3} \quad \text{the spherical permeability}$$

and

$$a = \sqrt{\frac{\pi k_z}{z_{VP}^2 \phi \mu c_t}} \quad m_s = \frac{q}{4} \left( \frac{\mu}{\pi k_s} \right)^{3/2} \sqrt{\phi c_t}$$

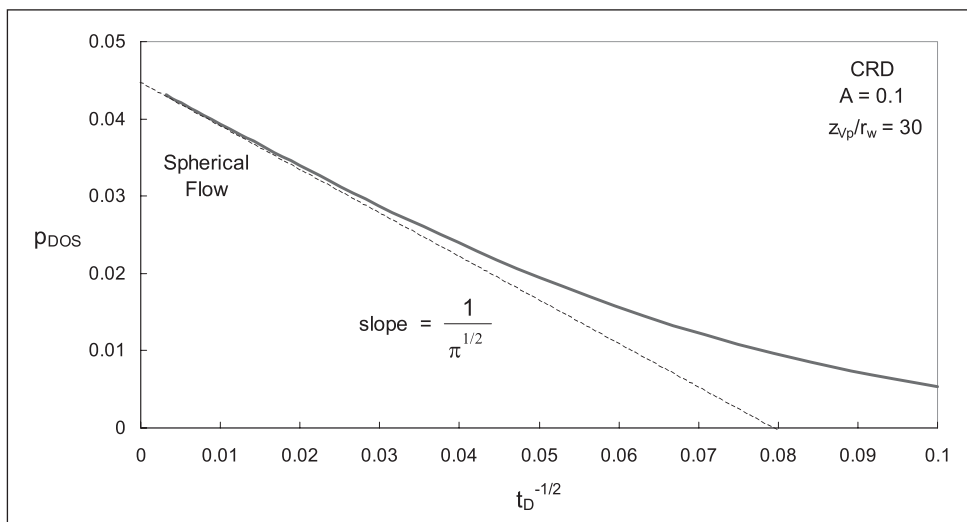


Fig. 12-40. Reciprocal square root of time plot (dimensionless)

In SPE field units, the slope  $m_s$  becomes

$$m_s = \frac{887.2}{\sqrt{0.0002636}} \frac{q}{4} \left( \frac{\mu}{\pi k_s} \right)^{3/2} \sqrt{\phi c_t} = 54637 \frac{q}{4} \left( \frac{\mu}{\pi k_s} \right)^{3/2} \sqrt{\phi c_t} \quad (12-76)$$

Thus the probe pressure response can be analyzed on an RSRT plot with the slope  $m_s$ , yielding the spherical permeability  $k_s$  as usual. The form of the RSRT graph is shown in figure 12-41, and in principle the combination of the slope and intercept  $m_s$  and  $p_{vp}(t=0)$  allows both permeabilities to be calculated. Defining an intercept permeability as

$$k_i = \frac{k_r}{\sqrt{A}} = \frac{k_r^{3/2}}{k_v^{1/2}} \quad (12-77)$$

the intercept equation takes the form

$$p_{vp}(t=0) = p_i - \frac{887.2 \times q\mu}{4\pi k_r z_{vp}} \sqrt{A} \quad (12-78a)$$

i.e.,

$$p_{vp}(t=0) = p_i - \frac{887.2 \times q\mu}{4\pi k_i z_{vp}} \quad (12-78b)$$

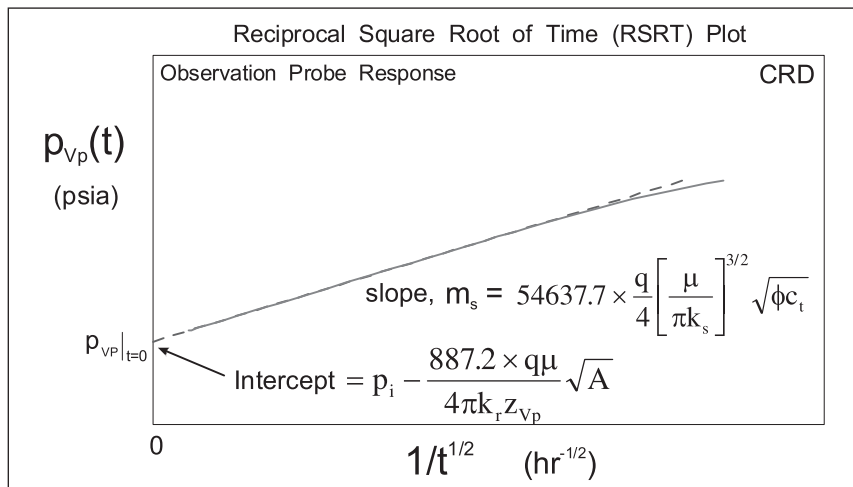


Fig. 12-41. Slope and intersect constructions on the RSRT plot

Knowledge of  $p_{vp}(t=0)$  and the reservoir parameters allows the quantity  $k_i$  to be determined, while the slope allows  $k_s$  to be estimated. The actual permeabilities  $k_r$  and  $k_v$  follow as

$$k_r = (k_s^3 k_i^2)^{1/5} \quad (12-79a)$$

$$k_v = \frac{k_r^3}{k_i^2} \quad (12-79b)$$

This is a benefit of having a vertical observation probe, and these permeability estimates from the RSRT plot can be used as starting values for a nonlinear regression fit of the observation probe model.

In figure 12–42, the effect of anisotropy  $A$  on the observation probe behavior is examined, and it can be seen that the amplitude of the pressure response and the time scale of the derivative response are strongly dependent on  $A$ . Hence, a nonlinear regression based on the probe model will be able to identify both  $k_r$  and  $k_z$ .

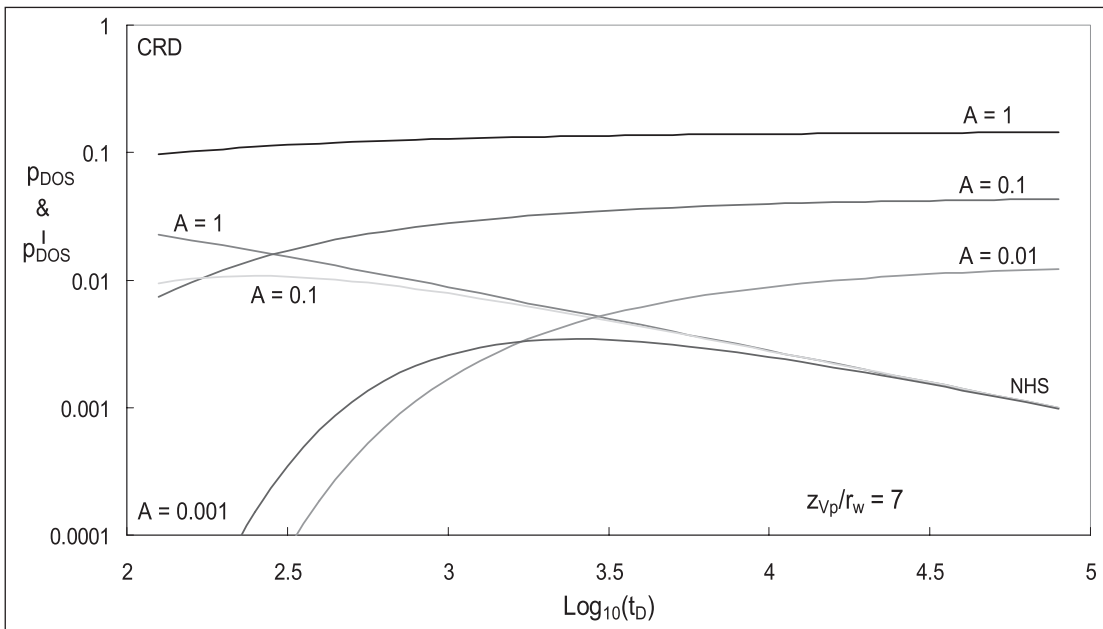


Fig. 12–42. Effect of anisotropy on the observation probe response

The behavior of the probe pressure after the sink probe has been shut in is given by superposition, i.e.,

$$p_{\text{DOSB}} = p_{\text{DOS}}(t_{\text{pD}} + \Delta t_{\text{D}}) - p_{\text{DOS}}(\Delta t_{\text{D}}) \quad (12-80)$$

where

$$p_{\text{DOSB}} = \frac{(p_i - p_{\text{svp}}(\Delta t))4\pi\bar{k}r_w}{q\mu}$$

In a buildup, the quantity  $p_{\text{DOSB}}$  is decreasing as the probe pressure returns to  $p_i$ ; hence it is convenient to plot  $-p_{\text{DOSB}}$  so that the dimensionless graph has the same shape as an actual pressure buildup specialized plot. Here  $p_{\text{DOS}}(t_{\text{D}})$  is the constant sink rate, which is the drawdown solution given by Eq. (12–71). A buildup following a flow period of  $t_{\text{pD}} = 3,064$  was simulated using the superposition Eq. (12–80), and the logarithmic derivative  $p'_{\text{DBO}}$  was computed as

$$p'_{\text{DOSB}} = \frac{dp_{\text{DOSB}}}{d \ln \Delta t_{\text{De}}} \quad (12-81)$$



where  $\Delta t_{De} = \frac{t_{pD} \Delta t_D}{t_{pD} + \Delta t_D}$  i.e., the Agarwal equivalent drawdown time.

This is the accepted definition of the buildup logarithmic derivative, and the dimensionless log-log derivative diagnostic plot is presented in figure 12-43. The buildup derivative also exhibits a negative half slope (NHS) indicating spherical flow, which is confirmed by the straight line section on the TRSR plot shown in figure 12-44. The dimensionless semilog plot (in  $\Delta t_{De}$  rather than Horner form) is given as figure 12-45, where it is apparent that the pressure at the observation probe is nearly constant at early buildup time. The observation probe pressure at early shut-in time is presented in figure 12-46, where it can be seen that  $p_{sVP}(\Delta t)$  is still decreasing at early time and exhibiting drawdown behavior. There is a delay in the interference of the active probe shutin, and this is emphasized in the derivative diagnostic focused on early shutin time given as figure 12-47. The derivative changes sign as the pressure trend reverses, and there is a characteristic sharp “spike” in the graph; note that the absolute value of  $p'_{DBO}$  has been plotted.

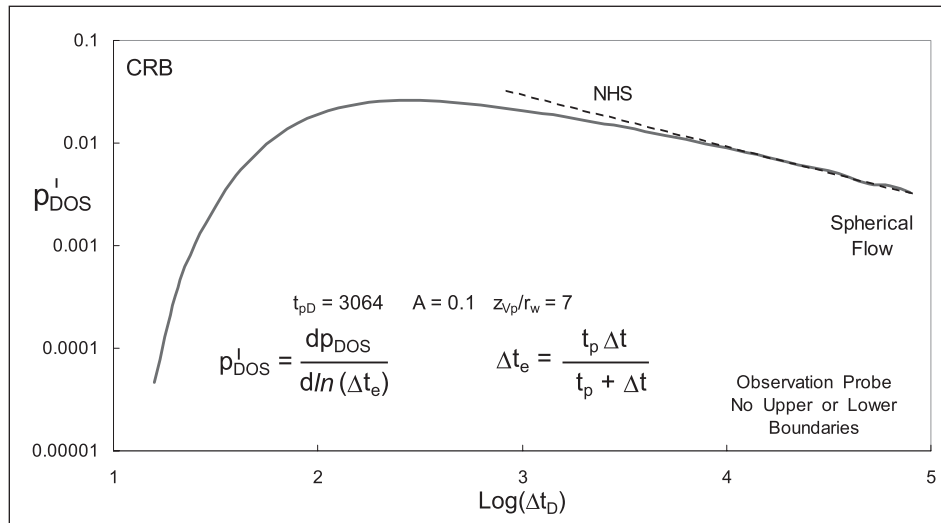


Fig. 12-43. Log-log derivative diagnostic (dimensionless)

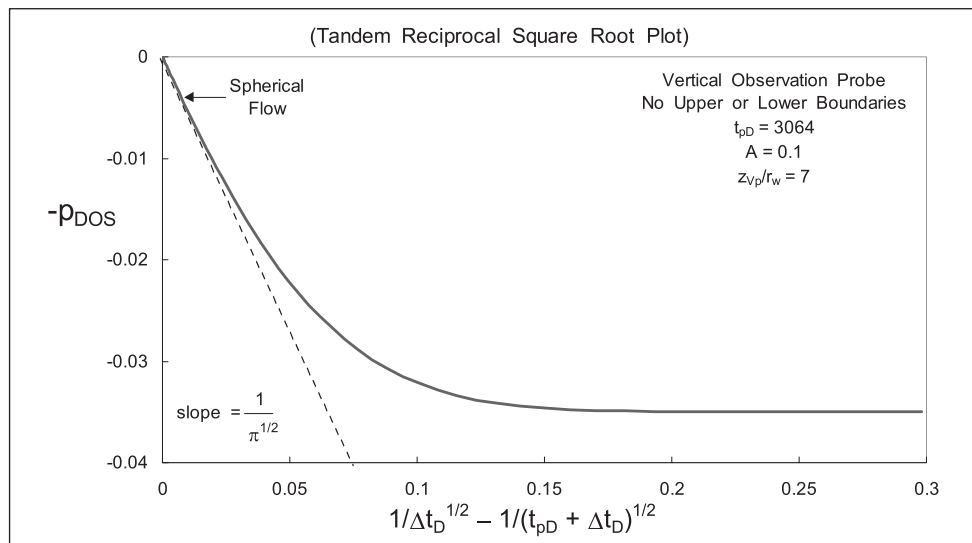


Fig. 12-44. Buildup reciprocal root of time graph (dimensionless)

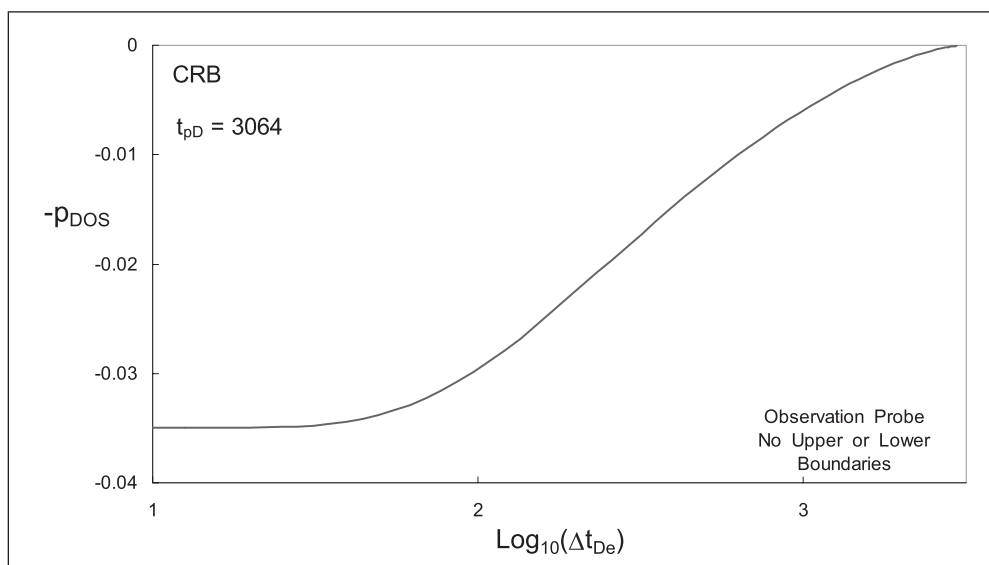


Fig. 12-45. Dimensionless semilog plot

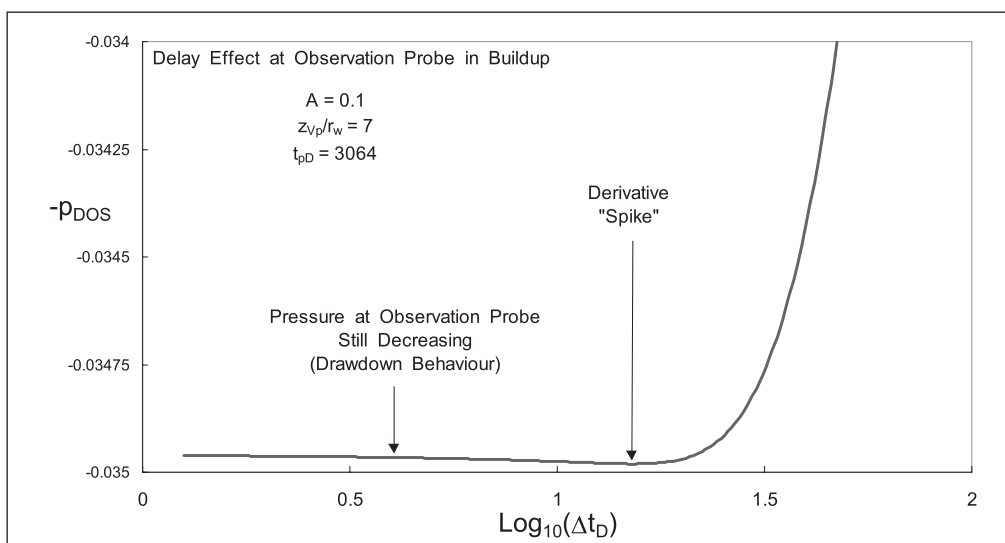


Fig. 12-46. Dimensionless observation probe pressure in early time buildup

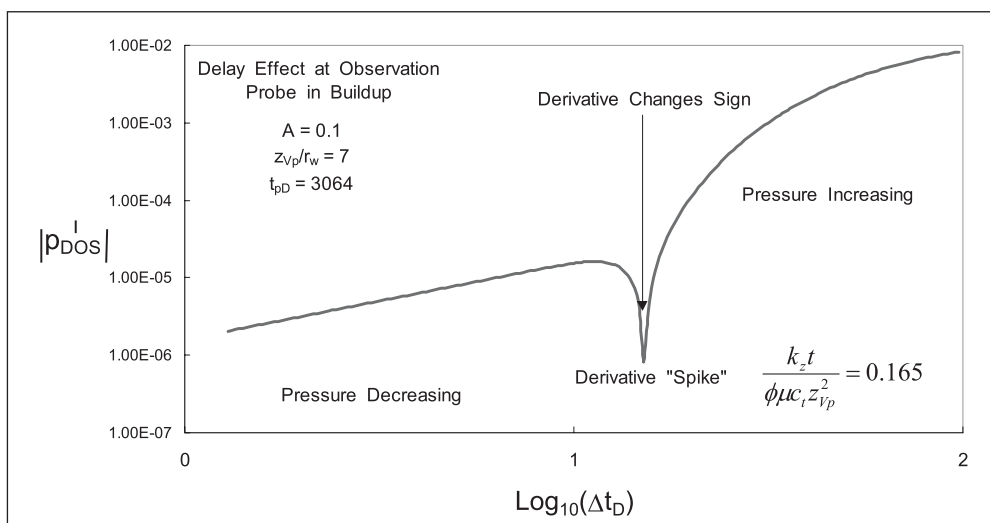


Fig. 12-47. Early time buildup log-log derivative diagnostic

The preceding results refer to the case where upper and lower boundaries are absent and an infinite-acting spherical flow can develop. Attention is now turned to the situation where perfect no-flow boundaries are present, as illustrated in figure 12–48, and the simulated case has  $h/r_w = 166.7$ . The quantity  $z$  is the location of the observation probe measured as a distance from the nearest boundary, and  $z_s$  is the location of the point source. The CRD solution at the observation probe is now given by Eq. (12–82), based on the method of images.

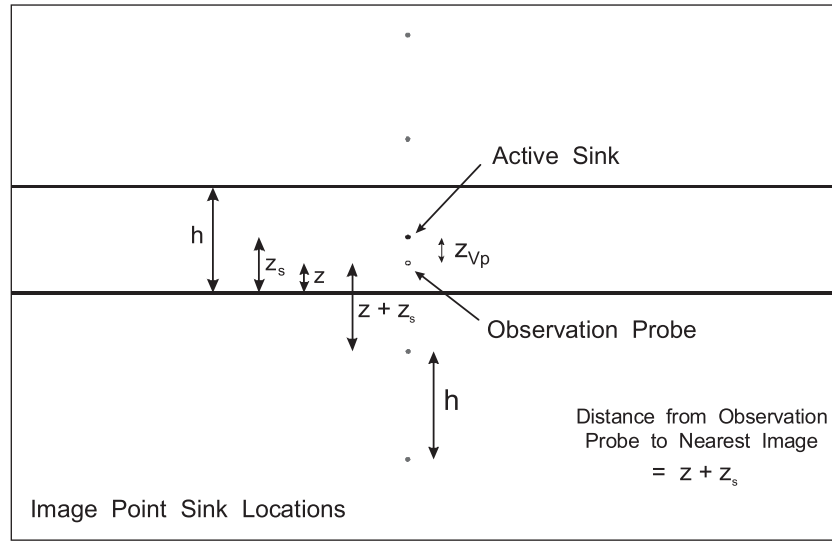


Fig. 12–48. Confined zone geometry

$$P_{DCOS} = \frac{1}{2\sqrt{\pi}} \int_0^{t_D} \sum_{i=-\infty}^{\infty} \left[ \left( \frac{e^{-\gamma_1(i,\beta)}}{\beta^{1.5}} + \frac{e^{-\gamma_2(i,\beta)}}{\beta^{1.5}} \right) G_o(\beta) \right] d\beta \quad (12-82)$$

where

$$\gamma_1(i,\beta) = \frac{[z - (2hi - z_s)]^2}{4\beta r_w^2 A} \quad \text{and} \quad \gamma_2(i,\beta) = \frac{[z - (2hi + z_s)]^2}{4\beta r_w^2 A}$$

The subscript “C” refers to the confined case where the presence of upper and lower boundaries will give rise to a final radial flow. In this case, it is more convenient to use a dimensionless pressure based on radial flow, i.e.,

$$P_{DCO} = \frac{(p_i - p_{vp}(t)) 2\pi k_r h}{q\mu} = \frac{h}{2r_w \sqrt{A}} P_{DCOS}$$

A computation of the CRD dimensionless response for  $h/r_w = 166.7$ ,  $z_s/r_w = 16.67$ ,  $z_p/r_w = 33.3$  is shown in figure 12–49, where a clear derivative plateau for radial flow is apparent. The formation thickness is large enough for the later stage of spherical flow to appear, with the derivative exhibiting something close to a negative half slope. The final derivative plateau is radial flow, and the semilog graph in figure 12–50 exhibits an MTR, i.e., a semilog straight line of ideal slope, based on  $k_r h$ . The effect of changing the anisotropy is also illustrated in figure 12–49, where the responses for  $A = 0.1$  and  $0.01$  are overlaid. Note that the dimensionless pressure

changes at the observation probe are quite small at early time. Once again, the issue of practical gauge resolution is the key, and proper attention must be paid to what can actually be measured with a quartz transducer.

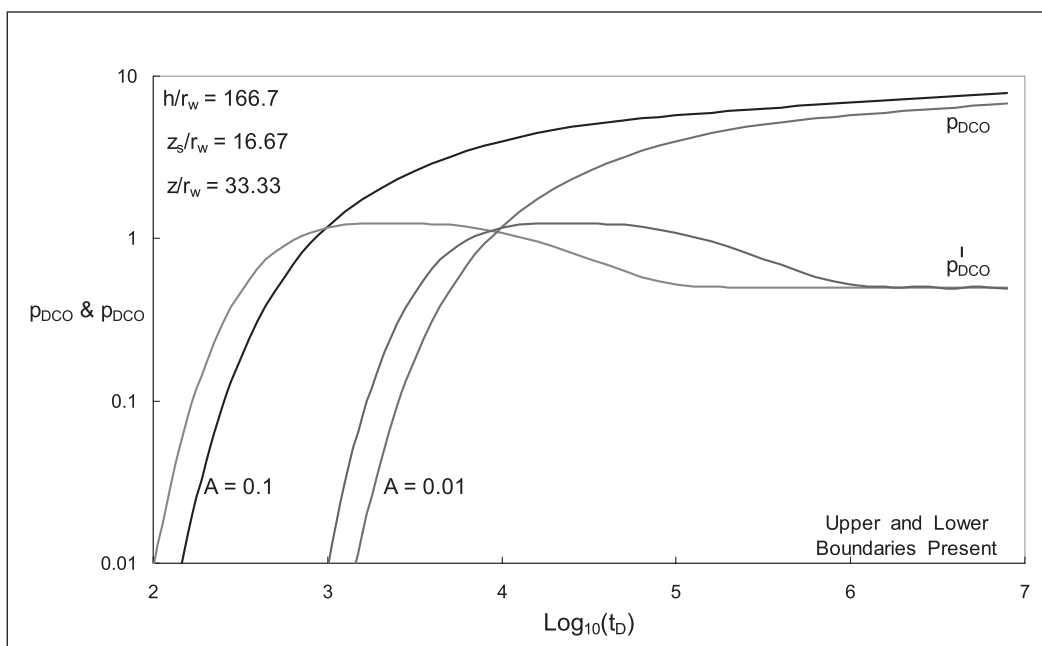


Fig. 12-49. Observation probe dimensionless response

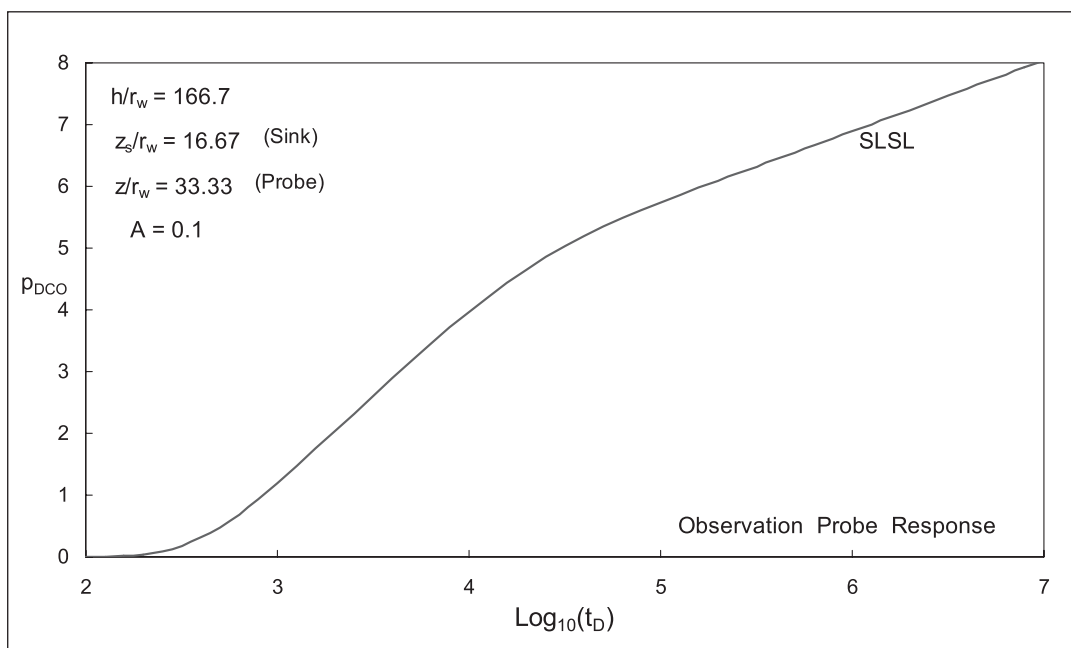


Fig. 12-50. Bounded case dimensionless semilog plot

The analytical CRD model for the probe (observation) pressure is the fundamental model for constant rate at the sink. In practice, there will be a wellbore (chamber) storage effect on the rate,

and the probe pressure has to be computed with storage included. The real-time superposition algorithm can be used for this purpose, and this problem will be treated later.

A buildup response is shown in figure 12–51 and, as expected, the time functioning, i.e.,  $\Delta t_e$ , gives the expected derivative plateau with the corresponding straight line on the semilog shown in figure 12–52. In this example, the formation is thin ( $h/r_w = 30$ ) and only radial flow is apparent.

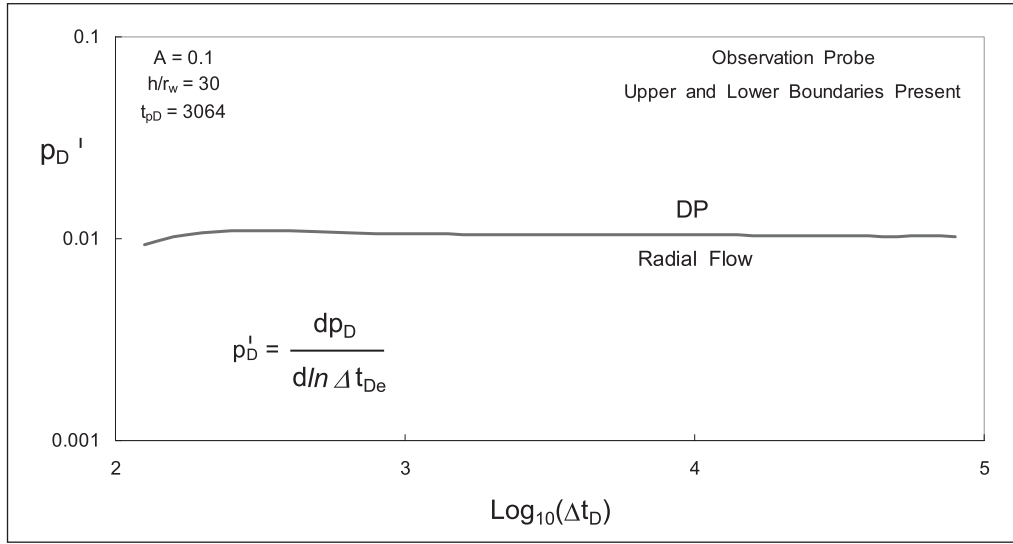


Fig. 12–51. Log–log buildup derivative diagnostic (dimensionless)

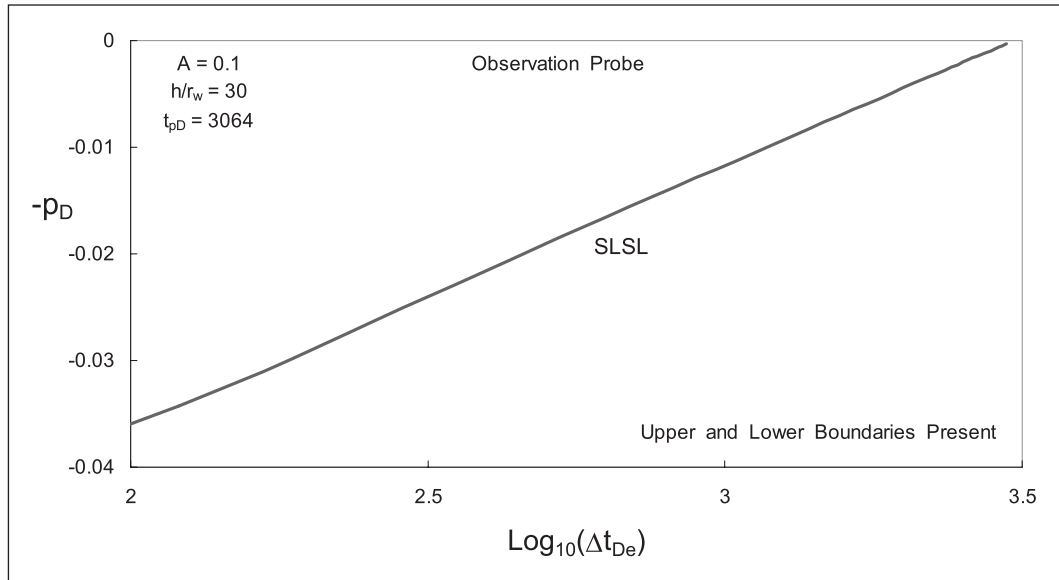


Fig. 12–52. Buildup semilog plot (dimensionless)

In the context of test design and quicklook interpretation, it is of considerable interest to have information on the time delay in buildup to see the derivative “spike,” i.e., the minimum in the observation probe pressure, as illustrated in figures 12–53 and 12–54. Several simulations were

carried out with the objective of determining the elapsed time at the occurrence of the minimum; this is denoted  $\Delta t_{\min}$ . The dimensionless characteristic time is defined as

$$\Delta t_{Dz,\min} = \frac{0.000263679 \times k_z \Delta t_{\min}}{\phi \mu c_t z_{VP}^2} \quad (12-83)$$

and in figure 12–55 this quantity is plotted against the anisotropy  $A$  for two values of  $h/z_{VP}$  and  $t_{pD} = 1,076$ . At low values of  $A$ , a limiting value of approximately 0.16 is observed and the data in the diagram could be used to design tests, i.e., how long should the buildup be to see the derivative spike that allows  $k_z$  to be identified. As usual in design, the hard part is to obtain a permeability estimate on which to base the prediction. Equation (12–83) set to the limiting value of 0.16 is in the form of a depth of investigation formula for vertical diffusion. In figure 12–56, the same information for a shorter producing time, viz.,  $t_{pD} = 358.7$ , is presented and it is apparent that producing time has quite a small effect on the time delay as expected. In interpretation mode, the elapsed time corresponding to the spike (leading edge) can be used in conjunction with the correlation to yield a starting value for  $k_z$ , for example.

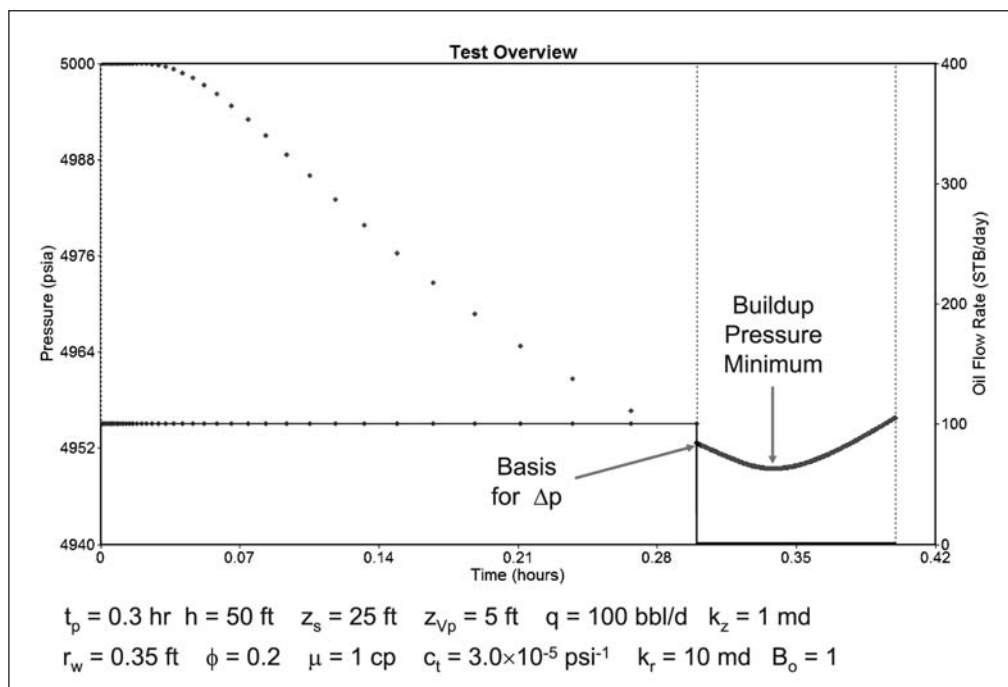


Fig. 12–53. Observation probe response

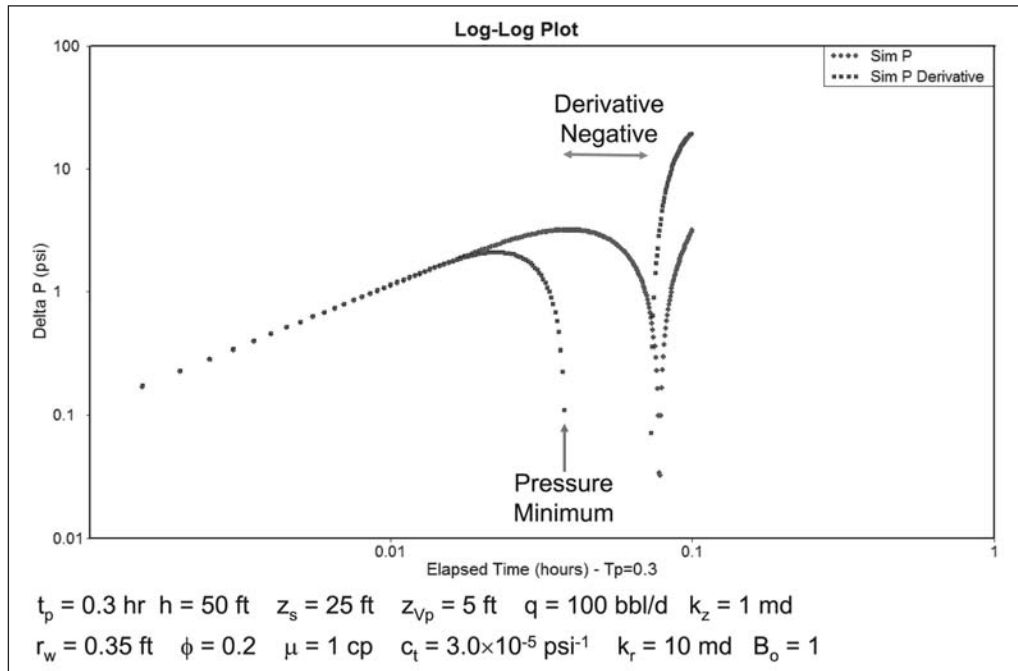


Fig. 12-54. Buildup derivative spike on log-log diagnostic plot

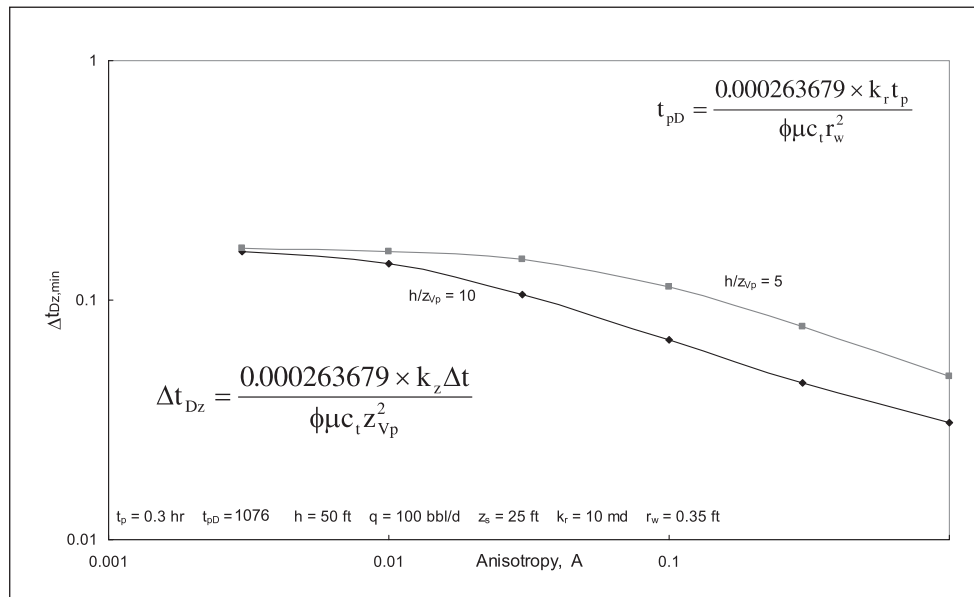


Fig. 12-55. Dimensionless elapsed time to pressure minimum

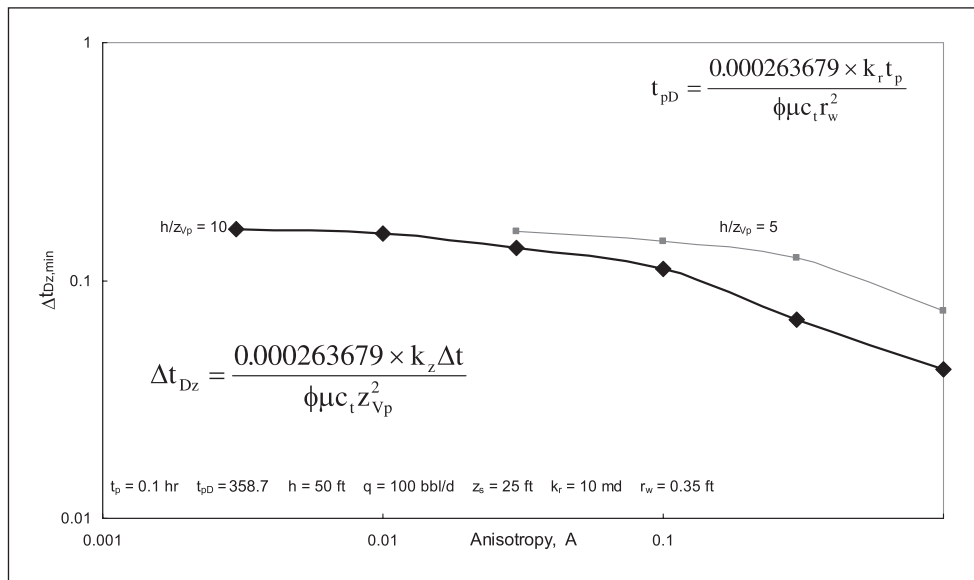


Fig. 12-56. Case of shorter producing time

The observation probe response has been computed for a constant sandface rate, and the corresponding buildup can be determined by a simple superposition of this solution. In this latter case, the sandface flow rate is assumed to be a step function and no wellbore storage effect is allowed. In order to introduce storage, the active probe response must first be computed and the sandface rate  $q_{sf}(t)$  determined as illustrated in figure 12-57; here, the convolution algorithm linking storage and the active probe  $p_D$  function has been utilized to generate  $q_{sf}(t)$ . This sandface rate schedule is then used in superposition mode—operating on the  $p_{DO}$  model—to predict an observation probe response with active probe storage and skin. An observation probe response generated using this algorithm and including the effect of active probe flowline storage is shown in figure 12-58. Thus the two models have to be computed in tandem if storage effects are to be handled properly. The observation probe model is treated as a variable rate process with the sandface flow schedule specified.

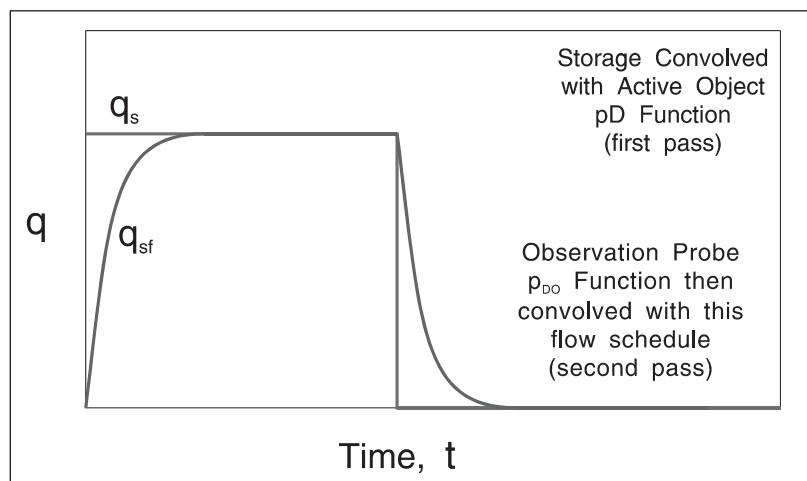


Fig. 12-57. First pass convolution of active object (probe)



# 13

## Reservoir Engineering Aspects of Production

---

### Basic Reservoir Engineering

#### Introduction

In this chapter a review of the reservoir engineering concepts that directly affect production will be presented. Additional material on reservoir engineering is also included in chapters 5 and 6 on material balance and coning and displacement phenomena. It is one objective of this chapter to emphasize the need to integrate reservoir and production engineering and for this reason considerable attention to reservoir engineering has been included. The treatment here is complementary to the material in *Well Test Design and Analysis* on pressure transient analysis. As a prelude to the study of completions, which is one subject of this chapter, it is useful to define production enhancement as "well level analysis, design, engineering and technologies needed to boost production at individual wells." In this text the term production optimization will be utilized for the wider procedure of "integrated well and surface network analysis, design, engineering and technology needed to create, monitor and maintain the overall system of downhole and surface equipment producing at the optimum level possible."

The optimization of production is carried out at distinctly different levels corresponding to the gathering system and individual wells. Attention will be focused here on the well completion and reservoir engineering phenomena relating to production. The last 25 years has seen a concerted and successful effort to properly link reservoir engineering and geology and the concept of an integrated team has been used to achieve this objective. The reservoir simulator has been the vehicle through which the reservoir engineers and geoscientists have coordinated their activities.

The present text is focused on the problem of linking reservoir and production engineering and it is important to extend the concept of the integrated team to allow reservoir, production, and facilities engineers to work in close contact. The production simulator, of which ReO is the first truly integrated form, is the vehicle that allows these activities to be coordinated. It has been estimated by a major operating company that approximately 60% of surface facility

installations are wrongly sized with respect to reservoir deliverability and it is evident that there is a substantial economic benefit from integrated design.

During the course of an asset management training program, a senior manager in PDVSA indicated that roughly seven out of ten workovers carried out in Venezuela produced little incremental oil production. It is relatively easy to analyze a pressure build-up test to determine the well skin factor and the current local reservoir pressure, but it is quite another problem to determine a suitable workover treatment to alleviate a skin problem, if it exists. Many different causes of formation damage are possible and it is quite a task to unravel the relevant mechanism and devise a successful treatment. This issue will be addressed here and special core analysis and PVT studies will form part of the recommended methodology. Another illustration of production wisdom from Venezuela arose in a seminar in Caracas where the production engineers made a case for adequate hole size to be able to run appropriate “jewelry” if production problems—usually water breakthrough—eventually occurred. This is an introduction into the subject of real option (Black and Scholes) economic analysis which considers the benefit of spending money “up-front” to allow problems to be solved at a later date. Conventional discounted cash flow economic analysis discriminates against such expenditure and the advocates of intelligent wells, for example, have adopted the real option approach to justify such completions.

An important aspect of production optimization is the subject of downtime of facilities, for example, as a result of platform maintenance. Shell consider this to be key driver in their strategy to maximize production. The treatment of electric submersible pumps focuses on the monitoring of pump performance in order to achieve a reasonable run life especially in circumstances where the intervention cost is high. The issue of downtime minimization is not covered directly in this text, but the act of building a production model does lead to improved knowledge of the operation of the system, and this will contribute to better, i.e., sustained, performance.

In the early 1980s, the author made a presentation to the then-CEO of Schlumberger, Jean Riboud, on the potential benefits of cased-hole services such as production logging. At the same time, a geophysicist, Francis Mons, made a presentation on the future application of seismic measurement, especially 3D. At the time Schlumberger embarked on a major development of seismic interpretation and cased hole did not receive the same focus despite the author’s plea. In retrospect, the development of 3D seismic has been the outstanding innovation in petroleum engineering in the last quarter century, and figure 13–1 illustrates the dramatic reduction in finding and development cost that has been achieved. Figure 13–2 indicates that 3D seismic has had a key role in this cost reduction and increased exploration success. According to Daniel Yergin of Cambridge Energy Research Associates (author of “The Prize,” a renowned history of the oil industry), technology played a key role in this process and he cites

- Improved seismic acquisition—3D seismic vessels, navigation, processing on-board
- Improved seismic processing—technical, computing, visualization
- Horizontal wells
- SPARs and TLPs

as the important drivers. It is the author’s opinion that production optimization, particularly in real time, will be the next major advance in petroleum engineering.

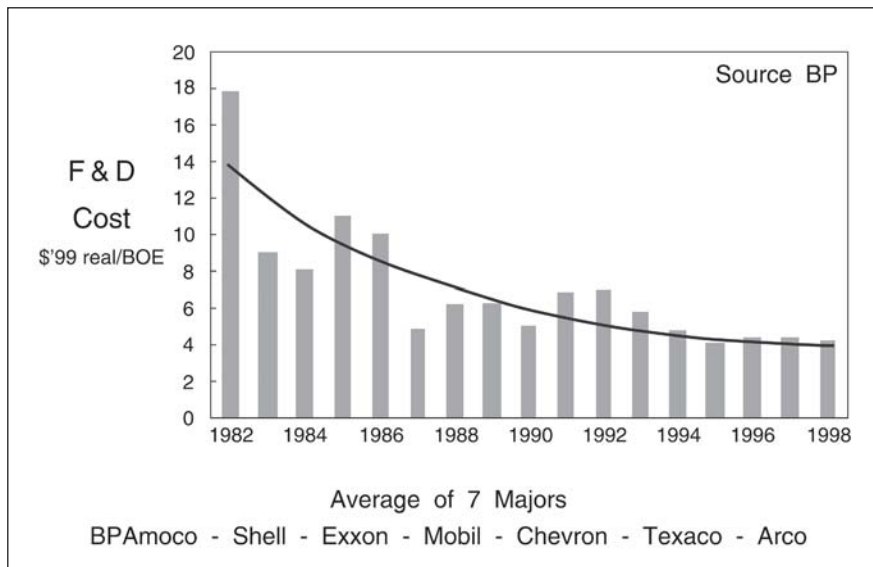


Fig. 13–1. Improvement in oil and gas industry productivity and efficiency

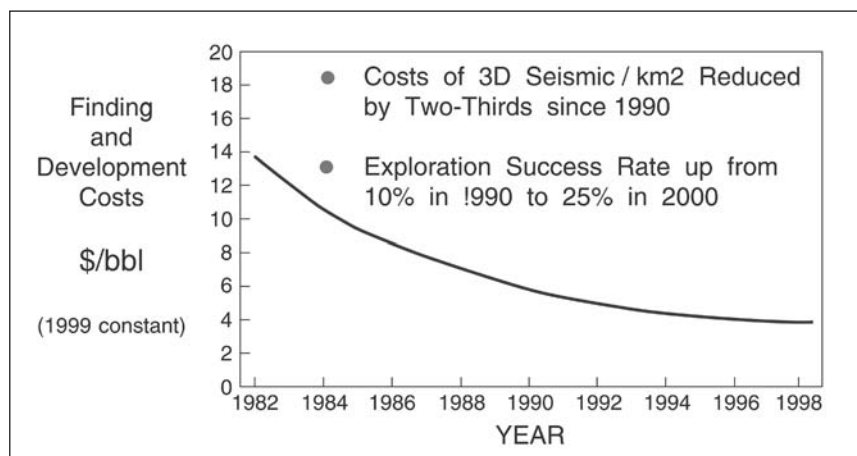


Fig. 13–2. Drivers for industry efficiency improvement

## In-Fill Drilling

The logo shown in figure 13–3 was adopted for an in-house Shell forum on production optimization in Oman. The Omani engineers who devised the logo did not appreciate that it had been used in the 1970s in the context of enhanced oil recovery (EOR) which turned out to be a largely disappointing technology; the one form of EOR that has produced results has been gas injection in permeable, dipping reservoirs such as Oseberg (Norwegian North Sea) where hydrocarbon gas was available from the nearby Troll field. Also, in the Norwegian sector the application of foam-water-alternating-gas (FWAG) has been successful in the Snorre field. Where carbon dioxide is cheaply available, e.g., four corners area in the US, CO<sub>2</sub>-enhanced recovery has been successful and at the present time renewed interest in CO<sub>2</sub> disposal (termed sequestration) by injection into reservoirs or aquifers is attractive in the light of concerns over global warming and climate change.

The outstanding technical and commercial success of the last two decades has been the development of improved oil recovery (IOR) through in-fill drilling. The term improved oil recovery was adopted since the descriptor using the almost synonymous word “enhanced” had been discredited. When an oil field is in the mature stage of development and the production is perhaps constrained by separator capacity, the most beneficial effect on production is to drill a new well into a part of the field which has been bypassed by the initial water flood process. As mentioned in the preceding section, it has been the advent of 3D seismic that has allowed better fault delineation and hence revealed reservoir compartmentalization leading to bypassed oil. Targeting a well into such “sweet spots” can be the single biggest contributor to increased oil production in a mature field. In the Mast (mature assets) project of BP in the North Sea, a proposed horizontal well in the Clyde field is delineated in figure 13–4. The improved fault description from 3D seismic was entered into the reservoir simulator and it was demonstrated that the existing locations of injection wells would not allow the region to be flooded. A 4,000-ft measured length horizontal well with gas lift was calculated to flow in the range 2–4–6 Mbbl/d in the low-permeability ( $k \sim 50$  md) reservoir. In fact, the well came in at 8 Mbbl/d of dry oil but within a year the production was down to 700 bbl/d oil at 50% water-cut. This field example shows the importance of the transient aspect of production in low-permeability reservoirs, a topic which will be addressed later in this chapter. The well was considerably better in terms of rate than a vertical well and the trajectory went through several faults helping to reduce the effect of compartmentalization. An interesting anecdote from the Mast project related to the Thistle field where a well had been shut in several years before because of a high water-cut of 60%; because of personnel changes, the existence of this well had been overlooked and only on the transfer of data to the new mast team did its potential become apparent. The well was reopened to flow and it became one of the best producers in the field. What was a poor well 10 years earlier in the middle stage of field development became a good well when the water-cut was in the 90%–99% range. This illustrates the importance of a maintained database, and the operating companies now recognize the danger of too frequent staff changes and the need to retain engineers who are familiar with the field history.

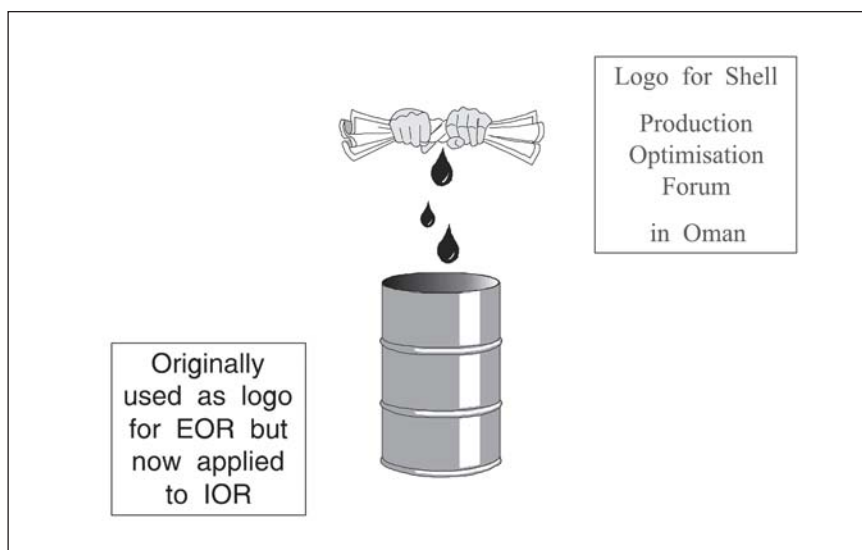


Fig. 13–3. Logo for production optimization forum

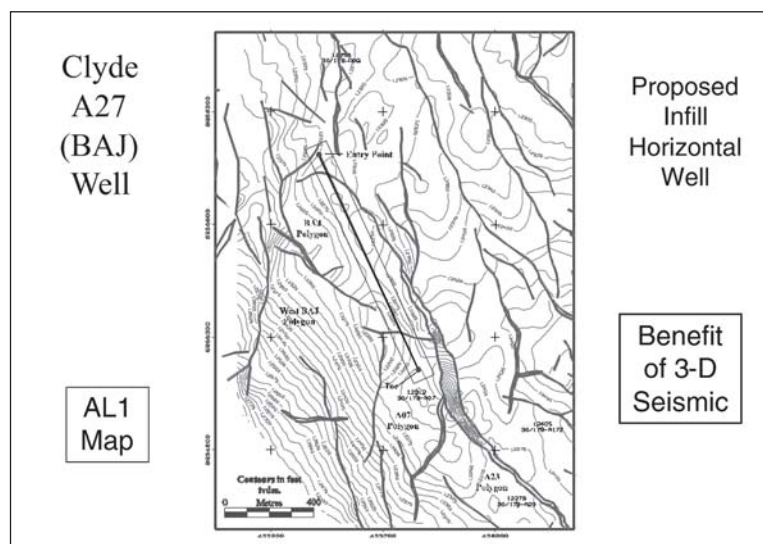


Fig. 13–4. Proposed infill horizontal well

A dual-drain horizontal well in the North Sea Dunbar field illustrated in figure 13–5 again demonstrates the utility of 3D seismic in giving improved connection with the reservoir. The large length of connection will have an immediately quantifiable effect on well productivity index (PI) but the consequence for recovery efficiency is much more difficult to tie down. An excellent example showing the benefit of 3D seismic comes from the Ekofisk field in the Norwegian sector of the North Sea; the field is operated by Phillips Petroleum (now Conoco-Phillips) and the fault map is shown in figure 13–6. The production history of well CO6 is plotted in figure 13–7, where the water-cut with the well in original position A showed a dramatic increase; the well was then sidetracked to location C and the water rate decreased substantially. When a field is water-handling-limited, this type of transformation in well performance is of huge benefit and the cost of running the 3D survey is well justified.

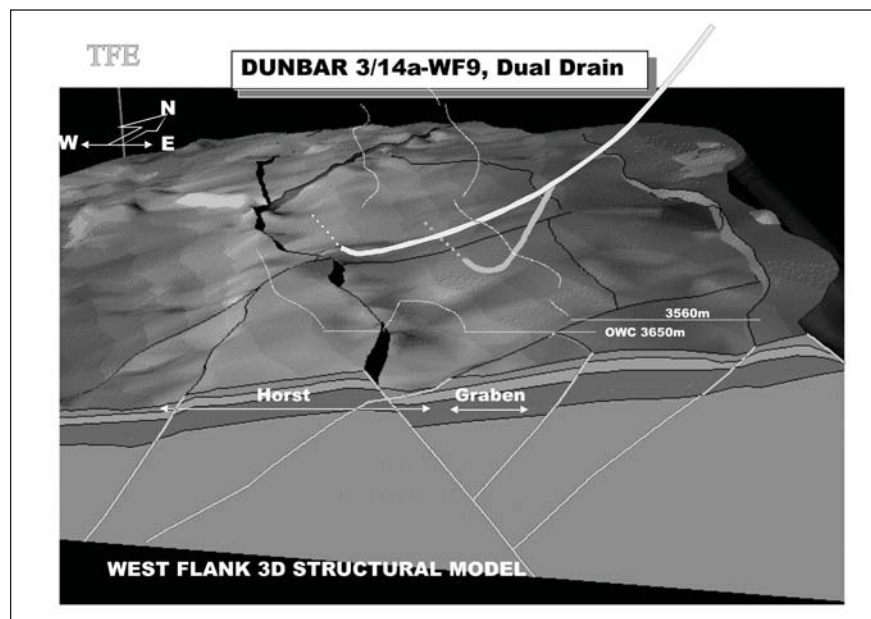


Fig. 13–5. Dunbar dual drain

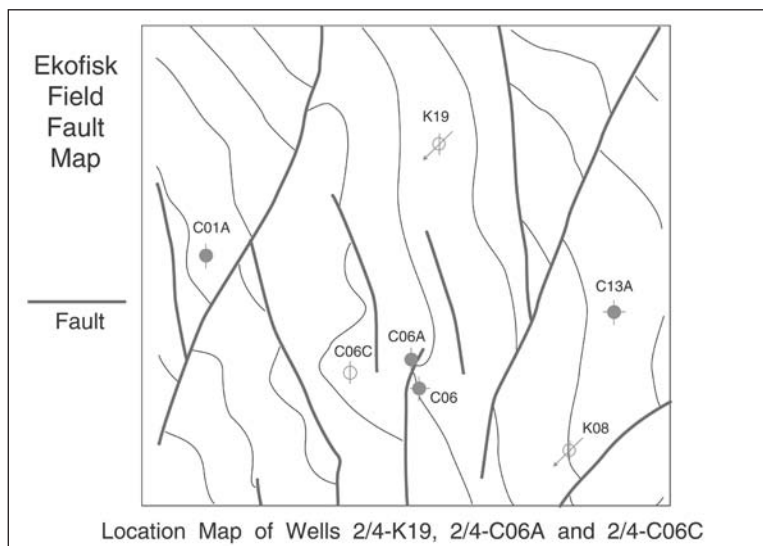


Fig. 13-6. Ekofisk field fault map

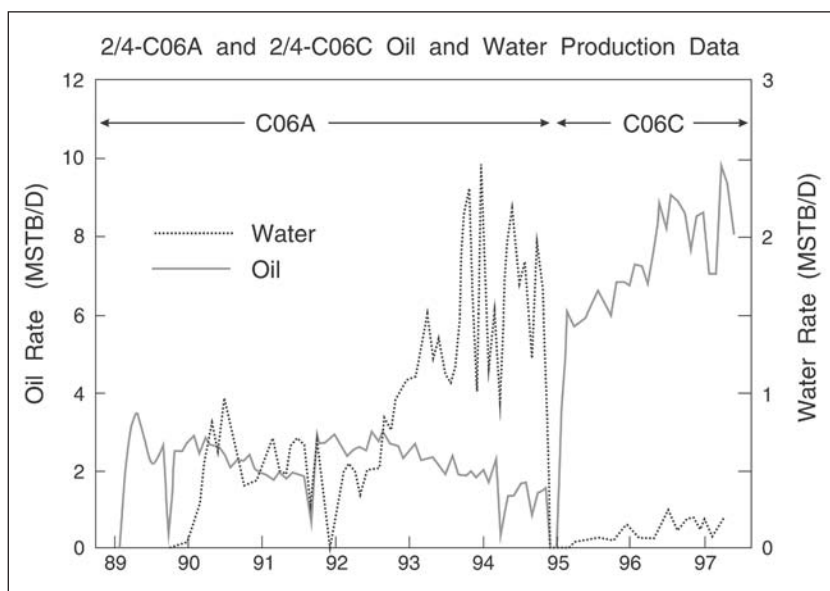


Fig. 13-7. Oil and water production data

## Layered Reservoirs

### Introduction

One of the key developments in reservoir engineering in the last 25 years has been distributed pressure measurement in observation wells using wireline formation testers (WFTs). It has been demonstrated by the author that distributed pressure data in producing fields should be accompanied by distributed flow measurement in the active producers or injectors. Whether interpretation is carried out using a relatively low-level model such as the complex



material balance or a full reservoir simulation, it is axiomatic that layer pressure data must be complemented by layer flow data. The process of distributed flow measurement in a flowing well is, of course, known as *production logging* and the contraction PLD—production logging device—will be used as a generic descriptor for spinner-type production logging tools. The use of production logging has increased dramatically over the last decade as reservoir engineers have come to recognize the importance of such measurements in understanding reservoir behavior. The output of a PLD survey is a flow profile which shows the proportion of the total flow emanating from each zone of the reservoir. Production logging is important where thick reservoirs are produced commingled into a common wellbore; a PLD survey is then the only way of assessing individual layer performance. The mechanics of running a spinner flow meter survey, the calibration of the device using up and down passes, and the computation of the flow profile will not be treated here. An excellent review by Hill<sup>1</sup> gives details of the practical aspects of production logging methodology. In the context of reservoir engineering application of PL measurements, perhaps the main point to make is that the accuracy of the measurement is much better when single-phase flow conditions exist in the wellbore, i.e., gas wells, water injection wells, and oil wells, where the bottom-hole pressure is above the bubble point. In these circumstances, quantitative use can be made of the distributed flow information in terms of identifying layer properties such as PI. When two-phase conditions exist—particularly in deviated wells—the errors in distributed flow measurement become quite severe; unfortunately, the service companies' promise to introduce new generation PL devices has not yet been fulfilled. Pressure can be measured with great accuracy but the determination of downhole flow is much less precise. However Darcy's law shows that the calculation of permeability, for example, requires knowledge of both pressure and flow rate and at the present time the weak link in the use of distributed flow information is the poor resolution of production logging devices.

In undersaturated reservoirs, the important period of primary depletion, when the reservoir is drawn down and pressure differences are allowed to develop, will also coincide with single-phase conditions in the wellbores of oil producers. Hence the WFT pressure data in new development wells is accompanied by good-quality PLD flow data from existing producers. After water breakthrough occurs, the main objective of production logging is to determine in which layers water entries are occurring; this information is also extremely important in understanding reservoir internal structure. In two-phase production logging interpretation, the flow profile of both phases is measured but, as previously mentioned, with much less precision than the single-phase case.

Thus distributed flow measurement is complementary to distributed pressure measurement and this information takes the form of a flow profile determined by up and down passes of the PLD. A typical single-phase flow profile is illustrated in figure 13–8. In a thick reservoir with commingled production from multiple zones or layers into a common wellbore, the flow profile is controlled by

- permeability distribution,
- skin factor distribution, and
- pressure distribution.

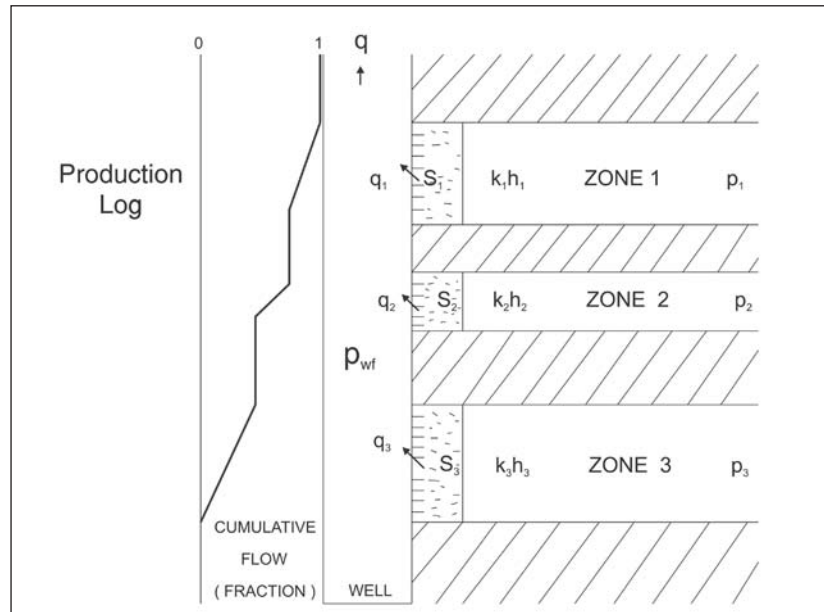


Fig. 13–8. Typical flow profile in a commingled reservoir

A schematic reservoir description for a commingled system is shown in figure 13–9 with each layer assigned its own permeability, skin factor, and pressure. The objective of layered well testing is to determine these three quantities for a system composed of layers separated by horizontal no-flow barriers. In this chapter the use of straightforward up and down passes of the flow meter—i.e., the flow profile—will be reviewed; the complicated subject of the design and interpretation of layered well tests involving the measurement of simultaneous rate and pressure transients is treated separately in the companion volume on well testing. The problem of poor resolution of spinner flow measurement places a practical limitation on what can be achieved in terms of identifying reservoir structure and it is necessary to restrict flow detection to the contribution of major zones only. The spinner device, in fact, registers cumulative flow and this signal has to be differentiated to obtain individual layer rates.

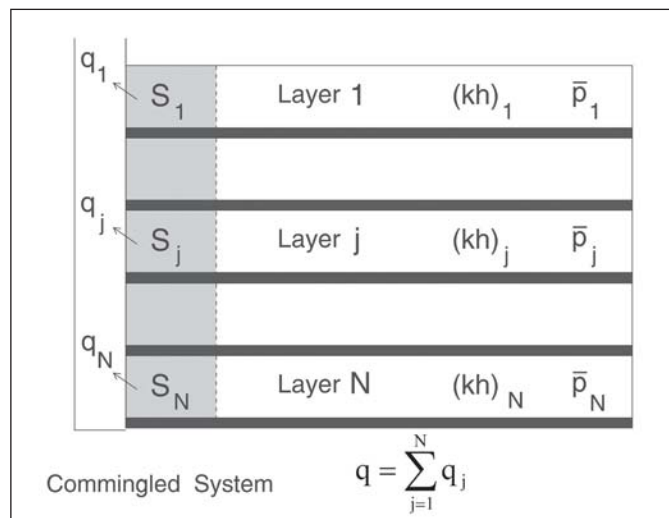


Fig. 13–9. Schematic commingled reservoir description



Some of the reasons for running production logs are summarized below:

#### Decisions on workover

- Is the well performing below its potential due to excessive skin?
- Which zones (if any) would benefit from reperforation?
- Are there any problems with the completion such as channelled cement and leaks in tubing, casing or packers?

#### Reservoir management

- Are the layers producing or accepting fluid at a rate compatible with good reservoir management (profile control)?
- Is there of detection of water or gas entries?
- Is there tuning of single-well models in reservoir simulators?

Extensive use of production logging is the natural consequence of the decision to opt for commingled production.

An interesting reservoir situation is illustrated in figure 13–10, where the possible effect of faulting on reservoir communication is apparent. The major zone 3 is of sufficient thickness that there is still partial juxtaposition across the fault plane and communication exists between the producing and injecting wells. However, although juxtaposition is present in the two thin layers 1 and 2, communication has been inhibited by diagenesis; this form of complexity in which the thin layers have been effectively blocked is quite a common occurrence and leads to severe problems in waterflooding the reservoir. Initially, all three layers will produce according to their individual PI as shown in the well performance diagram in figure 13–11. However, as the well is produced, the layers 1 and 2 will deplete more rapidly than layer 3 which has a much larger pore volume. In addition, layers 1 and 2 are not supported by the injection well, whereas layer 3 pressure will be maintained since communication to the injector is present. Production logging carried out on a regular basis will show the contribution of layers 1 and 2 gradually decreasing with time. When water breaks through in layer 3, the well bottom-hole pressure will rise and layers 1 and 2 will stop producing as shown in figure 13–12.

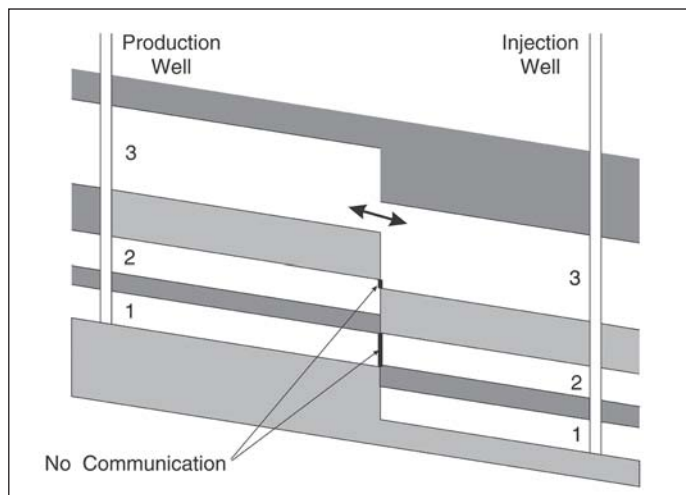


Fig. 13–10. Reservoir description illustrating lack of communication in thin layers

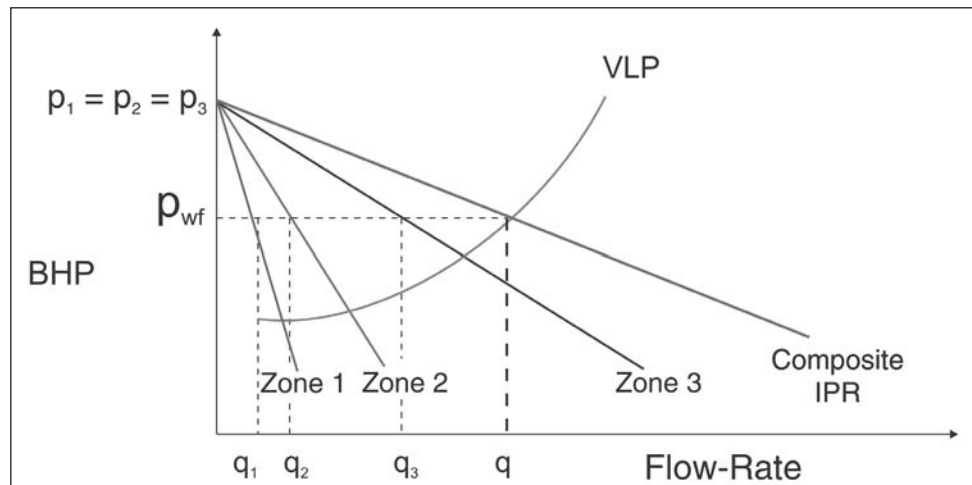


Fig. 13–11. Well performance diagram with three layers at the same initial pressure

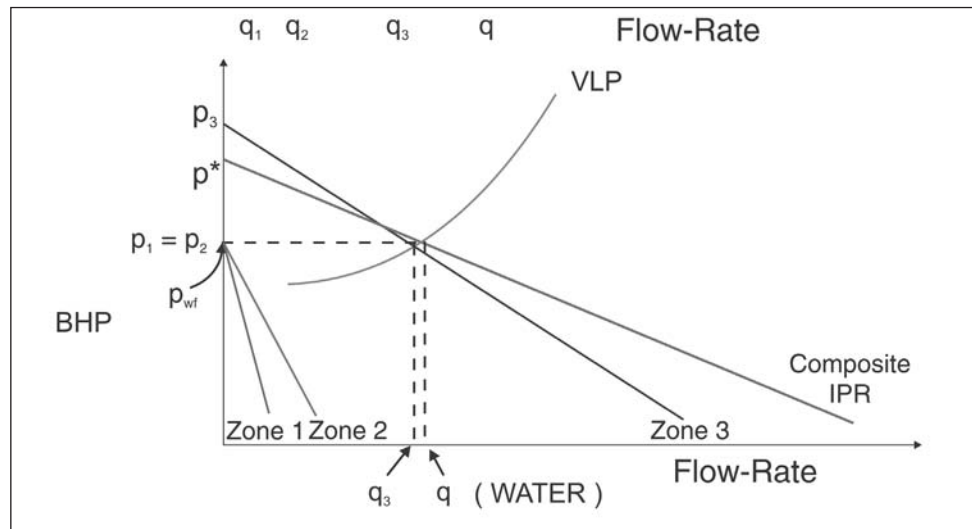


Fig. 13–12. Unsupported Layers at Zero Flow Dynamic Equilibrium with BHP

An interpreted production log in a well producing oil and gas is shown in figure 13–13, where it is clear that the upper group of perforations is hardly flowing. With the well cut back on the small choke, it also appears that the second and third top groups of perforations are accepting fluid, i.e., wellbore crossflow is occurring. Most of the flow is entering the well from the zone at 3,700 m and the bottom groups of perforations are also inactive; indeed, there is a standing water column up to the point (3,700 m) where the formation begins to flow. With the well rate increased at a larger choke of 3/4," the production log changes to the form shown in figure 13–14 with negligible injection now taking place; presumably, the bottom-hole flowing pressure is now less than the lowest pressure zone. Thus the production log gives detailed insight into the mechanism, i.e., distribution of inflow. Note, however, that in two-phase flow conditions—oil and gas in this case—the relation between spinner speed and fluid volumetric rate is subject to considerable uncertainty, particularly if the well is deviated and segregated flow is occurring.

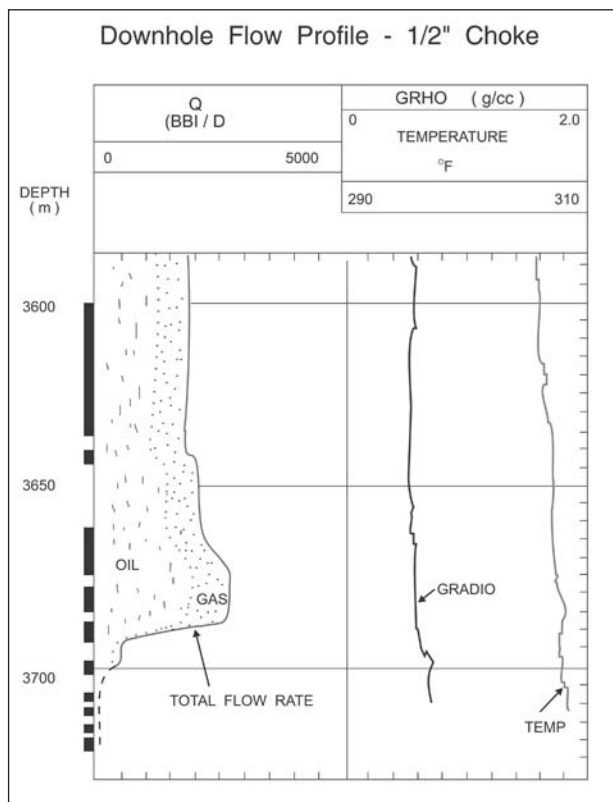


Fig. 13-13. Production log for a well producing on a 1/2" choke

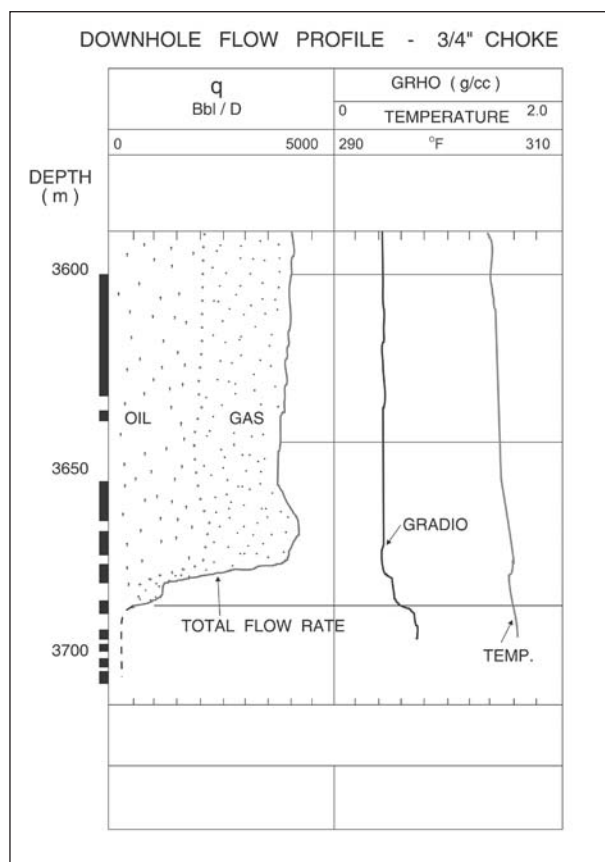


Fig. 13-14. Production log at increased rate i.e. lower bottom-hole flowing pressure

## Some Reservoir Engineering Applications of Production Logging

In this section, some of the basic reservoir engineering applications of production logging will be reviewed. In the development of the North Sea province, it was the engineers responsible for the Piper field who first appreciated the importance of production logging surveys in the monitoring of a layered reservoir. In a Europec conference in 1978, Stewart<sup>2</sup> demonstrated that in order to correctly track the waterfront movement in each layer using a reservoir simulator it was necessary to tune the simulator well models to production logging surveys. This is illustrated in figure 13–15, where it is evident that, provided no crossflow between layers is occurring, the location of the front is largely controlled by the injection rate into a layer and its cross-sectional area. Modern simulators allow the individual layer skin factors to be adjusted until the flow contributions calculated by the simulator well model match the flow profile measurements from PL surveys. This process of matching the simulator predictions to distributed flow data from producers and injectors is complementary to the parallel process of matching simulator layer pressures to WFT data in observation wells. Figures 13–16a and 13–16b show the type of flow profile match obtained by Bayat and Tehrani<sup>3</sup> in the Ninian field simulation study.

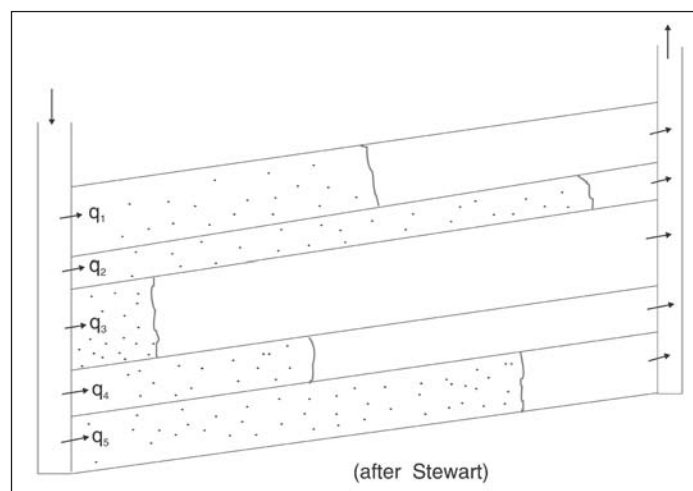


Fig. 13–15. Tracking water front locations in a reservoir simulator

The first paper to discuss the reservoir engineering applications of production logging by Stewart and Wittman<sup>4</sup> showed how a single-well model can be used to interpret production logging flow distribution measurements in conjunction with pressure measurements. Note that modern PL devices transmit simultaneous downhole flow and pressure data. An important use of production logging was described in this paper; figure 13–17 is a flow meter log from the giant Gawar field in Saudi Arabia which has a superpermeability streak present over a large area of the field. This thin band—about 2 ft thick—is due to fenestral (lagoonal) deposition and as can be seen that all the well’s production emerges from the very high permeability “thief” zone. Interestingly, the zone is embedded in low-porosity dolomite beds and, due to the shoulder effect on the logs, it is not evident at all that a thin high-porosity layer is present. Accordingly, the first production logs showing the massive flow concentration were regarded with some scepticism; however, the problems of early water production soon demonstrated the adverse affect on field performance of such a thief zone. Eventually, many wells had to be shut in because facilities were not available at the time for treating salty crude.

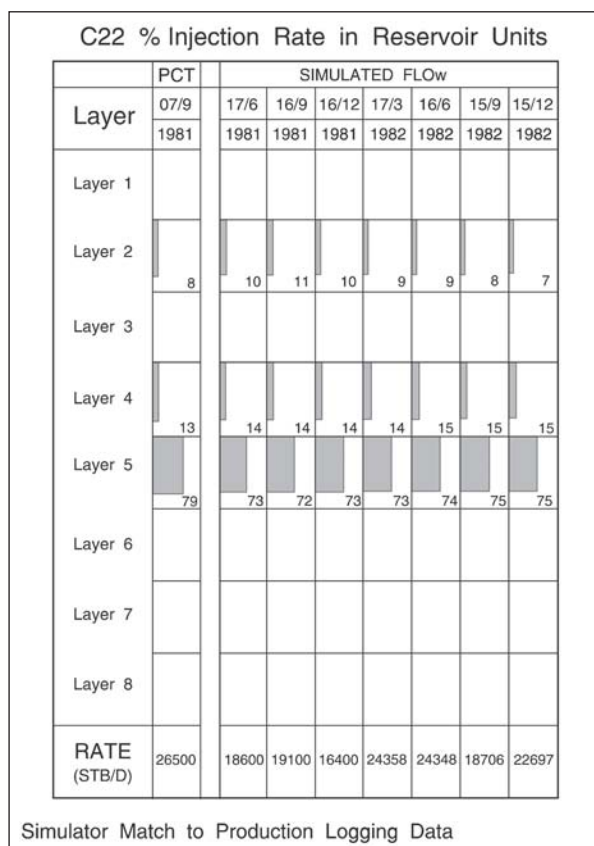


Fig. 13-16a. Ninian field flow profile match

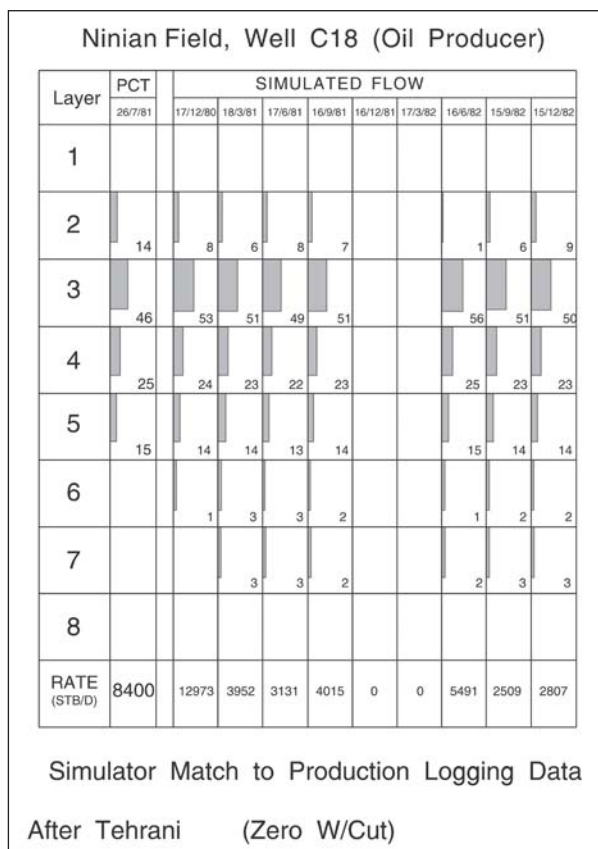


Fig. 13-16b. Ninian Field flow profile match (Well C18)

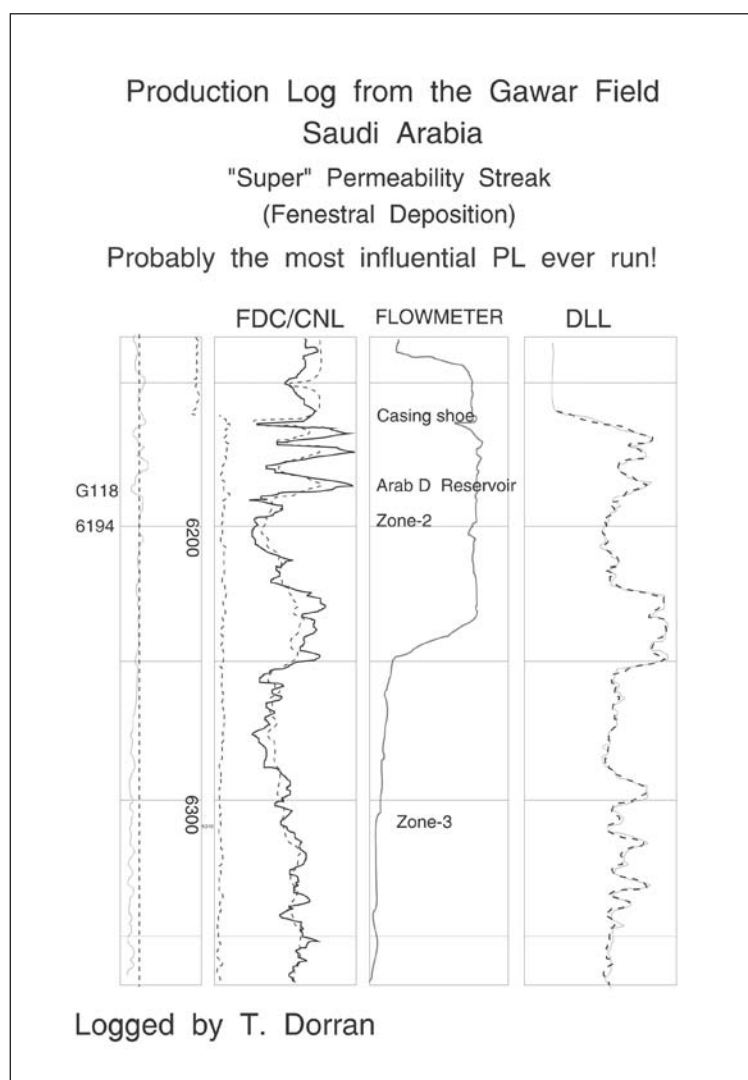


Fig. 13–17. Super-permeability streak

A related problem was mentioned in the paper by Stewart and Wittman that had become apparent also in connection with the Piper field. The most permeable zone in Piper is the F sand which has a permeability of the order of 10 darcy; however, the sand is so unconsolidated that it is almost impossible to obtain any core recovery from this formation. Consequently, knowledge of the permeability of the most prolific zone is difficult to obtain and, in fact, it was production logging data matched with a single-well model that tied down the F sand permeability. In the design of waterfloods, the most important information is data on permeability differences between layers and, if the most permeable zones cannot be cored, the presence of high permeability thief zones may be missed. Hence production logging surveys are a valuable addition to core analysis work.

The problem with permeability determination from production logging is that the flow profile is affected by individual layer skin factors in addition to their permeability. Thus if there is a variation of skin from layer to layer, it will be difficult to determine permeability. As previously mentioned, the detailed treatment of transient layered well testing, which allows a complete

determination of layer pressures, permeabilities, and skin factors, is given in chapter 14 of *Well Test Design and Analysis*.

Figure 13–18 illustrates, in a sense, the opposite of a high-permeability continuous thief zone, i.e., an isolated sand lens of limited extent. In a short-term transient well test of such a commingled system with equal initial pressures, the slope of the semilog plot will give the total  $kh$  of the two layers. However, the production from the sand lens will soon become negligible as its pressure quickly declines to a value very close to the flowing bottom-hole pressure. Thus the pressure of the low-capacity unit will reach a dynamic equilibrium with the bottom-hole pressure controlled by the performance of the dominant layer as shown previously in figure 13–12. This simple situation demonstrates the benefit of time-lapse production logging since the flow profile measured at different times will show the flow contribution from layer 1 gradually declining to a negligible value. Again the problem of reservoir storage, i.e., a two-layer system with the permeable zone bounded, is treated at length in the well testing context in chapter 14 of the companion volume. Another common geological situation is depicted in figure 13–19, where a high-permeability sand lens is embedded in a lower permeability matrix. In this case, the lens will force flow concentration and the production log will indicate the flow emanating from the high-permeability region. A well test will indicate a negative skin—even although the well has not been artificially stimulated in any way—and this case has been termed “geoskin” in the well testing context. Thus flow concentration can result from a specific permeability distribution or from a skin distribution and the production log needs to be considered in conjunction with a transient well test in order to distinguish between the different geological possibilities.

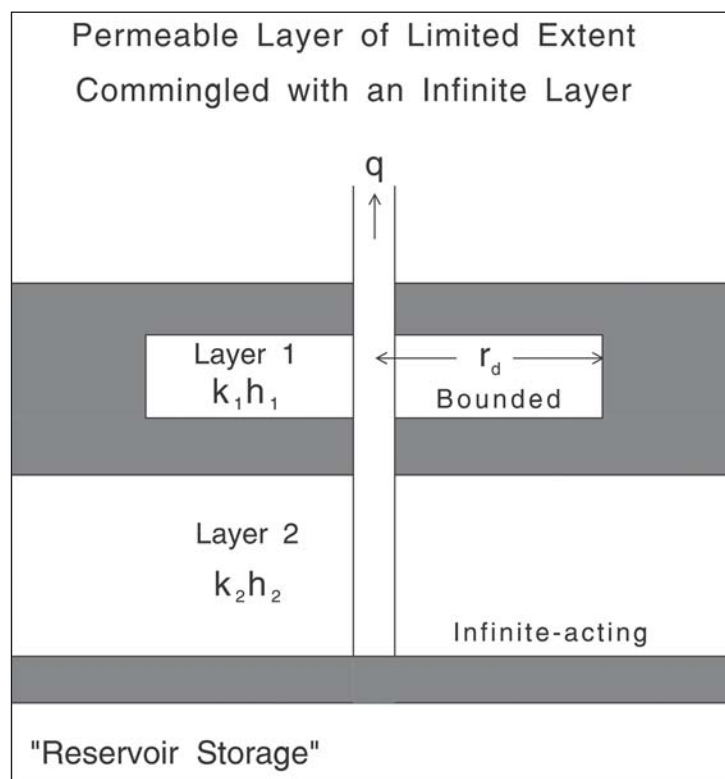


Fig. 13–18. Bounded high permeability layer commingled with an infinite tight zone



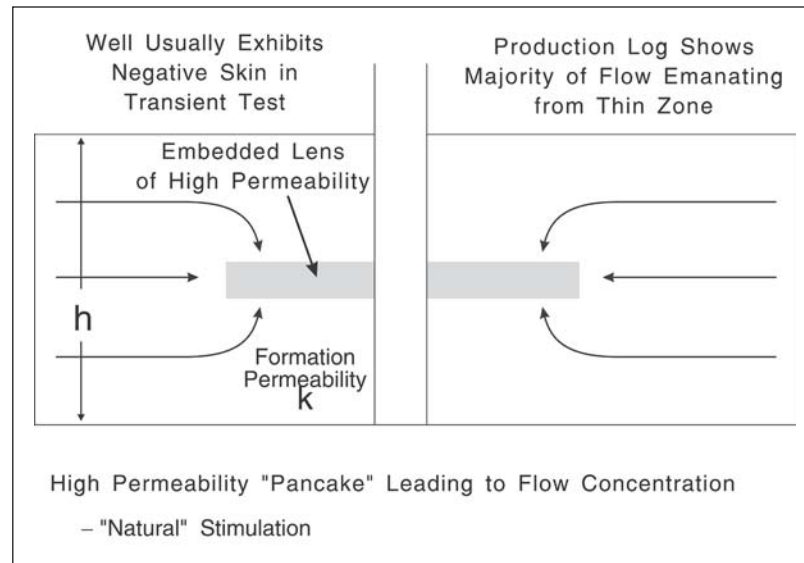


Fig. 13–19. Embedded permeable lens of limited extent

## Layer Skin Distribution

It is interesting to observe how the skin factor may vary from zone to zone. From the point of view of formation damage, it is the layers that have the highest content of water-sensitive clay minerals, e.g., montmorillonite, which might be expected to suffer most formation damage when wells are drilled with water-based mud. Hence the low-permeability layers, usually being the shaliest, would be expected to exhibit the larger skin. In water injection wells, the higher permeability layers will accept more water and therefore be subject to a greater degree of cooling due to the cold sea water. Again, the thermal fracturing associated with the cold ring will probably mean that the higher permeability layers will also have smaller, i.e., more negative, skin factors than the tighter zones. In completions that are perforated overbalanced (relatively rare in recent times with the preponderance of tubing-conveyed perforation), there is a tendency for high-permeability layers to clean up first and then there is not sufficient drawdown for the perforations in the remaining layers to unplug leading to high skin factors in the poorer zones. Thus, in general, it can be expected that the high-skin zones are often those with low permeability, which poses a serious problem in achieving balanced injection and production.

To summarize, the layer skin factor distribution is affected by

- perforation characteristics such as shot density and perforation depth and the problem of plugged perforations;
- formation damage like clay swelling with some zones being more sensitive than others; and
- formation alteration such as thermal fracturing in water injection wells and scale deposition.

Profile control is the name given to the exercise of adjusting the shots per foot in individual layers to try and achieve balanced production or injection since, from a reservoir management point of view, production or injection should occur in proportion to the layers pore volume.



The problem of plugged perforations is illustrated in figure 13–20, where the additional localized flow convergence causes the skin factor to be larger than anticipated. However, it often occurs that whole groups of perforations do not produce as shown in figure 13–21 and the well exhibits a limited entry. This detection of poor well performance due to unintentional limited entry is one of the most important applications of production logging and much influences decisions about workover. While on the subject of the practical application of production logging, it should be mentioned that the detection of leaks is one of the most common outcomes of a survey.

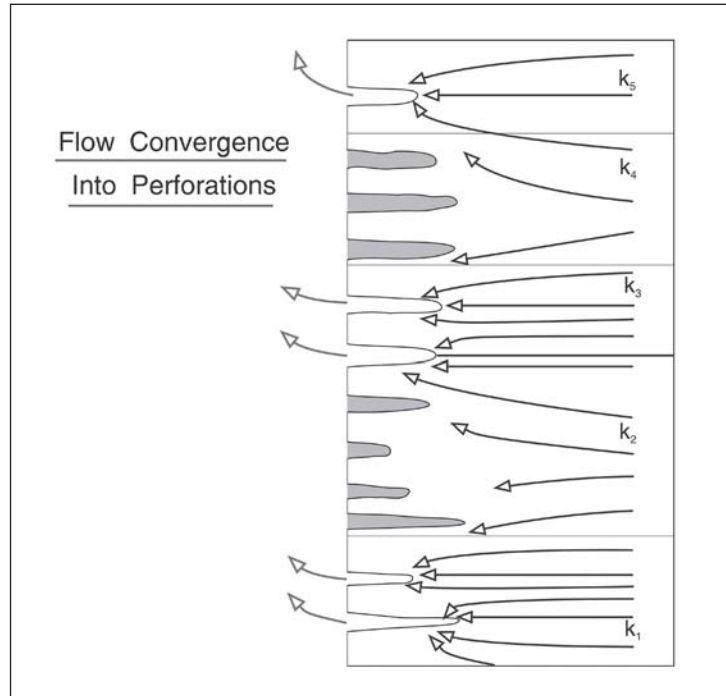


Fig. 13–20. Problem of plugged perforations and additional flow convergence

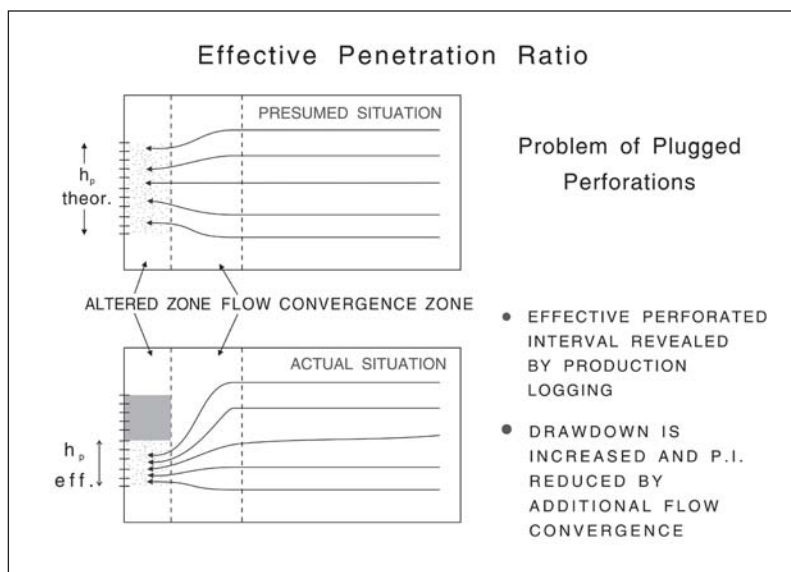


Fig. 13–21. Well limited entry as a result of a bank of perforations not flowing

In an attempt to improve understanding of perforated completions, Schlumberger developed a horizontal flow meter comprising two anemometer-type cups as illustrated in figure 13-22; the idea is to detect the jet entries associated with individual perforations. It is interesting to recount that the first attempt to measure the number of active perforations was carried out by Shell who hung off painted drillpipe in a well and counted the number of erosion marks. In this way it was established that only about 30%–40% of perforations actually flow (in the days before underbalanced tubing-conveyed perforation). The first experimental log from the horizontal flowmeter, run in Abu Dhabi, is shown in figure 13-23 and the entries corresponding to individual perforations are clearly visible. Unfortunately, this device was not developed into a commercial service.

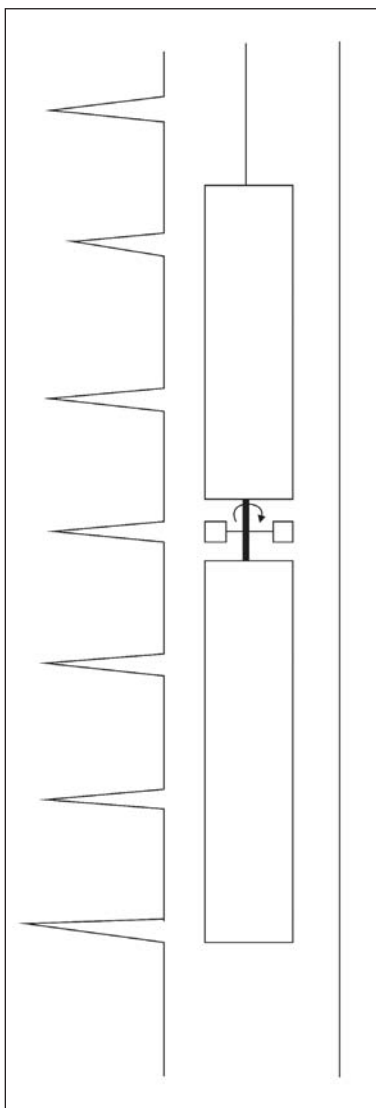


Fig. 13-22. Horizontal flowmeter

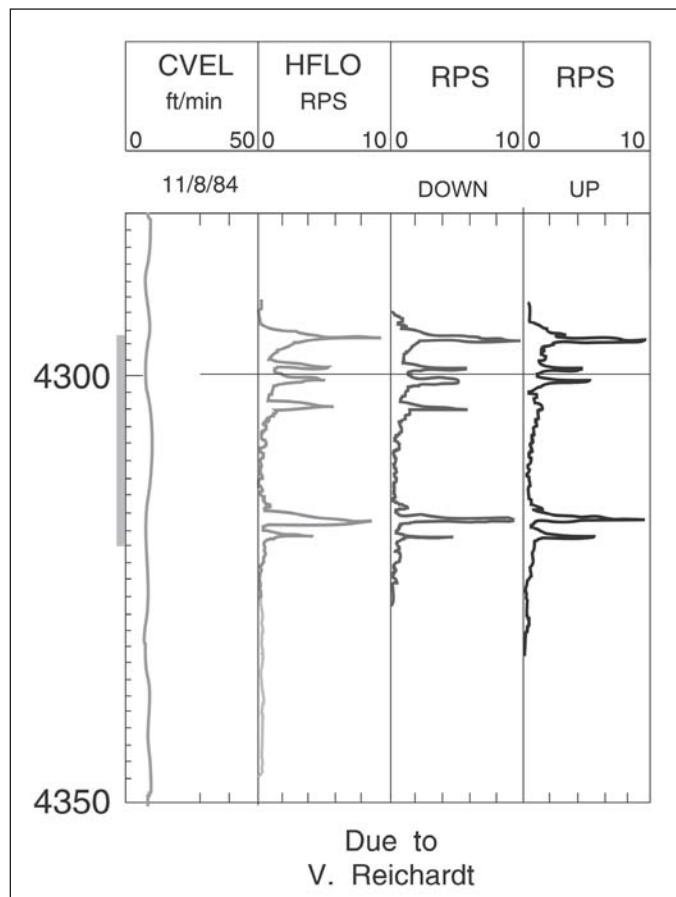


Fig. 13-23. Horizontal flow indicator (HFI) log

## Zonation

The flow distribution is obtained by differentiation of the cumulative flow profile and, as already mentioned, measurement error restricts this process to the determination of the contribution of major zones separated by barriers. Hence the poor quality of the measurement forces a degree of zonation on the interpretation of the production log. The layered reservoir description for a commingled system recognizes these limitations and the flow contribution from layer  $j$  can be written formally as

$$q_j = f_j(p_j^e, k_j h_j, S_j, p_{wf}) \quad (13-1)$$

with the total well flow rate given by the summation

$$q = \sum_{j=1}^N q_j \quad (13-2)$$

The distributions of flow, external pressure, permeability–thickness product, and skin factor can therefore be expressed as lists:

$$\mathbf{q} = \begin{pmatrix} q_1 \\ \dots \\ q_j \\ \dots \\ q_N \end{pmatrix} \quad \mathbf{p}^e = \begin{pmatrix} p_1^e \\ \dots \\ p_j^e \\ \dots \\ p_N^e \end{pmatrix} \quad \mathbf{kh} = \begin{pmatrix} k_1 h_1 \\ \dots \\ k_j h_j \\ \dots \\ k_N h_N \end{pmatrix} \quad \mathbf{S} = \begin{pmatrix} S_1 \\ \dots \\ S_j \\ \dots \\ S_N \end{pmatrix}$$

A typical zonation from a layered reservoir description study is shown in figure 13–24, where the zonation from logs has been presented along with the core analysis data and the flow profile. The last column is the permeability distribution which will be used in the reservoir simulation work.

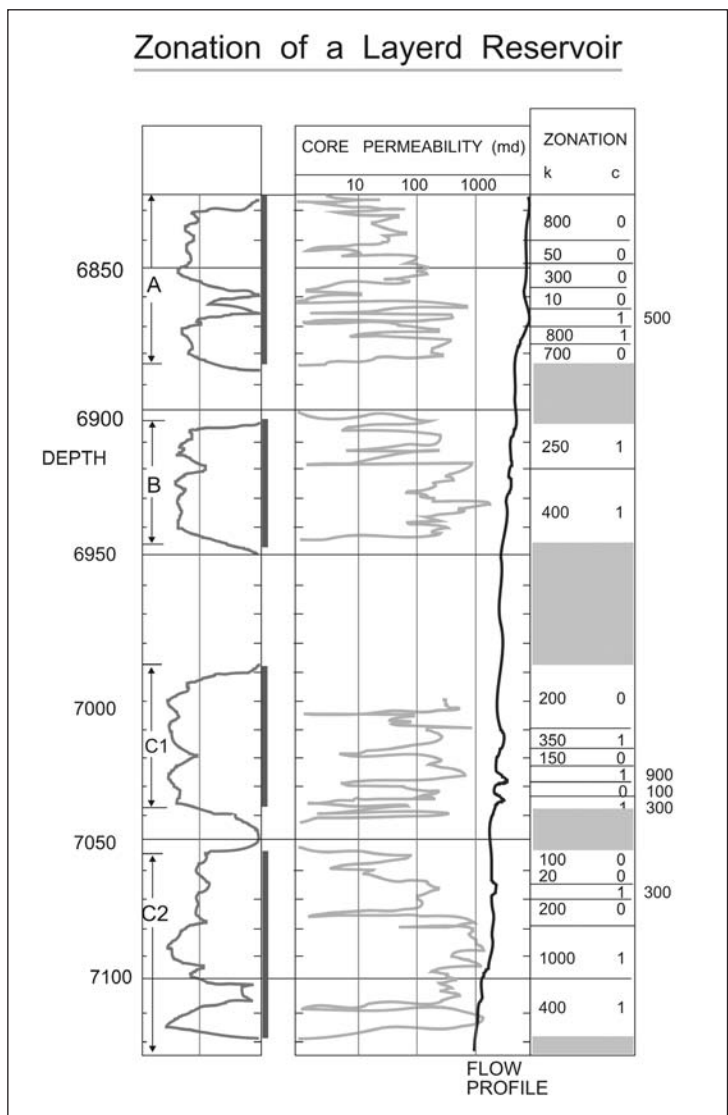


Fig. 13–24. Zonation of a commingled reservoir

## Direct Measurement of Layer Pressures

It has already been pointed out that when a new well is drilled into a produced field, the layer initial pressures  $p_j^e$  may be quite distinct due to differential depletion of the reservoir by existing producers. Whenever it is felt that differential depletion is occurring, a WFT survey will be run before the well is cased to directly measure these layer pressures; this is illustrated in figure 13–25. Here the term initial pressure does not refer to the original reservoir pressure but rather the current layer pressures in the vicinity of the new well. If the reservoir exhibits stratified characteristics, and especially when water or gas injection will be carried out, there is a strong case for carrying out a layered well test as part of the standard appraisal procedure. In this case the initial pressures  $p_j^e$  will already be known from the WFT survey and this information should be used in the design and analysis of the multilayer test. In addition, the WFT survey gives an excellent picture of the proper zonation and the number of layers that need to be carried in the reservoir description.

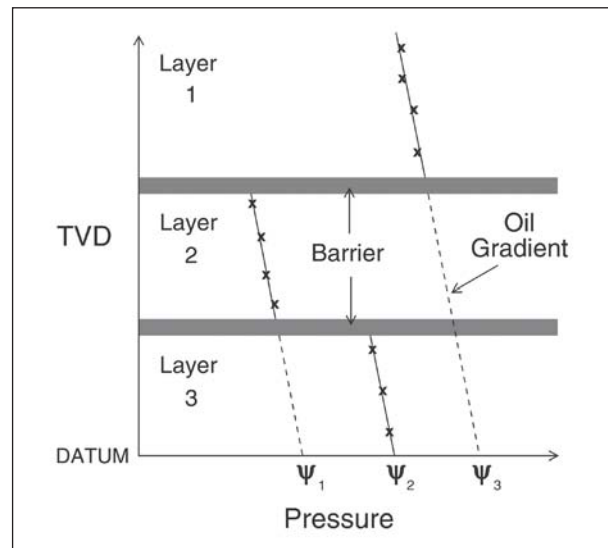


Fig. 13–25. Differential depletion

It is also possible to make a direct measurement of layer pressures in existing producing or injection wells using the cased-hole version of the wireline formation tester. If a well is killed for a workover and is inactivated by mud, as illustrated in figure 13–26, the cased hole WFT can be run to measure the layer pressure provided the well has been inactivated long enough for the buildup to essentially stabilize. The cased-hole tool has the capability of shooting a single new perforation, which is automatically isolated by the packer, and constitutes an observation perforation for direct pressure monitoring. Note that in the workover situation there is no wellbore crossflow since all layers are blocked by the overbalanced mud. This technique has been used with considerable success in the Prinos field in the North Aegean Sea where an extensive reservoir monitoring campaign has allowed the development of water production to be significantly deferred. Decisions concerning workover, e.g., the setting of casing patches, bridge plugs, or exclusion liners to seal particular layers, require knowledge of both layer pressure and water-cut and the cased-hole WFT along with saturation monitoring has been the key to improved recovery in this field. The permeabilities of the layers are high enough that supercharging by mud filtrate invasion is not significant and pressure stabilization following shutin occurs relatively quickly.

A second application of the cased-hole WFT is illustrated in figure 13–27, where the pressure of a zone not yet perforated has been accessed with the wireline device. It is very useful to know the pressure of such layers before they are perforated so that the effect of adding an additional zone to the commingled system can be properly considered in advance; the optimization of cumulative oil production from all layers needs to be assessed. Some operators have expressed reservations about leaving an unplugged hole in the casing if it is decided not to perforate the unproduced zone but the ability to measure pressure in advance allows better decision making to take place.

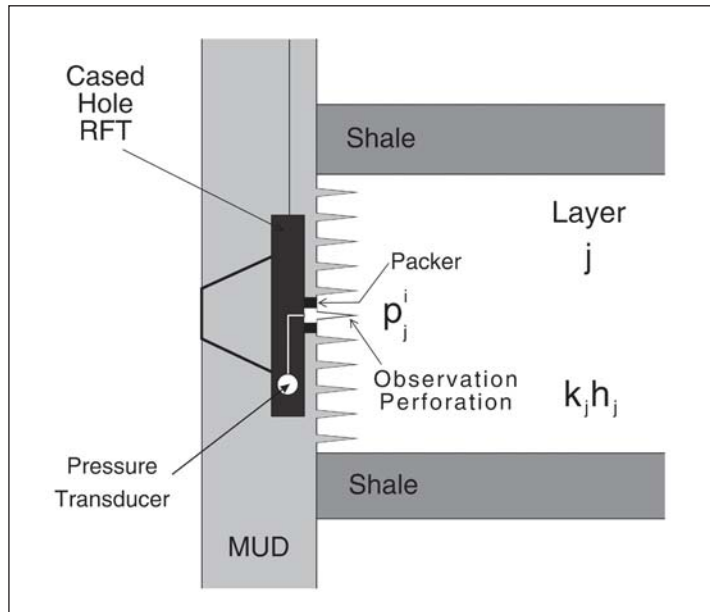


Fig. 13–26. Cased hole RFT in workover situation

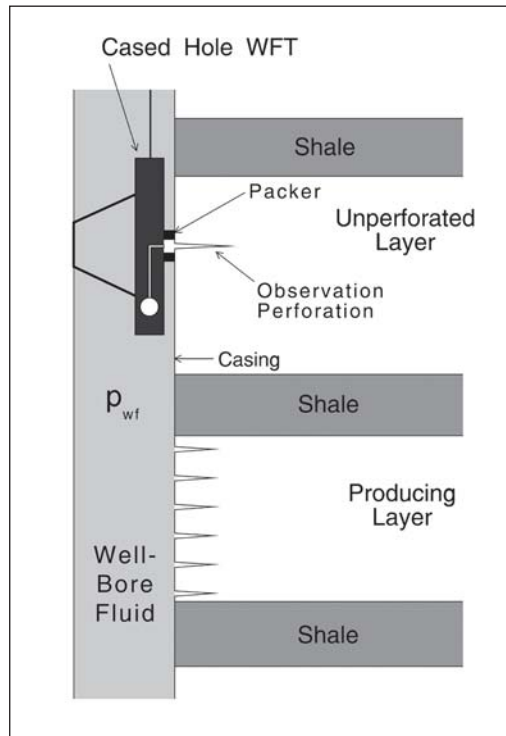


Fig. 13–27. Use of cased hole WFT to access pressure of an unperforated zone

In the treatment of layered well testing using PLTs given in this chapter, the indirect determination of layer pressures will be addressed in detail and an important objective of such testing is simply to allow layer pressures to be estimated using transient analysis techniques. However, it must always be remembered that cased hole WFT devices provide an alternative approach which in the correct circumstances may be advantageous. By the same token, selective

interval testing, illustrated diagrammatically in figure 13–28, using packers and perhaps coiled tubing units also offers a means of determining the same information. However, a danger associated with selective interval testing is presented in figure 13–29, where an invalid assumption concerning layer thickness and the interval being tested arises because the supposed impermeable barrier extends only a short distance from the well. Field examples have been published where the same interval was, in fact, tested twice and each of the presumed layers given much too high a permeability since the individual thicknesses were employed to decompose the same  $kh$  (combined layer) product. Each method must obviously be considered on its merits in a given situation.

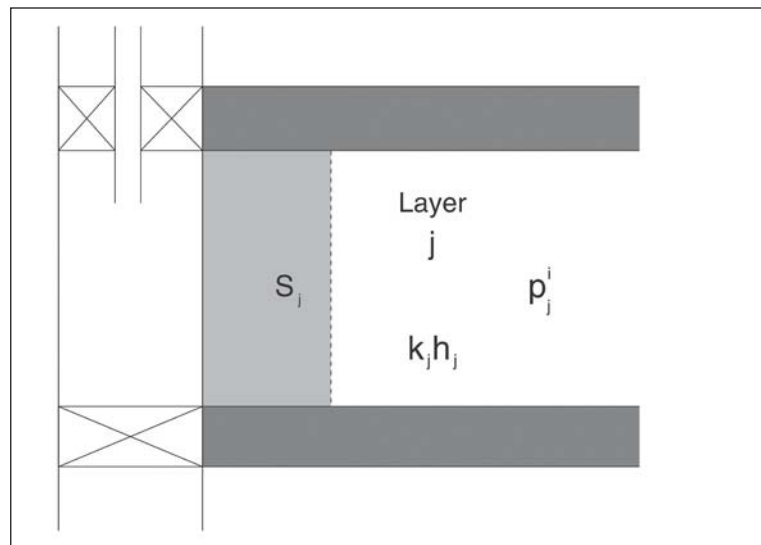


Fig. 13–28. Selective interval testing using packer technology

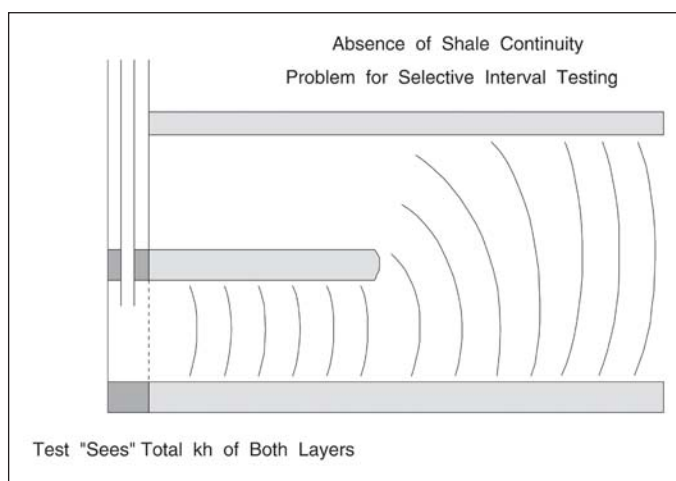


Fig. 13–29. Invalid layer identification arising from shale discontinuity

## Profile Control

The term profile control refers to the situation where some well completion technique is used to try and ensure the injection and production from layers which optimizes recovery. In waterflooding, for example, it may be beneficial to flood each layer at the same rate i.e. the injection and production per zone should be roughly proportional to layer thickness. In a balanced waterflood, the injection and production rates for each layer, on an in situ basis, are equal resulting in a stabilized maintained pressure. Note that the concept of profile control implies a commingled system with negligible reservoir crossflow between layers.

One of the first attempts at profile control was instituted in the Brent formations of the North Viking Graben. The very permeable Etive formation was perforated at a very small shot density, while the adjacent lower permeability Rannoch sand was completed conventionally at four shots per foot. However, this attempt to balance the layer contributions was unsuccessful and it was not until the advent of high slant wells in the limestone formations of the Middle East that profile control began to be realized. Here the length of the well in a particular layer was made inversely proportional to its average permeability which attempted to equalize the  $kL$  product between the various layers.

## Well Workover

During the course of a seminar in Edinburgh, a senior manager from PDVSA indicated that roughly seven out of ten workovers in Venezuela did not result in significant increased oil production and this situation is replicated in other regions of the world. It is straightforward to determine the skin factor in a single-layer reservoir from a build-up interpretation. However, it is quite another problem to deduce the origin of the damage and therefore an appropriate workover strategy to remedy the problem. It is remarked elsewhere in this chapter that often it is not known whether the poor production from a zone is due to low pressure or high skin. These difficulties are obviously compounded when multilayer systems are involved and the ensuing section will treat this situation in detail. The research of Bennion and coworkers in Canada has been of great value in identifying the origin of formation damage and therefore the design of a workover.

## Flowing Gradient Surveys

The basic understanding of the production of a well is the performance diagram, introduced into the industry by Gilbert, which is a plot of bottom-hole flowing pressure versus oil flow rate as illustrated in figure 13–30. In an oil well with the bottom-hole pressure above the bubble point, the inflow performance relation (IPR) is linear with a slope governed by the well productivity index  $J_{SS}$ . The topic of well testing is largely concerned with identifying the determinants of the IPR, i.e., the reservoir pressure, the zone permeability–thickness product, and the skin factor. Much of this chapter is concerned with measuring these parameters on a layer-by-layer basis. For example, the succeeding section deals with selective inflow performance, a technique which employs production logging passes to determine layer pressures and PIs. However, the well operating point is controlled by the intersection of the IPR with the vertical lift performance (VLP) curve, as shown in figure 13–30, and it is just as important to identify the parameters that



control the nature of the VLP relation; here it is suggested that an effective pipe diameter is the preferable method of matching a mechanistic vertical lift model to a measured FBHP and phase flow rate. In the case of the formation, well testing in the reservoir monitoring mode is tracking changes in formation pressure and skin factor and consequent variation of the IPR. Note that it is absolutely essential to distinguish between production problems caused by low reservoir pressure and problems associated with formation damage such as scaling, asphaltene deposition, water sensitivity, or perforation plugging; a workover must focus on the correct target.

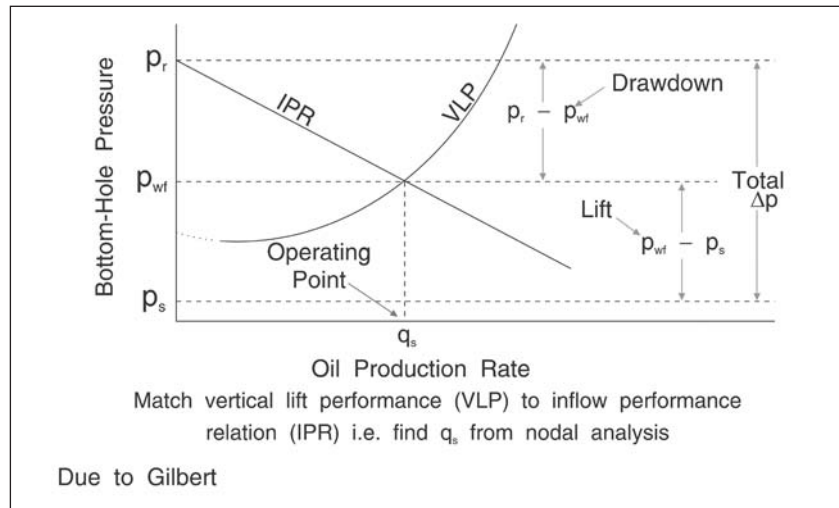


Fig. 13–30. Well performance diagram

## Selective Inflow Performance

### Single-phase Flow

WFT devices have shown the importance of measuring the pressures of the various layers in a reservoir as they deplete differentially. However, a WFT survey is possible only when a new well is drilled into the field. As the development drilling program comes to an end, the opportunity to access the evolution of layer pressures is curtailed unless there is much in-fill drilling. From the point of view of reservoir monitoring, it is desirable to go on measuring layer pressures. In the Gulf of Thailand, where multiple stacked gas reservoirs are produced commingled, the onset of sand production in a given layer is linked to its pressure. The zones that deplete rapidly will be the first to require a gravel pack and hence it is necessary to track individual layer pressures. It is possible to develop methods for the determination of layer pressures in active wells using production logging to give information on layer flow rates. The first application of production logging to layered reservoir analysis was devised for gas wells and has been called the *selective inflow performance* (SIP) technique. The idea was based on the well performance diagram for a reservoir comprising a number of isolated layers, i.e., a commingled system. Assuming

semi-steady-state (SSS) conditions with each layer having its own individual external pressure  $p_j^e$  and productivity index  $J_j$ , the individual layer inflow performance relations are given by

$$q_j = J_j(p_j^e - p_{wf}) \tag{13-3}$$

This assumes that the external pressures at radius  $r_e$ —the same for all layers—are essentially constant during the test period and the well in question is at the SSS. The SSS PI is related to the layer permeability and skin factor by the familiar equation

$$J_j = \frac{2\pi k_j h_j}{\mu B \left( \ln \frac{r_e}{r_w} - \frac{3}{4} + S_j \right)} \tag{13-4}$$

These layer IPRS can be plotted on a well performance diagram, i.e., a graph of bottom-hole flowing pressure  $p_{wf}$  versus flow-rate  $q_j$ , as illustrated in figure 13-31; this diagram was first presented in an early text book on production by a British mathematician called Nind.<sup>5</sup> For this purpose, Eq. (13-3) may be written as

$$p_{wf} = p_j^e - \frac{1}{J_j} q_j \tag{13-5}$$

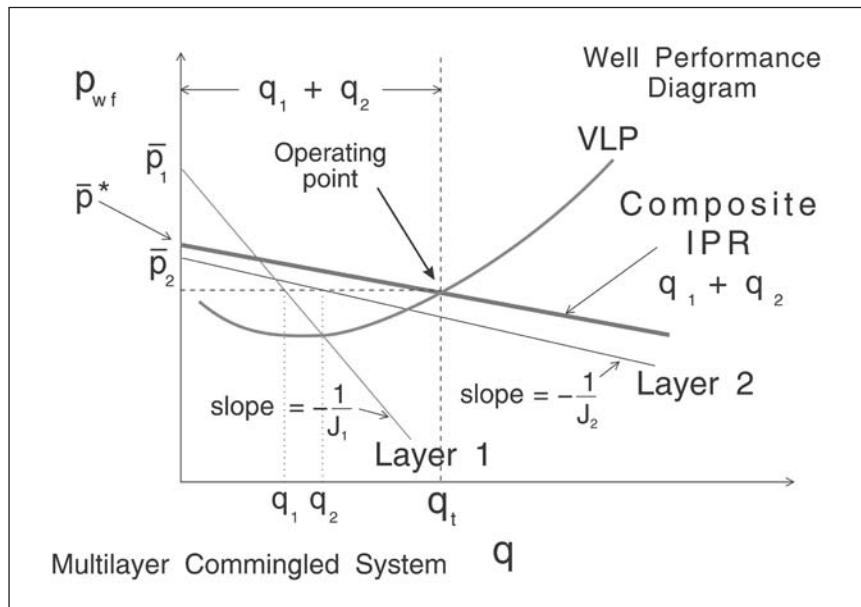


Fig. 13-31. Surface flow-rate schedule for a SIP test

Thus each individual layer IPRs has a slope  $-1/J_j$  and intercept  $p_j^e$ ; these are illustrated diagrammatically in figure 13-31. For a given value of  $p_{wf}$ , the total well flow  $q$  is given by

$$q = \sum q_j = \sum J_j(p_j^e - p_{wf}) \tag{13-6}$$

and prediction of the well inflow requires knowledge of the layer PIs,  $J_j$ , and the layer external pressures  $p_j^e$ . The total flow rate  $q$  obtained by the summation (13-6) is also a linear function of  $p_{wf}$  having the form

$$q = J(p_w^* - p_{wf}) \quad (13-7)$$

where

$$J = \sum J_j \quad (13-8)$$

and

$$p_w^* = \frac{\sum J_j p_j^e}{\sum J_j} = \frac{\sum J_j p_j^e}{J} \quad (13-8)$$

This is the composite IPR and it is also shown in figure 13-31. Provided  $p_{wf}$  is less than  $p_w^*$ , the well will be a net producer. For all layers to flow,  $p_{wf}$  should be less than the smallest external pressure denoted  $(p_j^e)_{\min}$ . If  $p_{wf}$  is intermediate between  $p_w^*$  and  $(p_j^e)_{\min}$ , some layers will be accepting fluid. The steady-state production characteristics of a well in a commingled system can be readily understood through the well performance diagram especially when the well VLP curve is plotted simultaneously with the composite IPR. The intersection of these two gives the well operating point. It is apparent that both layer productivity indices  $J_j$  and layer external pressures  $p_j^e$  must be known before well performance can be assessed. If a conventional total system build-up analysis is carried out in a layered reservoir, the pressure obtained from extrapolation of the Horner plot is essentially the quantity  $p_w^*$  and the slope of the semilog straight line yields the arithmetic average permeability given by

$$\bar{k}h = \sum_{j=1}^N k_j h_j \quad (13-9)$$

In the SIP technique, the well is flowed at a series of total rates as shown in figure 13-32. Each flow period  $i$  is of sufficient duration that the SSS is reached, i.e., the bottom-hole flowing pressure  $p_{wf}$  and the individual layer flow rates  $q_j$  have stabilized. At the end of the flow period, a production logging device is used to measure the flowing pressure  $p_{wf}(T_i)$  and the flow profile  $q_j(T_i)$ ,  $j = 1, \dots, L$ , where time  $T_i$  indicates the end of the  $i$ -th flow period. The assumption is made that each individual layer rate can also be presumed to be constant as illustrated in figure 13-33; in practice, the individual layer rates are not constant and rate transients occur as shown in figure 13-34. Provided each flow period is long enough for essentially SSS conditions to be attained, then the data points for each layer, viz.,  $p_{wf}(T_i)$  and  $q_j(T_i)$ , can be plotted on a well performance diagram as shown in figure 13-35. The slope of the straight line for layer  $j$  gives the layer steady-state PI  $J_j$ , while the intercept gives the layer external pressure  $p_j^e$ . This shows how a step-rate well test can yield the layer pressures using measurements of  $p_{wf}$  and layer flow rates. The SIP technique allows estimation of the layer productivity index  $J_j$ . If the layer permeability  $k_j$  is assumed known, say from core analysis, then the skin factor can be obtained from Eq. (13-2).

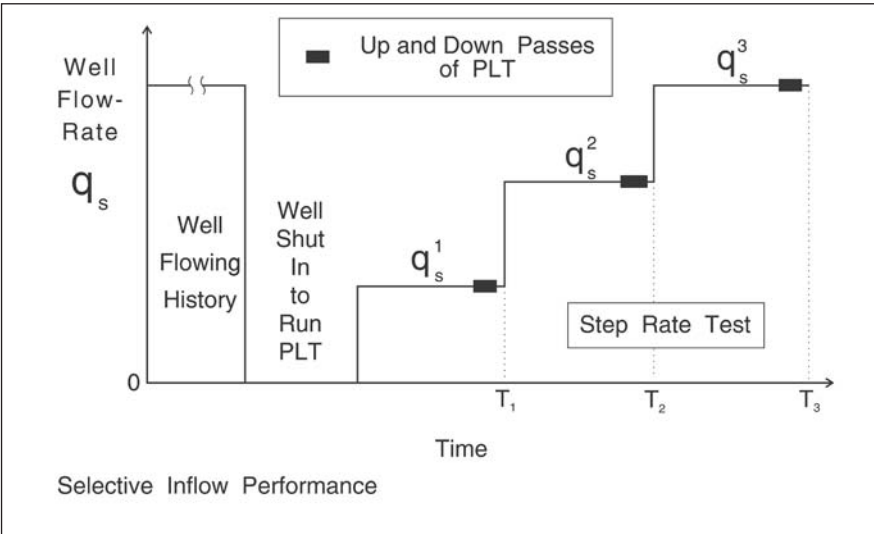


Fig. 13-32. Surface flow-rate schedule for a SIP test

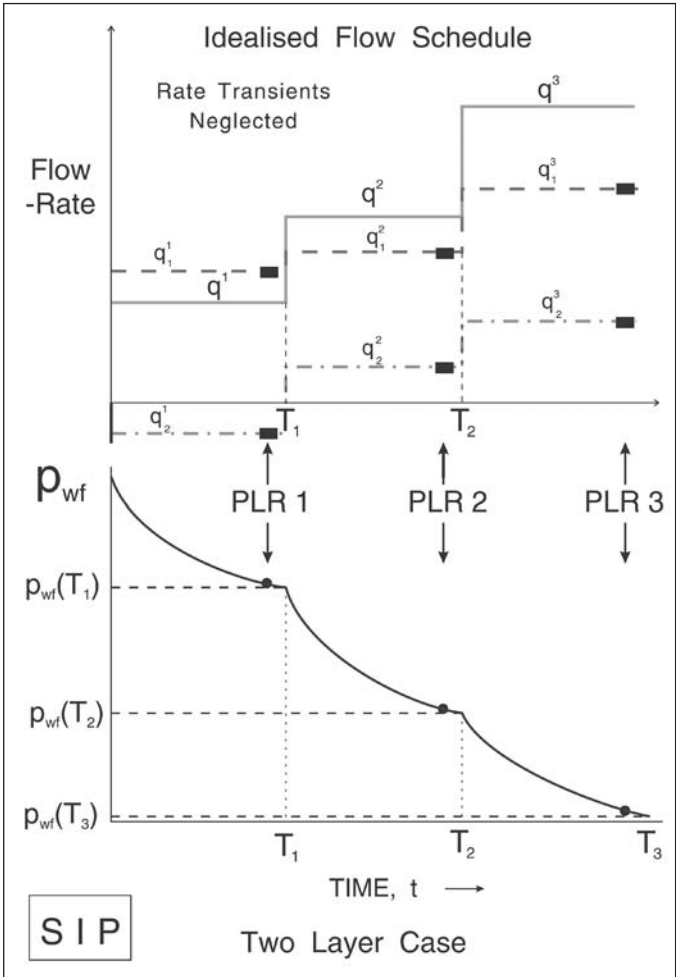


Fig. 13-33. Presumed downhole flow schedules for a SIP test

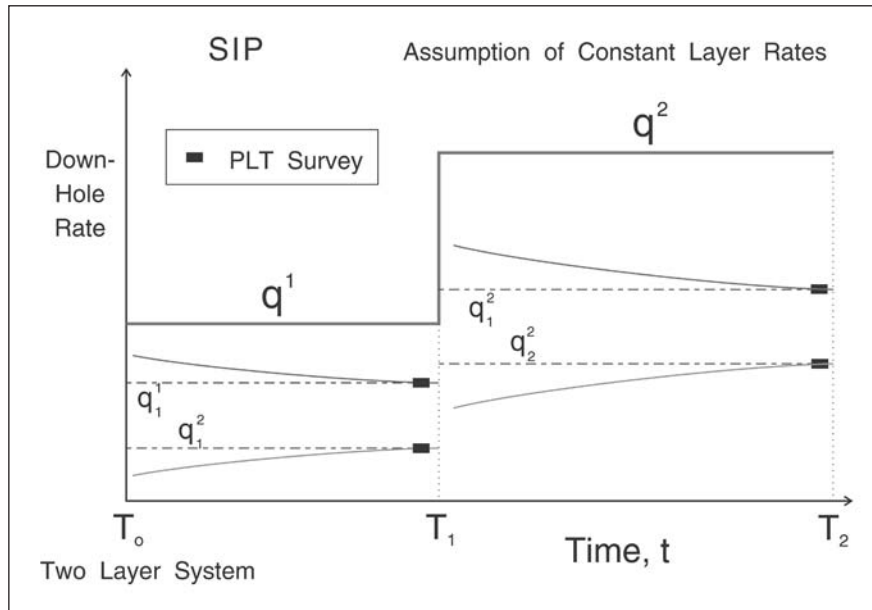


Fig. 13–34. Layer rate transients

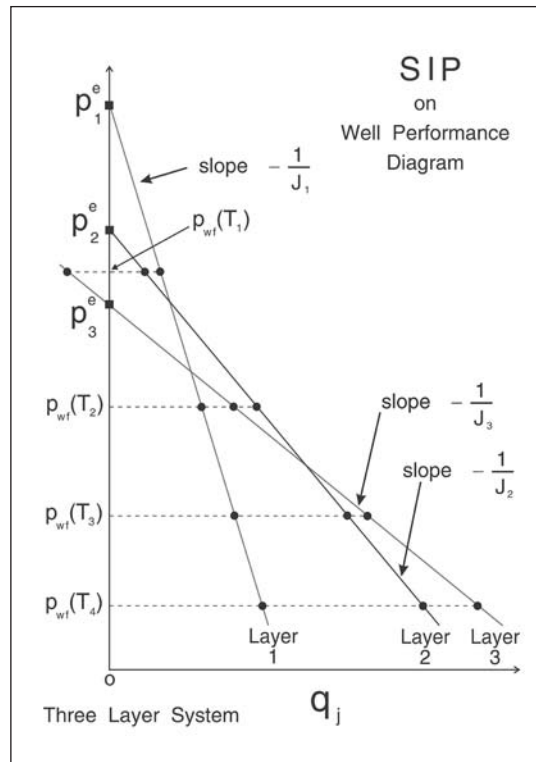


Fig. 13–35. SIP results presented on a well performance diagram

The SIP technique has been successfully employed in gas wells where it can also help to elucidate non-Darcy skin effects; in this case the IPRs are not straight and show curvature at high rate. It has also been employed in oil wells, a field example being shown in figure 13–36. However, the technique has the disadvantage that steady-state conditions must be attained. This is

controlled by the layer of lowest permeability ( $k_j$ ) and by the oil viscosity  $\mu$ . Note that what is implied is a quasi-steady-state (QSSS) in a multiwell system. However, the main problem is the time necessary to reach such a QSSS.

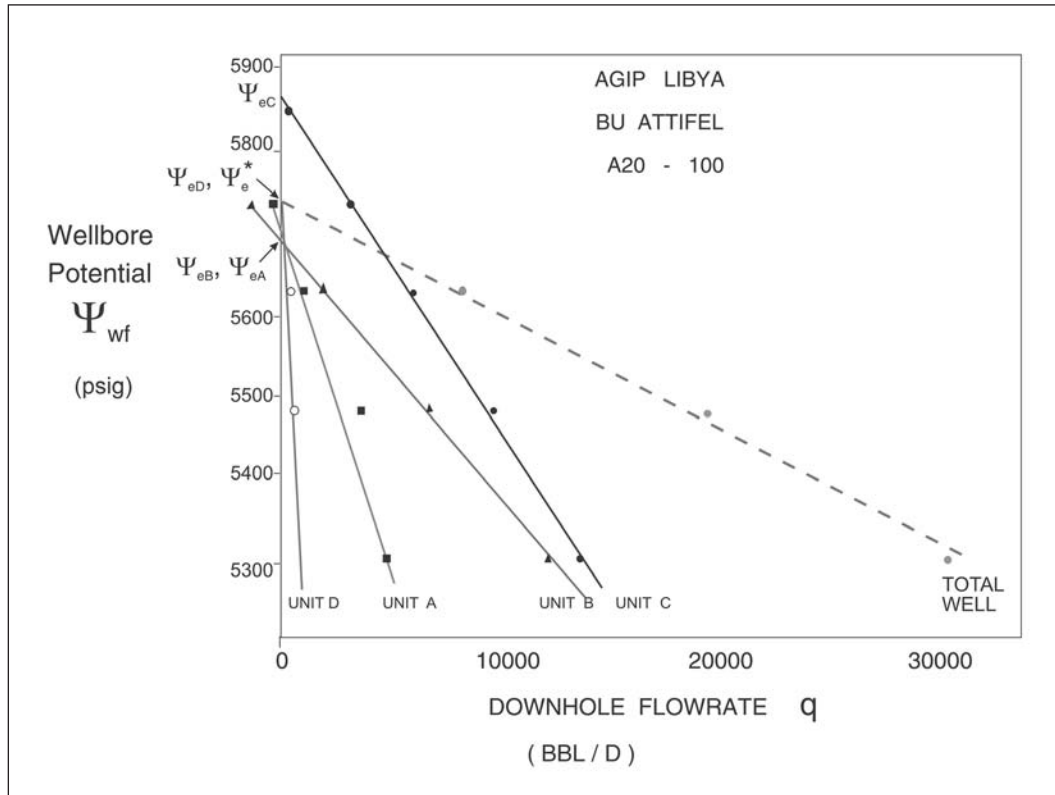


Fig. 13-36. SIP field example from libya

In order to demonstrate the effect of flow period duration on a SIP analysis, a synthetic example was run on an analytical layered reservoir simulator using a decreasing rate schedule. The specified properties of the layers and the simulation data and results are given in table 13-1. In this example, the model chosen for each layer was infinite-acting and the productivity index,  $J_{ss,j}$ , has to be based on the concept of drainage radius,  $r_{d,j}$ , where

$$r_{d,j} = 0.75 \sqrt{\frac{4k_j t}{\phi \mu c_t}} \tag{13-10a}$$

$$J_{ss,j} = \frac{2\pi k_j h_j}{\mu B \left( \ln \frac{r_{d,j}}{r_w} + S_j \right)} \tag{13-10b}$$

The example can be termed transient SIP since each layer is infinite-acting and the pressure disturbance propagates out to different distances according to the layer permeability.

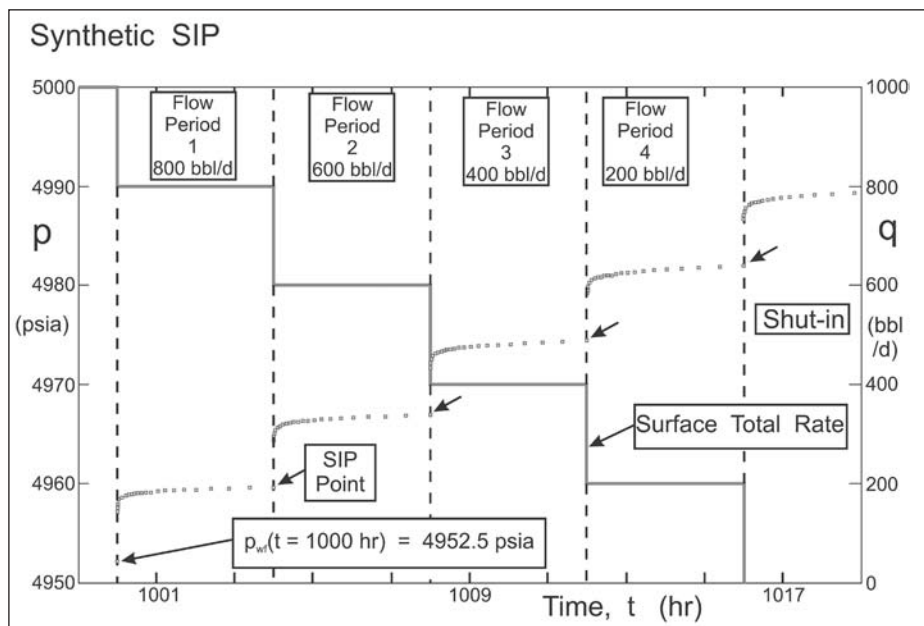
**Table 13–1a.** Parameter values for SIP simulation with decreasing rate

Layer	$h_j$ (ft)	$p_j^i$ (psia)	$k_j$ (md)	$S_j$	Common layer properties	
1	33	5,050	500	5	$r_w = 0.33$ ft	$\phi = 0.2$
2	33	5,000	300	3	$\mu = 1.0$ cp	$B_o = 1.0$
3	33	4,950	700	7	$c_t = 3.0 \times 10^{-5}$ psi <sup>-1</sup>	

**Table 13–1b.** SIP simulation results

Time (h)	$p_{wf}$ (psia)	Surface rate $q_s$ (bbl/d)	Layer 1 rate (bbl/D)	Layer 2 rate (bbl/D)	Layer 3 rate (bbl/D)
1,004	4,959.6	800	692.5	211.8	-104.3
1,008	4,966.9	600	624.1	161.8	-185.9
1,012	4,974.4	400	555.6	112.0	-267.6
1,016	4,981.9	200	487.2	62.3	-349.5

In this example, the well was flowed for 1,000 h at a constant rate of 1,000 bbl/d and then 4-h SIP flow periods were employed, and the synthetic data is plotted in figure 13–37a; the corresponding SIP plot is shown in figure 13–37b. The data appear to fall on straight lines but the slopes are too low and the layer PIs are overestimated. Correspondingly, the layer pressures are underestimated by up to 15 psi.

**Fig. 13–37a.** Synthetic field example—pressure data

When an increasing rate schedule is employed, the layer pressures are overestimated; thus the estimate of pressure is a function of flow history. These effects occur because the bottom-hole flowing pressure has not stabilized. Another field example (from the North Sea) is shown in figure 13–38, where three layers have been identified at substantially different pressures. Although straight lines have been put through the data, they are not well defined and considerable

uncertainty in the estimated pressures is present. Again the effect of nonstabilized conditions places much doubt on the SIP technique in oil wells. There is a great incentive to reduce the duration of each flow period and to carry out an SIP analysis based on transient theory. In this situation, the well is assumed to be infinite acting throughout the step rate test; the theory of this approach is treated in chapter 14 on layered well testing in *Well Test Design and Analysis*.

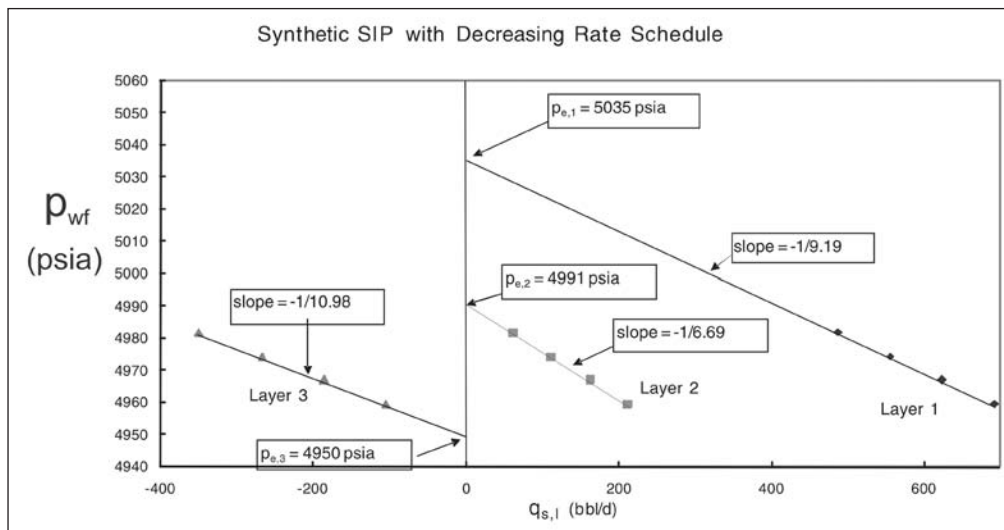


Fig. 13–37b. Synthetic field example—SIP plot

Table 13–2. Results from the interpretation of the synthetic example

Layer	Drainage radius $r_{d,j}$ (ft)	True $p_j^i$ (psia)	SIP $p_j^i$ (psia)	True $J_{ss,j}$ (bbl/d/psi)	SIP $J_{ss,j}$ (bbl/d/psi)
1	9,373	5,050	5,035	7.69	9.19
2	7,260	5,000	4,991	5.42	6.69
3	11,091	4,950	4,950	9.43	10.98

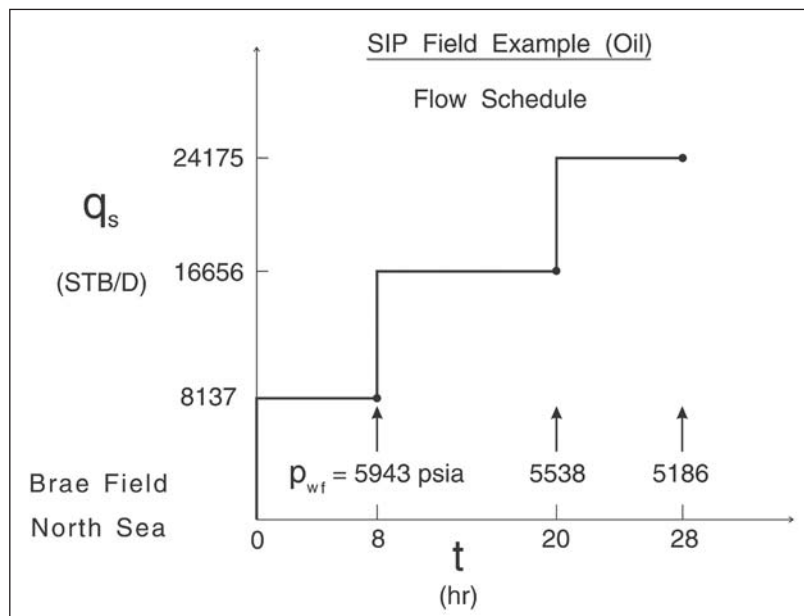


Fig. 13–38a. North sea SIP example (brae field)



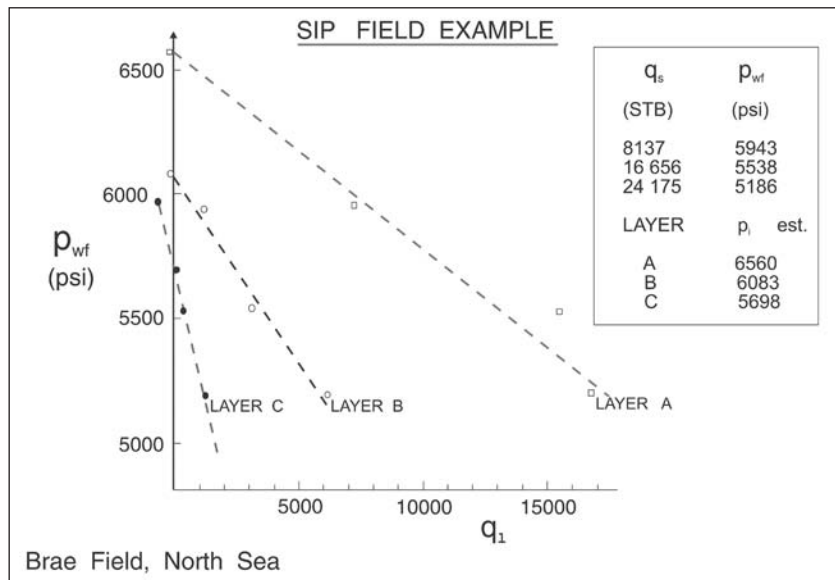


Fig. 13–38b. SIP field example (data plot)

## Gas Well Quadratic IPRs

The basic theory of the SIP procedure depends on straight line IPRs and, in the case of gas wells where non-Darcy flow is appreciable, some modification is necessary. Suppose that the individual layer IPRs, in terms of pressure, are given by equations of the form

$$\bar{p}_j - p_{wf} = A_j Q_j + B_j Q_j^2 \quad (13-11a)$$

i.e.,

$$Q_j = \frac{\sqrt{A_j^2 + 4B_j(\bar{p}_j - p_{wf})} - A_j}{2B_j} \quad j = 1, \dots, N \quad (13-11b)$$

then, for a range of assumed values of  $p_{wf}$ , the total flow can be computed from the summation

$$Q = \sum_{j=1}^N Q_j \quad (13-12)$$

Thus the composite IPR may be readily constructed; however, it does not have a quadratic form even though the underlying layer IPRs are indeed quadratic. This is illustrated in figure 13–39 for a liquid system, where a composite IPR has been compiled from the individual (quadratic) IPRs of a two-layer reservoir.

The first extensive application of the SIP technique in gas wells was carried out in the Hassi Messaoud field in Algeria, and figure 13–40 shows the plotted layer IPRs for a well labeled 3 (table 13–3).

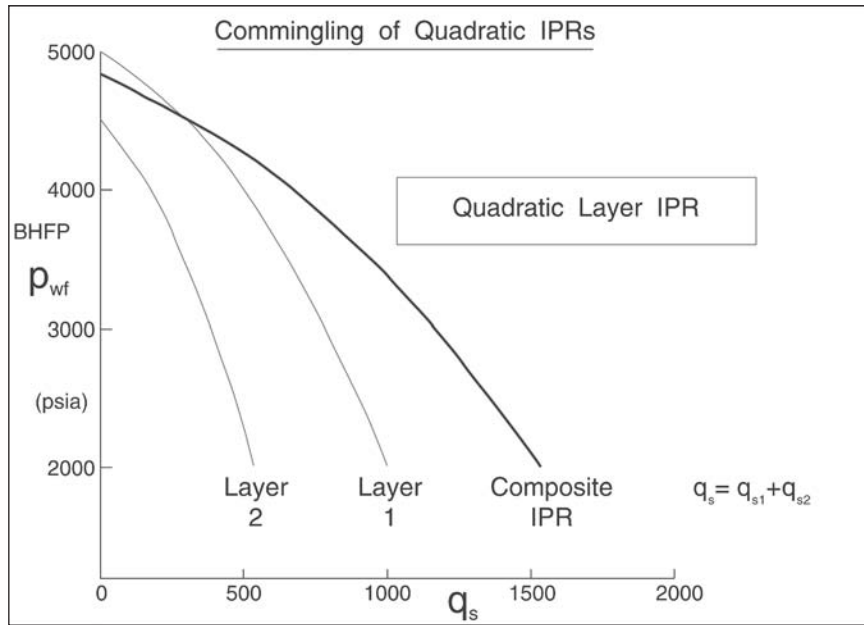


Fig. 13–39. Commingling of quadratic layer IPRs

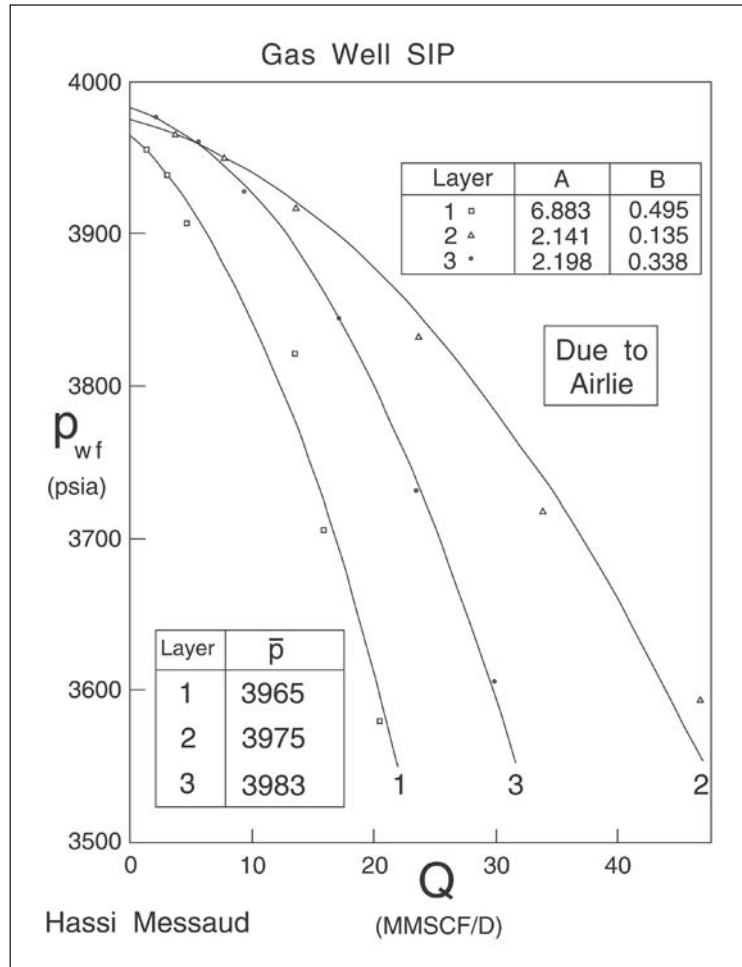


Fig. 13–40. Gas well SIP from Algeria (Hassi Messaoud)

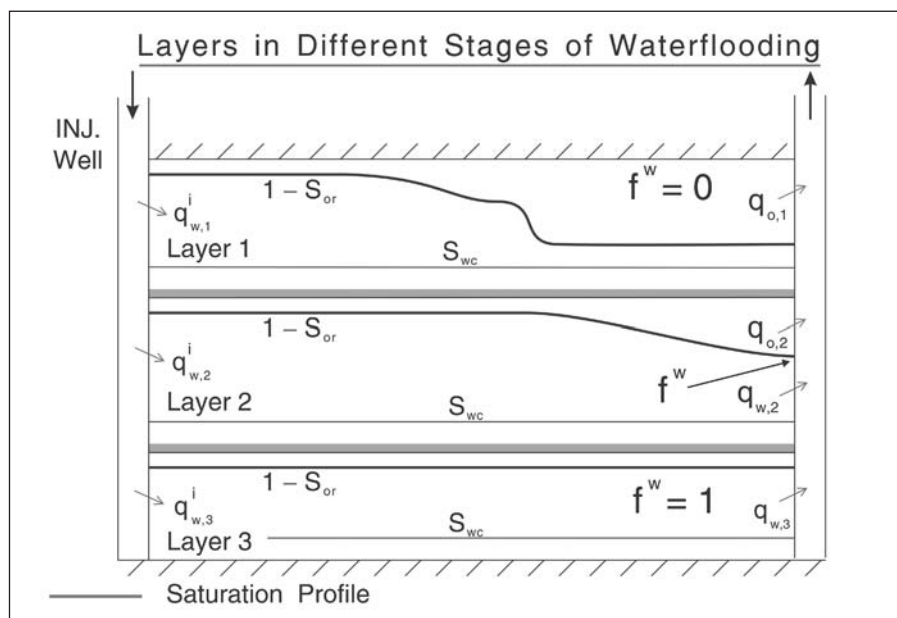
**Table 13–3.** Data for Hassi Messaud field example

Layer	h (ft)	$h_p$ (ft)		
1	57.5	33	$T = 93.8^\circ\text{C}$	$r_w = 0.35$ ft
2	65.6	59	$P_c = 648.7$ psia	$\phi = 0.2$
3	33	23	$T_c = 392^\circ\text{R}$	$\mu = 0.0245$ cp
			$\gamma = 0.787$	$c_t = 0.0002$ psi <sup>-1</sup>
			$r_e = 2,300$ ft	

The information on differential depletion and actual layer production rates was extensively used in the reservoir management of this giant gas condensate field.

## Two-Phase Flow

For water drive systems, the objectives of reservoir monitoring also include the detection of water breakthrough in the various layers and the subsequent periodic measurement of the developing water-cut. A diagrammatic representation of the waterflooding of a stratified system is shown in figure 13–41. In layer 1, the saturation front has not yet reached the producing well and only oil flows from this layer. Layer 2 has been flooded to such an extent that water breakthrough has occurred and it produces both oil and water. Layer 3 has been completely swept to waterflood residual oil saturation  $S_{or}$  and produces only water; obviously, this layer should be closed off. In a balanced system where oil production is more or less exactly tied to water injection (on an in situ basis), reservoir pressures tend to stabilize and in the history-matching of the reservoir simulator the main criterion is to correctly model the development of the water-cut on a layer-by-layer basis. The occurrence of water breakthrough in a well usually heralds the onset of production problems like scale deposition or fines migration and hence the detection of the first water production is an important event. The time to breakthrough also yields information on continuity of sands between wells and sometimes provides additional evidence of the existence of thief zones.

**Fig. 13–41.** Water flooding of a stratified system

In the two-phase situation, the interpretation of the production logs will be aimed at obtaining the water-cut (or fractional flow  $f^w$ ) of each layer. However, it must be emphasized that the resolution of the measurement is poor and the ability to accurately tie down the relative flows of oil and water from individual layers is limited. For this reason, the information from production logging is complemented by pulsed neutron capture (PNC) logging which attempts to measure saturation through casing. The assignment of the total water production of the well to individual layers may be difficult, but decisions on workover depend on knowledge of the origin of the produced water. For the present purpose, it is assumed that the water cut or fractional flow is known on a layer-by-layer basis as indicated in figure 13–41.

The stratified system illustrated in figure 13–41, with the layers separated by completely impermeable barriers, provides the opportunity to control production through dual completions and squeeze treatments. However, it is essential that the impermeable and continuous nature of the barriers has been established before such remedies are applicable. In the treatment of the two-phase production characteristics of such stratified systems, it will be assumed that no reservoir communication exists between the layers. The problem of the poor resolution of downhole flow measurement has already been mentioned in the context of single-phase conditions; in two-phase flow the difficulties increase dramatically and this imposes severe limitations on the implementation of two-phase SIP, for example.

A multilayer system is illustrated in figure 13–42, where commingled production from different zones to a common wellbore is taking place. Each individual layer  $j$  produces at its own water-cut  $f_j^w$ , which must be measured by production logging surveys and is fixed by the water advance in the separate zones. The external pressures  $p_j^e$  in the layers are also variable due to differential depletion and/or support. For the moment, attention will be confined to two-phase incompressible flow of water and oil above the bubble point where a single-layer inflow performance relation of the form

$$q_{t,j} = q_{o,j} + q_{w,j} = J_j(p_j^e - p_{wf}) \quad (13-13)$$

is applicable. The individual (downhole) phase flow rates are given by

$$q_{o,j} = (1 - f_j^w)q_{t,j} \quad q_{w,j} = f_j^w q_{t,j} \quad (13-14)$$

and the well total in situ rates are obtained by summation, i.e.,

$$q_w = \sum_{j=1}^N q_{w,j} \quad q_o = \sum_{j=1}^N q_{o,j} \quad (13-15)$$

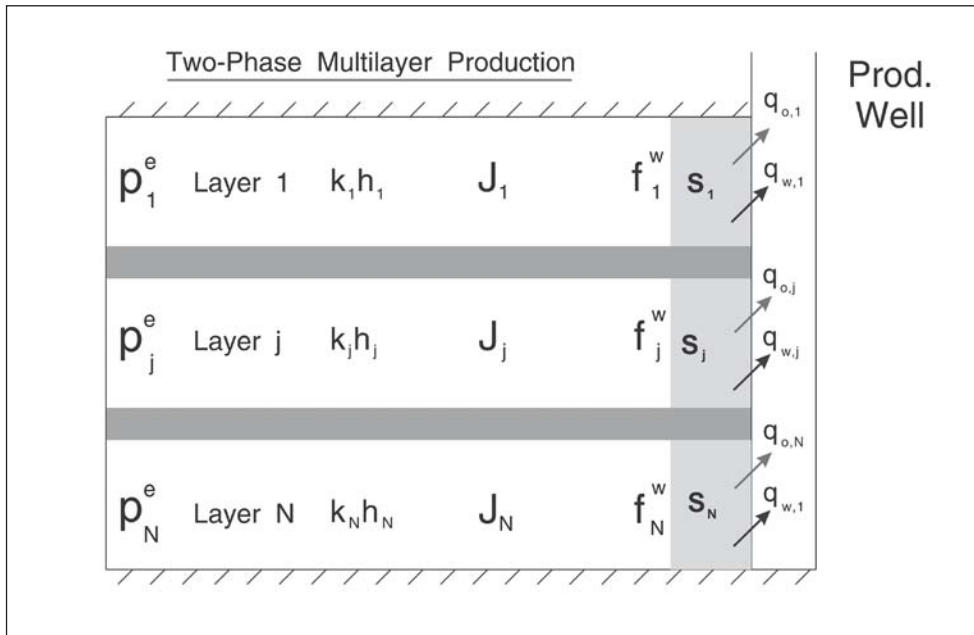


Fig. 13–42. Commingled system with layers producing at different water-cuts

The well producing water-oil ratio (WOR) then becomes

$$\text{WOR} = \frac{q_{sw}}{q_{so}} = \frac{B_o q_w}{B_w q_o} \quad (13-16)$$

The theory of two-phase incompressible flow is treated in chapter 3 on well performance, where the individual layer two-phase PI based on in situ total flow  $J_j$  was shown to be

$$J_j = \frac{2\pi k_j h_j \left( \frac{k_{ro}}{\mu_o} + \frac{k_{rw}}{\mu_w} \right)}{\left( \frac{1}{2} \ln \frac{4A}{\gamma C_A r_w^2} + S_{a,j} \right)} = \frac{2\pi k_j h_j \left( k_{ro} + \frac{k_{rw} \mu_o}{\mu_w} \right)}{\mu_o \left( \frac{1}{2} \ln \frac{4A}{\gamma C_A r_w^2} + S_{a,j} \right)} = \frac{2\pi h_j \left( \frac{k_j}{\mu} \right)_t}{\left( \frac{1}{2} \ln \frac{4A}{\gamma C_A r_w^2} + S_{a,j} \right)} \quad (13-17)$$

Note that in Eq. (13–17) the saturation  $S_w$  at which  $k_{ro}$  and  $k_{rw}$  are evaluated is different from layer to layer, i.e., it should be subscripted  $j$  since it depends on  $f_j^w$ . For the moment, it will be presumed that these layer two-phase PIs will be determined by the SIP technique (or full transient multilayer well testing) and it is only necessary at this stage to demonstrate that they may be treated as constants for well production analysis. In this commingled production model, it is also assumed that the individual layer water-cuts  $f_j^w$  are constant and not affected by rate—which may not be the case in a coning situation. However, the overall producing WOR is dependent on the bottomhole flowing pressure  $p_{wf}$  which poses a problem in trying to find the well operating point on a performance diagram.

The SIP technique can be used to determine the layer pressures, water-cuts, and PIs necessary for a full production analysis as illustrated in figure 13–43. A composite IPR based on total liquid rate is again valid where

$$q_t = J(p^* - p_{wf}) \quad (13-18)$$

with

$$J = \sum_{j=1}^N J_j \quad \text{and} \quad p^* = \frac{\sum_{j=1}^N J_j p_j^e}{J} \quad (13-19)$$

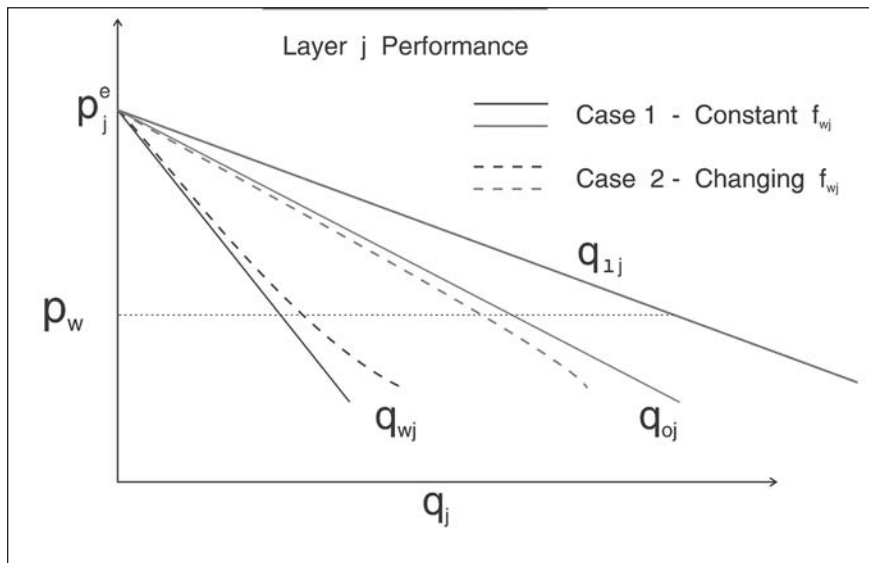


Fig. 13–43. Two-phase SIP analysis

It is also possible to derive composite IPRs for the oil and water phases as follows:

$$q_o = J_o(p_o^* - p_{wf}) \quad (13-20)$$

where

$$J_o = \sum_{j=1}^N (1 - f_j^w) J_j \quad \text{and} \quad p_o^* = \frac{\sum_{j=1}^N (1 - f_j^w) J_j p_j^e}{J_o}$$

$$q_w = J_w(p_w^* - p_{wf}) \quad (13-21)$$

where

$$J_w = \sum_{j=1}^N f_j^w J_j \quad \text{and} \quad p_w^* = \frac{\sum_{j=1}^N f_j^w J_j p_j^e}{J_w}$$

A well performance diagram showing typical composite behavior is shown in figure 13–44, where the straight line IPRs giving total liquid, total oil, and total water are plotted; this is similar in form to a two-layer system one of which produces oil and the other water. The slopes of the IPR lines are  $-1/J$ ,  $-1/J_o$ , and  $-1/J_w$ , respectively, and the intercepts are fixed by the quantities  $p^*$ ,  $p_o^*$ , and  $p_w^*$  as defined above.

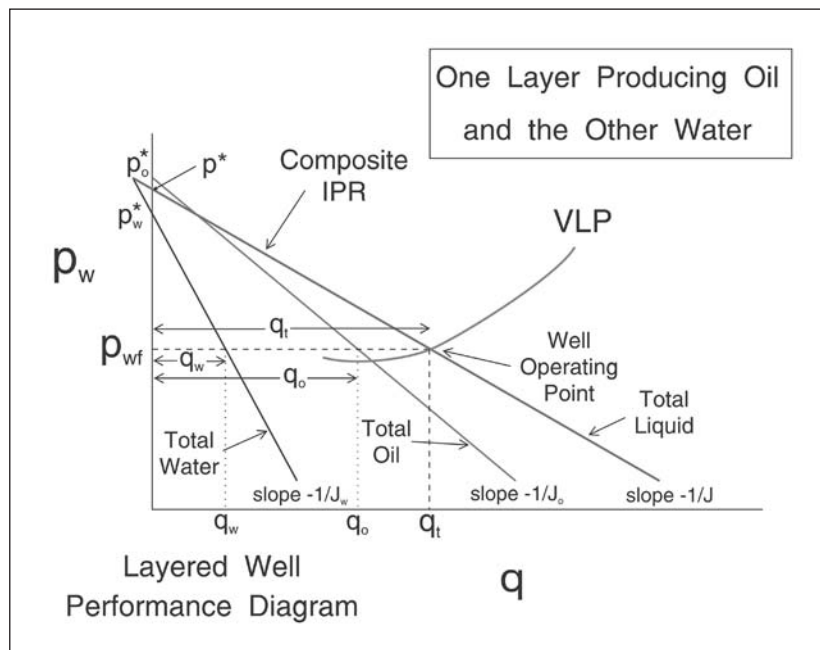


Fig. 13–44. Well performance diagram showing two-phase composites

When the layer external pressures  $p_j^e$  are different—which is generally the case—the overall water-cut denoted  $f_t^w$  and defined as

$$f_t^w = \frac{q_w}{q_w + q_o} = \frac{\sum_{j=1}^N q_{w,j}}{\sum_{j=1}^N q_{w,j} + \sum_{j=1}^N q_{o,j}} \quad (13-22)$$

depends on the well total rate  $q_t$  as illustrated in figure 13–45; this reflects the alteration in the balance of the layer contributions as the bottom-hole pressure  $p_{wf}$  changes. Thus in a two-phase well performance diagram, it is necessary to plot the total fractional flow  $f_t^w$  as a function of total liquid rate from (13–2). In order to carry out this calculation, the individual layer pressures, PIs, and fractional flows must be known. The important point is that the VLP

depends strongly on the overall water-cut and the determination of the well operating point as the intersection of the composite IPR and the VLP curve requires the appropriate function to be specified. Unfortunately, the correct value of  $f_t^w$  for the generation of the VLP relation is not known in advance and must be computed iteratively; the problem of the correct determination of the well operating point is illustrated in figure 13–46. Here the VLP curves marked upper (**u**) and lower (**l**) have been used to bracket the actual operating curve which is determined by interpolation. When the layer pressures are all equal, as illustrated in figure 13–47, the overall water-cut  $f_t^w$  is independent of total rate and the determination of the correct value does not require iteration.

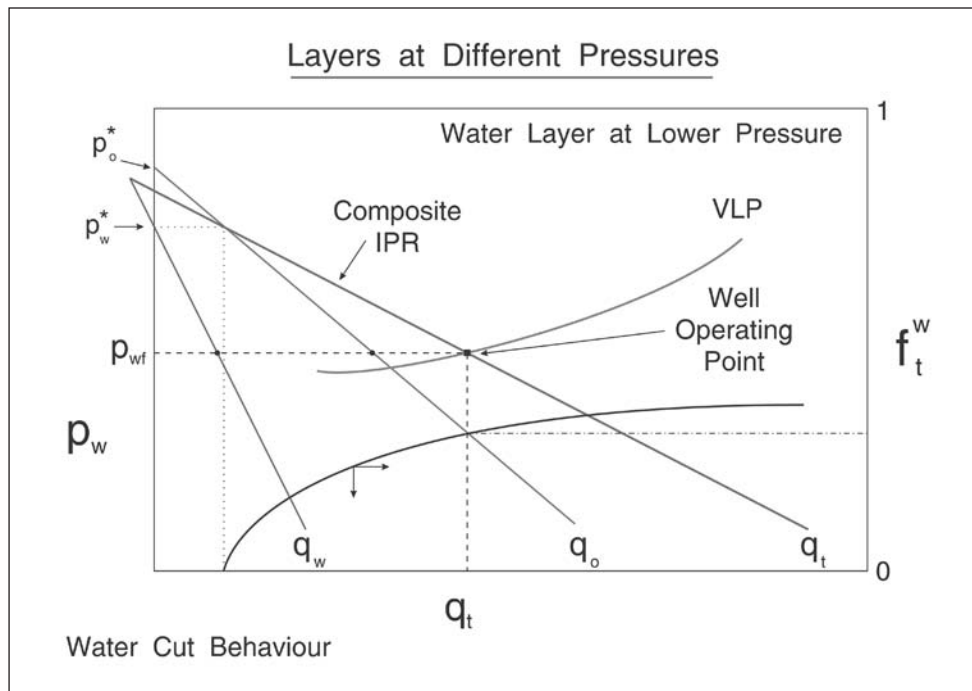


Fig. 13–45. Water-cut as a function of total rate on a well performance diagram

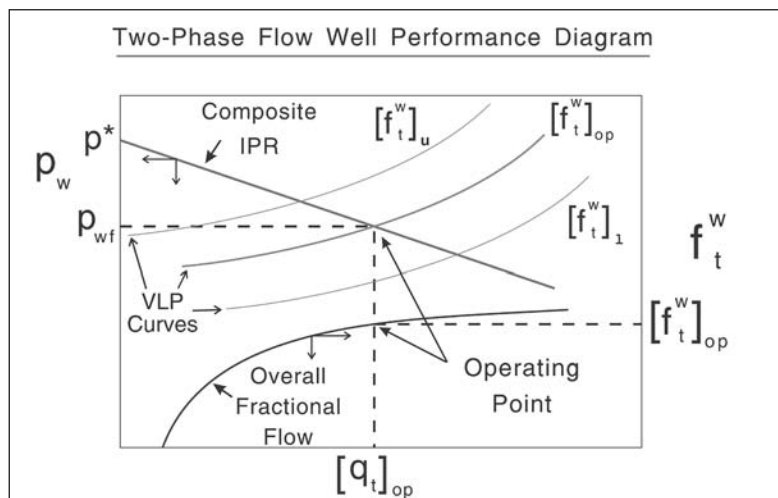


Fig. 13–46. Determination of the operating point for a well with unequal layer pressures



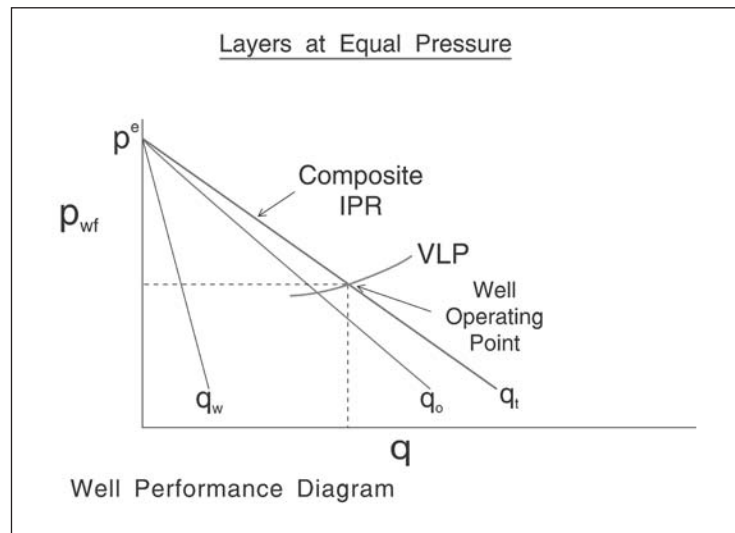


Fig. 13-47. Overall water-cut independent of total rate for equal layer pressures

The key issue in multilayer production with two-phase flow is probably the decision to workover the well and try and inhibit the water production. Recently, there have been significant advances in the technology of water shutoff and considerable improvement to well performance can be achieved. In figure 13-48, a well performance diagram is shown for a two-layer system where layer 1 is producing both oil and water with a high proportion of the latter. In addition, the pressure of layer 1,  $p_1^e$ , is high because it is well supported by the water injection. Layer 2 is at low pressure  $p_2^e$ , but is still producing oil alone, i.e.,  $f_2^w = 0$ . The composite IPR and its intersection with the appropriate VLP curve give the current well operating point marked  $q_{t|op}$  with a total oil production from the two layers of  $q_{o,1} + q_{o,2}$ . If layer 1 were to be shut off, say by a casing patch or squeeze job, the VLP curve would revert to oil alone marked  $f_t^w = 0$  on the diagram. The intersection of the layer 2 IPR line with this VLP gives an oil production  $q_{o,2|alone}$ , which is higher than the base case of both zones producing. This example demonstrates the importance of knowing the layer pressures in order to make intelligent workover decisions.

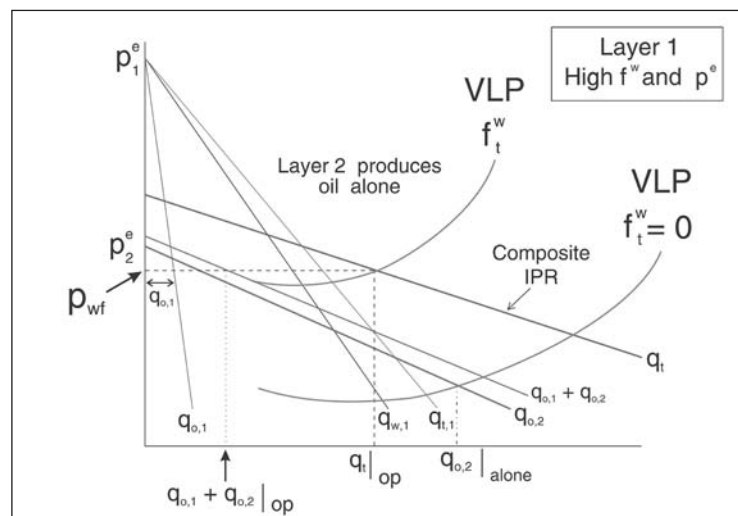


Fig. 13-48. Consequence of layer shut-off

## Integration with Transient Well Testing and Core Analysis

Considering the single-phase SIP interpretation, the slope of the straight lines is associated with the inverse of the PI of the individual layers. Thus the layer PI, i.e.,  $J_{SSS,i}$ , is given by an expression of the form

$$J_{SSS,i} = \frac{2\pi\bar{k}_i h_i}{B\mu \left( \ln \frac{r_e}{r_w} \right) - \frac{3}{4} + S_i} \tag{13-23}$$

Suppose the well has been the subject of a core analysis study and the estimates of the layer permeabilities by averaging core plug data are denoted  $\hat{k}_i$ ,  $i = 1, \dots, N$  as illustrated in figure 13-49. These estimates are in error as a result of inadequacies in the method of averaging and alteration of the core between the in situ state in the reservoir and the modified state in the laboratory. It is difficult to say which of these effects is the more important. Now presume that in addition to the SIP production logging survey in drawdown, a standard buildup has been carried out and the overall average permeability, i.e.,  $\bar{k}$ , has been determined from the semilog slope  $m$ . If the individual zone average permeabilities are written as  $\bar{k}_i$ , then for a commingled system

$$\bar{k}h = \sum_{i=1}^N \bar{k}_i h_i \tag{13-24}$$

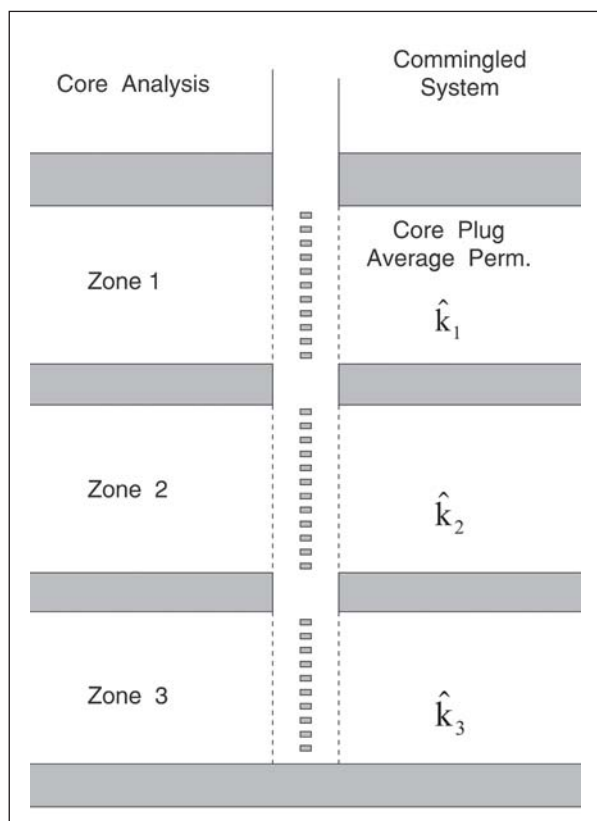


Fig. 13-49. Average zone permeabilities from core plug data

Here  $\bar{k}_i$  is the macroscopic average permeability of unit  $i$  for which  $\hat{k}_i$  is an estimate. Suppose that a common correction factor  $a$  for all units can be defined through the relation

$$\bar{k}_i = a\hat{k}_i \quad (13-25)$$

Substituting (13-25) into (13-24) gives

$$\bar{kh} = \sum_{i=1}^N a\bar{k}_i h_i \quad (13-26a)$$

i.e.,

$$a = \frac{\bar{kh}}{\sum_{i=1}^N \bar{k}_i h_i} \quad (13-26b)$$

where the quantity  $\bar{kh}$  is determined from the slope of the semilog straight line (MTR) of the buildup. Here,  $a$  is simply a normalizing factor which modifies the zone average permeabilities from core analysis to agree with the overall average from a transient well test.

If the layer productivity index,  $J_{SSS,i}$ , is known from the SIP analysis and  $\bar{k}_i$  from corrected core data, then the layer skin factor follows from (13-23). This is a very useful extension of the SIP technique since it will allow the reservoir monitoring process to track the zone pressures and skin factors which is the real objective of the whole procedure.

In figure 13-50, the core data from a well in the Piper Field is plotted on a logarithmic scale and a synthetic production log has been generated on the basis of cumulative  $kh$ , i.e., it has been assumed that skin is zero and the pressure is uniform. In this case, the flow profile simply follows the cumulative  $kh$  profile.

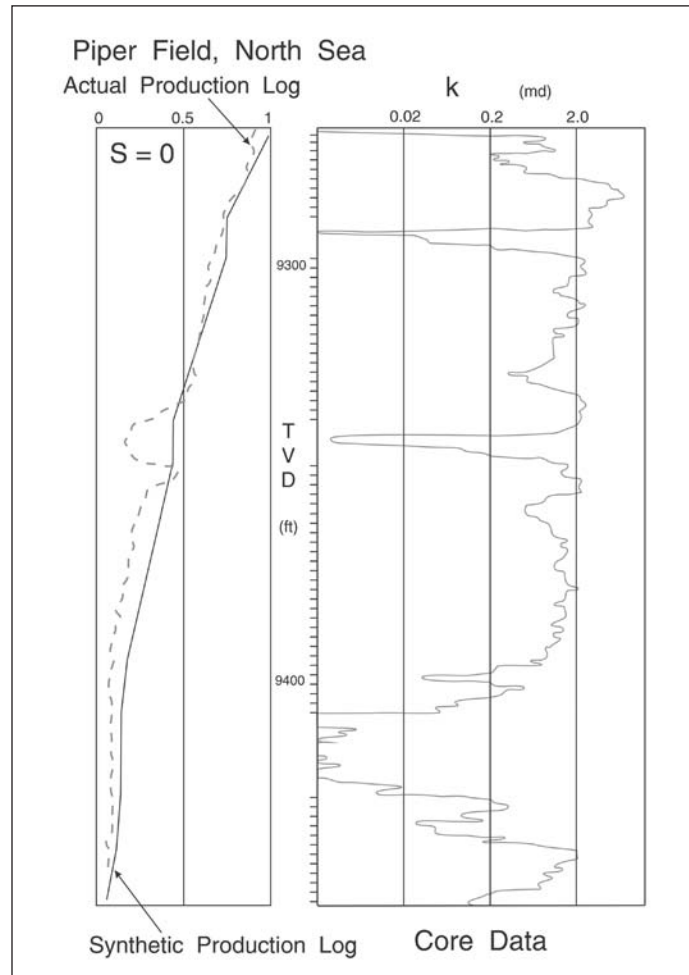


Fig. 13-50. Synthetic production log from core data

The actual production log (single phase oil flow) from the well overlays the zero-skin, uniform pressure prediction quite well and in this case there is no evidence of plugged perforations or unusual damage in particular zones. The core data here has not been normalized to a transient buildup  $kh$ . The assumption that the flow profile is a reflection of the permeability distribution is often made by geoscientists, but it must be emphasized that, in many cases, the skin and pressure distributions also influence the measured flow profile.

## Borehole Video Camera

The most recent innovation in production logging is the use of borehole video cameras to monitor the fluids coming from perforations. The development of lenses with special wettability characteristics allow such devices to be used in oil wells in addition to gas wells, where the first application was made. The video camera clearly indicates the fluids emerging from the perforations and is particularly useful in pin-pointing the zones having substantial water production. The borehole video camera is complementary to conventional production logging since it is a qualitative measurement but it holds promise with respect to maintaining production from wells in mature fields where workover strategy is crucial.

## Water Shut-off Treatments

In the situation where there is no communication between the layers (termed commingled here), there is a large incentive to block the flow emanating from a zone when its water-cut approaches 100%; this is referred to as a *water shut-off* (WSO). There are two basic approaches to blocking the flow of a water-producing layer. In the first, described as a sandface shut-off, the zone is plugged in the vicinity of the well using one of the following methods:

- Casing patch
- Coiled tubing cement squeeze
- Bridge plug or straddle packer

The latter procedure is most commonly used when it is the bottom layer that is producing water and many reservoirs are developed “bottom up” to force this situation. These sandface shut-off techniques will be effective only if the layers are not communicating in the reservoir. When reservoir communication is present, it is necessary to use the second approach to shut-off which takes the form of a deep-set polymer plug extending a large distance from the well. In practice, this latter treatment is much less successful. It is interesting to note that intelligent wells using sliding sleeves and control valves are often a form of sandface shut-off and it is necessary to establish that reservoir communication is negligible before a well can be a candidate for this technology. The subject of “smart” or “intelligent” wells will be addressed later in this chapter.

## Sandface Shutoff

The use of bridge plugs will be described in the context of a field example from a well in the Forties field in the North Sea. Figure 13–51 shows the measured production data from the well and it is apparent that there is a marked jump in the water-cut at a certain point in time (ca. July 1997). This is a change in the well behavior and spotting such anomalies is referred to as *trend*

or *exception analysis*. In this case, the production data is simply displayed on a spreadsheet plot and the step change in water cut observed manually. However, with the increasing application of SCADA systems and databases, software is being developed that will automatically detect such exceptions and post a warning to the production engineer. The question now arises as to where the water is entering the wellbore, and the solution lies in running a production log as shown in figure 13–52; in this case it is evident that the water is entering at the base of the formation and a shutoff requires only a bridge plug. This reservoir has bottom water drive (augmented with water injection) and it was likely that this would be the case. The result of the workover was an incremental oil production of 1.75 Mbbl/d which justified the \$47,000 for the production log and the \$71,000 for plugs. In discounted cash flow economics, typically the economic value of accelerated production is one fifth of the oil price. Even with this discounting the workover pays for itself in about 10 days! It would have been interesting to know what the prediction for the increase in well rate was from a run of the well modeling software before the job was carried out. Reducing the WOR improves the vertical lift performance since the density of the flowing mixture is reduced, allowing the well to flow with a reduced bottom-hole flowing pressure.

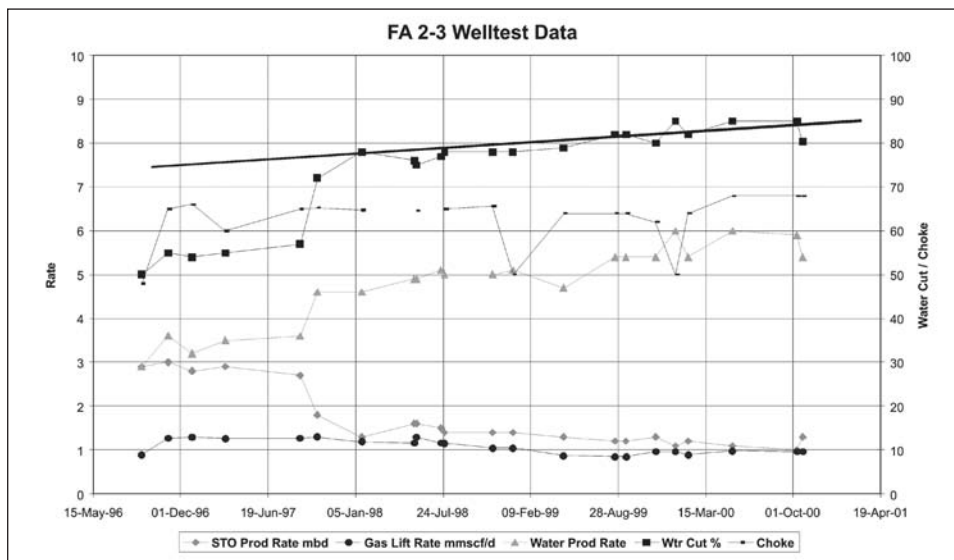


Fig. 13–51. Trend analysis and diagnosis

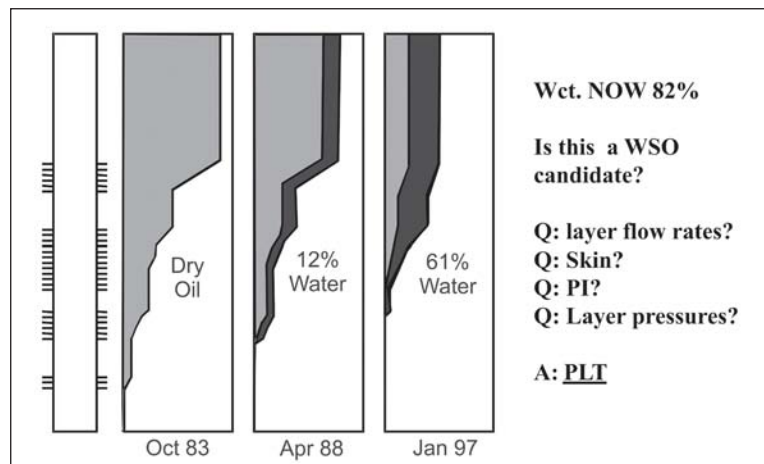


Fig. 13–52. Benefit of production logging

# 14

## Compartmentalized Material Balance

---

### Introduction

In the classic theory of well testing, the concept of semi-steady-state (SSS) depletion of an isolated fault block or reservoir unit is well known and forms the basis of reservoir limit testing. The idea of SSS depletion is usually discussed in terms of a single-well reservoir—the famous well in the center of a closed circle—or a multiple well system through the concept of drainage areas as proposed by Dietz. The essence of the extended drawdown test is simply that the average pressure of the system declines according to the elementary material balance expression

$$c_t V \frac{d\bar{p}}{dt} = -q^p = -q_s^p B_o \quad (14-1)$$

where

- $c_t$  = total compressibility,
- $V$  = connected pore volume,
- $q^p$  = total production rate at reservoir conditions,
- $q_s^p$  = total production rate at surface (standard) conditions, and
- $B_o$  = oil formation volume factor.

A Cartesian plot of reservoir average pressure  $\bar{p}$  versus time  $t$  will give a straight line of slope  $m^* = -q^p/(c_t V)$  if the rate is constant. The time taken to reach the SSS condition, at which the flowing bottom-hole pressure differs by a fixed amount from the material balance average pressure, depends on the size and shape of the drainage area and the well location within it. Tables of values of  $(t_{DA})_{SSS}$  are given for different geometrical configurations. At the SSS the flowing bottom-hole pressure follows the average pressure, as illustrated in figure 14–1, and measurement of  $dp_{wf}/dt$  is equivalent to measuring  $d\bar{p}/dt$ . If measured data are obtained in the transient period, the actual flowing bottom-hole pressure  $p_{wf}$  has to be transformed to the corrected value  $p_{wf}^{corr}$  which corresponds to SSS behavior. An approximate deconvolution algorithm for carrying out such a transformation is described in chapter 5 of *Well Test Design and Analysis* on variable rate analysis; when measured well flowing pressures are used for matching in the parameter estimation mode, it will be assumed that corrected values have been obtained. It is important to appreciate that the material balance equations predict only bottom-hole pressure at SSS conditions corresponding to  $p_{wf}^{corr}$  on figure 14–1.

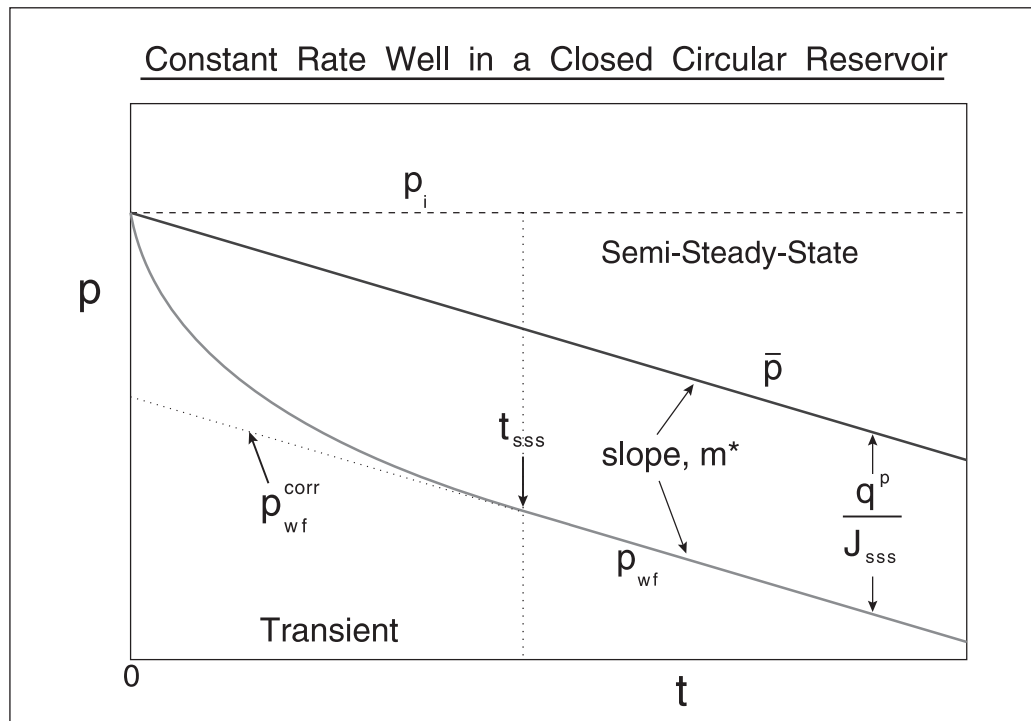


Fig. 14–1. Transient and semi-steady-state well bottom-hole flowing pressure

The application of conventional reservoir limit test theory to real situations is rarely feasible. For example, it is very difficult to keep the rate constant over an extended flow period, and variable rate methods of analysis have to be employed. More importantly, reservoirs are much more complicated in structure than the homogeneous, perfectly closed model implied by classic theory.

The elementary material balance expression (14–1) is essentially based on single-phase conditions. Although the total system compressibility  $c_t$  allows for the presence of more than one phase, e.g., oil and connate water or trapped gas, the assumption of a constant  $c_t$  implies no saturation change within the system. Note that, when  $c_t$  is taken to be constant, the material balance equation becomes linear; this is a very important property which allows an elegant treatment of the material balance. A linearized material balance equation for depletion modeling is companion to the linearized diffusivity equation used to describe transient flow. In many reservoir situations, particularly when the pressure is above the bubble point, the assumption of constant compressibility is quite valid.

Equation (14–1) is an ordinary differential equation in which the well rate  $q^p$  in general is a time-dependent function. The differential volumetric balance (14–1) may be simply integrated from  $t = 0$  to  $t = T$  when the compressibility–volume product is constant, i.e.,

$$c_t V(p_i - \bar{p}) = \int_0^T q^p dt = N_p B_o \quad (14-2)$$



where  $N_p$  is the volumetric cumulative production at standard (stock tank) conditions. The classical Schilthuis volumetric balance equation is based on this integral formulation. Note that solving the differential equation (14–1) by a numerical method (when the rate  $q^p$  is time dependent) is exactly equivalent to the formulation (14–2). In the method suggested here, the explicit time dependence of pressures is modeled by numerical forward integration of differential equations for cellular (compartmentalized) systems. This approach satisfies the mass or volume balance in integral form, and history-matching of such a model is analogous to the classical formulation of the material balance. In a modern framework, sophisticated nonlinear regression techniques (giving error bounds) are used to identify model parameter values and obtain estimates of oil-in-place (OIP) and water influx, for example. Results obtained as functions of real time can always be displayed in terms of cumulative production in order to maintain parity with conventional methods; this aspect is developed later. The differential form of the material balance emphasizes the relation between material balance, i.e., depletion, and transient well test analysis, particularly extended drawdown testing where some form of SSS has been attained.

The development of reservoir pressure monitoring using wireline formation testers (WFTs) showed significant pressure variation over real reservoirs both in the areal and vertical sense. These variations in pressure over a producing field are due to differential depletion of the system, and it became apparent that major pressure discontinuities were due to permeability barriers of one kind or another. Near horizontal barriers—such as shales or micaceous intervals—were associated with tight zones of sedimentary origin in clastic systems. Near-vertical barriers are often associated with fault planes and the partially communicating fault has been modeled by a continuous barrier of low permeability and negligible capacity. Single-phase flow through such a barrier is described by an equation of the form

$$q = \left( \frac{kA}{l\mu} \right)_b \Delta p = T_b \Delta p \quad (14-3)$$

where  $T_b$  = transmissibility index of the barrier,  
 $\Delta p$  = pressure difference over the barrier, and  
 $q$  = flow through barrier (in situ, i.e., reservoir, conditions).

In this approach, communication by way of windows in completely impermeable zones is modeled by a continuous barrier of low, but finite, permeability. The effective permeability, thickness, and area of the tight region are all lumped into the barrier transmissibility index  $T_b$ .

Thus, direct monitoring of reservoir pressure during depletion using WFTs has shown that many reservoirs are essentially compartmentalized into cells or blocks separated by no-flow or semipermeable barriers of the type just described. The pressure within individual cells is approximately uniform, with major pressure discontinuities occurring over cell interfaces. In this situation, the well-known lumped parameter approach to modeling behavior is appropriate, in which the reservoir is regarded as a connected system of tanks with essentially uniform conditions pertaining within each one. Input and output to or from individual cells is either due to flow across juxtaposed boundaries via semipermeable barriers or by well production or injection. A linear material balance equation incorporating these terms will be written for each cell; the ensemble of equations will be referred to as the *complex material balance*.



The idea of a compartmentalized reservoir arose essentially from systems of partially communicating fault blocks as illustrated in figure 14–2. In this case, the origin of compartmentalization is tectonic. However, other sedimentary environments give rise to similar systems. For example, a sequence of stacked channel sands from a fluvial deposition shows individual sand bodies demarcated by shales but with the possibility of some communication between adjacent units. Similarly, aeolian environments lead to individual sand bodies (dunes) each completely surrounded by a low-permeability envelope. Thus, the concept of a compartmentalized reservoir is of general interest and the behavior of such systems is worthy of investigation. Note that the compartmentalized reservoir—where the rectangular network is composed of zero or very low permeability planar regions—is the exact inverse of the familiar dual porosity system involving high permeability natural fractures.

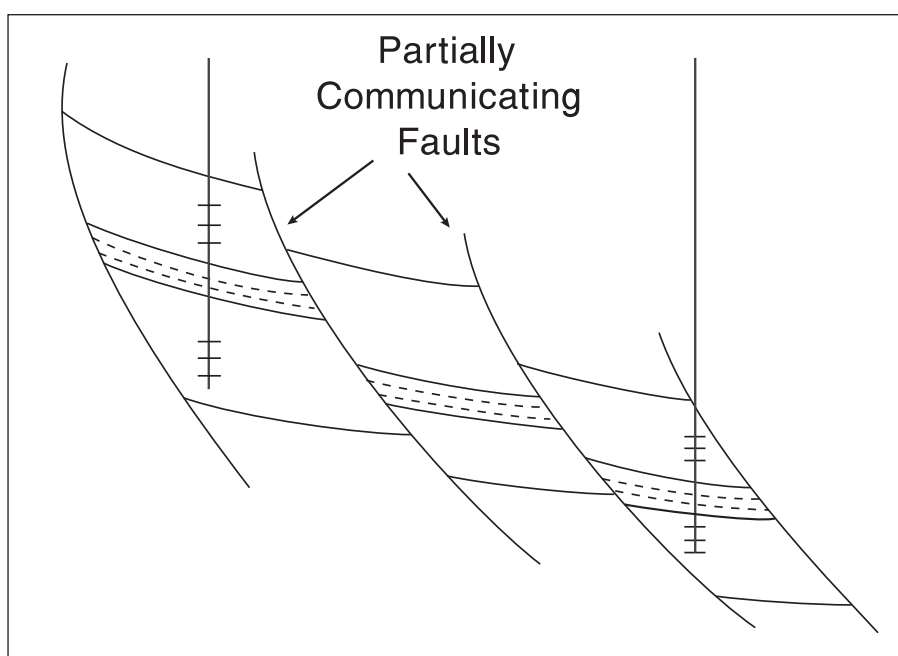
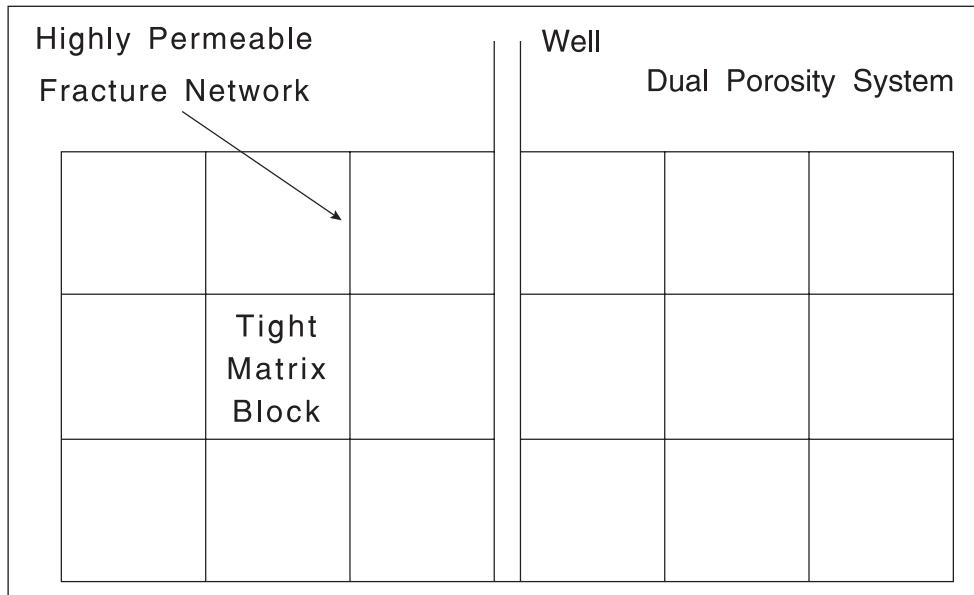


Fig. 14–2. Compartmentalized reservoir

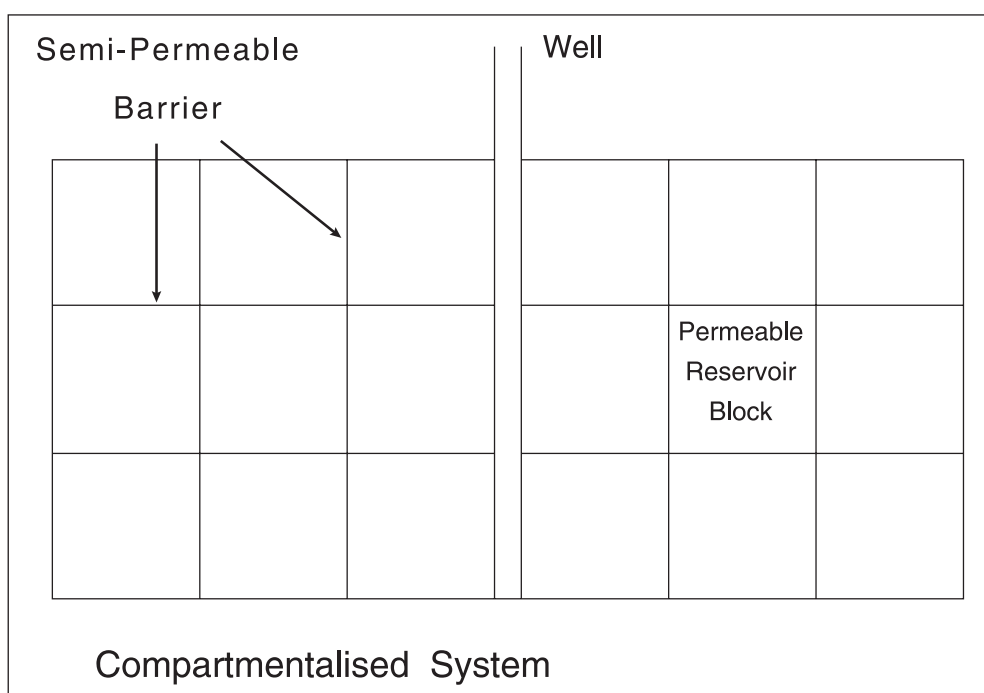
The material balance approach is limited, of course, to the examination of the long-term pressure response of the produced reservoir. It cannot model saturation changes for which a full reservoir simulation is necessary. Nor can the lumped parameter material balance handle the very early time transient pressure response of a well in the infinite-acting period before boundary effects are manifested. However, complex material balance modeling of pressure depletion, particularly in the early life of a field, can be of great value in delineating macroscopic reservoir structure. Identification of the major compartments and the degree of connection between them by pressure depletion analysis is a precursor to detailed reservoir simulation. The complex material balance was developed as a device for the interpretation of WFT pressure data in conjunction with production logging data on the flow profile in producing and injecting wells.

The literature of reservoir engineering and transient well testing has many references to naturally fractured (dual porosity) systems in which a network of permeable fractures are fed from tight matrix blocks as illustrated in figure 14–3; this is the well-known “sugar cube” model

of a fractured reservoir due to Warren and Root.<sup>1</sup> However, many reservoirs comprise blocks of high permeability separated by a network of semipermeable or impermeable barriers as indicated diagrammatically in figure 14–4—the compartmentalized reservoir discussed here. There are very few papers on this topic and the treatment given here is an attempt to redress the imbalance. The original ideas on compartmentalized systems were much influenced by discussions at various times with Lee Yaxley of Shell who was working on the Cormorant field and with Terry Beardall and Matt Fox of Conoco studying the behavior of the Murchison south flank.



**Fig. 14–3.** Warren and Root 'sugar cube' model of a naturally fractured reservoir



**Fig. 14–4.** Cubic compartmentalized reservoir

## Complex Reservoirs

In order to develop the complex material balance based on the concept of a compartmentalized reservoir, it is necessary to devise an efficient method of specifying the structure of such a system. The layered fault block reservoir shown in figure 14–5 comprising six interconnected units can be represented by the block diagram of figure 14–5, where the cells have been numbered from 1 to 6 and the possible connections between them indicated by arrows. In this example, the horizontal barrier is assumed to be impermeable and only linkages over fault planes—five in number—have been allowed. The system dimensions are given by

$NC = 6$     the number of cells,  
 $NL = 5$     the number of connections,  
 and         $NW = 2$     the number of wells.

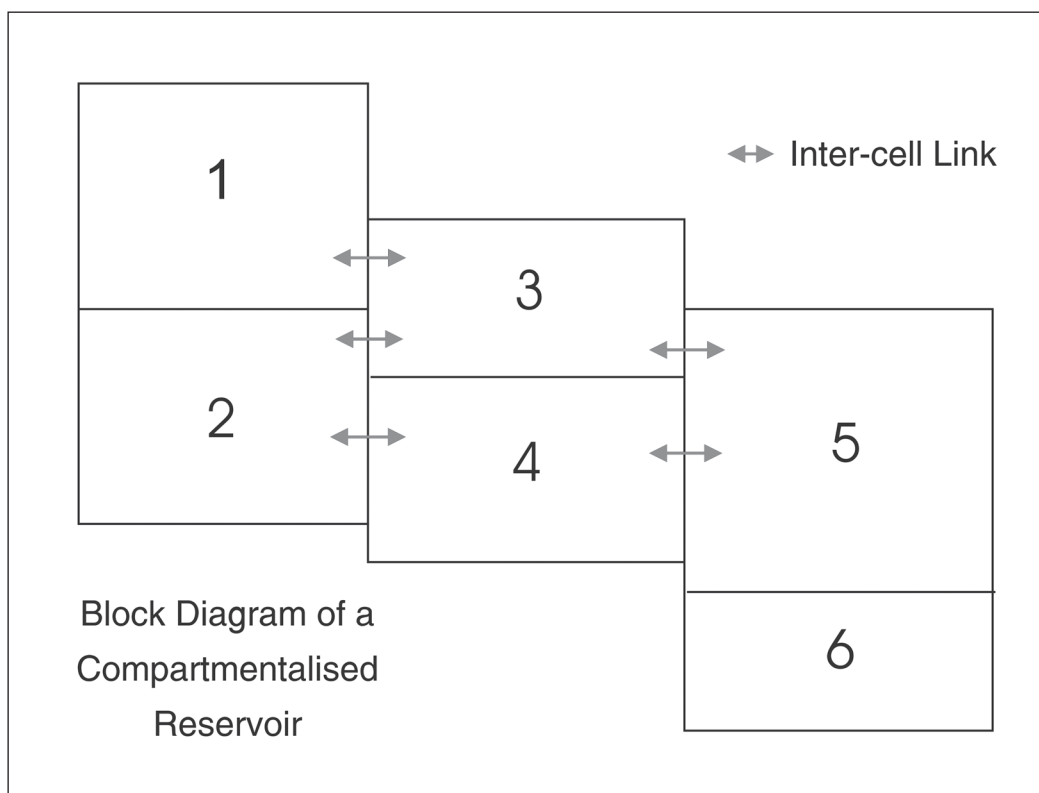


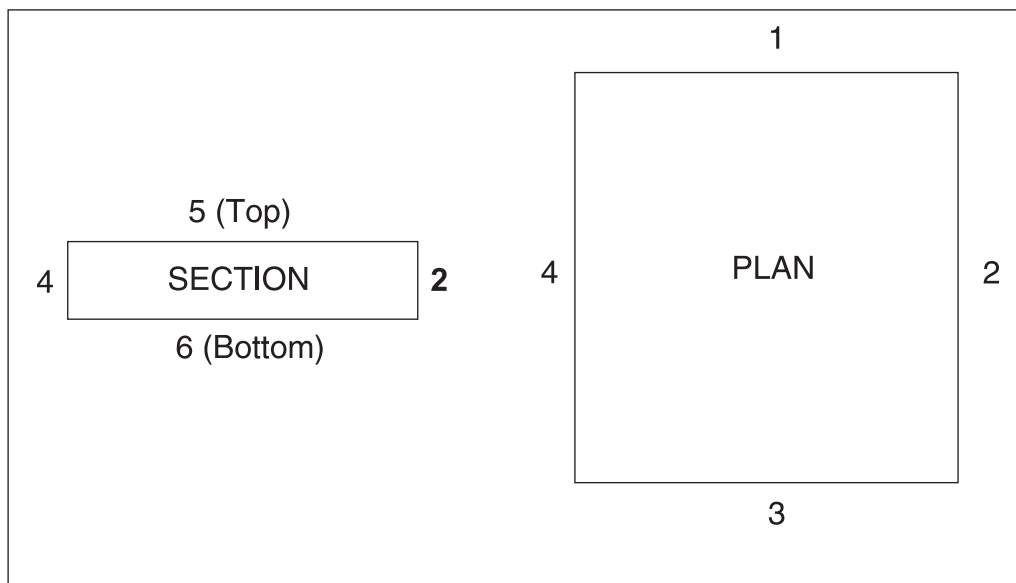
Fig. 14–5. Block diagram of a compartmentalized reservoir

It is now necessary to specify numerically how the various cells are connected. This problem has been much studied in relation to electrical networks and process flowsheets in chemical engineering. The usual approach is to define an integer connection or linkage matrix whose elements define the structure of the system. In the context of a complex reservoir, the compartments are assumed to be approximately rectangular in shape with each cell having six faces. These faces are labeled in a logical fashion as shown in figure 14–6; the four vertical faces are numbered clockwise from 1 to 4 and the top and bottom are denoted 5 and 6, respectively. A cell geometry corresponding to a rectangular parallelepiped is very convenient for setting up

three dimensional block systems and this cell geometry corresponds quite well to reality since most reservoirs have a small vertical dimension relative to areal extent. The integer cell linkage matrix ICLM has one row for each connection in which the cell and face number of the two connecting faces are identified. Thus, the cell linkage matrix has dimensions of ICLM (NL, 4) and it takes the form provided on table 14–1.

**Table 14–1.** Cell linkage matrix ICLM

	Cell	Face	Cell	Face
Link 1	1	2	3	4
Link 2	2	2	3	4
Link 3	2	2	4	4



**Fig. 14–6.** Cell face ordering scheme

This particular cell linkage matrix corresponds to the four-compartment, three-connection, one-well system shown in figure 14–7; thus  $NC = 4$ ,  $NL = 3$ , and  $NW = 1$ . The linkage matrix contains nonzero integer elements from which the structure of the block system can be deduced. This is a very convenient way of setting up quite complicated systems of interacting compartments. In addition to specifying the connections between blocks, it is also necessary to identify the connections to wells; this is done through the well linkage matrix IWLM. As shown in figure 14–7, a given well may intersect more than one block. This information is encoded in IWLM, which has one row for each well. The first element in a row is the number of blocks that the well intersects. This is followed by the cell numbers of these blocks. Again, for the example of figure 14–7, the well linkage matrix is as in table 14–2.

**Table 14–2.** Well linkage matrix IWLM

Well 1	2	1	2
--------	---	---	---

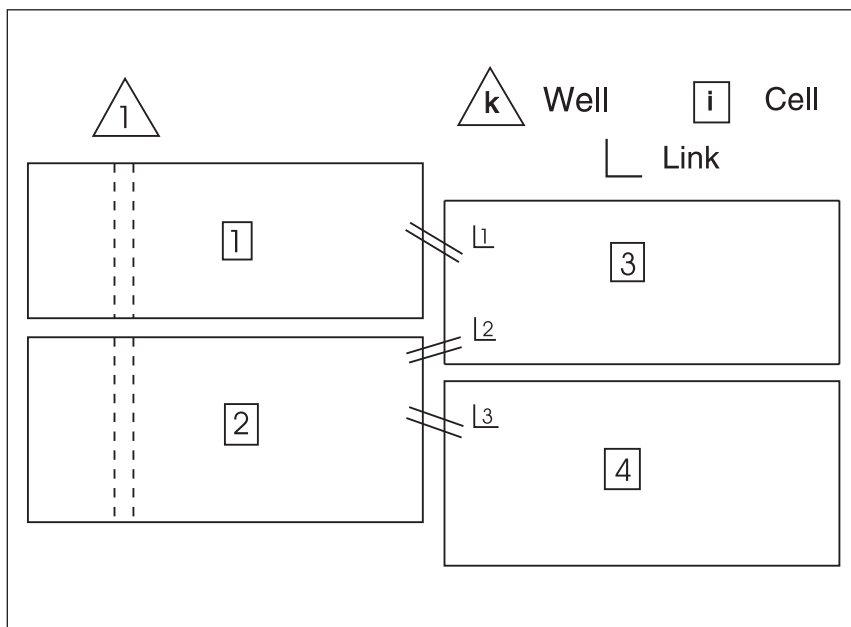


Fig. 14-7. Prototype four cell system

Once an intercell connection has been identified from cell  $i$  to cell  $j$  via the cell linkage matrix, the magnitude of the instantaneous flow across the interface is given by the equation

$$q_{i,j} = T_{i,j}(\bar{p}_j - \bar{p}_i) \tag{14-4}$$

where  $\bar{p}_i$  = cell  $i$  average pressure,  
 $\bar{p}_j$  = cell  $j$  average pressure,  
 $T_{i,j}$  = transmissibility index of the link  $i$ - $j$ ,  
 and  $q_{i,j}$  = interblock flow from cell  $j$  to cell  $i$ .

The units of the transmissibility as defined here are the same as those of a well productivity index  $J$ . Some authors have called the quantity  $T_{i,j}$  the interblock productivity index (PI). Note that Eq. (14-4) is time-dependent and  $q_{i,j}$  varies as the cell pressures change. Equation (14-4) presumes a linear relation between interblock flow  $q_{i,j}$  and the instantaneous pressure differential  $\bar{p}_j - \bar{p}_i$ .

Referring to the system of cells illustrated in figure 14-7, the lumped parameter material balance equations may be written as

$$\begin{aligned} \text{cell 1:} \quad & (c_t V)_1 \frac{d\bar{p}_1}{dt} = T_{1,3}(\bar{p}_3 - \bar{p}_1) - q_{1,1}^p \\ \text{cell 2:} \quad & (c_t V)_2 \frac{d\bar{p}_2}{dt} = T_{2,3}(\bar{p}_3 - \bar{p}_2) + T_{2,4}(\bar{p}_4 - \bar{p}_2) - q_{1,2}^p \end{aligned}$$

$$\text{cell 3:} \quad (c_t V)_3 \frac{d\bar{p}_3}{dt} = T_{1,3} (\bar{p}_1 - \bar{p}_3) + T_{2,3} (\bar{p}_2 - \bar{p}_3)$$

$$\text{and cell 4:} \quad (c_t V)_4 \frac{d\bar{p}_4}{dt} = T_{2,4} (\bar{p}_2 - \bar{p}_4) \quad (14-5)$$

This represents four simultaneous equations for the four cell pressures  $\bar{p}_1$ ,  $\bar{p}_2$ ,  $\bar{p}_3$ , and  $\bar{p}_4$ . The key parameters in these equations are as follows:

- the cell pore volumes  $V_1$ ,  $V_2$ ,  $V_3$ , and  $V_4$ ;
- the interblock transmissibilities  $T_{1,3}$ ,  $T_{2,3}$ , and  $T_{2,4}$ ;
- the cell total compressibilities  $(c_t)_1$ ,  $(c_t)_2$ ,  $(c_t)_3$ , and  $(c_t)_4$ .

As previously mentioned, these cell material balances are linearized by assuming that the total compressibilities  $c_t$  and interblock transmissibilities  $T_{ij}$  are constant. Thus, the model is appropriate to liquid systems above the bubble point and it neglects saturation changes. The terms  $q_{1,1}^p$  and  $q_{1,2}^p$  represent the production into well 1 from blocks 1 and 2, respectively, on an in situ basis. It is convenient to introduce a simplified commingled well inflow model of the form

$$q_{1,1}^p = J_{1,1} (\bar{p}_1 - \bar{p}_{1,w}) \quad (14-6a)$$

$$q_{1,2}^p = J_{1,2} (\bar{p}_2 - \bar{p}_{1,w}) \quad (14-6b)$$

$$\text{and} \quad q_1^p = q_{1,1}^p + q_{1,2}^p \quad (14-6c)$$

where  $p_{1,w}$  = well 1 bottom-hole flowing pressure,  
 $J_{1,1}$  = well 1 productivity index into cell 1,  
 $J_{1,2}$  = well 1 productivity index into cell 2,  
and  $q_1^p$  = well total rate.

Note that the PIs  $J_{k,i}$  are defined here in terms of in situ flow rates. Eliminating the common wellbore pressure  $p_{1,w}$  from Eq. (14-6a, b, and c) yields

$$q_{1,1}^p = \frac{J_{1,1}}{J_{1,1} + J_{1,2}} \left( q_1^p + J_{1,2} (\bar{p}_1 - \bar{p}_2) \right) \quad (14-7a)$$

$$\text{and} \quad q_{1,2}^p = \frac{J_{1,2}}{J_{1,1} + J_{1,2}} \left( q_1^p + J_{1,1} (\bar{p}_2 - \bar{p}_1) \right) \quad (14-7b)$$

Here the block well rates  $q_{1,1}^p$  and  $q_{1,2}^p$  have been related to the well total rate  $q_1^p$  and the cell pressures through the individual well cell PIs  $J_{1,1}$  and  $J_{1,2}$  which are also taken as constant. This is the conventional well model for the apportionment of the total flow between blocks penetrated by the well. The material balance equations now take the following form

$$\begin{aligned}
 (c_t V)_1 \frac{d\bar{p}_1}{dt} &= T_{1,3} (\bar{p}_3 - \bar{p}_1) - \frac{J_{1,1} J_{1,2}}{J_{1,1} + J_{1,2}} (\bar{p}_1 - \bar{p}_2) - \frac{J_{1,1}}{J_{1,1} + J_{1,2}} q_1^p \\
 (c_t V)_2 \frac{d\bar{p}_2}{dt} &= T_{2,3} (\bar{p}_3 - \bar{p}_2) + T_{2,4} (\bar{p}_4 - \bar{p}_2) - \frac{J_{1,1} J_{1,2}}{J_{1,1} + J_{1,2}} (\bar{p}_2 - \bar{p}_1) \\
 &\quad - \frac{J_{1,2}}{J_{1,1} + J_{1,2}} q_1^p \\
 (c_t V)_3 \frac{d\bar{p}_3}{dt} &= T_{1,3} (\bar{p}_1 - \bar{p}_3) + T_{2,3} (\bar{p}_2 - \bar{p}_3) \\
 (c_t V)_4 \frac{d\bar{p}_4}{dt} &= T_{2,4} (\bar{p}_2 - \bar{p}_4)
 \end{aligned} \tag{14-8}$$

Collecting terms, Eq. (14-8) may be written as

$$\begin{aligned}
 (c_t V)_1 \frac{d\bar{p}_1}{dt} &= \left( -T_{1,3} - \frac{J_{1,1} J_{1,2}}{J_{1,1} + J_{1,2}} \right) \bar{p}_1 + \frac{J_{1,1} J_{1,2}}{J_{1,1} + J_{1,2}} \bar{p}_2 + T_{1,3} \bar{p}_3 \\
 &\quad - \frac{J_{1,1}}{J_{1,1} + J_{1,2}} q_1^p \\
 (c_t V)_2 \frac{d\bar{p}_2}{dt} &= \frac{J_{1,1} J_{1,2}}{J_{1,1} + J_{1,2}} \bar{p}_1 + \left( -T_{2,3} - T_{2,4} - \frac{J_{1,1} J_{1,2}}{J_{1,1} + J_{1,2}} \right) \bar{p}_2 + T_{2,3} \bar{p}_3 \\
 &\quad + T_{2,4} \bar{p}_4 + \left( -\frac{J_{1,2}}{J_{1,1} + J_{1,2}} \right) q_1^p \\
 (c_t V)_3 \frac{d\bar{p}_3}{dt} &= T_{1,3} \bar{p}_1 + T_{2,3} \bar{p}_2 + (-T_{1,3} - T_{2,3}) \bar{p}_3 \\
 (c_t V)_4 \frac{d\bar{p}_4}{dt} &= T_{2,4} \bar{p}_2 + (-T_{2,4}) \bar{p}_4
 \end{aligned} \tag{14-9}$$

Thus, the complex material balance takes the form of a set of linear simultaneous ordinary differential equations (ODEs) in the cell pressures. The interaction between the equations occurs because of cell and well connections. The form of these equations depends on the structure of the system as defined in the cell and well linkage matrices. The coefficients of pressure in the linear differential system are constants (time-invariant). In general, the objective of the material balance is to adjust the parameters of the model (cell volumes and interblock transmissibilities in particular) until the predicted response obtained by the solution of (14–9) matches field measurements, i.e., parameter estimation will be achieved by history matching.

## Oil field units

In terms of the oilfield units defined in table 14–3, the liquid material balance equations take the form

$$\frac{d\bar{p}_i}{dt} = \frac{5.61458}{c_t V} \left( T_{i,j} (\bar{p}_j - \bar{p}_i) - q_s B_o \right) \quad (14-10)$$

**Table 14–3.** Definition of oil field units

$p$ : psi	$t$ : day	$V$ : ft <sup>3</sup>
$c_t$ : psi <sup>-1</sup>	$T$ : bbl/d/psi	$q_s$ : bbl/d

## General form of the commingled well model

In the general case, the commingled model for well  $k$  having  $NC$  connections takes the form

$$q_{k,i}^p = J_{k,i} (\bar{p}_i - p_{k,w}) \quad (14-11)$$

and

$$\sum_{i=1}^{NC} q_{k,i}^p = q_k^p \quad (14-12)$$

where the summation is taken over the cells linking to well  $k$ . The total well rate is given by the familiar commingled flow expression

$$q_k^p = J_k^* (p^* - p_{k,w}) \quad (14-13)$$



where

$$J_k^* = \sum_{i=1}^{NC} J_{k,i} \quad \text{and} \quad p^* = \frac{\sum_{i=1}^{NC} J_{k,i} \bar{p}_i}{J_k^*}$$

Equation (14–13) can be solved for  $p_{k,w}$  giving

$$p_{k,w} = p^* - \frac{q_k^p}{J_k^*} \tag{14-14}$$

and hence the general formula for the individual well cell rates takes the form

$$q_{k,i}^p = J_{k,i} \left( \bar{p}_i - p^* + \frac{q_k^p}{J_k^*} \right) \tag{14-15}$$

Note that equation (14–20) below can be used to compute the well bottom-hole flowing pressure at any time step once the cell average pressures have been computed by the integration algorithm. During a period of well shutin, i.e.,  $q_k^p = 0$ , the model will, of course, allow cross flow through the wellbore with the individual layer rates  $q_{k,i}^p$  positive or negative but summing to zero. In a simulation, it is therefore important to distinguish between a shut-in well with cross flow between perforated layers and a well which is totally inactive, i.e.,

$$q_{k,i}^p = 0 \quad i = 1, \dots, NC \tag{14-16}$$

If wells are drilled at different times, the no-flow condition for all layers (14–16) must be implemented up until the point that the well is completed. The starting times of the wells should be clearly indicated and, if a well is cemented off, again condition (14–16) should be invoked.

This model can also be written on a basis of surface rates and the conventional PI denoted  $J_{ks,i}$ ; the system then takes the equivalent form

$$q_{ks,i}^p = J_{ks,i} (\bar{p}_i - p_{k,w}) \tag{14-17}$$

$$\sum_{i=1}^{NC} q_{ks,i}^p = q_{ks}^p \tag{14-18}$$

$$q_{ks}^p = J_{ks}^* (p^* - p_{k,w}) \tag{14-19}$$

$$J_{ks}^* = \sum_{i=1}^{NC} J_{ks,i} \quad \text{and} \quad p^* = \frac{\sum_{i=1}^{NC} J_{ks,i} \bar{p}_i}{J_{ks}^*}$$

$$p_{k,w} = p^* - \frac{q_{ks}^p}{J_{ks}^*} \quad (14-20)$$

and

$$q_{ks,i}^p = J_{ks,i} \left( \bar{p}_i - p^* + \frac{q_{ks}^p}{J_{ks}^*} \right) \quad (14-21)$$

## State space representation of the complex material balance

Physical processes described by systems of linear time-invariant ODEs occur in many branches of engineering and it is convenient to write the complex material balance in matrix form by defining the state vector  $\mathbf{x}$  as follows:

$$\mathbf{x} = (\bar{p}_1, \bar{p}_2, \bar{p}_3, \bar{p}_4)^T$$

i.e.,

$$\mathbf{x} = \begin{bmatrix} \bar{p}_1 \\ \bar{p}_2 \\ \bar{p}_3 \\ \bar{p}_4 \end{bmatrix}$$

which is an  $(NSV \times 1)$  column vector where NSV is the number of state variables (in this case 4).

In most cases, the number of state variables NSV is equal to the number of cells NC. Similarly, the forcing function vector  $\mathbf{u}$  is defined as

$$\mathbf{u} = (q_1^p)^T$$

i.e.,

$$\mathbf{u} = \begin{bmatrix} q_1^p \end{bmatrix}$$

which is an  $(NFV \times 1)$  column vector where NFV is the number of forcing functions (in this case 1)

The number of forcing functions NFV is usually equal to the number of wells NW. The linear differential system may now be written as

$$\mathbf{D}_M \dot{\mathbf{x}} = \mathbf{A}_M \mathbf{x} + \mathbf{C}_M \mathbf{u} \quad (14-22)$$

where  $\mathbf{D}_M$  is an (NSV  $\times$  NSV) diagonal capacity matrix, i.e.,

$$\mathbf{D}_M = \begin{vmatrix} (c_t V)_1 & 0 & 0 & 0 \\ 0 & (c_t V)_2 & 0 & 0 \\ 0 & 0 & (c_t V)_3 & 0 \\ 0 & 0 & 0 & (c_t V)_4 \end{vmatrix}$$

and  $\mathbf{A}_M$  is an (NSV  $\times$  NSV) material balance coefficient matrix which in this case is

$$\mathbf{A}_M = \begin{vmatrix} \left[ -T_{1,3} - \frac{J_{1,1}J_{1,2}}{J_{1,1} + J_{1,2}} \right] & \frac{J_{1,1}J_{1,2}}{J_{1,1} + J_{1,2}} & T_{1,3} & 0 \\ \frac{J_{1,1}J_{1,2}}{J_{1,1} + J_{1,2}} & \left[ -T_{2,3} - T_{2,4} - \frac{J_{1,1}J_{1,2}}{J_{1,1} + J_{1,2}} \right] & T_{2,3} & T_{2,4} \\ T_{1,3} & T_{2,3} & \left[ -T_{1,3} - T_{2,3} \right] & 0 \\ 0 & T_{2,4} & 0 & -T_{2,4} \end{vmatrix}$$

Note that the coefficient matrix  $\mathbf{A}_M$  is symmetric. The forcing function matrix, designated  $\mathbf{C}_M$ , is an (NSV  $\times$  NFV) matrix which in this example takes the form

$$\mathbf{C}_M = \begin{vmatrix} \frac{J_{1,1}}{J_{1,1} + J_{1,2}} \\ \frac{J_{1,2}}{J_{1,1} + J_{1,2}} \\ 0 \\ 0 \end{vmatrix}$$

In order to achieve a standard formulation of the problem, each row of the system must be divided through by the relevant compressibility–pore volume product ( $c_t V$ ), i.e., row 1 by  $(c_t V)_1$ , etc. This may be written symbolically as

$$\dot{\mathbf{x}} = \mathbf{D}_M^{-1} \mathbf{A}_M \mathbf{x} + \mathbf{D}_M^{-1} \mathbf{C}_M \mathbf{u} \quad (14-23)$$

$$\text{i.e.,} \quad \dot{\mathbf{x}} = \mathbf{A} \mathbf{x} + \mathbf{C} \mathbf{u} \quad (14-24)$$

$$\text{where} \quad \mathbf{A} = \mathbf{D}_M^{-1} \mathbf{A}_M \quad \text{and} \quad \mathbf{C} = \mathbf{D}_M^{-1} \mathbf{C}_M$$

Equation (14–24) is the usual mathematical way of representing linear differential systems of ODEs; here,  $\mathbf{A}$  is the (NSV  $\times$  NSV) coefficient matrix of the state variables, while  $\mathbf{C}$  is the (NSV  $\times$  NFV) coefficient matrix of the forcing variables. The matrix  $\mathbf{D}_M^{-1}$  is simply the reciprocals of the diagonal elements of  $\mathbf{D}_M$ , i.e.,

$$\mathbf{D}_M^{-1} = \begin{vmatrix} \frac{1}{(c_t V)_1} & & & \\ & \frac{1}{(c_t V)_2} & & \\ & & \frac{1}{(c_t V)_3} & \\ & & & \frac{1}{(c_t V)_4} \end{vmatrix}$$

For the present example

$$\mathbf{C} = \begin{vmatrix} -\frac{J_{1,1}}{J_{1,1} + J_{1,2}} \cdot \frac{1}{(c_t V)_1} \\ -\frac{J_{1,2}}{J_{1,1} + J_{1,2}} \cdot \frac{1}{(c_t V)_2} \\ 0 \\ 0 \end{vmatrix}$$

The first advantage of the state space formulation of the material balance

$$\dot{\mathbf{x}} = \mathbf{A} \mathbf{x} + \mathbf{C} \mathbf{u}$$

is that the form of the coefficient matrices  $\mathbf{A}$  and  $\mathbf{C}$  can readily be deduced from the system dimensions NC, NL, and NW and the linkage information matrices ICLM and IWLM. This allows a great deal of flexibility in setting up and altering the structure of the block system. The terms in  $\mathbf{A}$  and  $\mathbf{C}$  involve the reservoir parameters  $c_t$ ,  $V$ ,  $T$ , and  $J$  (subscripted as necessary) and in order to define the simulation problem all these quantities must be specified. The values of  $c_t$  and  $V$  for each cell can be stored in a cell parameter matrix CPM, while the well connection factors  $J$  can be held in a well parameter matrix WPM. The transmissibility indices of the links  $T$  are stored in a transmissibility vector.

The linear differential system (14–24) is an initial value problem in which the starting values of the state variables at time  $t = 0$  are specified. In the complex material balance, this corresponds to the initial cell pressures; the starting state vector is designated  $x_0$ . The solution of (14–24) for the given initial condition also requires that the forcing functions  $u$ , i.e., the well total rates, be specified as functions of time; thus,  $u(t)$  must be known over the period of a simulation. The solution of (14–24)—known as *a trajectory* in systems engineering—subject to the initial condition and the forcing function yields the time variation of the state variables  $x(t)$ , i.e., the evolution of the cell pressures in response to the known production or injection history.

## Forcing functions

In the present formulation of the complex material balance, it has been chosen to regard the total well rates as known functions of time and to compute the system pressure response given this knowledge of well flow rate. This conforms to the general approach in well testing where the rate is specified and the pressure response is computed. Note that in the analysis of production data—which is the essential aim of material balance studies—the major source of error is in the measurement of rate and this must be recognized in an interpretation. It is sometimes, in fact, preferable to compute rates from measured pressure information because the latter can be measured very accurately. However, for the moment, in history-matching or simulation mode, it will be assumed that the rate data are known and the pressure response is generated by the model. Thus, for each well in the system a rate history must be specified as shown in figure 14–8; the rate data is stored simply as a table of times and flow rates known as *a rate schedule*. In general, the flow information is stored as surface rates, denoted  $q_{ks}^p$ , and the in situ (reservoir condition) rate is obtained by multiplying by the formation volume factor  $B_o$ ; thus

$$q_k^p = q_{ks}^p B_o \quad (14-25)$$

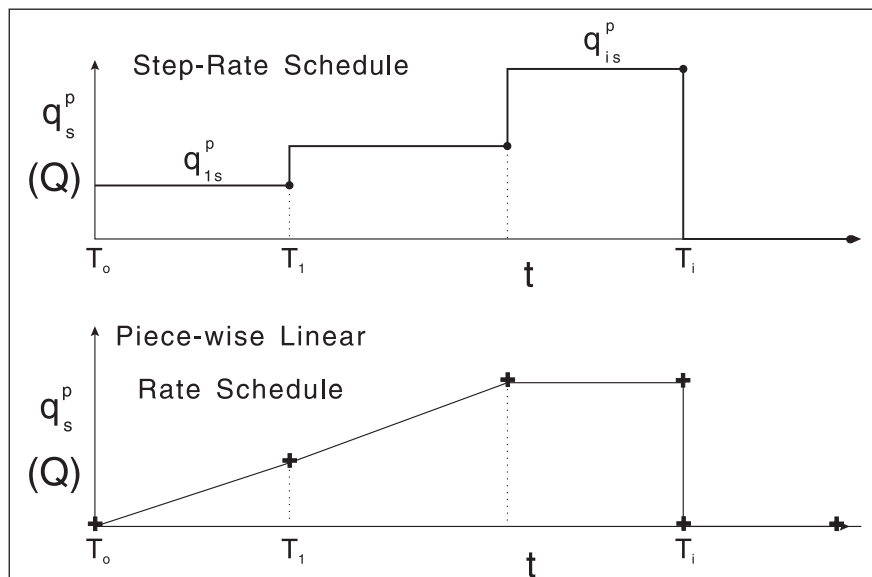


Fig. 14–8. Step function or piecewise linear rate schedule

The rate schedule can be treated as either a step function or a piecewise linear function as indicated in figure 14–8. The numerical integration algorithm, i.e., the Runge–Kutta method, will recognize that the time dependence of the forcing function can follow either of these forms. Obviously, the piecewise linear approximation will give a better representation of the flow history provided the method of rate measurement justifies its use. Note that it may be necessary to smooth field rate data before it is used in a material balance study. The process of generating a pressure response for a variable rate history is known as *convolution* and in the complex material balance model this process is limited to step or piecewise linear approximations to the underlying continuous function. Given the practical problems of field rate measurement, this is not a serious limitation.

The material balance is primarily a technique for analyzing production data in conjunction with pressure measurements. In the approach proposed here, attention has been focused on the time–rate record illustrated in figure 14–8. However, it must be recognized that actual production data are not usually available in this form. The manipulation of field production data is usually carried out on a spread sheet program of some type and a well file typically consists of a table of date or time versus period production as illustrated in table 14–4.

**Table 14–4.** Typical well production data file

<b>Date or Time (days)</b>	<b>Period production (STbbl or MMSCF)</b>	<b>Cumulative production (STbbl or MMSCF)</b>	<b>Rate over period (STbbl/d or MMSCF/d)</b>
—	—	—	—
—	—	—	—
—	—	—	—

Here, the period production implies the oil produced between the present and previous date or time. Given this information, it is a simple matter to compute the additional two columns comprising the cumulative production to date and the average (step) rate over the period. In fact, it is only necessary for one of the three production columns to be filled in and the other two can immediately be calculated. This form of file is easily generated on a spread sheet and this will be the normal form of input to the material balance program. Such a file is required for each well in the study and the starting date or time may be different from well to well.

## **Solution of the State Space System**

In the original formulation of the complex material balance, as described by Stewart,<sup>2</sup> the solution of the linear system (14–24) by analytical methods based on an eigenvalue decomposition was proposed. In retrospect, it has proved preferable to obtain solutions using numerical techniques, in particular the well-known Runge–Kutta methods formulated in numerical analysis treatises. The shift to numerical integration of the differential system was motivated by the desire to model gas reservoirs where the total compressibility  $c_t$  is dependent on the pressure. Thus, in gas reservoir engineering, the equations are nonlinear through the terms in the capacity matrix  $D_M$ ; since the state space analytical techniques are limited to linear systems, it is advantageous to consider only numerical methods of integration. The modern Runge–Kutta algorithms are, in fact, very fast and do not require the manipulation of large sparse matrices.

The main problem with a numerical technique is the optimal selection of a step size control algorithm that guarantees adequate precision in the generated responses and prevents instability in the solution.

A second-order Runge–Kutta (modified Euler) method is illustrated in figure 14–9 for the single differential equation

$$\frac{dx}{dt} = f(t, x) \quad t = 0 : x = x_0$$

and the method may be written for step i:

$$\bar{x}_{i+1/2} = x_i + \frac{\Delta t}{2} f(t_i, x_i) \quad \text{predictor}$$

and

$$x_{i+1} = x_i + \Delta t f\left(t_i + \frac{\Delta t}{2}, \bar{x}_{i+1/2}\right) \quad \text{corrector.}$$

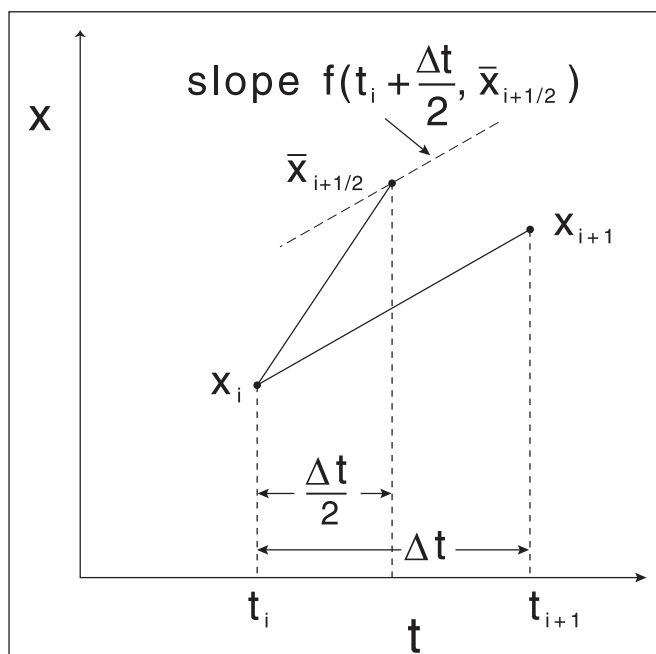


Fig. 14–9. Second-order Runge–Kutta method

Higher order Runge–Kutta methods for systems of simultaneous nonlinear ODEs

$$\frac{dx}{dt} = f(t, x) \quad t = 0 : x = x_0$$

are very efficient and, as already mentioned, the step size  $\Delta t$  can be automatically adjusted to maintain accuracy in the numerical solution. In the case of the material balance equations, it is particularly step changes in well rates (i.e., forcing functions,  $u$ ) that necessitate adaptive step size control algorithms. The trajectory may change dramatically if a new well is brought in or an existing one subjected to a large change in total rate. However, a fourth-order Runge–Kutta method has been found to be very effective for the forward integration of systems of material balance equations, and step changes in rate are handled perfectly adequately. Setting an upper limit on the step size ensures that sufficient pressure information is generated; however, since the pressure generation (simulation) mode will be used as a single function evaluation by the nonlinear regression routine, it is essential that the integration process be as rapid as possible. Hence, the desired accuracy specified to the adaptive step size control algorithm should not exceed the actual measurement error of the pressure detection systems. The analytical solution based on eigenvalues of the coefficient matrix  $A$  is useful in verifying the performance of the numerical forward (marching) integration process. The cell pressures will be computed at unequal times because the adaptive stepsize control algorithm will be continually adjusting  $\Delta t$ ; however, pressures at intermediate times may easily be generated by suitable interpolation. In the interests of overall computation time, it is important that as large steps as possible are used in the stepwise integration process. The large errors that occur in well rate measurement also indicate that the solution process of the material balance equations need not be overly accurate. Note that the systems of ODEs generated from the lumped parameter approach are not “stiff” in the mathematical sense since the cells are all of comparable volume; this is the advantage of handling the near-well flow analytically.

## Subsidiary variables

The material balance equations have been formulated in terms of the state variables (cell average pressures)  $\mathbf{x}$  and the forcing functions  $\mathbf{u}$  where the latter are the total well rates. In any study of this sort, it is also of interest to examine the intercell flows  $q_{i,j}$  given by the equation

$$q_{i,j} = T_{i,j}(\bar{p}_j - \bar{p}_i) \quad (14-26)$$

For example, if the support cell is an aquifer block, this represents the water influx into the reservoir. In addition, the individual layer flow rates into well  $k$  from cell  $i$  are given by

$$q_{k,i}^p = J_{k,i}(\bar{p}_i - p_{k,w}) \quad (14-27a)$$

$$\begin{aligned} q_{ks,i}^p &= J_{k,i}(\bar{p}_i - p_{k,w}) \frac{1}{B_o} \\ &= J_{ks,i}(\bar{p}_i - p_{k,w}) \end{aligned} \quad (14-27b)$$

Once the cell average pressures have been computed, the individual intercell flows and layer well inflows can be calculated from Eqs. (14–26) and (14–27a and b) and it is useful to define vectors of subsidiary variables  $\mathbf{y}$  and  $\mathbf{z}$  comprising these flows and the well bottom-hole flowing pressures  $p_{k,w}$ .



## Natural water influx

An important part of the classical material balance approach has related to the study of natural water influx into a reservoir. The problem of natural water drive is illustrated in figure 14–10, where an aquifer is shown to be in communication with an oil column. This situation may be represented by a two block system as shown. The oil block—labeled 2—has a compressibility  $(c_t)_2$  corresponding to an oil-filled system at connate water saturation and a pore volume  $V_2$ . The aquifer block—labeled 1—has a compressibility  $(c_t)_1$  corresponding to 100% water saturation and a pore volume  $V_1$ . The aquifer communication factor  $T_{12}$  in a lumped parameter model presumes all the resistance to water inflow to be localized in a barrier between blocks 1 and 2. The quantity  $T_{12}$  in this context has been called *the aquifer productivity index* by Fetkovich.<sup>3</sup> The differential system describing the simplified two block model (with a production well in block 2) takes the form

$$(c_t V)_1 \frac{d\bar{p}_1}{dt} = T_{12}(\bar{p}_2 - \bar{p}_1) \tag{14-28a}$$

and

$$(c_t V)_2 \frac{d\bar{p}_2}{dt} = T_{12}(\bar{p}_1 - \bar{p}_2) - q_{1,2}^p \tag{14-28b}$$

where

$$(c_t)_1 = c_{f1} + c_w$$

$$(c_t)_2 = c_{f2} + S_{wc}c_w + (1 - S_{wc})c_o$$

and

$$q_{1,2}^p = J_{1,2}(\bar{p}_2 - p_{1,w})$$

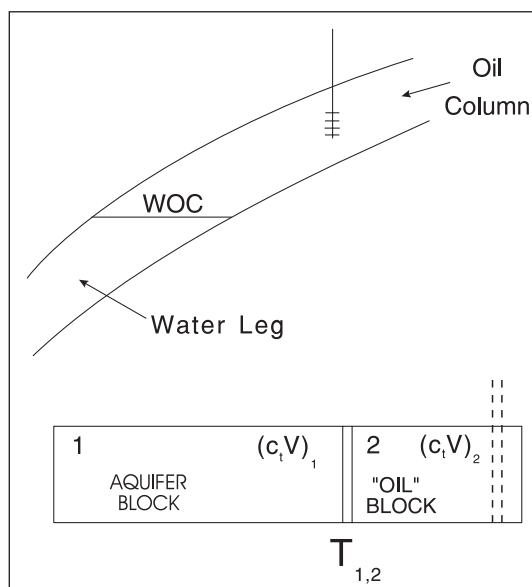


Fig. 14–10. Natural water influx

This aquifer model has two key parameters—the pore volume  $V_1$  and the aquifer PI  $T_{12}$ —and the lumped parameter approach to representing natural water influx was first proposed by Fetkovich. In the basic Fetkovich method, which is described in detail in the textbook by Dake,<sup>4</sup> the cumulative influx is calculated for a known pressure history, i.e., the single equation

$$(c_t V)_1 \frac{d\bar{p}_1}{dt} = T_{12} (\bar{p}_2(t) - \bar{p}_1) \quad (14-29)$$

is solved where  $\bar{p}_2(t)$  is a specified time function. An integrated form of (14-29) is used to predict the cumulative aquifer influx. In the present approach, the aquifer and oil reservoir equations (14-28a) and (14-28b) are solved simultaneously to give the pressure response of the overall system.

The obvious limitation of this approach to aquifer influx is, of course, that the saturation, and hence compressibility change of the oil block, is not accounted for. Thus, there is a progressive error in the pressure prediction as the water saturation rises in block 2. This can be compensated for quite simply by restarting the problem with an updated value of  $(c_t)_2$ . However, if large saturation changes take place, a two-phase simulation is warranted. The single-phase material balance is most useful early in the field development when pressure depletion monitoring is being used to improve reservoir description.

In Eq. (14-28a and b), the quantity  $T_{12}$  may represent a physical barrier near the oil–water contact. However, often it is the low permeability of the aquifer block that controls the water influx. In a succeeding section, it will be shown how to lump the resistance due to block permeability along with a barrier resistance to give a combined effective interblock transmissibility for use in the complex material balance model.

The material balance equations are presented in simulation mode, i.e., given the parameters—in this case  $V_1$ ,  $V_2$ , and  $T_{12}$  and the compressibilities—the pressure response can be predicted. In practice, of course, measurements are made of the cell pressures or the well flowing bottom-hole pressures, and a parameter set that matches the model to the observations is sought. This is the inverse problem of parameter estimation. Given a set of pressure observations  $p^{\text{obs}}$  and a corresponding set of predictions of these pressures  $p^{\text{calc}}$  from the model, it is possible to define a sum of squares objective function

$$\chi^2 = \sum \left( \frac{p^{\text{obs}} - p^{\text{calc}}}{\sigma} \right)^2 \quad (14-30)$$

which should be minimized by adjustment of the model parameters, i.e.,  $V_1$ ,  $V_2$ ,  $T_{12}$ , in the present situation. The vector of unknown parameters to be determined by matching is denoted  $\mathbf{a}$ ; in this case,

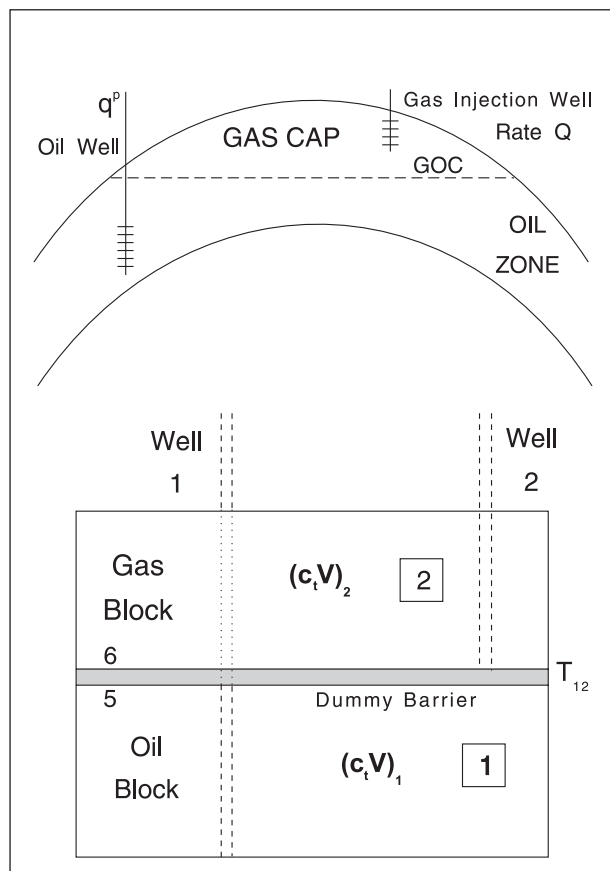
$$\mathbf{a} = \begin{vmatrix} V_1 \\ V_2 \\ T_{1,2} \end{vmatrix} \quad (14-31)$$

This is the basis of the material balance method—the search for a parameter set that will match the model to the observations, i.e., the measured pressure history. This search can be carried out manually by trial, or semiautomatically using a nonlinear optimization method for a sum of squares objective function.

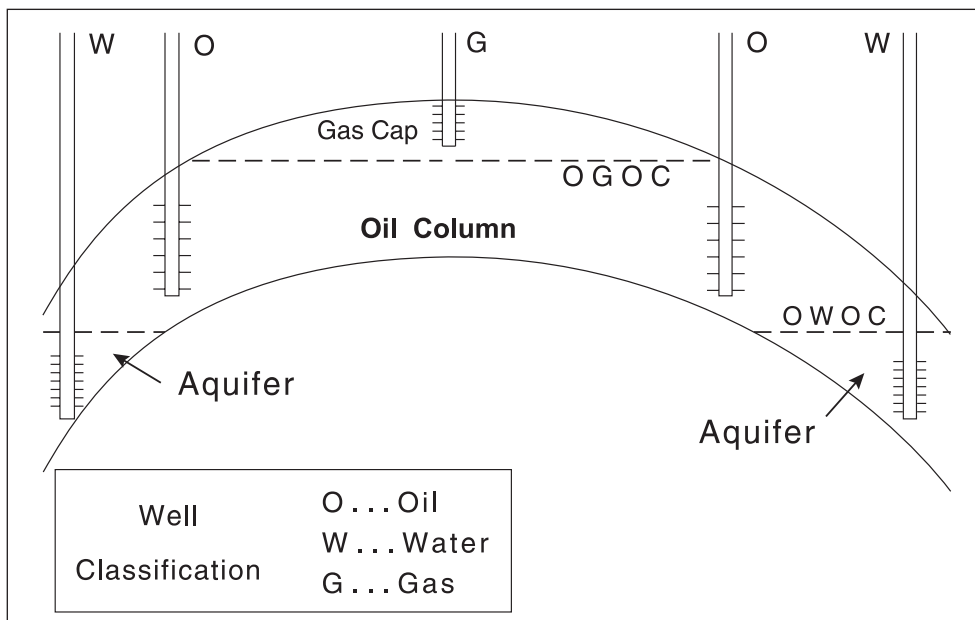
In the aquifer problem, the pore volumes  $V_1$  and  $V_2$  of the water and oil blocks occur as parameters. On the basis of pressure data alone, it can be very difficult to obtain discrimination between  $V_1$  and  $V_2$ , especially when there is reasonable aquifer communication. In this model,  $V_2$  represents oil reserves and  $V_1$  the aquifer size. This illustrates the classic problem (“pressure dilemma”) of the material balance in any form—the pressure response reflects the total connected system. There must be independent volumetric estimates that can be supported by material balance considerations. Hence, the geological model is very important in defining block structure and cell volumes and is an adjunct to depletion studies. The conditional nature of the matching process is reflected in the choice of unknowns selected for minimization, i.e., defining the elements of a is an important part of the procedure. In a constrained optimization, additional conditional relations can be imposed, e.g.,  $V_1 + V_2$  may have to be less than some quantity. In the minimization process, it is certainly necessary to impose upper and lower limits  $a_{\min}$  and  $a_{\max}$  on the search process to prevent physically impossible values being used.

## Gas cap drive

In the preceding section it was shown how the problem of aquifer support could be handled by defining blocks saturated with water only. It is possible to model the effect of gas cap drive in exactly the same way by specifying certain blocks to contain gas as illustrated in figure 14–11. The compressibility of gas is much higher than that of oil and the pressure behavior of the total system will reflect the support of the gas cap. Fluid flow will occur predominantly from the gas blocks to the oil blocks and there will, of course, be a progressive error as the flux into the oil block is assumed to be oil. The same problem occurred in the aquifer case and this lack of ability to recognize saturation is the main limitation of the complex material balance method as described here. The compressibility of gas is also a function of pressure and the material balance problem becomes nonlinear in this case. This effect can be handled by the use of pseudopressure and the methodology is described in the section “Material Balance in Terms of Pseudopressure and Pseudotime.” In the complex material balance model, it is necessary to stipulate whether a cell is oil-, water-, or gas-bearing in order that the fluxes of water and gas can be estimated separately. In addition, a well is only allowed to be completed in cells of one category; thus a well can be an injector or producer of oil, water, or gas depending on the cell fluid type of its connections. This is illustrated in figure 14–12. In the formulation of the cell mass balances, it is assumed that the flux into a cell is of the fluid type corresponding to that cell, e.g., gas, is transformed into oil (in terms of reservoir volumes) on crossing an interface between a gas and an oil cell.



**Fig. 14–11.** Modeling of a gas cap by allocation of gas bearing blocks



**Fig. 14–12.** Well classification by fluid type

In the case of a liquid system, the material balance equation for a cell containing a well has the form

$$(c_t V)_i \frac{d\bar{p}_i}{dt} = T_{i,j}(\bar{p}_j - \bar{p}_i) - q_{k,i}^p \quad (14-32)$$

Here, the well flow rate  $q_{k,i}^p$  is at reservoir (in situ) conditions and, if the rate at surface (stock tank) conditions is denoted  $q_{ks,i}^p$ , then Eq. (14-32) may be written alternatively as

$$(c_t V)_i \frac{d\bar{p}_i}{dt} = T_{i,j}(\bar{p}_j - \bar{p}_i) - q_{ks,i}^p B_o \quad (14-33)$$

where  $B$  is the conventional formation volume factor. In the case of a gas well, the flow rate is usually expressed in terms of volume at standard conditions (e.g., MMSCF/D) and the gas formation volume factor is used to convert to in situ conditions. Therefore, in the case of a gas block the material balance equation assumes the form

$$(c_t V)_i \frac{d\bar{p}_i}{dt} = T_{i,j}(\bar{p}_j - \bar{p}_i) - Q_{k,i} B_g^o \quad (14-34)$$

where  $B_g^o$  and  $c_t$  are evaluated at the initial cell pressure  $\bar{p}_i^o$ . At high pressure, there is very little error in treating gas as a liquid of constant compressibility in this fashion. However, as the pressure declines, it is necessary to allow for the changing compressibility of the gas phase in the material balance equation, i.e., the capacity term  $(c_t V)_i$  becomes pressure dependent. Thus

$$c_t = (1 - S_{wc})c_g + S_{wc}c_w + c_f \quad (14-35)$$

where

$$c_g = \frac{1}{p} - \frac{1}{z} \frac{\partial z}{\partial p}$$

Fortunately, the exact behavior of a real gas in the context of the material balance can simply be handled using the concept of normalized pseudopressure and allowing the term  $(c_t V)_i$  to be pressure dependent. Equation (14-34) is written in the form

$$\frac{d\psi(\bar{p}_i)}{dt} = \frac{\mu^o}{(\mu c_t V)_i} \left( T_{i,j} \left( \psi(\bar{p}_j) - \psi(\bar{p}_i) \right) - Q_{k,i} B_g^o \right) \quad (14-36)$$

Since the modified capacity term  $\frac{\mu^o}{(\mu c_t V)_i}$  is pressure dependent, the material balance equation for gas is nonlinear; here,  $\mu^o$  is the gas viscosity and  $B_g^o$  the gas formation volume factor both at the reference pressure. Fortunately, the presence of such nonlinearity makes no difference to the Runge-Kutta method and gas reservoir material balance (in the case where there are no oil cells)

can be handled in a fashion which recognizes the variation of compressibility factor  $z$  with pressure. It is simply a convenience to use the real gas pseudopressure to handle this effect—an approach that has already been successfully used in transient analysis of gas wells. The full derivation of the pseudopressure method is given in a later section.

In connection with overpressured gas reservoirs, the formation compressibility  $c_f$  is not constant and depends on the current pore pressure  $\bar{p}_i$ ; the information on pressure-dependent rock compressibility may be specified as a table of  $c_f$  versus  $p$  which can be interrogated by interpolation as shown in figure 14–13. In addition, when two-phase conditions exist, e.g., below the dew point for gas or below the bubble point for oil, the hydrocarbon compressibility denoted  $c_{mph}$  is also pressure dependent. Accordingly, Eq. (14–35) is written in the form

$$c_t = (1 - S_{wc})c_{mph} + S_{wc}c_w + c_f \quad (14-37)$$

where both  $c_{mph}$  and  $c_f$  are pore-pressure-dependent. The single-phase gas compressibility  $c_g$  or the two-phase hydrocarbon compressibility  $c_{mph}$  is tabulated with the normalized pseudopressure function since both quantities are required for material balance calculations. The total compressibility  $c_t$  should therefore be computed dynamically from Eq. (14–37) in the course of the simulation.

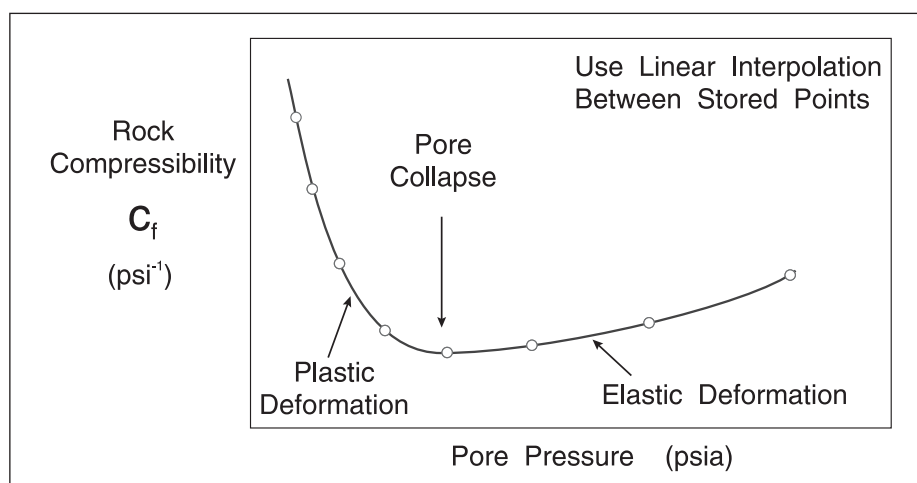


Fig. 14–13. Pore-pressure-dependent rock compressibility

For communication between gas cells, the interblock flow  $q_{i,j}$  is given by the expression

$$q_{i,j} = T_{i,j} \left( \psi(\bar{p}_j) - \psi(\bar{p}_i) \right) \quad (14-38)$$

and this will be computed as in situ bbl/day. However, if the communication is between an oil and a gas cell, e.g., gas cap support, it is not possible to mix pressure and pseudopressure; in this case, the interblock flows must be calculated on the basis of actual pressure, viz.,

$$q_{i,j} = T_{i,j} (\bar{p}_j - \bar{p}_i) \quad (14-39)$$

This logic must be incorporated into the material balance program.

The use of pseudopressure also allows gas cells to include the case of gas condensate where the effective compressibility  $c_{m\text{ph}}$  of a two-phase constant composition mixture will be utilized.

## Gas field units

In terms of the gas field units defined in table 14–5, the gas cell material balance takes the form

$$\frac{d\psi(\bar{p}_i)}{dt} = \frac{5.61458\mu^o}{(\mu c_t V)_i} \left( T_{i,j} \left( \psi(\bar{p}_j) - \psi(\bar{p}_i) \right) - \frac{QB_g^o \times 10^6}{5.61458} \right) \quad (14-40)$$

**Table 14–5.** Definition of gas field units

$(p)$ : psi	$t$ : days	$\mu$ : cp
$c_t$ : psi <sup>-1</sup>	$V$ : ft <sup>3</sup>	$T$ : bbl/d/psi
$Q$ : MMSCF/D	$B_g^o$ : ft <sup>3</sup> /SCF	

## Solution gas drive

Similarly if a two-phase pseudopressure is specified for an oil cell, the effect of solution gas drive can be modeled as the cell pressure falls below the bubble point. Thus, the complex material balance methodology allows for the following principal reservoir drive mechanisms:

- depletion drive (liquid or gas compressibility);
- natural water influx;
- gas cap drive (in the case of an oil reservoir);
- solution gas drive (including volatile oil);
- compaction drive;
- pressure maintenance by water or gas injection.

## Cumulative production and influx

In the complex material balance model, a cell can be one of three basic fluid types, viz.

- oil,
- water, and
- gas.

This refers to the fluid initially occupying the cell and, obviously, the question of initial hydrocarbon in place is tied to the sum of the pore volumes of the oil and gas cells. Since the material balance model does not allow for saturation changes, wells penetrating the gas cap are

only allowed to flow or inject gas. Similarly, wells completed in aquifer blocks are only allowed to inject or produce water. Also, a given well cannot intersect cells of different type. The cell volumes  $V_i$  refer to initial in situ volumes of fluid (oil, gas, or water) at reservoir conditions and it is useful to define the summations

$$V_{\text{oil}} = \sum_{\text{oil}} V_i \quad (14-41a)$$

$$V_{\text{gas}} = \sum_{\text{gas}} V_i \quad (14-41b)$$

$$V_{\text{water}} = \sum_{\text{water}} V_i \quad (14-41c)$$

where the summations are taken over all the cells of the specified type. In terms of volumes at standard surface conditions, the formation volume factors of the phases are designated  $B_o$ ,  $B_{gi}$ , and  $B_w$ , respectively, and the hydrocarbon and water originally in place are given as follows:

$$\text{Oil:} \quad N_i = \frac{V_{\text{oil}}}{B_o} \quad \text{denoted OIIP} \quad (14-42a)$$

$$\text{Gas:} \quad G_i = \frac{V_{\text{gas}}}{B_{gi}} \quad \text{denoted GIIP} \quad (14-42b)$$

$$\text{Water:} \quad W_i = \frac{V_{\text{water}}}{B_w} \quad (14-42c)$$

The well rates also refer to the fluid type, and the cumulative productions of oil, gas, and water may be written as

$$\text{Oil:} \quad N_p(t) = \sum_{\text{oil}} \int_0^t q_{ks}^p dt = \sum_{\text{oil}} N_k^p \quad (14-43a)$$

$$\text{Gas:} \quad G_p(t) = \sum_{\text{gas}} \int_0^t Q dt = \sum_{\text{gas}} N_k^p \quad (14-43b)$$

$$\text{and Water:} \quad W_p(t) = \sum_{\text{water}} \int_0^t q_{ks}^p dt = \sum_{\text{water}} N_k^p \quad (14-43c)$$



The individual cumulative production (standard volume) per well may be computed from the appropriate integral:

$$N_k^P(t) = \int_0^t q_{ks}^P dt \quad \text{or} \quad G_k^P(t) = \int_0^t Q_k dt$$

These integrals may be easily determined by quadrature, e.g., the trapezoidal rule, since piecewise linear rate schedules, at most, are specified. The cumulative amounts may be positive (production) or negative (injection). The integration process may be extended to the intercell flows  $q_{i,j}$ ; for example, if certain blocks have been designated as aquifer cells, it is useful to keep track of the total amount of water that has entered hydrocarbon regions. The water influx can be computed as

$$W_e(t) = \sum_{\text{water}} \int_0^t q_{i,j} dt \quad (14-44)$$

Here, the summation is taken over all links from water-bearing cells to hydrocarbon cells and only positive rates, in the sense that the flow is in the direction water cell to hydrocarbon cell, are allowed in the quadrature. The cumulative water influx is an important quantity in reservoir engineering terms.

In the present formulation of the material balance, it has been assumed that an oil well produces only oil and associated gas and that the formation volume factor  $B_o$  is constant. However, some wells will eventually produce a water-cut and it is necessary to allow for this in the calculations. The important point is that the product of  $q_{ks}^P$  and  $B_o$  is the reservoir barrels per day of liquid produced by the well. If the well is flowing  $q_{so}$  STbbl/day of oil at a water-cut of BSW (fraction total stock tank liquid), then the number of reservoir barrels per day of liquid is given by

$$q_t = q_{so} \left( B_o + \frac{BSW}{1 - BSW} B_w \right) \quad (14-45)$$

and it is possible to define an equivalent oil rate  $q_{so}^{\text{equiv}}$  by the relation

$$q_{so}^{\text{equiv}} = q_{so} \left( 1 + \frac{BSW}{1 - BSW} \frac{B_w}{B_o} \right) \quad (14-46)$$

This quantity may be used to represent the in situ liquid stream and allows the material balance model to be matched to wells producing a water cut. Of course, the compressibility will still be modeled as oil if the block has been so declared. Again, such calculations are readily performed on the spread sheet used to assemble the production database.

## Cellular Systems

### Three-cell problem

In order to demonstrate the idea of a compartmentalized reservoir and to show how the complex material balance can be used, a simple three-cell problem, shown in figure 14–14, will be studied. Here, three cells of equal volume and all oil bearing are connected in line. Cell 1 is intersected by a well that is flowed at constant rate. There are two links in the system and the transmissibility indices  $T_{1,2}$  and  $T_{2,3}$  are made equal. This is a prototype cellular system and the initial pressures are also made equal, i.e.,  $\bar{p}_1 = \bar{p}_2 = \bar{p}_3$ . The trajectory computed by the material balance model is shown in figure 14–15, where the response exhibits a dynamic period followed by a joint (total system) SSS where the cell average pressures all decline linearly with time at the same rate. This SSS condition is illustrated in figure 14–16 and is defined by the condition

$$\frac{d\bar{p}_1}{dt} = \frac{d\bar{p}_2}{dt} = \frac{d\bar{p}_3}{dt} = -\frac{q^p}{c_t V_t} \quad (14-47)$$

where

$$V_t = \sum_{i=1}^3 V_i \quad \text{the total pore volume.}$$

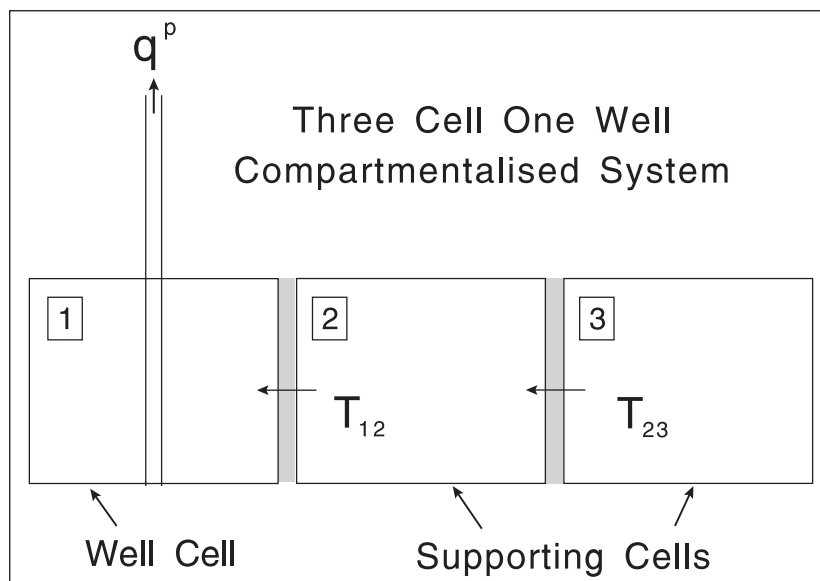


Fig. 14–14. Three-cell problem

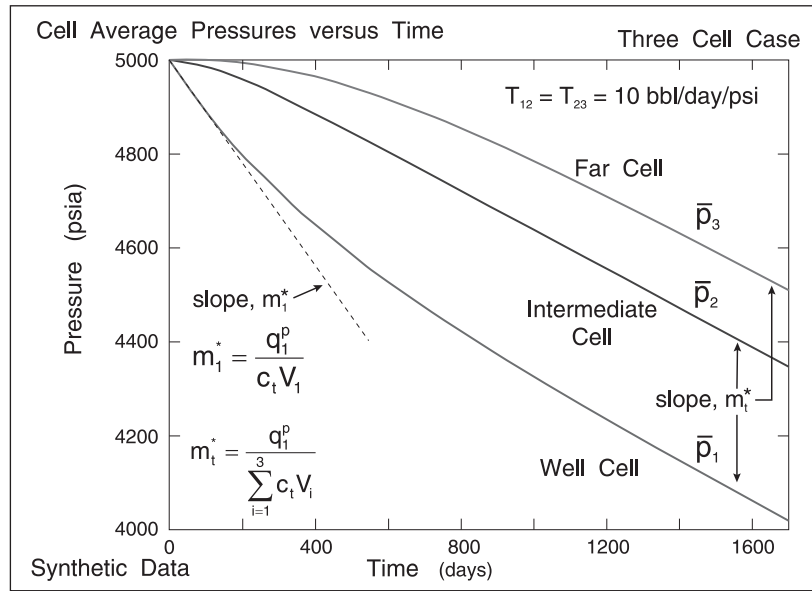


Fig. 14-15. Cell average pressure response for a three-cell system

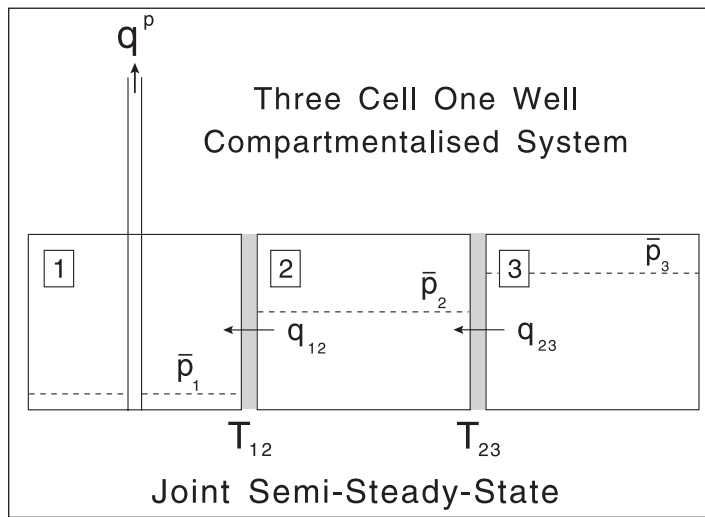


Fig. 14-16. Joint (total system) semi-steady-state of three-cell system

At the SSS, the intercell flows are given by

$$q_{3,2} = \frac{V_3}{V_t} q^p \quad \text{and} \quad q_{2,1} = \frac{V_2 + V_3}{V_t} q^p \quad (14-48)$$

i.e., the net flow from each cell is proportional to its pore volume assuming the compressibilities are identical. The differences between the cell pressures have stabilized such that this condition is satisfied and it can be shown that

$$\bar{p}_2 = \bar{p}_1 + \frac{1}{T_{1,2}} \frac{V_2 + V_3}{V_t} q^p \quad (14-49a)$$

and 
$$\bar{p}_3 = \bar{p}_2 + \frac{1}{T_{2,3}} \frac{V_3}{V_t} q^p \quad (14-49b)$$

i.e., 
$$\bar{p}_3 = \bar{p}_1 + \left( \frac{1}{T_{1,2}} \frac{V_2 + V_3}{V_t} + \frac{1}{T_{2,3}} \frac{V_3}{V_t} \right) q^p \quad (14-49c)$$

These relations define the differences between cell average pressures at joint (total system) SSS.

## Idealized cellular system

The simple three-cell problem discussed in the previous section is a particular case of the general idealized cellular system illustrated in figure 14–17, where a system of identical cells is connected in series with equal interblock transmissibilities. If the forcing function, i.e., the well rate, is excluded for the moment, the material balance equations take the form

$$\frac{d\bar{p}_1}{dt} = \frac{T}{c_t V} (-\bar{p}_1 + \bar{p}_2)$$

$$\frac{d\bar{p}_i}{dt} = \frac{T}{c_t V} (\bar{p}_{i-1} - 2\bar{p}_i + \bar{p}_{i+1}) \quad i = 2, \dots, N-1$$

and 
$$\frac{d\bar{p}_N}{dt} = \frac{T}{c_t V} (\bar{p}_{N-1} - \bar{p}_N) \quad (14-50)$$

i.e., 
$$\dot{\mathbf{x}} = \mathbf{A} \mathbf{x}$$

where  $N$  is the number of cells. In this homogeneous form with no forcing function, intercell flow will take place only if the block initial pressures  $x_0$  are different. The coefficient matrix  $A$  is of the form

$$\mathbf{A} = \frac{T}{c_t V} \mathbf{TD} \quad (14-51)$$

where  $TD$  is the tridiagonal, pressure coefficient matrix shown in Eq. (14–50); for a given value of  $NC$ , this matrix is specific to the identical cells in series model and the particular character of the system is lumped into the multiplier  $\frac{T}{c_t V}$  which has the dimensions of reciprocal time.

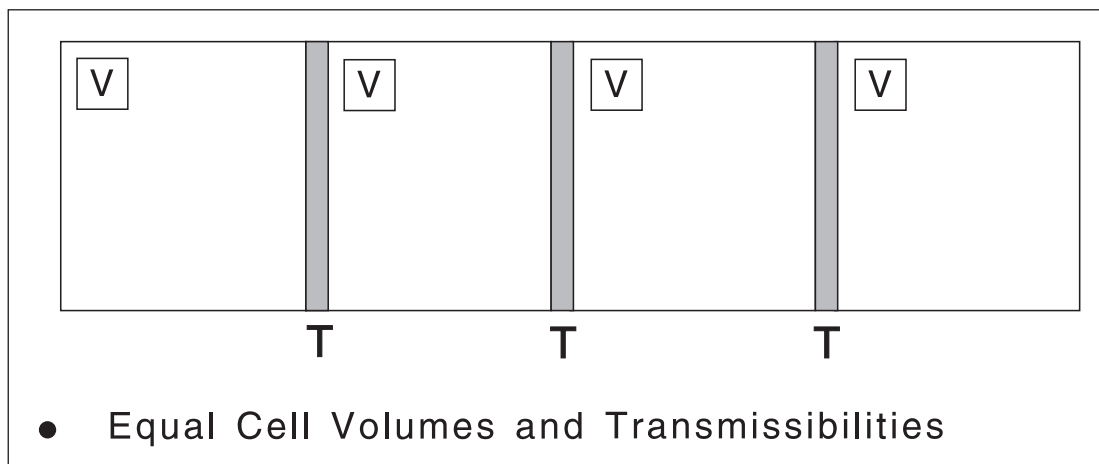


Fig. 14–17. Idealized cellular system

The dynamics of the system is controlled by the smallest (absolute value) eigenvalue of the matrix A where

$$\lambda_{\min}^A = \frac{T}{c_t V} \lambda_{\min}^{TD} \tag{14-52}$$

Thus, the smallest eigenvalue of A is related to the smallest eigenvalue of the tridiagonal matrix of fixed coefficients TD. The quantity  $\lambda_{\min}^{TD}$  depends on the number of cells NC and is tabulated below.

Table 14–6. Eigenvalues of Tridiagonal Coefficient Matrix, A

No. of Cells	Eigenvalues, $\lambda^{TD}$				
2	-2.0				
3	-1.0	-3.0			
4	-0.5858	-2.0	-3.4142		
5	-0.3820	-1.382	-2.618	-3.618	
6	-0.2679	-1.0	-2.0	-3.0	-3.7321

A system time constant  $\tau$  can be defined as the reciprocal of the dominant eigenvalue ( $\lambda_{\min}^{TD}$  is in second column i.e. smallest absolute value)

$$\tau = \frac{1}{|\lambda_{\min}^A|} \tag{14-53}$$

and from Eq. (14–52), this is proportional to  $\frac{c_t V}{T}$ . Hence, for systems with small transmissibilities T, the controlling time constant  $\tau$  is large and it takes a long time to reach joint SSS conditions. In material balance systems with symmetric coefficient matrices, there is always one eigenvalue

equal to zero and such systems will attain a steady-state (SS) if  $u$  is zero. Analogously, if  $u$  is constant, the system will attain the joint SSS as seen in the last section from the numerical results. Thus, in the analytical solution, the zero eigenvalue  $\lambda_0 = 0$  gives rise to terms as follows:

$$e^{\lambda t} = 1 \dots \text{SS} \quad \text{and} \quad \frac{e^{\lambda t} - 1}{\lambda} = t \dots \text{SSS}$$

The approach to the SS or SSS, as the case may be, is governed by terms in the analytical solution of the form

SSS –  $u$  constant

$$\bar{p}_i = d + c_0 t + c_1 e^{\lambda_1 t} + c_2 e^{\lambda_2 t} + \dots \quad (14-54a)$$

SS –  $u$  zero

$$\bar{p}_i = d + c_1 e^{\lambda_1 t} + c_2 e^{\lambda_2 t} + \dots \quad (14-54b)$$

where the eigenvalues of  $A$  are negative. The smallest eigenvalue in absolute value is  $\lambda_1$  and the second smallest  $\lambda_2$ , etc.; at some point in time, the terms corresponding to  $\lambda_2$  and larger eigenvalues become negligible and the solution is dominated by a single exponential form based on  $\lambda_1$ . This will be termed the *exponential approach region* (EAR) which is illustrated diagrammatically in figure 14–18 for the case where  $u = 0$ . For values of  $t > 3\tau$  approximately where  $\tau = \lambda_1^{-1}$ , Eq. (14–54a) reduces to

$$\bar{p}_i = d + c_0 t \quad (14-55a)$$

—the familiar linear variation of pressure with time for a well produced at constant rate in SSS drawdown. In this formula,  $c_0$  is the same for all cells  $i$  and equal to the quantity  $-\frac{q^p}{c_t V_t}$  defined earlier;  $d$ , of course, is different for each individual cell. When the forcing term is zero and flow occurs because of the imbalance in initial pressures, then at long time Eq. (14–54b) assumes the form

$$\bar{p}_i = d \quad (14-55b)$$

where  $d$  is now associated with the total system volumetric average pressure  $\bar{p}$  defined in the next section; it is this case that is illustrated in figure 14–18.

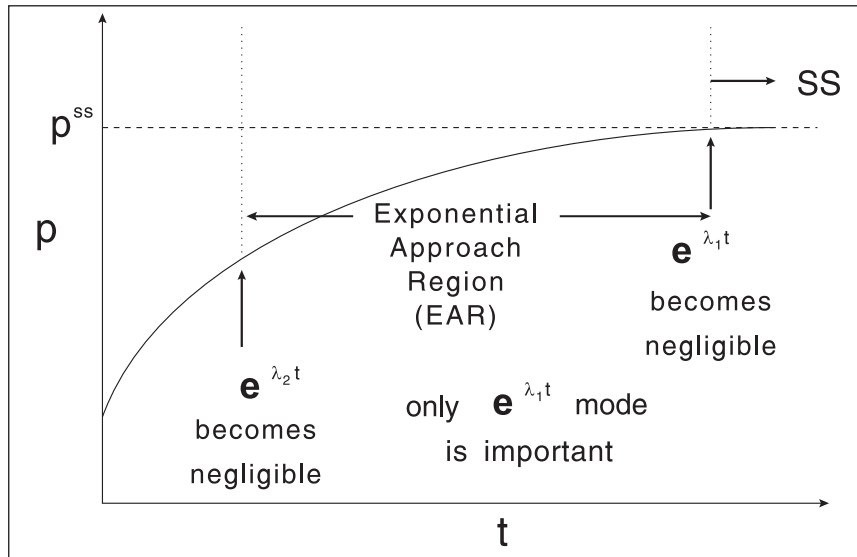


Fig. 14–18. Exponential approach region (EAR)

### Extended buildup in a compartmentalized reservoir

It is interesting to consider an extended buildup in a compartmentalized reservoir since this is very relevant to the process that takes place, for example, in gas wells shut in for the summer period. The pressure distribution at the moment of shutin for the well cell of a three-cell system has the form indicated in figure 14–19. Initially, there is a classical period of transient buildup in the well cell, which is controlled by the formation permeability and the well skin factor if storage is present. This is labeled the middle time region (MTR) on the semilog (Horner) plot as shown in figure 14–20; the time taken for the conventional buildup to occur is given by the approximate condition

$$t_{DL_f} = \frac{k\Delta t}{\phi\mu c_t L_f^2} = 0.3 \quad (14-56)$$

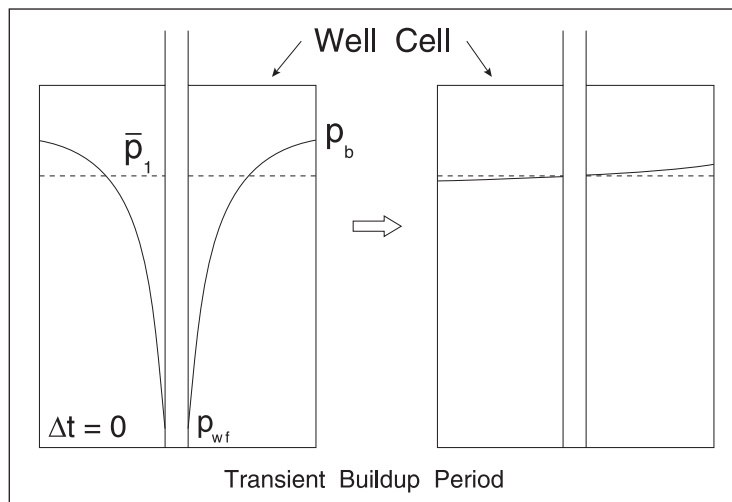


Fig. 14–19. Pressure distribution in well cell at the moment of shutin

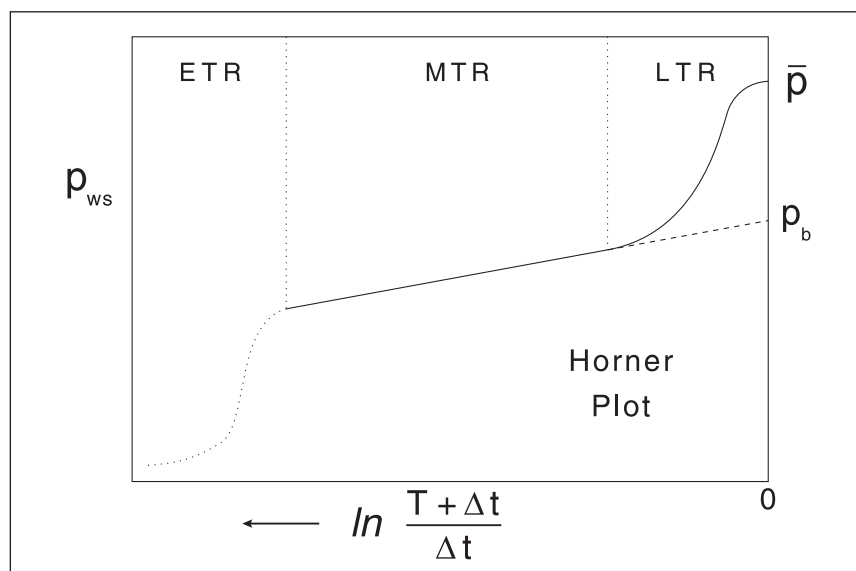


Fig. 14–20. Horner plot of an extended buildup in a compartmentalized reservoir

This corresponds to the depth of investigation traveling to the far boundary of the well cell a distance  $L_f$  away from the wellbore. After this period, the well becomes an observation point for the cell average pressure  $\bar{p}_1$  which is being recharged by support from the other cells in the system. The pressures in the cellular train after the well cell has essentially reached a uniform average pressure are illustrated in figure 14–21. The final equilibrium pressure when all the cells have come to the same level is denoted  $\bar{p}$  — the overall volume average pressure—defined by the equation

$$\bar{p} = \frac{\sum_{i=1}^{NC} V_i \bar{p}_i}{V_t} \quad (14-57)$$

where  $\bar{p}_i$ ,  $i = 1, \dots, NC$  are the individual cell average pressures at the moment of shut-in. In the late time region (LTR) indicated in figure 14–20, the cells are equalizing in pressure by cross flow and the response is governed by Eq. (14–50) where the forcing term is zero and the flow is driven by the imbalance in cell (initial build-up) pressures at  $\Delta t = \Delta t_{SSS}$ . The analytical solution shows that, towards the end of this extended buildup, the well cell pressure, which is being measured in the shut-in observation well, is following an exponential approach to equilibrium as illustrated in figure 14–22. Note that the Cartesian plot is the appropriate method of displaying these data since the compression of the time scale on a semilog graph has no relevance to the intercellular equilibration process controlled by the barrier strength. The final approach to equilibrium (EAR) follows the equation

$$\Delta p = ae^{-bt}$$

or

$$p_1 = \bar{p} - ae^{-t/\tau} \quad (14-58)$$



where  $\tau$  is an exponential time constant given by the relation

$$t_{Cr} = \frac{T\tau}{c_t V} \tag{14-59}$$

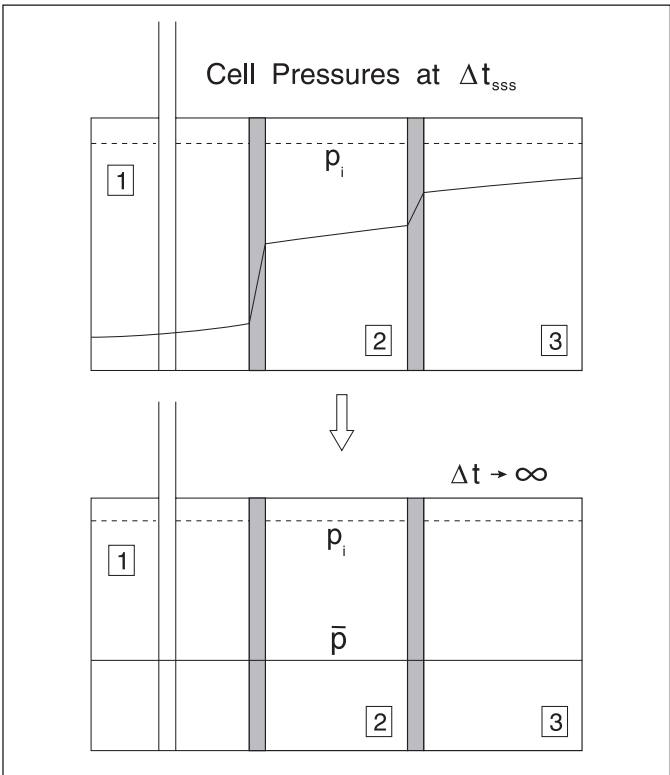


Fig. 14-21. Long-term equilibration between compartments by crossflow

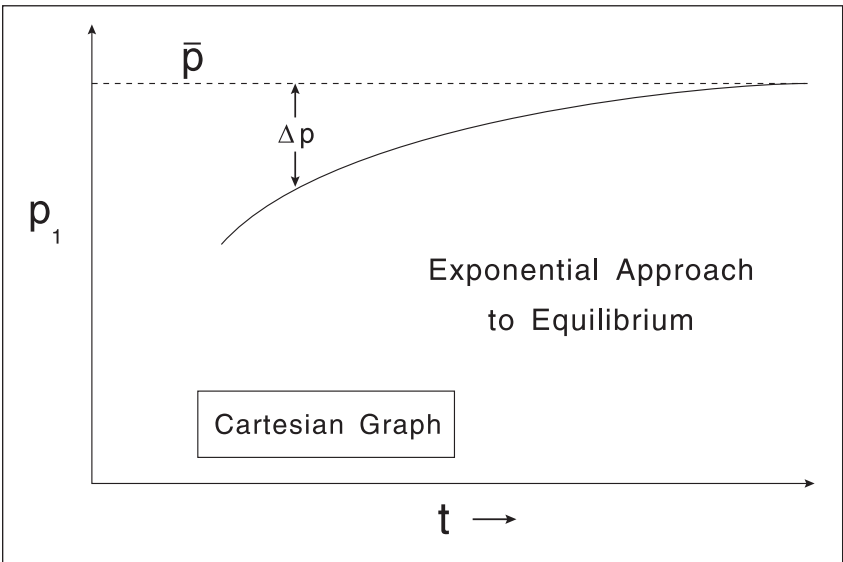


Fig. 14-22. Extended buildup showing exponential approach to equilibrium

Here,  $t_{Cr}$  is a dimensionless time constant based on barrier transmissibility and cell compressibility–volume product that characterizes the dynamics. It is interesting to observe that a plot of  $\ln \Delta p$  versus  $t$  will be a straight line of slope  $-\frac{1}{\tau}$  and intercept  $\ln a$  as shown in figure 14–23; this form of semilog graph was originally suggested by Muskat (in a quite different context). Note that this plot requires knowledge of  $\bar{p}$  in order to form  $\Delta p = \bar{p} - p_w = \bar{p} - p_1$  and is therefore not useful for extrapolating the pressure. This is best carried out on a Cartesian graph as illustrated in figure 14–24; here, three equally spaced points in time have been selected and the extrapolated pressure (asymptote of the exponential process) follows from the analytical formula

$$\bar{p} = \frac{p^1 p^2 - (p^3)^2}{p^1 + p^2 - 2p^3} \quad (14-60)$$

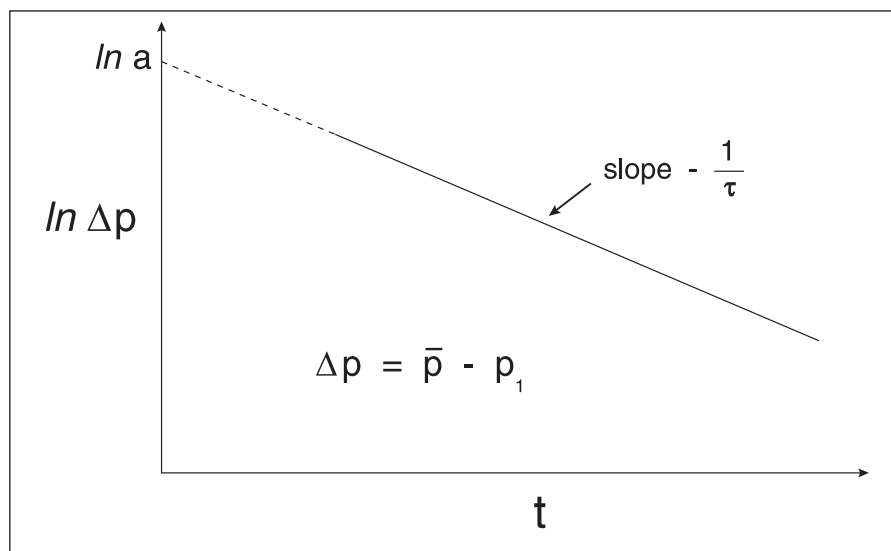


Fig. 14–23. Muskat form of semilog plot

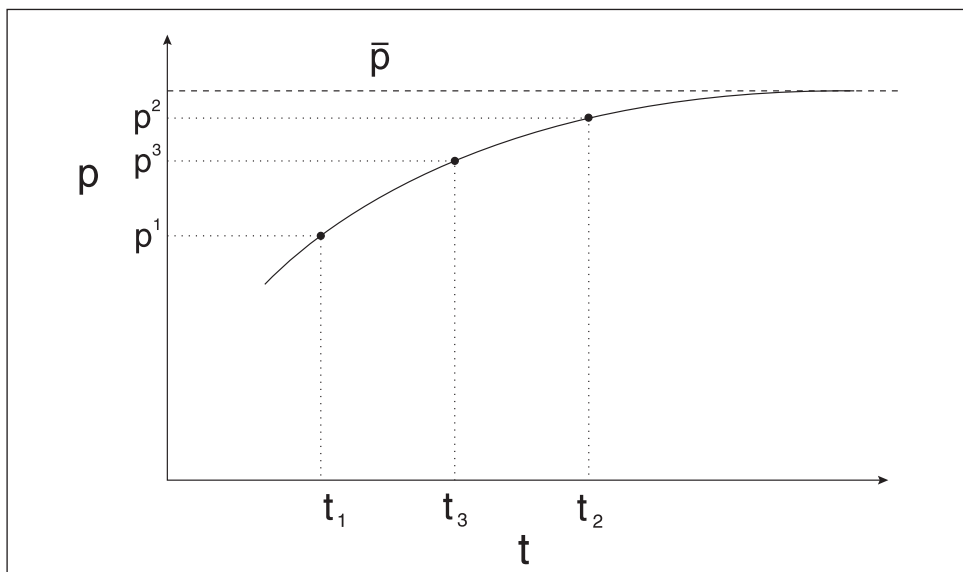


Fig. 14–24. Determination of average pressure on the Cartesian graph

Equation (14–60) is specific to an exponential form described by Eq. (14–58). In practice, it is better to employ nonlinear regression, e.g., the Levenberg–Marquardt algorithm, on a selection of data points in the exponential approach region as illustrated in figure 14–25; Eq. (14–58) is a three-parameter  $(\bar{p}, a, \tau)$  form and a least-squares objective function on  $p_w$  can be minimized to yield the three values one of which is the desired extrapolated pressure. This approach is very similar to the rectangular hyperbola method (RHM) proposed by Mead<sup>5</sup> and further investigated by Kabir.<sup>6</sup> However, in the present case there is rigorous theoretical support for the functional form (EAR) used in the fitting process, whereas the rectangular hyperbola is purely empirical. The technique also results in the characteristic time constant  $\tau$  from which it is possible to extract information on the ratio  $\frac{T}{c_t V}$  using Eq. (14–59).

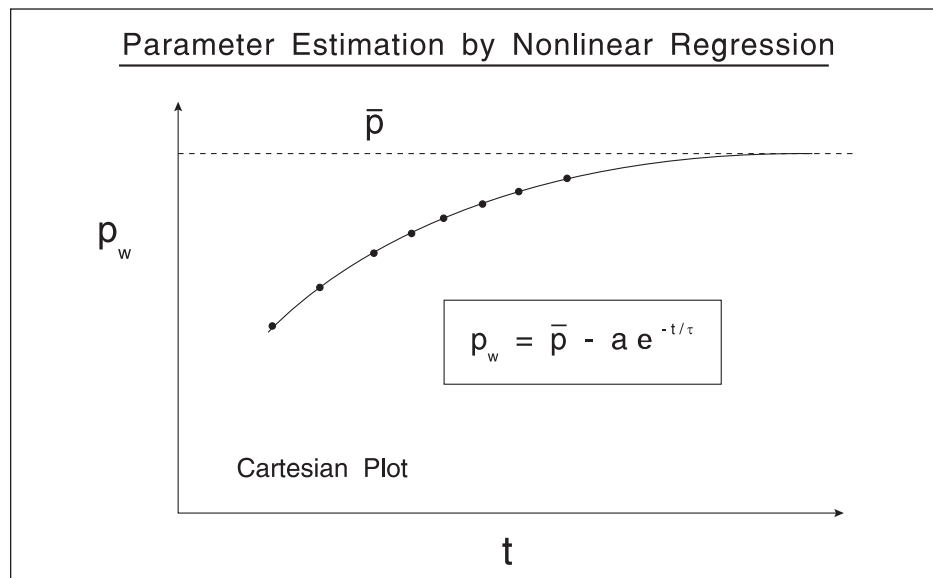


Fig. 14–25. Use of nonlinear regression to determine the total system average pressure

It is important to appreciate that, when the barrier strength is strong, i.e.,  $T$  is small, the duration of the buildup will be very long indeed. Conventional ideas based on formation permeability and well cell dimensions are not relevant to compartmentalized behavior which is controlled by cell volume and barrier strength.

## Average (steady-state) permeability of a cellular system

It is useful to derive an expression for the average permeability of a cellular system based on SS conditions as illustrated in figure 14–26; in this realization, a constant pressure  $p_o$  is imposed on the left face of cell 1 and a fixed pressure  $p_f$  is imposed on the right face of the last cell. This comprises a set of resistances in series, and SS flow through the system is described by the equation

$$p_o - p_f = \left( \frac{\mu L_1}{k_1 A_1} + \frac{1}{T_{12}} + \frac{\mu L_2}{k_2 A_2} + \frac{1}{T_{23}} + \frac{\mu L_3}{k_3 A_3} + \frac{1}{T_{34}} + \frac{\mu L_4}{k_4 A_4} \right) q \quad (14-61)$$

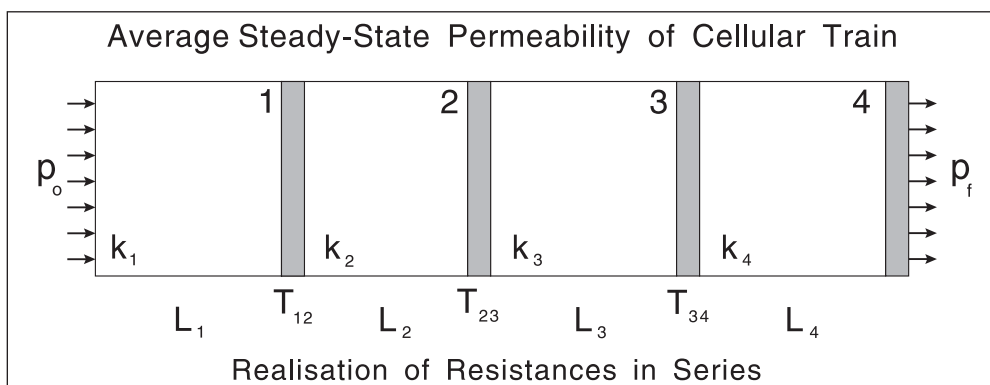


Fig. 14-26. Average permeability of a cellular train

Defining the average permeability as

$$p_o - p_f = \frac{\mu \sum L}{\bar{k}A} q \quad (14-62)$$

Gives, on comparing Eqs. (14-61) and (14-62),

$$\bar{k} = \frac{\sum L}{A} \left( \frac{1}{\frac{L_1}{k_1 A_1} + \frac{1}{T_{12}} + \frac{L_2}{k_2 A_2} + \frac{1}{T_{23}} + \frac{L_3}{k_3 A_3} + \frac{1}{T_{34}} + \frac{L_4}{k_4 A_4}} \right) \quad (14-63)$$

## Effective interblock transmissibility

The whole concept of the complex material balance was founded on high-permeability North Sea reservoirs which were compartmentalized by partially communicating faults. In such systems, the major areal and vertical pressure differences occur across semipermeable barriers. However, some areal pressure gradient will appear in the blocks themselves and it is useful to obtain at least an estimate of this effect. Two cells  $i$  and  $j$  separated by a tight zone of transmissibility  $T_{ij}$  are shown in figure 14-27; the intercell flow is given by

$$q_{j,i} = T_{i,j} (p_{j,m} - p_{i,m}) \quad (14-64)$$

where  $p_{j,m'}$  and  $p_{i,m}$  are the face pressures on either side of the barrier. Following the treatment given in the section “Linear Flow Theory,” the individual pressure drops may be written as follows:

$$1. \quad \bar{p}_j - p_{j,m'} = F_{j,m'} q_{j,i} \quad \text{where} \quad F_{j,m'} = \left( \frac{1 \mu L_2}{3 kA} \right)_{j,m'} \quad (14-65a)$$

$$2. \quad p_{j,m'} - p_{i,m} = \frac{1}{T_{i,j}} q_{j,i} \quad (14-65b)$$

$$3. \quad p_{i,m} - \bar{p}_i = F_{i,m} q_{j,i} \quad \text{where} \quad F_{i,m} = \left( \frac{1 \mu L_2}{3 kA} \right)_{i,m} \quad (14-65c)$$

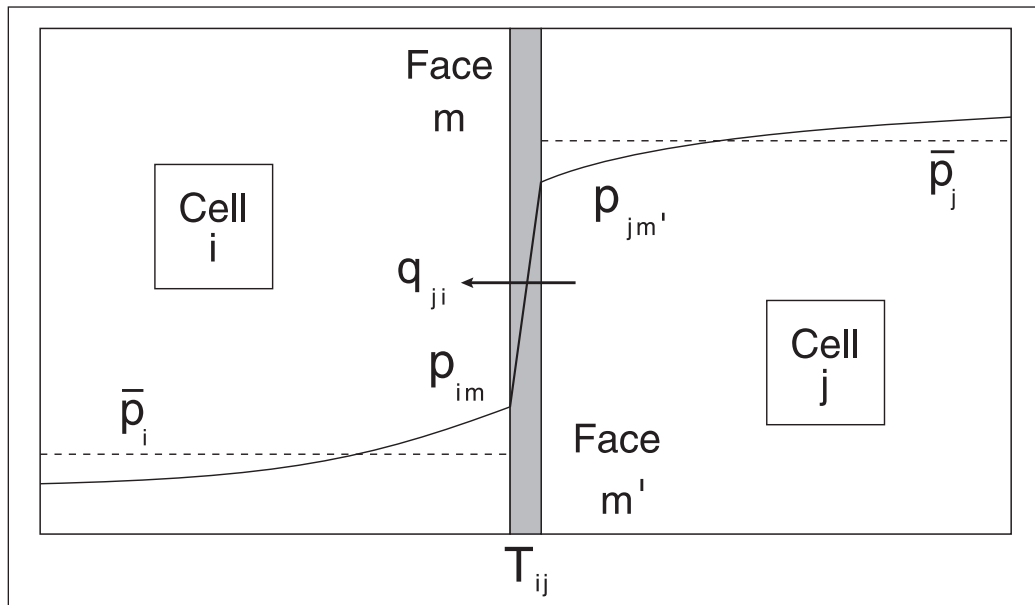


Fig. 14-27. Effective interblock transmissibility

The inverse transmissibility terms  $F$  are explained in the section “Linear Flow Theory” and allow for the pressure drop between the cell average pressure and the face boundary pressure; these depend naturally on the block permeabilities. Adding (14-65a), (14-65b), and (14-65c) gives

$$\bar{p}_j - \bar{p}_i = \left( F_{j,m'} + \frac{1}{T_{i,j}} + F_{i,m} \right) q_{j,i} \quad (14-66)$$

Hence, defining an effective interblock transmissibility  $T_{ij}^{eff}$  by the equation

$$q_{j,i} = T_{ij}^{eff} (\bar{p}_j - \bar{p}_i) \quad (14-67)$$

gives the result

$$\frac{1}{T_{i,j}^{\text{eff}}} = F_{j,m'} + \frac{1}{T_{i,j}} + F_{i,m}$$

i.e.,

$$T_{i,j}^{\text{eff}} = \frac{1}{F_{j,m'} + \frac{1}{T_{i,j}} + F_{i,m}} \quad (14-68)$$

This is a very useful result that allows the effect of cell internal flow resistance to be incorporated into an effective block transmissibility modeling the intrinsic barrier transmissibility  $T_{i,j}$  and the resistances  $F$  to flow across the blocks. The exact theory of cell resistance in the general case is fully developed in the section “Linear Flow Theory,” but this approximate method, in fact, gives excellent results and may be used to account for cell internal resistance in a very simple way. In all the previous results concerning time constants, the effective interblock resistance may be used to characterize the system.

## Apparent semi-steady-state of well cell alone

Returning to the three-cell problem discussed in the section “Three-cell Problem” it is interesting to observe the behavior when the barrier transmissibility becomes quite small; a trajectory for this case is shown in figure 14–28. For a certain period, it appears from the well block pressure that the cell is perfectly closed and the pressure is declining linearly with time at a rate given by

$$\frac{d\bar{p}_1}{dt} = - \frac{q^p}{(c_t V)_1} \quad (14-69)$$

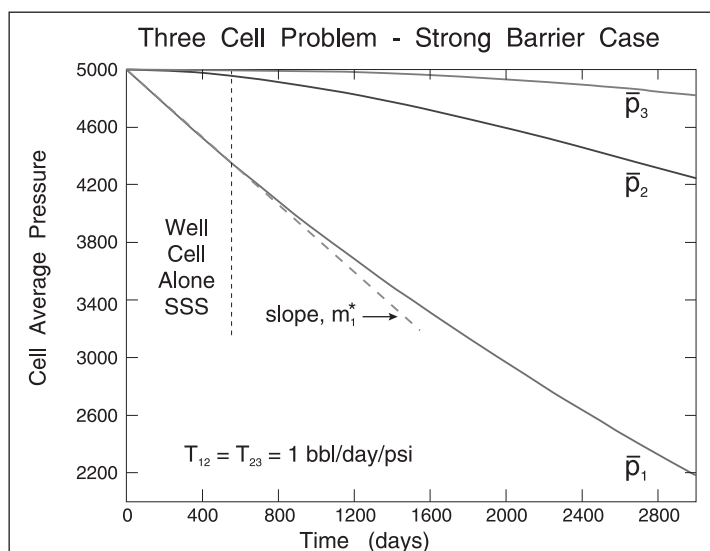


Fig. 14–28. Trajectory for three-cell problem with small interblock transmissibility

At early time, the support is negligible because the pressure difference across the barrier is not large enough to yield an appreciable cross flow; it therefore appears as if the well cell alone is acting as a closed system. As the pressure difference across the barrier increases, the support becomes substantial and the rate of change of the well cell pressure becomes less. At very late time, the total system joint SSS is attained. Thus, in an extended draw-down test, the size of the system appears larger, the longer the well is flowed, and support from compartments screened by tight zones and not penetrated by a well eventually becomes important. This type of behavior is particularly prevalent in gas reservoirs.

## Field Example

The first published application of the complex reservoir material balance model was a study of a terrace fault block system in the south flank of the Murchison field shown in figure 14–29. A geological study indicated a system of six communicating fault blocks as indicated in figure 14–30, where block D was identified to be in connection with the main field. The material balance model was matched to a variety of pressure data; the data from well M21 are shown in figure 14–31.

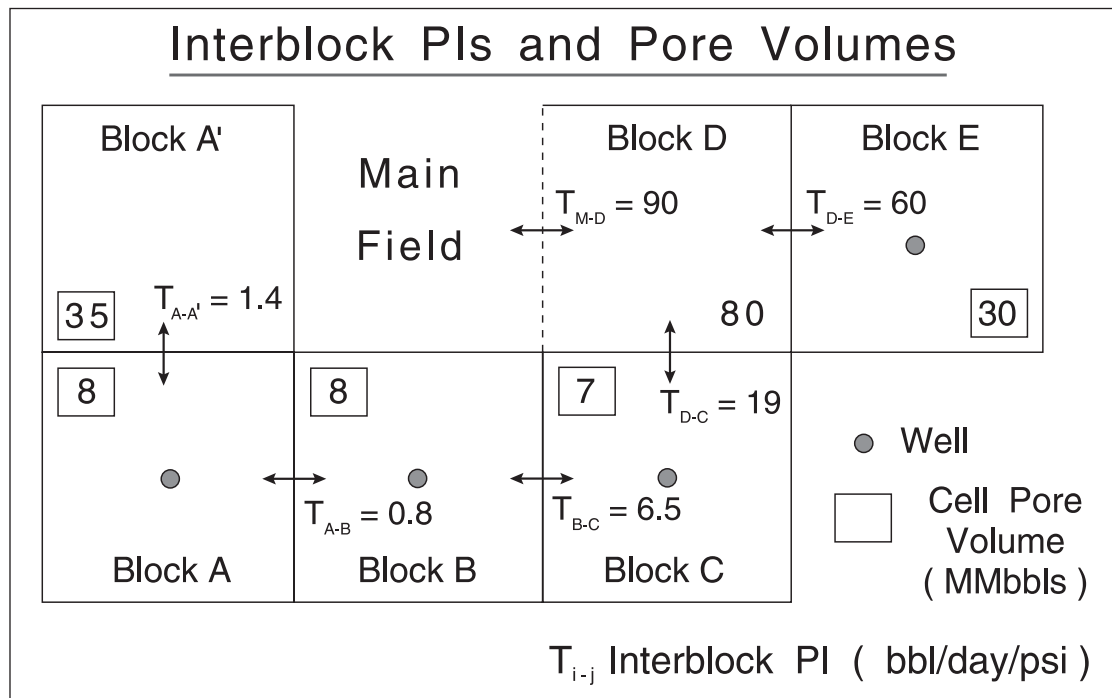
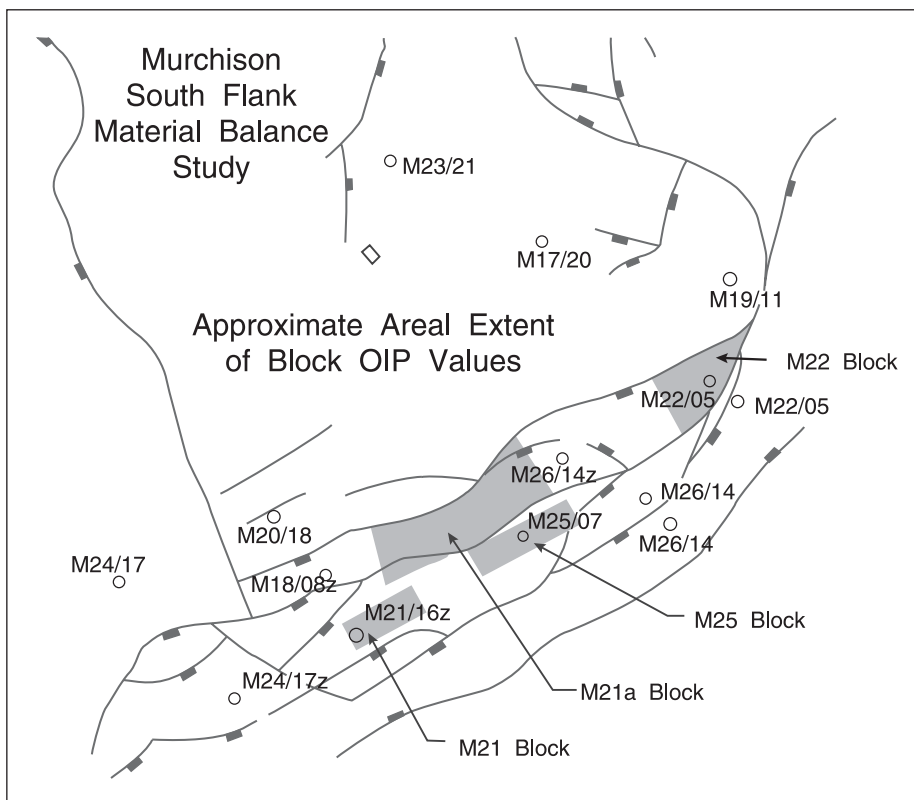
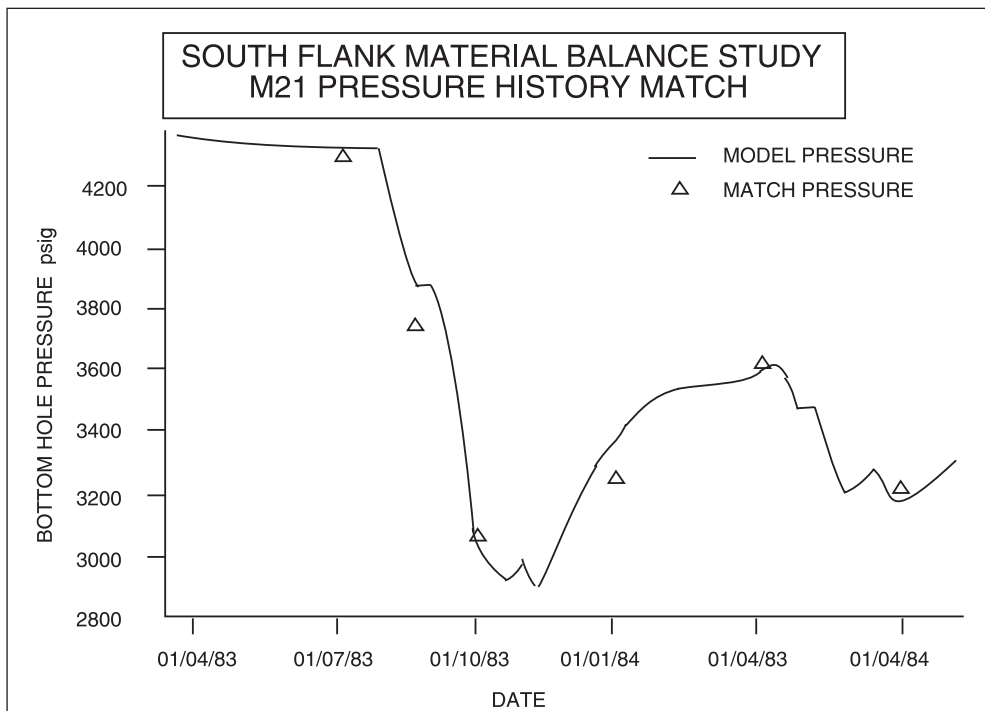


Fig. 14–29. Terrace fault block system of the Murchison south flank



**Fig. 14–30.** Pore volumes and interblock productivity indices (PIs) determined by matching



**Fig. 14–31.** History match for well M21



## Linear Flow Theory

In many reservoirs, it is possible to represent the material balance compartments by thin rectangular blocks illustrated diagrammatically in figure 14–32. Usually, the vertical thickness  $h$  of a cell is small compared to its areal extent; also the areal width  $L_1$  is frequently significantly less than the areal length  $L_2$ . For example, systems of down-thrown fault blocks or fluvial channel sands conform approximately to rectangular geometry. In such situations, linear flow takes place along the major axis of the sand body. The theory of linear SSS flow in rectangular geometry has been developed by Yaxley.<sup>7</sup>

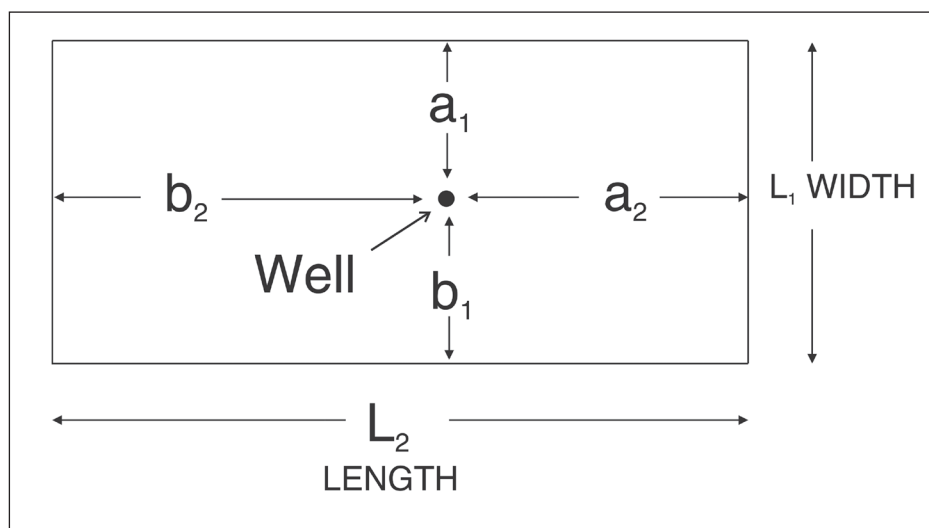


Fig. 14–32. Rectangular block geometry

It is useful first to consider a rectangular block with no-flow outer boundaries and a well as shown in figure 14–32. Suppose initially that the well production  $q^p$  is represented by a plane source normal to the linear flow direction. The closed rectangle is producing by SSS linear flow and a pressure distribution develops as shown in figure 14–33. The pressure at the plane source is denoted  $p_s$  and the average pressure in the cell is  $\bar{p}$ . It was shown by Yaxley that the difference between the average and source face pressures is given by

$$\bar{p} - p_s = \left( \frac{a_D^3}{3} + \frac{b_D^3}{3} \right) \frac{\mu L_2}{kA} q^p \quad (14-70)$$

where

$$a_D = \frac{a_2}{L_2} \quad b_D = \frac{b_2}{L_2} \quad \text{and} \quad A = L_1 h$$

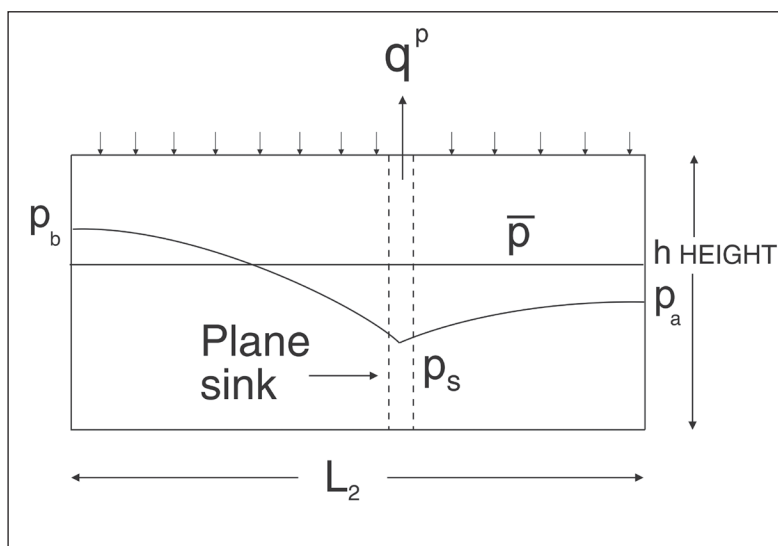


Fig. 14-33. Cell pressure distribution

For a well in the center of the rectangle ( $a_D = b_D = 0.5$ ), this reduces to

$$\bar{p} - p_s = \frac{1}{12} \cdot \frac{\mu L_2}{kA} q^p \tag{14-71}$$

Here,  $q^p$  is positive for production as usual.

Equation (14-70) accounts for SSS linear flow along the channel major axis to a plane sink. For an actual well, there is an additional pressure drop due to areal flow convergence as illustrated in figure 14-34. It was shown by Hantush<sup>8</sup> that this is given by

$$p_s - p_w = \frac{q^p \mu}{2\pi k h} \left( \ln \frac{L_1}{r_w 2\pi s \sin(\pi c_D)} + S \right) \tag{14-72}$$

where

$$c_D = \frac{\min(a_1, b_1)}{L_1}$$

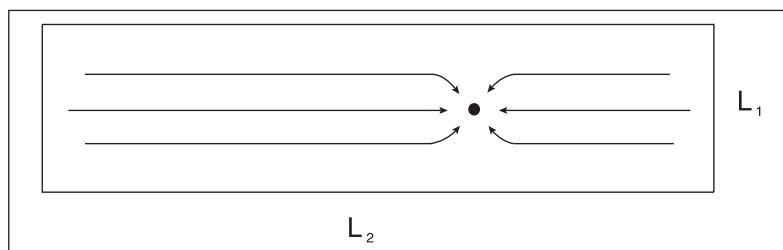


Fig. 14-34. Areal flow convergence

Hence, the total pressure drop is given by

$$\bar{p} - p_w = q^p \left( \left( \frac{a_D^3}{3} + \frac{b_D^3}{3} \right) \frac{\mu L_2}{kA} + \frac{\mu}{2\pi kh} \left( \ln \frac{L_1}{r_w 2\pi \sin(\pi c_D)} + S \right) \right) \quad (14-73)$$

where  $p_w$  is the well flowing bottom-hole pressure and  $S$  is the conventional well skin factor. Defining

$$G = \left( \frac{a_D^3}{3} + \frac{b_D^3}{3} \right) \frac{\mu L_2}{kA} + \frac{\mu}{2\pi kh} \left( \ln \frac{L_1}{r_w 2\pi \sin(\pi c_D)} + S \right) \quad (14-74)$$

this may be written as

$$\bar{p} - p_w = Gq^p \quad (14-75)$$

The quantity  $G$  is the reciprocal of the conventional well PI,  $J_{SSS}$ , based on drainage area average pressure. The PI is usually defined in terms of the Dietz shape factor  $C_A$ :

$$J_{SSS} = \frac{2\pi kh}{\mu \left( \frac{1}{2} \ln \frac{4\bar{A}}{\gamma C_A r_w^2} + S \right)} \quad (14-76)$$

Equating  $G$  and  $1/J_{SSS}$  from (14-74) and (14-76), respectively, and solving for  $C_A$  result in

$$C_A = \frac{4\bar{A}}{\gamma r_w^2 \exp \left( \frac{4\pi L_2}{L_1} \left( \frac{a_D^3}{3} + \frac{b_D^3}{3} \right) + 2 \ln \frac{L_1}{r_w 2\pi \sin(\pi c_D)} \right)} \quad (14-77)$$

It was shown by Yaxley that this equation gives remarkably accurate values for the Dietz shape factor for closed rectangles with any well position.

The SSS linear flow analysis of a rectangular cell can be extended to the case where flow occurs over the end faces. This is illustrated in figure 14-35, where cell input flows  $q_a$  and  $q_b$  are specified. The pressure distribution in the cell is affected by the magnitude of these inputs from adjacent blocks. In this situation, a SSS linear flow analysis yields the result

$$\bar{p} - p_w = G_a q_a + G_b q_b + G_p q^p \quad (2-78)$$

where

$$G_a = \frac{\mu L_2}{kA} \left( \frac{a_D^2}{2} - \frac{a_D^3}{3} - \frac{b_D^3}{3} \right)$$

$$G_b = \frac{\mu L_2}{kA} \left( \frac{b_D^2}{2} - \frac{a_D^3}{3} - \frac{b_D^3}{3} \right)$$

and

$$G_p = \left( \frac{a_D^3}{3} + \frac{b_D^3}{3} \right) \frac{\mu L_2}{kA} + \frac{\mu}{2\pi kh} \left( \ln \frac{L_1}{r_w} - 2\pi \sin(\pi c_D) + S \right)$$

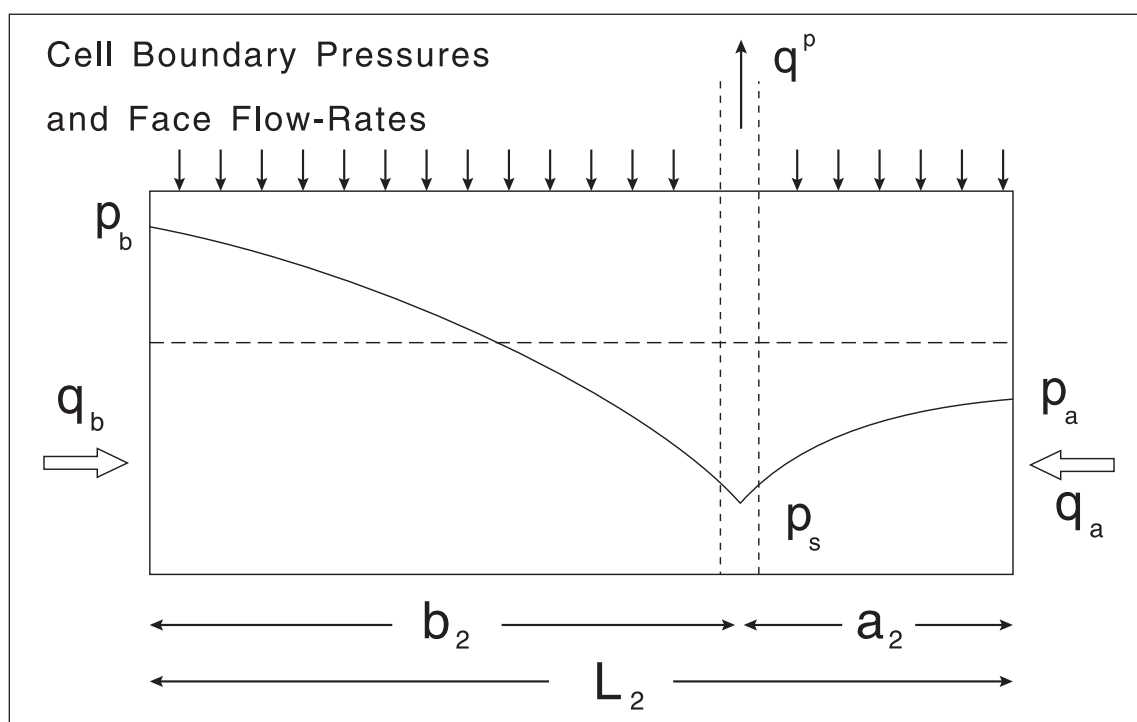


Fig. 14-35. Cell face flows

The quantities  $G_a$ ,  $G_b$ , and  $G_p$  are termed *partial PIs* and Eq. (14-78) is the generalized productivity expression for a rectangular cell. In Eq. (14-78),  $q_a$  and  $q_b$  are positive for input into the cell and the well rate is positive for production.

The observed pressure difference ( $\bar{p} - p_w$ ) is seen to be the result of superposition of the effect of three separate flows, viz.,  $q_a$ ,  $q_b$ , and  $q^p$ . The SSS pressure distribution in the cell is affected by the magnitude and direction of the inputs from adjacent blocks as well as by the production rate. Generalized inflow theory represented by Eq. (14-78) shows how the bottom-hole flowing pressure  $p_w$  is related to the cell average pressure (which is obtained by the complex material balance) and the cell input or output flows.

Equation (14–78) has been derived for the one-dimensional case where the inputs  $q_a$  and  $q_b$  occur over the end faces normal to the major axis. However, if inputs also occur over the other vertical faces (denoted  $c$  and  $d$ ) of the cell, then the superposition principle shows that the additional terms can be added to (14–78) to cover the general case, i.e.,

$$\bar{p} - p_w = G_a q_a + G_b q_b + G_c q_c + G_d q_d + G_p q^p \quad (14-79)$$

where  $G_c$  and  $G_d$  are analogous to  $G_a$  and  $G_b$  but with the cell dimensions reversed. If any cell face is a sealing boundary, the corresponding term is absent in (14–79).

Equation (14–78) was derived from SSS linear flow theory modified to account for specified fluxes over the end faces. Thus, the net production  $q^p - q_a - q_b$  is sustained by uniform expansion of the cell contents. However, if there is uniform flow over the top or bottom faces of the cell—indicated by the arrows in figure 14–35—the pressure distribution has exactly the same form and Eq. (14–78) or (14–79) still applies. The shape of the pressure distribution is the same whether uniform depletion or support is occurring. Hence, the lumped parameter model of the cell inflow behavior is quite general. It was pointed out by Yaxley that linear flow theory, corrected for flow convergence into a well, has much wider validity than the usual radial flow expression for a well in the center of a circle. Note that Eq. (14–79) gives excellent results for a well in the center of a square cell although it was conceived for rectangular blocks.

Well inflow theory is concerned with the relation between block average pressure and the bottom-hole flowing pressure of a well in the block. The problem of relating simulator block pressures to well flowing pressures, which of course are easy to measure, has long been recognized. However, it is also possible to relate the average pressure  $\bar{p}$  to the boundary pressures at the cell faces. This is also illustrated in figure 14–35 where the end face pressures are denoted  $p_a$  and  $p_b$ , respectively. Again, from the result of a SSS linear flow analysis it can be shown that

$$p_a - \bar{p} = F_{aa} q_a + F_{ab} q_b + F_{ap} q^p \quad (14-80)$$

where

$$F_{aa} = \frac{\mu L_2}{kA} \cdot \frac{1}{3}$$

$$F_{ab} = \frac{\mu L_2}{kA} \cdot \frac{1}{6}$$

and

$$F_{ap} = \frac{\mu L_2}{kA} \left( \frac{a_D^2}{2} - \frac{a_D^3}{3} - \frac{b_D^3}{3} \right)$$

The quantities  $F_{aa}$ ,  $F_{ab}$ , and  $F_{ap}$  will be termed *partial inverse transmissibility indices*; again  $q_a$  and  $q_b$  are positive for input.

Similarly, for the other boundary pressure  $p_b$

$$p_b - \bar{p} = F_{ba}q_a + F_{bb}q_b + F_{bp}q^p \quad (14-81)$$

where

$$F_{bb} = \frac{\mu L_2}{kA} \cdot \frac{1}{3}$$

$$F_{ba} = \frac{\mu L_2}{kA} \cdot \frac{1}{6}$$

and

$$F_{bp} = \frac{\mu L_2}{kA} \left( \frac{b_D^2}{2} - \frac{a_D^3}{3} - \frac{b_D^3}{3} \right)$$

Equations (14-80) and (14-81) show how the face pressures  $p_a$  and  $p_b$  are related to the cell average pressures  $\bar{p}$  given by the material balance. These equations are important since they allow for the flow resistance of the cell itself. Correspondingly, the equations for flow between cells, based on the interblock transmissibility  $T$ , should be written in terms of face pressures rather than cell average pressures. Note that Eqs. (14-79)–(14-81) represent linear algebraic equations between pressures and flows since the partial indices are constants dependent only on cell dimensions and properties ( $k$  and  $\mu$ ).

Equations (14-80) and (14-81) are lumped parameter expressions for the cell boundary pressures based on SSS linear flow analysis of a rectangular block. Again, the result is valid where uniform support flow occurs over the top or bottom face of the cell. In the two-dimensional case, the boundary pressures at faces  $a$  and  $b$  are not affected by transverse flow at  $c$  and  $d$ : hence, cross terms need not be included.

In figure 14-36, two adjacent cells  $i$  and  $j$  are shown with juxtaposed face pressures  $p_{i,m}$  and  $p_{j,m}$ . The flow between cells  $i$  and  $j$  is now given by the expression

$$q_{i,j} = T_{i,j}(p_{i,m} - p_{j,m}) \quad (14-82)$$

where

$$q_{i,j} = q_{i,m} = q_{j,m}$$

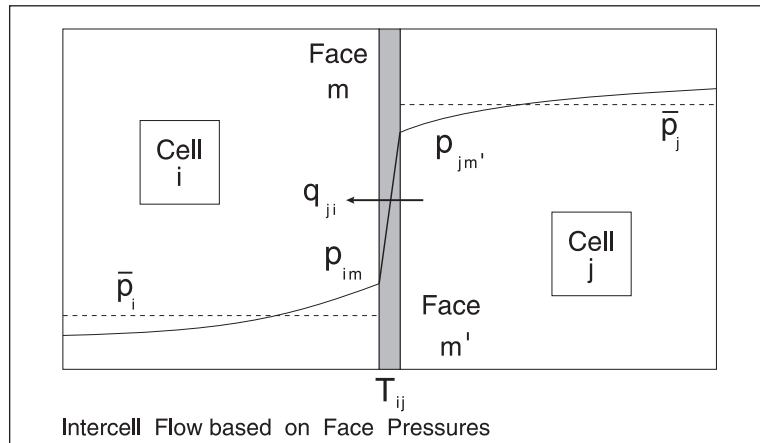


Fig. 14–36. Adjacent cells with juxtaposed face pressures

### Generalized complex material balance

In the simple treatment of the material balance given in the section “Complex Reservoirs,” the flow between adjacent cells was modeled on the basis of the cell average pressures. Now it is possible to write a more complete material balance model by incorporating the cell face pressures into the formulation for the vertical interfaces. For intercell flow across the top or bottom faces, the cell average pressure is still used; because the blocks are thin, it is not necessary to include vertical flow resistance within the cell itself. In order to demonstrate how the material balance system is set up, it is useful to consider the four-cell system considered in the section “Complex Reservoirs” and shown again in figure 14–37. The face pressures are now written in subscripted form, i.e.,  $p_{il}$  where  $i$  is the cell number and  $l$  is the face number ( $l = 1-4$ ) with the commas dropped for convenience. The material balance for cell 1 becomes

$$(c_t V)_1 \frac{d\bar{p}_1}{dt} = T_{13}(p_{34} - p_{12}) - q_{11}^p \tag{14-83}$$

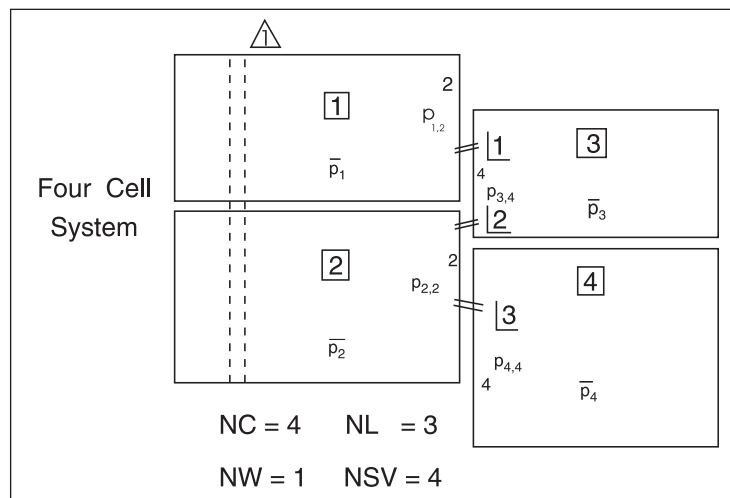


Fig. 14–37. Four-cell system with the inclusion of face pressures

In this equation, cell face pressures  $p_{12}$  and  $p_{34}$  have been used to define the intercell flow, i.e.,

$$q_{13} = T_{13}(p_{12} - p_{34}) \quad (14-84)$$

Here, the intercell flow has been subscripted  $q_{ij}$  where  $i$  and  $j$  are the respective cell numbers of the link. The well production terms are subscripted  $q_{ki}^p$  where  $k$  is the well number and  $i$  is the cell number. Equation (14-80) may now be used to obtain the expression for the face 2 pressure of cell 1, i.e.,  $p_{12}$ ; this takes the form

$$0 = \bar{p} - p_{12} + F_{122}T_{13}(p_{34} - p_{12}) + F_{12}^p q_{11}^p \quad (14-85)$$

Here, the flow across face 2, i.e.,  $q_{13}$ , has been written as  $T_{13}(p_{34} - p_{12})$ . The quantity  $F_{122}$  is the partial inverse transmissibility index for face 2 (corresponding to  $F_{aa}$  for cell 1 in (14-80)) and  $F_{12}^p$  is the partial inverse transmissibility index for the effect of well production. There is no term for face 4 ( $F_{ab}$ ) since this is a sealing boundary. Equation (14-85) is a linear algebraic equation relating the pressures and well flows.

Proceeding in a similar fashion for the other cells, the material balance equations take the following form:

Cell 1:

$$(c_t V)_1 \frac{d\bar{p}_1}{dt} = T_{13}(p_{34} - p_{12}) - q_{11}^p$$

$$0 = \bar{p} - p_{12} + F_{122}T_{13}(p_{34} - p_{12}) + F_{12}^p q_{11}^p$$

Cell 2:

$$(c_t V)_2 \frac{d\bar{p}_2}{dt} = T_{23}(p_{34} - p_{22}) + T_{24}(p_{44} - p_{22}) - q_{12}^p$$

$$0 = \bar{p} - p_{22} + F_{222}(T_{23}(p_{34} - p_{22})) + (T_{24}(p_{44} - p_{22})) + F_{22}^p q_{12}^p$$

Cell 3:

$$(c_t V)_3 \frac{d\bar{p}_3}{dt} = T_{13}(p_{12} - p_{34}) + T_{23}(p_{22} - p_{34})$$

$$0 = \bar{p}_3 - p_{34} + F_{344}(T_{13}(p_{12} - p_{34})) + (T_{23}(p_{22} - p_{34}))$$



Cell 4:

$$(c_t V)_4 \frac{d\bar{p}_4}{dt} = T_{24}(p_{22} - p_{44})$$

$$0 = \bar{p}_4 - p_{44} + F_{444} T_{24}(p_{22} - p_{44})$$

This represents a simultaneous system of linear algebraic and ordinary differential equations. In the present example, each cell has only one active face and there is one algebraic equation for each cell determining the active face pressure. In other examples, there may be more or less than one algebraic equation for a given cell. Obviously, the number of additional algebraic equations must equal the number of face pressures involved.

In addition to these linear algebraic equations representing the lumped parameter relations between average and boundary pressures and well flows, it is also necessary to consider the well inflow relations. For the example problem, there is only one well which intersects two blocks. The cell 1 inflow relation takes the form

$$0 = p_{1,w} - \bar{p}_1 + G_{12} T_{12}(p_{34} - p_{12}) + G_1^p q_{11}^p \quad (14-86a)$$

while for cell 2 the analogous expression is

$$0 = p_{1,w} - \bar{p}_2 + G_{22}(T_{23}(p_{34} - p_{22})) + (T_{24}(p_{44} - p_{22})) + G_2^p q_{12}^p \quad (14-86b)$$

In addition, the well layer rates must sum to the specified total rate  $q_1^p$ ; thus

$$0 = q_{11}^p + q_{12}^p - q_1^p \quad (14-86c)$$

These three linear algebraic equations determine the well flowing bottom-hole pressure, i.e.,  $p_{1,w}$ , and the allocation of the total rate, i.e.,  $q_1^p$ , between the blocks intersected by the well. This is a generalized form of the simple well inflow model developed in the section "Complex Reservoirs," which allows for the effect of intercell flows on well inflow.

The complex material balance may be put in mathematical form by defining the state vector  $\mathbf{x}$  and the forcing vector  $\mathbf{u}$  as before, i.e.,

$$\mathbf{x} = (\bar{p}_1; \bar{p}_2; \bar{p}_3; \bar{p}_4)^T \quad (\text{NSV} \times 1)$$

and

$$\mathbf{u} = (q_1^p)^T \quad (\text{NFV} \times 1)$$

and a subsidiary variable vector  $y$  defined as

$$\mathbf{y} = (p_{12}; p_{22}; p_{34}; p_{44}; p_{1,w}; q_{11}^p; q_{12}^q)^T$$

which contains NSUBV elements. The subsidiary variables are the cell face pressures, the well bottom-hole flowing pressure, and the well/cell production rates. The differential algebraic system may be written concisely as

$$\dot{\mathbf{x}} = \mathbf{Ax} + \mathbf{By} + \mathbf{Cu} \quad (14-87a)$$

$$0 = \mathbf{Dx} + \mathbf{Ey} + \mathbf{Fu} \quad (14-87b)$$

In the present example, there are four differential equations and four state variables (the cell average pressures) and seven algebraic equations and seven subsidiary variables.

The linear algebraic system (14-87b) can be formally solved for the subsidiary variables in terms of the state and forcing variables, i.e., Eq. (14-87b) can be written as

$$\mathbf{y} = -\mathbf{E}^{-1}\mathbf{Dx} - \mathbf{E}^{-1}\mathbf{Fu} \quad (14-87c)$$

which may be substituted into (14-87a) giving

$$\dot{\mathbf{x}} = \mathbf{Ax} - \mathbf{BE}^{-1}\mathbf{Dx} - \mathbf{BE}^{-1}\mathbf{Fu} + \mathbf{Cu}$$

i.e.,

$$\dot{\mathbf{x}} = (\mathbf{A} - \mathbf{BE}^{-1}\mathbf{D})\mathbf{x} + (\mathbf{C} - \mathbf{BE}^{-1}\mathbf{F})\mathbf{u}$$

or

$$\dot{\mathbf{x}} = \mathbf{A}'\mathbf{x} + \mathbf{C}'\mathbf{u} \quad (14-88)$$

where

$$\mathbf{A}' = \mathbf{A} - \mathbf{BE}^{-1}\mathbf{D} \quad \text{and} \quad \mathbf{C}' = \mathbf{C} - \mathbf{BE}^{-1}\mathbf{F}$$

provided the inverse matrix  $\mathbf{E}^{-1}$  exists. Thus, the simultaneous differential-algebraic system (14-87 a, b, and c) can be transformed into an equivalent differential system (14-88) involving only state and forcing variables. The system (14-88) may be solved by analytic or numerical methods as discussed previously. There is no problem, in fact, to handle mixed differential and algebraic systems especially when the latter are linear.

The dimensions of the system matrices A, B, C, D, E, and F are as follows:

$$\mathbf{A} = (\text{NSV} \times \text{NSV}) \quad \mathbf{B} = (\text{NSV} \times \text{NSUBV}) \quad \mathbf{C} = (\text{NSV} \times \text{NFV})$$

$$\mathbf{D} = (\text{NSUBV} \times \text{NSV}) \quad \mathbf{E} = (\text{NSUBV} \times \text{NSUBV}) \quad \mathbf{F} = (\text{NSUBV} \times \text{NFV})$$

and 
$$\mathbf{A}' = (\text{NSV} \times \text{NSV}) \quad \mathbf{C}' = (\text{NSV} \times \text{NFV})$$

For the present example NSV = 4, NSUBV = 7, and NFV = 1. It is also of interest to compute the intercell flows, which in the present example are given by

$$q_{13} = T_{13}(p_{12} - p_{34})$$

$$q_{23} = T_{23}(p_{22} - p_{34})$$

and 
$$q_{24} = T_{24}(p_{22} - p_{44})$$

In general form, this may be written as

$$\mathbf{z} = \mathbf{Gx} + \mathbf{Hy} \tag{14-89}$$

where z is the vector of intercell flows, i.e.,

$$\mathbf{z} = (q_{13} ; q_{23} ; q_{24})^T \quad \text{NL} \times 1$$

and G and H are (NL × NSV) and (NL × NSUBV) sparse output matrices whose elements depend on the transmissibilities  $T_{ij}$ .

In this form, the material balance model computes three distinct types of pressure information illustrated in figure 14–38; these are

- cell average pressures  $\bar{p}$ ,
- cell boundary pressures  $p_b$ , and
- well bottom-hole flowing pressures  $p_w$ .

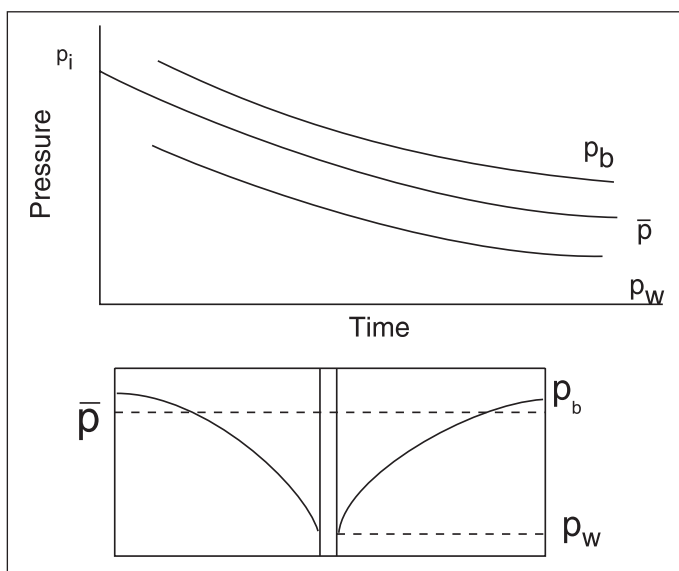


Fig. 14–38. Categories of pressure information

The cell average pressure  $\bar{p}$  is used to match direct observations of block pressures from WFT data. Since the extrapolated pressure from a buildup or a falloff corresponds to a cell boundary pressure  $p_b$ , well test pressures can be matched to the predicted cell face pressures. Alternatively, if build-up or fall-off data have been converted to cell average pressure  $\bar{p}$  using the Matthews, Brons and Hazebroek (MBH) correction, then well test results can be matched directly to the state variables. Finally, the model well bottom-hole flowing pressures  $p_w$  can be matched to actual measurements in flowing wells provided any transient effects have been corrected. This ability to predict all these pressure quantities is an important feature in the history matching process.

The formulation of the material balance for rectangular blocks allows only one well in a given cell; this can be either an injection or a production well. In the original conception of the complex material balance, the cell boundaries were identified with physical semipermeable barriers, either horizontal or vertical. However, when a physically homogeneous block contains more than one well, it is necessary to further subdivide it.

This is illustrated in figure 14–39 where a fault block containing two wells—perhaps a producer and an injector—is shown. In this case, the block is divided into two cells with a false barrier of high transmissibility located at the link. This effectively maintains the pressure continuously across the cell interface. The effect of employing virtual barriers to subdivide physical blocks is shown in figures 14–40a and b; obviously, areal reservoir pressure distributions are modeled with greater accuracy.

Cell boundaries can be classified into three categories:

- a) No flow:  $T_{i,j} = 0$   
e.g., sealing fault, reservoir limit, or sand pinchout;
- b) Semipermeable barrier:  $T_{i,j}$  small,  
e.g., partially communicating fault, tight zone, or an impermeable barrier with a window;
- c) Virtual cell boundary:  $T_{i,j}$  large.

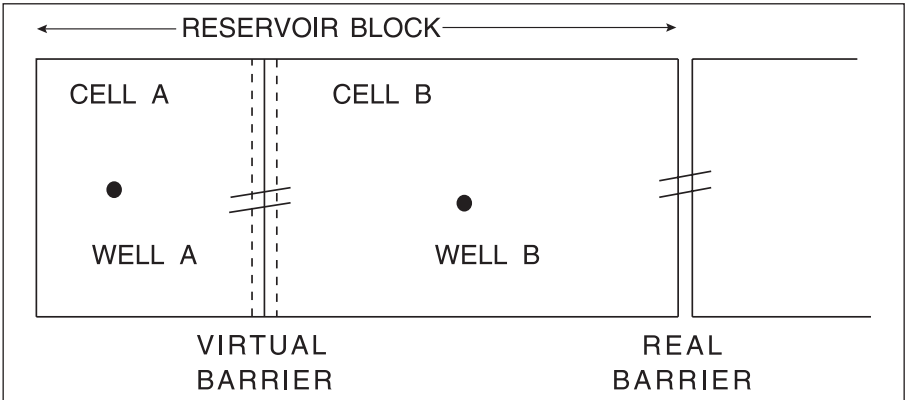


Fig. 14-39. Virtual barriers

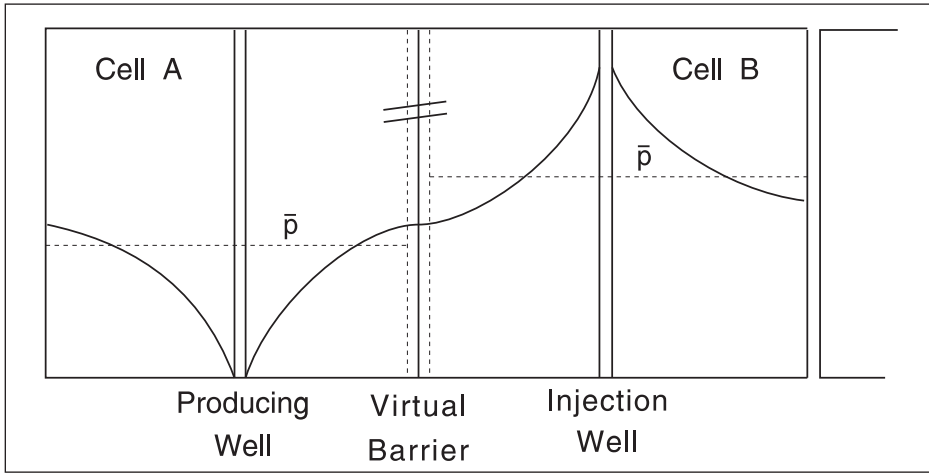
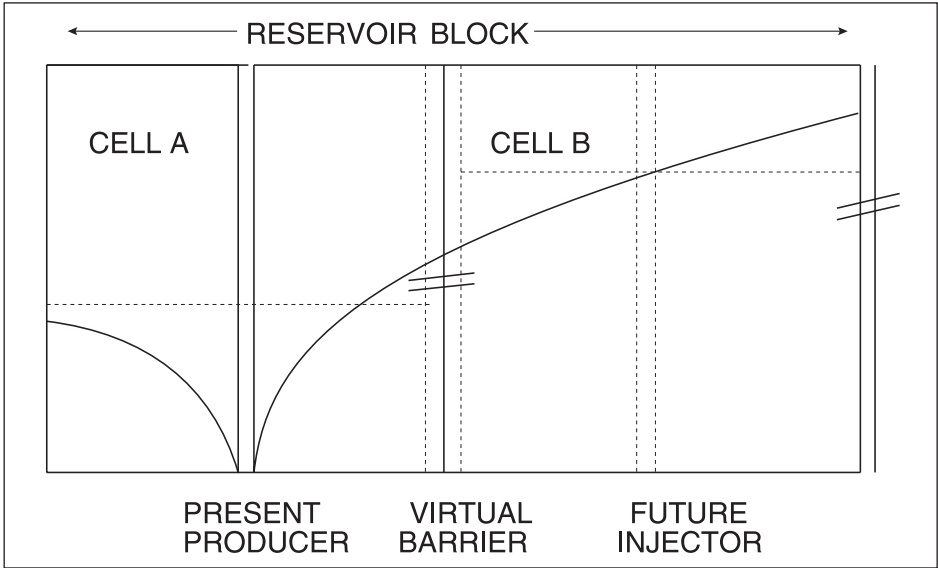
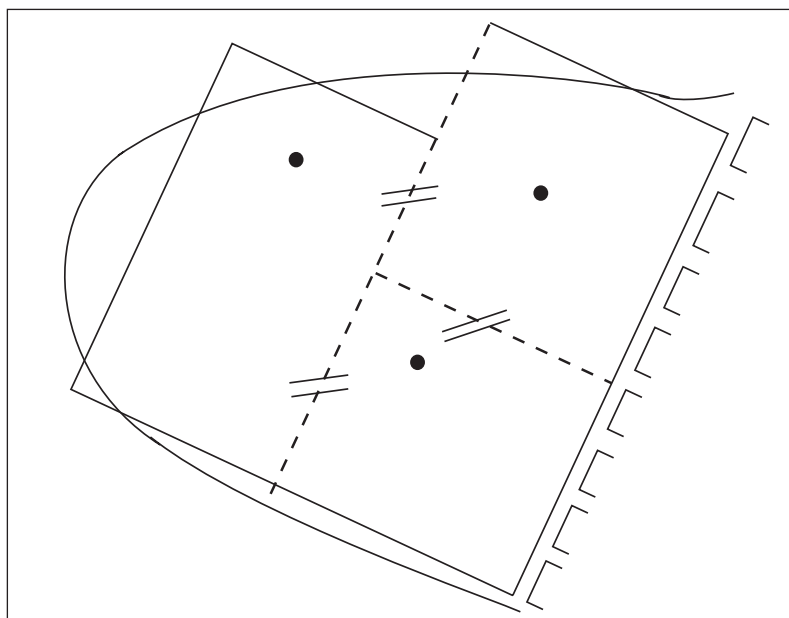


Fig. 14-40a and b. Block containing one producer and one injector

The virtual cell boundary is a synthetic device that allows the material balance model to better represent the areal pressure distribution. This introduces a finite-element character into the model where the internal pressure distribution within each cell is modeled by a lumped parameter (integral) approximation of considerable sophistication. Each well is associated with its own region of influence, i.e., drainage area. The dimensionality of the model, that is the number of cells, can be adjusted to suit the observed pressure variation.

The optimum placement of synthetic cell interfaces is illustrated in figure 14–41, where three producers are located in the same fault block. The Dietz concept of drainage areas has been used to define the best position of cell boundaries: this fixes the cell dimensions and the well position within it. The well test permeability and skin for the well located in the cell will be used in the calculation of the partial inverse productivity and transmissibility indices. In this situation of producers, only the virtual cell boundaries should coincide as far as possible with joint SSS virtual no-flow boundaries.



**Fig. 14–41.** Three producers in the same fault block

## Automatic Matching

In the simulation problem, the cell parameters, i.e., the volumes  $V_i$  and interblock transmissibilities  $T_{i,j}$ , are assumed known. However, the objective of a material balance study is, of course, to aid the identification of these quantities, and the question of parameter estimation is important. In essence, measurements of pressure are made and values of the parameters are sought that match the model predictions to the field data. The vector of unknowns which are to be fixed by nonlinear regression is denoted  $a$ ; here,  $a$  is an  $(NUP \times 1)$  vector comprising a user-defined selection of  $V_i$  and  $T_{i,j}$  values. For example, the volumes may be fixed from seismic maps, and the objective is to determine interblock transmissibilities. Alternatively, a mixture of

volumes and transmissibilities may be designated as matching variables. Cell compressibilities and well cell PIs are considered to be known in the material balance problem. Needless to say, this process is fraught with difficulty, and a considerable problem of lack of uniqueness is always present. The search process is conditional in the sense that other information has to be respected; in particular, the volumes of the compartments will be constrained by the seismic and log data. The lumped parameter formulation of the cell and well models allows the prediction of the three main types of pressure, i.e.,

- cell average pressure  $\bar{p}_i$ ,
- cell boundary pressure  $p_{b,i}$ , and
- well bottom-hole flowing pressure  $p_{k,w}$ .

In the history-matching process, it is common to have a variety of pressure measurements from WFT surveys and well tests carried out at different times and locations as illustrated in figure 14–42 for a three-cell two-well system. The material balance program has access to a measured pressure database, which comprises for each well

- pressure build-up or fall-off data,
- WFT surveys, and
- flowing bottom-hole pressure measurements.

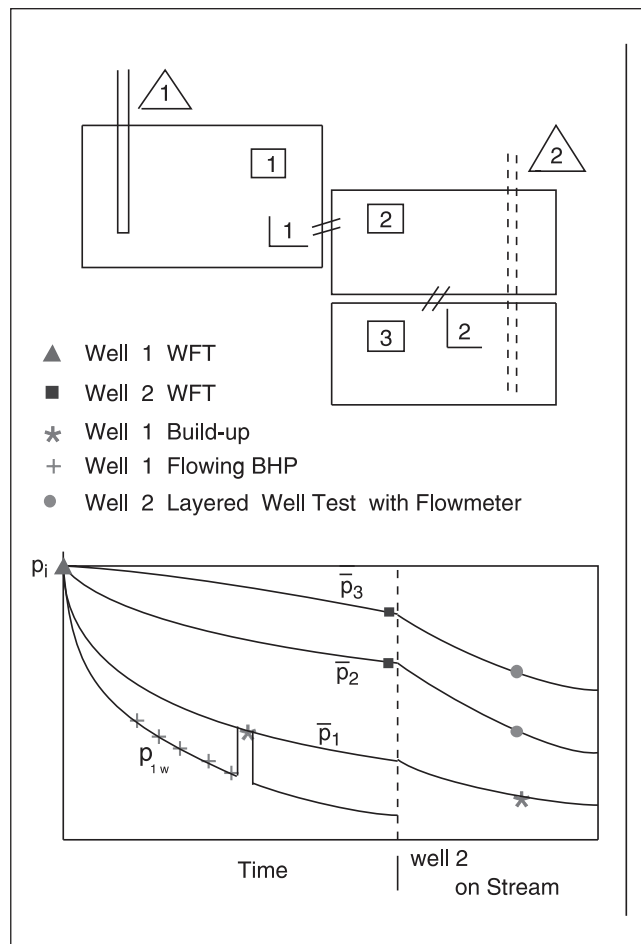


Fig. 14–42. Categories of pressure measurement

In conjunction with the measured pressure information, there is also a database of measured rate data comprising for each well

- complete rate history of production and/or injection and
- production logging surveys.

It is assumed that the skin factors implicit in the well cell PIs have been already adjusted to match flow distributions from PLT surveys. The matching of differential layer pressure depletion by a material balance approach is valid only if the model reproduces the actual flow division in the well. The pressure and rate database is a subset of a complete reservoir monitoring system. In general, a set of measured pressure data is available for matching, corresponding to points on the general Cartesian plot for cell  $i$  ( $i = 1, NC$ ) as illustrated in figure 14–43. A general pressure observation may be denoted simply as  $p_{i,k,t}^{\text{obs}}(T_m)$  where  $i$  refers to the cell,  $k$  to the well, and  $t$  to the type of pressure, i.e., average or boundary;  $T_m$  is the actual time of the measurement. The material balance model can predict any of these pressures for a specified parameter set  $a$ , and the objective function  $\chi^2$  may be defined as a summation over all the selected pressure measurements:

$$\chi^2 = \sum \left( \frac{p_{i,k,t}^{\text{obs}}(T_m) - p_{i,k,t}^{\text{pre}}(T_m)}{\sigma_{i,k,t}} \right)^2 \quad (14-90)$$

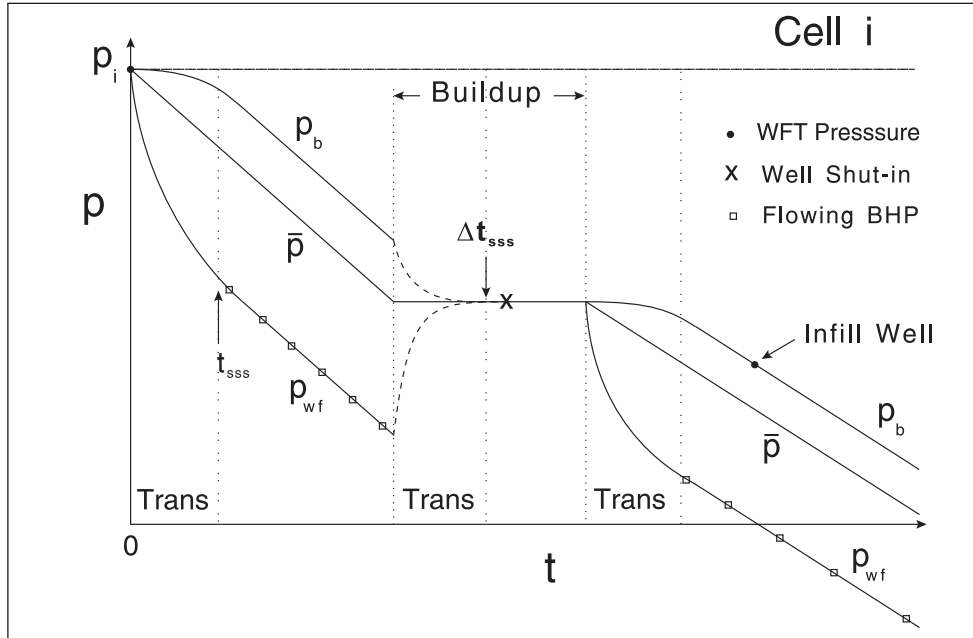


Fig. 14–43. Measured pressure data for cell  $i$  available for matching

In this definition of the objective function, the respective error estimates of the pressure measurements  $\sigma_{i,k,t}$  must be specified before the sum of squares can be calculated. It is up to the user to supply this information relating to the weight attributed to the various data sources. The number of points selected from each type will also affect the results achieved. The problem of parameter estimation then becomes a standard nonlinear regression where a parameter set



a is sought that minimizes the objective function. Such methods are described in chapter 14 in *Well Test Design and Analysis* in connection with transient well test analysis. Since one function evaluation involves a complete run of the complex material balance model, it is essential that the numerical integration process is very fast; it is for this reason that a modern Runge–Kutta method with adaptive step size control has been chosen as the integration algorithm. The classical Levenberg–Marquardt method, or an enhanced modification of it, can be used for the search process. The user must, of course, define which parameters are to be determined by regression and give starting values for those selected. With modern computers, it is quite possible to entertain such an approach to the material balance and use pressure data to greatest advantage in determining reservoir structure. It is very important that manual matching be carried out first to obtain reasonable starting values and give the user a good feel for the problem. Because the calculation time for the complex material balance is very rapid, indeed it is possible to carry out many runs in a short time. In this respect, such a study is an invaluable precursor to a full simulation which consumes a substantial amount of effort.

It is interesting to note that, in a detailed analysis of the Schilthuis volumetric balance equation (VBE) based on cumulative withdrawals, it was found by Tehrani<sup>9</sup> that the best approach to determining OIP and water influx was to minimize a sum of squares of observed and predicted reservoir pressures. This was shown to be equivalent to the best plotting technique for the classical integral method. However, Tehrani also highlighted the problem of lack of uniqueness and the difficulty in independently fixing OOIP and water influx. It is very difficult, on the basis of pressure and oil production information alone, to distinguish between oil and water in the reservoir; for this reason, conditional simulation bringing in data from other sources is essential. It cannot be expected that an automatic matching method will offer any improvement in this respect, and non-uniqueness will remain a problem. The introduction of the concept of compartmentalization makes it even more difficult to discriminate between hydrocarbon and water since retarded communication between oil or gas compartments will look exactly like aquifer influx in terms of pressure dynamics. This paradox will be treated at length later.

The use of nonlinear regression techniques, which have sophisticated error estimates for the fitted parameters, removes the need to try and pose the material balance equation in such a way that a straight line is obtained on some form of plot. Tehrani elegantly showed how this approach leads to an ill-conditioned formulation of the parameter estimation problem and the material balance method fell into disrepute because of such difficulties. The use of blocks with partial communication places the method described here somewhere between the classical material balance and a full reservoir simulation. In effect, a high-level pressure simulator has been developed using a simplified finite-element scheme; in this model, the saturation has essentially been held constant and the dynamic pressure behavior calculated. Such an approach has been often used in the past, and a material balance study is a very useful precursor to a full simulation of the reservoir. Much can be learned about reservoir structure simply by running the complex material balance model in simulation mode and manually adjusting parameters to try and achieve a match to the measured pressure information.

The selection of the number of cells in a complex material study balance and their connectivity should be based on a good understanding of the geology of the reservoir. Except in the case of virtual no-flow boundaries, the barriers (impermeable and semipermeable) are associated with geological features such as faults and shale layers. As in any simulation exercise, it is unwise to proceed without a basic understanding of the geological model. The determination of reserves,

i.e., original oil or gas in place by fixing the cell pore volumes,  $V_i$  should be constrained by the limits imposed by reservoir maps and geophysical information.

It is nowadays quite common to run permanent down-hole pressure gauges and so obtain almost continuous recording of bottom-hole flowing pressure for some wells. In this case, it is essential to select only a sparse dataset for automatic matching purposes; this is illustrated in figure 14–44. This problem of collocation, i.e., choosing a set of points which defines the shape of the measured response, is a familiar one in well test analysis by automatic matching methods.

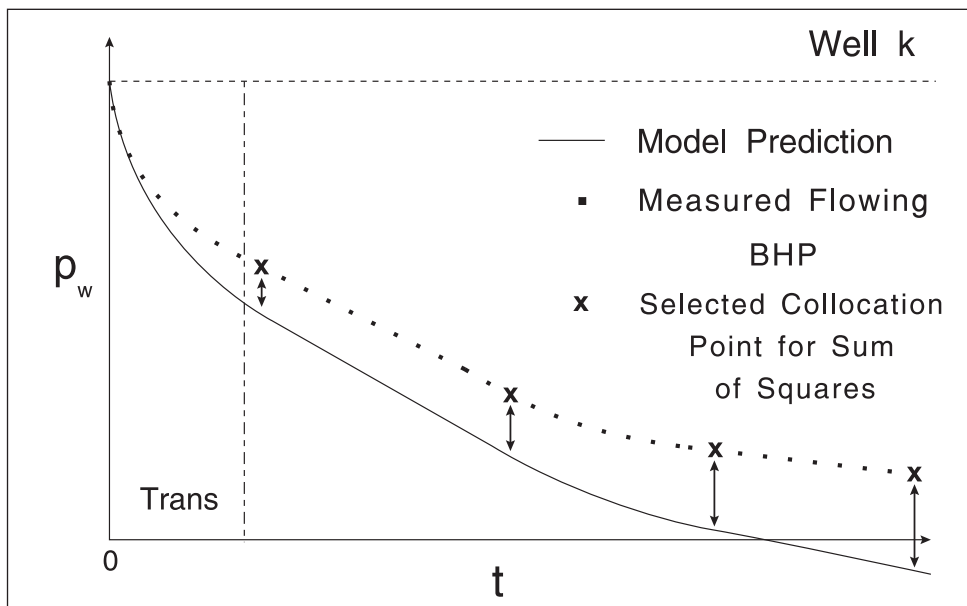


Fig. 14–44. Selection of pressure data points for matching purposes

The nonlinear regression algorithm sits above the material balance model as illustrated in figure 14–45.

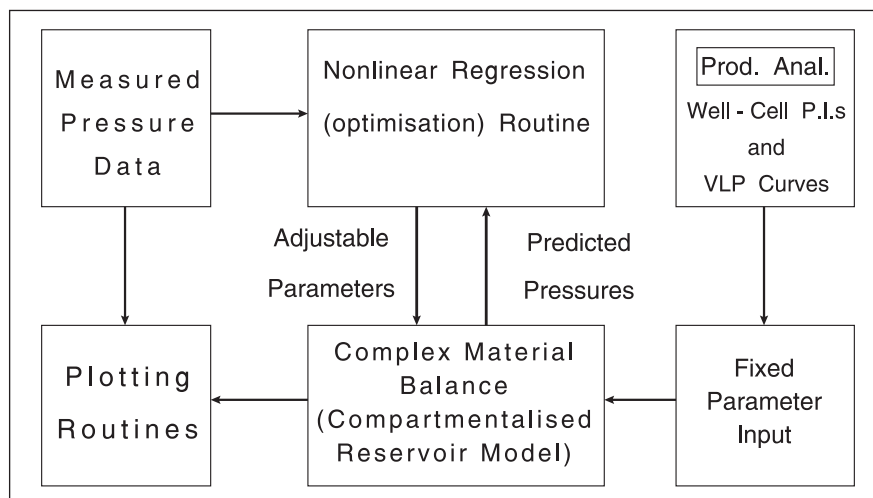


Fig. 14–45. Interaction between the material balance and the nonlinear regression routine

Note that it is only bottom-hole pressure data which are essentially at the SSS that can be used for matching a material balance model; data referring to transient conditions cannot be employed in this context. In chapter 5 of *Well Test Design and Analysis*, an approximate deconvolution algorithm was presented which removes the transient component of a response leaving the underlying depletion trend. This method requires knowledge of the well permeability and skin factor plus the location of any near faults. This deconvolution is illustrated diagrammatically in figure 14–46 and has been successfully used in material balance studies. This technique is an essential part of the approach proposed here and allows the effective use of bottom-hole pressure data in the variable rate situation. When field data from real extended draw-down tests are examined, it is rarely the case that quasi-constant rate conditions apply and the signal is usually strongly affected by transients which must be “cleaned up” by the deconvolution algorithm. The complex material balance method is used in conjunction with classical well test interpretation techniques and the deconvolved signal will usually originate from the transient analysis program.

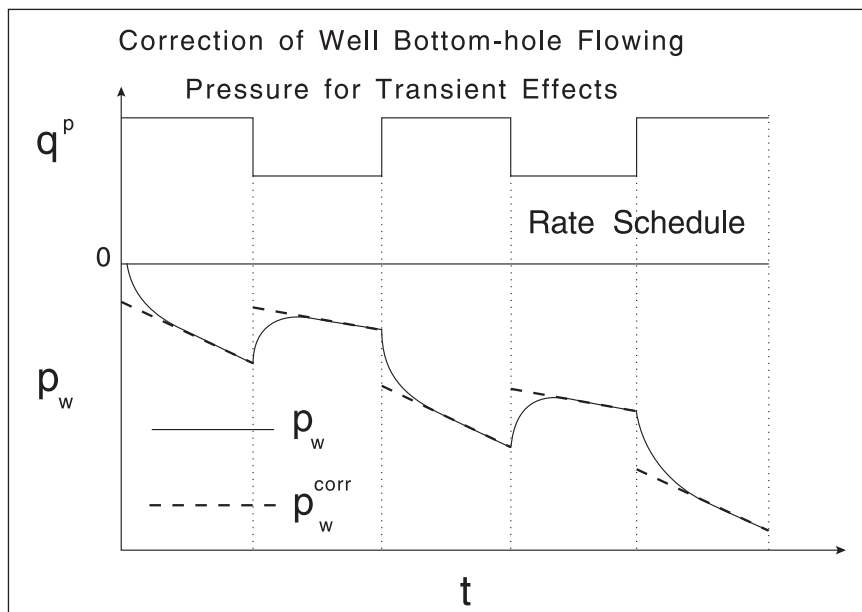


Fig. 14–46. Approximate deconvolution to remove transient components of a response

In many cases, the only pressure measurement available will be at surface, i.e., the wellhead. In this case, a vertical lift program can be used to convert wellhead data to downhole; this is a risky procedure, but in single-phase gas wells such an approach can yield reasonable results when the vertical lift correlation has been tuned to some good flowing well data. In multiphase flow, the generation of downhole pressures from surface data is much less satisfactory.

## Production Constrained Convolution

In the history-matching period of a complex material balance study, the forcing functions, i.e., the well total rates  $q_{ks}^p$  ( $k = 1, \dots, NW$ ) are specified time functions and the model parameters are adjusted by nonlinear parameter estimation techniques. In the forward mode it is desired

to predict the well rates and the evolution of the cell pressures for a given production scenario. In this situation, the cell volumes and interblock transmissibilities have been identified and it is now assumed that the behavior of each well is characterized by a VLP curve as illustrated in figure 14–47. A VLP curve is the relation between well flow rate  $q_{ks}^p$  and the corresponding bottom-hole flowing pressure  $p_{k,w}$  for a specified wellhead pressure. The VLP curve can either refer to the naturally flowing well or an artificial lift system such as an electrically submerged pump (ESP), or gas lift assembly can be incorporated. Thus, it may be appropriate to change the VLP characteristic at a certain time corresponding to a workover or change in well production model; this is illustrated in figure 14–48.

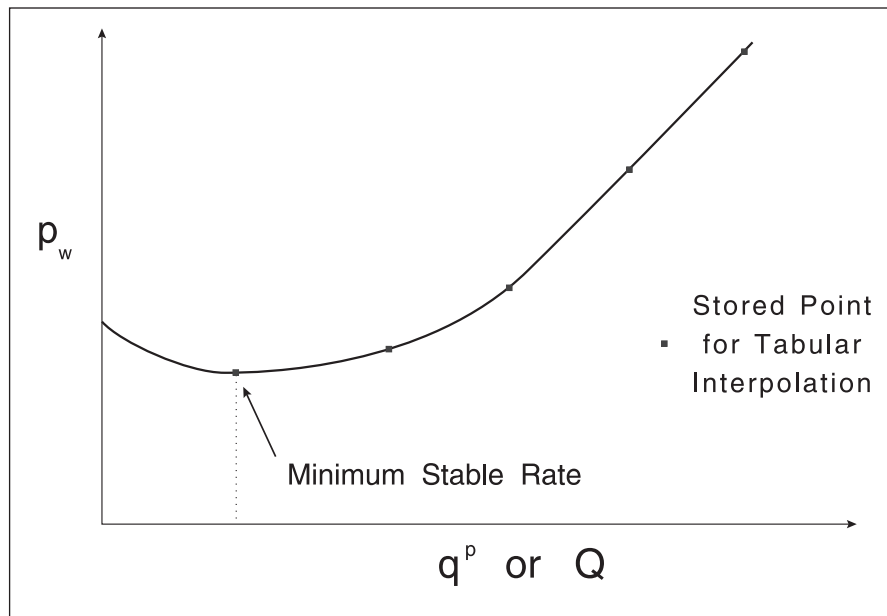


Fig. 14–47. Well vertical lift performance (VLP) curve

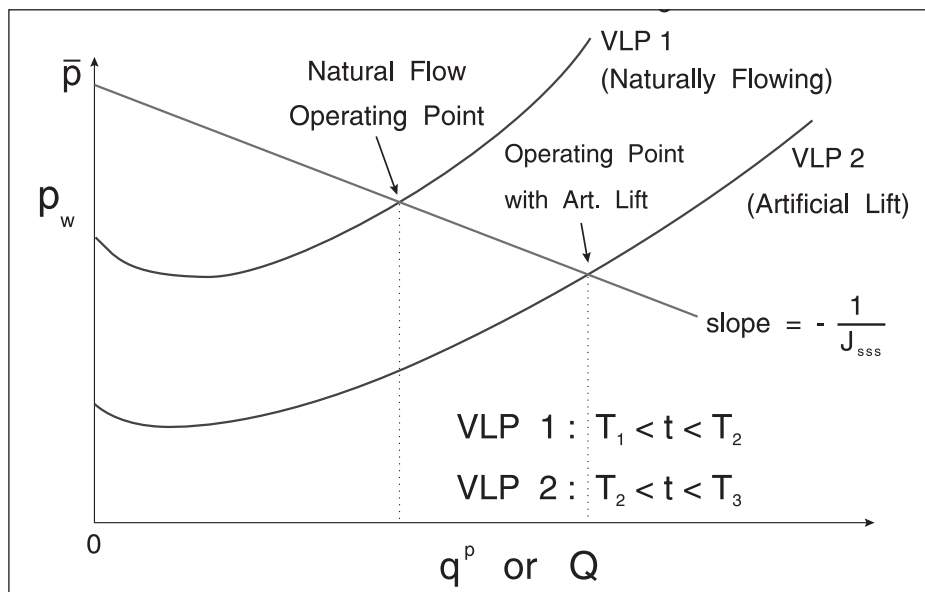


Fig. 14–48. Sequential selection of VLP curves as well production characteristic changes

The inflow model for well k now takes the form

$$q_{ks,i}^p = J_{ks,i} (\bar{p}_i - p_{k,w}) \tag{14-91a}$$

$$\sum_{i=1}^{NC} q_{ks,i}^p = q_{ks}^p \tag{14-91b}$$

and 
$$p_{k,w} = f_{VLP}(q_{ks}^p) \tag{14-91c}$$

This is equivalent to finding the intersection of the VLP curve and the total system inflow performance relation (IPR) straight line on a well performance diagram as shown in figure 14-49. In this mode, the tuned complex material balance model will predict well decline rates as the pressures in the cells deplete in response to the production constrained well rates. Most importantly, the effect of artificial lift on reservoir performance can be calculated.

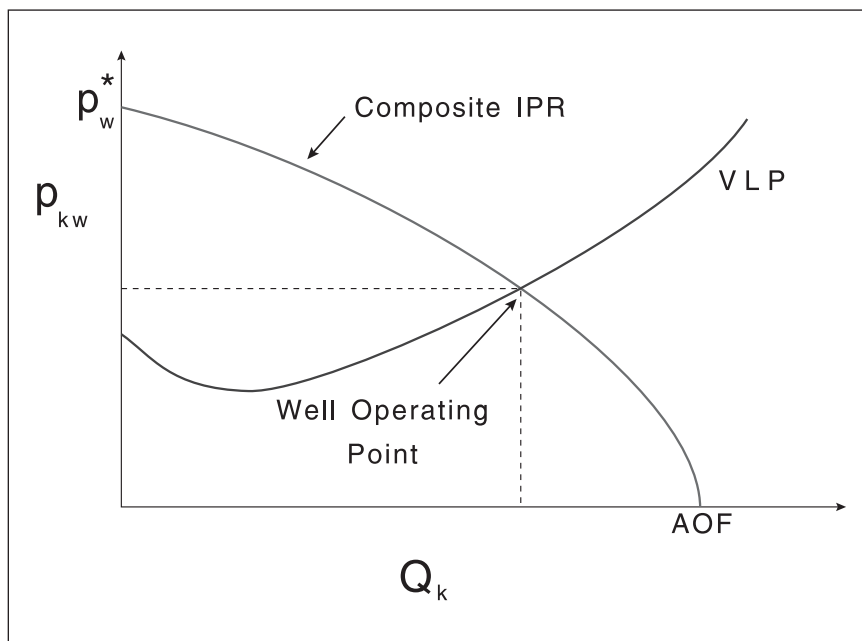


Fig. 14-49. System instantaneous operating point on a well performance diagram

In order to solve this system of equations (14-91a) and (14-91b), they may be combined to give one equation for the total flow rate, i.e.,

$$q_{ks}^p = J_{ks}^* (p^* - p_{k,w}) \tag{14-92}$$

where

$$J_{ks}^* = \sum_{i=1}^{NC} J_{ks,i} \quad \text{and} \quad p^* = \frac{\sum_{i=1}^{NC} \bar{p}_i J_{ks,i}}{J_{ks}^*} \quad (14-93)$$

The vertical lift equation may be linearized on the basis of a chord slope as illustrated in figure 14-50 giving the approximation

$$p_{k,w} = p_{k,w}^o + \frac{dp_w}{dq} (q_{ks}^p - q_{ks}^{p,o}) \quad (14-94)$$

where

$$\frac{dp_w}{dq} = \frac{p_w^- - p_w^+}{q^- - q^+}$$

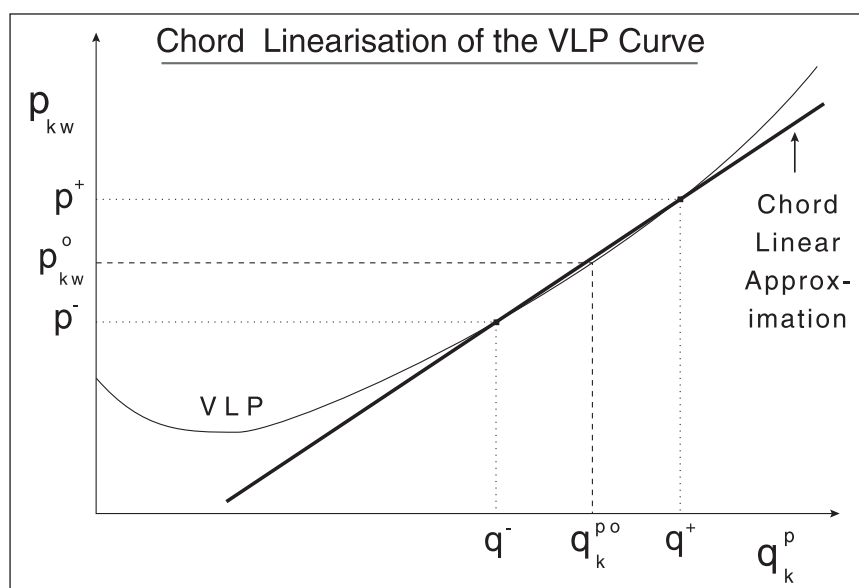


Fig. 14-50. Secant linearization of the VLP curve

The pair of linear algebraic equations (14-95) and (14-94) may be solved for  $p_{k,w}$  and  $q_{ks}^p$  respectively, using elimination; the individual cell well rates  $q_{ks,i}^p$  then follow from (14-91a). The pair of simultaneous linear algebraic equations

$$a_{11}x_1 + a_{12}x_2 = b_1$$

and

$$a_{21}x_1 + a_{22}x_2 = b_2$$

has the analytic solution

$$x_2 = \frac{b_2 - \frac{a_{21} b_1}{a_{11}}}{a_{22} - \frac{a_{21} a_{12}}{a_{11}}}$$

and

$$x_1 = \frac{1}{a_{11}}(b_1 - a_{12} x_2)$$

In the present case with  $x_1 \equiv q_{ks}^p$  and  $x_2 \equiv p_{k,w}$

$$a_{11} = 1 \quad a_{12} = J_{ks}^* \quad b_1 = J_{ks}^* p^* \quad (14-95)$$

$$a_{21} = \frac{dp_w}{dq} \quad a_{22} = -1 \quad b_2 = \frac{dp_w}{dq} q_{ks}^{p,o} - p_{k,w}^o \quad (14-96)$$

Equation (14-96) corresponds to a quasi-Newton method for solving the vertical lift characteristic and the fixed point  $(p_{k,w}^o, q_{ks}^{p,o})$ , on which the chord (i.e., linear interpolation in the VLP table) is based, may be iterated on if desired. Thus, the interpolating points, i.e.,  $(p^-, q^-)$  and  $(p^+, q^+)$  can be updated to achieve greater accuracy in the linear form until the solution is bracketed. The starting value of the fixed point for the linearization of the VLP curve can normally be taken from the previous time step.

In the production-constrained convolution mode, the well flows are predicted by the model and the rates decrease as the reservoir cell pressures reduce with depletion; in this form, the complex material balance constitutes a powerful future production prediction tool. In the history-matching mode, the measured production rates may well be decreasing with time and the nonlinear regression on hydrocarbon in place and/or interblock transmissibility becomes a sophisticated form of decline curve analysis which incorporates the major drive mechanisms.

In some circumstances, the wells are flowed essentially at a fixed bottom-hole flowing pressure denoted  $p_{k,w}^o$  ( $k = 1, \dots, NW$ ), i.e., constant terminal pressure conditions. In this case, the well rate is given by the expression

$$q_{ks}^p = J_{ks}^* (p^* - p_{k,w}^o) \quad (14-97)$$

where  $J_{ks}^*$  and  $p^*$  are evaluated as before (14-93) and change as the cells deplete. The well rates predicted in this case correspond to the classical decline curve model for a closed system which is compartmentalized into partially communicating blocks.

## Restart facility

In the preceding section, the ability to change from one VLP curve to another was shown to be important in assessing the impact of artificial lift on decline rate. However, it is also interesting to examine the effect of fracturing a well, for example, where a change in the PI is induced. One of the advantages of a cellular material balance approach is the fact that the state of the system is fixed by the cell pressures. Hence, it is possible to terminate a run at any point, retain the vector of cell pressures  $x$ , and restart a run with new well properties such as the VLP curve or connection productivity indices. The history is implicit in the current cell pressure vector and the cell pore volumes and transmissibility indices, i.e., the reservoir structure are left unaltered. This restart facility in simulation mode allows sensitivity studies to be carried out and greatly extends the application of decline curve analysis. The installation of gas compression, which changes the wellhead pressure and hence the VLP curve, can be modeled in this way in the case of a gas reservoir.

Note that the restart facility may also be used to update the block compressibilities if saturation changes have taken place.

## Cell of specified pressure history

The first successful application of the ideas suggested here was carried out by Fox and Chedburn,<sup>2</sup> who studied the south flank of the Murchison field in the North Sea. This comprised a system of down-thrown fault blocks and the communication between them was deduced from the simple material balance equations discussed in the section “Complex Reservoirs.” In this situation, the system of fault blocks was also in communication with the main field (source reservoir) as illustrated in figure 14–51. It is not necessary to simulate the history of the whole combined system using the material balance program; in such a case, the pressure of one block can simply be specified as a function of time and the performance of the reduced system simulated. This saves a great deal of effort and allows segments of a reservoir to be studied in isolation. Of course, the pressure history of the main reservoir block over the period of the complex material balance study must be known.

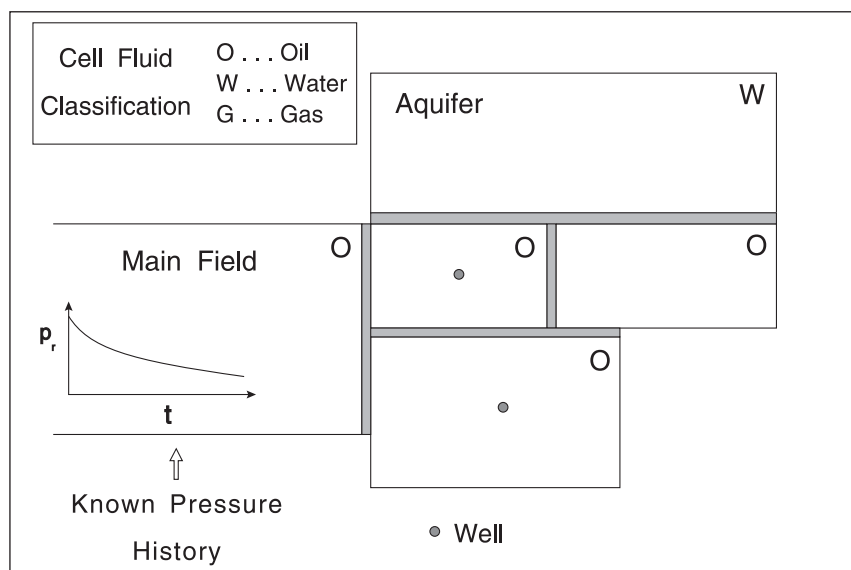


Fig. 14–51. System of fault blocks in communication with the main reservoir



## Desuperposition

One of the main reasons for the development of the complex material balance was to allow the identification of barrier transmissibility. It is possible to determine communication across faults by well-to-well interference testing under transient conditions. However, partially communicating faults usually occur in conjunction with sealing faults and unfortunately it is not possible to generate, for example, a rectangle comprising three sealing and one partially communicating fault by image wells. Some of the early well testing across faults showed the effects of depletion and did not follow infinite-acting or even semi-infinite-acting behavior.

A typical well testing situation is illustrated in figure 14–52, where two blocks in communication across a fault are shown. One block contains an active well and the other an observation well; this configuration is quite common in interference testing. The active well is flowed for a comparatively long time (extended drawdown test) and both the active well and observation well pressure responses are measured. If the blocks are large and the wells located relatively close to the communicating fault, the pressure responses initially will be predicted by the theory developed by Stewart and Westaway<sup>10</sup> and Yaxley<sup>11</sup> for the partially communicating fault. In this context, the partially communicating fault is regarded as a heterogeneity and the response of either well is regarded as infinite-acting until the influence of the sealing boundaries are felt; this defines the beginning of the late transient period.

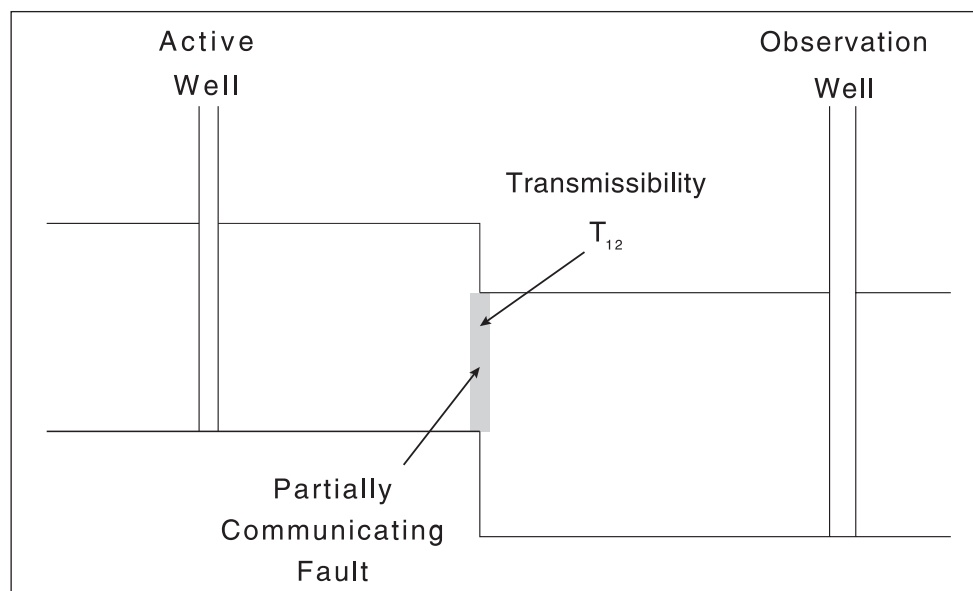


Fig. 14–52. Two blocks in communication across a fault

It is possible to generate the whole pressure response of a well, including the transient period, by combining the material balance method with the analytical solutions used in well test analysis. The superposition theorem shows the behavior of a block containing a well in a closed rectangle and the same cell with no well but specified fluxes through the faces. This is illustrated in figure 14–53. The important point is that the response of a well in closed rectangle can be obtained analytically using the method of images over all times, i.e., transient, late transient, and SSS.

When the block communicates with its neighbors, the face fluxes are calculated in the course of a material balance simulation.

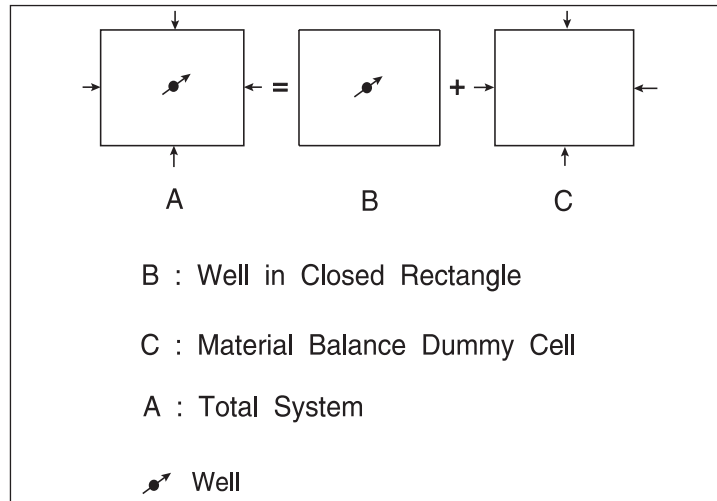


Fig. 14–53. Superposition of blocks

Now suppose that the response of a dummy block is computed, which has identical equations to the actual block containing the well but with the well terms removed. In particular, the face flows of the dummy block from adjacent cells are determined by the complex material balance model; this is illustrated in figure 14–54. The pressure response computed by the material balance model for this dummy cell is the response of the block without the well required for the superposition.

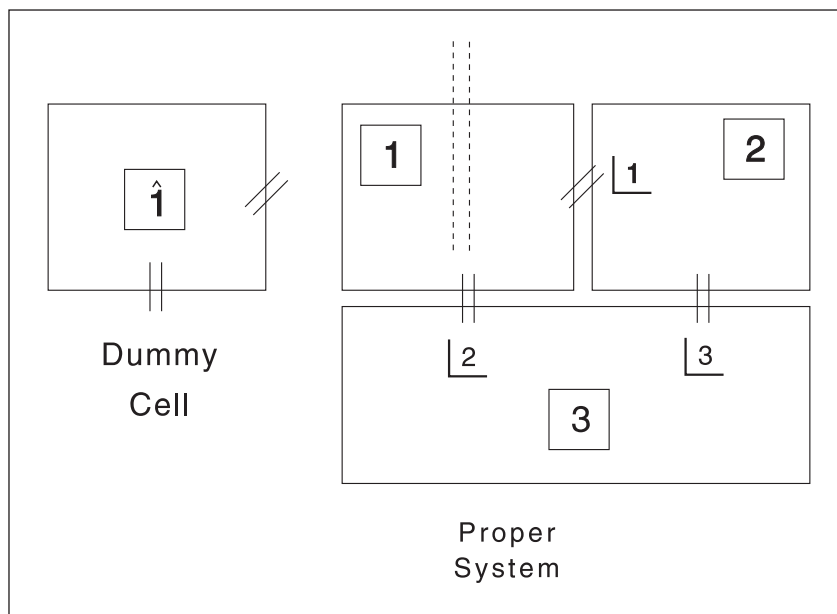


Fig. 14–54. Dummy block modeled with face flows only

The exact solution for the well in the closed rectangle is obtained by the method of images and the superposed correction for the effect of face fluxes yields the actual well response. This device allows the material balance model to be used in conjunction with analytic well simulators.

A two block system is shown in figure 14–55, with block 1 containing the active well in communication with block 2 through a semipermeable barrier. The complex material balance equations take the following form:

Cell 1: 
$$(c_t V)_1 \frac{d\bar{p}_1}{dt} = T_{12}(p_{24} - p_{12}) - q_{11}^p$$

$$0 = \bar{p}_1 - p_{12} + F_{122}T_{12}(p_{24} - p_{12}) + F_{11}q_{11}^p$$

Cell 2: 
$$(c_t V)_2 \frac{d\bar{p}_2}{dt} = T_{12}(p_{12} - p_{24})$$

$$0 = \bar{p}_2 - p_{24} + F_{224}T_{12}(p_{12} - p_{24})$$

Well 1: 
$$0 = p_w - \bar{p}_1 + G_{12}T_{12}(p_{24} - p_{12}) + G_1^p q_{11}^p$$

$$0 = q_{11}^p - q_1^p \tag{14-98}$$

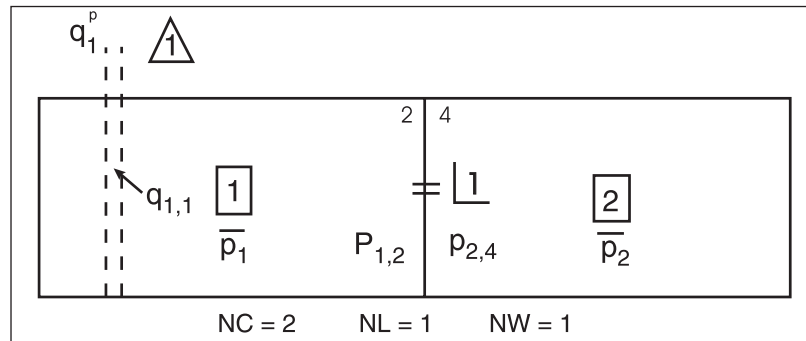


Fig. 14–55. Two-cell, one-well system

This state space system is self-contained and may be integrated forward in time in the usual way. A dummy cell is now set up which mimics the response of block 1 with the omission of the well term. This dummy block is denoted  $\wedge$  and the describing equations are as follows:

Desuperposition cell:

$$(c_t V)_1 \frac{d\hat{p}_1}{dt} = T_{12}(p_{24} - p_{12})$$

$$0 = \hat{p}_w - \hat{p}_1 + G_{12} T_{12}(p_{24} - p_{12}) \quad (14-99)$$

The material balance equation for the dummy cell has no well term and takes the flux over face 2 from the actual system model, i.e.,  $q_{12} = T_{12}(p_{12} - p_{24})$ . Note that the desuperposed cell average pressure  $\hat{p}_1$  does not enter any of the equations for the proper system. The algebraic equation relates the dummy cell average pressure  $\hat{p}_1$  to the pressure at the well location  $\hat{p}_w$ . The existence of the dummy cell in no way influences the behavior of the proper system.

The state vector is augmented by one variable, i.e.,

$$\mathbf{x} = (\bar{p}_1, \bar{p}_2, \hat{p}_1)^T$$

and the subsidiary variable vector is also augmented by one, i.e.,

$$\mathbf{y} = (p_{12}, p_{24}, p_w, q_{11}^p, \hat{p}_w)^T$$

The differential-algebraic system takes the form

$$\dot{\mathbf{x}} = \mathbf{A}'\mathbf{x} + \mathbf{C}'\mathbf{u}$$

and

$$\mathbf{y} = \mathbf{D}'\mathbf{x} + \mathbf{F}'\mathbf{u} \quad (14-100)$$

where the matrices have been augmented.

The pressure trajectory of the proper system is illustrated diagrammatically in figure 14-56, where the two cell average pressures and the well bottom-hole flowing pressure (based on the SSS inflow relation) are shown. This predicted well pressure response is, of course, quite erroneous at early time when the SSS assumption is invalid. The computed response of the desuperposition cell is also shown in figure 14-56; since flow occurs from cell 2 to cell 1, the pressure in the dummy cell increases with time.

The exact pressure response of cell 1 with  $T_{12} = 0$ , i.e., a closed rectangle, is shown in figure 14-57; this is labeled  $p_w^i$  and is correct at all times. In figure 12-57, the desuperposition is indicated by the addition of the dummy cell response  $\hat{p}_w$  to the closed rectangle response.  $p_w^i$ . Thus

$$p_w = p_w^i + \hat{p}_w \quad (14-101)$$

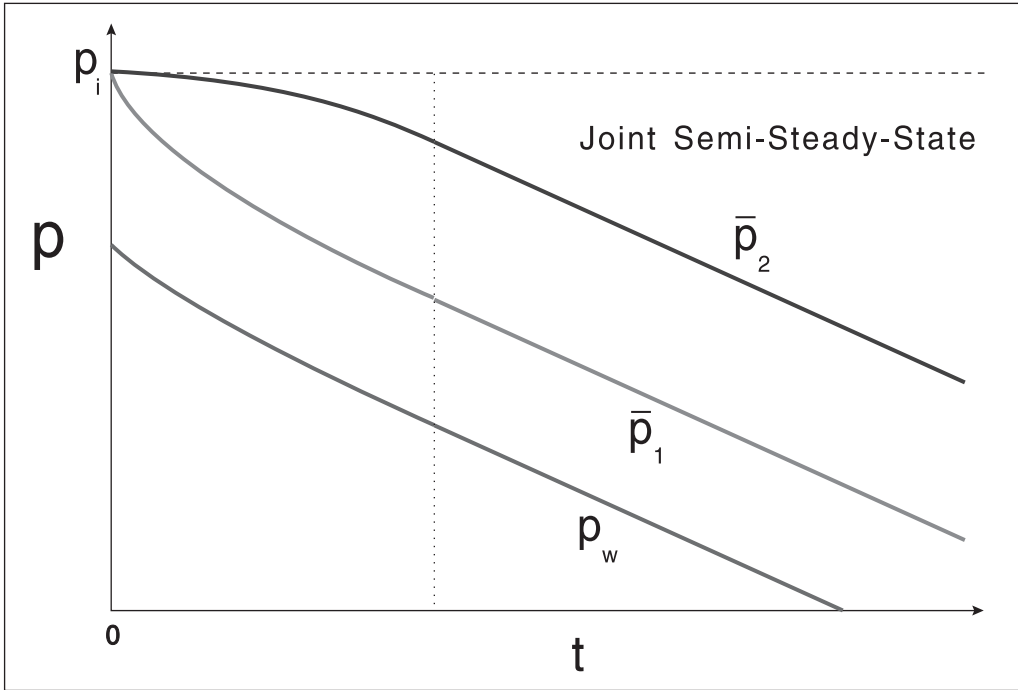


Fig. 14-56. Behavior of proper system

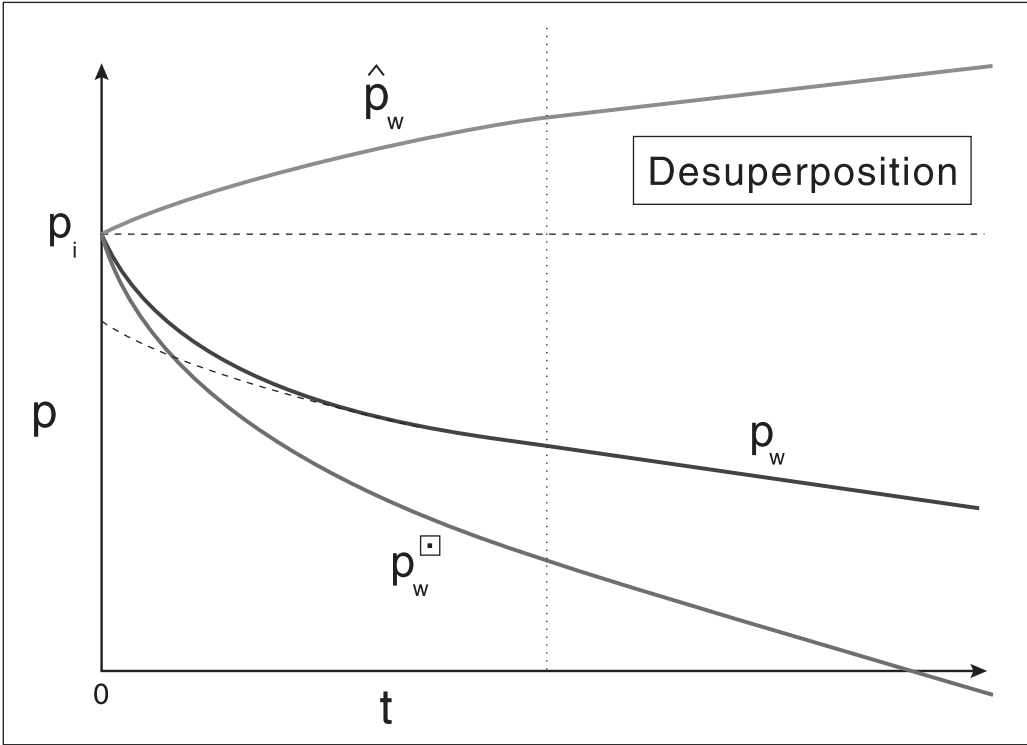


Fig. 14-57. Desuperposition

Here,  $p_w$  is the actual pressure response of the well.

## Material Balance in Terms of Pseudopressure and Pseudotime

The liquid phase material balance equations for a two-cell system with compartment 1 containing a well take the form

$$c_t V_1 \frac{d\bar{p}_1}{dt} = T_{12}(\bar{p}_2 - \bar{p}_1) - q_1^p \quad (14-102a)$$

and

$$c_t V_2 \frac{d\bar{p}_2}{dt} = T_{12}(\bar{p}_1 - \bar{p}_2) \quad (14-102b)$$

where  $T_{12}$  is the interblock transmissibility index and  $q_1^p$  is the well rate or forcing function. For a liquid, the compressibility  $c_t$  is constant and the material balance equations are linear. In the case of a gas reservoir, the assumption of constant compressibility is, of course, not valid and a different approach is necessary. In chapter 13 of *Well Test Design and Analysis*, the concepts of real gas normalized pseudopressure and pseudotime were introduced and it was shown that if a gas well is produced at constant mass rate, then, at the SSS, a Cartesian plot of pseudopressure versus pseudotime will be a straight line. For a single closed compartment, the differential material balance equation for gas may be written in the form

$$\frac{d\psi(\bar{p})}{dt_a} = \frac{m_g}{c_{ti} V \rho^o} = \frac{QB_g^o}{c_{ti} V} \quad (14-103)$$

where

$$\psi(p) = \frac{\mu^o}{\rho^o} \int_{p_b}^p \frac{\rho(p') dp'}{\mu(p')} \quad (14-104)$$

and

$$t_a = \mu^o c_{ti} \int_0^t \frac{dt'}{\mu c_t} \quad (14-105)$$

Here,  $\psi(p)$  and  $t_a$  are the normalized pseudopressure and pseudotime, respectively. Here, the superscript “o” has been used to indicate a quantity at the reference pressure (which may or may not be the initial cell pressure); the subscript “i” is reserved in this text for the layer number. In differential form, Eq. (14-105) may be written as

$$dt_a = \frac{\mu^o c_{ti}}{\mu c_t} dt \quad (14-106)$$

and substituting Eq. (14–105) in (14–102) gives

$$\frac{d\psi(\bar{p})}{dt} = \frac{\mu^{\circ}m_g}{\mu c_t V \rho^{\circ}} = \frac{\mu^{\circ}QB_g^{\circ}}{\mu c_t V} \quad (14-107)$$

This differential equation is nonlinear since the quantity  $\mu c_t$  is a function of pressure. The reason for expressing the gas material balance in this form is simply that the pseudopressure and  $\mu c_t$  functions are routinely computed for gas well test analysis and it is very convenient to have the material balance also written in terms of these quantities. In gas reservoir engineering, it is common to use the compressibility factor  $z$  in the material balance formulation. However, gas compressibility and compressibility factor are related through the equation of state

$$c_g = \frac{1}{p} - \frac{1}{z} \frac{\partial z}{\partial p} \quad (14-108)$$

and it does not matter which form is used. The total compressibility is given by

$$c_t = S_{wc}c_w + (1 - S_{wc})c_g + c_f \quad (14-109)$$

Note that in some overpressured gas reservoirs the formation compressibility  $c_f$  is highly pressure dependent and this effect must be allowed for in determining  $c_t$  as a function of pressure. As mentioned in chapter 4, the material balance is, of course, independent of viscosity which cancels between the two functions. Supposing that the ordinary differential equation is integrated forward in time using a numerical method such as the Runga–Kutta technique—presuming the well mass rate  $m_g$  is known as a function of time— Eq. (14–107) is of the form

$$\frac{d\psi}{dt} = f(\psi, m_g) = \frac{\mu^{\circ}m_g}{\mu c_t V \rho^{\circ}} = \frac{\mu^{\circ}m_g}{\overline{\mu c_t}(\psi) V \rho^{\circ}} = \frac{\mu_i QB_g^{\circ}}{\overline{\mu c_t}(\psi) V} \quad (14-110)$$

Here, the notation  $\overline{\mu c_t}(\psi)$  simply implies that the  $\mu c_t$  product has been tabulated as a function of pressure and for any given  $\psi$  the corresponding pressure  $p$  can be found from the  $\psi(p)$ – $p$  transform. Note that the quantity  $m_g/\rho^{\circ}$  may be replaced by  $QB_g^{\circ}$  if a formulation in terms of volumetric rate at standard conditions is required. Hence, given the two nonlinear functions  $\psi(p)$  and  $\overline{\mu c_t}(p)$ , the differential equation can be integrated numerically; both the pseudopressure  $\psi$  and the corresponding real pressure  $p$  are determined in the integration process. The treatment of total compressibility  $c_t$  for the case of pressure-dependent rock compressibility and two-phase reservoir conditions has already been discussed in the section “Gas Cap Drive.”

In the two-cell compartmentalized reservoir, the differential system becomes

$$\frac{d\psi_1}{dt} = \frac{\mu^\circ}{(\mu c_t V)_1 \rho^\circ} (T_{m12}(\psi_2 - \psi_1) - m_g) \quad (14-111a)$$

$$\frac{d\psi_2}{dt} = \frac{\mu^\circ}{(\mu c_t V)_2 \rho^\circ} (T_{m12}(\psi_1 - \psi_2)) \quad (14-111b)$$

where  $T_{m12}$  is an interblock transmissibility index on a mass flow basis; just as the well inflow is better posed in terms of pseudopressure, the interblock communication is better modeled on this basis. Given the forcing function  $m_g(t)$ , this nonlinear differential system can be integrated using a numerical method and the gas reservoir response simulated. In terms of volumetric rate at standard conditions, Eq. (14-111a and b) becomes

$$\frac{d\psi_1}{dt} = \frac{\mu^\circ}{(\mu c_t V)_1} (T_{12}(\psi_2 - \psi_1) - QB_g^\circ) \quad (14-112a)$$

$$\frac{d\psi_2}{dt} = \frac{\mu^\circ}{(\mu c_t V)_2} (T_{12}(\psi_1 - \psi_2)) \quad (14-112b)$$

Thus, for a gas reservoir (or gas cap cells in an oil reservoir) the material balance equations are expressed in terms of pseudopressure  $\psi$  and are nonlinear because the product  $(\mu c_t)$  is pressure dependent; the system may be written symbolically as

$$\frac{d\psi}{dt} = \mathbf{f}(t, \psi) \quad t = 0 : \psi = \psi_o \quad (14-113)$$

The Runge–Kutta numerical integration process will determine the trajectory for the pseudopressures  $\psi$  and at each time step the pseudopressure function is used to determine the corresponding cell pressures  $\mathbf{p}$ ; the methodology is illustrated in figure 14-58. Note that the viscosity–compressibility product  $(\mu c_t)$  should, in principle, be stored as a function of pseudopressure  $\psi$  rather than pressure  $p$  since the equations for integration are in terms of pseudopressure. However, both  $(\mu c_t)$  and  $\psi$  will be tabulated as functions of pressure and  $(\mu c_t)$  can be interpolated in terms of  $\psi$  or  $p$  as desired.



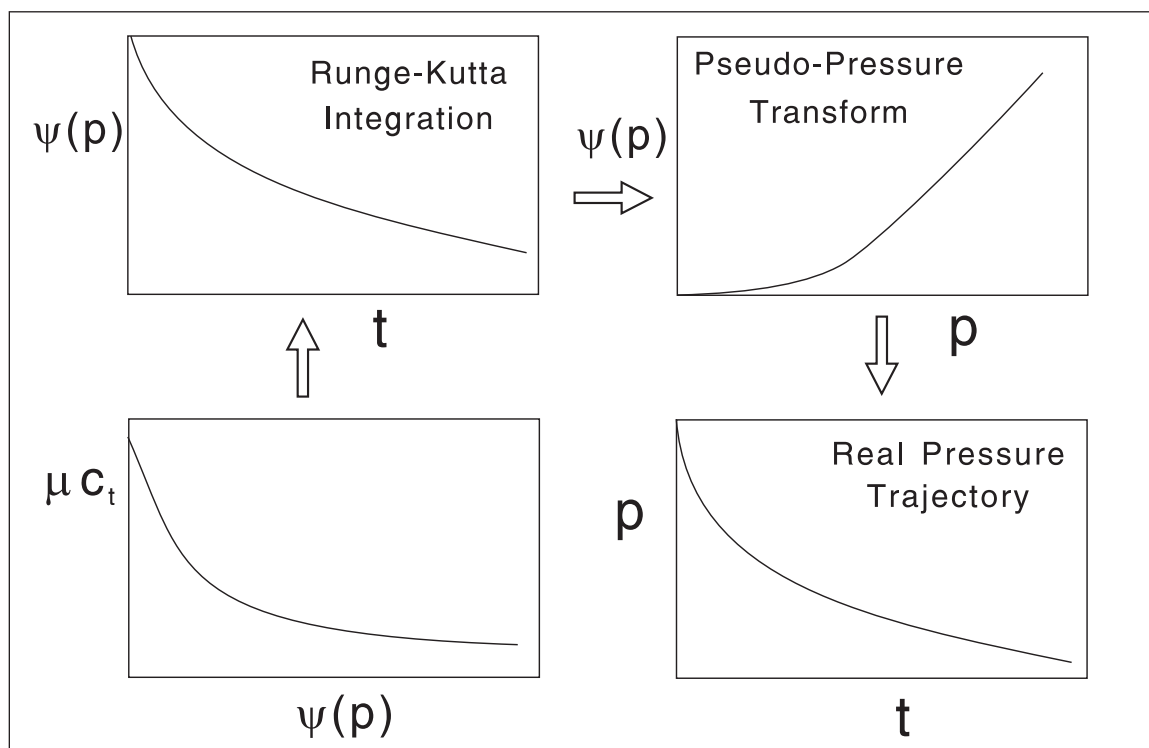


Fig. 14-58. Use of pseudopressure and viscosity-compressibility product

The application of the normalized pseudopressure function has been demonstrated in connection with a single-phase gas system but the case of gas condensate with retrograde condensation can be handled in exactly the same way. The imported two-phase pseudopressure function  $\psi(p)$  will allow for the effect of liquid dropout on mobility and well inflow and the effective compressibility  $c_{m\text{ph}}$  below the dew point will allow for mass transfer assuming equilibrium conditions. Material balance modeling of gas-condensate reservoirs therefore becomes feasible with the limitation that the overall mixture composition is held constant over the pore volume of a block. Again, the material balance model cannot accommodate saturation changes. In the case of gas-condensate wells, the flow rate  $Q_k$  refers to “wet” gas, i.e., the combined separator dry gas and liquid condensate equivalent to the mass flow rate of the stream.

## Commingled wellbore model for gas wells

In the general material balance case, more than one cell may produce into a given well  $k$  and the division of the total production between the commingled layers must be computed. The inflow relation for cell or layer  $i$  takes the form

$$\psi(p_{k,w}) = \psi(\bar{p}_i) - \frac{1}{J_{k,i}} Q_{k,i} - F_{k,i} Q_{k,i} |Q_{k,i}| \quad (14-114)$$

where the absolute value term in the non-Darcy component means that the expression is valid for both production and injection wells. The commingled aspect of the production is expressed by the summation

$$\sum_{i=1}^{NC} Q_{k,i} = Q_k \quad (14-115)$$

The algebraic system (14-114) and (14-115) constitute  $NC + 1$  equations in  $NC + 1$  unknowns  $\psi(p_{k,w})$  and  $Q_{k,i}$   $i = 1, \dots, NC$ . This may be written in functional form as

$$F_i = \psi(p_{k,w}) - \psi(\bar{p}_i) + B_{k,i} Q_{k,i} + F_{k,i} Q_{k,i} |Q_{k,i}| = 0 \quad i = 1, \dots, NC$$

$$F_{NC+1} = \sum_{i=1}^{NC} Q_{k,i} - Q_k = 0 \quad (14-116)$$

where the reciprocal of the Darcy PI, i.e.,  $1/J_{k,i}$ , has been written as  $B_{k,i}$ —the Darcy flow coefficient—following the usual convention for gas wells. The solution of this nonlinear algebraic system allows the layer rates  $Q_{k,i}$   $i = 1, \dots, NC$  and the bottom-hole pseudopressure  $\psi(p_{k,w})$  to be determined for specified block average pseudopressures, i.e.,  $\psi(\bar{p}_i)$ , and the well total volumetric rate  $Q_k$ . The actual bottom-hole pressure  $p_{k,w}$  then follows from the inverse transform. The forcing function is the total well volumetric rate  $Q_k$ .

For a given set of layer average pressures, i.e.,  $\bar{p}_i$   $i = 1, \dots, NC$  and corresponding pseudopressures, i.e.,  $\psi(\bar{p}_i)$   $i = 1, \dots, NC$  the individual layer deliverability curves can be plotted on a well performance diagram as shown in figure 14-59. For any selected value of the (common) bottom-hole pressure  $p_{k,w}$ , the individual layer flow rates can be determined from (14-114) and summed to give the total well rate  $Q_k$  as illustrated in the diagram. Note that there will be a range of bottom-hole pressures— $(\bar{p}_i)_{\min} < p_{k,w} < p^*$ —in which some of the layers will be in injection, i.e., wellbore cross-flow is taking place. The well operating point is given by the intersection of the composite nonlinear IPR with the VLP curve; this is also illustrated in figure 14-59. The quantity  $p^*$ , i.e., the maximum value of the wellbore pressure at which net flow will occur, is determined from the intersection of the composite nonlinear IPR curve; this will be very close to the value predicted by the formula ignoring the non-Darcy effect, i.e.,

$$\psi(p^*) = \frac{\sum_{i=1}^{NC} J_{k,i} \psi(\bar{p}_i)}{\sum_{i=1}^{NC} J_{k,i}} \quad p^* = \psi^{-1}(p^*) \quad (14-117)$$

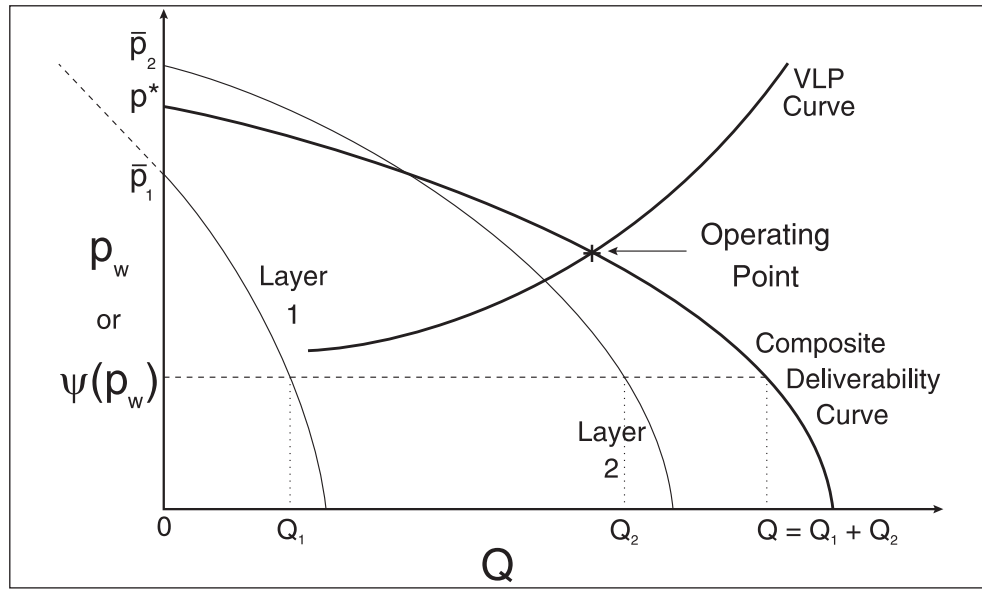


Fig. 14–59. Gas well composite deliverability curve

An iterative solution method for system (14–117) can be devised which converges fairly rapidly for a known total well rate  $Q_k$ . Suppose estimates of the individual layer or compartment rates are available denoted  $Q_{k,i}^{old}$  ( $i = 1, \dots, NC$ ); the functions  $F_i$  may be written in the form

$$Q_{k,i} \left( B_{k,i} + F_i^k \left| Q_{k,i}^{old} \right| \right) = \psi(\bar{p}_i) - \psi(p_{k,w})$$

i.e., 
$$Q_{k,i} = \hat{J}_{k,i} \left( \psi(\bar{p}_i) - \psi(p_{k,w}) \right) \tag{14-118}$$

where 
$$\hat{J}_{k,i} = \frac{1}{B_{k,i} + F_{k,i} \left| Q_{k,i}^{old} \right|} = \frac{J_{k,i}}{1 + J_{k,i} F_{k,i} \left| Q_{k,i}^{old} \right|}$$

The form (14–118) is identical in structure to the liquid equation (14–17) and the solution to the layer allocation problem may be written as

$$\hat{J}_k^* = \sum_{i=1}^{NC} \hat{J}_{k,i} \quad \psi(p^*) = \frac{\sum_{i=1}^{NC} \hat{J}_{k,i} \psi(\bar{p}_i)}{\hat{J}_k^*} \tag{14-119}$$

$$\psi(p_{k,w}) = \psi(p^*) - \frac{Q_k}{\hat{J}_k^*} \tag{14-120}$$

$$Q_{k,i} = \hat{J}_{k,i} \left( \psi(\bar{p}_i) - \psi(p^*) + \frac{Q_k}{\hat{J}_k^*} \right) \quad (14-121)$$

In the case of a layered gas well, this sequence is iterative since the quantities  $\hat{J}_{k,i}$  involve estimates of the layer flow rates  $Q_{k,i}^{\text{old}}$ . A possible starting set is simply to put

$$Q_{k,i}^{\text{old}} = \frac{Q_k}{NC} \quad i = 1, \dots, NC \quad (14-122)$$

i.e., equal allocation of the total well rate to the individual layers.

In most gas well deliverability models, the non-normalized pseudopressure  $m(p)$  is employed and Eq. (14-123) has the alternative form

$$m(p_{k,w}) = m(\bar{p}) - \tilde{B}_{k,i} Q_{k,i} - \tilde{F}_{k,i} Q_{k,i} |Q_{k,i}| \quad (14-123)$$

where the units of  $\tilde{B}_{k,i}$  and  $\tilde{F}_{k,i}$  are as follows:

$$\begin{aligned} \tilde{B}_{k,i} &: \text{psia}^2/\text{cp}/(\text{MMSCF}/D) \\ \tilde{F}_{k,i} &: \text{psia}^2/\text{cp}/(\text{MMSCF}/D)^2. \end{aligned}$$

The conversion to units of normalized pseudopressure takes the form

$$B_{k,i} = \frac{\mu^o z^o}{2p^o} \tilde{B}_{k,i} \quad (14-124a)$$

and

$$F_{k,i} = \frac{\mu^o z^o}{2p^o} \tilde{F}_{k,i} \quad (14-124b)$$

It is also possible to determine the well rate  $Q_k$  if the well vertical lift characteristic is known; thus, suppose the bottom-hole pressure has been determined as a function of total rate for a specified wellhead pressure  $p_{wh}$ . The VLP relation may be written symbolically as

$$p_{k,w} = f_{\text{VLP}}(Q_k) \quad \text{or} \quad F_{NC+2} = p_{k,w} - f_{\text{VLP}}(Q_k) = 0 \quad (14-125)$$

For production-constrained convolution, Eq. (14-125) constitutes an additional nonlinear algebraic relation fixing the well total volumetric rate  $Q_k$ . The functional relation  $p_{k,w} = f_{\text{VLP}}(Q_k)$  will normally be stored as a table of  $Q_k$  versus  $p_{k,w}$  and a continuous function generated by interpolation; the composite IPR can also be stored as a table of  $Q_k$  versus  $p_{k,w}$  and subjected to linear interpolation. The well operating point is found by the intersection of the two nonlinear functions as shown in figure 14-59, and an algorithm can be written that operates on the two tables to find the requisite root.

## Transient Production

In the formulation of the material balance equations, attention was focused on the SSS well productivity index  $J_{SSS}$  as defined by an equation of the form

$$q_{k,i}^p = J_{k,i}(\bar{p}_i - p_{k,w}) \quad (14-126)$$

where the index  $i$  refers to a cell and  $k$  to a well. In the case of a well intersecting a single layer or compartment, the well bottom-hole flowing pressure difference between the cell average pressure and the well bottom-hole pressure is fixed by the instantaneous well rate  $q_k^p$ . Considering the situation illustrated in figure 14-60, there is an initial transient period when the well bottom-hole flowing pressure is, in fact, fixed by the cell initial (rather than average) pressure  $p_i^o$  and the transient PI  $J_{tr}$  where  $J_{tr}$  is a time-dependent quantity. The transient analogue to Eq. (14-126) takes the form

$$q_{k,i}^p = J_{k,i}^{tr}(p_i^o - p_{k,w}) \quad (14-127)$$

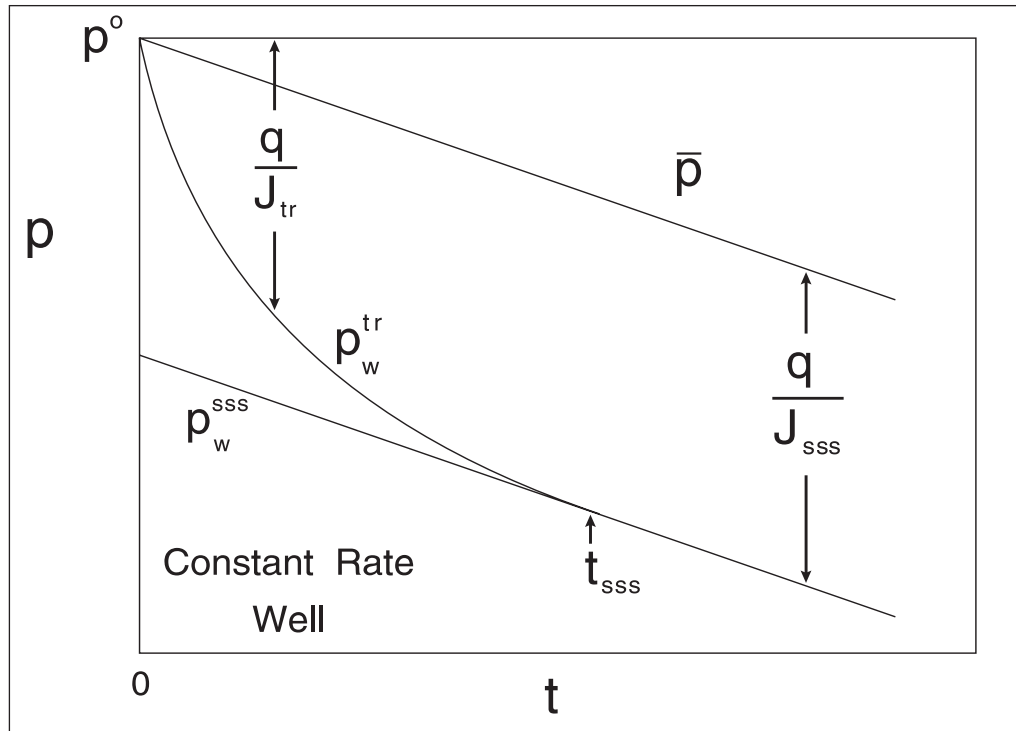
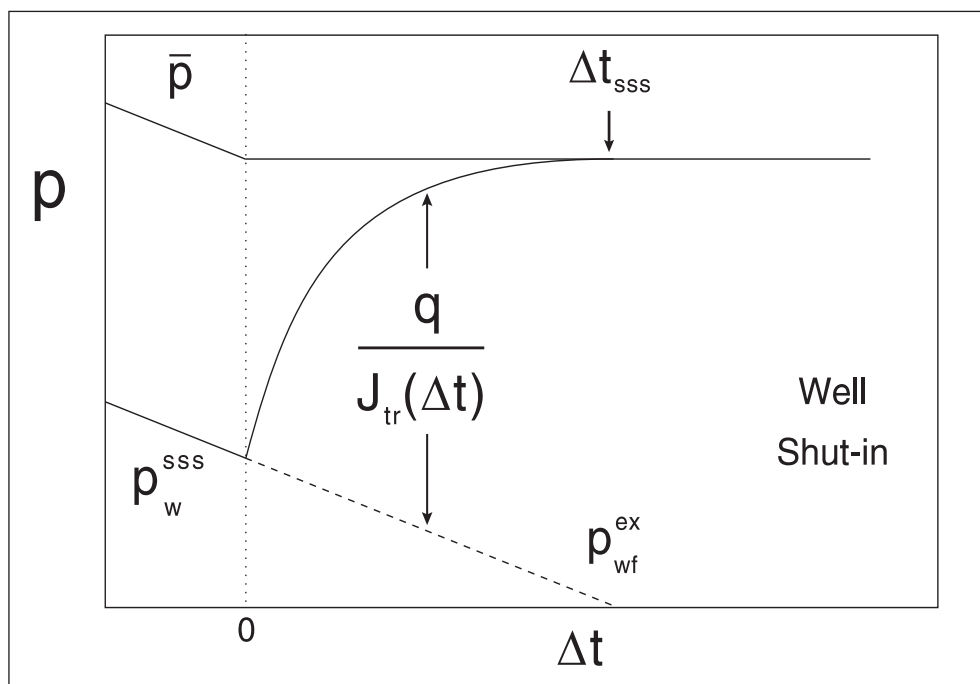


Fig. 14-60. Transient productivity index

In order to implement this formulation, it is necessary to import a transient PI function  $J_{tr}(t)$  into the material balance program and compute well bottom-hole flowing pressures from (14-127) in the early stages of the simulation. This has the effect, illustrated in figure 14-60, of eliminating sharp jumps in the bottom-hole flowing pressures as the well is switched on and

off. The concept of transient PI is mainly of importance in tight reservoirs where there is a long period of semi-infinite-acting behavior. When the well is shut in for a buildup, the same device can be used, as shown in figure 14–61.



**Fig. 14–61.** Use of transient productivity index in buildup

## Notes

- 1 Warren, J. E., and Root, P. J. "The Behaviour of Naturally Fractured Reservoirs," *JPT* 3 (3), (Sept. 1963): 245–255.
- 2 Fox, M. J., Chedburn, A. C. S., and Stewart, G. "Simple Characterisation of Communication Between Reservoir Regions," SPE 18360, (European Petroleum Conference, London, 1988).
- 3 Fetkovich, M. J. "A Simplified Approach to Water Influx Calculations: Finite Aquifer Systems," SPE 2603, *JPT* 23 (7), 1971.
- 4 Dake, L. P. *Fundamentals of Reservoir Engineering* (Amsterdam: Elsevier, 1978).
- 5 Mead, H. N. "Re-evaluation of the RHM, a Finite System Concept for Transient Pressure Behaviour," SPE 23465, 1991.
- 6 Chambers, K. T., Hallager, W. S., Kabir, C. S., and Garber, R. A. "Characterization of a Carbonate Reservoir With Pressure-Transient Tests and Production Logs: TengizField, Kazakhstan," SPE 72598, *SPERE* 4 (4), 2001, 250–259.
- 7 Yaxley, L. M. "New Stabilised Inflow Equations for Rectangular and Wedge-shaped Drainage Areas" SPE 17082, 1987.
- 8 Hantush, M. *Advances in Hydroscience* (New York: Academic Press, 1964), 281–432.
- 9 Tehrani, D. H. "An Analysis of a Volumetric Balance Equation for Calculation of Oil in Place and Water Influx" *JPT* 37 (9), (Sept. 1985): 1664–1670.

- 10 Stewart, G., Gupta, A., and Westaway, P. J. "The Interpretation of Interference Tests in a Reservoir with Sealing and Partially Communicating Faults," SPE 12967, (European Petroleum Conference, London, 1984).
- 11 Yaxley, L. M. "Effect of a Partially Communicating Fault on Transient Pressure Behaviour," *SPE Formation Evaluation* 2 (4), (Dec. 1987): 590–598.

# 15

## Reservoir Characterization from Underbalanced Drilling Data

---

### Introduction

Underbalanced drilling (UBD) is gaining popularity in the industry because of the advantages gained both in terms of the drilling process itself (e.g., higher rate of penetration and reduction of lost circulation) and for enhanced long-term productivity associated with reduced formation damage. In this chapter, a methodology to interpret the production associated with the drawdown maintained throughout the UBD will be developed using variable-rate well testing theory. One of the main targets of underbalanced operations is the drilling of differentially depleted zones, and a key issue in the reservoir characterization process is independent knowledge of the zone pressures. In new wells in unproduced fields, the pressure is likely to follow a hydrostatic gradient which is known from wireline formation tester (WFT) surveys in appraisal wells. In this case, the formation pressure is known when the first development wells are drilled. It will be shown later in the section on pressure and rate transient analysis that the identification of a permeability distribution is relatively easy when the pressure is known independently. When a new well is drilled into a depleted field, the major zones are likely to be at different pressures. It is obviously important for the design of the UBD operation to have an idea of what these pressures are, so that the appropriate degree of underbalance can be maintained. Such information may be obtained from nearby wells in which formation tester measurements have been made, either on wireline or drillpipe. It may be prudent to drill a hole in overbalance conditions just to run a formation tester for pressure information and then drill a sidetrack for the underbalance penetration into the reservoir with minimal formation damage. In the event that the formation pressure is not known accurately enough, then the reservoir characterization problem involves the determination of both permeability and pressure distributions. This is much more difficult, and attention will be paid here to establishing test designs which allow both distributions to be identified. Traditionally in well testing, buildup and drawdown periods have been used to achieve this objective. However, it has been demonstrated that a two-rate test is sufficient to allow both pressure and permeability



to be identified, and in the UBD case, if enough rate variation can be achieved, then the problem may be tractable. Note that in classical well testing only the average permeability and pressure of the whole formation is usually identified; in UBD it is possible to identify a permeability distribution which will allow the detection of high-permeability layers or other similar objects like fractures.

Many of the papers on this subject seek an integrated, transient model of the formation and the wellbore. In the approach adopted here, it is shown that the problem may be decoupled with independent models for the two parts of the system. This is illustrated in figure 15–1. A transient wellbore model is used to synthesize the downhole flow rate schedule from the formation into the wellbore, denoted  $q_o^{in}(t)$ , i.e., inlet to the well. In figure 15–2, the term virtual downhole flowmeter (VDF) is used to describe the inlet flow from the formation, reconstructed from the measurement of the surface oil flow emerging from the facilities. The simultaneous measured downhole pressure response  $p_{wf}(t)$  and synthesized flow response  $q_o^{in}(t)$  are analyzed as variable-rate well test with a progressively penetrating well. The theory of this for both vertical and horizontal wells, based on superposition, is presented later in this chapter.

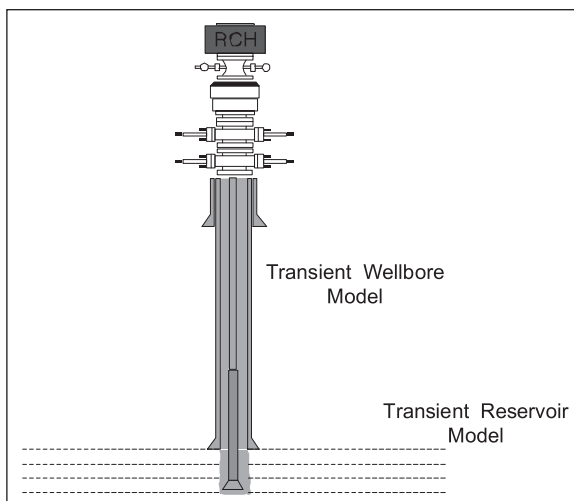


Fig. 15–1. Separation of wellbore and formation models

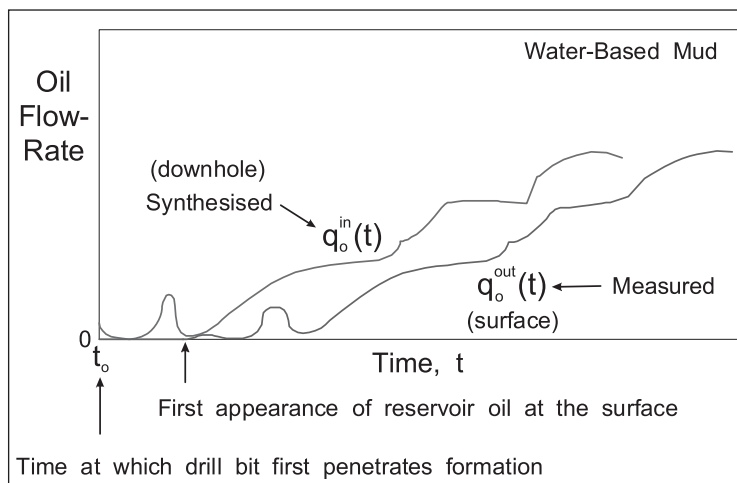


Fig. 15–2. Virtual downhole flowmeter

## Transient Well Model

A typical underbalance drilling system is shown in figure 15–3, where the main items of equipment are depicted. Here, the mud system is taken to be water-based and is designated “liquid”, and gas, usually nitrogen, is injected into the circulating mud to lighten the density so the desired underbalance can be achieved. The flow rates of fluid injected into the well are monitored and are referred to as upstream measurements. The fluids issuing from the well are denoted downstream and the flow rates of produced gas and oil are also measured. The produced gas is a mixture of injected nitrogen and associated hydrocarbon gas from the formation. In addition, the wellhead pressure and temperature as well as bottomhole pressure and temperature are continuously monitored. From a well testing point of view, the flow rate of the produced oil emanating from the formation is not measured directly. Normally, the injected gas is added to the injected fluid (mud) and the mixture enters the wellhead and emerges at the bit; however, in some cases the gas is injected separately, as in a gas-lifted well as shown in figure 15–4. The latter arrangement is referred to as a parasitic string.

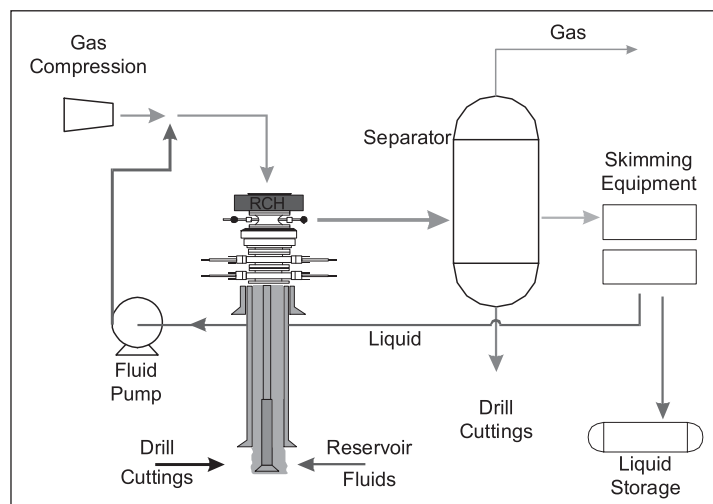


Fig. 15–3. Underbalance drilling system

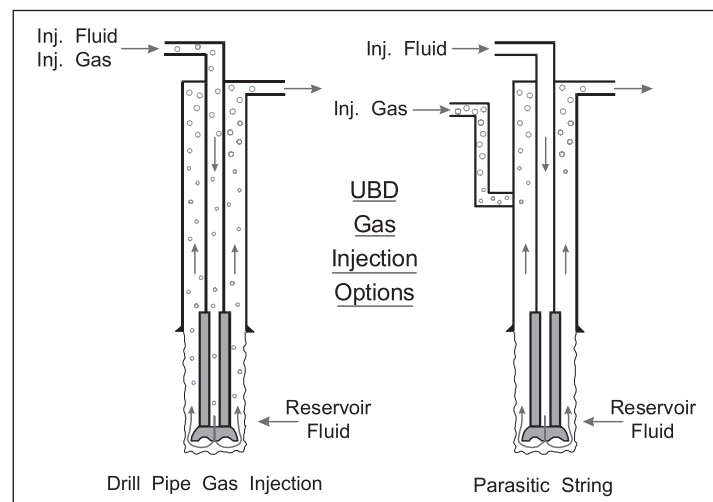


Fig. 15–4. UBD gas injection options

The objective of a transient wellbore model is to link the inputs and outputs of the system allowing for any accumulation that takes place. The basis of such a model is the unsteady-state mass conservation equations for the individual components. In the context of underbalance drilling, a black oil PVT formulation will usually be quite adequate, and the individual species are denoted as hydrocarbon gas (G), nitrogen (N), oil (O), water (W), and solid (S). Four phases are present which are denoted as gas (g), oil (o), water (w), and solid (s) and it is only the gas component G, which can be present in two phases, i.e., gas (g) and oil (o). The mass fraction of gas component in the oil phase is denoted x, and it is assumed that phase equilibrium exists at any location in the wellbore. The solubility of gas component in the oil phase follows from a PVT relation of the form

$$x = x(p, T) \tag{15-1}$$

The component conservation equations for one-dimensional pipe flow, based on the control volumes illustrated in figure 15-5, take the form

Oil  $\frac{\partial m_o}{\partial z} = - A_x \frac{\partial(\alpha_o \rho_o (1 - x))}{\partial t}$  (15-2a)

Gas  $\frac{\partial m_G}{\partial z} = - A_x \frac{\partial(\alpha_o \rho_o x + \alpha_G \rho_G y)}{\partial t}$  (15-2b)

Water  $\frac{\partial m_W}{\partial z} = - A_x \frac{\partial \alpha_w \rho_w}{\partial t}$  (15-2c)

Solid  $\frac{\partial m_S}{\partial z} = - A_x \frac{\partial \alpha_s \rho_s}{\partial t}$  (15-2d)

Nitrogen  $\frac{\partial m_N}{\partial z} = - A_x \frac{\partial \alpha_g \rho_g (1 - y)}{\partial t}$  (15-2e)

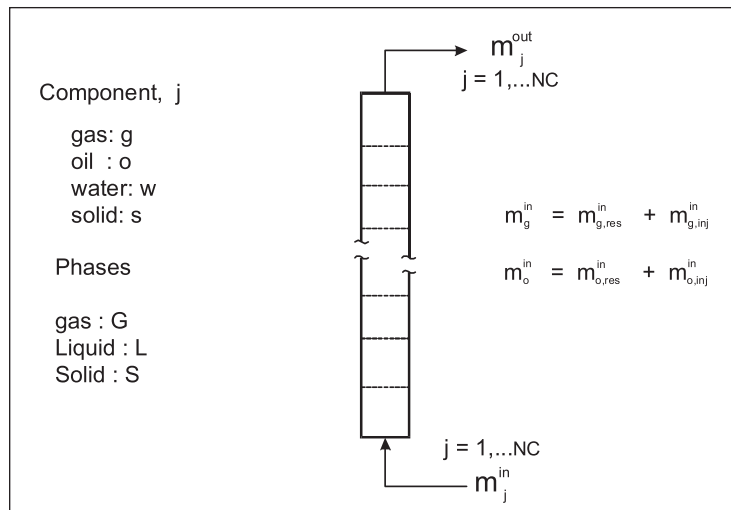


Fig. 15-5. Distributed mass conservation equations

It is assumed that there is no water component in the gas phase and no nitrogen component in the oil or water phases. The mass fraction of hydrocarbon gas component in the gas phase is denoted as  $y$ , and  $\alpha_p$ ,  $P = g,o,w,s$  is the volumetric fraction of the respective phases. System (15–2) constitutes a set of hyperbolic, partial differential equations (PDE) of the first order. The PDE will integrate to a steady-state operating condition, illustrated in figure 15–6, if the inlet flows are maintained constant.

In the context of underbalance drilling, the pressure and temperature at the wellhead and at bottomhole are measured throughout the operation. It will be assumed that the pressure and temperature along the length of the pipe, at any instant, can be obtained by a linear or cubic spline interpolation between the measured endpoints as shown in figure 15–7. This assumption will be examined later using a fully transient wellbore model for underbalance drilling. If the pressure and temperature are assumed to be known, there is no need to solve a transient pressure (momentum) equation, which greatly simplifies the wellbore model.

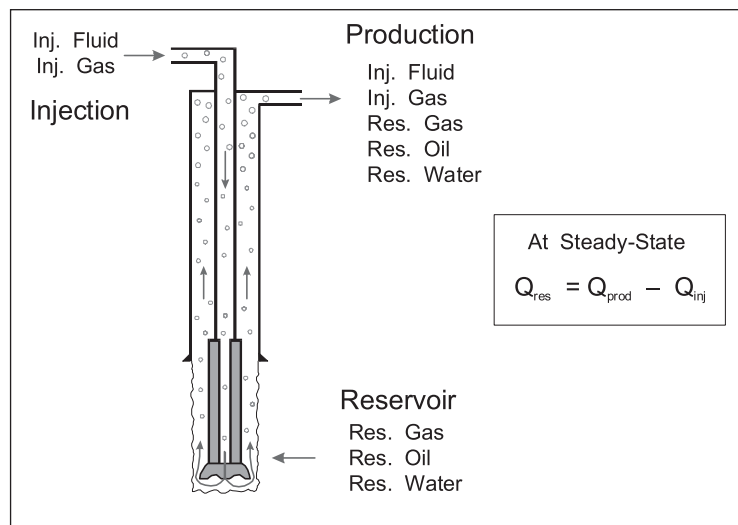


Fig. 15–6. System material balance

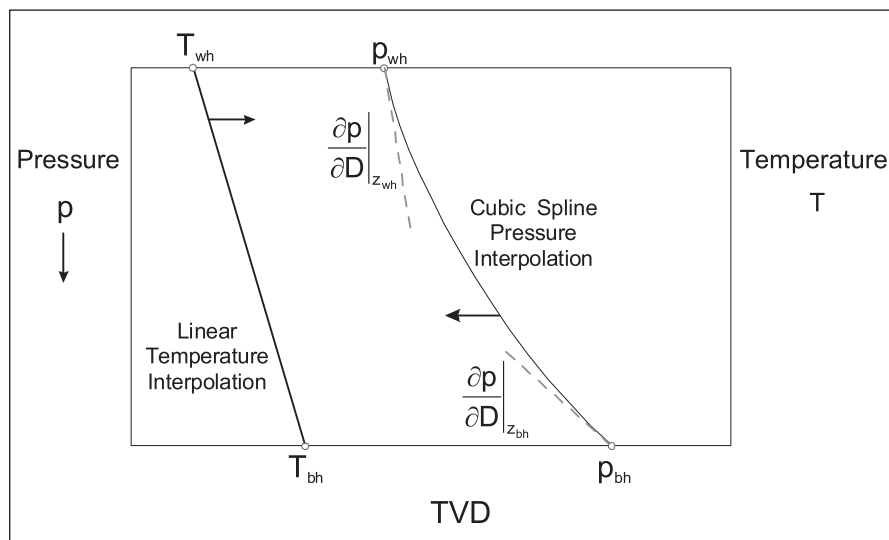


Fig. 15–7. Assumed pressure and temperature profiles

## Lumped Parameter Wellbore Model

The most sophisticated computer code for transient two-phase flow is the OLGA program developed in Norway. This software was originally focused on the problem of slugging in undulating pipelines but more recently the issue of slugging in the riser section of a gas-lifted well has been addressed. The key feature of OLGA is that the model predictions have been calibrated against both flow loop data (from the SINTEF loop in Norway) and field data from oil companies using the software. A special interface has also been written which allows the simulation of underbalance drilling. This program is called UBITS. An initial trial of OLGA indicated that it can be used as a virtual flow meter to determine the downhole flow rate from the measurements of surface flow rate and wellhead and bottomhole pressure. The idea of OLGA as a virtual flow meter has also been addressed in connection with conventional well testing, where the issue of nonideal wellbore storage has been a problem for many years. The application of OLGA in the UBD area is the subject of the next section of this chapter. The inflow model of OLGA (and therefore UBITS) is based on a steady- or semi-steady-state (SSS) productivity index (PI) and this is a severe limitation for either the well test situation or the UBD case. A modification to OLGA to allow a transient formation model is recommended. It will remain to be seen whether Scandpower adopts this suggestion. At the moment, the feeling in Weatherford is that UBITS is a qualitative tool for training but not quantitative in terms of detailed modeling of the UBD process. However, Scandpower has slides from a Shell presentation of a study using OLGA in real time to control the bottomhole pressure during UBD. This project included a multiphase flow meter upstream of the separator to give a direct measurement of the surface flow rate divorced from liquid level changes in the separator. The most likely weakness in UBITS is perhaps the inflow model, and rectifying this deficiency should considerably improve the predictions in the UBD situation.

As an alternative to using the OLGA code, which is expensive, it has been decided to also pursue another approach to the problem of estimation of downhole flow rate based on wellbore storage concepts in well testing. Here the wellbore is regarded as a tank containing compressible liquids, and a material balance equation links the input (downhole flow rate) and the output (surface flow rate) to the accumulation. This lumped parameter type of model will be modified to include dynamic changes in gas holdup and will be termed the LPW model. A wellbore with a distribution of gas holdup is shown in figure 15–8, where the pressure at inlet (bottomhole) and outlet (wellhead) are continuously monitored; these pressures are designated  $p_{wf}(t)$  and  $p_{wh}(t)$ , respectively. Since both the bottomhole and wellhead pressures are continuously monitored during a UBD operation, at any instant the interior pressure distribution can be obtained by interpolation as illustrated in figure 15–9. The simplest approach is a linear (straight line) interpolation between the terminal values  $p_{wf}(t)$  and  $p_{wh}(t)$ , and, since the bottomhole and wellhead temperatures  $T_{wf}(t)$  and  $T_{wh}(t)$  are also continuously measured, the same device can be used to approximate the internal temperature distribution. If information on the pressure gradient at the inlet and outlet ( $l = 0$  and  $l = L_m$ ) is supplied, a cubic spline can be fitted which will give a better approximation to the actual pressure distribution. A simple model assumes that the terminal pressure gradients are hydrostatic, i.e.,

$$\left. \frac{dp}{dl} \right|_{l=0} = - \left[ \left( \alpha_g \rho_g + (1 - \alpha_g) \rho_o \right) g \right]_{l=0} \quad (15-3a)$$

$$\left. \frac{dp}{dl} \right|_{l=L_m} = - \left[ (\alpha_g \rho_g + (1 - \alpha_g) \rho_o) g \right]_{l=L_m} \quad (15-3b)$$

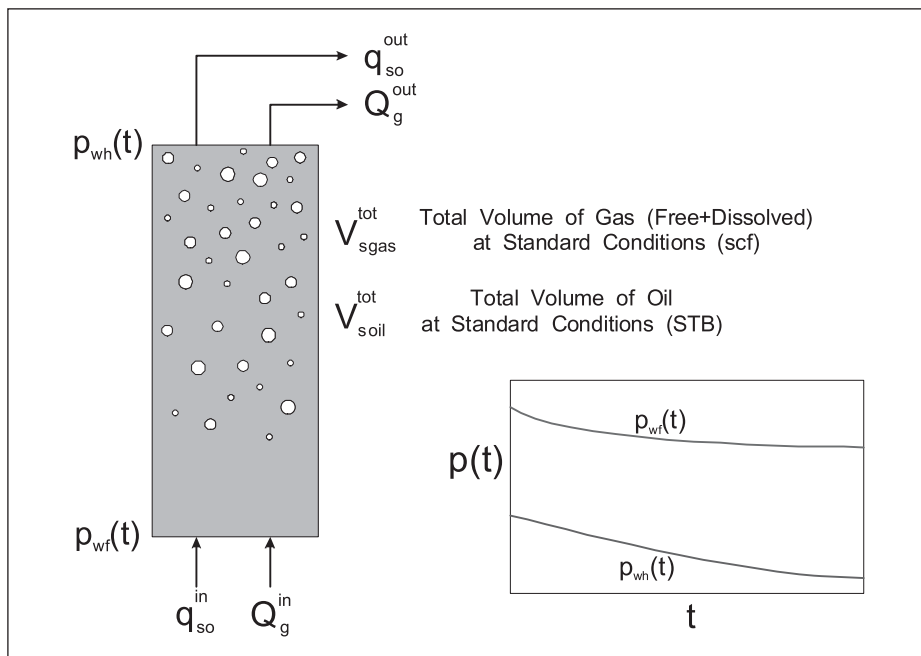


Fig. 15-8. Lumped parameter wellbore model

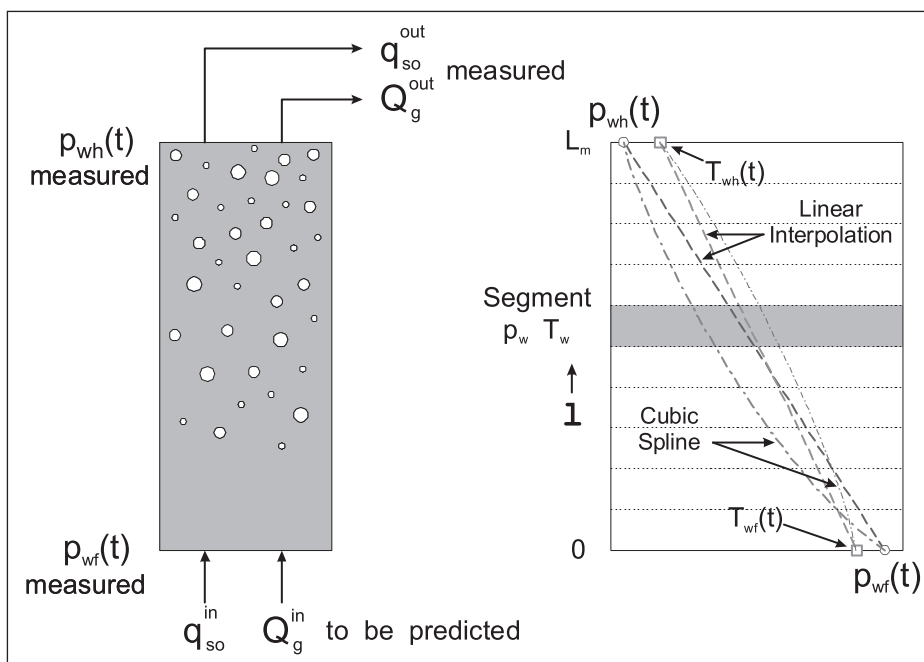


Fig. 15-9. Interpolation for interior pressure and temperature

In a lumped parameter approach, the volume of components in the “tank” will be calculated from a steady-state profile calculation. This is termed a quasi-steady-state (QSS) approximation and can be based on the measured surface flows at any instant. Thus the interior mass (or standard volume) flows of gas and oil components are held at the wellhead values and a steady-state pass is made by evaluating the holdup and property profiles as illustrated in figure 15–10. The pipe is divided into segments and the pressure and temperature at the mid-point of each is determined from the interpolation scheme. At each level the blackoil PVT model is used to compute the *in situ* volumetric rates of the phases  $q_g$  and  $q_o$ , as shown in figure 15–11. There is always a problem of nomenclature regarding black oil PVT models based on two components denoted oil and gas. For the purposes of material balance, the mass flow rates of these components have been written previously as  $m_O$  and  $m_G$ , i.e., the uppercase subscripts have been used to refer to components. In the black oil model, the liquid or oil phase contains both components, i.e., dissolved gas is present in the oil phase. When referring to phases, the lowercase subscripts o and g will be employed. The oil and gas components are described by a gravity or molecular weight, and the density of the pure component at standard conditions will be referred to as  $\rho_{SO}$  and  $\rho_{SG}$ , respectively, and are constants. The component mass flow rates may therefore be converted to volumes at standard conditions:

$$q_{SO} = \frac{m_O}{\rho_{SO}}; \quad Q_G = \frac{m_G}{\rho_{SG}} \tag{15-4}$$

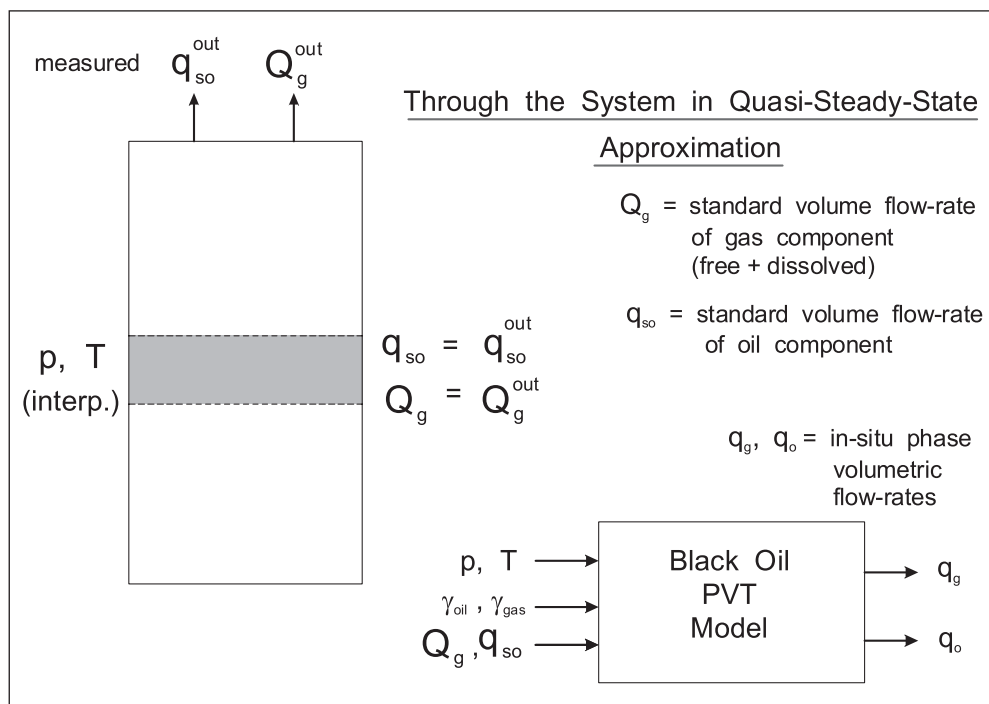


Fig. 15–10. Propagation of measured surface rates

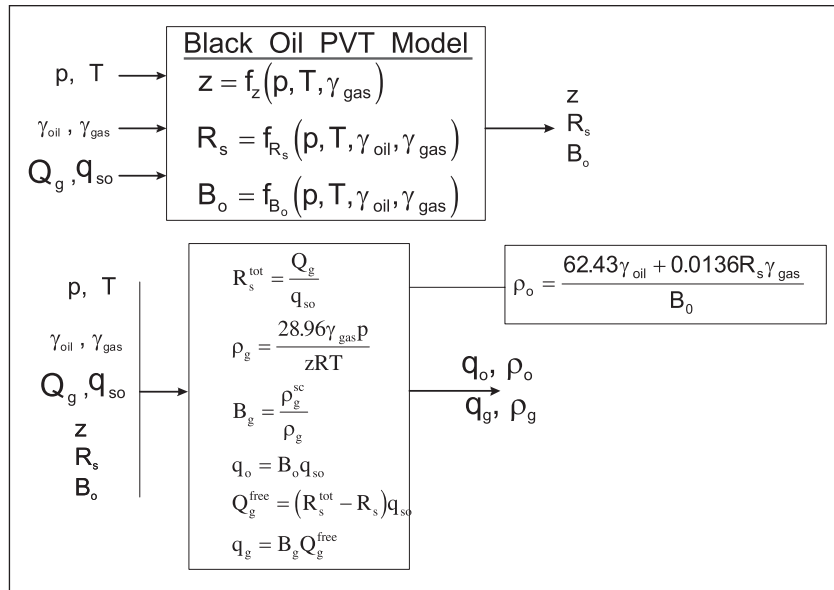


Fig. 15–11. Determination of in situ volumetric rates and phase densities

In the literature, these quantities are often written with lowercase subscripts, i.e.,  $q_{so}$  and  $Q_g$ . An oil flow rate with the subscript “s” or a gas flow rate with an upper case Q will always imply a component volume flow at standard conditions. These are entirely equivalent to component mass flow rates. Note that  $Q_g$  refers to the total amount of gas irrespective of whether it is present as free gas or dissolved gas. The gas solubility in the oil phase is given the symbol  $R_s$  and has units of vol/vol (standard) e.g., SCF/STB. This depends on pressure and temperature for a system of specified gravities. The standard conditions flow rate of free gas, i.e., gas phase, is given by

$$Q_g^{\text{free}} = Q_g - R_s q_{so}$$

The swelling of the oil phase due to the presence of dissolved gas is represented by the oil formation volume factor  $B_o$ , and the *in situ* volumetric flow rate of the oil phase  $q_o$  is given by

$$q_o = B_o q_{so} \quad (15-5)$$

In essence, a black oil model consists of two correlations relating  $R_s$  and  $B_o$  to pressure, temperature, and the gravities of the two components. In this chapter, the following expressions have been employed:

$$R_s = \gamma_g \left[ \left( 1.4 + \frac{p}{18.2} \right) 10^{-\left( 0.00091T_F - 0.0125\gamma_{API} \right)} \right]^{0.83} \quad (15-6)$$

$$B_o = 0.9759 + 0.00012 \left[ R_s \left( \frac{\gamma_g}{\gamma_o} \right)^{0.5} + 1.25T_F \right]^{1.2} \quad (15-7)$$



$$p : \text{psi} \quad T_F : ^\circ\text{F} \quad \gamma_{\text{API}} : ^\circ\text{API}$$

The preceding treatment has considered only a two-component system comprising of oil and a distributing gas component. In practice, there will normally be an additional two components, i.e., nitrogen and water. Nitrogen is taken to be insoluble in the liquid phases, and the free-gas phase contains the entire nitrogen present and free gas component. The solubility of gas in the oil phase is computed from the black oil model which is entered with the partial pressure of gas, viz.,

$$pp_g = (1 - y_{\text{N}_2})p \tag{15-8a}$$

i.e.,

$$R_s = \gamma_g \left[ \left( 1.4 + \frac{pp_g}{18.2} \right) 10^{- (0.00091T_F - 0.0125\gamma_{\text{API}})} \right]^{\frac{1}{0.83}} \tag{15-8b}$$

$$Q_{g,\text{free}} = Q_g - R_s q_{\text{so}} \tag{15-8c}$$

$$y_{\text{N}_2} = \frac{\frac{Q_{\text{N}_2} \rho_{\text{N}_2}^s}{28}}{\frac{Q_{\text{N}_2} \rho_{\text{N}_2}^s}{28} + \frac{Q_G \rho_g^s}{\gamma_{\text{HC}} 28.96}} \tag{15-8d}$$

A secant iteration is required to solve these simultaneous equations for  $y_{\text{N}_2}$ ,  $R_s$ , and  $Q_{g,\text{free}}$ , given the total pressure  $p$  and temperature  $T$ .

Once the *in situ* phase volumetric rates have been calculated at each segment mid-point, the generalized drift flux model, described in the preceding section, is then used to compute the local gas holdup as shown in figure 15-12. The PVT model will also have computed the phase densities and formation volume factors. The final stage, illustrated in figure 15-13, is to calculate the amount of each component in the segment from the equations

$$\Delta V_{\text{sgas}}^{\text{tot}} = \frac{\Delta I A_t \alpha_g}{B_g} + \Delta V_{\text{soil}}^{\text{tot}} R_s \tag{15-9a}$$

free dissolved

$$\Delta V_{\text{soil}}^{\text{tot}} = \frac{\Delta I A_t (1 - \alpha_g)}{B_o} \tag{15-9b}$$

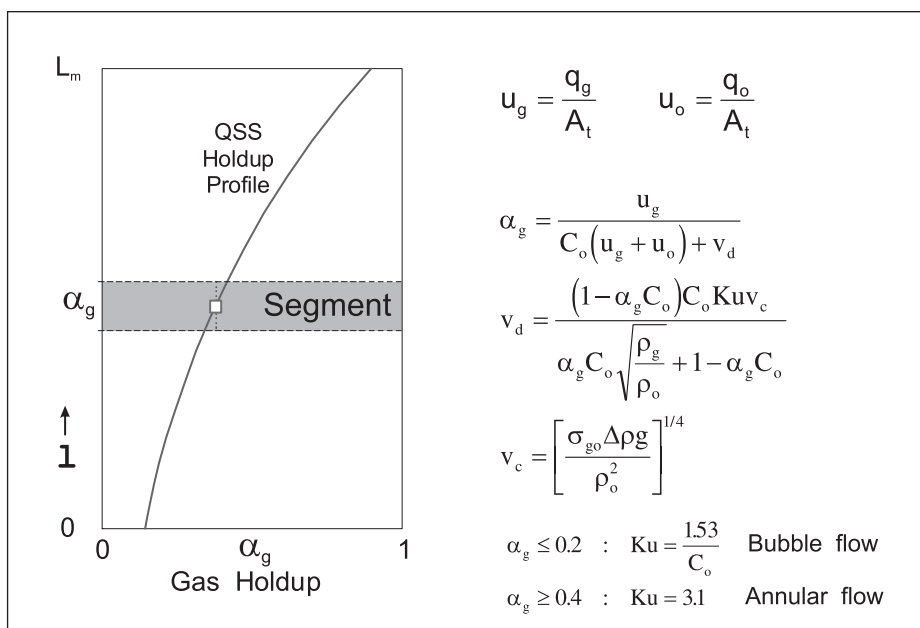


Fig. 15-12. Drift velocity holdup model

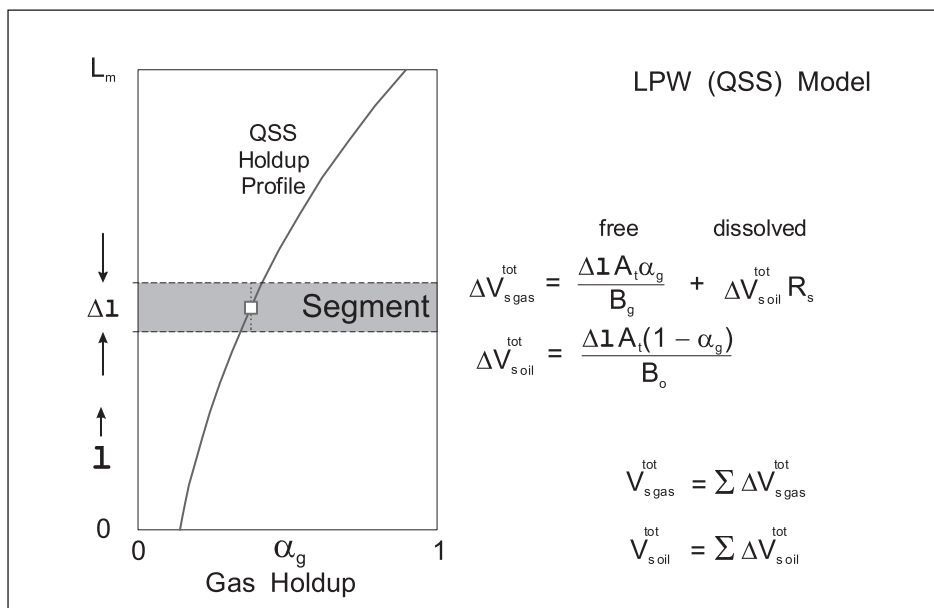


Fig. 15-13. Summation of standard volumes contained in segments

The summations over the segments yield the total amounts of gas and oil present in the tubing at the specified instant in time

$$V_{sgas}^{tot} = \sum_{ns=1}^{nsegm} \Delta V_{sgas}^{tot} \quad (15-10a)$$

$$V_{soil}^{tot} = \sum_{ns=1}^{nsegm} \Delta V_{soil}^{tot} \quad (15-10b)$$

The steady-state pass is based on the standard volume flow rates at the exit  $q_{so}^{out}$  and  $Q_g^{out}$ , since these are measured quantities. The gas holdup is greater at the low-pressure outlet end of the tubing, so using the exit stream as a basis is probably the best option. Fortunately, pressure and temperature are measured at both ends and the interpolation should provide a good interior profile of these quantities.

A calculated steady-state holdup profile for a well with the parameters given in table 15–1 is shown in figure 15–14; in this case the holdup at the wellhead (outlet) is less than 0.2 and hence the whole tubing is in the bubble flow regime. For this QSS snapshot, based on surface (outlet) rates, the amount of oil component present in the wellbore is 4.01 STB, while the gas content (free + dissolved) is 3,785 SCF. The profiles of gas component solubility  $R_s$  and gas phase density  $\rho_g$  are shown in figure 15–15. Note that the pressure at the inlet (5,000 psi) is less than the bubble point pressure at the inlet temperature of 660 °R and there is free gas over the whole length of the tubing. It is interesting to determine the time taken to replace the contents of the wellbore; for oil this time is given by

$$t_{R,oil} = \frac{4.01 \times 24 \times 3600}{2000} = 173 \text{ sec}$$

and for gas

$$t_{R,gas} = \frac{3785 \times 24 \times 3600}{2000 \times 1000} = 163 \text{ sec}$$

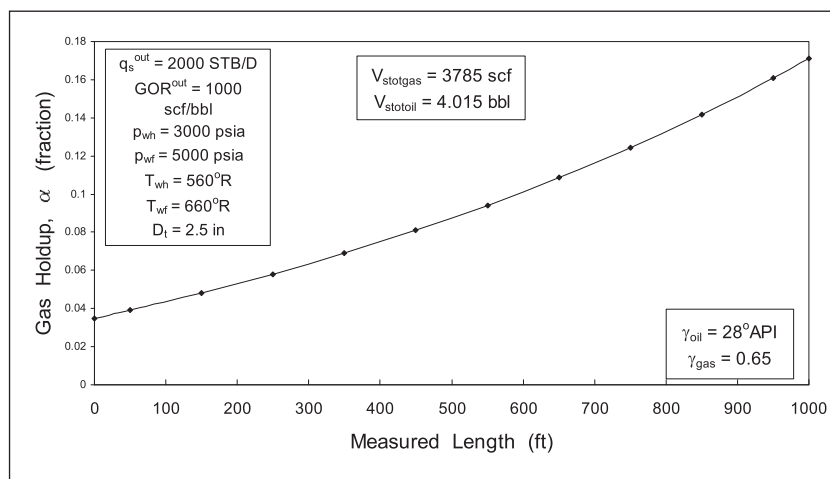


Fig. 15–14. Gas holdup profile

Thus the timescale of holdup changes in the wellbore is of the order of 3 min in this case, i.e., it is a fast process, which accounts for the numerical difficulty in trying to solve the fully distributed model in terms of partial differential equations.

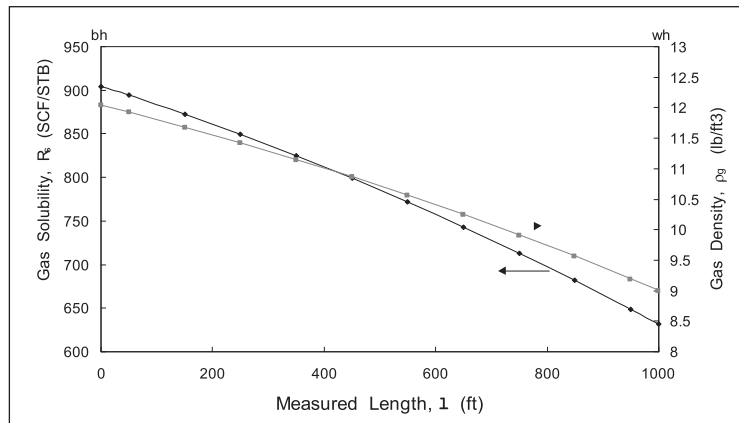


Fig. 15-15. Gas solubility and gas density profiles

Table 15-1. Parameter values for steady-state profile

$p_{wh} = 3,000$ psia	$p_{wf} = 5,000$ psia	$T_{wh} = 560^\circ R$	$T_{wf} = 660^\circ R$	$q_{sot}^{out} = 2,000$ STB/D
$GOR^{prod} = 1,000$ SCF/STB	$\gamma_g = 0.65$	$\gamma_{API} = 28$	$D_t = 2.5$ in.	$L_m = 1,000$ ft
$\sigma = 0.0245$ Pa.s	$\theta = 0$	Linear interpolation		

A second run was made with the producing gas–oil ratio (GOR) increased to 1,500 SCF/STB, all the other parameters remaining the same. The new gas holdup and drift velocity profiles are displayed in figure 5–16 and it can be seen that, over most of the length, slug flow is now occurring ( $0.2 \leq \alpha_g \leq 0.4$ ). The calculated drift velocity  $v_d$  goes up sharply in the slug-flow regime and the main attraction of the generalized slip model of Shi *et al* is its ability to handle this effect. The gas holdup is roughly double the levels in the base case and the trapped standard volumes are correspondingly different. The addition of nitrogen to the system is shown in figure 15–17, where the mole fraction  $N_2$  decreases as more gas flashes off up the tubing.

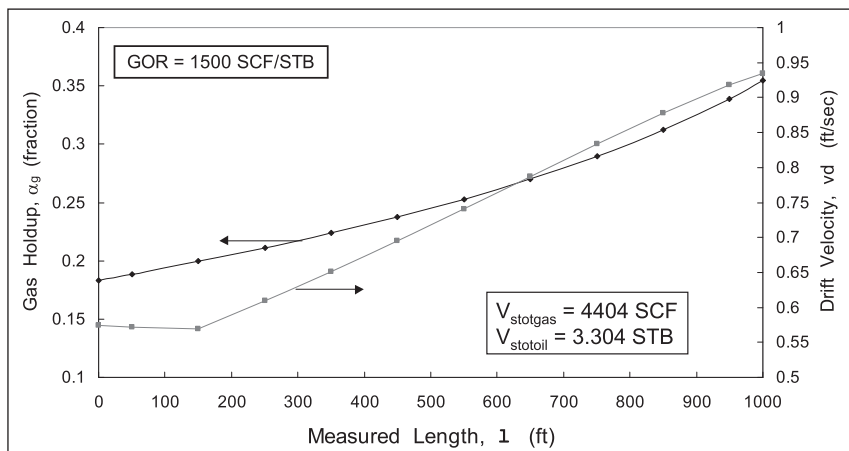


Fig. 15-16. Gas holdup and drift velocity profiles

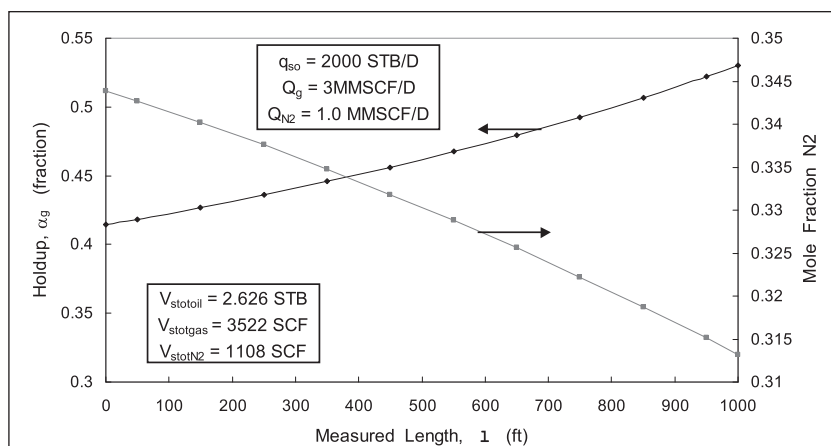


Fig. 15-17. Nitrogen mole fraction profile

The tank material balance equations for the components, i.e., oil and gas, take the form

$$q_{so}^{in} - q_{so}^{out} = \frac{dV_{soil}^{tot}}{dt} \tag{15-11a}$$

$$Q_{gas}^{in} - Q_{gas}^{out} = \frac{dV_{sgas}^{tot}}{dt} \tag{15-11b}$$

where mass has been converted to volumes at standard conditions. Solving for the inlet volume flow rates gives

$$q_{so}^{in} = q_{so}^{out} + \frac{dV_{soil}^{tot}}{dt} \tag{15-12a}$$

$$Q_{gas}^{in} = Q_{gas}^{out} + \frac{dV_{sgas}^{tot}}{dt} \tag{15-12b}$$

This simple model is useful only if a correlation can be obtained that relates the volumes of the components at standard conditions, i.e.,  $V_{soil}^{tot}$  and  $V_{sgas}^{tot}$ , to the flowing conditions at any time. One way of modeling transient phenomena is to regard the process as a sequence of steady states. Supposing attention is focused on the wellhead conditions of flow rate and pressure (also temperature), then for a given prescription of these quantities a steady-state pressure drop computation can be made integrating downward from the wellhead. This will generate a pressure and holdup profile in the tubing, which can be integrated to give the volumes required. Thus the wellbore gas and oil content can be related to the instantaneous wellhead conditions. As the wellhead pressure falls and more gas is present, these volumes will change. This information is then used in the dynamic material-balance model (15-12), where the accumulation term is calculated numerically as illustrated in figure 15-18. Obviously a steady-state wellbore model is required to achieve this and the generalized holdup model described in the section

“Transient Well Model” can form the basis of this calculation. In order to verify the accuracy of this procedure, some runs of a distributed model, i.e., OLGA, will have to be made. The surface flow measurement itself is susceptible to quite a degree of error, perhaps as much as  $\pm 10\%$ . The algorithm to reconstruct the downhole rate only needs to be of accuracy comparable to that of the rate measurement: i.e., a fair degree of error can be tolerated. The changes in holdup and gas density will not be large and the downhole rate will closely follow the surface rate which is measured. One issue, however, will be a change in inlet gas rate and how quickly a holdup redistribution in the wellbore will propagate through the system. This explains why some runs of OLGA will be necessary to validate a simple lumped-parameter model. In this approach, the pressure profile will be a smooth function, e.g., cubic spline, interpolating between the measured wellhead and bottomhole values. In figure 15–19, the effect of having a second liquid phase, i.e., water, is shown and the holdup profile now has both the volume fraction of gas phase and the volume fraction of oil in the combined liquid. In this run, there are four components and the trapped standard volume of each one has been computed. As a final example, the case where no hydrocarbon is present—only nitrogen and water—is illustrated in figure 15–20, where the gas-phase (nitrogen) holdup is plotted as a function of the measured length.

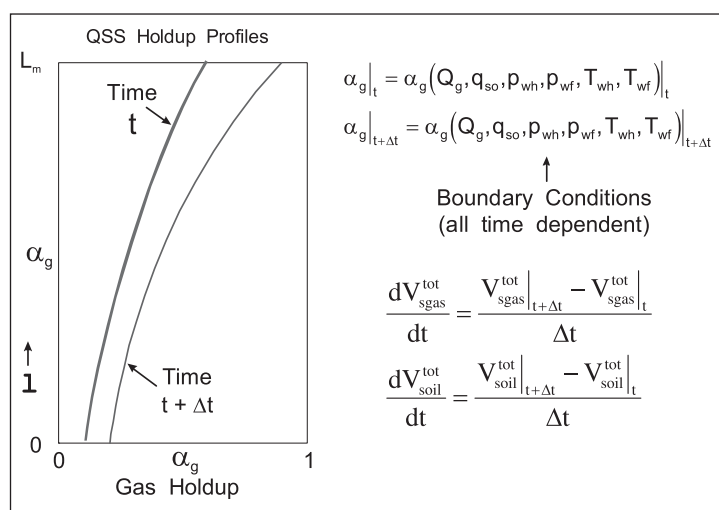


Fig. 15–18. QSS approximation

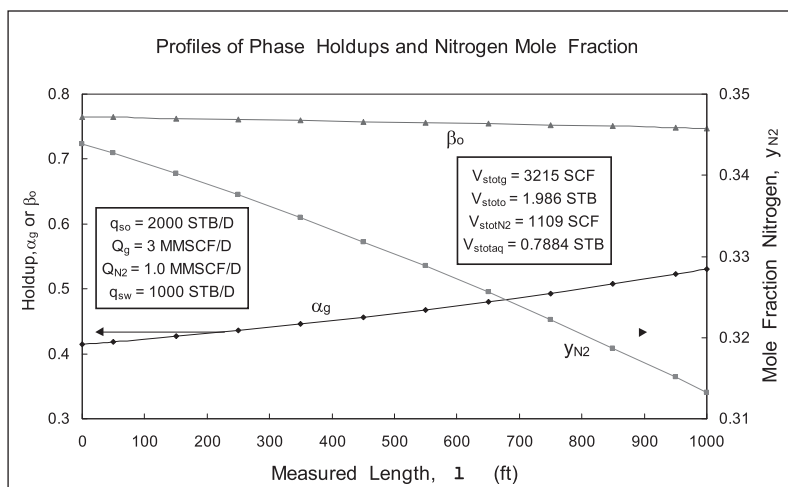


Fig. 15–19. Effect of a second liquid phase, i.e., water

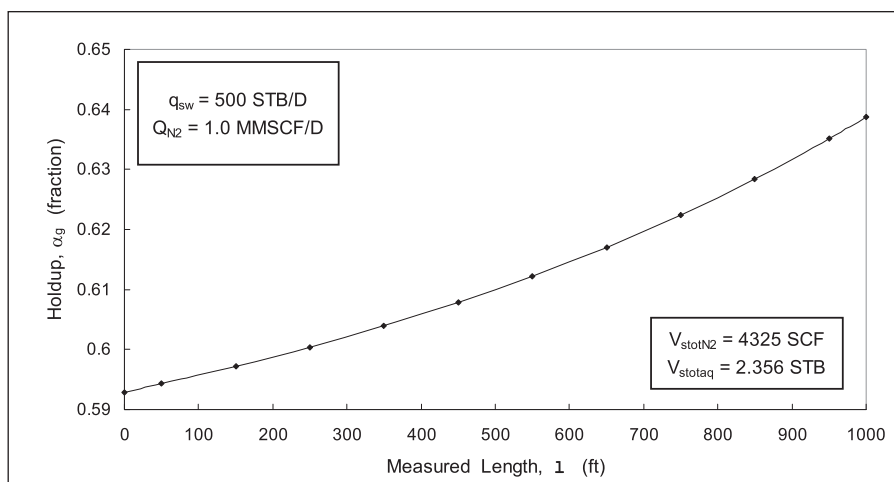


Fig. 15–20. Nitrogen holdup in N<sub>2</sub>-water system

In order to assess the importance of wellbore storage effects, it is interesting to use the two runs at steady-state conditions shown in figures 15–14 and 15–16, where the producing GOR is 1,000 SCF/STB in the first case and 1,500 SCF/STB in the second. Thus, if the GOR is changed from one value to another over a certain time period, the volume of oil (at stock tank conditions) held up in the 2.5" tubing goes from 4.015 STB to 3.304 STB. Thus the change in the liquid content is very small and essentially the input and output flow rates of oil differ only very little, i.e.,

$$q_{so}^{in} = q_{so}^{out} \tag{15-13}$$

In the present example, the surface flow rate of stock tank oil is 2,000 STB/D and it should be recognized that the error in flow measurement will be at least 5%, i.e.,  $\pm 100$  STB/D. Suppose the change in GOR occurs over a 1-h period; then the time derivative of oil volume is

$$\frac{dV_{soil}^{tot}}{dt} = (4.015 - 3.304) \times 24 = 17 \text{ STB/D}$$

which is negligible compared to the flow-rate measurement error.

In the system shown in figure 15–3, the surface flow rates are measured after the separator and hence any level changes in this device will mean there is a discrepancy between the wellhead flow rate and what is actually measured. It is therefore likely that this effect will be much more serious than the wellbore capacity problem. Since the proposed technique for determining formation permeability and pressure depends on sensitive rate measurement, it is necessary to minimize error whatever the cause. An improved system has been devised that has a multiphase flow meter in the transfer line from the wellhead. Shell have already tested such a system in the project to use OLGA to control the bottomhole pressure, i.e., underbalance. This scheme has an added attraction for the present project, since it could lead to much higher quality rate data.

## Distributed Parameter Wellbore Model

In the preceding section, the lumped parameter model was used to obtain estimates of the difference between the measured surface rate and the *in situ* rate entering the well from the formation. In this section, a fully distributed parameter wellbore model, i.e., OLGA, will be used to identify wellbore storage effects and examine in detail the idea of a VDF. Transient simulations in OLGA usually commence from a steady-state situation corresponding to time-independent boundary conditions. In the first test case, a vertical well of length 1,500 m and diameter 3" is modeled with a wellhead pressure of 30 bara and a bottomhole flowing pressure of 130 bara. Over the time period of 1.8–2.0 h, the bottomhole pressure is ramped up to 140 bara. The fluid entering from the reservoir is an oil phase and the OLGA trend plot of the simulation results is shown in figure 15–21. The wellhead pressure is maintained at 30 bara throughout the transient and the steady-state mass flow rate before the ramp change in  $p_{wf}$  is kg/s. In OLGA, pressure is a volume variable and the pressure at the mid-point of the first segment is plotted in figure 15–21. This changes from 128.3 bara to 138.3 bara over a 0.2 h ramp period. The mass flow at the inlet (Pipe 1,1) and the mass flow at the outlet (Pipe 1,30) are different during the transient period, with the inlet mass flow being greater than that at the exit due to the decreasing gas holdup in the well. In the plot, the liquid (oil) holdup is seen to increase; i.e., there is a “negative gas drive” process due to the compression of the gas phase as the pressure rises. At the steady state, before the ramp in inlet pressure, the two mass flows are identical at 12.52 kg/s. The final steady state at the new inlet pressure of 140 bara is 14.07 kg/s. During the ramp period, the inlet flow is approximately 1.4% higher (0.18 kg/s) than the exit flow and the difference is probably less than the resolution of the rate measurement. The liquid holdup in the exit segment increases from 0.2595 to 0.2617. Since this region is essentially at the exit pressure of 30 bara, this is a slip-related decrease in gas holdup, i.e., the higher rate means less importance of slip and therefore slightly smaller gas holdup. The steady-state profiles in the well before the disturbance in inlet pressure are shown in figure 15–22. The inlet pressure of 130 bara is just above the oil bubble point and there is a short region of single-phase flow. The inlet (reservoir) temperature is 70 °C and with an overall heat transfer coefficient  $U$  of 10 W/m<sup>2</sup>/°C the exit fluid temperature is 57°C. The whole of the two-phase region is in the bubble-flow regime.

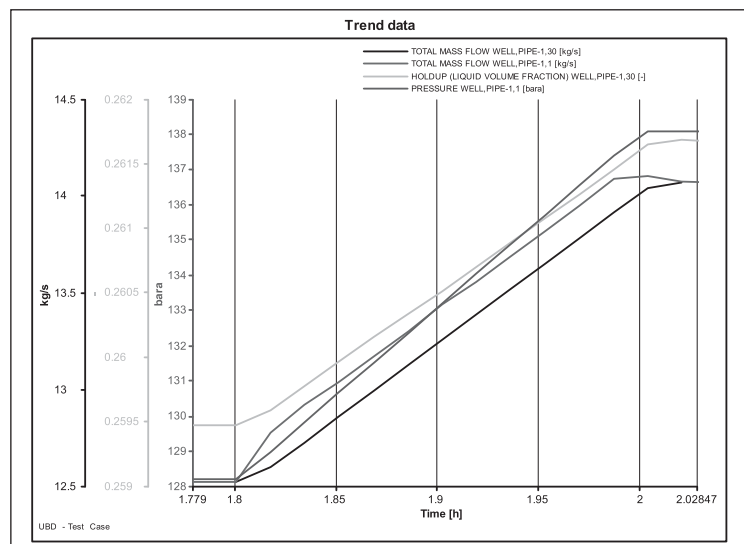


Fig. 15–21. Result of OLGA simulation—first segment



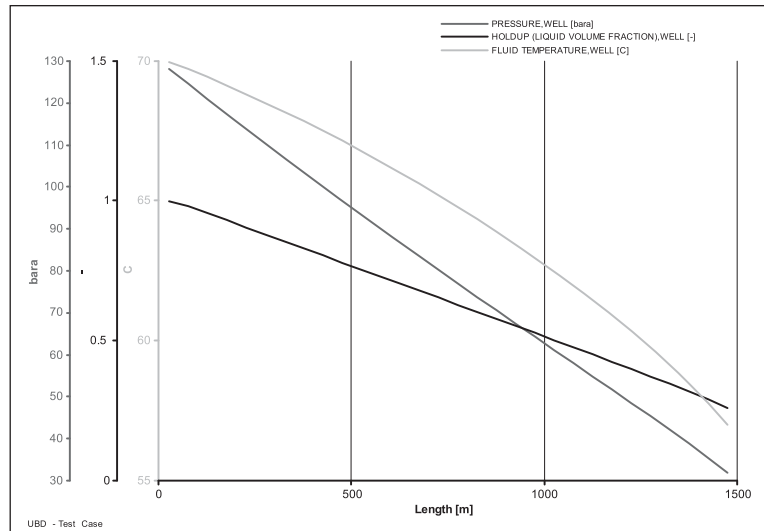


Fig. 15–22. Profile data at 1.669 h

In a second test case, the inlet pressure was reduced from 130 to 120 bara, which would reduce the mass flow rate to a final steady-state of 10.94 kg/s. In this case, the reduction in flowrate will tend to increase gas holdup through the slip, whereas the reduction in pressure will give rise to a “gas drive” effect associated with bubble expansion and hence will increase gas holdup. The second effect is dominant and the inlet mass flow is consistently less than that at the exit as shown in figure 15–23, which is the trend plot for the second case. Because of the opposing effects, the trend in liquid holdup at the exit end shows a complicated behavior as indicated in the diagram and exhibits a minimum, about half-way through the ramp. The maximum difference between inlet and exit mass flow rates at 1.87 h is 2.9% (0.35 kg/s), which is just large enough to warrant consideration.

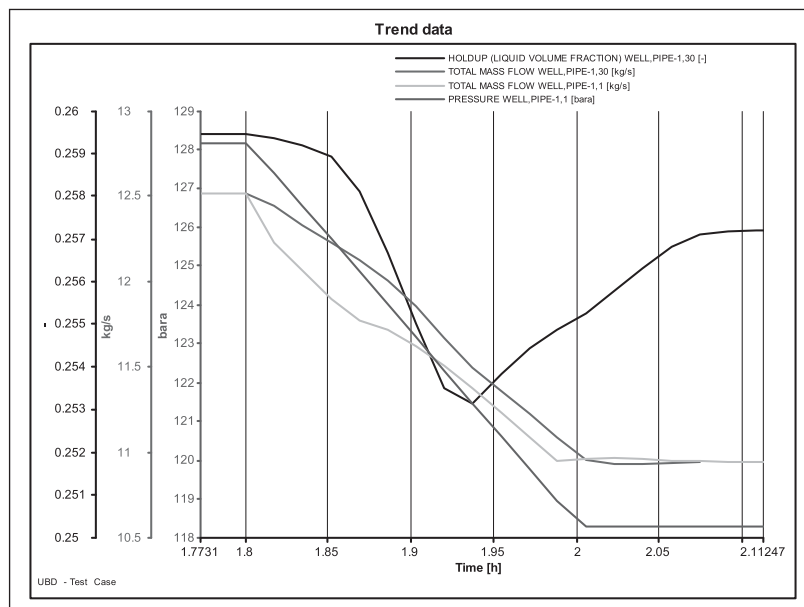


Fig. 15–23. Gas drive effect

These preliminary runs with OLGA also confirm that the wellbore capacity effects are quite small but, if the flow measurement accuracy merits this refinement, then OLGA is a useful tool to make the correction.

## Transient Formation Model

It will be shown later that the development of a practical methodology for layered well testing in the underbalance drilling context requires an algorithm that will compute the rate response of a layer given a measured pressure history. The basis of variable rate analysis is the convolution or superposition theorem which is illustrated in figure 15–24. The convolution equation takes the form

$$p_i - p_w(t) = \frac{\mu}{2\pi kh} \left( \sum_{i=1}^M q_i (p_D(t - T_{i-1})_D - p_D(t - T_i)_D) + q(t)p_D(t - T_M)_D \right) \quad (15-14)$$

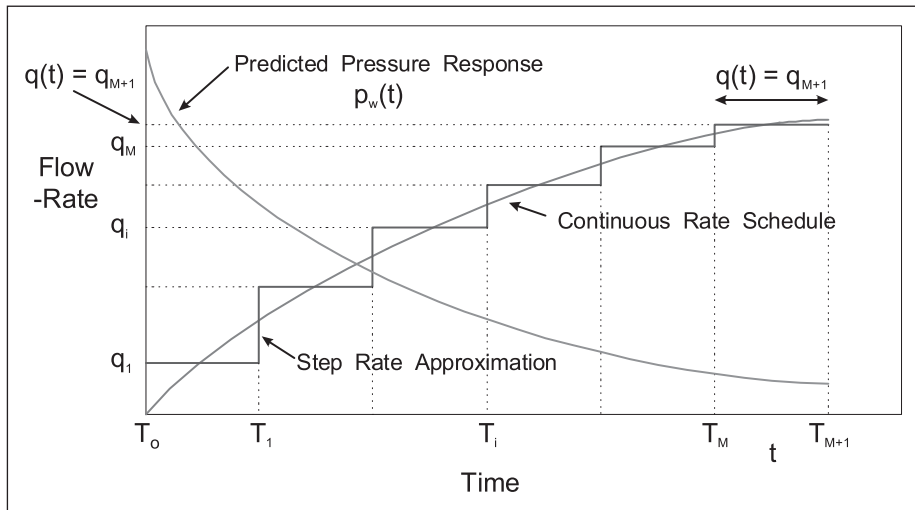


Fig. 15–24. General superposition based on step-rate approximation

Usually, this superposition principle is used to predict the bottomhole flowing pressure  $p_{wf}(t)$  knowing the rate history of the well. Here, the dimensionless constant rate  $p_D$  function often refers to an infinite-acting radial flow, i.e.,

$$p_D(t_D) = \frac{1}{2} \ln \frac{4kt}{\gamma \phi \mu c_t r_w^2} + S \quad (15-15)$$

However, in the UBD context the flowing pressure  $p_{wf}(t)$  is known and it is desired to predict the rate transient. Consider the problem of determining the rate in the time step between  $T_M$  and  $T_{M+1}$ , as indicated in figure 15–25. It is presumed that the rate in the preceding time steps has

already been computed. Since individual layers are involved, it is convenient to apply equations (15–14) and (15–15) to each layer  $j$  with starting time  $\tau_j = T_{lj}$ ; equation (15–14), subscripted  $j$  for a specific layer, can be solved for the new layer rate as follows:

$$q_{M+1,j} = \frac{2\pi k_j h_j (p_j^i - p_w(T_{M+1}))}{\mu p_{Dj} (T_{M+1} - T_M)_{Dj}} - \frac{\sum_{i=lj+1}^M q_{ij} (p_{Dj}(T_{M+1} - T_{i-1})_{Dj} - p_{Dj}(T_{M+1} - T_i)_{Dj})}{p_{Dj}(T_{M+1} - T_M)_{Dj}} \quad (15-16)$$

Here the integer  $lj$  is the index of the time step at which layer  $j$  commences to flow. Since the wellbore pressure is measured very accurately, this ability to compute the layer flow-rate response  $q_j(t)$  for a forced-pressure transient and assumed model parameters forms an essential part of the testing method. The generated flow response mode is illustrated in figure 15–25. The pressure and time points are now recognized as input to the sequential calculation of  $q_j(t)$  ( $j = 1, \dots, N$ ) using step-rate formula (15–16). Equation (15–16) applies when the imposed pressure is specified from time  $t = 0$  and the initial layer pressure, i.e.,  $p_j^i$  is known. In figure 15–25, the flowing bottomhole pressure (FBHP)  $p_{wf}(t)$  is depicted as constant and the computed flow schedule is the transient response to a step change in the wellbore pressure. This constant underbalance case is the canonical behavior for UBD analysis. The idea of computing the rate response for a specified pressure history using equation (15–16) was developed for layered well testing using up-and-down passes of a production logging tool.

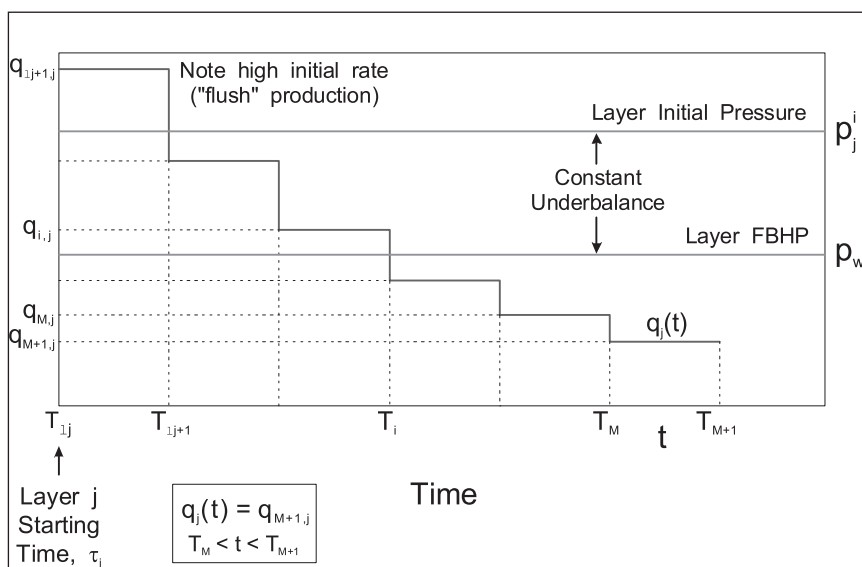


Fig. 15–25. Layer  $j$  flow schedule

In the preceding treatment, the convolution is based on the constant rate solution to the diffusivity equation, i.e., equation (15–15), following the approach adopted in conventional well test interpretation. However, it is also possible to derive a convolution based on the constant terminal pressure solution of Jacob and Lohman, which takes the form

$$q_D = \frac{1}{\frac{1}{2} \ln \frac{4t_D}{\gamma} + S} \quad (15-17)$$

where

$$q_D = \frac{\mu q(t)}{2\pi kh(p_i - p_{wf})} t_D = \frac{kt}{\phi \mu c_t r_w^2}$$

Here the time-dependent rate  $q(t)$  is predicted for a step change  $\Delta p = p_i - p_{wf}$  in the inner boundary (wellbore) pressure. The dimensionless rate transient according to (15-17) is plotted in figure 15-26 for  $S = 0$ , which again illustrates the initial flush production at early time. However, note that (15-17)—the log approximation—is not valid at very small values of  $t_D$ . In fact, Jacob and Lohman<sup>1</sup> refer to equation (15-17) as the long-time solution, but in modern well test parlance this would be referred to as the middle-time region. Typically, the log approximation is valid for dimensionless times  $t_D$  greater than 25.

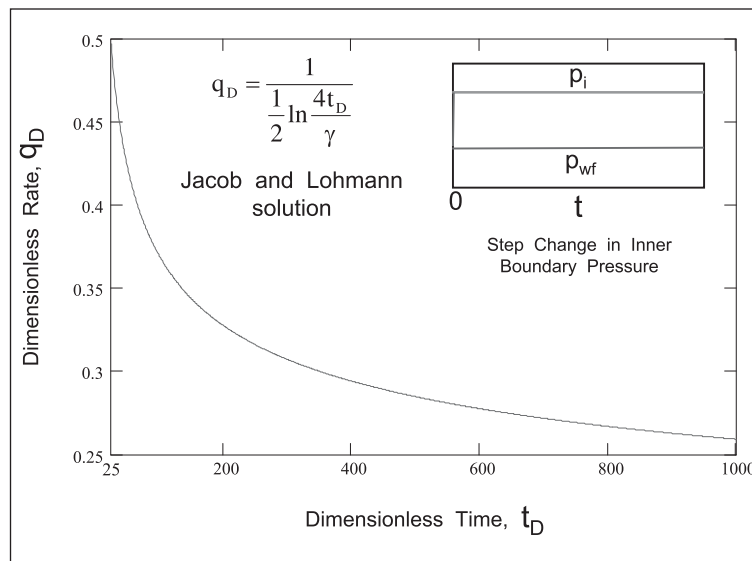


Fig. 15-26. Dimensionless rate transient

In the context of the inverse problem of parameter estimation, the analytical solution is of the form

$$\frac{1}{q(t)} = \frac{\mu}{4\pi kh(p_i - p_{wf})} \left( \ln t + \ln \frac{4k}{\gamma \phi \mu c_t r_w^2} \right) \quad (15-18)$$

In this formulation, the skin has deliberately been set to zero, which conforms to the UBD scenario. A semilog plot of  $1/q(t)$  i.e.  $q^{-1}(t)$ , versus  $\ln t$  will exhibit a straight-line form (as shown in figure 15-27):

$$q^{-1}(t) = m \ln t + b \quad (15-19)$$

where the slope 
$$m = \frac{\mu}{4\pi kh(p_i - p_{wf})} \tag{15-20}$$

and the intercept 
$$b = \frac{\mu}{4\pi kh(p_i - p_{wf})} \ln \frac{4k}{\gamma\phi\mu c_t r_w^2} \tag{15-21}$$

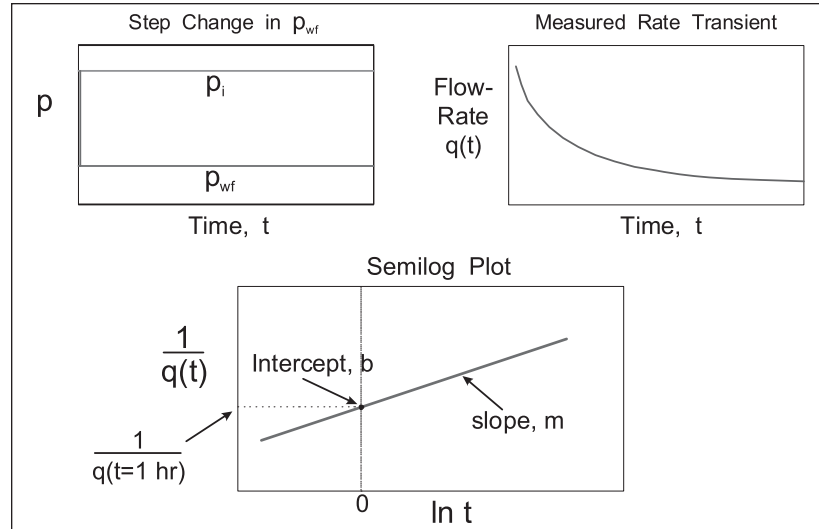


Fig. 15-27. Constant drawdown test

Thus, if the slope and intercept  $m$  and  $b$ , respectively, of the semilog plot are determined, these values can be used to identify the permeability  $k$  and the formation pressure  $p_i$ , since there are two equations (15-20) and (15-21) in two unknowns  $k$  and  $p_i$ . It is only possible to determine the pressure in a single-step drawdown because the skin is deemed to be zero, but this is an interesting theoretical result for the constant terminal pressure situation. In this theory of a single-layer system, it is assumed that the drawdown can be applied instantaneously to the whole zone, obviously if the UBD situation progressive penetration occurs.

In the case where the inner pressure boundary condition is time dependent, a superposition principle takes the form

$$q = \frac{2\pi kh}{\mu} \left( \Delta p_1 q_D(t_D) + (\Delta p_2 - \Delta p_1) q_D(t_D - T_{1,D}) + (\Delta p_3 - \Delta p_2) q_D(t_D - T_{2,D}) + \dots \right) \tag{15-22}$$

This form is used, for example, in the classical treatment of transient aquifer influx and in cases where the  $q_D$  function is available. This gives a better solution for the prediction of rate transients given the pressure history than the form (15-16). However, constant rate  $p_D$  functions are available for a wide range of models because of their application in conventional pressure transient analysis and hence the approach based on (15-16) is useful to have. In figure 15-28, the response of the rate to a pulse change in wellbore pressure, computed from the superposition (15-22), is plotted. The reservoir data for this simulation are listed in table 15-2.

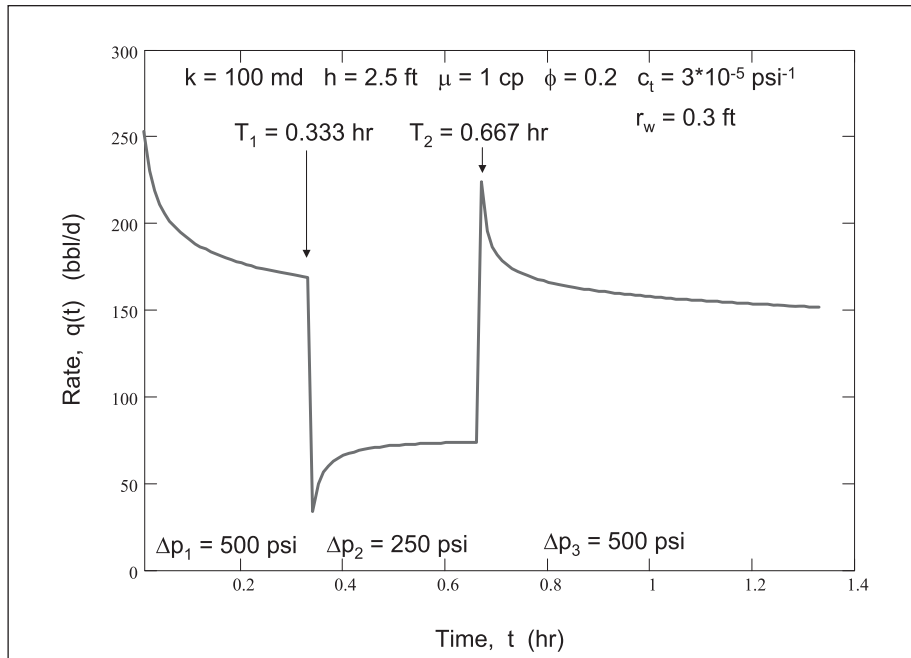


Fig. 15–28. Drawdown pulse rate response

Table 15–2. Reservoir data for pulse change in drawdown (three period test)

$\mu = 1 \text{ cp}$	$\phi = 0.2$	$r_w = 0.3 \text{ ft}$	$c_t = 3 \times 10^{-5} \text{ psi}^{-1}$	$h = 2.5 \text{ ft}$
$k = 100 \text{ md}$	$p_i = 5,000 \text{ psia}$	$T_1 = 0.333 \text{ h}$	$T_2 = 0.667 \text{ h}$	$\Delta p_1 = 500 \text{ psi}$
$\Delta p_2 = 250 \text{ psi}$	$\Delta p_3 = 500 \text{ psi}$			

The semilog plot for the first drawdown period ( $0 < t < 0.333 \text{ h}$ ) is shown in figure 15–29, where the predicted straight line is apparent. Substituting the fitted slope and intercept in equations (15–20) and (15–21) and solving for  $k$  and  $p_i$  yield the values listed in table 15–2, viz.,  $k = 100 \text{ md}$  and  $p_i = 5,000 \text{ psia}$ .

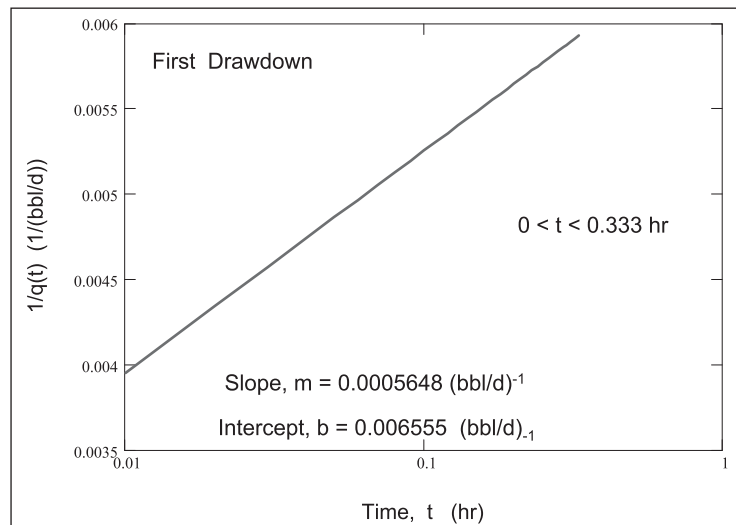


Fig. 15–29. Rate transient semilog plot

It is interesting to examine the behavior of a two-drawdown test, which corresponds to the first two periods in figure 15–28. In this case, the rate during the second period is given by (15–22) with two terms, i.e.,

$$q_2 = \frac{2\pi kh}{\mu} \left( \Delta p_1 q_D(t_D) + (\Delta p_2 - \Delta p_1) q_D(t_D - T_{1,D}) \right) \quad (15-23)$$

which on substitution of the model ( $q_D$  function) (15–17) becomes

$$q_2 = \frac{4\pi kh}{\mu} \left( \frac{\Delta p_1}{\ln \frac{4t_D}{\gamma}} + \frac{\Delta p_2 - \Delta p_1}{\ln \frac{4(t_D - T_{1,D})}{\gamma}} \right) \quad (15-24a)$$

or

$$q_2 = \frac{4\pi kh}{\mu} \left( \Delta p_1 \left( \frac{1}{\ln \frac{4(T_1 + \Delta t)_D}{\gamma}} - \frac{1}{\ln \frac{4(\Delta t)_D}{\gamma}} \right) + \frac{\Delta p_2}{\ln \frac{4(\Delta t)_D}{\gamma}} \right) \quad (15-24b)$$

In the special case where  $\Delta p_2 = 0$ , i.e.,  $p_{wf} = p_i$ , during the second period this becomes

$$q_2 = \frac{4\pi kh \Delta p_1}{\mu} \left( \frac{1}{\ln \frac{4(T_1 + \Delta t)_D}{\gamma}} - \frac{1}{\ln \frac{4(\Delta t)_D}{\gamma}} \right) \quad (15-25a)$$

For the data listed in table 15–2, the drawdown in the second and third periods was set to zero, and the predicted rate response is plotted in figure 15–30. The function in the brackets is a tandem reciprocal log form that asymptotically approaches zero from below as shown in figure 15–31. This is the constant drawdown analog of a buildup, and the flow schedule during such a test which is shown diagrammatically in figure 15–32. Such a test can be conveniently described as a step-return process. The process of pressure equilibration in the step-return drawdown situation is illustrated in figure 15–33 and it can be seen that the effect of setting the sandface pressure back to  $p_i$  is quite different from setting  $\frac{\partial p}{\partial r}$  equal to zero in a shutin. In particular the rate immediately goes to negative when  $p_{wf}$  returns to  $p_i$ .

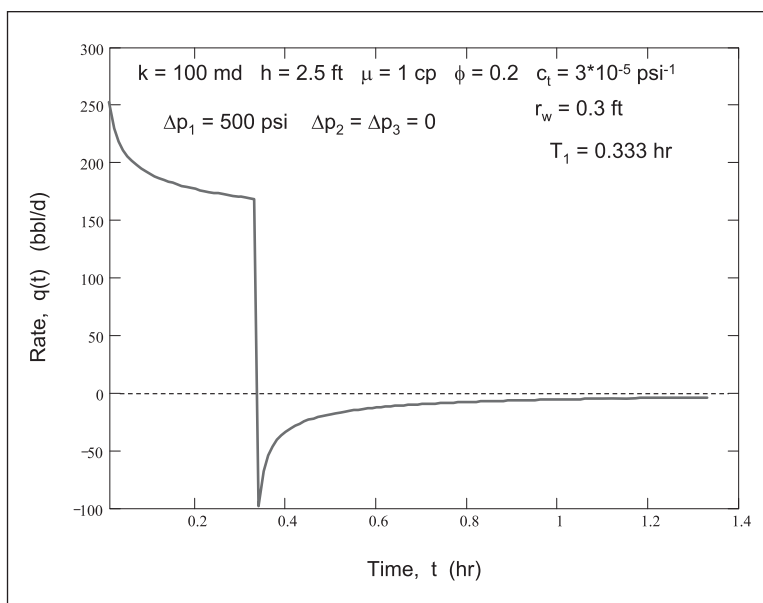


Fig. 15-30. Drawdown step-return rate response

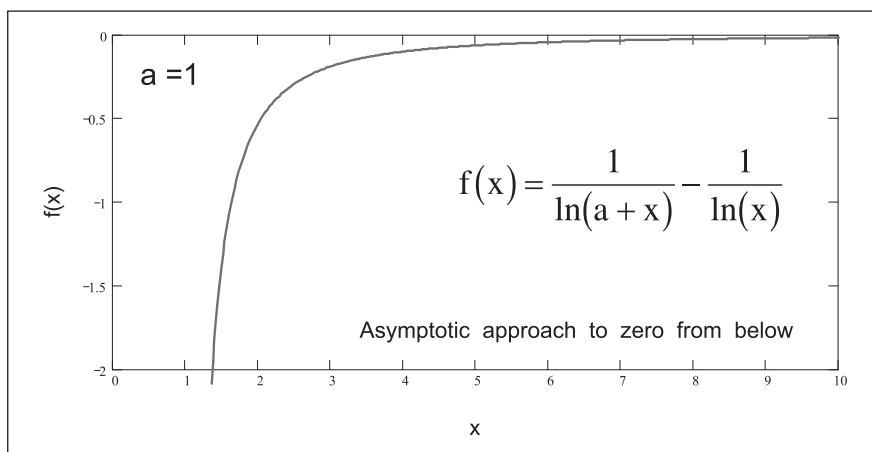


Fig. 15-31. Tandem reciprocal log function

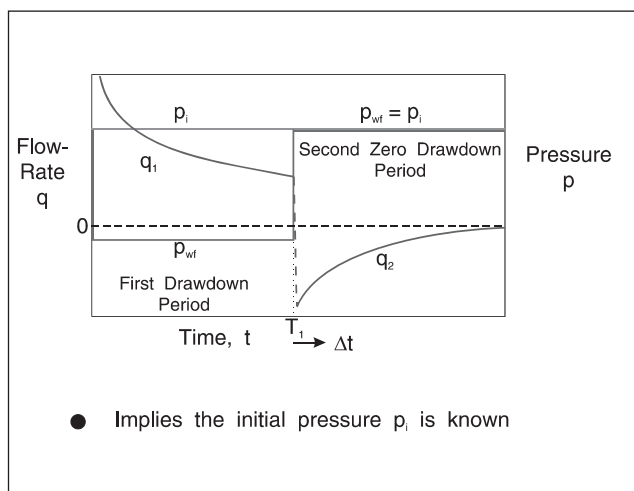


Fig. 15-32. Step-return drawdown test



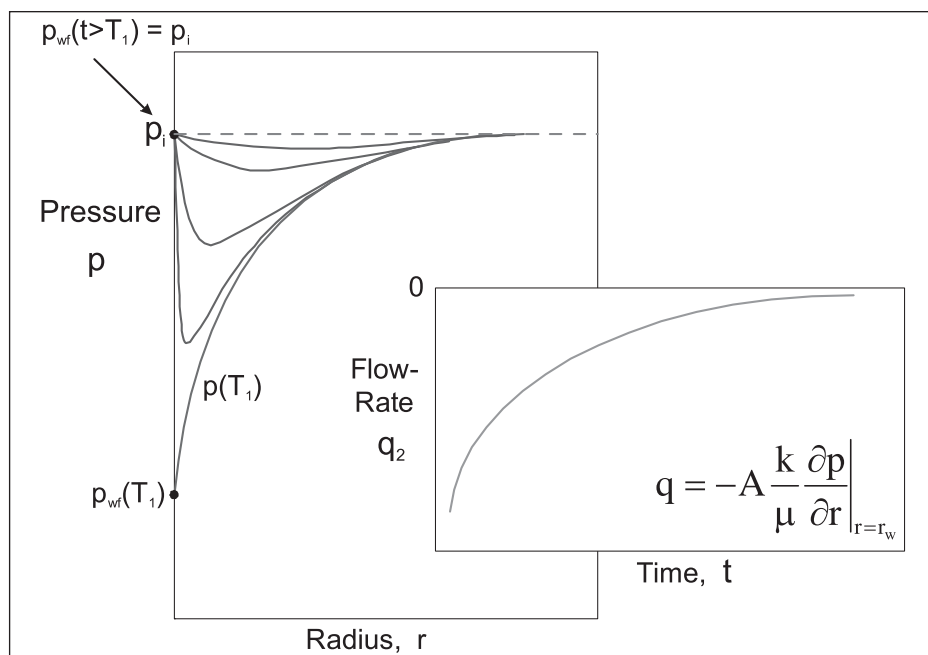


Fig. 15-33. Pressure equilibration process

In the general case where  $\Delta p_2 \neq 0$ , the second-rate period can be analyzed by desuperposition, as illustrated in figure 15-34, or by nonlinear regression, as illustrated in figure 15-35. Unfortunately, equation (15-24) does not lead to a convenient superposition time function through which a direct, specialist semilog plot can be formulated even when  $\Delta p_2 = 0$ . Trials using the Mathcad-supplied minimization routine on the test problem data of figure 15-28 (second period) showed that the permeability and initial pressure could be determined by nonlinear regression provided the starting value for  $k$  was higher than the actual.

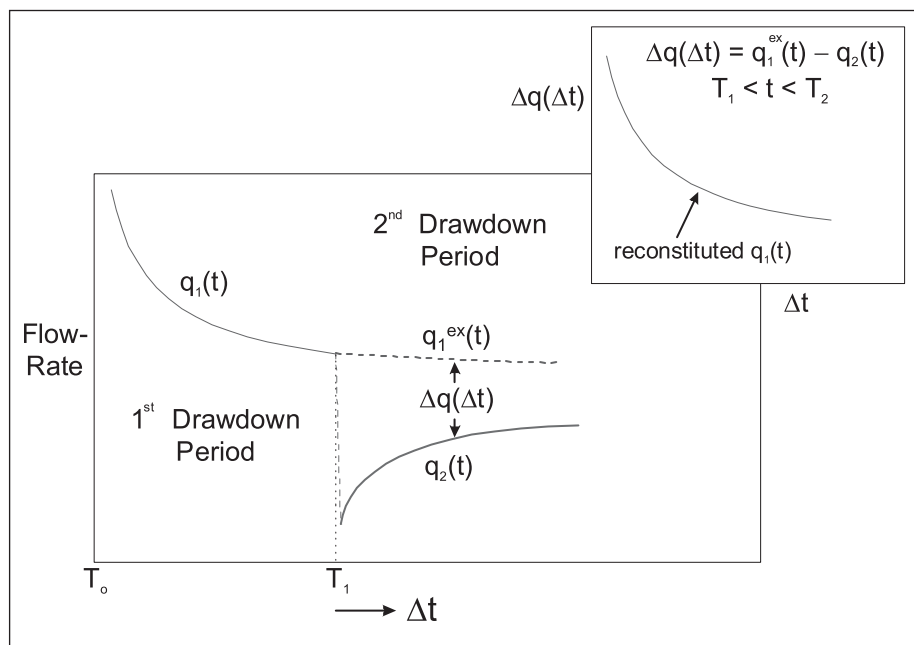


Fig. 15-34. Desuperposition method for a two-drawdown test

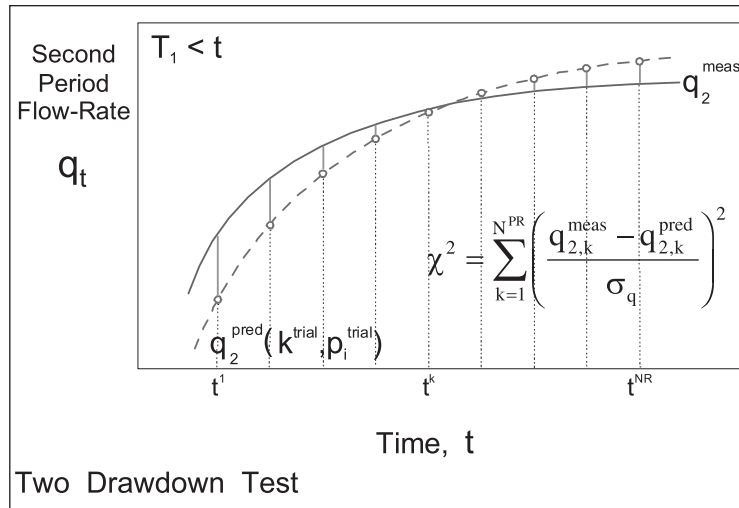


Fig. 15–35. Nonlinear regression on second-flow period data

A negative rate excursion of the form illustrated in figure 15–30 is highly undesirable from an UBD point of view since mud invasion leads to formation damage. It is interesting to determine the maximum change in underbalance, which just avoids a negative rate excursion. In the present example with  $\Delta p_1 = 500$  psi, the rate response with a second period where  $\Delta p_2 = 200$  psi is shown in figure 15–36; the rate falls to a value just greater than zero. A smaller drawdown in the second period will lead to negative rates. The ability to forecast conditions under which negative rate excursions will occur is an important application of the theory developed here. The maximum permissible reduction in the underbalance is denoted by  $\Delta p_{red}$ , and in the preceding example this is 300 psi, i.e., the underbalance can be reduced from 500 psi to 300 psi. Simulations using the Mathcad program showed that, for any degree of underbalance in the initial period  $\Delta p_1$ , then the corresponding permissible reduction may be expressed as a fraction  $F_{max}$  where

$$F_{max} = \frac{\Delta p_{red}}{\Delta p_1}$$

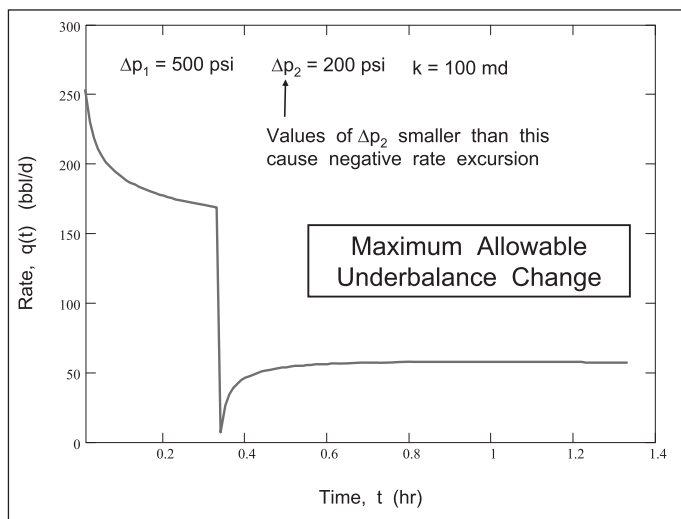


Fig. 15–36. Drawdown step-return rate response

Sensitivity runs were made using the software to examine the effect of permeability  $k$  and initial flowing time  $T_1$  on the ratio  $F_{max}$ . The results for oil are shown in figure 15–37 and for gas in figure 15–38a. The properties for the two cases are shown in table 15–3.

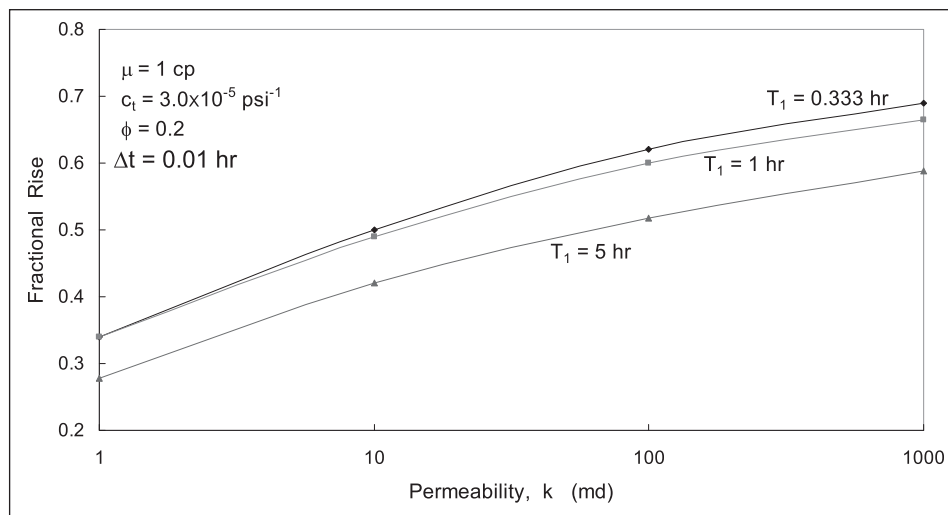


Fig. 15–37. Maximum allowable fractional pressure rise (oil)

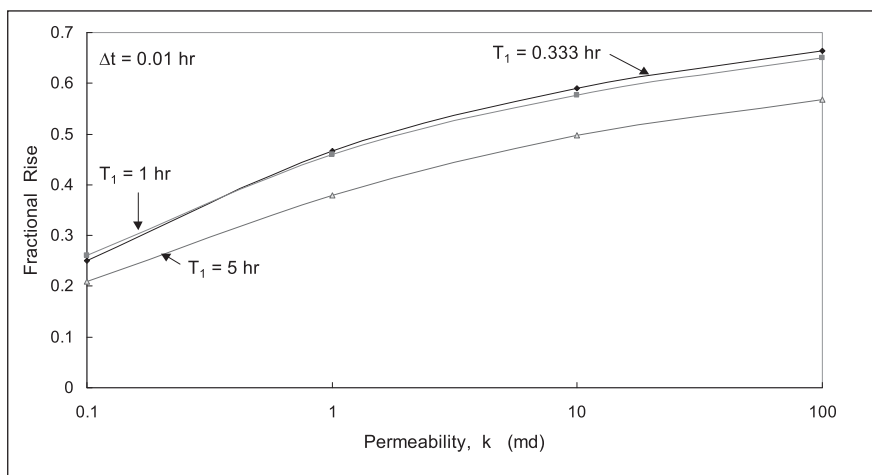


Fig. 15–38a. Maximum allowable fractional pressure rise (gas)

Table 15–3. Reservoir parameters for allowable underbalance sensitivities

$\mu_o = 1.0 \text{ cp}$	$c_{to} = 3.0 \times 10^{-5} \text{ psi}^{-1}$	$\mu_g = 0.02 \text{ cp}$	$c_{tg} = 3.0 \times 10^{-4} \text{ psi}^{-1}$
$r_w = 0.3 \text{ ft}$	$\phi = 0.2$		

The allowable ratio decreases with decrease in permeability and also decreases as the flowing time becomes longer. In the computation of the results in figure 15–38, the time-step was set at  $\Delta t = 0.01 \text{ h}$  in the superposition algorithm. This results in an almost instantaneous step change in pressure. A set of sensitivities was also run with a longer time step, viz.,  $\Delta t = 0.1 \text{ h}$  to examine the effect of spreading out the pressure disturbance. The results of this work are shown in

figure 15–38b, where it is apparent that much larger changes in underbalance can be tolerated if the pressure disturbance is controlled. The flow history of one of these cases is shown in figure 15–39 and it is apparent that the sharp spike has been (numerically) dispersed.

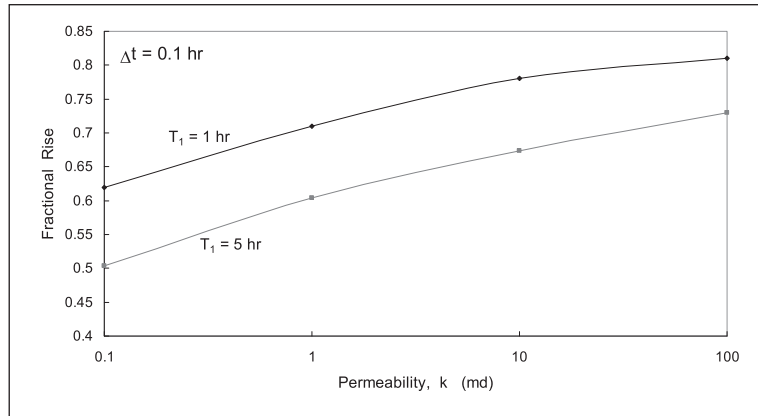


Fig. 15–38b. Maximum allowable fractional pressure (MAFP) rise (gas)

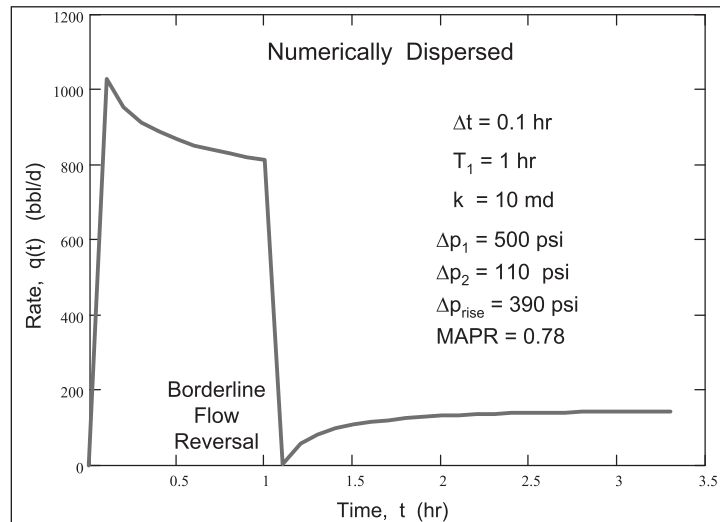


Fig. 15–39. Dual drawdown rate response

The preceding work was based on the Jacob and Lohman line-source analytical solution to the constant wellbore pressure solution. For early time phenomena, the finite wellbore radius (FWBR) solution should properly be used and the PanFlow option in the PanSystem software can be used to generate rate responses for specified pressure conditions using convolution of the constant rate solution. In order to check the validity of the correlations derived previously, runs were made in PanFlow using exactly the same conditions. For the case of  $k = 1$  md,  $T_1 = 1$  h, and  $\Delta t = 0.01$  h, the result of a PanFlow simulation is shown in figure 15–40. This has employed the FWBR model. The maximum allowable fractional pressure rise (MAPR) ratio is 0.36, which is very close to the value of 0.34 obtained using Jacob and Lohman theory and given in figure 5.14. The second bottomhole pressure of 680 psia was found by trial and error such that the rate just avoided going negative. Thus the error in using the log approximation for the line source is quite small.

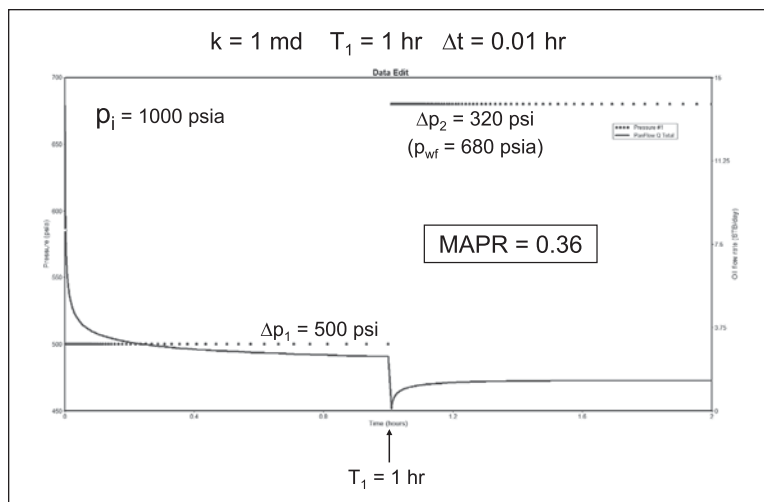


Fig. 15–40. PanFlow oil simulation based on FWBR solution

In many cases the target of underbalance drilling is fractured zones described by the dual porosity model. The problem of predicting rate, given a pressure signal and a model with identified parameters arose in the interpretation of layered well tests using production logging data. In the PanSystem software this facility is known as PanFlow and it can be used to run the calculations for negative rate excursions. It is simply necessary to generate a pressure response exhibiting two periods each at constant wellbore pressure. This can be conveniently done in Excel and the time–pressure file can be imported into PanSystem. A dual-porosity model has two additional dimensionless variables  $\omega$  and  $\lambda$ . The capacity parameter  $\omega$  is the ratio of the porosity of the fracture network divided by the total porosity and a typical value for this quantity is 0.01. The interporosity flow parameter  $\lambda$  is related to the matrix block height  $h_m$  and the matrix permeability  $k_{mb}$  and is defined as

$$\lambda = \frac{60k_{mb}r_w^2}{k_{fb}h_m^2}$$

Here,  $k_{fb}$  is the bulk permeability (based on total area of matrix plus fractures) of the fracture network. A large value of  $\lambda$ , corresponding to quite a small matrix blocks, is  $10^{-5}$ . The first flow regime in dual porosity is radial flow in the fracture system alone.

Initially a PanFlow run was made for  $k = 100$  md and  $\phi = 0.2$ , which yielded an MAPR ratio of 0.61 ( $\Delta t = 0.01$  h). The Jacob and Lohman theory gave 0.6 for this case, and again the agreement is excellent. The model was then changed to dual porosity with  $\omega = 0.01$  and  $\lambda = 10^{-5}$ , and the pressure in the second drawdown adjusted until the rate again just failed to go negative. The PanFlow result is shown in figure 15–41, where the MAPR ratio is now 0.92, which is substantially higher than the homogeneous result of 0.61. Thus it may be concluded that the correlations given here (Figure 5.14 for oil) are conservative for fractured zones. Note that the permeability becomes the bulk fracture network permeability  $k_{fb}$ . The reason for the marked contrast between the homogeneous and dual-porosity situations is the low porosity  $\phi_f$ , which controls the initial fracture system alone, in the present case  $\phi_f = 0.01\phi_{m+f}$ . Thus in a fractured reservoir case, there is little capacity in the fracture network, and the rate transient

following a change in FBHP occurs essentially in the period with no support from the matrix. This is good news, since many candidates for UBD are fractured zones, where the MAPR ratios are much larger than those predicted by homogeneous theory. The PanFlow option in PanSystem is an excellent tool for studying the conditions under which negative rate excursions will occur. The example quoted here ( $k_{fb} = 100$  md,  $\phi_{f+m} = 0.2$ ,  $\omega = 0.01$ , and  $\lambda = 10^{-5}$ ) refers to typical but specific parameter values and this can be extended to appropriate particular parameter sets relevant to actual field conditions. The problem is the assignment of the block size and the matrix permeability.

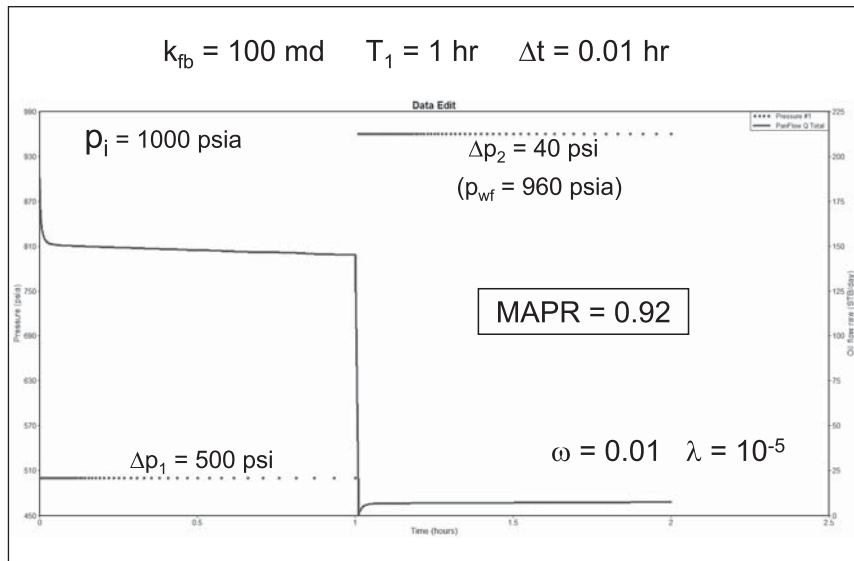


Fig. 15–41. PanFlow simulation of dual porosity case

A case where a natural fracture intersects the wellbore can be modeled almost exactly with the FWBR model with  $r_w$  replaced by  $r_{w,eff} = x_f/2$ . The FWBR radius model predicts linear flow at very early time and then radial flow with a transition region separating the two flow regimes. The results for three wellbore radii are shown in figure 15–42, where it is clear that the presence of a natural fracture greatly reduces the allowable pressure rise. The effective wellbore radius of 5 ft corresponds to a 10-ft half-length natural fracture. The result for an intersecting fracture is completely the opposite to that of a fracture network and it is therefore important to assess which of these cases correspond to a given well condition.

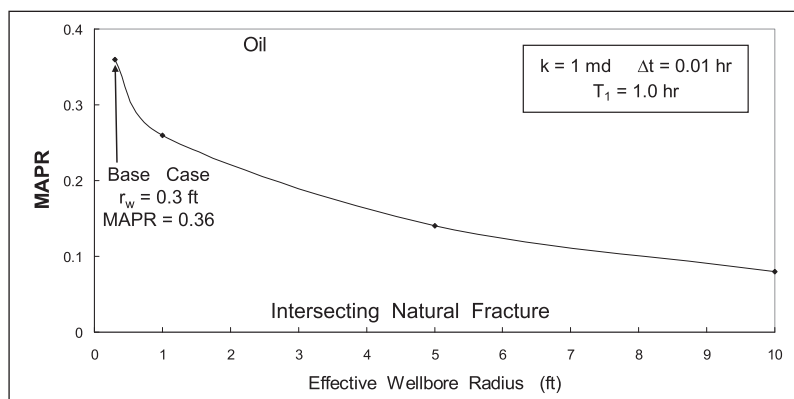


Fig. 15–42. MAPR ratio as a function of effective wellbore radius

## Application to Underbalanced Drilling

The multilayer convolution algorithm has an important application in UBD, where the well is flowing during the drilling process as illustrated in figure 15–43. As the well progressively penetrates the reservoir, more layers become available for flow and the superposition equation for an individual layer takes the form

$$p_j^i - p_w(t) = \left( \frac{\mu}{2\pi kh} \right)_j \left( \sum_{i=1}^M q_{ij} \left( p_{Dj}(t_j - T_{i-1})_{Dj} - p_{Dj}(t_j - T_i)_{Dj} \right) + q_j(t) p_{Dj}(t_j - T_M)_{Dj} \right) \quad (15-26)$$

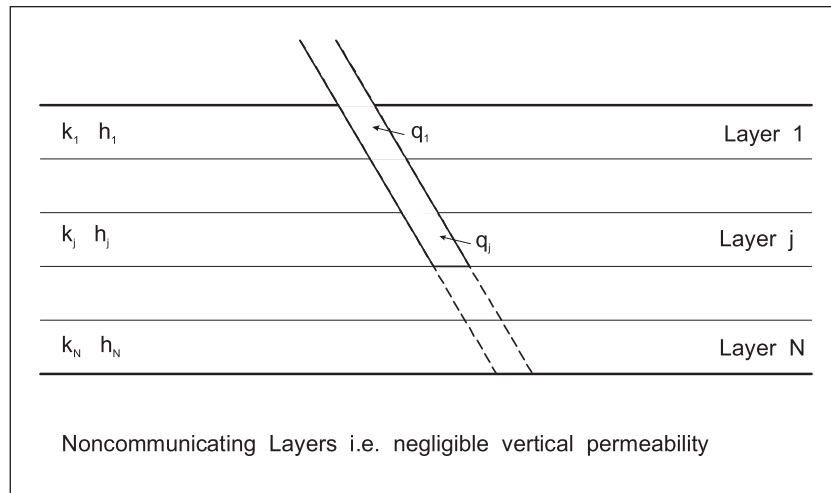


Fig. 15–43. Progressively penetrating well in an underbalanced drilling

Here each layer has its own starting time  $\tau_j$  measured as the point where the drill bit penetrates, and the quantity  $t_j$  is the total flowing time for layer  $j$  given by

$$t_j = t - \tau_j \quad (15-27)$$

In the summation,  $l$  is the period at which layer  $j$  starts to flow as illustrated in figure 15–44, and for the moment it will be assumed that the layer pressures  $p_j^i$  are known independently. In UBD, the bottomhole pressure  $p_w(t)$  is measured and the algorithm given above, with minor modifications, can be used to predict the layer flow rates as a function of time if the permeability distribution is given. Thus

$$q_j(t) = \frac{2\pi k_j h_j (p_j^i - p_w(t))}{\mu p_{Dj}(t_j - T_M)_{Dj}} - \frac{\sum_{i=lj+1}^M q_{ij} \left( p_{Dj}(t_j - T_{i-1})_{Dj} - p_{Dj}(t_j - T_i)_{Dj} \right)}{p_{Dj}(t_j - T_M)_{Dj}} \quad (15-28)$$

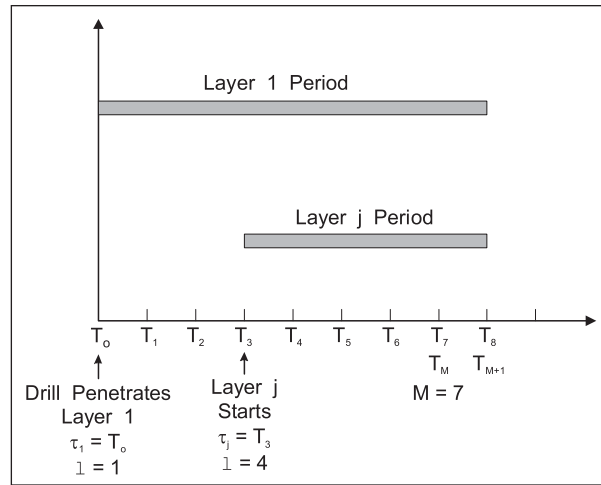


Fig. 15-44. Starting time for individual layers

Substitution of the canonical radial flow model, i.e., equation (15-27), and writing  $t_j = T_{M+1,j}$  yield

$$q_{M+1,j} = \frac{2\pi k_j h_j (p_j^i - p_w(T_{M+1}))}{\mu \frac{1}{2} \ln \frac{4k_j (T_{M+1} - T_M)}{\gamma \phi \mu c_t r_w^2}} - \frac{\sum_{i=l_j+1}^M q_{ij} \left( \frac{1}{2} \ln \frac{T_{M+1} - T_{i-1}}{T_{M+1} - T_i} \right)}{\frac{1}{2} \ln \frac{4k_j (T_{M+1} - T_M)}{\gamma \phi \mu c_t r_w^2}} \quad (15-29)$$

The total flow follows is

$$q(t) = \sum_{j=1}^{N_a} q_j(t) \quad (15-30)$$

where  $N_a$  is the number of active layers at time  $t$ .

The case where the vertical permeability is negligible, corresponding to noncommunication in the reservoir, implies that the appropriate  $p_D$  function is infinite-acting radial flow, i.e.,

$$p_{Dj}(t_{Dj}) = \frac{1}{2} \ln \frac{4k_j t}{\gamma \phi \mu c_t r_w^2} + S_j \quad (15-31)$$

In UBD, the mechanical skin is presumed to be zero and the skin contribution in (15-31) is only geometric. Thus, the effect of well deviation can be handled by the Cinco and Miller negative skin formulation. Kardolus and van Kruijsdijk have compared the noncommunicating progressive layer model to a numerical simulation using the boundary element method allowing vertical communication between the layers. The comparison in terms of dimensionless flow rate is shown in figure 15-45, where it can be seen that the difference is small, suggesting that vertical



permeability does not have a large influence on reservoir behavior in the condition of progressive penetration. Kardolus and van Kruijsdijk concluded that the analytical model is quite sufficient for determination of formation parameters.

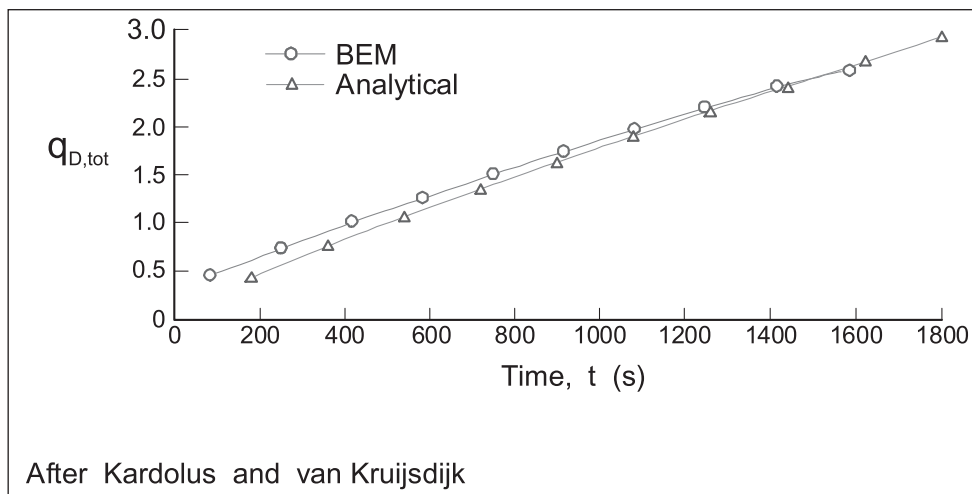


Fig. 15-45. Comparison of boundary element model and analytical model

The main problem with the analytical model is the “steppiness” of the computed total flow due to the finite thickness of the layers. An individual layer commences flowing when the drill bit reaches the mid-point of the layer with a high rate due to the flush production effect. This means there is a “kick” in the predicted total flow each time a layer mid-point is reached. The initial or flush production from a layer is given by

$$q_{1j+1,j} = \frac{2\pi k_j h_j (p_j^i - p_w(T_{1j+1}))}{\mu \frac{1}{2} \ln \frac{4k_j (T_{1j+1} - T_{1j})}{\gamma \phi \mu c_t r_w^2}} \tag{15-32}$$

which depends on the magnitude of the time step  $\Delta t = T_{1j+1} - T_{1j}$  and becomes infinite as  $\Delta t \rightarrow 0$ . In practice, the layer is opened progressively as the drill bit penetrates and the superposition based on step rate behavior only handles this effect in a discretized fashion. In order to minimize this effect, the layer thickness must be kept small, i.e., a large number of layers are required to adequately represent the special inner-boundary condition of progressive penetration.

In the formulation of layered reservoir models in well test theory, it is common practice to use layer potentials, i.e., pressures referred to a common datum, using the hydrostatic reservoir fluid gradient  $\hat{\rho}$ . Thus the initial layer pressure quantities  $p_j^i$  used above are, in fact, potentials and not actual pressures as measured with a WFT device. In a layered reservoir at hydrostatic equilibrium, i.e., exhibiting an oil or gas gradient on a pressure–depth diagram, the potential of the individual layers is identical, as illustrated in figure 15-46. If the datum is chosen as the top formation then

$$p = p_{\text{datum}} + \hat{\rho} D \tag{15-33}$$

where  $p$  = actual pressure  
 $D$  = true vertical depth measured from datum  
 $p_{\text{datum}}$  = potential (pressure at top reservoir).

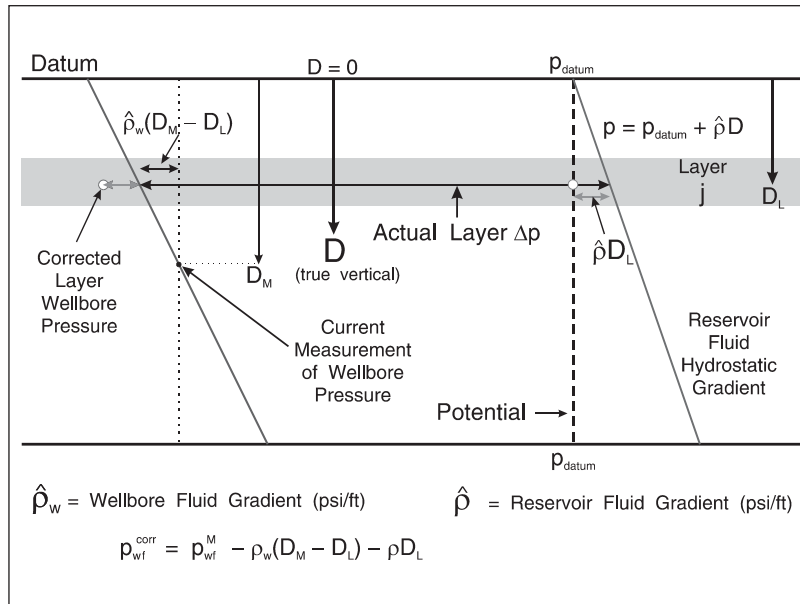


Fig. 15–46. Potential diagram

For layer  $j$ , the actual formation pressure is

$$p_j = p_{\text{datum}} + \hat{\rho} D_L \quad (15-34)$$

In the progressive penetration of the reservoir, the bottomhole gauge measures the pressure at the current depth of the assembly, again illustrated in figure 15–46. The actual pressure in the wellbore opposite the various layers is given by

$$p_{\text{wf},j} = p_{\text{wf}}^{\text{M}} - \hat{\rho}_w(D_M - D_L) \quad (15-35)$$

where  $p_{\text{wf},j}$  = actual pressure opposite layer  $j$  (assuming negligible friction)  
 $\hat{\rho}_w$  = hydrostatic gradient of wellbore fluid  
 $D_M$  = current true vertical depth (TVD) of assembly  
 $D_L$  = TVD of layer  $j$  midpoint.

However, if the formation pressure is adjusted to datum, then a corrected wellbore pressure must be likewise employed so that the layer  $\Delta p$  in potential is identical to the actual  $\Delta p$  illustrated in figure 15–46. From the geometry of the diagram, the corrected wellbore pressure is given by

$$p_{wf}^{corr} = p_{wf}^M - \hat{\rho}_w(D_M - D_L) - \hat{\rho}D_L \tag{15-36}$$

It is this corrected pressure that should be used in the transient formation model and equation (15–29) becomes

$$q_{M+1,j} = \frac{2\pi k_j h_j (p_j^i - p_w^{corr}(T_{M+1}))}{\mu \frac{1}{2} \ln \frac{4k_j(T_{M+1} - T_M)}{\gamma \phi \mu c_t r_w^2}} - \frac{\sum_{i=j+1}^M q_{ij} \left( \frac{1}{2} \ln \frac{T_{M+1} - T_{i-1}}{T_{M+1} - T_i} \right)}{\frac{1}{2} \ln \frac{4k_j(T_{M+1} - T_M)}{\gamma \phi \mu c_t r_w^2}} \tag{15-37}$$

In the preceding treatment, it has been tacitly assumed that the formation is horizontal, i.e., the dip angle  $\beta$  is zero. In figure 15–47, a formation dipping at an angle  $\beta$  to the true horizontal plane is intersected by a deviated well at angle  $\alpha$  to the true vertical plane. In the case of a horizontal formation, the thickness of a layer is simply given as the difference between successive TVD values, i.e.,

$$h_j = TVD_j - TVD_{j-1} \tag{15-38}$$

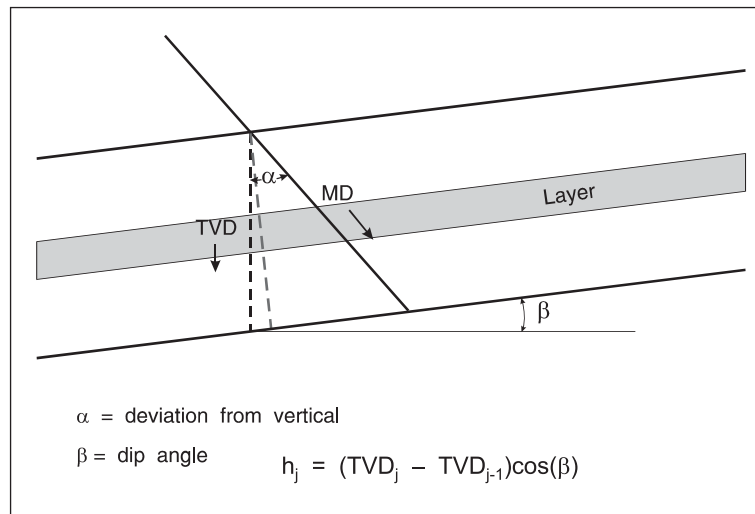


Fig. 15–47. Correction from TVD to dip normal thickness

If the formation is dipping, the dip normal thickness, i.e., the dotted line in figure 15–47, is given by

$$h_j = (TVD_j - TVD_{j-1})\cos(\beta) \tag{15-39}$$

Since the well trajectory has been converted to TVD, the effect of deviation angle  $\alpha$  has already been taken into account. However, the formation dip  $\beta$  must be entered as a reservoir parameter into any analysis so that estimated permeability are based on dip normal formation thicknesses.

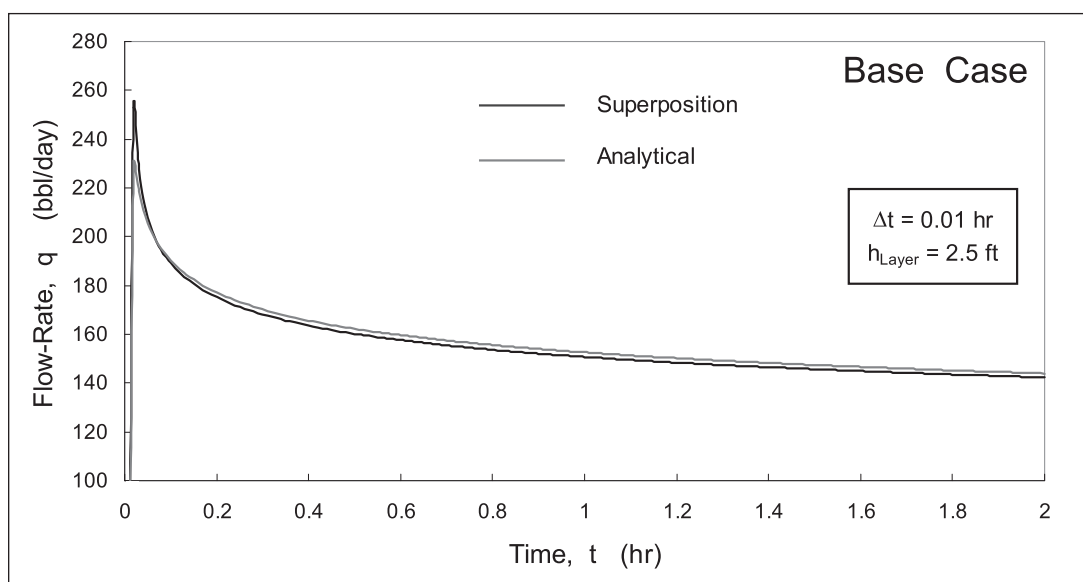
## Demonstration Simulation

In order to appreciate the nature of the problem, it is useful to generate flow transient results for various underbalance scenarios. The analytic simulation formulas (15–29) and (15–30) were programmed into a Mathcad spreadsheet and the rate response generated for different cases. The base situation was a 100-ft thick zone of uniform permeability  $k = 100$  md, which was drilled over a 1-h period with a vertical well. The well and reservoir properties are listed in table 15–4.

**Table 15–4.** Base case reservoir and well properties

$h = 100$ ft	$k = 100$ md	$\mu = 1$ cp	$r_w = 0.3$ ft	$c_t = 3.0 \times 10^{-5}$ psi <sup>-1</sup>
$\phi = 0.2$	$\gamma = 1.781$	$p_j^i = 5,000$ psia	$p_{wf}(t) = 4,500$ psia	$h_{lay} = 2.5$ ft

The individual flow prediction for the first layer is shown in figure 15–48, where the initial (flush) production is 253 bbl/d for a 2.5-ft layer. In this simulation, the 100-ft zone was divided into 40 layers and the drilling took 1 h. The simulation was extended to 2 h so that all the layers were flowing in the interval  $1 < t < 2$  h. The individual layer flow schedule is quite smooth and exhibits the familiar form of a transient rate decline for a constant-terminal-pressure inner boundary condition. The flow transient for deeper layers has exactly the same form but displaced in time. The constant drawdown analytical solution, i.e., equation (15–17) is also plotted in figure 15–48 and the superposition based on the constant rate drawdown (CRD) solution, i.e., (15–29), is seen to have an error of the order of 1%, which is quite acceptable.



**Fig. 15–48a.** Individual layer flow-rate

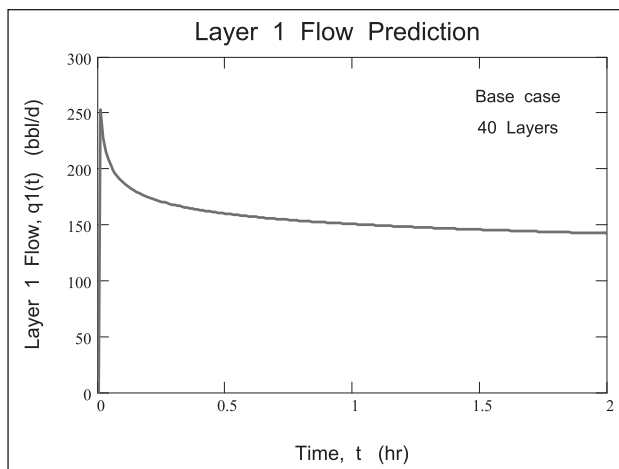


Fig. 15–48b. Individual layer flow-rate

The total flow given by summation (15–30) is plotted in figure 15–49, and this exhibits the steppiness alluded to earlier, even though 40 layers were used. The steppiness occurs because, as each new layer is added, its contribution is immediately in steep decline. The upward kicks are due to the new layers entering the process. It is possible to define an instantaneous transient PI at any moment in time based on the definition

$$J_{tran} = \frac{q(t)}{P_i - P_{wf}(t)} \tag{15-40}$$

and this quantity is plotted for the base situation in figure 15–49. Since the bottomhole flowing pressure is constant in this test case, the transient P.I. follows the total flow rate q(t), and exhibits the same steppiness. A continuing increase in the value of  $J_{tran}$  has been taken as evidence that the formation is not being damaged by the drilling process. Existing software also plots the cumulative oil production, and this is plotted in figure 15–50 for the demonstration simulation. In figure 15–51, the discretized flow history has been smoothed using a supplied Mathcad algorithm and this is felt to be a better representation of the true physical situation. Note that smoothing was only carried out on the active period of 1 h during which drill bit penetration was occurring.

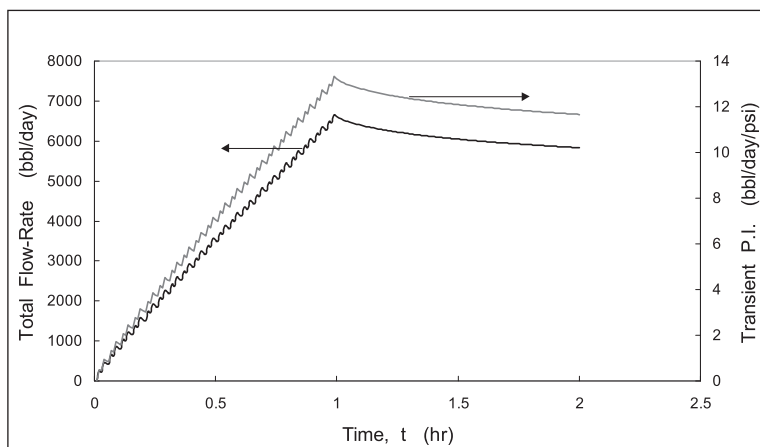


Fig. 15–49. Total flow and transient PI

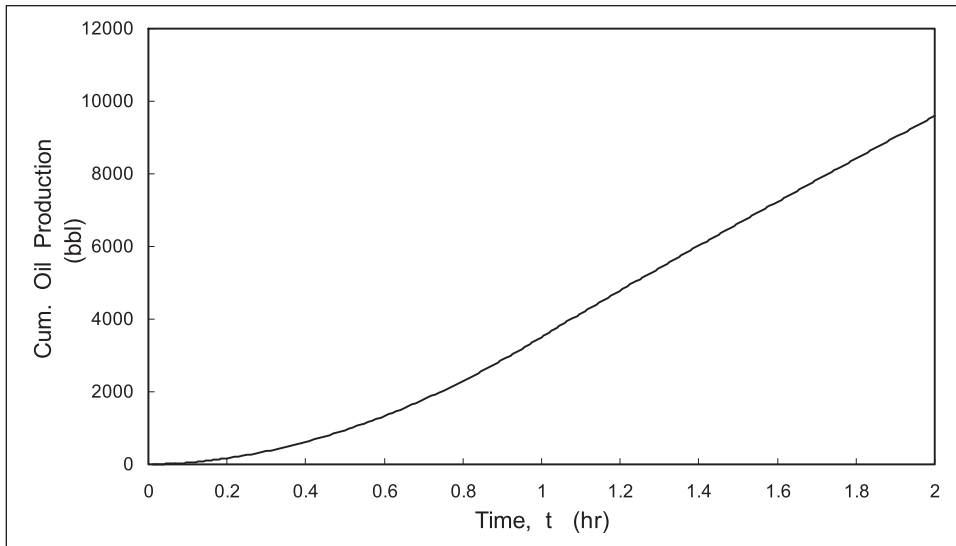


Fig. 15-50. Cumulative oil production

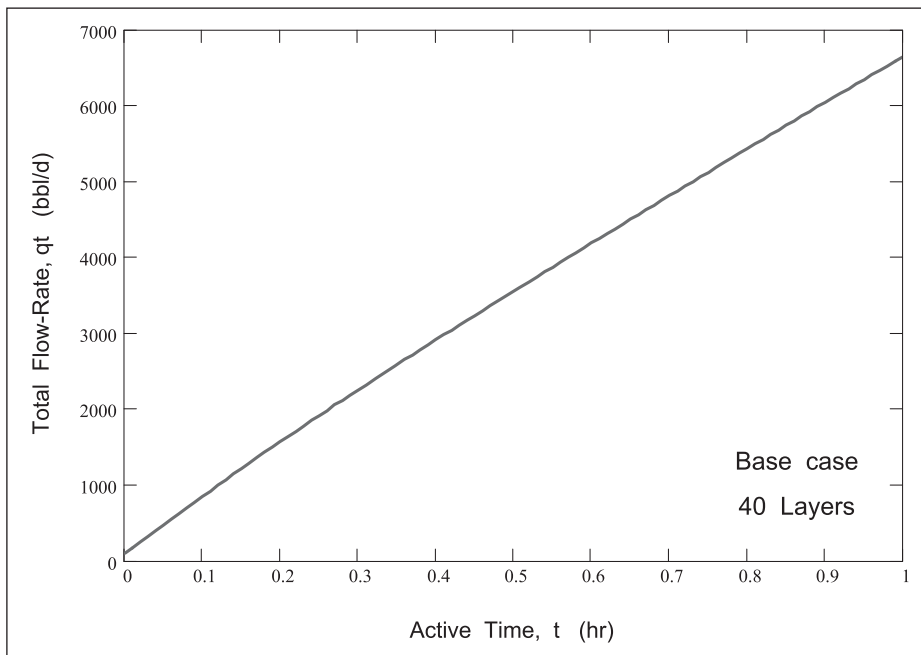


Fig. 15-51. Smoothed total flow versus time

The average permeability of the formation  $\bar{k}$  can be determined from the cumulative production at the end of the drilling phase. This will be denoted  $N_p^f$ , as illustrated in figure 15-52. If the superposition model, using the measured bottomhole pressure  $p_{wf}(t)$ , is run with a uniform permeability  $\bar{k}$ , this will generate a predicted cumulative production  $N_{pred}^f$ , which can be compared with the measured value  $N_{meas}^f$ . An iterative search for a value of  $\bar{k}$ , which minimizes the objective function  $(N_{pred}^f - N_{meas}^f)^2$  yields the average permeability of the formation for the given value of the formation pressure  $p_i$ .

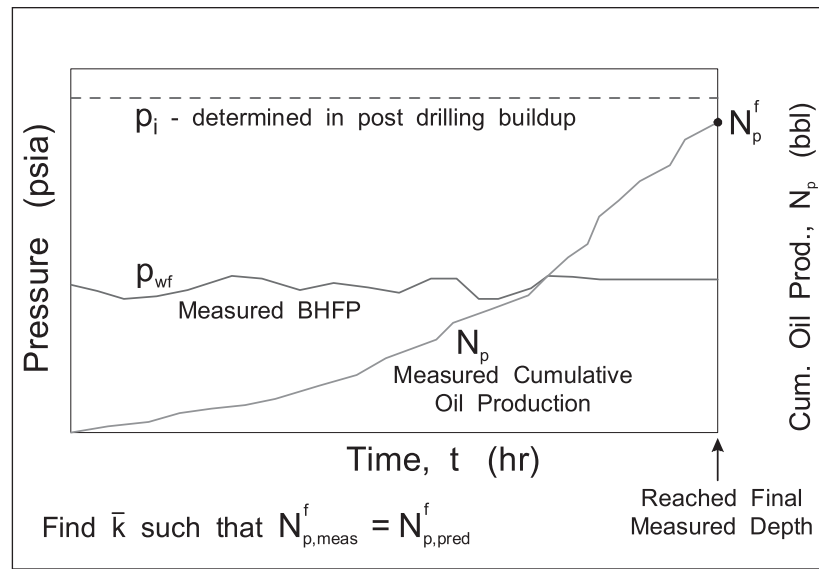


Fig. 15-52. Determination of average permeability

It will be demonstrated shortly through analytical simulation that the average permeability defined by this procedure is not the same as the arithmetic average permeability of a layered system which controls the eventual SSS PI. A much better approach is to develop the permeability profile sequentially based on a zonation of the system. Suppose a selection of points on the cumulative flow plot have been identified as shown in figure 15-53. The reservoir has been partitioned into zones and the times, labeled  $t_z$  in figure 15-53, correspond to the drill bit exiting a given zone. The zonation will be based on the surface flow rate, i.e., kicks in flow will indicate high permeability zones and decreasing flow rates will indicate tight regions. The cumulative flow from the first zone is designated  $N_p^1$  and the average permeability of the zone can be found by adjusting  $\bar{k}^1$  until  $f(\bar{k}^1) = (N_{pred}^1 - N_{meas}^1) = 0$ . Thus the problem of determining  $\bar{k}^1$  has been reduced to the solution of a functional equation in one variable, and a secant method, illustrated in figure 15-54, can be used to iterate to a solution. For the second zone of average permeability  $\bar{k}^2$  the functional equation may be written  $f(\bar{k}^2) = (N_{pred}^2 - N_{meas}^2) = 0$ . In the simulation using the superposition algorithm, to generate  $N_{pred}^2$  the permeability of zone 1 is already known and it is only the permeability of the additional segment that must be determined. This process is repeated until all zones have been identified and a complete permeability distribution is obtained. At this level, the formation pressure  $p_i$  has been treated as uniform, i.e., all zones are at the same potential. This may be determined from a post-drilling buildup.

# 16

## Effect of Mud Filtrate Invasion on WFT Measured Pressure

---

### Introduction

Wireline formation testers (WFTs) do not make a direct measurement of the undisturbed formation pressure. The pressure and saturation distributions around the wellbore are altered by the invasion of mud filtrate. This is a dynamic process which continues as long as open-hole conditions exist in the well. It is therefore necessary to study the mechanics of mud filtrate invasion in order to understand the physical significance of WFT measurements. The invaded zone constitutes a buffer between the undisturbed formation and the measurement system. In many instances, the stabilized probe pressure is essentially the same as the pressure of the continuous phase in the reservoir. For example, if a well is drilled with water-based mud and it penetrates a high-permeability water-bearing sand, then the WFT will register the water phase pressure as a function of depth. However, in a low-permeability formation—frequently in the case of aquifers—the sandface pressure detected by the probe will be greater than the local undisturbed formation pressure due to the viscous pressure drop associated with mud filtrate injection into the system. This is the phenomenon of supercharging, which depends on the local formation permeability and mud fluid loss rate. Unfortunately, those two quantities are extremely difficult to predict or measure.

In a WFT test, the probe is positioned on the sandface and sealed with a concentric packer by hydraulic action. A small volume of fluid is then withdrawn to disrupt the mud filter cake and establish communication with the formation. The pressure response is monitored at the surface and allowed to stabilize. In a high- or moderate-permeability formation, the buildup following fluid withdrawal is very rapid and the reservoir pressure at the setting depth is obtained. However, there is still the question of what pressure is being detected. In the capillary transition zone, for example, there are two mobile phases present, i.e., water and oil or gas, whose pressures differ by the capillary  $P_c$ . It is not clear which of these two pressures will be



registered. In high-permeability formations, the difference is small and the capillary transition zone is of limited vertical extent. Above the transition zone, it has been tacitly assumed that the WFT detects the hydrocarbon phase pressure in the oil or gas columns. This, of course, is borne out by the majority of field examples in unproduced reservoirs where oil and/or gas gradients are observed.

When a WFT is used for sampling into large chambers, it is usually found that the first fluid to be produced is mud filtrate. The pressure being detected by the measurement system should therefore correspond to the sandface pressure of the mud filtrate which has invaded the formation. In the new generation of WFT devices, there will be a fluid analyzing system on the sample line which will allow the nature of the flowing fluids to be determined. However, for the moment it will be assumed that the WFT measures sandface mud filtrate pressure and accordingly it is necessary to investigate how this quantity is related to the undisturbed phase pressure outside the invaded region around the well.

The mechanics of mud filtrate invasion depend, of course, on the nature of the drilling mud and its fluid loss characteristics. Obviously water-based muds (WBM) and oil-based muds (OBM) have quite different properties, with the mud filtrate being an aqueous phase in the WBM case and an oleic phase in the OBM case. Since it will be shown that capillary pressure plays an important role in the invasion process, it is important to consider any changes in wettability which may be induced. It is common practice to add surface-active agents to mud systems which will be present in the filtrate and can alter wettability. Hence the chemical composition of the filtrate is also of concern when considering invasion effects.

In the earliest analysis of observed pressure gradient intersections (OPGI) on a pressure–depth diagram, it was tacitly assumed by Stewart and Wittman<sup>1</sup> that the OPGI was coincident with the free water level (FWL) based on the theory of gravity–capillary equilibrium. The examples given here show that, in certain situations, this simplified model is not valid and capillary pressure shifts in WFT data must be recognized. Since fluid contacts are of extreme importance in reserve estimation and unitization agreements, the issue becomes a “political hot potato.” New-generation wireline formation testers (NGWFTs), such as the Modular Dynamic Tester (MDT) and the Reservoir Evaluation System (RES) tool will, allow additional measurements which may be useful in unravelling complex effects due to capillary pressure. Recently, Carnegie<sup>2</sup> has revisited thick transition zones in Middle East reservoirs and shown the presence of a distinct jump in the data between a water phase and a shifted oil phase pressure; this phenomenon needs to be explained by the invasion theory. The dynamic model of invasion is felt by the author here to be a better explanation of observed phenomenon than the “large or small hole observer” theory of Desbrandes and Gualdron.<sup>3</sup>

## Filtrate Invasion Model

In this section, the theory of invasion developed by Stewart and Phelps<sup>4,5</sup> will be derived and used to simulate pressure and saturation profiles in the near-wellbore region; this model is two dimensional and does not allow for gravity segregation effects. The invasion model is based on the conservation of mass as expressed by the continuity equation for each incompressible phase:

$$-\nabla \cdot \mathbf{u}_w = \frac{\partial(\phi S_w)}{\partial t} \quad (16-1a)$$

$$-\nabla \cdot \mathbf{u}_o = \frac{\partial(\phi S_o)}{\partial t} \quad (16-1b)$$

and the conservation of momentum in each phase described by Darcy's law and the concept of relative permeability:

$$\mathbf{u}_w = -\frac{k k_{rw}(S_w)}{\mu_w} \nabla P_w \quad (16-2a)$$

$$\mathbf{u}_o = -\frac{k k_{ro}(S_o)}{\mu_o} \nabla P_o \quad (16-2b)$$

For one-dimensional radial flow, the operators  $\nabla$  and  $\nabla \cdot$  are, respectively,

$$\frac{\partial}{\partial r} \quad \text{and} \quad \frac{1}{r} \frac{\partial(\cdot r)}{\partial r}$$

The pressures and saturations in the phases are related through the ancillary equations

$$P_c(S_w) = P_o - P_w \quad (16-3)$$

$$S_o + S_w = 1 \quad (16-4)$$

The capillary pressure relation, i.e.,  $P_c(S_w)$ , and the relative permeability curves  $k_{rw}(S_w)$  and  $k_{ro}(S_o)$  must be specified in any particular case. There are several ways of combining these equations which help in devising an efficient numerical solution technique. One formulation which is compatible with the known boundary conditions is

$$\frac{1}{r} \frac{\partial}{\partial r} \left[ r [\lambda_w + \lambda_o] \frac{\partial P_o}{\partial r} - r \lambda_w \frac{dP_c}{dS_w} \cdot \frac{\partial S_w}{\partial r} \right] = 0 \quad (16-5)$$

$$\frac{1}{r} \frac{\partial}{\partial r} \left[ r \lambda_o \frac{\partial P_o}{\partial r} \right] = -\phi \frac{\partial S_w}{\partial t} \quad (16-6)$$

where  $\phi$  has been assumed constant.

The classical differential equations describing two-phase, immiscible, incompressible displacement, including the effect of capillary pressure, have been derived. The four dependent

variables are the phase pressures and saturations; in addition to the two partial differential equations (16–5) and (16–6), the two algebraic relations (16–3) and (16–4) are necessary for a determined system. These equations are based on a continuum model of two-phase flow involving the concepts of relative permeability as defined in (16–2a) and (16–2b) and capillary pressure embodied in (16–3). Any saturation variation in the system will lead to flow inducing pressure gradients, and capillary forces are accounted for. The evolution of the system, i.e., the growth of the invaded region, occurs as a result of the imposed boundary conditions for saturation and pressure.

The invaded region is taken to be contained within a radial zone between the sandface at  $r_w$  and some external radius  $r_e$  which is greater than the deepest depth of invasion of mud filtrate. The relevant initial condition corresponds to the undisturbed formation at the vertical depth level in question. Supposing this lies above the capillary transition zone adjacent to the oil–water contact (OWC), then the initial water saturation in the region of interest, i.e.,  $r_w \leq r \leq r_e$ , is  $S_{wc}$ —the connate water saturation. The pressure in the oil phase at this level is denoted  $p_o^f$ ; from the capillary pressure equation (16–3), the initial water phase pressure must be give by

$$P_c(S_{wc}) = p_o^f - p_w^f \quad (16-7)$$

Note that far above the oil–water contact,  $p_w^f$  can be considerably less than  $p_o^f$ . The initial conditions in the region subsequently invaded by filtrate are shown in figure 16–1. The undisturbed oil phase pressure at the given vertical depth, i.e.,  $p_o^f$ , is the key variable in the interpretation process. It is this quantity that is desired to be measured by a WFT device.

In the case of WBM, the inner boundary condition at the sandface is based on a specified injection rate of water denoted  $q_w(t)$ . The mud fluid loss rate per unit length of well is time dependent and changes sharply when dynamic filtration (mud circulating) is replaced by static filtration (mud stationary). The mechanics of mud fluid loss are discussed in detail in the section “Simulation of the Invasion Process.” For the moment, it is sufficient to note that often the fluid loss history can be approximated by a simple two-rate schedule of the form illustrated in figure 16–2:

$$\begin{aligned} q_w(t) &= q_{w,1} & t < T_d \\ &= q_{w,2} & t > T_d \end{aligned}$$

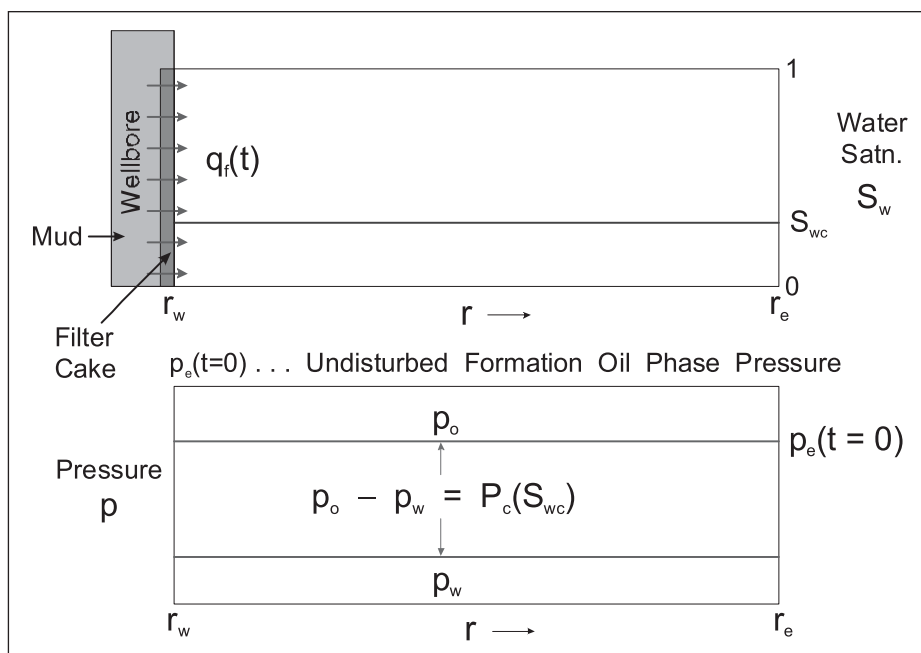


Fig. 16-1. Initial conditions for mud filtrate invasion model

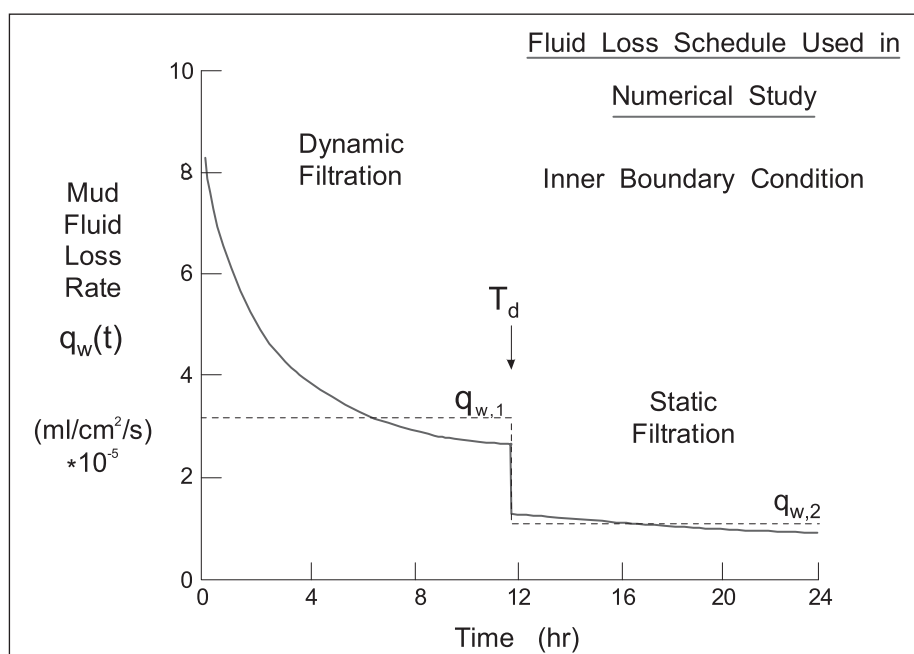


Fig. 16-2. Filtrate two-rate injection schedule

Here  $q_{w,1}$  is the equilibrium dynamic fluid loss rate of the mud,  $q_{w,2}$  is the approximately constant static fluid loss rate, and  $T_d$  is the time at which circulation was stopped (measured from the time at which bit penetration occurred).

The prescription of a specified injection rate per unit length is equivalent to fixing the water phase pressure gradient at the sandface. Thus the inner boundary condition may be written as

$$u_w|_{r_w} = \frac{q_w(t)}{2\pi r_w} = - \frac{kk_{rw}(S_w^s)}{\mu_w} \cdot \frac{\partial p_w}{\partial r} \Big|_{r_w}$$

i.e.,

$$\frac{\partial p_w}{\partial r} \Big|_{r_w} = - \frac{q_w(t)\mu_w}{2\pi r_w kk_{rw}(S_w^s)} \quad (16-8)$$

Here,  $S_w^s$  is the water phase saturation at the sandface, i.e.,

$$S_w|_{r_w} = S_w^s$$

No specific condition is placed on this quantity; in particular,  $S_w^s$  is not forced to be equal to  $1 - S_{or}$ , where  $S_{or}$  is the waterflood residual oil saturation. The model does not presume that the invaded region is completely swept in the vicinity of the sandface. Since oil does not pass through the filter cake, the flux of oil at  $r_w$  is zero and hence

$$\frac{\partial p_o}{\partial r} \Big|_{r_w} = 0 \quad (16-9)$$

The actual sandface pressure and saturation,  $p_w^s$  and  $S_w^s$ , respectively, will be determined from the solution of the model as time dependent quantities.

The outer boundary at  $r_e$  is infinite-acting with respect to saturation, i.e.,

$$S_w|_{r_e} = S_{wc} \quad (16-10)$$

$$S_o|_{r_e} = 1 - S_{wc} \quad (16-11)$$

These are the undisturbed reservoir fluid saturations. In an incompressible model, if there is an injection  $q_w(t)$  over the inner face, there must be an exactly equal production over the outer face at  $r_e$ ; accordingly

$$q_w(t) = q_o(t)|_{r_e} \quad (16-12)$$

This condition will be inherent in the model and it is not necessary to include (16-12) specifically as a boundary condition. However, the flow of oil over the outer face at  $r_e$  influences the external face

pressure denoted  $p_o^e(t)$ . Initially, at time  $t = 0$ , the pressure at  $r_e$  is  $p_o^f$ —the undisturbed formation pressure—but as injection into the formation proceeds the pressure at  $r_e$  increases with time. The classical line source transient solution may be used to compute the quantity  $p_o^e(t)$ , where

$$p_o^e(t) = p_o(t) \Big|_{r_e}$$

For the approximating two-rate injection schedule of figure 16–2, this is given by

$$p_o^e(t) = p_o^f + \frac{q_{w,2}\mu_o}{4\pi k k_{ro}} \left[ \frac{q_{w,1}}{q_{w,2}} \ln \frac{T_d + \Delta t}{\Delta t} + \ln \Delta t + \ln \frac{k k_{ro}}{\phi \mu_o c_t r_e^2} + 0.80908 \right] \quad (16-13)$$

Thus the formation outside the region affected by saturation changes is treated as an infinite-acting reservoir with respect to pressure and the standard analytical solution from well testing theory is used to describe its behavior. A numerical solution of the two-phase invasion problem in the annular region around the wellbore, i.e.,  $r_w \leq r \leq r_e$ , in which saturation is varying is linked to an analytical model of the pressure response of the formation for  $r > r_e$ . This continuation device, illustrated in figure 16–3, means that the numerical solution is only required over the region where mud filtrate has invaded—typically a few feet. Obviously,  $r_e$  has to be chosen large enough to exceed the maximum depth of penetration of mud filtrate; it is therefore an arbitrary quantity chosen for convenience. The actual depth of invasion is time-dependent and will be determined by the model itself. In equation (16–13),  $\Delta t$  is the time of static filtration conditions; as  $\Delta t$  increases, the pressure  $p_o^e(t)$  also increases according to two-rate transient theory. Note, however, that  $q_{w,2}$  is a very low injection rate and  $p_o^e(t)$  is appreciably different from  $p_o^f$ —the undisturbed formation pressure—only if  $k$  is small, typically less than about 5 md.

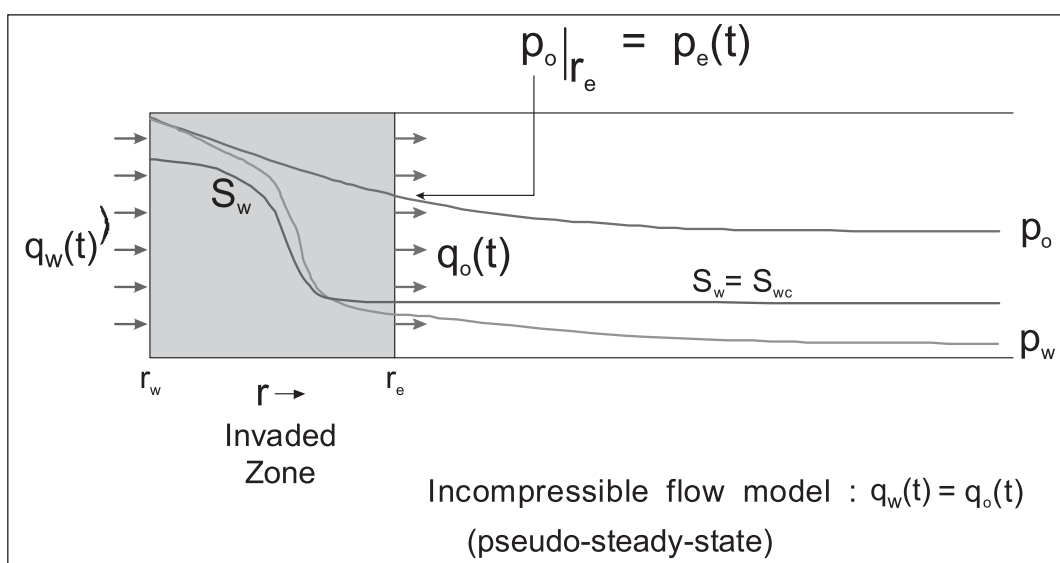


Fig. 16–3. Invaded zone incompressible flow pressure model

The saturation at  $r_e$  remains at the initial value, i.e.,

$$S_w|_{r_e} = S_{wc}$$

and only oil is flowing at this location since  $k_{rw}(S_{wc}) = 0$ . The composite model assumes incompressible, two-phase conditions in the invaded region and single-phase, compressible conditions for  $r > r_e$ .

Before a numerical solution of the invasion model can be obtained, it is also necessary to specify the relative permeability relations and the capillary pressure function. These quantities depend strongly on the wetting conditions in the porous medium. The influence of wettability on capillary pressure and relative permeability has recently been extensively reviewed by Anderson.<sup>6</sup> In the undisturbed formation, all conditions of wetting from strongly water-wet (WW) through neutral or mixed wettability to strongly oil-wet (OW) are possible in an oil column. In the case of gas or condensate reservoirs, strongly WW conditions are most probable. However, for oil reservoirs recent evidence from properly restored state core has shown that neutral or mixed wettability is prevalent at reservoir conditions. Jackson *et al.*<sup>7</sup> have demonstrated the wettability variation through transition zones in carbonate reservoirs. Certainly, there is much evidence against the common assertion of strongly WW rock. In the case of invasion phenomena, a complicating factor is the variety of surface-active chemicals that are added to mud systems. Hence the wetting conditions in the invaded region can be substantially changed by the incursion of filtrate. This makes the prediction of wettability very difficult indeed. Invasion will have typically taken place for tens of hours before a WFT survey is run; this is quite sufficient for significant changes in wettability to occur.

For the purposes of simulation, the relative permeability curves were assumed to have the form

$$k_{rw}(S_w) = k_{rw}^o \left[ \frac{S_w - S_{wc}}{1 - S_{or} - S_{wc}} \right]^n \quad (16-14a)$$

$$k_{ro}(S_w) = k_{ro}^o \left[ \frac{1 - S_w - S_{or}}{1 - S_{or} - S_{wc}} \right]^m \quad (16-14b)$$

These are common parametric representations of relative permeability relations based on the work of Corey. Typical values of  $n$  and  $m$  (dependent on pore size distribution and wettability) are 3–4 and 2–3, respectively, for WW conditions. The most important parameters are the critical saturations  $S_{wc}$  and  $1 - S_{or}$ , and the end point relative permeabilities  $k_{rw}^o$  and  $k_{ro}^o$ , as shown in figure 16–4.

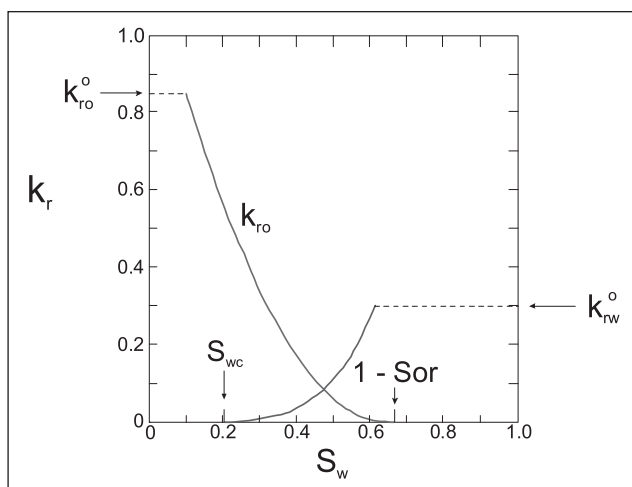


Fig. 16-4. Typical relative permeability curves

Capillary pressure information was put in parametric form using the Leverett J function, i.e.,

$$P_c[S_w] = J[S_w] \sigma \cos \theta \left( \frac{\phi}{k} \right)^{1/2} \quad (16-15)$$

where  $J(S_w)$  is a dimensionless function of saturation which normalizes a set of capillary pressure curves for cores of differing permeability and porosity. Suppose that the capillary pressure curve for a rock sample of permeability  $k_b$  (base case) is available as shown in figure 16-5. Then the capillary pressure relation for a sample of permeability  $k$  and the same porosity is given by

$$P_c[S_w] = P_{cb}[S_w] \left( \frac{k_b}{k} \right)^{1/2} \quad (16-16)$$

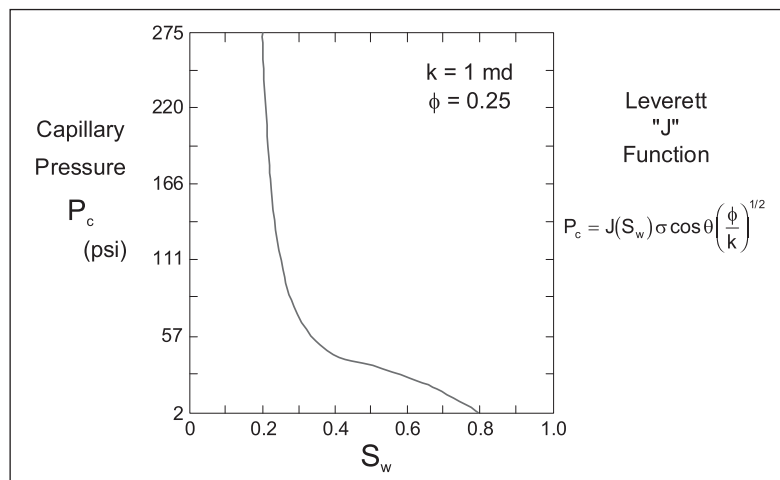


Fig. 16-5. Base case capillary pressure curve



This embodies the important scaling rule that capillary pressure is inversely proportional to the square root of permeability. This is the basis of the Leverett normalizing procedure. The parametric form of  $J(S_w)$  was taken from an extensive study of core capillary pressure data from a North Sea reservoir.

For WBM, the invasion process is two phase in the oil or gas columns, whereas in the aquifer it is a single-phase process not affected by capillary phenomena. In the case of OBM with a hydrocarbon (diesel) filtrate, it is invasion in the water column that will exhibit two phase behavior. The governing equations, i.e., (16-3)–(16-6), are the same; only the initial and boundary conditions are different. In the aquifer, the usual situation is that initially no oil is present, i.e.,  $S_w = 1$ . The undisturbed water phase pressure is  $p_w^f$ . The mud fluid loss inner boundary condition now becomes a specified oil (diesel) injection rate denoted  $q_o(t)$ ; thus

$$u_o \Big|_{r_w} = \frac{q_o(t)}{2\pi r_w} = - \frac{kk_{ro}(S_w^s)}{\mu_o} \cdot \frac{\partial p_o}{\partial r} \Big|_{r_w}$$

i.e.,

$$\frac{\partial p_o}{\partial r} \Big|_{r_w} = - \frac{q_o(t)\mu_o}{2\pi r_w k k_{ro}(S_w^s)} \quad (16-18)$$

Again, no specific value is given to  $S_w^s$ , the sandface water saturation. In the case of oil injection, it is the drainage capillary pressure which is relevant. The aquifer will be resumed to be strongly WW since only water is usually present in the undisturbed formation. Hence a nonwetting fluid is displacing a wetting fluid. However, it should be pointed out that OBMs also contain additives that are surface-active. In particular, chemicals are added to the mud which render cuttings OW. These will be present in the filtrate and may strongly affect rock wettability in the invaded region. The outer boundary condition takes the form

$$p_w^e(t) = p_w^f + \frac{q_{o,2}\mu_w}{4\pi k k_{rw}} \left[ \frac{q_{o,1}}{q_{o,2}} \ln \frac{T_1 + \Delta t}{\Delta t} + \ln \Delta t + \ln \frac{k k_{rw}}{\phi \mu_w c_t r_e^2} + 0.80908 \right] \quad (16-19)$$

## Simulation of the Invasion Process

### Water-Based Mud

The nonlinear differential system modeling near wellbore filtrate invasion was solved numerically using a finite difference scheme; this has been described in detail by Phelps.<sup>4,5</sup> The computational mesh was based on a logarithmic grid, and an implicit in pressure, explicit in saturation (IMPES) scheme was employed. This imposes a stability limit on the size of time step, but in a one dimensional situation computation time is not a problem. The inclusion of capillary pressure avoids the problem of shock fronts that occurs in hyperbolic systems, and

accurate numerical solutions for the saturation and pressure profiles through the invaded region were obtained.

The first case to be examined involved WBM and a strongly WW formation. The normalized capillary pressure curve is shown in figure 16–5 and the relative permeability curves in figure 16–4. The static mud fluid loss rate  $q_{w,2}$  is 0.04163 bbl/D/ft, which is typical for a WBM; the dynamic rate  $q_{w,1}$  is twice this value.

A typical saturation invasion pattern is shown in figure 16–6 for a constant rate mud fluid loss of 0.04163 bbl/D/ft in a low-permeability formation of  $k = 1$  md. The sandface saturation is at waterflood residual oil, i.e.,  $S_w^s = 1 - S_{or}$ , and the progressive advance of the filtrate is evident. The saturation profile is somewhat smeared out by capillary imbibition but the invasion is predominantly piston-like; the depth of invasion may be associated with the leading edge of the saturation distribution. Due to the radial nature of the process, the frontal advance rate slows down with time.

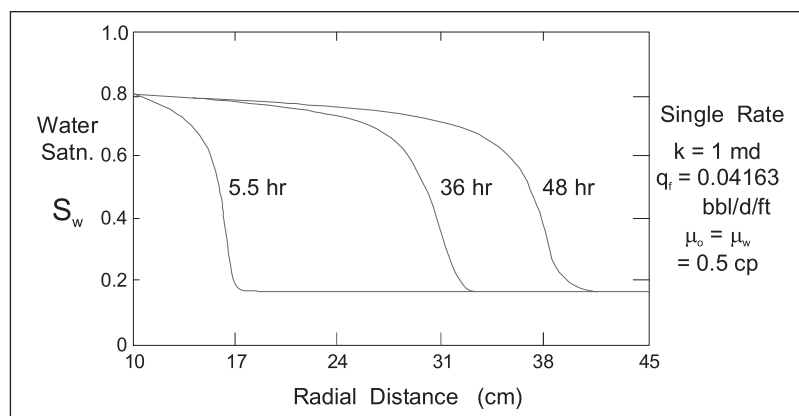


Fig. 16–6. Water-based mud invasion saturation profile

Invasion into an even lower permeability formation,  $k = 0.1$  md, is shown in figure 16–7 where now a two-rate fluid loss schedule has been employed with 12 h of dynamic filtration at  $q_{w,1} = 0.08326$  bbl/D/ft. The saturation profiles are even more piston-like especially at the higher dynamic rate. The displacement in low permeability rock is very close to that predicted by the Buckley–Leverett theory in which capillary pressure effects are neglected. The viscous forces predominate over the capillary pressure effects which are of little consequence. Typical pressure profiles are given in figures 16–8 a and b, which illustrate that the total pressure drop over the uninvaded part of the system. Even after 12 h of low-rate static filtration following the 12 h of dynamic filtration, the very low permeability (0.1 md, figure 16–8a) results in the sandface pressure  $p_w^s$  being 60 psi greater than the undisturbed oil phase pressure  $p_o^f = 2203$  psi. The difference  $p_w^s - p_o^f$  will be termed the “supercharging”; this aspect will be considered in detail in the section “Supercharging Analysis.” Note that the sandface water saturation  $S_w^s = 1 - S_{or}$ , i.e., complete displacement resulting in the phase pressures being equal at  $r_w$ ; this is a consequence of the particular form of the capillary pressure curve used, which has the property that  $P_c(1 - S_{or}) = 0$ . Note that it is only for very strongly WW conditions that an imbibition capillary pressure curve is like this. In the case of a 10 md formation, shown in figure 16–8b, the viscous effect is negligible and essentially  $p_w^s = p_o^f$  since  $P_c$  is also zero at the sandface.

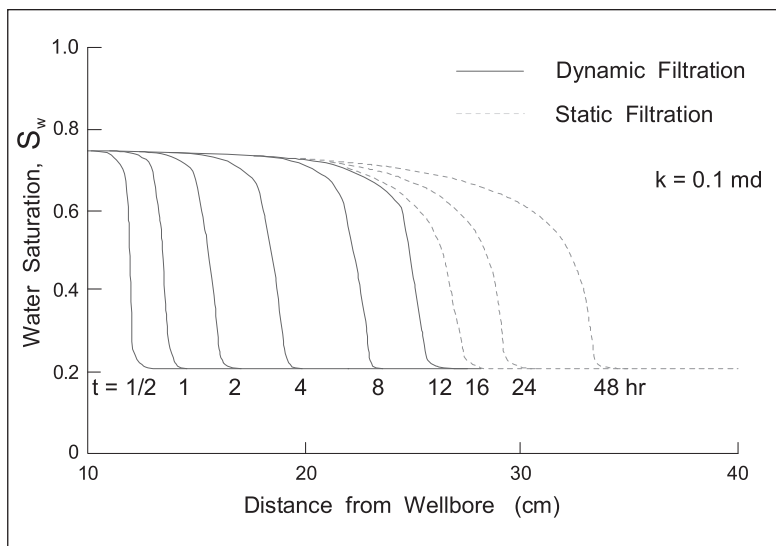


Fig. 16-7. Invasion saturation profile for a low permeability formation

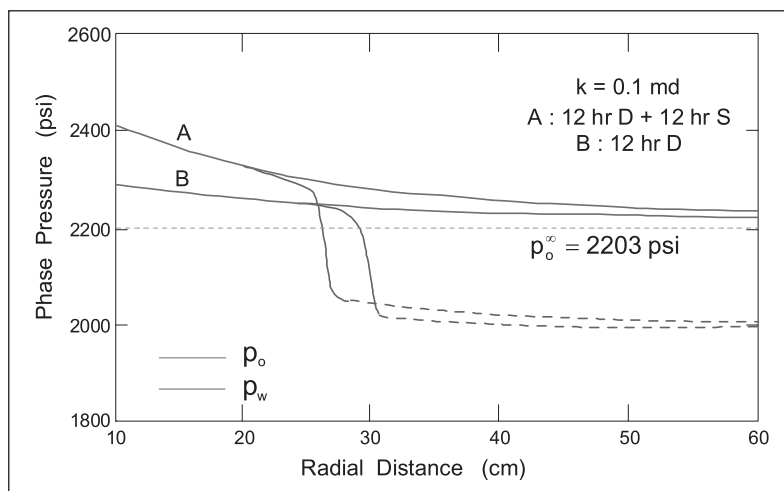


Fig. 16-8a. Invasion pressure profiles  $k = 0.1$  md

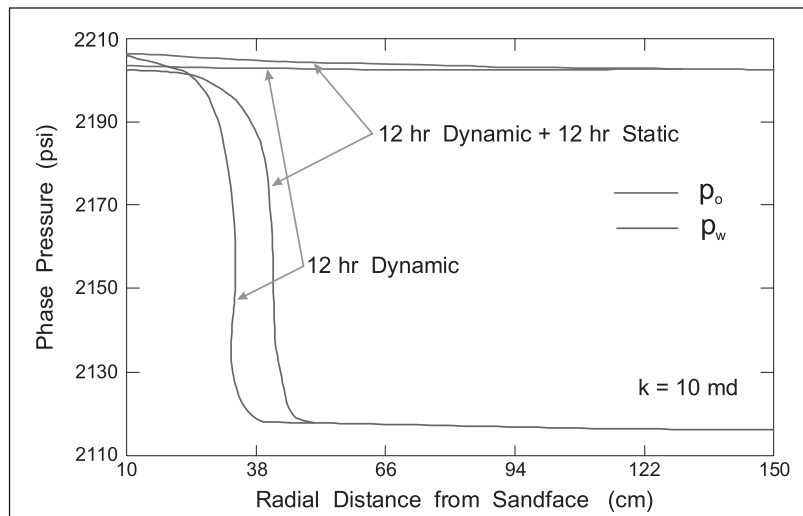


Fig. 16-8b. Invasion pressure profiles  $k = 10$  md

The contrasting case of a 100 md formation is illustrated in figures 16–9 and 16–10, in which the capillary pressure curve has been scaled down according to equation (16–16). The first observation is that the saturation profiles are now much more diffuse with correspondingly deeper invasion as defined by the leading edge of the saturation front. The second is that, not only has the water saturation at the sandface not reached  $1 - S_{or}$ , but it has in fact dropped below the maximum value attained at the end of the dynamic filtration period. Thus capillary imbibition is acting strongly to pull water away from the sandface, keeping  $S_w^s$  less than  $1 - S_{or}$  especially at the lower static filtration rate. This difference in behavior compared to the 0.1 md formation is due to the increased importance of capillary forces in higher permeability formations.

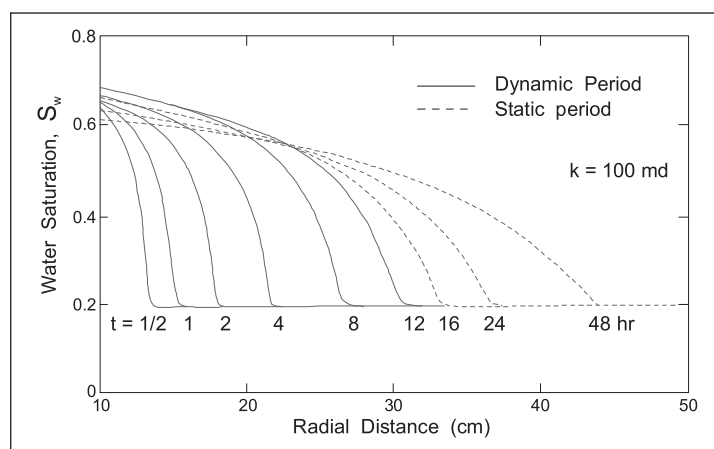


Fig. 16–9. Saturation profiles for a 100 md formation

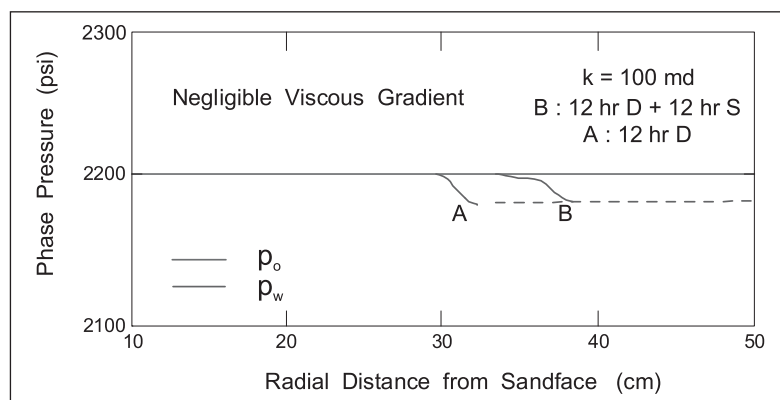


Fig. 16–10. Pressure profiles for a 100 md formation

The paradoxical situation arises where, although the capillary pressure is less in a high permeability formation, its effect on saturation distribution is greater. The explanation of the apparent anomaly is that capillary pressure is inversely proportional to the square root of permeability whereas flow resistance is inversely proportional to permeability directly. Although the magnitudes of the capillary gradients in the 100 md formation are  $\sqrt{1000}$  times less than in the 0.1 md rock, the ratio of capillary to viscous forces is  $\sqrt{1000}$  times greater. This is a consequence of the invasion rate being controlled by the filter cake and not the formation.

From figure 16–10, it can be seen that the overpressure due to viscous flow of filtrate in the 100 md formation is negligible, i.e.,  $p_w^s = p_o^r$ . However, since  $S_w^s < 1 - S_{or}$ , there must be a phase pressure difference at the sandface. In this particular example, because of the assumed shape of the capillary pressure curve, the difference is about 1 psi corresponding to  $S_w^s = 0.61$ . For capillary pressure curves applicable to formations with a wider pore size distribution, for example many carbonate formations, this pressure difference could be of the order of 10 psi. The effect will be enhanced by lower fluid loss rates since the filtrate is being imbibed into the formation faster than it is being supplied through the filtercake, resulting in lower near-wellbore saturations.

The conclusion is that in very strongly WW conditions and moderate permeability the sandface filtrate pressure  $p_w^s$  measured by a WFT may be slightly less than the undisturbed oil phase pressure  $p_o^f$ ; thus

$$p_w^s - p_o^f = - P_c(S_w^s) \tag{16-20}$$

if viscous pressure drops are negligible. A negative “supercharging” due to capillary pressure is present and the hydrocarbon gradient will be shifted to the left on a pressure–depth diagram giving too high a gradient intersection. In high permeability, this shift will be negligible because capillary pressure is so small, whereas in low permeability it does not exist since  $S_w^s = 1 - S_{or}$  and viscous supercharging is all important. The effect is most likely to be seen in gas reservoirs where strongly WW conditions exist. The influence of permeability on saturation distribution in the invaded region, for a fixed fluid loss schedule, is illustrated in figure 16–11.

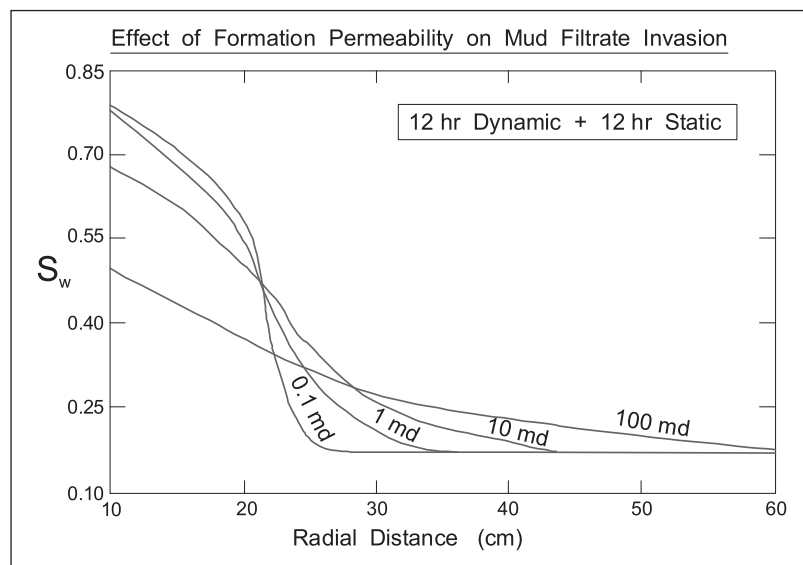


Fig. 16–11. Influence of permeability on saturation distribution

On the scale of a reservoir displacement and at the rate concerned, it is quite justifiable to neglect capillary pressure gradients and use the Buckley–Leverett theory. However, on the very much smaller length scale of an invasion process and at the very much lower displacement rate, capillary pressure effects can become very important.

The pronounced effect of capillary pressure on the shape of the saturation profile at high permeability has far reaching implications for logging measurements. Most log interpretation methods assume a piston-like displacement of reservoir fluid by invading filtrate a completely swept annular invaded zone essentially at residual oil saturation  $S_{or}$ , i.e.,  $S_w = 1 - S_{or}$ . In a strongly WW system, where imbibition plays an important role, this is clearly not the case. The saturation profile is smeared out and, for a fixed mud fluid loss rate governed by the filtercake, the invasion is deepest in high-permeability rock; this is quite contrary to the commonly held belief that invasion is deepest in low permeability. The main point is that, if diffuse conditions exist, a model based on sharp piston-like displacement should not be used for interpretation. Also  $S_{xo}$ —the measured near sandface water saturation using very shallow depth of investigation resistivity devices—is certainly not synonymous with  $1 - S_{or}$ .

The preceding discussion has been based on invasion simulations using the capillary pressure curve of figure 16–5, where  $P_c(1 - S_{or}) = 0$ . However, an imbibition capillary pressure curve in a WW system will generally not have this character. A more typical imbibition capillary pressure curve taken from the excellent review of wettability effects by Anderson<sup>6</sup> is shown in figure 16–12. At high water saturations, the imbibition capillary pressure becomes negative, i.e.,  $p_w > p_o$ , with the sample showing OW characteristics. This is the condition of mixed wettability where pores occupied by oil have become OW. Thus, in practice, the capillary pressure does not go to zero as  $S_w \rightarrow 1 - S_{or}$  but becomes negative. In order to simulate this much more realistic situation, the capillary pressure curve of figure 16–5 was simply shifted downwards, as shown in figure 16–13, so that it exhibits negative  $P_c$  at high water saturation. Recent evidence from carefully restored-state core experiments has shown that in the oil column the condition of mixed wettability is much more common than has been realized.

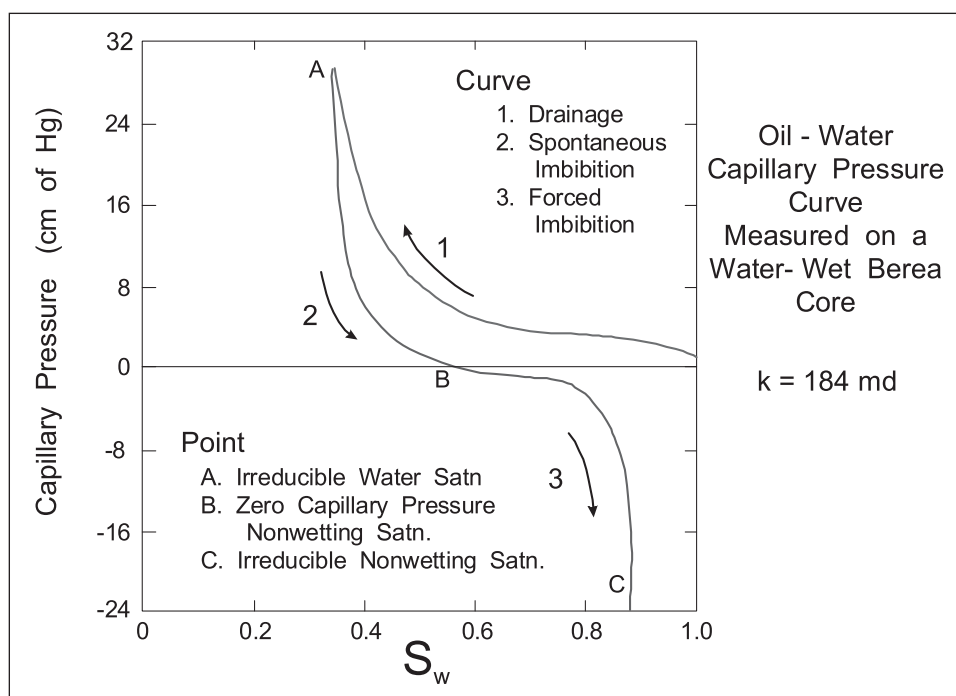


Fig. 16–12. Realistic imbibition capillary pressure curve

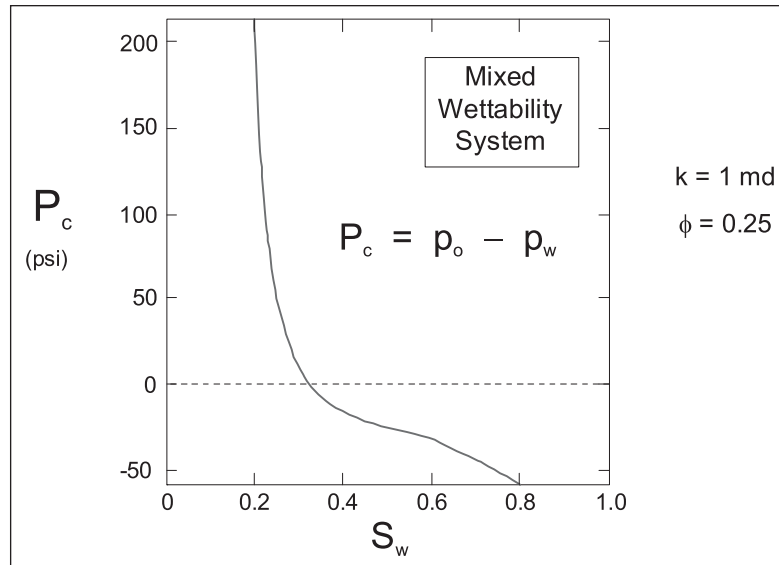


Fig. 16-13. Shifted capillary pressure curve

The pressure profiles from a simulation using the shifted, mixed wettability capillary pressure curve (figure 16-13) and a formation permeability of 1 md are shown in figure 16-14. The permeability is low enough for complete displacement to occur at the sandface, resulting in  $S_w^s$  being equal to  $1 - S_{or}$ , i.e.,  $S_w^s = 0.8$ . The phase pressures at the sandface accordingly differ by 60 psi, with the water phase pressure now significantly greater than the oil phase pressure; thus

$$p_w^s - p_o^s = -P_c(S_w^s) \quad (16-21)$$

where  $P_c(S_w^s) = P_c(1 - S_{or}) = P_c(0.8) = -60$  psi. The capillary pressure at the sandface is now negative due to the mixed wettability condition. Note that the shift of the capillary pressure curve was 60 psi; this is a purely arbitrary number simply to demonstrate the effect of mixed wettability. The important point is that the sandface water pressure now lies above the sandface oil pressure by an amount  $-P_c(S_w^s)$ . This is a very important result since it indicates that the water-phase pressure at the sandface measured by the WFT is greater than the undisturbed oil-phase formation pressure  $p_o^f$  due to the negative capillary pressure effect. This is superimposed on the viscous pressure drop supercharging which is present in this example but only to a small extent. Thus the excess pressure at the sandface is the sum of two contributions:

$$\Delta p^s = p_w^s - p_o^f = \Delta P_c + \Delta p_v \quad (16-22)$$

where

$$\Delta P_c = -P_c(S_w^s)$$

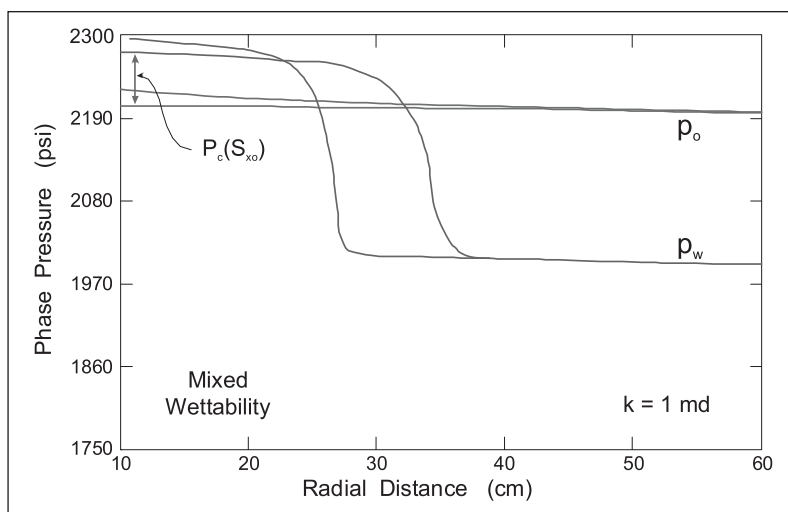


Fig. 16–14. Pressure profiles for mixed wettability

In this equation,  $\Delta p_v$  is the conventional supercharging effect due to viscous flow resistance.

It is interesting to examine the behavior in the other limiting case of a strongly OW system. A typical capillary pressure curve, again taken from the review paper of Anderson, is shown in figure 16–15. For WBM and aqueous filtrate invasion, it is now the (oil) drainage capillary pressure curve—labelled 1 in figure 16–15—which is relevant.

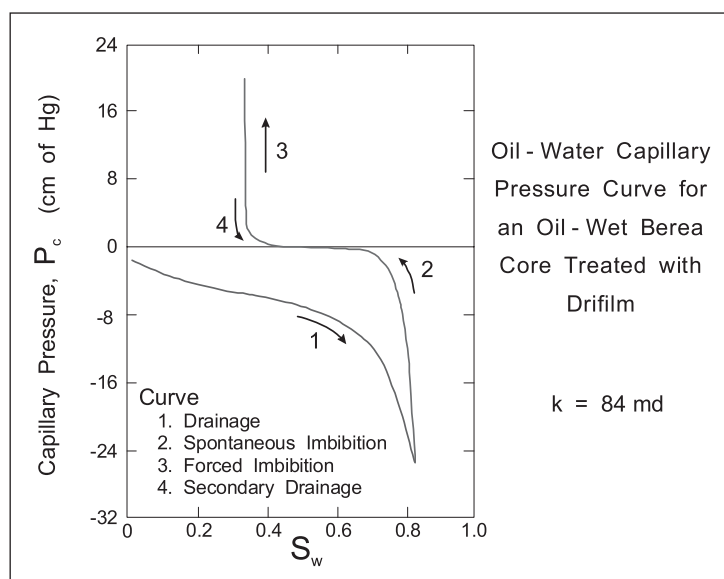


Fig. 16–15. Strongly oil-wet capillary pressure curve

The capillary pressure is negative at all saturations but approaches zero at low water saturation. The pressure profiles in an invasion process (with nonwetting fluid displacing wetting fluid) are shown diagrammatically in figure 16–16. In principle, for a strongly OW reservoir, the connate water saturation is essentially zero and at low water saturations, near the leading edge of the water front, the phase pressures are nearly equal. However, at the sandface where the water



saturation is high, the capillary effect is greatest and the water (nonwetting phase) pressure is much higher than the oil (wetting) phase pressure. This is quite the reverse of the strongly WW case. The implication for WFT pressure measurement is obvious—capillary effects are most likely to occur when a nonwetting phase displaces a wetting phase!

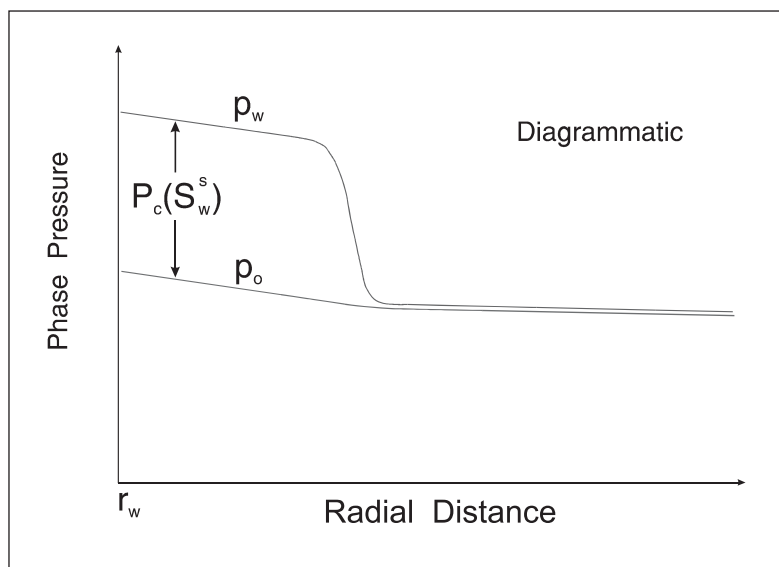


Fig. 16–16. Pressure profiles in a strongly oil-wet system

## Oil-Based Mud

The discussion so far has been concerned with the invasion of aqueous filtrate from a WBM in the oil or gas column. However, for various reasons many wells—for example 70% in the North Sea in 1986—are drilled with OBM. The principal advantages of OBM are faster drilling and clay stabilization. However, log interpretation is much more difficult and OBM, in fact, is an invert emulsion with oil (diesel) as the continuous phase, and laboratory studies have indicated that the filtrate that passes through the filtercake comprises oil only. However, it is by no means certain that at reservoir conditions water does not pass through the filtercake. In the mud itself, water remains suspended as very small droplets with maximum size of the order of 100  $\mu\text{m}$ . Emulsifying agents are required and these may act to make solid surfaces, e.g., drill cuttings, OW. These chemicals will also be present in the filtrate and hence may change the wettability in the invaded zone.

As previously mentioned, with OBM and an oleic filtrate, two-phase displacement will occur in the aquifer zone. It may be presumed that the reservoir rock in the water column is strongly WW and hence the invading diesel filtrate is very much a nonwetting phase unless any surface-active agents present in the filtrate drastically alter the rock wettability. The appropriate capillary pressure curve is therefore the primary (water) drainage curve for a strongly WW system, i.e., curve 1 in figure 16–12. The oil-phase pressure will always be greater than the water-phase pressure. Following the concepts developed on displacement in this section, the pressure profiles for oil filtrate invasion will have the form illustrated in figure 16–17.

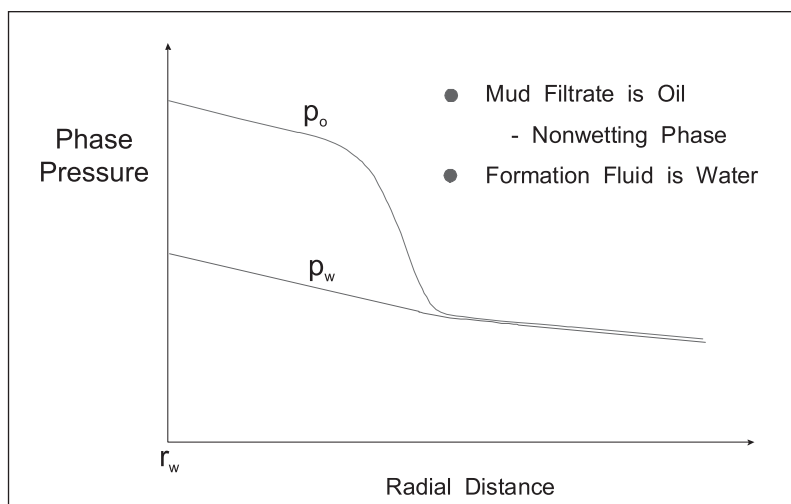


Fig. 16–17. Pressure profiles for oil filtrate invasion

In fact, figure 16–17 is identical to figure 16–16 except the phase profiles are reversed, in the present case (OBM: aquifer), oil is the nonwetting invading phase and its pressure listed above is that of the displaced wetting phase, i.e., water. The WFT will, of course, register the oil (filtrate) phase pressure at the sandface, i.e.,  $p_o^s$ . The excess pressure is now defined as

$$\Delta p^s = p_o^s - p_w^f = \Delta P_c + \Delta p_v \quad (16-23)$$

where

$$\Delta P_c = p_o^s - p_w^s = \Delta p_c(S_w^s)$$

When a nonwetting fluid displaces a wetting fluid, it is very difficult to reach the residual saturation: in this case, the oil floods residual water saturation  $S_{wr}$  (or  $S_{wc}$ ) without the passage of many pore volumes of fluid. Hence the sandface water saturation  $S_w^s$  will not be as low as  $S_{wr}$ . However, it is apparent that in the case of OBM there is a distinct possibility of a large capillary pressure effect  $\Delta P_c$  in addition to any supercharging  $\Delta p_v$  that may exist. Since the aquifer usually exhibits low permeability due to uninterrupted diagenesis and both terms of the excess pressure equation viz  $\Delta P_c$  and  $\Delta p_v$  increase with decreasing permeability, severe problems in determining water zone pressures  $p_w^f$  can be anticipated when OBM is used. One mitigating factor is that mud fluid loss rates are generally smaller in the case of OBM and viscous supercharging is less severe.

The mud filtrate invasion model developed by Phelps and Stewart<sup>4</sup> has been used by Beardsell<sup>8</sup> to simulate OBM invasion in the aquifer leg. In this study, a coupled model of filtercake deposition was used to estimate the diesel fluid loss rate during the dynamic filtration period (12 h) and the subsequent static filtration period (36 h). The formation initially contains only water and is strongly WW. The capillary pressure and relative permeability curves are shown in figures 16–18 and 16–19, respectively; the irreducible water saturation  $S_w$  is 0.4, at which the capillary pressure is 50 psi. The results are, of course, specific to the mud fluid loss rate predicted by the filtercake model and the assumed capillary pressure and relative permeability functions. The invasion front after 36 h of static filtration is shown in figure 16–20. It has penetrated only to a depth of 0.4 m after two days, which indicates a very low mud fluid loss rate. Hence the results are applicable

to low fluid loss conditions; note that very little is known of actual filtration rates of OBM in the wellbore at the reservoir temperature and pressure. The main feature of the saturation front is that the sandface water saturation  $S_w^s$  is 0.72 compared to the irreducible value of 0.4; hence the invaded zone is nowhere near well-swept. This is typical of the displacement of a wetting fluid (water) by a nonwetting fluid (diesel). The important corollary of this is that the capillary pressure at the sandface  $p_c(S_w^s)$  is much less than the potential maximum value of  $P_c(S_{wr})$ ; thus

$$P_c(S_w^s) = P_c(0.72) = p_o^s - p_w^s = 1.25 \text{ psi}$$

$$p_c(S_{wr}) = P_c(0.40) = 50 \text{ psi}$$

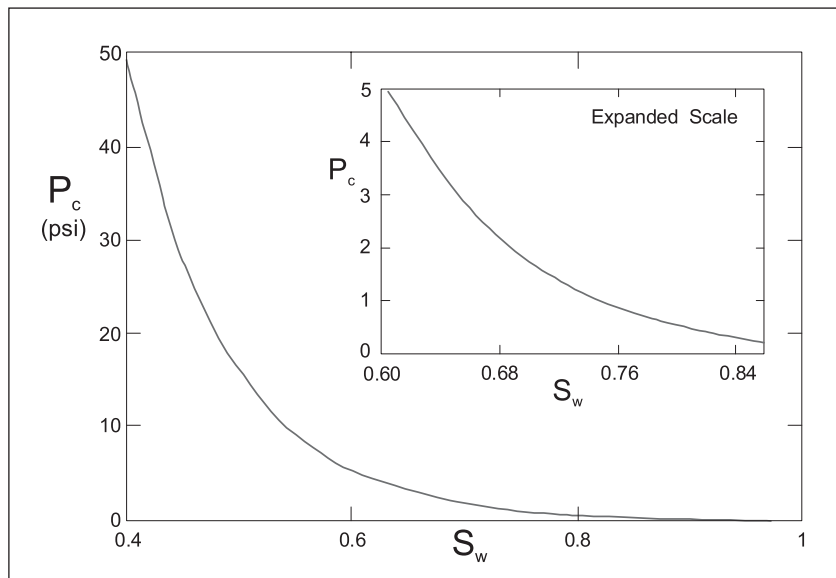


Fig. 16-18. Capillary pressure curve for OBM invasion

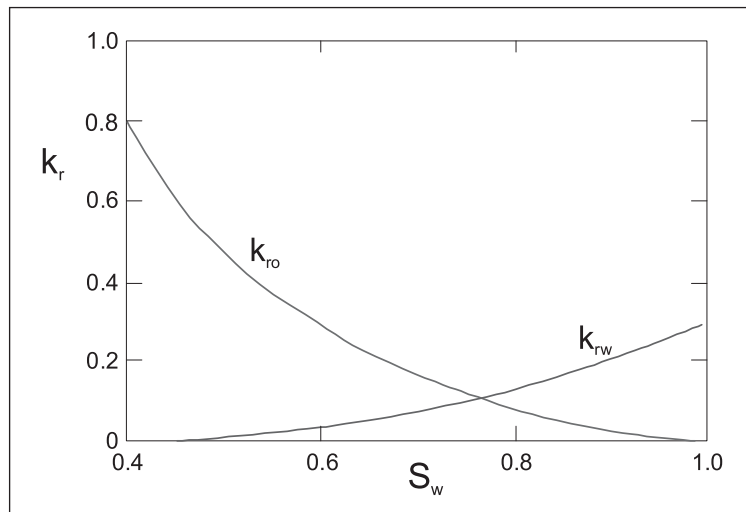


Fig. 16-19. Relative permeability curves for OBM invasion

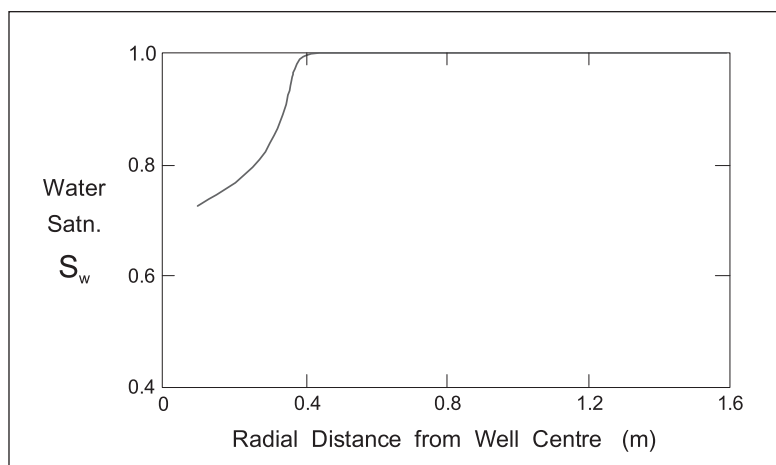


Fig. 16–20. Invasion front for OBM invasion

The actual sandface water saturation does not approach the irreducible value as would be predicted by Buckley–Leverett piston-like displacement. In fact, examination of figure 16–21, which shows the water saturation at the sandface as a function of time, reveals that while  $S_w^s$  was decreasing during the dynamic filtration period it is increasing during the period of declining rate static filtration.

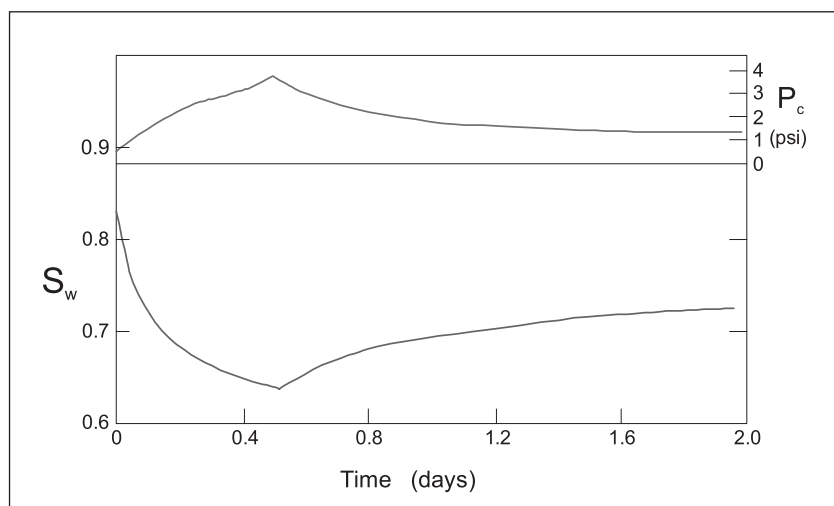


Fig. 16–21. Water saturation at the sandface in oil-based mud case

The phase pressures of the oil and water are shown in figure 16–22. As expected, the oil phase pressure lies above the water phase pressure in the invaded zone by an amount equal to the capillary pressure. In the simulation the undisturbed water phase pressure  $p_w^f$  was 10 psi and the viscous (supercharging) effect in the 2 md formation is evident—of the order of 1 psi. This is quite small due to the very low static mud fluid loss rate predicted by the model. The oil pressure profile shows a negative gradient corresponding to injection. However, the striking feature of figure 16–22 is that near the sandface the water-phase pressure exhibits a positive gradient indicating counterflow of water towards the wellbore. Thus, following the injection of oil at a relatively high rate during the dynamic filtration period, there is a redistribution of fluid during the static filtration period of much lower injection rate. Note that the rate drops drastically when static filtration begins and continues

to decline through the static period. Countercurrent capillary re-imbibition draws water back into the invaded region; this explains why the water saturation at the sandface is increasing during the static period. The redistribution process is still continuing even after 36 h of static filtration.

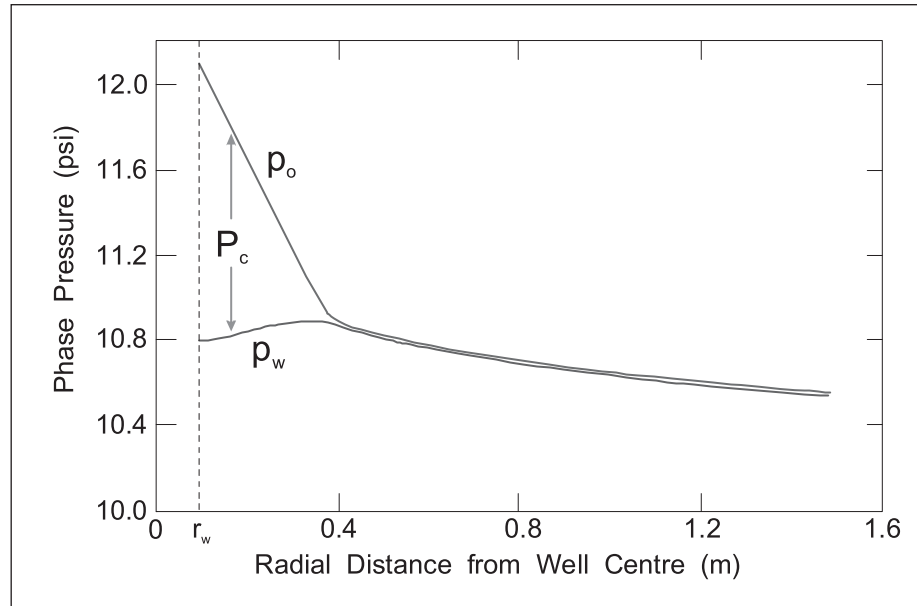


Fig. 16-22. Phase pressures in the oil-based mud case

The main conclusion of this study is that the water phase saturation at the wellbore  $S_w^s$  is prevented from reaching the lower limiting value of  $S_{wr}$  corresponding to complete displacement by

- (a) the displacing phase (diesel filtrate) being nonwetting;
- (b) countercurrent capillary re-imbibition after fluid loss rate reduction on the onset of static conditions.

The sandface capillary pressure effect  $\Delta p_c = p_c(S_w^s)$  is consequently considerably less than the maximum possible amount of  $P_c(S_{wr})$ . Thus the mechanics of the displacement process mitigate the effect of capillary pressure. These conclusions apply only to low fluid loss rate situations. The phenomena are very rate-dependent and in other circumstances the capillary pressure effect may be much more significant. The present example serves to highlight the complicated nature of the problem and to increase understanding of the physics of the invasion process with OBM.

## Field Examples Showing Capillary Pressure Effects

### Water-Based Mud

The simulation study of mud filtrate invasion has shown that, in some circumstances, the excess pressure  $\Delta p^s$  has a significant capillary pressure component which may be either positive or negative. The undisturbed phase pressures in a virgin reservoir are illustrated on a

pressure–depth diagram in figures 16–23a and b; case (a) shows the WW reservoir situation and case (b) corresponds to OW conditions. In the WW case, the oil–water contact (OWC) lies above the free water level (FWL) and in the OW case the reverse is true as indicated. If the WFT measured the true phase pressures, the gradient intersection would yield the FWL; this can be above or below the OWC depending on the wettability. In the case of a gas reservoir, only the WW condition is relevant and the FWL lies below the gas–oil contact (GOC).

It is useful, in fact, to first consider field examples from gas reservoirs which are really the only ones where strongly WW conditions may be expected. The invasion dynamics for the strongly WW case and WBM are summarized in figure 16–24, where the sandface water saturation  $S_w^s$  is less than the water saturation corresponding to residual swept gas, i.e.,  $1 - S_{gr}$ .

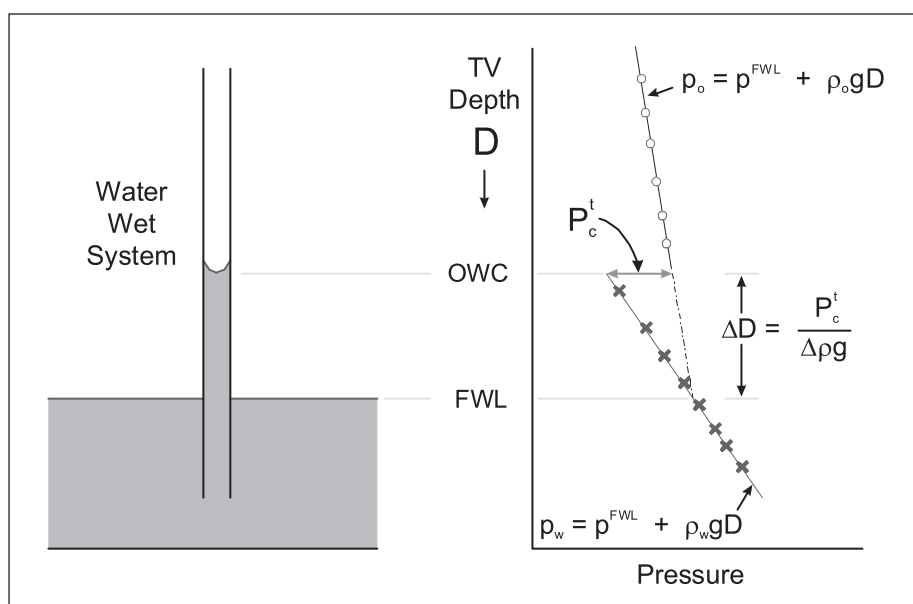


Fig. 16–23a. Undisturbed phase pressures in a virgin reservoir: WW

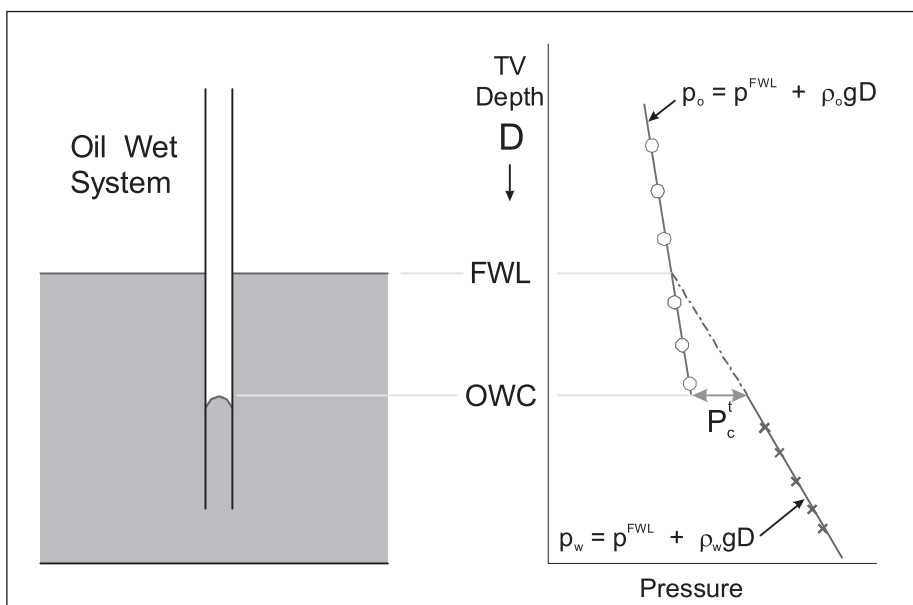


Fig. 16–23b. Undisturbed phase pressures in a virgin reservoir: OW

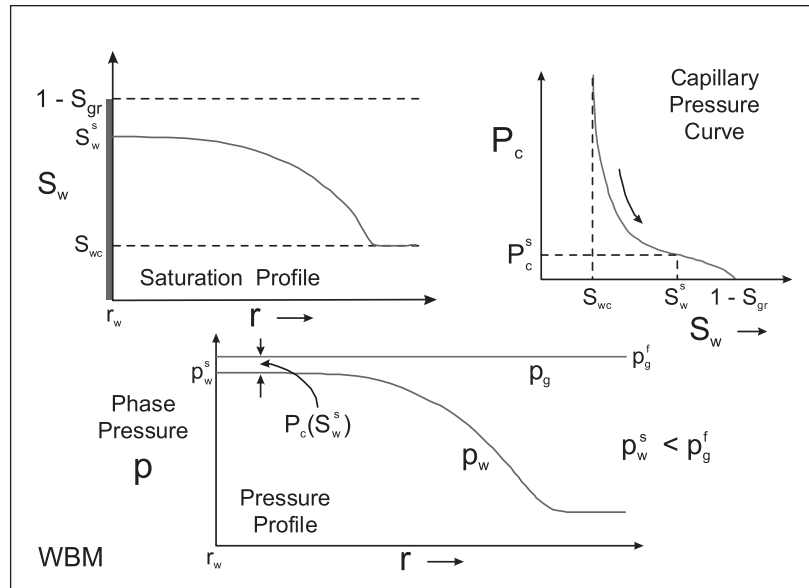


Fig. 16-24. Invasion dynamics for strongly WW case

The capillary pressure effect is negative, i.e.,

$$\Delta p^s = p_w^s - p_g^f = \Delta P_c = -P_c(S_w^s)$$

and the WFT-measured pressures are less than the true gas phase pressures at the same level; accordingly, there is a shift to the left on a pressure–depth diagram as shown on figure 16-25. The OPGI will lie above the FWL and probably above the gas–water contact (GWC).

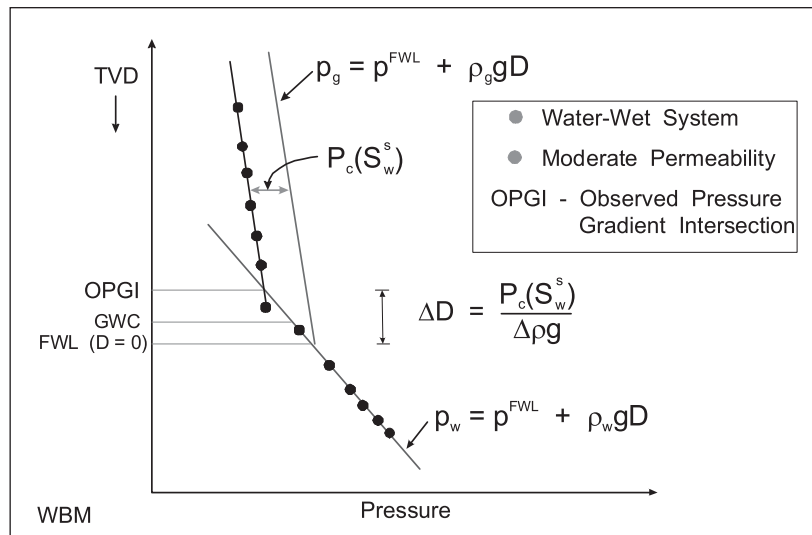


Fig. 16-25. Capillary pressure shift on pressure–depth diagram: gas well

This effect was first seen in the field by Awad,<sup>9</sup> who cites two gas wells in Pakistan with 500 m gas columns. For each well, pressure gradient lines were established for the gas and water phases; the results are shown in figures 16-26a and b and 16-27a and b. In both cases, the observed

gradient intersection lay above the log GWC. Awad used the log derived  $S_{xo}$ —the physical measurement of  $S_w^s$ —to correct the WFT-measured pressures. This depends on having available a capillary pressure J function and local permeability and porosity measurements. The correction shifted the intersection by 10 m as shown in the figures. The publication of this evidence of a WFT capillary pressure effect prompted the study of mud filtrate invasion described here.

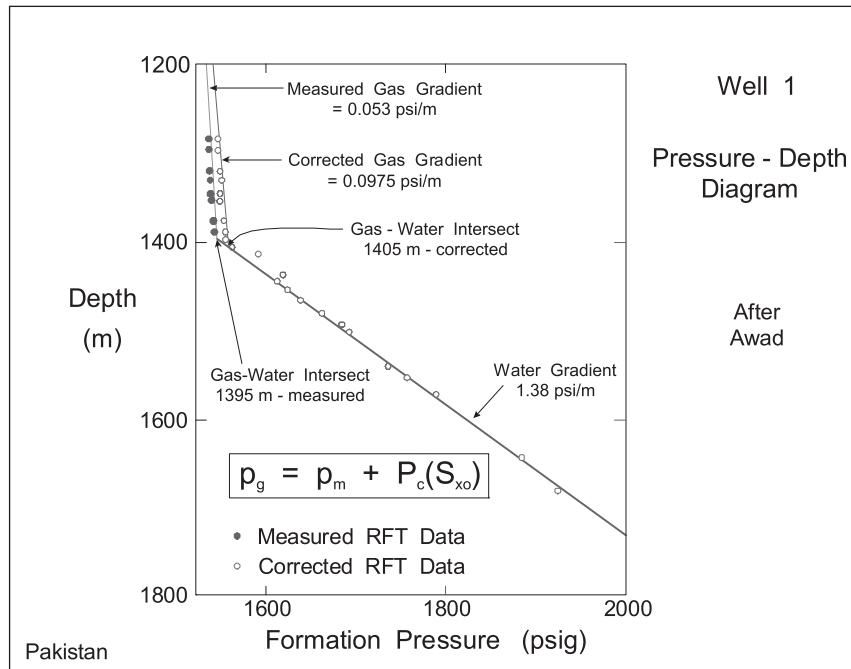


Fig. 16-26a. Field example of apparent capillary shift in a gas well: well 1

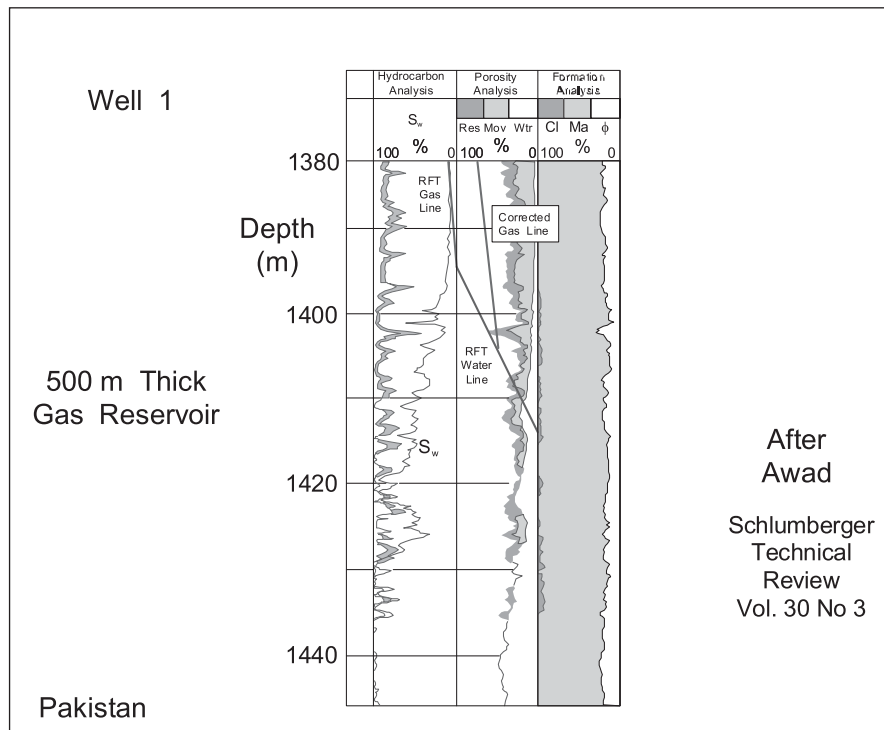


Fig. 16-26b. Computer processed log interpretation: well 1



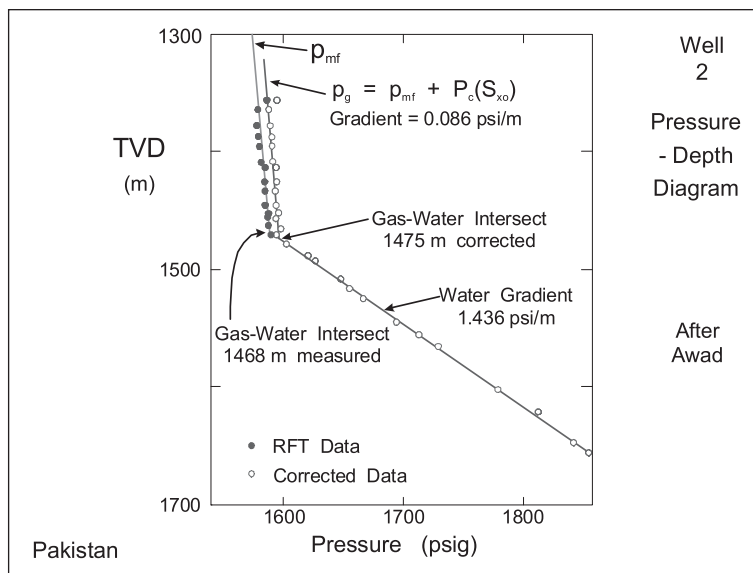


Fig. 16–27a. Second example of gas well capillary pressure shift

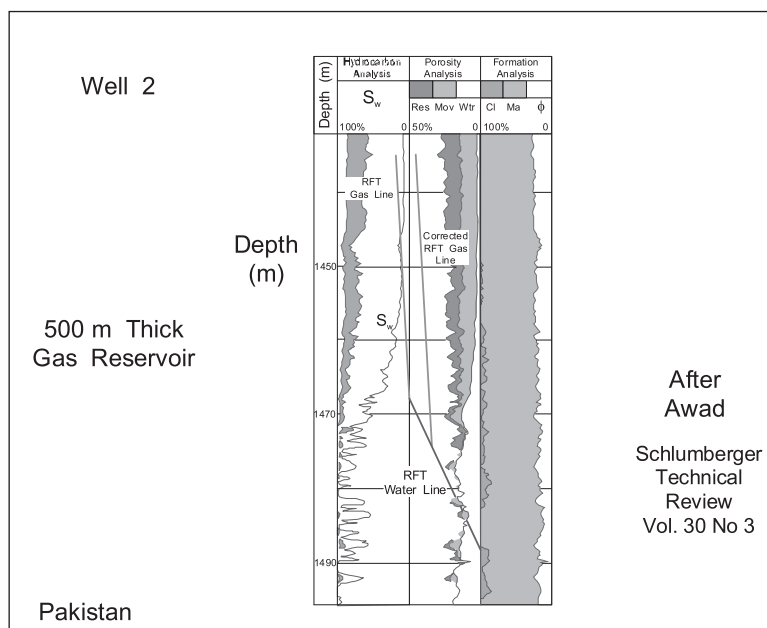


Fig. 16–27b. Computer processed log interpretation: well 2

The classical primary drainage capillary pressure curve for a porous medium with a narrow pore size distribution is reproduced in figure 16–28; the threshold capillary pressure is denoted  $P_c^t$ . Suppose the sandface water saturation lies somewhere in the range indicated by the arrows; then the capillary pressure effect  $\Delta P_c$  will be more or less equal to  $-p_c^t$ . This means that the observed pressure gradient intersection will lie exactly at the GWC. Hence the WFT gradient intersection, for this particular shape of capillary pressure curve, will be closer to the GWC than the FWL provided  $S_w^s$  is in the range indicated. This may explain why in many field examples the OPGI is indeed remarkably close to the GWC. The examples discussed here, where this is not the case, are the exceptions rather than the rule. Note that the upper limit for the OPGI is the top of the capillary transition zone; thus the theory of mud filtrate invasion brackets the OPGI between the FWL and the top of the transition zone.

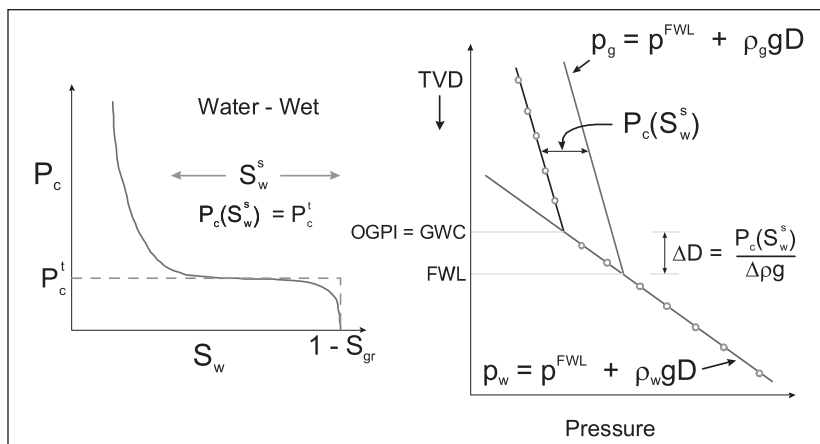


Fig. 16–28. Classical drainage capillary pressure curve

Two further WBM field examples from the southern North Sea province are shown in figures 16–29 and 16–30. In both these gas wells, the fluid gradients are well defined and the OPGI lies above the log indicated contact (although the latter quantity may be difficult to pin-point with precision). Obviously, this raises important questions about reserves and the validity of WFT surveys. For these wells, the OPGI is about 40 ft above the log GWC. This effect is now well known and can be explained by the invasion theory developed here. However, if the log contact was not well defined (say because of fresh formation water), it is difficult to estimate *a priori* the WFT intersection upward shift. The only approach is a good resistivity log which has a very shallow depth of investigation—and a correction based on measured capillary pressure data. This is essentially the method used by Awad. Note that the WFT intersection is conservative in relation to reserves estimation.

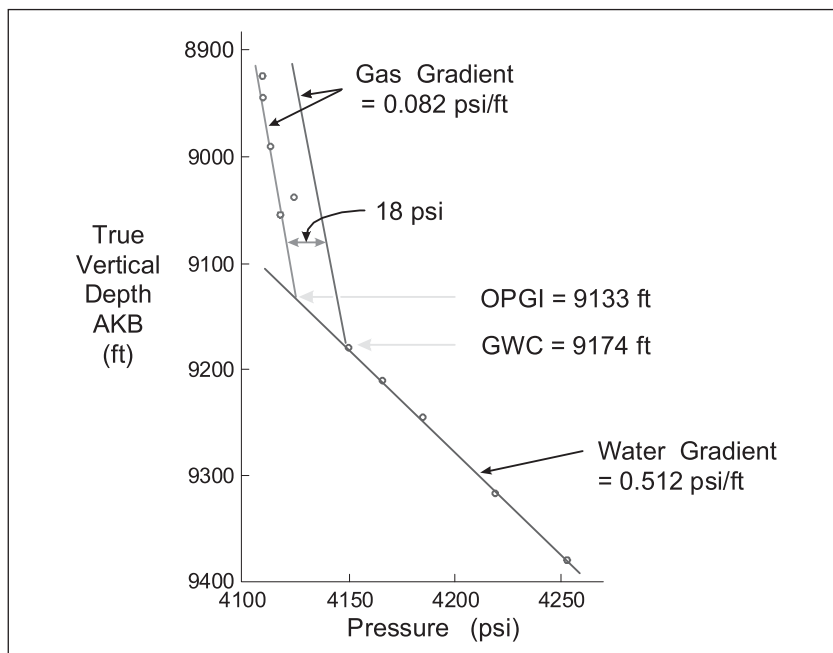


Fig. 16–29. North Sea field example of gas well with apparent capillary pressure shift

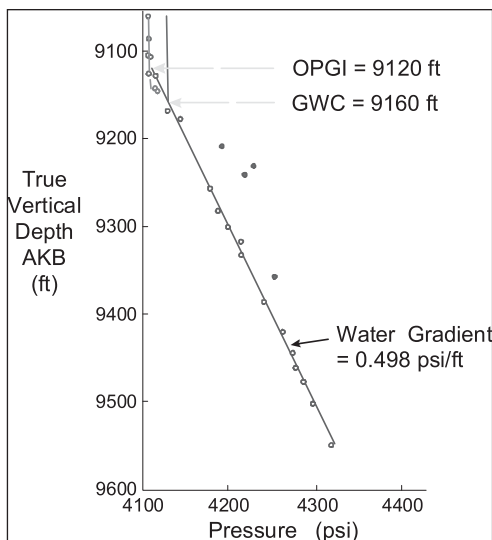


Fig. 16–30. Second North Sea gas well field example

As a final and interesting study of a gas well wireline formation tester (WFT) survey, a field example considered in detail by Airlie<sup>10</sup> will be discussed; this is designated well WBMI, and the depths and pressures have been shifted for reasons of confidentiality. The pressure–depth plot is shown in figure 16–31, where a good gas gradient has been identified but the observed water gradient has a slope of 0.95 psi/ft which is physically impossible in an unproduced field. The intersection of the best fit lines occurs at 384 ft which, in fact, is in very good agreement with the log contact as shown in figure 16–32; here, 384 ft corresponds to the bottom of the capillary transition zone, i.e., the GWC. However, the observed water gradient is quite unacceptable. Analysis of the individual test drawdown in the aquifer using spherical flow analysis gave permeabilities decreasing downwards through the water zone. There appears to be continually deteriorating permeability with depth in the aquifer, and at these low permeabilities a progressive increase in supercharging is likely.

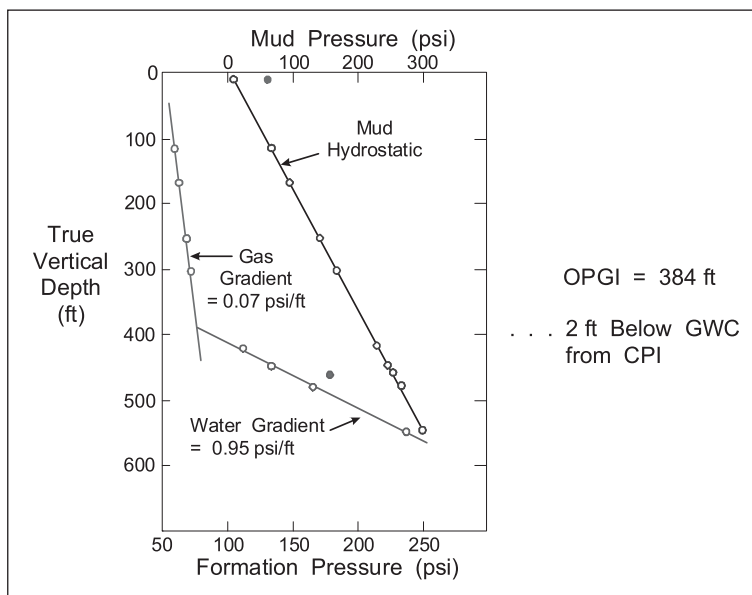


Fig. 16–31. Gas well field example due to Airlie

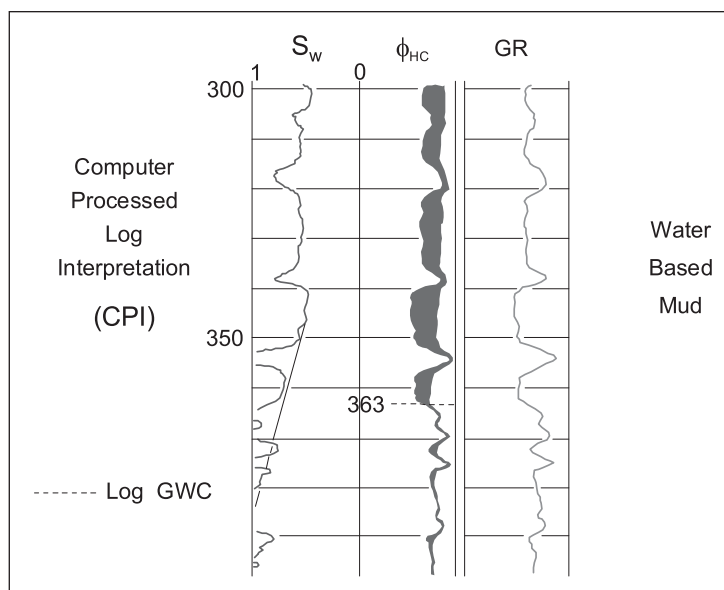


Fig. 16-32. Comparison of log contact and WFT intersection

The forced gradient supercharging analysis method described in chapter 9 was therefore used to correct the measured pressures in the water zone. A value for the formation water density was obtained by determining the salinity from logs and converting to a density. This was equivalent to a hydrostatic gradient of 0.52 psi/ft, which was later verified by a formation water sample. The supercharging analysis plot of  $p - \rho_w g D$  versus  $F(t)$  with  $q_2/q_1 = 0.5$  is shown in figure 16-33, the slope of which gives a value of the static mud fluid loss rate of 0.029 bbl/d/ft. The supercharging correction was then made to the water zone points, with the results shown in figure 16-34. This plot now has the proper water gradient and represents the hydrostatic pressure in the aquifer. The corrected gradient intersection lies at 384 ft—some 20 ft higher. The intersection lies between the apparent log GWC and the top of the capillary transition zone. Besides defining the phase pressures in the reservoir, this survey has provided important permeability information on the aquifer which will be useful in predicting future water influx as the gas zone is depleted.

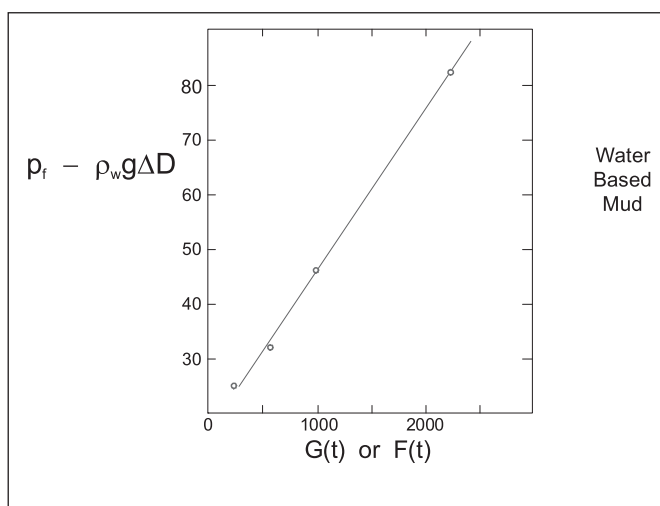


Fig. 16-33. Supercharging analysis

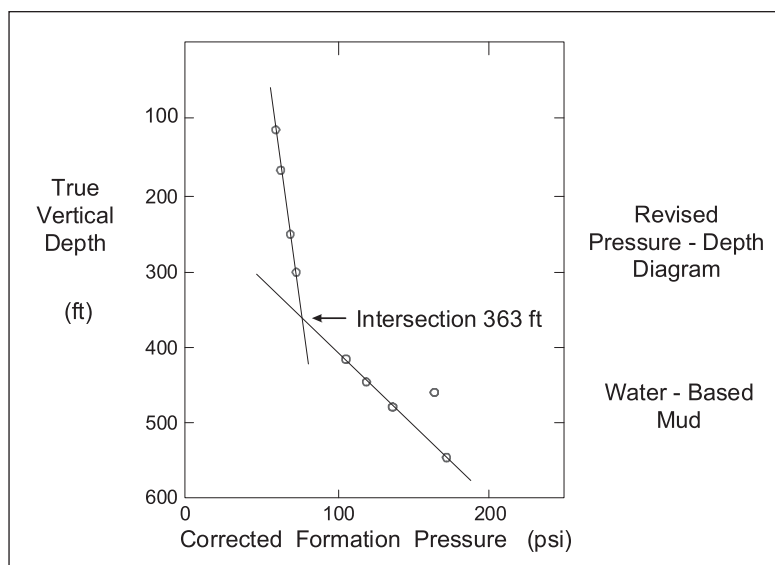


Fig. 16-34. Supercharging correction made to water zone

In the supercharging analysis, various values of the static–dynamic fluid loss ratio  $q_s/q_1$  were tried, but the results were not sensitive at all to the choice of this quantity. The effect of supercharging in the water zone meant that a permeability of 1 md required a correction  $\Delta p_s$  of 15 psi; the bottom point in the aquifer where  $k_s = 0.2$  md was shifted by 64 psi.

The measured gas gradient in the gas zone of 0.07 psi/ft agreed exactly with the gas density from PVT analysis. The estimated spherical permeabilities in the gas zone range from 1 to 8 md, indicating that a small supercharging correction should be made here also. If the water zone estimated fluid loss rate of 0.029 bbl/d/ft is used to correct gas zone pressures, the excellent observed gas gradient is no longer obtained. For this reason, no supercharging correction was made to the gas column data.

This discrepancy in the apparent supercharging behavior is difficult to explain. There is possible some reason—connected with the mechanics of filtercake resistance—why mud fluid loss might be lower in the gas zone than in the aquifer. It is quite conceivable that, due to the much lower viscosity and higher compressibility of gas, a better filtercake is deposited in the gas column. Alternatively, the analysis of supercharging given in the preceding section may be deficient. The theory of the viscous pressure drop  $\Delta p_v$  is based on a one-dimensional model which does not allow any vertical communication. Thus the degree of supercharging is regarded as a local phenomenon depending on the point permeability as determined by spherical drawdown analysis of the pressure response. In practice, vertical communication will exist and the local mud fluid loss will adjust in response to small-scale permeability heterogeneity. Hence supercharging should be assessed in terms of some average rather than essentially a point permeability. One dimensional theory will tend to suggest large differences in supercharging from level to level if the spherical permeability  $k_s$  shows wide variation.

It is unfortunate that the WFT buildup permeability, which in principle is an average over a scale of about 3 ft, has been shown to be unreliable by Radcliffe;<sup>11</sup> spherical drawdown permeability reflects conditions in the immediate vicinity of the probe.

A final observation concerning this field example is relevant. Airlie found that the  $S_{x_0}$  values from log interpretation were in the range 0.2–0.3, which are very close to  $1 - S_{gr}$ . He concluded that displacement was essentially complete and that there was no capillary pressure effect. The OPGI at 363 ft was therefore associated with the beginning of movable gas. The gas shown on logs between 363 ft and 384 ft was presumed to be nonproducing; this is in agreement with the logs as shown in figure 16–32, which do not indicate any movable gas below 363 ft.

Consider now oil reservoirs, still with WBM, when mixed wettability conditions exist in the oil column. The invasion dynamics in the oil zone (irreducible formation water saturation) are illustrated diagrammatically in figure 16–35. The sandface water saturation  $S_w^s$  is less than  $1 - S_{or}$  but still yields a negative capillary pressure. Thus the sandface water pressure  $p_w^s$  is greater than the formation oil-phase pressure  $p_o^f$  by an amount  $-P_c(S_w^s)$ . The oil gradient is accordingly displaced to the right as shown in figure 16–36; the shift is  $-P_c(S_w^s)$ . The OPGI is moved down closer to the OWC. Thus the effect of invasion dynamics is to bring the OPGI nearer to the OWC and away from the FWL. Note that this effect is due to mixed wettability in the oil zone above the capillary transition zone.

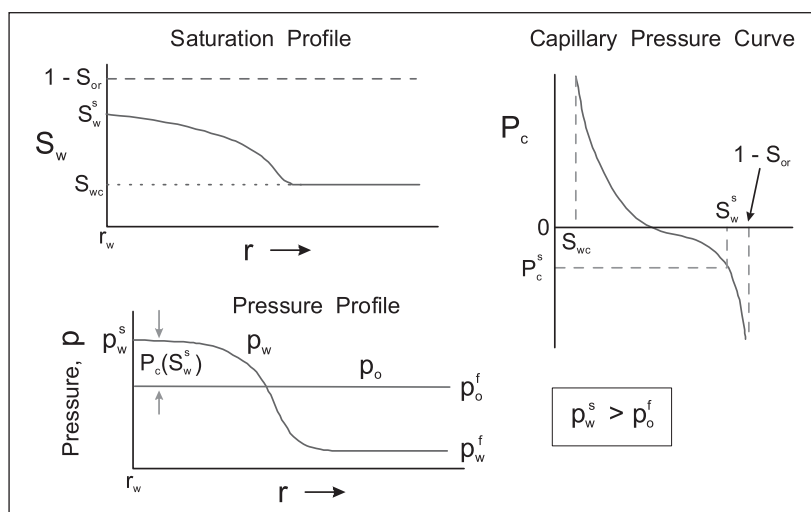


Fig. 16–35. Invasion dynamics in mixed wettability

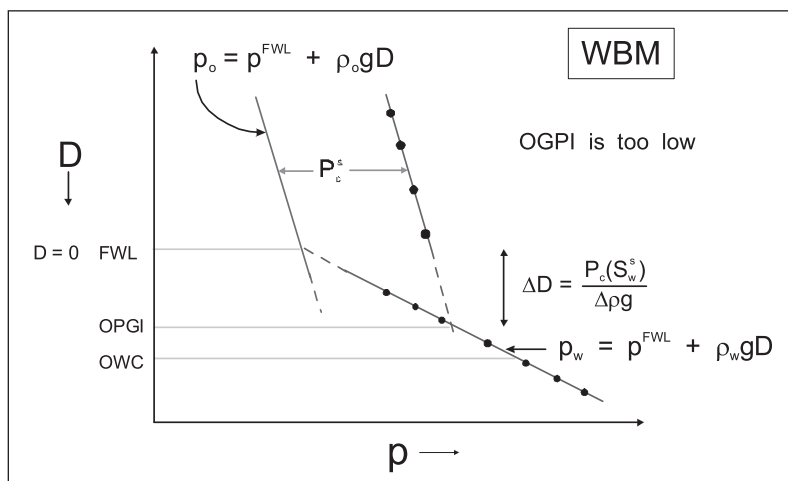


Fig. 16–36. Displacement of oil gradient in mixed wettability

Native or restored state wettability tests on core samples demonstrate that in many reservoirs WW conditions are present around the OWC, but higher up in the oil column mixed wettability prevails. In this case, behavior around the OWC will be classical WW but in the mixed wettability oil zone the invasion dynamics will cause the measured pressures to be shifted to the right by an amount  $-p_c(S_w^s)$ ; this is illustrated in figure 16–37. Hence the observed pressure gradient intersection is displaced below the true FWL and the apparent free water level lies far below the OWC. This feature is a possible clue that mixed wettability or oil wetness exists in the oil column. Figure 16–38 is a field example from Brazil exhibiting such behavior. Note that this data was originally used by the author (and later by Desbrandes and Gualdron) as an example of classical WW behavior. However, the whole capillary transition zone is much less than the distance between the apparent FWL and the OWC, which is extremely unlikely.

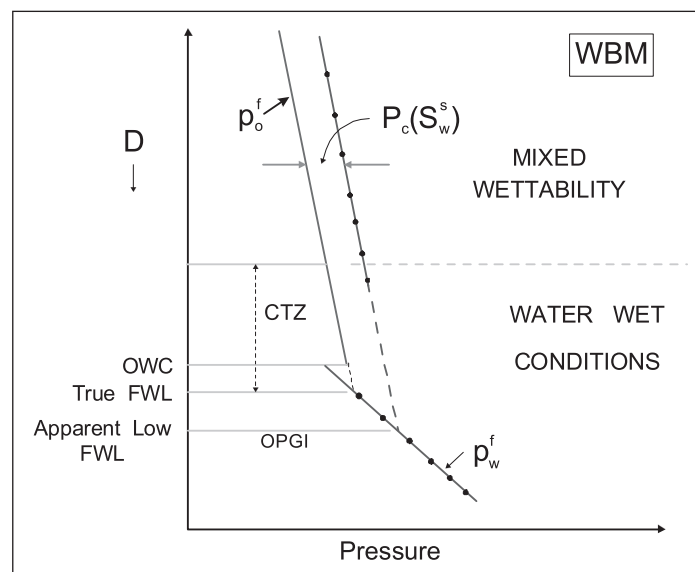


Fig. 16–37. Wettability variation with depth

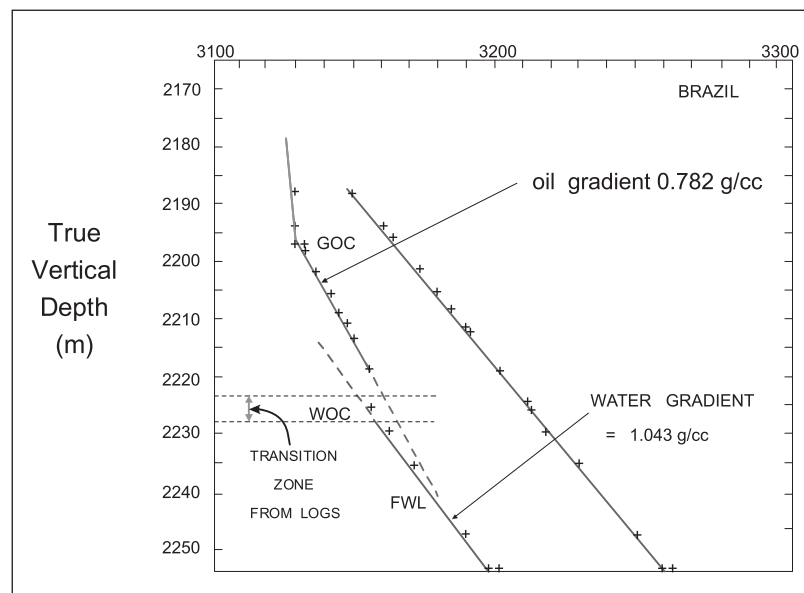


Fig. 16–38. Field example possibly exhibiting oil-wet behavior

# 17

## Tight Gas and Coal Bed Methane (CBM)

---

### Introduction

The development of unconventional gas reserves has become a large and important sector of the oil and gas industry in North America and elsewhere, e.g., Australia. The tight gas (including shales) and coal bed methane sectors are predominant, and companies have been aggressively developing capability in these areas. A key issue is the prediction of well deliverability in transient conditions often following a fracturing operation. Since the production forecast is essentially a particular form of variable rate analysis using a well test model (known as a constant rate drawdown (CRD)  $p_D$  function) as a basis for convolution, the PanSystem deliverability option has been one of the software's strongest assets particularly in connection with fractured wells in low-permeability reservoirs.

Existing well test models presume that the permeability is invariant but the two principal sectors mentioned above have the common feature that the permeability of the formation—low-permeability sand, shale bed, or coal seam—is dependent on pore pressure. The issue of compaction has been partially handled through the rock compressibility ( $c_p$ ) component in total compressibility  $c_t = S_w c_w + (1 - S_w) c_g + c_p$ ; this allows some element of compaction drive, i.e., change in porosity with pore pressure. However, the issue of associated permeability change has not been addressed in the well test software packages. One of the important advances in reservoir engineering in the last two decades has been much improved understanding of the role of rock mechanics. This was driven initially by the subsidence issue in the Norwegian chalk reservoirs and then by the fracturing of tight gas formations. However, it was pointed out by M. Smith at the recent Rio de Janeiro, Brasil, conference on Tight Gas (2007) that permeability was the prime factor in the design and eventual success of a fracture operation.

The analysis of production decline data using Agarwal–Gardner type curves has also been an important development particularly in Canada and the United States. PanSystem has an option for this type of analysis but again the permeability is presumed to be constant. At the present



time, the logarithmic derivative, which is used for diagnostic and interpretation purposes, is subject to noise problems in this application and the new wavelet processing is expected to significantly strengthen processing in this area. A further extension to include stress-dependent permeability has been a real boost to the software's capability.

In this chapter, the treatment of stress-dependent permeability and porosity (SDPP) in pressure transient testing and production forecasting will be addressed. The application of a pseudopressure transform, which is the traditional method for tackling the problem, will be described. It is interesting to note that multiphase pseudopressure for gas condensate and volatile oil transient testing was introduced by Raghavan of Phillips Petroleum. His Ph.D. thesis at Stanford was on stress-dependent rock properties where he had also proposed a pseudopressure approach following Muscat.

The SDPP pseudopressure method presumes that the rock mechanics model is already known. In the study described here, an alternative procedure termed "pseudo model" is proposed, where the rock mechanics parameters can be determined by the nonlinear regression facility available in well test software.

## Stress-Dependent Permeability

The slug test has been much used in the context of coal bed methane, as described in chapter 5 of *Well Test Design and Analysis* on variable rate, where it is important to determine the bulk permeability of the connected fissure (joint-cleat) system. The coal seams are also hydraulically fractured to enhance well deliverability allowing the water phase to be pumped off. In these systems, it has been shown that the permeability is stress dependent and changes in pore pressure will alter the effective stress (grain pressure). One approach to handling this effect, suggested by Raghavan *et al.*,<sup>1</sup> is to define a normalized pseudopressure of the form

$$\psi(p) = \frac{1 - \phi_i}{k_i} \int_{p_b}^p \frac{k(p')}{1 - \phi(p')} dp' \quad (17-1a)$$

or

$$\psi(p) = \frac{(1 - \phi_i)\mu_{wi}}{\rho_{wi}k_i} \int_{p_b}^p \frac{\rho_w k(p')}{(1 - \phi(p'))\mu_w} dp' \quad (17-1b)$$

Here it is presumed that only one phase—water—is present during the testing. Raghavan utilized a numerical simulator to model the pressure behavior in such situations, and the stress dependence used in the study is presented in figure 17-1a and b. When the pressure is transformed to a pseudopressure, the superposition principle is valid since the pseudopressure is the solution of a linear partial differential equation (PDE).

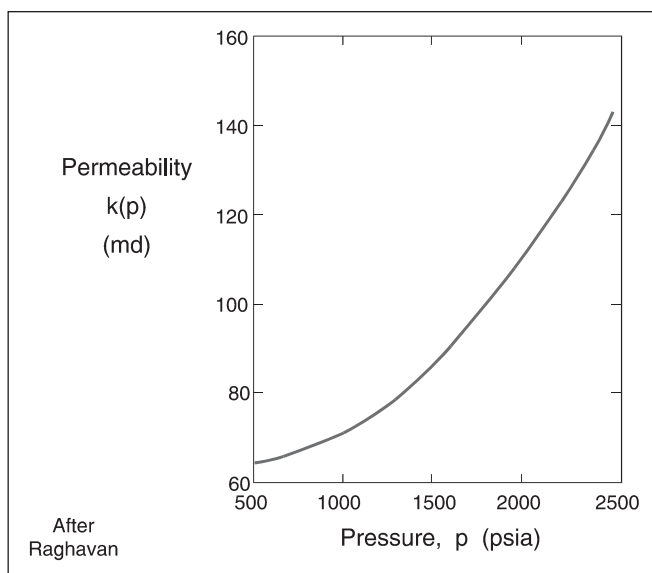


Fig. 17-1a. Stress-dependent permeability

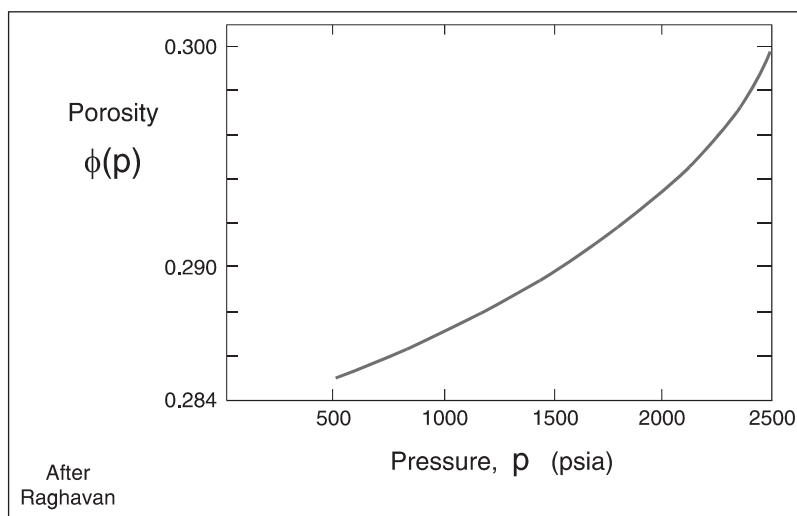


Fig. 17-1b. Stress-dependent porosity

Samaniego and Cinco<sup>2</sup> used the pseudopressure approach to analyze synthetic data generated by a numerical model, with the results shown in figure 17-2; here, the stress-dependent parameter,  $k(p)/(1 - \phi(p))$  has been determined as a function of pore pressure. These authors recommend a high rate drawdown so that an appreciable pressure range is investigated and they also suggest buildup analysis to give increased confidence to the stress dependence at pressures close to the initial. Thus storage effects in drawdown at early time mask the stress dependence effect at pressures close to  $p_i$ , whereas buildup at late time (and pressures close to  $p_i$ ) is not influenced by storage. However, buildup at late time is adversely affected by noise in the data. Raghavan did not investigate buildup behavior with his numerical model, but Samaniego showed that the application of stress-dependent pseudopressure to buildup was valid.

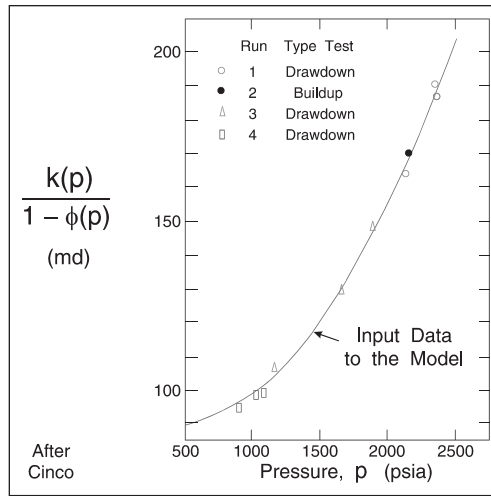


Fig. 17-2. Comparison between input and estimated parameter values

The concept of pseudopressure derives from an analysis of steady-state radial flow described by Darcy’s equation in the form

$$\frac{q}{A} = \frac{q}{2\pi rh(p)} = u_r = \frac{k(p) dp}{\mu dr} \tag{17-2}$$

In this form, the permeability is taken to be a function of pore pressure, which allows stress dependence to be catered for. Similarly, the effect of compaction on the formation thickness is modeled through a pressure dependence of the formation thickness, denoted  $h(p)$ , illustrated in figure 17-3. A volume balance gives

$$h_{\text{eff}} = h(p) = \frac{h(p_i)[1 - \phi_i]}{1 - \phi(p)} \tag{17-3}$$

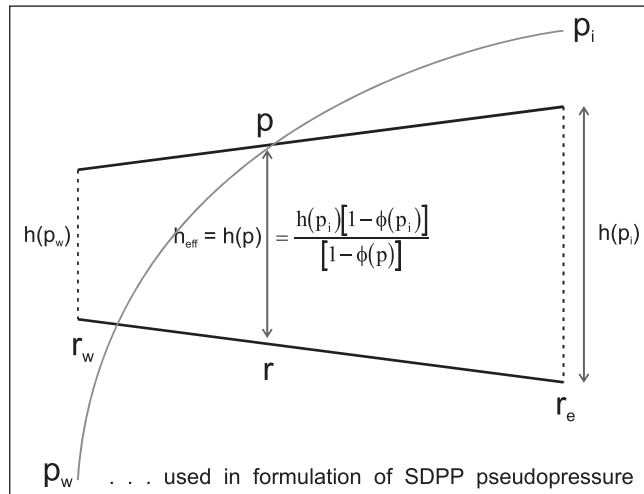


Fig. 17-3. Stress-dependent height compaction

This accounts for the compaction of the formation due to porosity change. Separating the variables in (17-2) yields

$$\frac{dr}{r} = \frac{2\pi h(p_i)[1 - \phi(p_i)]}{q\mu} \frac{k(p)}{1 - \phi(p)} dp \quad (17-4)$$

Integrating

$$\int_{r_w}^{r_e} \frac{dr}{r} = \frac{2\pi h(p_i)[1 - \phi(p_i)]}{q\mu} \int_{p_w}^{p_e} \frac{k(p)}{1 - \phi(p)} dp \quad (17-5a)$$

i.e.,

$$\ln \frac{r_e}{r_w} = \frac{2\pi h(p_i)[1 - \phi(p_i)]}{q\mu} \int_{p_w}^{p_e} \frac{k(p)}{1 - \phi(p)} dp \quad (17-5b)$$

↑  
reservoir integral

The form of (17-5b) suggests a normalized pseudopressure function of the form

$$\psi(p) = \frac{1 - \phi_i}{k_i} \int_{p_b}^p \frac{k(p')}{1 - \phi(p')} dp' \quad (17-6)$$

The integral in (17-6)—termed “the reservoir integral” by Raghavan—can be expressed as the difference between two pseudopressure integrals, i.e.,

$$\int_{p_w}^{p_e} \frac{k(p)}{1 - \phi(p)} dp = \int_{p_b}^{p_e} \frac{k(p')}{1 - \phi(p')} dp' - \int_{p_b}^{p_w} \frac{k(p')}{1 - \phi(p')} dp' \quad (17-7)$$

The steady-state radial inflow Eq. (17-5b) may therefore be written in the form

$$\ln \frac{r_e}{r_w} = \frac{2\pi k_i h_i}{q\mu} \{ \psi(p_e) - \psi(p_w) \} \quad (17-8)$$

The effect of skin and conversion to semi-steady-state (SSS) conditions can be achieved as follows:

$$\ln \frac{r_e}{r_w} - \frac{3}{4} + S = \frac{2\pi k_i h_i}{q\mu} \{ \psi(\bar{p}) - \psi(p_w) \} \tag{17-9a}$$

i.e.,

$$q = \frac{2\pi k_i h_i}{\mu \left( \ln \frac{r_e}{r_w} - \frac{3}{4} + S \right)} \{ \psi(\bar{p}) - \psi(p_w) \} \tag{17-9b}$$

Supposing a stress-dependent pseudopressure function has been computed, the well deliverability curve can be determined by the construction illustrated in figure 17-4. This approach is used in the prediction of gas well deliverability where the pseudopressure reflects changing fluid properties. The well deliverability curve is a translation of the shape of the pseudopressure curve as shown in figure 17-5.

In the SSS formulation, it is presumed that the current average reservoir pressure  $\bar{p}$  is known. It was demonstrated by Raghavan and Cinco and Samaniego that the steady-state pseudopressure, as defined here, can be used to linearize the transient flow equation, which then takes on the classical diffusion form; this assertion is validated by examining the results of a numerical simulation.

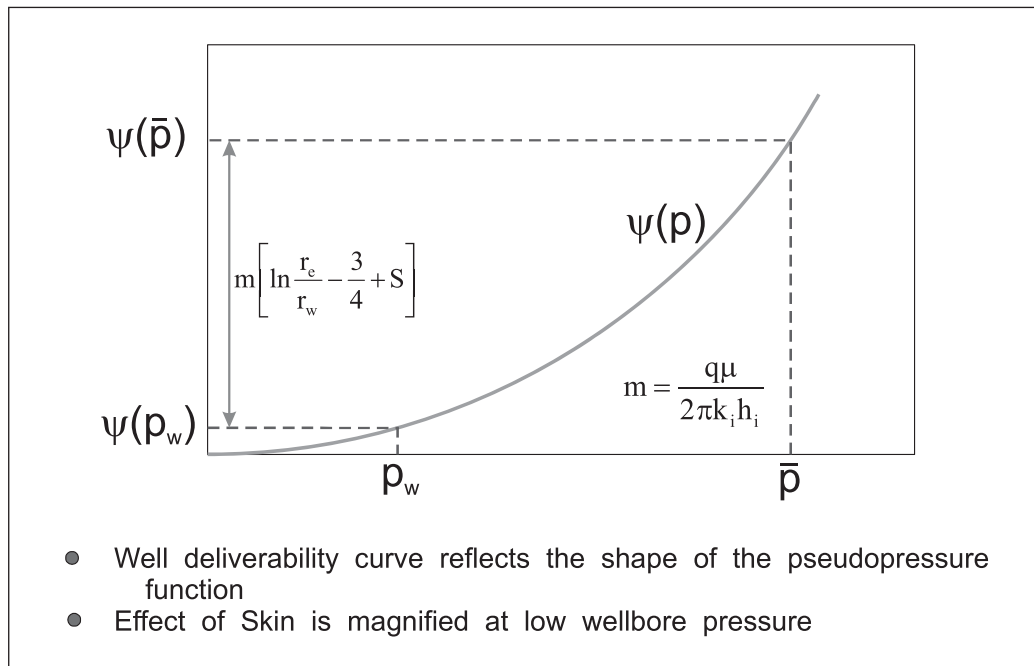


Fig. 17-4. Well SSS deliverability

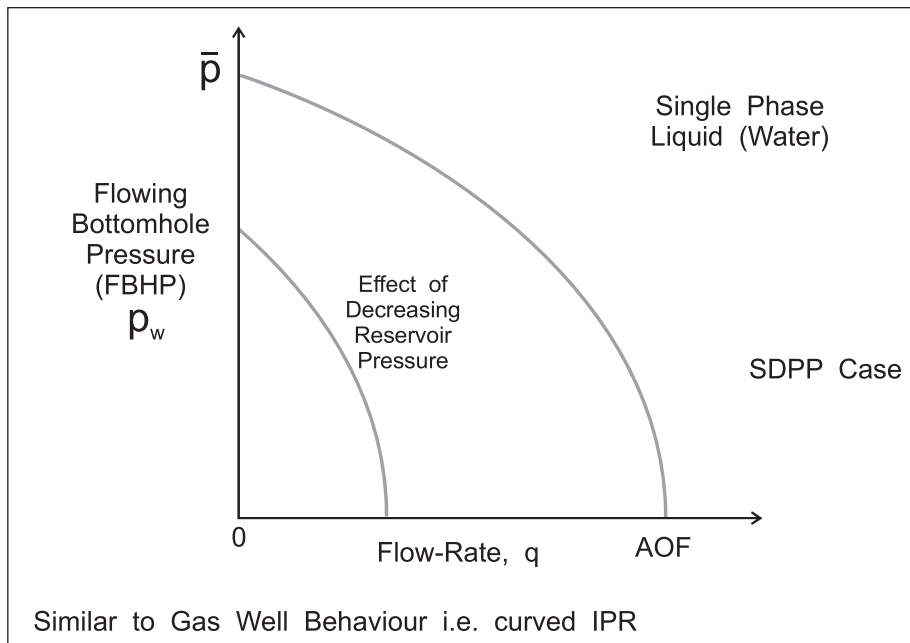


Fig. 17-5. Well deliverability curve

The stress dependence of permeability in coal beds has been investigated by Palmer and Mansoori,<sup>3</sup> who proposed the following model:

$$\frac{\phi}{\phi_i} = 1 + \frac{(p - p_i)}{\phi_i M} \quad (17-10a)$$

$$\frac{k}{k_i} = \left( \frac{\phi}{\phi_i} \right)^3 \quad (17-10b)$$

where  $M = E \frac{1 - \nu}{(1 + \nu)(1 - 2\nu)}$  constrained axial modulus (17-10c)

$$K = \frac{M}{3} \left( \frac{1 + \nu}{1 - \nu} \right) \quad \text{bulk modulus} \quad (17-10d)$$

and  $E = \text{Young's modulus}$  and  $\nu = \text{Poisson's ratio}$

Equation (17-10a) is the relation between porosity and pressure based on rock mechanics properties, while (17-10b) is the dependence of permeability on porosity. In the context of coal seams, it is a fracture system only (no matrix) that is present. In figure 17-6, the effect of pore pressure on permeability for typical San Juan basin coals is presented. In the treatment here, the rebound effect due to matrix shrinkage on gas desorption will not be considered. The present coding of the Palmer-Mansoori model does not allow the porosity to fall below 0.0001 ( $\phi$  cutoff).

The model is based on linear elasticity and will not handle pore collapse (plastic deformation). The change in effective formation height is secondary to permeability change, which is dominant. In the foregoing treatment, the basic rock properties are evaluated at the initial reservoir pressure  $p_i$ . In the event that the true initial pressure is unknown—in a buildup or falloff analysis for example—then the quantity  $p_i$  would be better referenced simply as  $p_{ref}$ . This is simply a convenient reference pressure at which the formation properties are evaluated. In this case, Eq. (17–10a) and (17–10b) are written in the form

$$\frac{\phi}{\phi_{ref}} = 1 + \frac{(p - p_{ref})}{\phi_{ref} M} \tag{17-10e}$$

$$\frac{k}{k_{ref}} = \left( \frac{\phi}{\phi_{ref}} \right)^3 \tag{17-10f}$$

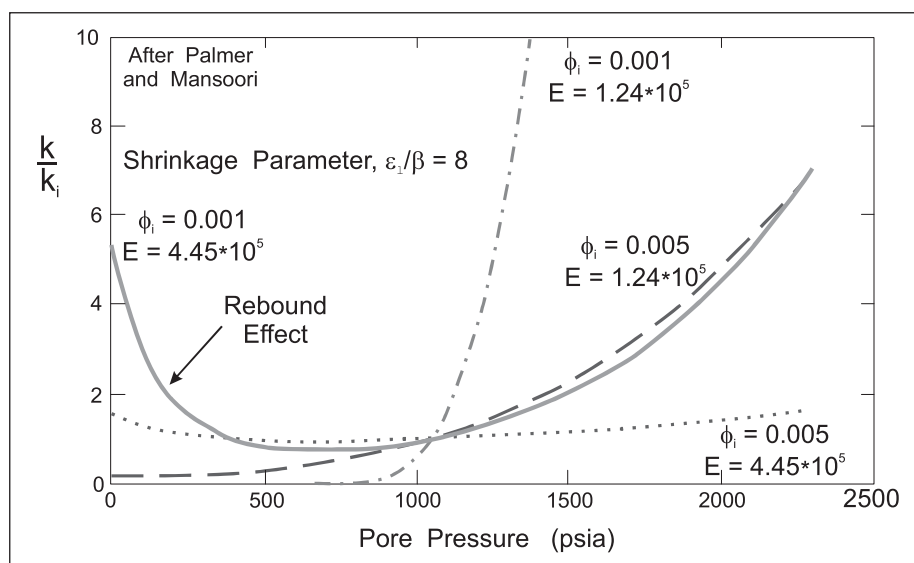


Fig. 17–6. Effect of pore pressure on coal permeability

In the paper by Samaniego and Cinco, emphasis is placed on analyzing the pressure signal directly, analogous to interpreting a gas condensate test using dry gas pseudopressure. The slope (derivative) of the semilog plot at a particular pressure reflects  $k(p)/(1 - \phi(p))$  and the logarithmic derivative diagnostic will take the form shown in figure 17–7. Thus the effect of stress-dependent permeability in drawdown has the derivative increasing with time, i.e.,  $k(p)/(1 - \phi(p))$  decreasing. In buildup, the derivative will decrease with shut-in time as the pore pressure increases and  $k(p)/(1 - \phi(p))$  also increases. In coal bed methane (CBM), much use is made of injection and falloff tests where the derivative behaviors will be reversed. It is presumed that the stress dependence is reversible and a model determined in injection and falloff (with pressures above  $p_i$ ) will be applicable in drawdown (DD) and buildup (BU) where pore pressures are less than  $p_i$ . It is useful to define an effective formation height  $h_{eff}$  as

$$h_{\text{eff}} = \frac{h(p_i)(1 - \phi(p_i))}{1 - \phi(p)} \quad (17-11)$$

and the slope of the semilog DD graph of pressure  $p_{\text{wf}}$  versus  $\ln(t)$  is given by

$$m = \frac{q\mu}{4\pi k(p)h_{\text{eff}}} \quad (17-12)$$

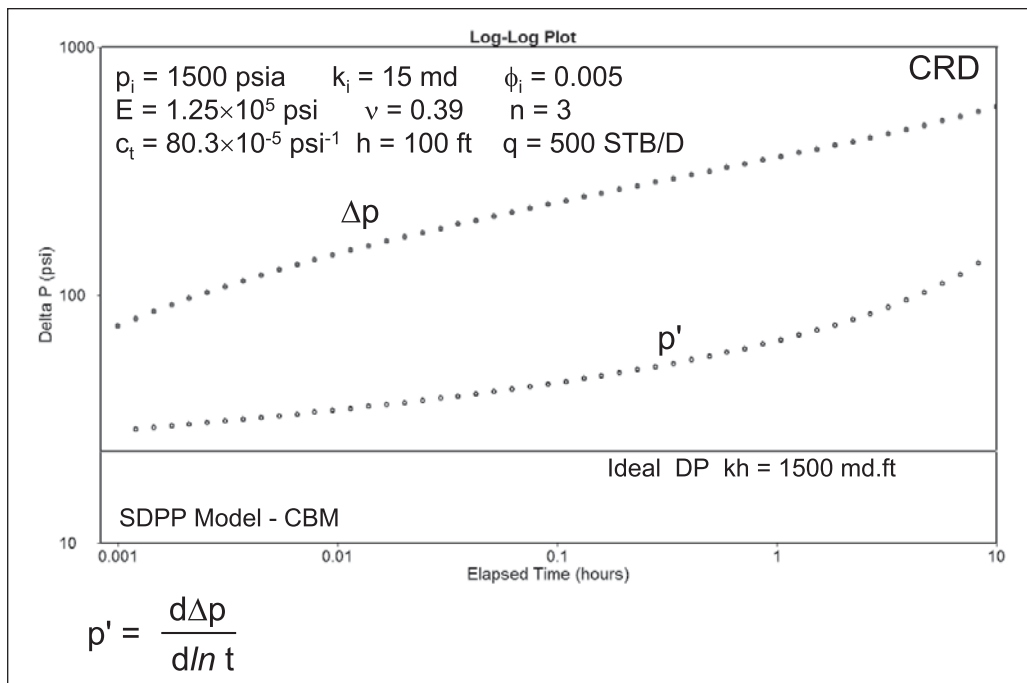


Fig. 17-7. Stress-dependent permeability and porosity

The method of Cinco and Samaniego based on the slope of the semilog plot, viz., the logarithmic derivative  $p'$ , is easily carried out in Pansystem. The test is simply analyzed directly in pressure, and the derivative plateau yields the value of  $k(p)h_{\text{eff}}(p)$  at any point as illustrated in figure 17-8. As the derivative steepens, the value of the permeability–thickness product decreases (in drawdown). Using the identity based on constant matrix volume

$$h_{\text{eff}}(1 - \phi) = h_i(1 - \phi_i) \quad (17-13)$$

the  $k(p)/(1 - \phi(p))$  ratio may be found; the appropriate pressure is read off the  $\Delta p$  curve on the L–L diagnostic plot. Note that this procedure implies a degree of averaging, which was examined by Yeh *et al.* in the context of radial composite behavior in water injection well falloff tests.



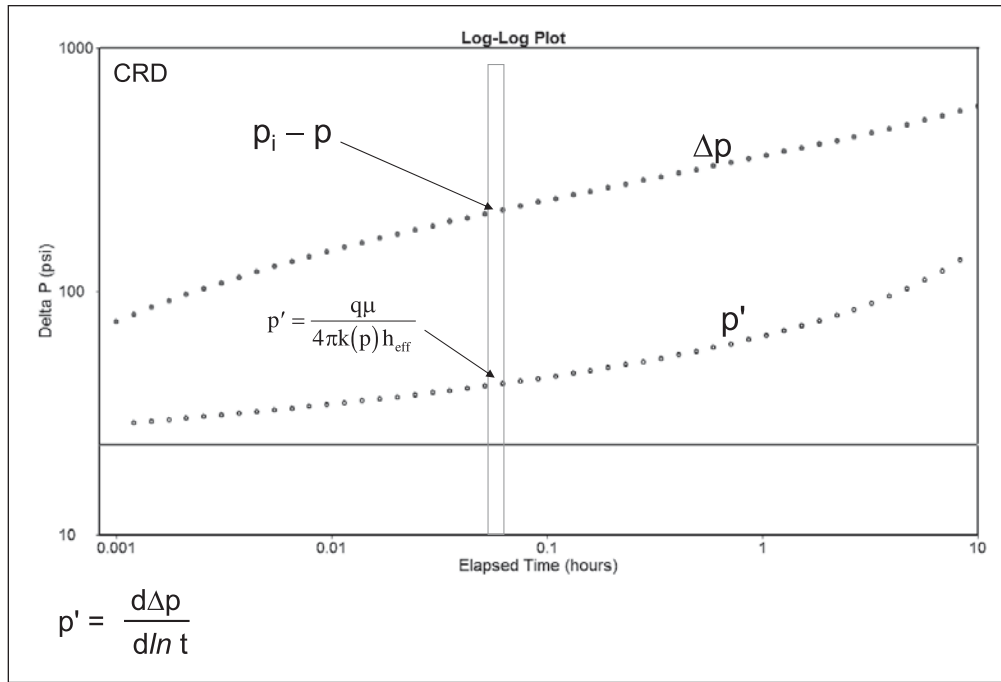


Fig. 17–8. Cinco and Samaniego derivative method

The fundamental model for test interpretation is taken to be I.–A. radial flow using the finite wellbore radius (FWBR) formulation written as  $P_D^{rw}(t_D)$  which will allow the presence of a negative skin if necessary; this is evaluated using the Stehfest algorithm. The Laplace space FWBR model takes the form

$$\tilde{P}_D(s) = \frac{K_o(\sqrt{s}r_D)}{s\sqrt{s}K_1(\sqrt{s})} \quad s \rightarrow t_D \quad (17-14)$$

The definition of dimensionless pseudopressure is

$$P_D = \frac{(\psi(p_i) - \psi(p_w))2\pi kh}{\alpha'_p q_s B\mu} \quad (17-15)$$

where  $\alpha'_p$  is a units conversion factor (= 887.217 for SPE oil field units). PanSystem allows the import of a normalized pseudopressure for oil or water and this facility can be used to analyze tests where stress dependence is an issue. Thus the pressure record is converted to pseudopressure using the transform, and pseudopressure results (e.g., extrapolated values on a semilog BU plot) are converted back to actual pressures. If the skin effect is zero or positive, then the line source approximation will be valid, i.e.,

$$P_D = \frac{(\psi(p_i) - \psi(p_w))2\pi kh}{\alpha'_p q_s B\mu} = \frac{1}{2} \ln\left(\frac{4t_D}{\gamma}\right) + S \quad (17-16a)$$

In the first instance, the dimensionless time  $t_D$  entering  $p_D^{r_w}(t_D)$  or the line source form (17-16) is based on properties at the initial reservoir pressure  $p_i$ ; thus

$$t_D = \frac{\alpha_t k(p_i) t}{\phi(p_i) \mu c_t r_w^2} \quad (\alpha_t = 0.000263679 \text{ SPE field units}) \quad (17-17)$$

The rock compressibility  $c_f$  entering  $c_t$  is also evaluated at initial reservoir pressure  $p_i$ ; note that  $E$  and  $c_f$  are closely related, i.e.,  $c_f = 1/(2E\phi_i)$  for coal beds. Samaniego and Cinco suggest the use of an Agarwal pseudotime to compensate for property variation in the accumulation term but this idea has not been followed up here. Using the Palmer and Mansoori model, the dependence of the ordinate  $k(p)/(1 - \phi(p))$  on pore pressure is illustrated in figure 17-9; this is based on typical coal bed rock mechanics properties as recommended by Palmer and Mansoori and outlined below. Thus, an approximately 10-fold decrease in  $k/(1 - \phi)$  is observed as the pore pressure is brought to low values approaching  $p_{\text{base}}$  (500 psia here).

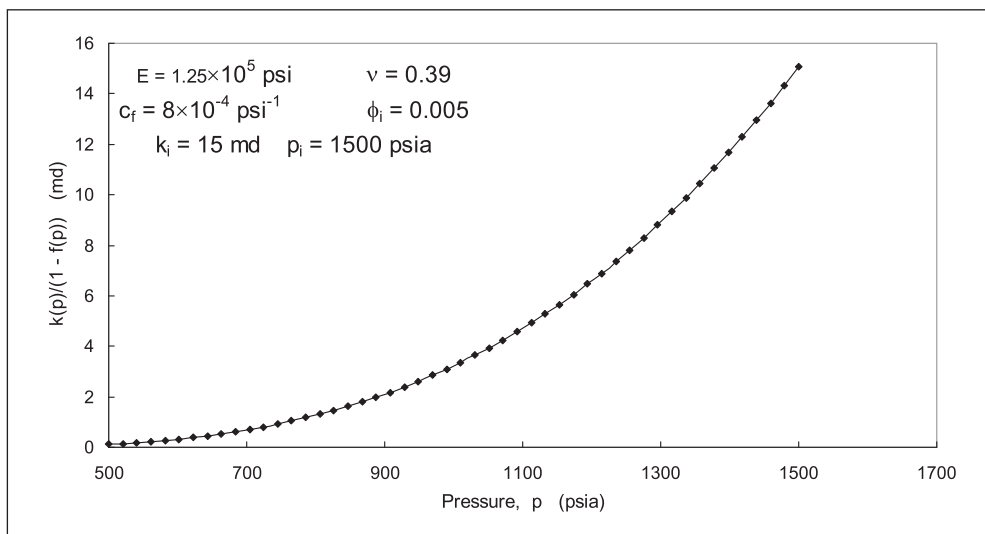


Fig. 17-9.  $k(p)/(1 - \phi(p))$  plot for coal bed methane

Representative values of the rock mechanics properties of coal seams are  $E = 1.25 \times 10^5$  psi and  $v = 0.39$ , while an initial porosity and permeability of 0.005 and 15 md are typical; for these parameter values, a normalized pseudopressure function  $\psi(p)$  is shown in figure 17-10a; this has been computed using Gaussian quadrature as illustrated in figure 17-11. The base for pseudopressure has been set at  $p_{\text{base}} = 500$  psia to avoid the danger of  $\phi$  becoming too small; often, bottomhole pressures will be greater than this. An extended range pseudopressure function with an upper limit on pressure of 2,000 psia is shown in figure 17-10b; it is necessary to compute pseudopressure to values higher than  $p_i$  ( $p_{\text{ref}}$ ) when the flowing period is an injection. Note that the function exhibits continuously increasing curvature unlike a real gas normalized pseudopressure which stabilizes at a unit slope.

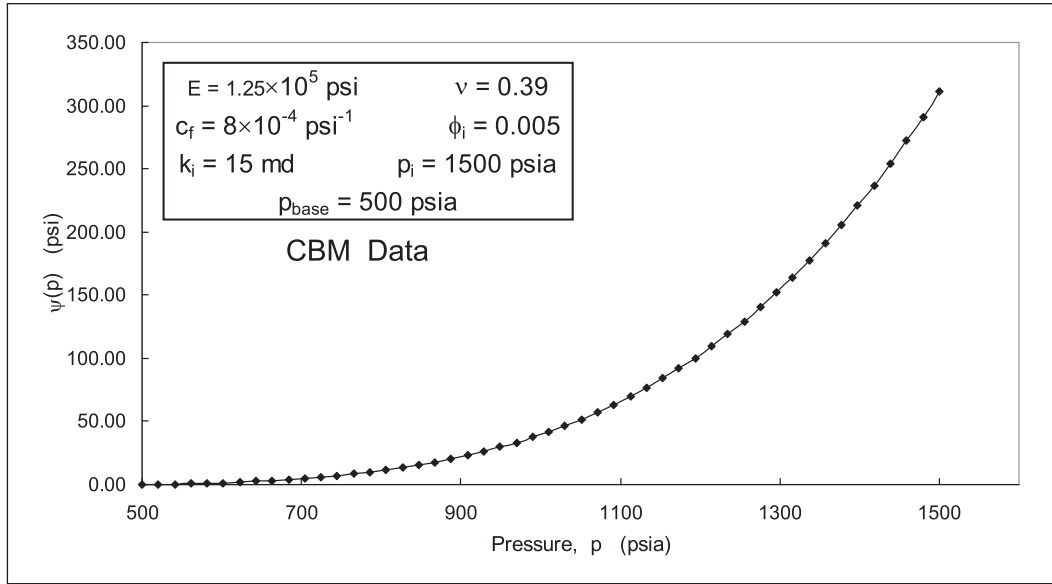


Fig. 17-10a. Stress-dependent  $k\text{-}\phi$  normalized pseudopressure transform

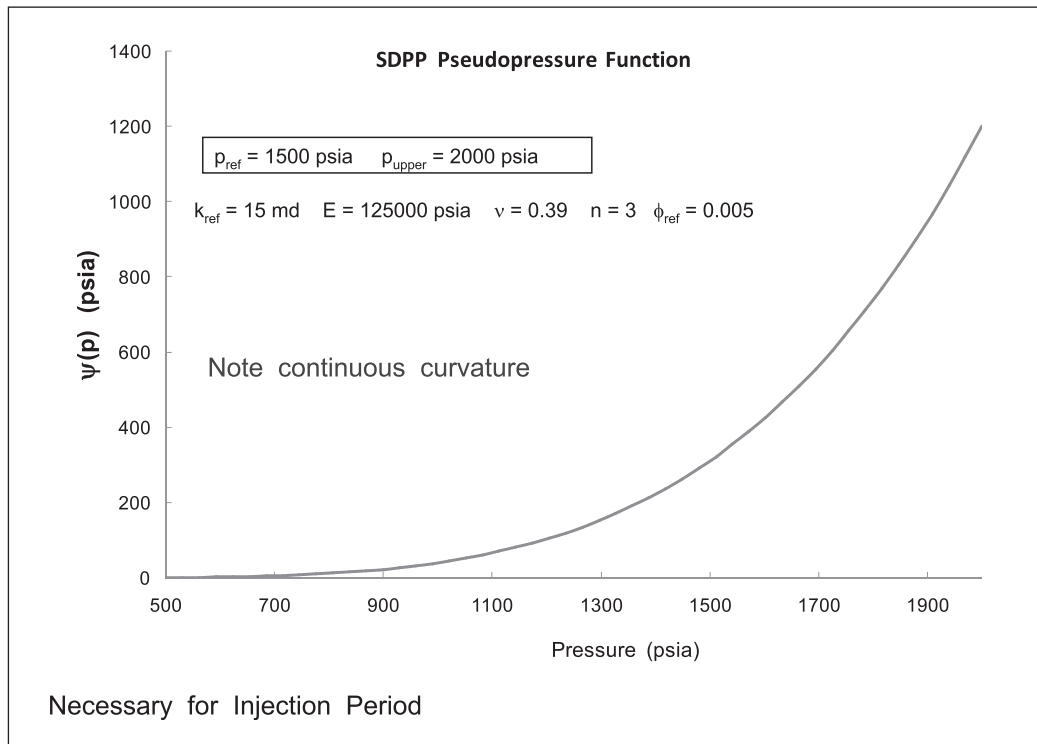


Fig 17-10b. Extended range SDPP pseudopressure function

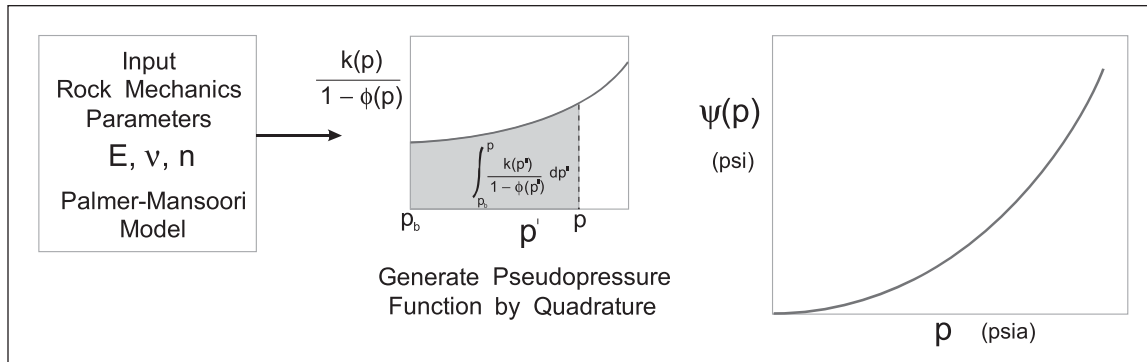


Fig. 17–11. Generation of the SDPP pseudopressure function

In buildup, the dimensionless pseudopressure is given by

$$p_D = \frac{(\psi(p_i) - \psi(p_{ws}))2\pi kh}{\alpha'_p q_s B\mu} = \frac{1}{2} \ln \left( \frac{t_p + \Delta t}{\Delta t} \right) \tag{17-18}$$

when the line source solution liquid is valid; this is simply the superposition result for constant rate buildup (CRB) in terms of pseudopressure.

An exact convolution algorithm for SDPP situations was written as an external program as illustrated in figures 17–12 and 17–13; this was used to generate synthetic data which could be used to check the well test software SDPP models. In constant rate flow (CRD or CRI) the well test software pseudomodel described in the next section behaves identically to the exact convolution shown in figure 17–12. However, in a shutin following the flow period, the exact convolution (fig. 17–13) computes the pressure based on the FWBR equivalent of (17–18) and refers to the initial pressure  $p_i$ . The exact convolution also models wellbore storage and allows boundary effects to be included.

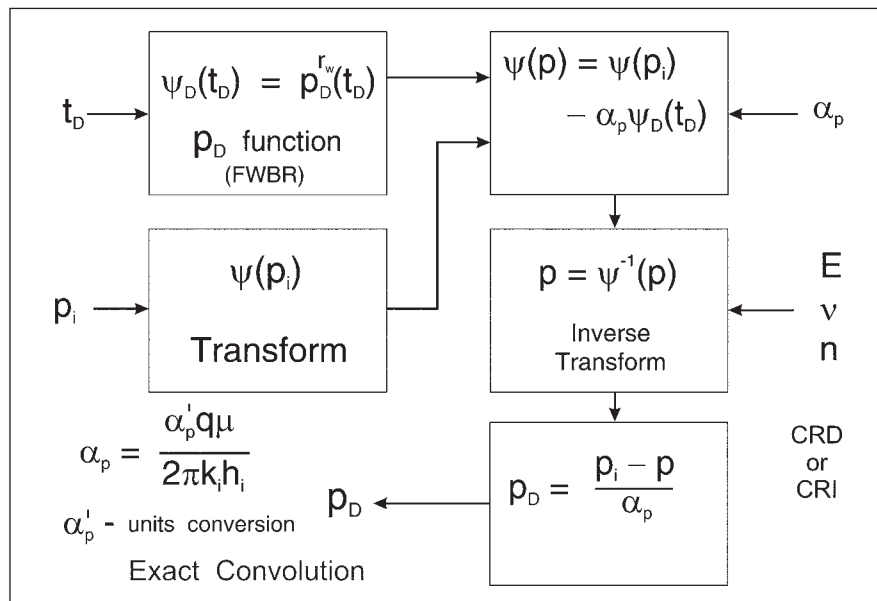


Fig 17–12. Dynamic pseudopressure algorithm (drawdown or injection at constant rate)

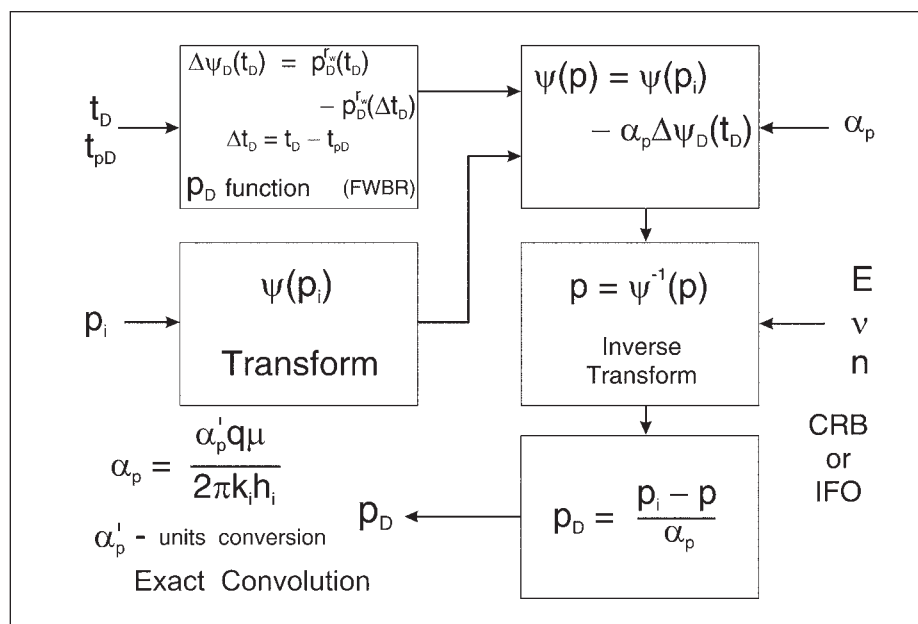


Fig 17-13. Dynamic pseudopressure algorithm (buildup or falloff)

## PanSystem Pseudo Model

However, a second approach is useful where the pseudopressure relation is embedded in the  $p_D$  function which returns actual pressure values as illustrated in figure 17-14a. In this case, the parameters of the rock mechanics model, e.g., the exponent in the permeability–porosity relation and the Young’s modulus, can be treated as regression quantities. The conventional approach allows parameter estimation by specialized plots and log–log diagnostics but the rock mechanics model is fixed. Figure 17-14a implies that the inverse transform be computed directly for the current rock parameter estimates; this can easily be achieved using a secant algorithm. The direct use of pressure via an SDPP pseudo  $p_D$  function is simply a means of utilizing the nonlinear regression algorithm available in Pan to allow estimates of rock mechanics properties to be made. Note that the SDPP effect is very sensitive to rate since it is drawdown-dependent. During injection—increasing pore pressure—permeability will increase. In order to utilize the SDPP pseudo model, data reduction must be employed to leave only a constant drawdown (or injection) and an ensuing buildup (or falloff). If the nonlinear regression option for  $E$ ,  $v$ , and  $n$  is desired, the test must be designed to have this form. The SDPP CRD pseudo  $p_D$  model requires the rate  $q_{ref}$  to be entered as a model (customer) parameter. Figure 17-14a refers only to a CRD or injection period during which the software will not carry out any superposition process. The model is termed Stressdependperm and the parameter set is indicated in figure 17-14b.

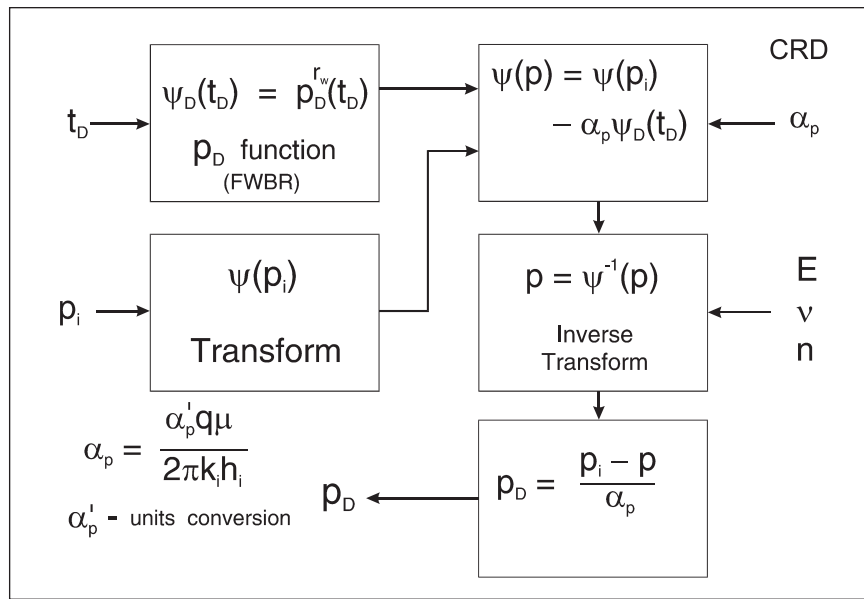


Fig. 17–14a. Pansystem pseudo model

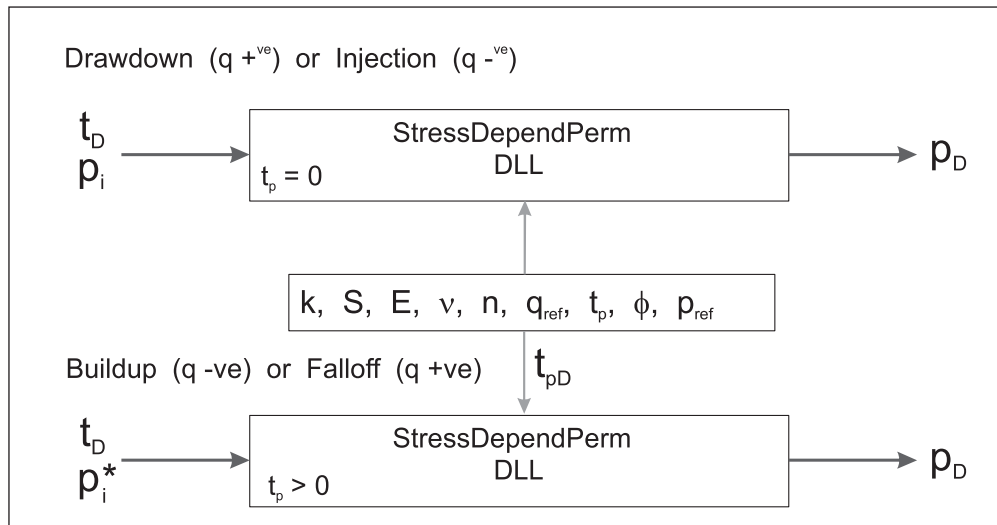


Fig. 17–14b. Pansystem SDPP model

When pressure is being treated directly, it is interesting to examine the nature of the logarithmic derivative fingerprint for stress-dependent properties. Figure 17–15b shows such a type curve (log–log plot of  $p_D'$  vs.  $t_D$ ) for typical coal parameters and CRD; figure 17–15a is the synthetic drawdown data plotted on a Cartesian scale. The version of the Palmer–Mansoori model implemented here does not include the “permeability rebound” associated with matrix shrinkage due to methane desorption. Hence it is intended for the interpretation of well tests to elucidate stress dependence of permeability and dewatering rates. The data in figures 17–15 was generated with the PanSystem pseudo model which generates pressure behavior directly using the inverse transform internally. The synthetic data was then analyzed using the traditional pseudopressure approach, illustrated in figure 17–16, with the result shown in figure 17–17; as expected the transformation of pressure has converted the data to liquid equivalent with

interpretation yielding  $k_i h_i$  and skin  $S$  (zero in this case). In this synthetic drawdown case, the values of the rock mechanics parameters  $E$ ,  $\nu$ , and  $n$  used in the generation (test design invoking the pseudo model) were then exactly known for the computation of the pseudopressure transform  $\psi(p)$ . The data was generated using the line source solution, whereas PanSystem always employs the FWBR model; this accounts for the small discrepancy at early time.

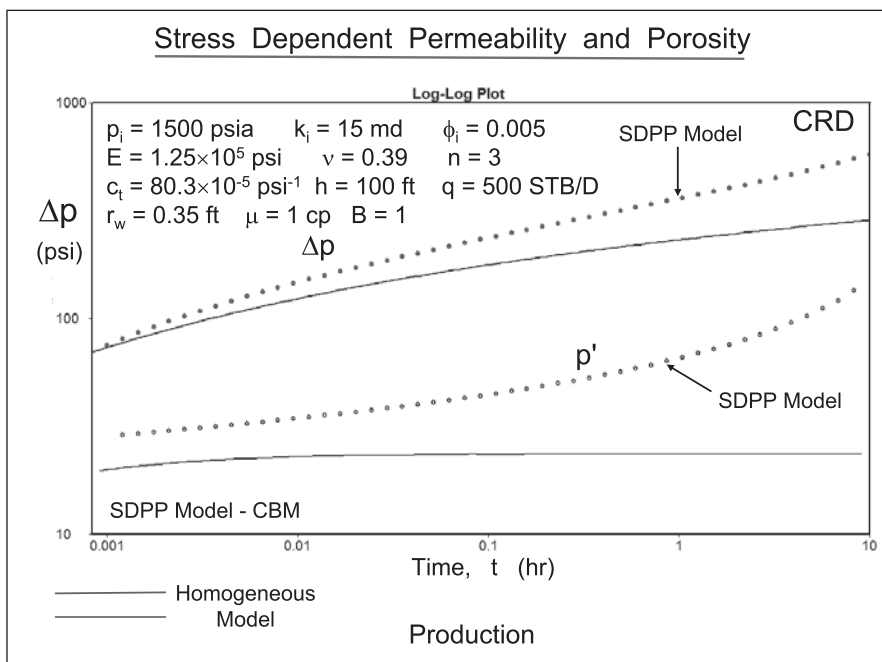


Fig. 17-15b. Log-log diagnostic for drawdown

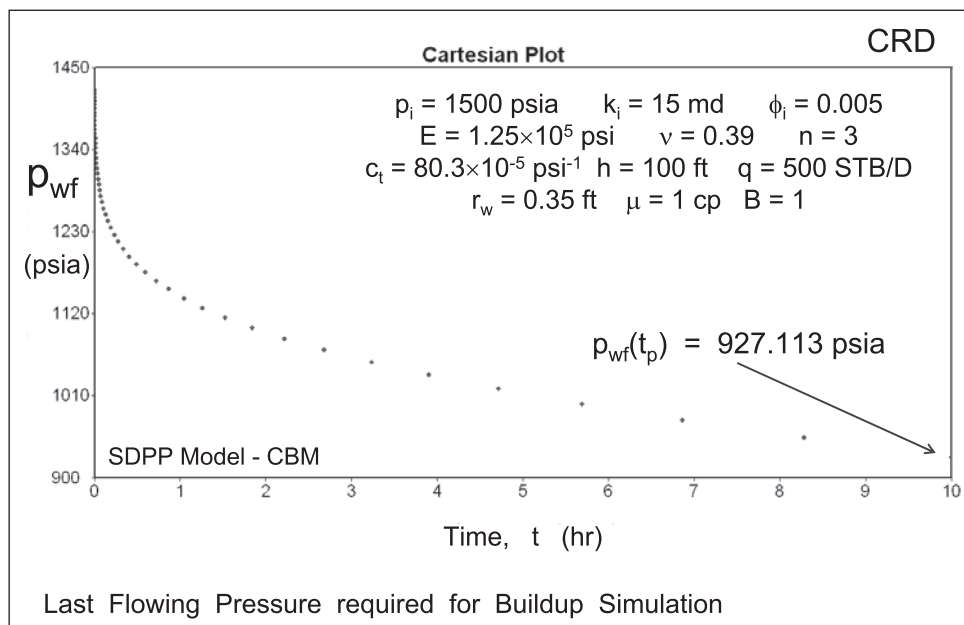


Fig. 17-15a. Simulation of constant rate production (test design)

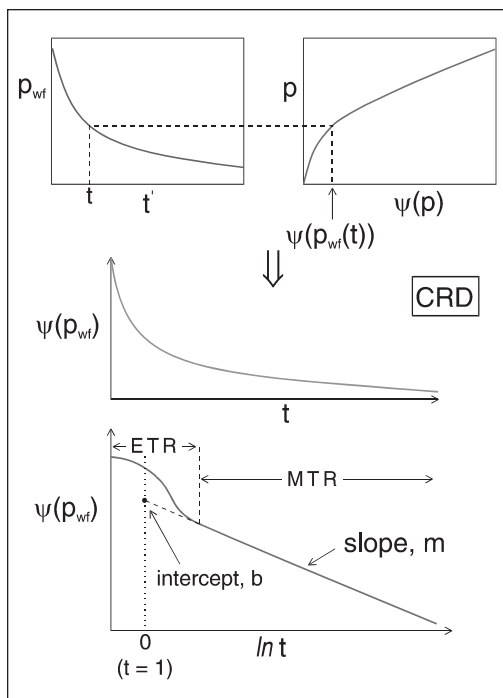


Fig. 17-16. Method 1 for CBM well testing

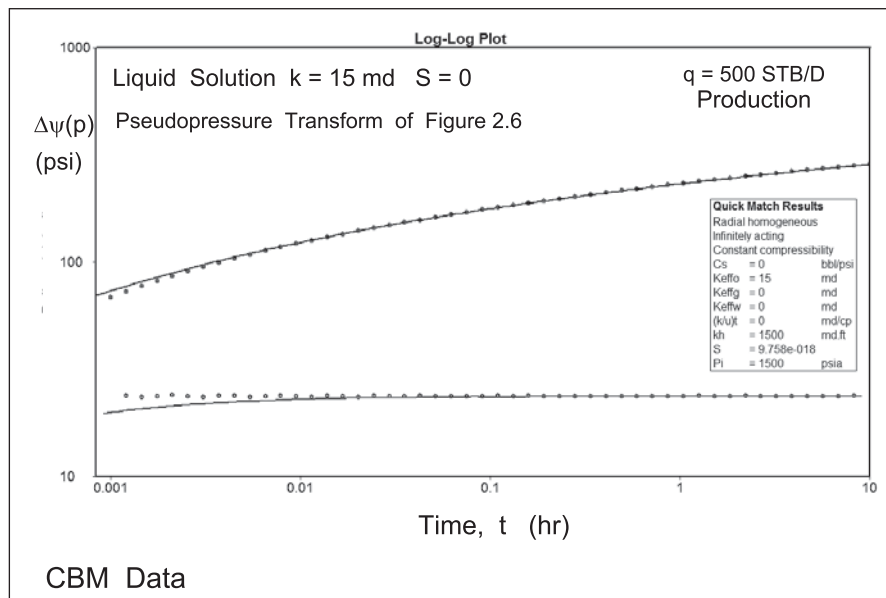


Fig. 17-17. Analysis of CRD using normalized pseudopressure

The drawdown data shown in figure 17-15 indicates the reduction in permeability at the vicinity of the sandface in a production period. This “choking” effect can be severe especially when the porosity at the initial pressure is small. In fact, there is a certain critical rate above which the formation cannot flow. In figure 17-18, a situation is shown where any increase in rate will cause the algorithm to “crash,” i.e., the rate of 500 bbl/d is critical for the parameter set indicated. The pseudopressure function for this parameter set in figure 17-19 exhibits



an almost flat segment at low pressure with a consequent influence on a calculated deliverability curve; flowing wellbore pressures below about 500 psia will not lead to any increase in flow rate. A different parameter set corresponding to the Mavor field example considered later is treated in figure 17–20, where a critical production rate of 7 bbl/d has been identified; this is very low indeed with a large implication for dewatering.

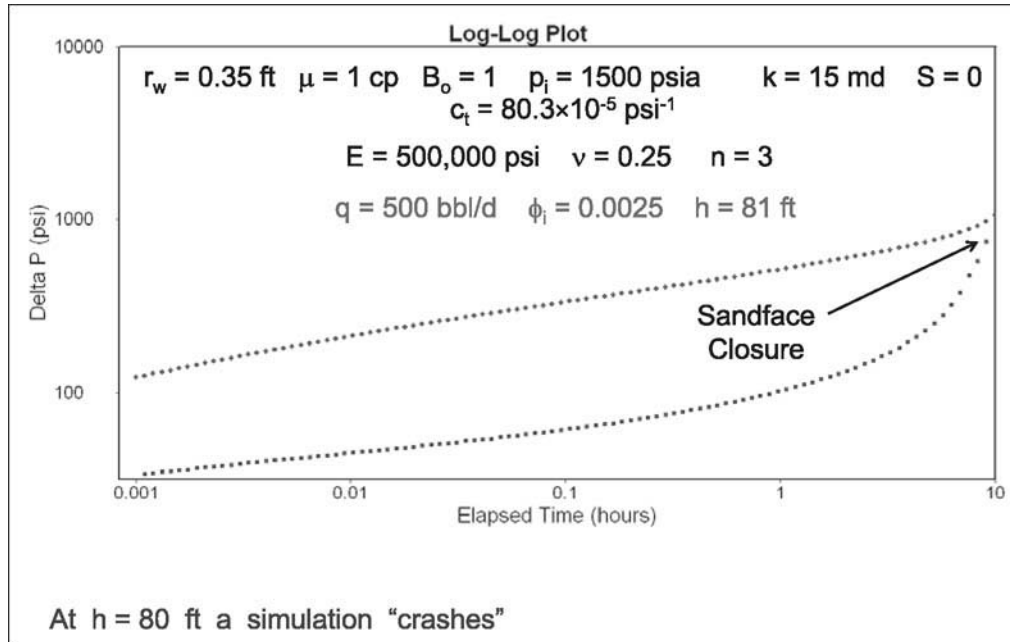


Fig. 17–18. Critical conditions in production (drawdown)

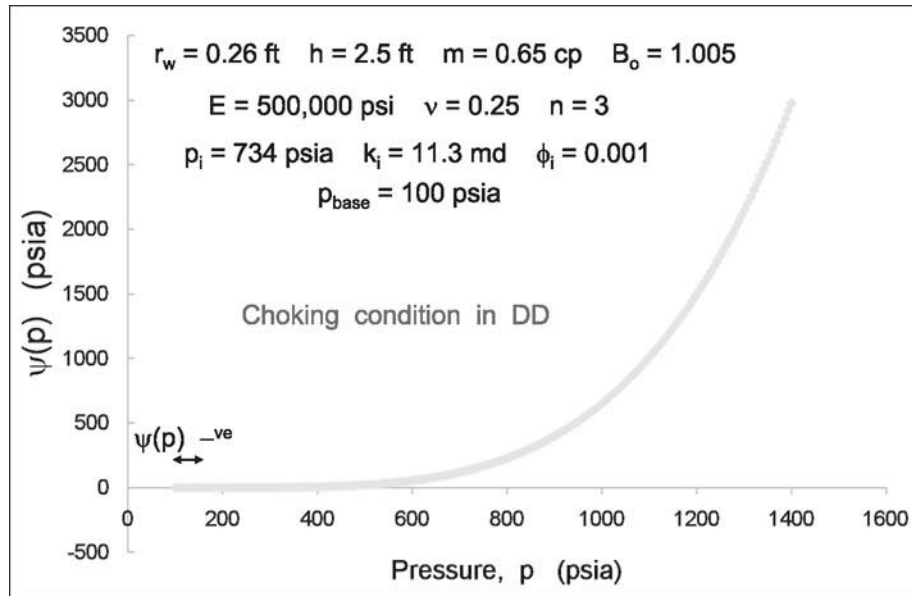


Fig. 17–19. Pseudopressure function  $\psi(p)$

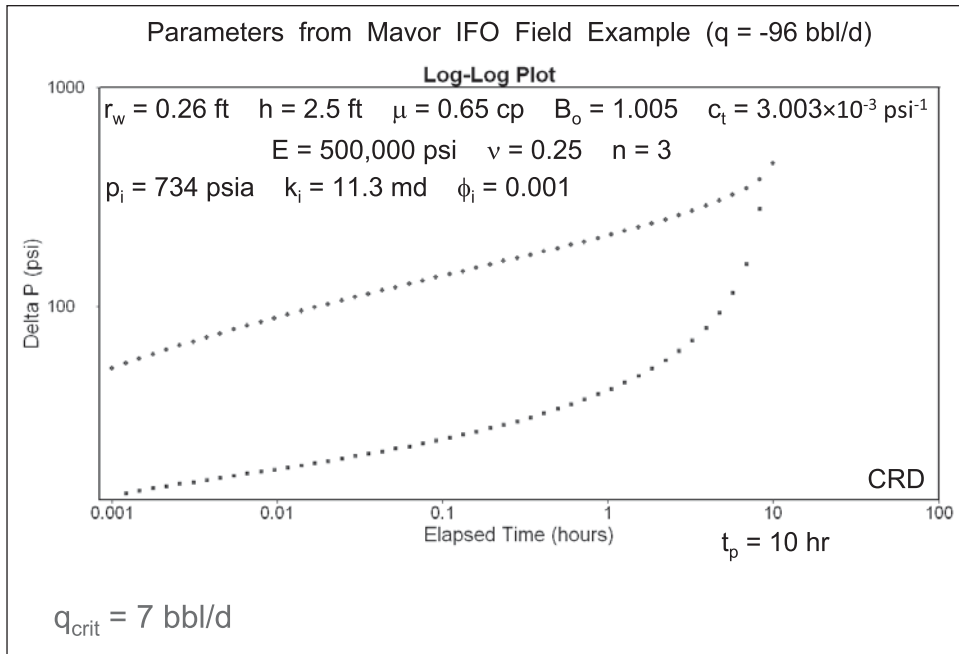


Fig. 17–20. Choking condition in production (drawdown)

The Palmer and Mansoori model involves the porosity at reservoir pressure  $\phi_i$ , Young's modulus  $E$ , and Poisson's ratio  $\nu$ . The formation (pore volume) compressibility  $c_f$  is related to these quantities by the relation

$$c_f = \frac{3(1 - 2\nu)}{E\phi_i} \quad (17-19)$$

The quantities  $\phi_i$ ,  $E$ , and  $\nu$  are essentially determined from logging surveys of the coal bed ( $E$  and  $\nu$  from the sonic log). The total compressibility  $c_t$  used in a well test interpretation is

$$c_t = c_w + c_f \quad (17-20)$$

and the appropriate values of  $\phi_i$ ,  $E$ , and  $\nu$  from log interpretation should be used in Eq. (17–19) to compute the correct rock compressibility. Both  $\phi_i$  and  $c_t$  are entered into Pansystem as fixed parameters; such quantities are not allowed to be used as adjustable model parameters in simulation or nonlinear regression. In the import pseudopressure method (i.e., method 1), it has been the practice to adjust the value of  $\phi_i$  in the matching process. In the Pansystem SDPP model, this approach is not possible since the model DLL structure does not allow a feedback path for a modified porosity. Instead, it is useful to define an effective Young's modulus  $E'$  as follows:

$$\frac{\phi}{\phi_i} = 1 + \frac{(p - p_i)}{\phi_i M} = 1 + \frac{(p - p_i)}{\phi_i E' f(\nu)} \quad (17-21a)$$

where 
$$f(\nu) = \frac{1 - \nu}{(1 + \nu)(1 - 2\nu)} \tag{17-21b}$$

Thus in the Pansystem SDPP model,  $\phi_i$  is held at the log value and the stress-dependent effect is modified by changing  $E'$ . The hydraulic diffusivity  $k_i/(\phi_i\mu c_t)$  is based on the hopefully correct  $\phi_i$  and  $c_t$  (both log derived), and modification of the stress effect is implemented through  $E'$  which will become distinct from the true value  $E$ . Note that  $k_i$  will be changed in the model matching process and the true (log) value of  $\nu$  is used in (17-21b).

In many of the CBM tests previously analyzed, the porosity at initial reservoir pressure  $\phi_i$  is entered into the pseudopressure evaluation as 0.001, which is considerably less than the log-based estimate; this value is then also used in the well test interpretation software. It is being suggested here that the porosity entered into the well test analysis program be the log estimate, say  $\phi_i = 0.01$ , and the effective Young's modulus  $E'$  be input as 50,000 psi rather than the true value of 500,000 psi, say.

In the PanSystem environment, the model ( $p_D$  function) will be called twice in the context of a CRB, i.e., the  $p_D$  function is superposed in the form

$$\Delta p = p_i - p_{ws} = \frac{q\mu}{2\pi kh} \{ p_D(t_D) - p_D(\Delta t_D) \} = \alpha_p \{ p_D(t_{pD} + \Delta t_D) - p_D(\Delta t_D) \} \tag{17-22}$$

However, when the pseudopressure is handled implicitly in the model which returns actual pressure, this is not valid. Thus the pressure in buildup must be computed as

$$\Delta \psi_D = \frac{(\psi(p_i) - \psi(p_{ws}))2\pi kh}{\alpha'_p q_s B\mu} = \frac{1}{2} \ln \left( \frac{t_p + \Delta t}{\Delta t} \right) \tag{17-23}$$

i.e., 
$$\psi(p_{ws}) = \psi(p_i) - \alpha_p \frac{1}{2} \ln \left( \frac{t_p + \Delta t}{\Delta t} \right)$$

$$p_{ws} = \psi^{-1}(\psi(p_{ws}))$$

$$\Delta p = p_i - p_{ws}$$

$$p_D = \frac{\Delta p}{\alpha_p}$$

One method of handling a shut-in period—buildup or falloff—in well test software is to convert to drawdown form using the concept of equivalent time; this approach is illustrated in

figure 17–21, where the falloff pressure change  $\Delta p_{\text{IFO}}$  is plotted against equivalent time  $\Delta t_e$ . The pseudopressure change in falloff is given by

$$\frac{(\psi(p_i) - \psi(p_{ws}))2\pi kh}{\alpha'_p q_s B\mu} = \frac{1}{2} \ln \left( \frac{t_p + \Delta t}{\Delta t} \right) \quad (17-24)$$

while the last flowing pressure is given by

$$\frac{(\psi(p_i) - \psi(p_{wf}(t_p)))2\pi kh}{\alpha'_p q_s B\mu} = \frac{1}{2} \ln \left( \frac{4t_{pD}}{\gamma} \right) + S \quad (17-16)$$

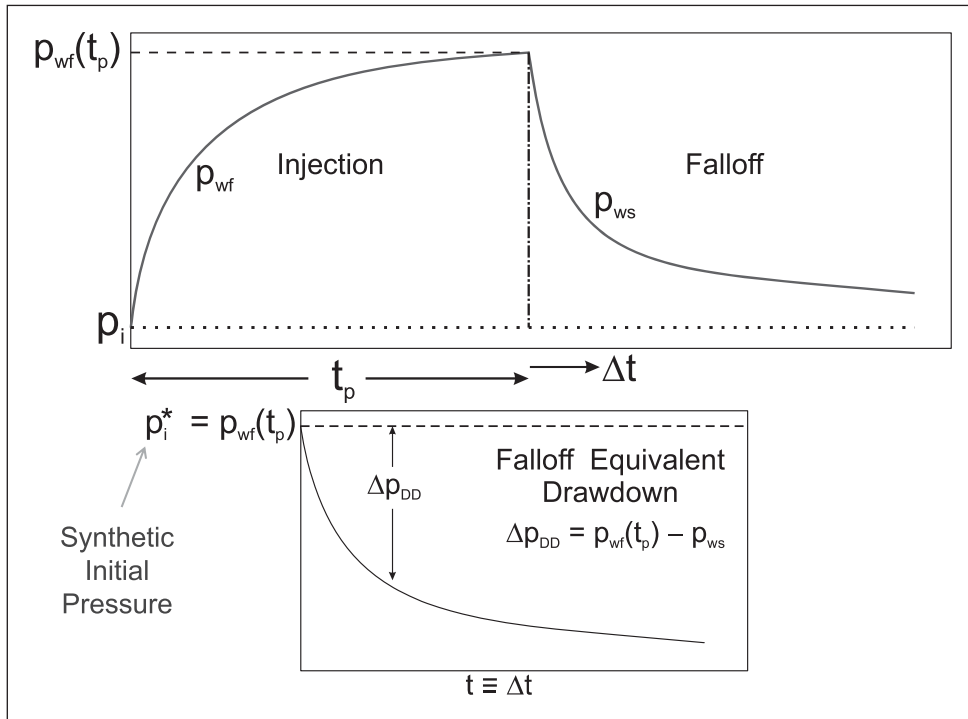


Fig. 17–21. Injection falloff (IFO)

Subtracting (17–24) from (17–16) gives the Agarwal form

$$\frac{(\psi(p_{ws}) - \psi(p_{wf}(t_p)))2\pi kh}{\alpha'_p q_s B\mu} = \frac{1}{2} \ln \left( \frac{4\Delta t_{eD}}{\gamma} \right) + S \quad (17-25)$$

where

$$\Delta t_e = \frac{t_p \Delta t}{t_p + \Delta t}$$

Thus the falloff pressure  $p_{ws}$  may be plotted against  $\Delta t_e$  as shown in figure 17–21 and the data treated as if it were CRD.

The preceding theory is based on the log approximation to the Ei function, which will usually be quite adequate for interpretation purposes. However, if the skin is negative, it will be advantageous to employ the finite wellbore radius solution, written as  $p_D^{r_w}(t_D)$ . The pseudopressure change in falloff becomes

$$\frac{(\psi(p_i) - \psi(p_{ws}))2\pi kh}{\alpha'_p q_s B\mu} = p_D^{r_w}(t_{pD} + \Delta t_D) - p_D^{r_w}(\Delta t_D) \quad (17-26)$$

while the last flowing pressure is given by

$$\frac{(\psi(p_i) - \psi(p_{wf}(t_p)))2\pi kh}{\alpha'_p q_s B\mu} = p_D^{r_w}(t_{pD}) \quad (17-27)$$

In this formulation, it is presumed that the skin factor has been absorbed into an effective wellbore radius. Again, subtracting (17–26) from (17–27) yields

$$\frac{(\psi(p_{ws}) - \psi(p_{wf}(t_p)))2\pi kh}{\alpha'_p q_s B\mu} = p_D^{r_w}(t_{pD}) + p_D^{r_w}(\Delta t_D) - p_D^{r_w}(t_{pD} + \Delta t_D) \quad (17-28a)$$

$$\text{or} \quad \psi(p_{ws}) = \psi(p_{wf}(t_p)) + \frac{\alpha'_p q_s B\mu}{2\pi kh} \left[ p_D^{r_w}(t_{pD}) + p_D^{r_w}(\Delta t_D) - p_D^{r_w}(t_{pD} + \Delta t_D) \right] \quad (17-28b)$$

$$\text{i.e.,} \quad \Delta\psi_D(t_D) = \left[ p_D^{r_w}(t_{pD}) + p_D^{r_w}(\Delta t_D) - p_D^{r_w}(t_{pD} + \Delta t_D) \right] \quad (17-28c)$$

The algorithm for computing  $p_{ws}(\Delta t)$  is shown in figure 17–22; this forms one basis for Quickmatch and Automatch calculations of the model-predicted response.

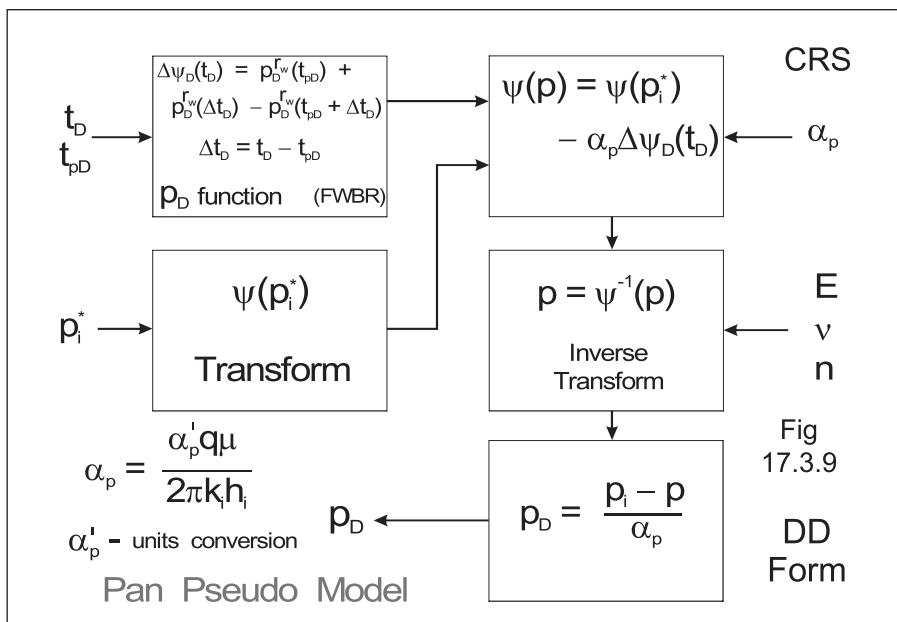


Fig. 17-22. Algorithm for computing shutin behavior

The test design mode and the pseudo model were then used to generate the response of a buildup following a period of CRD. The log-log diagnostic plot is shown in figure 17-23, where the derivative is opposite in character to that observed in the drawdown. When the pressure near the wellbore is low—at the beginning of the buildup—the derivative is large indicating low  $k/(1 - \phi)$ ; however, as the pressure rises in buildup, the derivative returns to a value characteristic of pressure close to  $p_i$ .

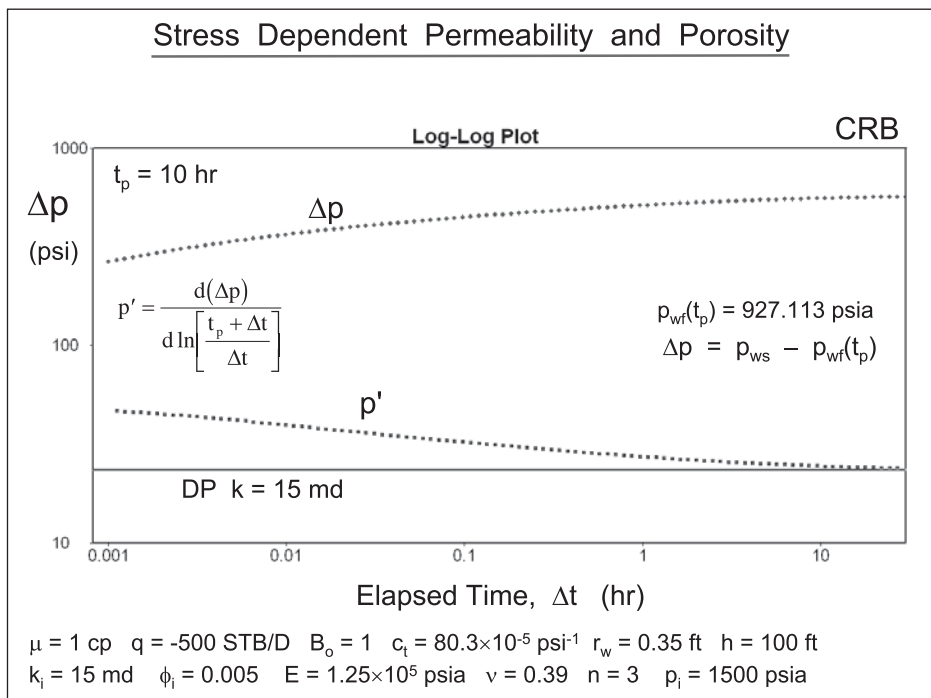


Fig. 17-23. Buildup following constant rate production

The buildup exhibits a derivative plateau as the pressure approaches the initial pressure corresponding to the value of permeability at  $p_i$ , i.e.,  $k_i$ . The semilog (Horner) plot for the buildup is shown in figure 17–24; this extrapolates to the known  $p_i$  of 1,500 psia but registers a skin of 5.1435 because the preceding drawdown has had additional pressure drop due to the stress-dependent effect. Note that the skin calculation for a buildup is based on the last flowing pressure  $p_{wf}(t_p)$ . This skin contribution can be referred to as the stress-dependent effect  $S_{\sigma}$ , representing the extra pressure drop in the drawdown due to stress dependency. In situations where the underlying derivative character is hidden by wellbore storage, only the final semilog straight line (SLSL) will be visible in the buildup and a conventional analysis will yield a high skin effect.

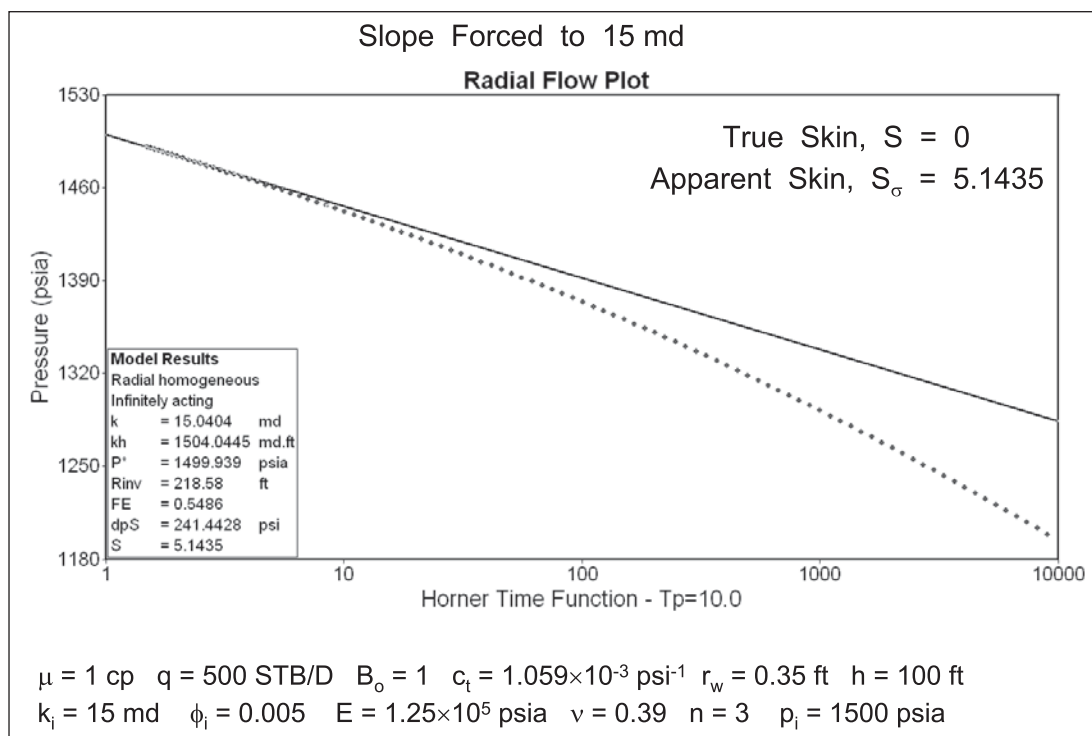


Fig. 17–24. Semilog analysis of buildup following a period of production

In buildup, the shut-in pressure  $p_{ws}$  is generated using Eq. (17–18). If a true skin of 1 is entered into this synthetic dataset, the well chokes at  $q = 500 \text{ bl/d}$ ! However, increasing the initial porosity  $\phi_i$  to 0.01 yields a weaker stress effect and the effect of true skin can be elucidated as shown in figure 17–25. As expected from the nature of the pseudopressure transform, the effect of true (mechanical) skin is strongly magnified ending in the well choking at  $S = 8$  in this case. It has been tacitly assumed that the pseudopressure concept allows the effect of mechanical skin, i.e., formation damage, to be modeled by Eq. (17–16). It has been postulated that there is also an effect of stress concentration in the near-wellbore region which would further enhance the magnification effect; however, this has not been investigated here. The present treatment is based on single-phase water flow above the methane desorption pressure. A free gas saturation in the near-wellbore region will block the flow of water leading to further skin effects based on relative permeability considerations. It is interesting that Raghavan went on to define a two-phase pseudopressure that will model gas block.

Palmer and Mansoori showed that there is a relation between the Young's modulus  $E$  and the traditional pore volume (PV) rock compressibility  $c_f$ ; this takes the form for coal beds

$$c_f = \frac{1}{2E\phi_i} \quad (17-29)$$

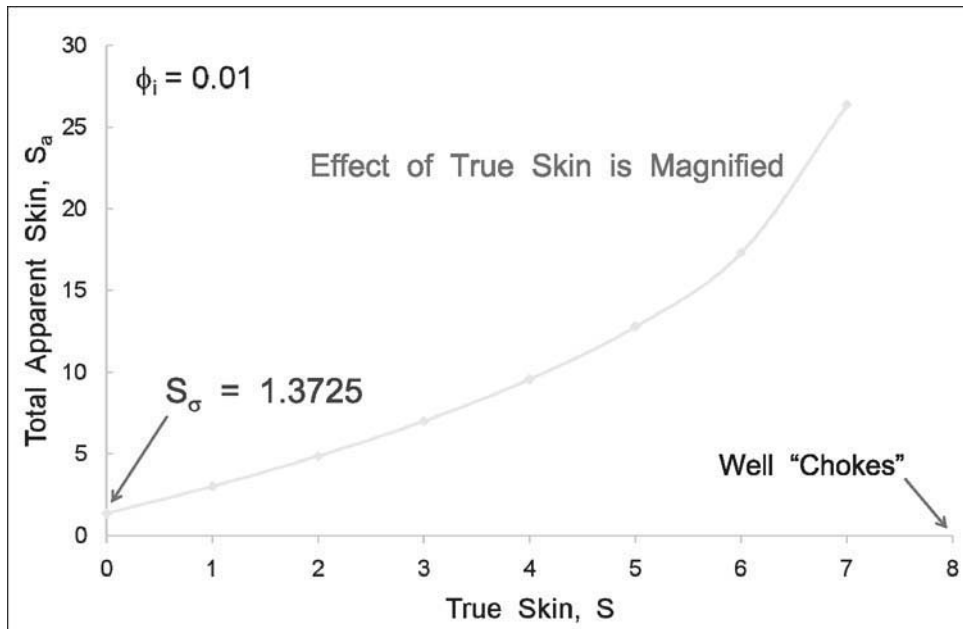


Fig. 17-25. Apparent skin from conventional buildup analysis

Van den Hoek<sup>4</sup> quotes the exact expression:

$$c_f = \frac{3(1 - 2\nu)}{\phi_i E} \quad (17-30)$$

which yields a result close to (17-29) when  $\nu = 0.39$ .

In a well test interpretation, the total compressibility  $c_t$  is defined as

$$c_t = S_{wc}c_w + (1 - S_{wc})c_g + c_f \quad (17-31a)$$

or 
$$c_t = c_w + c_f \quad (\text{if only water is present}) \quad (17-31b)$$

Fortunately, the slope of the semilog graph (derivative  $p'$ ) does not depend on total compressibility  $c_t$ , but if the Young's modulus  $E$  is found by regression, the value of  $c_t$  used in the interpretation should be iteratively updated. It was pointed out by Palmer and Mansoori that the rock compressibility in coal beds is a strong function of porosity and Young's modulus, as shown in figure 17-26. The SDPP formulation has been focussed on CBM applications. However, the



phenomenon of stress-dependent permeability is also important in tight gas applications and the SDPP pseudopressure and model approach will be extended to this domain. It is likely that different rock mechanics models will be required.

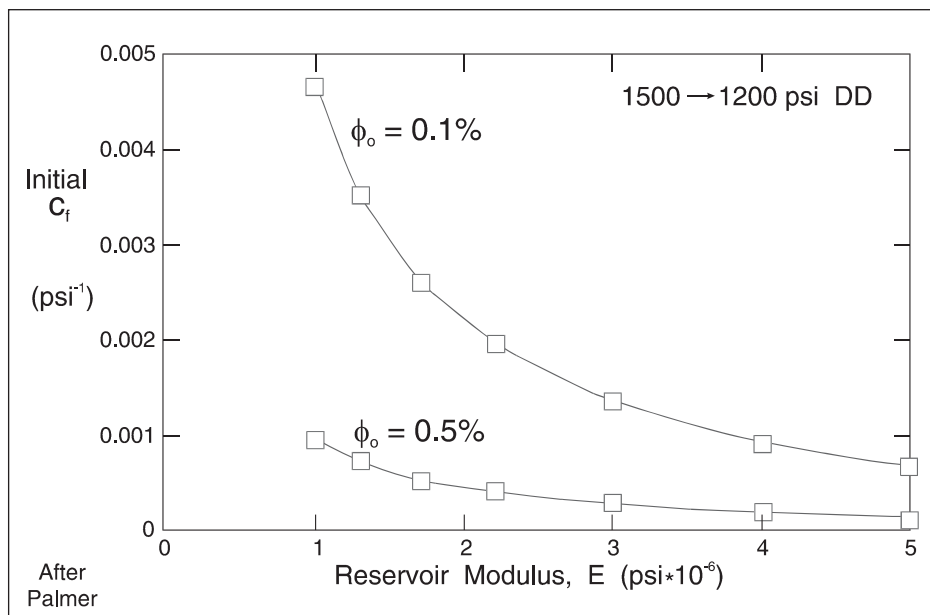


Fig. 17-26. Variation of initial PV compressibility

The synthetic examples so far have referred to production and buildup. The theory also applies to injection and falloff and figures 17-27b and 17-28b show the log-log diagnostic plots for this case; as previously mentioned, the form of the derivative fingerprints are reversed from the production-buildup cases. In injection, the permeability increases as the pressure rises and the derivative progressively becomes smaller. Conversely, the derivative progressively becomes larger in falloff as the permeability reduces to a value close to  $k_i$  with the pressure approaching  $p_i$ . Figures 17-27a and 17-28a are the Cartesian plots of the injection and falloff periods. In the injection period, two apparent derivative plateau are present—shown in figure 17-27c—registering 20 and 25 md, respectively. The semilog plot for the injection is given in figure 17-27d, with the ideal straight line of  $k = 15$  md and  $S = 0$  overlaid for information. In figure 17-27e, the first plateau (following the FWBR data) is subjected to semilog analysis, yielding  $k = 19.8$  md and  $S = -2.18$ ; the formation is already “ballooned” and at the central pressure of the plateau ( $p_{wf} = 1,597$  psia) permeability is higher than the base value of 15 md at  $p_i = 1,500$  psia. The data of figure 17-28b can also be analyzed using the SDPP pseudopressure function shown in figure 17-10b; the result is given in figure 17-27f. As before in the drawdown case, the derivative under the pseudopressure transformation reverts to the ideal plateau for radial flow. In figure 17-27c the porosity is 0.005, and in figure 17-27g the porosity has been reduced by an order of magnitude to  $\phi = 0.0005$ . This sensitivity analysis shows a much larger effect in terms of permeability levels but not much change in the shape of the derivative response on a log-log plot.

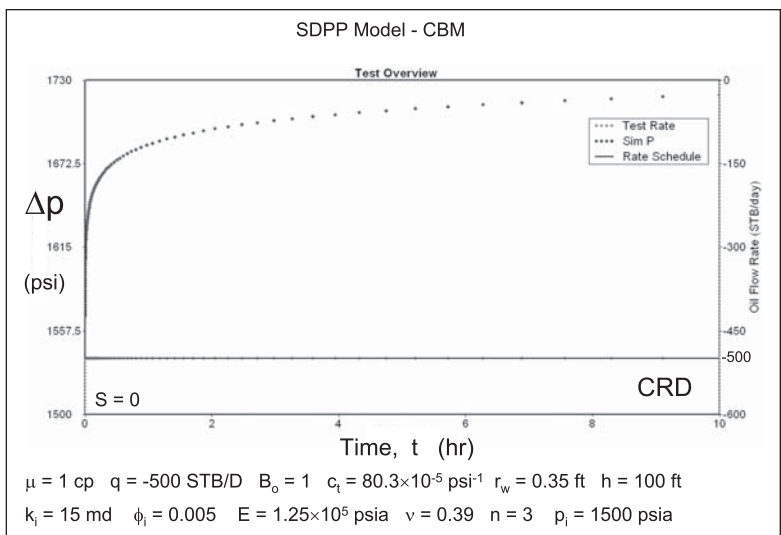


Fig. 17–27a. Injection period Cartesian plot

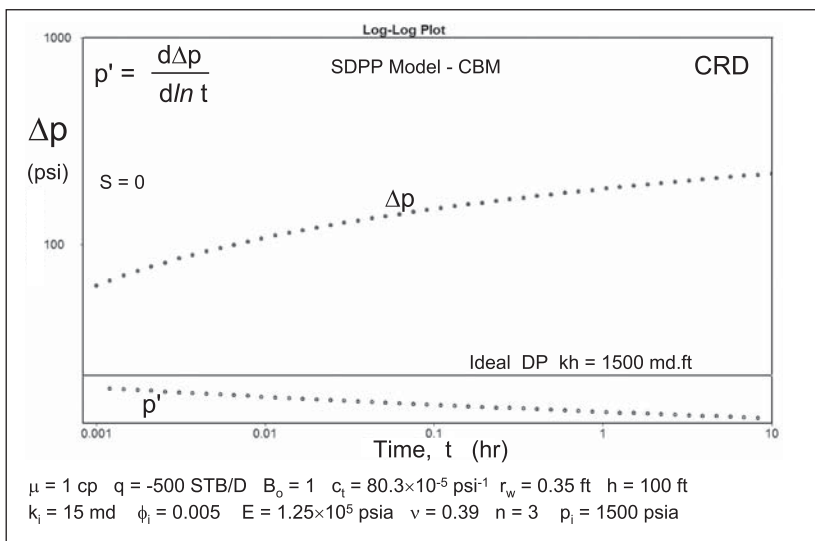


Fig. 17–27b. Injection period log–log diagnostic

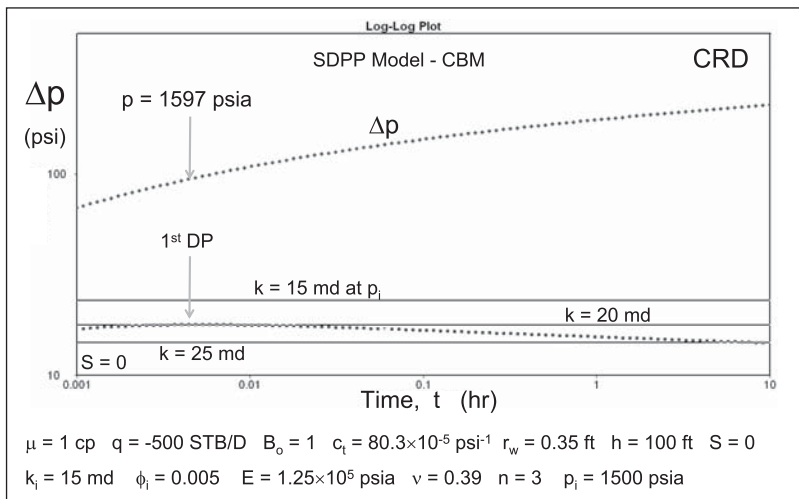


Fig. 17–27c. Injection period derivative plateaux

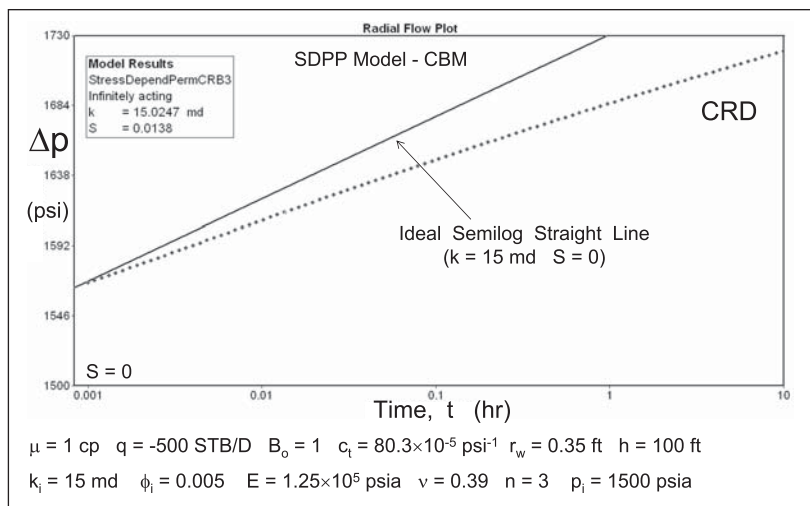


Fig. 17–27d. Injection period semilog

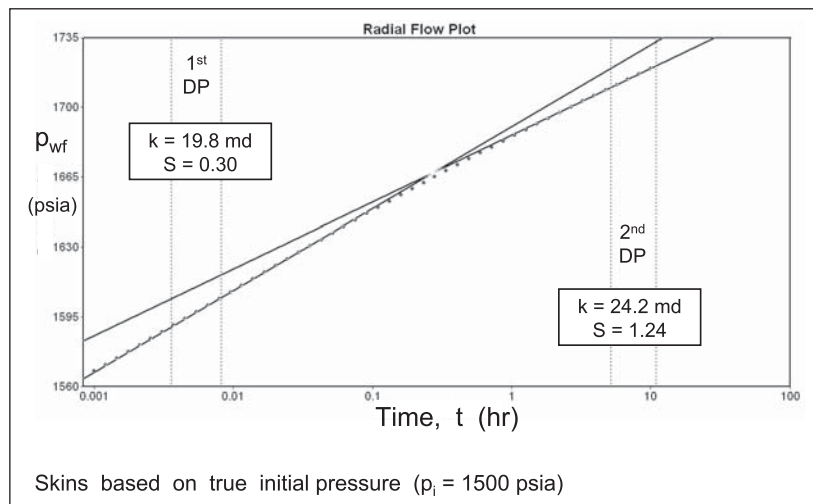


Fig. 17–27e. Semilog analysis of injection period

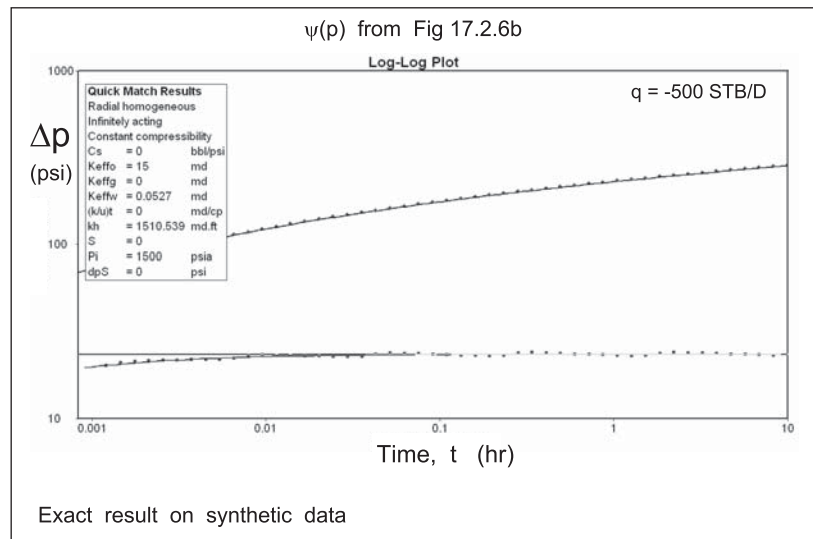


Fig. 17–27f. Analysis of injection period using SDPP pseudopressure

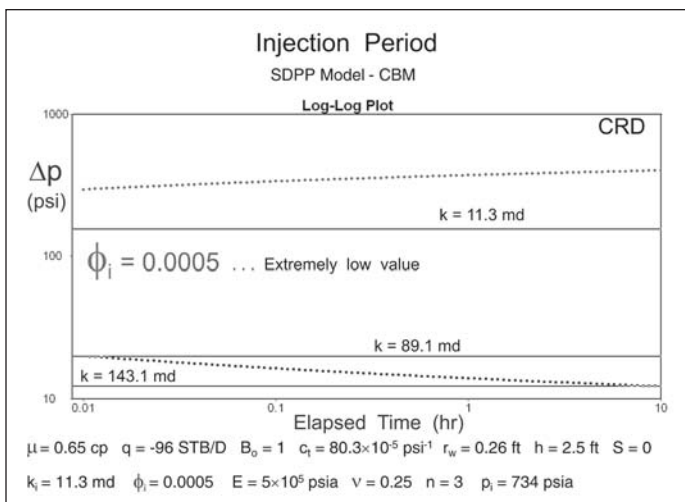


Fig. 17-27g. Sensitivity to porosity

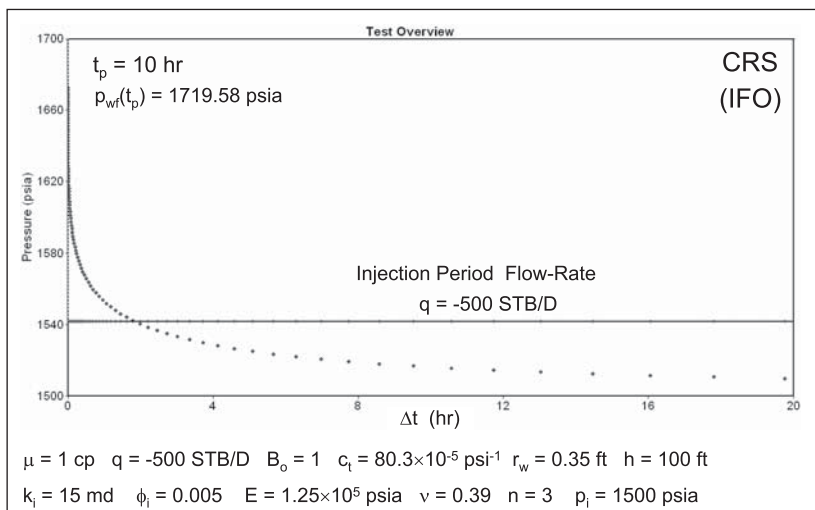


Fig. 17-28a. Falloff period Cartesian plot

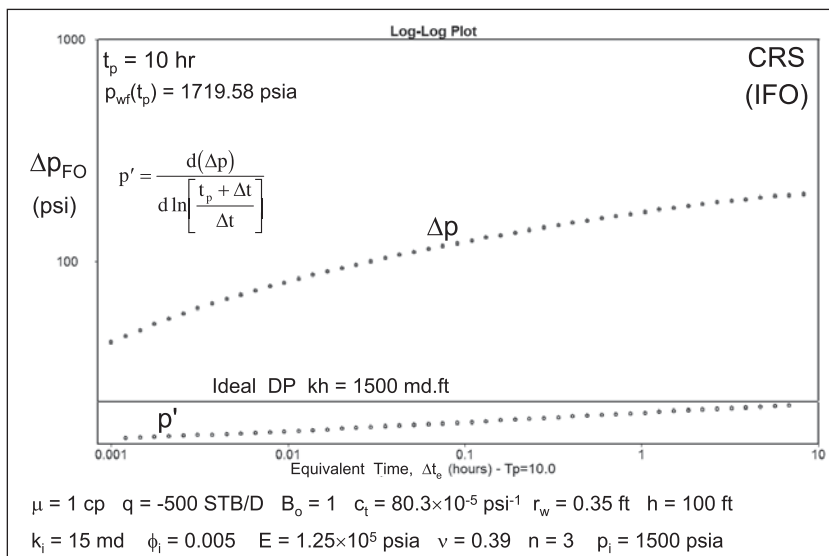


Fig. 17-28b. Falloff period log-log diagnostic

The effect of skin in the SDPP model is handled through effective wellbore radius for both positive and negative  $S$ . In figure 17–29, the effect of a positive skin ( $S = 2$ ) on the injection period response is presented on the log–log diagnostic plot. In the SDPP situation, the logarithmic derivative changes as well as the pressure since  $k$  is pressure dependent. At the end of the injection, the last flowing pressure is higher than in the base case—1,774.25 psia rather than 1,719.58 psia; hence the permeability at the end of the injection registers as 27 md (vs. 25 md for the base case).

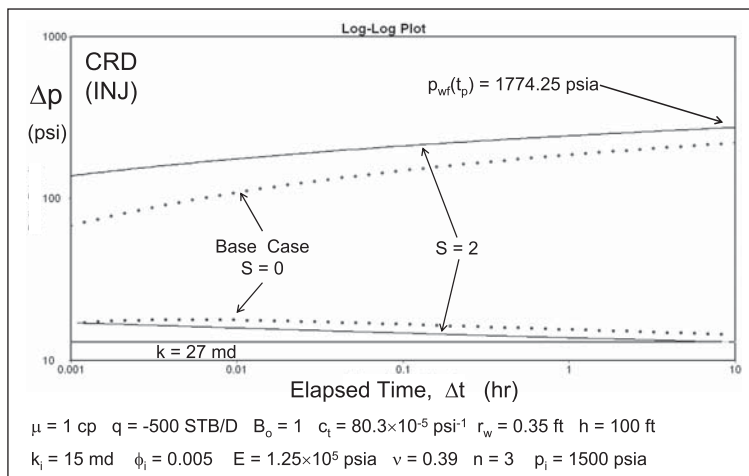


Fig. 17–29. Effect of positive skin on the injection period response

In the falloff period, illustrated in figure 17–28a, where the pressure is decreasing, the apparent permeability becomes smaller as the test proceeds; thus the derivative exhibits an upward trend as seen in figure 17–28b. As the pressure in falloff approaches the initial pressure  $p_i$ , equal to 1,500 psia, the permeability tends to the base case value of 15 md. However, the semilog plot of the last data, shown in figure 17–28c, gives  $k = 15.5$  md and  $S = -1.27$ ; this is because the last flowing pressure at  $t_p$ , i.e., 1,719.58 psia, was determined with the stress effect modeled. If homogeneous behavior had been present, this pressure would have been higher and the computed skin correct. The obtained negative skin of  $-1.27$  is due to the “ballooning” of the formation at the end of the injection.

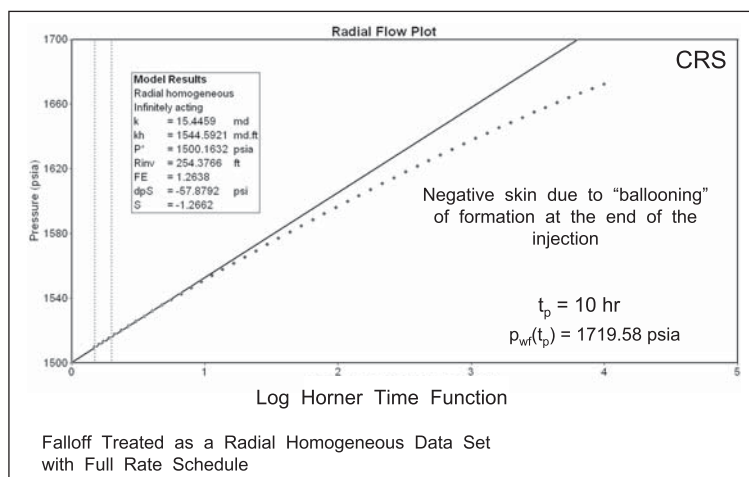


Fig. 17– 28c. IFO Horner (semilog) plot

The synthetic falloff pressure data generated by the SDPP model can be regarded as a dataset which can be interpreted using the pseudopressure function of figure 17–10b, as was done in the injection case. The result is shown in figure 17–30, and, as before, an exact liquid behavior is seen under the  $\psi(p)$  transformation. The semilog graph of the normalized pseudopressure versus  $\log\Delta t_e$  in figure 17–31 exhibits a perfect middle time region (MTR) straight line except for the early FWBR effect. Note that the skin from the intercept is now correctly zero.

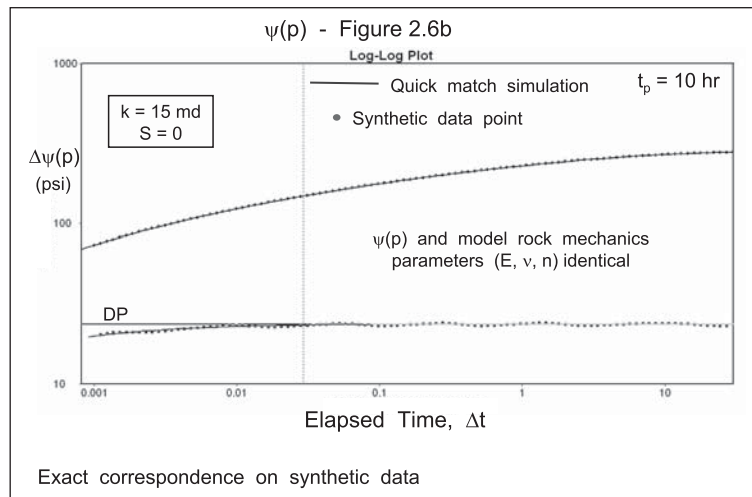


Fig. 17–30. Analysis of synthetic IFO data using SDPP pseudopressure

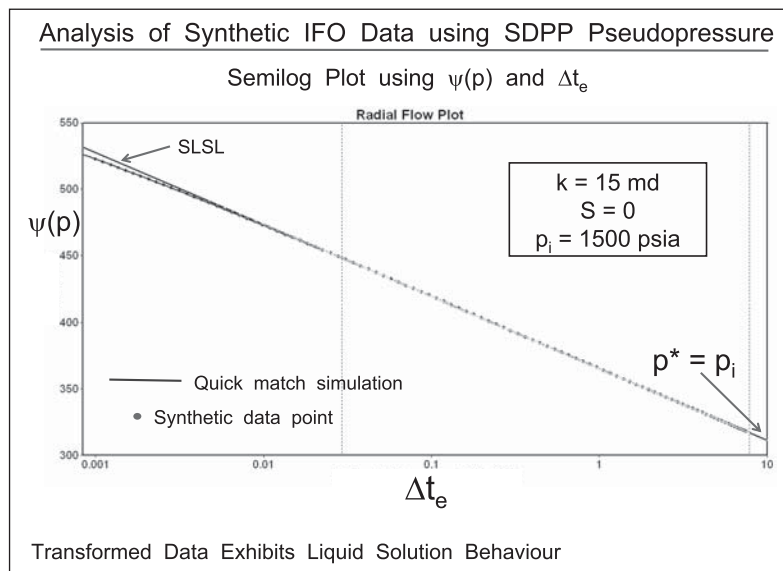


Fig. 17–31. Semilog plot using  $\psi(p)$

The responses examined so far have been obtained by simulation using the SDPP model in test design mode and it is interesting at this point to present actual field data. A typical dataset for an injection and falloff has been provided by Mavor, with the test overview shown in figure 17–32. It is apparent that the injection period is uninterpretable but the falloff period looks as if an analysis will be feasible. The log–log diagnostic for the falloff, shown in figure 17–33, indicates

a period of nonideal wellbore storage followed by a stress-dependent porosity and permeability effect. However, there is no sign of a final derivative plateau as the reducing pressure approaches  $p_i$  in the late stages of the falloff period. The falloff derivative fingerprint is similar to the drawdown fingerprint in production and does not resemble the synthetic fingerprints generated for injection falloff such as that portrayed in figure 17–28. It has been suggested by Mavor that the initial porosity  $\phi_i$  be treated as a parameter to be determined by matching rather than input as a constant known value (from logs) as is the case in conventional well test interpretation.

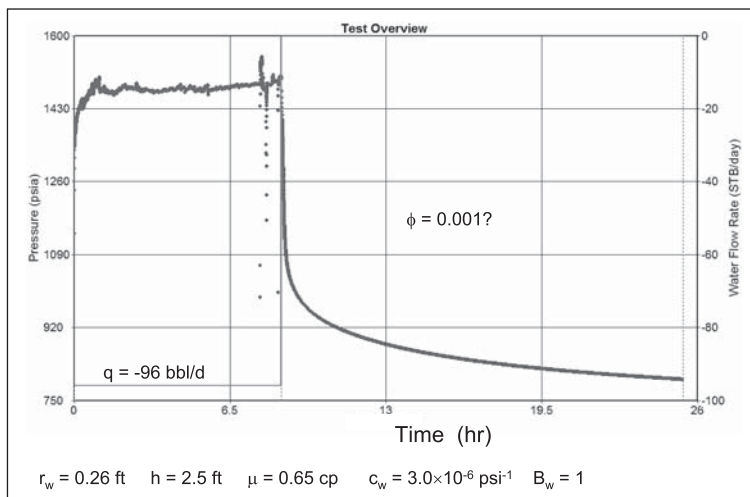


Fig. 17–32. Mavor field example

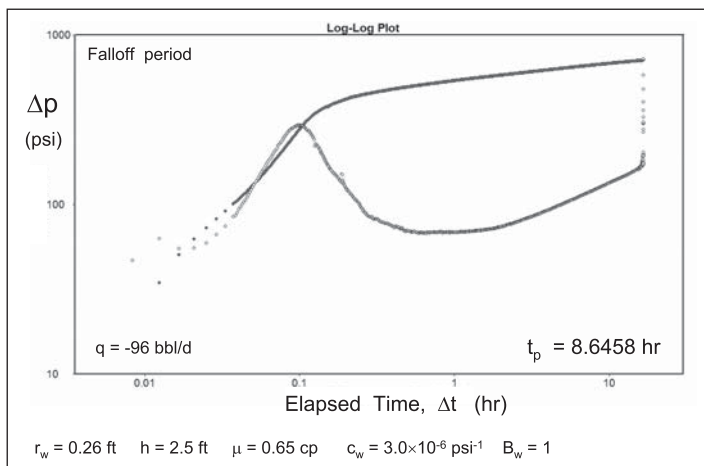


Fig. 17–33. Field example log–log diagnostic plot

A standalone program was written to compute pressure behavior in the stress-dependent situation so that the SDPP model in Pansystem could be verified; figure 17–34 shows a dataset generated externally and imported into Pansystem. The falloff was isolated as a single test, and figure 17–35 shows the match using the Pansystem pseudomodel for falloff; this test demonstrates that the suggested approach is viable. The conventional semilog interpretation of the falloff shown in figure 17–36 indicates a negative SDPP skin  $S_o$  of 4.28 due to the ballooning effect of the formation during the preceding injection.

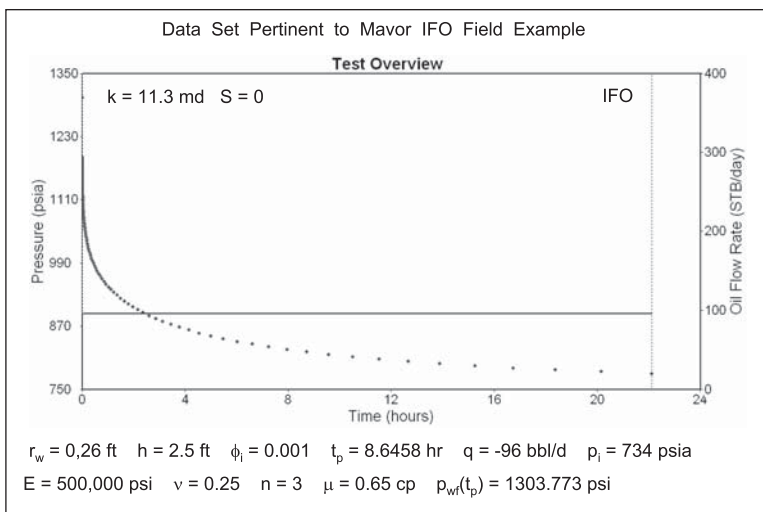


Fig. 17-34. Synthetic data generated in an SDPP program

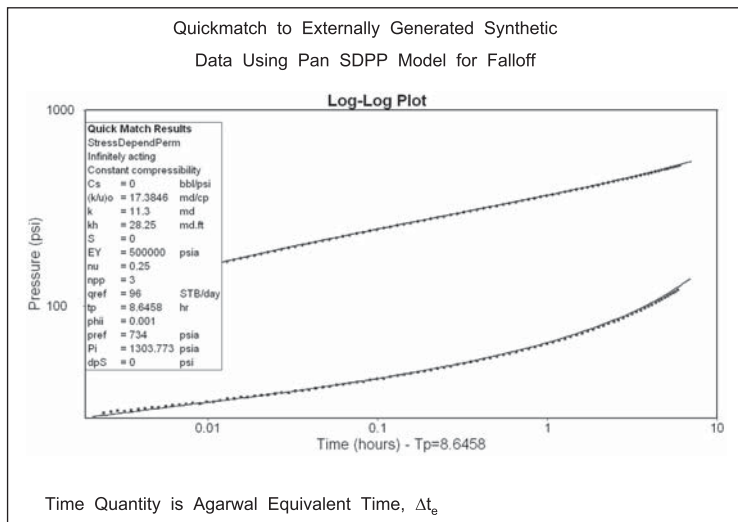


Fig. 17-35. Quickmatch to externally generated data

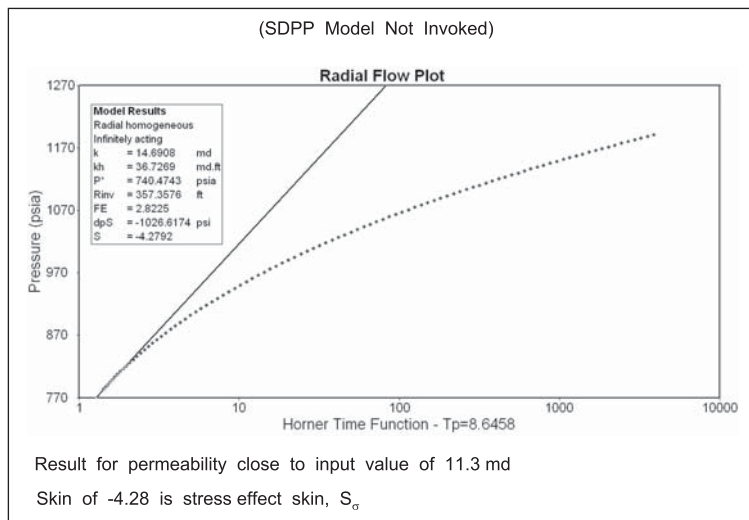


Fig. 17-36. Semilog analysis of falloff as a conventional test



The Mavor field example exhibits nonideal wellbore storage characterized by a sharp maximum feature on the derivative; this cannot be matched with the conventional constant-volume liquid compressibility storage model. It has first pointed out by Ramey that the volume of a fracture must be included with the wellbore volume in storage calculations. However, Van den Hoek<sup>4</sup> has shown that the closure of an unproppped fracture during shutin has the effect of changing the wellbore storage coefficient, i.e., the storage is nonideal. A derivative diagnostic plot from Van den Hoek’s paper, shown here as figure 17–37, has the same character as that observed in the Mavor data. The nonideal storage model of Van den Hoek has not been implemented in the present SDPP model, but the empirical, decreasing wellbore storage model of Hegeman *et al.* will be used to characterize the effect. In the  $p_D$  model developed here, the finite wellbore radius solution is used to model any effect of negative skin in the coal bed.

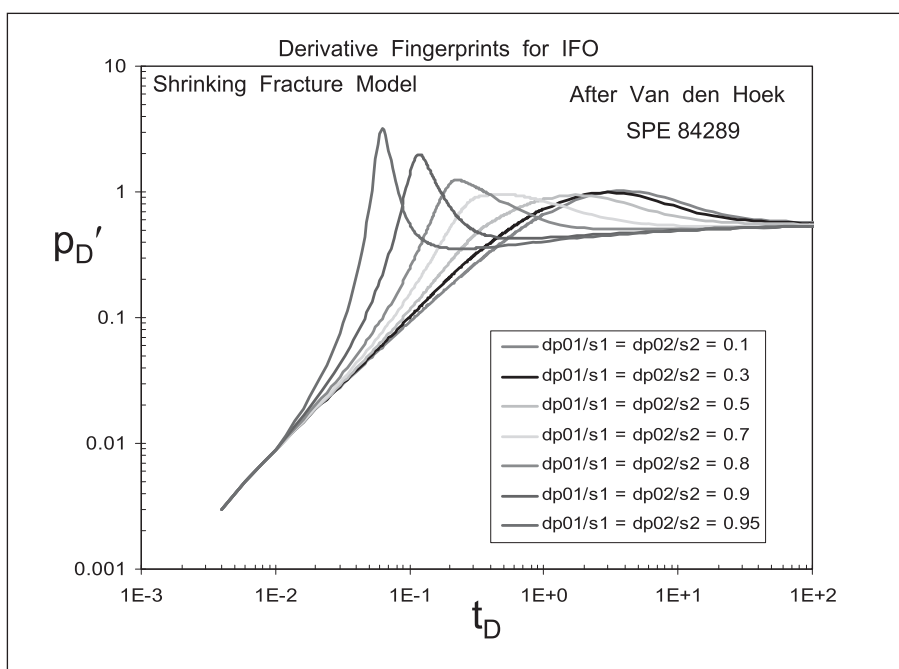


Fig. 17–37. Shrinking fracture model

## Inclusion of Wellbore Storage

The modeling of a wellbore storage effect can be accomplished by writing the superposition equation in the usual form for a liquid system:

$$p_w(T_M) = P_i - \alpha \left( \sum_{i=1}^{M-1} (q_i - q_{i-1}) p_D^*((T_M - T_{i-1})\beta) - q_{M-1} p_D^*((T_M - T_{M-1})\beta) + q_M p_D^*((T_M - T_{M-1})\beta) \right) \tag{17-32}$$

When a pseudopressure is introduced this becomes

$$\psi(p_w(T_M)) = \psi(p_1) - \alpha \left( \sum_{i=1}^{M-1} (q_i - q_{i-1}) p_D^*((T_M - T_{i-1})\beta) - q_{M-1} p_D^*((T_M - T_{M-1})\beta) + q_M p_D^*((T_M - T_{M-1})\beta) \right) \quad (17-33a)$$

and the wellbore storage equation has the form

$$q_{sf} - q_s = C_s \frac{dp_w}{dt} \quad (17-33b)$$

i.e.,

$$q_{sf} - q_s = C_s \frac{d\psi(p_w)}{dt} \frac{dp_w}{d\psi(p_w)} \quad (17-33c)$$

Equations (17-33a) and (17-33c) are solved simultaneously for  $\psi p_w(T_M)$  and  $q_{sf}(T_M)$  at the new time level, and then the inversion of  $\psi[p_w(T_M)]$  to actual wellbore pressure may be written formally as

$$p_w(T_M) = \psi^{-1} \left( \psi(p_w(T_M)) \right) \quad (17-34)$$

This represents a simple modification of the real-time convolution algorithm which allows the SDPP model to be computed including the effects of storage and skin. Note that here the skin effect is handled within the liquid  $p_D^*$  function using the FWBR model. A prototype program was written that embodies the exact storage convolution represented by Eq. (17-33a) and (17-33c), i.e., the superposition is in terms of pseudopressure.

The test problem was simulated in production with a storage coefficient  $C_s$  of 0.001 bbl/psi, and the drawdown period log-log diagnostic plot is shown in figure 17-38a; the early part of the response where radial flow based on  $k_i$  is observed is now completely obscured by the storage effect. In the framework of the current version of Pansystem, the convolution of storage will tacitly assume that the SDPP model is linear, i.e., an analytic solution to the diffusion equation at constant rate; strictly this is not the case. In figure 17-38b, the data has been generated externally using the exact convolution in pseudopressure. This data has been imported into Pansystem and analyzed using the SDPP model and it is apparent that a quickmatch perfectly overlays the exact data. Hence there is no need to include the exact convolution model into the software. Superposition assuming the model is linear is quite satisfactory. The convolution error is illustrated in figure 17-39 on a hugely exaggerated scale; the linearization is based on the reference rate rather than the current sandface rate.

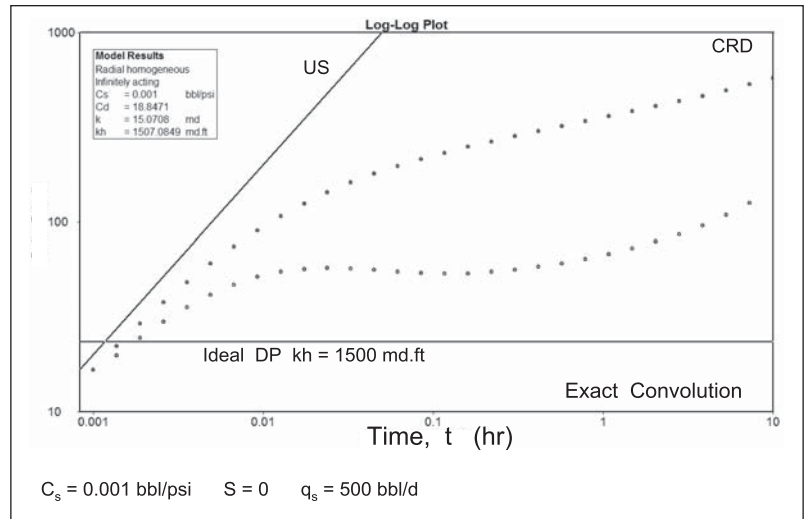


Fig. 17-38a. Effect of wellbore storage on SDPP behavior

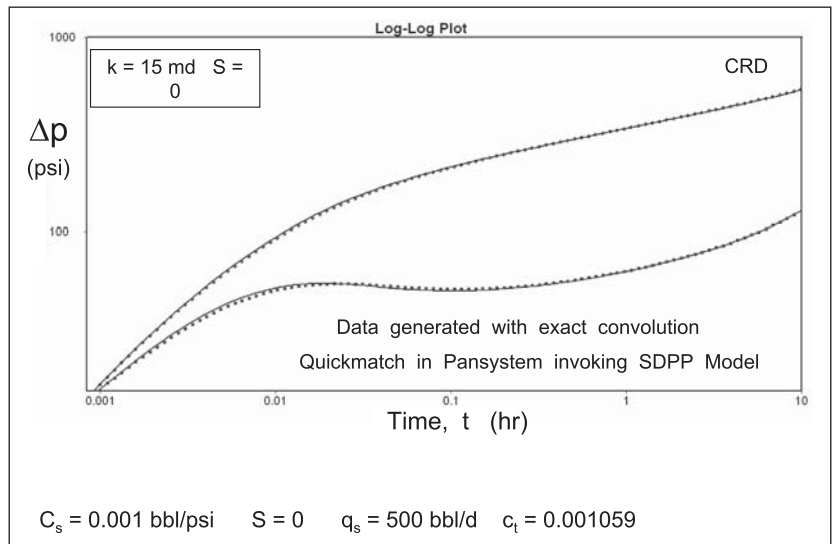


Fig. 17-38b. Ideal storage in production

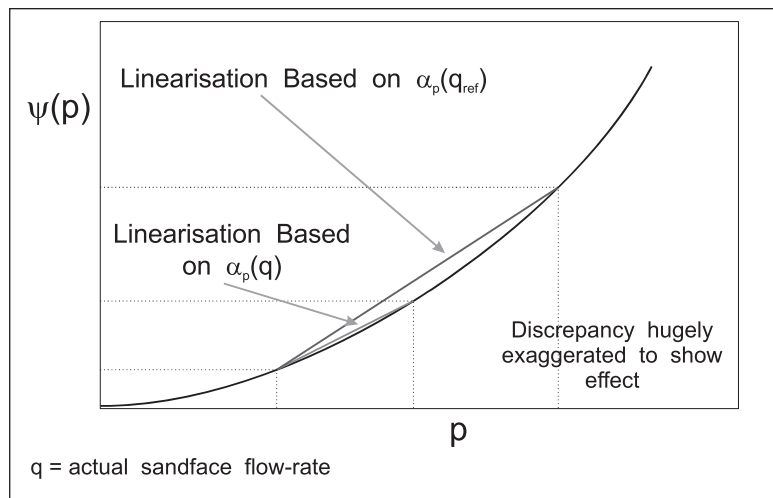


Fig. 17-39. Convolution error in modeling wellbore storage

The log-log diagnostic of the ensuing buildup is presented in figure 17-40, where it is evident that the effect of storage is much stronger. This is a result of the permeability at the end of the DD period being very low because of the drawdown and the well is “choked” with respect to delivering fluid to the wellbore to compress up its contents—analogueous to a tight gas well which has a high gas compressibility in the wellbore going into buildup. In figure 17-41, the effect of storage on a falloff has been computed; in a falloff, the permeability is high at the end of the preceding injection, which reduces the effect of wellbore storage since deliverability is enhanced.

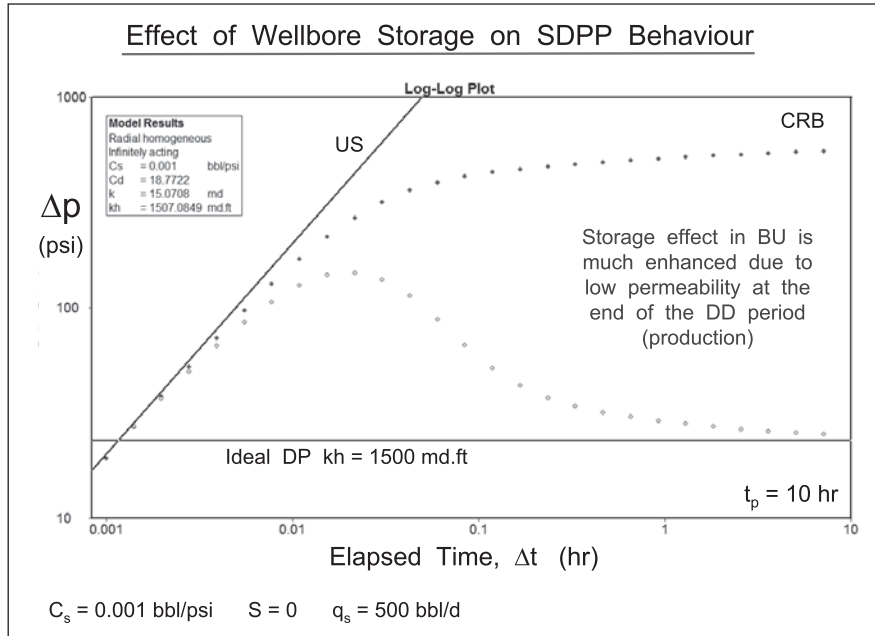


Fig. 17-40. Storage effect in buildup

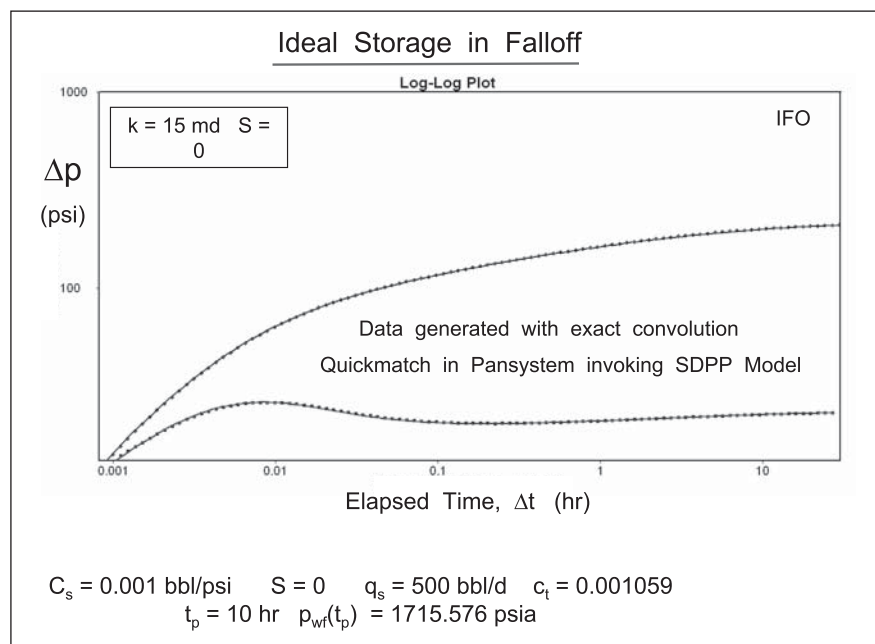


Fig. 17-41. Storage effect in falloff

The real-time convolution algorithm in terms of pseudopressure, as represented by Eqs. (17–33) and (17–34), has been derived for the case where the wellbore storage coefficient  $C_s$  is constant, i.e., ideal storage. The main reason why PanSystem adopts this approach is to allow nonideal storage to be modeled. There is no problem in a time-stepping algorithm to introduce nonideal, i.e., changing, wellbore storage. This is important, for example, in gas well testing where wellbore fluid compressibility is a function of wellbore pressure. In the context of CBM, it is the changing volume of near-wellbore fractures that introduces the possibility of nonideal storage effects, and the Van den Hoek model can be used to provide a useful model. This will be incorporated when the well skin factor is negative and the FWBR model is invoked. In the liquid  $p_D$  function, an effective wellbore radius  $r_{w,eff}$  is computed as

$$r_{w,eff} = r_w e^{-S} \quad (17-35)$$

and the equivalent fracture half length follows from the Goode and Wilkinson equation

$$x_f = 2.24r_{w,eff} \quad (17-36)$$

Following the work of Van den Hoek on injection fractures, the volume associated with near-wellbore fractures can be allowed to be stress-dependent and the dimensionless wellbore storage coefficient takes the form

$$\Delta t_D < \Delta t_D^{closure} \quad C_D = \frac{(V_w c_w + C_f)}{2\pi\phi_1 h r_w^2} = \frac{C_t}{2\pi\phi_1 h r_w^2} \quad (17-37)$$

Here,  $V_w$  is the volume of tubing and casing beneath the testing valve and  $C_f$  is a compliance associated with near-wellbore fractures. It had been pointed out by Hagoort that the effect of fracture compliance is similar to that of liquid compressibility and the quantity  $V_w c_w + C_f$  can be regarded as a total storage coefficient  $C_t$ . The closure of the fracture as the pressure declines in a falloff expels water into the wellbore and contributes to the afterflow. The theory of fracture closing is only applicable to falloff periods and a key parameter is the dimensionless time delay  $\Delta t_D^{closure}$ . Before the fracture closes, the storage is a total effect based on the value of  $C_t$ ; on closure, there is an abrupt change in storage coefficient to  $C_t = V_w c_w = C_s$ . It was pointed out by Van den Hoek that, in practice, fractures do not close like a hinge and the theory must be modified to allow for gradual fracture closure. The PanSystem real-time convolution algorithm can handle a changing value of  $C_t$  and hence the nonideal wellbore plus fracture storage can be modeled.

Van den Hoek analyzed the behavior of an elliptical fracture and suggested an expression for the fracture compliance  $C_f$  equal to the equivalent of a product of fracture volume and fluid compressibility, i.e.,  $C_f \equiv c_w V_f$ . Thus the model is based on a step change in the total storage coefficient:

$$\Delta t_D < \Delta t_D^{closure} \quad C_t = c_w V_w + C_f = C_\tau \quad (17-38a)$$

$$\Delta t_D > \Delta t_D^{closure} \quad C_t = c_w V_w = C_s \quad (17-38b)$$

The expression for compliance takes the form

$$C_f = \frac{2}{3} \pi \frac{1 - \nu^2}{E} \frac{hx_f \times \min(h, 2x_f)}{E(m)} \quad \text{where: } m = 1 - \left[ \min\left(\frac{h}{2x_f}, \frac{2x_f}{h}\right) \right]^2 \quad (17-39)$$

and  $E(m)$  is the complete elliptical integral of the second kind. In this model, the fracture closes at some particular stress (fixed by  $\Delta t_D^{\text{closure}}$ ). In reality, the fracture does not, in fact, close suddenly, and this theory has to be modified to accommodate actual behavior. However, the idea of a critical stress at which the fracture closes is a central idea.

The concept of decreasing wellbore storage was first considered by Hegeman *et al.*,<sup>5</sup> who extended the work of Fair<sup>6</sup> which referred only to increasing storage, i.e., phase redistribution. The models of nonideal storage associated with these authors are discussed in detail in chapter 14 of *Well Test Design and Analysis*, and the derivative responses produced by van den Hoek and shown in figure 17-37 are very similar in form to those that can be generated by the Hegeman nonideal storage model illustrated in figures 17-42a and 17-42b. The key feature is a change from an initial storage coefficient to a smaller one with attenuation of the transition. The Hegeman *et al.* model in real time takes the form

$$\frac{dp_w}{dt} = \frac{q_{sf}B - q_sB}{C_s} - C_\phi \frac{2}{\sqrt{\pi}} \frac{1}{\tau} e^{-\left(\frac{t}{\tau}\right)^2} \quad (17-40)$$

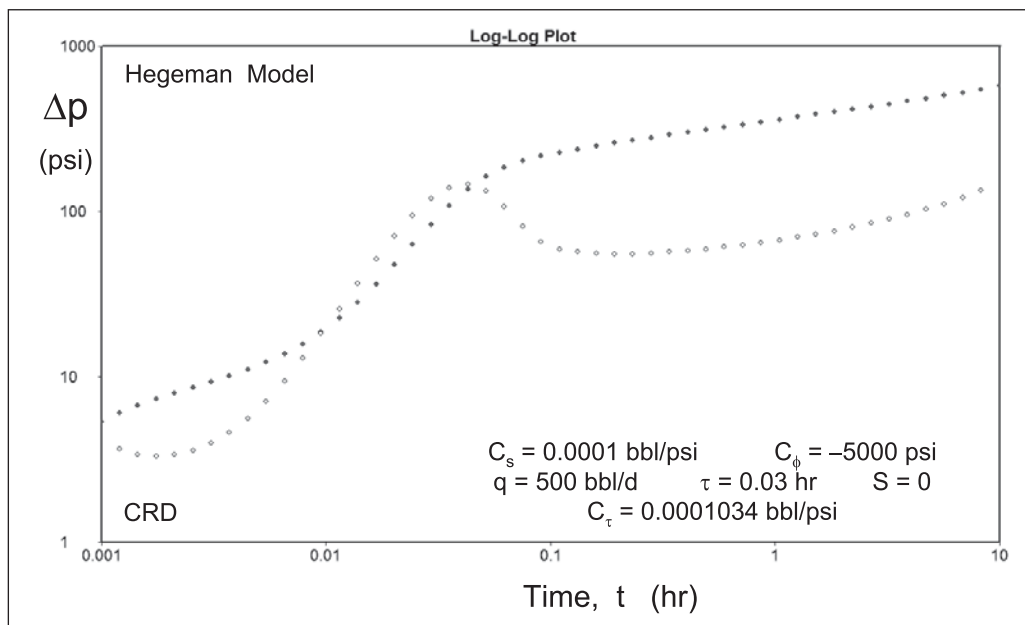


Fig. 17-42a. Effect of nonideal (decreasing) wellbore storage on production

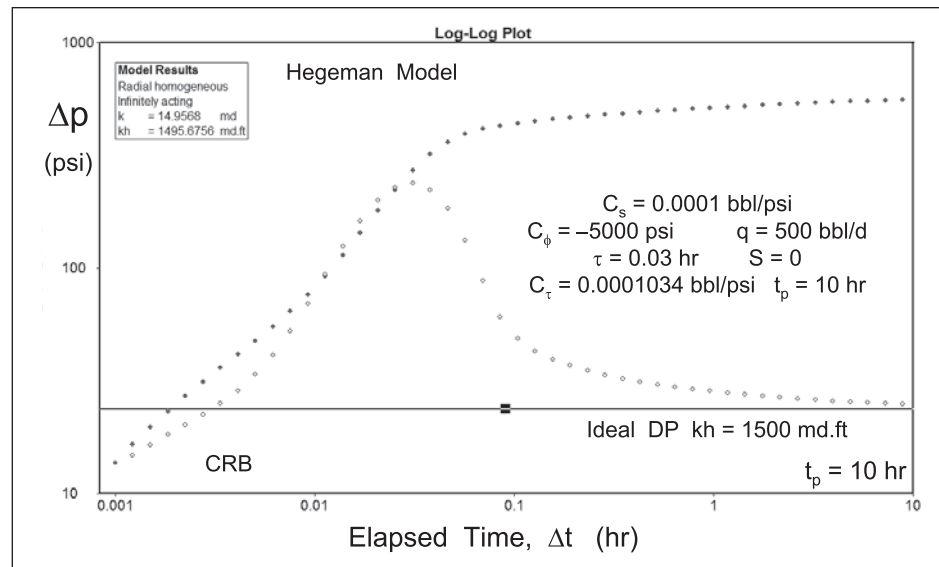


Fig. 17–42b. Effect of nonideal (decreasing) wellbore storage on buildup

At early time ( $t \rightarrow 0$ ), this model predicts a storage coefficient  $C_\tau$ , given by

$$\frac{1}{C_\tau} = \frac{1}{C_s} + \frac{C_\phi}{q_s B \tau} \quad (17-41)$$

In the context of decreasing storage, where  $C_\phi$  (psi) is negative, the value of  $C_\tau$  is larger the value at later time, which is  $C_s$ . The time function in (17–40) is totally empirical but the time constant  $\tau$  reflects the timescale of the transition from  $C_\tau$  to  $C_s$ . van den Hoek modeled the transition utilizing a rock mechanics model for a shrinking fracture, i.e., the compliance was pressure thus time dependent. The van den Hoek model is very complicated and for the present purposes the empirical function of Hegeman *et al.* will be deemed sufficient to model the fracture closure process.

The quantity  $C_\tau$  can be determined by the familiar unit slope construction on the log–log diagnostic plot and the inference can be made that there is information on rock mechanics properties in this value since  $c_w V_w + C_f = C_\tau$ , allowing fracture compliance  $C_f$  to be estimated if  $C_s = V_w c_w$  is known; this is related to Young’s modulus and Poisson’s ratio through Eq. (17–39). It will be seen shortly that nonlinear regression (automatch) invoking the nonideal storage model will yield both terms, viz.,  $C_\tau$  and  $C_s$ ; since the regression is in terms of  $C_s$  and  $C_\phi$ , Eq. (17–41) must be used to compute  $C_\tau$ .

A preliminary simulation of an injection falloff test (described in detail in the next section) is shown in figure 17–43 and the falloff yields the log–log diagnostic plot of figure 17–44.

# INDEX

---

Note: Page references in italics refer to figures.

Chapters on CD-ROM begin on page 1017.

## Index Terms

## Links

<u>Index Terms</u>	<u>Links</u>	
<b>A</b>		
A&H analytical model, <i>see</i> Abbaszadeh and Hegeman slant well model		
Abbaszadeh and Hegeman (A&H) slant well model	931	996–1002
Cinco model compared to	998	
numerical model compared to	1002–1014	
Abbaszadeh, M.	989	
nonintersecting fracture model	979–983	986–987
packer interval response	987–989	
Abgrall, E.		
critical gas saturation	531	
Ablewhite, P.K.		
FEM simulation of slant wells	198	200
abnormally pressured gas reservoir	402–406	
<i>see also</i> overpressured gas reservoir		
Abramowitz, M.	894	
absolute open-hole flow (AOF)	295	
solution gas drive	356	
Abu Dhabi		
detection of residual oil by WFT pressure survey	709	710
horizontal flow meter, first experimental log	844–845	
acid treatment		
horizontal well, using coiled tubing	1093–1094	
hydrochloric acid	157	
ACQ, <i>see</i> annual contract quantity		
active probe pressure response		
horizontal well, observation-active probe arrangement	992–995	
single horizontal barrier effect on	961–964	



## Index Terms

## Links

active probe pressure response ( <i>Cont.</i> )		
vertical well, analytical model	955–957	
vertical well, modified analytical model	964–976	
vertical well, numerical model	958–961	
active water drive		
dry gas reservoir with	580–585	
Addington gas coning model	588–593	
Aegean Sea		
Prinos field, cased-hole WFT	848	
Prinos field, through tubing casing patch	1069	
Agarwal-Gardner decline type curve		
based on cumulative production	656–666	
constant terminal pressure data and equivalent time	652–654	
gas reservoir data	654–655	
hydraulically fractured wells	656	664
production data analysis	1377–1378	
radial flow	651–652	657–663
Agarwal, R.G.	458	
Airlie, C.		
gas well selective inflow performance	862	
gas well WFT survey	1338–1341	
Al-Ajmi, F.A.		
workover program	1071–1074	
Algeria		
gas reservoir, gravity-capillary equilibrium	702	703
Hassi Messaoud field, selective inflow performance technique	862–863	
Al-Hussainy, R.	280	458
WFT pressure survey for reservoir description	788–792	
Al-Tawad, F.	1101	
Ambastha, A.K.	492	
American Petroleum Institute (API) test		
filter loss test	672	
shaped charge performance (RP 43)	118–120	
shaped charge performance (RP 43), fluid mechanics	128–134	

## Index Terms

## Links

Amoco	998			
analytical radial flow model	2			
Anderson, P.M.				
dynamic aquifer effects	744	745–746		
Anderson, W.G.				
capillary pressure curve	1327			
wettability effect on capillary pressure	1318			
anisotropy				
areal anisotropy in coal bed methane wells	1466–1481			
effect on core-derived permeability	694–695	696		
effect on observation probe response	917	994–995	1006	1013–1014
effect on RFT-derived permeability	687	688–689	694–695	696
effect on WFT-derived permeability, spherical flow conditions	877–878	893–895		
annual contract quantity (ACQ)	483			
AOF, <i>see</i> absolute open-hole flow				
API test, <i>see</i> American Petroleum Institute test				
apparent fracture conductivity	224–225			
appraisal well, <i>see</i> exploration well				
aquifer face skin	420–421	442		
linear aquifer	445–446			
aquifer influence function	419			
radial aquifer model	421–425			
aquifer influx	395			
case studies	452–456			
deconvolution method	448–449			
dry gas reservoir with active water drive	580–585			
enveloped high permeability streaks	450–452			
extended buildups	449			
inclusion of coning model	577–579			
inclusion of displacement model	579–580			
parameters determination	447–450			
reservoir limit testing	449–450			
reservoir pressure below bubble point	575–577			
tuning of material balance model	585			
undersaturated oil reservoir case	570–575			
variable rate drawdown analysis	418–421			

## Index Terms

## Links

aquifer material balance	425–426			
modified	438–439			
aquifer model				
discontinuous	450			
Fetkovich linear model	446			
Fetkovich radial model	424	434–435	437–438	
linear	444–446			
outcropping radial	443–444			
radial	421–443			
aquifer productivity index	1178–1179			
Archer, J.S., <i>see</i> Noman and Archer correlation				
for inertial resistance coefficient				
areal anisotropy				
coal bed methane wells	1466–1481			
areal displacement model				
gas recycling with	563–569			
areal flow convergence	38			
horizontal well in a rectangle	79–82			
areal pressure variation	417			
Argentina				
San Jorge Gulf basin, modular dynamic tester				
use	937–944			
arithmetic average permeability				
perfect layered systems	101–104			
three-layer system	1281–1284			
Arps empirical rate-time decline equation	616	621	622–623	631
	638			
non-applicability	618			
type curves	638	639		
Asaly, M.				
unusual measured well inflow performance	1074–1075			
Ascharsobbi, F.				
connected system of natural fractures	1452–1453			
asphaltene deposition	1084–1085			
associated aquifer	490	498		
Atkinson, J.P.	803–804	816–817		

## Index Terms

## Links

Australia		
coal bed methane wells, drill stem test	1437–1444	1445–1446
coal bed methane wells, injection fall-off test	1430–1433	1444–1445
Cooper Basin, fracturing multiple zones in stacked reservoirs	1118–1119	
Griffin field, sinusoidal well	1092	1093
Kingfish field, natural water influx	443	
Wanaea field, WFT pressure survey, dynamic aquifer effects	744	745
authigenic clay	798	
formation damage	49–51	
automatic model matching	419–420	
aquifer parameter determination	447–448	
Arps empirical model	633	
compartmentalized material balance	1215–1220	
<i>see also</i> nonlinear regression		
average permeability		
cellular system	1196–1197	
determination, underbalanced drilling data analysis	1277–1284	1308–1309
heterogeneous systems	101–105	
<i>see also</i> arithmetic average permeability		
average pressure		
during semi-steady-state depletion	24–26	
steady-state flow	20–22	
well inflow in terms of	36–37	
Awad, M.		
capillary pressure effects	1334–1337	
Ayestaran, L.	774	793
Ayoub, J.A.		
vertical observation probe pressure response, dual permeability model	944–948	
Aziz, K.	370	
<b>B</b>		
backpressure equation	301–302	
baffle	952–954	

## Index Terms

## Links

Banks correlation			
limitation	606		
waterfood simulation	563	603–604	
Barba, R.E.			
hydraulic fracturing program	232		
Bardon	333		
barium sulfate scale deposition	152–153		
Bath, P.G.H.	792		
Bayat, M.G.	787		
flow profile match	838	839	840
identification of fault zone through fault multiplier adjustment	802–803		
Beardall, T.J.	809–810	1163	
Beardsell, M.			
oil-based mud invasion in aquifer leg simulation	1329–1332		
Behrmann, L.A.			
perforation damage in underbalanced conditions	155		
Bell, W.T.	152		
Berea penetration multiplier	123		
Berea sandstone			
effect of capillary number on relative permeability curve	345–347		
effect of confining pressure on pore volume	11–12		
Berg correlation	10–11		
estimation of ideal permeability of gravel pack sand	175		
Bilhartz, H.L.	64		
Bishlawi, M.			
determination of effective vertical permeability	782–783		
Black and Scholes model	1018		
black oil pressure-volume-temperature model			
as an isochronic flash	519–520		
material balance study	506–510		
Blasinghame, T.A.	651	654	

## Index Terms

## Links

Blom, S.M.P., <i>see</i> Hagoort and Blom relative permeability weighting function				
Blount, E.M.	167			
blowdown limit model	367–370			
blow-through, <i>see</i> viscous stripping				
borehole video camera	874			
bottom water drive	571			
material balance study, Yang and Wattenbarger method	596–597			
boundary condition				
infinite conductivity	64			
steady-state radial flow model	15			
bounded drainage area				
well productivity	36–45			
boundary effect				
coal bed methane wells	1429–1430			
coal bed methane wells, stress-dependent permeability and porosity with	1448–1452			
Bourgoyne, A.T.	490			
Boyd, W.E.	458			
BP <i>see</i> British Petroleum				
Brazil				
field example, oil wet behavior	713–714			
Bremer, R.E.	795			
bridge plug	1060–1061			
<i>see also</i> straddle packer wireline formation tester				
Brigham	992			
British Petroleum (BP)	249	1109	1362	
gel treatment	1070			
high slant well	819–820			
Mast project	1020			
maximum allowable perforation velocity	181			
stimulation of fractured wells	220			
Brons and Marting correlation	62–64	71	73	113–114
	194	231		
Brons, F.	30			
Bruns, J.L.	490			

## Index Terms

## Links

Buckley-Leverett theory				
saturation profile	1321	1353–1354		
buildup analysis				
RFT-derived permeability	684–688	690–693	695–698	
Burton empirical correlation	199–200	1002		
<b>C</b>				
Campbell	150	198		
Canada				
Horseshoe Canyon, coal bed methane	1451–1452			
reservoir characterization, underbalanced				
drilling data analysis	1304–1305			
Canadian Fracmaster	1117			
capillary number				
effect on relative permeability	331–332	339	342–346	
capillary pressure effect				
oil-based mud invasion	1328–1332			
oil-based mud invasion, field examples	1343–1346			
water-based mud invasion	1320–1328			
water-based mud invasion, field examples	1332–1343			
carbonate reservoir				
thick oil-water transitions	1357–1358			
Carnegie, A.J.G.	1312			
thick oil-water transitions in carbonate				
zones	1357–1358			
Carslaw, H.S.	688	875	911	992–993
Carter, R.D.	644			
Cartesian plot/graph				
average pressure	1195			
average pressure in semi-steady-state				
depletion	25–26			
exponential approach to equilibrium	1193–1194			
FEM simulation of active probe pretest				
drawdown	958–959			
injection and fall-off periods, coal bed				
methane	1402	1403	1405	
pressure match quality	966	967		
production regimes in primary depletion	266–267			

## Index Terms

## Links

Cartesian plot/graph ( <i>Cont.</i> )			
rate-cumulative production decline	630–631		
rate-cumulative production decline for fractured wells	663–664		
rate-cumulative production decline for radial systems	657–658	659–660	661–662
reservoir pressure versus time for test problem	408–409	449	
cased-hole gravel pack			
maximum perforation velocity	179–184		
cased-hole wireline formation tester (CHWFT)			
measurement of layer initial pressure	847–849		
vertical interference test using	1063–1064		
Cason, L.D.			
gas field exhibiting water drive	452–454		
CBM, <i>see</i> coal bed methane			
CCE, <i>see</i> constant composition expansion			
CCPC, <i>see</i> cluster composite performance curve			
C factor	180		
CFE, <i>see</i> core flow efficiency			
Chang, Y.	1360		
invasion-supercharging model, mathematical formulation	1366–1369		
invasion-supercharging model, predictions	1369–1372		
Chan, K.S.			
water control diagnostic plots	1066–1068		
Chatas, A.T.	878		
Chedburn, A.C.S.	1225		
Chen, S.			
pressure maintenance	1075–1077		
Chesney, T.P.	458		
Chevron	100		
Chierici, G.L.			
decline curve analysis, example	635–637		
general form of volumetric balance equation	511		
residual gas saturation measurement	457		
China			
field example, WFT-derived permeability	902–903		



## Index Terms

## Links

choked fracture	233–234			
CHWFT, <i>see</i> cased-hole wireline formation tester				
Cinco-Ley, H.	72–73	196	208	931
effect of limited entry and slant well	199–200			
nonintersecting fracture model	979–983	986–987		
pseudopressure approach	1379–1380			
slant well model	998	1002	1005	
steady-state pseudopressure approach	1382			
stress-dependent permeability and porosity	1384–1387			
<i>see also</i> Wong, Harrington and Cinco-Ley				
type curve				
circular reservoir				
with a central well, semi-steady-state				
depletion	23–26			
Clancey, B.M.	214			
hydraulic fracturing of permeable oil wells	214			
Clarkson, C.R.	1451–1452			
classical cumulative influx superposition	428–432			
classical Schilthuis material balance	510–512			
clay minerals				
water sensitive	49–51	842		
clay smearing	798			
closed cylindrical reservoir				
semi-steady-state radial flow	31–34			
closed reservoir				
transient pressure behavior of single well at				
centre of	22–23			
closing fracture	1414–1415	1423		
cluster composite performance curve (CCPC)	385	387		
coal bed methane (CBM)	1377–1378			
areal anisotropy identification by interference				
test	1466–1481			
extended production testing	1481–1482			
geological structure	1429			
horizontal wells	1482–1483			
hydraulically fractured horizontal wells	1483–1491			
injection falloff test, field example	1407–1410	1417–1433		

## Index Terms

## Links

coal bed methane (CBM) ( <i>Cont.</i> )		
new-generation wireline formation tester		
applications	1492–1495	
production forecast	1433–1437	
radial composite behavior	1459	1461
skin effect	1452–1465	
slug test	1437–1448	
stress-dependent permeability and porosity	1378–1390	
stress-dependent permeability and porosity		
with boundary effects	1448–1452	
stress-dependent permeability and porosity,		
pseudo model	1390–1410	
Coleman, S.B.		
blowdown limit model	367–370	
gas well loadup	366–367	
Colley, N.	719	
commingled system, <i>see</i> compartmentalized		
system		
communicating layer		
arithmetic average permeability	102–103	
identification	1063–1064	
water shutoff	1060	
compartmentalized system		
average permeability	1196–1197	
complex material balance	1159–1163	
decline curve analysis	644	
extended buildup	1192–1196	
flow profile	832–833	
general form	1169–1171	
horizontal well in, production logging	1107–1108	
horizontal well in, productivity index	92–101	
<i>see also</i> layered compartmentalized system		
completion		
efficiency	1079–1086	
frac-pack	249–252	
horizontal	90	
open-hole, non-Darcy flow	166–167	
partial, <i>see</i> partial completion		

## Index Terms

## Links

completion ( <i>Cont.</i> )	
perforation, <i>see</i> perforated completion	
completion skin effect/factor	201–202
effect of limited entry	193–195
effect of slant well	196–198
effect of slant well with limited entry	199–201
complex material balance	1161–1169
automatic matching	1215–1220
cumulative production and influx	1184–1186
effective interblock transmissibility	1197–1199
extended buildup	1192–1196
field example	1200–1201
forcing functions	1174–1175
gas cap drive	1180–1184
idealized cellular system	1189–1192
natural water influx	1178–1180
<i>notion</i>	1161
state space representation	1171–1174
state space representation, by numerical	
integration	1175–1177
three-cell system	1187–1189
three-cell system with small interblock	
transmissibility	1199–1200
compositional flow	
two-phase, <i>see</i> two-phase compositional flow	
compositional material balance	
black oil model as isochronic flash	519–520
critical gas saturation	530–532
integration with production network model	534
material balance equation integration	520–522
nonlinear regression	533–534
solution gas drive cell	512–519
synthetic test problem	526–530
undersaturated liquid behavior	523–524
variable rate production data	532
well models in the material balance cell	524–526
coning, <i>see</i> gas coning; water coning	
connecting layer, <i>see</i> communicating layer	

## Index Terms

## Links

Conoco-Phillips	1021			
constant composition expansion (CCE)	338	508		
constant effective compressibility	492			
constant percentage decline	628			
constant rate buildup (CRB) analysis				
spherical flow	886–904			
constant rate drawdown (CRD) analysis				
observation probe pressure response	920–922			
spherical flow	886–904			
constant sandface rate				
observation probe pressure response	925			
constant terminal pressure (CTP)				
well rate prediction	1224			
constant terminal pressure (CTP) solution	425			
derivation of convolution	1260–1262	1267–1269		
determination of aquifer influx rate	433–434			
equivalent time and	652–654			
constant terminal rate case	424–425			
constant wellbore pressure test	617–619			
semi-infinite behavior	619–620			
contract year	483			
conventional pseudopressure	280			
convolution	1175			
in Laplace space, radial aquifer model	432–434			
<i>notion</i>	408			
production constrained convolution	1220–1225			
variable rate analysis, underbalanced drilling				
context	1259–1262			
<i>see also</i> real-time convolution algorithm				
Cook, C.C.	28–29	494	497	
Cooke, C.E. Jr.	222			
coordinate transformation				
deformation effect on well shape	84	197–198	877–878	989–990
	1000	1300	1467	1469
	1470–1473			
core analysis				
production logging integration with transient				
testing and	871–873			

## Index Terms

## Links

core-derived permeability	690–691			
heterogeneous systems	102–105			
RFT-derived permeability versus	693–698			
core flow efficiency (CFE)	152			
determination	120–121			
relation between crushed zone thickness and	122–123			
Corey exponent	303–305			
Cowan, G.	719			
CRB analysis, <i>see</i> constant rate buildup analysis				
CRD analysis, <i>see</i> constant rate drawdown analysis				
critical coning rate	69–71			
critical gas saturation	530–532			
critical gas velocity	365–367			
critical invasion rate	1359			
critical liquid saturation	329	333		
crossflow reservoir	1062–1066			
<i>see also</i> shutoff treatment				
crushed zone effect				
due to perforation	121	122–123	126	131–132
	136	152		
CTP, <i>see</i> constant terminal pressure				
Cuesta, J.F.				
evaluation of massive hydraulic fractured wells	228–233			
cumulative influx superposition	428–432			
cumulative production				
Agarwal-Gardner decline type curve	656–660			
Agarwal-Gardner decline type curve, applications	660–666			
decline curve analysis	628–631			
Cutler, W.W.	638			
cylindrical buildup analysis	685			
cylindrical gravel pack	184–185			
cylindrical reservoir				
semi-steady-state radial flow	31–33			
cylindrical reservoir with central well				
steady-state radial flow	14–15			

## Index Terms

## Links

### D

daily contracted quantity (DCQ)	482	483		
Dake, L.P.	1179			
black oil model	509–510			
general form of volumetric balance equation	511			
radial aquifer model behavior, test problem	435–438			
WFT pulse test	794–795			
damage envelope	152–153			
Danesh, A.	329	331–332	333	339
	345			
da Pratt, G.				
modular dynamic tester use, field examples	937–944			
Darcy flow shape factor	150–152			
Darcy's law				
<i>notion</i>	5			
radial flow	106			
single phase flow in porous medium	5–8			
Darcy units	6–7			
DCQ, <i>see</i> daily contracted quantity				
decline curve analysis	615–616			
Agarwal-Gardner	651–666			
constant wellbore pressure testing	617–620			
empirical rate-time equations	620–638			
Fetkovich	454–456	615	616	618
	626	638–645		
production constrained depletion	481–482	615		
semi-steady-state depletion	645–651			
deconvolution				
aquifer influx identification	448–449			
complex material balance	1220			
interpretation of variable rate drawdown				
analysis	419			
deep set gel treatment	1069–1071			
deliverability				
horizontal wells	90–91			
importance	2			
<i>notion</i>	483			
proximate wells	380–387			

## Index Terms

## Links

deliverability ( <i>Cont.</i> )				
semi-steady-state	1086–1094			
transient	1095–1100			
<i>see also</i> well rate				
deliverability constrained production	476			
Denmark				
chalk fields, rock compaction	29			
Dan field , hydraulic fracturing of horizontal well	219	252	253–255	1119
Deo, M.				
underbalance effects on perforation flow	134			
depletion				
semi-steady-state, <i>see</i> semi-steady-state depletion				
depressurization	1077–1078			
depth of investigation				
analysis	976–978			
effect on RFT-derived permeability	686			
radial and linear flow	1095–1096			
depth of penetration				
perforation tunnels	123–126			
derivative type curve				
horizontal well	987	988		
vertical observation probe response, limited entry model	936			
Desbrandes, R.				
large hole observer	704–706	713–715	1312	
design fracture half-length	1111–1113			
desuperposition				
compartmentalized material balance	1226–1230			
dew point pressure				
depletion above	549–550	557–559		
Dietz shape factor				
analytical formulae	40–45			
closed single well drainage areas	38–40			
four well cluster	380–384			
wedge-shaped drainage areas	43–45	387–390		

## Index Terms

## Links

differential depletion				
WFT pressure survey	762–767	793–794	847	
dimensionless external radius	17			
dimensionless fracture conductivity	205			
low	207–208			
dimensionless skin effect/factor				
idealized perforation pattern	137			
wellbore damage and	52–53	55		
well inflow performance, influence of				
damaged zone	111–113			
displacement model				
areal	563–569			
empirical	599–614			
inclusion in aquifer influx	579–580			
dissolved gas ratio	507			
distant fracture, <i>see</i> nonintersecting fracture				
distributed flow measurement	831–832			
distributed parameter wellbore model	1257–1259			
distributed pressure measurement	667–668			
using WFT, <i>see</i> wireline formation tester				
distributed pressure measurement				
Dorran, T.	839	841	1101	1102
drainage area				
bounded, well productivity	36–45			
determination	31	262–263		
semi-steady-state radial flow	30–34			
verification	765			
drawdown	3	668		
<i>notion</i>	2	17		
drawdown analysis				
RFT-derived permeability	682–683	685–695	697–698	
Drillflex	1069			
dry gas injection, <i>see</i> recycling				
dry gas reservoir				
with active water drive	580–585			
downtime	483	1018		



## Index Terms

## Links

dual permeability model				
vertical observation probe pressure response	944–952			
vertical observation probe pressure response, numerical simulation	950–954			
with limited entry	951–952			
dual porosity system	1162–1163			
coal bed test interpretation	1451–1452			
dual probe wireline formation tester (WFT)				
permeability estimation, field examples	938–944			
pressure response	909	910	911–912	
Duggan, J.O.				
Anderson “L” reservoir performance	490			
Duggan, T.P., <i>see</i> Morrison and Duggan				
correlation for inertial resistance coefficient				
Dumore	453			
dump flooding	1154			
Dussan, E.	955			
effect of anisotropy on probe permeability	688–689	878	900	
flow shape factors	882	893–895	898	901–902
dynamic aquifer				
detection by WFT pressure survey	739–747			
dynamic filtration	1358–1366			
<b>E</b>				
EAR, <i>see</i> exponential approach region				
Earlougher, R.	261	1466	1479	
East Irish Sea Basin				
South Morecambe field, paleocontact				
detection	719–720			
edge water drive	570–571			
incorporation into material balance	579–580			
effective barrier transmissibility				
estimation	793–794			
effective circular source radius	83			
effective interblock transmissibility	1197–1199			
effective perforation length	188–193			

## Index Terms

## Links

effective wellbore radius	86		
<i>notion</i>	74		
radial flow model	74–75		
skin effect in stress-dependent permeability and porosity	1406–1407		
Egan, F.	163	192	
FEM analysis of flow to confined perforation	129–131		
perforation geometries study	150–151		
Ehlig-Economides, C.A.			
vertical observation probe pressure response, dual permeability model	944–948		
vertical pulse test	795		
elliptical influence area	1476		
empirical displacement model			
layered systems	604–609		
multiple well situation	610–614		
unit mobility areal sweep	599–604		
waterflooding below bubble point	609–610		
empirical rate-time equation	620–625		
change in production conditions	633–635		
decline rate	628		
exponential decline for single compartment system	625–627		
field examples	635–638		
minimum economic rate	625		
production database	631–633		
transformation to cumulative production	628–631		
enhanced oil recovery (EOR)	1019		
enhanced voidage (EV)	1078		
EOR, <i>see</i> enhanced oil recovery			
equilibrium flash calculation, <i>see</i> isochoric flash; isothermal flash			
equivalent cylindrical aperture model	236		
wedge model of flow convergence compared to	237–238		
equivalent drawdown time			
shut-in period in well test software	1396–1400		
equivalent probe radius	132–133	144–146	875–876
Ergun equation	169		

## Index Terms

## Links

Euler method			
material balance equation integration	520–522	574	
EV, <i>see</i> enhanced voidage			
Evinger, H.H.			
two-phase pseudopressure	312	313	
exception analysis, <i>see</i> trend analysis			
exploration well			
detection of dynamic aquifers	739–747		
detection of immobile oil	706–712		
detection of mobile oil	712–713		
detection of tar mat	715–716		
forced gradient technique	721–727		
formation damage	48		
gravity-capillary equilibrium	700–706		
oil wet behavior	713–715		
overpressured reservoir	748–749		
pressure-depth diagram	1372	1373	
WFT pressure survey, field examples	717–720	740–747	
WFT pressure survey, objectives	699–700		
exponential approach region (EAR)	1191–1192		
exponential decline	621		
single compartment system	625–627		
single compartment system, field example	637–638		
extended production test			
coal bed methane wells	1481–1482		
Exxon	443	456	
<b>F</b>			
Fair, W.B.	1415		
fall-off test			
coal bed methane wells	1407–1410	1417–1433	1444–1445
fault detection/delineation			
WFT pressure survey	785–787		
fault transmissibility multiplier	801–804		
FEM numerical simulation, <i>see</i> finite element			
method numerical simulation			
Fenwick, D.			
perched water contact	735–737		

## Index Terms

## Links

Ferguson, C.K.				
mud fluid loss rates	672–674	1358–1359	1360	1367
	1368			
Fetkovich, M.J.	264	312	427	1124
	1178–1179			
approximation	267–268	1097–1098		
decline curve analysis	454–456	615	616	618
	626	638–645		
high pressure gas reservoir	490	494	496	498–501
linear aquifer model	446			
radial aquifer model	434–435	437–438	490	
radial aquifer model, quasi-semi-steady-state conditions	424			
solution gas drive well inflow performance	358–360			
Fevang, O., <i>see</i> Whitson and Fevang relative permeability curve; Whitson and Fevang weighting function				
field development				
well deliverability and	2–3			
WFT pressure survey, applications	751	755–777	793–814	847
WFT pressure survey, field examples	752–755	782–792	815–818	
WFT pressure survey, gradient determination accuracy	777–779			
field unit				
quantities entering Darcy's law	7			
well inflow performance at high production rates, equations	115			
film drainage	329–330			
filtrate invasion, <i>see</i> mud filtrate invasion				
finer migration				
formation damage and	56–58			
gravel pack	174			
unconsolidated formation	1121			
finite conductivity hydraulic fracture	1113–1114			
<i>notion</i>	1109			
pseudo-radial skin	204–214			

## Index Terms

## Links

finite element method (FEM) numerical simulation			
active probe pressure response	958–961		
active probe with spherical flow skin effect	964–976		
dual permeability model	950–954		
flow to a confined perforation	129–131		
high slant well	1015		
horizontal baffles	952–954		
nonintersecting fracture with limited entry	983–985		
observation probe pressure response	929	931–935	937
perforated completion, inflow behavior	140–141	147–148	150
slant wells	198		
slant well with limited entry	200–201		
slant well with limited entry, compared to A&H analytical model	1002–1013		
<i>see also</i> numerical simulation; PanMesh software			
finite wellbore radius solution	1269	1271	
Finklea, E.	875–876	877	
Firoozabadi, A.,			
critical gas saturation	531		
residual gas saturation	457–458		
<i>see also</i> Katz and Firoozabadi correlation for inertial resistance coefficient			
Fishlock, T.P.			
residual gas saturation	457–458		
five-layer system			
determination of permeability and pressure, synthetic problem	1291–1294		
five-spot waterflooding pattern			
displacement curve	603		
flow distribution	61		
flow convergence			
fracture	234–244		
perforations	64–68		
perforations, skin effect	136–138	843–844	
<i>see also</i> areal flow convergence			
flow efficiency	60–61	141–142	256

## Index Terms

## Links

flowing gradient survey	852		
flow regime			
slant well with straddle packer	999–1002		
flow shape factor	682–683		
Darcy flow	150–152		
non-Darcy flow, spiral pattern	163–166		
probe	186–187		
spherical flow	881–882	894–896	
flush production	1096–1097		
forced gradient technique	721–727		
Forcheimer equation			
flow in porous media	128		
linear flow	106		
linear flow integration	147		
linear incompressible flow	170		
radial flow integration	146		
steady-state, incompressible flow	143–144		
Fordham, E.J.			
critical invasion rate	1359		
filtration theory	1359–1363		
formation compaction	27–29		
formation damage	46	1081–1084	
analytical skin formulae	53–58		
dimensionless skin effect	52–53		
effect on RFT-derived permeability	687		
horizontal wells	1089		
hydraulic fracturing to overcome	226–228		
near-wellbore altered zone	46–49		
partial completion and	64–68		
radial, uniform altered region	155–159		
unusual case	1081		
water-sensitive authigenic clays and	49–51		
well deviation and	73		
formation pressure			
determination	671–676	733	747
determination, underbalance drilling data			
analysis	1284–1308		
<i>see also</i> wireline formation tester			

## Index Terms

## Links

four-cell system				
lumped parameter material balance model	808–809	1165–1168		
prototype	1165–1166			
four-well cluster	380–384			
Fox, M.J.	809–810	1163	1225	
frac-pack completion	249–250			
open-hole	183–184			
technology	250–252			
fracture choking	233–234			
fracture closure	1414–1415	1423		
fracture conductivity	219			
apparent	224–225			
effect of proppant size on	251–252			
fractured horizontal well	252–255			
fractured well				
productivity index	74–76			
fracture face damage	211–214			
fracture face skin effect/factor				
finite conductivity hydraulic fracture	211–214			
fracture root damage	211			
fracture root skin	212–213	233		
frictional pressure drop	91			
effect on horizontal well performance	96–100			
full gas recycling	566			
Fussel, D.D.	338–339			
<b>G</b>				
Garb, F.A.				
liquid recovery below dew point	552–554			
gas block	56	353	529	1456–1459
	1461			
gas cap				
detection by WFT pressure survey	729–731			
loss of oil	771–772			
gas cap drive				
complex material balance method	1180–1184			
secondary, evolution	534–549			

## Index Terms

## Links

gas condensate well				
depletion above dew point	549–550			
dry gas injection	556–563			
gravity segregation of condensate	555–556			
hydraulic fracturing	353			
inflow performance	335–339			
inflow performance, non-Darcy flow	351–352			
inflow performance, steady-state spherical non-Darcy flow	320–323			
retrograde condensation without gravity segregation	550–555			
two-phase pseudopressure	319–320	323–329	338–339	1129–1130
gas condensate well relative permeability curve	323–326	329–335	347–350	
gas coning	71	587–588		
material balance context	545–548			
material balance context, Addington model	547	588–593		
gas expansion factor	399			
gas-in-place (GIP)				
determination	399–402			
determination by decline type curves	651–652	660–666		
gas material balance	395	397–398	660–661	
abnormally pressured gas reservoirs	402–406			
aquifer influx	454–456			
areal pressure variation	417			
differential form	406–411			
high pressure gas reservoir	491–492			
including gas saturation effect	459–462			
including gas saturation effect, applications	465–474			
including gas saturation effect, synthetic test problem	463–465			
natural water influx scenario	413–417			
nonlinear regression	411–413			
no-water influx scenario	399–402			
radial aquifer	425–426	438–439		
rate measurement error	413			
volumetric reserves calculation	396–397			



## Index Terms

## Links

gas-oil ratio (GOR)	546–548	
calculation, Addington correlation	588–593	
solution gas drive reservoir	521–522	527–529
gas percolation	534–539	
<i>notion</i>	771	
Gas Research Institute (GRI), Texas	1115	
gas sales contract	482	
involving swing factor	483–490	
gas saturation, <i>see</i> residual gas saturation		
gas storage project		
differential material balance equation	465–474	
gas-water two-phase pseudopressure	360–365	
gas well		
capillary pressure effects, field examples	1333–1341	1343–1344
commingled wellbore model	1234–1237	
high-rate, <i>see</i> high-rate gas well		
non-Darcy skin analysis	298	
selective inflow performance	861–863	
water-cut, <i>see</i> gas well producing water		
gas well deliverability curve		
generation	299–301	
prediction	1382–1383	
gas well inflow performance relation (IPR)		
backpressure equation	301–302	
high pressure	296–298	
non-Darcy flow treatment	285–292	
pseudopressure	275–285	
quadratic	861–863	
steady-state	292–293	
<i>see also</i> gas condensate well: inflow		
performance		
gas well loadup	365–367	
gas well producing water	395	
blowdown limit model	367–370	
critical gas velocity	365–367	
standing water column	370–371	
two-phase pseudopressure	360–365	
<i>see also</i> gas material balance; water drive gas reservoir		

## Index Terms

## Links

gauge resolution				
impact on RFT-derived permeability	688			
Geffen, T.M.				
residual gas saturation measurement	457			
general mechanistic reservoir material balance	505–506			
aquifer influx	570–585			
black oil model	506–510			
classical Schilthuis equation	510–512			
compositional material balance	512–534			
evolution of secondary gas cap	534–549			
gas and gas condensate reservoirs	549–569			
geometric mean permeability	104–105			
geometric skin effect/factor, <i>see</i> completion skin effect/factor				
geopressured reservoir				
material balance approach	402–406			
geoskin	289	1309		
Germany				
Soehlingen gas field, hydraulically fractured				
horizontal well	1119–1120	1484		
Gilbert, W.E.	4	852		
Gilchrist, A.L.	178			
Gilchrist, J.M.				
gravel prepack design	177–178			
gravel prepack use	176			
GIP, <i>see</i> gas-in-place				
Glaze, C.E.	167			
Goode, P.A.	86	901–902		
active probe pressure response	955–957	964–965	968	971
analytical formula for areal flow convergence				
skin	80–81	84	216	
analytical formula for pure linear flow				
convergence skin	236–238			
dual probe formation tester pressure				
response	909	910		
effective circular source radius	83–84			
horizontal well deliverability	1089–1091			
observation probe pressure response	911–913	914–915	944	

## Index Terms

## Links

GOR, <i>see</i> gas-oil ratio				
gradient determination	777–779			
gravel pack efficiency	176			
gravel pack perforated completion				
effective perforation length	188–193			
effect of loss control material	176–179			
external cylindrical gravel pack	184–185			
horizontal well	1122–1125			
identical perforation and formation				
properties	185–187			
linear flow	169–176			
maximum perforation velocity	179–184			
pressure drop calculation	108–109	147	169–171	173
gravel pack well test	172			
gravity-capillary equilibrium				
WFT pressure survey	700–706			
gravity drainage of oil	771			
gravity segregation				
of condensate	555–556			
<i>notion</i>	768			
retrograde condensation without	550–555			
gravity vertical equilibrium, <i>see</i> vertical				
saturation equilibrium				
GRI, <i>see</i> Gas Research Institute				
Gualdron, A.				
large hole observer	704–706	713–715		1312
Guardia, M.A.				
reserves estimation	454–456			
Gulf of Campeche				
WFT pressure survey in production period	753–754			
Gulf of Mexico				
Burgos field, hydraulic fractures	1111–1113			
permeability and confining pressure	13			
sand control completions	1127			
Troika field, sand control completion	1124		1137	
water drive gas reservoirs	395			
Gulf of Thailand				
standing water column	370			

## Index Terms

## Links

Guppy, K.H.				
apparent fracture conductivity	224			
Gurley, D.G.	175			
<b>H</b>				
Hackney, R.M.				
reserves estimation	454–456			
Hagoort and Blom relative permeability				
weighting function	343–344			
Hagoort, J.	1414			
Haldorsen, H.	909			
Halford, F.				
heavy water gradient	748	749		
supercharging analysis	1351–1355			
supercharging analysis, field example	1355–1357	1358		
Halleck, P.M.				
underbalance effects on perforation flow	134			
Hammerlindl, D.J.	490			
abnormally pressured gas reservoirs	402–406			
Hammond, P.	898			
probe flow shape factor	187	895–896	897	957
	961			
Hann, J.H.				
dynamic aquifer effects	744	745		
Hantush, M.	927			
harmonic decline	622			
Harrington, A.G., <i>see</i> Wong, Harrington and				
Cinco–Ley type curve				
Harris, D.G.	805			
Harris, M.H.	150			
effect of perforation penetration on				
productivity	124	125	126	136
numerical solution to convergence flow				
problem into perforated well				
Harville, D.W.	490			
Hashem, M.N.	1345			
Hawkins, M.F.	490			
equation for skin effect	53–56	137	138	1079–1085

## Index Terms

## Links

Hazebroek, P.	30
HCPV, <i>see</i> hydrocarbon pore volume	
Hegeman, P.S.	989
nonideal wellbore storage model	1415–1417
packer interval response	987–989
slant well model, <i>see</i> Abbaszadeh and Hegeman slant well model	
hemi–pseudoradial flow	219–220
hemispherical flow	
disk aperture	186–187
Heriot–Watt University	
Berea relative permeability	345–347
relative permeability weighting function	343–344
heterogeneity index	180
heterogeneous system	
averaging methods	101–105
effect on RFT–derived permeability	686
perforation completion embedded in	166
Heum, O.R.	
dynamic aquifer effects	746–747
Hewlett–Packard (HP) quartz gauge	728
Higgins–Leighton displacement function	607–608
highly deviated well, <i>see</i> high slant well	
high–permeability straddling lens, <i>see</i> geoskin	
high pressure gas reservoir	490–491
effect of compressibility variation with stress	492–501
field examples	501–503
material balance model	491–492
<i>see also</i> overpressured gas reservoir	
high–rate gas well	
measurement of inertial resistance coefficient	168
non–Darcy flow in fracture	220–226
high slant well	
FEM simulation	1015
packer interval response	997–998
productivity index	1092–1093
WFT pressure survey	819–828

## Index Terms

## Links

Hill, A.D.	831	
Honarpour, M.	516	
Hong, K.C.	150	
nomograms for damage effect estimation	138	
numerical solution to convergence flow problem into perforated well	137	
perforated completion productivity	126	127
horizontal barrier		
detection, in reservoir testing	793–805	
effect on active probe pressure response	961–964	
horizontal barrier transmissibility	808–809	
horizontal flow meter	844–845	
horizontal gas well		
infinite conductivity wellbore	1128–1140	
lumped parameter vertical lift model	1148–1152	
wellbore friction	1140–1148	
horizontal well		
active and observation probe arrangement	992–995	
cementing	90	
coal bed methane	1482–1483	
compartmentalized reservoir, production logging	1107–1108	
compartmentalized reservoir, productivity index	92–101	
completion	90	
deliverability	90–91	96–100
dual-drain, in-fill drilling	1021	
dual packer interval response	987–989	
effect of isolated natural fractures	1101–1107	
general position in a large drainage area, productivity index	82–85	92
gravel pack completion	202–204	
hydraulically fractured	252–255	
hydraulically fractured, in coal bed methane	1483–1491	
hydraulically fractured, transient IPR	271–272	
multiple hydraulic fractures	1119–1120	
nose-to-tail	1154	
productivity index, field examples	87–90	

## Index Terms

## Links

horizontal well ( <i>Cont.</i> )			
observation probe pressure response	989–991		
in rectangular drainage area, pseudo-radial			
skin effect	85–86		
in rectangular drainage area, productivity			
index	76–82	92	
sand control completion	1120–1128		
semi-steady-state deliverability	1086–1094		
transient deliverability	1095–1100		
underbalanced drilling data analysis	1298–1304		
underbalanced drilling data analysis, field			
examples	1304–1308		
in wedge-shaped drainage area,			
pseudoradial skin effect	86–87		
<i>see also</i> horizontal gas well			
Horne, R.N.	1484	1489	1490
Horner plot	678		
average permeability determination	1308–1309		
buildup analysis, underbalanced drilling			
context	1308–1310		
extended buildup in compartmentalized			
reservoir	1192–1193		
total apparent skin from intercept	67–68		
Hower, T.L.			
modified material balance	438–439		
HP quartz gauge, <i>see</i> Hewlett-Packard quartz			
gauge			
Hurst, W.	53	138	425
cumulative influx superposition	428–429		
<i>see also</i> Van Everdingen and Hurst			
infinitesimal skin effect			
hyperbolic decline	622–625		
exponent	643–645		
hydraulic fracturing	74	1109–1119	1120–1121
applications	226–228		
damage mechanisms	211		
finite conductivity, <i>see</i> finite conductivity			
hydraulic fracture			

## Index Terms

## Links

hydraulic fracturing ( <i>Cont.</i> )			
flow convergence	234–244		
gas condensate wells	353		
with gravel packs	244–250		
in situ proppant permeability	219		
limited height fractures	217–219		
non-Darcy effect	220–226		
sand control	1120–1121		
spanning a rectangular drainage area	215–217		
two-stage treatment, <i>see</i> frac-pack completion			
<i>see also</i> massive hydraulic fracturing; multiple hydraulic fracturing of horizontal well			
hydrocarbon			
immobile, detection	706–712		
mobile, detection	712–713		
hydrocarbon pore volume (HCPV)	26	396	498
basic material balance model	491–492		
compositional material balance	511–517		
gas cap	541–543		
<b>I</b>			
idealized cellular system			
complex material balance	1189–1192		
Iffly, R.			
critical gas saturation	531		
imbibition capillary pressure curve	1325		
immiscible relative permeability curve	342–343		
improved oil recovery (IOR)	1020		
incompressible flow			
two-phase	302–309		
incompressible fluid			
steady-state linear flow	8–13		
steady-state radial flow	15–18		
India			
Tapti field, rate-dependent skin data	183	184	



## Index Terms

## Links

Indonesia			
exploration well, WFT pressure survey	711		
inertial resistance, <i>see</i> rate-dependent skin effect/ factor			
inertial resistance coefficient, <i>see</i> rate-dependent skin coefficient			
in-fill drilling	1019–1022		
infinite acting radial flow	23		
aquifer model	426–428		
infinite conductivity boundary condition	64		
infinite conductivity fracture			
<i>notion</i>	204–205		
pseudo-radial skin effect	205–207		
rate-time production decline type curve	656	664	
infinite conductivity wellbore			
horizontal gas well deliverability	1128–1140		
infinite conductivity vertical fracture			
pseudo-radial flow	75–76		
inflow performance			
high production rates	106–115		
perforated completion	139–140		
under semi-steady-state radial flow	34		
under steady-state non-Darcy flow	107–108		
under steady-state radial flow	20	114	
inflow performance relation (IPR)			
composite	866–868		
incompressible two-phase flow	308		
<i>notion</i>	3–4		
Peaceman model	376–380		
quadratic	110–111		
with vertical lift performance, effect on well rate	338	367–368	474–479
well inflow performance diagram	20		
<i>see also</i> gas well inflow performance relation; oil well inflow performance relation			
in-fracture flow convergence	234–244		
injection fall-off test			
coal bed methane wells, field example	1407–1410	1417–1433	1444–1445
formation damage	46		

## Index Terms

## Links

in situ proppant permeability	219			
instruments and devices				
borehole video camera	874			
bridge plug	1060–1061			
cased-hole wireline formation tester	847–849	1063–1064		
dual probe wireline formation tester	909	910	911–912	
Hewlett-Packard quartz gauge	728			
horizontal flow meter	844–845			
minipermeameter	681	682		
modular dynamic tester	668	676	681	711–712
	729			
multiprobe formation tester	909			
permanent downhole gauge	1122–1124	1481		
production logging device, <i>see</i> production logging device				
repeat formation tester, <i>see</i> repeat formation tester				
sand detection monitor	1123–1124			
strain-type pressure gauge	688	727–728	778	779
wireline formation tester, <i>see</i> wireline formation tester				
intelligent well	1152–1157			
interblock productivity index, <i>see</i> interblock transmissibility index				
interblock transmissibility index	800–801	809–810	1231	
interference test				
areal permeability anisotropy	1466–1481			
based on distributed pressure measurement	765–766			
IOR, <i>see</i> improved oil recovery				
IPR, <i>see</i> inflow performance relation				
Iran				
exploration well, WFT pressure survey	720			
Marun field, WFT pressure survey	780–781			
Mishrif, Sirri and Fateh fields, hydrocarbon accumulations	741			
open-hole completion	117			

## Index Terms

## Links

isochoric flash			
black oil model as	519–520		
calculation, dry gas reservoir	582–583		
calculation, solution gas drive	512–518		
calculation, undersaturated oil reservoir	575		
two region problem	538	556	559
isothermal flash	512–513	521	538

## **J**

Jacob and Lohman's constant terminal pressure				
solution	617–618	1260–1262	1267–1269	
Jackson, M.D.	1318	1357		
Jaeger, J.C.	688	875	911	992–993
Jensen, C.L.	694			
jet perforation	117–124	136		
Jewel, S.	28–29	494	497	
Johnson, H.D.	734–735			
Jones equation/formulation	167	296		
Jones, L.G.	67	167		
Jones, R.E.				
modified material balance	438–439			
Jorgensen, L.N.				
dynamic aquifer effects	744	745–746		
Juhasz, I.	898			

## **K**

Karakas, M.	151			
Kardolus, C.B.				
noncommunicating progressive layer				
model and boundary element model				
comparison	1273–1274			
Katz and Firoozabadi correlation for inertial				
resistance coefficient	109	164	168	
Katz, D.L.	465			
Kaufman, G.	792			
Keelan, D.K.				
residual gas saturation measurement	458			
Kharusi, M.S.	1106			

## Index Terms

## Links

King, G.E.				
underbalance effects on perforation flow	134–135			
Klotz, J.A.				
mud fluid loss rates	672–674	1358–1359	1360	1367
	1368			
perforated completion productivity	126	127		
Kucuk, F.J.	992			
<b>L</b>				
Lake, L.	909			
laminar-inertial-turbulent (LIT) analysis	296			
Laplace space convolution				
radial aquifer model	432–434			
large hole observer	704–706			
oil wet conditions	713–715			
Larsen, L.				
observation probe pressure response	930–931	952		
Larsen plot				
skin change during drawdown	882			
Lasmo	1156	1454		
layered compartmentalized system				
composite IPR	272–274			
production logs	832–837			
production logs in single-phase situations	853–860			
production logs in two-phase situations	863–871			
zonation	845–846			
layered system				
analogy between compartmentalized system and	100			
arithmetic average permeability	101–104			
displacement model	604–609			
<i>see also</i> layered compartmentalized system;				
multilayered system; three-layer system;				
two-layer system				
layered well test				
using production logging devices, <i>see</i>				
production logging: applications				
layer initial pressure				
direct measurement	847–850			

## Index Terms

## Links

layer potential	1274–1276			
layer skin factor distribution	842–845			
LCM, <i>see</i> loss control material				
leaky trap hypothesis	1373	1374		
Lee, R.L.	465			
Leighton, A.J., <i>see</i> Higgins-Leighton displacement function				
Leung, K.H.	435			
non-Darcy effect in high-rate fractured gas wells	222	223–225		
level-by-level model	1347	1352–1353		
Levenberg-Marquardt algorithm	419–420	447	449	633
estimation of permeability and pressure distribution	1289–1291			
estimation of permeability and pressure distribution, synthetic problem	1291–1294			
parameter estimation	1196	1218		
Lewis, R.C.	458			
Libya				
Bu Attifel field, selective inflow performance	855	857		
Elephant field, deep drilling solids invasion	1454			
Elephant field, formation damage	47	1081		
horizontal well	1107	1108		
limestone reservoir				
fine migration and formation damage	57–58			
limited entry	193–194			
deviation from true radial flow due to effect on completion skin effect	61–64			
effect on completion skin effect	193–195			
homogenous reservoir with progressive penetration, underbalance drilling context	1294–1298			
horizontal well compartment	96–97			
observation probe pressure response	926–937			
open-hole gas well	288–289			
partially completed well	113–114			
productivity of well with slant well, effect on completion skin effect	68			
slant well, effect on completion skin effect	199–201			
limited entry fracture	236–237			

## Index Terms

## Links

limited height fracture	217–219			
linear aquifer	444–446			
linear flow				
channel reservoir, transient IPR	271			
end faces	1204–1206			
generalized complex material balance	1208–1215			
gravel-packed perforation tunnel	169–176			
horizontal well in a closed rectangular drainage area	79–81			
rectangular geometry, semi-steady-state conditions	1202–1204			
line drive waterflooding pattern				
displacement curve	603			
liquid dropout curve				
compositional gas condensate reservoir	323	326–328	331	333
liquid phase compressibility				
compositional material balance	523–524			
liquid solution decline type curve	651–652			
LIT analysis, <i>see</i> laminar-inertial-turbulent analysis				
local permeability estimation				
using WFT	677–681			
Locke, S.	137	150		
nomogram for perforation skin effects	151–152			
perforated completion productivity	126	127		
relation between CFE and crushed zone thickness	122	123		
log-log derivative diagnostic plot				
observation probe pressure response	918	919		
spherical flow situations	885–886			
Lohman, S.W., <i>see</i> Jacob and Lohman's constant terminal pressure solution				
Longeron, D.G.				
mud fluid loss characteristics	1363–1365	1371		
longitudinal hydraulic fracture	1485–1488			
loss control material (LCM)				
effect on gravel pack skin	176–179			
types	176			

## Index Terms

## Links

low permeability reservoir				
buildup period	888–889			
hydraulic fracturing versus horizontal				
drilling	1089			
supercharging problem	671–676			
transient production	1020			
<i>see also</i> fractured well; horizontal well				
lumped parameter material balance model	805–814	1166–1167		
lumped parameter vertical lift model				
horizontal gas well deliverability	1148–1152			
lumped parameter wellbore model	1246–1256			
Lutes, J.L.	458			
<b>M</b>				
Madaoui, K.				
critical gas saturation	531			
Maersk Oil	1099	1110	1119	
major time step	483			
Mansoori, J.				
rock compressibility in coal beds	1401–1402			
stress-dependent permeability in coal beds	1383–1384	1387	1391	1395
	1423	1426	1427	
Maracit gel treatment	1070			
Maraseal gel treatment	1070–1071			
Marathon Oil Company	1070			
margin	483			
Markland, J.T.				
evaluation of massive hydraulic fractured				
wells	228–233			
Marquardt, D., <i>see</i> Levenberg-Marquardt				
algorithm				
Marting, V.E., <i>see</i> Brons and Marting correlation				
Mason, J.N.E.				
effective perforation length	188–192			
<i>see also</i> Pucknell and Mason correlation				
Massie, J.	783	795		
massive hydraulic fracturing (MHF)	253	1114		
applications	228–233			

## Index Terms

## Links

material balance iteration including swing	486–487	
material balance method, <i>see</i> complex material balance; gas material balance; general mechanistic reservoir material balance		
material balance shooting	479–481	
matrix acidization	157	
Matthews, Brons, and Hazebroek (MBH) method	400	
Matthews, C.S.	30	
Mavor, M.J.	1451	
injection and falloff, field example	1407–1410	1417–1433
Mayson, H.J.	694	
MBH method, <i>see</i> Matthews, Brons, and Hazebroek method		
McDaniel, B. proppant permeability	219	
McGuire and Sikora correlation	214	
McLeod, H.O.	155	
approximate model for perforated well productivity	142	161
McPhee, C.	316	
MDT, <i>see</i> modular dynamic tester		
measurement error		
depth measurement error	727	
flow measurement error effect on parameter estimation	1293–1294	
influence on gradient determination	757–758	778–779
influence on observed pressure gradient intersection	732–733	
rate measurement error	413	
zonation	845–846	
measurement while drilling (MWD) log horizontal well	1087–1088	
mechanical skin	156	191
MFH, <i>see</i> multiple hydraulic fracturing of horizontal well		
MHF, <i>see</i> massive hydraulic fracturing		



## Index Terms

## Links

### Middle East

carbonate reservoirs, thick oil-water				
transitions	1357–1358			
gas reservoir, edge water drive	471			
horizontal wells, acid treatment	1093–1094			
intelligent wells	1154–1155			
limestone reservoir, formation damage	57–58			
nose-to-tail horizontal wells	1154			
profile control	851			
reserve estimates	1087			
reservoir characterization, underbalanced				
drilling data analysis	1305–1308			
<i>see also</i> Abu Dhabi; Iran; Oman; Qatar; Saudi Arabia				
middle time region (MTR)	883–884	985	1192	1261
Mijnssen, C.				
horizontal well development	1105–1107			
Miller, F.G.	72–73	196		
effect of limited entry and slant well	199–200			
mini-drill stem test (DST)				
with straddle packer WFT	909	911		
with straddle packer WFT, coal bed methane appraisal	1492–1495			
with straddle packer WFT, depth of investigation analysis	976–979			
minimum economic rate	625			
minipermeameter	681	682		
minor time step	483			
miscible relative permeability curve	342–345			
mixed-wet	1357			
mobility	7			
Mobil Oil	1119	1484		
modular dynamic tester (MDT)	668	676	681	711–712
	729			
use, field examples	937–944			
Mons, F.	1018			

## Index Terms

## Links

Moore, R.L.			
determination of effective vertical permeability	782–783		
Moran, J.	875–876	877	
Morrison and Duggan correlation for inertial resistance coefficient	168		
MTR, <i>see</i> middle time region			
mud filtrate invasion	47–49		
effect on WFT measured pressure	1311–1312		
field example	1372–1375		
modeling	1358–1371		
natural fractures	1454		
Stewart and Phelps' model	1312–1320		
<i>see also</i> oil-based mud; supercharging; water-based mud			
multilayered system	390–393		
well performance diagram	853–855		
multiple hydraulic fracturing of horizontal well (MFH)	1119–1120		
hemi-pseudoradial flow	219–220		
multiple wells			
areal anisotropy, determination by interference test	1466–1481		
areal pressure variation	417		
displacement model	610–614		
drainage areas and virtual no-flow boundaries	30–34		
WFT pressure survey	727–733		
multiprobe formation tester			
permeability determination	944–948		
pressure response	909		
multirate test			
gravel-packed oil wells	178		
oil wells	360		
Muskat, M.	64	69	877
flow behavior analog study	139	150	
two-phase pseudopressure	312	313	
MWD log, <i>see</i> measurement while drilling log			

## Index Terms

## Links

### N

Nadir, F.T.

WFT pressure survey usage 765 783–788

naturally fractured reservoir

skin effect 1452–1454

WFT 738–739

natural water influx 443

complex material balance method 1178–1180

material balance method 413–417

negative rate excursion 1267–1271

negative skin effect/factor 53

Netherlands

field example, unusual measured well inflow  
performance 1074–1075

Groningen field, observations wells in a gas  
reservoir 503

Groningen field, well clusters 42–43 375 380

new-generation wireline formation tester

(NGWFT) 1312

applications in coal bed methane wells 1492–1495

with dual packer assembly 1063 1064

permeability estimation 937–944

NGWFT, *see* new-generation wireline formation

tester

Nigeria

Vrij field, retrograde condensation 552 554

nodal analysis

gas wells 367–368

*notion* 5

nodal analysis software

vertical lift performance 642–643 650–651

*see also* Wellflo software

no-flow boundary

compartmentalized horizontal wells 93–97 100–101

multiple well situations 30–34

Noik, S. 853

Noman and Archer correlation for inertial

resistance coefficient 168

## Index Terms

## Links

nominal decline rate	628		
nomogram			
damage effect estimation	138		
perforation skin effects	151–152		
non-Darcy flow			
approximate model for inflow into perforated completion	159–163		
flow shape factor for spiral pattern	163–166		
gas condensate well IPR	351–352		
gas condensate well IPR, in steady-state spherical situation	320–323		
gas well IPR	285–292		
hydraulically fractured wells	220–226		
influence of damaged zone including oil field units	111–113		
oil field units	109–111		
open-hole completion	166–167		
pressure drop	187–188	191–193	238–241
well inflow performance, in steady-state radial situation	107–108		
nonideal wellbore storage			
Hegeman model	1415–1417		
Van den Hoek model	1410	1414	1420
nonintersecting fracture			
analytical model	979–983	986–987	
numerical simulation	983–985		
nonlinear regression			
Arps empirical hyperbolic decline function	622–623		
complex material balance	1218–1219		
compositional material balance	533–534		
observation probe pressure response, dual permeability model	949–950		
material balance	411–413	474	
secondary gas cap evolution	549		
Slider's hyperbolic decline	624–625		
normalized pseudopressure	277–280		
coal bed methane, stress-dependent permeability	1378–1381		

## Index Terms

## Links

normalized pseudopressure (*Cont.*)

coal bed methane, constant rate drawdown

analysis

1391–1393

p2 form

293–296

299

North Sea

Alba field, area variation of reservoir

pressure

100

Beryl field, WFT pressure survey

788–792

Brae field, asphaltene deposition

1084

Brae field, selective inflow performance

860

Brae field, WFT pressure survey

815

Brent field, depressurization

1077–1078

Brent field, sand control method

1120–1121

Britannia field, gas condensate well IPR

347–350

chalk reservoir, pore collapse

494

496–497

Claymore field, hydrochloric acid treatment

157

Claymore field, pressure maintenance

1075–1077

Clyde field, 3D seismic measurement

1020

compartmentalized reservoirs, complex

material balance

1197

Cormorant field, WFT pressure survey

815–816

Dunbar field, 3D seismic measurement

1021

Dunlin field, WFT pressure survey

784

787

788

Ekofisk field, effect of formation compaction

27–28

Ekofisk field, 3D seismic measurement

1021–1022

Ekofisk field, WFT pressure survey, constant

pressure boundary effects

985–986

Ekofisk field, WFT pressure survey, dynamic

aquifer effects

744

Ekofisk field, WFT pressure survey, naturally

fractured reservoir

738–739

exploration well, RFT pressure survey

718–719

exponential decline

637–638

field development, WFT pressure survey

777

781

782–792

815–818

Forth field, loss control material use

176

177–178

Forties field, use of bridge plugs

1060–1061

Frigg field, influence of windows in barriers

1065–1066

Fulmar field, perched water contact

734–735

## Index Terms

## Links

### North Sea (*Cont.*)

gas reservoirs, capillary pressure effects	1337–1338	1343–1344
gas reservoirs, enveloped high permeability streaks	450–452	
Gullfaks field, frac-pack completion	250	
Gullfaks field, high-shot density perforation	173	
hydraulic fracturing of permeable oil wells	214	
Kraka field, dynamic aquifer effects	744	745–746
layered systems	604–605	
Leman gas field, massive hydraulic fracturing	228–233	
Magnus field, WFT pressure survey, horizontal barrier detection	803–804	816–817
Miller field, depletion by pressure decline	699	
Montrose field, WFT pressure survey	782–783	
Murchison field, compartmentalized complex material balance	1200–1201	1225
Murchison field, WFT pressure survey	783–784	795 809–810
multirate testing of gravel-packed oil wells	178	
Ninian field, flow profile match	838	839–840
Ninian field, WFT pressure survey	817–818	
North Viking Graben reservoir, profile control	851	
North Viking Graben reservoir, WFT pulse test perforated completions	794–795 117	
Pickerill field, perched water contact	735–737	
Piper field, production logging survey	838	840
Piper field, synthetic production logging	873	
Piper field, WFT pressure survey	772–774	
productivity index of wells	20	
Ravenspurn field, hydraulic fracturing	1117	
Ravenspurn field, stimulation of fractured wells	220	224
scale deposition problem	152–153	
Sleipner field, WFT pressure survey	674–676	
South East Forties field, WFT survey	1372–1375	
Tistle field, gel treatment	1070	
Tistle field, Mast project	1020	
Tistle field, WFT pressure survey	783–788	793

## Index Terms

## Links

### North Sea (*Cont.*)

Tistle field, WFT pressure survey, fault transmissibility	802–803			
Ula field, WFT pressure survey, dynamic aquifer effects	746–747			
Valhall field, effect of rock compaction	28	29	494	497
Wytch field, WFT pressure survey, high slant well	819–820	823–826		

### Norway

chalk fields, rock compaction	29			
Ekofisk field, effect of formation compaction	27–28			
Ekofisk field, 3D seismic measurement	1021–1022			
Ekofisk field, WFT pressure survey, dynamic aquifer effects	744			
Ekofisk field, WFT pressure survey, naturally fractured reservoir	738–739			
field example, WFT-derived permeability interpretation	930–931			
Frigg field, influence of windows in barriers	1065–1066			
Gullfaks field, use of high-shot density perforation	173			
multirate testing of gravel-packed oil wells	178			
Osberg reservoir, gas injection	1019			
Sleipner field, WFT pressure survey	674–676			
Snorre field, foam-water-alternating-gas application	1019			
Troll field, superwell configuration	390			
Troll field, wellbore friction effect on horizontal well deliverability	90–91	98–99		
Ula field, WFT pressure survey, dynamic aquifer effects	746–747			
Valhall field, effect of rock compaction on	28	29		

### numerical simulation

baffle	952–954			
finite conductivity fractures	1114			
mud filtrate invasion process	703	1320–1332		
Peaceman well model	376–380			
<i>see also</i> finite element method numerical simulation				

## Index Terms

## Links

### O

OBM, *see* oil-based mud

observation well

extended production testing 1481–1482

gas reservoirs 503

interference testing to determine areal

anisotropy 1466–1481

WFT pressure survey 751

WFT pressure survey, identification of

permeability barriers 760–762

observation probe pressure response

effect of anisotropy on 917 994–995 1006 1013–1014

horizontal well 987–991

horizontal well, active-observation probe

arrangement 992–995

slant well with limited entry 1013–1014

vertical wells 909–926 999–1000

vertical wells, dual permeability model 944–952

vertical wells, dual permeability numerical

model 950–954

vertical wells, limited entry model 926–937

observed pressure gradient intersection (OPGI) 1312 1334–1338

anomalies between log contacts and 723–727

large hole observer theory 704–706 722

quality control 1349–1350

Occidental 1154

ODE, *see* ordinary differential equation

offshore development

well deliverability and 2–3

oil-based mud (OBM)

fluid loss characteristics 1363–1365 1371

invasion process 1320

invasion process, field examples 1343–1346

invasion process, simulation 1328–1332

*see also* water-based mud

oil reservoir

material balance formulation, *see* general

mechanistic reservoir material balance



## Index Terms

## Links

oil well				
capillary pressure effects, field examples	1341–1343			
producing below the bubble point	354			
skin effect analysis	201–202			
oil well inflow performance relation (IPR)				
composite IPR of stratified system	272–274			
single layer IPR for semi-steady-state conditions	261–264			
transient	265–272	370		
OLGA software				
applications in underbalanced drilling	1246	1257–1259		
validation of lumped parameter wellbore model	1255			
Oman				
carbonate reservoir, p/z plot	400–401			
horizontal well cementing	90			
Yibal field	1154			
Yibal field, massive horizontal well development	1105–1107			
Onur, M.				
flow regimes of slant wells with straddle packer	999–1002	1006		
OOIP, <i>see</i> original oil in place				
open-hole completion				
fractured limestone reservoirs	117			
horizontal wells	1125–1127			
non-Darcy flow	166–167	288–289	295–296	
open-hole wireline formation pressure measurement	681			
OPGI, <i>see</i> observed pressure gradient intersection				
ordinary differential equation (ODE)				
numerical integration	341–342	406–407	408–409	435
	462			
ordinary differential material balance equation	459–462			
applications	465–474			
synthetic test problem	463–465			
original oil in place (OOIP)	26			

## Index Terms

## Links

Osborne, M.J.				
overpressure	748–749			
outcropping radial aquifer	443–444			
Ovens, J.				
evaluation of massive hydraulic fractured wells	228–233			
overbalance	161–162			
<i>notion</i>	48			
overpressured gas reservoir				
abnormally pressured	402–406			
detection	748–749			
<i>see also</i> high pressure gas reservoir				
Owens, K.A.	252	253–254		
Oyeneyin correlation				
gravel inertial resistance coefficient	175	176		
<b>P</b>				
p2 approach	293–296			
Pagan, C.				
clay smearing	798			
Pakistan				
gas reservoir, capillary pressure effect	1334–1336			
Palacio, J.C.	651	654		
paleocontact				
detection by WFT pressure survey	708–709	710	717–720	
<i>notion</i>	708			
Palmer, I.				
rock compressibility in coal beds	1401–1402			
stress-dependent permeability in coal beds	1383–1384	1387	1391	1395
	1423	1426	1427	
PanMesh software				
active probe response	958–961			
areal anisotropic reservoir simulation	1467–1469			
limitation	1009	1013		
wellbore storage	954			
PanSystem software				
forecasting	1099	1433–1437		

## Index Terms

## Links

PanSystem software ( <i>Cont.</i> )				
observation probe pressure response, limited entry model	927			
Panflow module	1269–1271			
ProbeProbeActive	968			
slant well model	998	1002		1005
stress-dependent permeability and porosity	1385–1387			
stress-dependent permeability and porosity, pseudo model	1390–1410			
<i>see also</i> PanMesh software				
Papadopoulos, I.S.	1466–1467			
parameter estimation	473–474	976		1012–1013
nonlinear techniques	1215–1220			
Parker, M.A.				
proppant permeability	219			
partial completion				
effect(s)	61–64			
effect on deviated wells	72–73			
formation damage and	64–68			
well inflow performance at high production rates	113–114			
partial inverse transmissibility	1206–1207			
partially communicating fault (PCF)	783–784	809–810		1162 1226
areal anisotropy of observation well	1471–1472			
detection, WFT pressure survey	795–805			
partial performance index	392			
particulate-based loss control material (LCM)	176			
PCF, <i>see</i> partially communicating fault				
PDG, <i>see</i> permanent downhole gauge				
PDVSA	1018	1066		
Peaceman probe radius	1459	1462		
Peaceman well model	376–380			
Pedersen	333			
penetration depth, <i>see</i> depth of penetration				
perched water contact	725–727	733–738		
Perez, C.	1156			

## Index Terms

## Links

perforated completion	1079–1086	1081–1085	
API RP 43 test	118–120	128–134	
jet perforation	117–124	136	
productivity	124–127		
quantities that control behavior	123–124		
skin effect	136–138		
skin effect approximate model	138–193		
skin effect approximate model, applications	255–258		
tubing conveyed perforation	141	142	
underbalance effects	134–135		
perforation damage	152–155		
perforation length			
alternative approach	192–193		
Pucknell and Mason approach	188–192		
perforation velocity	179–184		
Perkins, F.M.	610		
Perkins-Kern-Nordgren (PKN) fracture model	222–223		
permanent downhole gauge (PDG)	1122–1124		
production data analysis	1481		
permeability			
average, <i>see</i> average permeability			
core plug	9	1083–1084	
detrital rock	10–11		
effect of confining pressure on	11–13		
estimation, historical background	681–682		
estimation from core data	102–105	690–691	693–698
estimation from log data	11	1289–1290	
estimation, underbalanced drilling data analysis	1284–1308		
estimation, WFT, <i>see</i> wireline formation			
tester-derived permeability			
formation, <i>see</i> formation permeability			
impairment, reasons	46		
porous medium	5–13		
proppant	219		
sand pack	9–12		
spherical	148	150	679–681
stress-dependence, <i>see</i> stress-dependent			
permeability and porosity			

## Index Terms

## Links

permeability barrier			
identification, WFT pressure survey	760–768	785–787	792
Peru			
produced reservoir, WFT pressure survey	752		
Petroleum Development Oman	90		
Phelps, G.	780		
mud filtrate invasion model	1312–1320		
piecewise linear approximation (PLA)	387	630–631	
conversion of step-rate schedule to	633		
convolution process	433		
piecewise linear rate schedule	1174–1175		
pin-point fracturing	1118–1119		
piston displacement			
approximation	465–466		
gas cap expansion	541	557–558	
layered reservoir	604–605		
water drive	599–600		
PKN fracture model, <i>see</i> Perkins-Kern-Nordgren			
fracture model			
PL, <i>see</i> production logging			
PLA, <i>see</i> piecewise linear approximation			
planimetry	263		
PLD, <i>see</i> production logging device			
plugged perforation	161–162	165–166	843–844
effective penetration ratio and	256–257		
PNC log, <i>see</i> pulsed neutron capture log			
point source			
isotropic medium	876		
vertical observation probe and	909–926		
pore collapse	29	494–497	500–501
pore volume	403–405	412–413	459–460
high pressure gas reservoirs	491–501		
porous medium			
radial flow	1–5		
semi-steady-state-radial flow	22–36		
steady-state radial flow	14–22		
post-fracture test	228–230	1111	

## Index Terms

## Links

Prats, M.	75	81	83	205
	237			
fracture deliverability	1109–1111			
pressure approach	365			
pressure drop				
calculation	168			
frictional	91	96–100		
gravel-packed perforation tunnels,				
calculation	108–109	147	169–171	173
non-Darcy flow	187–188	191–193	238–241	
pure radial flow	149			
skin pressure drop	47	52–53	54	
<i>see also</i> drawdown				
pressure transient analysis (PTA)				
integration with production logging	851			
integration with production logging and core				
analysis	871–873			
Press, W.H.	469			
Price, H.S.	690			
primary gas cap				
evolution of secondary gas cap in presence of	539–545			
probe radius formula, <i>see</i> Peaceman probe radius				
produced reservoir				
WFT pressure survey, applications	751	755–777		
WFT pressure survey, field examples	752–755			
production constrained convolution	1220–1225			
production constrained depletion	481–482	615		
production decline analysis	1377–1378			
production engineering				
reservoir engineering and	1017–1019			
production enhancement	1017			
production forecast				
coal bed methane wells	1433–1437			
production logging (PL)	831–837			
applications	833	838–852		
applications, single-phase situations	360	853–860		
applications, two-phase situations	863–871			

## Index Terms

## Links

production logging device (PLD)	831	839
borehole video camera	874	
production logging device (PLD) survey	831	
production optimization	1017–1019	
completion efficiency and <i>notion</i>	1079–1086 1017	
productivity		
bounded drainage area	36–45	
effect of perforations on	117–138	
effect of permeability thickness product on with skin effects	19–20 58–61	
productivity index (PI)		
fractured well	74–76	
high slant wells	1092–1093	
horizontal well in a closed rectangular drainage area	76–82	
horizontal well in compartmentalized reservoir	92–101	
horizontal well in general position in a drainage area	82–85	
horizontal wells, field examples <i>notion</i>	87–90 2	20
oil wells	263–264	
steady-state radial flow	19–20	
North Sea wells	20	
productivity ratio, <i>see</i> flow efficiency		
profile control	843	851
pseudopressure		
material balance in terms of normalized pseudopressure, <i>see</i> normalized pseudopressure	1231–1237	
real gas	275–285	
three-phase flow	371	374–375
two-phase compositional flow	323–329	
two-phase incompressible flow	309–311	
pseudo-radial skin effect/factor		
fractured wells	74–76	
finite conductivity fractured wells	204–214	

## Index Terms

## Links

pseudo-radial skin effect/factor ( <i>Cont.</i> )				
horizontal wells	83–87			
infinite conductivity fracture	205–207			
pseudo-skin effect/factor				
Brons and Marting's	62–64	71	73	113–114
	194			
due to well deviation	72–73			
pseudo-time	654–655			
material balance in terms of	1231–1237			
PTA , <i>see</i> pressure transient analysis				
Pucknell and Mason correlation				
gravel inertial resistance coefficient	175–176			
Pucknell, J.K.				
calculation of total skin effect	198			
effective perforation length in gravel pack	188–192			
Pugh, V.J.				
residual gas saturation measurement	458			
pulsed neutron capture (PNC) log	450–452	470–471		864

## **Q**

### Qatar

Al Shaheen field, transient production				
decline	1099–1110			
horizontal wells	1103–1105			
North field, WFT pressure survey	725–727	733		
North field, WFT pressure survey, dynamic				
aquifer effects	740–744			

## **R**

Radcliffe, D.	681	685		691
WFT-derived permeability interpretation	897–900	959		1340
radial aquifer model				
aquifer influence functions	421–425			
classical cumulative influx superposition	428–432			
Dake's test problem	435–438			
effect of the invaded zone	438–443			
Fetkovich model	434–435	437–438		
infinite-acting behavior	426–428			



## Index Terms

## Links

radial aquifer model ( <i>Cont.</i> )				
Laplace space convolution	432–434			
material balance	425–426			
outcropping aquifer	443–444			
radial flow				
Darcy's law	106			
porous media	1–2			
deviation due to limited entry	61–68			
liquid solution decline type curve	651–652			
models	2			
rate-cumulative production decline type curve	657–663			
steady-state, <i>see</i> steady-state radial flow				
transient IPR	268–270			
well performance diagram	2–5			
radius of investigation, <i>see</i> depth of investigation				
Raghavan, R.	1378–1379	1400		
reservoir integral	1381			
steady-state pseudopressure approach	1382			
Ramesh, B.A.				
modification of Peaceman well model	379–380			
Ramey, H.J.	64	72–73	458	1410
	1466	1479		
effect of limited entry and slant well	199–200			
rate-dependent skin coefficient	7	222		
commercial proppants	1115–1116			
correlations	108–109	167–168		
evaluation using crushed zone permeability	161			
gravel pack sand	175–176	1125–1127		
high gravel pack skin and	173			
non-Darcy flow	285			
rate-dependent skin effect/factor	111–112	160	183	184
	223–224	239	1083–1084	
<i>notion</i>	108	1083		
rate-dependent relative permeability curve	339–350			
rate measurement error	413			
rate schedule	1174–1175			
Rawlins and Schellhardt method	301			

## Index Terms

## Links

real gas pseudopressure	275–285		
realization	104		
real option economic analysis, <i>see</i> Black and Scholes model			
real-time convolution algorithm			
computation of stress-dependent permeability and porosity along with wellbore storage	1411–1414		
rectangular drainage area			
Dietz shape factors	40–43		
horizontal well, pseudo-radial skin effect	85–86		
horizontal well, productivity index	76–82	92	
hydraulically fractured well spanning	215–217		
well in general position	382–383		
recycling	556–563		
with displacement model	563–569		
Reese, D.E.			
high pressure gas reservoir	494	496	498–501
relative permeability curve	303–304	1318–1319	
gas-oil	314–316		
gas-water	360–362		
immiscible	342–343		
miscible	342–345		
rate-dependent	339–350		
Whitson and Fevang's	339		
<i>see also</i> gas condensate relative permeability curve			
ReO production simulator	1017–1018	1084	
repeat formation tester (RFT)	667–668	676	
<i>see also</i> wireline formation tester			
repeat formation tester (RFT)-derived			
permeability	681	697–698	
analysis methods	690–693		
buildup versus core permeability	695–697		
drawdown versus core permeability	693–695		
interpretation	682		
interpretation, buildup analysis	684–685		
interpretation, drawdown analysis	682–683		

## Index Terms

## Links

repeat formation tester (RFT)-derived ( <i>Cont.</i> )			
interpretation, drawdown versus buildup	685–688		
interpretation, new developments	688–689		
reserves estimation			
gas reservoir material balance method, case studies	452–456		
reservoir			
description for a layered compartmentalized system	832–834		
description, WFT pressure survey	779–792		
description, underbalanced drilling context	1241–1242		
reservoir flow	1		
<i>see also</i> radial flow			
reservoir heterogeneity			
averaging methods	101–105		
reservoir integral	1381		
reservoir limit test			
aquifer parameter identification	449–450		
classic theory	1159–1160		
importance	792		
reservoir pressure			
above dew point	549–550		
below bubble point	575–577		
monitoring using WFT	1161		
reservoir simulator			
identification of permeability barriers	767–768		
reservoir testing	781		
horizontal barrier detection, WFT pressure survey	793–805		
reservoir tilting			
effect on water-oil contact	699	708	717–718
reservoir unit, <i>see</i> field unit			
residual gas saturation	457–458		
residual oil saturation			
effect of, detection by WFT pressure survey	706–712		
retrograde condensation			
without gravity segregation	550–555		
RFT, <i>see</i> repeat formation tester			

## Index Terms

## Links

Riboud, J.	1018			
Richardson, J.	1068			
Richardson, J.G.	610			
Robinson, B.M.				
effective fracture length	1111–1113			
Robinson, J.	198			
Robinson, J.C.				
hydraulic fracture stimulation	227–228			
rock compaction	28–29	494–495		497
observations wells to monitor	503			
rock mechanics	12			
coal beds	1417–1418			
implications for fracturing	232	253–255		1111
stress-dependent permeability and porosity	1390–1392			
Roodhart, L.P.	250			
effect of proppant size on fracture				
conductivity	251–252			
Rowan, G.	809			
Rowland, D.A.	67	137		
RP 43 test, <i>see</i> American Petroleum Institute test:				
shaped charge performance				
Runga-Kutta method				
formulation of complex material balance	1175–1177			
ordinary differential equation integration	286	321	342	408–409
	435	462	469–470	486
<b>S</b>				
Saidi, A.M.	531			
Samaniego, F.				
pseudopressure approach	1379–1380			
steady-state pseudopressure approach	1382			
stress-dependent permeability and porosity	1384–1387			
sand consolidation treatment				
skin effect calculation	53–56			
sand control completion	1120–1128			
sandface shutoff treatment	1060–1061			
<i>see also</i> crossflow reservoir				

## Index Terms

## Links

sand pack				
inertial resistance coefficient	108–109			
permeability, calculation	9–12			
Santos	1118			
saturation vertical equilibrium, <i>see</i> vertical				
saturation equilibrium				
Saucier criterion	251			
Saudi Arabia				
field example, tar mat detection	715–716			
Ghawar field, production log	839	841	1101	1102
Ghawar field, workover program	1071–1074			
Saulsberry, J.L.	1451			
scale deposition	152–153			
Scandpower	1246			
Schellhardt, M.A., <i>see</i> Rawlins and Schellhardt				
method				
Schilthuis, R.J.				
classical material balance equation for an oil				
reservoir with a gas cap	510–512			
Schlumberger	853	1018	1156	
CHDT	1063–1064			
horizontal flow meter	844–845			
MDT tool	668	676	681	711–712
	729	937–944		
repeat formation tester	667			
Schmidt-Wenzel equation				
prediction of gas compressibility factor	398			
Schulte, A.M.	333	335		
SDPP, <i>see</i> stress-dependent permeability and				
porosity				
sealing fault	268	270	785	1226
secant method	523			
average permeability determination	1280–1282			
material balance shooting	480–481			
secondary gas cap				
addition of coning model	545–548			
inclusion of primary gas cap	539–545			
nonlinear regression	549			

## Index Terms

## Links

secondary gas cap ( <i>Cont.</i> )			
upward percolation of free gas	535–539		
seismic measurement	1018	1020	1021–1022
selective inflow performance (SIP) technique	360	852	
borehole video camera	874		
coning situations	1066–1069		
crossflow reservoir	1062–1066		
depressurization	1077–1078		
gas well quadratic IPR	861–863		
gel treatment	1069–1071		
integration with transient well testing and core analysis	871–873		
pressure maintenance	1074–1077		
shutoff treatments	1060–1061		
single phase flow	853–860		
through tubing casing patch	1069		
two-phase flow	863–871		
workover field example	1071–1074		
selective interval test			
measurement of layer initial pressure	849–850		
semi-steady-state (SSS) deliverability			
horizontal wells	1086–1094		
semi-steady-state (SSS) depletion	23	1159–1160	
circular closed reservoir with a central well	23–26		
decline curve analysis	645–651		
semi-steady-state (SSS) differential depletion			
permeability barriers	762–767	793–794	
semi-steady-state (SSS) gas well deliverability	1382–1383		
semi-steady-state (SSS) inflow			
oil wells, single layer IPR	261–265		
semi-steady-state (SSS) inflow equation			
generalized form	37–40		
semi-steady-state (SSS) linear flow	1206–1207		
end faces	1204–1206		
generalized complex material balance	1208–1215		
rectangular geometry	1202–1204		

## Index Terms

## Links

semi-steady-state (SSS) radial flow	22–23			
drainage areas and virtual no-flow				
boundaries	30–34			
formation compaction	27–29			
solution technique	23–26			
well inflow in terms of average pressure	35–36			
well productivity with skin effects	59–61			
shaped charge	117–118			
Sharma, Y.	955			
effect of anisotropy on probe permeability	688–689	878	900	
flow shape factors	882	893–895	898	901–902
Sharpe, H.N.				
modification of Peaceman well model	379–380			
Shell	230–231	249	897	1109
	1119	1246	1256	
active perforation number estimation	844			
centrifuge relative permeability data	333–334			
clay smearing	798			
maximum allowable perforation velocity	181	182		
production optimization	1018	1019		
relative permeability scaling	346–347			
removal of mud filtrate invasion effects	1345			
reservoir depressurization	1077–1078			
subsidence monitoring	503			
superwell	376	390		
shooting method				
well deliverability	477–478			
shot density perforation	123–126	136	173	
shutoff treatment	1060–1061	1070–1071		
<i>see also</i> crossflow reservoir				
Siberia				
application of skin bypass fracture	1117–1118			
Simpson's rule	277			
simulation				
material balance including gas saturation				
effect	463–465			
perforated completions	126			
<i>see also</i> numerical simulation				

## Index Terms

## Links

single compartment system				
exponential decline	625–627	637–638		
material balance	406–411			
single phase flow				
selective inflow performance	853–860			
uniform vertical permeability	755–760			
single well				
at centre of a closed reservoir, transient				
pressure behavior	22–23			
drainage areas, Dietz shape factors	38–40			
sink probe, <i>see</i> active probe				
SIP technique, <i>see</i> selective inflow performance				
technique				
Sketne	7	285		
skin bypass fracture	1117–1118			
skin effect/factor				
analytical	53–58			
coal bed methane wells	1452–1465			
completion, <i>see</i> completion skin effect/factor				
dimensionless, <i>see</i> dimensionless skin effect/				
factor				
due to gravel packing	169–176			
due to partial completion and formation				
damage	64–68			
naturally fractured reservoirs	1452–1454			
layered systems	842–845			
non-Darcy	298			
<i>notion</i>	46	52–53	138	
oil wells	201–202			
perforated completion	136–138			
perforated completion, approximate model	138–193	255–258		
pseudo-radial, <i>see</i> pseudo-radial skin effect/				
factor				
rate-dependent	108	111–112	160	183
	184			
well productivity with	58–61			
skin pressure drop	52–53	54		
<i>notion</i>	47			



## Index Terms

## Links

slant well			
effect on completion skin effect	196–198		
intersecting a vertical fracture	234–235		
with limited entry, A&H analytical model	931	996–1014	
with limited entry, Cinco model	998	1002	1005
with limited entry, effect on completion skin effect	199–201		
with limited entry, numerical model	1002–1014		
<i>see also</i> high slant well			
Slider, H.C.	638		
hyperbolic decline	624–625		
slug test			
coal bed methane wells	1437–1448		
smart well, <i>see</i> intelligent well			
Smith, M.	1377		
Smith, M.B.	251		
software package, <i>see</i> nodal analysis software;			
PanSystem software; Wellflo software			
solution gas drive reservoir	311	353–354	
complex material balance method	1184		
inflow performance, Fetkovich method	358–360		
inflow performance, Vogel correlation	354–358		
oil well producing below bubble point	354		
two-phase pseudopressure	312	313	319–320
<i>see also</i> water drive gas reservoir			
spherical damage skin	878–880		
spherical flow			
steady-state, <i>see</i> steady-state spherical flow			
spherical flow analysis			
WFT-derived permeability	886–909		
spherical flow plot			
characteristics	978	979	
observable buildup duration	678–679		
permeability estimation	684–685	880–881	
spherical flow skin effect/factor			
active probe with	964–976		
near-tunnel damage	153–155		
role in perforation performance	132–134		

## Index Terms

## Links

spherical flow theory		
approximate model for inflow into perforated completion	143–146	
WFT-derived permeability	875–886	
spherical non-Darcy flow shape factor	163–166	
spherical permeability	148	150
estimation from observable buildup duration	679–681	886–909
spherical sink radius, <i>see</i> equivalent probe radius		
spinner-type production logging tool, <i>see</i> production logging device		
spurt loss	48	
SRT, <i>see</i> step rate test		
SSS, <i>see</i> semi-steady-state		
stabilized flow, <i>see</i> semi-steady-state radial flow		
stacked gas reservoir	370–371	
standing water column system	370–371	
static filtration	1358–1366	
statistical analysis		
multiple wells WFT pressure survey data	731–733	
Statoil	173	1117
shutoff treatment	1070–1071	
steady-state flow		
fully completed, deviated well	196–197	
steady-state gas well inflow performance	292–293	
condensate well	338–339	
steady-state linear flow		
Forcheimer equation integration	147	
incompressible fluid	8–13	
steady-state radial flow		
approximate model for inflow into perforated completion	147–150	
boundary conditions	15	
external boundary condition	22	
Forcheimer equation integration	146	
incompressible liquid	15–18	
single well model	14–15	
volume average pressure	20–22	
two-phase compositional flow	312–320	

## Index Terms

## Links

steady-state radial flow ( <i>Cont.</i> )				
well inflow performance	20	114		
well inflow performance, non-Darcy flow	107–108			
well productivity and	19–20			
well productivity with skin effect	58–59			
steady-state spherical flow				
gas condensate well inflow performance, non-Darcy flow	320–323			
Steele, L.				
WFT pressure survey usage for reservoir description	788–792			
Stegun, I.A.	894			
step rate test (SRT)				
coal bed methane wells	1462–1463	1464–1465		
Stevenson, P.M.	747			
Stewart and Roumboutsos algorithm	433			
Stewart, G.	687–688	738	766	774
	793	807	1086	1226
	1312	1372		
applications of production logging	839	840		
connected system of natural fractures	1452–1453			
constant pressure boundary effects in WFT applications	985–986			
depth of investigation analysis	976–978			
flow shape factor	881	893	902	957
	961			
mud filtrate invasion model	1312–1320			
vertically distributed single well model	1062			
supercharging analysis	1351–1355			
supercharging analysis, field example	1355–1357			
WFT pulse test	794–795			
Stewart, L.	1028			
production logging survey	838–839			
WFT pressure survey from Piper field	772–774			
Stiles waterfood simulation	604–605			
Stimlab	1115–1116			

## Index Terms

## Links

stimulation				
effect on decline behavior	633–634			
effect on perforated completion	138			
<i>see also</i> acid treatment; hydraulic fracturing				
Stone model II	373			
straddle packer wireline formation tester (WFT)				
mini-drill stem test	909	911		
mini-drill stem test, depth of investigation				
analysis	976–979			
slant well	996–1013			
<i>see also</i> bridge plug				
strain-type pressure gauge	688	727–728	778	779
Strelsova, T.D.	83	927		
stress-dependent permeability and porosity (SDPP)	1378–1390			
boundary effects with	1448–1452			
field example	1417–1433			
Palmer-Mansoori model	1383–1384	1387	1391	1395
	1423	1426	1427	
pseudo model	1390–1410			
pseudo model with wellbore storage	1410–1417	1424–1426		
strip model of flow convergence, <i>see</i> wedge model				
of flow convergence				
supercharging	667	671–681	723–727	779
	780	1346–1355		
Halford and Stewart method	1351–355			
Halford and Stewart method, field example	1355–1358			
invasion-supercharging model, mathematical				
formulation	1366–1369			
<i>see also</i> mud filtrate invasion				
superposition				
creation of progressively penetrating well	1294–1297			
variable rate drawdown for aquifer influx	419–421			
superwell	484–485			
deliverability of proximity wells	380–387			
multilayer systems	390–393			
<i>notion</i>	375–376			
Peaceman well model in numerical				
simulation	376–380			

## Index Terms

## Links

superwell ( <i>Cont.</i> )				
performance index	387			
wedge-shaped drainage systems	387–390			
Swarbrick, R.E.				
overpressure	748–749			
swing factor	482	483		
<b>T</b>				
3D seismic interpretation	1018	1020	1021–1022	1086
Tariq, S.M.	150	151	163	
tar mat				
detection by WFT pressure survey	715–716			
Taylor	131–132			
TCP, <i>see</i> tubing conveyed perforation				
Tehrani, D.H.	787	1218		
fault zone identification through fault multiplier adjustment	802–803			
flow profile match	838	839	840	
Temeng, K.O.	1484	1489	1490	
Tambynayagam, R.K.M.	901–902			
active probe pressure response	955–957	964–965	968	971
analytical formula for areal flow convergence skin	80–81	216		
analytical formula for pure linear flow convergence skin	236–238			
dual probe formation tester pressure response	909	910		
observation probe pressure response	911–913	914–915	944	
THL plot, <i>see</i> true horizontal length plot				
three-cell system				
complex material balance	1187–1189			
with small interblock transmissibility	1199–1200			
three-layer system				
determination of average permeability, synthetic problem	1281–1284			
three-phase flow	371–375			
three-phase pseudopressure	371	374–375		

## Index Terms

## Links

three-well cluster			
wedge-shaped drainage areas	387–390		
through tubing casing patch	1069		
Tiffin, D.L.		179	180
tight gas reservoir	1377–1378		
multiple hydraulic fractured horizontal wells	1119–1120	1483–1491	
massive hydraulic fractured wells			
performance	228–233		
perched water held up by capillary pressure	738		
stress-dependent permeability	1401–1402		
tight zone			
continuous, with communication	812	813	
differential depletion	765–767		
identification based on cumulative flow	1283–1284		
identification through pressure analysis	795		
near gas-water contact	420–421	438	
supercharging	779		
tilted water-hydrocarbon contact	741–742	744	
Timur Sea			
Sunrise-Troubador field, WFT pressure			
survey, dynamic aquifer effects	747		
tip screen-out (TSO) fracture	251	1109	1117
gas condensate wells	353		
Tjolsen, C.B.	304		
total apparent skin	143		
Toth, J.	741		
transient deliverability			
horizontal wells	1095–1100		
transient formation model	1259–1271		
transient inflow performance relation (IPR)	265–272		
applications	370		
transient pressure test, <i>see</i> pressure transient			
analysis			
transient production	266–268	271	
compartmentalized material balance	1238–1239		
constrained by tubing	1098–1099		
segmented horizontal well	1300		
transient productivity index	1098		

## Index Terms

## Links

transient radial flow, <i>see</i> infinite acting radial flow			
transient selective inflow performance (SIP)	858–859		
transient spherical flow	677–678		
transverse hydraulic fracture	253	254	1485–1489
trapped water, <i>see</i> perched water contact			
trend analysis	1060–1061		
Trice, M.L.	458		
TRT, <i>see</i> two-rate test			
true horizontal length (THL) plot	824–826		
true skin	142	256	
TSO fracture, <i>see</i> tip screen-out fracture			
tubing controlled	1085		
tubing conveyed perforation (TCP)	141	142	844
Turner critical velocity	366–368		
two-block depletion test	810–811		
two-block two-layer system			
depletion test	812–814		
lumped parameter material balance model	805–810		
two-drawdown test			
behavior	1264–1266		
two-layer system			
displacement model	605–606		
well performance diagram	870–871	1057	
with near-horizontal semipermeable barrier	821		
two-phase compositional system	311–312		
behavior of pseudopressure function	323–329		
radial steady-state Darcy flow	312–320		
spherical steady-state non-Darcy flow	320–323		
<i>see also</i> gas condensate well			
two-phase flow			
concurrent upward	774–777		
countercurrent	769–774		
selective inflow performance	863–871		
vertical saturation equilibrium	768–769		
two-phase incompressible flow	302–309		
pseudopressure function	309–311		
selective inflow performance	865–867		
two-phase pseudopressure	312	313	

## Index Terms

## Links

two-phase incompressible flow ( <i>Cont.</i> )				
gas condensate wells	319–320	323–329	338–339	1129–1130
gas-water	360–365			
two-rate test (TRT)				
permeability and pressure detection	1285			
type curve matching				
Agarwal-Gardner	651–666			
Fetkovich	638–645			
Wong, Harrington and Cinco-Ley's	211–212	1103		
<b>U</b>				
UBD, <i>see</i> underbalanced drilling				
Ugueto, G.	1345			
unconsolidated porous medium, <i>see</i> sand pack				
underbalance				
effect on perforation flow	134–135	155		
underbalanced drilling (UBD)	1241–1242			
coal bed methane wells	1454			
determination of permeability and formation				
pressure	1284–1308			
distributed parameter wellbore model	1257–1259			
final buildup	1308–1310			
limited entry model	1294–1298			
lumped parameter wellbore model	1246–1256			
multilayer convolution algorithm				
applications	1272–1284			
transient formation model	1259–1271			
transient wellbore model	1243–1245			
undersaturated oil reservoir				
aquifer influx	570–575			
uniform flux line source	931	990–991		
United Kingdom				
Brent field, depressurization	1077–1078			
Brent field, sand control method	1120–1121			
Claymore field, hydrochloric acid treatment	157			
Claymore field, pressure maintenance	1075–1077			
Cormorant field, WFT pressure survey	815–816			
Forth field, loss control material use	176	177–178		



## Index Terms

## Links

### United Kingdom (*Cont.*)

Rannoch formation, sand control completion	1120–1121	
Wych farm field, compartmentalized horizontal well	1107	1108

### United States

Alaska, horizontal wells in fault block	89–90	
Alaska, horizontal well trajectories	1086–1087	
Alaska, McKenzie River, fines migration and formation damage	56	
Alaska, Prudhoe Bay field, gas coning behavior	588	
Alaska, Prudhoe Bay field, gel treatment	1070	
Alaska, Prudhoe Bay field, tilting leading to residual oil zone	717–718	
Colorado, coal bed methane, injection and falloff	1417–1433	
Louisiana, Duck Lake field, aquifer influx	452–454	
Louisiana, North Ossum field, abnormally pressured gas reservoirs	403–406	
Oklahoma, AX-1 reservoir, decline curve analysis	635–637	
Oklahoma, South Wilburton field, aquifer influx	454–456	
Santa Barbara Channel, Dos Cuadras field, horizontal well development	87–89	
Texas, Anderson “L” reservoir	490	501–503
Texas, Ellenburger gas reservoir	501	502
Texas, overpressured reservoir, associated aquifer	490	
Texas, Pearsall field, fractured well	1101	1103
Texas, Sheridan field, retrograde gas condensation	552–553	
Texas, Spraberry trend, hydraulic fracturing	232	
Texas, West Seminole field, core and well test permeability	105	
Texas, West Seminole field, WFT pressure survey	792	

## Index Terms

## Links

United States ( <i>Cont.</i> )			
tight gas reservoir, perched water contact	738		
Wyoming, Powder River Basin, hydraulic fracture stimulation	227–228		
<i>see also</i> Gulf of Mexico			
unit mobility displacement	599–604		
Unocal	370		
U-tube effect	735	737	
<b>V</b>			
Valderrama, Patel and Teja (VPT) equation of state model	471–472		
Van den Hoek, P.J.	1401		
nonideal wellbore storage model	1410	1414	1420
Van der Post, N.	345		
Van Everdingen, A.F.	53	138	425
cumulative influx superposition	428–429		
Van Everdingen and Hurst infinitesimal skin effect	52		
Van Golf Racht, T.D.	738		
constant pressure boundary effects in WFT applications	985–986		
Van Kruijsdijk, C.P.J.W.			
comparison of noncommunicating progressive layer model and boundary element model	1273–1274		
Van Rijswijk, J.	784		
variable rate buildup (VRB) analysis			
spherical flow	904–909		
variable rate drawdown (VRD) analysis			
aquifer influx	418–421		
<i>via</i> deconvolution	419		
spherical flow	904–909		
VDF, <i>see</i> virtual downhole flowmeter			
VDSWM, <i>see</i> vertically distributed single well model			

## Index Terms

## Links

Vela, S.	795		
importance of fault location in interference testing	1476	1478	
Venezuela			
Dacion field, intelligent well	1156–1157		
field example, apure crocodile curve	1066–1067		
Furrial field, WFT pressure survey, vertical permeability	758–759		
produced reservoir, WFT pressure survey	754–755		
Santa Barbara and Piritital field, asphaltene deposition	1084		
workovers	1018		
vertical fracture			
horizontal wells	274–275		
vertical interference test			
with cased-hole WFT	1063–1064		
<i>see also</i> interference test			
vertical lift performance (VLP) curve			
compartmentalized material balance	1221–1225		
and IPR, effect on well rate	338	367–368	474–479
well performance diagram	4–5		
vertically distributed single well model (VDSWM)	1062–1063		
vertically fractured well			
pseudo-radial flow	75–76		
vertical permeability			
determination, WFT pressure survey	755–760	782–783	
vertical pulse test	795		
vertical saturation equilibrium	768–769		
vertical well			
active probe pressure response	955–957		
active probe pressure response, including spherical flow skin effect	964–976		
active probe pressure response, numerical model	958–961		
Addington gas coning model	588–593		
observation probe pressure response	909–926	999–1000	
observation probe pressure response, dual permeability model	944–952		

## Index Terms

## Links

vertical well ( <i>Cont.</i> )		
observation probe pressure response, dual		
permeability numerical model	950–954	
observation probe pressure response, limited		
entry model	926–936	
underbalanced drilling data analysis	1294–1298	
Yang and Wattenbarger water coning model	593–599	
virtual downhole flowmeter (VDF)	1242	
viscosity-based loss control material (LCM)	176	
viscous stripping	347–350	898
VLP curve, <i>see</i> vertical lift performance curve		
Vogel correlation		
solution gas drive well inflow performance	354–358	
voidage ratio	1078	
volume average pressure		
steady-state radial flow	20–22	
volumetric reserves calculation	396–397	
VPT EOS model, <i>see</i> Valderrama, Patel and Teja		
equation of state model		
VRB analysis, <i>see</i> variable rate buildup analysis		
VRD analysis, <i>see</i> variable rate drawdown analysis		
<b>W</b>		
Wallace, W.E.	490	
Walsh, D.M.		
non-Darcy effect in high-rate fractured gas		
wells	222	223–225
Warren and Root sugar cube model	1162–1163	
Warren, J.E.	690	
water-based mud (WBM)		
fluid loss characteristics	1363–1365	1371
invasion process	1320	
invasion process, field examples	1332–1343	
invasion process simulation	1320–1328	
<i>see also</i> oil-based mud		
water breakthrough (WBT)		
detection	863–871	

## Index Terms

## Links

water coning	69–71	587	1066–1069	1156
material balance context, Yang and Wattenbarger model	577–579	593–599		
water drive gas reservoir				
residual gas saturation	457–458			
vertical saturation equilibrium	768–769			
<i>see also</i> gas well producing water; solution gas drive reservoir				
waterflooding				
below bubble point, displacement model	609–610			
five-spot pattern	61	603		
layered system	863–864			
reservoir shapes	603			
unit mobility displacement model	599–604			
water injection well				
modeling of skin effect	158			
offshore development	3			
water-oil contact (WOC)				
effect of reservoir tilting on	699	708–709	717–718	
variable, over a field	709	710	712	
water-oil ratio (WOR)	302–303			
calculation, Yang and Wattenbarger method	578–579	593–599		
water recoverable oil contact (WROC)	706–708			
water shut-off (WSO) treatment	1060			
Wattenbarger, R.A., <i>see</i> Yang and Wattenbarger				
water coning model				
Watts, J.W.	67			
wavelet methodology	890–891			
WBM, <i>see</i> water-based mud				
WBS effect, <i>see</i> wellbore storage effect				
WBT, <i>see</i> water breakthrough				
WCPC, <i>see</i> well composite performance curve				
wedge model of flow convergence	236–241			
wedge-shaped drainage area				
Dietz shape factors	43–45	387–390		
weighting function of relative permeability	343–344			
Welge linear flow displacement function	606–607			
wellbore damage, <i>see</i> formation damage				

## Index Terms

## Links

wellbore friction			
effect on horizontal well deliverability	90–91	96–100	1153
effect on horizontal gas well deliverability	1140–1148		
wellbore storage (WBS) effect			
identification by distributed parameter			
model	1257–1259		
stress-dependent permeability and porosity			
model	1410–1417		
well cluster	375–376		
application of Dietz shape factors	42–43		
<i>see also</i> superwell			
well completion, <i>see</i> completion			
well composite performance curve (WCPC)	385	386	
well deliverability, <i>see</i> deliverability			
Wellflo software			
horizontal gas well deliverability	1128–1139		
horizontal gas well deliverability, effect of			
wellbore friction	1141–1148		
well inflow			
in terms of average pressure	35–36		
well inflow model	1–2	17	
well inflow performance, <i>see</i> inflow performance			
well inflow performance relation, <i>see</i> inflow			
performance relation			
well operating point			
determination	868–869		
<i>notion</i>	4–5		
well performance diagram	852		
multilayered compartmentalized system,			
selective inflow performance	853–855	857	
quadratic IPR for non-Darcy radial flow	110–111		
skin removal	60	1085–1086	
steady-state radial flow and	2–5		
transient IPR	268–269		
well deliverability in classical nodal analysis form	474–477		
well productivity, <i>see</i> productivity			

## Index Terms

## Links

well rate	2–3	474		
determination of end-of-the-plateau period	485–486			
effect of IPR-VLP relations on	474–479			
gas sales contract involving swing factor	482–485			
low permeability systems	1086–1128			
material balance iteration including swing	486–487			
material balance shooting	479–481			
production constrained depletion	481–482			
synthetic test	487–490			
Wells, P.R.A.				
hydrodynamic model	739–744			
Westaway, P.J.	1226			
wettability	715			
effect on capillary pressure and relative permeability	1318	1325–1327		
mixed	1341–1343			
WFT, <i>see</i> wireline formation tester				
Whitson and Fevang relative permeability curve	314	339		
Whitson and Fevang weighting function	343			
Whitson, C.H.				
high pressure gas reservoir	494	496	498–501	
Wilkinson, D.J.	86	214	898	
effective circular source radius	83–84			
horizontal well deliverability	1089–1091			
probe flow shape factor	187	895–896	897	957
	961			
pseudo-radial skin effect of finite conductivity fracture	208–209			
Willhite, G.P.	576	607	610	
Winterhalder, R.				
dynamic aquifer effects	744	745		
wireline formation tester (WFT)	667	668–671	1161	
dual probe	909	910	911–912	
effect of mud filtrate invasion	1311–1312			
effect of mud filtrate invasion, field examples	1332–1343			
hemispherical flow to a disk aperture	186–187			
open-hole version	681			

## Index Terms

## Links

wireline formation tester (WFT) ( <i>Cont.</i> )				
spherical flow	132–133			
<i>see also</i> cased-hole wireline formation tester;				
repeat formation tester				
wireline formation tester (WFT)-derived				
permeability				
background	681–682			
dual permeability model	944–954			
nonintersecting fracture	979–987			
nonlinear regression	949–950			
spherical flow analysis	886–909			
spherical flow theory	875–886			
vertical observation probe limited entry				
model	926–937			
vertical observation probe response	909–926			
<i>see also</i> repeat formation tester-derived				
permeability				
wireline formation tester (WFT) distributed				
pressure measurement				
exploration well applications	700–716	739–749	751	
exploration well applications, field examples	717–720	733–738		
exploration well, depth measurement errors	727			
exploration well, multiple well analysis	727–733			
exploration well, objectives	699–700			
field data	674–676			
field development applications	751	755–777	779–814	847
field development applications, field				
examples	752–755	782–792	815–818	
field development applications, gradient				
determination accuracy	777–779			
principles	668–671			
rapid local permeability estimation	677–681			
simplified supercharging analysis	671–676			
wireline formation tester (WFT) pulse test	794–795			
Wittman, M.J.	687–688	766	807	1312
depth of investigation analysis	976–978			
flow shape factor	881	893	902	957
	961			



## Index Terms

## Links

Wittman, M.J. ( <i>Cont.</i> )				
production logging applications	839	840		
vertically distributed single well model	1062			
Wong, G.K.				
maximum allowable perforation velocity	181–182			
Wong, Harrington and Cinco-Ley type curve	211–212			
horizontal well data	1103			
WOR, <i>see</i> water-oil ratio				
workover	1061			
design	1018			
field example	1071–1074			
influence of windows	1065–1066			
justification	1085–1086			
production logging	833	843	851	
with cased-hole WFT	847–848			
worm-holing	157			
WROC, <i>see</i> water recoverable oil contact				
WSO treatment, <i>see</i> water shut-off treatment				
<b>Y</b>				
Yang and Wattenbarger water coning model	578–579	593–597		
synthetic example	597–599			
Yaxley, L.M.	77	1163	1226	
formula for Dietz shape factor	40–45	85–86	87	95
	264	382		
leaky fault model	986			
linear semi-steady-state flow in rectangular geometry	1202–1204	1206		
Yeh, N.S.	1385			
Yergin, Daniel	1018			
yield point, <i>see</i> pore collapse				
<b>Z</b>				
Zimmerman, T.	132	186	677	683
	881–882	895		
zonation	784–785			
layered system	845–846			